XXXIX INTERNATIONAL SCIENTIFIC CONFERENCE ON INFORMATION, COMMUNICATION AND ENERGY SYSTEMS AND TECHNOLOGIES

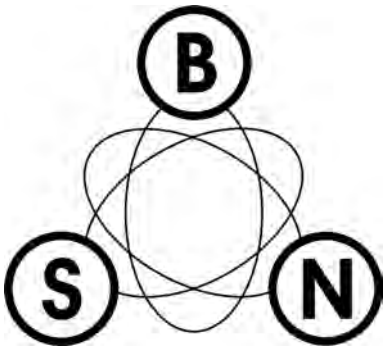

ICEST 2004

Proceedings of Papers

Volume 1

Bitola, 2004

XXXIX INTERNATIONAL SCIENTIFIC CONFERENCE ON INFORMATION, COMMUNICATION AND ENERGY SYSTEMS AND TECHNOLOGIES

-ICEST 2004-

Procedings of Papers – Volume 1 of 2 volumes

Editor: Prof. Dr. Cvetko Mitrovski

Technical Editor: Pargovski Jove

Published by: Faculty of Technical Sciences, Bitola, Macedonia

Printed by: MIKENA, Bitola, Macedonia

Total print run: 260

ISBN: 9989-786-38-0

CIP – Каталогизација во публикација
Матична и универзитетска библиотека
"Св. Климент Охридски", Битола

621.391:004(063)(082)
007.52(063)(082)
004.22(063)(082)
621.397.3:004(063)(082)
621.396.67(063)(082)
004.738.5(063)(082)

INTERNATIONAL scientific conference on information, communication and energy systems and technologies (39 ; 2004 ; Bitola)
ICEST 2004 : proceedings of papers / XXXIX International scientific conference on information, communication and energy systems and technologies ; [editor Cvetko Mitrovski]. - Битола : Технички факултет, 2004. – 2 св.
(XVI, 422 ; XVI, 422 стр.) : илустр. ; 28 см

Библиографија кон трудовите. – Регистар

ISBN 9989-786-38-0
1. Gl. Stv. nasl. 2. Mitrovski, Cvetko
а) Електроенергетски системи – Зборници б) Кодирање – Зборници в) Дигитална обработка на сигнали – Зборници г) Антени – Зборници д) Интернет – Зборници ѓ) Индустриска електроника – Зборници
COBISS.MK-ID 17470017

Dear Colleges,

On Behalf of the Technical Program Committee I was given the pleasure to wish you a welcome on the International Scientific Conference on Information, Communication and Energy Systems and Technology, **ICEST 2004**, which will be held from June 16 through 18, 2004 at the Winter-Summer Tourist Centre "Pelister" near Bitola.

The Conference is organized by the Faculty of Technical Sciences at the Saint Kliment Ohridski University of Bitola, Faculty of Electronics at the University of Nis and by the Faculty of Communications and Communication Technologies at the Technical University of Sofia, in cooperation with IEEE sections of Macedonia, Serbia and Montenegro, and Bulgaria. This year, the Faculty of Technical Sciences-Bitola has an honor for first time to be a host of the Conference under the ICEST acronym and we shall do our best to fulfill the standards established by our partners on the previous two ICEST Conferences.

This year, the Conference Program includes 222 papers for oral and poster presentation which are going to be presented by more than 150 participants of the Conference. Therefore the participants will have rather busy schedule, which I sincerely hope, won't affect their presentations. I also hope that the Conference will be the place where you can strengthen the collaboration among the institutions and the countries you are representing by sharing your ideas and your scientific results.

At last I want to express my gratitude to all our sponsors that has enabled the organization of this conference.

I wish you all a pleasant and a fruitful work on the ICEST-2004!

Assoc. Prof. D-r Cvetko Mitrovski
Conference Chairman

ICEST 2004

XXXIX INTERNATIONAL SCIENTIFIC CONFERENCE ON INFORMATION, COMMUNICATION AND ENERGY SYSTEMS AND TECHNOLOGIES

organized by

Faculty of Technical Sciences
University "St. Kliment Ohridski", Bitola, Macedonia

Faculty of Communications and Communications Technologies
Technical University of Sofia, Bulgaria

Faculty of Electronic Engineering
University of Niš, Serbia and Montenegro.

with support of

- Ministry of Education and Science Macedonia
- Macedonian Science Society-Bitola
- ETAI Macedonia
- ALCATEL Macedonia

in cooperation with

- IEEE Macedonia Section
- IEEE Bulgaria Section
- IEEE Serbia and Montenegro Section

ICEST HISTORY

The ICEST Conference appears to succeed a series of conferences started from 1963 at the Technical University of Sofia under the name "Day of the Radio". In 1977 the name of the Conference was changed into "Communication, electronic and computer systems".
Since 2000 it has become an international conference under the name EIST (Energy and Information Systems and Technologies). The first two EIST Conferences were organized by the Faculty of Communications and Communication Technologies, Sofia and the Faculty of Technical Sciences, Bitola.
In 2002 the Faculty of Electronic Engineering, Niš joined successfully the Conference organizers. Again, the Conference changed its name becoming ICEST (International Scientific Conference on Information Communication and Energy Systems and Technologies).
This year host of the ICEST conference is the Faculty of Technical Sciences, University "St. Kliment Ohridski", Bitola, Macedonia.

ORGANIZERS OF THE CONFERENCE

General Chairman:

C. Mitrovski	*University "St. Kliment Ohridski"- Bitola, Macedonia*

Vice Chairmen:

B. Milovanovic	*University of Niš, Serbia and Montenegro*
R. Arnaudov	*Technical University of Sofia, Bulgaria*

Members:

G. Dimirovski	*University of Skopje, Macedonia*
B. Dimitrijevic	*University of Niš, Serbia and Montenegro*
N. Dodov	*Technical University of Sofia, Bulgaria*
E. Ferdinandov	*Technical University of Sofia, Bulgaria*
M. Gusev	*University of Skopje, Macedonia*
Lj. Kocarev	*University of San Diego, USA*
Lj. Panovski	*University of Skopje, Macedonia*
V. Litovski	*University of Niš, Serbia and Montenegro*
M. Hristov	*Technical University of Sofia, Bulgaria*
L. Jordanova	*Technical University of Sofia, Bulgaria*
G. Milovanovic	*University of Niš, Serbia and Montenegro*
V. Milutinovic	*University of Belgrade, Serbia and Montenegro*
G. Stojanov	*Technical University of Sofia, Bulgaria*
M. Stojcev	*University of Niš, Serbia and Montenegro*
B. Spasenovski	*University of Skopje, Macedonia*
Lj. Trpezanovski	*University "St. Kliment Ohridski"- Bitola, Macedonia*
D. Velickovic	*University of Niš, Serbia and Montenegro*

ORGANIZING COMMITTEE

Chairman:

P. Mitrevski	*University "St. Kliment Ohridski"-Bitola, Macedonia*

Members:

M. Popnikolova-Radevska	*University "St. Kliment Ohridski"-Bitola, Macedonia*
I. Nedelkovski	*University "St. Kliment Ohridski"-Bitola, Macedonia*
G. Trombev	*University "St. Kliment Ohridski"-Bitola, Macedonia*
N. Acevski	*University "St. Kliment Ohridski"-Bitola, Macedonia*
D. Najdenov	*University "St. Kliment Ohridski"-Bitola, Macedonia*
B. Stevanovski	*University "St. Kliment Ohridski"-Bitola, Macedonia*
V. Ceselkoska	*University "St. Kliment Ohridski"-Bitola, Macedonia*
M. Kostov	*University "St. Kliment Ohridski"-Bitola, Macedonia*
M. Stojcev	*University of Niš, Serbia and Montenegro*
L. Lubih	*Technical University of Sofia, Bulgaria*
I. Docev	*Technical University of Sofia, Bulgaria*

CONFERENCE SECRETARIAT

M. Kostov	*University "St. Kliment Ohridski"-Bitola, Macedonia*
M. Atanasovski	*University "St. Kliment Ohridski"-Bitola, Macedonia*

Faculty of Technical Sciences, Bitola, Macedonia
I. L. Ribar, bb, 7000 Bitola
Phone:+389 47 207 701
Fax: +389 47 203 370

TECHNICAL SUPPORT

A. Kolevska	*University "St. Kliment Ohridski"-Bitola, Macedonia*
J. Pargovski	*University "St. Kliment Ohridski"-Bitola, Macedonia*

CONFERENCE INTERNET SITE

For further information, please visit the Conference Internet Site:
http://www. tfb.uklo.edu. mk/icest2004

TABLE OF CONTENTS

VOLUME 1

Power Transmission and Distribution Systems

Remote Ecological Monitoring

Signal Processing

Radio Communications, Microwave Technique and Antennas

Computer Systems and Internet Technologies

Industrial Electronics

Session PTDS:

Power Transmission and Distribution Systems

Model For Generation Planning In An Electric Power System

Anton Causevski*, Tome Bosevski**

*Faculty of Electrical Engineering - Skopje, Macedonia, caus@etf.ukim.edu.mk
**Macedonian Academy of Sciences and Arts, Skopje, Macedonia

Abstract - This paper presents the methodology for power generation planning in a complex electric power system. The model objective is to find an optimal power supply that meets the hourly electricity demand, and takes into account the operating conditions of the power generating stations. The model and the developed computer program are applied to the Macedonian Power System to provide a realistic application example, and to demonstrate the role and importance of the hydro power stations in the Macedonian Power Supply System.

1. THE MODEL FOR GENERATION PLANNING

This paper outlines the improvements of the original mathematical model developed by Bosevski and Causevski [1, 2, 3]. The improved model includes energy balancing, and power balancing in each time interval for each thermal power plant, as well as water inventory balancing for the hydro power plants. The optimisation procedure can be applied to different time intervals in each specific application. The calculations can be performed on time intervals wider than 24 hours, such as: on monthly, weekly and daily basis. In addition, the calculations can be performed with time subintervals down to 1 hour, or less, depending on the available data.

The total power load is defined as average value in a desired subinterval:

$$P_{tot} = \frac{W(\Delta t)}{\sum_{t_i=1}^{t_n} t_i} = \frac{\sum_{t_i=1}^{t_n} P(t_i)\cdot t_i}{\Delta t}, \quad (1)$$

where $\sum_{t_i=1}^{t_n} t_i = \Delta t$

If the Generation System consists of:
K –Thermal Power Plants
N – Connected Systems (Total Load)
V – Connected Systems (Variable Load)
M- Hydro Power Plants

The optimization function is minimizing the electricity generation expenses as following:

$$\sum_{k=1}^{K}\sum_{t=1}^{T}\left(K_k(P_{k,t}) + B_k\cdot(P_{k,t} - \overline{P_{k,Tkp}})^2\right)\cdot\Delta t + \quad (2)$$
$$\sum_{n=1}^{N}\sum_{t=1}^{T}\left(K_n(P_{n,t}) + A_n\cdot(P_{n,t} - \overline{P_{n,Tnp}})^2\right)\cdot\Delta t +$$
$$\sum_{v=1}^{V}\sum_{t=1}^{T}\left(K_v(P_{v,t}) + C_v\cdot(P_{v,t} - \overline{P_{v,Tvp}})^2\right)\cdot\Delta t \to \min$$

where:

$$K_i(P_{i,t}) = P_{i,t}\cdot\left(A + B\cdot P_{i,t} + C\cdot P_{i,t}^2\right) \quad i = k,n,v \quad (3)$$

The following conditions are included in the model:

$$\sum_{k=1}^{K} P_{k,t} + \sum_{n=1}^{N} P_{n,t} + \sum_{m=1}^{M} P_{m,t} = P_{l,t} \quad \text{total load:}$$

$$\sum_{m=1}^{M_a} P_{m,t} + \sum_{v=1}^{V} P_{v,t} = k_v\cdot P_{w,t} \quad \text{variable load}$$

$$\sum_{t=1}^{T} P_{k,t}\cdot\Delta t = W_k \quad \text{TPP's generation}$$

The model offers a high degree of flexibility, and can be applied in different situations because the optimisation period can be subdivided in as small subintervals depends on the examination and input available data. In order to achieve this flexibility, model improvements were introduced with respect to the terms covering the hydro power plants and the thermal power plants energy change representation.

Tab1.*Example of some calculation with the model*

Interval Duration	*No. of Intervals*	*Additional Water Balance*	*Matrix Dimension (N)*	*No. of Matrix Elements (N x N)*	*nonzero elements in the Matrix*		*Execution Time*
						%	s
Intervals > DAY							
month	12		22	484	250	51,65	<1
week	52		62	3,844	1.05	27,31	<1
day	364		374	139,876	7.29	5,21	1
Intervals < DAY							
6 i 18 h	728	182+364	1284	1,648,656	18,028	**1,09**	8
8 h	1092	52+364	1518	2,304,324	25,158	**1,09**	10
6 h	1456	58+364	1888	3,564,544	33,928	**0,95**	15
4 h	2184	364+364	2922	8,538,084	51,698	**0,60**	20
3 h	2912	58+364	3344	11,182,336	68,864	**0,61**	25
2 h	4368	364+364	5106	26,071,236	105,570	**0,40**	50
1 h	8736	364+364	9474	89,756,676	210,102	**0,23**	150

Tab.1 gives overview of some calculations for the Macedonian Electric Generation System depend on different intervals.

2. CONTROL OF THE HYDRO POWER PLANTS OPERATION

As the inflow of energy resulting from water inflow in an accumulation is expressed as

$$W_{m,Tmw}^{dotek} = \sum_{\Delta t\in Tmw} P_{m,t}^{dotek}\cdot\Delta t \quad (4)$$

and the generated energy from water outflow is expressed as

$$W_{m,Tmw}^{istek} = \sum_{\Delta t \in Tmw} P_{m,t} \cdot \Delta t \qquad (5)$$

than the expression:

$$S_m \cdot \sum_{t=1}^{T} \left(\frac{W_{m,Tmw}^{istek} - W_{m,Tmw}^{dotek}}{\sum_{\Delta t \in Tmw} \Delta t} \right)^2 \cdot \Delta t \qquad (6)$$

represents an additional condition that needs to be satisfied to optimise the generated power of a Hydro Power Plant (HPP) "m", as a result from water inflow during the period T_{MW}. This is particularly important for regulating the discharge as well as water storage level in the reservoir.

The inflow water volume $V_{m,Tmj}^{dotek}$ in the HPP "m" reservoir during the period T_{mj} can be expressed using the inflow volumetric flow rate $Q_{m,t}^{dotek}$:

(7)

The outflow water volume $V_{m,Tmj}^{istek}$ in the HPP's "m" reservoir during the period T_{mj} can be expressed using the discharge flow rate $Q_{m,t}^{istek}$:

$$V_{m,Tmj}^{istek} = \sum_{\Delta t \in Tmj} Q_{m,t}^{istek} \left(\frac{P_{m,t}}{H_{m,t}} \right) \cdot \Delta t \qquad (8)$$

The control of the water outflow (HPP power generation control) during the period T_{MJ} is achieved through the following term:

$$\sum_{Tmj=1}^{Tmv} \mu_{mj} \cdot \left(V_{m,Tmj}^{istek} - V_{m,Tmj}^{dotek} \right) \qquad (9)$$

This is particularly important for the reservoirs with small water inventories compared to the water inflow during the analysed period. This model feature helps to provide an appropriate treatment that is consistent with the reservoir water inventories (some reservoirs can be treated on yearly basis, whereas other reservoirs on seasonal, monthly, weekly, or daily basis).

3. MACEDONIAN ELECTRIC POWER SYSTEM

The model is applied to the Power Generation System of Macedonia to provide a realistic application example, and to demonstrate the role and importance of the hydro power stations in the Macedonian Power Supply System. The Macedonian Power Generation System consists of (Table 2)

a) 4 coal-fired thermal power plants (Bitola 1,2,3, each with 225 MW installed electric power, and Oslomej, with 120 MW installed electric power),
b) one oil fired thermal power plant (Negotino, with 210 MW installed electric power), and
c) 9 hydro power plants, 5 with storage water reservoirs, and 4 are direct river flow plants.

Tab2.*Overview of the general performances for storage HPP*

Storage HPP	Water Storage ($10^6 m^3$)	Gross Head (m)	Installed capacity (N x m^3/s)	Ave. yearly inflow (m^3/s)
Vrutok	277	572	4 x 8	9,90
Kozjak	260	102	2 x 50	21,20
Tikves	272	100	4 x 30	27,40
Globocica	228	101	2 x 27.4	28,50
Spilje	212	95	3x36	47,50

The electricity productions of the thermal power plants in Macedonian Power Generation System are set based on their production capability and fuel supply availability.

4. THE ROLE OF HYDRO POWER PLANTS

The results presented in this paper by an example of electricity generation planning in the Macedonian Power System, are aimed at demonstrating the capabilities of the improved model.

The analyzed period is 5 years (1996-2000), during which the energy demand is presented with 3654 points, and each day is divided in 2 intervals (8 & 16 hours on Fig.1).

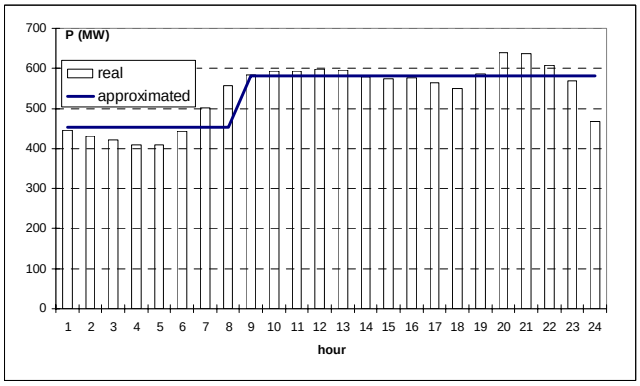

Fig. 1. Divided day into 2 intervals according (1)

The power generation in all nine hydro and five thermal power plants in the Macedonian Power Generation System are optimized, and the estimated energy demand is 40000 GWh in total during the 5-year period.

HPP Vrutok (high gross head) and HPP Globocica (large water inflow based on installed capacity), both with relatively large water inventory, can be used for saving water inventory during the 5year period. The other HPPs (Tikves Kozjak & Spilje) have a gross head of about 100(m), and water inventory capacity of over 200 mill m^3. These HPPs have a large water level to water inventory ratio, e.g. their power generation is sensitive to the reservoir water level, and these HPPs are not to be operated with large variation of the reservoir water level. Therefore, these HPPs need to use the water inflow over each year.

5. DISCUSSION OF RESULTS

Figure 1, 2 and 3 present the inflow energy, generated energy and accumulated energy, respectively, for the best 5 years (1979-1983) in terms of water inflow.

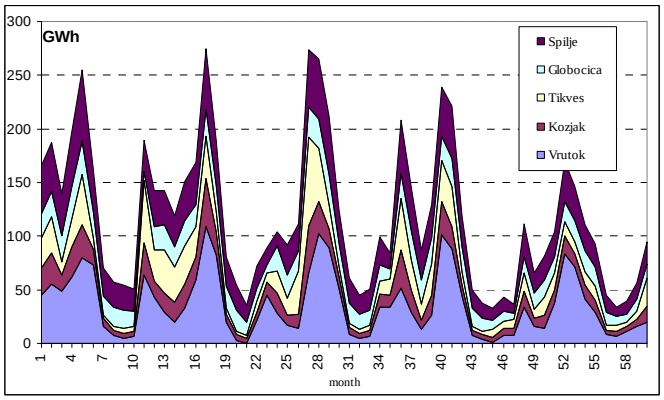

Fig. 2. Inflow energy in the reservoirs for wet period

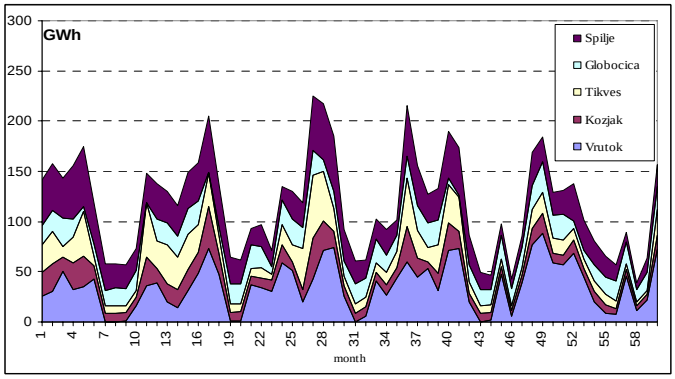

Fig. 3. Generated energy of the HPPs for wet period

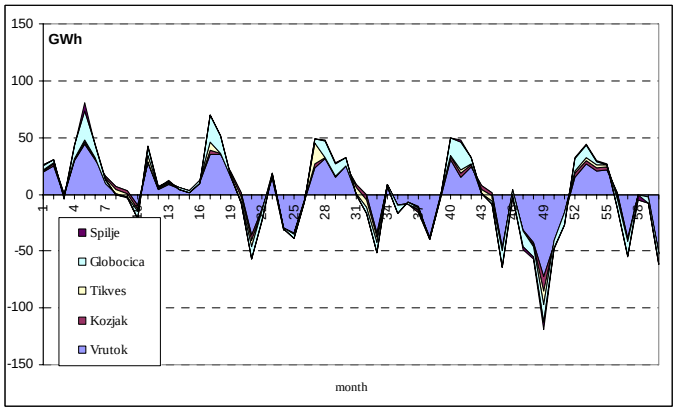

Fig. 4. Accumulated energy of the HPPs for wet period

Fig.5, Fig.6 and Fig.7 present the inflow energy, generated energy and accumulated energy respectively, for the average hydrology period of 5 years (1973-1977).

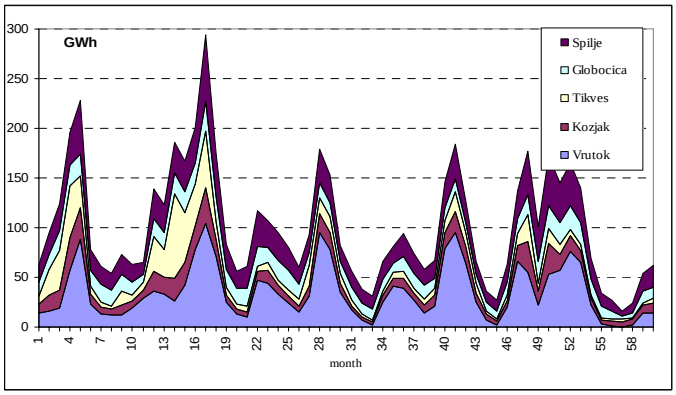

Fig. 5. Inflow energy in the reservoirs for average period

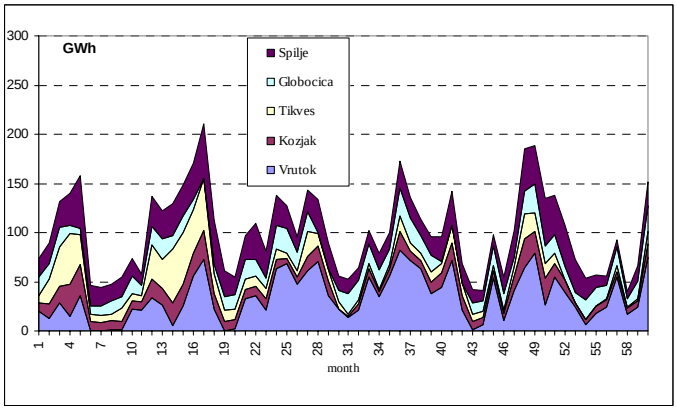

Fig. 6. Generated energy of the HPPs for average period

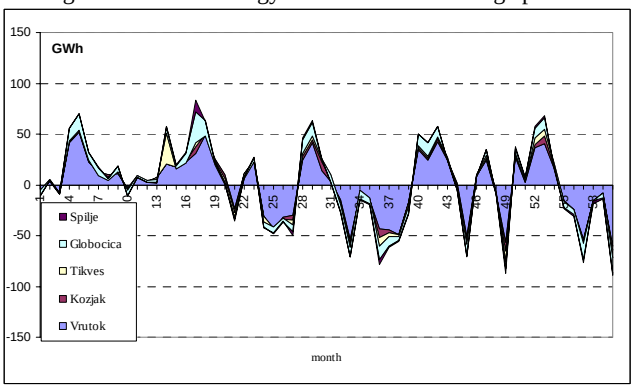

Fig. 7. Accumulated energy of the HPPs for average period

Fig.8, Fig.9 and Fig.10 present the inflow energy, generated energy and accumulated energy respectively, for the dry hydrology period of 5 years (1990-1994).

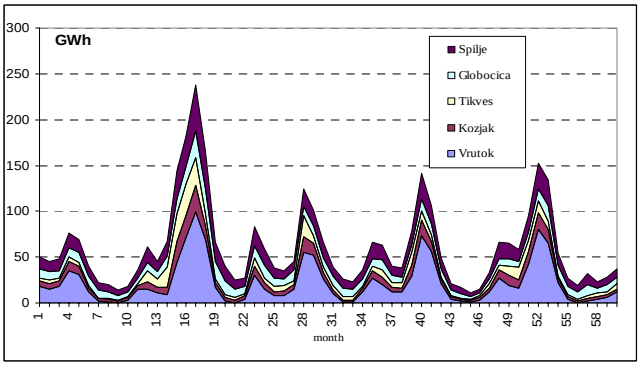

Fig. 8. Inflow energy in the reservoirs for dry period

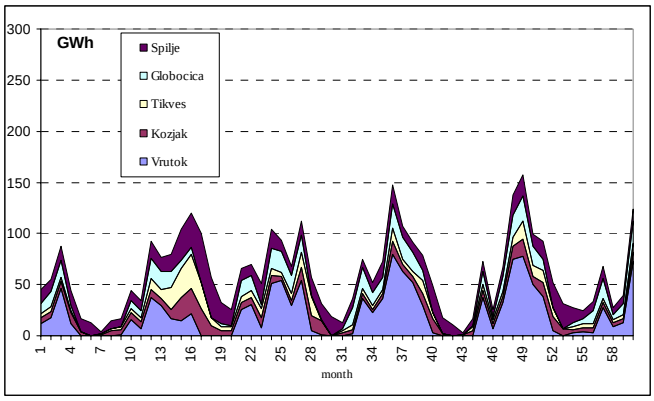

Fig. 9. Generated energy of the HPPs for wet period

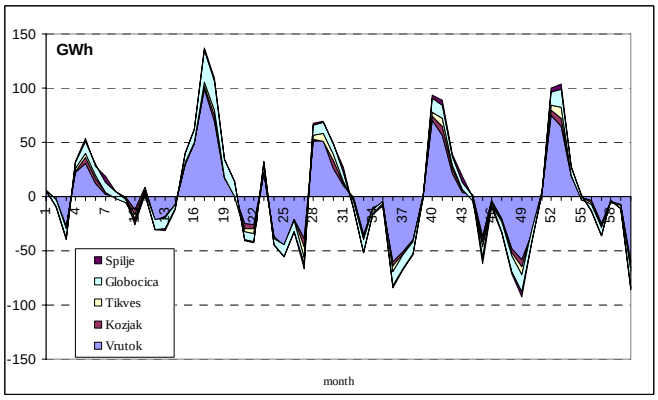

Fig. 10. Accumulated energy of the HPPs for average period

These figures demonstrate the role of the HPPs in different hydrology conditions with respect to the generated energy and accumulated water inventory. Obviously, saving water in the HPP reservoirs is greater in dry (Fig.10) than in average (Fig.7) or wet (Fig.4) periods. These results are obtained for the three hydrology periods with the same variations of the water reservoir levels, as follows: Mavrovo (HPP Vrutok) of about 15 (m), Ohrid lake (HPP Globocica) of 0,65 (m), and others reservoirs of about 10 (m).

6. CONCLUSION

The presented example of optimised planning of power generation in the Macedonian Power Generation System demonstrates the model capability in identifying the appropriate operating mode of the hydro power plants in the system. HPP Vrutok and Globocica have relatively large reservoir capabilities (can save water during the 5-year period.

The other HPPs, Kozjak, Tikves and Spilje, can save the water only over one-year period. Their contributions in the accumulated energy longer than 1 year are not significant, but on the other hand, the variation of the water level over 10 (m) will lead to significant energy loses.

The model capabilities can be used to ensure an optimised energy generation in a small power generation system, with an adequate energy supply that meets the projected energy demand each time interval.

The following points can be considered by using the presented model, aimed at improving the operation of the power generation system:

- Analyze hydrology influence on electricity generation of the HPPs,
- Define power plant operation to meet the electricity demand in a given time interval.
- Analyze operation of a series of linked HPPs, according to their hydro & technical parameters.
- Analyze pumping and generating operation using reversible HPPs,
- Determine the reservoir status of the existing storage HPP (water storage level during the period)
- Plan yearly operation, including outages of the thermal power plants, especially for the oil-fired plants, by taking into account the fuel price.
- Analyze the needs for increasing the installed capacity for some existing HPPs.
- Define the installed capacity and the operating role of the new HPPs & TPPs in the Power System.

REFERENCES

[1] T. Bosevski, A. Causevski, "Activities for Autonomy Work of the Macedonian Power System in New Energy Situation," *19th IAEE International Conference*, Conf. Proceedings, pp 407-414, May 27-30, 1996, Budapest.

[2] T. Bosevski, A. Causevski: "An Improved Method for Electricity Production Planning in a Complex Power System", *Conference and Exhibition on Modelling, Testing & Monitoring for Hydro Powerplants* - II Conf. papers, pp.677-686, July 8-11 1996, Lausanne.

[3] A. Causevski, "Analytical Numerical Improvements of the Models for Yearly Generation Planning in a Complex Power System," *the doctorial dissertation*, Faculty of Electrical Eng. Skopje, 2001.

[4] C-a. Li, E.Hsu. A.J. Svoboda, C. I. Tseng, R.B. Johnson, "Hydro Unit Commitment in Hydro-thermal Optimization", *IEEE Transaction on Power Systems*, *Vol.12*, No.2, May 1997.

Core Losses in Step-down Transformer Supplying Non-linear Loads

Georgi Ganev [1], George Todorov [2] and Atanas Kassamakov [3]

***Abstract* – The paper discusses the operation of a three-phase distribution transformer with a non-linear load connected. The influence of the harmonics, caused by the non-linear load, on the transformer's magnetic flux, magnetizing power and losses has been investigated. Analytical expressions for their calculation have been derived.**

Keywords: Harmonics, distribution transformer, core losses

I. INTRODUCTION

The wide usage of nonlinear electric power consumers (pulse-supplying sources with different purpose and power, supplying sources for different technological purpose, controlled motor drivers, etc) causes the electrical power quality aggravation. Due to its operation mode peculiarities this type of consumers deform the three-phase current waveforms. Therefore they become higher harmonics sources. The higher harmonics, which are distributed into supply grid, confuse the normal operation of the other consumers. On the other hand this harmonics cause the losses increasing in the equipment for energy transfer and distribution.

The aim of this paper is to study the influences of the harmonics, caused by the non-linear loads, upon the distribution transformer core losses.

II. NON-SYMMETRY MAGNITIC FLUXES IN THREE-PHASE TRANSFORMER WITH SYMETRIC SUPPLY

In the design and analysis procedures it is usually assumed that the magnetic flux is equal for all three cores of the three-phase transformer. The three-phase transformers with power less than 1600 kVA are usually of core design (three-leg core) and their magnetic current is non-symmetrical. It is preferred practice today since it is lighter, smaller, cheaper and slightly more efficient [4].

Assume that the primary winding is supplied with symmetrical three-phase voltage. The line voltages are equals to:

$$\dot{U}_{AB} = \dot{U}\,; \quad \dot{U}_{BC} = a^2.\dot{U}\,; \quad \dot{U}_{CA} = a.\dot{U}\,.$$

where $a = \exp\left(j\frac{2\pi}{3}\right)$ and $j = \sqrt{-1}$.

[1] Technical University – Sofia, branch Plovdiv, 25, Tzanko Dustabanov St., 4000, Plovdiv, BULGARIA,
e-mail: geoganev@yahoo.com

[2]Technical University – Sofia, Electrotechnical Department, 8, Kliment Ohridski St., bl.12, 1000, BULGARIA,
e-mail: gtto@tu-sofia.bg

[3]KCM-S.A., Assenovgransko shosse, 4009 Plovdiv, BULGARIA,
e-mail: atanas.kassamakov@kcm.bg

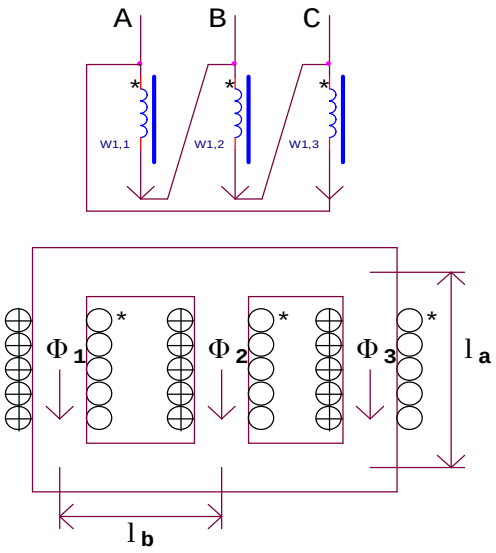

Fig.1.The three-phase core type transformer

Composing the three-phase core type transformer's equivalent circuit it is assumed that the leakage fluxes are negligible (fig.1). The useful magnetic fluxes in three cores are equals:

$$\begin{aligned}\dot{\Phi}_1 &= \left(\frac{1}{1+2r_\mu} - a^2\right)\Phi_0 \\ \dot{\Phi}_2 &= \left(a^2 - a\right)\Phi_0 = \left(-\,j.\sqrt{3}\right)\Phi_0 \\ \dot{\Phi}_3 &= \left(a - \frac{1}{1+2r_\mu}\right)\Phi_0\end{aligned} \qquad (1)$$

where Φ_0 - the provisional magnetic flux, is equal to:

$$\Phi_0 = \frac{3w_1 I_0}{\frac{1}{\Lambda_a} + \frac{2}{\Lambda_b}}$$

I_0 - mean value of the no-load current;
w_1 - number of the primary winding turns;
r_μ - ratio between core and yoke permeances (fig.1):

$$r_\mu = \frac{\Lambda_a}{\Lambda_b} = \frac{\mu.S_a}{l_a}.\frac{l_b}{\mu.S_b} = \frac{l_b}{l_a}.\frac{S_a}{S_b}$$

Λ_a,Λ_b -core and yoke permeances respectively equals to:

$$\Lambda_a = \frac{\mu.S_a}{l_a} \text{ и } \Lambda_b = \frac{\mu.S_b}{l_b};$$

S_a, S_b - core and yoke cross-section;
l_a, l_b - core and yoke length respectively.

Usually, the core and yoke cross-sections are equal. For the TMA type transformers type (manufactured by the Elprom

Trafo CH AG - Kjustendil, Bulgaria) the ratio l_b/l_a is about 0.55. Hence, the magnetic flux in inner core is almost 30% bigger than the fluxes in outside cores. Usually in the design procedures for three-phase transformer is used the magnetic fluxes mean value [5,6].

III. ELECTROMAGNETIC PROCESSES IN TRANSFORMER SUPLLYING NON-LINEAR LOAD

Nonlinear loads, connected to the low voltage supplying grid, cause an energy flow formed by higher harmonics with different numbers [7]. This energy flow is directed from the non-liner load to the step-down transformer and further to the medium voltage power-supplying grid. Hereafter it will be referred "Secondary Power Flow" (SPF) and will be designated with $W_{(k)}$, to be differentiated from the "Primary Power Flow" designated with $W_{(1)}$ comprising only the basic harmonic (fig.2) [5].

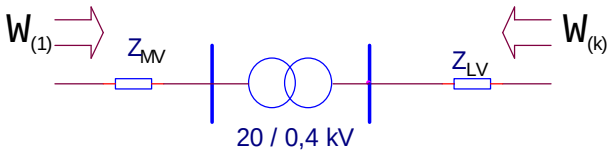

Fig.2. Scheme of the energy flow

It is typical of the discussed distribution transformer mode, that:

(a) The magnetic flux with frequency k^n, created in the magnetic core of the transformer by the secondary power flow and the main magnetic flux with grid frequency, generated by the primary winding and by the primary power flow, superimpose in the transformer magnetic core. The total magnetic flux of the transformer is a result of this superimposition and is non-sinusoidal.

(b) In terms of secondary power flow, the transformer is in a close to the short-circuit mode, as its primary winding is connected to middle voltage power supplying grid, with very low resistance for a harmonic with k^n frequency;

(c) While the primary winding is fed by a sufficiently powerful source (theoretically with unlimited power), regarding to the secondary power flow, the transformer feeding device has a limited power [1].

(d) The principle of superposition is not applicable in the analyses of the discussed mode. Therefore, we have to use the magnetization curves *B(H)* and take the momentary induction values for each of the harmonics. The position of the working point on the magnetization curve is determined by both magnetic fluxes - the basic frequency magnetic flux and the superimposed partial k^n frequency magnetic flux;

(e) Owing to the non-linear characteristics of the transformer and the presence of currents with different frequencies, it is necessary to transfer provisionally some of the parameters to one and the same basic frequency - the grid frequency. The following condition is accepted as the basis of this transferring – the core losses, caused by the k^n harmonic of the secondary winding current and the losses, transferred to the basic frequency, should be equal, that is:

$$P_{c(k)} = \hat{P}_{c(k)} \qquad (2)$$

It is accepted hereafter to use the symbol ˆ to denote quantities, caused by the secondary current harmonics, which have been transferred to the basic frequency.

From all that, it can be concluded that the operation of the nonlinear load, low voltage supplying grid, the step-down distribution transformer and middle voltage supplying grid should be analyzed as interrelated.

In the analysis of the electromagnetic processes, it is accepted that the partial voltage of the secondary winding has sinusoidal waveform. Consequently the magnetic flux $\Phi_{(k)}$ has also sinusoidal waveform and is added to the basic frequency magnetic flux $\Phi_{(1)}$.

What is characteristic of the discussed mode of operation is that the magnetization currents of the primary winding with basic frequency and the magnetizing currents of secondary winding with higher frequency, form independent of one another magnetic fluxes, which superimposed. Therefore we cannot define general magnetization current in the common sense of this term. We can only introduce and use it so long as it helps us determine the position of the working point on the magnetization curve and afterwards, to determine the value of the partial magnetizing current.

IV. CORE LOSSES DUE TO THE SECONDARY POWER FLOW

The core losses can be determined in the following way:

$$P_c = \sum_{j=1}^{n} p_{\frac{1,0}{50}} . B_{m,j}^2 \left(\frac{f}{50}\right)^{1,3}$$

where $p_{\frac{1,0}{50}}$ is the value of the relative core losses at peak flux density of 1T and frequency f=50*Hz*.

$B_{m,j}$ - the peak value of the flux density for the j^{th} element of the magnetic circuit.

Assuming that all elements of the magnetic circuit have equal cross-sections $S_j = Const$, it can be concluded that $B_{m,j} = Const$, and the transferring condition acquires the following expression:

$$\sum_{j=1}^{n} p_{\frac{1,0}{50}} . \hat{B}_{m,(k),j}^2 \left(\frac{f}{50}\right)^{1,3} = \sum_{j=1}^{n} p_{\frac{1,0}{50}} . B_{m,(k),j}^2 \left(\frac{k.f}{50}\right) \qquad (3)$$

After applying

$$k_{B(k)} = \sqrt{k^{1,3}} = k^{0,65} \qquad (4)$$

for the peak of the flux density transferred to basic frequency the result is:

$$\hat{B}_{m(k)} = k_{B(k)} . B_{m(k)} \qquad (5)$$

Due to the presence of two power flows through the transformer, the magnetic flux created by the k^n harmonic of the secondary winding current superimposes to the basic

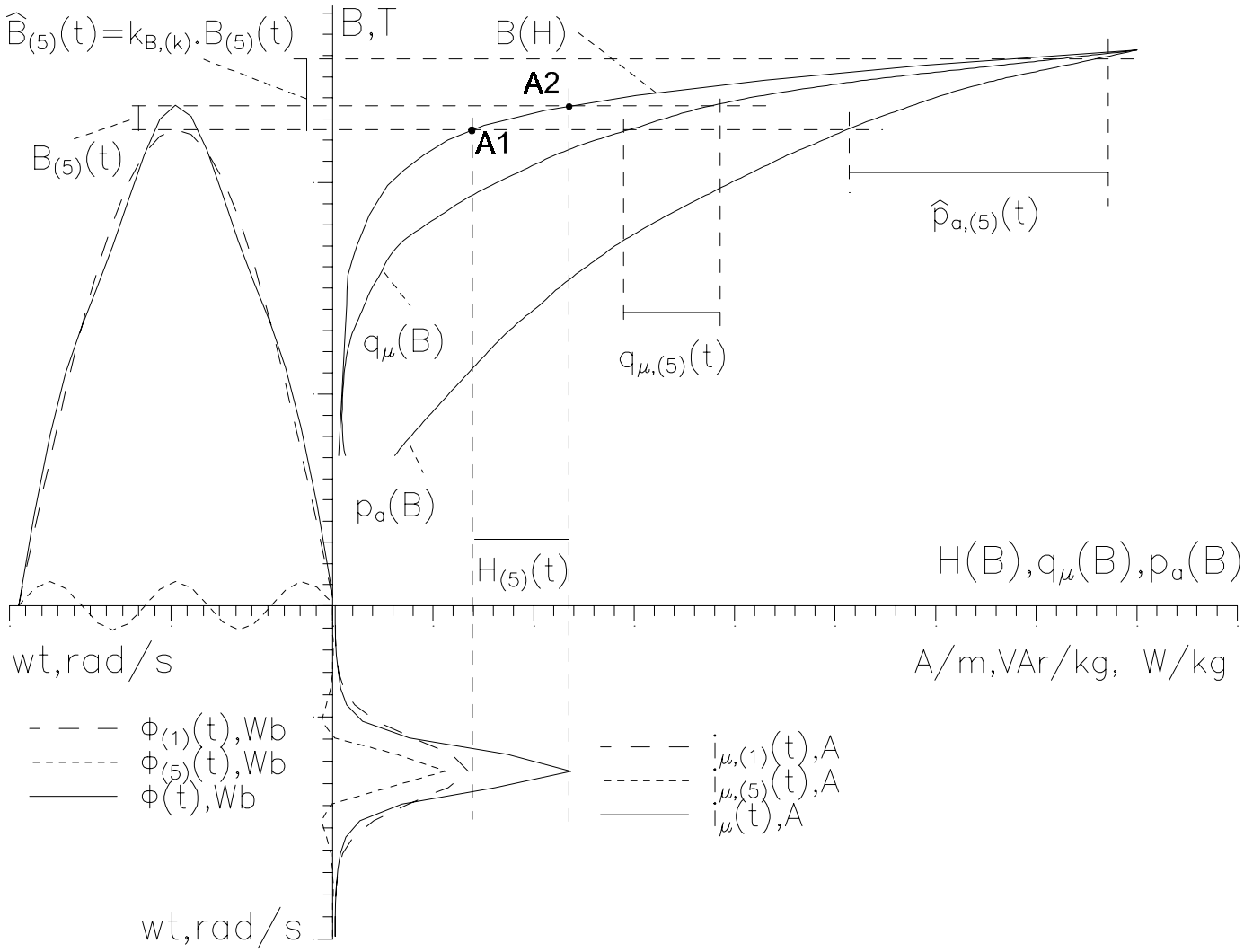

Fig.3. Determining the additional core losses of the transformer for the 5[n] harmonic

magnetic flux with grid frequency The value of the k[-n] harmonic magnetic flux can be presented as:

$$\Phi_{(k)}(\omega t) = \frac{\mu . w_2}{l_m} . S_a . i_{\mu(k)}(\omega t) \qquad (6)$$

where $i_{\mu(k)}(k\omega t)$ is the k[n] harmonic magnetization current,

of the secondary winding;

S_a - cross-section of the magnetic core;

l_m - the average length of the magnetic circuit.

The magnetization curve *B(H),* the relative core losses curve $p_a(B)$, and the relative magnetizing power curve $q_\mu(B)$ for the steel are used to determine the parameters of the transformer for the k[n] harmonic. For creating a precise model of a step-down transformer, it is necessary to take into account some other characteristics typical of its magnetic circuit, such as the magnetization power of the air gaps $q_{\mu,\delta}(B)$, the residual magnetic flux density B_r, etc. As the aim of this research is to investigate the influence of the harmonics to the transformer core losses they are not under consideration in this paper.

Fig 3 illustrates the core losses increasing due to the higher harmonics magnetic fluxes. It is assumed that only partial flux $\Phi_{(5)}$ superimposes to the basic magnetic flux $\Phi_{(1)}$. The basic magnetic flux $\Phi_{(1)}$ determines the basic working point on the magnetizing curve. With $\Phi_{(1)} = \Phi_{(1),max}$ the flux density $B_{(1)}$ reaches its peak value (designated with A1 in figure 3).

The sinusoidal voltage of the secondary winding creates a partial magnetic flux $\Phi_{(5)}$ with frequency 5 times the basic one. Supposing the magnitude of $\Phi_{(5)}$ is given. The flux $\Phi_{(5)}$ superimposed to the basic flux $\Phi_{(1)}$, causes partial hysteresis loop around the working point with frequency *kf=5f* and periodic oscillation of the magnetic induction $B_{(1)}$. In fig.3 with the given values, the magnetic induction *B* reaches the peak values, marked as A2 on the magnetization curve.

Owing to the strongly expressed non-linearity of the magnetization curve, the relative magnitude of the magnetic induction for the k[n] harmonic is determined graphically directly by the curve of *B = f(H);*

$$H_{(k)}(t) = H(t) - H_{(1)}(t) \qquad (7)$$

The magnetizing current $i_{\mu,(k)}$ of the k[n] harmonic is also plotted in quadrant 4. It can be determined by subtracting the magnetizing current with basic frequency $i_{\mu,(1)}$, from the resultant magnetizing current i_{μ}, determined by the total magnetic flux $\Phi(t)=\Phi_{(1)}(t)+\Phi_{(5)}(t)$.

$$i_{\mu(k)}(t)=i_{\mu}(t)-i_{\mu(1)}(t) \tag{8}$$

The curve $q_{\mu}=f(B)$, plotted in quadrant 1, allows to determine the magnitude of the relative magnetization power for the k[n] harmonic.

$$q_{\mu(k)}(t)=q_{\mu}(t)-q_{\mu(1)}(t) \tag{9}$$

Having the curve of the relative core losses at basic frequency $f=50Hz$ in quadrant 1, $p_a = f(B)$ the relative losses in the steel, caused by the k[n] harmonic in the secondary current, can be determined.

For this purpose, the obtained value of $B_{(k)}$ has to be transferred to the basic frequency by multiplying to the coefficient $k_{B,(k)}$. By adding the transferred magnetic flux density $\hat{B}_{(k)}$ to the magnetic flux density $B_{(1)}$, the peak value of the resultant magnetic flux density is obtained. This value is used to determine the total core losses. The relative active losses, due to the magnetic flux with frequency higher than the basic one, are determined with the equation:

$$\hat{p}_{a(k)}(t)=p_a(t)-p_{a(1)}(t) \tag{10}$$

The ration of the components of the power - $\hat{p}_{a(k)}$, $q_{a(k)}$, determines the loss angle for the k[n] harmonic.

$$tg\left(\alpha_{loss(k)}\right)=\frac{\hat{p}_{a(k)}(t)}{q_{a(k)}(t)} \tag{11}$$

The active component of the transformer current is:

$$\hat{i}_{a(k)}=i_{\mu(k)}.tg\left(\alpha_{loss(k)}\right) \tag{12}$$

It is important to note that all discussed values are the momentary ones.

The average values of the magnetizing power and the core losses for the k[n] harmonic are determined for one period of the basic harmonic. This is so, because it is the basic magnetic flux that determines the position of the working point, around which the partial hysteresis cycle with frequency kf is located.

Active power for the k[n] harmonic

$$P_{a(k)}=\frac{G_a}{T}.\int_0^T \hat{p}_{a(k)}(t).dt \tag{13}$$

where G_a is the core steel masse.

Reactive power for the k[n] harmonic

$$Q_{\mu(k)}=\frac{G_a}{T}.\int_0^T q_{\mu(k)}(t).dt \tag{14}$$

The core losses increasing is sum of losses causing by the harmonics with different frequency:

$$P_{a,SPF}=\sum_{k=1}^{\infty}P_{a(k)} \tag{15}$$

and respectively, the generalized magnetizing power is:

$$Q_{\mu,SPF}=\sum_{k=1}^{\infty}Q_{\mu(k)} \tag{16}$$

V. CONCLUSION

The nonlinear loads connected to the secondary winding cause higher harmonics power flow from the load to the transformer. It forms higher harmonics magnetic flux in the transformer magnetic core, which increases values of the flux density and moves the working point on the magnetization curve in saturation zone. As nowadays the transformer operate with a relatively high value of the magnetic flux density, this movement to the high saturation zone leads to sharp increase of the core losses. The additional core losses, due to the higher harmonics may have value commensurable with the losses due to the basic harmonic. On the other hand, due to the transformer core is non-symmetry, the magnetic flux, respectively magnetic flux density in the innes and the outside cores are different then the average values. Hence, the increase of the core losses is bigger for the inner core. The design engineers should take this fact into account when they design distribution transformer, supplying non-linear loads.

VI. REFERENCES:

[1] БДС EN 61000-1999.

[2] Генов Ст., А.Дачев, Проектиране на силови трансформатори, Техника, София,1990.

[3] Динов В. Електрически машини, Техника, София, 1985.

[4] Chapman St.J., Electric machinery fundamentals, McGray-Hill Inc. 1985

[5] Ganev G., G.Todorov, Influence of the Harmonics on the Step - Down Transformer Core Losses in the Case of Nonlinear Loads, SIELA'2003, vol.2, pp.63-69.

[6] Ganev G., G.Hristov, Determining the Step - Down Transformer Winding Losses in the Case of Nonlinear Loads, SIELA'2003, vol.2, pp.75-79.

[7] Stade D., L.Kuchumov, A.Novitskiy, A.Ivanov, Power Flows in Electrical Power Systems Containing Non-Linear and Non-Symmetrical Consumers, EMC'98, Wrocslav, pp 143-147

A Method for Additional Losses Determination in Distribution Transformer Supplying Nonlinear Load

Georgi Ganev [1], George Todorov [2] and Atanas Kassamakov [3]

***Abstract* – A method for additional core and winding losses calculation, is presented. It is intended for studying the steady-state mode of operation of a three-phase distribution transformer with non-linear loads. The method is applied to certain transformer and the results are compared to the measured values and values, obtained by another analytical methods. The comparison proves the new method's propriety and appliety.**

Keywords: Harmonics, distribution transformer, core losses, winding losses

I. INTRODUCTION

There are a lot of electrical power loads and electromechanical devices, which deform the three-phase voltage and current waveforms. So the "nonlinear loads" generate higher harmonics [8]. The harmonics distribute into the supply grid and cause power equipment losses increasing [2,4,8].

The aim of this paper is to study the influence of the harmonics, generated by the non-linear loads on the core and winding losses of the distribution transformer.

The method is derived supposing that three-phase symmetrical sinusoidal voltage supplies the transformer. It is assumed also that it is possible to measure the secondary winding voltage and current, and their harmonics spectra are known.

II. ADDITIONAL LOSSES DETERMINATION

Then the transformer supplies consumers with linear VA characteristics, efficiency coefficient is determined as:

$$\eta = P_2 / P_1 \qquad (1)$$

where P_2 is the output power measured on the transformer secondary side;

P_1 – the input power, supplying the transformer, determined as:

$$P_1 = P_2 + P_{nl} + P_{sc}.\beta^2$$

where P_{nl},P_{sc} are rated no-load and short-circuit losses respectively

β - load coefficient $\beta = I_2 / I_{2,nom}$;

$I_{2,nom}$,I_2 - rated secondary winding current and secondary winding current at the studied operation mode respectively.

In the case of the non-linear loads:

$$P_1 = P_2 + (P_{nl} + P_{a,SPF}) + (P_{sc} + P_{w,SPF})\beta^2 \qquad (2)$$

where $P_{a,SPF}$, $P_{w,SPF}$ are additional core losses and winding losses due to the secondary power flow (SPF) existing in low voltage grid [6,7]

After entering the symbols:

$\overline{p}_a$ -relative iron losses increasing due to the secondary power flow:

$$\overline{p}_a = P_{a,SPF} / P_{nl} ;$$

$\overline{p}_w$ -relative winding losses increasing due to the secondary power flow:

$$\overline{p}_w = P_{w,SPF} / P_{sc} ,$$

the transformer efficiency coefficient can be reexpressed as:

$$\eta = \frac{P_2}{P_2 + P_{nl}(1+\overline{p}_a) + P_{sc}(1+\overline{p}_w)\beta^2}, \qquad (3)$$

The two terms – $\overline{p}_a$ and $\overline{p}_w$, are integral measures for transformer additional core and winding losses magnitudes, which occurred if the secondary power flow exist. They depend on:

a/ distribution transformer type and design;

b/ values of total harmonic voltage distortion (THD_U) and total harmonic current distortion (THD_I) [8];

в/ magnitudes of each of current and voltage harmonics measured on the secondary winding outputs.

A. Relative core losses increasing

The main construction dimensions are determined so that it is realized optimal relation between iron core masse G_a, winding masse G_w and flux density B. In reference [3] is given a relationship between two iron masse values and respective flux density values. It is based on the constant no-load losses condition

$$G_2 = G_1 \left(K_2 + K_1 . \sqrt{\frac{B_1}{B_2}} \right) \left(\frac{B_1}{B_2} \right), \qquad (4)$$

where K_1, K_2 are coefficients, which values depend on the transformer's main dimensions [6].

As the transformer iron losses are $p_a = P_{nl} / G_a$, the equation (4) could be written as:

$$p_{a,1} = p_{a,2} \left(K_2 + K_1 . \sqrt{\frac{B_1}{B_2}} \right) \left(\frac{B_1}{B_2} \right) \qquad (5)$$

When the transformer supplies non-linear load and the secondary power flow exists:

[1] Technical University – Sofia, branch Plovdiv, 25, Tzanko Dustabanov St., 4000, Plovdiv, BULGARIA,
e-mail: geoganev@yahoo.com

[2]Technical University – Sofia, Electrotechnical Department, 8, Kliment Ohridski St., bl.12, 1000, BULGARIA,
e-mail: gtto@tu-sofia.bg

[3]KCM-S.A., Assenovgransko shosse, 4009 Plovdiv, BULGARIA,
e-mail: atanas.kassamakov@kcm.bg

$$\frac{P_{nl}}{G_a}=\frac{P_{nl}+P_{a,SPF}}{G_a}.\left(K_2+K_1.\sqrt{\frac{B}{B+\overline{B}}}\right).\left(\frac{B}{B+\overline{B}}\right) \qquad (6)$$

where $\overline{B}$ is flux density, due to the secondary power flow. It can be defined as sum of partial flux densities, created from the secondary power flow for one period of the supply voltage, which are transferred to basic frequency [6,7];

G_a – transformer iron masse.

The relative core losses, due to the secondary power flow, are:

$$\overline{p}_a=\frac{1+\overline{B}/B}{\left(K_1+K_2.\sqrt{1+\overline{B}/B}\right)}-1 \qquad (7)$$

Substitute: $B=\dfrac{U_{1(1)}}{4{,}44w_1 f.S}$

and respectively $B_{(k)}=\dfrac{U_{2(k)}}{4{,}44w_2 kf.S}$,

for main flux density creating for secondary power flow can be reexpressed as:

$$\overline{B}=\sum_{k=1}^{\infty}\hat{B}_{(k)}=\sum_{k=1}^{\infty}B_{(k)}k_{B(k)}=\sum_{k=1}^{\infty}\frac{U_{2(k)}}{4{,}44w_2 fS}\frac{\sqrt{k^{1,3}}}{k} \qquad (8)$$

where $U_{2,(k)}$ is voltage with frequency kf;

S - cross-section area of the core;

$k_{B,(k)}$ - flux density transforming coefficient. It is determined in [6,7] and it is equal to $k^{-0,65}$;

w_1, w_2 - primary and secondary winding turns respectively.

Assuming that:

$$K_{KU}=\sum_{k=1}^{\infty}\left(\frac{U_{2(k)}}{U_{2(1)}}k^{-0,35}\right), \qquad (9)$$

the equation (7) can be expressed as follow:

$$\overline{p}_a=\frac{\left(1+K_{KU}\right)^{3/2}}{\left(K_1+K_2.\sqrt{1+K_{KU}}\right)}-1 \qquad (10)$$

B. Relative winding losses increasing

For determination of the relative winding losses increasing it is necessary to separate the short-circuit transformer losses [1]:

$$P_{sc}=P_{dc}+P_{wt}+P_t+P_{se}$$

where P_{dc} are direct current winding losses;

P_{wt} - winding taps losses;

P_t - transformer tank losses;

P_{se} - losses which are caused from skin-effect and windings transposition.

The different transformer short-circuit losses portions depend mostly on the transformer rated power. Applying the coefficients k_t and k_{sc} [1,5] the tank losses P_t and the skin-effect losses P_{se} can be determine.

$$k_t=\frac{P_t}{S_{nom}}=0{,}578+0{,}325.10^{-3}.S_{nom},$$

$$k_{se}=\frac{P_{se}}{S_{nom}}=0{,}111+0{,}0264.\sqrt{S_{nom}},$$

In upper expressions the rated transformer power S_{nom} is measured in *kVA* [1]:

The additional winding losses causing from secondary power flow can be expressed as follow [5]:

$$P_{w,SPF}=\left(P_{dc}+P_{wt}\right).\left[\sum_{k=2}^{\infty}\left(\frac{I_{2(k)}}{I_{2,nom(1)}}\right)^2\right]+$$

$$+\left(P_t+P_{se}\right).\left[\sum_{k=2}^{\infty}\left(\frac{k.I_{2(k)}}{I_{2,nom(1)}}\right)^2\right] \qquad (11)$$

Transformer winding losses increasing $\overline{p}_w$, due to the secondary power flow is equal [5]:

$$\overline{p}_w=THD_I^2+\frac{S_{nom}}{P_{sc}}\left(k_{se}+k_t\right).\left(K_{KI}^2-THD_I^2\right) \qquad (12)$$

where K_{KI} is coefficient, defined as:

$$K_{KI}=\sqrt{\sum_{k=2}^{\infty}\left(\frac{k.I_{(k)}}{I_{(1)}}\right)^2} \qquad (13)$$

This coefficient K_{KI} is analogue to K-factor [8].

By reason of non-sinusoidal secondary current waveform, the load coefficient:

$$\beta^2=\left(\frac{I_2}{I_{2,nom}}\right)^2=\left(\frac{1}{I_{2,nom}}\sum_{k=1}^{\infty}I_{2(k)}\right)^2=\left(\frac{I_{2(1)}}{I_{2,nom}}\right)^2.\left[1+\sum_{k=2}^{\infty}\left(\frac{I_{2(k)}}{I_{2,nom}}\right)^2\right]$$

consequently:

$$\beta=\beta_{(1)}\sqrt{1+THD_I^2}$$

where $\beta_{(1)}$ is load coefficient giving by:

$$\beta_{(1)}=I_{2(1)}/I_{2,nom}$$

So, the efficient coefficient of transformer supplying non-liner consumer is:

$$\eta_{SPF}=\frac{P_2}{P_2+P_{nl}.\left(1+\overline{p}_a\right)+P_{cs}.\left(1+\overline{p}_w\right).\left(1+THD_I^2\right).\beta_{(1)}^2},$$

The general additional transformer losses increasing is:

$$\overline{p}_o=\frac{P_{nl}.\left(1+\overline{p}_a\right)+P_{cs}.\left(1+\overline{p}_w\right).\left(1+THD_I^2\right).\beta_{(1)}^2}{P_{nl}+P_{cs}.\beta_{(1)}^2}-1 \qquad (14)$$

III. RESULTS AND ANALYSIS

The experiments with three phase transformer type TT16002 manufacturing №88480 with parameters: S_{nom}=1200VA, U_1=380V, I_1=1,8A, U_2=110V, I_2=6,3A, and winding connected as Y/Δ. This transformer supplied three-phase bridge diode rectifier. The currents and voltages waveforms of phase A are given on fig.1 There are two case:

a/ if the rectifier supplies active-inductive load;

b/ if the rectifier supplies active-capacitive load.

For reliability verification of this developed method for transformer additional losses determining is made comparison between its results and the experimental results. In this calculation the coefficients K_1 and K_2 values are determined

for flux density varying from 1.2T to 1.8T [2]. The experiments was made as the rectifier loads are change such as transformer active output power are varying from 10% to 99% in comparison with nominal power S_{nom}.

For secondary voltage and current harmonics spectrum measuring in used power quality analyzer type MI 2192, №12091431, manufactured by METREL, Slovenia. The results are created the possibility the additional transformer losses calculating (see table 1). The measured values of THD_U, THD_I and input transformer power P_1 and the calculated values are approximately equals. This is the base to affirm that the proposed method usage cause to reliable results receiving

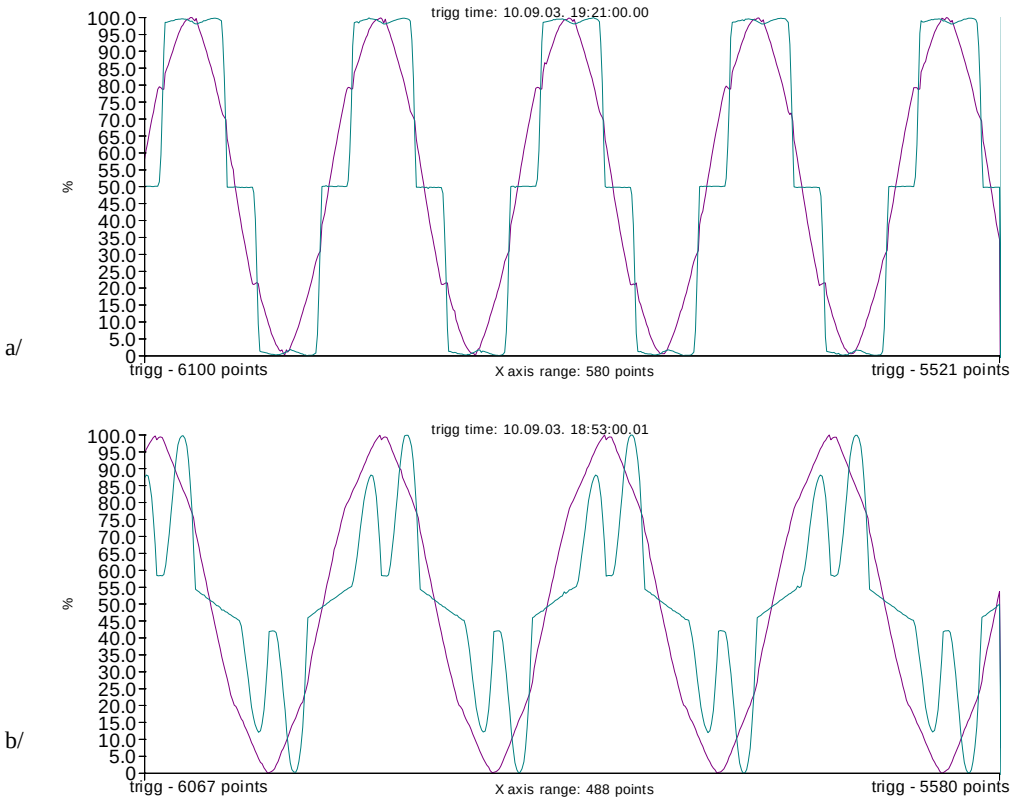

Fig.1. Voltage and current waveforms in phase A, if transformer supplied three-phase diode bridge rectifier with active-inductive load (a) and active-capacitive load (b) and with DC power P_{dc}=333W

TABLE 1.
HIGH HARMONICS CAUSED LOSSES.
AS THE NONLINEAR LOAD, GENERATING HIGH HARMONICS IS USED TRHEE PHASE DIODE BRIDGE RECTIFIER WITH ACTIVE-INDUCTIVE LOAD

№		P_2,W	$\beta_{(1)}$	THD_I,%	THD_U,%	K_{KI}	K_{KU},%	$\overline{p}_a$,%	$\overline{p}_w$,%	$\overline{p}_o$,%	P_1,W
1	M	126	-	29,43	3,27	-	-	-	-	-	149
	C	-	0,163	28,20	3	2,321	4,3	5,7	10,9	11,0	166
2	M	218	-	29,33	3,3	-	-	-	-	-	249
	C	-	0,164	28,10	3,1	2,31	4,4	5,8	10,8	11,2	259
3	M	333	-	28,83	3,43	-	-	-	-	-	368
	C	-	0,238	28,00	3,3	2,297	4,7	6,1	10,7	11,4	376
4	M	753	-	27,70	3,9	-	-	-	-	-	815
	C	-	0,604	27,20	3,7	2,176	5,0	6,6	9,9	13,0	818
5	M	1186	-	26,53	5	-	-	-	-	-	1290
	C	-	0,903	25,30	4,6	2,041	6,3	8,3	9,4	14,0	1282

Remarks: With M are signed measured values, with C – calculated values.

Comparison with another analytical methods for additional losses determining was made [2,4].

In [2] was proposed the relationship:

$$\Delta P_{R2} = P_{nl}\sum_{k=2}^{\infty}U_{(k)}^2 + 0{,}607.\frac{P_{sc}}{u_k^2}.\sum_{k=2}^{\infty}\frac{1+0{,}05.k^2}{k.\sqrt{k}}U_{(k)}^2, \quad (15)$$

and in [4]:

$$\Delta P_{R4} = 3\sum_{k=2}^{\infty} I_{(k)}^2 R_2 \sqrt{k} \ . \qquad (16)$$

The relative additional transformer losses increasing due to the secondary power flow, is:

$$\overline{p}_{o,R2} = \frac{\Delta P_{R5}}{P_{nl} + P_{sc}\beta_{(1)}^2} \qquad (15a)$$

and respectively:

$$\overline{p}_{o,R4} = \frac{\Delta P_{R7}}{P_{nl} + P_{sc}\beta_{(1)}^2} \qquad (16a)$$

The relationship between relative transformer losses versus to total distortion factor of voltage is given in fig.2. The secondary current harmonics spectrum influence to relative additional transformer losses is given in table 2. All values presented in fig.2 and table 2 are received by applying the proposed method and expressions (15a) and (16a).

Comparing the presented results, could make the following conclusions:

1. The core losses transformer increasing is due to the voltage harmonics (table 1). The increasing DC power cause the transformer influence increasing to the alternative current waveform. Increasing the overlap angle values cause to current harmonics spectrum improving (THD_I is changed from 28.2% to 25.3%) and the additional winding losses are decreasing – from 10.9 % to 9.4 %.

2. The equation (15) render an account of output transformer voltage harmonics. Of course, the harmonics exert main influence on additional core losses. The additional winding losses due to the skin-effect are determined by current harmonics. It is indirect rended an account of the second term of equation (15).

3. The term (16) render an account of skin-effect losses increasing but not the core losses increasing

4. After analysis of the proposed in fig.2, table 1 and table 2 results could make the conclusion that disregarding of each one of the additional losses parts could cause a big mistake.

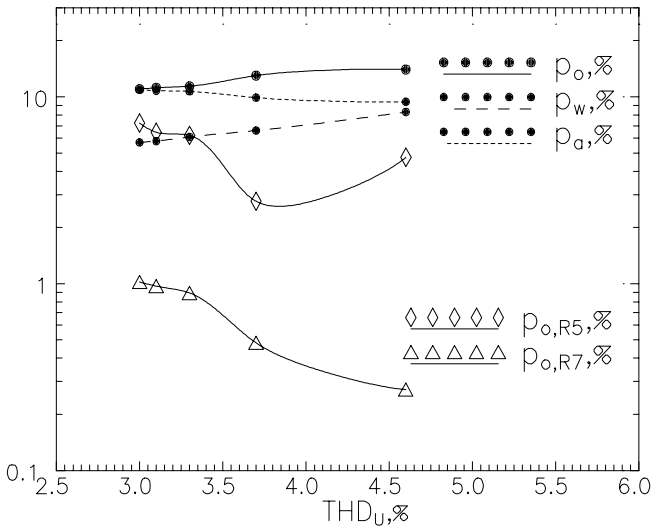

Fig.2. Distribution transformer losses increasing. Transformer is connected with three-phase diode bridge rectifier with active-inductive load

TABLE.2. RELATIVE TRANSFORMER LOSSES INCREASING VERSUS DIFFERENT TYPE OF RECTIFIERS DC LOAD (SEE FIG.1)

Load	RC		RL	
	M	C	M	C
P_2,W	333,6	-	333	-
β_1	-	23,8	-	12,8
THD_U,%	3,8	4,8	3,43	3,3
THD_I,%	57,8	58,3	28,83	28,00
K_{KU},%	-	8,2	-	4,7
K_{KI}	-	3,451	-	2,297
$\overline{p}_a$,%	-	10,8	-	6,1
$\overline{p}_w$,%	-	33,9	-	10,7
$\overline{p}_o$,%	-	37,2	-	11,4
P_1,W	365	357,3	368	376
$\overline{p}_{o,R2}$,%	-	43,501	-	6,213
$\overline{p}_{o,R4}$,%	-	7,473	-	0,891

Remarks: With M are signed measured values, with C – calculated values.

IV. CONCLUSION

The method for additional distribution transformer losses determining is presented. This method render an account of increasing frequency of nonlinear load generate harmonics. The additional winding and core losses are determining with secondary current and secondary voltages harmonic spectrum measuring.

V. REFERENCES

[1] Генов Ст., А.Дачев, Проектиране на силови трансформатори, Техника, София,1990.

[2] Овчаренко А.С., Д.И.Розинский, Повышение эффективности электроснабжения промышленных предприятий, Тэхника, Киев,1989.

[3] Тихомиров П.М., Расчет трансформаторов, Энергия, Москва, 1968.

[4] Фьодоров А.А, Г.В.Серебринксий, Справочник по электроснабжению промышленных предприятий. Промышленные электрические сети,. Энергоиздат, Москва, 1980

[5] Ganev G., G.Hristov, Determining the Step - Down Transformer Winding Losses in the Case of Nonlinear Loads, SIELA'2003, vol.2, pp.75-79.

[6] Ganev G., G.Todorov, Influence of the Harmonics on the Step - Down Transformer Core Losses in the Case of Nonlinear Loads, SIELA'2003, vol.2, pp.63-69.

[7] Ganev G., G.Todorov, A.Kassamakov, Core Losses in Step-down Transformer Supplying Nonlinear Loads, ICEST'2004 Bitola, Makedonia.

[8] Grady M., Understanding Power System Harmonics, September, 2000

Fuzzy Concept for Projects Evaluation in Power System Utilities

Atanas M. Iliev and Vangel V. Fustik

***Abstract*--This paper presents a new fuzzy concept for project evaluation in Power System Utilities which uses fuzzified economic criteria. For this purpose the classical economical criteria for accepting/rejecting a project are modified and upgraded in a fuzzy sense. The Investors point of view for successful project is modelled by triangular fuzzy number.**

Developed model is extension of the classical deterministic model and enables possibilities to perceive influence of the specific parameters and uncertainty to the rate of investment in specific project.

***Index Terms*- Project evaluation, Decision-making, Engineering economy, Fuzzy logic, Power system utilities.**

I. INTRODUCTION

Power systems projects, especially construction of new power plants and high voltage transmission lines are complex, occurring as unique projects undertaken to achieve exactly defined goals. They have to be finished in specified period, with limited budget and with guaranteed quality.

The projects in power system utilities are characterized with relatively long period of construction, intensive investments at the beginning of the project and many participants from different profiles and specialities. Within these projects a great number of parameters and indexes are necessary to be conducted the analyses with high degree of uncertainty and impreciseness. In the analyses of the technical and economical aspects of the power system project (that usually are in exploitation more than 20 years) it's unavoidable to use data, which have a high degree of uncertainty and impreciseness [4]. Therefore, studying, analyzing and energetic-economical valuation of such projects means a complex process which requires knowledge and experience in modelling and a vision of upbringing the correct decision.

The typical sequences in the projects in electric power utilities consist of an initial investments followed by operation and maintenance costs and returns in later years. The evaluation of these projects and investments are complicated by the fact that there are usually costs and benefits associated with an investment occurring at different points of time [1].

However, in many practical situations it is not possible to ignore the fact that the vagueness has an important role in the technical and economical valuation of the power system project evaluation [6, 7]. Thus, many essential project parameters such as:

- Price of electricity during the exploitation period of the power system project,
- Discount rate, that intends to capture the time value of the money,
- Time of construction of the project,
- Life-cycle of the project, etc.

may confuse the investors in power system utilities in an uncertain economic environment.

These variables are non-random and hence, not suitable for modelling by probabilistic theory. The next important issue is that these variables are unknown, but *bounded variables*. In order to take into account this uncertain future situation, imprecise character and vagueness, those variables could be modelled by fuzzy numbers [3, 9]. Thus, the expected discounted benefits of the undertaken power system project (**B**), as well as the discounted costs (**C**), are represented rather as fuzzy numbers than as ordinary crisp numbers [5].

II. MODIFIED FUZZY ECONOMIC CRITERIA FOR PROJECT EVALUATION

The most important and most used economical parameters for project evaluation [1] are:

- Net Present Value (NPV),
- Profitability Index (PI) and
- Internal Rate of Return (IRR).

Net Present Values means difference between discounted benefit and discounted cost of the project. In accordance to the classical terminology: if NPV > 0, project is economically acceptable. On the contrary, if NPV < 0 then the investments will not meet the desired results or, in other words the investments for the project will not be retrieved.

Profitability Index (PI) of the project is a ratio between the benefit and cost of the project, discounted on the base year [1]. Thus, if the ratio: PI=Benefit/ Cost >1 the project is acceptable for investment, but if the ratio PI=Benefit/Cost <1 the project is not acceptable from an economical point of view.

An investment's Internal Rate of Return (IRR) is defined as discount rate at which the investments NPV equals zero. The corresponding acceptance which to compare the IRR is the opportunity cost of capital to the company [1]. Thus, if the investment's IRR exceed the opportunity cost of capital, the investments is attractive from economic standpoint.

The main questions, in modelling the Investor standpoint in the decision making process, are:

Which NPVmin > 0 will be satisfactory for the investor, thus when NPV > NPVmin, the project will be accepted for investment?

Which value for B/C>1 will be acceptable, or which value will be satisfactory for the Investor? Would the investor for

A. M. Iliev is with Faculty of Electrical Engineering, Karpos bb, P.O.Box 574, 1000 Skopje, Macedonia, e-mail: ailiev@ieee.org

V. V. Fustik is with Faculty of Electrical Engineering, Karpos bb, P.O.Box 574, 1000 Skopje, Macedonia, e-mail: fustik@ukim.edu.mk

other reasons invest in a risky project with Benefit/Cost ratio lower than one?

Which is the minimal acceptable rate of return (MARR) which will satisfy the requirements of the investors in power system utilities, considering profit, risk and uncertainty?

When economic parameters of the projects are expressed by crisp number, the operation of ranking and ordering of the projects is well defined and clear. However, when the calculations of the Benefit and the Cost of the project are realized with fuzzy numbers, calculated Net Present Value (NPV) and the Profitability Index (PI), as final results, are fuzzy numbers [4-6]. In this case, checking of the fulfilment of the economic criteria needs applying the efficient method, which will compare a fuzzy number with a crisp number?

If the fuzzy logic concept is used for evaluation of the investments in the undertaken power system project, the basic economic parameters, as NPV, PI and IRR are not yet the crisp numbers, but the fuzzy numbers defined by theirs membership function. The procedure of evaluation of the projects with fuzzy economical parameters is more complicated and not always unique. Therefore, it's much more appropriate to calculate degree of plausibility in which the project A is much more worthwhile then project B, or equivalently, degree of plausibility that fuzzy economic parameter of project A is greater/lower than fuzzy economic parameter of project B. Moreover, modelling of the subjective Investor's point of view for successful project may be also realized in fuzzy sense by appropriate fuzzy number.

Following the advanced engineering logic in a fuzzy sense, the further modification of the economic criteria for acceptance of the project will be done. That way, the Investors point of view in a decision making process (with include accepted level of risk) will be expressed by fuzzy numbers.

Thus, the fuzzified economic criteria for project evaluation in power system utilities shall be:

$$\mathbf{NPV = B - C > Fuzzy\_Zero} \quad (1)$$

$$\mathbf{PI = B / C > Fuzzy\_One} \quad (2)$$

$$\mathbf{IRR > Fuzzy\_IRR} \quad (3)$$

where:

Fuzzy _ Zero - fuzzy number for defining of the criteria for accepting the project according to the NPV method.

Fuzzy _ One - fuzzy number (fuzzy one) for defining of the criteria for accepting the project according the Benefit/Cost method.

Fuzzy _ IRR - fuzzy number which defines the minimal (fuzzy) acceptable rate of return (**MARR**) of the project.

Each of this numbers is subjective and intuitive. Construction of the fuzzy numbers is in whole depending on the way of reasoning of the decision maker. One possible graphical presentation of the fuzzy numbers **Fuzzy_Zero** and **Fuzzy_One**, with their corresponding membership functions are shown on Fig.1. and Fig. 2. Similar presentation could be done for fuzzy number **Fuzzy_IRR**.

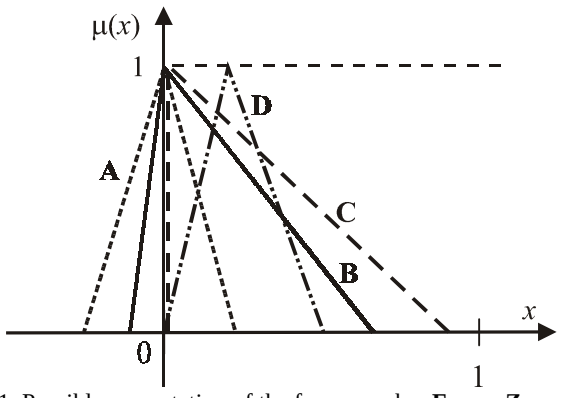

Fig.1. Possible presentation of the fuzzy number **Fuzzy_Zero** with triangular fuzzy numbers

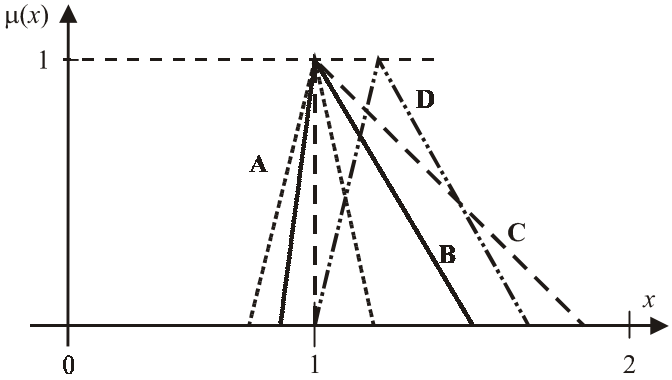

Fig.2. Possible presentation of the fuzzy number **Fuzzy_One** with triangular fuzzy numbers

Designed fuzzy numbers with triangular membership functions, shown on Fig. 1 and Fig. 2 could have the following *linguistic* description:

Fuzzy number **A** – accepting of the symmetrical risk in the project;

Fuzzy number **B** – accepting of the minimum risk with domination of the benefit from the project;

Fuzzy number **C** – zero risk and higher benefit;

Fuzzy number **D** – full rejecting of the risk with sure benefit for successful project.

III. RANKING THE FUZZY NUMBERS WITH SATISFACTION FUNCTION

Since the fuzzy numbers are described with a corresponding membership function, it is possible that the fuzzy numbers overlap, which makes the procedure of determining which fuzzy number is greater or lower than the other more difficult [4]. For example (Fig. 3), it is easy to conclude that fuzzy numbers **B** and **C** are larger than fuzzy number **A**. Otherwise, the comparison between fuzzy numbers **B** and **C** (Fig. 3) which are overlapping is not easy to perform and that is the reason why an appropriate procedure to work out a final decision is needed. Moreover, since two fuzzy numbers may overlap each others (like fuzzy numbers **B** and **C**), it is much more appropriate to talk about the degree of satisfaction of the fuzzy economic criteria than for strictly satisfaction of the economic conditions in classical form [4, 6].

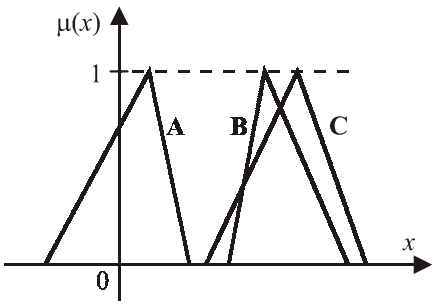

Fig. 3. Comparison between fuzzy numbers **A, B** and **C**

One of the most appropriate methods for comparison of two fuzzy numbers is the method based on the satisfaction function (SF) [2]. It determines the degree of satisfaction that fuzzy number **A** is greater than fuzzy number **B.** Thus, degree of satisfaction (degree of plausibility) that project (A) whose economic parameter is fuzzy number **A** is less worthy than project (B) described by fuzzy number **B** is:

$$S(\mathbf{A}<\mathbf{B})=\frac{\int_{-\infty}^{\infty}\int_{-\infty}^{y}\mu_{\mathbf{A}}(x)\circ\mu_{\mathbf{B}}(y)\mathrm{d}x\mathrm{d}y}{\int_{-\infty}^{\infty}\int_{-\infty}^{\infty}\mu_{\mathbf{A}}(x)\circ\mu_{\mathbf{B}}(y)\mathrm{d}x\mathrm{d}y} \tag{4}$$

Similarly, degree of satisfaction that project A is much more worth than project B (the fuzzy number **A** is greater than fuzzy number **B**) may be calculated by the following formula:

$$S(\mathbf{A}>\mathbf{B})=\frac{\int_{-\infty}^{\infty}\int_{y}^{\infty}\mu_{\mathbf{A}}(x)\circ\mu_{\mathbf{B}}(y)\mathrm{d}x\mathrm{d}y}{\int_{-\infty}^{\infty}\int_{-\infty}^{\infty}\mu_{\mathbf{A}}(x)\circ\mu_{\mathbf{B}}(y)\mathrm{d}x\mathrm{d}y} \tag{5}$$

In above equations " $\circ$ " is sign for T -norm operator, usually multiplication.

In cases where comparison between fuzzy and crisp number shall be performed, this formula have to be transformed. Thus, plausibility that the fuzzy number **A** is less than the crisp number k is given by:

$$S(\mathbf{A}<k)=\frac{\int_{-\infty}^{k}\mu_{\mathbf{A}}(x)\mathrm{d}x}{\int_{-\infty}^{\infty}\mu_{\mathbf{A}}(x)\mathrm{d}x} \tag{6}$$

while, plausibility that fuzzy number **A** is greater than crisp number k is:

$$S(\mathbf{A}>k)=\frac{\int_{k}^{\infty}\mu_{\mathbf{A}}(x)\mathrm{d}x}{\int_{-\infty}^{\infty}\mu_{\mathbf{A}}(x)\mathrm{d}x} \tag{7}$$

IV. Linguistic interpretation of satisfaction function for projects evaluation

Depending on the value of satisfaction function, which is used for comparison of the calculated economical parameter **A** of the project and adopted fuzzy number **B** for modelling the Investor's expectation for successful project, the following linguistic description could be suggested:

- If $S(\mathbf{A}>\mathbf{B})<0.15$, the project A is *significantly unsatisfactory* for investment;
- If $0.15\le S(\mathbf{A}>\mathbf{B})<0.30$, the project A is *very unsatisfactory* for investment;
- If $0.30\le S(\mathbf{A}>\mathbf{B})<0.45$, the project A is *unsatisfactory* for investment;
- If $0.45\le S(\mathbf{A}>\mathbf{B})\le 0.55$, the project A is *on the boundary* for profitable acceptance;
- If $0.55<S(\mathbf{A}>\mathbf{B})\le 0.70$, the project A *is favourable* for investment;
- If $0.70<S(\mathbf{A}>\mathbf{B})\le 0.85$, the project A is *very favourable* for investment; and
- If $0.,85<S(\mathbf{A}>\mathbf{B})\le 1$, the project A is *significantly favourable* for investment

V. Case Study: Project HPP St.Petka

Proposed approach for fuzzy evaluation of the hydroelectric project will be applied on the hydro project St. Petka (Republic of Macedonia). HPP St.Petka will be on the river Treska and it will be located between the HPP Kozjak (in construction) and the existing HPP Matka.

The main data of the HPP St.Petka are:

- Number of units 2
- Water discharge through turbines 2 x 40 m^3/s
- Net head 38.7 m
- Average water inflow in accumulation 21.89 m^3/s
- Average yearly production of electricity 60.27 GWh

Calculation of the expected yearly production of electricity from HPP St.Petka, is performed by a computer program based on the principle of a dynamical programming. It takes into account all relevant data and facts available in design phase [8], such as: design concept of the dam and machine hall, cascade type of system HPP Kozjak - HPP St.Petka - HPP Matka, irrigation and environmental limitations, characteristics of the units, friction losses, etc.

Construction costs are estimated on 30 millions $, and they are divided equally on the foreseen n-years for construction of the HPP St Petka.

For calculation of the fuzzy economic parameters of the project, discount rate is modelled by triangular fuzzy number $\mathbf{d}=(0{,}04;0{,}05;0{,}06)$, while the market price of electricity is $\mathbf{c}_1=(0{,}035;0{,}040;0.045)$ \$/kWh. It is considered that, the exploitation cost is 15% from the benefit obtained from electricity production.

Fuzzy economic parameters are calculated by methodology presented in [4]. Derived fuzzy economic parameters,

for Net Present Value (**NPV**), Profitability Index (**PI**) and Internal Rate of Return (**IRR**) of the specified project, are shown in Table1.

TABLE.I.
FUZZY ECONOMIC PARAMETERS OF THE HYDROELECTRIC PROJECT ST.PETKA DEPENDING ON THE YEARS OF CONSTRUCTION

Years of construction	Economic parameter		
	NPV	**PI**	**IRR**
3	[-4,08;3,14; 12,81]	[0,76; 1,10; 1,55]	[4,15; 5,23; 6,27]
4	[-4,62; 2,33; 11,78]	[0,74; 1,07; 1,54]	[4,11; 5,17; 6,20]
5	[-5,11; 1,57; 10,79]	[0,71; 1,05; 1,53]	[4,06; 5,12; 6,13]

Evaluation of the project parameter will be performed according calculated fuzzified Net Present Value, Profitability Index and Internal Rate of Return. In Tab.2 are shown results for project evaluation, when satisfaction function is calculated by (7). In this case fuzzy economic parameters are approximated by triangular fuzzy numbers.

TABLE II.
EVALUATION OF THE ECONOMIC PARAMETERS OF HYDRO PROJECT ST.PETKA DEPENDING ON THE YEARS OF CONSTRUCTION

Years of construction	Economic parameter		
	S **(NPV** > 0)	S **(PI** > 1)	S**(IRR** > 5%**)**
3	0.850	0,775	0,685
4	0.795	0,731	0,640
5	0.750	0,689	0,601

Presented results in Tab.2 show that according NPV and PI criteria hydro project St.Petka is a very favourable one for investment. According assumed value for IRR=5% the project belongs to the class of favourable projects for investment.

Next examples will ilustrate the concept in which the investor's point of view is modeled by triangular fuzzy number. Profitability Index of hydroelectric project St.Petka, given by triangular fuzzy number: $\mathbf{PI} = [0,76;1,10;1,55]$ will be compare with the fuzzy numbers which modeled the way of reasoning of the investor for:

- Accepting of a symmetrical risk (**PI_Inv_1**),
- Null risk and sure benefit (**PI_Inv_2**)
- Null risk and as much as bigger benefit (**PI_Inv_3**)

Calculated values for satisfaction function in these three cases are:

$$S(\mathbf{PI} > \mathbf{PI\_Inv1}) = \mathbf{S}\{[0,76;1,10;1,55] > [0,9;1;1,1]\} = 0,779$$

$$S(\mathbf{PI} > \mathbf{PI\_Inv2}) = \mathbf{S}\{[0,76;1,10;1,55] > [1;1,1;1,2]\} = 0,639$$

$$S(\mathbf{PI} > \mathbf{PI\_Inv3}) = \mathbf{S}\{[0,76;1,10;1,55] > [1;1,2;1,5]\} = 0,282$$

VI. CONCLUSION

In the proposed study fuzzufied economic criteria for evaluation of the investment in power system utilities are developed.

Investor's way of reasoning is modelled by fuzzy numbers: **Fuzzy_Zero**, **Fuzzy_One** and **Fuzzy_IRR**, depending on the specified economic criteria (NPV, PI or IRR) consequently. Each of this fuzzy number is subjective, intuitive and its definition is an attempt for modelling human decision making process. Depending on the value of the satisfaction function, linguistic descriptions for level of acceptance of the project is suggested.

Developed model is extension of the classical deterministic models and enables possibilities to perceive influence of the specific parameters and uncertainty to the rate of the undertaken project in power system utilities. It enables to perform simulation of various type of scenario which may include some external factors of the project, which could not be monetary quantified, or included in analyses in classical way.

The application of fuzzy-logic concept in model for energetic-economical evaluation of project in electric utilities, gives a special contribution to the up-to date engineer's upbringing, while making analyses without relevant data with multiple meaning.

VII. REFERENCES

[1] R.C. Himgins: Analysis for Financial Management, IRWIN, Homewood, Illinois 60430, 1989., pp. 205-279

[2] H. Lee-Kwang, J.Hyong Lee: A Method for Ranking Fuzzy Numbers and its Application to Decision Making, *IEEE Trans. on Fuzzy System*, Vol.7, No.6, December 1999, pp.677-685.

[3] A. Kaufman, M.M. Gupta, *Fuzzy Mathematical Models in Engineering and Management Science*, Amsterdam: Elsevier Science Publisher, 1988.

[4] A. M. Iliev, "Fuzzy logic approach for energetic and economic evaluation of hydroelectric projects" Ph.D. dissertation, University "St. Cyrill and Methodius", Faculty of Electrical engineering, Skopje, 2003.

[5] A. M. Iliev, V.V Fustik: Hydro Project Benefit Calculation in a Fuzzy Sense, Proceedings of Second Balkan Power Conference, BPC 2002, Beograd, 19-22 June 2002. pp.247-252.

[6] A. M. Iliev, V. V Fustik: Fuzzy Logic Approach for Hydroelectric Projects Evaluation, *IFAC Automatic Systems for Building the Infrastructure in Developing Countries, Third Int.Workshop, DECOM 2003*, Istanbul, June 26-28, 2003, pp.177-182.

[7] D. Kuchta, Fuzzy Capital budgeting, *Fuzzy Sets and Systems*, Vol. 111, Elsevier Science, pp.367-385, 2000.

[8] V. Fustik, A. Iliev, Z. Jakovlevski, V. Stojkovski, "Design concept of the machine hall and plant facilities in HPP St. Petka," Rev. *Energetic*, vol.32, Energetic Association of Macedonia, pp.24-29, Skopje, 03-2002.

[9] L. A. Zadeh: Fuzzy Sets and Application, Selected Papers by L.A. Zadeh, (Edited by R.R. Yager, S. Ovchinnikov, R.M. Tong and H.T. Nguyen), John Wiley & Sons, 1987.

Load Parameters in Low Voltage Distribution Networks

Lidija M. Korunovic[1], Dobrivoje P. Stojanovic[2] and Molodrag P. Kosarac[3]

Abstract – **Results of the experimental load model parameter determination on low voltage of distribution networks are shown in this paper. Static characteristic parameters of typical representatives of resistive load, indoor and outdoor lighting are determined and compared with literature data. Equivalent parameters of residential load and outdoor lighting are also obtained by measurements and compared with parameters of examined devices and literature data. Correlation of real and reactive power sensitivities on voltage and voltage value is analyzed.**

Keyword – **distribution network, load modeling, static characteristics**

I. INTRODUCTION

Exact load flow calculation is necessary for successful exploitation, control and planning of distribution networks. The accuracy of network condition calculation depends on the precision of input load parameter data. However, the value and component participation in the load, depends on the great number of factors: economic, social, climatic etc. Besides, distribution network loads vary during a day, depend on a day of a week and season and change in the exploitation period.

Therefore, many authors have investigated load models and determined concrete load model parameters. Although, the number of papers and professional books, which consider this subject, is large, the fact is that the exact determination of load characteristic is practically impossible, having in mind the change of load composition in time and number of load components.

According to the above-mentioned facts, load modeling is very important, but also a rather complex job. Even if the load composition is known, it will not be practical to present every load component separately, because there are plenty of components in the total system load. Therefore, the total load is being aggregated [1], and significant simplifications are being performed for load presentation [2].

All load models can be divided into two groups, static and dynamic, and their application depends on concrete problem.

[1]Lidija M. Korunovic is with the Faculty of Electronic Engineering, Beogradska 14, 18000 Nis, Serbia and Montenegro, E-mail: lidijak@elfak.ni.ac.yu

[2]Dobrivoje P. Stojanovic is with the Faculty of Electronic Engineering, Beogradska 14, 18000 Nis, Serbia and Montenegro, E-mail: dstojanovic@elfak.ni.ac.yu

[3]Milodrag P. Kosarac is with Joint Power Coordination Center Sarajevo, H. Cemerlica 2, 71000 Sarajevo, Bosnia and Herzegovina, E-mail: mkosarac@hotmail.com

Static models are used for steady-state condition calculations, but also for dynamic phenomena if the load bus encloses small part of electrical drives. Dynamic models are used for modeling of load that mostly consist of asynchronous and synchronous motors, air conditioners, as well as for research of lighting and thermostatically controlled load transients.

Most frequently used static models: exponential, polynomial and linear with neglected frequent dependence are considered in Section 2 of this paper. Having in mind the fact that load model parameters differ for certain low voltage devices and distribution network nodes [1, 3-8], these are empirically determined. Measurements are performed by means of power analyzer D 5135 - "NORMA".

II. MOST FREQUENTLY USED LOAD MODELS

Static load models express load characteristics at a certain moment as the functions of voltage value and frequency. This load models can be divided into several groups: exponential, polynomial, complex, fuzzy logic model [7, 8, 9]. Here will be presented only most frequently used ones.

Traditionally, load dependence on voltage and frequency is presented by exponential model. Network voltage is commonly varied much more than frequency. Therefore, frequency dependence can be ignored:

$$P = P_n \left(\frac{U}{U_n} \right)^{k_{pu}}, \quad (1)$$

$$Q = Q_n \left(\frac{U}{U_n} \right)^{k_{qu}}, \quad (2)$$

where

P and Q - real and reactive power at voltage U,

P_n and Q_n - real and reactive power of load at nominal voltage U_n,

k_{pu} and k_{qu} - selfregulation coefficients of real and reactive power.

When both exponents in the model (1) and (2) are equal to 0, 1 or 2, the load is of constant power, constant current or constant impedance type, respectively.

The selfregulation coefficients of this exponential model, k_{pu} and k_{qu}, show the percentage variations of real and reactive power, respectively, for the percentage of voltage change in the nominal voltage proximity [6]. Therefore, k_{pu} and k_{qu} can be named partial derivatives of real and reactive power with respect to voltage [1], or sensitivity coefficients [9].

Model, which is also frequently used for voltage dependence on load, is polynomial model. The second order polynomial model is most frequently used because the

approximation with higher order polynomial does not contribute to more exact load modeling, because during experimental or calculation static characteristic determination, certain mistakes are made. Widely used polynomial model is:

$$P = P_n\left[p_1\left(\frac{U}{U_n}\right)^2 + p_2\left(\frac{U}{U_n}\right) + p_3\right], \quad (3)$$

$$Q = Q_n\left[q_1\left(\frac{U}{U_n}\right)^2 + q_2\left(\frac{U}{U_n}\right) + q_3\right]. \quad (4)$$

The common name of this model is *ZIP* model, considering its composition of constant impedance (*Z*), constant current (*I*) and constant power (*P*) loads. If the total load is of constant impedance type, the coefficients are $p_1=q_1=1$, while all other are equal to zero. Load type of constant current is modeled by means of $p_2=q_2=1$ and constant impedance by means of $p_3=q_3=1$, while other coefficients are equal to zero.

III. Measurement Results

In order to determine load model parameters at 0.4kV voltage level, laboratory and field measurements that imply supply voltage variation are performed. The frequency was not measured, because this variable changed in a narrow proximity of its nominal value. Therefore, it was considered that all real and reactive power changes were due to voltage variations. Every experiment is repeated several times and static characteristics are obtained by the second order polynomial fitting using the least square method and network nominal voltage as base value. Then, partial derivatives of real and reactive power with respect to voltage, for different voltage values, are calculated.

Equivalent load static characteristics of one residential building and outdoor lighting are obtained. Also, components of these equivalent loads are chosen for experiments among plenty of low voltage devices. These are "typical" representatives of resistive load, indoor and outdoor lighting. Data of the devices are given in Appendix.

Static characteristic of single phase electric heater and hot plate real power are obtained in the voltage range $U \in [0.8-1.1\text{p.u.}]$:

$$P = -0.148 + 0.373\cdot U + 0.775\cdot U^2, \quad (5)$$

$$P = 0.251 - 0.473\cdot U + 1.222\cdot U^2, \quad (6)$$

and depicted in Fig. 1. These characteristics have dominant coefficient of square term. Fig. 2 shows partial derivatives of real powers with respect to voltage, i.e. real power sensitivities on voltage, $\partial P/\partial U$. Under nominal voltage these sensitivities are 1.92 and 1.97, respectively. In the literature [1, 3, 5-7], $\partial P/\partial U$ of resistive devices is specified as 2, which corresponds to constant impedance load type. Although the declinations of the sensitivities obtained by measurements from number 2 are mostly 4%, the results of these experiments show that constant impedance load type can not characterize even resistive devices.

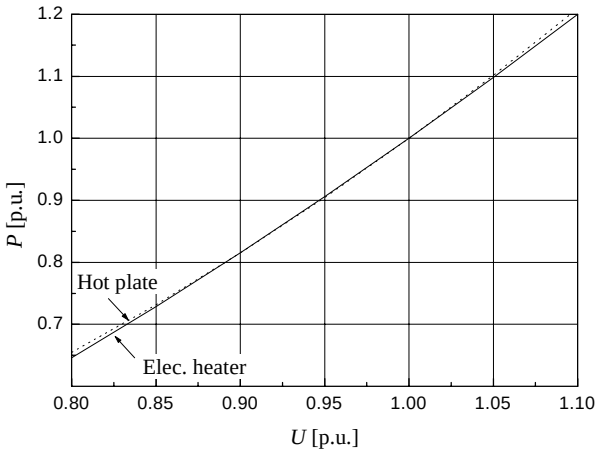

Fig. 1. Static characteristics of resistive load

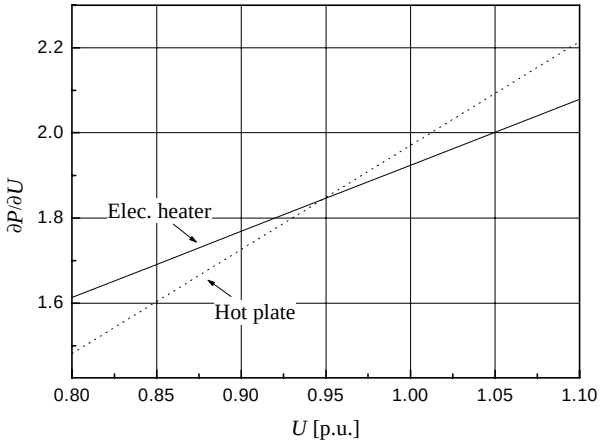

Fig. 2. Real power sensitivity on voltage of resistive load

Real power sensitivity on voltage of both devices changes with voltage variations, because their resistance changes with temperature. Thus, with voltage variation from 0.8 to 1.1p.u., sensitivity changes within the range 1.61-2.08 for electric heater and 1.48-2.21 for hot plate. This fact may be important when exponential load model, Eqs. (1) and (2), is used in the wide voltage range and therefore cause calculation mistakes.

Fluorescent lamp static load characteristics are

$$P = -0.102 + 0.511\cdot U + 0.592\cdot U^2, \quad (7)$$

$$Q = 3.495 - 9.574\cdot U + 7.081\cdot U^2 \quad (8)$$

in the voltage range $U \in [0.8-1.1\text{p.u.}]$. These are depicted in Fig. 3. On the basis of these polynomials, real and reactive power sensitivities on voltage are 1.69 and 4.67, respectively, in the close proximity on nominal voltage. These values are close to data specified in [2] for fluorescent lamp, but totally different from other literature values. For example, 0.96 and 7.4 are specified in [5]. According to the first derivative of Eq. (7) real power sensitivity coefficient changes from 1.46 to

1.82 with voltage variation from 0.8 to 1.1p.u. Reactive power sensitivity on voltage changes significantly, from 1.45 to 6.32 for the same voltage variation, owing to the larger square term coefficient. Declination of 1.45 from reactive power sensitivity on voltage in the proximity of U_n is even 69%.

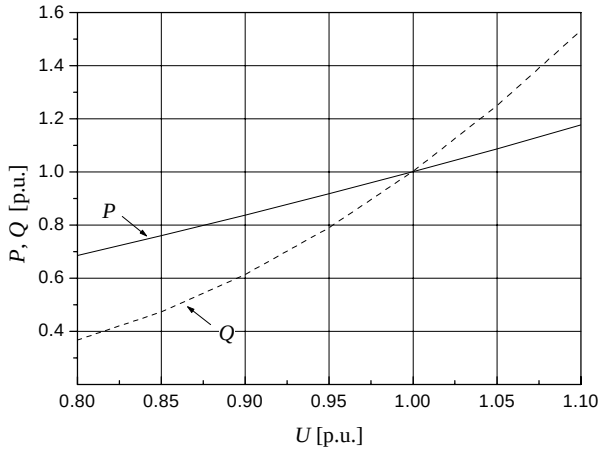

Fig. 3. Fluorescent lamp
real and reactive power dependence on voltage

The experiments are also carried out on mercury lamps for outdoor lighting of 125 and 250W rated power. These are denoted as lamp 1 and lamp 2, respectively. Static characteristics are specified in Table I and depicted in Fig. 4.

TABLE I

MERCURY LAMP STATIC CHARACTERISTICS FOR $U \in [0.85-1.1\text{p.u.}]$

Lamp Type	$P = F_1(U)$	$Q = F_2(U)$
Lamp 1	$-0.831+1.254\cdot U+0.577\cdot U^2$	$0.914 - 3.212 \cdot U + 3.299 \cdot U^2$
Lamp 2	$-2.027+3.769\cdot U-0.741\cdot U^2$	$-0.015 + 0.719 \cdot U + 1.302 \cdot U^2$

It may be noted that graphics of lamp 1 and 2 static characteristics are mutually similar. According to real power static characteristics of the lamps, linear term is dominant, and the dependence on voltage is approximately straight line. In the Eqs. of reactive power static characteristics, third term coefficient is greatest and the curves have parabolic shape.

Real power sensitivity on voltage in the proximity of nominal voltage is 2.41 and 2.29, for mercury lamp 1 and 2, respectively, and these values are close to the value specified in [3]. This coefficient is larger than the sensitivity of fluorescent lighting. Reactive power sensitivities in the proximity of rated voltage are 3.38 and 3.32 and significantly are higher than value in [3]. Real power sensitivities weakly change and opposite, reactive power sensitivities significantly change with voltage due to static characteristic shapes – nearly straight lines and parabolas. Power factors of mercury lamps are 0.55 and 0.58 because examined lamps operate without capacitor. Power factor of fluorescent lamps is significantly greater - 0.87. It was observed that power factor of both lamp types increases with voltage reduction and vice versa.

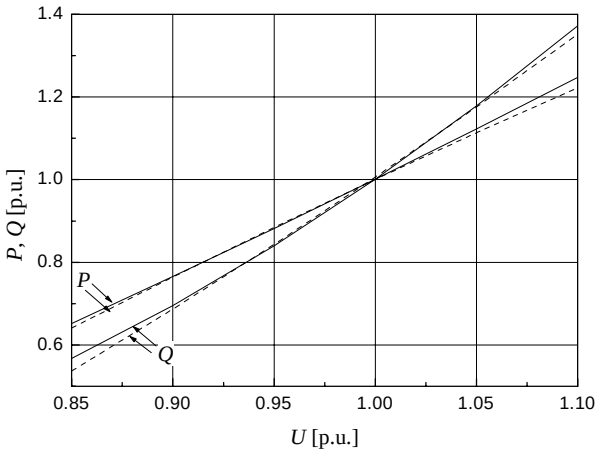

Fig. 4. Real and reactive power dependence on voltage
of mercury lamp 1 (————) and 2 (- - - - - -

Real and reactive power sensitivities show that none of examined devices belongs to the constant power, constant current or constant impedance load type. Also, the analysis reveals that these sensitivities are not constants and vary with voltage.

In next paragraphs, the experiment results of equivalent load static characteristics determination at 0.4kV voltage level are presented.

The measurements of total load of one residential building are performed during summer working day noon. This building also includes five offices. The voltage was varied by means of load tap changer at 110/35/10kV supply transformer station (Sarajevo 2).

Obtained static characteristics, in the voltage range $U \in [0.9-1.1\text{p.u.}]$ are

$$P = -0.575 + 1.324 \cdot U + 0.2506 \cdot U^2, \qquad (9)$$

$$Q = 5.0815 - 13.068 \cdot U + 8.986 \cdot U^2. \qquad (10)$$

These are presented in Fig. 5. Real and reactive power sensitivities on voltage in the proximity of nominal voltage are 1.83 and 3.81, respectively and power factor of the examined load is 0.979. In [5], for residential load class during summer are specified totally different values, $\partial P/\partial U = 1.2$, $\partial Q/\partial U = 2.9$ and $\cos\varphi = 0.9$. This may be explained by significant variety of load composition in different distribution networks that depends of economic, social, climatic and other factors. For example, in many countries, usage of air conditioners in summer increases. Their participation in total load influence on equivalent parameters and decrease them because typical parameters of window type air conditioner are $\partial P/\partial U = 0.468$, $\partial Q/\partial U = 2.5$ and $\cos\varphi = 0.82$ [5].

Experimentally obtained values of real power sensitivity on voltage and power factor, 1.83 and 0.979, confirm that non-resistive load participate in equivalent load. In the range 0.9-

$1.1U_n$, real power sensitivity on voltage changes from 1.78 to 1.88. Reactive power sensitivity varies in the wide range from 2.18 to 5.43 that exceeds ±42% of 3.81.

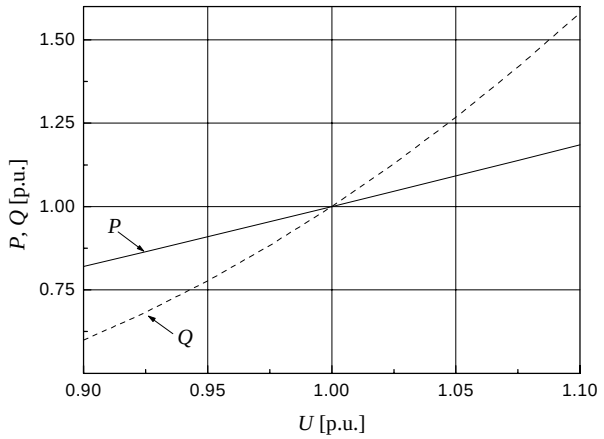

Fig. 5. Static characteristics of residential building load

The outdoor lighting load was simulated by 13 mercury lamps of 400W at each phase. These lamps are used as indoor lighting of IRCE High Voltage Laboratory in Sarajevo. The obtained static characteristics are

$$P = -1.630 + 2.572 \cdot U + 0.058 \cdot U^2, \qquad (11)$$

$$Q = 0.629 - 3.354 \cdot U + 3.725 \cdot U^2, \qquad (12)$$

and depicted in Fig. 6. Real and reactive power sensitivities on voltage for nominal voltage are 2.69 and 4.1, respectively, and power factor of the lighting is 0.7. Since real power characteristic is nearly straight line, real power sensitivity on voltage changes in narrow range from 2.68 to 2.7 for supply voltage from 0.9 to $1.1U_n$. Reactive power sensitivity on voltage changes from 3.35 to 4.84, i.e. declination from 4.1 is approximately 18%.

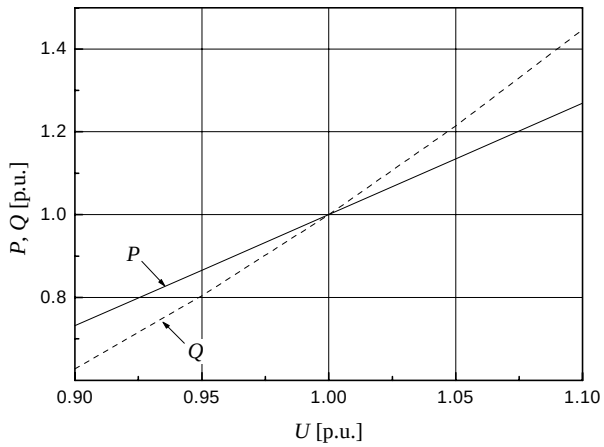

Fig. 6. Static characteristics of outdoor lighting

IV. Conclusion

The results of the paper show that none of the examined low voltage electric devices – representatives of resistive load, indoor and outdoor lighting belongs to the constant power, constant current or constant impedance load type. Real and reactive power sensitivities on voltage of these devices, of equivalent residential load and outdoor lighting, load differ from literature data. This points out the necessity of experimental load parameter determination and afterwards their incorporation in distribution network calculation. Also, real and reactive power sensitivities on voltage vary with voltage value and in some cases this variation is significant. It may cause larger calculation errors when exponential load model is used.

References

[1] J. Ribeiro, F. Lange, "A New Aggregation Method for Determining Composite Load Characteristics", *IEEE Trans. on Power Apparatus and Systems*, vol. PAS-101, no. 8, pp. 2869-2875, 1982.

[2] T. Thiringer, J. Luomi, "Comparison of Reduced-Order Dynamic Models of Induction Machines", *IEEE Trans. on Power Delivery*, vol. 16, no. 1, pp. 119-126, 2001.

[3] C. Concordia, S. Ihara, "Load Representation in Power System Stability Studies", *IEEE Trans. on Power Apparatus and Systems*, vol. PAS-101, no. 4, pp. 969-977, 1982.

[4] Н. Маркушевич, *Регулирование напряжения и экономия электроэнергии*, Москва, Энергоатомиздат, 1984.

[5] P. Kundur, *Power System Stability and Control*, New York, Mc Graw-Hill, 1994.

[6] C. Taylor, *Power System Voltage Stability*, New York, Mc Graw-Hill, 1994.

[7] W. Price, K. Wirgau, A. Murdoch, J. Mitsche, E. Vaahedi and M. El-Kady, "Load Modeling for Power Flow and Transient Stability Computer Studies", *IEEE Trans. on Power Systems*, vol. 3, no. 1, pp. 180-187, 1988.

[8] IEEE Task Force on Load Representation for Dynamic Performance, "Bibliography on Load Models for Power Flow and Dynamic Performance Simulation", *IEEE Trans. on Power Systems*, vol. 10, no. 1, pp. 523-538, 1995.

[9] L. Korunovic, D. Stojanovic, "Load Modeling in Distribution Networks", *Facta Universitatis (Nis), Ser.: Elec. Energ.* vol 15, no. 3, pp. 419-427, 2002.

Appendix

Resistive devices:

1. electric heater: type БДС 2099-85, P_n =1,6 kW, U_n =220 V, f_n=50 Hz, ЕЛІВА КВАРЦ – Bulgaria,
2. hot plate: type PR13, P_n =700 W, U_n =220 V, f_n=50 Hz, FVUE FERIZAJ – Urosevac, Serbia & Montenegro.

Lighting:

1. fluorescent lamps: type FC 40 W, DS 6500°K , U_n =220 V, f_n =50 Hz, TESLA – Pancevo, Serbia & Montenegro,
2. mercury lamps:
   - HPL-N 125 W, PHILIPS, Made in Belgium,
   - HPL-N 250 W, PHILIPS, Made in Belgium.

The Influence of Uncertain Load Parameter Data on Distribution Network Power Flow Results

Lidija M. Korunovic[1] and Dobrivoje P. Stojanovic[2]

***Abstract* – The influence of uncertain load parameter data on power flow results of radial middle-voltage distribution network is treated in this paper. The load flow calculation is performed on the basis of fuzzy logic, modeling load levels and real and reactive power sensitivities on voltage as fuzzy numbers. The parameters of fuzzy number functions are obtained using measurement data. The influences of supply voltage value and power sensitivities on voltage on the results are discussed.**

***Keyword* – power flow, distribution network, fuzzy logic, load parameters**

I. INTRODUCTION

Many papers have been dedicated to middle-voltage distribution network calculation. Necessary input data for this calculation are load parameters. However, these parameters are poorly known by rule, and they assuredly cause result mistakes. Therefore, great number of papers deals with load parameter determination [1, 2]. The number of paper destining a fuzzy logic approach to distribution network calculation increases, because uncertainty of load parameters can be taken into account in this way. The results of the calculation: load flows, branch currents, bus voltages, and power losses are fuzzy numbers that give the ranges of observed variables for every confidence level.

A fuzzy logic approach to load flow calculation of radial distribution networks is presented in [3]. This paper is based on the assumptions that the load at every node is a fuzzy variable with associated trapezoidal membership function and real and reactive power sensitivities on voltage are constants. Load representation by trapezoidal membership functions is capable when load data are obtained using utility worker experience. If a number of daily load curve measurements are available [4], the curve can be divided into five levels, and the load at each level modeled as one fuzzy variable. Since daily load curves are different for various load classes: residential, commercial and industrial, the measurements are performed at typical network buses, and results extrapolated to other buses that feed load of the same class.

There are different defuzzification methods, but it was found that the numbers obtained in this way are of low importance for engineers. Therefore, method for uncertainty level determination of fuzzy numbers on the basis of weighted intervals is suggested in [5]. It yields the bounds that are most reasonable for engineering decisions.

This paper models load values, as well as real and reactive power sensitivities on voltage as fuzzy variables. The assumptions are that daily load curves for different load classes are obtained by a number of measurements, and experiments of changing supply voltage for determining real and reactive power sensitivities on voltage are carried out. The results of power flow calculation in different operating conditions are analyzed on the example of IEEE test-network with 32 buses [6].

[1]Lidija M. Korunovic is with the Faculty of Electronic Engineering, Beogradska 14, 18000 Nis, Serbia and Montenegro, E-mail: lidijak@elfak.ni.ac.yu

[2]Dobrivoje P. Stojanovic is with the Faculty of Electronic Engineering, Beogradska 14, 18000 Nis, Serbia and Montenegro, E-mail: dstojanovic@elfak.ni.ac.yu

II. BASES OF FUZZY SET THEORY

A fuzzy set can be interpreted as a set of continual confidence intervals $A^{(\alpha)}$ which determine greater and greater uncertainty ranges with descending confidence levels. Confidence interval $A^{(\alpha)}$ can be defined as

$$A^{(\alpha)} = \left\{ x \in X : \ \mu_{\tilde{A}}(x) \geq \alpha \right\}. \tag{1}$$

It means that all values of fuzzy variable belonging to the interval $A^{(\alpha)}$ can be concerned possible with confidence level that is greater or equal to α. Confidence interval $A^{(\alpha)}$ has its lower and upper bound, $A^{(\alpha)} = \left[a_1^{(\alpha)}; a_2^{(\alpha)} \right]$, where $\alpha \in [0,1]$. Since $A^{(\alpha)}$ is decaying function of α, for every pair $\alpha_1, \alpha_2 \in [0,1]$

$$(\alpha_2 > \alpha_1) \ \Rightarrow \ A^{(\alpha_2)} \subset A^{(\alpha_1)}. \tag{2}$$

Therefore, basic arithmetic operations on fuzzy sets can be regard as generalization of interval arithmetic [7]. These arithmetic interval operations for every confidence level ($\alpha \in [0,1]$) and fuzzy sets $\tilde{A}$ and $\tilde{B}$ are:

$$\tilde{C} = \tilde{A}(+)\tilde{B} = \left[a_1^{(\alpha)} + b_1^{(\alpha)}; \ \ a_2^{(\alpha)} + b_2^{(\alpha)} \right], \tag{3}$$

$$\tilde{C} = \tilde{A}(-)\tilde{B} = \left[a_1^{(\alpha)} - b_2^{(\alpha)}; \ \ a_2^{(\alpha)} - b_1^{(\alpha)} \right], \tag{4}$$

$$\tilde{C} = \tilde{A}(\cdot)\tilde{B} = \left[a_1^{(\alpha)} \cdot b_1^{(\alpha)}; \ \ a_2^{(\alpha)} \cdot b_2^{(\alpha)} \right], \tag{5}$$

$$\tilde{C} = \tilde{A}(:)\tilde{B} = \left[a_1^{(\alpha)} / b_2^{(\alpha)}; \ \ a_2^{(\alpha)} / b_1^{(\alpha)} \right]. \tag{6}$$

In this paper, following interval operations are also used for each α:

$$\tilde{C} = \tilde{A}^{\tilde{B}} = \left[\min a_i^{b_j};\ \max a_i^{b_j}\right],\quad i,j=1,2, \qquad (7)$$

$$\left|\tilde{C}\right| = \left[\min\left(c_{Ri}^2 + c_{Ij}^2\right)^{1/2};\ \max\left(c_{Ri}^2 + c_{Ij}^2\right)^{1/2}\right],\ i,j=1,2. \qquad (8)$$

Here a_i and b_j are the bounds of confidence interval, $A^{(\alpha)}$ and $B^{(\alpha)}$, respectively, and c_{Ri} and c_{Ij} are the bounds of $C_R^{(\alpha)}$ and $C_I^{(\alpha)}$ that are confidence intervals of complex variable real and imaginary parts.

III. Load Parameter FN Functions

The assesment is that the load at 10kV voltage level can be devided into classes. Mean daily load curves of each class are obtained from great number of measurements during certain season and can be extrapolated to other nodes with load of the same class. However, declinations of these curves are objectivelly possible. Therefore, it is advicable to use lingvistic description of load level for every class expressed as percentage of transformer rated power: very small (VS) - 0-20%S_n, small (S) - 20-40%S_n, middle (M) - 40-60%S_n, large (L) 60-80%S_n, and very large (VL) - 80-100%S_n. Then, fuzzy variable x assigned to each load level and each load class may be modeled as normalized fuzzy number (FN) as depicted in Fig. 1. Kernel X_K of this triangular FN denotes mean value obtained from daily load curve for corresponding load level. Lower and upper bounds, X_{0l} and X_{0u}, are specified in previous paragraph for each load level. Interval of possible values of x with lower and upper bound, $X_{\alpha l}$ and $X_{\alpha u}$, is assigned to every confidence level.

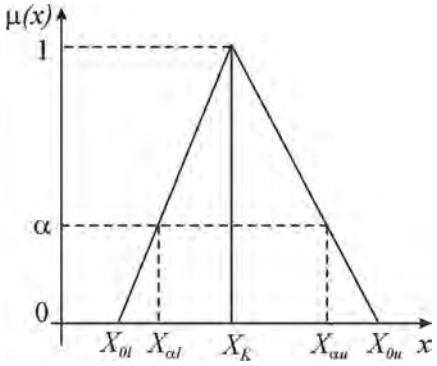

Fig. 1. Characteristic function of a FN

Also, fuzzy numbers can be assigned to real and reactive power sensitivities on voltage. Their bounds are minimal and maximal values obtained by measurements at different day intervals at nodes with certain load class. Kernels are mean values of real and reactive load sensitivities on voltage.

The uncertainty grade of every variable x, which is presented as fuzzy number in Fig. 1, may be determined as

$$UG = \frac{100}{X_K}\int_0^1 \left(X_{\alpha u} - X_{\alpha l}\right)(1-\alpha)\,d\alpha\,. \qquad (9)$$

It gives the interval of variable x values obtained by weighting all possible intervals of variable values by the uncertainty levels characterizing these intervals. Lower and upper bound relative declinations of X_K are

$$LU = \frac{100}{X_K}\int_0^1 \left(X_K - X_{\alpha l}\right)(1-\alpha)\,d\alpha\,, \qquad (10)$$

$$UU = \frac{100}{X_K}\int_0^1 \left(X_{\alpha u} - X_K\right)(1-\alpha)\,d\alpha\,. \qquad (11)$$

On the basis of former definitions, $LU+UU=UG$. Finally following bounds for variable x values may be taken as most reasonable for engineering decisions made under uncertainty

$$X_K\left(1-\frac{LU}{100}\right) \le x \le X_K\left(1+\frac{UU}{100}\right). \qquad (12)$$

IV. Algorithm

Input parameters for radial distribution network load flow calculation are: 1. Load class parameters – histogramic daily load curves, real and reactive power sensitivities on voltage obtained by measurements and power factor of every load class; 2. Network parameters – source voltage, sending and receiving node of each branch, its resistance and reactance, transformer rated power and class of the load connected to the branch receiving node.

The following algorithm can describe the calculation procedure:

1. FN function parameters, X_K, X_{0l} and X_{0u}, of five load levels are determined for every load class (mostly five). FN function parameters of real and reactive load sensitivities on voltage are provided for every load class;
2. For specified hour of the day, on the basis of daily load curves and load class distribution among network nodes, one FN function of load level is assigned to each consumer. FN functions of real and reactive power sensitivities on voltage are assigned to each consumer according to the load class connected to the node;
3. Flat voltage profile is adopted, and confidence level α is set to zero;
4. Lower and upper bounds of load level and bounds of real and reactive power sensitivities on voltage are determined for α at each network node regarding FN function parameters obtained in step 1. Following calculation is performed on the basis of Eqs. (3) – (8);
5. In ν^{th} iteration, load current components are calculated according to formulae

$$I_{pR}(i)^{(\alpha)\nu} = \frac{P_{pp}(i)^{(\alpha)\nu-1}\cdot U_R(i)^{(\alpha)\nu-1} + Q_{pp}(i)^{(\alpha)\nu-1}\cdot U_I(i)^{(\alpha)\nu-1}}{\left(U_R(i)^{(\alpha)\nu-1}\right)^2 + \left(U_I(i)^{(\alpha)\nu-1}\right)^2}, \qquad (13)$$

$$I_{pI}(i)^{(\alpha)\nu} = \frac{P_{pp}(i)^{(\alpha)\nu-1}\cdot U_I(i)^{(\alpha)\nu-1} - Q_{pp}(i)^{(\alpha)\nu-1}\cdot U_R(i)^{(\alpha)\nu-1}}{\left(U_R(i)^{(\alpha)\nu-1}\right)^2 + \left(U_I(i)^{(\alpha)\nu-1}\right)^2}, \qquad (14)$$

where $I_{pR}(i)^{(\alpha)\nu}$ and $I_{pI}(i)^{(\alpha)\nu}$ are real and imaginary components of i^{th} node load current, $U_R(i)^{(\alpha)\nu-1}$ and $U_I(i)^{(\alpha)\nu-1}$ are real and imaginary voltage components from previous iteration, and $P_{pp}(i)^{(\alpha)\nu-1}$ and $Q_{pp}(i)^{(\alpha)\nu-1}$ real and reactive power of the load from previous iteration. These powers are calculated with respect of real and reactive power at rated voltage ($P_p(i)^{(\alpha)}$ and $Q_p(i)^{(\alpha)}$), absolute voltage value at the node from previous iteration ($U(i)^{(\alpha)\nu-1}$) and sensitivities of real and reactive power on voltage corresponding the load connected to i^{th} node ($k_{pu}(i)$ and $k_{qu}(i)$)

$$P_{pp}(i)^{(\alpha)\nu-1} = P_p(i)^{(\alpha)} \cdot \left(\frac{U(i)^{(\alpha)\nu-1}}{U_n} \right)^{k_{pu}(i)}, \quad (15)$$

$$Q_{pp}(i)^{(\alpha)\nu-1} = Q_p(i)^{(\alpha)} \cdot \left(\frac{U(i)^{(\alpha)\nu-1}}{U_n} \right)^{k_{qu}(i)}; \quad (16)$$

6. Branch current components are obtained starting from the end toward the source node

$$I_R(i)^{(\alpha)\nu} = I_{pR}(i)^{(\alpha)\nu} + \sum_{j \in J} I_R(j)^{(\alpha)\nu}, \quad (17)$$

$$I_I(i)^{(\alpha)\nu} = I_{pI}(i)^{(\alpha)\nu} + \sum_{j \in J} I_I(j)^{(\alpha)\nu}, \quad (18)$$

where J is the set of branches that are directly feed from i^{th} node;

7. Voltages are calculated starting from the source node towards the end one

$$U_R(i)^{(\alpha)\nu} = U_R(j)^{(\alpha)\nu} - \left(R(i) I_R(i)^{(\alpha)\nu} - X(i) I_I(i)^{(\alpha)\nu} \right), \quad (19)$$

$$U_I(i)^{(\alpha)\nu} = U_I(j)^{(\alpha)\nu} - \left(R(i) I_I(i)^{(\alpha)\nu} + X(i) I_R(i)^{(\alpha)\nu} \right), \quad (20)$$

where j is the sending node of a branch i, and $R(i)$ and $X(i)$ are i^{th} branch resistance and reactance;

8. Iterative procedure is finished when the differences between lower (1) and upper (2) bounds of the confidence interval for real and imaginary voltage components in two neighbourhood iterations are less or equal to specified number ε

$$\left| U_{R1(2)}(i)^{(\alpha)\nu} - U_{R1(2)}(i)^{(\alpha)\nu-1} \right| \le \varepsilon, \; i = 1,\ldots,N, \quad (21)$$

$$\left| U_{I1(2)}(i)^{(\alpha)\nu} - U_{I1(2)}(i)^{(\alpha)\nu-1} \right| \le \varepsilon, \; i = 1,\ldots,N. \quad (22)$$

Then, α is increased by $\Delta\alpha$, and calculation continues with step 4. If conditions are not fulfilled, go to step 5;

9. If $\alpha > 1$, FN functions of certain output variables are plotted. Uncertainty grade and bounds of these variables are calculated according to Eqs. (9) – (12). If $\alpha \le 1$, go to step 4.

Based on this algorithm, estimation of daily real and reactive energy losses may be realized, too.

V. RESULTS

The calculations are performed in different operating conditions of distribution IEEE test-network with 32 buses. For easier result comparison here is presented results of the cases when all network consumers belong to the same class – daily load curve and real and reactive power sensitivities on voltage are the same.

It is assumed that the load belongs to large (L) level. Lower and upper bounds for proper FN function are 0.6 and 0.8, respectively, and data from daily load curve yield the kernel value amounts 0.675. Literature data provide different real and reactive power sensitivities on voltage. However, here are presented results for those that characterize constant power, constant current or constant impedance load type (k_{pu}=k_{qu}=0, 1 or 2, respectively). The results for sensitivities as deterministic values are compared with the cases when sensitivities are modeled as fuzzy numbers with:

1. X_K =0, LU=-0.5 and UU=0.5,
2. X_K =1, LU=0.5 and UU=1.5,
3. X_K =2, LU=1.5 and UU=2.5.

The supply voltage is modeled as deterministic variable for easier inference and it is varied in the wide range from $0.95U_n$ to $1.1U_n$.

In Figs. 2, and 3, current of the first branch for real and reactive power sensitivities on voltage modeled as deterministic variables and as fuzzy numbers are presented. Supply voltage of the results in Figs. 2 and 3 is assumed to be $1.1U_n$ and $0.95U_n$, respectively. Both figures present the spread of FN functions - increase of uncertainty grade when sensitivity coefficients are fuzzy numbers. Also, the greatest first branch current for supply voltage $1.1U_n$ is when the load is of constant impedance type, while for $0.95U_n$ it is for constant power load type. It was found that the network is practically indifferent on load type when supply voltage is $1.05U_n$, because in this case the average bus voltage in the network is U_n. In this case kernel values of I_{max} differ less than 1.93% from kernel mean value (134.54A) obtained for mentioned load types. These declinations exceed 6.6% for $1.1U_n$ and 8.2% for $0.95U_n$.

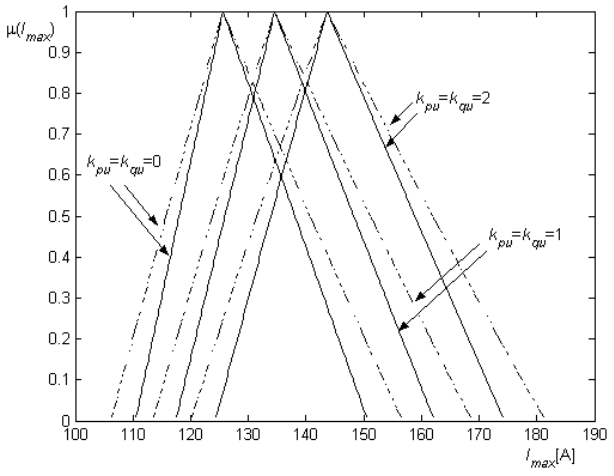

Fig. 2. I_{max} for U_0=$1.1U_n$ and power sensitivities on voltage as deterministic (———) and fuzzy variables (– · – · – ·)

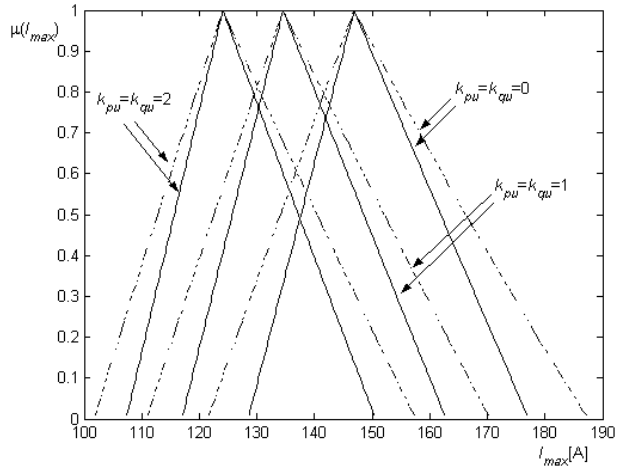

Fig. 3. I_{max} for U_0=0.95U_n and power sensitivities on voltage as deterministic (———) and fuzzy variables (– · – · – ·)

TABLE I

CALCULATION RESULTS

Quan-tity	U_0	Power sensitivities	Determin. or fuzzy	Kernel	*LU*	*UG*
I_{max} [A]	1.1	$k_{pu}=k_{qu}=0$	Determin.	125.6	3.98	10.54
			Fuzzy	125.6	5.12	13.15
		$k_{pu}=k_{qu}=2$	Determin.	143.67	4.46	11.45
			Fuzzy	143.67	5.49	14.00
	0.95	$k_{pu}=k_{qu}=0$	Determin.	146.86	4.13	10.89
			Fuzzy	146.86	5.71	14.59
		$k_{pu}=k_{qu}=2$	Determin.	124.07	4.46	11.45
			Fuzzy	124.07	5.96	14.73
U_{min} [p.u.]	1.1	$k_{pu}=k_{qu}=0$	Determin.	0.9591	0.29	0.46
			Fuzzy	0.9591	0.34	0.56
		$k_{pu}=k_{qu}=2$	Determin.	0.9542	0.35	0.58
			Fuzzy	0.9542	0.42	0.69
	0.95	$k_{pu}=k_{qu}=0$	Determin.	0.9444	0.41	0.67
			Fuzzy	0.9444	0.56	0.93
		$k_{pu}=k_{qu}=2$	Determin.	0.9542	0.35	0.58
			Fuzzy	0.9542	0.45	0.77

Numerical results of first branch current (I_{max}) and electrically most distant node voltage (U_{min}) for 1.1U_n and 0.95U_n supply voltage and power sensitivities on voltage as deterministic and fuzzy variables are presented in Table I. These results show noticeable increases of uncertainty grade and lower and upper bound declinations when power sensitivities on voltage are treated as fuzzy numbers. For example, *UG* of I_{max} changes more than 2.5%, while *LU* and *UU* change more than 1 and 1.5%. As real power losses are functions of square currents, increases of their *UG*, *LU* and *UU* are significantly greater and exceed approximately 2%, 3% and 5%, respectively. All mentioned increases would be more important under assumption that measurement based data of real and reactive power sensitivities on voltage in various seasons are not available. Also, results of the paper show that uncritical usage of literature data of these sensitivities can cause unacceptable power flow result mistakes.

VI. CONCLUSION

Presented distribution network load flow calculation treat uncertain load parameters as fuzzy numbers. Calculation results are the most reasonable ranges of output data. They show essential importance of real and reactive power sensitivities on voltage and supply voltage value on load flow results. Modeling of real and reactive power sensitivities on voltage as fuzzy numbers causes significant increase of uncertainty grade and lower and upper bound declinations of load flow output data. Suggested methodology may be used for energy loss estimation.

REFERENCES

[1] L. Hajagos, B. Danai, "Labaratory Measurements and Models of Modern Loads and Their Effect on Voltage Stability Studies", *IEEE Trans. on Power Systems*, vol. 13, no. 2, pp. 584-592, 1998.

[2] L. Korunovic, D. Stojanovic, "Load Modeling in Distribution Networks", *Facta Universitatis (Nis), Ser.: Elec. Energ*. vol 15, no. 3, pp. 419-427, 2002.

[3] A. Saric, M. Calovic, "Fuzzy Logic Approach to Load Flow Calculation in Distribution Networks", *The First Yugoslav Conference on Distribution Networks*, R-6.01, Zlatibor, 1998. (in Serbian)

[4] H.-C. Kuo, Y.-Y. Hsu, "Distribution System Load Estimation and Service Restoration Using a Fuzzy Set Approach", *IEEE Trans. on Power Delivery*, vol. 8, no. 4, pp. 1950-1957, 1993.

[5] J. Nahman, D. Peric, "Distribution System Performance Evaluation for Data Uncertainty", *IEEE Trans. on Power Delivery*, vol. 18, no. 3, pp. 694-700, 2003.

[6] M. Baran, F. Wu, "Network Reconfiguration in Distribution Systems for Loss Reduction and Load Balancing", *IEEE Trans. on Power Delivery*, vol. 4. no 2, pp. 1401-1407, 1989.

[7] M. Petkovic, *Introduction to interval arithmetic*, Belgrade, Naucna knjiga, 1989. (in Sebian)

Calculation of Energy Losses in Low Voltage Distribution Systems Using a Fuzzy Clustering Technique

Dragan S. Tasić[1] and Miodrag S. Stojanović [2]

Abstract – **A method for calculation of energy losses in low voltage distribution networks, based on the fuzzy clustering technique, is developed in this paper. The method required input data about the networks that can be collected easily: lengths of lines, number of line segments, number of customers, conductor's cross section area, conductor's material, electrical energy delivered by distribution transformers etc. The method is tested on the example of ninety low voltage networks. It is analyzed the optimal number of clusters as well as the optimal value of the parameter that defines fuzziness of fuzzy clustering.**

Keywords – **Low voltage networks, Energy losses, Fuzzy clustering.**

I. INTRODUCTION

Determination of electrical energy losses in low voltage distribution networks is very important for any electrical utility. For exact calculation of energy losses, the data about network parameters as well as the data about loads for any moment of the observed time interval are needed.

The reliability of data of network parameters, for low voltage distribution networks, is very small. Problem of the unreliability can be solved by further involvement on reviewing data base. Other, much difficult problem, when energy losses in low voltage distribution networks are calculated, lies is the fact that a small number of measuring exist in these networks. Therefore, the data bases about low voltage loads do not exist. The electric energy, delivered by distribution transformers, is usually the only available data about the loads.

In [1,2] the problem of low voltage losses calculation is simplified by classifying low voltage networks in two groups: town's and village's. In [2] is shown that regression method is suitable for calculation of losses in low voltage networks.

A method for calculation of energy losses in low voltage distribution networks, based on the fuzzy clustering technique, is developed in this paper. Fuzzy clustering is made on a spice that make objects with following attributes: lengths of lines, number of line segments, number of customers, conductor's cross section area, conductor's material, electrical energy delivered by distribution transformers etc.

[1] Dragan S. Tasić is with the Faculty of Electronic Engineering, University of Niš, Beogradska 14, 18000 Niš, Yugoslavia, E-mail: dtasic@elfak.ni.ac.yu

[2]Miodrag S. Stojanović is with the Faculty of Electronic Engineering, University of Niš, Beogradska 14, 18000 Niš, Yugoslavia, E-mail: miodrag@elfak.ni.ac.yu

II. FUZZY CLUSTERING ALGORITHM

Clustering is one of the most fundamental issues in pattern recognition. Given a finite set of data *X*, the problem of clustering is to find several cluster centers that can properly characterize relevant classes of *X*. In classical cluster analysis, these classes are required to form a partition of X such that degree of association is strong for data within blocks of the partition. When the requirement of a crisp partition of *X* is replaced with a weaker requirement of a fuzzy partition or a fuzzy pseudopartition of *X*, we refer to the emerging problem area as fuzzy clustering. Fuzzy pseudopartitions are often called fuzzy *c*-partition, where *c* designates the number of fuzzy classes in the partition. There are two basic methods of fuzzy clustering. One of them, which is based on fuzzy *c*-partitions, is called a fuzzy *c*-means clustering method.

Let $X = \{x_1, x_2, ..., x_n\}$ be a set of given data. A fuzzy pseudopartition or fuzzy *c*-partition of *X* is a family of fuzzy subsets of *X*, denoted by $P = \{A_1, A_2, ..., A_c\}$ witch satisfies:

$$\sum_{i=1}^{c} A_i(x_k) = 1, \quad k \in N_n \ , \tag{1}$$

for $N_n = \{1,2,...,n\}$, and

$$0 < \sum_{k=1}^{n} A_i(x_k) < n \quad i \in N_c \tag{2}$$

where c is positive integer and N_c set of integers $N_c = \{1,2,...,c\}$. Given a set of data $X = \{x_1, x_2, ..., x_n\}$, where x_k in general is a vector:

$$x_k = [x_{k1}, x_{k2}, ..., x_{ka}] \in R^a \tag{3}$$

for all $k \in N_n$, the problem of fuzzy clustering is to find a fuzzy pseudopartition and associated cluster centers by which the structure of the data is represented as best as posible.

The *c*-means algorithm is based on the assumption that the desired number of clusters *c* is given and, in addition, a particular distance, a real number $m \in (1, \infty)$, and a small positive number ε, serving as a stopping criterion, are chosen.

Step 1.

Let $t = 0$. Select an initial fuzzy pseudopartition $P^{(0)}$.

Step 2.

Calculate the *c* cluster centers $v_1^{(t)}, ..., v_c^{(t)}$ by relation

$$v_i = \frac{\sum_{k=1}^{n} [A_i(x_k)]^m x_k}{\sum_{k=1}^{n} [A_i(x_k)]^m} \quad (4)$$

For $P^{(t)}$ and the chosen value of *m*.

Step 3.

Update $P^{(t+1)}$ by the following procedure: For each $x_k \in X$, if $\left\|x_k - v_i^{(t)}\right\|^2 > 0$ for all $i \in N_c$, then define

$$A_i^{(t+1)}(x_k) = \left[\sum_{j=1}^{c} \left(\frac{\left\|x_k - v_i^{(t)}\right\|^2}{\left\|x_k - v_j^{(t)}\right\|^2} \right)^{\frac{1}{m-1}} \right]^{-1} \quad (5)$$

if $\left\|x_k - v_i^{(t)}\right\|^2 = 0$ for some $i \in I \subseteq N_c$, then define $A_i^{(t+1)}(x_k)$ for $i \in I$ by any nonnegative real numbers satisfying

$$\sum_{i \in I} A_i^{(t+1)}(x_k) = 1 \quad (6)$$

and define $A_i^{(t+1)}(x_k) = 0$ for $i \in N_c - I$.

Step 4.

Compare $P^{(t)}$ and $P^{(t+1)}$. If $\left|P^{(t+1)} - P^{(t)}\right| \le \varepsilon$, then stop; otherwise, increase *t* by one and return to Step 2.

In Step 4, $\left|P^{(t+1)} - P^{(t)}\right|$ denotes a distance between $P^{(t+1)}$ and $P^{(t)}$ in the space $R^{n \times c}$. An example of this distance is

$$\left|P^{(t+1)} - P^{(t)}\right| = \max_{i \in N_c, k \in N_n} \left|A_i^{(t+1)}(x_k) - A_i^{(t+1)}(x_k)\right|. \quad (7)$$

In the algorithm, the parameter is selected according to the problem under consideration. When $m \to 1$, the fuzzy *c*-means converges to a "generalized" classical *c*-means. When $m \to \infty$, all cluster centers tend towards the centroid of data set *X*. That is, the partition becomes fuzzier with increasing. Currently, there is no theoretical basis for an optimal choice for the value of *m*. However, it is established that the algorithm converges for any $m \in (1, \infty)$.

III. PROCEDURE OF CALCULATION OF ENERGY LOSSES

The presented fuzzy clustering algorithm can be applied for calculation of electrical losses in low voltage distribution networks. Following steps should be made:

Step 1

From the set of N_n low voltage networks, N_t test networks are selected. Additional measurements, that enable losses calculation by classical methods, are made on the test networks.

Step 2

A spice that consists of N_t objects is now formed. Any object has N_a attributes, whereat value of energy losses is one attribute (absolute or percentage).

Step 3

For chosen number of clusters *c* and real number $m \in (1, \infty)$, fuzzy clustering is made, and objects that represent cluster centers are stored in memory.

Step 4

A spice that consists of N_n-N_t objects with N_a-1 attributes is formed. Energy losses are not considered as attribute of objects.

Step 5

Using the modified *c*-means method, fuzzy clustering is made for cluster centers determined in step 3 without the energy attributes included. The modification of *c*-means method is following: on the step 2 of *c*-means algorithm shown in II, the centers of clusters are not determined then centers of the test networks are retained.

Step 6

For any object (low voltage networks), absolute or percentage energy losses are calculated summing the memberships values multiplied with attributes of corresponding center of cluster that represent energy losses.

The following questions required answer:

- what is optimal cluster number,
- what value of real number m is optimal,
- what attributes shall we consider.

These questions have not unique solution, and as will be seen from the following example, answers depend on number of disposed data.

IV. EXAMPLE OF ENERGY LOSSES CALCULATION

In order to analyse proposed method, calculation of energy losses are made for ninety low voltage networks. The authors made calculations of losses, using modified c-means method, for 23 different combinations of parameter m (1.05 to 1.75), number of clusters and chosen data set comprehended in analysis. Obtained values of percentage losses are shown in Table I. The following data are comprehended in analysis:

1. number of line sections,
2. median cross section area of first line section $(3 \cdot S_f + S_0)/4$,
3. the smallest median cross section area of line $(3 \cdot S_{f\min} + S_{0\min})/4$,
4. resistivity of conductor,
5. electrical energy delivered by distribution transformers,
6. load factor,

where S_p and S_n are cross section areas of phase and neutral conductors respectively.

For selection 1, shown in Table I, all available data are comprehended. Selection 2 does not comprehend resistivity of conductors, and selection 3 does not comprehend load factors.

TABLE I

ENERGY LOSSES CALCULATED USING FUZZY CLUSTERING METHOD

		selection 1												selection 2						selection 3					
m		1.05			1.2		1.4			1.75				1.05			1.2			1.05		1.2		1.4	
num. of clu.		6	12	20	10	20	6	12	20	6	12	20	6	12	20	10	15	20	10	20	12	20	12	20
1	16.05	18.5	16.2	18.1	16.3	16.4	6.19	16.4	17.3	10.6	17.9	14.8	6.36	14.4	16.8	16.4	20.4	17.4	15.6	18.1	16	9.79	15.6	13.7
2	1.213	3.46	3.36	3.2	3.54	3.74	3.82	3.67	4.65	5.01	4.57	4.98	3.52	4.54	3.2	3.55	4.5	3.15	4.45	2.55	3.28	3.09	3.31	3.15
3	25.46	18.5	16.2	18.1	16.2	16.3	6.27	15.4	16.3	10.1	17.2	22.8	6.36	14.5	25.5	16.3	18.9	17.6	15.6	18.1	15.4	25.4	13.5	25.5
4	1.913	3.46	3.36	3.2	3.54	2.38	3.83	3.65	4.7	4.74	4.58	4.9	3.52	4.54	3.2	3.56	4.5	3.13	4.45	5.25	3.28	3.68	3.32	3.7
5	38.79	18.3	29.6	38.8	29.6	38.8	10.4	29.3	38.7	7.87	8.64	11.6	29.3	32.1	38.8	29.6	29.6	38.8	29.6	38.8	29.6	38.8	29.5	29.5
6	3.038	3.46	3.36	3.2	3.54	2.32	3.83	3.64	4.67	4.64	4.57	5.06	3.52	4.54	3.2	3.56	4.5	3.13	4.45	5.25	3.28	3.68	3.32	3.7
7	2.143	3.46	3.33	3.15	3.46	3.02	6.12	4.23	3.19	5.46	4.54	4.93	6.33	1.93	2.78	3.87	2.39	2.85	3.29	12	3.57	2	3.45	7.02
8	6.113	8.41	16.2	11	12.2	10.5	5.27	9.4	7.82	9.07	8.61	8.26	6.34	4.88	9.29	13.2	8.06	6.23	6.15	6.73	5.04	6.55	6.62	7
9	2.91	1	1.63	2.91	1.09	1.64	3.27	2.18	2.92	5.17	3.55	2.87	2.01	3.17	4.59	4.58	4.59	4.59	1.19	2.91	1.19	1.31	1.28	1.29
10	0.68	1.02	0.84	1.06	0.86	1.04	2.37	1.4	1.04	3.39	3.71	5.04	6.36	1.93	0.64	4.39	2.19	0.67	1.19	1.06	1.22	1.06	1.84	1.05
11	0.448	0.29	0.27	0.27	0.28	0.24	0.51	0.34	0.38	1.09	1.04	1	0.47	0.32	0.24	0.24	0.24	0.24	1.89	0.24	0.24	0.24	0.27	0.62
12	0.28	1	0.84	0.52	0.85	0.71	1.03	0.92	0.71	1.23	1.32	1.31	0.47	0.93	0.93	0.93	0.93	0.93	1.19	0.52	1.19	1.31	1.21	1.26
13	2.530	3.46	3.36	2.86	3.63	3.72	4.36	3.24	2.94	5.52	4.66	4.62	3.52	2.63	2.24	3.46	2.63	2.29	4.45	2.55	3.28	2.48	3.59	2.93
14	1.825	3.46	3.33	2.86	3.42	3.03	5.79	3.18	3.28	5.25	4.1	4.25	3.52	2.63	2.78	3.81	2.64	2.87	3.29	12.2	3.84	3.11	4.43	6.37
15	0.50	1	0.45	0.5	1.04	0.52	2.61	0.95	0.53	4.43	0.89	0.54	2.01	0.32	0.5	0.41	0.45	0.45	0.42	0.5	0.42	0.5	0.48	0.5
16	1.154	0.29	0.29	0.29	1.58	1.14	1.5	3.01	2.89	3.29	3.84	4.33	2.01	0.38	0.25	0.77	0.96	1.1	1.89	6.12	0.35	4.55	0.99	0.9
17	0.05	0.29	0.27	0.27	0.29	0.24	0.64	0.4	0.44	2.41	2.35	3.35	0.47	0.32	0.24	0.24	0.24	0.24	0.05	0.24	0.24	0.24	0.29	0.06
18	1.064	3.46	3.33	3.15	3.4	3.78	6.17	4.17	4.26	5.28	4.98	5.2	6.36	1.93	3.55	3.84	2.17	8.24	3.29	3.18	3.57	1.9	3.4	1.96
19	1.125	3.46	3.33	3.17	3.43	3.69	5.64	3.95	4.12	5.48	4.86	5.26	3.52	1.93	3.65	3.86	2.87	5.71	3.29	3.33	3.8	2.22	4.38	3.94
20	2.15	3.46	3.34	2.86	3.92	1.25	5.05	3.8	1.32	5.61	4.91	2.23	3.52	0.93	0.93	0.93	0.93	0.93	1.89	1.25	2.92	1.25	2.86	2.48
21	9.048	5.1	6.34	10.4	3.85	9.05	6.16	4.68	8.93	6.46	5.83	9.06	6.91	4.54	9.23	6.42	4.52	9.18	4.45	6.73	3.97	6.43	4.66	5.5
22	11.84	7.16	11.8	11.8	7.19	11.8	7.48	7.02	11.7	8.09	6.72	11.8	6.91	9.36	9.69	6.45	9.34	11.8	7.2	11.8	7.19	9.43	7.14	11.8
23	1.351	3.46	3.33	11	5.39	3.8	5.83	4.76	4.61	8.07	5.87	2.04	6.36	1.93	0.64	4.24	3.65	0.97	3.29	3.19	3.58	1.91	3.62	2.4
24	0.34	1	1.63	0.34	1.05	1.6	3.78	0.44	0.34	5	0.49	3.79	2.01	3.17	0.34	0.43	0.34	0.34	0.42	0.34	0.42	0.34	0.34	0.34
25	12.39	13	9.06	11	10.6	4.9	6.02	6.38	5.69	9.89	6.38	12.3	6.36	14.4	9.3	8.71	6.67	14.8	6.12	12.2	7.44	12.8	7.18	12.8
26	1.249	3.46	3.36	3.2	3.54	2.2	3.84	3.65	2.71	4.47	3.6	3.93	3.56	4.54	3.2	3.67	4.5	3.47	4.45	2.55	3.28	2.45	3.32	2.47
27	0.35	0.3	0.27	0.27	0.33	1.25	2.3	1.87	1.31	4.03	4.02	1.57	0.47	0.93	0.93	0.93	0.93	0.93	1.89	1.25	2.92	1.25	2.81	2.4
28	0.393	3.46	3.35	2.86	3.53	3.03	5.66	3.2	3.28	5.53	4.36	4.45	3.52	2.63	2.78	3.79	2.64	2.86	4.3	12.2	3.95	4.87	4.64	6.94
29	0.132	0.29	0.27	0.27	0.64	0.58	0.97	2.11	2.22	2.76	3.43	3.89	1.82	0.32	0.26	0.53	0.55	0.63	1.89	0.24	0.24	0.24	0.27	0.62
30	6.64	3.48	6.34	11	7.33	4.35	5.49	5.88	5.41	7.77	5.98	8.6	6.91	7.91	9.3	4.59	5.98	13.2	3.32	12.2	4.79	8.17	5.84	11
31	0.47	1	0.59	0.52	1.04	0.71	1.25	1.35	1.44	2.94	2.48	3.29	0.47	0.32	0.24	0.24	0.24	0.24	1.19	2.39	1.14	1.31	1.26	1.28
32	2.60	0.3	0.27	0.27	0.43	1.25	2.26	2.28	1.71	3.92	4.08	3.85	0.47	0.93	0.93	0.93	0.93	0.94	1.89	1.25	2.92	1.25	2.81	2.4
33	0.71	3.46	3.33	6.72	3.6	2.85	5.87	4.25	3.53	5.87	5.02	5.2	4.11	1.93	2.78	2.96	2.18	4.1	3.29	12.2	3.72	2.96	4.42	7.91
34	11.17	18.5	16.2	18.1	16.1	16.2	6.18	15.2	15.8	8.98	15	14.3	6.36	12.9	25.5	16.1	6.95	17.6	15.6	18.1	15.8	25.4	14.2	14.8
35	2.758	3.46	6.34	3.2	3.56	2.19	4.14	3.74	2.37	4.54	3.31	3.01	6.91	4.54	7.43	6.44	4.5	5.92	4.45	2.55	3.28	2.48	3.31	2.59
36	3.50	3.46	3.36	2.86	3.62	3.76	4.69	3.18	2.94	5.58	4.55	4.63	3.52	2.63	2.24	3.55	2.63	2.29	4.45	2.55	3.31	2.47	3.8	2.71
37	7.546	9.78	6.34	8.11	8.48	8.11	12.4	8.15	7.84	7.19	8.25	8.03	6.91	9.36	9.69	6.43	9.34	8.11	4.79	5.25	8.08	8.11	7.99	8.09
38	7.03	7.16	5.65	5.65	7.17	5.65	6.81	6.65	5.73	6.91	7.19	6.74	3.52	4.87	9.3	3.93	6.83	5.94	7.2	8.23	7.19	9.43	7.15	5.81
39	0.24	1	0.45	0.5	1.04	0.52	2.48	0.96	0.53	4.32	0.94	0.57	2.01	0.32	0.5	0.41	0.45	0.45	0.42	0.5	0.42	0.5	0.49	0.5
40	4.95	1	1.62	2.91	1.72	2.17	2.4	2.67	3.68	4.48	3.86	5.07	6.91	9.36	8.68	6.14	8.79	8.17	1.19	2.91	1.28	1.37	2.05	2.59
41	14.33	18.5	6.35	10.4	9.49	8.53	11.1	8.76	8.48	10.4	8.51	8.51	6.91	10.1	9.73	5.56	10.9	10.7	15.6	18.1	16	12.8	14.6	9.64
42	0.90	1	0.71	0.53	1.05	0.77	1.44	1.21	1.93	3.51	2.37	3.29	1.59	0.32	0.24	0.31	0.33	0.36	1.19	2.91	1.08	1.3	1.27	1.29
43	0.71	1	0.84	0.52	0.92	0.79	1.07	1.44	1.84	2.51	2.78	3.72	0.47	0.98	0.98	2.02	2.28	3.52	1.19	2.91	1.19	1.31	1.24	1.27
44	2.34	3.53	1.63	0.34	2.15	2.81	4.59	2.19	3.16	5.24	3.66	5.43	2.01	3.17	0.34	0.99	0.35	0.35	0.42	0.34	1.05	0.49	1.59	2.24
45	0.20	1	0.45	0.5	1.22	0.6	3.12	1.87	2.27	4.56	2.9	3.72	2.04	4.13	0.5	1.21	2.29	2.64	0.42	0.5	0.43	0.51	1.33	1.07
46	3.131	3.46	6.34	3.2	3.55	2.19	3.96	3.67	2.35	4.46	3.37	2.86	6.91	4.54	3.2	6.38	4.5	3.15	4.45	2.55	3.28	3.64	3.32	3.46
47	0.83	1	0.84	1.06	0.85	1.04	1.3	0.92	1.04	1.95	2.2	3.37	6.35	1.93	0.77	4.29	2.26	8.2	1.19	1.06	1.19	1.06	1.23	1.05
48	0.08	0.29	0.27	0.27	0.28	0.24	0.52	0.32	0.28	1.52	1.34	1.98	0.47	0.32	0.24	0.24	0.24	0.24	0.05	0.24	0.24	0.24	0.28	0.06
49	0.59	1	1.62	0.34	1.1	1.16	2.95	0.85	1.1	4.44	2.29	4.04	2	0.34	0.34	0.53	0.45	0.46	0.42	0.34	0.42	0.34	0.34	0.34
50	3.375	3.46	3.33	3.31	3.41	3.8	6.17	4.2	4.36	5.31	5.03	5.8	6.36	1.93	9.3	3.85	2.2	8.66	3.29	11.8	3.58	2.04	3.61	7.53
51	1.38	1	0.84	0.52	0.85	0.71	1.04	0.92	0.71	1.26	1.37	1.39	0.47	0.93	0.93	0.93	0.93	0.93	1.19	0.52	1.19	1.31	1.21	1.26
52	6.11	9.78	6.34	6.11	8.48	8.9	12.8	8.18	8.78	7.66	8.48	6.71	6.91	8.9	8.9	4.53	8.9	6.11	15.6	3.17	15.9	14	14.7	4.33
53	23.30	18.5	16.2	18.1	16.2	16.3	6.19	15.9	16.6	8.48	12.7	12.3	6.36	14.3	4.38	16.2	16.4	16.9	15.6	18.1	16.1	5.33	15.9	12.3
54	4.359	3.46	3.36	2.86	3.55	3.76	3.99	3.62	3.07	5.17	4.8	5.06	3.52	2.63	2.24	3.52	2.67	2.29	4.45	2.55	3.28	2.47	3.48	2.83
55	0.224	0.29	0.27	0.27	0.28	0.24	0.51	0.28	0.27	0.97	0.53	0.49	0.47	0.32	0.24	0.24	0.24	0.24	1.89	0.24	0.24	0.24	0.28	0.62
56	0.459	3.46	3.36	2.86	3.55	3.77	4.07	3.72	3.24	5.62	4.84	5.44	3.52	2.63	2.24	3.55	2.67	2.36	4.45	2.55	3.32	2.46	3.84	2.68
57	9.37	17.9	6.34	10.4	8.48	8.9	10.2	7.94	8.74	8.38	7.93	6.92	6.91	8.9	8.9	4.1	8.9	11.7	3.29	12.2	3.57	7.39	3.43	13.1
58	11.29	18.5	6.34	10.4	8.53	8.78	10.4	7.78	8.2	9.17	7.66	7.6	6.91	8.9	8.89	4.11	8.84	11.6	3.29	3.17	9.7	13.3	7.95	9.97
59	8.86	18.5	15.9	10.9	14.2	4.3	6.26	6.26	5.27	11.2	6.91	7.85	6.36	14.4	2.11	4.85	7.15	12.3	4.56	3.2	3.81	14	5.09	10.6
60	0.17	1	0.84	0.52	0.85	0.72	1.03	1.07	0.95	1.65	2.15	2.84	0.47	0.93	0.93	0.96	0.99	1.12	1.19	0.52	1.19	1.31	1.21	1.26
61	8.08	3.5	6.07	10.9	5	4.25	4.87	5.54	5.54	7	6.01	7.56	6.7	4.54	8.98	6.44	5.73	7.81	4.45	6.08	5.28	6.05	5.82	6.28
62	2.04	3.62	3.33	3.16	4.64	3.94	6.14	4.82	4.63	7.44	5.75	5.05	6.36	1.93	0.64	4.91	2.17	1.87	3.29	11.8	3.57	2.05	3.52	5.23
63	0.41	1	0.84	1.06	0.85	0.74	1.04	0.88	0.83	1.18	1.2	1.61	3.55	0.93	0.93	1	1.04	1.58	1.19	1.06	1.19	1.08	1.19	1.25
64	1.01	1	0.84	0.52	0.85	0.71	1.03	0.96	0.74	1.34	1.64	1.94	0.47	0.93	0.93	0.93	0.93	0.93	1.19	2.91	1.19	1.31	1.21	1.26
65	3.48	3.46	3.36	9.83	4.11	2.57	4.63	4.33	3.66	6.11	5.15	5.93	3.52	1.5	9.19	2.76	3.08	5.21	4.45	1.45	3.07	3.27	3.92	4.68
66	2.371	3.46	3.36	2.86	3.55	3.77	3.95	3.42	3.02	5.51	4.64	5.08	3.52	2.63	2.24	3.55	2.64	2.29	4.45	2.55	3.28	2.45	3.31	2.48
67	2.391	3.46	3.33	2.86	3.41	3.02	6.06	3.16	3.17	5.01	3.54	3.1	3.52	2.66	2.78	3.84	2.93	2.85	3.29	5.82	4.5	6.39	4.81	6.52
68	2.29	1.18	0.84	1.06	0.86	1.04	2.4	1.27	1.05	3.14	3.43	4.76	6.36	1.93	2.73	4.09	2.17	4.3	1.19	1.06	1.23	1.06	1.92	1.06

		selection 1												selection 2						selection 3					
m		1.05			1.2		1.4			1.75				1.05			1.2			1.05		1.2		1.4	
num. of clu.		6	12	20	10	20	6	12	20	6	12	20	6	12	20	10	15	20	10	20	12	20	12	20
69	3.88	3.46	3.34	2.87	4.28	1.25	5.13	4.06	1.47	5.88	5.07	3.74	3.52	0.93	0.93	0.93	0.93	0.93	1.89	1.25	2.92	1.25	2.92	2.64
70	0.493	3.46	3.33	9.01	4.5	3.84	5.81	4.83	4.74	7.34	5.81	1.65	6.36	1.93	0.64	4.13	2.45	0.65	3.29	3.3	3.57	1.9	3.6	1.97
71	1.11	1	0.84	1.05	0.85	0.71	1.23	0.89	0.73	1.45	1.13	1.22	3.52	0.93	0.93	0.94	0.94	0.97	1.19	1.06	1.19	1.08	1.19	1.25
72	1.40	1	0.84	1.06	0.85	1.04	1.31	0.89	1.04	1.75	1.75	2.74	4.79	1.93	2.78	3.99	2.31	9.47	1.19	1.06	1.19	1.06	1.22	1.05
73	10.86	15.4	13.6	17.9	10.7	3.64	6.13	10.9	5.84	6.96	7.88	8.46	6.36	6.71	4.37	8.76	6.86	6.1	15.6	18.1	16.1	6.52	16.2	7.12
74	2.593	3.46	3.33	3.15	3.89	3.09	6	5.35	3.97	6.09	5.53	5.78	6.33	1.93	2.78	4.23	2.31	2.93	3.29	7.52	3.58	1.91	3.79	2.3
75	3.32	0.29	0.27	0.27	0.3	0.24	0.62	0.72	0.58	2.06	2.29	2.81	0.52	0.32	0.24	0.25	0.25	0.25	0.05	0.24	0.24	0.24	0.35	0.35
76	11.54	18.5	15.4	11	13.6	4.35	6.22	6.16	5.28	10.9	6.69	9.02	6.36	14.3	0.98	5.13	5.91	14.4	8.02	12.2	3.84	14	5.04	13.5
77	4.794	3.46	3.36	2.86	3.75	3.09	5.58	3.32	3.61	5.75	4.66	4.98	3.52	2.63	2.78	3.91	2.72	2.9	4.45	6.73	4.17	6.46	5.19	6.65
78	0.40	0.29	6.18	0.45	4.72	1.66	2.51	4.2	3.89	4.21	4.2	4.45	2.01	0.36	0.4	0.86	0.54	0.55	0.05	0.24	0.25	0.26	0.55	0.11
79	2.06	0.29	0.27	0.27	0.28	0.24	0.54	0.33	0.29	1.82	1.64	2.53	0.47	0.32	0.24	0.24	0.24	0.24	0.05	0.24	0.24	0.24	0.28	0.06
80	4.49	3.46	3.33	3.15	3.72	3.1	6.08	5.33	3.9	5.97	5.31	5.63	6.35	1.93	2.78	4.05	2.2	2.91	3.29	12.2	3.57	1.95	3.66	5.47
81	4.631	3.46	3.36	3.2	3.56	3.77	3.99	4.1	4.71	5.91	4.87	4.91	3.52	2.89	3.19	3.56	4.5	3.13	4.45	5.25	3.29	3.68	3.51	3.7
82	0.77	0.29	0.27	0.4	0.63	0.4	1.24	2.18	2.11	3.43	3.59	3.89	2	0.32	0.4	0.37	0.44	0.45	0.05	0.24	0.26	0.28	0.76	0.18
83	7.54	18.5	16.2	11.8	16.1	12.1	7.04	12	9.94	13	10.5	9.73	6.36	14.4	17.9	15.7	17	11.2	15.6	18.1	16.1	12.8	16.1	8.84
84	0.34	1	0.84	0.59	0.86	0.82	1.07	1.16	1.4	1.94	2.61	3.6	3.52	4.54	9.23	3.54	4.33	7.72	1.19	0.52	1.19	1.23	1.24	1.38
85	0.92	1	0.84	0.52	0.85	0.71	1.03	0.99	0.77	1.45	1.78	2.16	0.47	0.93	0.93	0.93	0.93	0.94	1.19	2.91	1.19	1.31	1.23	1.26
86	8.80	18.5	16.2	18.1	15.5	17	6.63	13.3	15.8	8.72	12.3	19.4	6.36	32.1	25.5	15.4	9.58	17.5	29	34.6	21	25.6	18.1	23.1
87	7.99	18.5	29.5	38.8	25.5	38.1	7.24	18.5	28.7	7.69	9.12	12.8	29.3	32.1	37.3	24.6	15.9	34.5	29.6	38.8	29.6	37.4	29.4	29.1
88	0.28	1	0.84	0.52	0.85	0.71	1.05	0.91	0.71	1.27	1.27	1.18	0.47	0.93	0.93	0.93	0.93	0.93	1.19	0.52	1.19	1.31	1.21	1.26
89	6.20	18.5	16.2	17.7	15.6	16.1	6.2	14.7	14.8	7.27	8.37	7.89	6.36	14.4	4.38	14.5	18.8	4.09	15.6	18	16.1	5.99	16.1	3.92
90	3.40	3.46	3.33	3.79	3.55	3.14	6.13	5.06	3.94	5.53	4.86	5.6	6.31	2.58	2.78	3.89	3.45	2.9	3.3	12.2	4.38	12	5.52	13

Column 2 of Table I shows value of percentage energy losses given by additional measurement, while columns 3-25 show calculated percentage energy losses.

Meaning of different colours in Table I is following:

- networks with a large value of electrical losses that are not identified,
- networks with a large value of electrical losses that are identified properly,
- networks for which a large value of electrical losses is identified erroneously.

On the basses of results shown in Table I, we can conclude the best results are given in following two cases:

- *m*=1.05, for 12 clusters and all data comprehended,
- *m*=1.4, for 20 clusters and all data comprehended.

Table I shows only a small piece of results. The authors was made analysis for different number of networks, and concluded following:

- requested number of test networks is 50 to 100,
- all available data shall be comprehended,
- optimal number of clusters depend on number of test networks and shall be 15% to 30% of the number of test networks,
- parameter *m* gives the optimal value in the range of 1 to 1.5, thereat value of *m* increase with increasing the number of clusters,
- total percentage electrical losses of all networks are quite accurate if previous conclusions are satisfied.

V. Conclusion

A new method for calculation of energy losses in low voltage distribution networks is developed in this paper. The method is based on the fuzzy clustering technique. Beside the data about parameters of networks, method requires electrical energies delivered by distribution transformers. Additionally, measurements, that enable losses calculation by classical methods, are made for selected test networks.

Optimal number of clusters depends on number of test networks. The authors suggest that number of cluster gives the value in the range of 15% to 30% of number of test networks. Parameter *m* that defines fuzziness of clustering shall be selected from the range of 1 to 1.5. For proposed values of parameter *m* and number of clusters, the calculated value of total electrical losses of all networks is quite accurate.

Acknowledgment

The work in this paper if partially funded by the Ministry of Science and Development of Republic of Serbia.

References

[1] Ю. С, Железко, Выбор мероприятий по снижению потери электроэнергии в электрических сетях, Энергоатомиздат, Москва, 1989.

[2] В. Э. Воротницкий, Ю. С. Железко, В. Н. Казанцев, В. Г. Пекелис, Д. Л. Файбисович, Потери электроэнергии в электрических сетях энергосистем, Энергоатомиздат, Москва, 1983.

[3] G. J. Klir, B. Yuan, “Fuzzy sets and fuzzy logic: Theory and Applications”, Prentice Hall, New Jersey, 1995.

[4] N. Rajaković, D. Tasić, M. Stojanović, “A Clustering Technique for Distribution Losses Calculation in Deregulated Environment”. proceedings of 2nd Balkan Power Conference, Beograd, June 19-21, 2002.

[5] N. Rajaković, M. Stojanović, D. Tasić, “An Improved Methods for the Electric Energy Losses Assessment in Distribution Networks”. 3rd Mediterranean Conference Med Power 2002, Athens, November 4-6, 2002.

[6] M. Stojanović, D. Tasić, “A fuzzy method of distribution energy losses calculation”, ICEST 2003, Sofia, October 2003, pp. 454-457.

Fast Method for Asymmetrical Load-Flow Solution in Sequence Domain

Ljupco D. Trpezanovski[1], Vladimir C. Strezoski[2] and Metodija B. Atanasovski[3]

***Abstract* – In this paper a new fast method for asymmetrical load-flow solution in sequence domain is presented. The entire power system is modelled with three decoupled positive-, negative- and zero-sequence circuits. The proposed method is consisted of a system of non-linear equations which represents the positive- and two systems of linear equations which represent the negative- and zero-sequence circuits. The solution of non-linear equations is by Newton-Raphson procedure and solution of linear systems of equations is by Gauss's method.**

***Keywords* – Asymmetrical load-flow, sequence domain, decoupled sequence circuits.**

I. INTRODUCTION

The load-flow studies are the most frequent calculations in the power system analysis. The steady state symmetrical load-flows studies (SLF) are performed in the more efficient and comfortable sequence domain instead of in the phase domain. Usually, power system states deviate more or less from the symmetrical states, therefore symmetrical states are only approximations of the actual states of three-phase power systems. Always, the three-phase electrical power system states are asymmetrical. The presence of long unbalanced (untransposed) transmission lines and asymmetrical or single-phase loads (as induction furnaces and electrical railways substations) cause: negative-sequence currents at generator terminals rise heating in their rotors; malfunctions of protective relays; zero-sequence currents increase greatly the effect of inductive coupling between parallel transmission lines; higher power system loss etc. Because of these reasons, for more precise analysis of three-phase power system states, the asymmetrical load-flow (ALF) analysis are required. Also, ALF calculations are required in the process of transmission line designing to study the effects of various phase arrangements, or in operating situation with single pole switching, etc.

Usually, the methods for ALF solutions are in phase domain [1-3]. The main reasons for avoiding the sequence domain in the ALF methods are: (1) presence of phase shifts of the three-phase transformers (ideal transformers with complex turns ratios in their sequence circuits); (2) mutually couplings among sequence circuits in the points of power system unbalances and (3) asymmetrical phase loads, which cannot be specified in the sequence domain. Applying new scaling concept [4], unbalanced line decoupled model in sequence domain and asymmetrical phase loads model specified in the sequence domain [5-7], the entire power system can be modeled with three decoupled positive, negative and zero-sequence circuits. For proper definition of the ALF methods in sequence domain an enhanced bus classification is proposed in [8], [9].

[1]Ljupco D. Trpezanovski and [3]Metodija B. Atanasovski are with the Faculty of Technical Sciences, University St. Kliment Ohridski, I. L. Ribar bb, 7000 Bitola, Macedonia,
E-mail: ljupco.trpezanovski@uklo.edu.mk

[2]Vladimir C. Strezoski is with the Faculty of Engineering, University of Novi Sad, Fruskogorska 11, 21000 Novi Sad, Serbija and Montenegro,
E-mail: streza@eunet.yu

II. ENHANCED BUS CLASSIFICATION

Usual bus classifications are performed in accordance with the specification of values of quantities associated with power system buses. Twelve real-valued quantities are associated with each three-phase bus: three pairs of voltage magnitudes and angles, as well as three pairs of active and reactive injected powers. Three pairs of active and reactive power balance equations, for each three-phase bus, describe these quantities. These equations are extended with relations representing control laws associated with buses in which the three-phase active powers and reactive powers or voltage magnitudes are controlled. To provide a correct treatment of reactive power limits enforcement at the generators, as well as to simplify the ALF method, the standard three types buses classification is enhanced to a new four types buses classification by introducing a new or $P_\Sigma Q_\Sigma$ type of buses (Table I). The new classification is independent of the domain which the ALF problem is stated in:

1. $P_\Sigma V$ bus is a bus in which the value of three-phase injected active power (P_Σ) and the control law of the automatic voltage regulator (AVR) are specified. Values of three pairs of magnitudes and angles of voltages, as well as values of three pairs of injected active and reactive powers are unknown. Applying the synthesizing procedure [8], [9], this bus is suppressed in the high voltage bus of the step-up transformer.
2. θV bus (slack bus) is a bus in which the angle of a voltage and the control law of the generator AVR are specified. Values of three magnitudes and two angles of voltages and values of three pairs of injected active and reactive powers are unknown. Applying the synthesizing procedure, this bus is suppressed in the high voltage bus of the step-up transformer.
3. $P_\Sigma Q_\Sigma$ bus is a bus in which values of three-phase injected active and reactive powers (sums of phase powers P_Σ and Q_Σ) are specified. Values of three pairs of magnitudes and angles of voltages and values of three pairs of injected active and reactive powers are unknown. It is newly introduced type of buses, which is necessary to provide the correct treatment of Q limits enforcement at $P_\Sigma V$ buses. Also, this type of bus is suppressed in the high voltage bus of the step-up transformer.

TABLE I. THE ENHANCED BUS CLASSIFICATION FOR THE ALF PROBLEM (c.l. – CONTROL LAW, PHASE DOMAIN *abc*, SEQUENCE DOMAIN *dio*).

BUS TYPE	$P_\Sigma V$		θV		$P_\Sigma Q_\Sigma$		PQ	
	abc	*dio*	*abc*	*dio*	*abc*	*dio*	*abc*	*dio*
SPECIFIED VALUES	P_Σ c.l. of AVR	P_Σ c.l. of AVR	θ_a c.l. of AVR	θ^d c.l. of AVR	P_Σ Q_Σ	P_Σ Q_Σ	P_a, P_b, P_c Q_a, Q_b, Q_c	P^d, P^i, P^o Q^d, Q^i, Q^o
UNKNOWN VALUES	U_a, U_b, U_c $\theta_a, \theta_b, \theta_c$ P_a, P_b, P_c Q_a, Q_b, Q_c	U^d, U^i, U^o $\theta^d, \theta^i, \theta^o$ P^d, P^i, P^o Q^d, Q^i, Q^o	U_a, U_b, U_c θ_b, θ_c P_a, P_b, P_c Q_a, Q_b, Q_c	U^d, U^i, U^o θ^i, θ^o P^d, P^i, P^o Q^d, Q^i, Q^o	U_a, U_b, U_c $\theta_a, \theta_b, \theta_c$ P_a, P_b, P_c Q_a, Q_b, Q_c	U^d, U^i, U^o $\theta^d, \theta^i, \theta^o$ P^d, P^i, P^o Q^d, Q^i, Q^o	U_a, U_b, U_c $\theta_a, \theta_b, \theta_c$	U^d, U^i, U^o $\theta^d, \theta^i, \theta^o$

4. *PQ* bus is a standard type of buses in which values of three pairs of injected active and reactive powers are specified. Values of three pairs of magnitudes and angles of voltages are unknown.

Three complex or six real equations, representing the current or power balances for each three-phase bus, are on disposal to solve the unknown values of quantities presented in Table 1. Six unknown values are fully covered by these equations for *PQ* buses only. Twelve unknown values associated with other buses are covered by eight equations only–six previously noted balanced equations and two relations corresponding to specified (controlled) values. Thus four equations have to be established to cover the remaining four unknown values. This problem is solved by applying new scaling concept [4] and synthesizing procedure [8], [9]. With the new scaling concept the transformer complex turn ratios are eliminated from the power system sequence circuits. The synthesizing procedure enables to suppress the equivalent parameters (of the generator and it's corresponding step-up transformer) of the negative and zero-sequence circuits in the transmission network. This suppression enables zero-valued injected currents and powers in the corresponding negative and zero-sequence nodes. Now, the issue of shortage of four equations corresponding to each $P_\Sigma V$, θV and $P_\Sigma Q_\Sigma$ bus in the sequence domain can be solved.

III. POWER SYSTEM SEQUENCE CIRCUITS DECOUPLING

When the power system elements (balanced or unbalanced) are modeled in phase domain there are mutual inductive and capacitive couplings between phases. But, if balanced elements (practically all generators, transformers and transposed lines) are modeled in sequence domain all mutual couplings between phases and sequence circuits are eliminated [7].

When the unbalanced lines are considered in sequence domain, there are couplings among positive-, negative- and zero-sequence and the line model cannot be presented with lumped-π decoupled sequence circuits. In this case, 6x6 node-admittance matrix representatives of the line is full with non-zero elements, just like the 6x6 node-admittance matrix in the phase domain. Thus, the power system model in sequence domain cannot be presented with three linear decoupled sequence circuits. The points of mutually coupling among positive-, negative- and zero-sequence power system circuits are just these unbalanced lines. Inductive and capacitive mutual couplings among positive-, negative- and zero-sequence are expressed with non-zero off-diagonal elements in 6x6 node admittance matrix. Instead of mutually admittances, the couplings can be expressed by compensation current sources [5], [7]. Thus, the unbalanced line model can be presented with three decoupled sequence circuits as it is depicted in Fig. 1a-c. The mutual couplings are replaced by corresponding controlled sources – current sources.

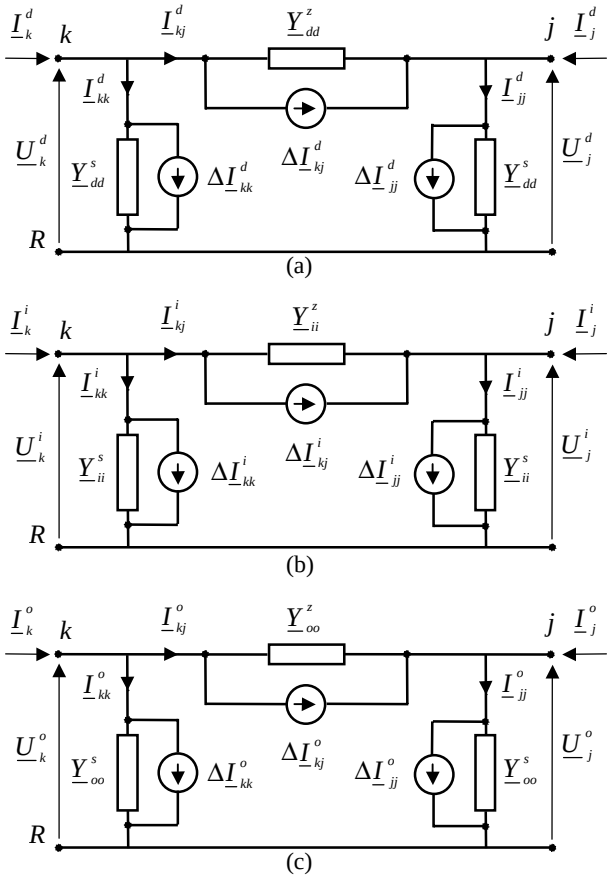

Fig. 1. Unbalanced line decoupled positive- (a), negative- (b) and zero-sequence circuit (c) in absolute value domain.

The current controlled sources in series and shunt branches of each sequence lumped-π circuit include the coupling influences from the other sequences. The self-admittances and the current sources currents in series and shunt branches of any sequence from the Fig. 1 can be calculated very easy as it is shown in [7], [9].

The injected currents in the ends *k* and *j*, of any sequence lumped-π circuit can be corrected by the compensation currents [7], [9]. These corrections enable the omit ion of the current sources from the sequence circuits in Fig. 1a-c and obtaining the final decoupled, compensated, scaled, unbalanced line model in sequence domain, depicted in Fig. 2.

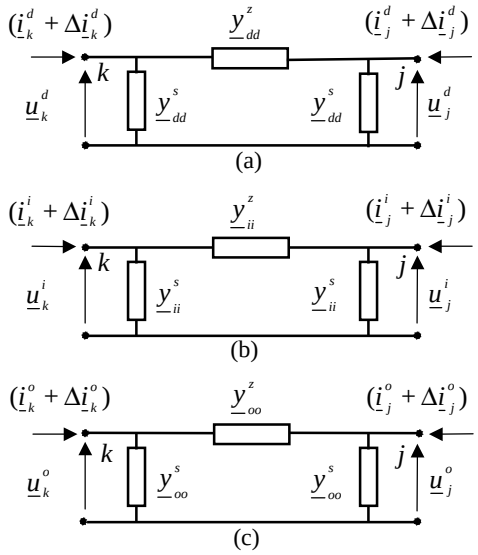

Fig. 2. Unbalanced line decoupled, compensated, scaled positive- (a), negative- (b) and zero-sequence (c) lumped-π circuits.

Applying above described unbalanced line model, new scaling concept, and synthesizing procedure the entire power system can be represented with three decoupled positive-, negative- and zero-sequence circuits.

IV. FAST METHOD DEFINITION

Each load-flow model is based on a power system linear model, which is stated in terms of complex voltages and currents. The most widely used linear power system model is that of the nodal voltage equation. For the power system with *n* three-phase buses, i.e. 3*n* phase nodes, this model in sequence domain (*dio*) says:

$$\underline{\mathbf{Y}}^{dio}_{3n\times 3n}\,\underline{\mathbf{U}}^{dio}_{3n\times 1}=\underline{\mathbf{I}}^{dio}_{3n\times 1}. \tag{1}$$

In the Eq. 1, $\mathbf{Y}^{dio}_{3n\times 3n}$ is node-admittance matrix of the power system equivalent sequence circuits. The complex voltages and injected currents in all power system buses are elements of vectors $\underline{\mathbf{U}}^{dio}_{3n\times 1}$ and $\underline{\mathbf{I}}^{dio}_{3n\times 1}$. They consist of sub vectors of dimensions 3×1, containing the sequence complex quantities. The node-admittance matrix is formed for a sequence circuits without ideal transformers with complex turn ratios. If the number of generators in the power system is n_g, the application of the synthesizing procedure enables power system buses reduction for $2n_g$ buses. Now, the power system can be treated as a system with $r=n-2n_g$ buses or $3r$ nodes. Therefore, the power system model given by Eq. (1) gets new form with reduced dimensions:

$$\underline{\mathbf{Y}}^{dio}_{3r\times 3r}\,\underline{\mathbf{U}}^{dio}_{3r\times 1}=\underline{\mathbf{I}}^{dio}_{3r\times 1}. \tag{2}$$

Finally, if the decoupled, compensated, scaled, unbalanced line model in sequence domain is applied, the entire power system can be represented by new model with three systems of linear equations:

$$\mathbf{Y}^{d}_{r\times r}\mathbf{U}^{d}_{r}=\mathbf{I}^{d}_{rc}, \tag{3}$$

$$\mathbf{Y}^{i}_{r\times r}\mathbf{U}^{i}_{r}=\mathbf{I}^{i}_{rc}, \tag{4}$$

$$\mathbf{Y}^{o}_{r\times r}\mathbf{U}^{o}_{r}=\mathbf{I}^{o}_{rc}. \tag{5}$$

Each of these systems of equations represent the nodal voltage equations for the power system positive-, negative- and zero-sequence decoupled circuits. The matrices of injected currents, corrected by compensation currents (as result of circuits decoupling) $\mathbf{I}^{d}_{rc}$, $\mathbf{I}^{i}_{rc}$ and $\mathbf{I}^{o}_{rc}$ for positive-, negative- and zero-sequence decoupled circuits respectively, are consisted of node injected complex currents. At first, the Eq. (3) can be conjugated and after that multiplied from the left by a diagonal matrix containing the complex positive-sequence voltages. As the result of this procedure, a new nonlinear system of equations representing the power system positive-sequence is obtained:

$$\mathbf{U}^{d}_{r,dij}\left(\mathbf{Y}^{d}_{r,r}\right)^{*}\left(\mathbf{U}^{d}_{r}\right)^{*}=\mathbf{S}^{d}_{rc}. \tag{6}$$

In Eq. (6), matrix $\mathbf{S}^{d}_{rc}$ represents complex, compensated injected powers in the positive sequence circuit nodes [9]. Applying the Taylor's procedure, the nonlinear system of equations given by matrix Eq. (6), can be transformed in the new linear system of equations. This new system is consisted of equations for differences between the injected specified and calculated powers $-\Delta\mathbf{S}^{d}_{kor}$ in the power system positive-sequence circuit nodes, represented by the Jacobian $\mathbf{J}^{d}$ (for this sequence circuit) and unknown differences of voltage magnitudes and angles given by the matrix $\Delta\mathbf{X}^{d}$:

$$\mathbf{J}^{d}\Delta\mathbf{X}^{d}=\Delta\mathbf{S}^{d}_{kor}. \tag{7}$$

or in the well known form with sub matrices:

$$\begin{bmatrix}\mathbf{H}^{d} & \mathbf{N}^{d}\\ \mathbf{M}^{d} & \mathbf{L}^{d}\end{bmatrix}\begin{bmatrix}\Delta\theta^{d}\\ \Delta\mathbf{U}^{d}/\mathbf{U}^{d}\end{bmatrix}=\begin{bmatrix}\Delta\mathbf{P}^{d}_{kor}\\ \Delta\mathbf{Q}^{d}_{kor}\end{bmatrix}. \tag{8}$$

Actually, the matrix Eq. (8) has the same form as the equations which represents the symmetrical load-flow model [10]. The Eqs. (8), (4) and (5) together represent the model of the new fast method for asymmetrical load-flow solution.

Because for the *r*-th, θV bus (or slack bus), the complex voltage is specified ($\underline{U}^{d}_{r,sp}=U^{d}_{r,sp}\angle\theta^{d}_{r,sp}$), the equations representing the power differences for this bus are not included in the system given by Eq. (8).

For all *g* buses, type $P_{\Sigma}V$, the three-phase injected power in phase domain $P^{\Sigma}_{g,sp}$ are specified. This power expressed through sequence voltages and currents is given by equation:

$$P_{g,sp}^{\Sigma} = 3\mathrm{Re}\left[\underline{U}_g^d \left(\underline{I}_g^d\right)^* + \underline{U}_g^i \left(\underline{I}_g^i\right)^* + \underline{U}_g^o \left(\underline{I}_g^o\right)^*\right],\ g \in \{P_\Sigma V\}. \quad (9)$$

As it was mentioned above, the synthesizing procedure enables to account with zero injected currents in this type of nodes in the negative- and zero-sequence circuits ($\underline{I}_g^i = 0$ and $\underline{I}_g^o = 0$). Taking into account this fact, the three-phase injected power given by Eq. (9) can be expressed as:

$$P_{g,sp}^{\Sigma} = 3\mathrm{Re}\left[\underline{U}_g^d \left(\underline{I}_g^d\right)^*\right] = 3\mathrm{Re}\left[\underline{S}_g^d\right] = 3P_g^d, \quad g \in \{P_\Sigma V\}. \quad (10)$$

From Eq. (10), the injected specified power in the buses type $P_\Sigma V$, in positive-sequence circuit is calculated very easy:

$$P_g^d = P_{g,sp}^d = \frac{1}{3} P_{g,sp}^{\Sigma}, \quad g \in \{P_\Sigma V\}. \quad (11)$$

Also, for this type of buses, the positive-sequence voltage magnitude $-U_{g,sp}^d$, is specified. Because, the value of the positive-sequence voltage angle $-\theta_{g,sp}^d$ is unknown, there is only one equation (for differences between the injected specified and calculated active powers) in matrix Eq. (8), for each bus of this type.

If the number of the $P_\Sigma Q_\Sigma$ type of buses is *q*, then for each bus there are two equations (in matrix Eq. (8)) for differences between the injected specified and calculated three-phase active and reactive powers. As specified powers in the nodes of the positive sequence circuit is taken one third of the three-phase active power and one third of the maximum or minimum possible injected reactive power (depending which limit of reactive power is achieved).

For all of *p* buses type PQ, there are two equations in the matrix Eq. (8). Because, for these buses the phase active and reactive powers are specified, it is necessary to express specified injected active power $-P_{p,sp}^d$ and reactive power $-Q_{p,sp}^d$ in the nodes of the positive-sequence circuit. This procedure is explained in [7], [9].

Taking into account the above explanations, the conclusion is that the whole number of equations in the system given by Eq. (8) is $k = 2p + 2q + g$. The solution of systems of equations Eq. (8), (4) and (5) is by iterative procedure.

With the above proposed fast method, the problem of ALF solution is transformed in the easy solution of SLF problem and solution of two systems of linear equations representatives of negative- and zero-sequence power system circuits.

V. METHOD VERIFICATION

The fast method is tested on the entire power system of the Republic of Macedonia consisting of 63 buses of 400, 220 and 110 kV voltage level, 53 lines, 5 interconecting transformers and 9 equivalent generators and step-up transformers. Eight states (variants) are considered. The comparison of the results obtained by Newton–Rapson's method for ALF in phase domain [1] and the proposed fast method in this paper is performed. The proposed fast method in sequence domain is very efficient and robust, because the amount of iterations/CPU time required for calculations and memory storage are significantly smaller then the Newton-Rapson's method for ALF in phase domain.

VI. CONCLUSION

In this paper the efficient fast method for asymmetrical load-flow solution is given. The efficiency is achieved by applying several advancements as: enhanced bus classification, sequence circuits decoupling, new scaling concept and synthesizing procedure. The form of the decoupled positive-sequence part of the presented ALF model is reduced to the form of the classical SLF problem. Thus, the same SLF Newton–Rapson procedure can be applied inside the ALF solution procedure. The negative- and zero-sequence parts of the presented ALF model are represented by two systems of linear equations and solved by Gauss's method of coefficient elimination.

REFERENCES

[1] J.Arrillaga, C.P.Arnold, B.J.Harker, *Computer Modelling of Electrical Power Systems*, John Wiley & Sons Ltd, 1983.

[2] R.G.Wasley, M.A.Shlash, "Newton-Raphson algorithm for 3-phase load flow", PROC. IEE, Vol. 121, No. 7, pp. 630-638, July 1974.

[3] J.Arrillaga, B.J.Harker, "Fast-decoupled three-phase load flow", PROC. IEE, Vol. 125, No. 8, pp. 734-740, August 1978.

[4] V.C.Strezoski, "New scaling concept in power system analysis", IEE Proc.-Gener. Transm. Distrib., Vol. 143, No. 5, pp. 399-406, 1996.

[5] X.-P.Zhang, H.Chen, "Asymmetrical three-phase load-flow study based on symmetrical component theory", IEE Proc.-Gener. Transm. Distrib., Vol. 141, No. 3, pp. 248-252, May 1994.

[6] X.-P.Zhang, "Fast Three Phase Load Flow Methods", IEEE Trans. on PS, Vol. 11, No. 3, pp. 1547-1554, August 1996.

[7] Lj.Trpezanovski, V.Strezoski, "Power System Elements Modeling in Sequence Domain", XXXVII International Scientific Conference on Information, Communication and Energy Systems and Technologies, Proceedings, Vol. 2, pp. 459-462, Nis, Yugoslavia, 2002.

[8] V.Strezoski, Lj.Trpezanovski, "Three–phase asymmetrical load–flow", International Journal of Electrical Power and Energy Systems, Vol. 22, No. 7, pp. 511-520, October 2000.

[9] Lj.Trpezanovski, *Three-Phase Asymmetrical Load Flow in Power Systems*, PhD thesis (in Serbian), University of Novi Sad, Faculty of Technical sciences, Novi Sad, July 2000.

[10] W.F.Tinney, C.E.Hart, "Power Flow Solution by Newton's Method", IEEE Trans. on PAS, Vol. PAS-86, No. 11, pp. 1449-1460, November 1967.

Single Chip Microprocessor Based Electric Power Monitoring and Controlling Meter

Xi Zhaohui[1], Wang Lin[2], Wang Xuewei[3]

Abstract: **The paper introduces a four-function electric power monitoring and controlling meter, which is composed of an induction watt-hour meter and a single chip microprocessor, and packed in two boxes. The sampling pulses sent by the induction watt-hour meter are fed to the single chip microprocessor, and the microprocessor measures the pulses to complete monitor and control.**

Keywords **– Meter, Microprocessor, Single chip.**

I. INTRODUCTION

The rise in economic importance of electric energy has resulted in the development of more instruments for electric energy monitoring, controlling and measurement. In China, electric energy management instruments have more and more effect on unity of electricity generation, supplying and consuming, and therefore efficiency of electricity production has been distinctly improved. From the late of 1980's microprocessor based electric energy management meters were put into application. This kind of meters has multi-function, small volume and is programmable. The use of them has saved labors and increased the management level, which will make wide application of microprocessor based electric energy management meters in the near future. In the other aspect, the new management meter now has some problems in reliability, which happens in the following situation.

1. Harbin University of Science & Technology
Add: 52 Xuefu Road, Nangang District, and Harbin, China 150080
E-mail: xichaohui@hotmail.com
2. Beijing University of Chemical Technology
3. Beijing University of Chemical Technology
No.15 beisanhuan Dong Road, Beijing China 100029
E-mail: wangxw@mail.buct.edu.cns

1) when large inductive load switches on or off in power supply circuit, the microprocessor run" fly "and" lock "(can't work correctly).

2) When electricity in the meters controlled power supply is switched on or off, the data, like
maximum demand are lost in the meters.

To overcome the problems, shielding technique and microprocessor system reliability design technique must be adopted and developed.

Because the developed shielding theory now can be used in a design, we focus our attention on reliability design of microprocessor system in this paper.

II. CONSTRUCTION OF THE METER

The meter is mainly composed of an induction watt-hour meter and an 89C51 single chip microprocessor system, as illustrated in Fig.1.

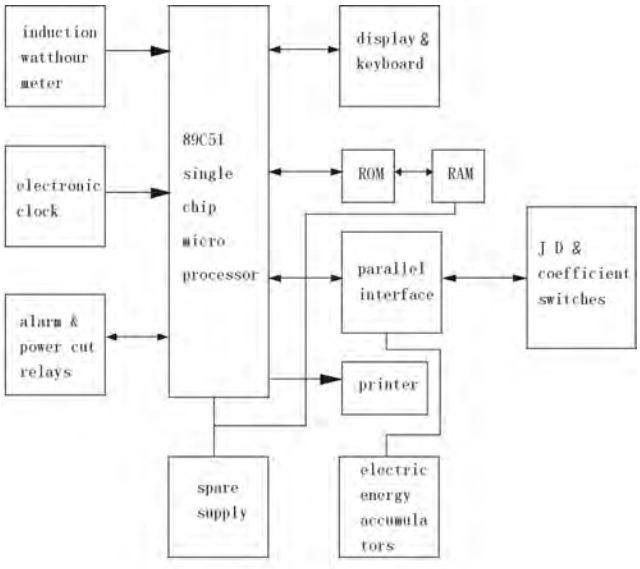

Fig.1 Block diagram of the electric energy monitoring and controlling meter

Other parts of the meter are electronic clock, printer, electric energy accumulators, display and relays. The induction watt-hour meter sends a sampling pulse every turn. The microprocessor receives the pulse, and performs the following function.

1) Display the instant electric power.

2) Display maximum demand, i.e. MD.

3) According to the time periods divided, record KWh separately in peak period, in valley period and in normal period.

4) In peak period, monitor consumer power, when consumer power exceeds stipulated kilowatt, the micro-process gives an alarm. If the consumer power is not decreased in ten minutes, the microprocessor cuts off power supply of the consumer.

5) At the end of every month, reserve the MD, electric energy KWh in peak, valley and normal periods and total energy KWh for printing values of them in the later time.

The turn speed of the induction watt-hour meter is in proportion to the power, so by measuring sampling pulse cycle the instant electric power is obtained. Supposing constant of the induction watt-hour meter is C turn/KWh, the electric power can be expressed as

$$P = \frac{3600 \times f}{C \times n} \qquad (1)$$

Where p instant electric power (KWh),

c constant of a induction watt-hour meter(turn/KWh),

f counting pulse frequency(Hz),

n value in counter between two sampling pulses.

Stipulated kilowatt, i.e. JD, is set in percent rated power of the induction watt-hour meter by two decimal switches. Supposing J is the percentage, the count up to the alarm in power counter can be calculated by the following equation.

$$n_0 = \frac{3600 \times f}{C \times J \times P_0} \qquad (2)$$

Where: n_0 the alarm count value:

J percentage:

P_0 rated power of induction watt-hour meter (KW).

Program design bases on the equation (1) and (2). Fig .2 shows block diagram of the instant power measurement, power exceeding alarm and power exceeding cut program.

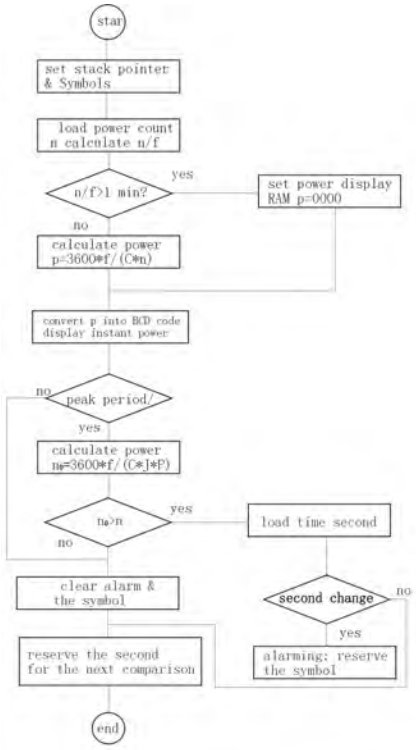

Fig.2 Block diagram of the instant power measurement, power exceeding alarm and cut program

III. RELIABILITY DESIGN OF THE MICROPROCESSOR SYSTEM

Single chip microprocessor is the kernel of the meter. In the microprocessor system design, its reliability is put in the most important position and method is using overlap of the program memory address, parted address between data and program memory and self-reset technique [(1)]. The memory of the 89C51 microprocessor has two different configurations, which is shown in Fig.3. This microprocessor memory structure is easy to “run fly and lock ” (program is not executed) in the appearance of disturbance. The reasons are described in the following.

1) CPU executes the machine code not in the sequence of program design.

2) CPU executes the random code beyond the memory address of the program and data.

3) CPU executes the code in data memory.

4) The state of symbol data changes, so the CPU can’t executes the program correctly.

For the first situation, CPU can enter the designed program flow after it executes 3~5 instructions, i.e. the execution of code program is recoverable. The

microprocessor system is working after disturbance. For the second situation, execution of the random code makes CPU run randomly also, as a result that microprocessor system is locked. For the third situation, the result is the same as the second situation. For the fourth situation, if the symbol data is not recoverable, the measurement and control is out of order. In order to overcome the second wrong working state, the program memory address must be overlap, which means that the unused program memory space is merged into memory space occupied by the program. This method makes CPU access the program only from used memory space. In the meter described here the overlapped program address space is only 8K byte. In order to overcome the third wrong working state, the program memory space must be parted from data memory space, which means the CPU can't load program code from date memory. This memory configuration is shown in fig.3. (b).

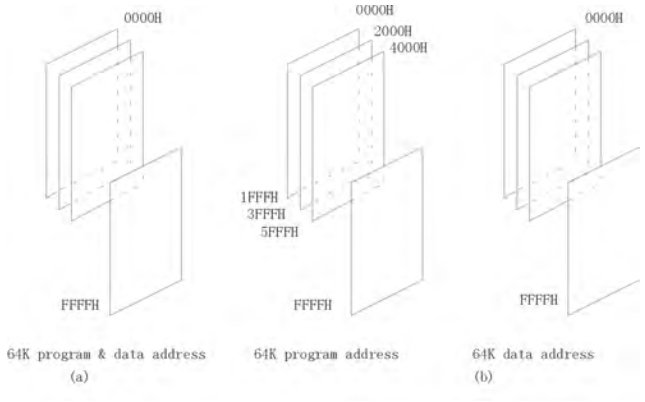

Fig.3 The two configuration of the 89C51 microprocessor memory

In order to overcome the fourth wrong working state, every symbol data is reserved in memory three-ply. When CPU reads the data, it compares the data with other two copies, and if two of the three data are identical, the data is usable, and if the three copies of the data is different, the data is useless and CPU sends wrong indication (Light a lamp).

For the sake of preventing CPU from going into dead loop, self-reset circuit was designed. Schematic diagram is shown in Fig.4.

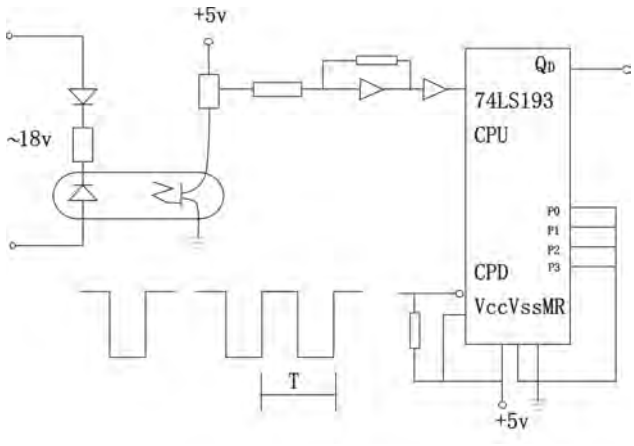

Fig.4 Self-reset circuit diagram

The 18V A.C. voltage passing through the photocopier and buffers is converted into square wave with 20ms cycle. The counter 74ls193 counts the square wave pulses and pin Q_D output pulses with the cycle 320ms. When CPU works, it sends clear pulse every T Millisecond. If the T<320ms, pin Q_D outputs low, no reset Pulse is sent to the CPU. When CPU does not work, no clear pulse is sent to the counter, the pulse on the pin Q_D restart the microprocessor system immediately.

IV. THE ANTI-DISTURBANCE EXPERIMENT

To proof anti-disturbance microprocessor system design theory proposed in the above section, three electric power monitoring and controlling meters were used to try the property of anti-disturbance on condition that disturbance generator and three meters used the same A.C. Supply and distance between them is no more than three meters. The shielding system of the meter is designed carefully. The disturbance generator is the pulse source in laser and the pulse strength is 10KV, 2KA and 50ns, therefore the disturbance is very strong. Ten group experiments were carried out with 20 min interval. Every group experiment was 10 min and pulse source discharged every second. In the disturbance period, the electric power monitoring and controlling meter worked in the normal condition, at the same time, the other electronic apparatus in the same room is out of order, Electric arc interference on the meter is also observed, when the power supply was switched on or off. In the experiments, the maximum demand, watt-hour and power display were right and data reserved were correct in this condition.

V. CONCLUSION

The electric power monitoring and controlling meter was put into application at the beginning of 1988, and worked more than two years. Practice shows that the microprocessor based electric power monitoring and controlling meter is capable of substituting the old electric energy management meters.

REFERENCE

(1) Wang Xuewei, Sun Yingda and Wang Lin, No. 1 1990 " The Anti-interference System in single Chip Computer ", Journal of Harbin University of Science and Technology, Vol.14, Sum No, 29, pp33 – 37.

Session REM:

Remote Ecological Monitoring

Heat – Technological Scheme for Cooling of Mineral Water

Georgi I. Valtchev[1] and Violeta Rasheva[1]

Abstract - **Republic Bulgaria is rich of mineral waters, which are used for drinking and curative purposes. The mineral water for drinking purposes is bottling in plastic bottles and the technology for bottling of the water requires to cool it to definite temperature before bottling.**

The aim of this paper is to be studied different heat-technological schemes for bottling of mineral water and be pointed out their advantages and disadvantages. In result of that the most effective scheme can be chosen at given conditions of bottling.

Keywords - **mineral water, bottling, heat schemes for cooling, heat exchangers**

I. Introduction

Republic Bulgaria is rich of mineral springs which waters possess curative qualities and they are used as drinking water in the our country and abroad. For meeting of market needs these waters are bottled in plastic bottles for single use. However in the most cases the temperature of the mineral waters is higher than the ambient temperature. This fact creates problems with the water bottling because deforming of the bottles after cooling of the water filled in them. That's why the mineral waters have to be cooled to temperature of 25 ^{0}C before their bottling.

Two heat - technological schemes of installations for cooling of mineral waters before their bottling are offered in this paper. The mineral water cooling is realized indirectly in a plate heat exchanger. Circulating water is used as cooling fluid. In the first heat - technological scheme this circulation water is cooled on the other hand in a coil heat exchanger, sunk in a natural or artificial water basin. A freezing plant is used for cooling of the circulation water in the second scheme.

The aim of the paper is to be studied different heat-technological schemes for cooling of mineral water before its bottling and to be pointed out their advantages and disadvantages.

II. Materials and Methods

In the studied case the mineral water which is subject to bottling has temperature of 47 ^{0}C and has to be cooled to temperature of 25 ^{0}C. The first variant of scheme for cooling of mineral water with sunk heat - exchanger is presented on fig. 1. The cooling of the mineral water occurs indirectly in a plate heat - exchanger 1 as for cooling fluid is used circulating in closed loop water. This water takes away the heat from the mineral water and on the other hand it is cooled in a heat - exchanger 2 sunk in a natural or artificial water basin.

[1]Georgy I. Valtchev is with the Department of Industrial Heat Engineering, University of Food Technologies, blvd. Maritza 26, 4002 Plovdiv, Bulgaria, E-mail: g_valtchev@abv.bg

[1]Violeta D. Rasheva - E-mail: v_rasheva@abv.bg

The last heat - exchanger represents pipe coil from two, three or four parallel pipes with diameter Φ60x3,5 and length in dependence of the mass flow rate of the cooled mineral water.

Two variants of the sunk heat - exchanger at volumetric flow rate of mineral water $\dot{V}_1$ = 20 m^3/h are presented on fig 2. In the first variant (fig. 2a) the coil is manufactured from two parallel pipes and in the second variant (fig. 2b) the coil is manufactured from three parallel pipes.

Other two variants of the sunk heat - exchanger at volumetric flow rate of mineral water $\dot{V}_2$ = 30 m^3/h are presented on fig 3. In the first variant (fig. 3a) the coil is manufactured from three parallel pipes and in the second variant (fig. 3b) the coil is manufactured from four parallel pipes.

In the second principle heat - technological scheme of installation for cooling of mineral water freezing plant is used instead of the sunk heat - exchanger.

III. Experimental Results and Data Analysis

A. Heat - technological scheme of installation with sunk heat - exchanger

Heat and constructional calculations of the plate and the sunk heat - exchangers are carried out and their parameters are determined as follow:

1.Determining of plate heat - exchanger parameters

It is accepted that the fluids in the heat - exchanger flow in countercurrent as the mineral water is cooled from temperature of 47 ^{0}C to temperature of 25 ^{0}C and the circulating water is cooled from temperature of 20 ^{0}C to temperature of 30 ^{0}C.

The mean temperature difference between the temperatures of the two fluids is determined from the equation of mean logarithmic temperature difference

$$\Delta t_{CP} = \frac{\Delta t_A - \Delta t_B}{\ln \frac{\Delta t_A}{\Delta t_B}}, \quad \text{K} \qquad (1)$$

where Δt_A and Δt_B are larger and smaller temperature differences in the two ends of the heat-exchange surface, K

The mass flow rate of the cooled mineral water is calculated from the equation

$$\dot{m}_{M.W} = \frac{\dot{V}_i \cdot \rho}{3600}, \quad \text{kg/s} \qquad (2)$$

where $\dot{V}_i$ is volumetric flow rate of the mineral water, m^3/h;

ρ - density of the mineral water, kg/m^3,

and the heat flow rate which has to be taken away from the mineral water in the plate heat - exchanger is determined from the equation of the energy balance of the heat - exchanger

$$\dot{Q}_P = \dot{m}_{M.W}.c_P.(t'-t''), \quad \text{kW} \qquad (3)$$

where c_P is a specific heat capacity of the mineral water, J/(kg.K);

t' and t'' - temperatures of the mineral water at the inlet and the outlet of the heat - exchanger respectively, K.

The necessary heat-exchange surface of the plate heat-exchanger is determined from the basic equation of heat transfer

$$F_P = \frac{\dot{Q}_P}{k_P.\Delta t_{CP}}, \quad \text{m}^2 \qquad (4)$$

where k_P is heat transfer coefficient, W/(m^2.K).

Its value is accepted according to [5].

The necessary mass flow rate of the circulating water is determined from the equation of the energy balance of the heat - exchanger

$$\dot{m}_{C.W} = \frac{\dot{Q}_P}{c_P.(t_W^{'} - t_W^{''})}, \quad \text{kg/s} \qquad (5)$$

where c_P is a specific heat capacity of the circulating water, J/(kg.K);

$t_W^{'}$ and $t_W^{''}$ - temperatures of the circulating water at the inlet and the outlet of the heat - exchanger respectively, K.

The results from the heat calculations of the plate heat exchanger for two different volumetric flow rates of the cooled mineral water ($\dot{V}_1$ = 20 m^3/h and $\dot{V}_2$ = 30 m^3/h) are presented in table I.

Table I

Results from the Heat Calculation of the Plate Heat Exchanger

N	Parameters	Sym-bol	Unit	Value at	
				$\dot{V}_1$=20 m^3/h	$\dot{V}_2$ =30 m^3/h
1	Mean temperature difference	Δt_{CP}	K	9,83	9,83
2	Mass flow rate of mineral water	$\dot{m}_{M.W}$	kg/s	5,55	8,33
3	Heat flow rate	$\dot{Q}_P$	kW	512	768
4	Heat transfer surface	F_P	m^2	26	39
5	Mass flow rate of circulating water	$\dot{m}_{C.W}$	kg/s	12	18,3

2.Determining of the parameters of the sunk heat - exchanger (coil)

It is accepted that the temperature of the water in the water basin is 14 ^{0}C and it is constant. The circulating water is cooled from temperature of 30 ^{0}C to temperature of 20 ^{0}C. Thus the mean temperature difference between the temperatures of the two fluid in the heat - exchanger is determined from the equation (1).

The heat flow rate which has to be taken away from the circulating water is determined from the equation of energy balance of the sunk heat - exchanger

$$\dot{Q}_C = \dot{m}_{C.W}.c_P.(t_W^{'} - t_W^{''}), \quad \text{kW} \qquad (6)$$

where c_P is a specific heat capacity of the circulating water, J/(kg.K).

The necessary heat-exchange surface of the coil heat-exchanger is determined from the basic equation of heat transfer

$$F_C = \frac{\dot{Q}_C}{k_C.\Delta t_{CP}}, \quad \text{m}^2 \qquad (7)$$

where k_C is heat transfer coefficient of the coil heat-exchanger, W/(m^2.K).

Its value is accepted according to [6].

The total length of the coil is determined from the equation

$$L = \frac{F_C}{\pi.d_{BH}}, \quad \text{m} \qquad (7)$$

where d_{BH} is outside pipe diameter, m.

Determining of the speed of the water in the coil pipe

The water speed is determined from the equation of continuity

$$w = \frac{\dot{m}_{C.W}.v}{f.n'}, \quad \text{m/s} \qquad (8)$$

where v is water specific volume, m^3/kg;

f - clear opening of one pipe, m^2;

n'- number of parallel pipe of the coil heat - exchanger.

Determining of the coil heat - exchanger pipe number with unit length ***l*** *= 6 m* (fig. 2a)

The pipe number of the coil heat - exchanger is determined as the total length is divided of the unit pipe length

$$n = \frac{L}{l}, \qquad (9)$$

and overall length of the coil heat - exchanger a (fig. 3a) depends on the interval between the two next pipes a' (fig. 3b) and pipe number n and it is calculated from the equation

$$a = a'.n, \quad \text{m.} \qquad (10)$$

Determining of the total mass of the coil heat - exchanger pipes

The mass of one linear meter pipe from carbon steel and with dimensions Φ60x3,5 is m' = 4,88 kg [1], and the total mass of the coil pipes is calculated from the equation

$m = m' . L$, kg. (11)

Costs for the coil heat - exchanger pipes

The price of the pipes is P_T = 2 BGL per kg and the total costs for the coil heat - exchanger pipes is calculated from the equation

$$C_T = P_T . m, \text{ BGL.} \quad (12)$$

The results from the heat and constructional calculations of the sunk heat exchanger for two different volumetric flow rates of the cooled mineral water ($\dot{V}_1$ = 20 m^3/h and $\dot{V}_2$ = 30 m^3/h) are presented in table II.

Table II

Results from the Heat and Constructional Calculation of the Coil Heat Exchanger

N	Parameters	Sym-bol	Unit	Value at	
				$\dot{V}_1$=20 m^3/h	$\dot{V}_2$ =30 m^3/h
1	Mean temperature difference	Δt_{CP}	K	10,2	10,2
2	Heat flow rate	$\dot{Q}_C$	kW	503	767
3	Heat transfer surface	F_C	m^2	82	125
4	Total length of the coil pipes	L	m	435	663
5	Mass flow rate of water in 1 pipe	$\dot{m}_1$	kg/s	6 [a]	6,1 [c]
6	Mass flow rate of water in 1 pipe	$\dot{m}_1$	kg/s	4 [b]	4,575 [d]
7	Speed of the water in the pipes	w	m /s	2,72 [a]	2,76 [c]
8	Speed of the water in the pipes	w	m /s	1,8 [b]	2,07 [d]
9	Pipes number	n	-	73	111
10	Overall length of the coil heat - exchanger	a	m	9	13
11	Total mass of coil pipes	m	kg	2 123	3 235
12	Costs for coil pipes	C_T	BGL	4 246	6 470

*Note

a/the variant with two parallel pipes of the coil and volumetric flow rate $\dot{V}_1$ = 20 m^3/h (fig. 2a);

b/the variant with three parallel pipes of the coil volumetric flow rate $\dot{V}_1$ = 20 m^3/h (fig. 2b);

c/the variant with three parallel pipes of the coil volumetric flow rate $\dot{V}_2$ = 30 m^3/h (fig. 3a);

d/the variant with four parallel pipes of the coil volumetric flow rate $\dot{V}_2$ = 30 m^3/h (fig. 3b).

B. Heat - technological scheme with freezing plant

The electrical power consumed from the freezing plant is N_{EL} = 90 kW and it is determined in result of the heat calculations of the freezing plant [2,3,4] and the heat flow rate which has to be taken away from the circulating water. The operating costs of the freezing plant compressor are determined at electrical energy price of 0,15 BGL per kWh.

For 24 hours they are - 2 160 kWh and 324 BGL.

IV. Conclusions

1.Two heat - technological schemes of installations for cooling of mineral water before its bottling are offered in this paper. The cooling of the mineral water is performed indirectly in a plate heat - exchanger as the circulating heat transfer carrier is cooled on the other hand in a sunk heat - exchanger in the first heat - technological scheme and a freezing plant is used in the second heat - technological scheme.

2.The operating costs for the first scheme with sunk heat - exchanger are significantly lower in comparison with these for the second scheme with a freezing plant.

3.The first heat - technological scheme could be used successfully if there is a natural or artificial water basin near by bottling plants.

4.The result from this investigation could be useful for the companies bottling mineral water.

References

[1] BDS 6007/80

[2] .St. Dichev. Freezing Plants, Plovdiv, Academic publishing house of HIFFI, 2002.

[3] G. Kimenov. Thermodynamic and Physical Properties of Materials, Reference book, Sophia, Technique, 1995.

[4] N. N. Kokoshkin and other. Heat and Constructional Calculations of Freezing Plants, Leningrad, Mechanical engineering, 1976.

[5] V. A. Milchev. Industrial Heat Installations, Sophia, Technique, 1993.

[6] K. F. Pavlov, P. G. Romankov, A. A. Noskov. Examples and Tasks for the Course of Processes and Apparatuses of Chemical Technology, Leningrad, Chemistry, 1981.

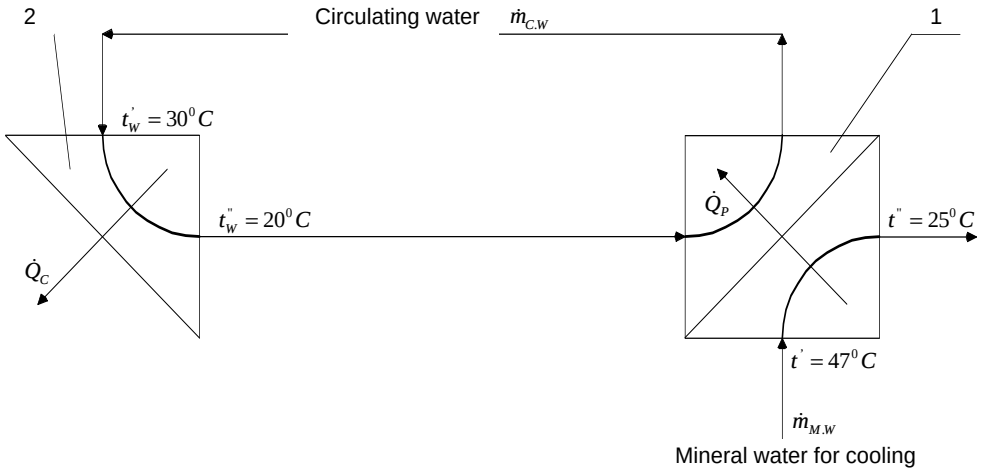

Fig. 1.Sceme of installation of mineral water cooling with sunk heat - exchanger
1 - Plate heat - exchanger; 2 - Sunk heat - exchanger (coil)

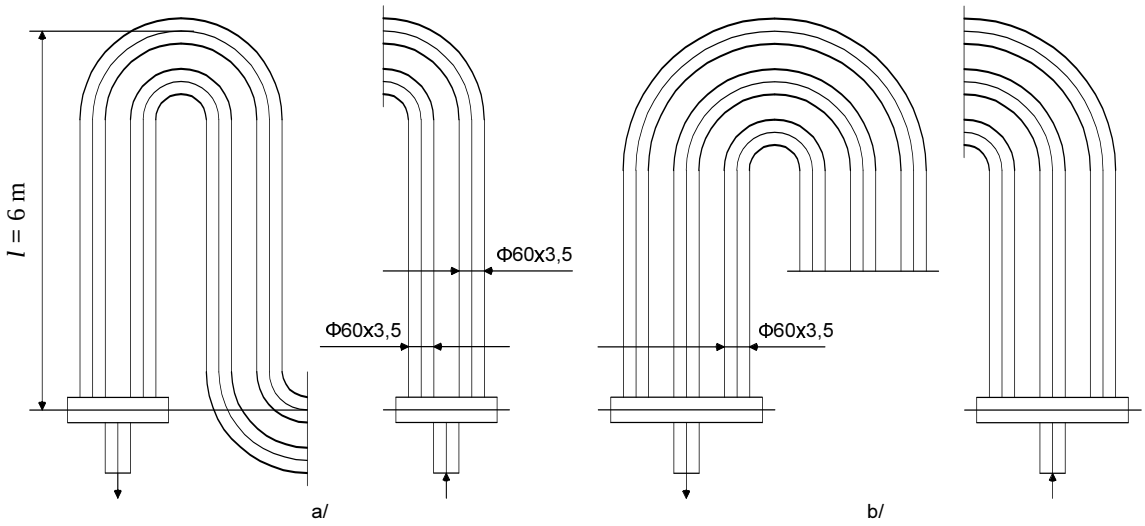

Fig. 2. Variant of the first scheme of installation with sunk heat exchanger at volumetric flow rate $\dot{V}_1$ = 20 m^3/h

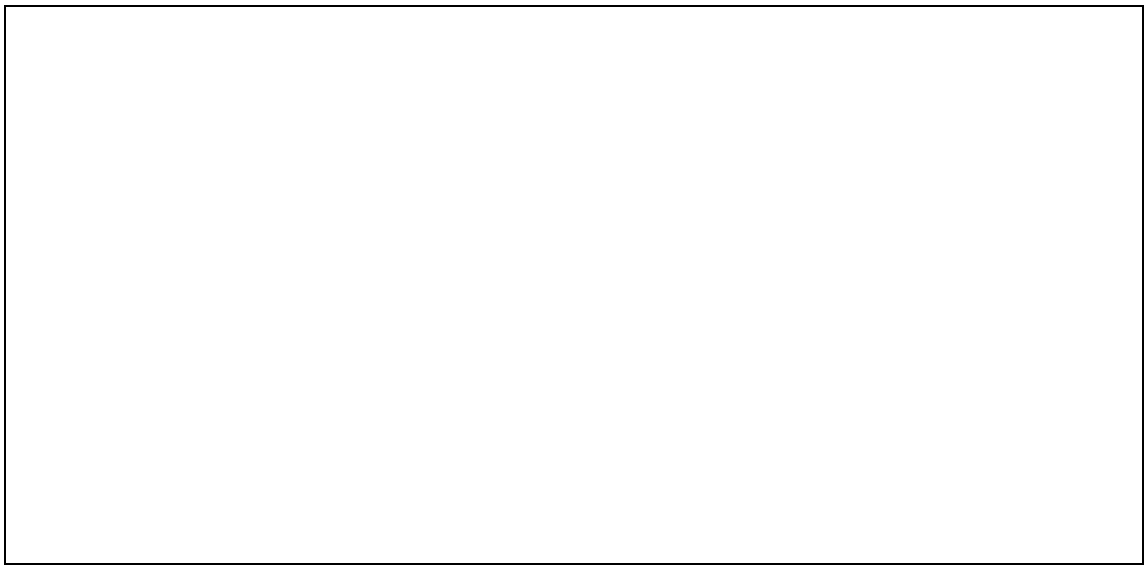

Fig. 3. Variant of the first scheme of installation with sunk heat exchanger at volumetric flow rate and $\dot{V}_2$ = 30 m^3/h

Automatic Station for Continuous Monitoring of Environmental Radiation

Mityo G. Mitev[1], Ludmil T. Tsankov[2], Chavdar B. Lenev[3]

***Abstract* – The problems concerning design of an automatic station for continuous monitoring of the environmental radiation are described. The structure of the station is presented as well as the implemented principles, methods and operation modes. Some problems arising from the continuous operation mode under open atmospheric conditions are also discussed.**

Keywords – Continuous measurements, absorbed dose-rate, logarithmic energy spectrum

I. INTRODUCTION

The actuality of the problem for continuous measurement and monitoring of the environmental radiation is still more increasing in the last years due to the frequently occuring armed conflicts, terrorists attacs, potential accidents in nuclear power plants etc. [1]. There are three main difficulties in this respect:

- the deficiency of equipment possessing high sensitivity and precision in order to measure near-background radiation level; (to achieve the necessary accuracy the energy distribution of the radiation has also to be taken into account);
- the increased requirements to the equipment working at heavy conditions – continuous outdoor operation in a wide temperature interval, precipitation etc.;
- the high price of the commercial equipment which can in part satisfy the above requirements.

A possible way to achieve both high sensitivity and high accuracy in a wide dose-rate range is to use two detector systems. The low levels are then measured by high sensitive detectors (e.g. based on NaI(Tl) scintillators) and the high dose rates – by ionisation detectors [1].

The progress in the electronic components during the laste decade has made possible to develop portable spectrometric systems having lower power requirements and lower price [2,3]. They can serve as a basis for high sensitive systems for continuous monitoring which conform with the above mentioned requirements.

The automatic station suggested in the present work is based on a portable multichannel analyser with a logarithmic energy scale [3]. It uses single detector system with a 3x3" NaI(Tl) crystal and two measurement modes.

The dose rate for weak radiation fields is determined by means of the spectrometric data collected during the measurement.

In the case of high radiation intensity (when the dead time of the spectrometric channel is considerably large) the dose rate is determined by the information generated from the radiometric channel which is a single-channel spectrometer with variable energy threshold (in order to flatten the energy dependence of the dose).

II DESIGN

A generalised structural scheme of the automatic station is shown on Fig.1. It contains the following main blocks:

A. Detector module

A scintillation crystal $\varnothing 3\times 3''$ is used combined with a FEU82 (Russia) photomultiplier.

B. Detector power supply

A diode-capacitive Cockroft-Walton multiplier is used to supply the PMT dynode system. A LM2578 pulse stabiliser is used which can directly stabilise negative voltage [4]. The dynode potentials are controlled by changing the value of a control voltage generated by integrating the PWM1 output signal of the used microcontroller. In this way, the PMT operation mode can be software controlled.

Total energy consumtion of the high voltage converter does not exceed 4mA at 12V source supply.

C. Spectrometric channel

The detector output signals are shaped and selected by a resonant charge-code converter [5]. Its operation principle is based on the idea to use a LC circuit as a load in the PMT anode chain and to count the maxima (or minima) of the generated fading oscillations until they 'sink' under a predefined reference level. The number of the counts serves then as a code to sort the event registered by the detector according to its energy. This addressing method is very simple; however, the channel numbers are proportional to the energy logarithm instead to the energy itself.

The number of the useful channels in such a multichannel analyser depends on the LC circuit's quality factor. It can be improved by a partial compensation of the energy dissipated inside the LC circuit. If a positive feedback is introduced, 256 channels of the spectrometer are achieved.

The pulses coming from the detector during the conversion time of the spectrometer are switched over to the radiometric channel using a differential current switch. In this

[1] Mityo G. Mitev is with the Faculty of Electronics and Electronic Technology, TU - Sofia, Bulgaria, E-mail: mitev@ecad.tu-sofia.bg

[2] Ludmil T. Tsankov is with the Faculty of Physics, University of Sofia, 1164 Sofia, Bulgaria, E-mail: ludmil@phys.uni-sofia.bg

[3] Chavdar B. Lenev is with the Institute for Nuclear Research and Nuclear Energy, BAS, Sofia, Bulgaria, E-mail: lenev@inrne.bas.bg

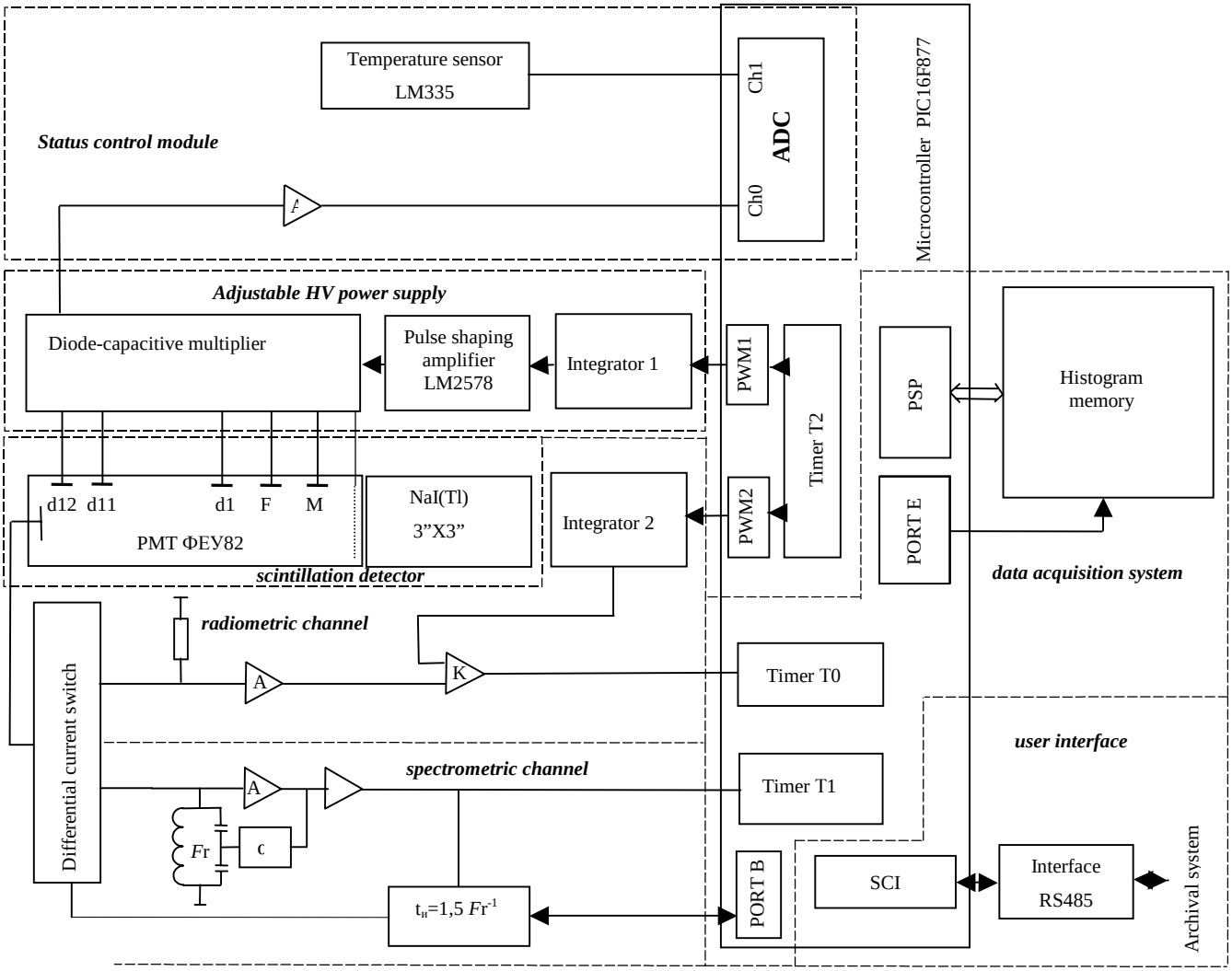

Fig. 1

way it is possible to account for the events lost during the dead time of the spectrometer channel.

D. Radiometric channel

The radiometric channel comprises of a linear amplifier of the PMT anode pulses and a comparator which converts them to standard CMOS levels. The comparator's threshold is controlled by the output voltage of a second integrator following the PWM2 output of the used microcontroller. So, it can be also controlled by the software.

If the count rate of the incoming pulses is low, the spectrometric mode is preferred. A low level value is given the comparator's threshold, so that all events entering the detector during the spectrometer's dead time are registered by the radiometric channel.

At higher count rates the dose is determined only by the radiometric channel. In that case, all pulses are switched to the radiometric channel via the differential current switch and the comparator's threshold is being varied so that the dose rate can be calculated by the JAERI method [6].

E. Data Acquisition System

The data acquisition system is based on a single chip microcontroller PIC16F877 of MicroChip and it uses extensively its peripheral systems.

Timer2 is used to generate the main time intervals of the system. It is used also in the two PWM pulse generators which control the PMT high voltage (PWM1) and the radiometric comparator's level (PWM2).

All shaped pulses bursts coming from the spectrometric channel are counted by the Timer1 which works in burst mode. The timer output code is used as address for sorting the current event into the spectrometric (histogram) memory.

The spectrometric memory is 128 kbyte. Its schematic is designed to exchange up to 16 bytes in burst mode. The memory contains up to 240 spectrograms which allows a long time standalone work of the system.

Timer0 is used to register the pulses coming from the radiometric channel.

Port B is used in interrupt mode to receive end-of-burst signal from the spectrometric subsystem. It can also control the differential current switch to redirect all the PMT anode pulses to the radiometric channel.

F. Interface

All data collected in the automatic station are transferred to a higher hierarchy control level in NRZ format via the serial communication interface (SCI) embedded in the microcontroller. All electric signals are RS485 compliant. The latter interface is preferred by two reasons:

- it ensures stable work at relative longer distances to the archiving station;
- it allows parallel operation of several units (such as a meteosattion, for example).

G. Status control

A status control channel is foreseen in the automatic station to monitor some of its current parameters.

The ADC embedded into the microcontroller is used to measure the current value of the PMT voltage (the potential between the anode and the last dynode which is proportional to the whole voltage supplied to PMT).

The temperature of the scintillation detector is also measured. The used sensor is of type LM335; it has sensitivity 10 mV/K, thus allowing a discretisation step of 0.5 ^{o}C.

H. Power supply of the station

The continuous operation mode of the automatic station sets strong requirements regarding the power supply module. All necessary voltage supply is taken from a pulse DC-DC converter (not shown in Fig.1) powered by 9-24V DC. The total energy consumption of the station does not exceed 90mA at 12V in all modes of operation.

The power for the DC-DC converter is received from a 220 V~ /12 V= AC-DC converter backed up by a 12V/3.2Ah lead accumulator. The load characteristic of the AC-DC converter is limited by output current to 400mA and by output voltage at 13.8V. Thus, an optimal recharging mode of the used accumulator is guaranteed. In case of power net failure the automatic station can work more than 24h with the backup accumulator.

III Operation modes

A. Determination of the dose rate in the spectrometric mode

The dose absorbed within the detector volume is determined by means of the spectral distribution of the registered gamma-rays. The charge appearing at the PMT anode is proportional to the energy deposited in the detector and it is independent on the kind of the interaction. The dose absorbed for the time interval of the measurement is:

$$D = k_d \cdot \sum_{I_{\min}}^{I_{\max}} N(I).E(I) \qquad (1)$$

where N(I) is the number of counts registered in the I-th channel;

E(I) is the average energy corresponding to the I-th channel;

k_d is a coefficient to account for the detector mass and geometry.

An advantage of this method is its high accuracy and sensitivity which are superior to any other methods at low dose rates (i.e. close to the natural background).

B. Determination of dose rate in the radiometric mode

At higher count rates the dead time of the resonant charge-code converter becomes rather high and causes considerable measurement errors. It is provided to use the radiometric channel in this case, when all PMT signals are redirected to that channel (by the differential current switch).

In this case, the method of the so called spectral weight function G(E) is used for dose calculations [6]. G(E) is indeed a conversion operator connecting the absorbed dose with the pulses distribution by:

$$D = \int_{E_{\min}}^{E_{\max}} F(E).G(E)dE \qquad (2)$$

where F(E) is the spectral distribution of the registered events in the energy range E_{min} - E_{max}.

In the measurement, the operator G(E) is replaced with a time dependent operator G(t), which repeats its characteristic during the integration time interval. This is made using the programmable threshold of the integral discriminator (the comparator in the radiometric channel):

$$D = k_d \int_{E\min}^{E_{\max}} N(E).G(E)dE = k_d^t \cdot \sum_{t_{\min}}^{t_{\max}} N(t).G(t) \qquad (3)$$

Here again k_d^t accounts for the detector characteristics.

In this case the automatic system works as a single-channel analyser. So, the length of the integration time interval $t_{\max} - t_{\min}$ should be sufficiently short (several seconds) to follow the dynamics of the radiation field. In fact, the time cycle in (3) is continuously repeated.

This method allows measurement of dose levels which are considerably higher than those achievable by the multichannel spectrometric method without replacing the detector system.

IV Problems arisig from continuous operation

The automatic station is designed for long term continuous outdoor work. The measurement conditions set additional requirements regarding its stability and reliability. Some of the more essential resulting problems are:

A. Temperature drift

The outdoor operation implies a temperature change in a very large interval (at least -20^{o}C to +40^{o}C). The temperature drift of the scintillation detectors is well pronounced. It is due mainly to the PMT instability. Hence, a stabilisation system is required to compensate temperature drift. In our system the temperature drift has been separately studied and the PMT high voltage supply is tuned during the operation using the temperature value measured continuously at the detector system.

B. Long term instability

The long term instability of the spectrometric systems is usually defined for 16h continuous work at count rate 1000 cps and constant operation conditions (temperature, power supply etc. [7]).

The long term continuous operation requires even stronger stability. For example, the change of the ambient air humidity influences the capacitive multiplier work and then it changes the overall PMT gain. Some additional constructive precautions have been taken to avoid that effect: the high resistance part of the PMT supply is carefully varnished and some absorbing substance is put into the hermetised volume (silica gel).

The ageing of the components also influences the long term stability of the system, e.g. the degradation of the last PMT dynode can decrease the anode current by 50-80% for 1000h operation.

Hence, an additional method for active stabilisation is required. A general solution is to control the centroid of the spectral line of a known isotope; the best candidate is the naturally occuring ^{40}K. This method is not applicable in some specific cases – if the reference line is masked by stronger lines in its vicinity (e.g. ^{60}Co). Then the active stabilisation is bypassed.

C. Power supply backup

The used power supply scheme allows continuous operation of the system for more than 24h without external power source.

V CONSTRUCTION FEATURES

The used non-standard spectrometer design makes possible to assemble the whole automatic system inside a single hermetic cylindrical container of magnetic soft material with outer dimensions $\varnothing 115 \times 300 mm$ (including the scintillator). It has a 4-wires connection: two for the DC power supply and two for the interface.

VI. CONCLUSION

Usually, the systems for radiation monitoring are based on doubled detector system – one high sensitive detector is used for the low doses and another – for elevated doses.

Combining a spectrometric method with that of the pulse height weighting function [6] makes possible to use the same detector for both high and low radiation fields keeping good accuracy and sensitivity in a large dose scale.

System parameters:

Detector system background	< 20 nGy/h
Energy range	50 keV – 10 MeV
Pulse height analysis	resonant charge-code converter at 1MHz, 256 channels
Conversion time	(4.4 + N.1) μs – N is the channel number
Histogram memory	128kB, 2^{16}-1 counts per channel, up to 240 spectra.
Dead time correction	counting the lost pulses

Adjustments
Automatic acquisition cycle – 0.01s to 167772s, step 10 ms
Hardware adjustment of the energy scale slope
HV adjustment – programmable, 500-2000 V, 1024 steps

Control interface - RS485

Power supply – 12V DC

Power consumption – < 100mA.

REFERENCES

[1] Moriai,K., H.Kawaguchi, S.Matsubara, N.Tateishi, M.Egawa, H.Kakihana. Development of High Stable Monitor for Measurering Environmental Radiation. Proc. 10-th IRPA International Congress, Hiroshima, May 2000, P-4a-286.

[2] Cardoso M., V.Amorim, R.Bastos, R.Madeira, J.Simões, C.Correia. A Very Low-cost Portable Multichannel Analyzer, IEEE NSS-2000 (IEEE Nuclear Science Symposium 2000), Lyon, France - October 2000.

[3] Mitev,M., L.Tsankov, Ch.Lenev. A Spectral Analyser With a Logarithmic Energy-Code Characteristic - Nature, Features, Advantages and Drawbacks. Proceedings of the 12 International Scientific and Applied Science Conference "Electronics ET'2003", book 2, p 30 - 35, Sozopol, September 24-26, 2003.

[4] Mitev,M., I.Mitroshanov, Cv.Lazarov. Provident High Voltage Power Supply for a Scintillation Detector. Proceedings of the 12 International Scientific and Applied Science Conference "Electronics ET'2003", book 2, p 36 - 41, Sozopol, September 24-26, 2003.

[5] Mitev M.G., T.B.Lenev, L.T. Tsankov. An Improved Resonant Charge-Code Transducer, Tenth International Scientific and Applied Science Conference "Electronics ET'2001", book 1, p 111 - 124, Sozopol, September 26-28, 2001.

[6] Moriuchi,S., I.Miyanaga. A Method of Pulse Height Weighting Using the Discrimination Bias Modulation. Healt Physics, Pergamon Press 1966, Vol. 12, pp 1481-1487

[7] Photomultiplier Tubes and Assemblies For Scintillation Counting & High Energy Physics. 1998 Hamamatsu Photonics K.K.
http://www.hamamatsu.com/

Investigation of lavender oil obtained in experimental cohobation installation

Stanislava Tasheva[1], Albena Stoianova[1], Georgi Valchev[1], Violeta Rasheva[1]

Abstract - **Primary distillation waters are processed in experimental cohobation installation. The quantity of the obtained secondary essentail oils is defined, and their composition and physico – chemical parameters are investigated. It is established that the basic components of the lavender oils are linalool (31,4 - 45,3 %), α –terpineol (13,8 -18,7 %), geraniol (5,5 – 8,6 %) and lavendulol (1,9 – 2,6 %). The content of essential oil in processed medium at different hights of the column is defined.**

Keywords **– lavender, essential oils, cohobation, distillation waters**

I Introduction

Lavender (Lavandula angustifolia Mill, from family Lamaceae) is perennial essential plant, which is growed and processed in Bulgaria. Primary essential oil with basic component linalilacetate is obtained by steam disttilation of the racemes. The oil is used in perfumery, medicine, technics and faience industris. Distillation waters, called primary are obtained as waste product from the process of steam distillation of lavender racemes. According to the literature data these primary disttilation waters contain about 0,01 – 0,06 per cent dissolved and emultionized oil, which could be extracted by continuons cohobation (redistillation). The secondary oil obtained in this way doesn't mix with the primary oil, because of the differce in their composition [4,5].

The purpose of this paper is to be studed the secondary lavender oils, obtained by processing of primary distillation waters in experimental cohobation installation with horizontal sheet packing, as well as to be determined the essential oil content in processed medium at different column heights.

II Materials and methods

Primary distillation waters, obtained by steam distillation of lavender racemes harvest 2003 year in village Pesnopoy, region Plovdiv are manufactured.

Two batch consigument (A and B) of the primary disttilation waters are processed. Essential oil content in the primary distillation waters and experimental tests are determined by water distillation in glass laboratory apparatus of British farmacopoeia, modified from Balinova –Diakov [1].

[1]Stanislava Tasheva is with the Department of Industrial Heat Engineering, University of Food Technologies (UFT), blvd. Maritza 26, 4002 Plovdiv, Bulgaria, E-mail: st_tasheva@abv.bg

[1]Albena Stoianova is with the Department of Essential oils, UFT, E-mail: alstst@yahoo.com

[1]Georgi Valtchev - E-mail: g_valtchev@abv.bg

[1]Violeta D. Rasheva - E-mail: v_rasheva@abv.bg

The experimental cohobation installation for extraction of secondary lavender oil is presented on fig.1 and it consists from: cohobation column 3, heat exchange apparatus 2, coil condenser 5, florentine flasks 8, reservoirs for distillation and working waters 1 and 7 respectively and tank for secondary distillation waters 9. The cohobation column is filled with horizontal sheet packing. The experimental cohobation installation is provided with devices for taking of tests from the processed medium. The tests could be taken from the distillation still, florentine flasks and from different heights of the column. Detailed description of the horizontal sheet packing and the installation work is presented in [2,3,8].

Some physical and chemical properties – Consistency, Specific Gravity d_{20}^{20}, Refractive Index n_D^{20}, Acid and Ester Numbers of the obtained secondary essential oils are investigated for comparison of its quality with known literature data [6].

The composition of obtained secondary oils is defined by GC/MS analyses. Gas chromathograph is a Hewlett Packard with a mass-spectrometer detector. The GC was filled with a 30 m x 0,25 mm; 0,25 μm film thickness capillary column HP - 5 MS, which was temperature programmed from 50 °C – 280 °C at 4 °C/min, 280 °C (10 min isothermal), injector temperature 250 °C, carried gas nitrogen, sample 0,2 μm, split ratio 1 : 150.

The statistic processing of the experimental results is carried out according to the standard methods for directly measured quantities. Two to three parallel tests are analysed at calculating the value of the controled parameters and their average value is accepted for real value.

III Experimental Results and Data Analysis

The processed primary disttilation waters before cohobation contain 0,06 (for consigument A) and 0,073 (for consigument B) per cent essential oil (Table II) which doesn't differ from the pointed in the literature data [4,5].

It is established that about 0,05 per cent essential oil is extracted from the primary distillation waters of consigument A in result of cohobation (which is about 83 per cent from the total quantity essential oil) and about 0,001 per cent essential oil remains dissolved in cohobation residue. And about 0,09 per cent desolved essential oil remains in the secondary disttilation waters and it will be very difficult to extract this oil.

The experimental results obtained for the amount of the essential oils extracted from the distillation waters of consigument B don't differ essentially from these for consigument A and they are present in table II. Content of the secondary essential oil in the processed medium (distillation

waters) from different column height is presented in table I. The physicochemical properties and chemical composition of the oil, represented in table I isn't analysed. The location of points I to VI is shown on fig. 1.

The cohobation column actually is the stripping part of rectification column and increasing essential oil content in processed medium with the upward flow of vapor is owing to that. The abrupt reducing of essential oil content of primary distillation waters with their flow down packing layers of the column is obvious. The essential oil content in the cohobation residue according the literature data is about 1 per cent from the passed for cohobation oil and there is agreemant with the obtained experimental results.

The physical and chemical parameters of the secondary oils, collected from different parts of the cohobation installation are shown in table II. The experimental results point that the analized parameters of the obtained secondary oils don't differ from the published literature data [4,5]. The lack of linalilacetate in the secondary oil can be explained with the hydrolysis of the esters which is occurred in the time of stay of the distillation waters before their processing. And the high per cent of α-terpineol can be explained with the decomposing of the linalool acetate via linalool to α-terpineol, and also terpinen-4-ol to α-terpineol. Higher values are established only for the ester number. The difference in the essential oil content in the two studied consiguments primary distillation waters is due to the fact that they are obtained at two different primary distillations of lavender racemes. There is a little disagreemant in the studied parameters of the secondary essential oils obtained from these two consignments primary distillation waters.

The chemical composition of the obtained secondary oils are present in table 3. The basic oil components are: linalool (31,4 - 45,3 %), α – terpineol (13,8 -18,7 %), geraniol (5,5 – 8,6 %) and lavendulol (1,9 – 2,6 %). The experimental data about the chemical composition of the secondary oils don't differ from the Bulgarian literate data of secondary lavender oils [4, 5]. There are some diviations of chemical composition of the studied oils and the literature data from the Russian references [7]. This diviations is probably due to the difference in the processed lavender racemes sort and in the methods for analyze.

IV Conclusion

1.The composition and quality of the secondary essential oils obtained by processing of primary distillation water in the experimental cohobation installation with horizontally sheet filling don't differ from respective literature data for the secondary lavender oils obtained by constinuously operating cohobator with ceramic filling of Rashing.

2.About 83 per cent essential oils from the total amount oils disolved in the primery disstilation water are extracted by the experimental cohobation installation. Therefor there is a minimum loss of essential oils.

3.The experimental results for the essential oil content in the processed medium of different column height show rapid redusing of the oil content at flowing down of the distillation waters throught the highes packing layers of the column. This means good dividing efficiency of the column packing.

4.The obtained date can be used from the producers of essential oils.

REFERENCES

[1]. Balinova, A., G. Diakov. Detailed apparatus for microdistillation of rose blossom. Vegetable sciences, vol.11, № 2, 1974

[2]. Valchev, G., S. Tasheva, V. Rasheva, A. Stoianova. Experimental installation for investigation of process cohobation. Science conference 20 years of Technical faculty, 16 – 18 may 2003

[3]. Valchev, G., S. Tasheva, V. Rasheva, A. Stoianova. Heat calculations of distillation installations in essential oil industry. Science conference 50 years of UFT, 16 – 18 october 2003

[4]. Georgiev, E. Technology of natural and synthetic products, Sofia, DI Zemizdat, 1995

[5]. Georgiev, E., D. Dimitrov. Reference book of expert in perfumery cosmetic industry, Sofia, DI Technic, 1989

[6]. Georgiev, E., A. Stoianova. Guidance for laboratory exercises, Plovdiv, 1997

[7]. Tanasienko, F. S. Essential oil content and composition in plants, Kiev,Sceince Dumka, 1985

[8]. Tasheva, S., G. Valchev, V. Rasheva, A. Stoianova. Heat-exchange in a semi-industrial cohobation installation. Science conference 40 years of EMF, vol. II, 31 october – 1 november, 2003.

TableI

Content of oil in the processed medium

Part on the column	Distillation still	Point I	Point II	Point III	Point IV	Point V	Point VI
Content of oil,%	0,001	0,0025	0,0025	0,0075	0,075	0,01	0,02

The oils presented in table 1 aren't analyzed, because there are a little quantaty from these oils.

Table II

Physicochemical properties of lavender oils

Parameters	Oil before cohobation		Oil obtained in the time of cohobation		Oil staied in the water medium[1]	
	A	B	A	B	A	B
Consistency	Liquid					
Color	Light yellow				Orange	
Odor	lavender					
Essential oil content, %	0,06	0,073	0,05	0,06	0,05	0,06
Specific Gravity at 20 ^{O}C d_{20}^{20}	0,908	-*	0,913	0,905	-*	0,903
Refractive Index at 20 ^{O}C n_{D}^{20}	1,472	-*	1,469	1,468	1,470	1,472
Acid Number , mg/KON g	-*	-*	2,29	3,23	2,35	2,80
Ester Number mg/KON g	-*	-*	58,53	66,23	11,73	64,92

-[1]that is oil, which is remained in the water in the florentine flasks about 24 hours, i.e. it's extracted after about a day

-* the oils aren't analyzed

Table III

Chemical composition of lavender oils, %

Components	Oil before cohobation		Oil obtained in the time of cohobation		Oil staied in the water medium	
	A	B	A	B	A	B
Z-linalool oxide	2,1	1,3	2,3	3,3	0,4	0,9
E-linalool oxide	1,5	0,9	1,7	2,4	0,3	0,5
camphor	0,9	0,6	0,8	0,8	0,6	0,6
linalool	35,1	33,6	34,6	31,4	45,3	34,1
terpinen-4-ol	26,2	25,7	24,6	25,0	22,4	23,6
lavandulol	2,5	2,3	2,1	1,9	2,6	2,5
α-terpineol	15,9	17,9	16,3	17,3	13,8	18,7
nerol	1,8	2,4	1,8	1,7	2,4	2,7
geraniol	5,5	7,4	5,7	5,5	6,8	8,6
non indefiziran	8,5	7,9	10,1	10,7	5,4	7,8

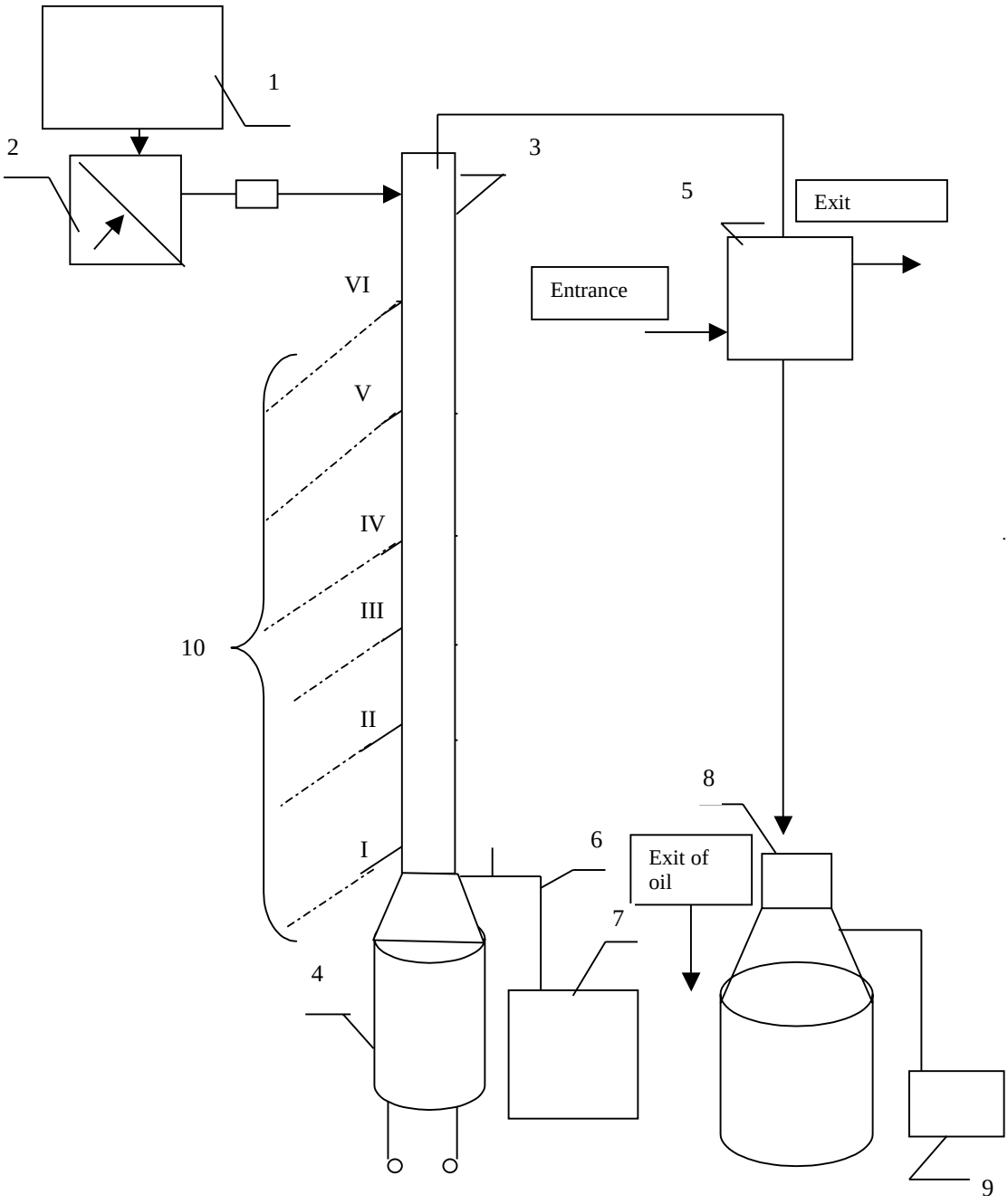

Fig.1 Experimental cohobation installation

1 - reservoir for distillation waters; 2 – heat-exchanger ; 3 – cohobation column; 4 – distillation still;
5 –coil - condenser; 6 – overflow; 7 – reservoir for waste waters; 8 – florentine flasks; 9 – reservoir for secondary distillation waters;
10 – devices for taking of processed medium tests

Energy Analysis of Heat Schemes of Installations for Dividing of Separate Components from Waste Waters

Georgi I. Valtchev[1]

Abstract - **An energy analysis of industrial installations for dividing of ethanol and methanol from waste waters is done. Suitable technical decisions for reduction in energy consumption of separating processes are offered. The quality of recovered components permits to use them repeatedly in the production process.**

Keywords - **recovery of organic solvents, dividing of waste waters, energy analysis, ethanol, methanol.**

I. Introduction

The multicomponent mixtures ethanol - water - non volatile impurities and methanol - water - non volatile impurities are received as waste products in different productions. With a view to achieve a definite economic and ecological effect it is necessary to recover the valuable components of these waste mixtures and to use them repeatedly in the production process.

Heat-technological schemes of industrial installations for dividing of the mentioned mixtures in their composite components are work out for solving of this problem.

The aim of this paper is to be carried out an energy analysis of the offered installations and of different technical decisions for energy costs reduction for the used dividing processes and on that base to be offered the most appropriate decisions for the case.

II. Materials and Methods

The waste mixtures ethanol - water - non volatile impurities and methanol - water - non volatile impurities are brown, light viscous, oleaginous liquids. Their color, viscosity and oiliness are owing to the non volatile impurities dissolved in them, because the rest components - water, ethanol and methanol are colorless and unviscous liquids. The non volatile impurities have concentration about 2000 ÷ 5000 μg/ml. If the amount of these impurities is ignored the ratio of the rest two components ethanol and water in the mixture ethanol - water - non volatile impurities vary about 20 ÷ 30 volume %. The same refers to the ratio of methanol and water in the waste mixture methanol - water - non volatile impurities

The binary solution ethanol-water is a solution with completely solubility components and has an azeotropic point with a minimal boiling temperature of 78 degree centigrade and composition 96 weight % ethanol и 4 weight % water [12]. Data about the vapor - liquid equilibrium in that binary system is published in [5,11,12].

The ethanol is one of the few alcohols which in small quantities is not poison for the people. In greater quantities it is toxic and explosion hazardous. At concentration of 0,6 to 0,9 % in the air it is not recommended long staying in the area.

[1]Georgy I. Valtchev is with the Department of Industrial Heat Engineering, University of Food Industries, blvd. Maritza 26, 4002 Plovdiv, Bulgaria, E-mail: g_valtchev@abv.bg

Its maximum allowable concentration of inflammation in the air is up to 19 volume %.

The binary solution methanol-water is a solution with completely solubility components and has not an azeotropic point. Data about the vapor - liquid equilibrium in that binary system is published in [5].

The methanol is explosion hazardous and strongly poisonous at swallowing, inhaling and contact with the skin. Its maximum allowable concentration in the air is 0,02 %.

The heat - technological scheme of the installation for dividing of the waste mixture ethanol - water - non volatile impurities in its composite components is presented on figure 1. It is work out on base of the theory of the mass - exchange processes [3,6,10] and of data about the purity of the recovered components, obtained at the preliminary carried out experiments for dividing of the studied waste mixtures [2,9]. The installation works at atmospheric pressure and it is build up from consistently connected a batch distiller in which the non volatile impurities are divided from the waste mixture, and a continuous operating rectification column in which the ethanol is divided from the binary solution ethanol - water. The last solution has to be heated to its boiling temperature before entering into the column. The distillate obtained from the rectification column contains 95 volume % ethanol. The distillation residue leaded away from the column contains over 95 volume % water.

The analysis of different technical decisions leading to energy costs reduction of used dividing processes (heat integration, vapor re-compression, complex configurations of the column apparatuses, the thermodynamic state of feed solution of the rectification column, optimization and so on) is done.

III. Experimental Results and Data Analysis

Greatest attention is paid to the rectification column because it consumes the largest part from the total energy costs [8]. The results from the analysis of different technical decisions for reduction of the energy costs for realization of the used dividing processes show that:

a/There is a dependence between the thermodynamic effectiveness of the rectification column for dividing of binary systems and the composition, thermodynamic state and relative volatile of the feed solution [1]. The optimal thermodynamic parameters of the rectification column feed solution have to be determined according to that dependence. In the investigated case the feed solution with concentration about 20 ÷ 30 volume % has to be entirely in liquid state and heated to its boiling temperature.

b/Thermal integration is possible only in the frames of the studied installation because of lack of data for the energy flows between the other equipment in the factory. In this aspect it is possible to utilize the heat of the residue from the

rectification column for heating of the initial waste mixture before entering in to the distiller and of the water - ethanol solution before its entering in to the rectification column.

c/The number of the rectification column contact trays is determined by means of the technico-economical optimization. The computer software from [7] is used for that purpose. Mathematical simulation from the type 2^4 is carried out. Therefore the variables are four and their areas of varying are: concentration of the feed solution x_f - (20 ÷ 30) volume %; ethanol content of the column residue x_W - (3 ÷ 5) volume %; reflux ratio R - from 1,59 to 2,8 (1,4.Rmin ÷ 1,8.Rmin); heating steam pressure - (0,2 ÷ 0,4) MPa. The coefficient of efficiency of the column trays is 0,54 for the stripping part of the column and 0,51 for the rectifying part and it is determined as function of the relative volatile and the dynamic viscosity of the operated medium [6]. The heating steam costs are calculated according to the present operating price of the heat power - 80 BGL per MWh. The ethanol price is 3,78 BGL per litre. The number of the real column trays - N, the number of the feed tray - N_F and the total reduced costs - K for producing of 1 dl absolute alcohol are determined in result of that optimization. The obtained results are shown in tables I and II.

TABLE I

Number of the real column trays - N and number of the feed column tray - N_F

№	x_f	R	x_W assigned	x_W obtained	N_F	N
-	mol %	-	mol %	mol %	№	Number
1	7,08	2,2	0,95	1,21	5	39
2	7,08	2,2	1,60	1,305	4	39
3	11,33	1,59	0,95	0,953	6	86
4	11,33	1,59	1,60	1,005	6	86
5	7,08	2,8	0,95	0,86	4	31
6	7,08	2,8	1,60	1,585	3	30
7	11,33	2,05	0,95	0,67	5	42
8	11,33	2,05	1,60	1,50	4	41

The equipment depreciation costs - K_{DEP}, the repairing costs - K_{REP}, the heating steam costs - $K_{H.S}$, the costs for the alcohol lead away with column residue - K_{RES} and the building depreciation costs - K_{BUIL} also are shown in table II.

TABLE II

Results from technico-economical optimization of the rectification column

№	K_{DEP}	K_{REP}	$K_{H.S}$	K_{RES}	K_{BUIL}	K
-	BGL per dl absolute alcohol					
1	0,1937	0,1937	0,6451	7,13	0,0232	8,19
2	0,1967	0,1967	0,6449	7,82	0,0236	8,88
3	0,2568	0,2568	0,5192	3,00	0,0308	4,06
4	0,2576	0,2576	0,5191	3,18	0,0309	4,24
5	0,1524	0,1524	0,7627	4,78	0,0183	5,87
6	0,1581	0,1581	0,7583	9,98	0,0190	11,08
7	0,1225	0,1225	0,6074	2,05	0,0147	2,92
8	0,1282	0,1282	0,6056	4,98	0,0154	5,86

The optimal variant is seventh and its parameters are: x_f = 30 volume %, R = 2,05 = 1,8.Rmin и x_W = 3 volume %. The heating steam pressure doesn't give substantial influence. The total reduced costs - K are 2,92 BGL per each obtained dl absolute alcohol and they are lowest in comparison with the other seven variants.

d/The vapor re-compression is one technical decision with wide application at separation of difficult dividing binary solutions but it isn't recommended for rectification columns for separation of water - ethanol solutions because of the relatively large temperature difference between the top and the bottom of the column. Using of vapor re-compression in such cases leads to quite great capital costs owing to the investments for the compressor (the compressor price is a function of the work which it has to do and of the volume of the re-compressed vapor) [8].

e/The complex configuration of column apparatuses (feed streams prefractioning; columns with side flows and other) are known but rarely used in practice. These configurations usually require greater capital costs and their introduction in production rear could excuse these investments[4].

The energy flows necessary for the waste mixture dividing are determined from the energy balances of the apparatuses from the installation and they are graphically shown on the energy flow diagram of Senkey (fig. 1). Dry saturated steam with pressure of 0,2 MPa is used as a heating carrier and industrial water with temperature of 16 degree centigrade is used as a cooling carrier. The heat loss are assumed to be 10 % from the heat necessary for the distiller and 4 % from the heat necessary for the rectification column.

1.The process of the waste mixture heating and evaporating in **the distiller 4** is a batch process and the duration of 1 cycle is 60 minutes. The amount of the mixture processed for 1 cycle is 1 m^3. It is experimentally established that the ethanol content in the distillation residue is below 0,2 weight % [2].

At these conditions the necessary heat flow rate is

$$\dot{Q}_{UTILL} = \dot{Q}_{HEAT} + \dot{Q}_{EVAP} = 537{,}1 \text{ кW}, \quad (1)$$

and the mass flow rate of the heating steam is

$$\dot{m}_{H.S} = (\dot{Q}_{UTIL} + \dot{Q}_{LOSS}) / r = 0{,}268 \text{ кg/s}, \quad (2)$$

where $\dot{Q}_{HEAT}$ and $\dot{Q}_{EVAP}$ are heat flow rates for heating and evaporating of the waste mixture respectively, кW;

$\dot{Q}_{UTILL}$ и $\dot{Q}_{LOSS}$ are utilized heat flow rate and heat loss respectively, кW;

r is a specific boiling heat of water, kJ/kg.

The energy coefficient of efficiency of the distiller is

$$\eta = \dot{Q}_{UTIL} / (\dot{Q}_{UTIL} + \dot{Q}_{LOSS}) = 537{,}1 / 590{,}78 \approx 0{,}91, \quad (3)$$

2.The condensation of the distillation vapors and the cooling of the obtained condensate to temperature of 86 degree centigrade are performed in **the condenser 5**. The heat flow lead away is

$$\dot{Q} = \dot{Q}_{KON} + \dot{Q}_{COOL} = 520 \text{ кW}, \quad (4)$$

and the cooling water flow rate –

$$\dot{m}_W = \dot{Q} / (C_P.\Delta t) = 2{,}07 \text{ кg/s}, \quad (5)$$

where $\dot{Q}_{KON}$ and $\dot{Q}_{COOL}$ are the heat flow rates necessary

for the vapor condensation and cooling of the obtained distillate respectively, κW;

C_P is water specific heat capacity, kJ/(kg.K);

Δt - the water temperature difference, K.

3.**The rectification column 9** is with the continuos operation and capacity 962,22 κg/h initial feed solution ethanol - water (with concentration of 30 volume). The initial solution according to point a/ has to be heated to its boiling temperature - 85,85 ^{0}C, and the obtained residue has temperature of 102 ^{0}C. The distillate contains 95 volume % ethanol, and the distillation residue contains 3 volume % ethanol.

The heat flow necessary for column bottom heating is

$$\dot{Q}_{UTIL} = 208{,}34 \text{ κW},$$

and the heating steam flow rate is

$$\dot{m}_{H.S} = (\dot{Q}_{UTIL} + \dot{Q}_{LOSS})/r = 217{,}02 / 2202{,}2 = 0{,}099 \text{ κg/s}.$$

The energy coefficient of efficiency of the rectification column is

$$\eta = \dot{Q}_{UTIL}/(\dot{Q}_{UTIL} + \dot{Q}_{LOSS}) = 208{,}34 / 217{,}02 \approx 0{,}96.$$

4.**The heat exchanger 8** is continuously operating and has purpose to heat the rectification column initial feed to its boiling temperature of 85,85 ^{0}C if there is a necessity. The rectification column residue heat is utilized for the aim.

5.**The reflux condenser 10** is continuously operating. Partial condensation of the distillation vapors is performed in it. The heat flow lead away is 134 κW, and the cooling water flow rate is 0,64 kg/s.

*6.***The condenser - cooler 11** is continuously operating. Condensation of distillation vapors and cooling of the obtained distillate to 25 ^{0}C is performed in it. The heat flow lead away is 75,8 κW, and the cooling water flow rate is 0,36 kg/s.

7.**The heat exchanger 2** is continuously operating. The initial waste mixture is heated in it to temperature of 70 ^{0}C, as the rectification column residue heat is utilized for that purpose. The necessary heat flow rate for heating of that mixture is $\dot{Q}_{UTIL}$ = 52,1 κW, and the heat loss - 5,2 κW. Therefore the total heat flow rate which have to bring in the heat exchanger 2 is 57,3 κW.

The heat flow of 52,1 kW is saved in result of this heat integration at ethanol recovery installation. This is about 24 % from the heat flow necessary for the rectification column and 6,5 % from the total heat flow necessary for the whole installation

About 0,394 kg/s heating steam flow rates with pressure 0,2 MPa are necessary for heating of the distiller and the rectification column, and 3,07 kg/s cooling water flow rates are necessary for condensation of vapors and cooling of the distillates from the distiller and the rectification column.

The energy analysis of the installation for dividing of the second waste mixture methanol - water - non volatile impurities shows that the processes for dividing of that mixture could be realized in the installation for dividing of the first waste mixture ethanol - water - non volatile impurities. The heat flow rates saved as a result of the heat integration in heat exchanger 2 at methanol recovery is 5,4 % from the total heat flow necessary for the whole installation.

Conclusions

1.Different technical decisions leading to reduction of energy costs for the dividing processes for recovery of the organic solvents from industrial waste waters are analyzed and the most appropriate of them (carrying out of technico-economical optimization of the rectification column for determining of the optimal column trays; selecting of the optimal thermodynamic state of the initial feed for the rectification column; heat integration in the frame of the installation) are selected for the investigated case.

2.The heating steam and the cooling water flow rates for the different apparatuses are calculated from the energy analysis of the offered installation.

3.Heat flow rates of 52,1 κW are saved only in result of heat integration in the frames of the installation for dividing of the first waste mixture ethanol - water - non volatile impurities. This is about 24 % from the heat flow necessary for the rectification column and 6,5 % from the heat flow necessary for the whole installation.

4.The heat flow rates saved as a result of the heat integration in heat exchanger 2 at methanol recovery is 5,4 % from the total heat flow necessary for the whole installation.

References

[1] Agrawal, R., D. M. Herron. Optimal Thermodynamic Feed Condition for Ideal Binary Mixtures. AIChE Journal, Vol. 43, N^0 11, November 1997, pp. 2984-2996.

[2] valtchev G., V. Rasheva, Regeneration of Ethanol from the Mixture "Ethanol - Water - Non volatile Impurities" at Antibiotic Production, Scientific Conference ЕМФ'98, TU - Sofia, Sozopol, May, 1998.

[3] Gelperin, N. I. Basic Processes and Apparatuses in Chemical Technology. Moscow, Chemistry, 1981.

[4] Ding, S.S., W.l. Luyben. Control of a Heat-Integrated Complex Distillation Configuration. Industrial Engineering Chemical Research, 29, 1990, pp. 1240-1249.

[5] Kogan, V. B., V. M. Fridman, V. V. Kafarov. Vapor - Liquid Equilibrium. Moscow - Leningrad, Science, 1966.

[6] Milchev, A. Industrial Heat installation. Sophia, Technique , 1993.

[7] Milenkov, B. G. Valtchev, O. Eneva, V. Rasheva. Software for Optimal Designing of Rectification Column for Separation of Binary Solutions, Jubilee Scientific Conference "50 Years UFT - Plovdiv", Scientific Works of UFT, Vol. L, Issue 4, Plovdiv, October 15-17, 2003.

[8] Muhrer, C. A., M. A. Collura, W. l. Luyben. Control of Vapor Recompression Distillation Columns. Industrial Engineering Chemical Research, 29, 1990, pp. 59-71.

[9] Rasheva, V., G. Valtchev, E. Shalapatova. Regeneration of Methanol from the Mixture "Methanol - Water - Non volatile Impurities" Obtained as Waste Product in the Pharmaceutic Industry. Scientific Conference with International Participation ЕМФ'2000, TU - Sophia, Varna, 25 - 28 June, 2000.

[10]Stabnicov, V. N. and other. Rectification in Food Industry: Process Theory, Machines, Intensification. Moscow, Light and Food Industries, 1982.

[11] Stabnicov, V. N., T. B. Protzuk, N. M. Uschenko. Investigation of vapor - liquid equilibrium in the system ethanol - water at different pressures, News from Higher Schools, Food technology, N^{0}3, Moscow, 1972.

[12]Stabnicov, V. N. Ethilov alcohol. Moscow, Food Industry, 1976.

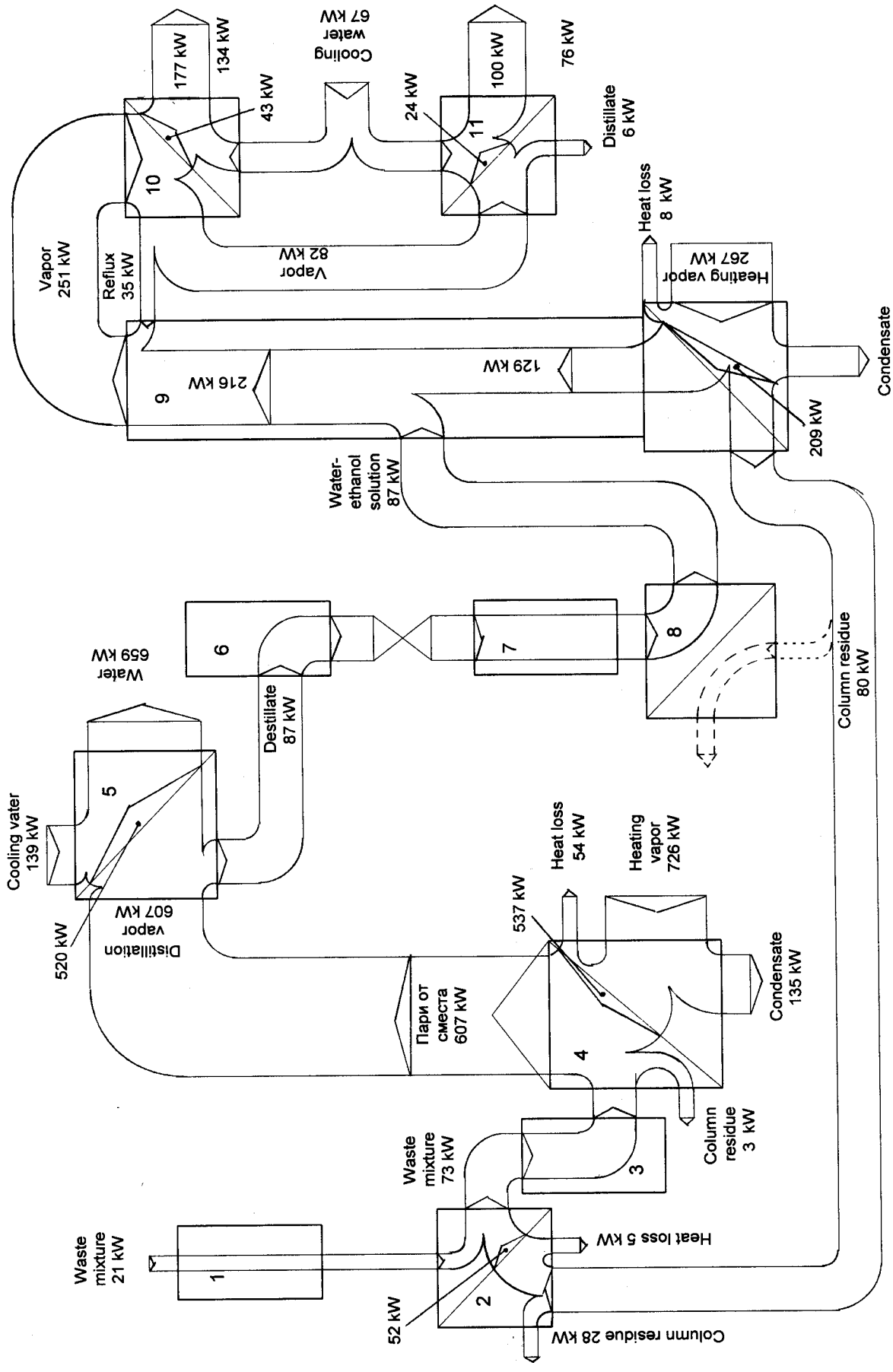

Fig. 1. Energy Diagram of Senkay of the Installation for Dividing of the Waste Mixture Ethanol - Water - Non Volatile Impurities

1 - Reservoir, 2 - Heat exchanger, 3 - Reservoir, 4 - Distiller, 5 - Condenser, 6 and 7 - Reservoirs, 8 - Heat exchanger, 9 - Rectification column, 10 - Reflux condenser, 11 - Condenser - Cooler

Session SP:

Signal Processing

Hausdorff LC Filters

Peter Apostolov[1]

Abstract - **This paper presents a method for synthesis of two kinds of inverse filters with Hausdorff-type transfer characteristic. The filter frequency characteristics are determined and a comparison with Chebyshev inverse filters is given.**

Keywords - **approximation, polynomial, synthesis, inverse LC filter, Hausdorff, Chebyshev, frequency characteristic**

I. Introduction

In modern filter theory the synthesis is performed by appropriate characteristic function approximation [2], [3]. Hausdorff filters are implemented by "shifted" Delta-function approximation [1] with the same form line as of an ideal characteristic function with Hausdorff polynomial, given on Fig. 1 and Equation (1):

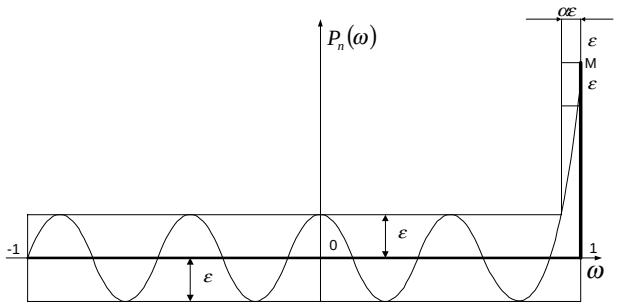

Fig. 1

$$P_n(\omega)=\varepsilon T_n\left(\frac{2\omega}{2-\alpha\varepsilon}\right)=\varepsilon T_n\left(\frac{\omega}{1-\alpha\varepsilon/2}\right). \qquad (1)$$

In this equation ε (Hausdorff dimension) is the best approximation with algebraic polynomial of "shifted" Delta-function in Hausdorff metrics [1], T_n is Chebyshev polynomial of first order and n degree; α is parameter, $\omega=2\pi f$ is frequency and the product $\alpha\varepsilon$ determines function steepness in an interval approximating the transition between filter pass-band (PB) and filter stop-band (SB). Given the filter order n and pass-band ripple DA [dB], the Hausdorff dimension ε and the product $\alpha\varepsilon$ could be found from the following equations (2) and (3), [4]:

$$\varepsilon=\sqrt{10^{0.1DA}-1}; \qquad (2)$$

$$\alpha\varepsilon=2\frac{\operatorname{ch}\left[\frac{1}{n}\operatorname{Ach}\left(\frac{1}{\varepsilon}\right)\right]-1}{\operatorname{ch}\left[\frac{1}{n}\operatorname{Ach}\left(\frac{1}{\varepsilon}\right)\right]+1}. \qquad (3)$$

Hausdorff filters transfer function takes the form:

$$|A(\omega)|=\sqrt{\frac{1}{1+\varepsilon^2T_n^2\left(\frac{\omega}{1-\alpha\varepsilon/2}\right)}}. \qquad (4)$$

As $\alpha\varepsilon$ values are in the interval (0,1) from the equation (4) can be seen that Chebyshev polynomial argument is divided by a positive number smaller than 1. That's why the Hausdorff filter transmission function appears to be "scale-shrunk" compared to Chebyshev ones with a coefficient of $(1-\alpha\varepsilon/2)$. Hausdorff and Chebyshev filters transmission functions are shown on Fig. 2. Both functions contain identical variation in pass-band and identical steepness out of it when the difference for the normalized frequency (cut-off frequency in this case) is equal to $\alpha\varepsilon/2$ [5].

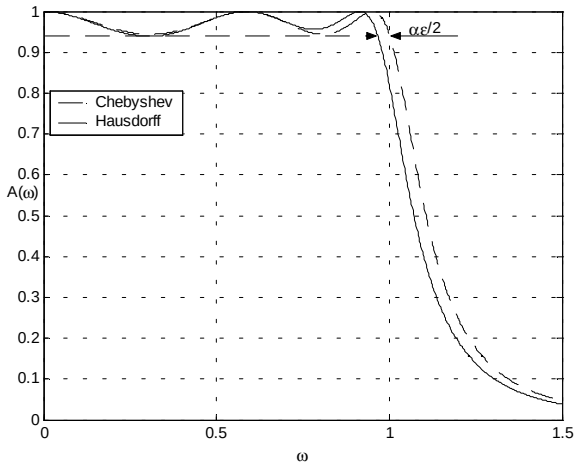

Fig. 2

II. Inverse Hausdorff Filters (IHF)

A. Inverse Hausdorff Filters from A-type

An inverse filter transmission function comes out through low-frequency filter-prototype transmission function transfer into high-frequency transmission function and the reciprocal value of argument is taken $\omega=1/\omega$:

$$|A_{nA}(\omega)|=\sqrt{\frac{\varepsilon^2T_n^2\left[\frac{1}{\omega(1-\alpha\varepsilon/2)}\right]}{1+\varepsilon^2T_n^2\left[\frac{1}{\omega(1-\alpha\varepsilon/2)}\right]}}. \qquad (5)$$

As can be seen from the last equation Chebyshev polynomial argument is multiplied by the expression $(1-\alpha\varepsilon/2)$. This comes to transmission function "scale-stretching" along the ω axis with a coefficient $(1-\alpha\varepsilon/2)$. Inverse Hausdorff and Chebyshev filters will have identical steepness and attenuation in stop-band, as ordinary (non-inverse) Hausdorff filters when filter order n and characteristics value k for limit frequency ω_c, are equal (Fig. 3).

[1] Peter S. Apostolov, Ms. Sc., Assoc. Fellow, IST-Sofia
E-mail: p_apostolov@abv.bg

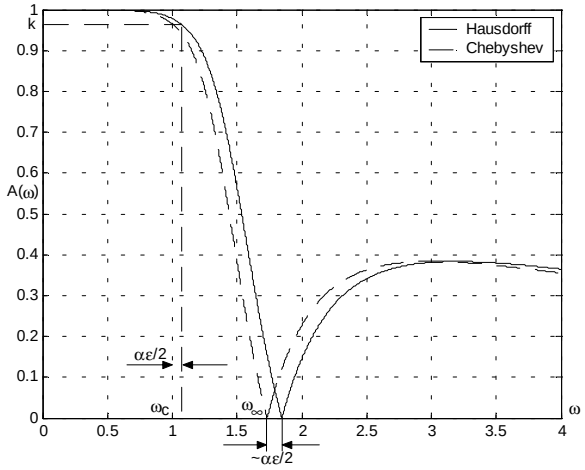

Fig. 3

The cut-off frequency shift ω_c is not acceptable in terms of filter design. As for inverse Hausdorff filters this can be overcome with the help of modern filter synthesis theory [2], [3]. An IHF is to be designed with limit frequency equal to a preliminary specified value of transfer function *k*, the pass band frequencies proportional to the product $\alpha\varepsilon$, as shown on Fig.4.

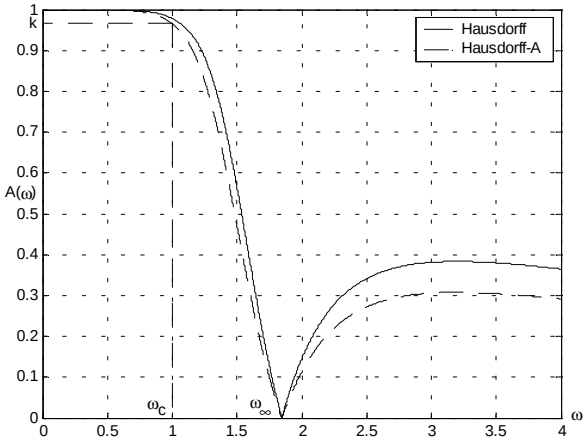

Fig. 4

Filter order *n*, cut-off frequency ω_c, transfer function attenuation for it *DA* in [dB], stop frequency ω_s and the product $\alpha\varepsilon$ are to be known for transfer function parameters specification. Transfer function limit frequency value is specified like in (2):

$$k = \sqrt{10^{0.1DA} - 1}. \qquad (6)$$

The product $\alpha\varepsilon$ can be specified by calculating transfer function value of inverse Chebyshev filter from the same order in stop frequency:

$$DS_{ch} = 10\log\left[k^2 \cosh^2\left(n \arccos h \frac{\omega_s}{\omega_c}\right) + 1\right]. \qquad (7)$$

Then ε of the low-pass filter-prototype can be calculated [6]:

$$\varepsilon = \frac{1}{\sqrt{10^{0.1DS} - 1}}. \qquad (8)$$

As it was mentioned in the beginning, the plain Hausdorff and Chebyshev filters when pass-band ripple is equal, the characteristics steepness is also equal, i.e. when the relation ω_s / ω_c is equal they will have equal attenuation. Therefore, the established value for will be equal to the value of Hausdorff dimension of the low-pass Hausdorff filter-prototype. When it is known, $\alpha\varepsilon$ can be determined from the equation (3).

The requirement that the cut-off frequency must remain the same leads to a change in stop-band maximums, which can be seen on Fig 4. The attenuation that IHF will have with $\omega_s(1-\alpha\varepsilon/2)/\omega_c$ as value of argument is calculated:

$$DS_{1A} = 10\log\left\{k^2 \mathrm{ch}^2\left[n\mathrm{Ach}\frac{\omega_s(1-\alpha\varepsilon/2)}{\omega_c}\right] + 1\right\}. \qquad (9)$$

From the established value IHF equivalent ripple ε_1 can be determined:

$$\varepsilon_{1A} = \frac{1}{\sqrt{10^{0.1DS_{1A}} - 1}}. \qquad (10)$$

Then the attenuation that IHF will have for stop-band ω_s will be:

$$DSH_A = 10\log\frac{\varepsilon_{1A}^2 \mathrm{ch}^2\left(n\mathrm{Ach}\frac{1}{1-\alpha\varepsilon/2}\right)}{1+\varepsilon_{1A}^2 \mathrm{ch}^2\left(n\mathrm{Ach}\frac{1}{1-\alpha\varepsilon/2}\right)}. \qquad (11)$$

B. Inverse Hausdorff filters from B-type

From the point of view of the synthesis it would be interesting to form an inverse filter transfer function taking in equation (1) reciprocal value of the whole expression containing the Chebyshev polynomial argument:

$$|A_{nB}(\omega)| = \sqrt{\frac{\varepsilon^2 T_n^2\left(\frac{1-\alpha\varepsilon/2}{\omega}\right)}{1+\varepsilon^2 T_n^2\left(\frac{1-\alpha\varepsilon/2}{\omega}\right)}}. \qquad (12)$$

In this case, in contrast to (5), the argument ω is divided by $(1-\alpha\varepsilon/2)$. This leads to "scale-compressing" of transfer function (Fig. 5) along the axis ω a coefficient of $(1-\alpha\varepsilon/2)$.

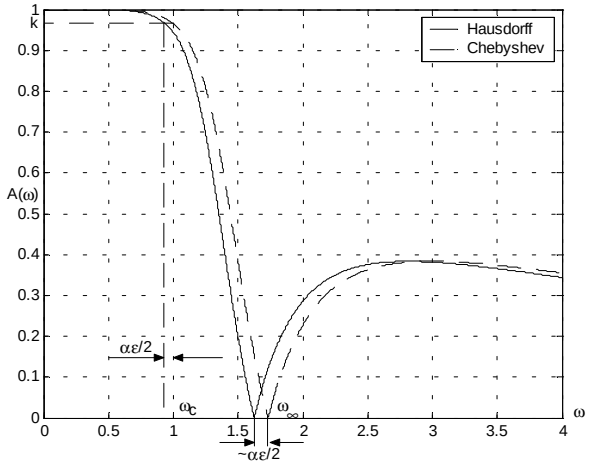

Fig. 5

The transfer function we want to realize is shown on Fig. 6. This type filter parameters can be defined as those for A-type. The product $\alpha\varepsilon$ is established from the equations (6), (7), (8) and (3) and the expressions (9), (10) and (11) take the form:

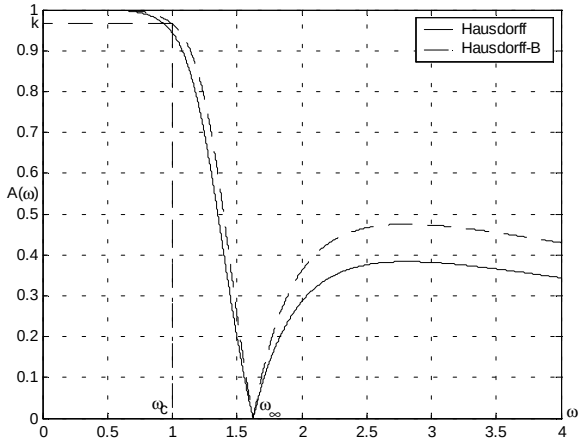

Fig. 6

$$DS_{1B} = 10\log\left\{k^2\mathrm{ch}^2\left[n\mathrm{Ach}\frac{\omega_s}{\omega_c(1-\alpha\varepsilon/2)}\right]+1\right\}; \quad (13)$$

$$\varepsilon_{1B} = \frac{1}{\sqrt{10^{0.1DS_{1B}}-1}}; \quad (14)$$

$$DSH_B = 10\log\frac{\varepsilon_{1B}^2\mathrm{ch}^2\left[n\mathrm{Ach}(1-\alpha\varepsilon/2)\right]}{1+\varepsilon_{1B}^2\mathrm{ch}^2\left[n\mathrm{Ach}(1-\alpha\varepsilon/2)\right]}. \quad (15)$$

III. Synthesis basics

The characteristics and transfer function are represented as relation of three polynomials $e(s)$, $p(s)$ и $q(s)$ of complex frequency $s = j\omega$. The polynomial $e(s)$ is Hurwitz strict polynomial and its zeros ω_i represent the filter own frequencies and these of $p(s)$ - the extreme frequencies $\omega_{\infty i}$, for which the transfer function has infinite attenuation. Calculating two of polynomials usually solves the synthesis task and the third is defined by Feldkeller equation:

$$e(s)e(-s) = p(s)p(-s) + q(s)q(-s). \quad (16)$$

The zeros of *e(s)* and *p(s)* can be found as follows:

For A-type:

$$\omega_i = \frac{1}{\left(1-\frac{\alpha\varepsilon}{2}\right)(\sigma_i + j\Omega_i)}; \quad (17)$$

$$\omega_{\infty i} = \frac{j}{\left(1-\frac{\alpha\varepsilon}{2}\right)\cos\left(\frac{2i-1}{n}\frac{\pi}{2}\right)}. \quad (18)$$

For B-type:

$$\omega_i = \frac{1-\frac{\alpha\varepsilon}{2}}{\sigma_i + j\Omega_i}; \quad (19)$$

$$\omega_{\infty i} = \frac{j\left(1-\frac{\alpha\varepsilon}{2}\right)}{\cos\left(\frac{2i-1}{n}\frac{\pi}{2}\right)}, \quad (20)$$

where:

$$\sigma_i = -\sin\left(\frac{2i-1}{n}\frac{\pi}{2}\right)\mathrm{sh}\left[\frac{1}{n}\mathrm{Ash}\left(\frac{1}{\varepsilon_{1A,B}}\right)\right]; \quad (21)$$

$$\Omega_i = \cos\left(\frac{2i-1}{n}\frac{\pi}{2}\right)\mathrm{ch}\left[\frac{1}{n}\mathrm{Ash}\left(\frac{1}{\varepsilon_{1A,B}}\right)\right], (i = 1 \div n). \quad (22)$$

Elements value calculation is carried by a method described in [17] via transformation of the variable *s* into a new variable *z*:

$$z = 1 + \frac{\omega_c^2}{s^2}. \quad (23)$$

Basing on this method two computer programs APPROX and LC are given in [3] where the filter is calculated. On input data load frequencies defined from the equations (18) and (20) must be introduced.

Through the described synthesis method two low-pass Hausdorff filters from third order (n=3) and cut-off frequency $f_c = 10\text{kHz}$, stop frequency $f_s = 15\text{kHz}$, $\alpha\varepsilon = 0.1239$, attenuation 0.3dB for cut-off frequency, normalized input and output resistance of 1Ω were calculated. Schematic diagrams 7 and 8 of the filters are shown below:

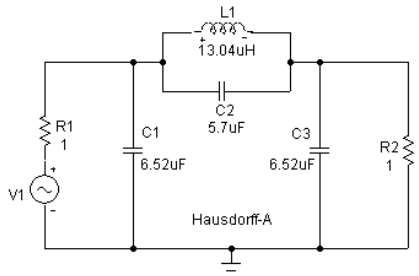

Fig. 7

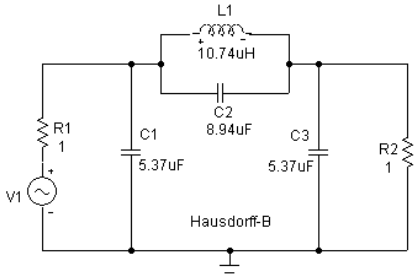

Fig. 8

IV. Inverse Hausdorff filters frequency characteristics

A. Magnitude (amplitude)-frequency characteristic

On Fig 9 are shown magnitudes responses of the two filters compared to that of inverse Chebyshev filter with the same input data.

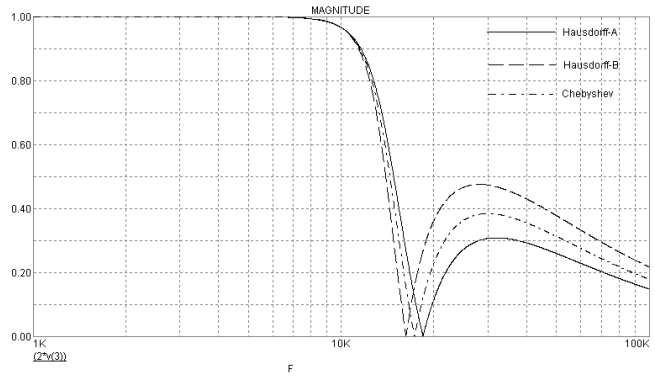

Fig. 9

The IHF from A-type have less steepness in interval (ω_c, ω_s) compared to the inverse Chebyshev. It is because their extreme frequencies are $(1-\alpha\varepsilon)^{-1}$ times higher than those of Chebyshev's (18). They have greater attenuation in stop-band. The extreme frequencies to IHF B-type are $(1-\alpha\varepsilon)$ times less than Chebyshev's, which defines the higher characteristic steepness in the interval (ω_c, ω_s) and less attenuation in stop-band.

B. Phase-Frequency Characteristic

Equations (17) and (19) solution defines the polynomials $e(s)$. Represented as rational function after a substitution $s = j\omega$, they expand into real a_R and imaginary e_I polynomials. The same operation is applied to the polynomials $p(s)$, defined from (18) and (20). Phase-frequency characteristic is:

$$\varphi(\omega) = \arctan\frac{p_I}{p_R} - \arctan\frac{e_I}{e_R}. \qquad (24)$$

On Fig 10 phase-frequency characteristics of the two types inverse Hausdorff filters are shown compared with that of Chebyshev's with the same input data.

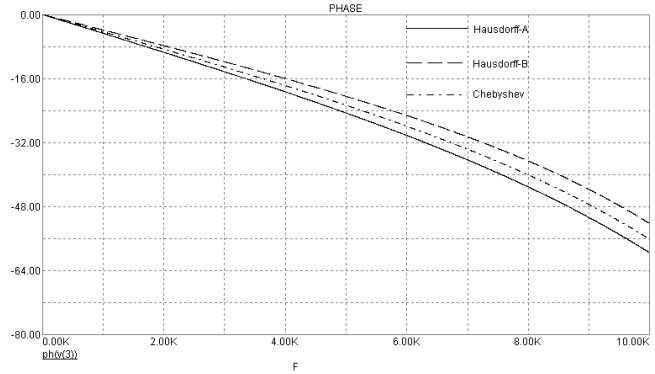

Fig. 10

The A-type inverse Hausdorff filter has more linear characteristics in pass-band compared to that of Chebyshev's and the B type's characteristic is more non-linear.

C. Group time-delay (GTD)

It can be defined from the equation:

$$t_{gr} = \mathrm{Re}\left[\frac{1}{e(s)}\frac{de(s)}{ds} - \frac{1}{p(s)}\frac{dp(s)}{ds}\right]. \qquad (25)$$

On Fig 11 group time delay of the two types inverse Hausdorff filters are shown compared to that of inverse Chebyshev filter with the same input data

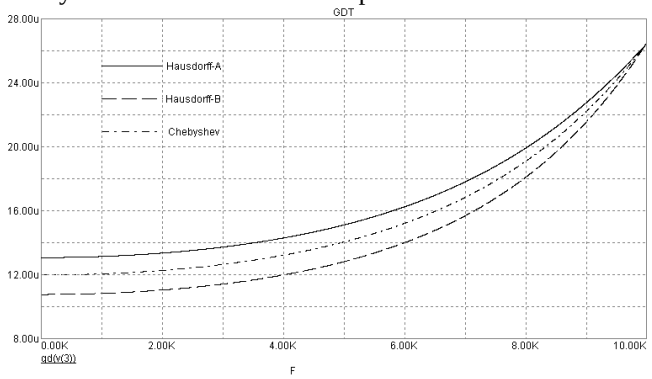

Fig. 11

The A-type inverse Hausdorff filter has more linear characteristic in pass-band GTD compared to that of Chebyshev's and the B-type is more non-linear.

IV Conclusion

We may say as a conclusion that the two types of inverse filters are complimentary of one another. Compared to Chebyshev's, the first type shortcomings are second type advantages. This leads to greater opportunities in filter design. The frequency characteristics specificity is defined from Hausdorff dimension. This means that the two types Hausdorff filters are unique and without analogous using other type of approximation.

Reference

1. Сендов, Бл., *Хаусдорфовые приближения*. С., БАН, 1979.
2. Стоянов, Г., И. Узунов, Л. Райковска и Р. Брадваров. *Анализ, синтез и проектиране на електрически филтри с персонални компютри*. С., Техника, 1991.
3. Темеш Г., С. Митра *Современная теория фильтров и их проектирование*. М., Мир, 1977.
4. Апостолов, П. С. *Синтез на предавателна характеристика на нискочестотен филтър с най-добро хаусдорфово приближение на "отместена" делта-функция*. – Сборник научни трудове, С., ИСТ-МВР, 2002, том XVI, 45-51.
5. Апостолов, П. С. *Синтез на многозвенен LC филтър с хаусдорфова предавателна характеристика, апроксимираща "отместена" делта-функция*. – Сборник научни трудове, С., ИСТ-МВР, 2002, том XVI, 52-56.
6. Orchard, H. J., G. C. Temes. *Filter design using transformed variables*. – IEEE trans. on circuit theory, 1968, CT-15, pp.385-408.

Investigation Spectral Characteristics of Onions in Training Neural Network

Nanko H. Bozukov[1], Chavdar I. Damyanov[2], Nikolai D. Bankov[3], Olga D. Rahneva[4]

Abstract **- One of the basic stages in fruits and vegetables grading includes the study of their spectral characteristics of transmittance and reflectance and the determining of those wavelengths, at wich the difference between the separate classes is the greatest. The structure of the objects investigated (onion tubers) and the development of diseases in them have shown that in order to use Neural Network (NN) during their quality evaluation (qualification), an information should be received concerning their total inner and outer status.**

Keywords **- Spectral Characteristics, Training, Neural Network, Qualification.**

I. INTRODUCTION

One of the main stages and vegetables grading is the study of their spectral characteristics of transmission and determining of those wavelengths in wich there is the greatest difference between the separate classes. The first step in this stage is the determining of the most suitable range for carrying out the spectrophotometric investigations upon the separate fruit or vegetable. According to the recommendations of some authors and the experience gained by the work team, the studies have been directed within the range 550-900 nm of the visible and a part of the near infrared region of the electromagnetic spectrum. They have been carried out on the spectrophotometric assembly for the two most widely spread varieties of onion in our country-"Liaskovski-58" and "Ispanska-482". A part of the data have been put down on the photometric assembly at the Department of "Automatics, Information and Control Technique" at the University of Food Technologies-Plovdiv, and another part have been obtaind by means of the of the sensor module of the sorting mashine aqs 602.

As a result of the scanning of the product along its lengthwise dimension, a realization of the following type has been obtaind:

$U = U_{\lambda i} / U_{\lambda j}$ ($U_{\lambda i}$ and $U_{\lambda j}$ are voltage signals,

[1]Nanko H. Bozukov HIFFI, Maritza blv. 26, 4002 Plovdiv, Bulgaria, E-mail: nankob@hiffi-plovdiv.acad.bg

[2]Chavdar I. Damyanov , HIFFI, Maritza blv. 26, 4002 Plovdiv, Bulgaria, E-mail: chavdam@yahoo.com

[3]Nikolai D. Bankov HIFFI, Maritza blv. 26, 4002 Plovdiv, Bulgaria, E-mail: bankov@hiffi-plovdiv.acad.bg

[4] Olga D. Rahneva HIFFI, Maritza blv. 26, 4002 Plovdiv, Bulgaria, E-mail: rahneva@hiffi-plovdiv.acad.bg

II. EXPERIMENTAL STUDIES

For the purpose of experimental studies, excerps of tubers have been selected, on which an expert assessment has been done, according to outer indications, by experts. All tubers have been divided into three qualities: 1 quality-corresponding to the requirements of the BSS(Bulgarian State Standard) and the European Standard(ES) for Class I; 2 quality-corresponding to the requirements of the latter standards for Class II; to this quality also belong some diseased tubers with a reserved commersial appearans; 3 quality-tubers, having diseases that have developed to such a degree that they have turned to be completely out of use.

Tables I, II, III present results from recording the spectral characteristics of transmission of the onion tubers. In I line it is the tuber number, in I column- it is the wavelenght in nm, while in the remaining cells of the table-there are the ratios between the two informative wavelengths in % [1], [2].

TABLE I

№ nm	1	2	3	4	5	6	7
550	6	6	0	1	6	2	13
575	9	7	0	1	8	3	15
600	12	11	0	2	12	3	21
625	15	16	0	2	16	4	26
650	19	21	0	3	23	5	33
675	22	26	0	5	30	6	41
690	25	30	2	6	37	7	47
700	17	33	5	9	43	10	50
725	32	40	13	26	54	21	60
740	38	46	17	33	63	26	66
750	45	59	26	44	70	35	73
775	54	63	43	59	78	49	82
800	85	82	88	89	100	86	90
825	100	100	100	100	100	100	100
850	98	100	77	95	100	86	112
875	88	100	61	78	81	69	102
900	88	100	61	61	76	69	100

TABLE II

№ nm	8	9	10	11	12	13	14
550	12	11	6	6	9	7	4
575	16	13	7	7	11	9	6
600	20	17	10	9	13	12	7
625	26	22	12	12	16	15	9
650	32	25	16	17	21	22	11
675	39	30	21	22	25	31	15
690	45	34	28	30	32	40	20
700	48	36	32	35	37	46	23
725	58	44	41	44	49	52	31
740	64	49	47	50	55	56	34
750	71	57	55	59	64	63	46
775	74	67	65	69	72	69	58
800	90	84	92	66	94	92	87
825	100	100	100	100	100	100	100
850	100	99	90	92	86	83	88
875	95	102	83	80	81	76	79
900	95	93	68	66	76	62	67

TABLE III

№ nm	15	16	17	18	19	20
550	4	10	4	2	7	0
575	5	12	6	6	12	1
600	6	15	8	10	16	2
625	8	20	11	13	20	3
650	11	24	15	18	21	6
675	14	29	20	24	20	9
690	19	34	27	48	52	19
700	23	36	31	61	64	27
725	33	45	41	53	65	36
740	38	49	47	54	62	41
750	46	58	56	66	71	51
775	55	66	67	78	79	64
800	86	80	91	108	115	97
825	100	100	100	100	100	100
850	86	97	97	72	68	86
875	81	91	80	67	52	80
900	68	86	73	67	46	72

Fig. 1 and 2 give the spectral characteristics, respectively of healthy (unaffected) (1 and 2 quality) and affected tubers (3 quality), after the data from tables I,II, III. On the X-axis, the wavelength in nm has been ploted, while on the y-axis, it is the ratio between the two informative wavelengths in % that has been plotted [3], [4]. From the spectral characteristics of transmission on unaffected and affected tubers it can be established that the most significant are the differences between them within the range of 700-750 nm and 850-900 nm [5].

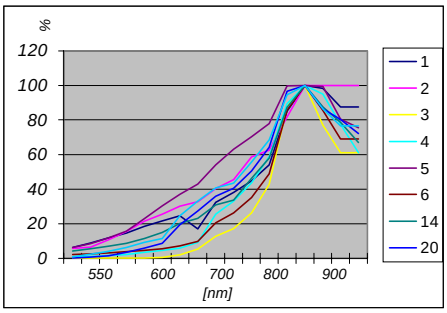

Fig. 1. Spectral characteristics of unaffected tubers

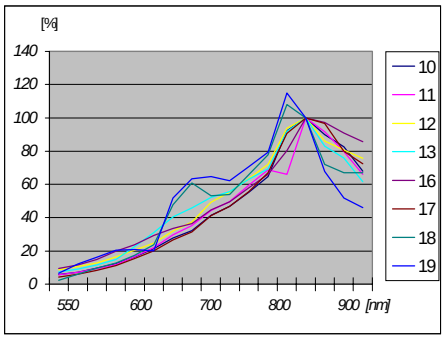

Fig. 2. Spectral characteristics of affected tubers

III. CONCLUSION

Onion as an object of NN training, as well as its grading by means of the so far training NN, is in itself a unhomogenious and changing structure, that has been connected with the variety peculiarity, variations of the shape and size, unhomogenious ageing, different himidity, etc. These parametres influence the data regirtering by using the spectral method.

REFERENCES

[1] T.C. Kirova, Neural Networks, Basic Architectural and Training Algorithms, Softex, Tempus JEP 1497, Sofia, 1995.

[2] H. Demuth and M. Beale, Neural Networks Toolbox, For Use with MatLab, User's Guide, The Mathworks, Inc.,1994.

[3] Matlab, High-Performahce Numeric Computation and Visualization Software, Classroon Kit Guide, The Mathworks, Inc., 1994.

[4] Matlab, Introductional Guide, Contemporary Systems for Control Centre, III. 1994.

[5] K. Hornik, Multilayer feedforward networks are universal approximators. Neural Networks, 2, 359-366,1989.

Method for Transformation of Principal Subspace Algorithms to Principal Components Algorithms

Marko Janković[1] and Hidemitsu Ogawa[2]

Abstract - **This paper proposes a general method which transforms known one-layer neural network PSA algorithms, into PCA algorithms. The method uses two distinct time scales. A given PSA algorithm is responsible, on a faster time scale, for the "behaviour" of all output neurons. At this scale, a principal subspace is obtained. On a slower time scale, output neurons compete to fulfil their "own interests". On this scale, basis vectors in the principal subspace are rotated toward the principal eigenvectors.**

Key words - **L*earning algorithm, neural networks, time hierarchy, PSA, PCA.***

I. INTRODUCTION

Neural networks provide a novel way for parallel on-line computations of the principal component analysis (PCA) or principal subspace analysis (PSA). Due to their parallelism and adaptivity to input data, such algorithms and their implementations in neural networks are potentially useful in feature extraction and data compression. It is well known that in the first step of any pattern recognition scheme, which is the representation of the objects from a usually large amount of raw data, some preprocessing and data compression is essential. In that case a minimal loss of information is a central objective. Many preprocessing, feature extraction and data compression techniques can be mathematically expressed as linear transformations. Since more economical representations than the original set of measurements are mostly desired, this transformation is a linear mapping to a lower-dimensional subspace. PCA is also used as a preprocessing step in independent component analysis (ICA).

Within last years various PCA and PSA learning algorithms have been proposed and mathematically investigated [1-3, 5, 6, 8-13,15-28]. Most of them are based on local Hebbian learning. Due to locality it has been argued that these algorithms are biologically plausible. PSA is essential for some problems such as subspace methods for pattern recognition. It seems that derivation of PCA algorithms is usually harder than that of PSA algorithms, since the number of known parallel PCA algorithms is much smaller. In this paper we propose a simple method for converting PSA algorithms to PCA algorithms. It is named the Time-Oriented Hierarchical Method (TOHM).

[1]Marko Jankovic is with the Institute of Electrical Engineering "Nikola Tesla", Koste Glavinica 8a, 11000 Belgrade, Serbia and Montenegro, E-mail: elmarkoni@ieent.org

[2]Hidemitsu Ogawa is with Tokyo Institute of Technology, Tokyo, Japan, 152-8552, E-mail: ogawa@og.cs.titech.ac.jp

The TOHM is introduced in Section II. Application of TOHM is presented in Section III. Section IV is devoted to mathematical analysis of the proposed method. Simulation results are presented in Section V. Section VI gives conclusions.

II. TIME-ORIENTED HIERARCHICAL METHOD

We shall introduce a general method for transformation of PSA algorithms to PCA algorithms. The main idea is that

Each neuron tries to do what is the best for its family, and then to do what is the best for himself.

We shall call this idea "the family principle". In other words the algorithm consists of two parts: the first part is responsible for the family-desirable feature learning and the second part is responsible for the individual-neuron-desirable feature learning. The second part is taken with a weight coefficient α which is smaller than 1. This means that we will make some time-oriented hierarchy in realization of the family and individual parts of the learning rules.

What was the motivation? In Fig. 1, a multivariate Gaussian probability density is shown. It is well known that principal axes of the hyper ellipsoid are parallel to the eigenvectors of the covariance matrix when the mean of input signals are zero. In the case when a PSA algorithm is used, weight vectors, which are shown by dotted lines in Fig.1, are rotated to principal axes. Now, a question is how to make an additional driving force for the rotation. Our proposal is to add one more term to the PSA algorithm.

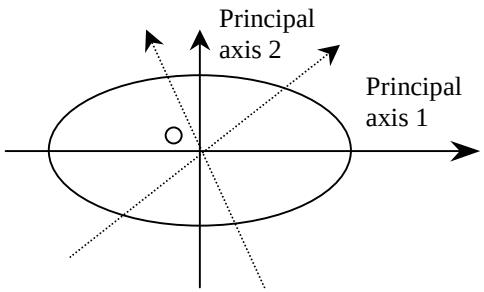

Fig.1 Illustration of the multivariate Gaussian probability density

In order to realize "the family principle", we propose the following general method, which transforms a PSA algorithm, denoted by FLA_{PSA}, to a PCA algorithm, denoted by LA_{PCA}:

$$LA_{PCA} = FLA_{PSA} + \alpha\, ILA\left(\max\left(E\left\{ \left(y^T y \right) \middle| \begin{matrix} w_k^T w_k = 1, \\ k = 1,2 \ldots N \end{matrix} \right\} \right) \right), \quad (1)$$

where α is a constant such that $|\alpha|<1$. ILA denotes an individual part. It is an algorithm for achieving maximization of $E(y^T y)$ under the constraints $w_k^T w_k=1$ for $k=1,2,\ldots,N$. We can see, that if homogenous PSA algorithm is used then we will have fully homogenous PCA algorithm.

Since $|\alpha| < 1$, the family part of the learning rule is implemented faster than the individual part. Equation (1) is roughly illustrated in Fig. 2.

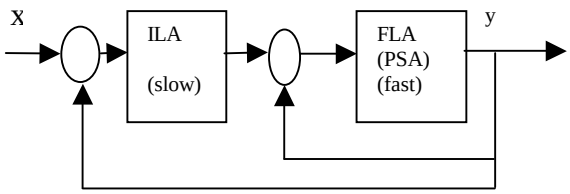

Fig. 2 Block schema of the realization of the proposed method

Due to symmetry of the proposed algorithm there is more than one solution (attraction point). It can cause the "conflict of interests" between individual neurons. From Fig. 1 we can see that one weight vector can move toward the positive direction of the principal axis 1, and at the same time second weight vector will have "intention" to move toward the negative direction of the principal axis 1. And then, the algorithm can stop somewhere in the middle or oscillate between some points. So, sometime algorithm can be sensitive to α selection.

Can we diminish that problem? The answer is yes if we introduce some asymmetry in the algorithm. We give different neurons different possibilities to achieve the principal eigenvector. The proposed method is given by the following equation:

$$LA_{PCA} = FLA_{PSA} + ILA\left(\max\left(E\left\{ \left((Dy)^T y \right) \middle| \begin{matrix} w_k^T w_k = 1, \\ k = 1,2 \ldots N \end{matrix} \right\} \right) \right), \quad (2)$$

where D is a diagonal matrix with nonzero elements d_n and such that $|d_n|<1$. Introduction of asymmetry brings additional time hierarchical organization of the realization of individual parts of learning rule. Obviously if all d_n are equal to α, we have the homogenous case.

III. Application of the TOHM

We shall show two typical applications of the TOHM. First one is to derive a new PCA algorithm from a PSA algorithm by using the TOHM. We shall use the Modulated Hebb Oja (MHO) algorithm as a PSA algorithm [13]. That is, applying Eq. (1) to method proposed in [13] yields

$$\begin{aligned} W(i+1) &= W(i) + \gamma(i)\left(x(i)^T x(i) - y(i)^T y(i)\right) \\ &\cdot \left(x(i)y(i)^T - W(i)diag\left(y_1(i)^2, \cdots y_N(i)^2\right)\right) \\ &+ \alpha\gamma(i)\left(x(i)y(i)^T - W(i)diag\left(y_1(i)^2, \cdots y_N(i)^2\right)\right). \end{aligned} \quad (3)$$

Some simulation results for the new PCA algorithm are presented in Section V.

The second application of the TOHM is to give a new interpretation of existing PCA algorithms. As an example, we shall show that the well-known weighted learning rule for PCA [21] can be derived from a PSA algorithm named Subspace Learning Algorithm (SLA) using TOHM. The weighted learning rule is given by

$$\begin{aligned} w_k(i+1) &= w_k(i) \\ &+ \gamma(i)\left[y_k(i)x(i) - \theta_k y_k(i) \sum_{m=1}^{N} y_m(i) w_m(i) \right]. \end{aligned} \quad (4)$$

This equation can be written as

$$\begin{aligned} w_k(i+1) &= w_k(i) \\ &+ \gamma(i)\theta_k\left[y_k(i)x(i) - y_k(i) \sum_{m=1}^{N} y_m(i) w_m(i) \right] \\ &+ \frac{(1-\theta_k)}{\sqrt{\theta_k}}\gamma(i)\left(\frac{y_k(i)x(i)}{1/\sqrt{\theta_k}} \right). \end{aligned} \quad (5)$$

If we assume that θ_k are nearly equal to one, having in mind Ref. [17] and the fact that the norm of the k-th weight vector is $1/\theta_k^{0.5}$ (see [21], [22]), this equation represents a special case of Eq. (2).

IV. Simplified Mathematical Analysis of the Proposed Principle

Although it is generally assumed that $|d_n| < 1$, we shall analyse only the case that $|d_n|$ is much less than 1. In this case, the "individual part" in Eq. (2) has almost no impact on the "family part" (idea used in multiloop control design [14]). Then the "family part" provides a principal subspace. This means that $W^T W=I$ and W spans a principal subspace. In this case, the "individual part" in Eq. (2) can be written as

$$\begin{aligned} &W(i+1) = W(i) \\ &+ \gamma(i)\left(x(i)y(i)^T - W(i)diag\left(y_1(i)^2, \cdots, y_N(i)^2\right)\right)D, \\ &\text{where } D \text{ is a diagonal matrix and } W \text{ is such that} \\ &W^T W = I \text{ and spans the principal subspace.} \end{aligned} \quad (6)$$

Corresponding differential equation is [15, 20]

$$\frac{dW}{dt} = \left(CW - W diag\left(W^T CW\right)\right)D, \tag{7}$$

where diag(W^TCW) is a diagonal matrix which consists of diagonal elements of W^TCW. If we write this equation for each column w_k, we have

$$\frac{dw_k}{dt} = d_k \left(Cw_k - \lambda_k w_k\right), \tag{8}$$

where λ_k is the k-th element of diag(W^TCW). We can easily conclude that the stationary points of these equations are eigenvectors of the matrix C. If the $w_k(i)$ of the corresponding discrete algorithm visits infinitely often a compact subset of the domain of attraction of the solution of Eq. (8), then the solution of Eq. (8) is also a solution for the corresponding discrete algorithm (2).

V. SIMULATION RESULTS

We shall consider small-scale numerical simulations whose results are given in Table I to Table IV. Two algorithms were examined. One is a PCA algorithm derived from the SLA by the TOHM, which is denoted by the TOHM SLA. The other is a PCA algorithm derived from the MHO algorithm by the TOHM, which is denoted by the TOHM MHO. The number of inputs was $K = 5$ and the number of output neurons was $N = 3$. Artificial zero-mean vectors with uncorrelated elements were generated by the following equations:

x(1,1) = sin(i/2);

x(2,1) = (rem(i,23) - 11)/9).^5;

x(3,1) = (rem(i,27) - 13)/9);

x(4,1) = ((rand(1,1) < .5) * 2 - 1). * log(rand(1,1) + .5);

x(5,1) = - .5 + rand(1,1).

In such a case, the three principal eigenvectors are $c_1 = (00100)^T$, $c_2 = (10000)^T$ and $c_3 = (01000)^T$. Let d be the vector which consists of d_k in Eq. (16). In Table I and Table II, a smaller $d = (0.08, 0.06, 0.04)^T$ is used. In that case both algorithms require big number of iterations (70000) to converge to a solution. In Table III and IV a bigger $d = (0.4, 0.2, 0.1)^T$ is adopted, and algorithms become faster. Results in the tables are achieved after 10000 iterations. The simulation results show that the TOHM is useful.

TABLE I
WEIGHT VECTORS OF THE TOHM SLA LEARNING ALGORITHM AFTER 70000 ITERATIONS; D=(0.08, 0.06, 0.04)^T

W		
0.0493	-0.9960	0.0932
0.0195	-0.0964	-0.9953
0.9907	0.0448	0.0062
-0.0283	-0.0356	0.0071
-0.1315	-0.0433	-0.0511

TABLE II
WEIGHT VECTORS OF THE TOHM MHO LEARNING ALGORITHM AFTER 70000 ITERATIONS; D=(0.08, 0.06, 0.04)^T

W		
-0.0871	1.0001	0.1439
-0.0289	0.0856	-0.9866
0.9960	0.0942	-0.0427
-0.0577	0.0244	-0.0164
-0.0427	0.0069	0.0060

TABLE III
WEIGHT VECTORS OF THE TOHM SLA LEARNING ALGORITHM AFTER 10000 ITERATIONS; D=(0.4, 0.2, 0.1)^T

W		
-0.0449	0.9977	0.0159
0.0212	0.0292	0.9907
-0.9987	-0.0074	0.0078
0.0535	-0.0084	-0.0189
0.0077	-0.0716	-0.0465

TABLE IV
WEIGHT VECTORS OF THE TOHM MHO LEARNING ALGORITHM AFTER 10000 ITERATIONS; D=(0.4, 0.2, 0.1)^T

W		
-0.0488	0.9905	0.2027
0.0295	-0.1062	0.9775
1.0014	-0.0632	-0.0343
0.0541	-0.0530	-0.0293
0.0142	0.0407	0.0283

VI. CONCLUSION

In this paper, a general method (named time-oriented hierarchical method – TOHM) is proposed, which transforms PSA algorithms into PCA algorithms. Introduction of the two distinct time scales is the novelty of the proposed method. This indirectly means that possible biological implementation of the network requires two types of the neurotransmitters. On a faster time scale a PSA algorithm is responsible for the "behaviour" of the all output neurons. On a slower scale, output neurons compete to fulfil their "own interests". On this scale, basis vectors in the principal subspace are rotated toward the principal eigenvectors. Some mathematical analysis and simulation results are presented.

REFERENCES

[1] P. Baldi and K. Hornik, "Learning in linear neural networks: A survey", IEEE Trans. Neural Networks, vol. 6, pp. 837-858, July 1995.

[2] C. Chatterjee, Z. Kang and V.P. Roychowdhury, "Algorithms for accelerated convergence of adaptive PCA", IEEE Trans. on Neural Networks, vol. 11, no. 2, pp. 338-355, March 2000.

[3] T. Chen, Y. Hua and W. Yan, " Global convergence of Oja's subspace algorithm for principal component extraction", IEEE

Trans. on Neural Networks, vol. 9, no. 1, pp. 58-67, January 1998.
[4] G. Deco and D. Obradovic, "An information-theoretic approach to neural computing", Springer-Verlag New York Inc., 1996.
[5] K.I. Diamantaras , "Robust principal component extracting neural networks", ICNN'96, USA, pp. 74-77, 1996.
[6] S.C. Douglas, S.Y. Kung and S. Amari, "A self-stabilized minor subspace rule", IEEE Signal Processing Letters, vol. 5, no. 12, pp. 328-330, 1998.
[7] J. Dowling, "The Retina: an approachable part of the brain", The Belknap Press of Harvard University Press, 1987.
[8] S. Fiori, "A theory for learning by weight flow on Stiefel-Grassman Manifold, Neural Computation, Vol. 13, No. 7, pp. 1625-1647, July 2001.
[9] C. Fyfe and R.J. Baddeley, "Finding compact and sparse distributed representations of visual images", Network: Computation in Neural Systems 6(3), pp. 334-344, 1995.
[10] C. Fyfe and R.J. Baddeley, "Nonlinear data structure extraction using simple Hebbain networks", Biological Cybernetics 72(6), 533-541, 1995.
[11] G. F. Harpur "Low entropy coding with unsupervised neural networks", Ph.D. thesis, Cambridge University, UK, 1997.
[12] M. Jankovic, "A new simple ∞OH neuron model as a biologically plausible principal component analyzer", IEEE Trans. on Neural Networks, vol. 14, pp. 853-859, 2003.
[13] M. Jankovic and H. Ogawa "A new modulated Hebb learning rule – Biologically plausible method for local computation of principal subspace", Int. J. Neural Systems, Vol.3, no.4, 2003.
[14] J.G. Kassakian, M.F. Schlecht, G.C. Verghese “Principles of Power Electronics”, Addison-Wesley Publishing Company, 1991.
[15] L. Ljung, "Analysis of recursive stochastic algorithms", IEEE Trans. Automat. Contr., vol. 22, pp. 551-575, 1977.
[16] H. Ogawa, "Karhunen-Loéve subspace", International Conference on Pattern Recognition, Hague, The Netherlands, pp. 75-78, 1992.
[17] E. Oja, "A Simplified neuron model as a principal component analyzer", J. Math. Biol., vol. 15, pp. 267-273, 1982.
[18] E. Oja, "Subspace Method of Pattern Recognition", Research Studies Press and J. Wiley, Letchworth, 1983.
[19] E. Oja, "Neural networks, principal components, and subspaces", Int. J. Neural Systems, 1, pp. 61-68, 1989.
[20] E. Oja and J. Karhunen "On stochastic approximation of the eigenvectors and eigenvalues of the expectation of a random matrix", J. Math. Anal., Appl., 106, pp. 69-84, 1985.
[21] E. Oja, H. Ogawa and J. Wangviwattana, "Principal component analysis by homogeneous neural networks, Part I: The weighted subspace criterion", IEICE Trans. Inf.&Syst., E75-D, 3, pp. 366-375, 1992.
[22] E. Oja, H. Ogawa and J. Wangviwattana, "Principal component analysis by homogeneous neural networks, Part II: Analysis and extensions of the learning algorithm", IEICE Trans. Inf.&Syst., E75-D, 3, pp. 376-382, 1992.
[23] S. Ouyang, Z. Bao and G. Liao, "Robust recursive least squares learning algorithm for principal component analysis", IEEE Trans. on Neural Networks, vol. 11, no. 1, pp. 215-221, January 2000.
[24] M. Plumbley, "On information theory and unsupervised neural networks", Technical Report CUED/F-INFENG/TR. 78, Cambridge University, UK, 1991.
[25] A. Weingessel and K. Hornik, "Local PCA algorithms", IEEE Transactions on Neural Networks, vol. 11, no. 6, pp. 1242-1250, November 2000.
[26] L. Xu, "Least mean square error reconstruction principle for self-organizing neural nets", Neural Networks, vol. 6, pp. 627-648, 1993.
[27] W. Yan, U. Helmke and J.B. Moore, "Global analysis of Oja's flow for neural networks", IEEE Trans. on Neural Networks, vol. 5, no. 5, pp. 674-683, 1994.
[28] Q. Zhang and Y. Leung, “A class of learning algorithms for principal component analysis and minor component analysis”, IEEE Trans. On Neural Networks, vol. 11, no. 2, pp. 529-533, March 2000.

Analysis of the Chaotic Signals, Produced from Some Radiocommunication Circuits

Stoitscho V. Manev[1] and Vladimir Iv. Georgiev[2]

Abstract - **In this paper analysis of the structure of some circuits, designed to generate chaotic signals, has been made. The main purpose of the paper is to investigate the influence of the nonlinearity in the analyzed circuits upon the properties of the generated signals. An algorithm, based on the algorithm of Eckmann, Kamphorst, Ruelle and Ciliberto for determination of the Ljapunov's exponents of chaotic signals, has been applied. After the determination of the Ljapunov's exponents, conclusions have been made.**

Keywords - **chaotic circuits, chaotic attractors, chaotic signals Ljapunov exponents**

I. INTRODUCTION

The implementation of the chaotic signals in radiocommunications is of great interest. This paper can be considered as a continuation of the investigations, made in [5]. Different circuits, designed to generate chaotic signals, have been suggested and discussed in the publications. One of these circuits, most often used for this purpose, is the circuit, known as the Chua's circuit. In the presented paper investigations upon signals, produced by different parameter sets of the Chua's circuit, have been made. These variants of parameter sets have been discussed in [5]. An analysis, based on the Shilnikov's theorems, has been made there. Using the results, obtained in [5], in the presented paper a mathematical model of the system of differential equations, discussed there, has been made.

The chaotic signals, generated by means of the constructed mathematical model, have been investigated. By the computation of the Ljapunov's exponents, an algorithm, based on the well known Eckmann, Kamphorst, Ruelle and Ciliberto (EKRC) algorithm, has been used. This algorithm has been applied by the investigations, carried out upon different parameter sets of the Chua's circuit. From the values of the Ljapunov's exponents, obtained by the investigations, conclusions about the behavior of the circuit by respective parameter sets have been made. Based on the obtained results, an estimate about the ability of the investigated parameter sets of the Chua's circuit to generate different types of chaotic signals can be made.

[1]Stoitscho Velizarov Manev - assistant in Dept. of Radiotechnic in Faculty of Communication and Communication Technologies in TU-Sofia, Bulgaria

[2]Vladimir Ivanov Georgiev - professor DSc. In Dept.of Theoretical Electrotechnic in TU-Sofia, Bulgaria

II. EXPERIMENTAL RESULTS

The dynamic behaviour of the observed circuits has been analyzed in 3-dimensional phase space. The phase space has been formed after the proposal, given in an example in [1].

The obtained digital values have been used as basis for further investigations. The time domain presentation and the autocorrelation function (ACF) of the signal have been shown in each considered case.

Following the methodology, proposed in [1], the value for the time delay (τ) in each case has been determined. An algorithm, based on the EKRC algorithm, has been implemented for determination of the Ljapunov's exponents and the Ljapunov's dimension.

For a fixed set of values of the parameters a chaotic signal has been produced. The initial conditions for the first parameter set of the Chua's circuit, which has been analyzed, are as follows:Ec=1V;E=8.3V;the conductance of the nonlinear element in the middle region Ga= -0.9167mS; the conductance of the nonlinear element in the outer regions Gb=-0.4091mS;the inductor L=23mH;the capacitor C1=15nF; the capacitor C2=100nF; the conductance G=0.625mS; u1=1e-12V;u2=2e-12V; i3=1e-12A.

Because of the restricted resolution by all graphical presentations of the investigated signals, only a highly reduced number of points have been presented. In fact, in the subsequent mathematical analysis much more points have been considered.

The generated signal has been shown in time domain, as follows bellow in Fig.1.

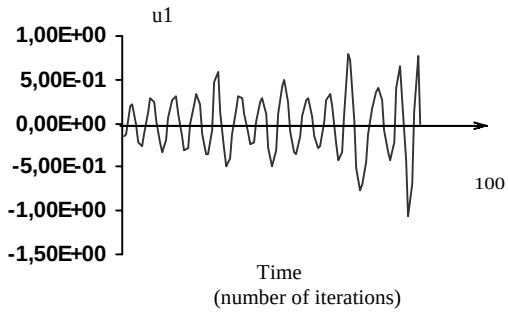

Fig.1

The accurate determination of the Ljapunov's exponents is from great importance for the study of the dynamical behaviour of the analyzed circuit. This requires analysis, based on the autocorrelation functions of the obtained signals. The precise calculation of the time value (τ), at which the autocorrelation function for the first time becomes equal to zero, is a necessary condition for the further

computation of the Ljapunov's exponents. This is the reason, for every obtained signal this value to be determined by means of the corresponding ACF [1-2].

The corresponding autocorrelation function of the signal, displayed in time domain in Fig.1, has been presented in Fig.2.

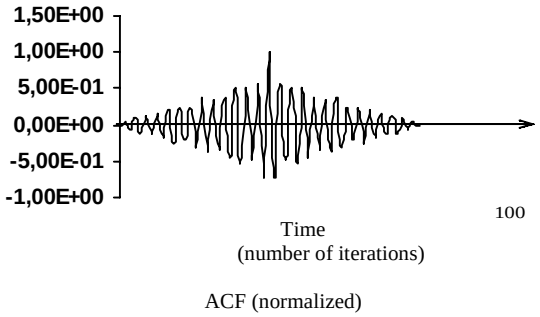

Fig.2

The value of τ for the discussed signal has been computed after calculations, based on the ACF , using the full number of iterations of the obtained signal, in contrast to the small fraction of points, presented in Fig.2, because of the limited resolution by the graphical representation of the results.

For determination of the Ljapunov's exponents and the Ljapunov's dimension an algorithm, based on the EKRC algorithm, has been implemented. The following results have been obtained:

$\lambda_1 = 0.1630, \quad \lambda_2 = -0.0600, \quad \lambda_3 = -0.3119,$

$D_{Ljap} = 3.7153,$

the sum of the positive Ljap exponents = 0.1630,

the sum of the negative Ljap exponents = - 0.3719.

The presence of: (1) Ljapunov's exponents with positive value,

(2) the satisfied inequality between the sum of the negative Ljapunov's exponents, dominated against the sum of the positive Ljapunov's exponents ,

(3) the small value of the second Ljapunov exponent,

are evidence for chaotic behaviour of the generated signal.

Let consider an another set of initial conditions: the conductance of the nonlinear element in the middle region Ga= - 0.9215 mS , the conductance of the nonlinear element in the outer regions Gb= - 0.3991 mS.

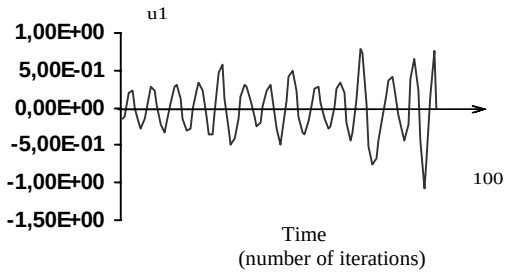

Fig.3.

By these initial conditions another chaotic signal has been obtained. The normalized characteristic in time domain has been presented respectively in Fig.3.

The corresponding autocorrelation function of the signal has been presented in Fig.4.

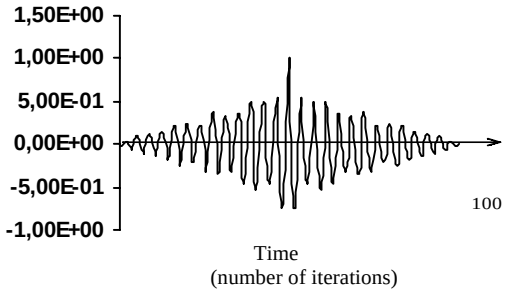

Fig.4.

The further computations of the Ljapunov's exponents lead to the following results:

$\lambda_1 = 0.1666, \quad \lambda_2 = -0.0511, \quad \lambda_3 = -0.3383,$

$D_{Ljap} = 4.2592,$

the sum of the positive Ljap exponents = 0.1666,

the sum of the negative Ljap exponents = - 0.3895.

The signal , displayed in Fig.4, is treated by the analysis, concerning the Ljapunov's exponents for the chaotic signal, explained above. By means of the Ljapunov's exponents chaotic behaviour in the presented investigated signal has been established. The Ljapunov's dimension is similar to the dimension, obtained in the previous case.

By a change of the initial conditions, as follows: Ec=1V; E=8.3V; L=18mH; C1=10nF; C2=100nF; G=(1/1700)S; Ga=(-55/60)mS ; Gb=(-9/22)mS, another chaotic signal has been generated.

The normalized chaotic signal in time domain has been shown in Fig.5

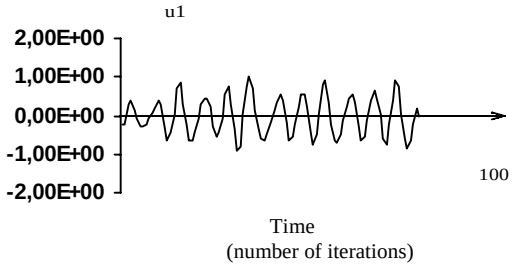

Fig.5

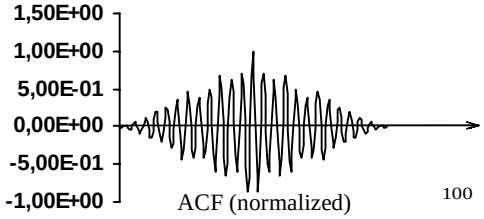

Fig.6

The corresponding normalized autocorrelation function of the obtained signal has been presented above in Fig.6.

The Ljapunov components and the Ljapunov's dimension, computed for the case, considered here, have the following values:

$\lambda_1 = 0.1404$, $\lambda_2 = -0.0832$, $\lambda_3 = -0.3406$

$D_{Ljap} = 2.6880$,

the sum of the positive Ljapunov exponents = 0.1404,

the sum of the negative Ljapunov exponents = - 0.4237.

The computation of the sums, respectively of the positive and the negative Ljapunov's exponents is from great importance for the precise identification of the obtained signals and the correct determination of their characteristics.

The results show, that the examined signal exhibits chaotic behaviour. The value of the Ljapunov's dimension is a small one comparing with the analogous values, obtained in the previous cases, but it is sufficient to prove the presence of chaotic behaviour of the analyzed signal.

Let change the parameter set of the initial conditions in the following way: Ga=(- 0.9215)mS;

Gb=(- 0.3991)mS;

In result a new chaotic signal has been generated.

The time domain presentation of the normalized new chaotic signal is displayed in Fig.7.

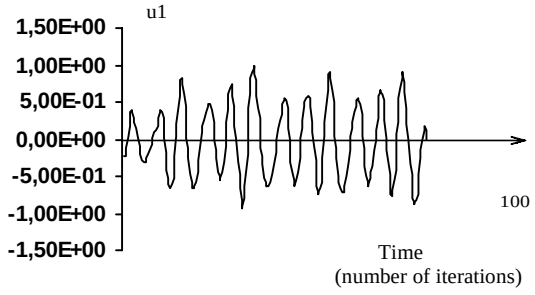

Fig.7

The normalized ACF, related to the signal, considered here, is shown bellow in Fig.8.

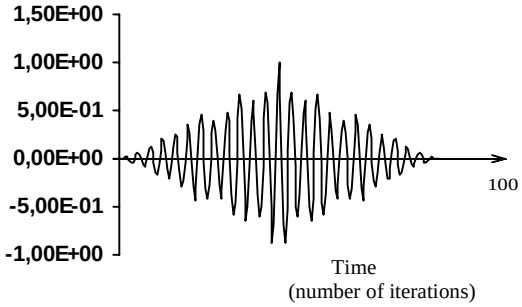

ACF (normalized)

Fig.8

After computations, using the full set of the discrete values for the produced signal, the following results for the Ljapunov's exponents and the Ljapunov's dimension have been obtained:

$\lambda_1 = 0.1648$, $\lambda_2 = -0.0833$, $\lambda_3 = -0.3289$,

$D_{Ljap} = 2.9777$,

the sum of the positive Ljap exponents is: 0.1648,

the sum of the negative Ljap exponents is: - 0.4122.

The value of the Ljapunov's dimension, calculated here, is bigger than the Ljapunov's dimension, obtained in the previous case.

Another initial conditions, as shown bellow:

L=16mH; C1=15nF; C2=100nF; G=(1/1500) S;

Ga= - 0.9167 mS; Gb= - 0.4091 mS are accepted.The obtained signal has been shown in time domain in Fig.9.

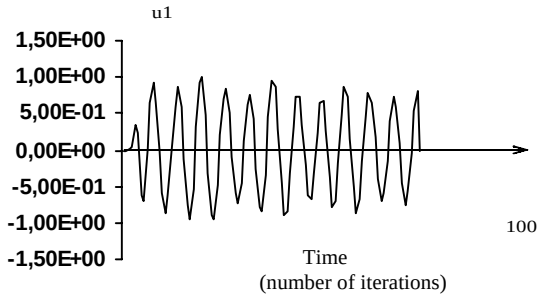

Fig.9

The corresponding ACF is presented in Fig.10.

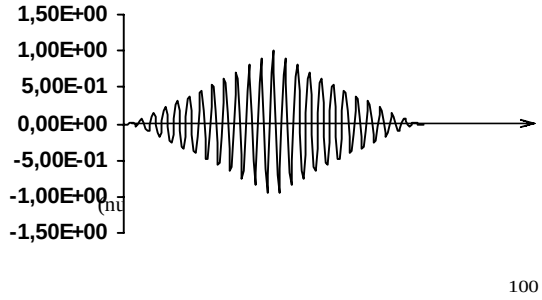

Fig.10

After computations, using the full set of the discrete values for the produced signal, the following results for the Ljapunov's exponents and the Ljapunov's dimension have been obtained:

$\lambda_1 = 0.2042$, $\lambda_2 = -0.1145$, $\lambda_3 = -0.3298$,

$D_{Ljap} = 2.7840$,

the sum of the positive Ljap exponents = 0.2042

the sum of the negative Ljap exponents = - 0.4443

A preliminary control of the values of the parameter set has been made, if the examined values satisfy the requirements of the Shilnikov's theorems. By means of the algorithm, proposed in [5], only these values have been selected, which are with accordance with the requirements, imposed by the theorems, considered in [5].

Changing the initial conditions, as shown bellow:

L=33mH; C1=22nF; C2=100nF; G=(1/1500)S;

Ga=(-55/60)mS; Gb=(-9/22)mS, an another chaotic signal has been obtained.

The examined signal has been presented in time domain respectively in Fig.11.

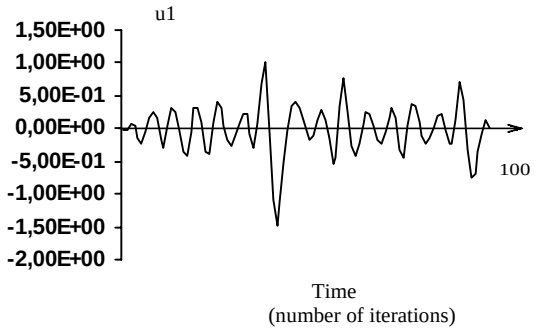

Fig.11

The autocorrelation function, related to the time domain characteristic, is presented bellow in Fig.12:

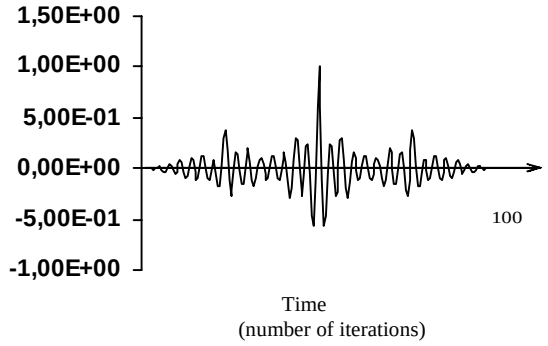

Fig.12

After computations, using the full set of the discrete values for the produced signal, the following results for the Ljapunov's exponents and the Ljapunov's dimension have been obtained:

$\lambda_1 = 0.2155, \qquad \lambda_2 = 0.0037, \qquad \lambda_3 = -0.2933$

$D_{Ljap} = 2.7472,$

the sum of the positive Ljap exponents = 0.2192 ,

the sum of the negative Ljap exponents = - 0.2933

The comparison between the obtained values allows, conclusion for presence of signal with chaotic behaviour to be made.

The values, obtained for the Ljapunov's exponents, show a variation, depending on the set of the values of parameters. As expected, the magnitudes of the Ljapunov's dimension are significant.

The analysis of the dependence between the structure of the Chua's circuit, designed to generate chaotic signals and the characteristics of the generated signals is from great importance for the understanding the processes in this circuit. The appropriate choice of the type of the nonlinearity, used in the circuit, permits signals with chaotic behaviour to be produced.

III. CONCLUSIONS

* A circuit, designed to generate chaotic signals, has been investigated.
* Numerous sets of values of the parameters of the elements, included in the Chua's circuit, have been examined.
* The dependence between the change in the sets of the values of their parameters and the corresponding change in the form of the obtained chaotic signals has been found.
* The sets of values of the parameters of the elements in the Chua's circuit are chosen in accordance with the requirements of the Shilnikov's theorems.
* Signals, obtained from the discussed circuits, have been analyzed and presented in time domain.
* The corresponding autocorrelation functions have been shown.
* Based on the obtained autocorrelation functions, computations, necessary for the determination of the Ljapunov exponents, have been carried out.
* The Ljapunov exponents have been obtained.
* The Ljapunov's dimensions have been computed.
* The Ljapunov's exponents made possible, a qualitative analysis of the examined chaotic signals to be done. By means of the values, obtained for the Ljapunov's exponents, the relationship between these exponents and the Kolmogorov's entropy can be investigated.
* Comparison between some of the obtained Ljapunov's dimensions has been made.
* Conclusions about the ability of the examined sets of values of the parameters of the elements for producing of chaotic signals have been made.
* All of the observed signals satisfy the criteria for the presence of chaotic behaviour.

REFERENCES

[1] Stoycho Panchev, "Theory of chaos" (with Examples and Applications) *Academic Publishing House "Prof. Marin Drinov"* , 1996 (in Bulgarian).

[2] Antonis Karantonis, M.Pagistas ,"Comparative study for the calculation of the Lyapunov spectrum from nonlinear experimental signals", pp. 5428 – 5444, *Ph.Rev.E*, Vol.53, No.5, May 1996.

[3] St. Manev , Vl. Georgiev, "Chaotic signals, generated by some circuits - comparative study (correlation analysis)", ICEST 2003 - Sofia.

[4] St. Manev, Vl. Georgiev, "Chaotic signals, generated by some circuits - comparative study (Ljapunov exponents)", ICEST 2003 - Sofia.

[5] Stoitscho V. Manev and Vladimir Iv. Georgiev, "Analysis of the processes in some radiocommunication circuits, designed to generate chaotic signals", ICEST - 2004.

Analysis of the Processes in Some Radiocommunication Circuits, Designed to Generate Chaotic Signals

Stoitscho V. Manev[1] and Vladimir Iv. Georgiev[2]

Abstract - **In this paper analysis of the processes in some radiocommunication circuits, designed to produce chaotic signals, is presented. Using mathematical approach it has been shown, that the proposed circuits are appropriate for developing of chaotic generators. Some experimental results are shown. The obtained results have been discussed.**

Keywords – **Chaotic circuits, Chua's circuit**

I. INTRODUCTION

The generation of chaotic signals is from great interest for communication purposes. The problem is discussed in many papers[1-5].

Devices, designed to produce chaotic signals, can be used in communications to obtain signals with certain properties. A lot of the devices, designed for this purpose, can be attached to the class of circuits, based on the well known Chua's circuit, presented in Fig.1[1-5]. In purpose to make the mathematical analysis easier, piecewise - linear approximation of the volt - current characteristic of the nonlinear element has been made. The obtained characteristic can be divided in two regions with negative slopes, as presented in Fig.2 [1-4].

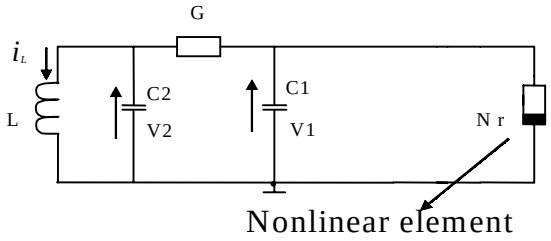

Fig.1.

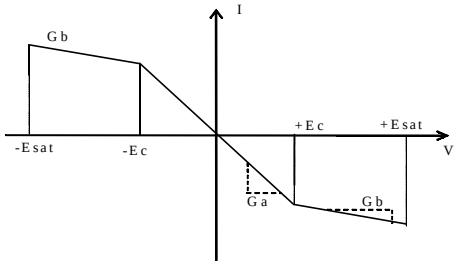

Fig.2

[1]Stoitscho Velizarov Manev - assistant in Dept. of Radiotechnic in Faculty of Communication and Communication Technologies in TU-Sofia, Bulgaria

[2]Vladimir Ivanov Georgiev - professor DSc. in Dept. of Theoretical Electrotechnic in TU-Sofia, Bulgaria

The processes in the Chua's circuit, can be described by means of the following equations [1]:

$$\frac{dv_1}{dt}=\frac{1}{C_1}.\left[G.(v_2-v_1)-\left(G_b.v_1+\frac{1}{2}(G_a-G_b).(\,|\,v_1+1|-|\,v_1-1|)\right)\right]$$

$$\frac{dv_2}{dt}=\frac{1}{C_2}.\left[G.(v_1-v_2)+i_L\right] \qquad (1)$$

$$\frac{di_L}{dt}=-\frac{v_2}{L}$$

In the equations, presented above, the admittances G_a and G_b are correlated to the graphical representation of the volt - current characteristic of the nonlinear element (Fig.2).

II. APPROACH, BASED ON SHILNIKOV'S THEOREMS

The trajectories, obtained from the output signal, are located in 3-dimensional space. In order to make the mathematical analysis easier, this space can be separated in 3 regions.

The processes in the middle region can be described, by means of the value of the parameter G_a. In the outer regions the parameter G_b is used.

After the piecewise-linear approximation the processes can be examined in each region. It can be described analytically as a linear one.

In the middle region the following system of differential equations is valid [3]:

$$\frac{d\,I_3}{d\,t} = -\frac{1}{L}.V_2$$

$$\frac{d\,V_2}{d\,t} = \frac{1}{C_2}.I_3 - \frac{G}{C_2}.(V_2 - V_1) \qquad (2)$$

$$\frac{d\,V_1}{d\,t} = \frac{G}{C_1}.V_2 - \frac{G_a'}{C_1}.V_1$$

where $G_a' = G + G_a$;

In this region the Jacobian matrix and the characteristic polynomial are [3]:

$$J_{F_a} = \begin{bmatrix} 0 & -\frac{1}{L} & 0 \\ \frac{1}{C_2} & -\frac{G}{C_2} & \frac{G}{C_2} \\ 0 & \frac{G}{C_1} & -\frac{G_a'}{C_1} \end{bmatrix} \qquad (3)$$

$$\lambda^3 + \left(\frac{G}{C_2} + \frac{G_a'}{C_1}\right).\lambda^2 + \left(\frac{1}{L.C_2} + \frac{G.G_a}{C_1.C_2}\right).\lambda + \frac{G_a'}{L.C_1.C_2}.$$

In order to analyse the behaviour of the Chua's circuit in the middle region, the eigenvalues of the Jacobian matrix have to be found. The processes in the outer regions can be described by the following system of differential equations [3]:

$$\frac{dI_3}{dt} = -\frac{1}{L}.V_2$$

$$\frac{dV_2}{dt} = \frac{1}{C_2}.I_3 - \frac{G}{C_2}.(V_2 - V_1) \qquad (4)$$

$$\frac{dV_1}{dt} = \frac{G}{C_1}.V_2 - \frac{G_b'}{C_1}.V_1 - \frac{I'}{C_1}$$

where:

$$G_b' = G + G_b,$$
$$I' = (G_b - G_a).E \quad if \quad V_1 < -E,$$
$$I' = (G_a - G_b).E \quad if \quad V_1 > E.$$

In the outer regions the Jacobian matrix and the characteristic polynomial are, as follows [3]:

$$J_{F_b} = \begin{bmatrix} 0 & -\frac{1}{L} & 0 \\ \frac{1}{C_2} & -\frac{G}{C_2} & \frac{G}{C_2} \\ 0 & \frac{G}{C_1} & -\frac{G_b'}{C_1} \end{bmatrix} \qquad (5)$$

$$\lambda^3 + \left(\frac{G}{C_2} + \frac{G_b'}{C_1}\right).\lambda^2 + \left(\frac{1}{L.C_2} + \frac{G.G_b}{C_1.C_2}\right).\lambda + \frac{G_b'}{L.C_1.C_2}.$$

The mathematical analysis, made in the outer regions, is similar to the analysis in the middle region.

In both cases after the determination of the eigenvalues, using the Jacobian matrices, the Shilnikov's method can be applied to prove the presence of chaotic behaviour .

Next, a general case of third order autonomous dynamical system is considered.

The equations, describing the processes in this system are, as follows [5]:

$$\frac{dX}{dt} = \zeta\ (X), \quad t \in R, \quad x \in R^3, \qquad (6)$$

where ζ is vector field.

Let $X_e \in R^3$. X_e is defined as an equilibrium point for (6), if $\zeta\ (X_e) = 0$.

Let the matrix $D\zeta\ (X_e)$ be:

1) real,
2) 3×3 dimensional,
3) the Jacobian derivative of ζ at X_e.

The equilibrium point X_e is defined as *hyperbolic saddle focus,* if the eigenvalues of $D\zeta\ (X_e)$ are of the form: $\gamma, \quad \sigma \pm j\omega, \quad \gamma.\sigma < 0, \quad \omega \neq 0$, where: γ, σ, ω are real [5].

The two theorems, presented bellow, give the background for the chaotic behaviour of the Chua's circuit in the sense of Shilnikov [5]:

Theorem1 (Homoclinic Shilnikov Method)

Given the third-order autonomous system in (6), where ξ is a C^2 vector field on R^3. Let X_e be an equilibrium point for (6). Suppose the following:

1) The equilibrium point is a saddle focus, whose characteristic eigenvalues satisfy the Shilnikov's inequality: $|\gamma| > |\sigma| > 0$

2) There exists a homoclinic orbit H based at X_e.

Then: 1) The Shilnikov map, defined in a neighbourhood of H, possesses a countable number of Smale horseshoes in its discrete dynamics.

2) For any sufficiently small C^1 - perturbation ζ of ξ^2, the perturbed system:

$$\frac{dX}{dt} = \zeta\ (X), \quad x \in R^3 \qquad (7)$$

has at least a finite number of Smale horseshoes in the discrete dynamics of the Shilnikov's map, defined near H.

3) Both the original system (equation (6)) and the perturbed system (equation (7)) exhibit horseshoe chaos (homoclinic chaos)[5].

Theorem2 (Heteroclinic Shilnikov Method)

Given the third - order autonomous system in (6), where ξ is a C^2 vector field on R^3. Let X_{e1} and X_{e2} be two distinct equilibrium points for (6). Suppose the following:

1) Both X_{e1} and X_{e2} are saddle foci that satisfy the Shilnikov's inequality: $|\gamma_i| > |\sigma_i| > 0 \quad (i = 1, 2)$

With the further constraint:

$$\sigma_1.\sigma_2 > 0 \quad or \quad \gamma_1.\gamma_2 > 0$$

2) There is a heteroclinic loop H_l, joining X_{e1} to X_{e2}, that is made up of two heteroclinic orbits $\mathrm{H}_i \quad (i = 1, 2)$.

Then: 1) The Shilnikov map, defined in a neighbourhood of H_l, possesses a countable number of Smale horseshoes in it's discrete dynamics.

2) For any sufficiently small C^1 - perturbation ζ of ξ^2, the perturbed system:

$$\frac{dx}{dt} = \zeta(x), \qquad x \in R^3 \tag{8}$$

has at least a finite number of Smale horseshoes in the discrete dynamics of the Shilnikov's map, defined near H_l.

3) Both the original system equation (6) and the perturbed system equation (8) exhibit heteroclinic chaos [5].

The aim of the analysis, made in the presented paper, is to examine the influence of the Shilnikovs inequalities (see above) on the character of the signal, produced from the Chua's circuit.

In order to achieve this, in the presented study the following algorithm has been developed:

1) For the initial conditions the Jacobian matrix (3) in the middle region has been constructed.

2) By means of the values of the parameters, given in the initial conditions, the Jacobian matrices (5) for the outer regions have been constructed.

3) The eigenvalues, respectively for the matrices (3) and (5), have been determined.

4) The real parts: γ and σ from the eigenvalues have been determined.

5) Using the Shilnikov's inequalities a procedure has been developed. The essence of this procedure is: such values of the parameters, taking part by the construction of the Jacobian matrices, to be determined, so as the Shilnikov's inequalities to be satisfied. To achieve this, the following steps are necessary:

* The eigenvalues should be checked up, if they satisfy the requirements, defined by the Shilnikov's inequalities.

* If these requirements are not fulfilled, another procedure starts. It includes search of such set of values of parameters, which is appropriate to satisfy the Shilnikov's inequalities.

III. EXPERIMENTAL RESULTS

As starting point for the investigations a circuit, analogous to this, presented in [3], has been used. In Fig.1 the structure of the analyzed circuit is presented. It consists of: an inductor L, two capacitors C1 and C2, a linear resistor G and a nonlinear element.

The values of the parameters are: the inductor L=23mH;the capacitor C1=15nF; the capacitor C2=100nF; the conductance: G=0.625m S;

In Fig.2 the volt-current characteristic is given. The negative signs indicate, that the slopes of the volt - current characteristic in the examined regions are both negative. In order to obtain characteristic in such a form (Fig.2), the absolute value of Ga must be greater then the absolute value of Gb. This requirement is included in the proposed algorithm. A search for values of the parameters Ga and Gb has been made, in order to satisfy the Shilnikov's inequalities.

The experimental results illustrate the above procedure. They are based on the following initial conditions:

* a conductance of the nonlinear element in the middle region Ga= - 0.9167 mS.

* a conductance of the nonlinear element in the outer regions Gb= - 0.4091 mS.

For this case for γ and σ, concerning the dynamics of the system in the middle region, the values:

γ = 2.4805e+004 ; σ = -5.8051e+003 have been obtained.

The eigenvectors for the middle region are the columns of the matrix, presented bellow:

$$\begin{bmatrix} 0.0011 + 0.0008i & 0.0011 - 0.0008i & -0.0002 \\ 0.4877 - 0.3385i & 0.4877 + 0.3385i & 0.1276 \\ -0.8047 & -0.8047 & 0.9918 \end{bmatrix}$$

The values, obtained for γ and σ by the investigations in the outer regions, are as shown bellow:

γ = - 2.1732e+004 ; σ = 544.0226 .

Respectively the eigenvectors, concerning the processes in the outer regions, are the columns of the matrix:

$$\begin{bmatrix} -0.0009 + 0.0008i & -0.0009 - 0.0008i & -0.0003 \\ 0.3151 + 0.3578i & 0.3151 - 0.3578i & -0.1734 \\ 0.8790 & 0.8790 & 0.9848 \end{bmatrix}$$

It is obvious, that the obtained values for γ and σ in the middle and in the outer regions fulfil the requirements from the Shilnikov's inequalities and their polarity are in accordance with the expected polarity, resulting from the analysis in [3].

Alternatively, another set of initial conditions:

Ga= - 0.9215 mS; Gb= - 0.3991 mS produce the following values for γ and σ in the middle region:

γ= 2.5117e+004 ; σ= - 5.7999e+003

The eigenvectors are the columns of the matrix

$$\begin{bmatrix} 0.0011 + 0.0008i & 0.0011 - 0.0008i & - 0.0002 \\ 0.4922 - 0.3381i & 0.4922 + 0.3381i & 0.1274 \\ - 0.8021 & - 0.8021 & 0.9919 \end{bmatrix}$$

For the outer regions γ = -2.2384e+004 , σ = 536.8802 have been obtained .The eigenvectors are presented as columns of the matrix

$$\begin{bmatrix} - 0.0009 + 0.0008i & -0.0009 - 0.0008i & - 0.0003 \\ 0.3272 + 0.3587i & 0.3272 - 0.3587i & - 0.1731 \\ 0.8742 & 0.8742 & 0.9849 \end{bmatrix}$$

The inequalities in the Shilnikov's theorems are satisfied.

Another set of initial conditions: L=18mH; C1=10nF; C2=100nF;G=(1/1700)S;G= 0.58824 mS; Ga=-0.9167mS; Gb=-0.4091 mS produce:

γ = 3.8713e+004 ; σ =-5.8762e+003

in the middle region. The eigenvectors in this region are presented as columns of the matrix:

$$\begin{bmatrix} 0.0011 + 0.0011i & 0.0011 - 0.0011i & -0.0001 \\ 0.5271 - 0.2845i & 0.5271 + 0.2845i & 0.0993 \\ -0.8008 & -0.8008 & 0.9951 \end{bmatrix}$$

For the outer regions the following values have been obtained: $\gamma = -2.6246e+004$; $\sigma = 1.2246e+003$. The corresponding eigenvectors are the columns of the matrix, shown bellow:

$$\begin{bmatrix} 0.0009 - 0.0008i & 0.0009 + 0.0008i & -0.0003 \\ -0.2952 - 0.2997i & -0.2952 + 0.2997i & -0.1402 \\ -0.9072 & -0.9072 & 0.9901 \end{bmatrix}$$

The change in the values of Ga and Gb, as follows:

Ga= -0.9215 mS; Gb= -0.3991mS;

leads to a respective change in the eigenvalues of the Jacobian matrices in the middle and in the outer regions:

In the middle region: $\gamma = 3.9168e+004$,

$\sigma = -5.8620e+003$.

The eigenvectors are the columns of the matrix

$$\begin{bmatrix} 0.0011 + 0.0011i & 0.0011 - 0.0011i & -0.0001 \\ 0.5316 - 0.2840i & 0.5316 + 0.2840i & 0.0988 \\ -0.7980 & -0.7980 & 0.9951 \end{bmatrix}$$

In the outer regions : $\gamma = -2.7203e+004$,

$\sigma = 1.2035e+003$.

The eigenvectors in the outer regions are displayed as columns of the matrix

$$\begin{bmatrix} 0.0009 - 0.0008i & 0.0009 + 0.0008i & -0.0003 \\ -0.3086 - 0.3009i & -0.3086 + 0.3009i & -0.1395 \\ -0.9023 & -0.9023 & 0.9902 \end{bmatrix}$$

It is obvious, that the inequalities in the Shilnikov's theorems are satisfied.

Experiments with another set of initial conditions: L=16mH; C1=15nF; C2=100nF; G=(1/1500)S; Ga = - 0.9167 mS; Gb= - 0.4091 mS, have been carried out. Respectively: $\gamma = 2.1856e+004$ and $\sigma = -5.9270e+003$ in the middle region have been obtained.

The eigenvectors in this region are the columns of the matrix

$$\begin{bmatrix} -0.0014 - 0.0008i & -0.0014 + 0.0008i & -0.0003 \\ -0.4176 + 0.3884i & -0.4176 - 0.3884i & 0.1159 \\ 0.8214 & 0.8214 & 0.9933 \end{bmatrix}$$

For the outer regions

$\gamma = -2.4002e+004$; $\sigma = 82.2005$

have been obtained. The eigenvectors in the outer regions can be obtained, using the columns of the matrix:

$$\begin{bmatrix} -0.0012 + 0.0010i & -0.0012 - 0.0010i & -0.0004 \\ 0.3308 + 0.4054i & 0.3308 - 0.4054i & -0.1519 \\ 0.8522 & 0.8522 & 0.9884 \end{bmatrix}$$

Experiments with another set of initial conditions, have been carried out:L=33mH; C1=22nF; C2=100nF; G=(1/1500)S; Ga= -0.9167 mS; Gb= - 0.4091 mS;

The following bellow values for γ and σ in the middle region have been obtained:

$\gamma = 1.6225e+004$; $\sigma = -5.7633e+003$.

The eigenvectors in this region are the columns of the matrix

$$\begin{bmatrix} -0.0011 - 0.0006i & -0.0011 + 0.0006i & -0.0003 \\ -0.4593 + 0.3588i & -0.4593 - 0.3588i & 0.1584 \\ 0.8126 & 0.8126 & 0.9874 \end{bmatrix}$$

For the outer regions the following values have been obtained: $\gamma = -1.8856e+004$

$\sigma = 240.9648$

Respectively the columns of the matrix:

$$\begin{bmatrix} -0.0009 + 0.0007i & -0.0009 - 0.0007i & -0.0004 \\ 0.3381 + 0.3880i & 0.3381 - 0.3880i & -0.2296 \\ 0.8574 & 0.8574 & 0.9733 \end{bmatrix}$$

are the eigenvectors in the outer regions.

From the results, obtained by the investigations of different sets of values of parameters of the elements of the Chua's circuit, becomes obvious, that the requirements of the inequalities in the Shilnikov's theorems are satisfied.

IV. CONCLUSIONS

* An algorithm to study chaotic signals by means of Chua's circuit, has been proposed.
* Some illustrative experiments have been carried out.
* The obtained results have been examined, if they are with accordance to the requirements, imposed by the Shilnikov's theorems.
* It has been shown, that by appropriate choice of the values of the components in the Chua's circuit, using the proposed algorithm, chaotic signals have been obtained.

REFERENCES

[1] L.Chua, G.N.Lin, "Canonical realization of Chua's circuit family", *IEEE Trans. CAS*, Vol. 37, No.7, 1990.

[2] M.P.Kennedy, "Three steps to chaos-part I: Evolution", *IEEE Trans.CAS* , Vol.40, No.10, 1993.

[3] M.P.Kennedy, " Three steps to chaos-Part II: A Chua's circuit primer", *IEEE Trans.CAS*, Vol.40, No.10, 1993.

[4] L.Chua, Ch.W.Wu, An.Huang, G.-Q.Zhong, "A universal circuit for studying and generating chaos - Part I: Routes to chaos", *IEEE Trans.CAS* , Vol.40, No.10, 1993.

[5] Christopher P.Silva, "Shilnikov's Theorem - A Tutorial", *IEEE Trans.CAS*, Vol.40, No.10, 1993.

[6] St. Manev , Vl. Georgiev, "Chaotic signals, generated by some circuits - comparative study (correlation analysis)", ICEST 2003 - Sofia.

[7] St. Manev , Vl. Georgiev, "Chaotic signals, generated by some circuits - comparative study (Ljapunov exponents)", ICEST 2003 - Sofia.

A new algorithm for Doppler ambiguity resolution

Rossen Miletiev[1], Rumen Arnaudov[2], Slavcho Lishkov

Abstract – A new algorithm for velocity ambiguity resolution in coherent pulsed Doppler radar is proposed, based on the spectrum analysis of the nonuniformly sampled data. The highest resolved Doppler ambiguity rate is estimated and simulations results are represented to show the algorithm effectiveness.

Keywords – Doppler ambiguity, single target

Introduction - In radar systems the periodically nonuniform sampling is used to avoid the blind speed effect. For a given set of PRFs, Chinese Remainder Theorem (CRT) has been established to resolve ambiguity [1]-[3]. The problem with the CRT approach is that a small range error on a single PRF (pulse repetition frequency) can course a large error in the resolved range and there is no indication that this has happened. To avoid this problem, a clustering algorithm is also suggested with the minimum square error criterion [4]. It has good anti-error ability and expensive computational throughout. An algorithm based on the choice of particular values for the PRFs is provided for velocity ambiguity resolution, where a quasi-maximum likelihood criterion is maximized for ambiguity order estimation [5].

Considering the blind area of both in time and frequency, this algorithm is so limited by particular PRFs that it is not fit for other combination of PRFs to resolve the velocity ambiguity. In view of the shown disadvantages of the described methods, a new algorithm is proposed to resolve the velocity ambiguity using the spectrum analysis of the nonuniformly sampled data.

Mathematical background – As is well known, the spectrum of a signal sampled uniformly in the time domain is periodic in the frequency domain. In contrast, the spectrum of a nonuniformly sampled signal is not periodic, which enables unambiguity frequency analysis at the frequencies above half the virtual sampling frequency, defined by the mean harmonious of the selected pulse repetition frequencies [6]. The proposed algorithm is based on this aperiodicity according to the spectrum estimation equation [6] using two consecutively changed *PRFs*:

$$X(m+pN/2)=X_{2k}(m)+e^{j\frac{2\pi}{N}(m+pN/2)(1-\rho)}X_{2k+1}(m), \quad (1)$$

where $\rho=\dfrac{PRF_1-PRF_2}{PRF_1+PRF_2}$ - nonuniformly sampling constant; N - number of sampling points; $m\in\left[0;N/2-1\right]$ - frequency bin number; p - integer number; X_{2k} and X_{2k+1} - *DFT* of even and odd samples respectively

The corresponding power spectrum is calculated by taking the modulus-squared spectral coefficients:

$$\left|X(m+pN/2)\right|^2=\left|X_{2k}(m)\right|^2+\left|X_{2k+1}(m)\right|^2+ \\ +\operatorname{Re}\hat{X}\cos\theta-\operatorname{Im}\hat{X}\sin\theta, \quad (2)$$

where $\theta=2\pi m/N-\pi p\rho$ and $\hat{X}=X_{2k}(m)\overset{*}{X}_{2k+1}(m)$

The Doppler ambiguity resolution is made by spectrum peak detection at two stages. The first stage defines the bin number of the spectrum peak below half the sampling frequency and the second stage locates the peak of the dominant alias frequencies envelope according to the equation:

$$\frac{\partial\left\{\left|X(m'+pN)\right|^2\right\}}{\partial p}=0 \quad (3)$$

By substituting the equation (2) into (3), the resolution equation is described as follows:

$$tg\left(\frac{2\pi}{N}m'-2\pi p\rho\right)+\frac{\operatorname{Im}\hat{X}}{\operatorname{Re}\hat{X}}=0, \quad (4)$$

From the known trigonometric formula $tg(\alpha-\beta)=\dfrac{tg\alpha-tg\beta}{1+tg\alpha tg\beta}$, the equation (4) is modified to the next equation:

$$tg(2\pi p\rho)=\frac{tg\left(\frac{2\pi}{N}m'\right)+\frac{\operatorname{Im}\hat{X}}{\operatorname{Re}\hat{X}}}{1-\frac{\operatorname{Im}\hat{X}}{\operatorname{Re}\hat{X}}tg\left(\frac{2\pi}{N}m'\right)}=Y \quad (5)$$

Since the trigonometric function $tg(x)$ is defined in the range $-\pi/2\le x\le\pi/2$, the Doppler ambiguity rate can be uniquely established when the following expression is implemented:

$$|p|\le(4|\rho|)^{-1} \quad (6)$$

In this case the Doppler ambiguity rate is calculated from the next equation:

[1]Rossen Miletiev – miletiev@yahoo.com
[2]Rumen Arnaudov – RA@tu-sofia.bg
Technical University of Sofia, Faculty of Communications and Communication technologies

$$p = \mathrm{int}\left(\frac{1}{2\pi\rho} arctgY \right) \qquad (7)$$

Therefore, the obtained equation (7) resolves the Doppler ambiguity of a single target in the limitation of equation (6) using spectrum analysis of the nonuniformly sampled data. It is clear that the highest resolved Doppler ambiguity rate is inversely proportional of the nonuniformly sampling constant, but the detailed analysis shows that in this case the proposed algorithm is more sensitive to the additive noise. So there is a settlement by compromise of this parameter.

Numerical example - The proposed algorithm is tested using Matlab® routine. To illustrate the significance of the algorithm, we consider a single sinusoidal waveform f=13kHz with added white Gaussian noise ($SNR=5dB$), sampled with two consequently changed PRFs – PRF_1=1818Hz and PRF_2=1723Hz in N=128 points. The chosen initial values specify the values of the nonuniformly sampling constant and the highest resolved Doppler ambiguity rate to 0,026829 and 9 respectively. The spectrum power of the signal is calculated below and above half the sampling frequency according to equation (1), and the simulation results are shown at fig. 1 and fig. 2 respectively. The figure 1 defines two spectrum peaks – one real spectrum peak at 622,4Hz and second parasitic one at 1493,3Hz. The parasitic spectrum peak is descended from the nonuniform sampling nature, described at our previous work [6]. The real resolved frequency is equal to 13,002kHz, which is the nearest point to the real simulated waveform. The second resolved frequency, defined by the parasitic spectrum peak, is equal to 15,658kHz, which is recognized as parasitic Doppler frequency due to extended spectrum analysis, shown at fig.2. It shows that the real Doppler frequency is located at the peak of the dominant alias frequencies envelope according to equation (3).

The figure 1 and figure 2 demonstrate the first and second stage of the Doppler ambiguity resolution respectively as they define the bin number of the spectrum peak and the value of the Doppler ambiguity rate, which is set to 7 according to equation (7).

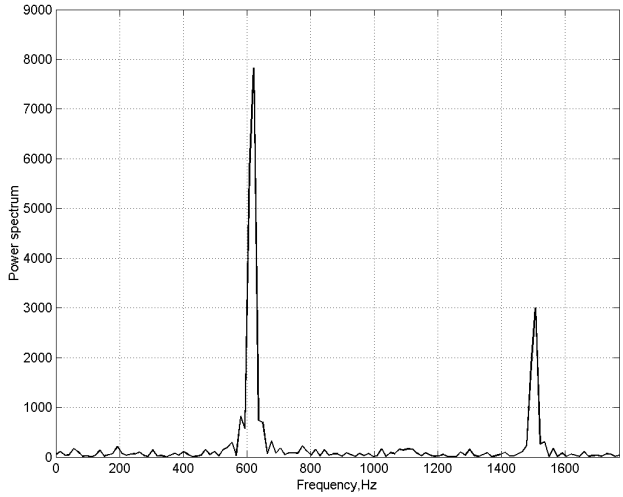

Figure 1 – Spectrum analysis at the frequencies below half the virtual sampling frequency

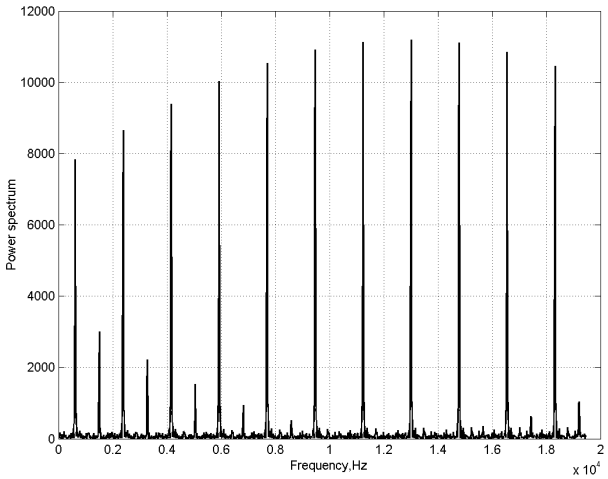

Figure 2 – Extended spectrum analysis at the frequencies above half the virtual sampling frequency

So the proposed algorithm resolves successfully the Doppler ambiguity in the low SNR environments using simple estimation technique as described in §2. The fast implementation of the unambiguous estimation procedure is based on the fast Fourier transform (*FFT*) and spectrum coefficients computation only at selected frequencies. The main disadvantage of the proposed algorithm consists in the inability to resolve the Doppler frequencies in the multiple target situations, when the difference of the target radial velocities is divisible by the virtual sampling frequency.

Conclusion - A new approach to PRF ambiguity resolving has been described. The presented algorithm allows resolving the Doppler ambiguity of a single target according to the obtained equation (7) and the highest resolved Doppler ambiguity rate is defined by equation (6). This algorithm provides good stability in low SNR environments and simple computation mechanism. It can find an application in advanced radar processors, included in low PRF search radars, or in other Doppler systems to determine the object radial velocity.

References

[1] Hovanessian, S.A. – An algorithm for calculation of range in multiple PRF radar, *IEEE Trans*., AES-18, 1982, No.3, pp.288-296

[2] Sirdhar, N.R. – Resolution of range and Doppler ambiguities in medium PRF radars in multiple target environment, *Signal Processing*, 1983, Vol.11, pp.223-226

[3] Misiurewitz, J. – Unambiguous Doppler frequency estimation in at MTI radar, *IEE 1997*, Radar 97, Edinburgh, 14-16 October 1997, Publication No.449, pp.530-534

[4] Trunk, G.; Brockett, S. – Range and velocity ambiguity resolution – *The record of 1993 IEEE International Radar Conference*, pp.146-149

[5] Ferrari, A.; Berenguer, C.; Alengrin, G. – Doppler ambiguity resolution using multiple PRF, *IEEE Trans. of Aerospace and Electronic Systems*, vol.33, No.3, pp.738-751

[6] Miletiev, R.G.; Arnaudov, R.I. – Spectrum analysis of nonuniformly sampled data, *Proceedings of Technical University - Sofia*, 2004, v.53, No.1

Real-time radar Doppler processing

Rossen Miletiev[1]

Abstract - This paper discusses the algorithm for coherent Doppler processing using consecutively changed PRFs and nonparametric spectral estimation method for the nonuniformly sampled data sequence. The described Doppler processing algorithm provides improved performance for target detection, especially in low SNR environments, and it is suitable for search Doppler radars with fast frequency changes and a relatively small number of echoes from a target.

Keywords – Doppler processing, real-time

I. Introduction – Radar serves to detect objects within the area of observation and to estimate their position coordinates. The echo characteristics provide information such as the range, angular location of the target, its trajectory if it is moving and predict future location [1-3]. The Doppler processing of the reflected signal is the primary tool at the detection, identification and classification of the targets and an estimation of its mean target velocity and position coordinate. It improves the moving target improvement factor of the system. Hence it improves the performance of the detector. A wide range of techniques for Doppler-based clutter suppression are practical due to advances in signal processing [4-6].

They often utilize parametric estimation methods, which require prolong computing time and impede the real-time operation. For that reason, the Doppler processing algorithm is described below, which is based on *FFT* technique and possesses the enhanced spatial resolution.

II. System design – The main problem, which the proposed algorithm decides, is associated with the relation between the target azimuth coordinates and its spectral characteristics. Therefore, the expedient *PRFs* alternation had to be chosen. If the radar transmits the first *n* pulses with the first *PRF* and the second *n* pulses with the second one then the analyzed data segment contains the different data bits of the each *PRF* and the spectral analyze requires the prolong computation time due to impracticable *FFT*. Therefore the real-time sliding spectral estimation is impossible. If the data sequence from each *PRF* is collected at blocks and transformed to frequency domain by *FFT*, then the frequency data bits are not associated with the target azimuth coordinates. For that reason the consecutively changed *PRFs* are used, i.e. the odd pulses are transmitted with the first *PRF* and the even pulses – with the second one.

[1]Rossen Miletiev – miletiev@yahoo.com, Technical University of Sofia, Faculty of Communications and Communication Technologies

This choice possesses the next advantages:

- Every data segment contains *N/2* bits for each *PRF*
- The spectral estimation method is based on *FFT* technique to ensure the great computing efficiency
- The 2D output matrix is produced for each returned echo. This fact allows to determine the target azimuth coordinate
- The spatial resolution is increased, because the algorithm can resolve multiple targets, which have the same azimuth coordinates, but different radial speed. Therefore, the algorithm gives an account of the finite dimensions of the antenna radiation pattern at *E* and *H*-plane.

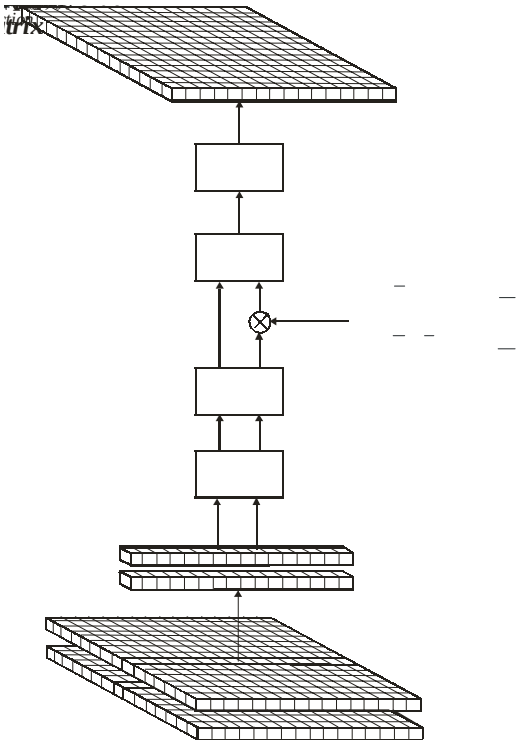

Fig.1. Real-time Doppler processing algorithm

The proposed algorithm for real-time Doppler processing is based on the accepted way of the *PRFs* alternation. The algorithm diagram is shown at fig.1 and contains the following steps:

- The discrete data sequence from the pulse compression matrix is divided in two sequences, which contain the odd and even bits respectively
- The created sequences are multiplied by window function to avoid the spectral leakage. The *Hamming* window is used due to its low sidelobe levels

- The *N/2* point *FFT* is applied to the odd and even windowed sequences
- The spectrum coefficients of the even sequence $X(2k+1)$ are corrected with the phase factor $\exp\left[-j\frac{2\pi}{N}m(1-\rho)\right]$, according to the reported spectrum estimation method [7]
- The segment frequency response is estimated by addition the spectrum coefficients of the odd and corrected even sequence
- The power spectrum is calculated from the segment frequency response
- The proposed algorithm is repeated from step 1 by shifting the segment to one bit to realize the sliding spectral analysis

III. Numerical example – The proposed Doppler processing algorithm is simulated using *MATLAB*® routine. The simulations are implemented at the following conditions:

1. A single target is presented at the scan area
2. If the target azimuth angle is equal to φ_0, then the input data sequence describes the scanning results from the azimuth range $\varphi = (\varphi_0 - 10^0; \varphi_0 + 10^0)$
3. The antenna radiation pattern is described by the equation and is shown at fig.2:

$$|F(\varphi)| = \left|\frac{\sin\frac{x_0}{\theta_0}\varphi}{\frac{x_0}{\theta_0}\varphi}\right| \cdot \frac{\theta_0^2}{|\theta_0^2 - \varphi^2|},$$

where $x_0 = 2.2629$ - constant, which describes the system parameters

$2\theta_0 = 0{,}9\deg$ - antenna beam width at -3dB

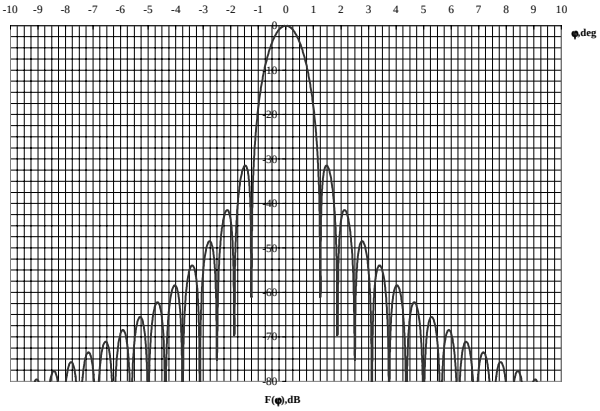

Fig.2 – Antenna radiation pattern

4. The white Gauss noise is added to the signal matrix

The calculations are made according to the described consistency at the algorithm with the next additional information:

1. *SNR=6dB – signal to noise ratio*
2. *PRF_1=2500Hz, PRF_2=2857Hz – pulse repetition frequencies*
3. *v_r=20m/s – radial target velocity*
4. *N_x=12min^{-1} – antenna revolution*
5. *R=21km – target distance*
6. *N_A=370 – number of azimuth bits*
7. *N_D=64 – number of Doppler bits*
8. *N_R=1024 – number of range bits*

The simulation results are represented at fig.3 and fig.4. The partial time domain 2D matrixs (*I* and *Q* channel) are shown at fig.3a and fig.3b. The shown azimuth bins are limited to 100 bits, which include the target ones. The generated CFAR matrixes, which are estimated by using the sliding window, are shown at fig.4a-c. The Doppler maximum is poorly discernable at the first and the last figures (fig.4a and fig.4c), which are thoroughly contained the noise. When the Hamming window maximum coincades with the target azimuth coordinate then the Doppler peak has the maximum value (fig.4b). Due to these algorithm properties the target azimuth coordinates are established.

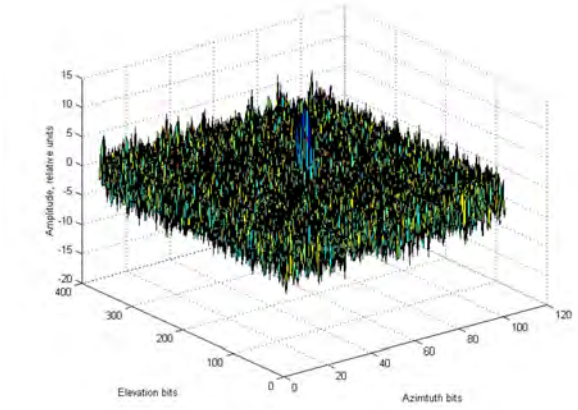

I matrix

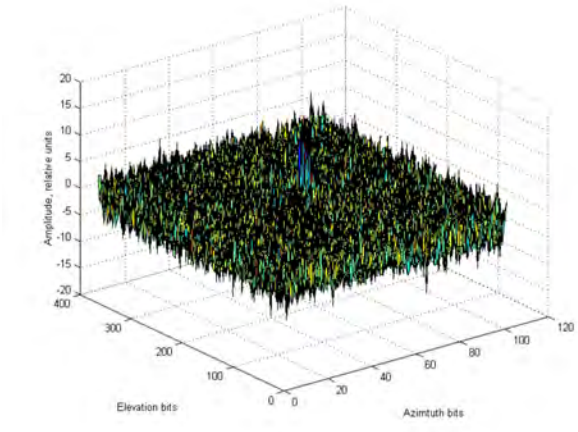

Q matrix

Fig.3 – Time domain 2D matrixes

Therefore, the simulations show that the sliding Doppler processing and the proposed spectrum analysis algorithm allow detecting the target azimuth coordinates from the generated CFAR matrix maximums using high speed *FFT* technique to ensure the real-time processing.

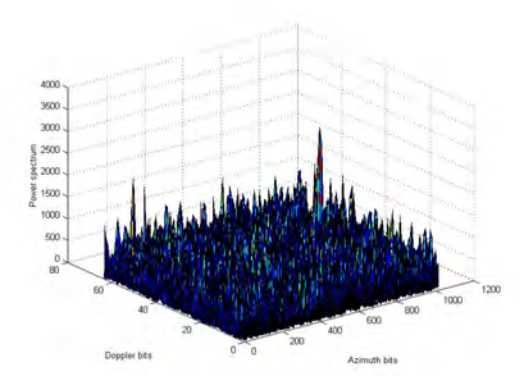

(a)

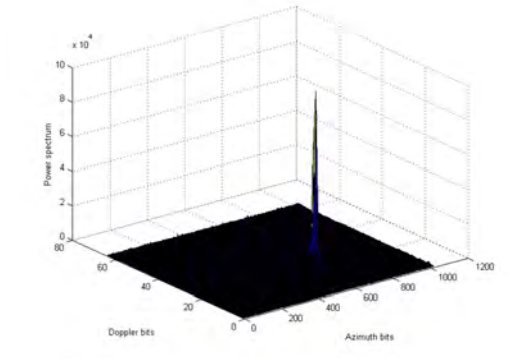

(b)

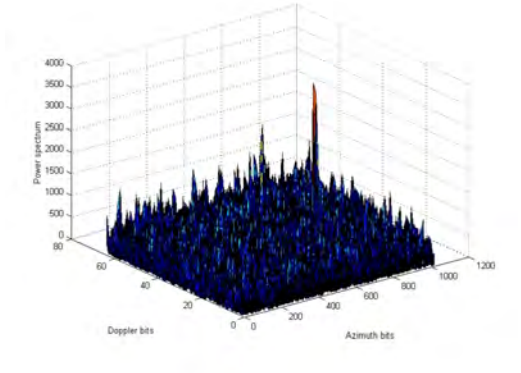

(c)

Fig.4 – The CFAR matrix

a) 16 bits before the target maximum
b) window coincides with the target maximum
c) 16 bits after the target maximum

IV. Conclusion – The discussed algorithm for coherent Doppler processing using consecutively changed *PRFs* and nonparametric spectral estimation method for the nonuniformly sampled data sequence. The described Doppler processing algorithm provides improved performance for target detection, especially in low *SNR* environments, and is distinguished with an enhanced spatial resolution and great computing efficiency. It is suitable for search Doppler radars with fast frequency changes and a relatively small number of echoes from a target.

V. References

1. Nathanson, Fred E. – "Radar design principles: signal processing and the environment", New York, McGraw-Hill, 1991
2. Edde, Byron – "Radar: principles, technology, applications", N.J., Prentice Hall, c1993
3. Skolnik, M.I.– "Radar handbook**"**, McGrawHill, 1970
4. Schleher, D. Curtis – "MTI and pulse Doppler radar", Boston, Artech House, c1991
5. Barton, David K. – "Radars – Frequency agility and diversity**"**, vol.6, Artech House Inc., London, 1989
6. Armstrong, B.C. – "A comparison of conventional, adaptive and hybrid Doppler processing techniques", Communications and Signal Processing, COMSIG '92, pp: 127 -134
7. Miletiev, R.G.; Arnaudov, R.I. – Spectrum analysis of nonuniformly sampled data, *Proceedings of Technical University - Sofia*, 2004, v.53, No.1

New First-Order Very Low Sensitivity Narrow-Band Hypercomplex Digital Filter Sections

Zlatka Nikolova[1]

Abstract **- In this paper a new strategy to obtain very low sensitivity narrow-band orthogonal hypercomplex coefficients first-order IIR digital filter sections with canonic number of elements is developed. It is shown that the new filters behave much better in a limited word-length environment in comparison with other known structures of this type.**

Keywords **– complex filters, orthogonal hypercomplex digital filter sections, sensitivity**

I. INTRODUCTION

As a rule hypercomplex numbers are defined as an expansion of complex numbers [1]. Hamilton's quaternion belongs to the group of hypercomplex numbers and has its main application in the field of image processing and computer graphics as a coordinate transform of 3-D images. They have been also employed by the aerospace engineering, where their convenient representation of rotation has proved useful in such matters as stabilization and altitude control. Shutte and Wenzel proved that Hamilton's quaternions and biquaternions are not well suited for the purpose of digital signal processing (DSP) and in Ref. [2] the modified version as "reduced biquaternions (RB)" is offered. Some authors call RB "bicomplex numbers". Several research studies concerning applications of bicomplex numbers to DSP have been reported. Computational efficiency and stability criterion of digital filters with bicomplex coefficients are investigated in Ref. [9], [8]. Colour image filters based on hypercomplex convolution are defined and utilized for autocorrelation and cross-correlation of color image processing in Ref. [10]. Hypercomplex filters also make use of image recognition, smoothing the colour image components, design of two-dimensional transfer functions with applications in image processing of both grey scale and colour images.

The filters with RB coefficients can reduce the order of the filters to 1/4 of the one with real coefficients, and to 1/2 of one with complex coefficients, which is one of the most significant advantages of using hypercomplex numbers. Reduction of the number of multipliers and additions by efficient algorithms is another advantage.

In many applications high accuracy filter realizations with heavily quantized coefficients are required and they are achieved by structures with lower sensitivity. In this paper some new first-order narrow-band hypercomplex digital filter sections with very low coefficients sensitivity are developed and investigated.

[1] Technical University-Sofia, Faculty of Communication Technology, Dept. of Telecommunications, Bulgaria, E-mail: zvv@tu-sofia.bg

II. PROPERTIES OF HYPERCOMPLEX NUMBERS

A quaternion may be represented in hypercomplex form as follows:

$$q = a + bi + cj + dk\ , \tag{1}$$

where *a*, *b*, *c* and *d* are real numbers, while *i*, *j*, and *k* are orthogonal complex operators which obey the following rules:

$$\begin{gathered} i^2 = j^2 = k^2 = ijk = -1 \\ ij = k \quad jk = i \quad ki = j \quad ji = -k \quad kj = -i \quad ik = -j\,. \end{gathered} \tag{2}$$

Regarding the arithmetic lows of a quaternion, addition of two quaternions is commutative and associative, and multiplication is associative but not commutative, which make them not applicable to DSP systems. To avoid this problem reduced biquaternion (RB) has been proposed, which is derived as follows: *a* and *b* in Eq. (1) are expanded to complex numbers and *c* and *d* are set to zero. This modification is equivalent to the expansion of each element of a complex number to a complex number, i.e. a quaternion is a complex number with complex real and imaginary parts. On account of that RB is also called bicomplex number:

$$\begin{aligned} A = A_S + iA_V &= (A_1 + jA_2) + i(A_3 + jA_4) = \\ &= A_1 + jA_2 + iA_3 + kA_4 \end{aligned} \tag{3}$$

where A_1, A_2, A_3 and A_4 are real numbers, j is the imaginary unit with $j^2 = -1$ and i is the vector unit with $i^2 = -1$. The first two terms A_S are called "scalar part" and the last two A_V - "vector part". The properties of the imaginary units for RB are as follows:

$$\begin{gathered} i^2 = j^2 = -1 \quad k^2 = 1 \\ ij = ji = k \quad jk = kj = -i \quad ki = ki = -j\,. \end{gathered} \tag{4}$$

Two types conjugate of *A* can be defined – the vector conjugate:

$$A^+ = A_S - iA_V \tag{5}$$

and the complex conjugate:

$$A^* = A_s^* + iA_v^* = (A_1 - jA_2) + i(A_3 - jA_4)\,. \tag{6}$$

Applying Euler's formula for the complex exponential generalized to hypercomplex form any quaternion *q* may be represented in polar form as:

$$q = |q|e^{\mu\Phi}\,. \tag{7}$$

μ and Φ are referred as the eigenaxis and eigenangle of q, respectively. Φ is analogous to the argument of a complex number, but is unique only in the range $[0, \pi]$, because the value greater than π can be reduced to this range by reversing of eigenaxis. μ is a unit (pure) quaternion and identifies the direction in three-space of the hypercomplex number's vector part. The requirement for μ is $|\mu| = 1$.

Hereafter in this publication each coefficient and internal signal of hypercomplex digital filters will be encoded as a bicomplex number.

III. HYPERCOMPLEX SECTIONS DERIVATION PROCEDURE OUTLINE

If the variable z in a N-order real coefficients digital transfer function $H_R(z)$ is substituted by

$$z = ze^{-j\theta} = z(\cos\theta - j\sin\theta), \quad (8)$$

the complex coefficients transfer function $H_C(z) = H(e^{-j\theta})$ will be obtained. $H_C(z)$ may be easily presented by two $2N$-order real coefficients transfer functions:

$$H_C(\hat{z}) = H_{R1}(z) + jH_{R2}(z), \quad (9)$$

where "R" denotes real, "C" – complex and "$\hat{z}$" – complex variable.

If $H_R(z)$ is a low-pass (LP) type, $H_{R1}(z)$ and $H_{R2}(z)$ will be of band-pass (BP) type only, while high-pass (HP) $H_R(z)$ will produce band-stop (BS) type transfer functions as well. $\theta = \pi/2$ substituted in Eq. (8) brings to

$$z = -jz \quad (10)$$

and respectively $H_C(z) = H(-jz)$ will be complex transfer function called "orthogonal".

In this work the idea proposed by Okabayashi and Takahashi [7] is used in order to derive a first-order hypercomplex (bicomplex) orthogonal transfer function $H_{HC}(z)$ presented by fourth-order real coefficients transfer functions $H_1(z)$, $H_2(z)$, $H_3(z)$ and $H_4(z)$:

$$\begin{aligned} H_{HC}(z) &= H_1(z) + jH_2(z) + iH_3(z) + kH_4(z) = \\ &= H_{C1}(\hat{z}) + iH_{C2}(\hat{z}). \end{aligned} \quad (11)$$

Scalar part $H_{C1}(\hat{z})$ and vector part $H_{C2}(\hat{z})$ have complex coefficients and "HC" marks hypercomplex. The coefficients of $H_{HC}(z)$ are bicomplex numbers represented by Eq. (3).

If "j" is replaced by "i" in Eq. (9), bicomplex coefficients transfer function will be retrieved:

$$H_{HC}(z) = H_{R1}(z) + iH_{R2}(z), \quad (12)$$

but the coefficients of $H_{R1}(z)$ and $H_{R2}(z)$ will be still real because $H_{HC}(z)$ has coefficients whose scalar and vector components are with zero imaginary parts:

$$A = (A_1 + j0) + i(A_3 + j0) = A_1 + iA_3 \quad A_1, A_3 \in R. \quad (13)$$

This corresponds to the orthogonal transformation $z = -iz$ applied on real transfer function $H_R(z)$ and leads to the orthogonal bicomplex function Eq. (12).

Then, the complex frequency transformation according to j imaginary unit

$$z = \hat{z}e^{-j\theta} \quad (14)$$

is applied on $H_{R1}(z)$ and $H_{R2}(z)$ in order to get:

$$H_{HC}(\hat{z}) = H_{C1}(\hat{z}) + iH_{C2}(\hat{z}). \quad (15)$$

$H_{C1}(\hat{z})$ and $H_{C2}(\hat{z})$ have complex coefficients because now the imaginary parts of scalar and vector components are not zero:

$$A = (0 + jA_2) + i(0 + jA_4) = j(A_2 + iA_4) \quad A_2, A_4 \in R. \quad (16)$$

Orthogonal form of the frequency transformation Eq. (14)

$$z = \hat{z}e^{-j\frac{\pi}{2}}, \quad (17)$$

applied on $H_{R1}(z)$ and $H_{R2}(z)$, will make possible the presentation of $H_{C1}(\hat{z})$ and $H_{C2}(\hat{z})$ in the terms of real transfer functions:

$$\begin{aligned} H_{C1}(\hat{z}) &= H_1(z) + jH_2(z), \\ H_{C2}(\hat{z}) &= H_3(z) + jH_4(z). \end{aligned} \quad (18)$$

Thus the representation of a bicomplex orthogonal transfer function by four real transfer functions Eq. (11) is achieved.

IV. FIRST-ORDER ORTHOGONAL HYPERCOMPLEX FILTER SECTIONS DERIVATION

After intensive search among the most often used first-order LP filter sections it was found that MHNS-section (Fig.1a) is rather appropriate prototype having canonic number of elements. Its transfer function is:

$$H_R^{MHNS}(z) = \frac{1-\alpha}{2}\frac{1+z^{-1}}{1-\alpha z^{-1}}. \quad (19)$$

In [3] a method of circuit transformation is proposed permitting also to obtain orthogonal complex filters with canonic number of elements. Applying this method on the section in Fig.1a, the complex orthogonal structure from Fig.1b is obtained [5]. Having two inputs and two outputs as well, this section is able to realize four real coefficients transfer functions at its different outputs which are equal in couples as follows:

$$H_{R1}^{MHNS}(z) = H_{RR}(z) = H_{II}(z) = \frac{(1-\alpha)}{2} \cdot \frac{1-\alpha z^{-2}}{1+\alpha^2 z^{-2}}, \quad (20)$$

$$H_{R2}^{MHNS}(z) = H_{RI}(z) = -H_{IR}(z) = \frac{(1-\alpha^2)}{2} \cdot \frac{z^{-1}}{1+\alpha^2 z^{-2}}. \quad (21)$$

They are obtained after orthogonal transformation Eq. (10) is applied on Eq. (19) and all four are of BP type. They can be considered as real and imaginary parts respectively of the complex transfer function:

$$H_C^{MHNS}(z) = H_{R1}^{MHNS}(z) + jH_{R2}^{MHNS}(z). \quad (22)$$

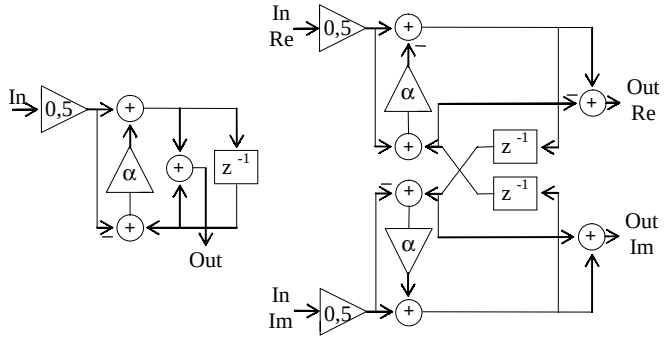

Fig.1. (a) First-order LP MHNS-prototype real sections; (b) MHNS-based orthogonal BP complex section

Similar transformation, producing orthogonal bicomplex filter structures with canonic number of elements, could easily be developed. Realization by real elements (multipliers, delays and additions) is expected to be rather complicated circuit having four inputs and the same number of outputs. Therefore sixteen fourth-order transfer functions will be carried out four by four equal with $\pm$ sign.

According to the above presented method we apply orthogonal frequency transformation Eq. (17) on $H_{R1}^{MHNS}(z)$ and $H_{R2}^{MHNS}(z)$. As a result the following orthogonal fourth-order real coefficients transfer functions are obtained:

$$H_1^{MHNS}(z) = \frac{1-\alpha}{2} \cdot \frac{1+\alpha^3 z^{-4}}{1-\alpha^4 z^{-4}}, \quad (23)$$

$$H_2^{MHNS}(z) = \frac{\alpha(1-\alpha^2)}{2} \cdot \frac{z^{-2}}{1-\alpha^4 z^{-4}}, \quad (24)$$

$$H_3^{MHNS}(z) = \frac{\alpha^2(\alpha^2-1)}{2} \cdot \frac{z^{-3}}{1-\alpha^4 z^{-4}}, \quad (25)$$

$$H_4^{MHNS}(z) = \frac{\alpha^2-1}{2} \cdot \frac{z^{-1}}{1-\alpha^4 z^{-4}}. \quad (26)$$

They form the bicomplex transfer function $H_{HC}^{MHNS}(z)$.

It was shown in [5] that in the case of narrow-band LP filter (pole near z=1) the MHNS-structure (Fig. 1a) has very high coefficients sensitivity. Using Nishihara's method [4] of sensitivity minimization through coefficient conversion, the section shown in Fig.2a and named LS11 is derived. Its transfer function is:

$$H_R^{LS11}(z) = \frac{\beta}{2} \frac{1+z^{-1}}{1-(1-\beta)z^{-1}}. \quad (27)$$

Following the procedure applied on the MHNS-section, we derive the complex structure in Fig.2b with real coefficients transfer functions:

$$H_{R1}^{LS11}(z) = H_{RR}(z) = H_{II}(z) = \frac{\beta}{2} \cdot \frac{1-(1-\beta)z^{-2}}{1+(1-\beta)^2 z^{-2}}, \quad (28)$$

$$H_{R2}^{LS11}(z) = H_{RI}(z) = -H_{IR}(z) = \frac{\beta}{2} \cdot \frac{(2-\beta)z^{-1}}{1+(1-\beta)^2 z^{-2}}, \quad (29)$$

being parts of the orthogonal complex transfer function.

The orthogonal bicomplex transfer function's real parts are

$$H_1^{LS11}(z) = \frac{\beta}{2} \cdot \frac{1+(1-\beta)^3 z^{-4}}{1-(1-\beta)^4 z^{-4}}, \quad (30)$$

$$H_2^{LS11}(z) = \frac{(1-\beta)\left[1-(1-\beta)^2\right]}{2} \cdot \frac{z^{-2}}{1-(1-\beta)^4 z^{-4}}, \quad (31)$$

$$H_3^{LS11}(z) = \frac{(1-\beta)^2\left[(1-\beta)^2-1\right]}{2} \cdot \frac{z^{-3}}{1-(1-\beta)^4 z^{-4}}, \quad (32)$$

$$H_4^{LS11}(z) = \frac{(1-\beta)^2-1}{2} \cdot \frac{z^{-1}}{1-(1-\beta)^4 z^{-4}}. \quad (33)$$

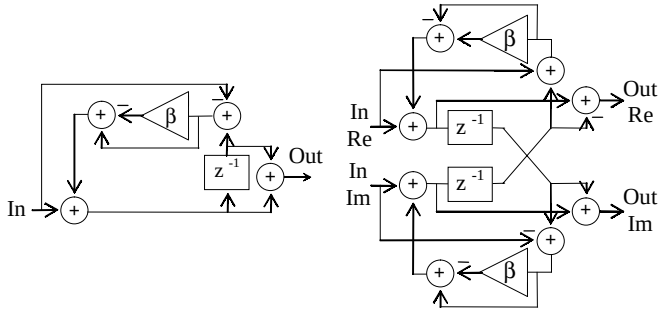

Fig.2. (a) First-order LP LS11-prototype real sections; (b) LS11-based orthogonal BP complex section

V. SENSITIVITY INVESTIGATIONS

In this section the coefficients sensitivity of all three type (real, complex and bicomplex) filter sections will be investigated. The case of narrow-band orthogonal filter which is the most likely in practice is achieved for α=0.99 (β=0.01). Canonic sign-digit (SD) code representation and fixed point arithmetic were used and the word-length was changed from infinite (ideal case) to 2 bits only.

Under this conditions the real prototype-sections (Fig.1a and 2a) have been investigated. We have shown [5], [6] that coefficients sensitivity of LS11 LP first-order filter section is about hundred times lower that this of MHNS-section. It was shown also that the low-sensitivity properties of the LP-prototype circuits are directly

inherited in the complex coefficients orthogonal structures.

In order to verify the reported results a number of computer simulation were conducted with respect to the bicomplex filter sections, derived in this publication. All eight transfer functions (23)-(26) for MHNS-based and (30)-(33) for LS11-based section were simulated for the same pole disposition near the unit circle. Poles $p_{1,2} = \pm 0{,}99$ and $p_{3,4} = \pm j0{,}99$ are achieved for $\alpha = 0{,}99$ (MHNS-based) and $\beta = 0{,}01$ (LS11-based) structures. In Fig.3a and 3b some of the results concerning $|H_1|$ and $|H_3|$ of the MHNS- and the LS11-based structures are shown for different coefficient word-lengths. It is seen that the LS11-structure has a magnitude response almost coinciding with the ideal one even when the word-length is reduced to 2 bits only. The MHNS-based structure response (Fig. 3b) is considerably changed when the word-length is only limited to 3 bits. The similar results were obtained also for $|H_2|$ and $|H_4|$.

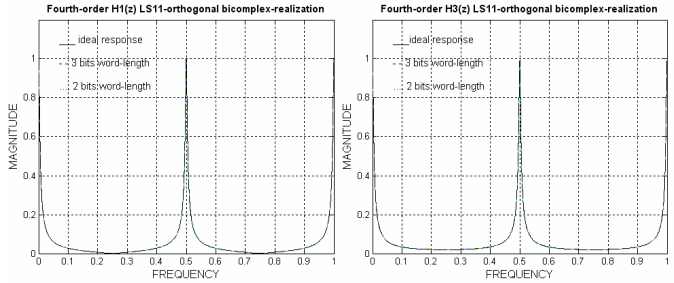

(a)

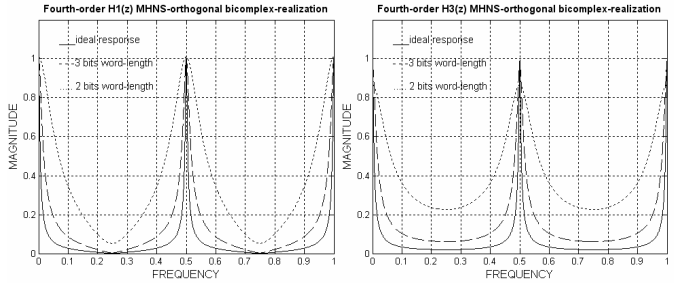

(b)

Fig. 3. Magnitude responses of the first-order bicomplex orthogonal sections for different word-lengths: (a) LS11-based for β=0.01; (b) MHNS-based for α=0.99

VI. Conclusions

A method for design of hypercomplex (bicomplex) coefficients first-order orthogonal filter sections was proposed in this publication. Second-order BP real coefficients transfer functions, composing a first-order complex function, were transformed into fourth-order real coefficients transfer functions after orthogonal frequency transformation. The first-order bicomplex transfer function can be presented by them which reduce four times the order in comparison with the real one.

As narrow-band orthogonal filters are most often used, the developed transfer functions were investigated on these terms for different word-length of the coefficients.

It was experimentally demonstrated that the magnitude response of the LS11 low sensitivity hypercomplex section does not change considerably even when two bits of SD-code is used, while the magnitude response of MHNS-structure is completely destroyed when the word-length is reduced to three bits. These properties, including sensitivity of the LP-prototype structures will be inherited by the new bicomplex structures. Many new sections can be derived and investigated following the proposed approach.

The presented method for design of hypercomplex sections is also appropriate for second-order filter section's derivation which will permit cascade filter realizations.

The new hypercomplex structures are suitable for realization of high quality narrow-band orthogonal filters. Additionally, the possibility for simplification of the circuits and further parallelism will make them very attractive for telecommunications and other DSP applications and will ensure a considerable reduction of the complexity and the cost of the equipment.

References

[1] I.L. Kantor and A.S. Solodovnikov. "*Hupecomplex numbers: An elementary introduction to algebras*", Springer Verag, 1989.

[2] H.D. Schutte and J. Wenzel. "Hypercomplex Numbers in Digital Signal Processing", Proc. IEEE Singapore Int. Symp. Circuits and Systems, pp.1557-1560, 1990.

[3] E. Watanabe and A. Nishihara, "A Synthesis of a Class of Complex Digital Filters Based on Circuitry Transformations". IEICE Trans., vol. E-74, No.11, pp.3622-3624, Nov. 1991.

[4] A. Nishihara and Y. Moriyama, "Minimization of Sensitivities in Digital Filters by Coefficient Conversion". Electronics and Communications in Japan, vol.68, No8, pp.7-14, 1980.

[5] G. Stoyanov, M. Kawamata and Zl. Valkova, "Very Low Sensitivity Complex Coefficients Bandpass Filter Sections", Technical Report of IEICE, Sc. Meeting on Digital Signal Processing, Tokyo, Japan, vol.96, No.424, (Rep. DSP96-103), pp. 39-45, Dec. 13, 1996.

[6] G.Stoyanov, M. Kavamata, Zl. Valkova. "New First and Second-order Very Low-sensitivity Bandpass/bandstop Complex Digital Filter Sections", Proc. IEEE 1997 Region 10th Annual Conf. "TENCON'97", Brisbane, Australia, vol.1, pp.61-64, Dec. 2-4, 1997.

[7] K. Okabayashi and S. Takahashi, "Reference Networks for Simultaneous Realization of Complex IIR Digital Filters", IEEE Pacific Rim Conference on Communications, Computer and Signal Processing, vol.1, pp.165-168, Rim, Italy, 1997.

[8] H. Toyoshima, "Computationally Efficient Implementation of Hypercomplex Digital Filters", IEICE Trans. Fundamentals, Vol.E85-A, No.8, pp. 1870-1876, August 2002.

[9] V.S.Dimitrov, T.V.Cooklev and B.D.Donevsky, "On the Multiplication of Reduced Biquaternion and Applications". Infor. Process. Lett., vol.43, No.3, pp.161-164, 1992.

[10] S.J.Sangwine and T.A.Ell, "Color Image Filters Based on Hypercomplex Convolution", IEEE Proc.-Vis. Image Signal Process., Vol.147, No.2, pp. 89-93, April 2000.

Optimization of output spectrum of direct digital synthesizers for application in hybrid frequency synthesizers

Ognian I.Petkov

Abstract- **Investigation of the output spectrum of direct digital synthesizers for best performance in hybrid DDS and PLL synthesizers. Optimization of the connection between the output of the DDS and the output filter for best impedance matching.**

Keywords- **Direct Digital Synthesizers, noise, spurious and alias frequencies, output filters impedance matching.**

I. INTRODUCTION

Direct Digital Frequency Synthesis (DDFS) becomes a very popular technique for generating frequencies whenever very precise frequency resolution and fast frequency switching is needed. The most common DDFS architecture includes a periodically overflowed phase accumulator, for generating and storing phase information and uses a ROM based look up table to compute the sine function. The digitally generated sine from the ROM is next passed to a digital to analog converter (DAC) where it is converted to a pulsed analog form and finally this form is filtered by a low pass filter. The frequency of the generated sine wave is controlled by the Frequency Control Word (FCW). The output frequency could be defined from Eq. (1):

$$f_{out} = FCW \frac{f_{clk}}{2^j} \quad (1)$$

Where f_{out} is the synthesized frequency, f_{clk} is the clock frequency and "j "is the word length of the phase accumulator. The spectral density of the generated signal could be expressed with the help of the formulae, given in Eq. (2):

$$S(f) = e^{-j\pi f/f_{clk}} \frac{\sin(\pi f/f_{clc})}{\pi f/f_{clc}} \sum_{n=-\infty}^{\infty} \sum_{m=-\infty}^{\infty} c_m \sigma(f - nf_{clk} - mf_{out}) \quad (2)$$

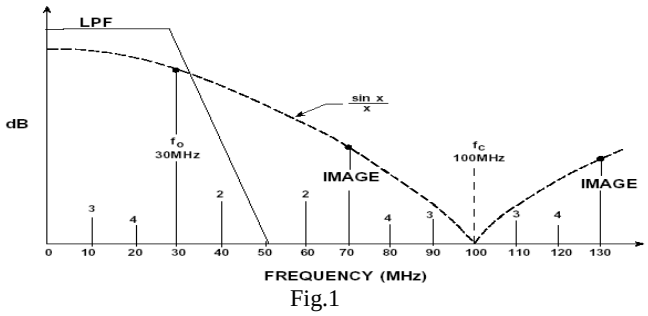

Fig.1

Ognian I. Petkov is with the Faculty of Electronics, Technical University - Varna, Studentska 1, 9010 Varna, Bulgaria, E-mail : oipbg@yahoo.com

As can be seen from Fig.1 the DDFS causes all frequency components residing in the generated signal to be aliased about every harmonic of the clock frequency fclk. If the output is a perfect sine wave, then the spectrum contains the frequencies $nf_{clk} \pm f_{out}$. The component, corresponding to n=0 is the desired sine wave and the others are the images or alias frequencies. It is of great importance to define the location and the amplitudes of the spurious components in the output spectrum. In many hybrid synthesizers the quality of the output signal depends to a great degree from the appropriate choice of the clearest part of the spectrum of the DDS.

For many applications, the DDS solutions have distinct advantages over the equivalent frequency synthesizers, employing PLL circuitry. These advantages could be used more completely if we know the real nature of the synthesized output sine wave in DDS. One important subject is the generation of spurious spectrum lines and the noise at the output of the DDS and the appropriate measures for diminishing their influence on the purity of the output spectrum.

In this paper the sources of the noise and spurious frequencies will be analyzed and the influence of the output impedance matching between the output of the DDS and the antialias filter on the quality of the generated signal will be discussed.

II. NOISE AND SPURIOUS SOURCES IN DDS

As we have seen before, the most dangerous and difficult to handle are the spurious frequencies, arising from the digital nature of the generated signal. But the output spectrum contains additional spurious frequencies and wideband noise, which had to be taken in consideration. The most important of them are:

1. Spurious lines and noise due to the truncation of the phase accumulator bits addressing the sine ROM.
2. Noise due to the distortion from the compression of the sine ROM.
3. Errors, due to the limited precision of the samples, stored in the ROM.
4. Noise from the nonlinearities in the digital to analog conversion.

We need to know the carrier to noise (C/N) ratio for every one of these noise and spurious sources. From [2] it is calculated that the worst case C/N caused from the truncation of the least significant bits in the phase accumulator is from Eq. (3):

$$C_t/N \approx 6.02\,K - 3.92 \quad \text{dBc} \qquad (3)$$

where k is the number of most significant bits of the phase accumulator, used for programming the ROM table.

The finite character of the quantization in the sine ROM values also leads to the output DDFS spectrum impairments. The carrier to noise ratio for this case could be calculated from Eq. (4):

$$C_q/N \approx 6.02\,m + 1.76 \quad \text{dBc} \qquad (4)$$

III. OUTPUT SPECTRUM OPTIMIZATION

A program was created in MATLAB in which all of the factors were taken in consideration. With the help of this program it is possible to choose the frequency range where the spurious frequencies have lowest values and this range could be used for reference frequency in a hybrid PLL plus DDS synthesizers. Graphical results are shown for two different frequencies for a direct digital synthesizer with accumulator length of 32 bits, 21 truncated bits and 12 bits for the ROM. The clock frequency of the DDS is 12.8 MHz.

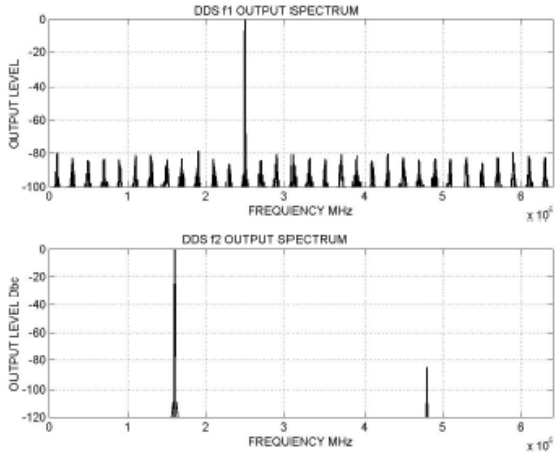

Fig.2

In high speed and high resolution (>10 bits,>50 MHz) DDFS most of the spurs are generated from the analog errors in the DAC. In the advanced high speed DDFS the DAC is the most critical component. The anomalies in the output spectrum, caused by the DAC do not follow the sin(x)/x roll off response.

The carrier to noise ratio on the output of the DAC could be defined from the well known formulae in Eq. (5):

$$C_n/N \approx 6.02\,n + 1.8 \quad \text{dBc} \qquad (5)$$

where "n" is the number of bits in the DAC. In almost every state of the art DDS the number of bits after truncation in the phase accumulator is big enough in comparison with the bits in the DAC, so here one can assume that the main source of wideband noise at the output of the DDS is the quantizing noise of the DAC, which can be well predicted. For an example if we take the AD9854, which has 48 bits phase accumulator, 17 bits after truncation and 12 bits DAC the C/N from the truncation can be calculated and is more than 102dB and the C/N from the DAC in this case is 72 dB.

Another important consideration is that, unlike a PLL-based system, the higher order harmonics of the fundamental output frequency will fold back into the baseband, because of aliasing. These harmonics cannot be removed by the antialiasing filter as shown in fig.1. For instance if the clock frequency is 100 MHz and the output frequency is 30 MHz the second harmonic of the 30 MHz signal appears at 60 MHz out of band but also at 100 – 60 =40 MHz, and the fourth at 120 – 100 = 20 MHz. Higher order harmonics products also fall within the Nyquist bandwidth.

The nonlinear process in the DAC is generating harmonically related spurs in the output spectrum. The amplitude of the spurs is difficult to predict, but the location of the spurs is harmonically related to the output frequency of the synthesizer. A detailed analysis could be done for every particular DAC. At this stage of the development of the direct digital synthesis it could be seen that only the lack of high frequency and linear DACs is that stops their more intense application in the frequency bands for portable and computer wireless communications. The comparatively high level of wideband noise and the presence of alias and image frequencies prevents their applications in precise measurment equipment. On fig.3 the output spectrum of the synthesizer after the DAC for two frequencies is shown. Clear degradation of the spectrum can be seen for the two frequencies.

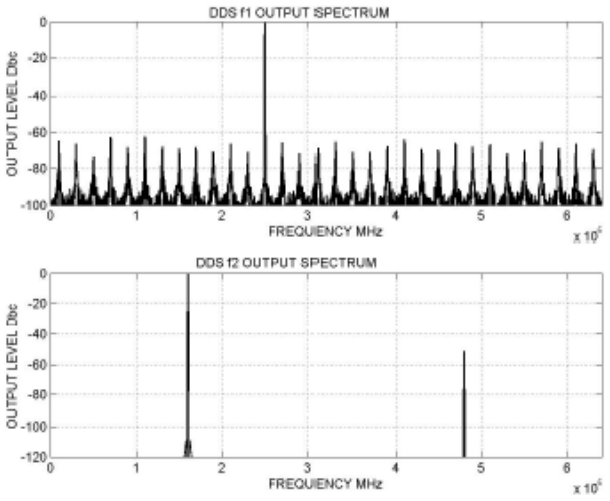

fig.3

If we summarize the analysis we can make the conclusion that the main sources of spurious frequencies and noise at the DDS output are the digital nature of the signal at the output and the quantizing and nonlinearities noise from the DAC.

IV. OUTPUT INTERFACE CONSIDERATION

High speed DDS IC's with integrated DAC's provide an output current witch can be pumped into any resistive load as long as voltage, developed at the DAC output does not exceed the maximum level. Normally the outputs are terminated to ground through a resistor as shown in fig.4.

For example the AD 985X family DDS will source current into a load, according to the equation: Iout= 39.93/Rset. The DDS/DAC output resistance specification is the combined impedance of the CMOS devises that comprise the switches and the current source circuitry. The DAC output resistance is very high and can be ignored in our calculations. Another important feature of the mentioned DDS is that the output current is unipolar and if the terminating resistor is connected to the ground the voltage will vary from zero to some positive value. This causes that the output sine wave will be DC offset from the load termination potential by one half of the full-scale voltage. This may be an important consideration when applying this signal to a dc coupled amplifier.

One solution to this problem is if we use the two outputs of the DAC witch are 180 degrees out of phase**.** These two signals can be combined in a center-tapped RF transformer to produce a symmetrical output waveform as shown in fig.4. When combining these two complementary currents in a transformer the dc offset is lost and the signal can be easily filtered and amplified. The low impedance way to ground through the transformer center tap is better than taking the reactive pathway through a LC filter that is terminated only at the filter output.

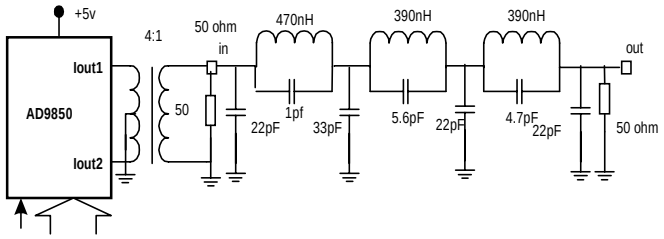

fig.4

Without a transformer, the next best method is to apply the DAC current output to a LC filter that is doubly-terminated, as shown in fig.5.

Regardless of what output termination scheme is chosen, experience has shown that optimum spurious and harmonic suppression are achieved when both Iout1 and Iout2 outputs are terminated equally. This is very important at higher output frequencies, where every dB of SFDR (spurious-free dynamic range) counts and this practice will give a cleaner output spectrum, lower spurs and higher SFDR. This practice is especially applicable to situations where only one of the outputs is utilized**.**

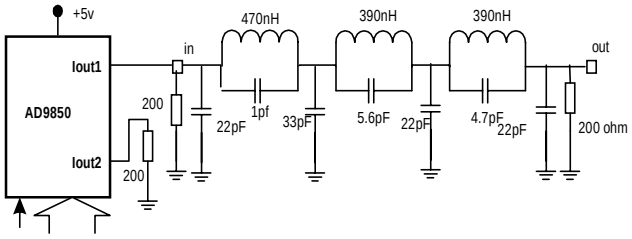

fig.5

V. FILTER DESIGN CONSIDERATIONS

For every particular application of the DDS these spurious frequencies have to be minimized to levels that are compatible with the spectrums of the other frequency sources. In almost every DDS this is accomplished from the low pass filter after the DAC. The frequency response of an ideal low pass filter would be 1 over the Nyquist band $(0 \leq f \leq Fs/2)$ and 0 elsewhere. Such a filter is not physically realizable and this results in the sacrifice of some portion of the available output bandwidth in order to match the no ideal response of the antialias filter.

The parameters of the output filters are very important for the overall performance of the DDS and the requirements they have to met define the purity of the synthesized signal.

The proper choice of the filter is connected with the reaching of some compromise between the contradictionary requirements for the great steepness of the transitional part of the frequency response of the filter and the flatness of the group delay time characteristic, which is needed for digital communication systems.

For a proper choice of a filter we need to define the different applications of the DDS and we can divide the applications in three types:

Direct digital synthesizers used individually or as a part of hybrid synthesizer where the whole possible frequency band has to be utilized.

DDS, used for a reference oscillators for hybrid DDS-PLL combination, where the only a part of the possible band of DDS is used and no need for wide band digital modulation.

DDS for a relatively narrow frequency band in mixer type hybrid synthesizers where wide band digital modulations have to be implemented.

Every one of these types has a need from particularly designed low pass filter. The most serious demands are for the first application where the aim for achieving a wider bandwidth leads to reaches to the Nyquist limit of fclk/2 in which case the first image fclk-fout is getting closer to fout and it becomes impossible to separate these two frequencies with the known filter approximations.

An important parameter of the filter is the group delay time or GDT, which is the first derivation of the phase and is a measure for the delay of different frequencies, when passing through the filter. GDT could be comparatively easily measured and used for criteria for the time domain characteristics of the filter.

There are lot types of filters known from the theory [3] and practice but the most popular are Butterworth, Chebyshev and Kauer (elliptic) approximations.

On the basis of these analysis and consideration a program in MATLAB [4] was designed where the input parameters are the $(f_{clk}\text{-}f_{out}/f_{out})\text{-}\Omega$ ratio, the ripple in the passband and the minimal attenuation in the stopband. The definition of the limits for all these parameters depends exclusively on the specific application of the synthesizer but for the start a ripple of 1dB, Ω of 1,2 and attenuation of 60dB and 80dB were chosen. A filter for cut off frequency of 100 MHz designed with this program is connected to the output of the DAC as shown in fig.5.

When the requirements to the purity of the output spectrum of the signal of DDS are more stringent there is a possibility for further improvements with the use of tunable or bandpass filters.

VI. CONCLUSION

In this paper an analysis of the output spectrum of the DDS is done with respect to their application in the hybrid frequency synthesizers.

Three ways of optimization were analyzed and proposed in this paper:

First an optimal choice of a frequency band is done for minimal parasitic lines in the output spectrum.

Second the choice of optimal matching network for the output of the DAC is analyzed and experimented.

Third the choice of the output antialiased filter is discussed in respect of optimal filtering and matching of the DDS output.

Two programs in MATLAB are made for the investigation of the most appropriate output frequency range for reference clock applications. Solutions for best interface between the output of the DDS and the antialias filter are proposed.

REFERENCES

[1] A.V. Oppenhaim, and R.W. Schafer, "*Digital Signal* Processing", Prentice Hall Englewood Cliffs, New Jersey, 1975.

[2] Y .C. Jeng ,"*Digital Spectra of Nonuniformly Sampled Signals – Digital Look- Up Tunable Sinusoidal Oscillators*," IEEE Trans. On ins. And Meas., Vol. 37, No.3,pp 358- 362, Sept. 1988.

[3] G. Stojanov, *Theoretical Foundations of telecommunication technics,* Sofia , Technica, 1993.

[4] O. Petkov, *"Optimization of parameters of output filters for direct digital synthesizers"*, ICEST 2003, pp 47-49, Oct. 2003 .

Design and Study of Digital FIR Filters

Pesha D. Petrova[1] , Boyan D. Karapenev[2]

Abstract **- An algorithm for the design of digital FIR filters by using DSP TMS320C5x and MATLAB program package has been developed. A program code for DSP control has been created. Low-pass filter, High-pass filter, Band-pass filter and Band-stop filter of various orders at various sample frequencies have been designed. Amplitude frequency responses from the study and simulation of the designed variants have been presented. The results allow the correct register adjustment of the analog interface of DSP. They indisputably support the correctness of the algorithm proposed.**

Keywords **– FIR filters, DSP, amplitude frequency response, MATLAB**

I. INTRODUCTION

It is known [1], [2] that the output signal *y(n)* of FIR filters at a certain moment *n* is a function of the input signal *x(n)* at this moment and of its previous values *x(n-i).* A mathematical representation in direct form of a FIR filter is given as

$$y(n) = F\big((x(n), x(n-1),..., x(n-M)\big), \qquad (1)$$

where M determines the filter order and *n =0, 1, …., N-1 (N* - the number of samples).

For constant parameter linear filters the functional relation is set by a linear combination of input samples *x(n-i)* by coefficients of proportionality b_i , $i = 0,....,M$. Where at

$$y(n) = b_0 x(n) + b_1 x(n-1) + ... + b_M (x-M) = \sum_{i=0}^{M} b_i x(n-i) \qquad (2)$$

is obtained.

This equation is the result from the vector inner product between the filter coefficient vector *b* and the order-reversed input data vector *x*.

The same equation is presented graphically in Fig.1.

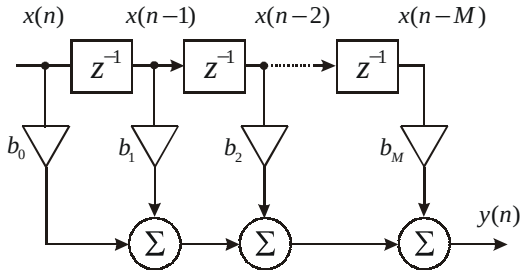

Fig. 1. Direct-form FIR.

[1]Pesha D. Petrova is with the Department of Communication Equipment and Technologies, Technical University of Gabrovo, 5300 Gabrovo, 4, Hadji Dimitar St.,Bulgaria, E-mail: daneva@tugab.bg

[2]Boyan D. Karapenev is with the Department of Communication Equipment and Technologies, Technical University of Gabrovo, 5300 Gabrovo, 4, Hadji Dimitar St.,Bulgaria, E-mail: bkarapenev@tugab.bg

The design and study of FIR filters is reduced to determining b_i coefficients by defined parameters and filter type [3], block diagram synthesis, visualization and analysis of functional characteristics and parameters.

These problems can be solved successfully by suitable software and digital signal processors (DSP).

II. DESIGN AND STUDY OF FIR FILTERS

The MATLAB [4] – DSP medium is particularly suitable for the design and study of FIR filters. The principal stages in the design-study process of FIR filters by MATLAB and DSP TMS320C5x [5] are represented in the block diagram in Fig.2.

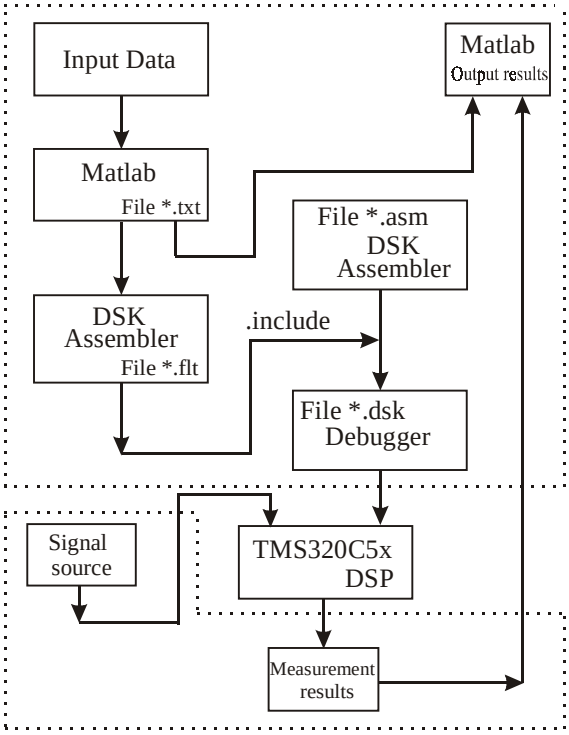

Fig. 2. Block diagram of FIR filters design-study process.

The procedure of filter synthesis and analysis is reduced to:

1. Calculating the filter coefficients

The coefficients of the filter designed are calculated, scaled and recorded in a text file *.txt by MATLAB file which contains the following input data:

- filter type: low-pass filter, high-pass filter, band-pass filter, band-stop filter;
- filter order;
- sampling frequency;
- cut-off frequency.

2. Creating a file *.flt

The coefficients from *.txt file are recorded in *.flt file by means of the directives .set and .word. Since delay circuits are also needed for the design of FIR filter, then information about them is entered in *.flt file by the directive .word.

3. Creating a file *.asm

This file contains the major source code of the digital filtration program. The adjustments of registers of the analog integrated circuit (AIC) are contents of great importance while creating the file. They can be set by the DSP program in order to adjust the sampling frequency of the AIC as well as the cut-off frequencies in several built – in filters. TA and TB are necessary for transmitting data to the AIC (D/A converting) whilst RA and RB are used for receiving data (A/D converting). Thus, there can have different sampling frequencies for either direction. Each mentioned register works in conjunction with a counter, which is loaded with the value hold in the corresponding register. The counters are decremented each clock cycle and generate an interrupt if zero is reached. They are then reloaded with the register value again. There are two counters for each direction because two frequencies have to be set – the sampling frequency and the switched capacitor frequency which controls the several band-pass and low-pass filters. The input band-pass filters can be switched off by the software and are not used by default. The output filter however is always active, thus, has to be taken in consideration. It is a low-pass filter that cuts - off frequencies above a special threshold. The A registers (TA or RA) define this threshold. The switched capacitor frequency f_{SCF} can be expressed by

$$f_{SCF} = \frac{f_{MCLK}}{2counter_A} \tag{3}$$

where f_{MCLK} is the frequency produced by the DSP timer, i.e. Master Clock Frequency. It is usually 10 MHz and $counter_A$ is defined by TA or RA.

The cut-off frequency of output filter can be expressed by

$$f_{cut-off} = \frac{f_{SCF}\,3700}{288000}. \tag{4}$$

To adjust the sampling rate it has to set the B registers accordingly. The sample rate should be double the cut-off frequency if frequencies in this range are expected. So

$$f_s = \frac{f_{SCE}}{counter_B} = \frac{f_{MCLK}}{2counter_A.counter_B} \tag{5}$$

where $counter_B$ is defined by TB or RB.

RA and TA (and RB and TB) should have equal values in order to get predictable results because TA/TB control the output sampling frequency but RA/RB however clock the algorithm which generates the desired output waveform. Thus, they have a direct relationship.

4. Creating a file *.dsk

By the command

dsk5a [filename] [options]

a file *.dsk is created by means of which DSP is controlled and the desired digital filter is realized. The files *.asm and *.flt are linked by the directive .include.

5. Experimenting the designed FIR filters

Before starting the loaded *.dsk file, a constant amplitude signal is sent from a source signal to DSP. When the program code is correct the type of filter, fixed by the code, is designed. The output signal amplitude for various frequencies is measured and it is useful to display its wave, which is a criterion of the correctness of the scaling coefficients. The latter are corrected if required.

6. Processing of results

In the procedure of design and study of filters it has been made possible the theoretical and experimental results to be processed by MATLAB. To this purpose a data file is formed about the measured amplitude-frequency response and the coefficients recorded in *.txt file by which the filter amplitude-frequency response is simulated. The real and simulated characteristics are visualized in a general system of coordinates. The summarized file from Fig.3 performs the overall data processing.

```
%************************************************
%Amplitude Frequency Responses of FIR Filters
%************************************************
%Calculate the FIR filter coefficients
b = fir1(M, w_n, 'ftype');
c = round(b*2^k);  %k is the scaling factor
%************************************************
%Create a formatted data file
fid = fopen(filename.txt, 'w');
fprint(fid, '%d\n', c);
fclose(fid);
%************************************************
%Simulate the FIR filter amplitude-frequency response
[h,w] = freqz(b, 1, n); m = abs(h);
%************************************************
%Generate vectors containing measured data
f = [];  %frequencies
m1 = [];  %amplitudes
%************************************************
%Visualization of real and simulated frequency responses
plot(f, m1,'k--', m,'k');
%************************************************
```

Fig.3. Summarized MATLAB file for simulation and visualization of real and simulated frequency response of FIR filters.

In order to estimate the results promptly and make a proper choice of parameters and adjustment when designing digital filters with defined parameters, in addition to MATLAB, we recommend processing of the experimental data by EXCEL as well.

III. Experimental and Simulated Results

To estimate the presented approach, low-pass, high-pass, band-pass and band-stop FIR filters of various order for various sampling frequencies have been designed and studied. The design is based on DSP TMS320C5x and a suitable program code created. In compliance with Eqs. (3), (4) and (5)

and the recommendations in [6], [7] Table I shows variants of parameter values necessary for the development of the filters.

TABLE I
VALUES OF TA/RA, TB/RB, FS AND SNR

TA/RA	TB/RB	F_S, kHz	SNR, dB
10	50	10.000	80
16	31	10.081	60
5	50	20.000	67
8	31	20.161	78
4	26	48.077	60

The information from Table I is represented graphically in Fig.4.

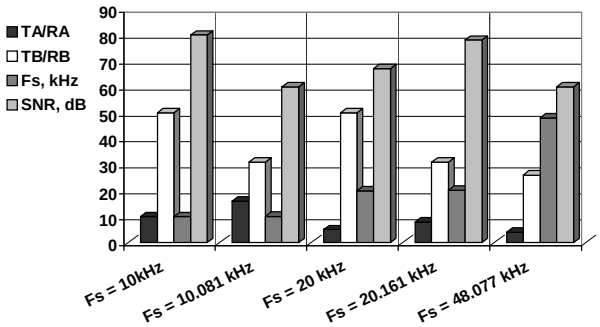

Fig.4. Relations between TA/RA, TB/RB, Fs and SNR.

The graphic representation shows indisputably that the values of registers TA/RA and TB/RB, which determine the sampling frequency, depend substantially on the signal/noise ratio. This fact has to be taken into account when adjusting the registers in the process of design of digital filters.

The simulation and experimental results of designing FIR filters of 85th order are given below.

For each of the 4 types of filters (low-pass, high-pass, band-pass and band-stop) the measurement data are processed by MATLAB and by EXCEL.

Fig. 5, Fig. 6, Fig. 7 and Fig. 8 show the experimentally obtained and simulated by MATLAB amplitude frequency response, respectively for low-pass filter, high-pass filter, band-pass filter and band-stop filter at sampling frequency of Fs=10.081 kHz.

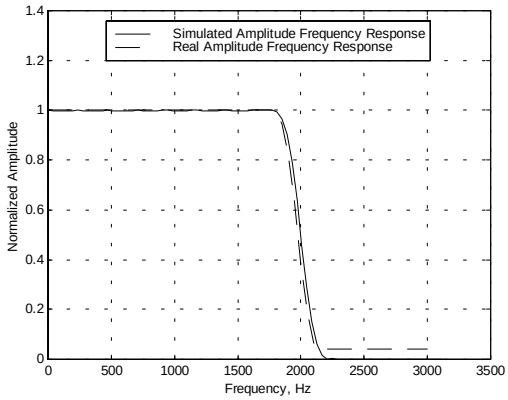

Fig. 5. Measured and simulated amplitude frequency responses for low-pass filter.

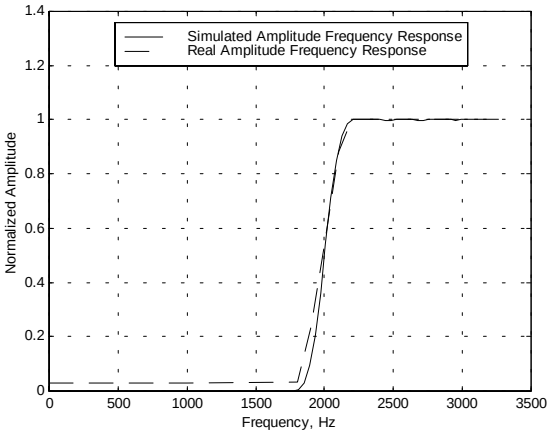

Fig. 6. Measured and simulated amplitude frequency responses for high-pass filter.

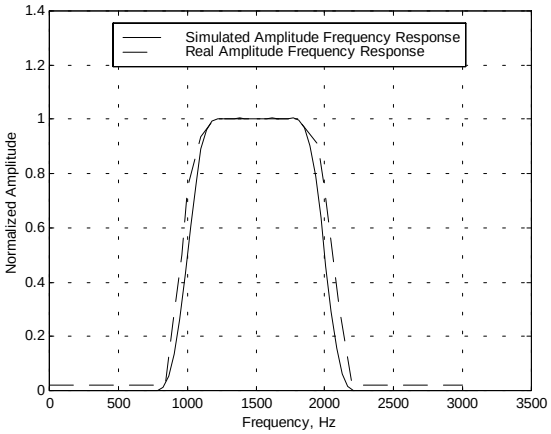

Fig. 7. Measured and simulated amplitude frequency responses for

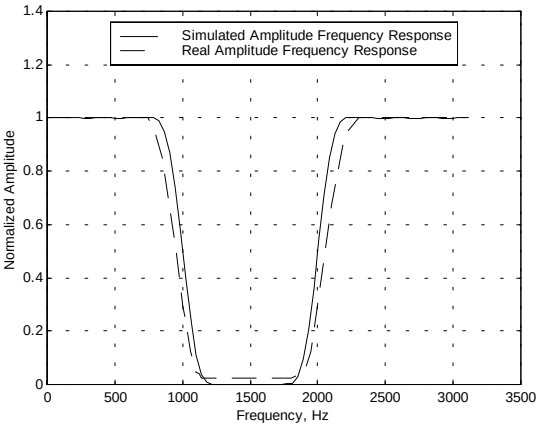

Fig. 8. Measured and simulated amplitude frequency responses for band-stop filter.

As it is seen in the figures, the simulated and real characteristics are very close. From the obtained amplitude frequency response of the designed filters at various sampling frequencies, the cut-off frequencies are determined and the summarized results from the various types of filters are illustrated in Fig.9 (low-pass filter and high-pass filter), Fig.10 (band-pass filter) and Fig.11 (band-stop filter). From the

diagrams in Fig.9 it follows that with increasing the sampling frequency for low-pass filter and high-pass filter the cut-off frequency increases, i.e. the slope of amplitude frequency response decreases. For band-pass filter (Fig.10) and band-stop filter (Fig.11) when the sampling frequency increases, besides the increase in cut-off frequencies, the pass-band width of the respective filter varies and this variation is proportional to the sampling frequency.

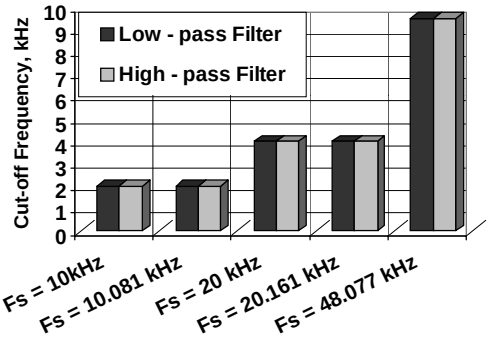

Fig. 9. Dependence of cut-off frequencies of low-pass filter and high-pass filter on sampling frequency.

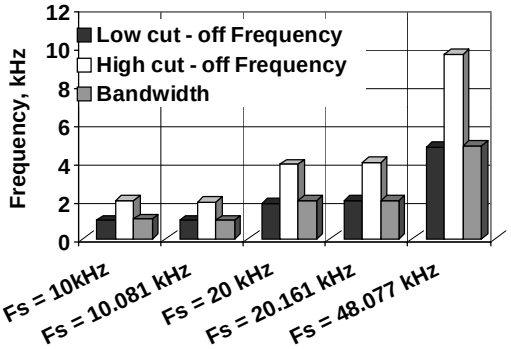

Fig. 10. Dependence of cut-off frequencies and bandwidth of band-pass filter on sampling frequency.

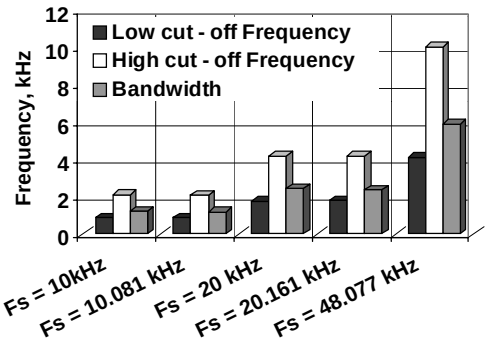

Fig. 11. Dependence of cut-off frequencies and bandwidth of band-stop filter on sampling frequency.

IV. CONCLUSION

An algorithm for the design and study of digital FIR filters by using DSP TMS320C5x and MATLAB and EXCEL software has been proposed. A program code for DSP control in designing various types of filters has been created. Frequency characteristics and parameters for low-pass filter, high-pass filter, band-pass filter and band-stop filter at various requirements to them, have been obtained by experiments and simulations. The experimental and simulated outcomes support the efficiency and correctness of the proposed approach to design and study of digital FIR filters.

REFERENCES

[1] J. Smith, “Introduction to Digital Filters”, Stanford University, California, 2003.

[2] R. Hamming, “Digital Filters”, Dover Publications, Inc, Canada, 1989.

[3] D. Schlichtharle, “Digital Filters: Basics and Design”, Springer Verlag, 2000, ISBN 3540668411.

[4] MATLAB User’s Guide, MathWorks Inc., 2002.

[5] TMS320C5x User’s Guide, Texas Instruments Inc., 1997.

[6] S. Smith, “Digital Signal Processing: A Practical Guide for Engineers and Scientists”, Publisher: Newnes, 2002, ISBN 075067444X.

[7] T. Heinrich, “DSP Starter Kit and Filter programming”, 2002.

Neural modeling of speech coding prediction

Sn.Pleshkova- Bekjarska [1] M.Momtchedjikov[2]

Abstract: **The neural networks are used in many applications as picture processing, computer vision, control system, signal processing etc. It is possible to use the neural networks for speech recognition. The goal of this article is to use the neural networks modeling in speech coding prediction.**

Keywords: **speech, speech coding, speech prediction, neural networks, predictive neural networks.**

I. INTRODUCTION

There are two general methods for using neural networks in speech coding: direct and hybrid. In the first case speech signal is applied to neural networks and it is supposed that the neural networks whole coding algorithm after an effective learning [1, 2]. In this case it is possible to achieve a compression of speech information if the numbers of neural network outputs are less than the inputs in a speech frame. The advantages of these methods are that the coding depends only from neural networks structure and his performances. The disadvantages are that it is not possible to use the specific characteristics of speech signals (sample frequency, pitch, voiced/unvoiced separation etc.).

These advantages are not present in the second group of hybrid methods, in which it is used the classical speech coding algorithms (LPC, CELP etc.), but some (or all) of the parts of these algorithms are modeling with a suitable neural network structure. The advantages in these cases are that it is possible to use the specific characteristics of speech signals. The disadvantages are the more complex and not regular structure of speech coders and decoders.

The goal of this article is to apply the second hybrid method for speech coding prediction, which is a part of many classical speech coding methods (LPC, CELP, FS-1016 etc.).

[1]Sn.Pleshkova is with the Faculty of Communications and Communications Technologies, Technical University, Kliment Ohridski 8, 1000 Sofia, Bulgaria,
E-mail: snegpl@tu-sofia.bg.
[2]M.Momchedjikov is with the Faculty of Communications and Communications Technologies, Technical University, Kliment Ohridski 8, 1000 Sofia, Bulgaria,
E-mail: snegpl@tu-sofia.bg.

II. NEURAL NETWORK STRUCTURE

The proposed neural networks structure is shown in Figure 1.

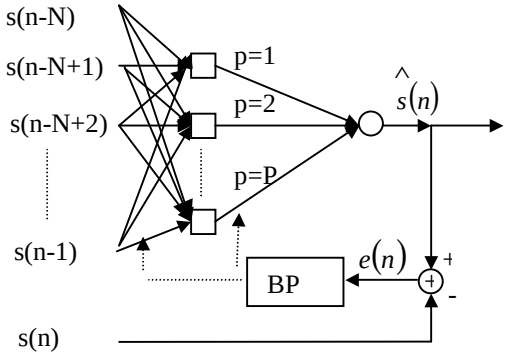

Fig.1. Neural networks structure.

It is chosen as a neural networks structure a two layers perception. The first layer is a hidden layer, which serve for a transformation of each input speech frame $(s(n-1) \div s(n-N))$ with dimension N with correspondence of a given numbers of $p = 1 \div P$ prediction elements (coefficients).

The second layer calculate the current value of predicted speech sample $\hat{s}(n)$, which is compared with real speech sample $s(n)$. The error $e(n)$ is used in learning algorithm. It is chosen the back propagation (BP) as a learning algorithm.

III. NEURAL NETWORK ANALYSIS

The neural network characteristics definitions are made in correspondence with speech prediction conditions. The number N of input samples in speech signal $s(n)$ depend from speech frame dimensions NF, which is used in speech coding method. Usually from coding standards sample frequency speech signal statistics etc., the speech frame dimension is chosen $NF = 160 \div 240$ samples. For a right neural network learning of first hidden layer with sufficient representatives in the input learning sequence, it is necessary to satisfy the condition:

$$N \le NF . \qquad (1)$$

The value of N chosen from (1) must satisfy the following contradicting requirements: the reducing of N lead to increasing of number of representatives in learning sequence, but the prediction accuracy decrease and the necessary time of learning increase. In practical cases N is chosen from (1) with estimation of real prediction error. It can be shown from

experimental tests, that a chosen suitable value of number *N* of input samples is $N = 20$.

The number *P* of neurons (cells) in second layer also depends from speech coding standards and is chosen usually in range of:

$$P = 10 \div 16. \qquad (2)$$

The analysis of proposed neural network structure from Fig.1 can be made with representing of the current speech frame to neural network as a vector:

$$\vec{S}_n = [s(n-1), s(n-2), \ldots, s(n-N)]^T. \qquad (3)$$

As a result of neural network action the output of neural network $\hat{s}(n)$ is the current predicted samples from the input vector $\vec{S}_n$:

$$\hat{s}(n) = F(\vec{S}_n), \qquad (4)$$

where

F is whole activation function of neural network.

Since the structure of neural network is composed from two layers the whole activation function *F* can be represent with the functions of activation of the first the second layer:

$$F = G_W . H_a, \qquad (5)$$

where

G_W is activation function of first hidden neural network layer with vector $\vec{w}$ of weights;

H_a - activation function of second neural network layer with vector $\vec{a}$ of weights.

The transformation of input vector $\vec{S}_n$ can be represented with respect of (4) end (5):

$$\vec{Z}_n = G_W(\vec{S}_n), \qquad (6)$$

$$\vec{s}_n = H_a(Z_n), \qquad (7)$$

where

Z_n is the output vector of the first layer of neural network $\vec{Z}_n = [z_1(n), z_2(n,), \ldots, z(n)]$.

From the expressions (5), (6) and (7) it can be shown, that the current predicted speech sample $\hat{s}(n)$ depend from whole neural network activation function *F* and from corresponding activation functions G_W and H_a of the first and second neural network layer.

The particular activation functions G_W and H_a can be chosen linear or nonlinear (for example sigmoid function) and corresponding neural network, work as a linear or nonlinear predictor of speech signal. This is an advantage of neural network prediction in correspondence of classical methods for speech predictions, which are all only linear methods.

The weights in the vectors $\vec{w}$ and $\vec{a}$ for corresponding first and second layer of neural network can be calculated in the learning phase of neural network by using minimization of quadratic prediction error $e(n)$:

$$e(n) = \sum_n \left(s(n) - \hat{s}(n) \right)^2. \qquad (8)$$

The error $e(n)$ from expression (8) is calculated as a sum of all possible representatives in learning sequence in each given speech frame. The number of these representatives in accordance with expression (1) is:

$$n = 1 \div (NF - N) \qquad (9)$$

The error expression can be generalized for all frames $i = 1 \div L$, for which the learning is made:

$$e_i(n) = \sum_i \sum_n \left(s_i(n) - \hat{s}(n) \right)^2. \qquad (10)$$

It is possible to make a substitution of the expressions (6) and (7) in the expression (10):

$$e_i(n) = \sum_i \sum_n (s_i(n) - H_{ai} . G_W(s_i(n))). \qquad (11)$$

The expression (11) can be used in the first phase of learning for calculating the weights $\vec{w}$ of the first hidden layer of neural network.

At this phase of learning the goal of second layer learning of weights in vector $\vec{a}$ is to improve the precisions of calculating the weights in vector $\vec{w}$ for the first hidden neural network layer using all presented speech frames in learning sequences.

The second phase of learning algorithm used the calculating in the first phase weights in vector $\vec{w}$ unchanged. Only the weights in vector $\vec{a}$ are changed of updated in this phase of learning. The second phase of learning is made only with the representatives in the current speech frame. This second learning can serve as prediction in speech coding of current speech frame. The reason for this are the expressions (6) and (7) shows that current predicted speech sample $\hat{s}(n)$ is directly calculated from the activation function H_a of the second layer of neural network. In H_a are the weights of vector $\vec{a}$ and this weights can be tread as prediction weights or coefficients and the prediction can be linear or nonlinear depending of choose of activation functions H_a and G_W, respectively for second and first layer of the neural network.

The calculation of error in the second learning phase is made only for the representatives in the current speech frame. It is possible to use the equation (8) modified with index *i* to show the number of speech frame:

$$e_i(n) = \sum_n (s_i(n) - \hat{s}_i(n)), \qquad (12)$$

but the sum is only in the current speech frame.

The effectiveness of the prediction with this proposed neural network can be calculated and estimated with the definition of the so called prediction gain:

$$G_i = 10\log_{10}\left(\sum_n s_i(n)^2 / \right.$$
$$\left. / \sum e_i(n)^2 \right). \qquad (13)$$

IV. NEURAL NETWORK TESTING

The purposed neural networks have been simulated with Matlab. The input speech signal (Fig.2) is a pronunciation of letter "a" as a fest signal for neural network. It is shown at the Fig.3 an input speech frame. The sample frequency is $f_s = 11025Hz$, the frame dimension *NF*=240 samples.

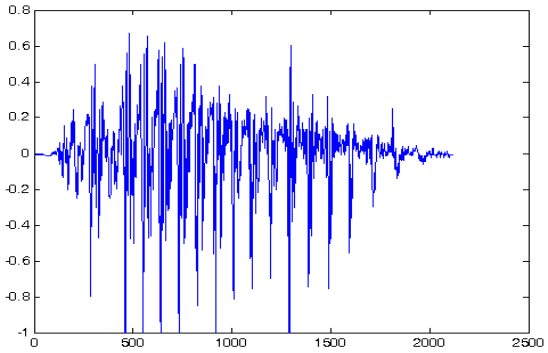

Fig.2. Input speech signal.

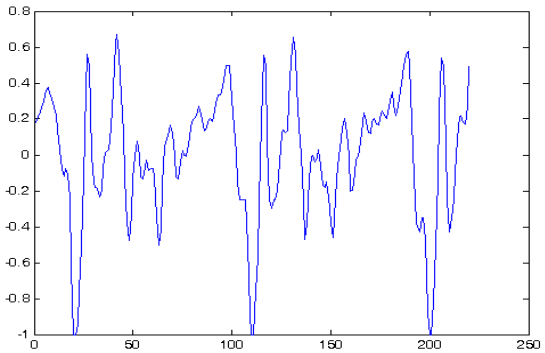

Fig.3. A frame of input speech signal.

At the Fig.4 is an assembly plot of input frame (solid line) and predicted frame (_. line) as an output of neural network. At the Fig.5 is an assembly plot with the same signal as at Fig.4, but here it is added the plot of error (x line).

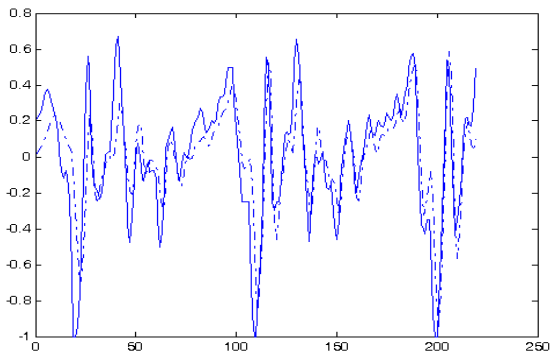

Fig.4. Input and predicted frame as an output of neural network.

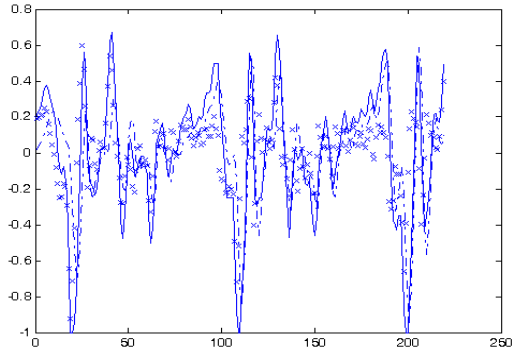

Fig.5. Input, predicted frame and error signal.

V. CONCLUSION

The test of proposed neural network show the possibility to modeling of the speech prediction, which is frequently used in speech coding methods. As a future work it is necessary to investigate the whole properties of this neural network: the error minimization, the complexity of software or hardware realization etc.

REFERENCE:

[1] S. Morishima, H. Harashima and Y. Katayama. Speech Coding based on a multiplayer neural network. IEEE Transac-tion on Signal processing. Vol.40, No.4, pp.429-432, 1990.

[2] Br. Verma and Vallipuram Muthukkuma-rasamy. Speech Compression for VOIP: Neural Network Vs. G723.1. School of Information Technology. Griffith University, Australia.

[3] J. Thyssen, D.S. Hansen Using Neural Networks for Vector Quantization in low Rate Speech Coders, IEEE Transactions on Signal Processing, Vol.4, 1993.

[4] S.C. Ahalt, A.R. Krishnamurthy, D.E. Melton, and P. Chen Neural Networks for Vector Quantization. IEEE Yournal of Selected Areas in Communications, Vol. 8, No. 8, pp. 1449-1457, 1990.

[5] E. Shlomot, V. Cuperman, and A. Gresho Hybrid Coding: Combined Harmonic and Waveform Coding of Speech at 4kb/s. IEEE Transactions on Speech and Audio Processing. Vol. 9, pp. 632-646, 2001.

GUI Based Tool for Watermarking Attacks

Jovan Spasik[1], Dimitar Taskovski[2] and Sofija Bogdanova[3]

Abstract **- Many watermarking techniques for image watermarking were proposed in the last few years. At the same time the large numbers of attacks are presented. Watermarking algorithm developers need a tool, which may help them to test the robustness of their proposed algorithms to these attacks. The tool that implements most of the standard image processing operations (watermarking attacks) is presented in this paper. The main characteristics of the proposed tool are: GUI - Graphical User Interface, simplicity of use and speed.**

Keywords **– Watermarking, Attacks, Evaluation, GUI.**

I. INTRODUCTION

We are witnesses of enormous growth of Internet and Internet sharing applications and data. The advancement in technology offers new solutions, but in the other way, creates new problems as well. Digital media (e.g. audio, images, video, etc.) offers many benefits: It can be stored, duplicated and distributed everywhere in the world, with no loss of fidelity, but in contrary, it can also be manipulated and modified easily, often only with personal computer and appropriate software, and sometimes even unintentionally. While these properties are desirable in general, they can create problems for parties who own digital media and want to distribute it, but at the same time, want to protect it from illegal multiplication and distribution.

Because of that, there is a need for protecting the intellectual property rights. Digital watermarking has been proposed as a solution for the copyright protection. It is a process of embedding hidden copyright information directly into the digital data by making small, unnoticed for human eye, modifications to them.

A digital watermark should possess certain properties, although their relative importance can vary depending upon the application [1]. The most important characteristics for effective watermarking are invisibility and robustness. This means that the watermark should be embedded into the image so as to be invisible over all image types. Also, it should be robust to intentional or unintentional image processing operations, which preserve the desired image quality.

[1]Jovan Spasik is with the Faculty of Electrical Engineering, University "Ss. Cyril and Methodius", 1000 Skopje, R.Macedonia, E-mail: vanja@mail.net.mk

[2]Dimitar Taskovski is with the Faculty of Electrical Engineering, University "Ss. Cyril and Methodius", 1000 Skopje, R.Macedonia, E-mail: dtaskov@etf.ukum.edu.mk

[3]Sofija Bogdanova is with the Faculty of Electrical Engineering, University "Ss. Cyril and Methodius", 1000 Skopje, R.Macedonia, E-mail: sofija@etf.ukim.edu.mk

A lot of watermarking algorithms that meet these two main requirements for effective watermarking have been proposed in recent years. An overview of more than 100 proposed methods is given in [2].

In the period of time required for marked data to reach the watermark receiver, an embedded watermark may be accidentally, inadvertently, but most of the time purposely, impaired from some processes. Any processing that may impair detection of the watermark is called watermark attack. An attack is succeeds if it impairs the watermark beyond acceptable limits while maintaining the perceptual quality of the attacked data. All attacks could be performed intentionally or unintentionally. Unintentional attacks are results of common signal processing operations done by legal user of watermarked works. Intentional attacks are usually performed by more competent people with more knowledge of watermarking systems and more resources to make the attacks.

As fast as new watermarking algorithms are proposed the large numbers of attacks are presented [3-6]. These attacks have shown that far more research is required to improve the quality of existing watermarking methods.

The complete theoretical analysis of the watermarking algorithm performance with respect to different attacks is rather complicated. In general, the developers of watermarking algorithms refer to the results of experimental testing, and they usually claim that proposed watermarking method is robust although only few experimental tests (e.g. JPEG compression, insertion of noise, cropping, etc) are performed to only few images. In order to overcome this problem with evaluation of the watermarking algorithm performance several benchmarks are proposed [7-9]. The benchmarks usually combine some of the possible attacks into a common framework and weight the resulted performances depending on the possible application of the watermarking technology. All these benchmarks include tools for watermarking attacks implementation. The main disadvantages of this tools are that some of them are very complex for use, some of them do not offer GUI, parameters of some predefined attack cannot be change and they do not include some of the standard attacks.

In this paper we present a GUI based tool that implement most of the standard image processing operations. This tool can help watermarking algorithm developers to test the robustness of their proposed algorithms. Benefit of this proposed tool, beside GUI, is that in same place it comprises many standard operations for image processing - watermark attacks, saves quality time, it may work on multiple images simultaneously and it is very simple for use.

In the next section, we briefly summarize the watermarking attacks and coarsely categorize them. Then, we propose GUI based tool that implements most of these attacks, classified in two main groups: simple and geometrical attacks.

II. CLASSIFICATION OF WATERMARKING ATTACKS

The watermark attacks can be classified in many different ways. In this paper we followed the categorization proposed in [4] where watermarking attacks are grouped in four main groups: Simple attacks, Geometrical attacks, Ambiguity attacks and Removal attacks.

A. Simple attacks

The main characteristic of this type of watermark attacks is that they manipulate on whole image and therefore attacks the embedded watermark. So they do not try to separate or to identify the watermark from the host image. Examples may include linear and general nonlinear filtering, JPEG compression, addition of noise and gamma correction.

B. Geometrical attacks

Sometimes the affect of the attack over the watermarked image is to make the image undetectable by watermark detector. These types of attacks disable the synchronization of the watermark detector, and usually include geometric transformation like cropping, rotation, shifting, permutations or removal of pixels or any other geometric transformation of the data. The main goal of these attacks is to make the watermark unreadable even though it is still present in the modified image.

C. Ambiguity attacks

Attacks often can be made and by insertion of confusion with creation of fake original or watermarked data. In other cases this attacks can discredit the authority of original watermark by embedding one or several additional watermarks such that it is unclear which the first, original watermark was.

D. Removal attacks

These are the most sophisticated attacks since they take into account prior knowledge about watermarking process. They first analyze the image, and than try to separate the watermark from the host data. After the removing of watermark, the original image is vulnerable to further illegal use. Examples are collusion attacks, denoising and some non-linear filter operations.

It should be noted that the properties of the attacks make its classification very hard, and then an attack may belong to more than one group. Cropping for example can be regarded as either a simple attack or a geometrical attack.

III. GUI BASED TOOL FOR WATERMARKING ATTACKS

We have chosen MATLAB [10] as the environment for developing our GUI. MATLAB contains extensive library of built-in functions that greatly simplifies programming and most of the watermarking system designers first implement their algorithms in MATLAB. They also need a tool for testing the performances of their algorithms.

With the proposed tool (Fig. 1) the process of testing is simplified and unified. This tool also saves time, because in one turn more than one image and attack can be chosen. The name of the modified images is compound from the names of the used attacks, and just one look at the name of the images shows which attack is implemented on that image.

In this tool the available attacks are classified in 2 groups: Geometrical and Simple attacks. The realization of other two groups of attacks will be discussed in further releases.

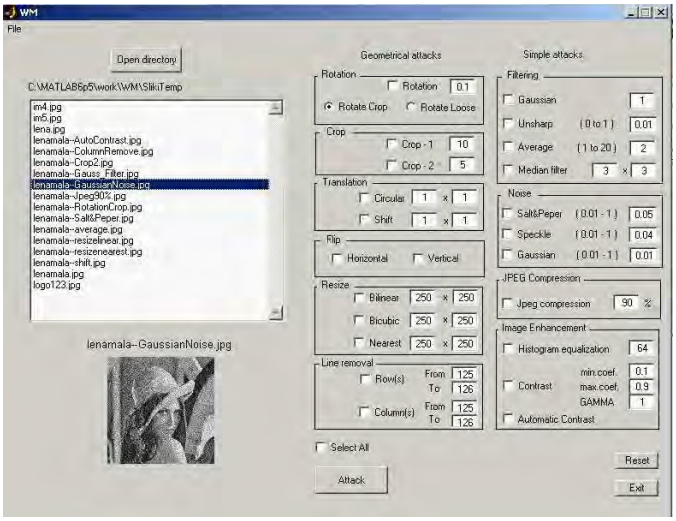

Fig.1. GUI based tool for watermarking attacks

We do not make difference between intentional and unintentional attacks.

The components of *Geometrical attacks* group are:

Rotation: This attack does not usually change the commercial value of the image but can make the watermark un-detectable. Rotations are used to realign horizontal features of an image. In this tool rotate attack can be made in two ways (with or without crop).

Cropping: Usually, attackers are just interested in the central part of the copyrighted material, so in this case cropping is ideal solution for breaking the synchronization and making recovery of the watermark impossible.

Translation: Disabling the synchronization can also be easily done with this type of attack. Proposed tool presents two translation attacks: shifting in one direction and circular shift

Flip: The very few watermarking systems can survive horizontal and vertical flip, although there is no loosing of information in the image with this type of attacks.

Resize: Resizing of the image can be done using three different interpolation methods: bilinear, bicubic and nearest. A lot digital watermarking methods are resistant to this kind of attacks.

Line removal: This attack can removes selected number of row(s) and column(s) from the image and it is very efficient against any simple implementation of spread-spectrum techniques in the spatial domain.

The second group named *Simple attacks* is compound of four subgroups: Filtering, Noise, JpegCompression and Image Enhancement group.

Commonly used linear and non-linear filters are: symmetric Gaussian low pass filter, standard average filter and median filter. In Filtering group there is also sharpening filter. These filters can be used as an effective attack on some watermarking schemes.

In the communication theory and signal processing theory literature, additive noise and uncorrelated multiplicative noise have been largely addressed. Authors often claim that their watermarking techniques survive this kind of attack, however many forget to mention the maximum level of acceptable noise. Proposed tool includes these types of noises:

Salt & pepper - adds "salt and pepper" noise to the image,

Speckle - adds multiplicative noise to the image,

Gaussian - adds Gaussian white noise to the image.

One of the most widely used intentional or unintentional attacks is JPEG compression algorithm. Because of that, every watermarking system should be flexible to some degree of JPEG compression. In this tool we can experiment with different values of compression by changing quality factor in the edit box. Here we can point out that attackers often use this attack in combination with some geometrical transformation (e.g. cropping and rotation).

The final group of attacks is named Image Enhancement. These attacks usually do not prevent watermark detection, and they are often applied before detection is performed to obtain better results. Histogram equalization is attack that includes histogram stretching or equalization, which are sometimes used to compensate poor lightening conditions. Contrast attack adjusts image intensity values. Here we can choose Gamma factor that specifies the shape of the curve describing the relationship between the values in input and output picture.

IV. CONCLUSIONS

The aim of this tool is to help the watermark algorithm developers to test the robustness of their watermarking algorithms. This can be done by testing the behavior of watermarked image, attacked by most of the existing attacks. In proposed tool this could be done from the same location in just one turn. Beside this, the presented tool is easy for using thanks to GUI, saves quality time and may work on multiple images simultaneously.

REFERENCES

[1] I. Cox, M. Miller and J. Bloom, “Watermarking applications and their properties,” Int. Conf. on Information Technology’2000, Las Vegas, 2000.

[2] F. Hartung and M. Kutter, “Multimedia watermarking techniques,” Proceedingg of the IEEE, Special Issue on Protection of Multimedia Content, vol. 87, July 1999.

[3] F.A.P. Petitcolas, R.J. Anderson and M.G. Kuhn, “Attacks on copyright marking systems” in Second Workshop on Information Hiding, Portland, OR, USA, Apr. 1998.

[4] F. Hartung, J.K. Su, and B. Girod, “Spread Spectrum Watermarking: Malicious Attacks and Counterattacks”, Proc. of SPIE: Security and Watermarking of Multimedia Contents, vol. 3657, San Jose, CA, Jan 1999.

[5] S. Voloshhynovskiy, S. Pereira, A. Herrigel, N. Baumgartner and T. Pun, “Generalized watermark attack based on watermark estimation and perceptual remodulation,” in Proc. Electronic Imaging 2000, Security and Watermarking of Multimedia Contents II, vol. 3971, San Jose, CA, Jan 2000.

[6] M. Kutter, “Watermark copy attack,” in Proc. Electronic Imaging 2000, Security and Watermarking of Multimedia Contents II, vol. 3971, San Jose, CA, Jan. 2000.

[7] http://www.cl.cam.ac.uk/~fapp2/watermarking/stirmark

[8] V. Solachidis, A. Tefas, N. Nikolaidis, S. Tsekeridou, A. Nikolaidis, I.Pitas, “A benchmarking protocol for watermarking methods”, 2001 IEEE Int. Conf. on Image Processing (ICIP'01), Thessaloniki, Greece, October, 2001

[9] Shelby Pereira, Sviatoslav Voloshynovskiy, Maribel Madueño, Stéphane Marchand-Maillet and Thierry Pun, “Second generation benchmarking and application oriented evaluation,” in Information Hiding Workshop III, Pittsburgh, PA, USA, April 2001.

[10] http://www.mathworks.com

Realization of Variable IIR Digital Filters as a Cascade of Third or Higher Order Identical Sub-filters

Georgi Stoyanov[1], Ivan Uzunov[2] and Masayuki Kawamata[3]

Abstract – **A new approach to design high tuning accuracy variable IIR filters as a cascade of *N* identical filters of order higher than second is proposed in this paper. The identical sub-filters are realized as parallel allpass structures and their sensitivities are minimized to obtain higher accuracy and wider range of tuning compared to other known variable filters. All theoretical results derived are verified experimentally.**

Keywords – **IIR Digital filters, Variable/tunable digital filters, Sensitivity, Tuning accuracy, Cascade realization**.

I. INTRODUCTION

Variable IIR filters are usually designed by employing the spectral (allpass) transformations of Constantinides (TC) [1], [2]. But when the prototypes are IIR filters, delay-free loops appear after the TC. Due to the attempts to eliminate these delay-free loops, no precise, without limitations, real-time tuning of IIR filters is known until now – all methods are approximate and valid only in a narrow range of values of the tuned parameter and over some limited frequency range. Most of the known methods are based on truncated Taylor series expansions, applied on real or complex coefficient parallel-allpass-structure [3] (called MNR-method after the names of the authors Mitra, Neuvo and Roivainen) or on cascade [4] and wave [5] realizations. The MNR-method is considered as the best known, but we have shown in Ref. [6] that the magnitude characteristics are degrading even when the LP/HP (lowpass/highpass) filter cutoff frequency or the bandpass and bandstop (BP/BS) bandwidth (BW) are tuned over a very limited frequency range. We have increased considerably the range and the accuracy of tuning by introducing a sensitivity minimization as an additional design step [6]. We have developed also a new approach [7], [8], based on a cascaded connection of several identical sub-filters. It permits an easy tuning of the cutoff frequency of the LP filter without having to use TC and truncated Taylor series expansions when using sub-filters of first or second order. We have developed and investigated [8],[9] such tunable sub-filter structures (of first and second order) with a very high tuning accuracy for narrow-band realizations.

[1]Georgi Stoyanov is with the Faculty of Communication Engineering, Technical University of Sofia, 8 Kl. Ohridski Str., 1756 Sofia, Bulgaria, E-mail: stoyanov@ieee.org
[2]Ivan Uzunov is with the Institute of Communication Engineering, Tampere University of Technology, P.O. Box 553, FIN-33101, Tampere, Finland, E-mail: uzunoviv@cs.tut.fi
[3]Masayuki Kawamata is with the Graduate School of Engineering, Tohoku University, Aramaki Aza Aoba 05, Sendai 980-8579, Japan, E-mail: kawamata@mk.ecei.tohoku.ac.jp

In this work we propose to realize the sub-filters of higher than second order as parallel allpass structures and investigate the applicability and the merits of such an approach.

II. APPROXIMATION USING A PRODUCT OF SEVERAL EQUAL TRANSFER FUNCTIONS

Our new method of design and realization of variable digital filters (VDF) is based on the usage of several cascaded identical filter blocks, each of them providing a very simple tuning of a given frequency parameter by varying a single multiplier coefficient. We are concerned with development of approximation procedures meeting only lowpass filter specifications. Variable BP/BS filters are obtained then by applying the constrained TC [1][2] on the variable LP filter. This transformation provides also an independent tuning of the central frequency, while the tuning of the cutoff frequency of the prototype LP filter is varying the BW of these BP/BS filters.

The magnitude specifications of the desired LP variable filter are: pass-band (PB) from 0 to ω_p (for digital filters) or Ω_p (for analog), stop-band (SB) from ω_s or Ω_s to infinity, maximum variation of the PB attenuation A_p, dB and minimum SB attenuation A_s, dB. And we have to find a total transfer function (TF) $H(z)$ (digital) or $T(s)$ (analog) represented as a product of N equal individual TFs $H_i(z)$ or $T_i(s)$, each of them of order n:

$$H(z) = H_i^N(z), \qquad T(s) = T_i^N(s), \tag{1}$$

$$H_i(z) = \frac{a_0 + a_1 z^{-1} + a_2 z^{-2} + \ldots\ a_n z^{-n}}{1 + b_1 z^{-1} + b_2 z^{-2} + \ldots\ b_n z^{-n}}, \tag{2}$$

$$T_i(s) = \frac{a_0 + a_1 s + a_2 s^2 + \ldots\ a_m s^m}{b_0 + b_1 s + b_2 s^2 + \ldots\ b_n s^n},\ m \le n. \tag{3}$$

These TFs might be of Butterworth, Chebyshev or elliptic type and in the process of design we have to determine the minimal number N of the individual TFs $H_i(z)$ or $T_i(s)$, necessary to meet the specifications with given (selected) type (maximally flat, equiripple or other) and order n. A step-by-step design procedure for this is given in [7][8], it is performed in the analog domain and is using the popular in the classical filter theory Characteristic function $k(\Omega)$.

An approximation using N equal terms is far from optimal and there are many limitations that have to be clearly defined. These limitations depend on the type of the individual TF and on the selected approximation parameters. It might be even impossible to meet some difficult filter specifications doesn't

matter how high the number N is taken. These limitations are investigated in details in [7][8]. Here we need a more general evaluations taking into account the order n of the individual TFs and some simple parameter describing how difficult the specifications are. We choose to use the "rectangularity coefficient" r (calculated in s- or in z-domain) as such parameter:

$$r = \frac{\Omega_s}{\Omega_p} \quad \text{or} \quad r = \frac{\tan\frac{\omega_s \tau}{2}}{\tan\frac{\omega_p \tau}{2}}, \tag{4}$$

where τ is the sampling interval and r is taking values within the limits $1 \le r < \infty$ with r=1 for an ideal LP filter.

If $A_{s_{\max}}$ is the highest value that A_s can achieve at its points of minimum (in the stop-band) for a given approximation and values of n while $N \to \infty$, we can derive very handy formulae connecting only A_p, r and $A_{s_{\max}}$ and permitting the most general possible way of comparing different approximations.

For Butterworth-type of individual TF we get (starting from the results in [7][8])

$$A_{s_{\max}} = A_p r^{2n}, \tag{5}$$

which is used to calculate the curves shown in Fig. 1.

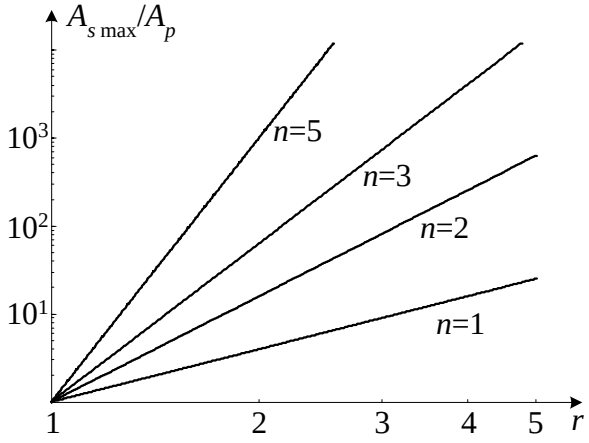

Fig. 1 Upper limits of the SB attenuation for different order n of the individual Butterworth type transfer functions

It is clear from Fig. 1 that the ratio $A_{s_{\max}} / A_p$ cannot exceed the value of 100 even for very easy filter specifications (r=3, for example) if we use an unlimited number of Butterworth-type second-order sections as individual sub-filters.

If the individual TFs are of Chebyshev type, we obtain the following very general expression

$$A_{s_{\max}} = A_p \operatorname{ch}^2(n \operatorname{Arch} r). \tag{6}$$

A family of curves, obtained by using Eq. (6), is shown in Fig. 2. It is seen once again that in order to obtain a filter with quite a high selectivity (r<2), it will be necessary to use individual sub-filters of order higher than second even when these sub-filters are with Chebyshev type of TF. These filters are, on the other hand, much more capable, compared to the filters with Butterworth individual TF (which is very easy to anticipate).

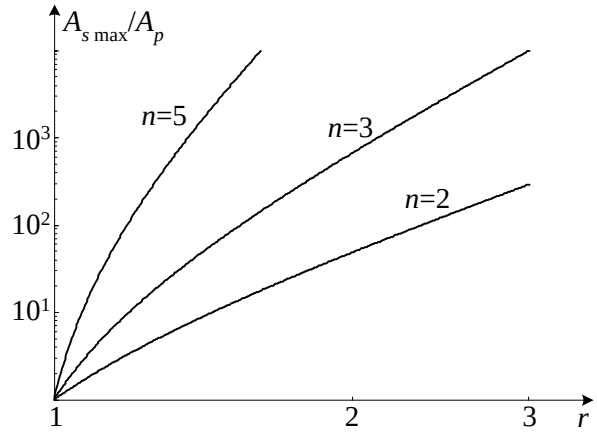

Fig. 2 Upper limits of the SB attenuation for different order n of the individual Chebyshev type transfer functions

It is impossible to derive a single compact formula for the case of elliptic type of individual TFs. In [7][8] we have derived very general expressions (different for n even and n - odd), which are used to obtain the following more concrete formulae:

$$A_{s_{\max}} = \frac{A_p r^4}{\operatorname{sn}^8\left(\frac{K(1/r)}{2}\right)} = A_p r^4 \left(1 + \sqrt{1 - \frac{1}{r^2}}\right)^4 \quad \text{for } n = 2, \tag{7}$$

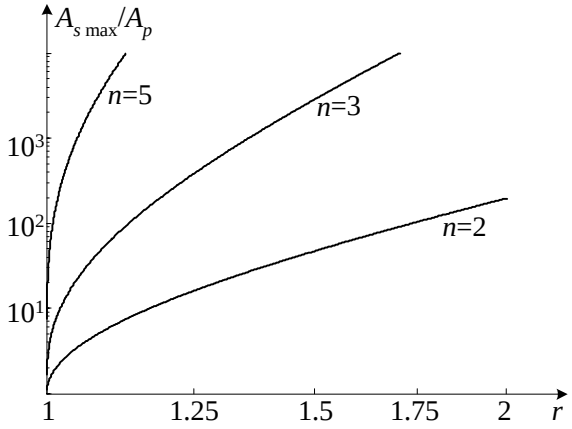

Fig. 3 Upper limits of the SB attenuation for different order n of the individual elliptic type transfer functions

$$A_{s_{\max}} = \frac{A_p r^8}{\operatorname{sn}^8\left(\frac{K(1/r)}{3}\right)} \quad \text{for } n = 3, \tag{8}$$

$$A_{s\,\max} = \frac{A_p r^{12}}{\operatorname{sn}^8\left(\frac{K(1/r)}{5}\right)\operatorname{sn}^8\left(\frac{3K(1/r)}{5}\right)} \quad \text{for } n = 5, \tag{9}$$

where sn is the Jacobi's "sinus elliptic" function and $K(1/r)$ – the function of Jacobi, calculated as a complete elliptic integral of first kind (see [8] for details).

It is seen from Fig. 3 that almost any kind of difficult filter specifications will be met if elliptic transfer functions with order higher than second are used to realize the individual sub-filters.

In Fig. 4 the upper limits of the stop-band attenuation, achievable with identical first- (IFOS) and second-order sections (ISOS), are given in order to have a base for comparisons. These limits are, in fact, much lower because instead of $N \to \infty$, we are using only several IFOS or ISOS.

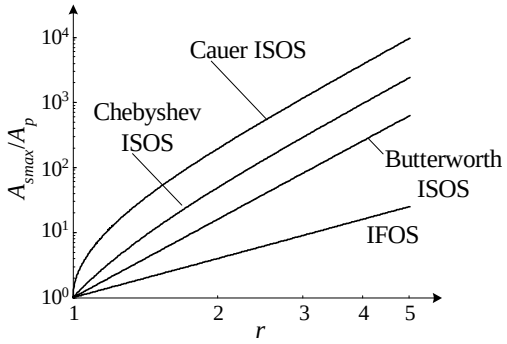

Fig. 4 Upper limits of the SB attenuation with IFOS or ISOS

III. REALIZATION OF THE HIGHER ORDER SUB-FILTERS

We have developed and investigated in [8],[9] excellent variable first and second order filter sections for IFOS and ISOS with truly independent high accuracy tuning without using any truncated Taylor series expansions. It appeared, however, to be impossible to synthesize such structures with higher than second order. No such structures have been found also in the literature. In order to solve the problem, we have to accept the MNR approach (to use truncated Taylor series expansions) [3] but only for the realization of the sub-filters. It will provide an easy tuning of the cutoff frequency of the LP individual filters by varying a single multiplier coefficient. But as our structure is a cascade of several low-order order sections (even though obtained as parallel-allpass-structures) , it will have much lower sensitivity in the stop-band, compared to that of the totally parallel allpass structure, which is behaving really badly, as shown in [6]. Next, we propose to use our approach advanced in [6], namely to introduce an additional step in the design of the sub-filers, consisting of a sensitivity minimization (within the frequency range of interest) of the first- and second-order allpass sections used to realize these sub-filters. There is another problem with the parallel-allpass-structure – it cannot realize even-order LP TFs with real coefficients. We could still use it to realize our even-order sub-filters with complex coefficients, but they will be quite impractical (complex structures with low tuning accuracy). Thus we shall concentrate mainly on the realization of third- and fifth-order sub-filters, putting, in fact, out of consideration only sub-filters of fourth-order (it is also impractical to use sub-filters of order higher than fifth, because we lose then all the merits of the cascade realization).

Once it is decided, the design problem is reduced to development of convenient first- and second-order allpass sections with low sensitivities for the frequency range over which the filter will be tuned. We have shown in [6] that for the most common case – variable narrow-band LP filter (having all his TF poles near z=1) – our very low sensitivity allpass sections, shown in Fig. 5b and Fig.6b and named respectively ST and LS, are by far the best known.

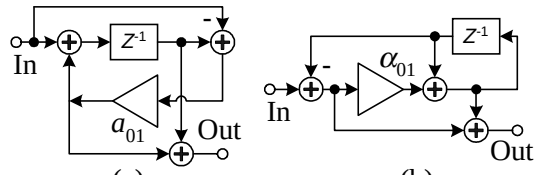

Fig. 5. First-order all-pass sections: (a) MH section, (b) ST section

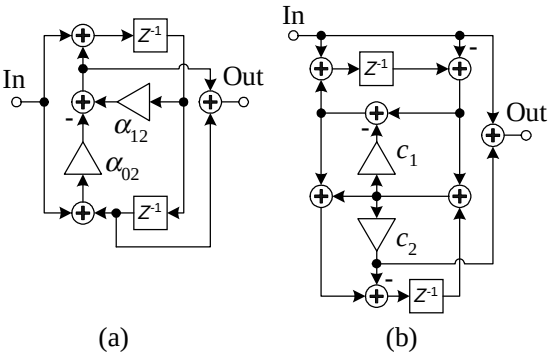

Fig. 6. Second-order all-pass sections: (a) MH2B, (b) LS

They realize the following TFs

$$H(z)_{ST} = \frac{z^{-1} - (1-\alpha_{01})}{1-(1-\alpha_{01})z^{-1}}, \qquad (10)$$

$$H(z)_{LS} = \frac{1-c_2-(2-2c_1-c_2)z^{-1}+z^{-2}}{1-(2-2c_1-c_2)z^{-1}+(1-c_2)z^{-2}}. \qquad (11)$$

In Figs. 5a and 6a we have shown the allpass sections most often mentioned in the literature [3] – these of Mitra and Hirano, called respectively MH and MH2B.

The design of third and fifth-order sub-filters as parallel-allpass-structures (Fig. 7a) might be very simple and straightforward. Once $H_i(z)$ (2) is determined, its poles p_0 and $p_{1,2} = r_1 e^{j\theta_1}$ (for n=3) and p_0, $p_{1,2} = r_1 e^{j\theta_1}$, $p_{3,4} = r_3 e^{j\theta_3}$ (for n=5) are readily known. Then, for n=3, $A(z)$ (Fig. 7a) will be a second-order allpass TF with poles $p_{1,2}$, while $B(z)$ will be of first-order with a real pole p_0. The denominator polynomials of $A(z)$ and $B(z)$ are thus easily found and the corresponding nominators are their mirror image polynomials.

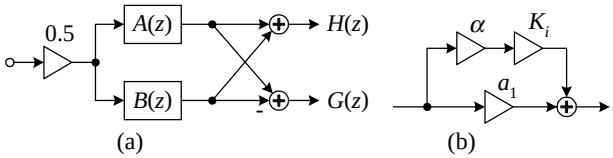

Fig. 7. Parallel-allpass-structure-based realization (a) and variable coefficient realization (b)

For n=5 $A(z)$ will be a third-order allpass TF with poles p_0 and $p_{3,4}$, while $B(z)$ will be of second-order with poles $p_{1,2}$ (supposing $\theta_3 > \theta_1$).

For n=3 and usage of the ST and LS sections it produces:

$$\alpha_{01} = 1 - p_0,\ c_1 = 0.5(1 - 2r_1 \cos\theta_1 - r_1^2),\ c_2 = 1 - r_1^2. \quad (12)$$

Each multiplier then is made tunable as shown in Fig. 7b by adding a parallel branch αK_i, where α is the tuning factor and K_i is calculated as

$$K_\alpha = \alpha_{01}(\alpha_{01} - 2); \quad (13)$$

$$K_{c1} = c_1(2c_1 + c_2 - 4); \qquad K_{c2} = c_2(2c_1 + c_2 - 2). \quad (14)$$

Similar formulae are easily derived for the design of ST and LS for n=5.

IV. EXPERIMENTS

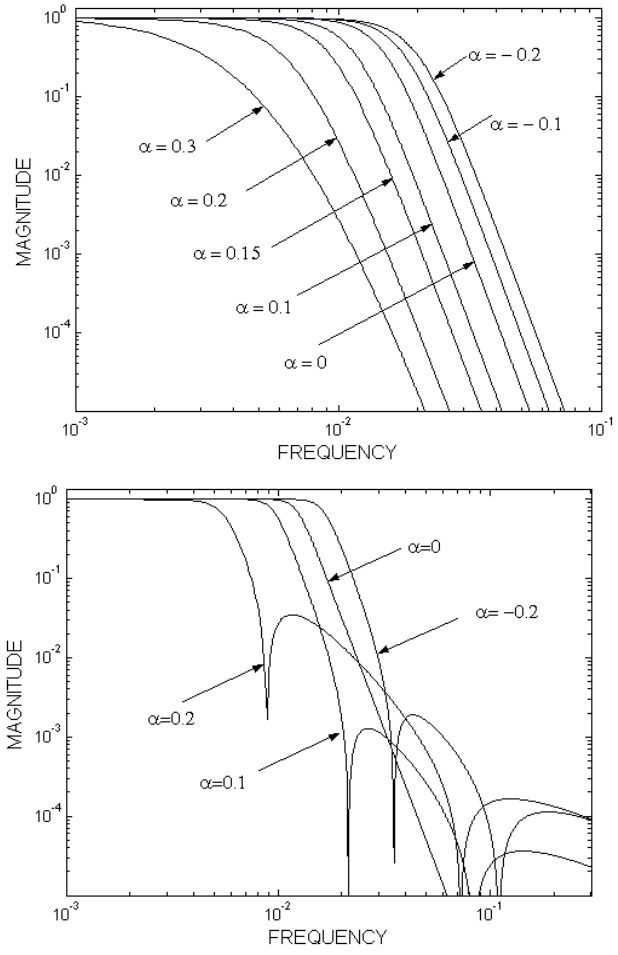

Fig. 8. Tuning of a Butterworth variable filter realized as a cascade of three 3rd order sub-filters (a) and as a MNR-filter (b)

In order to verify the proposed approach and the derived expressions, we have designed and simulated many variable filters based on cascades of identical third or fifth order sub-filters. In Fig. 8a, b the results are shown for filter meeting the following specifications: ω_p=0.01 (tunable from 0.005 to 0.015), ω_s=0.03, A_p=2 dB and A_s=55 dB and using a Butterworth approximation. Our method is producing a 9th order TF, realized as a cascade of 3 sub-filters of 3rd order while the MNR-filter is of 7th order and is realized with MH and MH2B sections. It is seen in Fig. 8 that our filter is easily tuned even over wider frequency range while the SB magnitude of the MNR-filter is destroyed and gone out of the specifications and some transmission zeros are appearing even when $\alpha < |0.1|$.

V. CONCLUSIONS

A new approach to design high tuning accuracy variable IIR filters as a cascade of N identical sub-filters of order higher than second is proposed in this paper. The identical sub-filters are realized as parallel all-pass structures and their sensitivities are minimized to obtain higher accuracy and wider range of tuning compared to other known variable filters. The limitations of the new approach are investigated and simple design procedures are proposed. All theoretical results and the superiority of our method are verified experimentally.

REFERENCES

[1] G. Stoyanov and M. Kawamata, "Variable digital filters", *J. Signal Processing*, vol. 1, No.4, pp. 275-289, July 1997. Available: http://www.mk.ecei.tohoku.ac.jp/papers/articles/Stoyanov-JSP-1997.html.

[2] A. Constantinides, "Spectral transformations for digital filters", *Proc. Inst. Elec. Eng.*, Vol. 117, pp. 1585-1590, 1970.

[3] S. K. Mitra, Y. Neuvo and H. Roivainen, "Design of recursive digital filters with variable characteristics", *Int. Journal Circuit Theory Appl*., Vol. 18, pp. 107-119, 1990.

[4] N. Murakoshi, E. Watanabe, and A. Nishihara, "A synthesis of variable IIR digital filters", *Trans. IECE of Japan*, vol. E 75-A, pp. 362-368, March 1992.

[5] E. Watanabe, M. Ito, N. Murakoshi and A. Nishihara, "A synthesis of variable wave-digital filters", *IEICE Trans. Fundamentals*, Vol. E77-A, No. 1, pp. 263-271, 1994.

[6] G. Stoyanov and M. Kawamata, "Improved tuning accuracy design of parallel-allpass-structures-based variable digital filters", *Proc. ISCAS'98*, Monterey, California, vol. 5, pp. V-379-V-382, May 1998.

[7] G. Stoyanov, I. Uzunov and M. Kawamata, "Design of variable IIR digital filters using equal sub-filters", *Proc. 2000 IEEE International Symp. On Intelligent Signal Processing and Communications Systems* (*ISPACS'2000*), Honolulu, Hawaii, vol. 1, pp. 141-146, Nov. 5-8, 2000. Available: http://www.mk.ecei.tohoku.ac.jp/papers/proceedings/Stoyanov-ISPACS-2000.html

[8] G. Stoyanov, I. Uzunov and M. Kawamata, "Design and realization of variable IIR digital filters as a cascade of identical sub-filters", *IEICE Trans. Fundamentals*, vol. E84-A, No.8, pp. 1831-1839, August 2001. Available: http://www.mk.ecei.tohoku.ac.jp/papers/articles/Stoyanov-IEICE-Trans-Fundamentals-2001.html

[9] G. Stoyanov and M. Kawamata, "Variable biquadratic digital filter section with simultaneous tuning of the pole and zero frequencies by a single parameter", *Proc. ISCAS'2003*, Bangkok, Thailand, vol. 3, pp. III-566–III-569, May 2003.

Input-output based discrete-time disturbance estimator using sliding mode approach

Boban Veselić[1], Čedomir Milosavljević[2] and Darko Mitić[3]

***Abstract* – This paper proposes input-output based discrete-time disturbance estimator structure, in which conventional passive digital filters are replaced with an active digital sliding mode controlled subsystem. In ideal sliding mode, complete disturbance rejection occurs and plant output follows nominal system. Estimator robustness is actively gained by providing sliding mode existence conditions. Simulation results show effectiveness of the proposed disturbance estimator.**

***Keywords* – Disturbance estimator, external disturbances, model uncertainties, sliding mode, robustness.**

I. INTRODUCTION

In almost every control environment the presence of external disturbances and model uncertainties is inevitable, which has significant impact on the performance of a controller. Hence, the performance of a control system is evaluated through its disturbance rejection ability and robustness to model uncertainties.

One approach in handling external disturbances and model uncertainties, which is usually regarded as an equivalent or generalized disturbance, is an employment of disturbance observers. The concept of disturbance observer is that the disturbance action can be efficiently compensated by feedback of the observed disturbance. Thus, disturbance observer enables real plant to behave like the nominal plant.

Generally, there are two methods in a disturbance observer design. The first is the design of a state space disturbance observer, which requires disturbance model to be employed in an augmented state observer. This approach is suitable for simple disturbances, such as bias and periodic disturbances. It is hardly used for arbitrary disturbances. However, it is proposed in [1] a design of discrete-time robust control system, containing a state space disturbance observer, in which modeling of disturbances is not required.

The other method of a disturbance observer design is based on transfer function approach. Conventionally, the disturbance observer is designed using inverse dynamic of a plant, [2]. Disturbance observer efficiency is dependent on the design of the so-called Q filter, which is essentially utilized for the causality of the observer. Q filter determines robustness and disturbance rejection performance, which is proved to be contradictory requirements, [3].

This approach may be viewed from the aspect of internal model concept. The IMPACT (Internal Model Principle And Control Together) structure incorporates both internal models of nominal plant and disturbances, in order to obtain rejection of known class of disturbances, robustness to parameter perturbations and desired dynamic response. Compensation of an arbitrary external disturbance may be obtained by on-line adaptation of disturbance internal model, [4]. A simplified IMPACT controlling structure [5] may be treated as a disturbance estimator.

As a nonlinear robust control strategy, which is theoretically insensitive to model uncertainties and external disturbances, variable structure systems (VSS) with their associated sliding mode behavior are very attractive for perturbed system control. Sliding mode control (SMC) essentially utilizes a switching control law to drive the state of the concerned system to a predefined sliding surface in the state space and to maintain the sliding motion along the surface into the equilibrium point [6]. Due to digital realization of VSC algorithms, analysis of discrete-time sliding mode control (DSMC) systems shows that in general only quasi-sliding modes can be achieved, i.e., the system trajectories are in a small bounded vicinity of the sliding surface.

Among many versatile applications, SMC has found its role in a system state observation [6], and thereby in disturbance observers. Discontinuous disturbance estimators, where VSS equivalent control theory is employed in disturbance estimation, are proposed in [7,8].

This paper proposes sliding mode controlled input-output based discrete-time disturbance estimator. Conventional passive digital filters responsible for estimator robustness and disturbances rejection are replaced with an active DSMC structure, due to its emphasized robustness property. If an ideal sliding mode is established, complete disturbance rejection occurs and plant output follows nominal system. Estimator robustness (stability) against model uncertainties is actively gained by providing sliding mode existence conditions. Thus, robustness and good external disturbances rejection property are no longer contradictory requests.

II. DSMC BASED DISTURBANCE ESTIMATOR

Consider a single-input single-output continuous time dynamic system described by the state space model

[1] Boban Veselić is with the Faculty of Electronic Engineering, Medvedeva 14, 18000 Niš, Serbia and Montenegro, E-mail: bveselic@elfak.ni.ac.yu

[2] Čedomir Milosavljević is with the Faculty of Electronic Engineering, Medvedeva 14, 18000 Niš, Serbia and Montenegro, E-mail: milosavljevic@elfak.ni.ac.yu

[3] Darko Mitić is with the Faculty of Electronic Engineering, Medvedeva 14, 18000 Niš, Serbia and Montenegro, E-mail: darkom@elfak.ni.ac.yu

$$\dot{\mathbf{x}}(t)=\mathbf{A}\mathbf{x}(t)+\mathbf{b}u(t)+\mathbf{j}v(t),\ y(t)=\mathbf{c}\mathbf{x}(t), \quad (1)$$

where the state $x\in R^n$, the control $u\in R^1$, the external disturbance $v\in R^1$ and the output $y\in R^1$; $\mathbf{A}$, $\mathbf{b}$, $\mathbf{j}$, $\mathbf{c}$ are the constant matrix and vectors of appropriate dimensions. The discrete time representation of the dynamic system (1) is obtained by applying u through a zero-order-hold,

$$\mathbf{x}(k+1)=\mathbf{E}\mathbf{x}(k)+\mathbf{f}u(k)+\mathbf{w}(k),\ y(k)=\mathbf{c}\mathbf{x}(k), \quad (2)$$

where T is a sampling period and

$$\mathbf{E}=e^{\mathbf{A}T},\ \mathbf{f}=\int_0^T e^{\mathbf{A}t}\mathrm{d}t\mathbf{b},\ \mathbf{w}(k)=\int_0^T e^{\mathbf{A}t}\mathbf{j}v(kT+T-t)\mathrm{d}t. \quad (3)$$

By assuming zero initial conditions, Z-transform of (2) yields

$$Y(z)=\mathbf{c}(z\mathbf{I}-\mathbf{E})^{-1}\mathbf{f}U(z)+\mathbf{c}(z\mathbf{I}-\mathbf{E})^{-1}\mathbf{W}(z). \quad (4)$$

Using Eq. (4), the system output y in terms of the control u and the external disturbances d may be expressed as

$$y(k)=G(z)u(k)+d(k), \quad (5)$$

where

$$G(z)=\frac{z^{-1}B(z^{-1})}{A(z^{-1})},\ d(k)=\frac{z^{-1}\mathbf{H}(z^{-1})}{A(z^{-1})}\mathbf{w}(k),$$
$$A(z^{-1})=z^{-n}\det(z\mathbf{I}-\mathbf{E}),\ B(z^{-1})=z^{-n+1}\mathbf{c}\,\mathrm{adj}(z\mathbf{I}-\mathbf{E})\mathbf{f}, \quad (6)$$
$$\mathbf{H}(z^{-1})=z^{-n+1}\mathbf{c}\,\mathrm{adj}(z\mathbf{I}-\mathbf{E})=\left[H_1(z^{-1})\quad H_2(z^{-1})\right].$$

The polynomials $A(z^{-1})$ and $B(z^{-1})$ are assumed to be stable and relatively prime, where z^{-1} denotes unit-delay operator.

The main concept is to compensate action of the equivalent disturbance, consisting of model uncertainties and external disturbance, by feedback of the observed equivalent disturbance, and thereby to obtain nominal model behavior. Consider the control structure proposed in Fig. 1., which is composed of the real plant (5) and the disturbance estimator in the local loop. The extraction of the equivalent disturbance q in the disturbance estimator is obtained using discrete transfer function of the nominal model $G_n(z)$. The mismatch between the real plant and nominal model inevitably exists due to uncertainties of the plant parameters. The real plant may be reliably described by

$$G(z)=G_n(z)(1+\delta G(z)), \quad (7)$$

where its perturbation is limited by the multiplicative bound of uncertainties $|\delta G(e^{j\omega T})|\le\gamma(\omega),\ \omega\in[0,\pi/T]$. According to Eq. (7) and Fig. 1., the extracted equivalent disturbance is

$$q(k)=d(k)+G_n(z)\delta G(z)u_k(k). \quad (8)$$

In order to improve disturbance estimator robustness, an active controlling structure is employed instead of conventionally used passive digital filter. A reasonable choice is a DVSC system due to its emphasized robustness property. Signal $\hat{q}$ is an estimation of the compensated equivalent disturbance portion. If DSMC ensures $\hat{q}=q$ (an ideal sliding mode occurs), the control signal may be described as $u_{sm}(k)=G_n^{-1}(z)q(k)$. It can be easily proved that the system output behaves as a nominal model $y(k)=G_n(z)u(k)$. Since DSMC systems enables only quasi-sliding mode, certain but small bounded error between q and $\hat{q}$ will exist, whose value depends on the employed control algorithm.

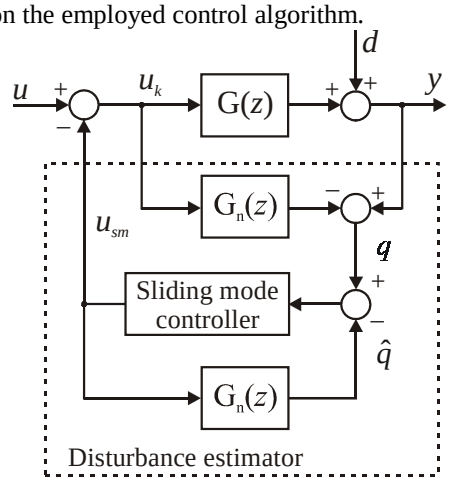

Fig. 1. Structure of DSMC based disturbance estimator

Robustness against model uncertainties is actively gained by providing sliding mode existence conditions. Thus, robustness and good external disturbances rejection property are no longer contradictory requests. From the control design aspect, the proposed method of equivalent disturbance compensation may be treated as a discrete-time tracking control problem with measurable but unknown in advance reference signal $q(k)$. Since digital controller steers a nominal model not a real plant, all state variables are available. This enables variety of DSMC algorithms to be utilized, which successfully handle this control task.

III. DSMC Design

Robust chattering-free DSMC algorithm [9] based on state-space approach is chosen for the digital sliding mode controller. Controller design is demonstrated on the second order system. Consider a discrete-time nominal model.

$$\mathbf{x}(k+1)=\mathbf{E}\mathbf{x}(k)+\mathbf{f}u_{sm}(k),\ y(k)=\mathbf{c}\mathbf{x}(k), \quad (9.a)$$

$$\mathbf{E}=e^{\mathbf{A}T}=\begin{bmatrix}e_{11}&e_{12}\\e_{21}&e_{22}\end{bmatrix},\ \mathbf{f}=\int_0^T e^{\mathbf{A}t}\mathrm{d}t\mathbf{b}=\begin{bmatrix}f_1\\f_2\end{bmatrix},\ \mathbf{c}=\begin{bmatrix}1&0\end{bmatrix}. \quad (9.b)$$

It is more convenient to consider tracking error dynamics, which may be obtained using coordinate transformation. A new state space vector $z(k)=[z_1\quad z_2]^{\mathrm{T}}$ is introduced, defined as $z_1(k)=q(k)-x_1(k),\ z_2(k)=z_1(k)-z_1(k-1),\ \hat{q}(k)=x_1(k)$, which has to be driven to zero by the control force $u_{sm}(k)$. The discrete-time model (9) is transformed to

$$\mathbf{z}(k+1)=\mathbf{E}_x\mathbf{z}(k)+\mathbf{f}_x u_{sm}(k)+\mathbf{h}x_2(k)+\mathbf{g}q(k+1)+\mathbf{p}q(k),$$
$$\mathbf{E}_x=\begin{bmatrix}e_{11}&0\\e_{11}-1&0\end{bmatrix},\mathbf{f}_x=\begin{bmatrix}-f_1\\-f_1\end{bmatrix},\mathbf{h}=\begin{bmatrix}-e_{12}\\-e_{12}\end{bmatrix}, \quad (10)$$
$$\mathbf{g}=\begin{bmatrix}1\\1\end{bmatrix},\mathbf{p}=\begin{bmatrix}-e_{11}\\-e_{11}\end{bmatrix}.$$

The basic sliding mode control philosophy comprises global stabilization of the control system by steering system states onto predefined sliding surface, and maintaining

subsequent motion along that surface into the state space origin. Let the switching function be

$$s(k)=\boldsymbol{\sigma}\mathbf{z}(k),\ \boldsymbol{\sigma}=[\sigma\quad 1] \tag{11}$$

Control law $u_{sm}(k)$ should be determined which provides the desired motion constrained into the quasi-sliding domain, defined as small bounded vicinity of the sliding line $s(k)=0$. Sliding line parameter σ defines sliding mode dynamics, that is, compensation dynamics of the equivalent disturbance. An adequate adoption of the slope σ should provide stable system eigenvalues with desired dynamics.

According to Eqs. (11) and (10), system motion toward the sliding line is presented by

$$\begin{aligned}s(k+1)=s(k)+\boldsymbol{\sigma}[(\mathbf{E}_x-\mathbf{I})\mathbf{z}(k)+\mathbf{f}_x u_{sm}(k)\\ +\mathbf{h}x_2(k)+\mathbf{g}q(k+1)+\mathbf{p}q(k)].\end{aligned} \tag{12}$$

Let the control signal be in the form

$$\begin{aligned}u_{sm}(k)=\frac{-1}{\boldsymbol{\sigma}\mathbf{f}_x}\{\boldsymbol{\sigma}[(\mathbf{E}_x-\mathbf{I})\mathbf{z}(k)+\mathbf{h}x_2(k)+(\mathbf{p}+2\mathbf{g})q(k)\\ -\mathbf{g}q(k-1)]+\operatorname{sgn}(s(k))\min(|s(k)|,\alpha T)\},\end{aligned} \tag{13}$$

under constraint $\boldsymbol{\sigma}\mathbf{f}_x\neq 0$. Control signal has two modes. The first mode, nonlinear with respect to $s(k)$ and active outside the region $|s(k)|<\alpha T$, ensures reaching the region in a finite number of steps; afterwards, the second linear mode provides reaching the quasi-sliding domain in one step. Thus, a discrete-time sliding mode is achieved employing smooth control signal, [9].

To prove that the proposed control law (13) ensure above described motion, and to determine the related switching gain as well as the width of the quasi-sliding domain, the following two supportive lemmas are given.

Lemma 1, [10]**:** *System trajectories described by*

$$s(k+1)=s(k)+f(k+1)-\alpha T\operatorname{sgn}(s(k)) \tag{14}$$

where $f(k)$ *is some bounded function and* $\alpha>|f(k+1)|/T$, $\forall k\in N$, *will reach region* $|s(k)|<\alpha T$ *from any initial state* $s(0)$ *in finite number of steps.*

Lemma 2, [10]**:** *If* $q(t)$ *is an arbitrary smooth function with bounded time derivative* $|\ddot{q}(t)|\le R$, *then the following discrete time inequality holds* $|q(kT+T)-2q(kT)+q(kT-T)|\le 2T^2R$.

The designed discrete time variable structure controller is summarized by the following theorem.

Theorem: *Consider the discrete time system (10) under the action of the control signal (13), where the switching function is chosen as (11). If the switching gain satisfies*

$$\alpha>2TR|\boldsymbol{\sigma}\mathbf{g}|, \tag{15}$$

the discrete-time quasi-sliding mode will arise from any initial state in a finite number of steps in the domain defined by

$$|s(k+1)|\le 2T^2R|\boldsymbol{\sigma}\mathbf{g}|. \tag{16}$$

Proof: Since the system motion starts outside the region $|s(k)|<\alpha T$, by virtue of Eq. (13), Eq. (12) becomes

$$s(k+1)=s(k)-\alpha T\operatorname{sgn}(s(k))+\boldsymbol{\sigma}\mathbf{g}[q(k+1)-2q(k)+q(k-1)]. \tag{17}$$

Under condition (15), according to lemmas 1 and 2, system trajectories (17) will reach the region in a finite number of steps. Governed further by the linear phase of the control (13), system motion is described by

$$s(k+1)=\boldsymbol{\sigma}\mathbf{g}[q(k+1)-2q(k)+q(k-1)], \tag{18}$$

indicating that the quasi-sliding domain is entered in the next step, whose width (16) is proved by (18) and lemma 2. □

It is evident from (16) that $s(k+1)=0$ if $\ddot{q}(t)=0$, implying that the proposed sliding mode based disturbance estimator completely rejects step and ramp like equivalent disturbances. In all other cases, when $R\neq 0$, it provides $O(T^2)$ accuracy.

VI. Simulation Results

The effectiveness of the proposed DSMC based disturbance estimator has been investigated by simulation. The plant is a DC motor, whose continuous-time model (1) is defined with

$$\mathbf{x}=\begin{bmatrix}\omega\\ i_r\end{bmatrix},\mathbf{A}=\begin{bmatrix}0 & k/J\\ -k/L_r & -R_r/L_r\end{bmatrix},\mathbf{b}=\begin{bmatrix}0\\ 1/L_r\end{bmatrix},\mathbf{j}=\begin{bmatrix}-1/J\\ 0\end{bmatrix},\mathbf{c}^{\mathrm{T}}=\begin{bmatrix}1\\ 0\end{bmatrix} \tag{19}$$

The nominal plant (model) parameters are: $R_{rn}=1\Omega$, $B_n=0$ $L_{rn}=2.5\cdot 10^{-3}H$, $J_n=3.267\cdot 10^{-3}kgm^2$, $k_n=0.33$. Using the discrete-time model (2) with the sampling time $T=10^{-3}s$ the following nominal discrete transfer function is obtained according to Eqn. (6)

$$G_n(z)=\frac{z^{-1}(0.0177384+0.0155257z^{-1})}{1-1.65934z^{-1}+0.67032z^{-2}}. \tag{20}$$

The plant is subjected to parameter and external disturbances. Load torque, shown in Fig. 2., acts as an external disturbance. Model uncertainty, i.e., the mismatch between the real plant and the nominal model, is defined by the following values: $R_r=R_{rn}\cdot 1.3$, $L_r=L_{rn}\cdot 1.2$, $J=J_n\cdot 2$, $k=k_n\cdot 1.1$. Consequently, the real plant discrete transfer function is

$$G(z)=\frac{z^{-1}(0.00805062+0.00696901z^{-1})}{1-1.64289z^{-1}+0.648344z^{-2}}. \tag{21}$$

Parameters of the digital sliding mode controller have been selected as: $\alpha=10$, $\sigma=10$. The main control loop contains linear digital controller $G_r(z)=(1-0.985z^{-1})/(1-z^{-1})$, which involves an integral action. The controlled DC motor is subjected to a step angular velocity reference.

Step responses of the controlled systems with and without disturbance estimator are shown in Fig. 2, as well as the load torque. Due to the integral action of the main loop controller, the uncompensated system output $y_0(t)$ has zero error only in the section of step like disturbance action. In other sections, system error is significant. The compensated system output $y(t)$ demonstrates an excellent disturbance rejection performance.

According to the enlarged scale of the switching function plotted in Fig. 3., it is confirmed the complete rejection of step and ramp like disturbances by the proposed disturbance estimator. The deviation from the zero value in other sectors is significantly small.

Error signal of he compensated system is shown in Fig. 4. in the enlarged scale also. It may be noticed that the system

has no error in the case of step, ramp and parabolic like disturbance action. This is a result of the combined action of the disturbance estimator and the main controller with integral action.

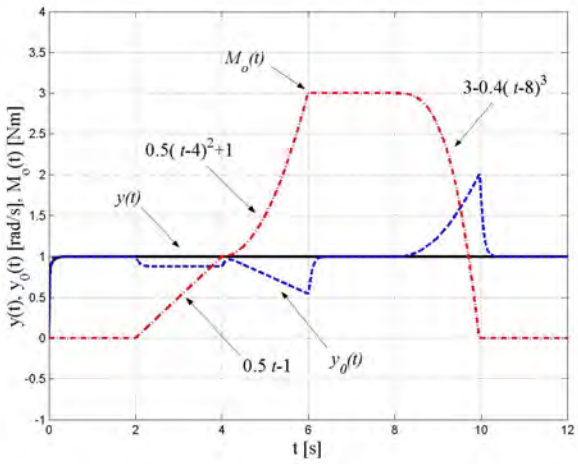

Fig. 2. Step responses of uncompensated system $y_0(t)$, compensated system $y(t)$; and external disturbance $M_o(t)$.

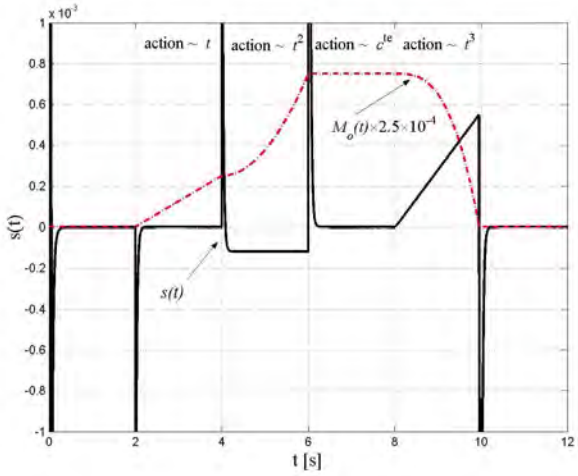

Fig. 3. Switching function $s(t)$.

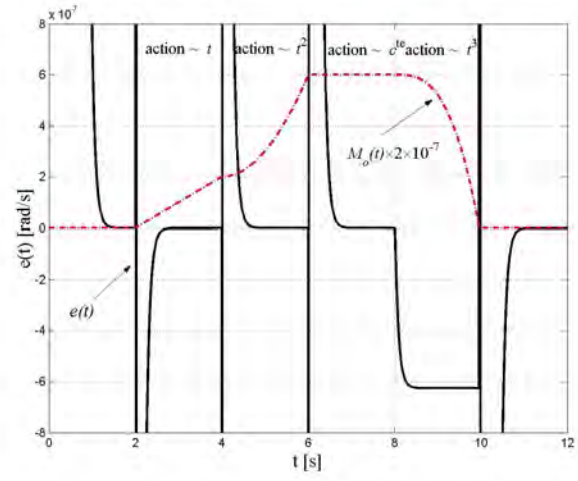

Fig. 4. Error signal $e(t)$ of the compensated system.

V. Conclusion

The proposed input-output based discrete-time disturbance estimator structure, where conventional passive digital filters are replaced with active DSMC subsystem, inherits recognized sliding mode properties with respect to internal and external perturbations. Estimator robustness against model uncertainties is actively gained by providing sliding mode existence conditions. Thus, robustness and good external disturbances rejection property are no longer contradictory requests.

From the control design aspect, the proposed equivalent disturbance compensation method may be viewed as a discrete-time tracking control problem with measurable but unknown in advance reference signal. Sliding mode digital controller governs a nominal model not a real plant, where all state variables are available, offering variety of DSMC algorithms to be utilized. The applied state-space DSMC algorithm enables complete rejection of step and ramp like equivalent disturbances. In all other cases it provides an $O(T^2)$ accuracy.

References

[1] S.M. Suh, C.C. Chung and S.H. Lee, "Discrete-time track following controller design using a state space disturbance observer", Microsystem Technologies, no. 9, pp. 352-361, 2003.

[2] S. Komada, K. Nnomura, M. Ishida and T. Hory, "Robust force control based on compensation for parameter variations of dynamic environment", IEEE Trans. Industrial Electronic, vol. 40, no. 1, pp. 89-95, 1993.

[3] Y. Chou, K. Yang, W.K. Chung, H.R. Kim and H. Suh, "On the robustness and performance of disturbance observers for second-order system", IEEE Trans. Automatic Control, vol. 48, no. 2, pp. 315-320, 2003.

[4] M.R. Stojić and M.S. Matijević, "Structural design of digital control system with immeasurable arbitrary disturbances", The th Mediterranean Conference on Control and Automation, Proceedings of Conference, Dubrovnik, Croatia, 2001.

[5] M.R. Stojić, M.S. Matijević and S. Korać, "Design of IMPACT controlling structure with conventional digital controllers", (invited paper), XLVII ETRAN Conference, Proceedings of Conference, vol. 1, pp. 263-268, Heceg Novi, Serbia and Montenegro, 2003.

[6] V.I. Utkin, *Sliding Modes in Control and Optimization*, Berlin, Springer-Verlag, 1992.

[7] P. Korondi, K.K.D. Young and H. Hashimoto, "Discrete-time sliding mode based feedback compensation for motion control", 1996 IEEE Workshop on Variable Structure Systems, Proceedings of Conference, pp. 127-131, Tokyo, Japan, 1996.

[8] X. Chen, S. Komada and T. Fukuda, "Design of nonlinear disturbance observer", IEEE Trans. Industrial Electronics, vol. 47, no. 2, pp429-437, 2000.

[9] G. Golo and Č. Milosavljević, "Robust discrete-time chattering free sliding mode control", Systems & Control Letters, vol. 41, pp. 19-28, 2000.

[10] B. Veselić, G. Golo and Č. Milosavljević, "Discrete time sliding mode approach to synchronization of modulated two-phase harmonic oscillator", Electrical Engineering, (in press) DOI 10.1007/s00202-003-0209-z, http://dx.doi.org/10.1007/s00202-003-0209-z.

Neural network for polar image processing

Al.Bekiarski[1]

***Abstract*: The wide application of neural network in image processing is less developed in polar image direction. The polar image transformations give the specific advantages for some classes of images, which are composed of objects with circular performances. It is the goal of this article to propose a suitable neural network structure for polar image processing.**
***Keywords*: Polar Images, Neural network, Image processing.**

I. INTRODUCTION

The polar images are very important for some applications in which it is necessary to select the objects with circular performance [1]. The classical methods for image segmentation can do this selection, bur it is not possible to use the specific features of circular objects in images. The other direction of polar image processing are the active image processing, are the active image processing systems [2], in which it is used the eye point of view as a origin of image sampling and processing. These systems are similar and a simple model of some animal eyes system [3]. The application of these methods of polar image processing is very useful in robotic systems.

The goal of this article is to propose a suitable and efficient structure of a neural network for polar image processing.

II. THE POLAR IMAGES REPRESENTATION

Most of the polar images processing systems used a non-uniform sampling as a model of an animal eye. This method give an image representation with densest sample points in the centre and regions of interest, whilst maintaining a wide field of view, but it requires camera movements to allow such regions to be selected. This disadvantages of this is the necessarily of special cameras. The non-uniform method of sampling, which is used very often, is log-polar sampling. In log-polar sampling, pixels are indexed by ring number *R* and wedge number *W*, related to ordinary *x*,*y* image coordinates by the mapping:

$$r = \left[(x - x_c)^2 + (y - y_c)^2 \right]^{1/2} \tag{1}$$

$$\theta = \tan^{-1}\left(\frac{y - y_c}{x - x_c} \right) \tag{2}$$

$$R = \frac{(n_r - 1)\log(r / r_{\min})}{\log(r_{\max} / r_{\min})} \tag{3}$$

$$W = \frac{n_w \theta}{2\pi}, \tag{4}$$

where

r, θ are polar coordinates;

x_c, y_c - position of the centre of the log-polar sampling pattern;

n_r and n_w - the numbers of rings and wedges, respectively;

$r_{\min}$ and $r_{\max}$ - radii of the smallest and largest rings of samples.

A log-polar sampling image is one whose samples are centered on points mapping to integral *R* and $W, R \in \{0, ..., n_r - 1\}, W \in \{0, ..., n_w - 1\}$. this separation. The separation between sample points is proportional to distance from the sample centre. This arrangement appears to be approximated by the ganglion cells of the primate retina and the visual cortex. In this representation, image expansion and rotations about (x_c, y_c) become shifts in *R* and *W*, but image transaction has a more complex effect.

In order to keep a pixel's nearest neighbors in orthogonal directions at approximately equal distance from it, the following constraint is needed:

$$r_{\min} = r_{\max} \ell^{-2\pi(n_r - 1)/n_w}. \tag{5}$$

Log-polar images are displayed on orthogonal (R, W) axes, but this is misleading since it leads them to be regarded as "distorted" representations.

It is possible to define:

$$\rho = \log r = -\log \cos \theta. \tag{6}$$

The graphical relation between ρ and θ is shown in Fig.1.

[1] Aleksanser Bekiarski is with the Faculty of Communications and Communications Technologies, Technical University, Kliment Ohridski 8, 1000
Sofia, Bulgaria, E-mail: aabbv@tu-sofia.bg

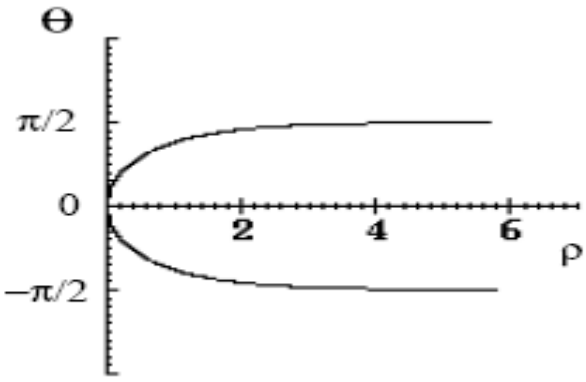

Fig.1. Graphical relation between ρ and θ.

The objects representation in log-polar images is very important, because it give the possibility to decide, which objects are easy to select and separate in log-polar images. As an example of an object representation, in log-polar images here is a representation of straight line:

$$\rho = \rho_l - \log\cos(\theta - \theta_l). \tag{7}$$

The peak of the convolution output will be at (ρ_l, θ_l). The cases for straight line $x = 1$ in orthogonal Cartesian axes give from expression (7):

$$\rho = -\log\cos\theta \tag{8}$$

and is shown in Fig.1.

It is possible to perform an efficient convolution by multiplication in the Fourier domain. It is possible to find a closed – form expression for the Fourier transform of the straight line in log-polar space.

To find the Fourier transform, it is possible to taka a path integral along the line in log-polar space. Let *S* be the standard line $\rho = -\log\cos\theta$ from the equation (8) with element $d\rho$ in (ρ, θ) space, then the integral is:

$$F(k_\rho, k_\theta) = \int_s \ell^{-ik_\rho \rho}\, \ell^{jk_\theta \theta}\, w(\rho,\theta)\, ds, \tag{9}$$

where

$w(\rho,\theta)$ is the wiegnt factor to allow convergence:

$$w(\rho,\theta) = (\cos\theta)^{1-\alpha} \quad 0 \langle \alpha \langle 1. \tag{10}$$

The larger values of α make *F* more localized to the minimum of ρ. An suitable value of α is 0.2.

If substitute $d\theta / ds = \cos\theta$, the integral becomes:

$$F(k_\rho, k_\theta) = \int_{-\pi/2}^{+\pi/2} (\cos\theta)^{ik_\rho - \alpha}\, \ell^{-ik_\theta \theta}\, d\theta. \tag{11}$$

III. THE NEURAL NETWORK FOR POLAR IMAGES PROCESSING

The general methods for polar images processing is based on using local logical on arithmetic operators for object feature selection (lines, edges, bars etc.). It is possible to propose a suitable structure of a neural network and to use the ability of the neural network to be learning for the object feature extraction in log-polar images. The structure of this proposed neural network is shown in Fig.2.

As an input image it is possible to use a conventional Cartesian image following by a log-polar transformation or an active camera input image which is directly represented in log-polar coordinates. The structure of polar neural network can be chosen from traditional types of neural networks: perception Hopfield, Kehonen etc. with appropriate layers, inputs and layers numbers. The neural network input can be represented as a two vectors:

$$IM_R = \begin{bmatrix} ir_0 \\ ir_1 \\ . \\ . \\ ir_{n_r - 1} \end{bmatrix} \quad R \in \{0, ..., n_r - 1\} \tag{12}$$

$$IM_W = \begin{bmatrix} iw_0 \\ iw_1 \\ . \\ . \\ iw_{n_w - 1} \end{bmatrix} \quad W \in \{0, ..., n_w - 1\} \tag{13}$$

in accordance with equations (1), (2), (3) and (4). The learning process can be performed with the following rules: forward, back propagation, associative etc. and is used to collect the objects features as edges, lines etc. At the fig.2 it is shown a last general block named feature, processing as an example to using the extracted the proposed neural network features. This feature processing can be made for a concrete application and output of this block can be used for a following post processing. But as a general necessary application of the output information it is shown at Fig.2 with dashed line the definition and updating of origin (x_c, y_c) of current input image if this is a real complete log-polar image processing system with an active controlled camera.

IV. TEST AND CONCLUSION

A Matlab simulation is prepared for the proposed neural network structure for log-polar images processing. Some of practical results of learning and classification with this neural network for some typical features in polar images edges, bars etc. are shown in Fig.3.

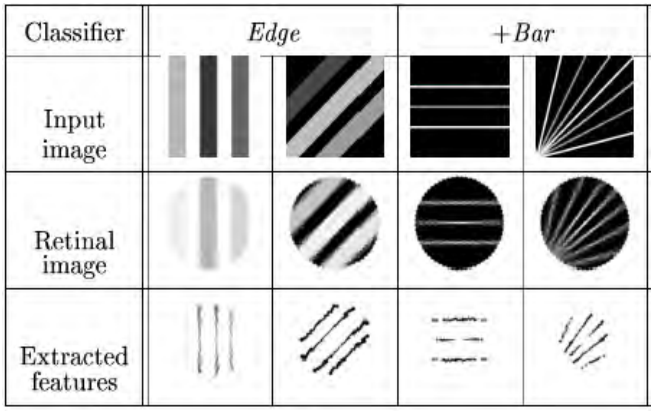

Fig.3. Practical results of neural network testing.

These practical results are only for a confirming the possibility of using such neural network structure and to continue its investigation, extension and real practical applications.

REFERENCE:

[1] Schwarts E.L. Special mapping in the primate sensory projection: analytic structure and relevance to perception. Biological Cibernetics, 25, pp.181÷194, 1998.

[2] Tistarelli M., Sandini G. Dynamic aspects in Active Vision. CVGIP: Image Understanding, 56, pp.108÷129, 1992.

[3] Lim F.L., West G.A.W., Vencatesh S. Use of log-polar space for foveation and feature recognition. IEE Proc.Vis. Image Signal Processing, 144, pp.323÷331, 1997.

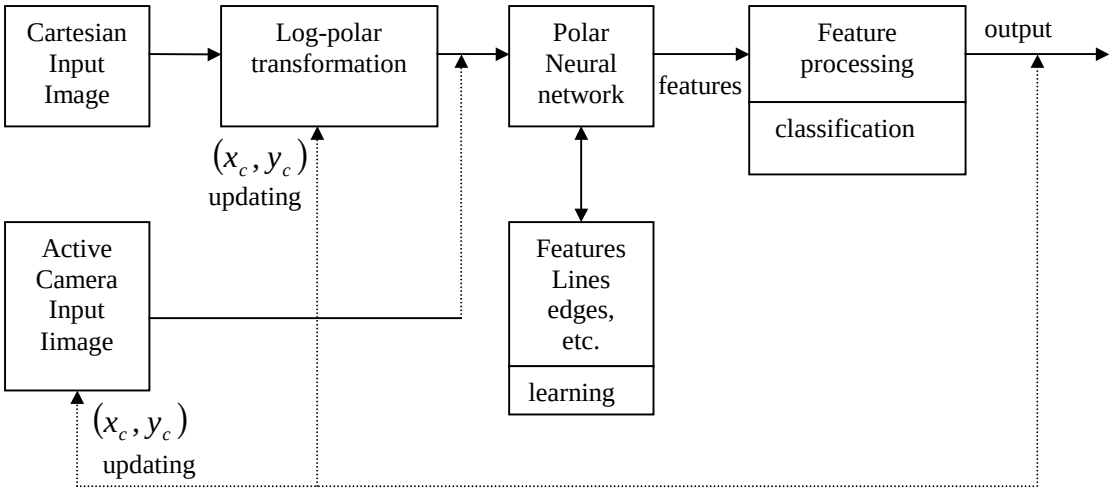

Fig.2. Structure of proposed neural network

Automatic Face Detection in Frontal Color Images

Ognian Boumbarov[1] and Strahil Sokolov[2]

Abstract - **In this work we propose an approach to automatic detection of faces in color images. The proposed approach consist these parts: color space selection, human skin-color modeling, and human skin-color segmentation to identify probable regions corresponding to human faces and facial feature extraction.**

Keywords - **Skin color model, Human skin segmentation, Facial features extraction.**

I. INTRODUCTION

Face tracking and face recognition are basic needs for many fields including surveillance and security, human-machine interfaces, object-based video coding, virtual reality, and automatic 3-D modeling. Although face tracking and recognition is a fundamental part in a fully automated facial analysis system, the first important step is detecting faces in static image and video sequences. There are many variations of image appearance such as pose variation (front and profile), occlusion, image orientation, lighting condition and facial expression [1-2].

In this work we propose an approach to automatic detection of faces in color images. The proposed approach consist of three parts: *color space selection* and *human skin modeling*, *human skin segmentation* to identify probable regions corresponding to human faces and *facial feature extraction.*

The paper is organized as follows. In the following Section the choice of suitable skin color space is described. In Section 3 the use of lighting compensation and single Gaussian modeling for the modeling human of skin is discussed. The face skin color segmentation is given in Section 4. The human skin segmentation employs a model-based approach to represent and differentiate the background colors and skin colors. The final facial feature detection is presented in Section 5. Experimental results evaluating the performance of the algorithm are given in Section 6.

II. MATHEMATICAL DESCRIPTION

Color space selection

Color information is an important feature of human faces. Using skin color as a feature for detecting face skin regions has several advantages. In particular, processing color is faster than processing other facial features. The more so as color information is invariant to face geometrical transformations. However, even under a fixed ambient lighting, people have different skin color appearance.

[1]Ognian Boumbarov is with Faculty of Communication Technics and Technology, Technical University of Sofia, Kl. Ohridski 8, 1000 Sofia, Bulgaria, E-mail: olb@tu-sofia.bg

[2]Strahil Sokolov is with the Faculty of German Engineering Education and Industrial Management (FDIBA), Technical University of Sofia, Kl.Ohridski 8, 1000 Sofia, Bulgaria, E-mail: strahil@gmx.net

Furthermore, to successfully use skin color for face detection, we need to choose color space, in which human skin colors cluster tightly together and cluster in different color spaces. Different color spaces tend to enhance characteristics of images at the expense of reside remotely to background color[1-2]. Color space is a method of color information obtained from a static image and video sequences. Human skin color tends to others[1],[5],[6]. Some color spaces are discussed in this paper.

The RGB color space (or the normalized color space RGB) is one of the most widely used color spaces for processing and storing of digital image data [2],[5],[6].

However, high correlation between the color components, mixing of the chrominance and the luminance data make RGB color space an unfavorable choice for color analysis and recognition.

In the YCbCr color space, color is represented by luma, constructed as a weighting sum of RGB values, and two color difference values Cb and Cr that are formed by subtracting luma from RGB red and blue components [5 - 6]. The transformation simplicity and explicit separation of luminance and chrominance components make this color space very attractive for skin color modeling.

The family of color spaces HSI (V, L) – Hue, Saturation, Intensity (Value, Lightness) was introduced when there was a need for the user to specify color properties numerically[2]. *Hue* defines the dominant color of an area; *saturation* measures the colorfulness of an area in proportion to its brightness. The “intensity”, “lightness” or “value” is related to the color luminance. The explicit discrimination between luminance and chrominance components made this color spaces popular for skin color segmentation. Besides YCbCr color space, several other linear transform of the RGB color space was employed for human skin detection – YES, YUV and YIQ [2], [8], [9].

Many works on face skin detection discard the luminance component of the color space. This decision seems logical, because this is a dimensionality reduction. The goal of any color-based approach is diminishing the influence of the lighting conditions. The chrominance-only color analysis will make the approach partially independent from the lighting conditions.

We choose YCbCr as the processing color space since it is perceptually uniform and separate the luminance and the chrominance components. In our implementation only the CbCr components are used to model the distribution of skin colors. The YCbCr space is of particular interest because it is widely used in still-images and video coding standards such as JPEG, MPEG, and H.263.

Modeling human skin

The purpose of skin color modeling is to build a decision rule that will discriminate between skin and not-skin pixels. The techniques for skin color modeling in YCbCr space can be classified into following categories: parametric, non-parametric, and semi-parametric. A parametric skin color model has a specific functional form (single or mixture Gaussian) [1].[2],[10] with adjustable parameters chosen to fit the model to the input data. A non-parametric model does assume any particular form (e.g. histogram thresholding). A semi- parametric approach applies a very general form with adaptive parameters systematically varied in number as wellas in value in order to create flexible models [11].

Our approach employs a two-dimensional normalized Gaussian probability distribution function for modeling skin color in Cb-Cr space.

Let P_{skin} (C) be the probability of a pixel with chrominace vector C = $[Cb,Cr]^t$ belonging to skin color class. We can shape the distribution of the chrominance components in a Cb-Cr skin space as follows [14]:

$$\text{Pskin (C)} = \frac{1}{2\pi\sqrt{Det\{K\}}}\exp\left[-\frac{(\vec{C}-\vec{\mu})^t K^{-1}(\vec{C}-\vec{\mu})}{2}\right]$$

where $\mu=[\mu_b, \mu_r]^t$ and [K]=Cov(C, μ) respectively are the mean and covariance matrix for the Cb-Cr skin space. The mean and covariance matrix are estimated from a training set. The chrominace vector C= $[Cb,Cr]^t$ is calculated for each color pixel (Cb(i,j), Cr(i,j)) at spatial position (i,j) from the two color components Cb and Cr of the color space YCbCr. The result obtained by skin color modeling with the normalized Gaussian probability distribution function is displayed on **Fig.3** as normalized grayscale map of expected skin regions.

Skin color segmentation

In order to detect a skin color region we must map the skin pixels into a region. Generating of binary skin/non-skin maps strongly depends on lighting conditions and the tuning of the camera. This is supported by the histograms of the normalized grayscale maps of expected skin regions, shown on **Fig.4.**

The abovementioned two facts impose that the skin-color segmentation is implemented via adaptive thresholding. In addition, there are 5 skin-types: white, black, yellow, brown, and red.

In the course of our work were researched various methods of automatic adaptive thresholding for the purpose of intensity segmentation of the grayscale maps of the expected face regions: 1D Fuzzy, 2D Fuzzy, NIR, QIR, and Otsu. Best results were generated by the Otsu-method, as shown on **Fig.5**.

Facial features extraction

In our approach a geometrical model of face representation is chosen, described in [11]. The purpose of this algorithm is automation of the process of feature extraction from full-face images and their representation as multidimensional vector.

There are various methods used for feature extraction. One of them is the method of adjustment of a flexible template [11, 12, 13]. According to this method, the form of the facial elements is approximated with a set of geometrical shapes, whose equations are known. In this way the eyes and the mouth are easily described. Their templates consist of parabolas representing their outlines, and the iris is approximated by a circumference. On the other hand, the eyebrows, the outline of the face, the hair and the nose, cannot be approximated by simple templates, due to their complex shapes. In the described face model are used extraction and analysis only of theeyes and mouth, using the algorithm of face region segmentation using skin color, described in the previous section. The resulting binary map of the expected skin regions of the face (**Fig.5**) considerably narrows the region of search (region of making a decision) and increases the accuracy of extraction of the facial features. Limiting the zones of interest in an input image speeds up the feature-extraction process. The approach for facial features extraction can work separately in recognition of full-face frontal images.

The algorithm for automated extraction of the facial features “eyes” and “mouth” comprises the following basic steps:

- Finding the eyes, or more precisely drawing their surrounding rectangles;
- Estimation of the mouth location by its surrounding rectangle;
- Precise adjustment of the form and location of both eyes and the mouth by setting up flexible templates;
- Extraction of the vector with the features, saving it to a file, designed for neural-network recognition

III. EXPERIMENTAL RESULTS

Photos are usually taken under various lighting conditions. This is the reason why they have variations in quality, color, position, pose and facial expression. Our algorithm has been evaluated on various images from the World Wide Web. We present the evaluation on a set of images from our local database.The experiment took place in the following steps. First, a training set of ten skin samples is loaded, shown on **Fig.1**. Next, the sequence of original images is shown on **Fig.2.** A grayscale map of the expected skin region, shown on **Fig.3,** is generated with the normalized Gaussian probability distribution function. After finding the optimal threshold value with the algorithm of Otsu for every image we obtained a binary mask of the expected skin region, **Fig.5.** Using the binary mask we extract the expected skin region, ingnoring the non-skin regions of the image, as can be seen on **Fig.6.** Finally we use the limited region of the skin to search for facial features, with the algorithm described the previous section. The templates have been precisely adjusted to the eyes and mouth regions of every full-face frontal image, **Fig.7.**

The experiment was implemented on a system, running WindowsXP SP1with a 2.6 GHz Pentium 4. Both algorithms have shown good robustness and reasonable accuracy for the photos from our test sets. The whole facial feature set is detected automatically. The overall feature extraction time with the described algorithms is about 1-2 seconds per one photo on our system.

IV. CONCLUSION

We have presented a method for face detection in frontal images and feature extraction from a detected face region. First of all, our method generates a normalized Gaussian probability distribution of face region in the image.After generating an optimal mask, the face region is being extracted from the original image and is subjected to the algorithm for detection of facial features.The detected features are saved in a file, used for recognition by a neural network. Results for some photos of our test set ave been presented. Our approach is particularly suitable for embedding in surveillance and security systems. Our goal is to implement a system that detects faces and facial features and uses them as patterns for recognition in images and video streams.

ACKNOWLEDGEMENT

This work has been sponsored by the Project 311-7/2003 R & D Department, TU-Sofia.

REFERENCES

[1]. M.Yang, D. Kriegman, N. Ahuja, “Detecting Face in Image: A Survey, IEEE Trans. on PAMI, vol.1, pp. (34-58), January, 2002.

[2]. V.Vezhnevets, V. Sazonov, A. Andreeva, “A survey on pixel-based skin color detection techniques”, Proc. Graphicon-2003, September 2003.

[3]. D. Mayo, D. Miltonic, Real-time face location o gray-scale static images, Pattern Recognition, vol.33, no.9, pp.1525-1539, September 2000.

[4]. H. Rowley, S. Beluga, T. Canada, Neural Networks based face detection, IEEE Trans. PAMI, vol.20, pp. 23-38, January 1998.

[5]. K. Sung, T. Poggie, Example-based learning for view-based human face detection, IEEE Trans. PAMI, vol.20, no.1, January 1998.

[6]. A., Jain, Fundamentals of digital image processing, Prentice – Hall, 1989.

[7]. W., Pratt, Digital I mage processing. AWiley-Interscience Publication. John Wiley&Sons, Inc. 2001.

[8]. E. Saber, A. Tekalp, Frontal-view face detection and facial features extraction using color, shape and symmetry based cost functions, Pattern Recognition Letters, vol.9, pp669-680, 1998.

[9]. F. Marques, V. Vilaplana, A morphological approach for segmentation and tracking of human faces, Int. Conf. on Pattern Recognition (ICPR’00), vol1, pp.5064-5068, 2000.

[10]. Rein-Lien Hsu, M. Abdel-Mottaleb, A. Jain, Face detection in color space, IEEE Trans. PAMI, vol.24, no.5, pp.696-706, 2002.S.Phung, D.Chai, A. Bouzerdoum, A universal and robust human skin color model using neural networks, IEEE, vol. pp.2844-2899, 2001.

[11]. O.Boumbarov, I.Ankov, Feature extraction for face recognition on frontal images, Proc. of International Scientific Conference on Energy and Information Systems and Technologies’2001, vol.2, pp.593-599, Bitola, Macedonia.

[12]. N. Roeder, X.Li, Accuracy Analysis for Facial Feature Detection, Pattern Recognition, vol.29, pp.143-157, 1999.

[13]. J.Deng, F.Lai, Region-Based Template Deformation and Masking for Eye-Feature Extraction and Description, Pattern Recognition, vol.30, pp.403-419, 1997.

[14]. Ed. A. D. Poularikas, The Handbook of Formulas and Tables for Signal Processing, CRC Press LLC, 1999.

Fig.1 Experimental training set of ten color images of faces

Fig.2 Original images of faces

Fig.3 Normalized grayscale maps of expected skin regions

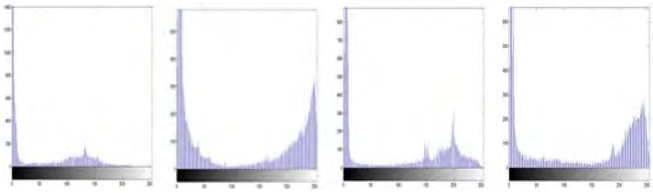

Fig.4.Histograms of normalized grayscale maps of expected skin regions

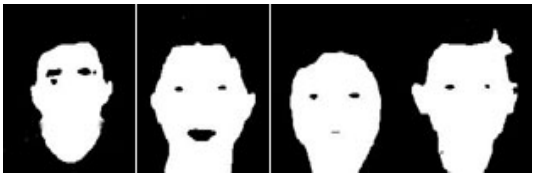

Fig.5 Binary map of expected skin regions

Fig.6 Colormap of expected skin regions

Fig.7 Templates adjusted to original image

Bayesian Super Resolution Estimation for EBCOT Compressed Video

Zoran Ivanovski[1], Ljupcho Panovski[1], Cvetko Mitrovski[2]

Abstract - **In this paper, a new approach to video enhancement based on super-resolution is presented. The proposed method is used to enhance video sequences compressed with the MotionJPEG2000 standard. It is based on a spatial-domain Bayesian maximum a posteriori probability estimator. Simulations and real video experiments show improvement in the peak signal-to-noise ratio as well as improvement in visual quality.**

Keywords - **super-resolution, enhancement, EBCOT, compressed video, MAP estimator.**

I. INTRODUCTION

In the past twenty years, the area of super-resolution (SR) has received considerable attention. Since its beginning, dating back to the work of Huang and Tsai in 1984, numerous algorithms have been proposed with different levels of success. Some of the algorithms approach the SR problem in the frequency domain [1], [2]. Some exploit mapping of low-resolution images onto a HR image plane followed by interpolation and restoration [3]. Another approach to SR, which incorporates prior knowledge about the solution into the reconstruction process, is based on Projection onto Convex Sets (POCS). This is done by restricting the solution to be a member of a closed convex set of vectors that satisfy a particular property [4]. Reconstruction constraints have also been used in a statistical estimation framework. The constraints can be easily embedded in a Bayesian estimator incorporating a prior knowledge about the HR image. Both the Maximum Likelihood (ML) and Maximum a Posteriori Probability (MAP) estimators have been used. Tom and Katsaggelos [5] proposed an ML estimator that estimates the subpixel shifts, the noise variance of each image, and the HR image simultaneously. A MAP estimator that uses an edge preserving Huber-Markov random field for an image prior was proposed by Shultz and Stevenson [6]. Hardie et al. used a MAP estimator for simultaneous estimation of the image registration parameters and the HR image.

Recently, as the use of compressed video grew higher, the problem of enhancing compressed video came into focus.

[1] Zoran Ivanovski and Ljupcho Panovski are with the Faculty of Electrical Engineering, Karpos II bb, 1000 Skopje, Macedonia, E-mails: mars@cerera.etf.ukim.edu.mk; panovski@ukim.edu.mk

[2] Cvetko Mitrovski is with the Faculty of Technical Sciences, Ivo Ribar Lola bb, 7000 Bitola, Macedonia, E-mail: cvetko.mitrovski@uklo.edu.mk

In the last few years several techniques for enhancing compressed video have been proposed. Early techniques usually estimate subpixel motion vectors (using the information from the transmitted ones) before applying the SR process [8], [9], [10]. Later on, techniques that simultaneously estimate motion field and high resolution frame were proposed [11]. Patti and Altunbasak demonstrated the importance of the proper handling of the quantization information and proposed a solution that explicitly exploits the compression process by incorporating the quantization information into a POCS-based algorithm that operates in the compression domain [12], [13]. In order to establish a stochastic framework that can utilize the quantization information, Gunturk et al. in [14] model the additive noise and than transform it to the compressed domain. A Gaussian model for conditional probability is used. In [15] a method to experimentally estimate the conditional probability is proposed. Bayesian reconstruction methods have also been proposed for the minimization of the artifacts introduced by the compression process [10], [16].

Although the framework developed in most of the aforementioned works is general and can be used with all video coding standards where the transform utilized is linear, most of them deal with DCT-based standards. On the other side, new compression techniques are mostly wavelet-based. Usually, the wavelet transform is applied to the image, without dividing it into blocks (tiles), although the possibility of tiling is still given in JPEG2000. The avoidance of tiles eliminates the blocking effect as one of the artifacts of the compression process, and consequently the necessity to optimize the SR technique for its elimination. High compression ratio in JPEG2000 is achieved by optimizing the compression through minimization of the MSE for the desired bit-rate (Tier 2 coding). The minimization (bit-stream generation) phase makes the modeling of the conditional probability density function very difficult. In this paper we demonstrate the possibility of the use of a Gaussian model for the conditional PDF in combination with a prior PDF model based on Markov Random Fields.

II. IMAGING MODEL

The observation model for the low-resolution images in the video sequence assumes that low-resolution images are generated from the high-resolution (HR), ideal, and undegraded images, $\mathbf{z}_k$. These HR images are representing scene values sampled at or above the Nyquist rate. The pixels in the low-resolution image are defined as a weighted sum of appropriate HR pixels with additive noise, with weighting being used to model the blurring that is due to the finite detector size and point spread function (PSF) of the detector and the optics.

Consider low-resolution frames of size $N_1 \times N_2$ pixels. The values of the pixels in the k-th low-resolution frame of the sequence can be expressed as

$$y_{k,m} = \sum_{r=1}^{q^2 N_1 N_2} w_{k,m,r} z_{k,r} + \eta_{k,m} \qquad m = 1,..., N_1 N_2 \tag{1}$$

where $\eta_{k,m}$ is additive noise representing the error in estimating $w_{k,m}$. The noise, $\eta_{k,m}$, is assumed to be an independent and identically distributed (i.i.d.) Gaussian random variable. In Eq. (1), $z_{k,r}$ is the r-th element of the lexicographic representation of the k-th undegraded HR image. Different model weights for every pixel in the low-resolution frames correspond to different amounts of motion at each pixel during the acquisition of each frame. The subpixel motion of every low-resolution pixel relative to the HR grid is essential for the estimation of the HR image. We can express Eq. (1) in matrix notation as

$$\mathbf{y}_k = \mathbf{w}_k \mathbf{z}_k + \mathbf{n}_k \tag{2}$$

The relation between the HR images in a video sequence can be expressed as:

$$\mathbf{z}_k = \mathbf{C}(\mathbf{d}_{k,k-i}) \mathbf{z}_{k-1} \tag{3}$$

where $\mathbf{C}(\mathbf{d}_{k,k-i})$ represents the motion compensation matrix from frame k to frame k-i and $\mathbf{d}_{k,k-i}$ are motion vectors. Hence, the relation between low the resolution images and the different HR images is:

$$\mathbf{y}_{k-i} = \mathbf{AHC}(\mathbf{d}_{k,k-i}) \mathbf{z}_k + \mathbf{n}_{k-i} \tag{4}$$

where $\mathbf{A}$ is the downsampling matrix, and $\mathbf{H}$ is the filtering matrix.

The low resolution images are than compressed before transmission and decompressed at the receiver, yielding

$$\mathbf{g}_{k-i} = \mathbf{T}_{DWT}^{-1} Q^* \left[Q \left[\mathbf{T}_{DWT} \left(\mathbf{AHC}(\mathbf{d}_{k,k-i}) \mathbf{z}_k + \mathbf{n}_{k-i} \right) \right] \right] \tag{5}$$

where $\mathbf{T}_{DWT}$ and Q are the transform matrix and the quantization operator, respectively.

II. Bayesian Map Estimator

In order to estimate the high resolution image $\mathbf{z}_k$ at time k, and the matrix of motion vectors $\mathbf{d}$ that describes the motion between $\mathbf{z}_k$ and M_F+M_B neighboring frames, we form a Bayesian MAP estimator given the low-resolution decompressed frames $\mathbf{g}$ and the appropriate prior. The estimate can be computed by maximizing the a posteriori probability $\Pr(\mathbf{z}_k, \mathbf{d} | \mathbf{g})$, which, according to Bayes theorem, gives:

$$\hat{\mathbf{z}}_k, \hat{\mathbf{d}} = \arg\max \{ \Pr(\mathbf{g} | \mathbf{z}_k, \mathbf{d}) \Pr(\mathbf{z}_k) \Pr(\mathbf{d}) \} \tag{6}$$

or by maximizing the log-likelihood function

$$\begin{aligned} \hat{\mathbf{z}}_k, \hat{\mathbf{d}} = \arg\max \{ & \log \left[\Pr(\mathbf{g} | \mathbf{z}_k, \mathbf{d}) \right] \\ & + \log \left[\Pr(\mathbf{z}_k) \right] + \log \left[\Pr(\mathbf{d}) \right] \} \end{aligned} \tag{7}$$

The probability $\Pr(\mathbf{d})$ is ignored since it is not a function of $\mathbf{z}_k$ or $\mathbf{d}$. It is assumed that $\mathbf{z}_k$ and $\mathbf{d}$ are statistically independent.

The first term in Eq. (7) is a conditional probability that models the errors in estimating the motion vectors, errors introduced during the conversion of the high resolution image to the low resolution observation and the noise introduced during the compression. Assuming that the error between frames is zero-mean i.i.d. Gaussian, we can write:

$$\Pr(\mathbf{g} | \mathbf{z}_k, \mathbf{d}) \propto \exp\left\{ -\frac{1}{2} \beta \sum_{i=-MB}^{MF} \left\| AC(\mathbf{d}_{k,k-i}) \mathbf{z}_k - \mathbf{g}_{k-i} \right\|^2 \right\} \tag{8}$$

where $\beta = \dfrac{1}{\sigma_n^2}$ and σ_n^2 is the noise variance.

The second term in Eq. (7) is the prior HR image model. We assumed a local conditional PDF based on Markov Random Fields which penalizes the difference between the pixel intensity and the averaged intensity value of its four neighboring pixels:

$$\Pr(\mathbf{z}_k) \propto \exp\left\{ -\frac{1}{\lambda} \left\| \mathbf{z}_k - \mathbf{a}\mathbf{z}_k \right\|^2 \right\} \tag{9}$$

where $\mathbf{a}$ represents the four neighbors averaging matrix and λ is a "tuning" parameter.

By substituting Eqs. (8) and (9) into Eq. (7) we obtain:

$$\hat{\mathbf{z}}_k, \hat{\mathbf{d}} = \arg\min \left\{ \beta \sum_{i=-MB}^{MF} \left\| AC(\mathbf{d}_{k,k-i}) \mathbf{z}_k - \mathbf{g}_{k-i} \right\|^2 + \frac{1}{\lambda} \left\| \mathbf{z}_k - \mathbf{a}\mathbf{z}_k \right\|^2 \right\} \tag{10}$$

The minimization of Eq. (10) is accomplished through a cyclic coordinate-descent minimization procedure. At each iteration n, the motion parameters estimates are updated through a search procedure to minimize Eq. (10) with respect to $\mathbf{d}$, given that $\mathbf{z}_k = \hat{\mathbf{z}}_k^n$.

$$\hat{\mathbf{d}}^n = \arg\min \left\{ \beta \sum_{i=-MB}^{MF} \left\| AC(\mathbf{d}_{k,k-i}) \mathbf{z}_k^n - \mathbf{g}_{k-i} \right\|^2 \right\} \tag{11}$$

Adaptive block-matching algorithm is used as a search procedure.

Once the estimate for the motion parameter is found, a steepest descent technique is employed to minimize Eq. (10) with respect to $\mathbf{z}$ and to estimate $\hat{\mathbf{z}}_k^{n+1}$.

IV. Experimental Results

Two sets of experiments were conducted to test the performance of the algorithm. The first set of experiments was performed on a simulated sequence of images. A single HR image was used to produce a sequence of low-resolution images, with given subpixel motion. The generated sequence of low-resolution images was compressed and decompressed using the EBCOT compression algorithm (JPEG2000). In the second set of experiments, a real video sequence was used.

In the first set of experiments, the "cameraman" image was used to produce a sequence of three 144 × 176 low-resolution images, the second image being shifted -0.3 pixels in both directions, and the third being shifted 0.5 pixels in both directions. All three images were then compressed with the EBCOT algorithm to a compression ratio of 40:1 and decompressed. The decompressed images were used as the input for the SR estimation procedure. Despite the fact that only three images were used, a PSNR gain of 0.85 dB was achieved. The visual quality of the image also improved. Fig. 1(a) shows the original image, Fig. 1(b) shows the compressed image, and Fig. 1(c) shows the image obtained after the SR procedure was applied. The results shown were achieved with $\lambda = 1$ and with a fixed-size block matching algorithm in a motion estimation procedure with 0.1 pixel accuracy. The procedure was stopped after 2 iterations, since no further significant visual improvement was noticed.

Fig. 1(a) The original "cameraman" image

Fig. 1(b) The reconstruction of the EBCOT compressed "cameraman" image

Fig. 1(c) The SR enhanced reconstruction of the EBCOT compressed "cameraman" image

In the second set of experiments, the “coastguard” video sequence was used, consisting of 300 frames with resolution 144×176, recorded at 30 fps. Fig. 2 shows the PSNR gain for all frames following the applicatoin of the SR procedure with $\lambda = 1$ and motion estimation with 0.1 pixel accuracy. Again, the procedure was stopped after 2 iterations, since no further significant visual improvement was noticed. The region with large negative values in Fig. 2 demonstrates that the SR procedure could be destructive for the quality if inappropriate parameters are applied. Namely, this region corresponds to a particular part of the "coastguard" video sequence, which contains very large motion shifts, much larger than the range of the motion estimation search window. However, outside this region, the average PSNR gain is at the level of 0.5 dB.

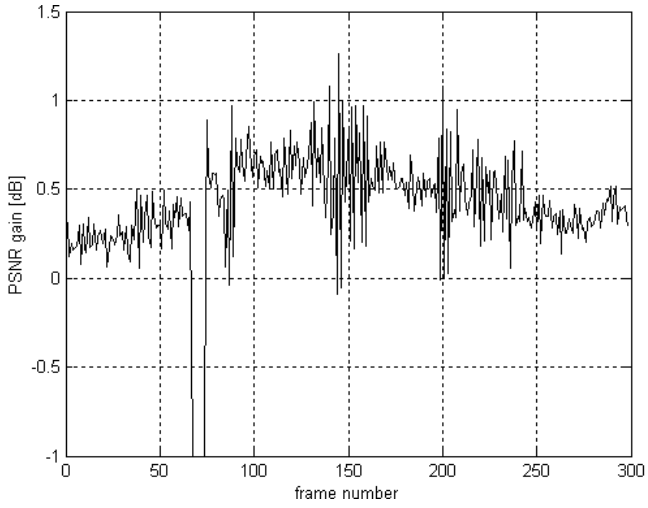

Fig 2. PSNR gain for the "coastguard" sequence

Figs. 3 (a), (b) and (c) show frame #145 of the original, of the compressed, and of the SR processed sequence, respectively.

Fig 3(a) Frame #145 of the original "coastguard" sequence

Fig. 3(b) Reconstruction of frame #145 of the EBCOT compressed "costguard" sequence

Fig. 3(c) SR enhanced reconstruction of frame #145 of the EBCOT compressed "coastguard" sequence

V. CONCLUSIONS

An algorithm for video enhancement of video sequences compressed with MotionJPEG2000 is proposed, which is based on a spatial-domain Bayesian maximum a posteriori probability estimator. Simulations and real video experiments show improvements in the peak signal-to-noise ratio of up to 1 dB both in the case of simulated video sequences and in real video. At the same time, along with the improvements in the PSNR, improvements in the visual quality are achieved as well.

REFERENCES

[1] R. Y. Tsai and T. S. Huang, "Multiframe Image Restoration and Registration", *Advances in Computer Vision and Image Processing*, vol. 1, pp. 317-339, JAI Press Inc., 1984.

[2] S. P. Kim, N. K. Bose and H. M. Valenzuela, "Recursive Reconstruction of High-Resolution Image from Noisy Undersampled Multiframes", IEEE Trans. Acust., Speech, Signal Processing, vol. 38, No. 6, pp. 1013-1027, 1990.

[3] N. Nguyen and P. Milanfar, "An Efficient Wavelet-Based Algorithm for Image Superresolution", Proc. Int. Conf. Image Processing, vol. 2, pp. 351-354, 2000.

[4] H. Stark and P. Oskoui, "High Resolution Image Recovery from Image-Plane Arrays, Using Convex Projection", J. Opt. Soc. Am. A, vol. 6, pp. 1715-1726, 1989.

[5] B. C. Tom and A. K. Katsaggelos, "Reconstruction of a High-Resolution Image by Simultaneous Registration, Restoration, and Interpolation of Low-Resolution Images", Proc. 1995 IEEE Int. Conf. Image Processing, vol. 2, pp. 539-542, 1995.

[6] R. R. Shultz and R. L. Stevenson, "Extraction of High-Resolution Frames from Video Sequences", IEEE Transaction on Image Processing, vol. 5, no. 6, pp. 996-1011, 1996.

[7] R. C. Hardie, K. J. Barnard and E. E. Armstrong, Joint MAP Registration and High-Resolution Image Estimation Using a Sequence of Undersampled Images", IEEE Transaction on Image Processing, vol. 6, no. 12, pp. 1621-1633, 1997.

[8] Y. Altunbasak and A. J. Patti, "A Maximum A Posteriori Estimator for Higher Resolution Video Reconstruction from MPEG Video", Proc. of the IEEE ICIP, Vancouver, BC, Canada, Sept. 10-13, 2000.

[9] A. K. Katsaggelos and N. P. Galatsanos, eds. *Signal Recovery Techniques for Image and Video Compression and Transmission*, Kluwer Academic Publishers, 1998.

[10] J. Mateos, A. K. Katsaggelos and R. Molina, "Resolution Enhancement of Compressed Low Resolution Video", Proc. of ICASSP 2000, vol. 4, pp. 1919-1922, 2000.

[11] J. Mateos, A. K. Katsaggelos and R. Molina, "Simultaneous Motion Estimation and Resolution Enhancement of Compressed Low Resolution Video", Proc. of ICASSP 2000, 2000.

[12] Y. Altunbasak, A. J. Patti and R. M. Mersereau, "Super-Resolution Still and Video Reconstruction from MPEG-Coded Video", IEEE Trans. Circuits Syst. VId. Technol., vol. 12, pp. 217-226, Apr. 2002.

[13] Y. Altunbasak and A. J. Patti, "Artifacts Reduction for Set Theoretic Super Resolution Image Reconstruction with Edge Adaptive Constraints and High-Order Interpolants", IEEE Trans. Image Processing, vol. 10, pp. 179-186, Jan. 2001.

[14] B. K. Gunturk, Y. Altunbasak and R. M. Mersereau, "Bayesian Resolution Enhancement Framework for Transform-Coded Video", Proc. IEEE ICIP, vol. 2, pp. 41-44, 2001.

[15] B. K. Gunturk, Y. Altunbasak and R. M. Mersereau, "Multiframe Resolution-Enhancement Methods for Compressed Video", IEEE Signal Processing Letters, vol. 9, no. 6, pp. 170-174, June 2002.

[16] C. A. Segall, R. Molina, A. K. Katsaggelos and J. Mateos, "Bayesian High-Resolution Reconstruction of Low-Resolution Compressed Video", Proc. ICIP, vol. 2, pp. 25-28, 2001.

Audio Watermarking in the Phase-Frequency Domain

R. Kountchev[1], R. Mironov[2]

Abstract - **A new approach for audio watermarking in the phase-frequency domain is presented, based on the Inverse Difference Decomposition with Complex Hadamard Transform. The main advantages are the absence of quantization noise, the lower computational complexity and the ability for the owner of the audio contents and for the authorized distributors to insert different watermarks in the protected audio signal.**

Keywords: digital audio watermarking, inverse difference decomposition, Complex Hadamard transform

I. INTRODUCTION

In correspondence with the up-to-date methods for audio watermarking [1,2], the watermarks are inserted in the time- or frequency domain of the audio signal, using some kinds of masking effects, which concern the sound perception in accordance with the human auditory system (HAS) [3]. In order to make the distortions, resulting from the watermark insertion in the time domain smaller [1], the watermark is presented as a pseudo-noise binary sequence, which is added to the corresponding discrete values of the audio segments. In the cases, when the watermarking is performed in the audio signal spectrum [2], usually are modified the amplitudes and the phases of selected complex low-frequency coefficients, obtained using one of the known discrete linear transforms: Fourier, Fourier-Mellin, Radon, etc. The second approach was developed for discrete cosine and wavelet transforms [4], for which the corresponding spectrum coefficients are real numbers. In this case is used modulation of selected cosine coefficients in the middle-frequency band of the audio signal, or the pseudo-random sequence is inserted in some components of its wavelet decomposition. The basic qualities of the spectrum approach for watermark insertion [1] are its practical inaudibility (transparency), the high resistance against pirates and fraud attacks, audio compression, time scaling, amplitude corrections, linear and nonlinear filtration, noising and applying of special effects.

In this work is offered a high-efficient method for audio watermarking, based on the modification of the phases of the spectrum coefficients in every level of their Inverse Difference Decomposition (IDD) with Complex Hadamard Transform (CHT), in correspondence with [5].

II. MATHEMATICAL DESCRIPTION

Audio Watermarking Based on IDD with CHT.

The new principle is based on CHT of the discrete audio signal components x(k) for k=0,1,..,N-1 and $N=2^n$, decomposed with two-level IDD, with number l=0,1:

$$x(k)=\tilde{x}_0(k)+\tilde{e}_0^s(k)+e_1(k)\,. \qquad (1)$$

For the level l=0 the component $\tilde{x}_0(k)$ is described with the approximation model of x(k), defined by the relations (2):

$$\tilde{x}_0(k)=CHT^{-1}\{F_0[y_0(u)]\}\,,\; y_0(u)=CHT[x(k)]\,,\; k,u=\overline{0,N-1}\,.$$

The operators CHT[•] and CHT[•]$^{-1}$ represent the direct and the inverse CHT of the signal x(k), by (3):

$$y(u)=\sum_{k=0}^{N-1}x(k)t(u,k)=y_{Re}(u)+jy_{Im}(u)\,,\; x(k)=\frac{1}{N}\sum_{u=0}^{N-1}y(u)t^*(u,k)$$

where: $y_{Re}(u)$ and $y_{Im}(u)$ are correspondingly the real and the imaginary part of the complex coefficient $y(u)=M(u)\exp[j\varphi(u)]$, M(u) and φ(u) represent the amplitude and the phase spectrums of the audio signal x(k), and t(u,k) and $t^*(u,k)$ are the elements of the matrices for the direct and inverse CHT:

$$t(u,k)=j^{-uk}h(u,k)\;;\; t^*(u,k)=j^{uk}h(u,k), \qquad (4)$$

$$h(u,k)=\begin{cases}1 & \text{for} \quad n=2;\\ \prod_{r=3}^{n}(-1)^{\lfloor u/2^{r-1}\rfloor\lfloor k/2^{r-1}\rfloor} & \text{for } n=3,4,...\end{cases} \qquad (5)$$

Here $\lfloor * \rfloor$ is an operator, which represents the integer part of the result, obtained after the division.

For the level l=1 at first is defined the zero difference $e_0(k)=x(k)-\tilde{x}_0(k)$, from which is calculated its approximation model:

$$\tilde{e}_0^s(k)=CHT^{-1}\{F_1[y_1^s(u)]\}\,,\; y_1^s(u)=CHT[e_0(k)] \text{ for } s=1,2. \qquad (6)$$

Here for s=1 the components $\tilde{e}_0^s(k)$ and $y_1^s(u)$ are defined from the difference $e_0(k)$, when k=0,1,..,(N/2)-1. For s=2 these components are defined from $e_0(k)$, when k=(N/2),(N/2)+1,..,N-1. The operators $F_0[.]$ and $F_1[.]$ represent the filtration of the spectrum of every segment in the levels l=0,1 of IDD, consisting in truncation of a selected part of the spectrum coefficients. The retained coefficients must be even number, complex-conjugated couples.

For the inverse CHT the "truncated" coefficients should be substituted with zeros. The last, residual component in the decomposition of Eq. (1) is defined as:

$$e_1(k)=e_0(k)-\tilde{e}_0^s(k)\,, \text{ for } s=1,\,2. \qquad (7)$$

In particular, in case, that from the spectrum of every segment in the levels l=0,1 are selected the complex-

[1]Roumen Kountchev is with the Faculty of Telecommunications, Technical University of Sofia, Boul. Kl. Ohridsky, 8, Sofia 1000, Bulgaria. E-mail: rkountch@tu-sofia.bg

[2]Roumen Mironov is with the Fac. of Telecomm., TU of Sofia, Boul. Kl. Ohridsky 8, Sofia 1000, Bulgaria. E-mail: rpm@tu-sofia.bg

conjugated coefficients with frequencies $u_1=4m+1$ and $u_2=4m+3$ only, is obtained:

$$y_0(u_1)=CHT[x(k)]=y_{0Re}(u_1)+jy_{0Im}(u_1)=y_0^*(u_2) \quad (8)$$

$$M_0(u_1)=M_0(u_2)\,, \qquad \varphi_0(u_1)=-\varphi_0(u_2)\,, \quad (9)$$

$$y_1^s(u_1)=CHT[e_0(k)]=y_{1Re}^s(u_1)+j\,y_{1Im}^s(u_1)=y_1^{s*}(u_2)\,,\ s=1,2, \quad (10)$$

$$M_1^s(u_1)=M_1^s(u_2)\,, \quad \varphi_1^s(u_1)=-\varphi_1^s(u_2) \quad (11)$$

The watermark elements w_l, which are inserted in the levels l=0,1 of IDD, modify the phases $\varphi_1^s(u_1)$ and $\varphi_1^s(u_2)$ of the corresponding spectrum coefficients $y_1^s(u_1)$ and $y_1^s(u_2)$ in accordance with:

$$\varphi_{lw}(u_1)=\varphi_l(u_1)+w_l(u_1)\,,\ \varphi_{lw}(u_2)=-\varphi_{lw}(u_1)\,. \quad (12)$$

In the level l=1 of IDD for every value of s=1,2 could be changed the corresponding phases $\varphi_1^s(u_1)$ and $\varphi_1^s(u_2)$ of the two coefficients couples $y_1^s(u_1)$ and $y_1^s(u_2)$, i.e. there could be inserted two different values $w_1^1(u_1)$ and $w_1^2(u_1)$. In order to retain the subjective quality of the watermarked signal equal with that of the original one, the maximum value of every element of the watermark w_l for a given IDD level must be restricted in correspondence with the requirement $|w_l|\le 0{,}05$ rad ($\le 3^0$). This ensures practical inaudibility of the changed phases of the spectrum components with frequencies (u_1) and (u_2) in the two IDD levels, in case that the sequence of w_l elements has a pseudorandom structure, without zero values. The requirement for watermark sign secrecy is answered performing the function "exclusive OR" for every w_l element with its corresponding element from the pseudorandom sequence, which represents the chosen secret key.

The audio signal $x_w^l(k)$, watermarked in accordance with Eq. (14) for the level l of IDD is correspondingly:

$$x_w^0(k)=\tilde{x}_{0w}(k)+e_0(k)=\tilde{x}_{0w}(k)+x(k)-\tilde{x}_0(k) \quad \text{for l=0,} \quad (13)$$

$$x_w^1(k)=\tilde{x}_{0w}(k)+\tilde{e}_{0w}^s(k)+e_0(k)-\tilde{e}_0^s(k) \quad \text{for l=1 and s=1,2} \quad (14)$$

Here $x_w^0(k)$ contains the element w_0, and $x_w^1(k)$ - respectively the elements w_0, w_1^1 and w_1^2.

The components $\tilde{x}_{0w}(k)$, $\tilde{e}_{0w}^s(k)$, in Eqs. (13) and (14), are defined in correspondence with:

$$\tilde{x}_{0w}(k)=CHT^{-1}\{F_0[M_0(u)\exp\varphi_{0w}(u)]\}\,, \quad (15)$$

$$\tilde{e}_{0w}^s(k)=CHT^{-1}\{F_1[M_1^s(u)\exp\varphi_{1w}^s(u)]\} \quad \text{for s=1,2,} \quad (16)$$

Here, using $F_0[\bullet]$ and $F_1[\bullet]$ from the spectrum in levels l=0,1, are selected only the coefficients with frequencies (u_1) and (u_2), whose phases $\varphi_{0w}(u_1)$ and $\varphi_{1w}^s(u_2)$ for s=1,2 are modified in correspondence with Eq. (14). The described watermarking principle permits the insertion of (L+2R) elements w_l of the watermark signs in every N-dimensional audio segment, modifying the phases of the 2L complex conjugated CHT coefficients from the level l=0, and of the 4R coefficients - in the level l=1 (L and R are selected in the interval from 1 to N/4).

The watermark extraction from the watermarked audio signal $x_w^0(k)$ or $x_w^1(k)$, defined from Eqs. (13) and (14), could be performed using the original signal x(k). In this case the elements $w_0(u_1)$ are defined using the relations:

$$y_{0w}(u_1)=CHT\{x_w^0(k)\vee x_w^1(k)\}, \quad y_0(u_1)=CHT\{x(k)\}\,. \quad (17)$$

Then, if $\varphi_0(u_1)\neq 0$, from Eqs. (14) and (21) follows:

$$w_0(u_1)=\varphi_{0w}(u_1)-\varphi_0(u_1)\,. \quad (18)$$

The elements $w_1^1(u_1)$ and $w_1^2(u_1)$ for s=1,2 are defined in accordance with:

$$y_{1w}^s(u_1)=CHT\{e_{0w}^s(k)\}\,, \quad y_1^s(u_1)=CHT\{e_0^s(k)\}\,. \quad (19)$$

In Eq. (19) the differences $e_{0w}^s(k)$ and $e_0^s(k)$ are equal to:

$$e_{0w}^s(k)=x_w^l(k)-\tilde{x}_{0w}(k)\,, \ e_0^s(k)=x(k)-\tilde{x}_0(k)\,. \quad (20)$$

Here $x_w^l(k)$, $\tilde{x}_{0w}(k)$ and $\tilde{x}_0(k)$ are calculated, using Eqs. (14), (15) and (2).

In case, that $\varphi_1^s(u_1)\neq 0$, the elements of the watermark are defined with the relation: $w_1^s(u_1)=\varphi_{1w}^s(u_1)-\varphi_1^s(u_1)$. (21)

In order to obtain higher reliability for the watermark detection, the elements w_l, extracted from the audio segments, must be compared with their originals w_l^*. For this purpose is used the coefficient of the normalized cross correlation ρ_l of the two sequences w_l and w_l^* [2]. The solution for the watermark detection in the first IDD level is taken when the condition in Eq. (22) for l=0,1 is answered:

$$\rho_l(w_l,w_l^*)=\left\{\sum_{n=1}^{N_l} w_l(n)\,w_l^*(n) \Big/ \sqrt{\sum_{n=1}^{N_l} w_l^2(n)}\sqrt{\sum_{n=1}^{N_l} w_l^{*2}(n)}\right\}\ge T_l$$

Here T_l is a threshold, selected in advance, and N_l is the number of segments, containing the elements w_l.

Algorithm for Watermarking of Audio Segments.

Based on the already described principle here follows the algorithm for watermarking of a couple of complex conjugated CHT coefficients, generalized for M couples. In case, that from all the CHT coefficients of the N-dimensional audio segment in the level l=0, we retain only the couple $y_0(u_1)$ and $y_0(u_2)$, its approximation model is defined in accordance with the Eqs. (2)-(6) and (8)-(9), as follows:

$$\begin{aligned}\tilde{x}_0(k)&=(1/N)[y_0(u_1)j^{(u_1)k}h(u_1,k)+y_0(u_2)j^{(4m+3)k}h(u_2,k)]=\\&=(1/N)M_0(u_1)h(u_1)j^k[e^{j\varphi_0(u_1)}+(-1)^k e^{-j\varphi_0(u_1)}].\end{aligned} \quad (23)$$

Here:

$$y_0(u_1)=y_0^*(u_2)=\sum_{k=0}^{N-1} x(k)h(u_1,k)j^{-k}=C_0(u_1)+jD_0(u_1) \quad (24)$$

$$C_0(u_1)=\sum_{v=0}^{(N/4)-1}[x(4v)-x(4v+2)](-1)^{\alpha_0(m,v)},$$
$$D_0(u_1)=\sum_{v=0}^{(N/4)-1}[x(4v+3)-x(4v+1)](-1)^{\alpha_0(m,v)}, \quad (25)$$

where: $\alpha_0(m,v)=\sum_{r=3}^{\lg_2 N}\lfloor m/2^{r-3}\rfloor\lfloor v/2^{r-3}\rfloor$.

The module and the phase of the coefficient $y_0(u_1)$ are represented with:

$$M_0(u_1)=\sqrt{C_0(u_1)^2+D_0(u_1)^2},\ \varphi_0(u_1)=\mathrm{arctg}[D_0(u_1)/C_0(u_1)]. \quad (26)$$

From Eqs. (27-30) follows that after watermarking in accordance with the Eqs. (12-13) is obtained the marked audio signal for the level l=0 - $x_w^0(p)=x(p)-[\tilde{x}_0(p)-\tilde{x}_{0w}(p)]$. For p=4v, 4v+1,4v+2,4v+3 and v=0,1,..,(N/4)-1 following:

$$x_w^0(4v)=x(4v)-a_0(m), \quad x_w^0(4v+1)=x(4v+1)-b_0(m), \quad (27)$$
$$x_w^0(4v+2)=x(4v+2)+a_0(m), \quad x_w^0(4v+3)=x(4v+3)+b_0(m), \quad (28)$$

where: $a_0(m)=\frac{2}{N}[C_0(u_1)\beta_0(m)+D_0(u_1)\delta_0(m)]$, (29)

$$b_0(m)=\frac{2}{N}[C_0(u_1)\delta_0(m)-D_0(u_1)\beta_0(m)], \quad (30)$$

$$\beta_0(m)=1-\cos[w_0(u_1)],\ \delta_0(m)=\sin[w_0(u_1)],$$

These relations are used as a base for the algorithm for watermark insertion in the IDD level l=0. At the beginning, in the Eq. (25) are calculated the values of $C_0(u_1)$ and $D_0(u_1)$, which after that are substituted in Eqs. (29) and (30) for the calculation of $a_0(m)$ and $b_0(m)$. Then, from Eqs. (27)-(28) are calculated the values of the marked signal $x_w^0(k)$.

The watermark extraction from $x_w^0(k)$ is performed using the original x(k), $a_0(m)$ and $b_0(m)$, defined with the differences:

$$a_0(m)=x(4v)-x_w^0(4v)=x_w^0(4v+2)-x(4v+2), \quad (31)$$
$$b_0(m)=x(4v+1)-x_w^0(4v+1)=x_w^0(4v+3)-x(4v+3). \quad (32)$$

From Eq. (25) are calculated $C_0(u_1)$ and $D_0(u_1)$, and together with the obtained values for $a_0(m)$ and $b_0(m)$ they are substituted in:

$$w_0(u_1)=\arcsin\left\{\frac{N[a_0(m)D_0(u_1)+b_0(m)C_0(u_1)]}{2[C_0(u_1)^2+D_0(u_1)^2]}\right\} \quad (33)$$

The last relation is the solution of the system of Eqs. (29)-(30) concerning the element $w_0(u_1)$ of the corresponding watermark in the case, when l=0. In similar way are inserted and extracted the watermarks w_1^1 and w_1^2. The described algorithm is generalized for the watermarking of M complex-conjugated couples of CHT coefficients in every level of IDD.

In the cases, when the watermark extraction does not require the original audio signal, could be used correlation detection based on the sequence of watermark elements, known in advance:

- In correspondence with Eqs. (40)-(45), for the level l=0 of the IDD the watermarked audio signal could be represented with a sequence of N-dimensional vectors of the kind: $Z_0=X+G_0=X+w_0S_0(M)$, where: $X=[x(0), x(1), x(2),..., x(k),..., x(N-1)]^t$ is the vector of the original audio segment; $G_0=w_0S_0(M)$ - vector with elements $g_0(k)=w_0s(k)$ for $k=\overline{0,N-1}$ and Z_0 – vector with elements $z_0(k)=x(k)+g_0(k)=x_w(k)$, corresponding with the watermarked audio segment.

- Let $W_0=w_0[-1,-1,+1,+1,...,-1,-1,+1,+1]^t$ represents the N-dimensional vector for watermark in the level l=0. In this case, the coefficient of the normalized cross correlation ρ_0 of the couple of vectors Z_0 and W_0 from the sequence of N-dimensional audio segments is defined with:

$$\rho_0(Z_0,W_0)=(Z_0W_0)/\|W_0\|^2=$$
$$=[1/(w_0N)]\left|\sum_{v=0}^{(N/4)-1}[x_w(4v+2)+x_w(4v+3)-x_w(4v)-x_w(4v+1)]\right| \quad (34)$$

The condition for the detection of the element w_0 of the watermark in the level l=0 of IDD for every audio segment could be represented with the relation: $\rho_0(r)>T_0$, where:

$$\rho_0(r)=\left|\sum_{v=0}^{(N/4)-1}[x_w(4v+r+2)+x_w(4v+r+3)-x_w(4v+r)-x_w(4v+r+1)]\right|.$$

For r=0,1,…,N-1 should be found the maximum of ρ_0. It must not be bigger than the threshold T_0, which defines the probability for false alarm or missing the element w_0. The elements w_1^1 and w_1^2 in the level l=1 of IDD for every audio segment could be extracted in similar way, using the corresponding correlation, ρ_1.

The main advantage of the described algorithm for watermark extraction is its universality, due to the fact, that it does not require the use of the original audio signal. In this case, however, the probability for false detection or missing is higher.

III. Evaluation of the Watermark Efficiency

As criteria for the watermark quality evaluation in every IDD level, could be used the mean square error (MSE) of the watermarked audio signal $x_w^0(k)$ or $x_w^1(k)$ in respect to the original, x(k). For a segment of N discrete values MSE is defined from the relation:

$$\overline{\varepsilon_l^2}=\frac{1}{N}\sum_{k=0}^{N-1}[x(k)-x_w^l(k)]^2 \quad \text{for } l=0,1. \quad (35)$$

Then the signal/noise ratio (SNR) is defined with:

$$SNR_l=10\lg_{10}\{\sum_{k=0}^{N-1}x(k)^2/\overline{\varepsilon_l^2}\}\ \text{dB} \quad \text{for } l=0,1. \quad (36)$$

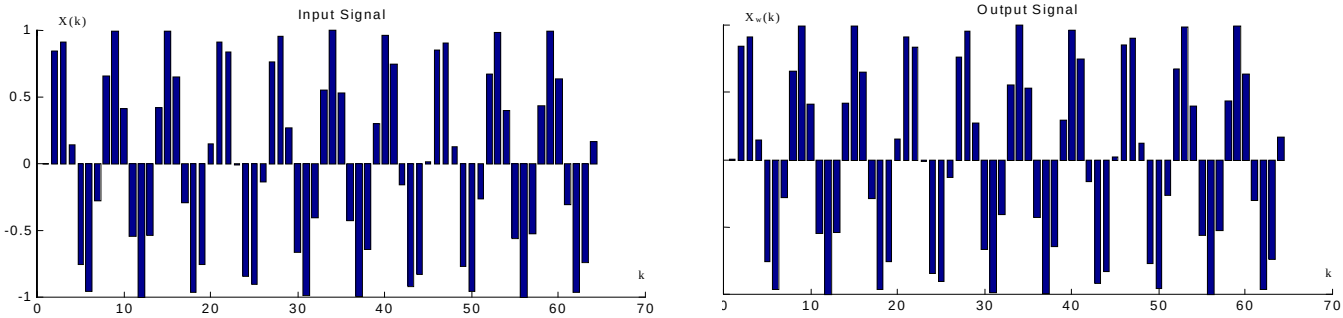

Fig.1. The original and watermarked test signals with 64 samples each.

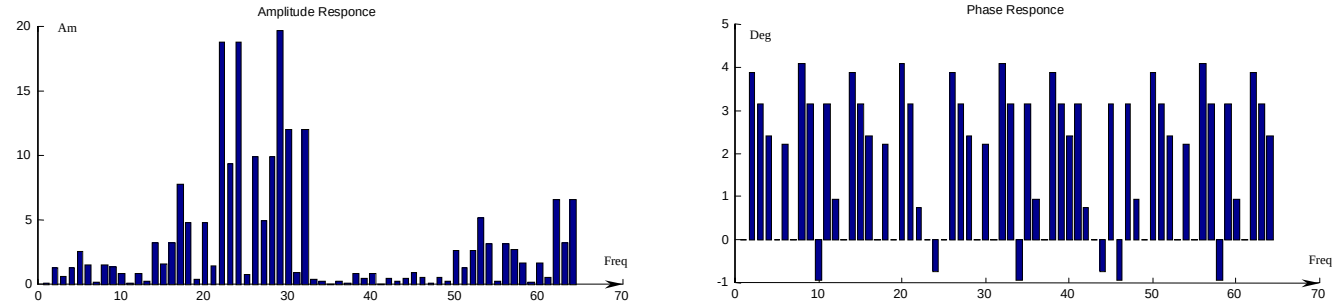

Fig.2. Amplitude and phase responses of the tested signal.

From the Eqs. (35) and (36) follows that the relation SNR_l grows together with the increasing of N and the decreasing of the value of the watermark element w_l.

The described method for audio watermarking was tested with great number of test audio signals, with length 25s, stored as WAVE files, with sampling frequency 44.1 kHz, 16 bits. The audio signals were divided in segments, 256 samples each. For L=R=1 and m=0 were modified the phases of the complex-conjugated couples for $y_0(1)$ and $y_0(3)$ from the level l=0, and $y_1^s(1)$ and $y_1^s(3)$ for s=1,2 – from the level l=1 of IDD for every segment. The obtained results proved the high efficiency of the watermarking with SNR>80 dB when the values of the watermark elements are in the range $\pm 3^0$ and are coded with 5 bits per element, missing the code 00000. In this case the maximum speed for watermark data transmission in the level l=0 is approximately 860 bps, and in the level l=1 - correspondingly 1.72 кbps.

On Fig. 1 an input test sinusuidal signal with 64 samples, and the corresponding marked signal are presented. The 5 bits watermark is set to the 3^{th} coefficient. The amplitude and phase responses of the input signal are presented on Fig.2. These results were obtained with program simulitaion on MATLAB 5.3.

IV. Conclusion

A new method for audio watermarking in the phase spectrum with two-level IDD, was developed. The method is based on the limited spatial resolution of the Human Auditory System in respect to the direction of the sound source, which results in practical inaudibility of the inserted watermarks. Advantage of the method is the fact that there is no quantization of the transform coefficients, the method has relatively low computational complexity and permits the insertion of different watermark with high information capacity in every IDD level.

The method offers exact watermark extraction, high resistance against frauds and pirates' attacks with multiple lossy compression or different kinds of audio transforms and the ability for exact watermark extraction without using the original audio signal. The insertion of different watermarks in every IDD level makes the identification of the manufacturers and of the authorized distributors of multimedia production much easier.

Acknowledgement

The authors thank the National Fund for Scientific Research of the Bulgarian Ministry of Education and Science for the financial support by the contract I-1304/2003.

References

[1] M. Swanson B. Zhu, A.Tewfik, L. Boney. Robust audio watermarking using perceptual masking, Signal Processing, Vol. 66, 1998, pp. 337–355.

[2] F. Hartung, M. Kutter. Multimedia Watermarking Techniques. Proc. IEEE, Vol. 87, No 7, 1999, pp. 1079-1107.

[3] R. Garcia. Digital Watermarking of Audio Signals Using a Psycho-acoustic Auditory Model and Spread Spectrum Theory, 107-th AES Convention, Sept. 1999.

[4] X. Wang, H. Yang. A Content-Based Fragile Digital Audio Watermarking Algorithm. IEEE Intern. Conf. on Information Reuse and Integration, IRI'2003, Las Vegas, USA, October, 2003.

[5] R. Kountchev, M. Milanova, C. Ford, S. Rubin. Multimedia Watermarking with Complex Hadamard Transform in the Inverse Pyramid Decomposition, IEEE Intern. Conf. on Information Reuse and Integration, IRI'2003, Las Vegas, USA, October, 2003, pp. 305-310.

Lossless Image Compression With IDP Decomposition

R. Kountchev[1], Vl. Todorov[2], R. Kountcheva[3]

Abstract **- A recursive algorithm for lossless compression of halftone and colour images, in correspondence with the decomposition method INVERSE DIFFERENCE PYRAMID (IDP), based on two-dimensional orthogonal transforms, is described in this paper. Special investigation was performed on the results obtained with highest quality or lossless coding applied for different kinds of images: natural, graphics, medical, etc. The results are compared with those for JPEG and JPEG2000.**

Keywords **- lossless image compression, inverse difference pyramid decomposition.**

I. INTRODUCTION

In the paper are presented the specific features of the Inverse Difference Pyramid decomposition [1,2], used for lossless still image compression. In the section II are presented the basic principles of the method. In the section III are given the results, obtained with the IDP lossless compression for medical ultrasound images, natural grayscale and colour images and graphics, and are pointed some of its main advantages, compared with the widely used standards JPEG and JPEG2000 [3,4]. In the section IV are presented the most efficient trends for future method development.

II. BASIC PRINCIPLES OF THE IDP DECOMPOSITION

The Inverse Difference Pyramid (IDP) decomposition is presented in brief, as follows. The basic approach is that the matrix [X] of the original image is divided in sub-images with size $2^n \times 2^n$ and each is processed with a two-dimensional (2D) orthogonal transform using only a limited number of spectrum coefficients. The values of the coefficients, calculated in result of the transform, constitute the first pyramid level. Using the values of these coefficients, the sub-image is restored with the corresponding inverse orthogonal transform and subtracted pixel by pixel from the original one. The difference sub-image with elements $e_p(i,k)$ in the level p of the IDP is defined as:

$$e_p(i,k)=\begin{cases} x(i,k)-\tilde{x}(i,k) & \text{for} \quad p=0; \\ e_{p-1}(i,k)-\tilde{e}_{p-1}(i,k) & \text{for } p=1,2,..,P, \end{cases} \qquad (1)$$

where x(i,k) is the pixel (i,k) in a sub-image with size $2^n \times 2^n$ of the input image [X] (Fig.1a); $\tilde{x}(i,k)$ and $\tilde{e}_{p-1}(i,k)$ are the pixels of the recovered input and difference sub-images in the level p of the IDP, obtained with the inverse orthogonal transform using the selected spectrum coefficients only. The obtained difference sub-image is divided in 4 sub-images with size $2^{n-1} \times 2^{n-1}$. Each sub-image is processed with the 2D orthogonal transform again; the values of the transform coefficients build the second pyramid level. Then the image is restored again and the second difference image is calculated. The process continues in a similar way with the next pyramid levels. In this way all pyramid levels, consisting of coefficients values only, are calculated. The processing of the image is shown in Fig. 1.

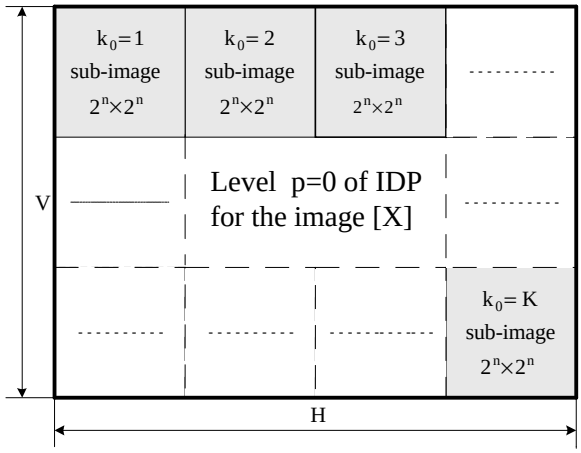

a. The original image [X], divided in K sub-images ($2^n \times 2^n$) for pyramid level p=0.

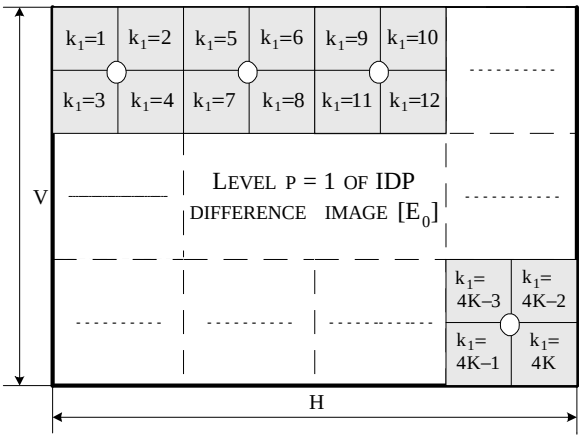

b. Each sub-image of difference image [E_0] the level p=0, is divided in 4 sub-images ($2^{n-1} \times 2^{n-1}$) in the pyramid level p=1

Fig.1. The IDP levels p=0,1 for the image with HxV pixels.

Usually the processing does not require all the pyramid levels to be used, because the necessary image quality is

Roumen Kountchev is with the Faculty of Telecommunications, Technical University of Sofia, Boul. Kl. Ohridsky, 8, Sofia 1000, Bulgaria. E-mail: rkountch@tu-sofia.bg

Vladimir Todorov is with T&K Engineering, Mladost 3, P.O.Box 12, Sofia 1712, Bulgaria. E-mail: vtodorov@yahoo.com

Roumiana Kountcheva is with T&K Engineering, Mladost 3, P.O.Box 12, Sofia 1712, Bulgaria. E-mail: rkountcheva@yahoo.com

obtained earlier, in one of the lower levels. Such pyramid is called "truncated". The only requirement for the case of lossless image coding is that in the last pyramid level all the possible coefficients should be used.

The approximation models of the input or difference image in the level p could be represented with the relations:

$$\tilde{x}(i,k) / \tilde{e}_{p-1}(i,k) = IT[y_p(u,v)], \quad (2)$$

$$y_p(u,v) = T[x(i,k) / e_{p-1}(i,k)]$$

where T[•] is the operator for the "truncated" direct two-dimensional linear transform applied on the input block with size $2^n \times 2^n$, or on the difference sub-image with size $2^{n-p} \times 2^{n-p}$ from the pyramid level p=1,2,..,P (Fig. 2b); IT[•] is the operator for the inverse linear transform of the spectrum coefficients, $y_p(u,v)$ from the level p of the "truncated" transform $2^{n-p} \times 2^{n-p}$, obtained in result of the transformation of every ¼ part of the difference sub-image, $e_{p-1}(i,k)$.

Specific for IDP is that the set of coefficients of the orthogonal transform, chosen for every pyramid level, can be different. The coefficients obtained in result of the orthogonal transform from all pyramid levels are sorted in accordance with their frequency, and scanned sequentially. The obtained one-dimensional massif of spectrum coefficients for the s-th frequency band of the two-dimensional linear transform of the input or of the difference image for the level p of the IDP is represented with:

$$y_p(s) = y_p[u=\varphi(s), v=\psi(s)], \quad (3)$$

where $u=\varphi(s)$ and $v=\psi(s)$ are the functions, which define the transformation for the two-dimensional massif of spectrum coefficients in the s-th frequency band for the level p. In order to achieve higher compression ratio the data is processed, applying adaptive entropy and run-length coding, performed in two steps: adaptive coding of the lengths of the series of equal symbols (run-length encoding, RLE), and adaptive coding with modified Huffman code (HE). The compressed and decompressed data of the one-dimensional massif of spectrum coefficients for the s-th spectrum band in the level p is presented as follows:

$$\alpha_p(s) = RLE / HE[y_p(s)]; \quad y_p(s) = RLD / HD[\alpha_p(s)] \quad (4)$$

where RLE/HE[•] and RLD/HD[•] are operators for entropy coding and decoding with Run-Length and Huffman coding.

The recovered sub-image x(i,k) is calculated recursively from the components of all the (P+1) IDP levels:

$$x(i,k) = \tilde{x}(i,k) + \sum_{r=1}^{P} \tilde{e}_{r-1}(i,k). \quad (5)$$

In the start of the arranged data sequence is inserted a special header, which contains information about the number of the used pyramid levels, the retained "meaning" coefficients, the kind of the selected orthogonal transform for every level (usually DCT or WHT), the kind of the lossless coding, etc. The process of the image decompression is performed in reverse order. The block diagram of the described IDP algorithm is shown in Fig. 2.

III. Results and Evaluation

The experiments were performed for the following basic image kinds: graphics, text, medical ultrasound images, natural grayscale images, fingerprints, and colour images. In the investigation were used hundreds of images, but in TABLE 1 are presented only a part of the results, which show the specific features of the method behavior best. The used orthogonal transform was Walsh-Hadamard (WHT). The most typical images, used as examples and shown in Fig.3 were as follows: *Graphics***:** Circles, Squares, Crosses; *Text images***:** Text1, Text2, Text5; *Medical images*: Coronal, Axial, Cells; *Natural grayscale images*: Lena, Peppers, Souliers; *Uniform Color images*: Yellow, Blue, Green, White.

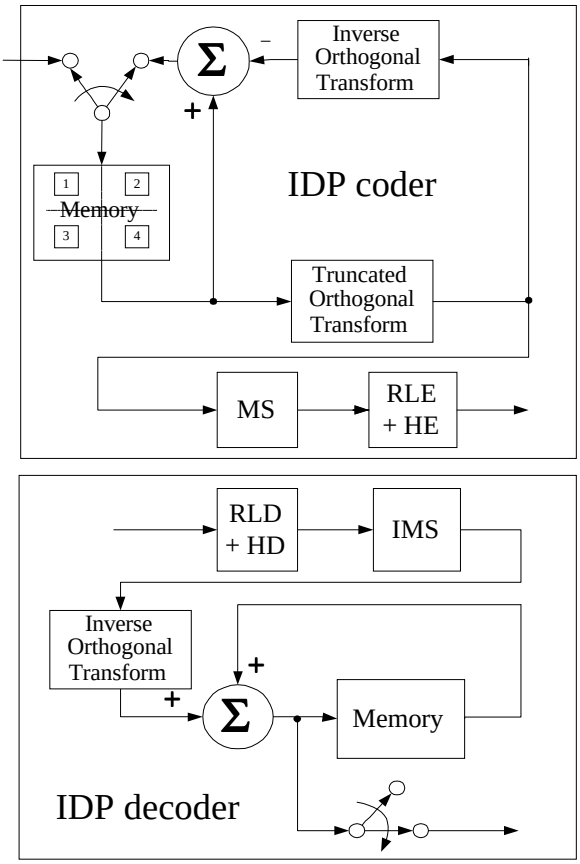

Fig. 2. Block diagram of the IDP algorithm: MS and IMS are the blocks for direct and inverse processing of the two-dimensional data massif consisting of coefficients' values; M is the memory, and (RLD+HD) and (RLE+HE) are the blocks for decoding and coding with RLE and Huffman code.

Fig.3a. Circles (256x256, 8bpp) b. Squares (256x256, 8 bpp)

```
void *operator new(size_t) throw(std::bad_al
void operator delete(void *) throw();
void *operator new(size_t, void *);
void *operator new(size_t, void *);
void *operator new(size_t, void *);
void *operator new(size_t, std::nothrow_t cor
void *operator new(size_t) throw(std::bad_al
void operator delete(void *) throw();
void *operator new(size_t) throw(std::bad_al
void operator delete(void *) throw();
void *operator new(size_t) throw(std::bad_al
void operator delete(void *) throw();
void *operator new(size_t, std::nothrow_t cor
void *operator new(size_t) throw(std::bad_al
void operator delete(void *) throw();
void *operator new(size_t) throw(std::bad_al
void operator delete(void *) throw();
void *operator new(size_t) throw(std::bad_al
void operator delete(void *) throw();
void operator delete(void *) throw();
void *operator new(size_t) throw(std::bad_al
void operator delete(void *) throw();
void *operator new(size_t) throw(std::bad_al
void operator delete(void *) throw();
```

c. Text 2 (512x512, 8bpp)

d. Peppers ((512x512, 8bpp)

e. Souliers (551x369, 8 bpp)

f. Fingerprint 2 and Fingerprint 3 (128x88, 8 bpp each)

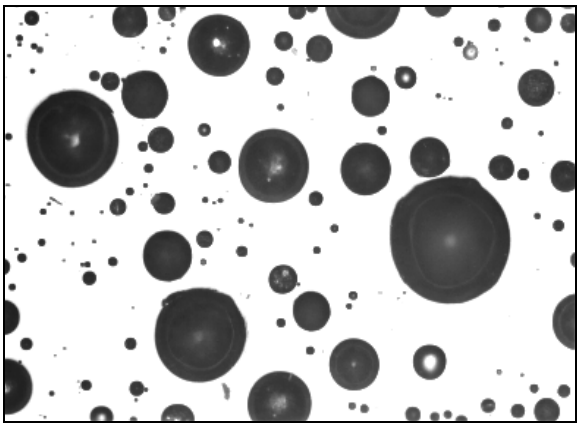

g. Cells (390x277, 8 bpp)

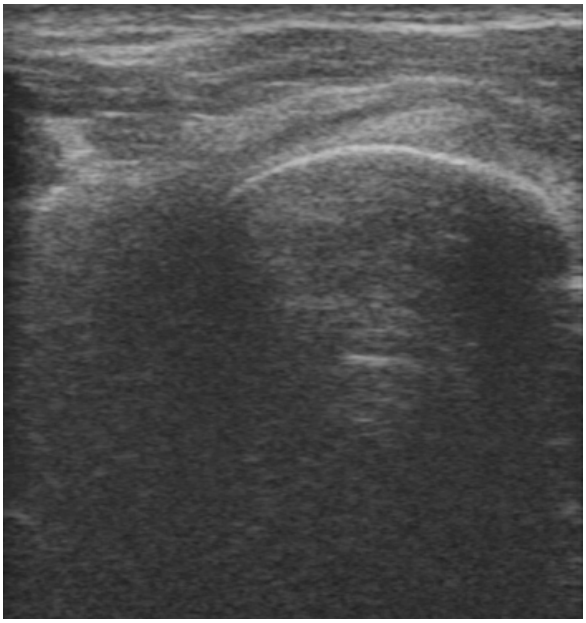

h. Coronal (350x432, 24bpp)

Fig.3, a - h. Example test images.

This investigation was done only for lossless compression. The compression with JPEG was performed with MS Photo Editor, and for JPEG2000 was used LuraTech Algovision. With MS Photo Editor is impossible to perform lossless image compression, but the results show that for best quality compressions the image quality for JPEG was worse than that obtained with IDP.

The results, presented in TABLE 1, illustrate the following specific features and advantages of the method:

- The IDP method offers much higher lossless compression for graphic images. All text images were compressed with unchanged quality and the compression ratio was higher than that, obtained with JPEG and JPEG2000.
- Very good results were obtained for uniform color examples (images Yellow, Blue, Green-1024x1024 pixels). In these cases, the compression ratio for lossless IDP was extremely high.
- The comparison with JPEG standard shows better results for IDP lossless compression. In some cases, the highest quality with JPEG lossless compression resulted even in enlarging of the image file (pictures Text1, Fingerpr2 and Fingpr3).
- The IDP method has lower computational complexity than JPEG2000.
- For natural images (peppers, Lena, etc.) the results, obtained with IDP, are worse than these with JPEG and JPEG2000.

IV. Future method development

In case, when the IDP method is used for surveillance applications, the basic processing should be made more flexible, setting regions of interest. For this purpose, the sub-images of the picture should be processed with different masks, in order to select the most suitable set of coefficients, and to increase the compression efficiency.

- Special stress will be put on the lossless compression and data base management for fingerprints and graphics.
- The compression method permits the insertion of digital watermark in every pyramid level. This makes the application area of the method very wide, including multimedia contents protection and authorized distribution check, performed together with the compression.

ACKNOWLEDGEMENT

The authors thank the National Fund for Scientific Research of the Bulgarian Ministry of Education and Science for the financial support. (Contract No. I 1304/2003).

References

[1] R. Kountchev, V. Haese-Coat, J. Ronsin. Inverse Pyramidal Decomposition with multiple DCT. Signal Processing: Image Communication, Vol. 17, January 2002, pp. 201-218.

[2] R. Kountchev. Image Compression with Recursive IDP Algorithm. ICEST 2003, 16-18 Oct. Sofia, Bulgaria, pp. 273-276.

[3] G. Wallace. The JPEG Still Image Compression Standard. IEEE Trans. Consumer Electronics, Vol. 38, No.1, Feb. 1992.

[4] M. Rabbani, R. Joshi. An Overview of the JPEG 2000 Still Image Compression Standard. Signal Processing: Image Communication, Vol.17, Jan.2002, pp.3-48.

TABLE 1

Image	IDP lossless	IDP PSNR[dB]	JPEG HQ Compr.	JPEG HQ PSNR[dB]	JPEG2000 compr.	JPEG2000 PSNR[dB]
Coronal	5.11	Infinity	5.59	58.48	6.62	Infinity
Axial1	5.35	Inf.	5.73	58.43	6.67	Inf.
Axial2	5.89	Inf.	5.70	18.52	6.56	Inf.
Text5	12.87	Inf.	2.50	65.96	4.31	Inf.
Text1	13.46	Inf.	0.85	60.83	1.89	Inf.
Text2	7.54	Inf.	1.19	62.79	2.25	Inf.
Squares	468.11	Inf.	55.02	Inf.	43.92	Inf.
Crosses	42.17	Inf.	3.13	67.11	7.45	Inf.
Circles	46.38	Inf.	4.85	68.15	8.57	Inf.
Cells	2.97	Inf.	1.95	62.43	2.74	Inf.
Souliers	1.74	Inf.	2.29	58.58	2.53	Inf.
Fingerp3	6.15	Inf.	0.57	63.32	12.09	Inf.
Fingerpr2	4.97	Inf.	0.55	63.02	9.24	Inf.
Peppers	1.36	Inf.	1.59	58.51	1.80	Inf.
Lena	1,21	Inf.	1,47	58,45	1.69	Inf.
Yellow	27594.00	Inf.	61.62	Inf.	3972.00	Inf.
Blue	27594.00	Inf.	61.62	Inf.	3972.00	Inf.
Green	27594.00	Inf.	61.62	Inf.	3972.00	Inf.

TABLE 1. Results from the compression with IDP, JPEG and JPEG 2000 (LuraTech)

Analysis of two-dimensional LMS Error -Diffusion Adaptive Filter

Rumen P. Mironov[1]

Abstract - **An analysis of error-diffusion adaptive filter for image halftoning is presented. The filter coefficients are adapted on the basis of 2D LMS algorithm. The received results shown that the filter leads to more uniform values distribution in the homogeneous areas and more precise edges reproduction in the output bi-level image.**

Keywords - image quantization, error diffusion, adaptive filtration, LMS adaptation.

I. INTRODUCTION

Digital image halftoning is used to transform gray scale images into bi-level ones, which give the appearance of containing various shades of gray. Most widespread are the following two basic transforming techniques - "error diffusion" and "ordered dither" [1], [2], [3]. The use of error diffusion methods results in a better edge reproduction, but also to appearance of artefacts in the homogeneous image areas. This disadvantage is due to the constant values of weights of the two-dimensional error filter, which deals with image pixels in a certain causal window.

In order to minimize the image distortions an adaptive error-diffusion filter is presented. The coefficients of error filter are adapted with the help of generalized 2D LMS Widrow algorithm [5], [6], [7] and the compare threshold on the base of the image histogram is calculated [7].

II. MATHEMATICAL DESCRIPTION

The input m-level halftone image and the output n-level ($2 \le n \le m/2$) image of dimensions *M x N* can be represented by the matrices:

$$\begin{aligned} \boldsymbol{C} &= \{\mathbf{c}(k,l) \,/\, k = \overline{0,M-1};\; l = \overline{0,N-1}\}, \\ \boldsymbol{D} &= \{\mathbf{d}(k,l) \,/\, k = \overline{0,M-1};\; l = \overline{0,N-1}\}. \end{aligned} \tag{1}$$

Transformation of the image elements **c**(k,l) into **d**(k,l) is accomplished by the adaptive error diffusion quantiser (AEDQ) shown on Fig. 1. The quantiser operation is described by the following equation:

$$\mathbf{d}(k,l) = Q[\mathbf{c}_f(k,l)] = \begin{cases} q_{0,} & \text{if } \mathbf{c}_f(k,l) < T_0 \\ q_{p,} & \text{if } T_{p-1} < \mathbf{c}_f(k,l) < T_p \;\; (p = \overline{1,n-2}) \\ q_{n-1,} & \text{if } \mathbf{c}_f(k,l) < T_0 \end{cases} \tag{2}$$

where $q_p \le q_{p+1} \le m$ $(p = \overline{0,n-2})$ are the values of the function Q[.].

[1]Rumen P. Mironov is with the Faculty of Communication Technics and Techology, Technical University of Sofia, Kl.Ohridsky 8, 1000 Sofia, Bulgaria, E-mail: rpm@vmei.acad.bg

Thresholds for comparison are calculated by $T_p = (C_p + C_{p+1})/2$, where C_p represents the gray values dividing the normalized histogram of the input halftone image $\boldsymbol{C}$ into n equal parts. The value of the filtered element $\mathbf{c}_f(k,l)$ in Eq. (2) is:

$$\mathbf{c}_f(k,l) = \mathbf{c}(k,l) + \mathbf{e}_0(k,l)\,. \tag{3}$$

The summarized error can be expressed as:

$$\mathbf{e}_0(k,l) = \sum_{(r,t)\in \boldsymbol{W}} \sum \mathbf{w}_{k,l}(r,t)\,\mathbf{e}(k-r,l-t) = \mathbf{W}_{k,l}^{t}\,\mathbf{E}_{k,l}\,, \tag{4}$$

where $\mathbf{e}(k,l) = \mathbf{c}_f(k,l) - \mathbf{d}(k,l)$ is the error of the current filtered element when its value is substituted by q_p; $\mathbf{w}_{k,l}(r,t)$ are the filter weights defined in the certain causal two -dimensional window $\boldsymbol{W}$; $\mathbf{W}_{k,l}$ and $\mathbf{E}_{k,l}$ are the vectors of the weights and their summarized errors, respectively.

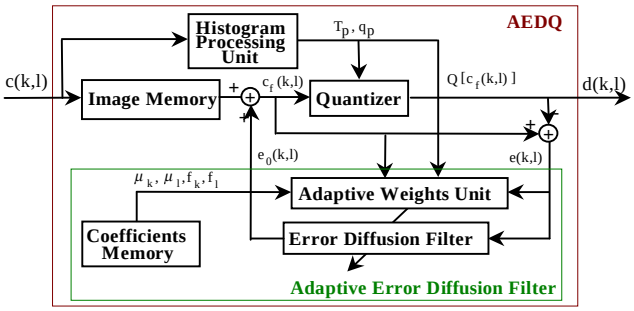

Fig.1 Adaptive error-diffusion quantiser

According to 2D-LMS algorithm [7] the adaptive error diffusion filter (AEDF) weights can be determined recursively:

$$\mathbf{W}_{k,l} = f_k\,\mathbf{W}_{k,l-1} - \mu_k \nabla_{k,l-1} + f_l\,\mathbf{W}_{k-1,l} - \mu_l \nabla_{k-1,l}\,, \tag{5}$$

where: $\nabla_{k,l-1}$ and $\nabla_{k-1,l}$ are the gradients of the squared errors by the quantisation in horizontal and vertical directions; f_k, f_l - coefficients, considering the direction of the adaptation, where : $f_k + f_l = 1$; μ_k, μ_l - adaptation steps in the respective direction.

According to [5] the convergence and the stability of the AEDF adaptation process is given by the following condition:

$$\left|f_k - \mu_k \lambda_i\right| + \left|f_l - \mu_l \lambda_i\right| < 1\,, \tag{6}$$

where λ_i are the eigenvalues of the gray-tone image covariance matrix .

Sequence (5) is 2D LMS algorithm of Widrow summary from which the following two particular cases should hold:

First. If $f_k=1, \mu_k=\mu, f_l=\mu_l=0$ then the adaptive calculation of the weights is proceeded only in the horizontal direction:

$$\mathbf{W}_{k,l} = \mathbf{W}_{k,l-1} + \mu_k(-\nabla_{k,l-1}) = \mathbf{W}_{k,l-1} - \mu \frac{\partial \mathbf{e}^2(\mathbf{k},\mathbf{l-1})}{\partial \mathbf{W}_{k,l-1}}. \quad (7)$$

Second. If $f_l=1, \mu_l=\mu, f_k=\mu_k=0$ then the adaptive calculation is proceeded only in the vertical direction:

$$\mathbf{W}_{k,l} = \mathbf{W}_{k-1,l} + \mu_l(-\nabla_{k-1,l}) = \mathbf{W}_{k-1,l} - \mu \frac{\partial \mathbf{e}^2(k-1,l)}{\partial \mathbf{W}_{k-1,l}}. \quad (8)$$

The derivatives by the quantization error in the respective directions are determined by the Eqs. (1), (2), (3), (4) and (5). For the derivative in horizontal direction is obtained:

$$\frac{\partial \mathbf{e}^2(k,l-1)}{\partial \mathbf{W}_{k,l-1}} = 2\mathbf{e}(k,l-1)\mathbf{E}_{k,l-1}\left[1-Q'_{\mathbf{c}_f}(k,l-1)\right] \quad (9)$$

where:

$$Q'_{\mathbf{c}_f}(k,l\text{-}1) = \begin{cases} 0, & \text{if: } \mathbf{c}_f(k,l\text{-}1) \neq T_p \\ q_{p+1}-q_p, & \text{if: } \mathbf{c}_f(k,l\text{-}1) = T_p. \end{cases}$$

In the same way for the derivative in the vertical direction is obtained:

$$\frac{\partial \mathbf{e}^2(k\text{-}1,l)}{\partial \mathbf{W}_{k\text{-}1,l}} = 2\mathbf{e}(k\text{-}1,l)\,\mathbf{E}_{k\text{-}1,l}\left[1-Q'_{\mathbf{c}_f}(k\text{-}1,l)\right] \quad (10)$$

For the AIHF weights the condition must be hold:

$$\sum_{(r,t)\in \boldsymbol{W}}\sum \mathbf{w}_{k,l}(r,t) = 1, \quad (11)$$

which guarantees that $\mathbf{e}(k,l)$ is not increased or decreased by its passing through the error filter.

On the basis of analysis, made in Eqs. (7) to (11) the sequence for the components of $W_{k,l}$ is

$$\begin{aligned} w_{k,l}(r,t) &= f_k w_{k,l-1}(r,t) \\ &\quad -2\mu_k e(k,l\text{-}1)e(k\text{-}r,l\text{-}t\text{-}1)\left[1-Q'_{\mathbf{c}_f}(k,l\text{-}1)\right] \\ &\quad +f_l w_{k\text{-}1,l}(r,t) \\ &\quad -2\mu_l e(k\text{-}1,l)e(k\text{-}r\text{-}1,l\text{-}t)\left[1-Q'_{\mathbf{c}_f}(k\text{-}1,l)\right]. \end{aligned} \quad (12)$$

III. Experimental Results

An error diffusion filter with 4 coefficients has been used for the evaluation of the efficiency of the developed filter. The spatial disposition, shown on Fig.2, and the initial values of weights correspond to these in the Floyd-Steinberg filter [1].

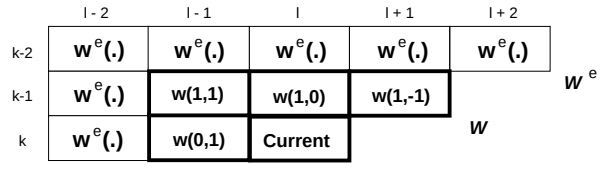

Fig.2. Spatial disposition of the weights $w_{k,l}(r,t)$ in $\boldsymbol{W}$.

For the calculation of each one $w_{k,l}(r,t)$ are used the weights $w^e_{k,l}(.)$ from the extended window $\boldsymbol{W}^e$.

The analysis of 2D variation of peak signal to noise ratio (PSNR) depending on parameters f and μ ($f_k=f, f_l=1\text{-}f, \mu_k=\mu_l=\mu.$) is made in [7] and [8].

The coefficients f and μ are changed in the following way: f =0.0 to 1.0 with step 0.1 and $\mu = 1.0\text{x}10^{-6}$ to $2.0\text{x}10^{-6}$ with step $1.0\text{x}10^{-8}$.

The peak signal to noise ratio is determined by the equation

$$PSNR = 10\,lq\frac{m^2}{\sum_{k=0}^{N}\sum_{l=0}^{M}[e(k,l)]^2}, dB.$$

The examination of the function PSNR (f, μ) showed that the most proper mean values of f and μ are $f=0.7, \mu=1.67\text{x}10^{-6}$. In this case AIHF leads to increasing of PSNR with about 0.6 dB in comparison with the 4 coefficient ($f=1, \mu=0$) non-adaptive filter of Floyd and Steinberg.

On Fig.3 the experimental results from the simulation of AEDQ for the test image "LENNA" with: M=N=512, m=256 levels, n=2 bits, $f_k=0.7$, $f_l=0.3$, $\mu_k=\mu_l=1.67\text{x}10^{-6}$ are presented.

The average variation of weights $w_{k,l}(r,t)$ is presented on Fig.4. The given results show that the weights point to a value for which the mean square error (MSE) is minimized for the current image. A second image transform with scanning the pixels in reverse direction is performed for further decrease of mean square error. The initial values of the weights are equal to the last ones obtained from the direct transform. In this case a better convergence of the adaptation is obtained, the phase distortions are decreased and PSNR increased in addition with about 0.2 dB.

IV. Conclusion

The developed generalized AEDQ results in the following particular cases: the wide-spread non-adaptive error diffusion filter of Floyd and Steinberg (for n=2, $f_k=1, \mu_k=\mu_l=f_l=0$); adaptive error diffusion using the weights only in the horizontal (from the same image row - $f_k=1, f_l=0$) or only in the vertical direction (from the previous image row - $f_l=1, f_k=0$). The adaptive filter provides minimum reconstruction error, uniform distribution of the arranged structures in the homogeneous areas and precise reproduction of edges in the output multilevel images. The coefficients f_k, f_l, μ_k, μ_l must be selected on the basis of PSNR analysis and keeping of Eq. (7) as is done in [7]. The developed AEDQ is appropriate for realization on special VLSI circuit to accelerate calculation of image transform.

The presented error diffusion filter can be used for transformation of color palettes or brightness of pixels in

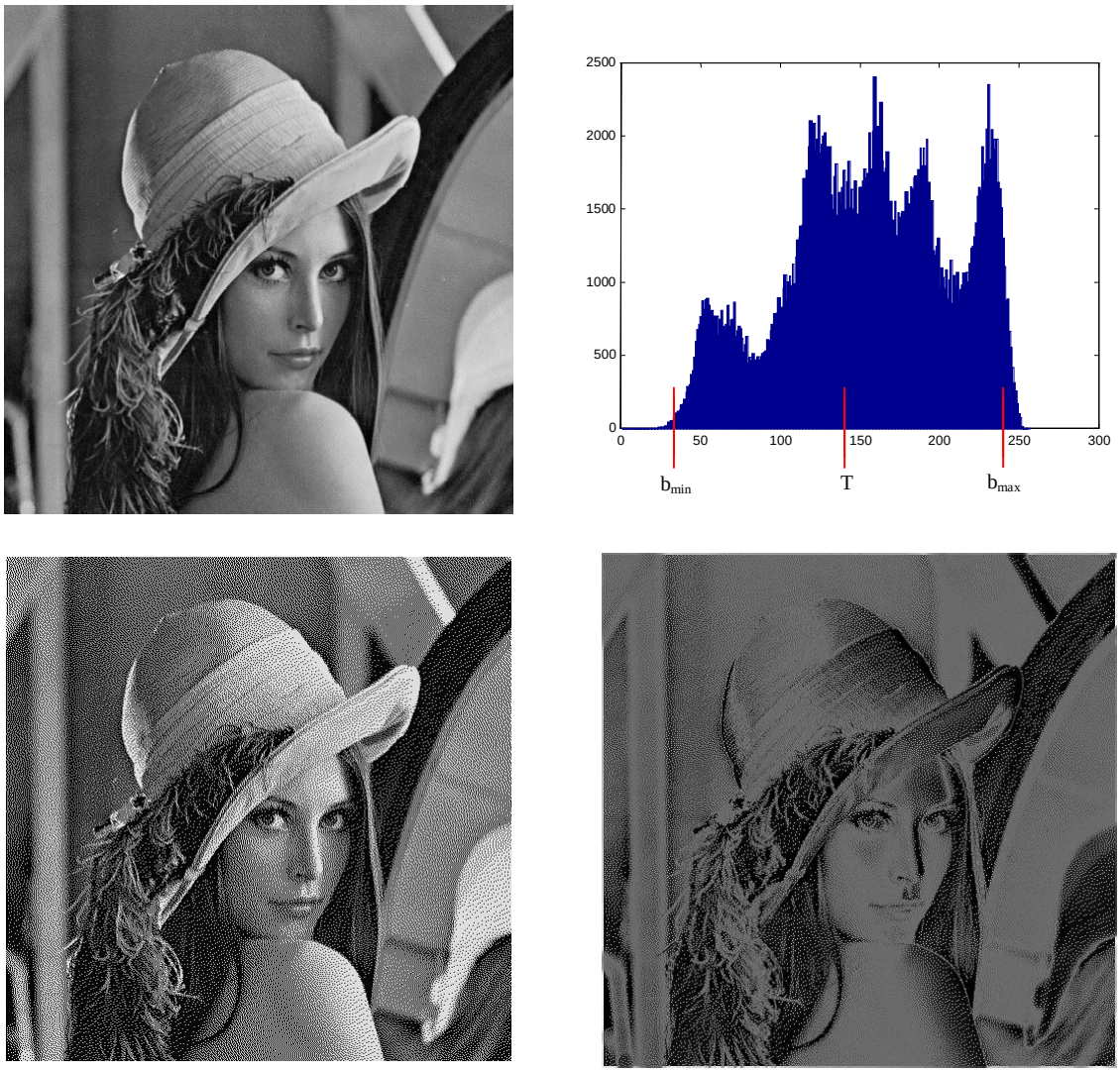

Fig.3. Experimental results - input image "LENNA", histogram of image, output bi-level image end error image.

multimedia systems, for printing color and halftone images and transmission by facsimile devices.

ACKNOWLEDGEMENT

The authors thank the National Fund for Scientific Research of the Bulgarian Ministry of Education and Science for the financial support by the contract I-1304/2003.

REFERENCES

[1] R.Floyd and L.Steinberg. "An adaptive method for spatial gray scale". SID Dig., vol.36, 1975.

[2] J.F.Jarvis, C.N.Judice and N.J.Ninke. "A survey of techniques for the display of continuous - tone pictures on bilevel displays". Computer Graphics, Image Processing, vol.5, pp.13-40, 1976.

[3] R.A. Ulichney, "Dithering with blue noise", *Proc. of IEEE*, Vol.76, No.1, January 1988, pp.56-79.

[4] Maher A. Sid-Ahmed, *Image Processing: Theory, Algorithms, and Architectures*. McGaw-Hill, Inc., 1995.[5] Mohiy M. Hadhoud, David W. Thomas, "The Two-Dimensional Adaptive LMS (TDLMS) Algorithm".*IEEE Trans. on Circuits and Systems*, vol. CAS-35, No.5, pp.485-494, May 1988.

[6] Makoto, O., S. Hashiguchi, "Two-Dimensional LMS Adaptive Filters", *IEEE Trans. on Consumer Electronics*, Vol.37, No.1, February 1991, pp.66-73.

[7] R.Mironov, R.Kunchev, "Adaptive Error-Diffusion Method for Image Quantization". *Electronics Letters, IEE An Intr. Publication the Institution on Electrical Engineers*, 11-th November 1993,Vol.29, No.23, pp. 2021-2023.

[8] R.Mironov. *Algorithms for Local Adaptive Image Processing.* XXXVII International Scientific Conference on Information, Communication and Energy Systems and Technologies. ICEST 2002, Niš, Yugoslavia, October 1-4, 2002, pp.193-196.

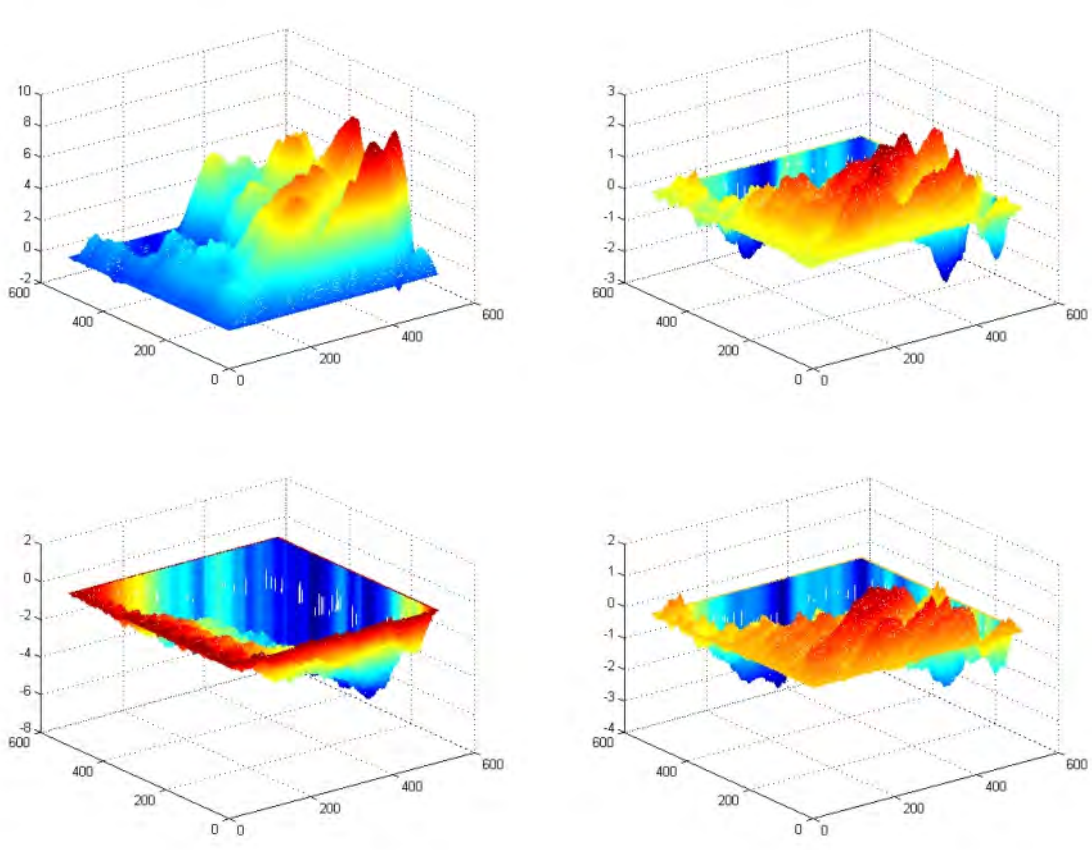

Fig.4. Variation of weights $w_{k,l}(r,t)$ for the test image "LENNA".

On Wavelet Selection for Nuclear Medicine Images Processing

Cvetko D. Mitrovski[1] and Mitko B. Kostov[2]

Abstract – **This paper presents some experimental results of NM image filtering by using several types of wavelets. For this purpose, one set of wavelets that belong to different wavelet families is chosen. Based on these experiments, the Coiflet 5 wavelet is identified as the best wavelet. The aim of the paper is identifying the best wavelet for filtering of NM images in order to develop sophisticated diagnostic software that could automatically offer the optimal positions and the shapes of the regions of interest needed for the heart studies.**

Keywords – **Nuclear medicine image, wavelets, filtering, compression.**

I. INTRODUCTION

Wavelet transforms have received significant attention recently from mathematicians, signal analysts and engineers as a new tool for feature extraction, signal and image compression, edge detection and de-noising. Unlike the traditional Fourier techniques, wavelets are localized both in time and frequency domain. This feature makes them suitable for the analysis of non-stationary signals. At present, there exist no theoretical results that can predict which wavelet is suitable for a particular type of signal. Usually, the best wavelet is chosen by comparing the performances of several types of wavelets.

One interesting area of wavelet applications is biomedical engineering. Wavelets have been applied to several problems in biomedical signals, but analysis of *Nuclear Medicine* (NM) images by using wavelet transforms has not be widely explored yet.

Nuclear medicine images are diagnostic digital images, which provide both anatomical and functional information. They present the projection of distribution of radioisotope(s) in a body of a patient after injection of adequate dose of radioisotope(s). The raw NM images are based directly on the total counts detected over a fixed observation period by computerized gamma cameras and have a low signal-to-noise ratio (SNR) due to the nature of the gamma ray emission process and the operational characteristics of the gamma cameras. Therefore, the NM image analysis must be preceded by a certain image preprocessing, which ought to provide an accurate recognition of anatomic data of the patient (the boundaries of the various objects – organs, on the images). This process can be much diversified, since it should be adjusted to the organs and tissues.

In this paper we demonstrate the potential use of different types of wavelets for chest-region NM image filtering. Based on experimental experiments, the Coif5 is identified as the best wavelet. The result can be used in noise removal in NM images and automatic extracting of the anatomic data from the chest region dynamical NM images. The paper is organized as follows. The wavelet theory is summarized in Section II. Section III outlines the scheme used in wavelet filtering of NM images. The experimental results are presented in Section IV. Filtering with different types of wavelets are applied to real images captured with our own gamma camera upgrading system, developed at the department of NM in Bitola. Section V concludes the paper.

II. AN OVERVIEW OF THE DISCRETE WAVELET TRANSFORM

The Discrete Wavelet Transform (DWT) decomposes a signal into a set of orthogonal components describing the signal variation across the scale [3]. The orthogonal components are generated by dilations and translations of a prototype function ψ called *mother wavelet.*

$$\psi_{i,k}(t) = 2^{-i/2}\psi(t/2^i - k), \quad k,i \in Z \tag{1}$$

The above equation shows that the mother function is dilated by the integer i and translated by the integer k. In analogy with other function expansions, a function f may be written for each discrete coordinate t as sum of a wavelet expansion up to certain scale J plus a residual term, that is:

$$f(t) = \sum_{j=1}^{J} \sum_{k=1}^{2^{-j}M} d_{jk}\psi_{jk}(t) + \sum_{k=1}^{2^{-J}M} c_{Jk}\phi_{Jk}(t) \tag{2}$$

The estimation of d_{jk} and c_{Jk} is carried out through an iterative decomposition algorithm, which uses two complementary filters h_0 (low-pass) and h_1 (high-pass). Since the wavelet base is orthogonal, h_0 and h_1 satisfies the quadrature mirror filter conditions (QMF) [4]. Filter bank theory is closely related to wavelet decompositions and multiresolution concepts. For this reason, it is helpful at this point to view the scaling function ϕ as a low pass filter h_0 and wavelet function ψ as a high pass filter h_1. The mother and scaling functions are defined as follows [3]:

$$\psi(t) = \sum_n 2^{1/2} h_1 \psi(2t - n) \tag{3}$$

[1]Cvetko D. Mitrovski is with the Faculty of Technical Sciences, I.L.Ribar bb, 7000 Bitola, Macedonia, E-mail: cvetko.mitrovski@uklo.edu.mk

[2]Mitko B. Kostov is with the Faculty of Technical Sciences, I.L.Ribar bb, 7000 Bitola, Macedonia, E-mail: mitko.kostov@uklo.edu.mk

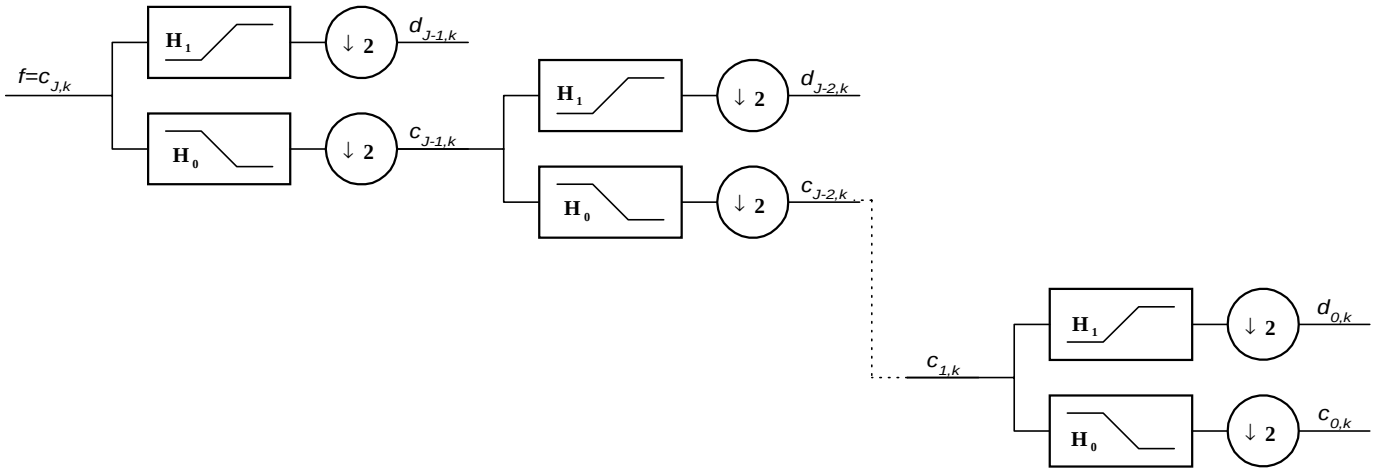

Fig. 1. Discrete Wavelet Transform Tree

$$\phi(t) = \sum_n 2^{1/2} h_0 \phi(2t - n) \tag{4}$$

For computation of wavelet transform, the following pyramidal algorithm is used:

The QMF bank decomposes the signal into low and high frequency components respectively. Convolving the signal with h_1 gives a set of wavelet coefficients $c_{J,k}$, while the convolution with h_0 gives the approximation coefficients $d_{j,k}$. Because of the redundancy of information, these filters are down-sampled, throwing away every other sample at each operation, thus halving the data each time. The approximation coefficients $d_{j,k}$ are then convolved again with the filters h_0 and h_1 to form the next level of decomposition. The backward algorithm simply inverts the process. It combines two linear filters with up-sampling operation. Fig. 1 shows the operation involved in the wavelet decomposition and synthesis of the signal.

At present, there exist no theoretical results that can predict which wavelet is suitable for a particular type of signal. Usually, the best wavelet is chosen by comparing the performances of several types of wavelets.

III. Filtration of NM Images

To demonstrate the potential of wavelets for NM image filtering, we use the most popular form of wavelet-based filtering, commonly known as *Wavelet Shrinkage*. For this purpose, we choose one set of wavelets that belong to different wavelet families including the following wavelet bases Daubechies (Db6 and Db10), Biorthogonal (Bior3.5 and Bior6.8), Coiflets (Coif3 and Coif5) and Symlets (Sym4 and Sym7). In order to identify the best wavelet, *Non-zero pixels compression ratio* (NZPCR) and *Percent root-mean-square difference* (PRD) are defined as follows. The non-zero pixels compression ratio is closely intertwined with the threshold in the wavelet shrinkage, because the bigger the threshold is, the bigger the non-zero pixels compression ratio is. So, we want to find the best wavelet for a set non-zero pixels compression ratio (threshold). As the best wavelet for a set NZPCR, we identify the one for which the PRD is minimal.

First, we calculate the wavelet coefficients of the observation, w_i, and then we filter contribution of a particular wavelet basis function in the signal expansion by weighting the corresponding coefficient w_i by a number h_i; $0 \le h_i \le 1$. That is, we modify the wavelet coefficients according to:

$$\hat{w}_i = w_i \cdot h_i. \tag{5}$$

In the wavelet shrinkage program that we use, the shrinkage filter corresponds to the "hard threshold" nonlinearity

$$h_i^{(\text{hard})} = \begin{cases} 1, & \text{if } |w_i| \ge \tau \\ 0, & \text{if } |w_i| < \tau \end{cases}. \tag{6}$$

After obtaining the filtrated coefficients, we calculate the non-zero pixels compression ratio and Percent root-mean-square difference that are defined below.

The Non-zero pixels compression ratio is defined as:

$$\text{NZPCR} = \frac{\sum \omega_f}{\sum \omega_{\hat{f}}} \tag{7}$$

where $\sum \omega_f$ is number of coefficients different than zero before, and $\sum \omega_{\hat{f}}$ is number of coefficients different than zero after applying the wavelet shrinkage. The threshold value can be adjusted to alter the number of preserved coefficients, thereby changing the non-zero pixels compression ratio.

Percent root-mean-square difference measures the numerical distortion between the original and the reconstructed NM image. We analyze PRD in relation to a set threshold:

$$\text{PRD} = \sqrt{\frac{\sum \left(f_i - \hat{f}_i\right)^2}{\sum f_i^{\,2}}} \times 100 \tag{8}$$

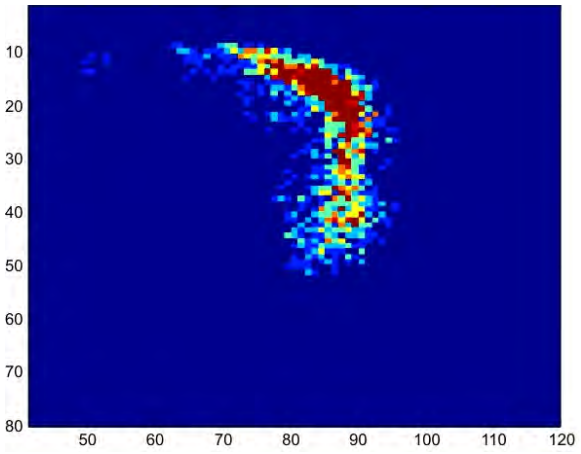

Fig. 2 The analyzed NM image

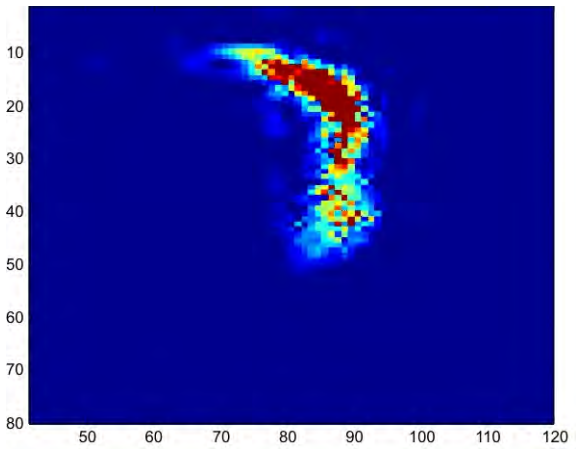

Fig.3 The filtrated NM image

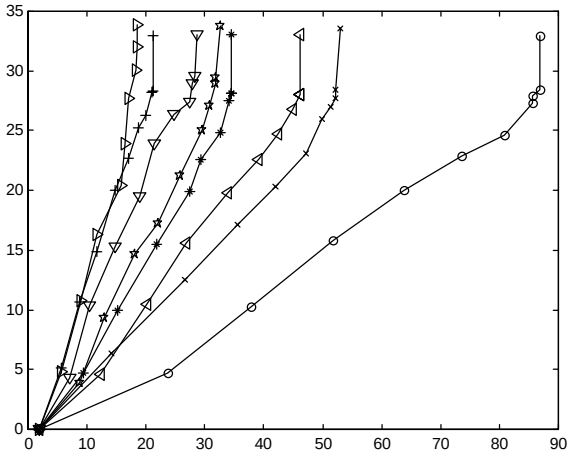

Fig.4 PRD versus NZPCR

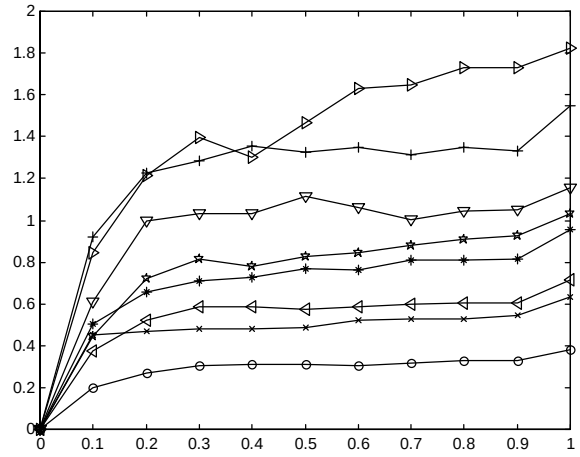

Fig. 5 PRD/CR versus threshold

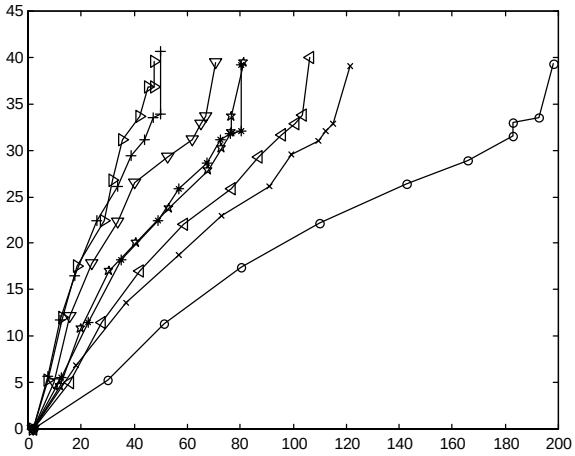

Fig.6 PRD versus NZPCR

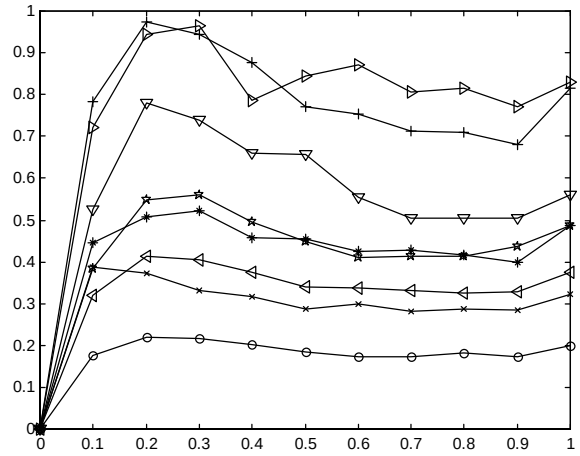

Fig. 7 PRD/NZPCR versus threshold

Legend for Figs. 5-8: db6 v, db10 x, bior3.5 >, bior6.8 *, coif3 <, coif5 o, sym4 +, sym7 p

where f_i is a pixel of the original image f, and $\hat{f}_i$ is the corresponding pixel of the filtered image $\hat{f}$.

IV. EXPERIMENTAL RESULTS

As a sample image in our experiments we use one NM image matrix of resolution 128x128. Fig. 2 shows the NM image used for the experimentation. The image contains part of the vein and part of the heart of a patient. Autocorrelation low-pass filtering technique was applied to the image in order to remove salt and pepper noise. But, it still contains rather high level of noise due to: a) mixing the radionuclide with the blood and the spreading of this mixture, b) hydrodynamic processes in the blood vessels caused by the pumping work of the heart and c) by the randomness of the gamma rays emission and their detection by the gamma camera.

Taking into consideration this, we want to adequately preprocess the raw images in order to extract the anatomy information about the position of the vena cava superior and the heart. According to this information, the optimal position (and the shape) of the regions of interest (ROI's) for the heart study can be proposed [2].

A number of experiments were performed to identify the best wavelet for this type of images. In our experiments, first, we apply the wavelet shrinkage program to the image. We use the following set of wavelet bases Daubechies (Db6 and Db10), Biorthogonal (Bior3.5 and Bior6.8), Coiflets (Coif3 and Coif5) and Symlets (Sym4 and Sym7). As a result, all the wavelet detail coefficients with magnitudes larger than the threshold value are retained with full accuracy and the remaining coefficients are truncated.

Next, we calculate the rate distortion curves (PRD versus non-zero pixels compression ratio) for eight wavelets by using decomposition at level one. The curves are shown in Fig. 4. The ratio PRD/CR versus threshold is illustrated on Fig. 5. From the both figures, it can be noticed that for any set threshold or non-zero pixels compression ratio, the percent root-mean-square difference is smallest for the Coiflet 5 wavelet. So, in terms of the best wavelet within the chosen set of wavelets, the Coiflet 5 wavelet performs better results than the other wavelets. General characteristic of Coiflets wavelets is that they are compactly supported wavelets with highest number of vanishing moments for both ϕ and ψ for a given support width, which is useful for compression purpose.

The rate distortion curves, obtained for the same eight wavelets when decomposition at level two is used, are shown in Fig. 6. Now, the wavelet shrinkage program is applied to the detail coefficients from the both levels: one and two. The ratio PRD/CR versus threshold is illustrated on Fig. 7. Again Coiflet 5 is identified as the optimal wavelet.

The filtrated image obtained by using wavelet filtration at level 2 by the optimal wavelet and a threshold equal to 30% of intensity of the pixel with maximal intensity is shown in Fig. 3.

V. CONCLUSION

In this paper we demonstrate the potential use of different types of wavelets for chest-region NM image filtering. Based on these experiments, the Coiflet 5 wavelet is identified as the best wavelet from one set of wavelets that belong to different wavelet families. The result can be used in noise removal in NM images and automatic extracting of the anatomic data from the chest region dynamical NM images. Anatomical data can be determined in order to upgrade the software with an expert system that could identify the optimal positions and shapes of the regions of interest needed for the heart study.

REFERENCES

[1] General Electric, *Gamma Camera Technical Reference Manual*, 1980.

[2] G. Strang and T. Nguyen, *Wavelets and Filter Banks*. Wellesley-Cambrige Press, 1996.

[3] P.P.Vaidyanathan, *Multirate Systems and Filter Banks*, Prentice – Hall (1992).

[4] Cvetko D. Mitrovski and Mitko B. Kostov, "A Wavelet Domain Approach On Noise Filtration Of Nuclear Medicine Images", *International Scientific And Applied Science Conference Electronics ET'2002*, Sozopol, Sept. 2002.

Text Regions Segmentation in Image Printed Documents

Antoaneta A. Popova[1], Milen A. Dimitrov[2], Vasil G. Grancharov[3]

Abstract – **The paper deals with a suitably developed algorithm and designed program system that is being used to separate text regions from image and graphics regions. A combination is used of an edge detection, a dilatation, a recognition text blocks by features as a periodicity of 90^0, an uniformly/ regularity of 0^0 and a similarity of 45^0 and 135^0 projections.**

Keywords – **Page segmentation, Text extraction, Edge detection, Document image understanding.**

I. INTRODUCTION

The image documents analysis is part of the conversion task from a hard copy to a soft copy with text recognition in the office automation. The goal of a document image understanding system is to convert a raster image scanned by a document scanner, into an appropriate symbolic form [1]. One of the applied approaches is a morphological closing or only erosion on the different directions (60°, 120°), using a structural element of 5x5 in order to eliminate non-text objects [2]. The X-Y tree method (pyramid) assumes that a document can be represented in the form of nested rectangular blocks. A "local" peak detector is applied to the horizontal and vertical "projection profiles" to detect local peaks [3]. In the above and most of the previous works [4,5,6] the features for block classifications are extracted from the binarized document images. This has some difficulties such as the determination of the threshold value for the binarization and the lack of enough information for detailed block classification. So, for an efficient block classification, the feature extraction from gray images is applied in this work. In Section 2, is described in detail the approach for automatic text segmentation algorithm from gray-scaled images. Experimental test results are presented in Section 3. Finally, the conclusions are given in Section 4.

[1]Antoaneta A. Popova is with the Faculty of Telecommunication, Technical University- Sofia
Bulgaria, E-mail: Antoaneta.P@komero.net
[2]Milen A. Dimitrov is with Komero Technolodgies Int. Ltd., Sofia, Bulgaria, E-mail: Milen.D@komero.net
[3]Vasil G. Grancharov is with Orbitel Ltd., Sofia, Bulgaria

II. TEXT SEGMENTATION ALGORITHM

The function of the segmentation algorithm is to locate the information blocks in the document image. Two approaches, *boundary-based* (edge information transition from background to the information object block) and *region-based* (fill-up and segment these blocks).

Fig. **1**. illustrates the flow diagram for the segmentation algorithm.

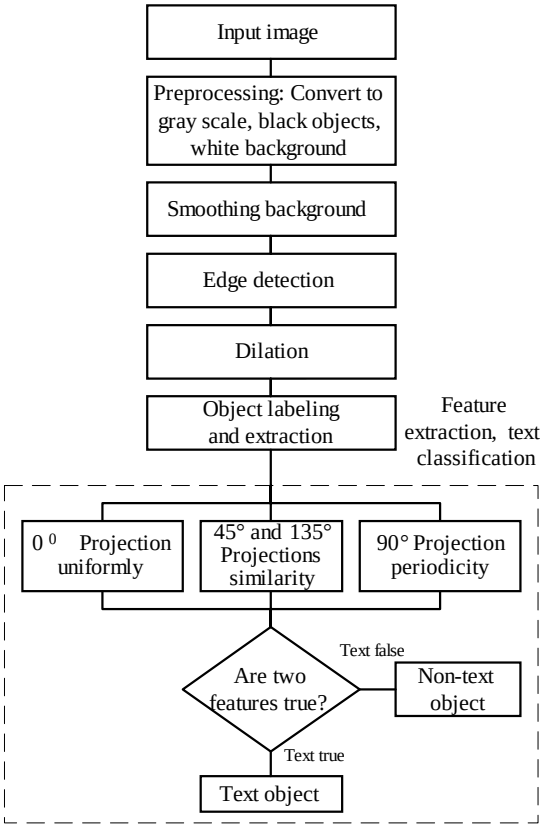

Fig. 1. Flow diagram for segmentation algorithm

Smoothing Background: This operation removes slight variation in the background by the histogram *h(i)* analysis. The threshold is set to retain 18% of pixels with the lowest intensities. Pixels *Z(i)* with intensities *i* above the threshold are set to 255 (background intensity level). If in the intensity interval 254-127 there isn't 18 % pixels all pixels in this interval are set to 255.

For k=0 to 127 $If \sum_{i=254}^{254-k} h(i) = (18 * \sum_{i=0}^{255} h(i))/100$ (1)

$Z(i)_{254-k}^{254} = 255$

$If \sum_{i=254}^{127} h(i) < (18 * \sum_{i=0}^{255} h(i))/100$ (2)

$Z(i)_{254}^{127} = 255$

Edge-detection: The edge detector seeks for gradient transform of the gray scale image *A*, using the Prewitt method. It realizes a convolution of two filter masks horizontal *Px* and vertical *Py* (Fig. 2.). The current pixel *Z8* is in the center of the window operator *A1-A9*.

-1	0	1
-1	0	1
-1	0	1

-1	-1	-1
0	0	0
1	1	1

A1	A2	A3
A4	A5	A6
A7	A8	A9

Fig. 2. Prewitt filter masks *Px, Py* and image area *A*

As the convolution result of the gray scale in the current pixel and his neighbors with masks *Px*, *Py* are obtained two scalar components *Hx*, *Hy*. The image area *A* is considered, when *A1..A9* are gray scale values. *Hx* and *Hy* are calculated by multiply the image area with *Px* и *Py*.

$$Hx = (A3 + A6 + A9) - (A1 + A4 + A7) \quad (3)$$

$$Hy = (A7 + A8 + A9) - (A1 + A2 + A3) \quad (4)$$

The magnitude *H(x,y)* and orientation *Q(x,y)* of the gradient can be computed from the standard formulas for rectangular-to-polar conversion:

$$H(x,y) = \sqrt{H_x^2(x,y) + H_y^2(x,y)} \quad (5)$$

$$Q(x,y) = \mathrm{Arctan}(H_y / H_x)$$

Then is calculated *H(x,y)*, and compared with a threshold 100. If *H(x,y)* value is less or equal to threshold the current pixel is set 0 (black) or in the other case is set 255 (white). In this way is done edge detection and binarization.

Dilation: A square structuring operator 3x3 is used. The dilation/ closing operation aims to fill-up the region and increase the connectivity within pixels so that labeling can be done more accurately. A square-structuring element is therefore a suitable candidate. The dilation is done repeatedly until there is no change in the output of this operation. If the current pixel is 0 and there is at list one neighbor with intensity *i=255* in 3x3 matrix the current pixel is set to 255.

In this method is applied the morphological nonlinear operation dilation on the binary page document image. The dilation operation $\otimes$ combines two sets *A* and *B*, using a vector sum. Dilation $A \otimes B$ is pixels set of all possible vector sums of couple pixels, by one from each pixel sets *A* and *B*.

$$A \oplus B = \{p \in \varepsilon^2 : p = a + b, a \in A, b \in B\} \quad (6)$$

Using structural operator *B* 1x2 is obtained the original object *A* closing on horizontal direction. The dilation example is given on (
Fig. **3**.), and with *X* is marked the coordinate system origin.

$$A = \{(1,0),(1,1),(2,1),(1,2),(3,2),(1,3),(4,0)\} \quad (7)$$

$$B = \{(0,0),(1,0)\} \quad (8)$$

$$A \otimes B = \{(1,0),(1,1),(2,1),(1,2),(3,2),(1,3),(0,4),(1,4),(2,3),(2,2),(4,2),(3,1),(2,0)\} \quad (9)$$

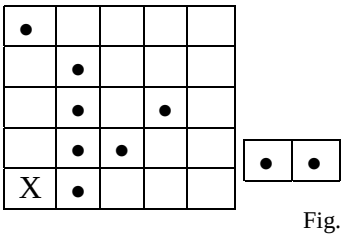

Fig. 3. Dilation: original object, operator, closing object

Objects labeling and extraction: A connected component is a set of connected pixels that share a specific property *V* (same color, intensity). Two pixels *p* and *q* are connected if there is a path from *p* to *q* of pixels with property *V*. The image will be represented by an array *A* that has *N* columns and *M* rows.

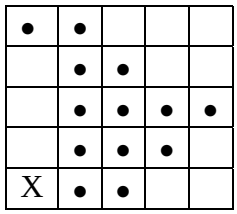

A[*x,y*] refers to the element in column *x* and row *y*, with $x \in \{0, N-1\}, y \in \{0, M-1\}$. Let *Q* be an array that is the same size as *A* and will hold the connected component labels *L*. For the beginning *L*=0 and is incremented for a new connected component. The goal is to end up with all of the pixels in each connected component having the same label *L* and all of the distinct connected components having different labels *L*. Some of the pixels in the same connected component will end up with different labels and it will be resolved at the end of the labeling process. A vector EQ will hold the equivalence class relations that are discovered as the algorithm is running.

The pixels with value zero are image background. The following algorithm will be described for 4-connected neighborhoods, applied on the binary image.

Step 1: Label pixel A[0,0]. If *A*[0,0]>0 then increment *L* and set *Q*[0,0]=*L*. This takes care of the first pixel in the image.

Step 2: Label the pixels in row y=0. For *x*=1 to *N*-1, check the value of *A*[x,0]. If *A*[x,0]>0 and *A*[x,0]=*A*[x-1,0] then set *Q*[x,0]=*Q*[x-1,0]. If *A*[x,0]>0 and $A[x,0] \neq A[x-1,0]$ then increment *L* and set *Q*[x,0]=L. This will cause

neighboring pixels in the first row that have the same value to have the same label (Fig. 4.).

0	1	1	1	1	0	0	2	2	2	2	0	0	0	3	3	0	0	4	4

Fig. 4. Sample of the first row pixels labeling

Step 3: Label the rest of the rows. The first element of each row is handled a little differently than the rest of the elements, since it has no left neighbor. For y=1 to M-1 do the following. If $A[0,y]>0$ and $A[0,y]=A[0,y\text{-}1]$ then set $Q[0,y]=Q[0,y\text{-}1]$. If $A[0,y]>0$ and $A[0,y] \neq A[0,y\text{-}1]$ then increment L and set $Q[0,y]=L$. This takes care of labeling the first element in the row.

Labeling the rest of the elements in a row requires that we look at both the neighbor above and the neighbor to the left. For simplicity, let us refer to the current pixel as p, the neighbor to the left as s and the one above as t. If $A[p]=A[s]$, but $A[p] \neq A[t]$ then set $Q[p]=Q[s]$. If $A[p] \neq A[s]$, but $A[p]=A[t]$ then set $Q[p]=Q[t]$. If $A[p] \neq A[s]$ and $A[p] \neq A[t]$, then increment L and set $Q[p]=L$. If $A[p]=A[t]$ and $A[p]=A[s]$ and $Q[s]=Q[t]$, then set $Q[p]=Q[t]$. This takes care of all the cases except if $A[p]=A[t]$, $A[p]=A[s]$ and $Q[s] \neq Q[t]$. This means that pixels s and t have the same values but different labels, and they are in the same component. We therefore label pixel p with the smaller of the two labels and record the fact that the larger label value is equivalent to the smaller one. Let $L1$ be the smaller value and $L2$ be the larger value, then set $Q[p]=L1$ mark $EQ[L2]=L1$. The first three rows are shown in Fig. 5.

0	1	1	0	0	0	2	0	0	3
0	0	1	0	4	4	2	0	5	3
0	0	1	0	0	4	0	0	0	0

Fig. 5. The first three image rows labeling

Features extraction and text classification: The purpose is to segment the image into text and non-text regions as best as possible, and then let the OCR system do make symbol recognition. The used features are the following:

0^0 Projection uniformly/ regularity feature: The most intuitive characteristics of text are its regularity. If the average of each three neighbors projection values are approximately equal (small dispersion) the regularity/ uniform feature test is true/ positive.

45^0 and 135^0 Projections similarity feature: The difference between the autocorrelation of 45^o projection and the cross-correlation between 45^o and 135^o projections is first computed.

The used equation for the cross-correlation normalized function is:

$$r = \frac{\sum_m [(x(m) - x_{aver}) * (y(i-d) - y_{aver})]}{\sqrt{\sum_m (x(m) - x_{aver})^2} \sqrt{\sum_m (y(m-d) - y_{aver})^2}} \quad (10)$$

where x,y are the projection pixel coordinates and i, m are projection elements numbers. If $r>=0,90$ can be accepted that these projections similarity is a positive feature.

90^0 Projection periodicity feature: The peak detection is carried out. Next the intervals between the peaks are extracted and the mean value of the interval calculated. If there are more than 50% of the intervals with regular spacing, the test is positive.

Our system takes advantage of the distinctive above characteristics of text that make it stand out from other image material. The text classification in two classes text and non-text is done if two of the above extracted features are true.

III. Experimental Test Results

The segmentation algorithm was tested on digitized paper documents. The proposed method was tested on 8 newspaper images with 23 separated text, images and graphics objects. Image size varied to 1024-768 pixels and 256 grey scale levels. Most of the text blocks were successfully separated from non-text regions. The algorithm for locating text is relatively fast.

Details of the implementation: The results obtained for this segmentation algorithm are shown in the below figures.

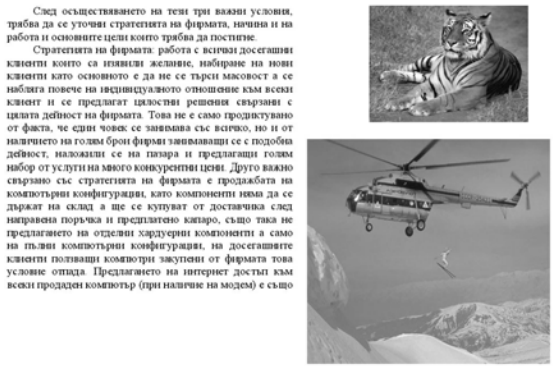

Fig. 6. Input original document image with text and plane

Fig. 7. After smoothing background and edge detection

Fig. 8. After dilation for connected component analysis

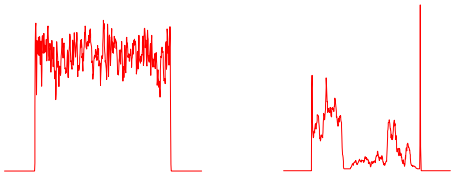

Fig. 9. 0^0 Projection uniformly feature (text, plane)

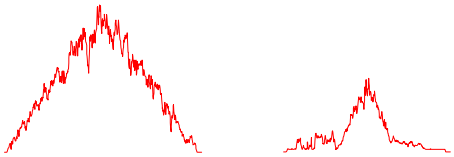

Fig. 10. 45^0 Projections for similarity feature (text, plane)

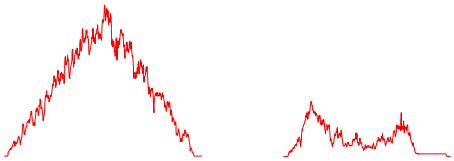

Fig. 11. 135^0 Projection for similarity feature (text, plane)

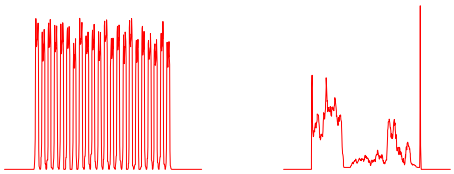

Fig. 12. 90^0 Projection periodicity feature (text, plane)

The developed algorithm was implemented as a Delphi program and tested in a Laboratory Television, Faculty of Communication and Technologies, Technical University-Sofia. Two computers' configurations were used under MS Windows 2000: Celeron 1700/ 500 MHz, RAM 512/ 128 MB. The final performance result for both configurations was less than one second. This good performance due to using for image manipulations "memory bitmap"and "scanline".

IV. Conclusions

In conclusion, a text segmentation algorithm is developed in two steps, segmentation and text classification. The two steps are implemented and tested. The programming realized algorithm is independent of the size and type of the characters and the position of the text in the document. This paper proposes a segmentation method that clusters successfully the regions of a mixed-type document image into text for OCR input and non-text areas.

There are some difficulties if the text object has only one row and the feature *Periodicity* 90^0 will be negative. This text region can be mixed-up with some texture region. In the future this research will be extended with exploring of the 0^0 projection for periodicity corresponding to the symbols' columns and space between them, using on word identification to make the algorithm more robust and suitable to different cases. A weighting function can be implemented instead of the hard AND operation in the final output of classification.

Reference

[1] S. Srihari, S. Lam, V. Grovindaraju, R. Srihari "Document image understanding", CEDAR, State University of New York at Buffalo, 1999.

[2] C. Ngin, "Text segmentation in printed documents", Computer Society Press, EE368A Final Project Report, 2001.

[3] "Project DEBORA", Instituto Superior Técnico (PT), 1999.

[4] Q. Yuan, C. Tan, "Page segmentation and text extraction from gray scale image in microfilm format", National University of Singapore, 2002.

[5] V. Wu, "Finding text in images", Computer Science Department, University of Massachusetts, 2001.

[6] R. Gonzalez, R. Woods, "Digital Image Processing", A-W Publishing, 1993.

An Algorithm for GPS Synchronized Power System Controllers and Information Networks

Angel B. Colov[1] Ilia G. Iliev[2] Rumen I. Arnaudov[3]

Abstract – The paper discusses an algorithm for synchronization of energy information measurement systems using GPS. The algorithm computes a future moment of time used for synchronization of the measurement controllers in the information network. The results derived by prediction are sufficient for the synchronization and measurement of Power Energy Systems (PES) necessities.

Keywords - GPS time synchronization, energy information networks.

I. INTRODUCTION

There are many publications about the application of GPS for network synchronization, synchronization of energy data network, energy information networks, cellular communication networks (GSM, CDMA) etc. There are on the market many devices, for this purpose, working with determined time accuracy. There are also GPS receivers specially designed for uniform time synchronization with high accuracy for computer networks, information-measurement system etc. Special algorithms for increasing the accuracy of the defined time are built-in their software (RIAM algorithms). The error is the order of dozens nanoseconds. This advantage is paid by the price. For synchronization purpose, it may be used reception of GPS signals and synchronization from one point either, or distributed, differential synchronization [1,3].

[7] discusses the applicability of general GPS receivers for synchronization in one point of Energy Information Measurement Networks. The sources and the types of errors received in the determination of the time through GPS are analyzed. Based on the analysis, the rate of variation of the informative quantities in the system for telemeasurement, control and management is discussed. The admissible quantization time error and the admissible time error for registration are determined. Based on these, the paper proposes an algorithm for synchronization with general GPS receiver and time prediction. The time determination error obtained by a general GPS receiver is not greater than 60 ms and taking into account the variation rate of the informative quantities in the system for telemeasurement, control and management in the PES we may conclude that the precision of the described in [7] methods for determination of the unified time (synchronization) with GPS is sufficient for the PES necessities.

[1] Angel Belchev Colov – assistant in Dept. of Electric Power Production in Faculty of Electrical Engineering in TU – Sofia E-mail abc@vmei.acad.bg

[2] Ilia Georgiev Iliev – assistant in Dept. of Radiotechnic in Faculty of Communications and Communication Technologies in TU – Sofia E-mail igiliev@vmei.acad.bg

[3] Rumen Ivanov Arnaudov – assoc. prof. in Dept. of Radiotechnic in Faculty of Communications and Communication Technologies in TU – Sofia E-mail ra@vmei.acad.bg

II. CHARACTERISTICS OF THE SYNCHRONIZATION SIGNALS AND DATA FROM GPS

GPS receiver is able to transmit information about the coordinates and the time in a message every one second. This message is transmitted over standard interface RS232 with pre-defined data rate. For receiving the full information, minimum 10ms are necessary. The signal time diagram and the data packages, received by the GPS receiver are shown on Fig.1. Besides this, the received data is time delayed compared to the time reference 1PPS.The signal 1PPS is a time reference, transmitted every 1 second, and defines the received data validity.

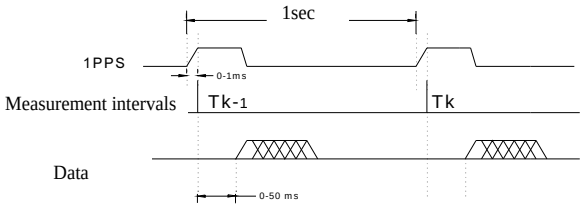

Fig.1

This signal has the following parameters:

- Rising time of the signal is approximately (20÷30) ns;
- The duration of the logical "1" of the impulse is approximately 200ms±1ms;
- Precision in self mode <130ns;
- Precision in hold mode <50ns.

The data is received for a time not greater than 50ms after this signal. This delay results in inaccuracy in determination of the time and it is comparative to the duration of the processes in PES and its influence must be removed. The time precision must be sufficient to be used for measurement of the values of the fast variance analog quantities. If they are measured and scanned by 10-bit ADC, the smallest conversion time is 36μs. Consequently the precision of the obtained time by GPS must be considered with the conversion time. For overcoming the data time delay of 10ms towards the reference time and the time adjustment of every measurement controller, it is necessary to use additional specialized communication controller included to the multi-computer system for control in real time (Fig.2).

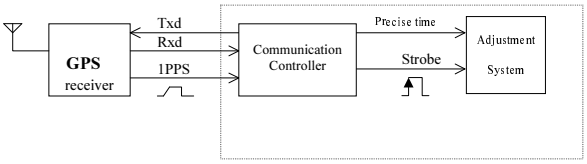

Fig.2

The functions of the communication controller of the system are widened with the algorithms for analysis and prediction of the real time. The prediction purpose is to obtain data every 1 second for the time from the GPS receiver and the computed prediction for the current second. The time calculation by the communication controller is based on the full data from the status message of the receiver. Data like: availability and number of the tracked satellites, Doppler frequency shift, a correction for the fraction part of the second (there is a time delay in the path from the satellite to the Earth), are necessary for authenticity of the computed time. The data for the fraction of the second is transmitted in 2 bytes in I/O message. The value formed from these bytes increases monotonically with rate dependant on every GPS receiver and the current data for correction from satellite. When this value becomes maximum it zeroes and start increasing again. The physical explanation in the increasing is that the value formed by this data is a liner increasing function with overloading constraint or ramp function ***R(t)***. (Fig.3)

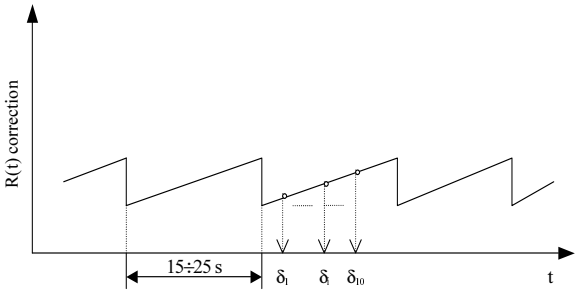

Fig.3

The time of variance form 0 to maximum value of this function is different for the different GPS receivers even though they are in one and the same point. This time varies from 15 to 25 s. Fig.4 shows the error variation, formed by the difference between the times obtained by the GPS receiver and stationary standard atom clock.

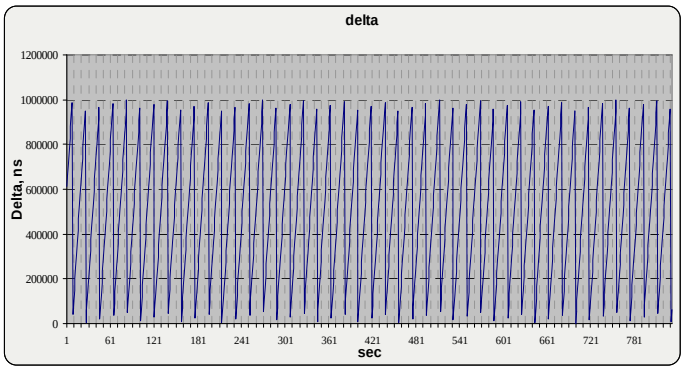

Fig.4

To be able to predict the time, the communication controller must carry out a synchronization signal toward the system that needs the precision time, based on the ramp function data. In the moment of transmitting the synchronization strobe impulse (Fig.5) it is transmitting the synchronized precise time.

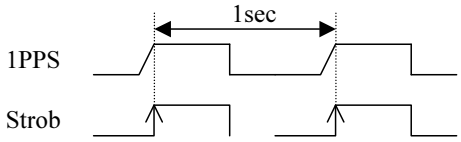

Fig.5

It is a value that is received by every controller by the GPS receiver with zero time of data processing.

Fig.6 shows the value variation derived by two bytes, carrying the information about the fraction part of the second.

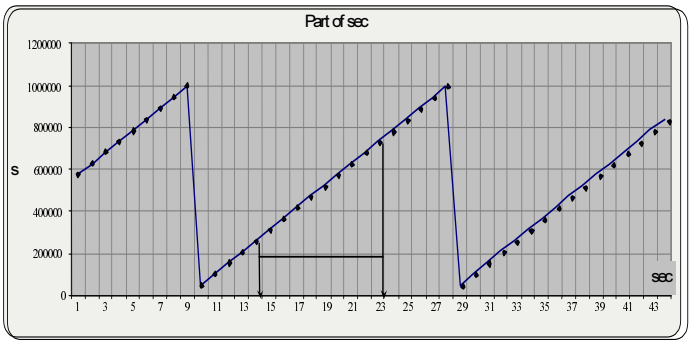

Fig.6

III. Time Prediction Algorithm by GPS Receiver Measurement

The paper proposes the following time prediction algorithm:

1. Scanning the moment from overloading to zero of the ramp function;
2. Searching 10 contiguous function values, where the last one has positive derivative (interval of constant increasing of the function);
3. Omitting the first and the last value;
4. Calculating the prediction correction based on the remaining 8 values:

$$\delta_{cp.} = \frac{1}{8}.\sum_{i=1}^{8}\delta_i \qquad (1)$$

5. Adding the computed prediction to the time data from the GPS receiver in the next moment;

The corrected data is transmitted to the synchronized system. The main system controller zeroes the internal free-running timer in the moment of receiving the precision time by the communication controller. The internal timer accumulates the time value automatically for 1 or more seconds. This time is necessary for the registration of the measured quantities for one period of comparison of the time. It is supposed that for a small period of time the internal

quartz oscillator (the clock oscillator of the measurement controller) has minimal frequency deviation.

The predicted time, formed by δ_{cp}, changes only when the number of the tracked satellites by the GPS receiver is changed. In this case, the prediction controller makes a new measurement in an interval of 15 to 22 s to form a new δ_{cp}. During this interval, the time is transmitted with the old prediction. Fig.7 shows the program algorithm for synchronization.

IV. Measurement Data

Fig.8 shows the deviation of the absolute error between the predicted and the real time obtained by the GPS receiver. The predicted time is computed following the previously described algorithm.

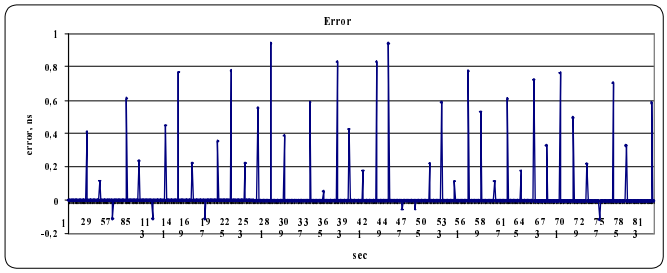

Fig.8

The root-mean square (RMS) error of the computed absolute error is not greater than 0.318ns. Fig.9 shows the absolute error deviation for the changing the number of the tracked satellites.

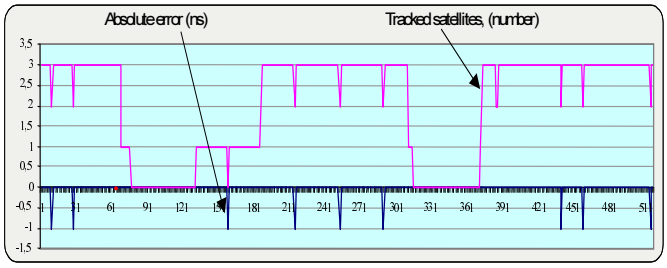

Fig.9

According to the measured data we may conclude that the time prediction algorithm works with sufficient error. The maximum deviation of the predicted results is not greater than 1ns and the RMS error is not greater than 0.318ns. When the number of the tracked satellites is changed the error is of the order of 1ns.

V. Conclusion

The application of general GPS receiver (without specialized built-in function for increasing the time precision) is real the synchronization of information measurement in the Systems in the Energy Systems the only drawback of the method is that the precision time data is delayed towards the time reference computed by the GPS receiver correlator. Consequently this signal 1PPS cannot be used for direct time correction of the separate measurement controller. The proposed algorithm removes this drawback by prediction of the time value in a future moment of appearing the signal 1PPS. In this way first data for the unified time is loaded in the measurement controllers and after receiving the reference signal they are actualized as real unified time. The measurement data for prediction error is satisfactory and the error value is not greater than 1ns, including the case of changing the number of the tracked satellites.

References

[1] Sangeeta Nagrare, M. R. Sivaraman, Synchronization for WAAS over Indian Airspace using GPS, The Asian GPS Conference 29-30 October 2001, New Delhi.

[2] Pratap Misra, Brian P. Burke, Michael M. Pratt, GPS Performance in Navigation, Proceedings of the IEEE, Vol. 87, No. 1, January 1999

[3] Enge, P.K. Global positioning systems: signals, measurements, and performance, *International J. Wireless Information Networks* 1(2)

[4] John F. Hauer, Jeff E. Dagle, Pacific Northwest National Laboratory, White Paper on Review of Recent Reliability Issues and System Events, Transmission Reliability Program U.S. Department of Energy

[5] G. Gross (UIUC), A. Bose (WSU), C. DeMarco (UWM), M. Pai (UIUC), J. Thorp (Cornell U) and P. Varaiya (UCB) PSERC, White Paper on Real-Time Security Monitoring and Control of Power Systems, Transmission Reliability Program U.S. Department of Energy

[6] H. Quinot, H. Bourlès, T. Margotin, "Robust Coordinated AVR+PSS for damping large scale power systems ", article accepted for publication in the IEEE PES Transaction

[7] I Iliev, A Colov, R Arnaudov, "Application analysis of GPS used for synchronization in energy information networks", ICEST 2003, Sofia, pp462 - 465

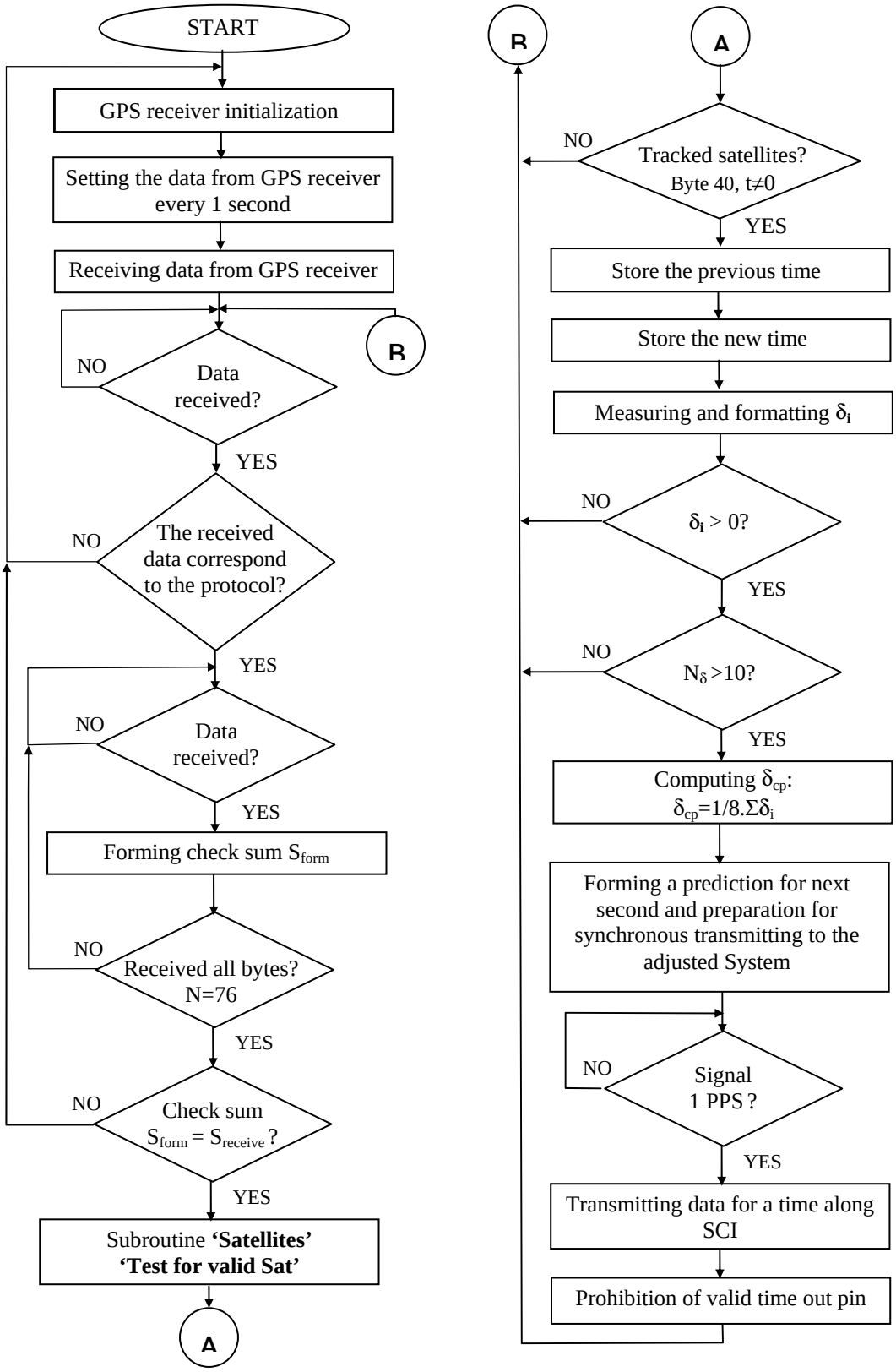
START
GPS receiver initialization
Setting the data from GPS receiver every 1 second
Receiving data from GPS receiver
R
NO
Data received?
YES
NO
The received data correspond to the protocol?
YES
NO
Data received?
YES
Forming check sum S_{form}
NO
Received all bytes? N=76
YES
NO
Check sum $S_{form} = S_{receive}$?
YES
Subroutine **'Satellites'** **'Test for valid Sat'**
A
R
A
NO
Tracked satellites? Byte 40, t≠0
YES
Store the previous time
Store the new time
Measuring and formatting δ_i
NO
$\delta_i > 0$?
YES
NO
$N_\delta > 10$?
YES
Computing δ_{cp}: $\delta_{cp}=1/8.\Sigma\delta_i$
Forming a prediction for next second and preparation for synchronous transmitting to the adjusted System
NO
Signal 1 PPS ?
YES
Transmitting data for a time along SCI
Prohibition of valid time out pin

Fig.7

Complex Behavior in Sigma-Delta Modulator

Cvetko D. Mitrovski

Abstract: **In this paper we investigate the dynamic behavior of a general class of second order single loop sigma delta modulators driven by a constant input. The proposed approach is based on nonlinear dynamic analysis of the piece wise linear model of the modulator.**

Keywords: **Sigma-delta modulator, trajectories, fractals, attractor, phase space.**

I. INTRODUCTION

The sigma delta modulation, as a method of analog to digital conversion has attracted much research interest since it was for the first time presented in 1962[1]. This technique is now finding widespread use in various signal processing applications, which is motivated by both, simplicity of the design and the fault tolerance to fabrication errors. The last two factors make the sigma delta modulators very suitable to integrated circuit applications.

The devices designed on the principle of sigma-delta modulation are non-linear systems which convert a time sampled analog signal to a stream of bits. Usually, they consists one or two integrators and a one bit quantiser in a feedback loop. In general, the basic structure could be modified by substituting the integrator(s) with any subsystem with low-pass or band-pass characteristics, while the other parts remain the same. This configuration can be generalized as a non-linearity within a feedback path, which is a classic route to complex behavior [2]. Therefore, the exact analyze of any sigma delta modulator is highly nontrivial.

In this paper we use nonlinear dynamic to discover the properties of a class of single loop second order modulators realized with an arbitrary band pass filter operating on the boundary of its stability region. This problem is actually generalization of the problem of band-pass sigma delta modulation analyzed in [3][4].

In this paper we first model the sigma delta modulator by piece wise linear model and after that we analyze the nature of its trajectories and their dependence on the parameters and the initial conditions. At the end we give some conclusions illustrated by our simulation results.

II. BASIC SIGMA–DELTA MODEL

The general structure of basic Sigma delta modulator consists of integrator and a one bit quantizer in a feedback loop. In general case, the integrator can be substituted by any subsystem with a properly chosen transfer function, as shown in Figure 1.

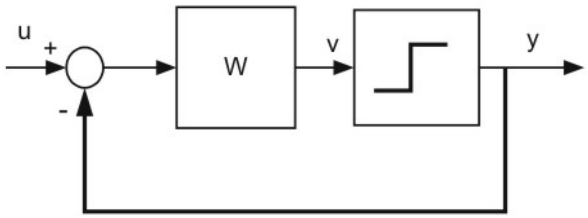

Figure 1. Block diagram of single loop sigma delta modulator

In our study we suppose that the integrator(s) is(are) substituted by the second order subsystem

$$W(z) = \frac{b_1 z^{-1} + b_0 z^{-2}}{1 - 2\cos(\theta) z^{-1} + z^{-2}}, \qquad (1)$$

where: b_1 and b_0 are arbitrary parameters and θ is the angle which determines the pole positions of W(z) on the unit circle. This model is an extension of the model analyzed in [4], in which the parameters b_1 and b_0 were chosen to be

$$b_1 = 2\cos(\theta); \quad b_0 = -1 \qquad (2)$$

The dynamic behavior of this model, can be described by the following system of difference equations

$$\begin{aligned} x_1(k+1) &= x_2(k) \\ x_2(k+1) &= 2\cos(\theta) x_2(k) - x_1(k) - f(.) \end{aligned} \qquad (3)$$

where:

$$\begin{aligned} f(.) = b_1 &\left(u(k) - \mathrm{sign}(x_2(k))\right) + \\ &+ b_0 \left(u(k-1) - sign(x_1(k))\right), \end{aligned} \qquad (4)$$

and $x_i(k)$, i=1,2 are the internal states of the modulator.

Table -1

i	Ri	$x_1(k)$	$x_2(k)=x_1(k+1)$	f(i)
0	R_0	$x_1(k)=0$	$x_2(k)=0$	$U(b_1+b_0)$
1	R_1	$x_1(k)>0$	$x_2(k)>0$	$U(b_1+b_0)-b_1-b_0$
2	R_2	$x_1(k)<0$	$x_2(k)>0$	$U(b_1+b_0)-b_1+b_0$
3	R_3	$x_1(k)<0$	$x_2(k)<0$	$U(b_1+b_0)+b_1+b_0$
4	R_4	$x_1(k)>0$	$x_2(k)<0$	$U(b_1+b_0)+b_1-b_0$
5	R_5	$x_1(k)=0$	$x_2(k)>0$	$U(b_1+b_0)-b_1$
6	R_6	$x_1(k)=0$	$x_2(k)<0$	$U(b_1+b_0)+b_1$
7	R_7	$x_1(k)<0$	$x_2(k)=0$	$U(b_1+b_0)+b_0$
8	R_8	$x_1(k)>0$	$x_2(k)=0$	$U(b_1+b_0)-b_0$

[1]Cvetko D. Mitrovski is with the Faculty of Technical Sciences, I.L.Ribar bb, 7000 Bitola, Macedonia, E-mail: cvetko.mitrovski @uklo.edu.mk

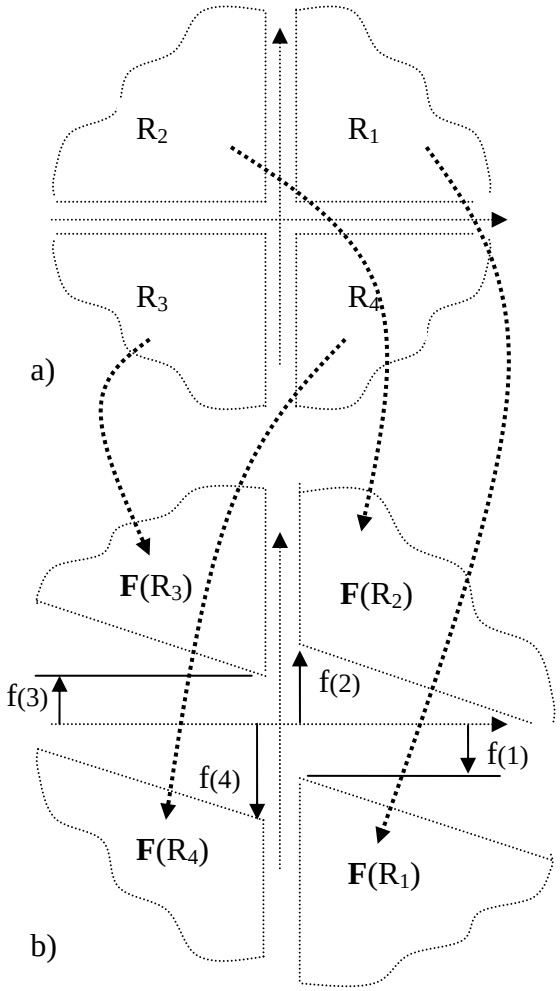

Figure-2. a) Regions of the phase space of the map b) Images of the regions R_i,i=1,2,3,4.

Since f(.) depends on the terms sign(x_2(k) and sign(x_1(k), in case of constant input u(k)=u(k-1)=U, its values will belong to a finite set of nine values given in the table 1.

III. Piece Wise Linear model

The above system can be modeled by the piecewise-linear map $\mathbf{F}(\mathbf{x}(k)): R^2 \rightarrow R^2$ defined by

$$\mathbf{x}(k+1) = \mathbf{A}\mathbf{x}(k) + \mathbf{b}s_i \quad \text{for } \mathbf{x}(\mathrm{k}) \in R_i \qquad (5)$$

where:

$$\mathbf{x}(k) = \begin{vmatrix} x_1(k) \\ x_2(k) \end{vmatrix}; \quad \mathbf{A} = \begin{vmatrix} 0 & 1 \\ -1 & 2\cos(\theta) \end{vmatrix}; \quad \mathbf{b} = \begin{vmatrix} 0 \\ 1 \end{vmatrix},$$

R_i, i=0,1,2,3,4,5,6,7,8 are disjoint subspaces that cover R^2 and s_i=f(i).

The matrix **A** is the Jacobian of the map and it has an unit module (|det(**A**)|=1) for any θ. Therefore, the transformation **A** is a rotation on an ellipse with center in origin (0, 0) and axis at $\pm\pi/4$.

According to this, each trajectory starting from any initial point will visit the regions R_i i=0,1,…,8 in some order by generating an infinite symbolic sequence "$s_0s_1…s_k…$" composed by the indexes of the visited regions. These symbolic sequences are generated by some patterns, which could be determined by analyzing the position of the images of the disjoint regions R_i, (**F**(R_i)), i = 0,1,2,..,8 and their originals.

In Figure-2 we have illustrated the transformations of the regions R_1, R_2 R_3 and R_4 by the map (5) while the transformation of the other regions (positive and negative parts of the axes Ox_1 and Ox_2) are not shown.

The relative position of the images of the regions **F**(R_i) depend on the parameters of the map. If b_0<0, then the regions **F**(R_1) and **F**(R_2) (**F**(R_3) and **F**(R_4) are overlapping while for b_0>0 they are not.

If **F**(R_1) and **F**(R_2) are overlapping, then the images of R_5, R_6, R_7 and R_8 satisfy the following relations:

$$\mathbf{F}(R_5) \subset \mathbf{F}(R_1) \cap \mathbf{F}(R_2) \qquad (6)$$

$$\mathbf{F}(R_6) \subset \mathbf{F}(R_3) \cap \mathbf{F}(R_4) \qquad (7)$$

$$\mathbf{F}(R_7) \cup \mathbf{F}(R_8) \subset R_5 \cup R_6 . \qquad (8)$$

Otherwise, **F**(R_5) (**F**(R_6)) is equidistant to the parallel sides of **F**(R_1) and **F**(R_2) (**F**(R_3) and **F**(R_4)).

By changing the parameter θ we modify the angle of open sectors **F**(R_i), i=1,2,3,4, while by changing of b_0, b_1 and U we influence on their vertical position in R^2 and on their relative position. With that, we influence on the map dynamics by modifying the transition patterns among the regions. Typical example for this is the transition from R_1 to R_1, which could be enabled or disabled by choosing the appropriate value for the corner points of **F**(R_1) below or above the x_1 axis.

IV. Unbounded trajectories

If b_0 >0 ($2b_0$=f(2)-f(1)=f(3)-f(4)) the images of the regions **F**(R_1) and **F**(R_2) (**F**(R_3) and **F**(R_4)) will not overlap. In that case any trajectory starting from any initial condition will diverge spirally toward infinity. This phenomenon is obvious when f(1)*f(2) <0 (f(3)*f(4) <0) because in that case, in each iteration, the shifting part of the map pushes the image toward the exterior of the ellipse.

If f(1)*f(2)>0 (f(3)*f(4) >0) the trajectories remain globally expanding, but they have some local contractions. The smaller the gap between **F**(R_1) and **F**(R_2) is, the more dominant local contractions are. In this case the trajectories while evolving in some regions are pushed, sometimes toward the interior of the ellipses and sometimes toward its exterior. Therefore the trajectories create curved ellipse like patterns which are appearing periodically in the phase space (Figure-3a). By increasing the value of b_0, the gap between **F**(R_1) and **F**(R_2) is increased and the intensity of the local contractions in the

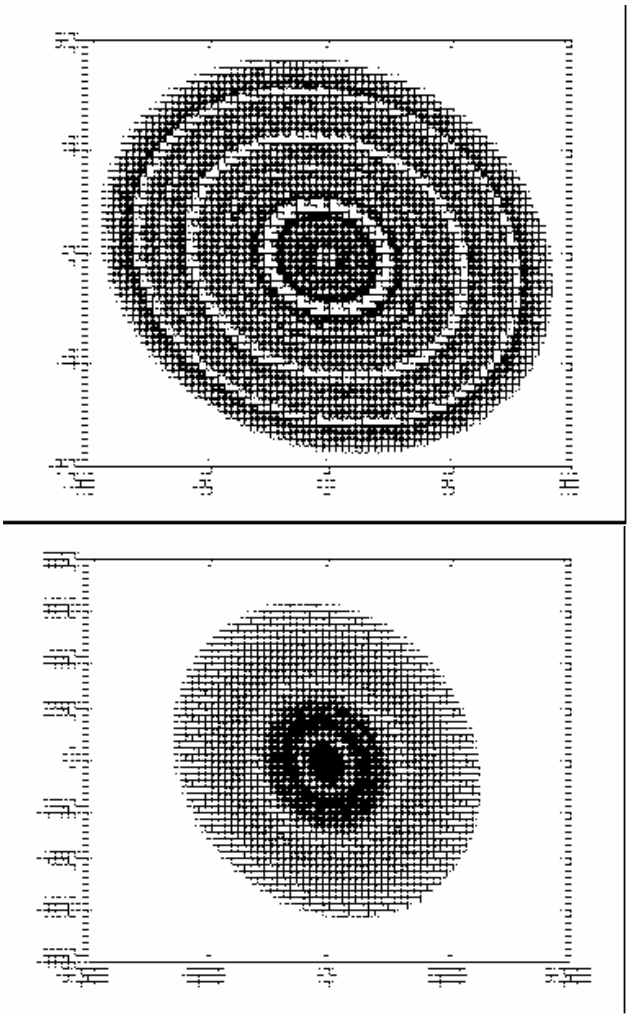

Figure 3 Expanding trajectories starting from **x**(0)=(0.00237, -0.0123) of the map with parameters θ=1.73, b_1=2*cos(1.73) a) and b_0=0.0001. b) b_0=0.05

expanding trajectories is reduced. That leads to elimination of the ellipse like curvatures in the expanding trajectories as illustrated in Figure 3b).

V. BOUNDED TRAJECTORIES

If b_0 (b_0<0) enables even a slightest overlapping of **F**(R_1) and **F**(R_2) (**F**(R_3) and **F**(R_4)), then the trajectories of the map (5) are bounded by an open concave eight corner polygon. In case of U=0, this polygon has a central symmetry.

No matter whether $U \neq 0$ or U=0, all the trajectories that start out of this polygon are trapped in it (after a certain number of iterations). Therefore we shall concentrate on the trajectories which are starting from the interior of this polygon and remain in it for all the time. While evolving, these trajectories also generate infinite symbolic sequences composed of the indexes of the visited regions.

If the generated symbolic sequence is periodic, then the trajectory is either periodic (finite set of points), or dense on a finite number of ellipses. If they are periodic, then the corresponding trajectories are fractal, and if they are eventually periodic, then the trajectories posses his irregular

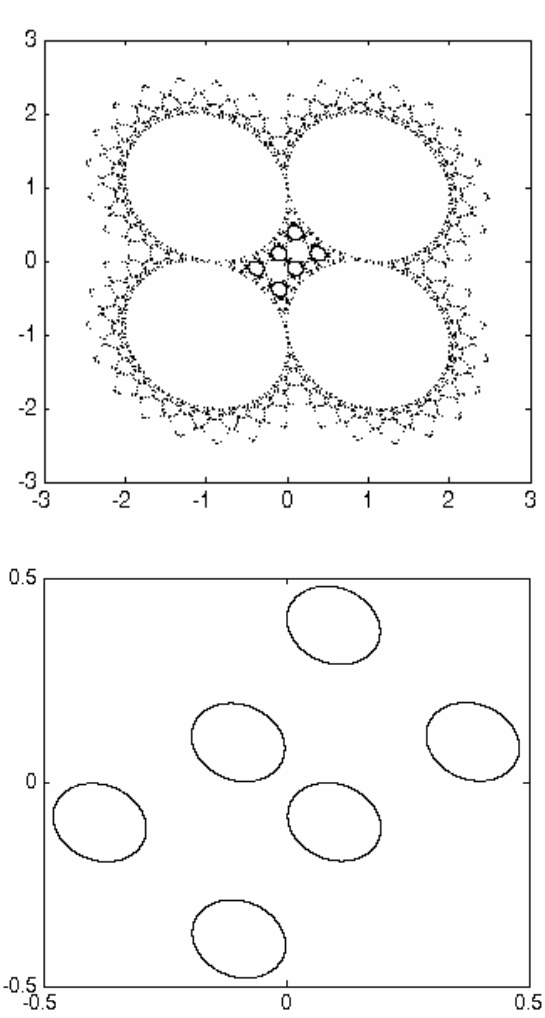

Figure 4. Bounded trajectory of the map U=0, θ =1.73, b_1 = 2*cos(θ), b_0 =-0.001 a) starting from **x**(0)=(0.00237, -0.0123) b) starting from **x**(0)=(0.00512, -0.0626).

part after which they are attracted either by a sets of fixed points or by a sets of dense ellipse like orbits.

The existence of various types of trajectories is illustrated in Figure-4 and Figure-5.

The trajectory shown in Figure-4a has irregular (fractal like) initial part which converges to a set of six small ellipses, while the trajectory starting from **x**(0)=(0.00512, -0.0626) remains on six dense ellipses.

In case when b_1 = 2*cos(θ) and b_0 =-1, the map (5) models the band-pass sigma delta modulator [4]. For this combination of parameters b_1 and b_0, the map generates all tree types of trajectories. In figure 5, we illustrate a fractal trajectory of this map, starting from **x**(0)=(0.016,-0.0485), which visits infinite number of ellipses. While evolving it shapes almost all the ellipse regions in the phase space from which only regular trajectories could be generated (sets of periodic points and sets of dense ellipses).

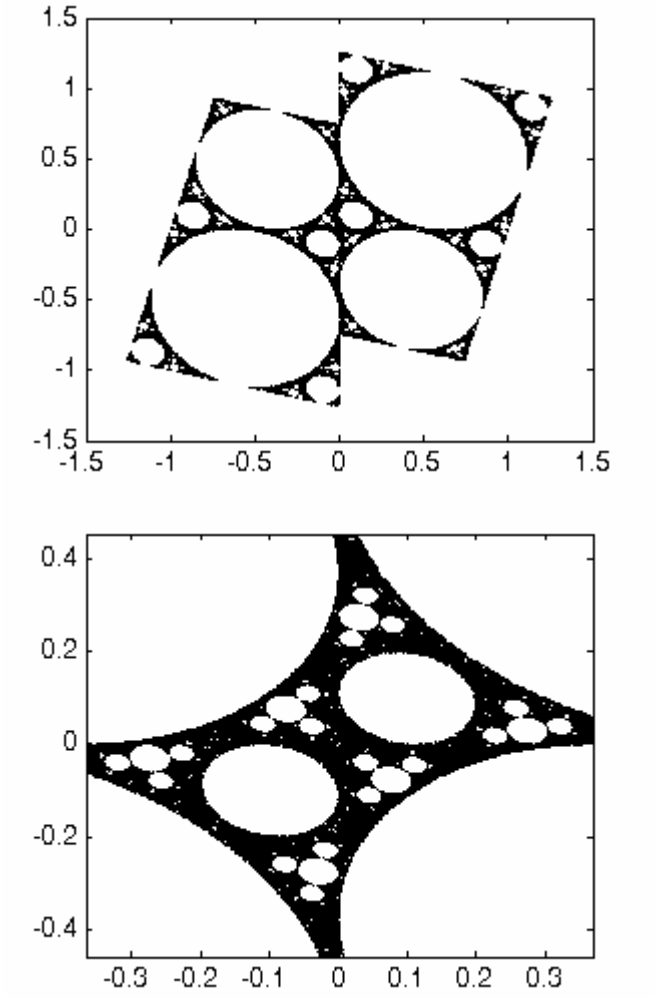

Figure 6. Fractal trajectory of the map U=0, θ =1.7, b_1 = 2*cos(θ), b_0 =-1 starting from **x**(0)=(0.016, -0.0485). b) Zoomed detail

So, for a constant input U we could obtain various symbolic sequences in dependence of the initial conditions. Since the symbolic sequence determines the bit stream output of the modeled sigma delta modulator, it means that we could have different, even false outputs.

VI. CONCLUSION

In this paper we have observed a wide class of constant input driven sigma delta modulators realized with a second order digital filter (operating on the boundary of its stability region) and one bit quantizer in a feedback loop. For this class of devices we have determined the piece wise liner map which describes its internal behavior. After that we have determined that the parameter b_0 determines the safe operation space.

In case when b_0 >0 the map exhibits unbounded trajectories which means that the modeled real sigma delta modulator could be damaged due to excessive internal dissipation. In cases when b_0<0, the map exhibits bounded trajectories which cannot damage the modeled device, but its complex behavior could lead to different and sometimes false output streams of the constant driven real device.

REFERENCES

[1] H. Inose, Y. Yasuda and J. Marakami, *"A telemetering system by code modulation, delta-sigma modulation,"* IRE Trans. on Space, Electronics and Telemetry, SET-8, pp. 204-209, Sept. 1962.

[2] L. O. Chua and T. Lin "Chaos in digital filters", *IEEE Trans. Circuits and Systems*, Vol 35 pp 648-658, June 1988.

[3] O. Feely and D. Fitzgerald "*Nonlinear Dynamics and Chaos in Sigma–Delta Modulation*", Journal of the Franklin institute, Vol 331B, pp 903-936, 1994.

[4] O. Feely and D. Fitzgerald "Band-pass Sigma-Delta Modulation –An Analysis From the Perspective of Nonlinear Dynamics", IEEE *J. Circuit Theory and Applications*, vol 18, pp 146-149, 1996.

[5] C.W. Wo and L. O. Chua "Symbolic dynamics of Piecewise-Linear Maps", *IEEE Trans. Circuits and Systems II,* Vol 41 pp 420-424, June 1994.

Session RCMTA:

Radio Communications, Microwave Technique and Antennas

Fixed Beam Antenna Effectiveness Study in Remote Control Radio Systems

Boncho G. Bonev[1] and Emil S. Altimirski[2]

***Abstract* - The paper describes fixed beam antenna effectiveness at a remote control system base station. Data acquisition time and message missing probability at different beam numbers and terminal dislocations are being analyzed.**

***Keywords* - antenna array, remote control systems**.

I. INTRODUCTION

One of the main restriction factors for communications is interference. It could be caused by different reflected signals, as well as by simultaneous function of more than one transceiver at the same frequency. It could cause radio link disturbances at a wireless system and severely decrease its functionality. As a result adaptive antenna array are being widely applied in the last years. They are mainly used at mobile communications systems [1,2].

The paper analyses fixed direction beam antenna array at remote control systems.

II. THE PROBLEM

The system described herein comprises a base station (BS), which acquires dislocated objects information, the latter being also stationary, equipped with radio-terminals each of them, used for parameters estimation. Some of the terminals are at objects with mains power supply and are permanently switched on (RT – P). Data is acquired from them upon a request from the base station, and subsequently all radio-terminals send the appropriate information in a sequence. If a given parameter is not within the predefined boundaries, messages are being transmitted upon a request from the radio-terminal. The rest (RT – A) are dislocated at objects without a mains power supply and are supplied by means of batteries. They send the measurements data upon an individual initiative at a given time interval.

The base station antenna is not directed towards a horizontal plane and radio link is achieved by means of a single radio channel. The latter leads often to noise occurrences, as a result of a simultaneous transmit of more than one radio-terminal, as well as loss of information.

The article proposes a method for noise reduction, by means of base station antenna pattern division into a given number of beams, thus allowing parallel exchange with the terminals.

[1] Boncho G. Bonev is with Faculty of Communications and Communications Technologies, Technical University, 1000 Sofia, Bulgaria, E-mail: bbonev@tu-sofia.bg

[2] Emil S. Altimirski is with Faculty of Communications and Communications Technologies, Technical University, 1000 Sofia, Bulgaria, E-mail: altimir@tu-sofia.bg

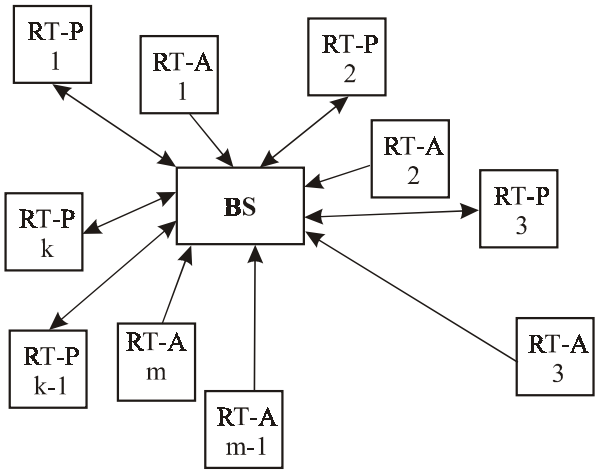

fig. 1

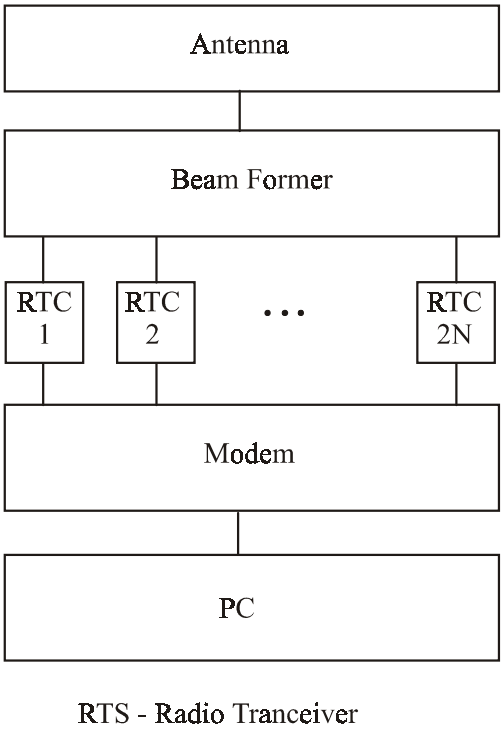

RTS - Radio Tranceiver

fig. 2

2N beams are being formed by means of a Beam Former (fig.2), consisting of phase–shift circuits. 2N transceivers, receiving and transmitting the corresponding beam signals are

connected to it. By means of a modem data is being send to a personal computer (PC) for processing and storage.

Antenna system is being realised by means of one or more antenna arrays. As a result the following diagram is being achieved (fig.3).

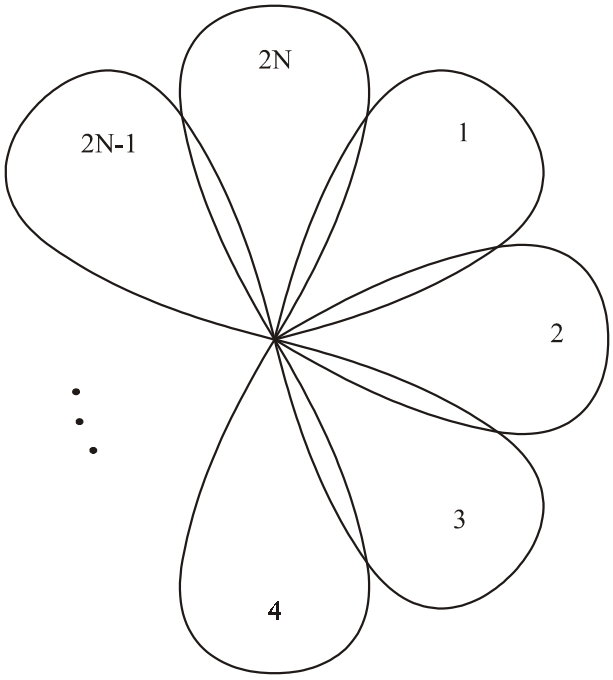

fig. 3

In this case the base station acquires first of all data from all radio terminals, situated at beam zones with an odd number, thereafter from those with an even number. Simultaneous service of odd and even number beam zones leads to noise occurrences between adjacent zones and will not allow the desired effect to take place.

III. INVESTIGATION RESULTS

Antenna pattern division into beams aims data acquisition time reduction at radio terminals, as well as missing message probability reduction at stations with a battery power supply.

By means of a computer simulation based on real data, terminals data acquisition time dependence in cases of equal and real radio-terminals dislocation is being derived. The latter is shown in fig. 4.

In case of an equal distribution, data exchange time is proportional to 1/N. In case of a real nonequal distribution, it decreases with beam number increase as well, but is greater, as a result of radio – terminals concentration at given beams. In cases of antennas with 10 and more beams, data exchange time does not decrease considerably with beam number increase. Additional complication and price rise of the appropriate hardware are to be expected in this case.

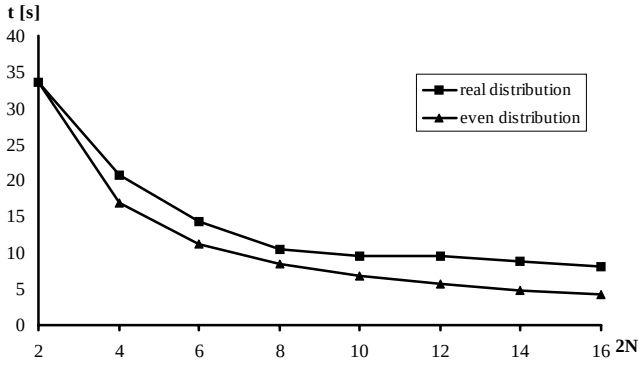

fig. 4

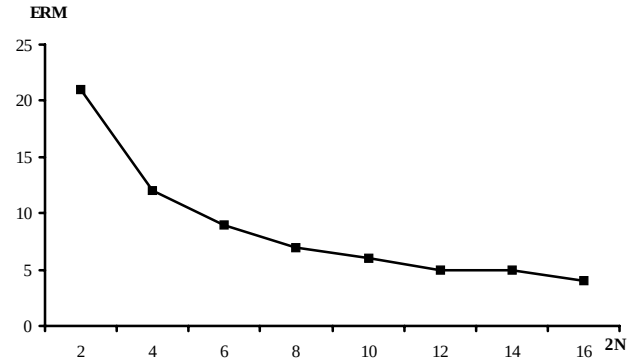

fig. 5

Besides of data exchange time decrease, fixed – beam antenna application leads to missing messages number reduction at radio – terminals upon a corresponding self-initiative. Fig. 5 represents missing messages number dependency in twenty - four hours.

IV. CONCLUSIONS

As a result of the analysis, it could be concluded that fixed beam antenna application at base station leads to a significant data exchange time and missing messages number reduction. Besides of that, the above mentioned parameters decrease with the increase of beam number, considerably for antennas with 8 – 10 beams. Usage of a greater number of beams is not justifiable from a technical and economical point of view, due to transceivers number increase and complications in single beam signals processing.

REFERENCES

[1] M. L. Dukić, M. L. Janković, B. L. Odadžić, “Analysis of SDMA&Smart Antenna Techniques for Existing and New Mobile Communication Systems”, Telfor’2001, Belgrade.

[2] M. A. Halim, “Adaptive Array measurment in communications”, Artech house, 2001,Boston - London.

Scattering Parameters of Exponential Transmission Line

Zlata Cvetkovic[1]

Abstract– **Exponential lossless transmission line as two port network is observed in the paper. Its *ABCD* parameters are determined using Picard-Carson's method. Conversion of *ABCD* parameters to scattering parameters is also done. Scattering parameters are plotted using program package Mathematica 3.0.**

Keywords–**Scattering parameters, *ABCD* parameters, Exponential transmission line, Picard –Carson method.**

I. INTRODUCTION

Scattering parameters are important in microwave design because they are easier to be measured and to work with at high frequencies than other kinds of two port network parameters [1].

In the paper [2] formulas for conversions between various networks matrices are presented. While four of these matrices, *Z, Y, h* and *ABCD*, relate voltage and current at the ports, the other two, *S* and *T*, relate wave quantities. The equations developed in [2] are valid for complex and unique impedances on input and output ports.

Relationships presented in paper [3] between different two port network matrices are valid for homogeneous transmission line.

Author of the paper [4] comments relationships between various two port network matrices presented in paper [3] and in other presented papers and points out that results depend on the chosen reference impedance.

The scattering parameters of a lossless, exponential transmission line are studied in detail both in frequency and time domains [5]. Time domain scattering parameters are obtained by taking the inverse Laplace's transform of their corresponding functions in frequency domain. By taking the causality condition into consideration, the time domain scattering parameters in a rapid convergence power series are cast. Each term of the power series represents a signal component generated by the exponential line when the signal travels around trip.

A new approach for the time domain simulation of transients on a dispersive and lossy transmission line terminated with active devices is presented in [6]. The method combines the scattering matrix of an arbitrary line and the nonlinear causal impedance functions at the loads to derive expressions for the signals at the near and far ends. A time domain formulation is proposed using the scattering matrix representation. The algorithm assumes that dispersion and loss models for the transmission lines are available and that the frequency dependence is known.

Conversion from *ABCD* parameters to scattering parameters is performed in this paper. The scattering parameters for lossless exponential transmission line are determined using given expressions. *ABCD* parameters of transmission line are calculated using Picard-Carson's method.

II. SCATTERING PARAMETER FORMULATION

Any linear two port network can be described as a set of scattering parameters which relate two reflected and two incident waves. These waves are variables, which depend on the total currents and voltages at the two ports.

Scattering parameters are defined as,

$$b_1 = S_{11}\ a_1 + S_{12}\ a_2\,, \tag{1}$$

$$b_2 = S_{21}\ a_1 + S_{22}\ a_2\,, \tag{2}$$

where a_1, a_2, b_1 and b_2 are defined as the incident and reflected waves from Port 1 and Port 2, respectively. S_{ij}, for $i, j = 1, 2$, are the scattering parameters.

In generally, they tell us how much power "comes back" or "comes out" when we "throw power at" a network. They also contain phase shift information.

S_{11} and S_{22} are simply the forward and reverse reflection coefficients with the opposite port terminated with reference impedances, which are equal to the characteristic impedances of the exponential line at left and right sides, respectively. S_{12} and S_{21} are the forward and reverse gains assuming reference impedances equal to characteristic impedance of the exponential line at left and right sides, respectively.

The signal flow graph in Fig. 1 gives the situation for the scattering parameter interpretation in voltages.

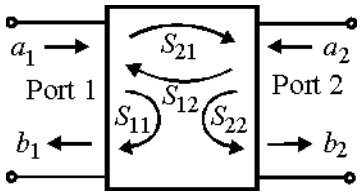

Fig. 1. Two port network represented with scattering parameters.

ABCD parameters for a two port network shown in Fig. 2 are written as

$$U_1 = A\,U_2 - B\,I_2\,, \tag{3}$$

$$I_1 = C\,U_2 - D\,I_2\,. \tag{4}$$

A relation between the *ABCD* parameters of a lossless exponential transmission line and the associated scattering parameters can be derived.

[1] Zlata Z. Cvetkovic is with the Faculty of Electronic Engineering, University of Nis, Beogradska 14, 18 000 Nis, Serbia, Yugoslavia, E-mail: zlata@elfak.ni.ac.yu

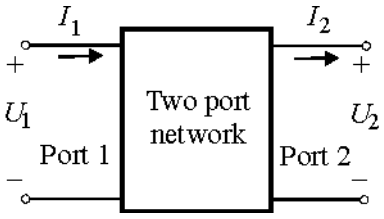

Fig. 2. A general two port network.

If we assume that reference impedances at Port 1 and Port 2 are pure real and equal to characteristic impedance of the exponential line at left and right sides, R_{01} and R_{02}, respectively, we can start from relations

$$a_j = \sqrt{R_{0j}}\, I_{ji} \tag{5}$$

and

$$b_j = \sqrt{R_{0j}}\, I_{jr}, \tag{6}$$

where R_{0j} is the reference impedance for the j-th port [2], [3..

I_{ji} and I_{jr} are the incident and reflected currents for the j-th port, so

$$I_j = I_{ji} - I_{jr} \tag{7}$$

and

$$U_j = U_{ji} + U_{jr} \tag{8}$$

where U_{ji} and U_{jr} are the incident and reflected voltage at the j-th port.

After substitution of relations (5), (6), $U_{ji} = I_{ji} \cdot R_{0j}$ and $U_{jr} = I_{jr} \cdot R_{0j}$ into (7) and (8) we obtain

$$I_j = \frac{1}{\sqrt{R_{0j}}}\left(a_j - b_j\right) \tag{9}$$

$$U_j = \sqrt{R_{0j}}\left(a_j + b_j\right). \tag{10}$$

These equations are used as the starting equations for conversion from *ABCD* parameters to scattering parameters.

Substituting (9) and (10) into (3) and (4), we get the following expressions for the scattering parameters:

$$S_{11} = \frac{A R_{02} + B - C R_{01} R_{02} - D R_{01}}{A R_{02} + B + C R_{01} R_{02} + D R_{01}}, \tag{11}$$

$$S_{12} = \frac{2(AD - BC)\sqrt{R_{01} R_{02}}}{A R_{02} + B + C R_{01} R_{02} + D R_{01}}, \tag{12}$$

$$S_{21} = \frac{2\sqrt{R_{01} R_{02}}}{A R_{02} + B + C R_{01} R_{02} + D R_{01}} \tag{13}$$

and

$$S_{22} = \frac{-A R_{02} + B - C R_{01} R_{02} + D R_{01}}{A R_{02} + B + C R_{01} R_{02} + D R_{01}}. \tag{14}$$

Unlikely *ABCD* parameters, scattering parameters are dependent upon the source and load impedances.

III. $ABCD$ PARAMETERS OF DISTRIBUTED NETWORKS

To describe the voltage and current behaviour on the non-uniform transmission line, we have Telegraph's equations:

$$\frac{\mathrm{d}U(s,\, x)}{\mathrm{d}\, x} = -Z(x, s) I(s,\, x) \tag{15}$$

and

$$\frac{\mathrm{d}\, I(s,\, x)}{\mathrm{d}\, x} = -Y(x, s) U(s,\, x), \tag{16}$$

where $Z(x,\, s) = r(x) + l(x)s$ is serial impedance and $Y(x,\, s) = g(x) + c(x)s$ is the shunt admittance per unit length of the distributed network. $r(x)$, $l(x)$, $g(x)$ and $c(x)$ are unit length resistance, inductance, admittance, and capacitance, which are functions of position x, for a nonuniform line.

In this paper a successive approximation method, Picard-Carson's method is used to solve transmission line equations (15) and (16). This method is a powerful method in getting a power series solution for the distributed network [7]. Picard–Carson's method solves ordinary differential equations by an iterative sequence

$$U_n = U_0 - \int_0^x Z(x, s) I_{n-1}(x, s)\, \mathrm{d}\, x \quad \text{and} \tag{17}$$

$$I_n = I_0 - \int_0^x Y(x, s) U_{n-1}(x, s)\, \mathrm{d}\, x, \tag{18}$$

for n=1,2,3,…, where U_0 and I_0 are the voltage and current at the input port, $x = 0$, Fig. 3.

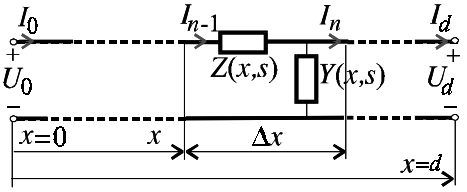

Fig. 3. Transmission line and model of elementary line length.

Since the terms inside the integrals are continuous and bounded, the sequences will converge to the true solutions

$$U(s, x) = \lim_{\Delta x \to 0} U_n(s, x) \tag{19}$$

and

$$I(s, x) = \lim_{\Delta x \to 0} I_n(s, x). \tag{20}$$

Equations (17) and (18) may be written in the form of

$$U(s, x) = U_0 - \int_0^x Z(x, s) I(s, x)\, \mathrm{d}\, x, \tag{21}$$

$$I(s, x) = I_0 - \int_0^x Y(x, s) U(s, x)\, \mathrm{d}\, x. \tag{22}$$

Using Picard–Carson's method we can show these solution in the form of two port parameters [7],

$$U(s,x)=U_0\sum_{n=0}^{\infty}\zeta_{2n}-I_0\sum_{n=0}^{\infty}\zeta_{2n+1} \qquad (23)$$

$$I(s,x)=U_0\sum_{n=0}^{\infty}\psi_{2n+1}-I_0\sum_{n=0}^{\infty}\psi_{2n}\ . \qquad (24)$$

From equation (23) and (24), the *ABCD* parameters are:

$$A(x)=\sum_{n=0}^{\infty}\psi_{2n},\qquad B(x)=\sum_{n=0}^{\infty}\zeta_{2n+1}\ , \qquad (25)$$

$$C(x)=\sum_{n=0}^{\infty}\psi_{2n+1}\ \text{ and }\ D(x)=\sum_{n=0}^{\infty}\zeta_{2n}\ . \qquad (26)$$

To start iteration, we can choose

$$\zeta_0=1\quad\text{and}\quad\psi_0=1, \qquad (27)$$

as initial values. The other terms in the summations are found by evaluating the following integrals iteratively:

$$\zeta_n=\int_0^x Z\,\psi_{n-1}\,\mathrm{d}\,x \qquad (28)$$

and

$$\psi_n=\int_0^x Y\,\zeta_{n-1}\,\mathrm{d}\,x\,. \qquad (29)$$

IV. *ABCD* PARAMETERS OF LOSSLESS TRANSMISSION LINE

For example of Picard–Carson's method we consider a lossless exponential transmission line of known characteristic impedance,

$$Z_C(x,s)=Z_{C0}\,\mathrm{e}^{k\,x}, \qquad (30)$$

with $k=\dfrac{1}{d}\ln\dfrac{Z_{Cd}}{Z_{C0}}$ and $Z_{C0}=\sqrt{\dfrac{l_0}{c_0}}$,

where Z_{C0} and Z_{Cd} are the characteristic impedances of the exponential line at the left (source) and right (load) sides, respectively. l_0 and c_0 are the inductance and capacitance per unit length. $Z(x,s)=l_0 s\,\mathrm{e}^{k\,x}$ and $Y(x,s)=c_0 s\,\mathrm{e}^{-k\,x}$ are serial impedance and the shunt admittance per unit length of the line.

Starting from (27) and using equations (28) and (29), a few first terms of series are

$$\zeta_1(x)=\frac{l_0 s}{k}\left(\mathrm{e}^{k\,x}-1\right),\ \psi_1(x)=\frac{c_0 s}{k}\left(\mathrm{e}^{-k\,x}-1\right),$$

$$\zeta_2(x)=\frac{l_0 c_0 s^2}{k^2}\left(1-\left(\mathrm{e}^{k\,x}-k\,x\right)\right),$$

$$\psi_2(x)=-\frac{l_0 c_0 s^2}{k^2}\left(1-\left(\mathrm{e}^{-k\,x}+k\,x\right)\right),$$

$$\zeta_3(x)=\frac{{l_0}^2 c_0 s^3}{k^3}\left(2-2\,\mathrm{e}^{k\,x}+\left(1+\mathrm{e}^{k\,x}\right)k\,x\right),$$

$$\psi_3(x)=-\frac{l_0 {c_0}^2 s^3}{k^3}\left(2-\mathrm{e}^{-k\,x}\left(2+\left(1+\mathrm{e}^{k\,x}\right)k\,x\right)\right),$$

$$\zeta_4=\frac{{l_0}^2{c_0}^2 s^4}{k^4}\left(3+\frac{1}{2}\left(-6\,\mathrm{e}^{k\,x}+2\left(2+\mathrm{e}^{k\,x}\right)k\,x\right)+k^2\,x^2\right)$$

$$\psi_4=\frac{{l_0}^2{c_0}^2 s^4}{k^4}\left(3+\frac{1}{2}\left(-6\,\mathrm{e}^{-k\,x}-2\left(2+\mathrm{e}^{-k\,x}\right)k\,x\right)+\mathrm{e}^{k\,x}\,k^2\,x^2\right)$$

$$\zeta_5=\frac{{l_0}^3{c_0}^2 s^5}{k^5}\left(-6+\frac{1}{2}\left(12\,\mathrm{e}^{k\,x}-6\left(1+\mathrm{e}^{k\,x}\right)k\,x\right)+\left(\mathrm{e}^{k\,x}-1\right)k^2\,x^2\right)$$

$$\psi_5=\frac{{l_0}^2{c_0}^3 s^5}{k^5}\left(6+\frac{1}{2}\left(-12\,\mathrm{e}^{-k\,x}-6\left(1+\mathrm{e}^{-k\,x}\right)k\,x\right)+\left(\mathrm{e}^{k\,x}-1\right)k^2\,x^2\right)$$

$$\vdots$$

After substitution these terms into (18) and (19), we obtain the *ABCD* parameters.

V. RESULTS FOR SCATTERING PARAMETERS

In this paper, we consider an exponential transmission line, which is used as impedance transformer from $Z_{C0}=100\,\Omega$ to $Z_{Cd}=400\,\Omega$ [5]. If the length of transmission line is $d=0.5\,\mathrm{m}$ then k will be $k=0.5753641$.

For chosen transmission line *ABCD* parameters are

$$A(d)=\sum_{n=0}^{\infty}\psi_{2n}(d)=1+\psi_2+\psi_4+\psi_6+\cdots\approx$$

$$\approx 1+0.11(s\tau)^2+0.0023(s\tau)^4+0.000019(s\tau)^6,$$

$$B(d)=\sum_{n=0}^{\infty}\xi_{2n+1}(d)=\zeta_1+\zeta_3+\zeta_5+\cdots\approx$$

$$\approx Z_{C0}\left[0.579s\tau+0.024(s\tau)^3+0.0003(s\tau)^5+1.79\times10^{-6}(s\tau)^7\right]$$

$$C(d)=\sum_{n=0}^{\infty}\psi_{2n+1}(d)=\psi_1+\psi_3+\psi_5+\psi_7+\cdots\approx$$

$$\approx\frac{1}{Z_{C0}}\left[0.43s\tau+0.018(s\tau)^3+0.00023(s\tau)^5+1.34\times10^{-6}(s\tau)^7\right]$$

and

$$D(d)=\sum_{n=0}^{\infty}\xi_{2n}(d)=1+\zeta_2+\zeta_4+\zeta_6+\cdots\approx$$

$$\approx 1+0.14(s\tau)^2+0.0029(s\tau)^4+0.000025(s\tau)^6.$$

where τ is time rise,

$$\tau=\sqrt{l_0 c_0}\ . \qquad (31)$$

Comparing to the first term in the given series, the high order terms can be neglected. In order to simplify the expression, we focus on the first three terms of A and D parameters and the first two terms of B and C parameters. After substitution of given values of *ABCD* parameters into (11)–(14), we obtain approximate values for the scattering parameters in Laplace's domain. The time domain scattering parameters $S_{ij}(t)$ are the inverse Laplace's transforms of the frequency domain scattering parameters. This gives

$$S_{ij}(t)=L^{-1}\left[S_{ij}(s)\right],\qquad (i,j=1,2). \qquad (32)$$

where L^{-1} represents the inverse Laplace's transform.

The inverse Laplace's transform of scattering parameters is done in program package Mathematica 3.0 in this paper. Scattering parameters are plotted using the same program. All results are calculated for impedance ratio $Z_{Cd} / Z_{C0} = 4$.

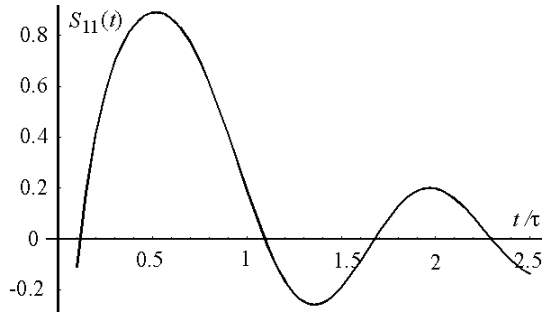

Fig. 4. Time domain scattering reflection coefficient $s_{11}(t)$.

Figs. 4 and 5 show the time domain input and output reflection coefficients $s_{11}(t)$ and $s_{22}(t)$, respectively. These magnitudes are always less than 1. The steady state values of $s_{11}(t)$ and $s_{22}(t)$ are zero.

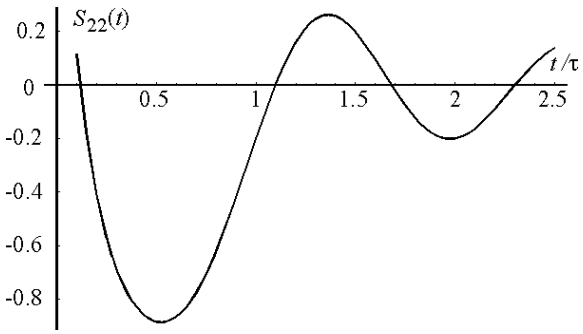

Fig. 5. Time domain scattering reflection coefficient $s_{22}(t)$.

In the Fig. 6 the reverse transmission coefficient $s_{12}(t)$ is plotted and forward transmission coefficient $s_{21}(t)$ in the Fig.7.

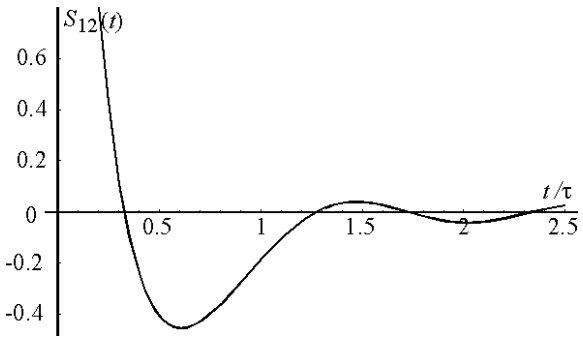

Fig. 6. Time domain scattering coefficient $s_{12}(t)$.

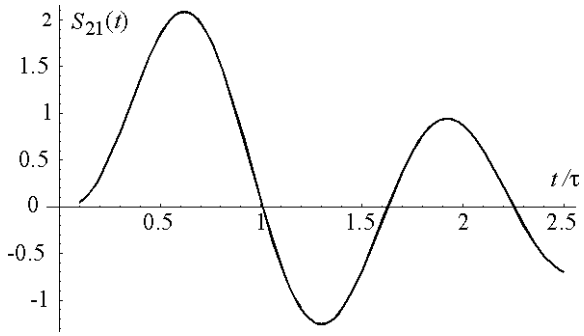

Fig. 7. Time domain scattering coefficient $s_{21}(t)$.

We can conclude that according to (25) and (26), if we carry out the iteration for infinite times, scattering parameters will thus contain infinite number of terms a power of s. These parameters are directly related to the moments of the function. In this paper we only make use of first four poles. So these results depend on number of chosen terms and on used program package.

VI. Conclusion

The Picard–Carson's method of determining the parameters of the general distributed two port network is used as a practical method for obtaining *ABCD* parameters of the two port network of nonuniform transmission line in this paper. The scattering parameters are obtained using formulas, which are obtained by conversions from *ABCD* parameters. *ABCD* parameters are approximated by first a few terms (of first four poles) of a series. Obtained scattering parameters are plotted using program package Mathematica 3.0.

References

[1]http://eesof.tm.agilent.com/docs/iccap2002/MDLGBOOK/1MEASUREMENTS/3VNA/3SPAR/1SparBasics_1.pdf

[2] Markovic, V., *Modelling of Noise of Microwave Transistors*, Memoir, Nis, 2002.

[3] Frickey, D. A., "Conversions Between S, Z, Y, h, ABCD, and T Parameters which are Valid for Complex Source and Load Impedance", *IEEE Trans. Microwave Theory Tech.*, Vol. 42, No. 2, pp. 205211, 1994.

[4] Marks, R. B., and Williams, D. J., "Comments on 'Conversions Between S, Z, Y, h, ABCD, and T Parameters which are Valid for Complex Source and Load Impedance' ", *IEEE Trans. Microwave Theory Tech.*, Vol. 43, No. 4, pp. 914–915, 1995.

[5] Hsue, C. W., "Time-Domain Scattering Parameters of an Exponential Transmission line", *IEEE Trans. Microwave Theory Tech.*, Vol. 39, No. 11, pp. 1891–1895, 1991.

[6] Schutt-Aine, J. E., and Mittra, R., "Scattering Parameter Transient Analysis of Transmission lines Loaded with Nonlinear Terminations", *IEEE Trans. Microwave Theory Tech.*, Vol. 38, No 8, pp. 1023-1030,

[7] Ghausi, S. M., and Kelly, J. J., *Introduction to Distributed-Parameter Networks*, Holt, Rinehart and Winston, Inc., New York, 1968.

SCP Technology – the New Challenge in Broadband Satellite Communications

D-r Veselin B. Demirev[1]

Abstract – **A new approach for solving the problems of the tracking antenna systems for broadband satellite communications is proposed. It includes additional pilot signal transmitted in the band of information signals and available in the receiver by one of the known methods of radio access. The receiver terminal is equipped with random phased antenna array. The random phase spread information and pilot signals correlate in a correlator. Its output signal at low intermediate frequency or at baseband is the recovered information signal. Matrix presentations of the signals in a SCP system, as well as their correlation matrix are given in the report. The Spatial Cross Correlation Function of a SCP system is defined as a measure of the isolation among the satellites, sharing the same frequencies.**

Keywords – **Spatial correlation processing, Broadband satellite communications, Tracking antenna array system**

I. INTRODUCTION

Satellite Communication Ground Systems (SCGS) are currently a strong growth market, driven chiefly by major projects to deploy vast regional or world-wide networks. One of the biggest technical problems of SCGS is the antenna system. The need to change the polarisation, to track Low Earth Orbiting Satellites (LEO,s) or to select one of several Geo Stationary Orbit Satellites (GSO,s) positions, as well as the requirements for mobile reception, low price and mass market production lead to unsolved by traditional antennas problems. The solving of the SCGS antennas problems needs entirely new approach, subject of this report. The name of the new technical proposal (Ref.1) is Spatial Correlation Processing (SCP). Its main objectives include:

- Receiving one or more radio signals coming from one or several spatially distributed sources (satellites), insuring high gain of the antenna systems and using fixed or mobile receiving terminals, equipped with SCP signal processing systems.
- Insuring spatial selectivity high enough to cancel the same frequency channel interference, coming from different space directions, using simple one-channel receiver and patented signal processing principle.

[1] Veselin B. Demirev is with the Faculty of Communications and Communications technologies, TU – Sofia, "Kl. Ohridsky" blvd. N8, 1756 – Sofia, Bulgaria, E-mail: vedem@tu-sofia.bg

The objectives stated above are achieved by a method for radio communications, which proposes application of additional pilot signals transmitted in the band of information signals and available in the receiver by one of the known methods of access (Fig.1). The SCP receiver terminal antenna array is with equal in amplitude and random in phase aperture excitation. The phase shifts of the signals, received by the different antenna elements, are random at the antenna output regardless of the information source direction. These phase spread signals correlate with the recovered pilot signals, phase spread in the same manner. Since the pilots come from the same direction and propagate in the same random environment to the antenna output they should have the same phase spread ("poly-phased" signature) as the information signals. The results of the correlation process are the recovered information signals at low intermediate frequency or at base band. The signals coming from other satellites will propagate from antenna aperture to the antenna output in different random environment. Their phase spreads will be different from these of the chosen pilots and they will not correlate during the signal processing. This lack of correlation insures the spatial and polarization selectivity of the SCP system.

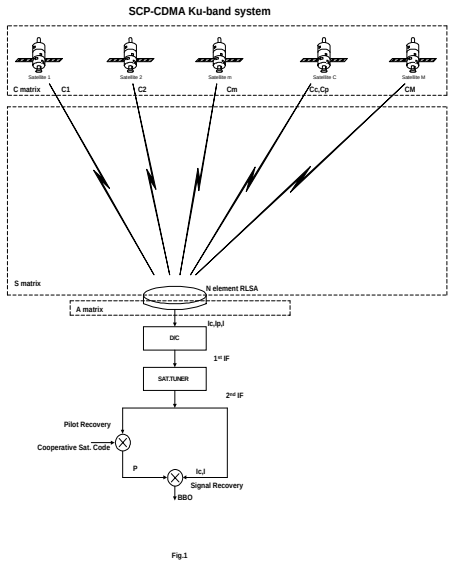

SCP system architecture

One of the main parts of the SCP system is the random phase antenna. In principle all kind of antenna arrays can be used, but for Ku band particular suitable for this purpose is the Radial Line Slot Antenna (RLSA). Until now it was used as phased array for fixed satellite reception. The main features of the SCP approach are:

- Simple and cheap passive RLSA, suitable for mass production in Ku and Ka frequency bands.
- One channel microwave receiver with simple signal processing.
- Omnidirectional for the cooperative satellite, but with high figure of merit G/T.

- Selection of different satellites and polarizations by PN-codes.
- Soft handover and virtual multibeams features.
- Receive only system, but with possible applications in transmitting systems too.
- Applications in existing S-DVB with minor modifications of the ground transmitters, compatible with the existing satellite transponders.
- High value of the patented intellectual property.
- Possible applications in fixed and mobile GSO S-DVB and in wideband GSO and NGSO satellite communication systems, as well as in the fixed and mobile terrestrial Local Multipoint Distribution Systems (LMDS).

II. Basic Matrix Expressions of the Signals in a SCP System

The SCP system is a multi source one output system and therefore can be represented by a block diagram, shown in fig. 1. Being a multi source system, it involves a cooperative signal source located in a position, given with its angular coordinates in the coordinate system (fig.2) and a number interference signal sources randomly distributed on both sides of the boresight. To analyze such a system, the most suitable mathematical tools available involve matrix and vector algebra. This results in relatively complex mathematical expressions which can be easy calculated by means of the Matlab software.

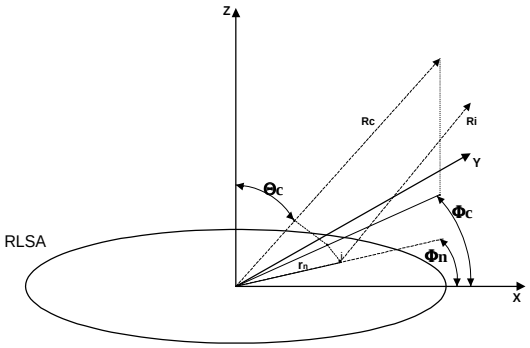

Fig. 2

SCP coordinate system

The SCP system under consideration involves both the cooperative information signal c_c with pilot c_p and the interference signal sources $c_{1,2,3...m...M}$ distributed throughout space. The signals from all of these sources will travel through space to reach the RLSA, where they will be picked up by every slot and collected by the Radial line to the input of the receiver. Here, after downconversion, the collected signals correlate with the recovered phase spread pilot signals for information signal recovery, result of phase despreading procedure. The cooperative signal source is located at angular coordinates ϕ_c, θ_c and distance R_c. The interference signal sources are located correspondingly to $\phi_{1,2...m...M}, \theta_{1,2...m...M}, R_{1,2...m...M}$.

Each slot of the N-elements RLSA will pick up signals from all the signal sources, cooperative and interference, and deliver them to its output. Thus the RLSA output will carry signals from all the signal sources. Let s_{nm} be the transfer function between m-th interference signal source and the n-th element of RLSA. Then

$$s_{nm} = L_{snm}.e^{-j\psi_{nm}} \tag{1}$$

where L_{snm} are the space propagation losses, $\psi_{nm} = k.r_n.\sin\theta_m.\cos(\phi_m - \phi_n)$ is the phase of the signal received by n-th slot of RLSA relative to its center, $k = 2\pi/\lambda$ - free space phase constant, r_n, ϕ_n - the coordinates of the n-th slot of RLSA, ϕ_m, θ_m - the angular coordinates of m-th source.

Let $\mathbf{s}_m$ represents the transfer functions between m-th signal source and all slots of RLSA, then:

$$\mathbf{s}_m = \begin{vmatrix} s_{1m} \\ s_{2m} \\ \cdots\cdots \\ s_{nm} \\ \cdots\cdots \\ s_{Nm} \end{vmatrix} \tag{2}$$

where $\mathbf{s}_m$ is called a column matrix or vector. The transfers functions among all interference sources and RLSA slots can be represented by means of matrix $\mathbf{S}$, given by:

$$\mathbf{S} = |\mathbf{s}_1, \mathbf{s}_2, \ldots\ldots \mathbf{s}_m \ldots\ldots \mathbf{s}_M| = \begin{vmatrix} s_{11} & s_{12} \ldots\ldots s_{1m} \ldots\ldots s_{1M} \\ s_{21} & s_{22} \ldots\ldots s_{2m} \ldots\ldots s_{2M} \\ \cdots\cdots\cdots\cdots\cdots\cdots\cdots\cdots \\ s_{n1} & s_{n2} \ldots\ldots s_{nm} \ldots\ldots s_{nM} \\ \cdots\cdots\cdots\cdots\cdots\cdots\cdots\cdots \\ s_{N1} & s_{N2} \ldots\ldots s_{Nm} \ldots\ldots s_{NM} \end{vmatrix} \tag{3}$$

In analogy the transfer function for information and pilot signals from the cooperative source will be given by:

$$\mathbf{s}_c = \begin{vmatrix} s_{c1} \\ s_{c2} \\ \cdots\cdots \\ s_{cn} \\ \cdots\cdots \\ s_{cN} \end{vmatrix} \quad \text{and} \quad \mathbf{s}_p = \begin{vmatrix} s_{p1} \\ s_{p2} \\ \cdots\cdots \\ s_{p3} \\ \cdots\cdots \\ s_{pN} \end{vmatrix} \tag{4}$$

If $c_1, c_2, ..., c_m .....c_M$ are the signals transmitted by the interference signal sources 1,2,.....*m*, respectively, then the signals at the n-th RLSA slot due to the signals from the m-th interference signal source will be given by:

$$x_{nm} = s_{nm}.c_m \tag{5}$$

and that from the cooperative signal source will be given by:

$$x_{cn} = s_{cn}.c_c, x_{pn} = s_{pn}.c_p \tag{6}$$

Therefore the signal vector, combining the signals from all signal sources, interference and cooperative, at the n-th slot of RLSA is:

$$\begin{aligned} \mathbf{x}_{\mathrm{n}} &= \left| \; x_{n1} \quad x_{n2} ....x_{nm} ....x_{nc} x_{np} \; \right| = \\ &= \left| \; s_{n1}.c_1 \quad s_{n2}.c_2 ....s_{nm}.c_m ....s_{nM}.c_M \quad s_{cn}.c_c \quad s_{pn}.c_p \; \right| \end{aligned} \tag{7}$$

Considering the interference signals only, the interference signal vector at all slots of RLSA due to interference signal sources can be represented by:

$$\begin{vmatrix} \mathbf{x}_1 \\ \mathbf{x}_2 \\ ..... \\ \mathbf{x}_{\mathrm{n}} \\ ..... \\ \mathbf{x}_{\mathrm{N}} \end{vmatrix} = \begin{vmatrix} s_{11} & s_{12} & s_{13} ... s_{1m} ... s_{1M} \\ s_{21} & s_{22} & s_{23} ... s_{2m} ... s_{2M} \\ ..... \\ s_{n1} & s_{n2} & s_{n3} ... s_{nm} ... s_{nM} \\ ..... \\ s_{N1} & s_{N2} ..... & s_{Nm} ... s_{NM} \end{vmatrix} X \begin{vmatrix} c_1 \\ c_2 \\ c_3 \\ .... \\ c_m \\ .... \\ c_M \end{vmatrix}$$

or $\mathbf{x} = \mathbf{S}.\mathbf{c}$, where

$$\mathbf{x} = \begin{vmatrix} \mathbf{x}_1 \\ \mathbf{x}_2 \\ ..... \\ \mathbf{x}_{\mathrm{n}} \\ ..... \\ \mathbf{x}_{\mathrm{N}} \end{vmatrix} \text{ and } \mathbf{c} = \begin{vmatrix} c_1 \\ c_2 \\ c_3 \\ .... \\ c_m \\ .... \\ c_M \end{vmatrix} \tag{8}$$

Thus the column vector $\mathbf{x}$ represents all signals from all interference signal sources at all slots of RLSA while column vector $\mathbf{c}$ represents all signals transmitted by all interference signal sources. In addition to the signals from all interference signal sources, all slots will also receive the information and pilot signals from the cooperative signal source, as follows:

$$\mathbf{x}_{\mathrm{c}} = \mathbf{s}_{\mathrm{c}}.c_c, \mathbf{x}_{\mathrm{p}} = \mathbf{s}_{\mathrm{p}}.c_p \tag{9}$$

As it was mentioned above, the RLSA will transport all signals, received by different slots, to the RLSA output and the SCP receiver. Let the transfer functions between all RLSA slots and its output be represented by the column vector $\mathbf{a}$:

$$\mathbf{a} = \begin{vmatrix} a_1 \\ a_2 \\ a_3 \\ ..... \\ a_n \\ ..... \\ a_N \end{vmatrix} \tag{10}$$

where $a_n = L_{an}.e^{j\varphi n}$, L_{an} - gain of a single slot, RLSA propagation losses are included, $\varphi_n = 2\pi.r_n / \lambda_g + \Delta\varphi_n$, where $2\pi.r_n / \lambda_g$ - phase shift due to RLSA, $\Delta\varphi_n$ - phase shift due only to the inner slots and to the slot inclination if Circular Polarization (CP) is used.

Due to the finite transfer function that exists between the input and output ports of a RLSA, the signals appearing at its output will be those at the input slots modified by the transfer function $\mathbf{a}$. The signal vector $\mathbf{I}$, combining all interference signals appearing at the RLSA output, is:

$$\mathbf{I} = \left| \; a_1.\mathbf{x}_1 \quad a_2.\mathbf{x}_2 \quad a_3.\mathbf{x}_3 .... \quad a_n.\mathbf{x}_{\mathrm{n}} .... \quad a_N.\mathbf{x}_{\mathrm{N}} \; \right| = \mathbf{a}.\mathbf{X} \tag{11}$$

In analogy the signal vectors, combining all cooperative information $\mathbf{i}_c$ and pilot $\mathbf{p}$ signals will be given by:

$$\begin{aligned} \mathbf{i}_{\mathrm{c}} &= \left| \; a_1.x_{c1} \quad a_2.x_{c2} \quad a_3.x_{c3} .... \quad a_n.x_{cn} .... \quad a_N.x_{cN} \; \right| \\ &= \mathbf{a}.\mathbf{x}_{\mathrm{c}} \end{aligned} \tag{12}$$

$$\begin{aligned} \mathbf{p} &= \left| \; a_1.x_{p1} \quad a_2.x_{p2} \quad a_3.x_{p3} .... \quad a_n.x_{pn} .... \quad a_N.x_{pN} \; \right| \\ &= \mathbf{a}.\mathbf{x}_{\mathrm{p}} \end{aligned} \tag{13}$$

The received by RLSA signals are amplified in Low Noise Amplifier (LNA), downconverted, amplified and correlated in the Correlator unit. Consider for simplicity the process without math description of code spreading and dispreading, which in principle will not change the investigated interference environment and thermal noise properties. The total receiver gain *G*, product of the above mentioned procedures, will be:

$$G = G_{LNA}.G_{DC1}.G_{IFA1}.G_{DC2}.G_{IFA2} \tag{14}$$

where G_{LNA} is the gain of the LNA, G_{DC1} is the gain of the first downconverter, G_{IFA1} is the gain of the first IFA, G_{DC2} is the gain of the second downconverter and G_{IFA2} is the gain of the second IFA.

The output signal, product of the multiplication process, will be:

$$G(\mathbf{i}_c.\mathbf{p}) = G\begin{vmatrix} i_{c1}.p_1 & i_{c2}.p_1 .... & i_{cn}.p_1 .... & i_{cN}.p_1 \\ i_{c1}.p_2 & i_{c2}.p_2 .... & i_{cn}.p_2 .... & i_{cN}.p_2 \\ ..... & & & \\ i_{c1}.p_n & i_{c2}.p_n .... & i_{cn}.p_n .... & i_{cN}.p_n \\ ..... & & & \\ i_{c1}.p_N & i_{c2}.p_N .... & i_{cn}.p_n .... & i_{cN}.p_N \end{vmatrix} \quad (15)$$

Where the term $j-k$ consists of:

$$(i_{cj}.p_k) = \pm i_c.e^{j\left[\omega_{II}.t - k.r_j.\sin\theta_c.\cos(\phi_c-\phi_j)+k_g.r_j\right]} .e^{j\left[\omega_{II}.t - k.r_k.\sin\theta_c.\cos(\phi_c-\phi_k)+k_g.r_k\right]} \quad (16)$$

In Eq. (16) $\pm i_c$ is the amplitude of the information signal per slot (BPSK modulation and uniform amplitudes of the antenna elements are considered), the same for the pilot is chosen to be 1. Assume the pilots are noise free due to the high CDMA Processing gain *PG).

By means of Eq.

$$\cos A.\cos B = 0{,}5\cos(A-B) + 0{,}5\cos(A+B)$$

Eq. (16) can be represented in real form as:

$$\begin{aligned} \mathrm{Re}(i_{cj}.p_k) = \pm\, & 0{,}5.i_c.\cos\left[-k.r_j.\sin\theta_c.\cos(\phi_c-\phi_j)\right. \\ & \left. + k_g.(r_j - r_k) + k.r_k.\sin\theta_c.\cos(\phi_c-\phi_k)\right] \\ & \pm 0{,}5.i_c(2\omega_{II}t + ...) \end{aligned} \quad (17)$$

The second term of Eq. (17) is with double intermediate frequency and after Low Pass Filtering (LPF) it cancels.

A basic requirement of the SCP technology (in order to obtain smooth omnidirectional cooperative pattern) is the sum of the off-diagonal terms of the matrix (15) to be zero. This requirement is fulfilled when the signals phase Probability Density Function (PDF) is uniform in the interval 0 – 360 degrees, the channel is real with Additive White Gaussian Noise (AWGN), RLSA is frequency dispersive and the process of correlation is digital. The real part of the n-th diagonal term of matrix (15) consists of:

$$\begin{aligned} \mathrm{Re}(i_{cn}.p_n) = \pm\, & i_c.\cos^2\left[\omega_{II}.tr_n\right. \\ & \left. - k.r_n.\sin\theta_c.\cos(\phi_c-\phi_n) + k_g\right] \end{aligned} \quad (18)$$

Equation (18) can be presented by means of Eq. $\cos^2 A = 0{,}5.(1+\cos 2A)$ as follows:

$$\mathrm{Re}(i_{cn}.p_n) = \pm\, 0{,}5.i_c \pm 0{,}5.i_c.\cos(2\omega_{II}.t + ...) \quad (19)$$

The second term of Eq. (19) vanishes after LPF. The first term represents the demodulated information signal per antenna element at baseband. The total baseband output signal will be N times more, equal to the trace of the matrix (15) (the N diagonal elements of (15) are in phase):

$$\mathbf{BBO}_c = \pm\, 0{,}5.G.i_c.N \quad (20)$$

The formal mathematical way to describe the above mentioned correlation process and the result (20) in matrix form is:

$$\mathbf{BBO}_c = \mathrm{timeaver}\, G.(\mathbf{i}_c.\mathbf{p}) = G.\mathrm{Tr}(\mathbf{i}_c.\mathbf{p}^H) \quad (21)$$

where $\mathbf{p}^H$ is the Hermitian (transpose and conjugate) matrix of $\mathbf{p}$.

In analogy the interference signals:

$$\mathbf{BBO}_{\text{interference}} = \mathrm{timeaver}\, G.(\mathbf{I}.\mathbf{p}) = G.\mathrm{Tr}(\mathbf{I}.\mathbf{p}^H) \quad (22)$$

The Spatial Cross - Correlation Function (SCCF) can be introduced for the spatial interference analysis, as follows:

$$\mathbf{SCCF}(\phi,\theta)(dB) = 10\lg\left[\mathbf{BBO}_{\text{inter.}}(\boldsymbol{\varphi},\boldsymbol{\theta})/\mathbf{BBO}_c\right] \quad (23)$$

The total system interference from several satellites could be represented by means of Protection Ratio (PR), defined as the ratio of the cooperative BBO to the total interference.

ACKNOWLEDGMENTS

The author thanks SkyGate BG Ltd. for the financial and technical support of this report.

REFERENCES

[1] V. Demirev, Method and system for radiocommunications, Bulgarian Patent Office applicant report, N 105671/ 04.07.01., PCT(BG02) 00016, Geneve, 13.02.2004.

[2] R. Mailloux, Phased Array Antenna Handbook, Artech House, 1994.

SCP-CDMA GSO,s System Proposal

D-r Veselin B. Demirev [1] and Alexander Efremov [2]

Abstract - **The practical implementation of the SCP approach leads to the problem of pilots transmission through the same propagation environment as that of the cooperative information signals. The requirements to the pilot transmission technology are defined in the report. A proposal for CDMA pilot spreading and transmission in the frequency band of the information signal is given too. The basic SCP-CDMA systems parameters are defined by means of modified link budget calculations per slot. Matlab matrix simulations of a SCP-CDMA system, K-u band version, used for S-DVB application, are given in the report too. The goal is to define the Spatial Cross Correlation Function (SCCF) between cooperative satellite and the others. It is calculated for 0, 30 and 60 degrees of the pilot tilt angles. The computed SCCF is in fact the virtual antenna pattern at baseband. Its sidelobes satisfy the satellite regulations levels and promise low BER properties for the future SCP-CDMA S-DVB systems.**

Keywords – **SCP technology, SCP-CDMA, S-DVB, Spatial cross correlation function**

I. INTRODUCTION

A description of a new radio-communication technology, based on random phased antenna arrays approach and autocorrelation signal processing (SCP), as well as Matrix presentations of the signals and the basic signal processing procedures, is given in Ref. 1 and Ref.2. The goal of this report is to propose a SCP-CDMA GSO,s system, as well as to simulate its SCCF (Spatial Cross Correlation Function) pattern.

II. PILOT SIGNAL TRANSMISSION

The practical implementation of the SCP approach leads to the problem of pilots transmission through the same propagation environment as that of the cooperative information signals. The requirements to the pilot transmission technology could be summarized as follows:

[1] Veselin B. Demirev is with the Faculty of Communications and Communications technologies, TU – Sofia, "Kl. Ohridsky" blvd. N8, 1756 – Sofia, Bulgaria, E-mail: vedem@tu-sofia.bg

[2] Alexander Efremov was with SkyGate BG Ltd., E-mail: efremov_a@hotmail.com

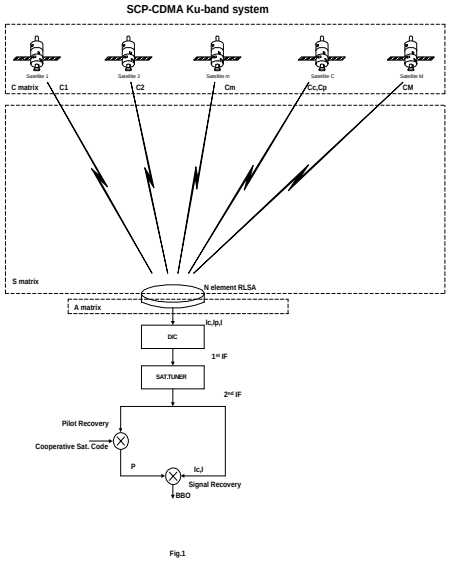

SCP system architecture

- It should occupy minimum additional frequency spectrum resources, as well as additional hardware.
- It should not cause interference over the cooperative information signals.
- It should ensure easy access to the chosen combination of pilots in the case of mass implementation of SCP technology in satellite communications.
- It should not generate any significant intermodulation noise in the satellite transponders, working near to the saturation point (zero back-off).
- Bearing in mind the frequency dispersive phase shifts, introduced by Radial Line Slot Antenna (RLSA) to the information and to the pilot signals, their career frequencies should be as close as it is possible.

The common used methods for access to the base stations resources in wireless communications are Frequency Division Multiple Access (FDMA), Time Division Multiple Access (TDMA) and Code Division Multiple Access (CDMA). All of them could to be used for pilot transmission in SCP technology, but the CDMA approach (Ref.3) matches in the best way to the above mentioned requirements. The system architecture of a SCP-CDMA system is shown in Fig.1. Its frequency spectrum is shown in Fig.2.

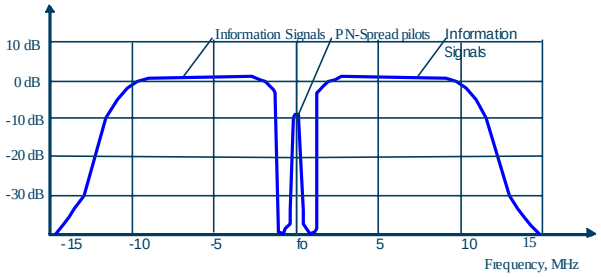

Fig.2. Frequency spectrum of SCP-CDMA system

III. SCP-CDMA GSO,S SYSTEM PARAMETERS

As a result of the random RLSA slots distribution and inclination, the different slots signals phases are random, uniformly distributed between 0 and 360 degrees. Their amplitudes can be calculated, using conventional link budget equations with the following assumptions for simplicity:

- The slot directivity pattern is omni directional (which is exactly correct for high elevation angles).
- The slot gain Gs=1,6 dbi (based on published experimental results for RLSA, the transmission losses in the antenna are included).
- Simplified forms of link budget equations are used (Ref.4).

Bearing in mind the above simplifications and the particular values for a S-DVB satellite:

- EIRP=50 dbw for each component of the QPSK modulated signals,
- S=38000 km (distance to the GSO satellite),
- f=12,5 GHz (microwave frequency in the midle of the Ku band),
- L=206 db (calculated propagation losses)
- R=20 MBt/s (standard information signal data rate),
- Rc=1,23 MCh/s (chosen spreading code chirp rate for the pilots),
- Receiver noise figure 1 db, antenna noise temperature 50 grad. K (equal to phase array antenna with the same aperture), system noise temperature Ts= 125 grad. K, Ts(db)=21 dbgrad.K,
- G/T per slot=-19,4 dbi/gradK (calculated),
- Ladd=2 db (additional losses due to propagation phenomena),
- Lpol.loss=3 db (because of the circular polarization),
- N=2700 (number of available slots in 60 cm diameter RLSA according to the published data), N(db)=34,3db

For the parameters listed above, the following values are computed:

- Information signal to noise ratio per slot (Eb/No)ips=-24,81 db.
- Information signal power per slot Cips=-159,4 dbW.

The multiplication of the information and the pilots signals from a given slot in the Correlator unit and the following Low Pass Filtering (LPF) is process of coherent demodulation. The result is N in phase base band components, which sum is the demodulated base band signal. Bearing in mind that the signal to noise ratio for the pilot is about 20 db higher than the same for the information signal (it is noise free), the total (Eb/No)t=N.(Eb/No)ips, (Eb/No)t(db)=N(db)+(Eb/No)(db)ips=34,3-24,81=9,49 db. The last result is several db above the specified in EN 300421 standard values.

In analogy the total figure of merit (G/T)t(db)=N(db)+G/T per slot(db)=34,3-19,4=14,9dbi/grad.K.

The thermal noise was calculated by means of standard procedure for PSK signals. The detailed SCP thermal noise properties are under investigation now and will be published soon.

IV. RADIAL LINE SLOT ANTENNA

It was shown that the SCP requirement to obtain smooth omnidirectional cooperative pattern needs the off-diagonal output signals to cancel for all possible elevation and azimuth angles of the cooperative satellite. It is zero when the antenna slots signals phase probability density function is uniform from 0 to 360 deg. for all spatial angles of the signal direction. A random distribution of the slots over RLSA surface was proposed for this purpose. The slots coordinates were chosen by means of random generator with some restrictions. The practical implementation of this procedure was not quite successful because:

- There were areas on the RLSA surface where the neighbour slots were at equal distance to the centre of the RLSA. As a result the signals from these slots are in phase (they are strong correlated) and the phase probability density function has maximum for low phase values.
- The neighbour slots were placed close and at equal distances each other in radial direction. Bearing in mind the low permittivity of the RLSA core, the signals from these slots were close in phase. The phase probability density function has maximum for low phase values too. The RLSA works as a leaky-wave antenna in this particular case.
- The small interslots spacing (used for high efficiency of the RLSA) leads to high values of mutual coupling among the neighbour slots. The result is the existence of high correlated areas on the RLSA surface, due to non-random phase excitement.

The existence of strong correlated areas leads to statistically uncompensated **cros** signal output (the BBO correlation matrix is not equal to its trace). The **cros** output is summed with the omnidirectional **cor** output and as a result the high ripples in the SCP output signal appear. It means that the system sensitivity is not equal for the different azimuth and elevation angles. The only way to obtain smooth SCP cooperative pattern is to decorrelate as much as it is possible the signals from the RLSA slots, bearing in mind the influence of the RLSA core, to receive with low signal to noise ratio (where the AWGN channel theory is valid) and to use digital correlators.

The latest algorithm for the slots distribution and orientation represents a combination of the previously used approaches for phase randomization and radial distributed pins fed slots with the following characteristics:

- random element position
- the slots are normal, or at angles ±45 deg to the radius of the antenna, or radial with exciting pins
- the positions of the exciting pins are alternatively changed so that the phase difference for the radial slots equally spaced from the antenna center and with different pins positions is 180 deg.

One of the most important parameters of the receiving S-DVB systems is the cross polarization isolation between Left and Right Hand Circular Polarization (LH, RH, CP). The problem here is its degradation for high tilt angles. The cross polarization isolation and the switching of the received polarizations in the SCP systems are based on entirely new principle of operation. The slots design assures the both CP to be received in the most efficient way. The choice of the polarization is based on the correlation of the chosen pair of pilots for given CP with the corresponding information signals. The signals, received by LH and RH CP, are not correlated because of the opposite direction of rotation and about 15 MHz frequency offset between the selected pilot signals and the opposite CP signals. Very good cross polarization properties, independent on the tilt angles, are expected in this way.

The developed math model of the SCP system, as well as the Mathlab simulations, do not include the polarization properties of the RLSA slots. As it was stated early, the best way to randomise the phase distribution is to incline the slots in random manner and to use circular polarization. The math description of the SCP approach in this case should to involve the antenna-wave interaction from polarization point of view. The detailed developing of this method for the SCP case should to be done in the future work.

The developed math model for the slots signals phases deals with the space distribution among antenna slots and the cooperative satellite (the outer solution), as well as the slots positions on the RLSA aperture (the inner solution). It does not include the influence of the inner slots and fed probes to the outer slots signal phases, as well as the mutual coupling phenomena.

V. SCP SYSTEM SIGNAL SIMULATIONS, KU-BAND S-DVB APPLICATION

The matrix simulations of a SCP-CDMA system, K-u band version, used for S-DVB application, should start with a simplified analysis. The goal is to define the Spatial Cross Correlation Function (SCCF - Ref.1) between cooperative satellite and others.

$$\mathbf{SCCF}(\phi,\theta)(dB) = 10\lg\left[\mathbf{BBO}_{\text{inter.}}(\boldsymbol{\varphi},\boldsymbol{\theta})/\mathbf{BBO}_{\text{c}}\right]$$

For this purpose the following assumptions and simplifications are used in the calculations:

- space propagation losses $L_{snm} = 1$, $\lambda = 2{,}5cm$,
- $r_n = 5 - 28{,}5cm, \phi_n = 0 - 360^0$.
- ϕ_m, θ_m – angular coordinates of interference satellites, entries for S-matrix calculation, $\phi_c, \theta_c, \phi_p, \theta_p$ – angular coordinates of the cooperative satellite. Three possible scenarios should be calculated – in zenith, 30 and 60 degrees tilt from zenith, pure south.
- $c_1 = c_2 = ... = c_M = c_p = c_c = 1$ – amplitudes of interference, pilot and cooperative information signals.
- RLSA propagation losses $L_{an} = 1$. The phase shift due to inner slots and slot inclination $\Delta\varphi_n = 0$.
- The total receiver gain G=1.

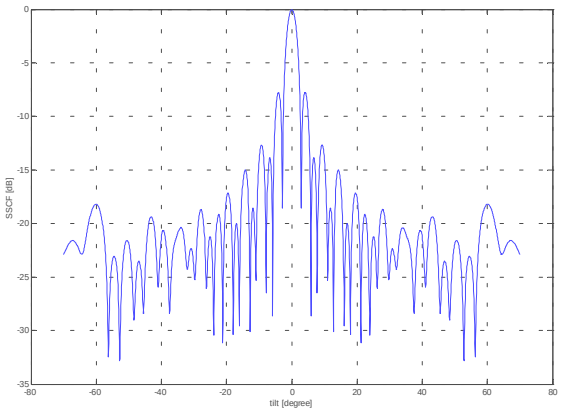

Fig.3. SCCF of RLSA Diameter – 0,57 m, N = 2501, λ = 2,5 cm,

$\phi_p = 0^o, \theta_p = 0^o$, $\phi_m = 0^o, \theta_m = -70^o \div 70^o$

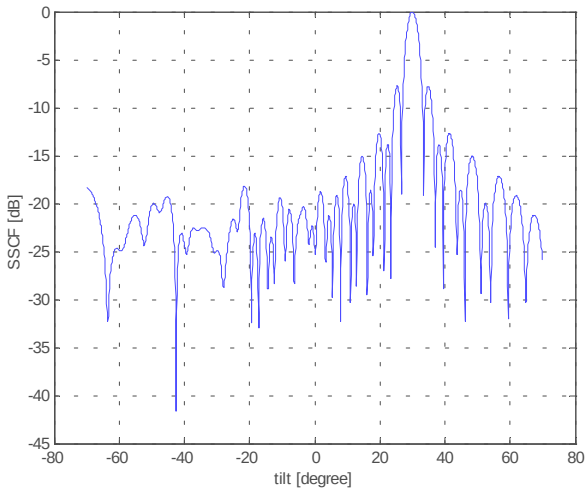

Fig.4. SCCF of RLSA Diameter – 0,57 m,
$N = 2501,\ \lambda = 2{,}5\,\text{cm},\ \phi_p = 0^o, \theta_p = 30^o,$
$\phi_m = 0^o, \theta_m = -70^o \div 70^o$

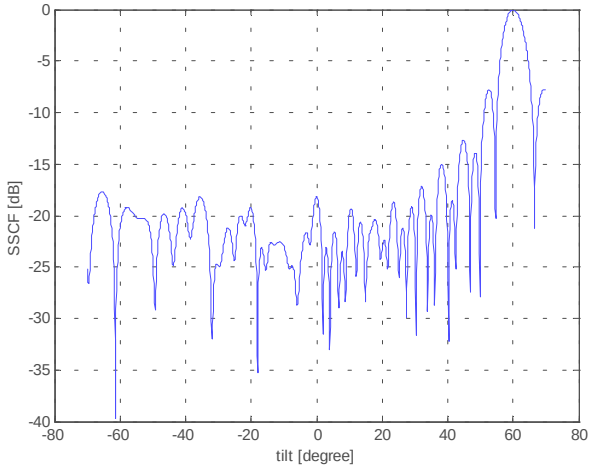

Fig.5 SCCF of RLSA Diameter – 0,57 m,
$N = 2501,\ \lambda = 2{,}5\,\text{cm},\ \phi_p = 0^o, \theta_p = 60^o,$
$\phi_m = 0^o, \theta_m = -70^o \div 70^o$

ACKNOWLEDGEMENTS

The authors thank SkyGate BG Ltd. for the financial and technical support of this report.

REFERENCES

[1] V. Demirev, SCP technology – the new challenge in broadband satellite communications, ICEST,04, Bitola, Macedonia, 2004.
[2] V. Demirev, Method and system for radiocommunications, Bulgarian Patent Office applicant report, N 105671/ 04.07.01., PCT(BG02) 00016, Geneve, 13.02.2004.
[3] J. Lee, L. Miller, CDMA Systems Engineering Handbook, Artech House, 2001.
[4] G. Gordon, W. Morgan, Principles of Communications Satellites, John Wiley&Sons, 1993.

The Probability Theory with Application in SCP Technology

D-r Veselin B. Demirev[1]

Abstract – **The probability theory is used to investigate some of the basic properties of the SCP technology. Central limit theorem is used too to prove the gain of the random phased antenna array, as well as the Gaussian probability properties of the antenna array output signals.**

Keywords – **SCP technology, Random phase process, Central limit theorem, Gaussian PDF**

I. INTRODUCTION

A description of a new radio-communication technology, based on random phased antenna arrays approach and Spatial Correlation Processing (SCP), as well as Matrix presentations of the signals and the basic signal processing procedures, are given in Ref. 1. A GSO,s system, based on SCP-CDMA approach, as well as Matlab computer simulations of the system spatial resolution properties are given in Ref.2 too. The goal of this report is to represent some of the basic SCP system phenomena by means of probability theory, obtaining better understanding for the SCP unique properties.

II. THE RANDOM PHASE PROCESS

A basic property of the SCP approach is the random phase spread among the signals, received by the different antenna array elements. Consider (Ref.3) the theory of a random process, which in the best way describes the SCP signals. Consider the time function:

$$X(t) = A\cos(\omega_0 t + \theta) \qquad -\infty \prec t \prec \infty \tag{1}$$

Where A, ω_o are constants, θ is the random variable with uniform probability density function in the interval $[0,2\pi]$. The collection of all possible such waveforms together with the underlying probability assignment is called a phase random process. Each realization of a particular waveform is referred as a sample function. In SCP case each such sample function corresponds to a particular signal, obtained from a given antenna array element. Uniform amplitude distribution (A=const.) is considered for simplicity.

The mean value of the random phase process, given with Eq. (1) is:

$$E[X(t)] = \int_0^{2\pi} A\cos(\omega_0 t + \theta)\frac{d\theta}{2\pi} = 0 \tag{2}$$

The mean square value is:

$$E[X^2(t)] = \int_0^{2\pi} A^2\cos^2(\omega_0 t + \theta)\frac{d\theta}{2\pi} = \\ = \int_0^{2\pi} \frac{A^2}{2}\frac{d\theta}{2\pi} + \int_0^{2\pi} \frac{A^2}{2}\cos 2(\omega_0 t + \theta)\frac{d\theta}{2\pi} = \frac{A^2}{2} \tag{3}$$

The variance is:

$$\sigma_x^2(t) = E[X^2(t)] - \{E[X(t)]\}^2 = \frac{A^2}{2} - 0 = \frac{A^2}{2} \tag{4}$$

The autocorrelation function is:

$$R_x(t, t+\tau) = E[X(t)X(t+\tau)] = \\ = \int_0^{2\pi} A^2\cos(\omega_0 t + \theta)\cos[\omega_0(t+\tau) + \theta]\frac{d\theta}{2\pi} = \frac{A^2}{2}\cos\omega_0\tau \tag{5}$$

III. THE CENTRAL LIMIT THEOREM (CLT)

If the random variables (Ref. 4, 7 and 8) $X_1, X_2, \ldots\ldots\ldots, X_n$ are independent and identically distributed with probability density functions $f_x(x)$, means μ_x and variance σ_x^2, then the probability distribution function of the sum $Y = X_1 + X_2 + \ldots\ldots + X_n$ is approximately Gaussian with mean $\mu_y = n\mu_x$ and variance $\sigma_y^2 = n\sigma_x^2$ as long as n is "large enough". This result is called the Central Limit Theorem.

Applying CLT to the SCP phase random process, we obtain for the output antenna signal the sum $Y = X_1 + X_2 + \ldots\ldots + X_n$ with mean $\mu_y = n\mu_x = 0$ and variance:

$$\sigma_y^2 = n\sigma_x^2 = n\frac{A^2}{2} \tag{6}$$

In this particular case (zero mean), the variance is equal to the mean square value (the energy of the signal, or to the autocorrelation value at zero time off-set) resp. of the individual antenna element and of the total SCP antenna.

[1] Veselin B. Demirev is with the Faculty of Communications and Communications technologies, TU – Sofia, "Kl. Ohridsky" blvd. N8, 1756 – Sofia, Bulgaria, E-mail: vedem@tu-sofia.bg

The equation (6) proves the basic SCP property that the total antenna gain is sum of the gains of the individual slot radiators.

The sum Y is Gaussian with Probability Distribution Function (PDF) (Ref.5 and 6), given by:

$$p_y(\alpha) = \frac{1}{\sqrt{2\pi}\sigma_y} e^{-\alpha^2 / 2\sigma_y^2} \quad (7)$$

The Cumulative Distribution Function (CDF) of such process is given by:

$$F_y(\alpha) = \Pr[Y \le \alpha] = \int_{-\infty}^{\alpha} \frac{1}{\sqrt{2\pi}\sigma_y} e^{-\frac{\lambda^2}{2\sigma_y^2}} d\lambda = 1 - Q(\alpha / \sigma_y) \quad (8)$$

Where $Q(\alpha)$ is defined as Complementary Cumulative Probability Distribution Function (CCDF) of a standard zero-mean, unit variance Gaussian random variables, $G(0,1)$:

$$Q(\alpha) = \int_{\alpha}^{\infty} \frac{1}{\sqrt{2\pi}} e^{-\frac{\lambda^2}{2}} d\lambda \quad (9)$$

The root mean square value of the envelope of such process (Rayleigh) is (Ref.5):

$$R_{rms} = \sqrt{2}\sigma_y \quad (10)$$

IV. Cross-correlation properties of orthogonal random phase-spread signals

Matrix presentation of the RLSA poly-phase signals, as well as matrix description of the SCP correlation processes are given in Ref.1 only for BPSK modulated signals. In the real broadband satellite systems QPSK modulation is used in order to double the system information capacity. An important issue of QPSK SCP systems is the isolation between ***I*** and ***Q*** channels. This isolation depends on the cross-correlation properties between ***I*** channel pilot signal P_I and ***Q*** channel information signal I_Q (and vice versa). For this reason the cross-correlation properties of orthogonal poly-phase spread signals are considered below, following Ref. 10.

Consider the above-mentioned pair of QPSK SCP signals $P_I(t)$ and $I_Q(t)$ that are related to a random wide-sense stationary process $X(t)$ as follows:

$$\begin{aligned} P_I(t) &= X(t)\cos(2\pi f_c t + \theta) \\ I_Q(t) &= X(t)\sin(2\pi f_c t + \theta) \end{aligned} \quad (11)$$

Where f_c is a carrier frequency, and the random variable θ is uniformly distributed over the interval $(0,2\pi)$. Moreover, θ is independent of $X(t)$. One cross-correlation function of $P_I(t)$ and $I_Q(t)$ is given by:

$$\begin{aligned} &R_{IQ}(\tau) = E[P_I(t)I_Q(t-\tau)] = \\ &E[X(t)X(t-\tau)\cos(2\pi f_c t + \theta)\sin(2\pi f_c t - 2\pi f_c \tau + \theta)] = \\ &E[X(t)X(t-\tau)]E[\cos(2\pi f_c t + \theta)\sin(2\pi f_c - 2\pi f_c \tau + \theta)] = \\ &0{,}5R_X(\tau)E[\sin(4\pi f_c t - 2\pi f_c \tau + 2\theta) - \sin(2\pi f_c \tau)] = \\ &0{,}5R_X(\tau)\sin(2\pi f_c \tau) \end{aligned} \quad (12)$$

Where in the last line we have made use of the phase uniform probability density distribution. At $\tau = 0$, the factor $\sin(2\pi f_c \tau)$ is zero and therefore:

$$R_{IQ}(0) = E[P_I(t)I_Q(t)] = 0 \quad (13)$$

This shows that the random variables, obtained by simultaneously observing the QPSK modulated signals P_I and I_Q at some fixed value of time t, are orthogonal to each other.

Particularly for the SCP system Eq.13 means that after the process of signal recovery and PSK demodulation the I and Q channels are isolated.

Acknowledgements

The author thanks SkyGate BG Ltd. for the financial and technical support of this report.

References

[1] V. Demirev, SCP technology – the new challenge in broadband satellite communications, ICEST,04, Bitola, Macedonia, 2004.

[2] V. Demirev, A. Efremov, SCP-CDMA GSO,s system proposal, ICEST,04, Bitola, Macedonia, 2004.

[3] P. Zimerman, Digital communications and spread spectrum, 1985.

[4] A.P.Felzer, ECE 315 – Continuous random variables – invest 17, The Central Limit Theorem, Winter, 2003 (Internet).

[5] J.S.Lee, L.E. Miller, CDMA System Engineering Handbook, Artech house, 1999.

[6] M.K. Simon, Probability Distributions Involving Gaussian Random Variables, Kluwer Academic Publishers, 2002.

[7] J. M. Wozencraft, I. M. Jacobs, Principles of Communication Engineering, John Willey&Sons, 1965. (Теоретические основы техники связи, Изд. Мир, Москва, 1969)

[8] A. Leon-Garcia, Probability and Random Processes for Electrical Engineering, Addison-Wesley Publishing Company, 1994.

[9] А. Зиновьев, Л. Филиппов, Введение в теорию сигналов и цепей, М., Высшая школа, 1973.

[10] S. Haykin, Communication systems, Artech House, 1993.

An Overview of Microstrip Transmission Line Resonators

Dobri M. Dobrev and Marin V. Nedelchev

Abstract: This paper presents closed form formulas for the input admittance and the admittance slope parameter for different microstrip resonator types. Generalized formula for the admittance slope parameter of stepped impedance resonator is derived. Closed form formula for the input admittance for a hairpin resonator with stub elements is derived. The resonance conditions of different resonator types are discussed.

Keywords: Microstrip resonator, resonance condition, input admittance, admittance slope.

I. INTRODUCTION

Microstrip filters are widespread in the microwave devices for their compactness, reliability, simplicity and easy manufacturing. The resonator topology defines, in a great extent, the filter amplitude characteristic. The comparatively low unloaded Q factor of the resonators leads to high insertion loss in the passband and low steepness of the amplitude response of the filter. Using cross-coupled filters, dual-mode resonator filters or 0° feed structure of the filter solves these problems.

The cross-coupled filters have higher selectivity, because of the placing of transmission zeros in the stopband. The dual-mode resonators may be used as a doubly tuned resonant circuit and therefore the number of resonators required for a *n*-degree filter is reduced by half, resulting in a compact filter configuration. 0° feed structure means placing the input and the output feed points at the opposite locations about the center of the resonator. This creates two transmission zeros in the stopband.

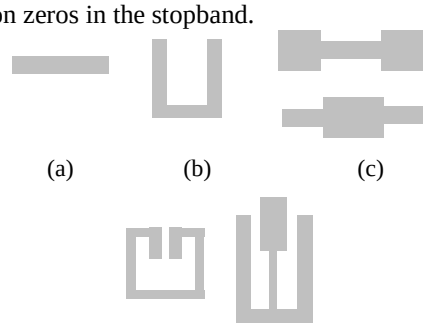

(a) (b) (c) (d) (e)

Fig.1. Different microstrip resonator types.
(a). *λ/2* length (b) hairpin *λ/2* length (c) Stepped impedance.
(d) Miniaturized hairpin (e) hairpin resonator with stub element

Dobri M. Dobrev – Assoc. Professor in Dept. of Radiotechnic in Faculty of Communications and Communication Technologies in TU –Sofia E-mail: dobrev@tu-sofia.bg
Marin Veselinov Nedelchev – PhD student in Dept. of Radiotechnic in Faculty of Communications and Communication Technologies in TU –Sofia E-mail mnedelchev@abv.bg

λ/2 length (Fig.1a) [1] and hairpin *λ/2* length (Fig.1b) [2] are the most frequently used microstrip resonators. Because of their resonance response periodicity, the filters based on these resonators have also periodicity in the amplitude response. The spurious passbands are of the second or the third harmonic of the fundamental resonance. Breaking the regularity in the resonator structure results in breaking the periodicity in the filter amplitude response. This is desirable for filters placed after mixers, power amplifiers working in class C or filters in the resonance system of microwave oscillators, where suppressing the second and the third harmonic is necessary. Stepped impedance resonators (SIR) are proposed in [3] (Fig.1c). They have smaller dimensions than the *λ/2* length resonator and the first spurious frequency is not at $2f_0$. In [4] is proposed miniaturized hairpin resonator (Fig.1d), where coupled lines are joined to the main resonator line to reduce the overall resonator dimensions. The first spurious frequency is not at $2f_0$ too. For increasing the filter amplitude response steepness, the authors of [5] propose a hairpin resonator with stub elements (Fig.1e). This resonator has two parallel and one serial resonant frequency.

The paper presents closed form formulas for the input admittance and the admittance slope parameter for different types of microstrip resonators. They are necessary for calculating the resonance frequencies and the coupling coefficients of the filter. A general formula for the SIR admittance slope parameter and a formula for the input admittance of the hairpin resonator for stub elements are derived.

II. BASIC STRUCTURES OF MICROSTRIP RESONATORS AND RESONANCE CONDITIONS.

A. *λ/2 length resonator*

The *λ/2* length resonators are the most frequently used resonators in the microstrip filters, because of their simple structure and easy adjustment. A network model of *λ/2* length resonator is shown on Fig.2. The resonator consists of a transmission line with characteristic impedance Z_c and physical length of *λ/2*.

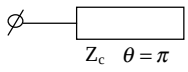

Fig.2 Network model of *λ/2* resonator

The resonator physical length is unacceptable high for low frequencies. Compact filters based on *λ/2* resonators are obtained in the X-band. The formula for the input admittance is:

$$Y_{in} = jy_c tg\theta \quad (1),$$

where θ is the electrical length of the resonator, and $y_c = 1/Z_c$

When $\theta = \pi$ rad , then $Y_{in} = 0$ and the resonance is parallel. The admittance slope parameter is defined in [6]:

$b = \frac{\omega_0}{2}\frac{\partial Y_{in}}{\partial \omega}\Big|_{\omega=\omega_0}$, where ω_0 is the resonant frequency.

The admittance slope parameter of *λ/2* resonator is [6]:

$$b = \frac{\pi}{2} y_c \tag{2}$$

An electromagnetic (EM) simulation is made and the resonance response is shown on Fig.3.

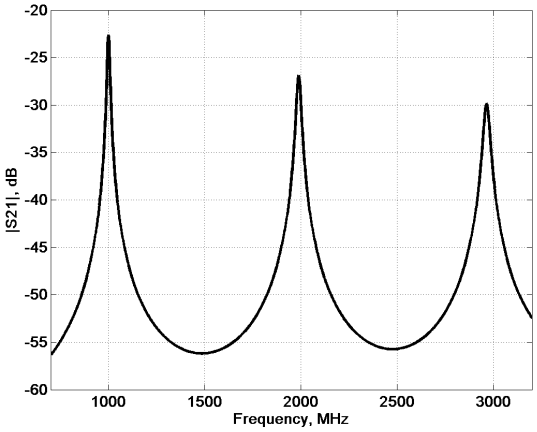

Fig.3 EM simulated frequency response on substrate *h=1.5mm* and ε_r*=4.5*

It is seen the periodicity of the resonance characteristic and the first spurious frequency is twice greater than the fundamental frequency. This results in the periodicity of the filter based on the *λ/2* resonator.

B. Stepped Impedance Resonator

Network model of SIR is shown on Fig.4. SIR consists of transmission line with characteristic impedance Z_1 and $2\theta_1$ long, loaded in its ends by open stubs with characteristic impedance Z_2 and θ_2 long. The discontinuity, introduced by the impedance difference, leads to decreasing the overall resonator length in comparison to *λ/2* resonators and shifts the first spurious frequency from $2f_0$.

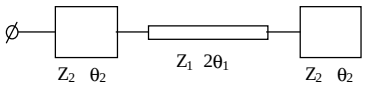

Fig.4 Network model of SIR

The formula for the input admittance of SIR is derived in [3]:

$$Y_{in} = jY_2 \frac{2\left(Rtg\theta_1 + tg\theta_2\right)\left(R - tg\theta_1 tg\theta_2\right)}{R\left(1-tg^2\theta_1\right)\left(1-tg^2\theta_2\right) - 2\left(1+R^2\right)tg^2\theta_1 tg^2\theta_2} \tag{3}$$

where $R = Y_1/Y_2 = Z_2/Z_1$ is the impedance ratio.

The condition for the fundamental parallel resonance is:

$$R = tg\theta_1 tg\theta_2 \tag{4}$$

The general formula for admittance slope parameter of SIR is:

$$b = -Y_2 \frac{\left(tg\theta_1 + \cot g\theta_1\right)\left(\frac{2R\theta_1}{\sin 2\theta_1} + \frac{\theta_2 \sin\theta_1}{\cos^3\theta_1}\right)}{\left(1-tg^2\theta_1\right)\left(1-R^2\cot g^2\theta_1\right) - 2\left(1+R^2\right)} \tag{5}$$

The normalized first spurious frequency over the fundamental resonance frequency as a function of the impedance ratio is shown on Fig.5.

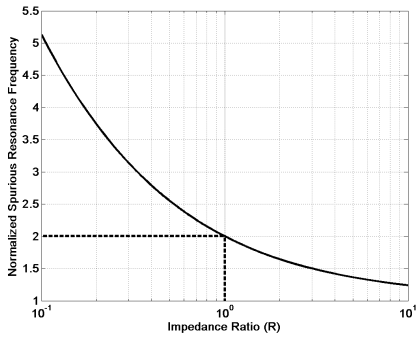

Fig.5 First spurious resonance frequency of SIR

It is obvious that for $R = Y_1/Y_2 = 1$, $f_s = 2f_0$, e.g. SIR degenerates to *λ/2* resonator.

For the most practical cases it is preferable to choose $\theta_1 = \theta_2 = \theta$. The resonance condition becomes:

$$\theta_0 = arctg\sqrt{R} \tag{6}$$

where θ_0 is the lines' length for the resonance frequency.

The expression for the admittance slope parameter is derived from (5):

$$b = 2\theta_0 Y_2 \tag{7}$$

When $\theta_0 = \pi/4$ rad, e.g. the resonator physical length is *λ/2*, the admittance slope is (2), as it is derived in [6].

The SIR filters have a transmission zero for the serial resonance frequency. They are suitable for applications with mixers and power amplifiers.

C. Miniaturized Hairpin Resonator

The miniaturized hairpin resonators proposed in [4] are much smaller than the conventional hairpin resonator. Network model is shown on Fig.6

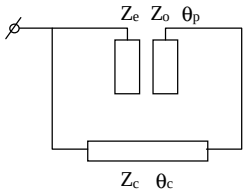

Fig.6 Network model of a miniaturized hairpin resonator

The coupled lines acts as a capacity connected to both ends of the main resonator line. This reduces the resonator dimensions and makes the resonator usable up to 3GHz. The resonator dimensions become too small above this frequency and it makes the resonator sensitive to manufacturing tolerances. A network model of miniaturized hairpin resonator is shown on

Fig.6. This resonator is a modification of SIR. The input admittance and the admittance slope parameter are derived in [7]:

$$Y_{in} = -j\frac{\left[\begin{array}{l}-(Z_e - Z_o)\cot g\theta_p + (Z_e + Z_o)\cot g\theta_p \cos\theta_s + \\ + \left(\frac{Z_e Z_o}{Z_c}\cot g^2\theta_p - Z_c\right)\sin\theta_s\end{array}\right]}{2Z_e Z_o \cot g^2\theta_p \cos\theta_s - Z_c(Z_e + Z_o)\cot g\theta_p \sin\theta_s} \quad (8)$$

$$b = -\frac{1}{2}\frac{A+B}{C} \quad (9)$$

where

$$A = \frac{(Z_e - Z_o)\theta_p}{\sin^2\theta_p} + \frac{(Z_e + Z_o)\theta_p \cos\theta_s}{\sin^2\theta_p} + (Z_e + Z_o)\theta_s \sin\theta_s \cot g\theta_p$$

$$B = \theta_s \cos\theta_s \left(\frac{Z_e Z_o}{Z_c}\cot g^2\theta_p - Z_c\right) + \frac{2Z_e Z_o \theta_p \cot g\theta_p \sin\theta_s}{Z_c \sin^2\theta_p}$$

$$C = 2Z_e Z_o \cot g^2\theta_p \cos\theta_s - Z_c\left(Z_e + Z_o\right)\sin\theta_s \cot g\theta_p$$

and Z_e and Z_o are the even and odd mode impedances of the coupled lines;

θ_p and θ_c are the electrical length of the coupled lines and the main resonator line respectively.

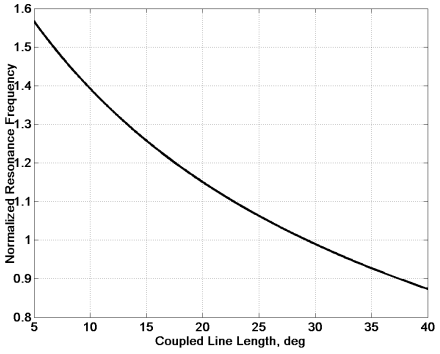

Fig.7 Normalized resonance frequency of a miniaturized hairpin resonator

Fig.7 shows the normalized resonance frequency as a function of the coupled line length for Z_e=*75Ω*, Z_o=*33.3*Ω, θ_c=*100*deg.

In [8] closed form formulas are derived for the fundamental and the first spurious resonance frequency:

$tg\frac{\theta_c}{2} = \frac{Z_o}{Z_c}\cot g\theta_o$, for the fundamental frequency, where θ_0 is the odd mode electrical length of the coupled lines.

$cotg\frac{\theta_c}{2} = -\frac{Z_e}{Z_c}\cot g\theta_e$, for the first spurious frequency, where θ_e is the even mode electrical length of the coupled lines.

D. Hairpin resonator with stub elements

A network model of hairpin resonator with stub elements is shown on Fig.8.

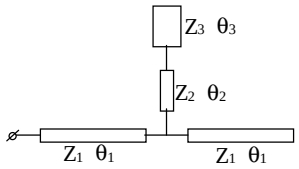

Fig.8 Network model of a hairpin resonator with stub elements.

The additional stub elements are connected in the middle of the *λ/2* line and have two resonances-a parallel and a serial. The frequency of the parallel resonance of the stub is chosen close to the passband of the filter. Two parallel and one serial resonance are the advantages of this resonator. The stubs and the resonator are connected in parallel in order to decrease the overall resonator losses. This resonator may be used for narrow bandwidth filters and high selectivity. Usually these filters are built by two or three resonators, because higher number of resonators makes difficult the resonance controlling and filter adjustment. The formula for the input admittance is:

$$Y_{in} = -jY_1\frac{2Atg\theta_1 + B}{Atg^2\theta_1 + Btg\theta_1 - A} \quad (10),$$

where $A = Y_1\left(Y_2 - Y_3 tg\theta_2 tg\theta_3\right)$

$B = Y_2\left(Y_3 tg\theta_3 + Y_2 tg\theta_2\right)$.

It is assumed that the main resonator line and the stub elements do not have influence. When $\theta_1 = \pi/2$ rad, then the input admittance is zero for the resonance frequency. The serial and the second parallel resonance are as a result of the common action of the stubs and the right *λ/4* open-end line (Fig.8). They are transformed through the approximately *λ/4* length line for the frequencies of parallel and serial resonances. The resonance frequencies are shifted, because of the inaccurate transformation (θ_1 is not *π/2* for the serial and the parallel resonance). Fig.9 shows EM simulation of hairpin resonator with stub elements. The serial and both parallel resonances are clearly seen.

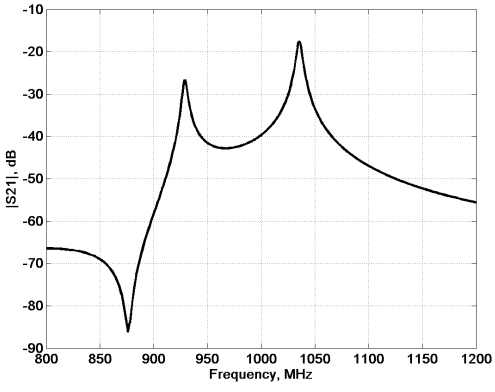

Fig.9 EM simulated frequency response on substrate *h=1.5mm* and ε_r=*4.5*

V. CONCLUSION

The paper describes the most frequently used microstrip transmission line resonators. Closed form formulas for the input admittance and the admittance slope parameter

are presented for all of the resonators. General formula for the admittance slope parameter and a formula for the input admittance of the hairpin resonator with stub elements are derived. The frequency range and the desired filter characteristics conduct the proper resonator choice for the filter design. In many applications is suitable the use of two different resonator types. This allows the combining the advantages of different resonators for obtaining the filter characteristic.

REFERENCES

[1] S.B. Cohn. Parallel-Coupled Transmission-Line-Resonator Filters. IEEE Transactions on MTT, 1958 pp.223-231.

[2] Cristal, E.G., Frankel, S., Hairpin-Line and Hybrid Hairpin-Line/Halfwave Parallel-Coupled Filters, IEEE Trans. On MTT Nov. 1972.

[3 Makimoto, M., Yamashita, S., Bandpass Filters Using Parallel Coupled Stripline Stepped Impedance Resonators, IEEE Trans. on MTT-28, 1980, pp.1413-1417.

[4] Sagawa, M. Takahashi, K., Makimoto, M., Miniaturized Hairpin Resonator Filters and Their Application to Receiver Front-End MIC's, IEEE Trans. On MTT-37, Dec. 1989, pp.1991-1997

[5] . A. A. Aleksandrovsky, B. A. Belyaev, and A. A. Leksikov, Synthesis and Selective Features of Microstrip Filters Based on Hairpin Resonators with Stub Elements, Journal of Communications Technology and Electronics, Vol. 48, No. 4, 2003

[6] Matthaei, G., Young, L., Jones, E.M.T., Microwave Filters, Impedance-Matching Networks, and Coupling Structures, Artech House, Norwood, MA, 1980

[7 Iliev I. G., CAD of Microwave Bandpass Filters Based on Miniature U Resonators, TELEKOM-95, Varna, pp.90-96, 1995

[8] Lee, S. -Y., Tsai, C. -M. A New Network Model for Miniaturized Hairpin Resonators and its Applications, IEEE MTT-S, Digest, 2000, pp.1161-1164.

Comparative Analysis of Analytical Models for Patch Antenna Approximation

Nicola I. Dodov[1] and Peter Zh. Petkov[2]

Abstract – **This study explores the behaviour of the two most - often used analytical models of printed antennas in the frequency domain. The article also contains recommendations for their use.**

Keywords – **cavity model, transmission line model**

I. INTRODUCTION

Microstrip antenna arrays are commonly used antennas in modern communication systems for telemetry and control, as well in radar and navigation technology. Design techniques are based on two main analytical models – the Transmission line model and the Cavity model. As usual, both techniques have good performance and in general produce accurate results, but detailed examinations show that properties of material structure should be taken into account when selecting the techniques.

II. BRIEF DESCRIPTION OF THE MODELS

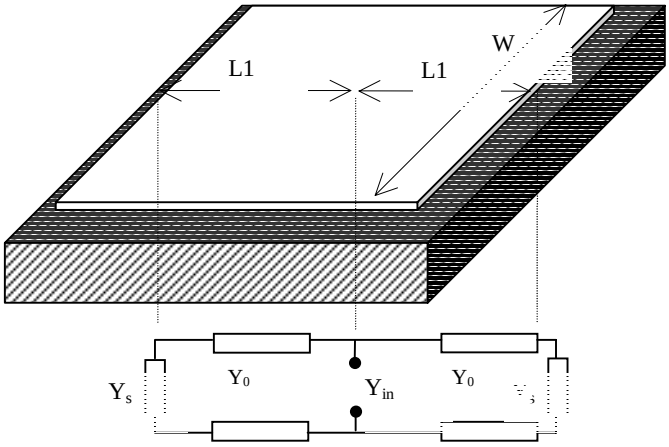

Fig. 1. Transmission Line Model

- Transmission Line Model interprets the radiating element as 2 parallel connected transmission lines with characteristic impedance, loaded with radiating edge impedance (Fig. 1). The total input admittance is presented in Eq. 1.

$$Y_{in} = Y_o \left[\frac{Y_0 + jY_s \tan(\beta l_1)}{Y_s + jY_0 \tan(\beta l_1)} + \frac{Y_0 + jY_s \tan(\beta l_2)}{Y_s + jY_0 \tan(\beta l_2)} \right] + jB_{in} \quad (1)$$

Where Y_0 is the characteristic admittance of the transmission line, B_{in} is imaginary part of the input admittance; Y_s – admittance of the radiating edge and l_1, l_2 is the length of the transmission lines, $l_1 + l_2 = L$ – the electrical length of the patch.

- Cavity model. The cavity model is based on the Eigen solution of the Helmholtz equation – Eq. 2

$$\nabla^2 E_z + k^2 \nabla^2 E_z = j\omega\mu_0 z^{\varpi} J$$
$$E_z(x,y) = \sum_m \sum_n A_{mn} \psi_{mn}(x,y) \quad (2)$$

For a rectangular patch the boundary conditions as shown in Eq. 3 apply and the final form of the Eigen solution is shown in Eq. 4.

$$\left.\frac{\delta \psi_{mn}}{\delta x}\right|_{x=0} = \left.\frac{\delta \psi_{mn}}{\delta x}\right|_{x=L} = 0$$
$$\left.\frac{\delta \psi_{mn}}{\delta y}\right|_{y=0} = \left.\frac{\delta \psi_{mn}}{\delta y}\right|_{y=W} = 0 \quad (3)$$
$$\left(\frac{\partial^2}{\partial x^2} + \frac{\partial^2}{\partial y^2} + k_{m,n}^2\right)\psi_{m,n} = 0$$

$$\psi_{mn}(x,y) = \sqrt{\frac{q_m q_n}{LW}} \cos(k_m x)\cos(k_n y)$$

Where m,n= 0, 1,2,…i; $k_m = m\pi/L$, $k_n = n\pi/W$, $k^2mn = k_n^2 + k_n^2$. As a result, the input impedance is a function of the Eigen solution (Eq. 4). C_{feed} is a constant that takes into account the influence of the feeder (microstrip feeding line).

$$Z_{in} = -j\omega\mu_0 h \sum_m \sum_n \frac{\psi_{mn}^2(x_0,y_0) C_{feed}}{k_0^2 \varepsilon_r (1 - j\delta_{eff}) - k_{mn}^2} \quad (4)$$

[1]Nicola I. Dodov is with the Faculty of Communication Technique and Technologies. Technical University of Sofia, 1000 Sofia, Bulgaria. E-mail: ndodov@tu-sofia.bg

[2]Peter Zh. Petkov is with the Faculty of Communication Technique and Technologies. Technical University of Sofia, 1000 Sofia, Bulgaria. E-mail: pjpetkov@tu-sofia.bg

III. RESULTS

Analysis of the structures was performed with electromagnetic simulation software, based on the method of moments at frequency of 5 GHz. The results are taken as reference in the examination. TRL and Cavity lines at the drawings are based on values calculated using the methods mentioned above, and with consideration that Z_{in} depends only of S_{11}.

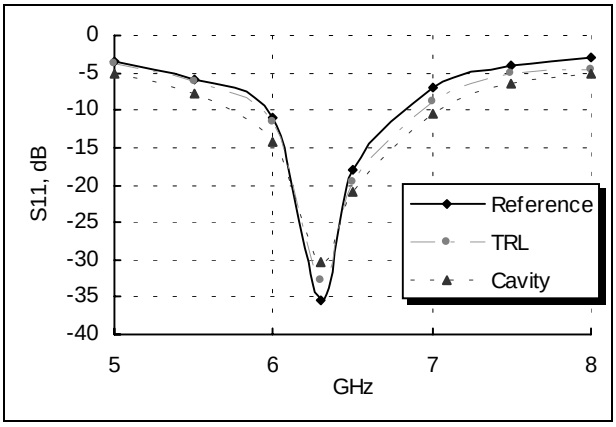

Fig. 2. Substrate thickness λ/30

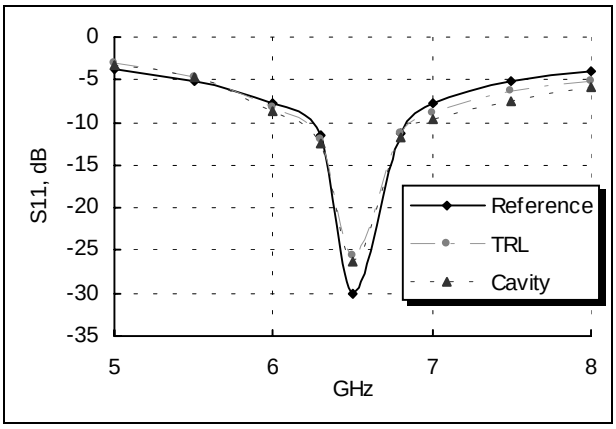

Fig. 3. Substrate thickness λ/20

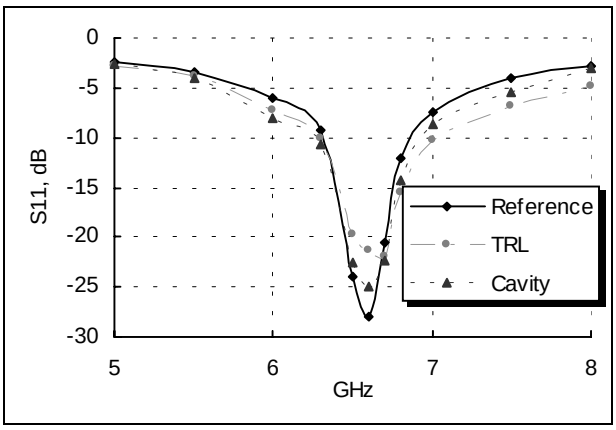

Fig. 4. Substrate thickness λ/10

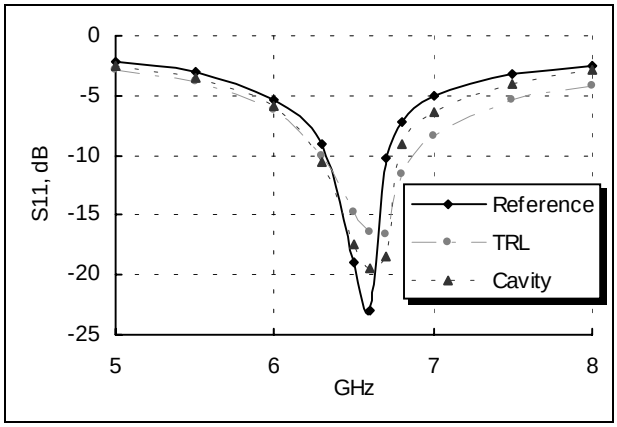

Fig. 5. Substrate thickness λ/5

From the Figures 2÷5 and theoretical background outlined above the following conclusions can be drawn:

1. The Transmission Line Model is simple, easy to use and gives accurate results in thin substrates. A very convenient feature is that it is easy to use in antenna arrays. A negative side is that it cannot solve the problems concerning circular patches and structures with existence of higher modes.

2. The Cavity Model is more complex and is based on physical processes in the microstrip radiating structure. It yields the most accurate results in cases with relatively thick substrates therefore its use in such cases is highly recommended. It determines the current distribution of electric and magnetic currents not only for the base mode, but also for the higher modes and multilayer antennas. That also gives the possibility for analytical determination of the antenna pattern. Its main disadvantage is the fact that it cannot be used for analysis of antenna arrays.

IV. CONCLUSION

This paper examines and explains the basic features of two methods for modelling patch antennas. The main conclusion is that both models give accurate enough results when they are selected taking into account substrate properties. Future research in this field will be focused on the analysis of model behaviour with regard to the dielectric permittivity of the substrate.

REFERENCES:

[1] David M. Pozar and Daniel H. Schaubert, "Microstrip Antennas : The Analysis and Design of Microstrip Antennas and Arrays ", Wiley-IEEE Computer Society Pr, 01 May, 1995

[2] Keith R. Carver and James W. Mink “Microstrip Antenna Technology” *IEEE Trans. Antennas Propagat.*, vol. A-P 30, pp. 13-33, Nov. 1981

Input Impedance and Polarization Properties of Rectangular Microstrip Edge-Fed Patch

Nikola I. Dodov[1] and Alexander G. Toshev[2]

Abstract — **Dependence of the input impedance of rectangular microstrip edge-fed patch from the position of the junction point of the feeding microstrip line is investigated. Polarization properties of the radiated far field with respect to the feeding point are investigated and presented as well. Simulation results of the rectangular patch utilizing Moment Method are presented for verification of the results.**

Keywords — **Microstrip rectangular patch, Input impednace, Polarization properties**

I. INTRODUCTION

Microstrip patches are often used as radiating elements for phased array antennas [2]. These radiating elements are commonly narrowband [1], but wide used PCB technology for their production is very attractive and low cost. For that reason many investigations have been made in the resent years concerning modeling of the patches [1], [3]; impedance matching and bandwidth widening; polarization purity improvement of the radiated field etc.

The most popular models of microstrip patches are: transmission-line model [1], [4], [7]; cavity model [5], [4]; and full-wave analysis mainly involving moment methods (MoM) [6].

This paper emphasizes on a rectangular microstrip edge-fed patches operating at its dominant TM_{010} mode [1]. Input impedance of such patches is investigated in [1] using the results obtained from transmission-line model and cavity model. According to the cavity model it is obtained that input impedance does not depend upon location of the feeding line along the feeding edge of the patch, because for TM_{010} mode electric field is constant along this edge. Subject of this paper is investigation of the dependence of the input impedance with respect to the position of the feeding microstrip line along the edge of the patch and scope of applicability of the cavity model for analysis of such structure. Polarization properties are also taken into account when results are presented. The moment method is used for analysis of the structures.

[1]Nikola I. Dodov is with the faculty of Communications and Communications Technologies, TU Sofia, "Kl. Ohridsky" blvd. N8, 1756 – Sofia, Bulgaria, E-mail: ndodov@tu-sofia.bg

[2]Alexander G. Toshev is with the faculty of Communications and Communications Technologies, TU Sofia, "Kl. Ohridsky" blvd. N8, 1756 – Sofia, Bulgaria, E-mail: toshev_a@skygate.bg

II. MATHEMATICAL BACKGROUND AND RESULTS FROM TRANSMISSION-LINE AND CAVITY MODELS

When fringing effects can be neglected (L/h>>1 on Fig.1) field between microstrip patch and substrate is well described using cavity model [1]. Using coordinates designated on Fig.1 for the dominant TM_{010} mode the following expressions for the field are valid [1]:

$$\begin{aligned} E_x &= E_0 \cos\left(\frac{\pi}{L} y'\right) \\ H_z &= H_0 \sin\left(\frac{\pi}{L} y'\right) \\ E_y &= E_z = H_x = H_y = 0 \end{aligned} \tag{1}$$

where y' is used to designate the fields inside the cavity; $E_0 = -j\omega A_{010}$ and $H_0 = \frac{\pi}{\mu L} A_{010}$. The magnitude of the field is A_{010} and its structure is depicted on Fig. 1. The resonant frequency is determined by [1]:

$$(f_r)_{010} = \frac{v_0}{2L\sqrt{\varepsilon_r}} \tag{2}$$

where v_0 is the speed of light in the free space.

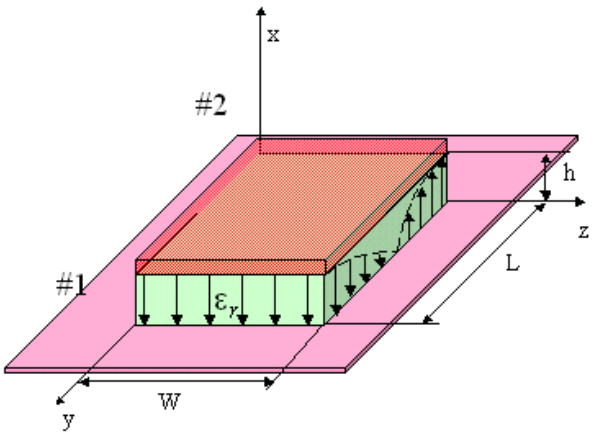

Fig. 1: Rectangular microstrip patch and its dominant TM_{010} mode

Because of the fringing effects resonant length of the patch is smaller than its electrical length. The extension ΔL that

takes into account fringing is dependent on the ratio $\frac{W}{h}$ and is given by [1]:

$$\Delta L = 0.412 \frac{(\varepsilon_{reff} + 0.3)(W/h + 0.264)}{(\varepsilon_{reff} - 0.258)(W/h + 0.8)} \quad (3)$$

where ε_{reff} is effective permittivity of the transmission line of width W. The effective length of the patch is $L_{eff} = L + 2\Delta L$. This influences also the resonant frequency, given with Eq. (2), where ε_{reff} and L_{eff} should be used.

The TM_{010} field is not dependent on z coordinate and therefore input impedance should not depend on the position of the feeding line along W dimension of the patch – Fig. 2. If the feeding microstrip line is parallel to y-axes, the patch has two radiating slots designated on Fig. 2, with equivalent conductance G_1 and susceptance B_1, determined by the fields, given with Eq. (1) from the cavity model [1]. Input resonant impedance of the inset-fed rectangular patch is determined by the two radiating slot separated by the transmission line of width W [1]:

$$R_{in}(y = y_0) = \frac{1}{2(G_1 - G_{12})} \cos^2\left(\frac{\pi}{L} y_0\right) \quad (4)$$

where G_{12} is mutual conductance between radiating slots and y_0 determines inset-feed point as shown on Fig. 2. Eq. (4) is valid if $G_1 / Y_c << 1$ and $B_1 / Y_c << 1$, where Y_c is the characteristic admittance of the feeding line. Inset-feed is used for matching between characteristic impedance of the input line and input impedance of the patch as described in [1]. According to Eq. (4) input impedance of the patch does not depend on z-coordinate, because neither G_1 nor G_{12} depend on it.

III. Moment Method Analysis – Simulation Results

For adequate estimation of the input impedance Z_{in} of the patch and its variation with respect to the position z_{feed} of the inset feeding microstrip line, with characteristic impedance Z_c and width w_0, cavity model of the patch and transmission line model are not sufficient, because they do not take into account fringing effects as feeding line approaches edges of the patch. Full wave analysis and particularly Moment Method is good approach for these purposes.

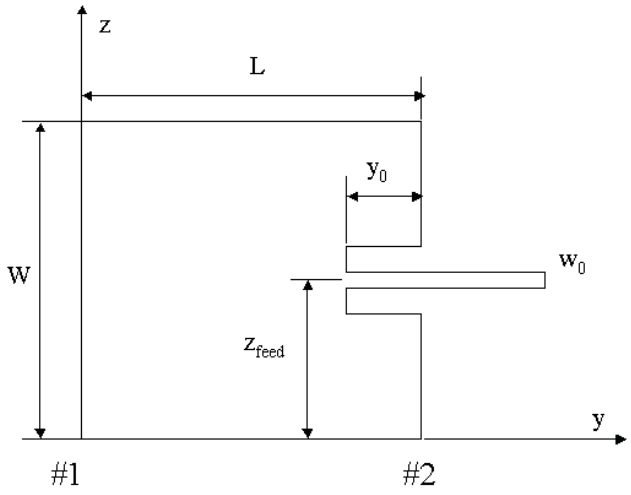

Fig. 2: Rectangular patch inset-feed dimensions

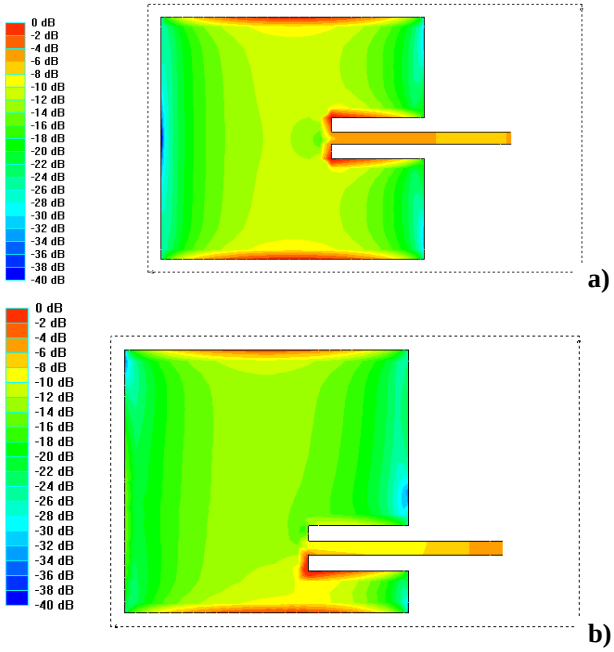

Fig. 3: Excitation average current density (MoM solution) for edge-fed microstrip patch operating at f=12.5GHz – a) - $z_{feed} / W = 0.5$; b) $z_{feed} / W = 0.25$

The following results treat microstrip edge-fed patches with approximately square shape ($W \approx L$). When feeding point is placed in the center of the patch ($z_{feed} / W = 0.5$) excitation current distribution is shown on Fig. 3 a). In the central part of the patch, when $z_{feed} / W \approx 0.5$, excitation current density is symmetrical and fringing effects are negligible as shown on Fig. 3 a). When feeding microstrip line approaches non-radiating edge of the patch ($z_{feed} / W \approx 0$ or $z_{feed} / W \approx 1$) excitation current distribution becomes asymmetrical and it is concentrated close to the approached

non-radiating edge. This situation is depicted on Fig. 3 b) for the case $z_{feed}/W = 0.25$. Since the excitation current concentrates close to the non-radiating edge, it may excite parasitic TM_{001} mode with smaller amplitude than dominant TM_{010} mode. Thus the patch starts to operate in dual mode regime and its input impedance changes according to the ratio between amplitudes of the parasitic and dominant modes.

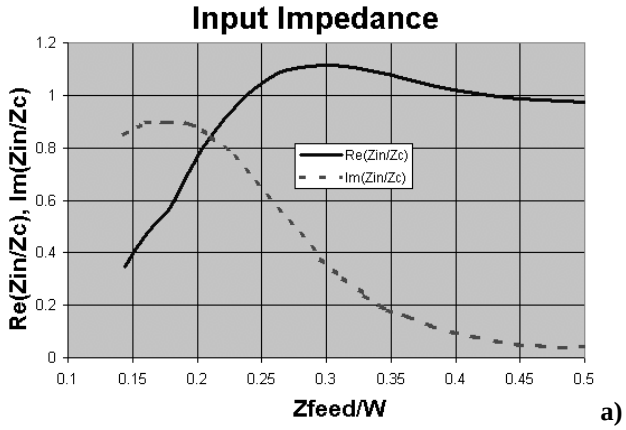

Fig. 4: Input impedance – a) and input reflection – b) for edge-fed microstrip patch (f=12.5GHz) with respect to the position of the feeding line (z_{feed}/W)

The normalized real and imaginary parts of the input impedance (Z_{in}/Z_c) are shown on Fig. 4 a). The input impedance is almost constant only in central part of the patch ($z_{feed}/W \approx 0.5$) and it becomes different in the regions close to the non-radiating edges. On Fig. 4 b) is shown input reflection of the patch as a function of the position of the feeding line. The curves are presented only in the range $0 < \frac{z_{feed}}{W} < 0.5$, because the other halves are symmetrical to the presented ones. Practical rule could be extracted based on the simulation results. For square microstrip edge-fed patches in order to obtain input reflection less than –10dB, position of the feeding line could be in the region:

$$0.25 < \frac{z_{feed}}{W} < 0.75 \qquad (5)$$

If Eq. (5) is satisfied the amplitude of the parasitic TM_{001} mode is not large enough to destroy significantly input matching of the patch.

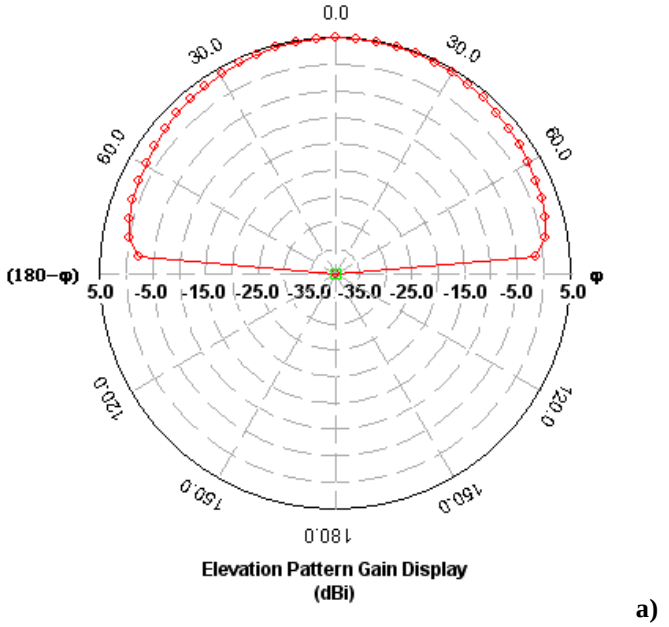

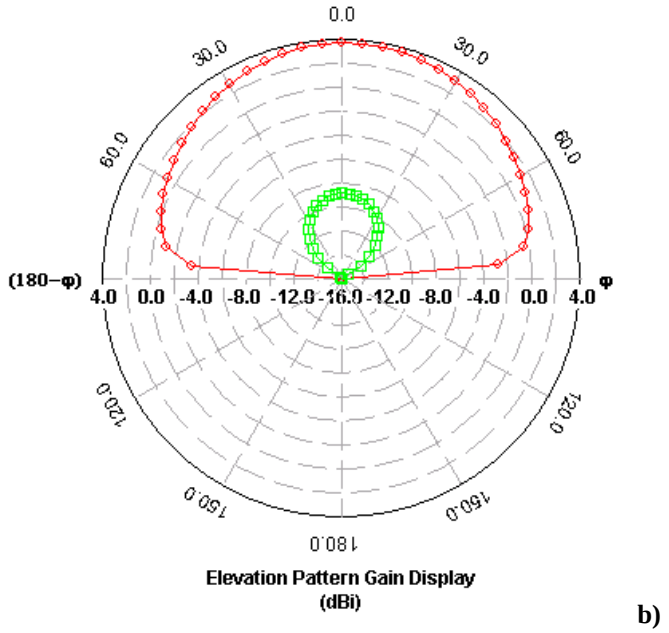

Fig. 5: Radiation in the E-plane, (x,y) plane, for square microstrip edge-fed patch (f=12.5GHz) for the case: a) - $z_{feed}/W = 0.5$ and b) - $z_{feed}/W = 0.25$

Very interesting is the question about radiating properties of the patch, when feeding line approaches non-radiating edges. The dominant TM_{010} mode radiates with the radiating slots #1 and #2 designated on Fig. 1 and Fig. 2. The field of the TM_{010} mode is polarized in the plane (x,y), which is the E-plane for

this mode - Fig. 1. The parasitic TM_{001} mode has radiating slots orthogonal to slots #1 and #2 and therefore radiates linear polarized field in the plane orthogonal to that of TM_{010} mode. The plane (x,z) is H-plane for TM_{010} mode and E-plane for TM_{001} mode. Therefore radiation from the parasitic TM_{001} mode is orthogonal to that of the dominant TM_{010} mode. In other words non-radiating slots become partially radiating (because of the parasitic TM_{001} mode) when position of the feeding line approaches edge of the patch.

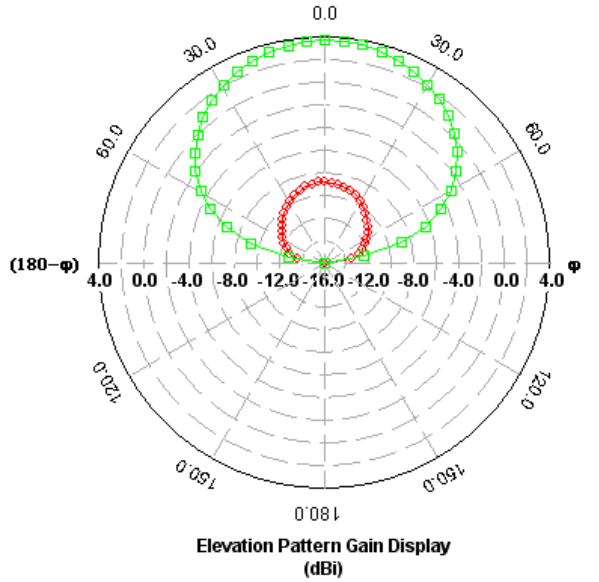

a)

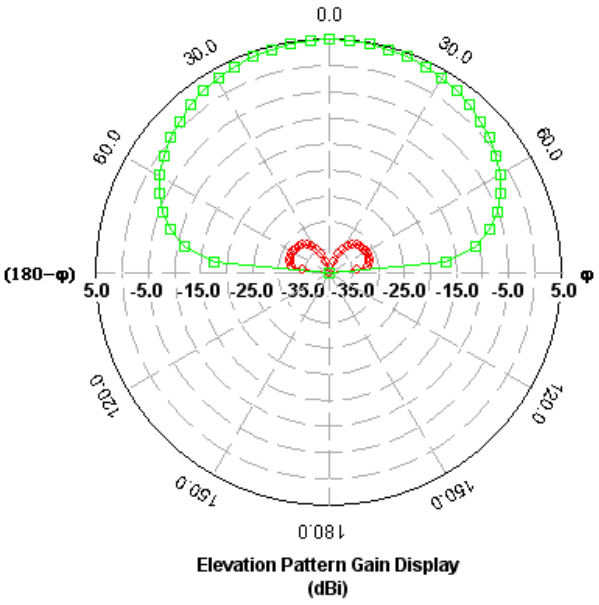

b)

Fig. 6: Radiation in the H-plane, (x,z) plane, for square microstrip edge-fed patch (f=12.5GHz) for the case: a) - $z_{feed}/W = 0.5$ and b) - $z_{feed}/W = 0.25$

The level of the crosspolarization is determined with the ratio between dominant TM_{010} and parasitic TM_{001} modes. It is interesting to know the level of the crosspolarization when Eq. (5) is satisfied. Radiation patterns in the E-plane of the patch calculated upon excitation currents, shown on Fig. 3, are presented on Fig. 5 a) and b) for the cases $z_{feed}/W = 0.5$ and $z_{feed}/W = 0.25$ respectively. Radiation patterns in the H-plane of the patch are presented on Fig. 6 a) and b) for the same cases. The level of the crosspolarization is of order of –12dB when $z_{feed}/W = 0.25$. This leads to the conclusion that amplitude of the parasitic TM_{001} mode is more than 10 dB lower than that of the dominant TM_{010} mode.

IV. Discussion and Conclusion

Investigation of the input impedance of rectangular microstrip edge-fed patch with respect to the position of the feeding line along radiating edge has been presented. It has been shown that cavity and transmission line models are not sufficient for estimation of the input impedance of the patch when feeding line approaches non-radiating edge because they do not take into account fringing effects. Moment method has been employed for analysis. Dependence of the input impedance and input reflection from the position of the feeding line has been presented. Practical design rule for almost square patches has been extracted for placement of the feeding line along radiating edge in order to obtain not large degradation of the input reflection of the patch. Crosspolarization degradation of the not-center-fed microstrip patch has been explained based on cavity model and dominant TM_{010} and parasitic TM_{001} modes.

References

[1] Constantine A. Balanis, *Antenna Theory – Analysis and Design*, John Wiley & Sons, Inc., New York 1997

[2] Robert J. Mailloux, *Phased Array Antenna Handbook*, Artech House, 1994

[3] *Microstrip Antennas – The Analysis and Design of Microstrip Antennas anmd Arrays*, edited by David M. Pozar and Daniel H. Schaubert, IEEE PRESS ,1995

[4] K. R. Carver and J. W. Mink, "Microstrip Antenna Technology", *IEEE Trans Antennas and Propagat.*, Vol. AP-29, No1, pp. 2-24, January 1981

[5] Y. T. Lo, D. Solomon, W. F. Richards, "Theory and Experiment of Microstrip Antennas", *IEEE Trans Antennas and Propagat.*, Vol. AP-27, No2, pp. 137-145, March 1979

[6] J. R. Mosig and F. E. Cardiol, "General Integral Equation Formulation of Microstrip Antennas and Scatterers", *Proc. Inst. Elect. Eng.*, pt. H., Vol. 132, No2, pp. 424-432, 1985

[7] J. R. James and P. S. Hall, *Handbook of Microstrip Antennas*, Vols. 1 and 2, Peter Peregrinus, London, UK, 1989

Mutual Coupling between the Resonators in the Planar Microstrip Antennas
Part I. Principles and Basic Microstrip Resonators

Nikola Ivanov Dodov[1] and Nikolay Mitrev Stoyanov[2]

***Abstract* – In recent years there has been considerable interest in microstrip antenna arrays. One of the basic disadvantage of this type of antennas is the presence of surface waves. Because of this reason in this paper are shown the basic principles for excitation and propagation of the surface waves. There is made a comparison between basic constructions of microstrip resonators. The numerical data of reflection and transmission coefficients are evaluated by the method of moments. The results can be used in design of microstrip antenna arrays.**

I. INTRODUCTION

The dielectric coated ground plane of a printed antenna supports a finite number of surface wave modes, which propagate in a direction parallel to the air-dielectric interface. The properties of surface waves in absorbing layers are not well known. Only recently, they have been studied in details by few authors [1], [2].

In particular, it was found that in absorbing dielectric layers, TM surface wave cannot propagate if the frequency exceeds the so-called upper cutoff frequency. At this upper cutoff frequency, a TM-surface wave becomes a regular plane wave incident on an absorbing layer at the Brewster angle [3].

The power launched into the surface waves is power, which will eventually be lost. Hence, the excitation of surface waves lowers the overall radiation efficiency of the antenna. For finite-size substrates, the surface wave power will diffract from the edges of the substrate resulting in a disturbance of the radiation pattern [4]. Furthermore, the excitation of surface waves also results in increased mutual coupling between distant antenna elements, since the surface wave fields decay more slowly with radial distance than the space-wave fields [5]. Because of these reasons, the excitation of surface waves is generally on desirable. Since the dominant TM_0 surface wave of a grounded dielectric layer has a zero cutoff frequency, a microstrip antenna will in generally always excite some surface-wave power.

In the paper, basic types of microstrip antennas resonators are presented which are with reduced mutual coupling. A comparative evaluation in respect of excitation of surface waves, frequency band, and technology is made.

[1]Nikola Ivanov Dodov - Technical University, Department of Radiocommunications, Sofia, Bulgaria
[2]Nikolay Mitrev Stoyanov - Technical University, Department of Radiocommunications, Sofia, Bulgaria, e-mail: n_m_stoyanov@abv.bg

The surface wave excitation is avoided by specific design of the radiating element and the one of the dielectric substrate geometry.

II. Surface Waves

In this paragraph a short expression of the surface wave propagated in a grounded dielectric slab with perfect conductivity plane is given. The dispersion equation and Pointing's equations are given. Let the dielectric slab is placed in plain (x,z) and y is normal to (x,z). The dielectric slab has a height *h* orientated along *y* and it has a permittivity ε and permeability μ. The space over the slab is air with ε=μ=1.

The both TM and TE surface waves are considered. The TM waves are described by equations

$$H_x = e^{jk_1(y-h)}e^{j\beta_z}, \qquad E_y = -\frac{\beta}{k_0}Z_0 H_x,$$

in the free-space (y>h) and by equations

$$H_x = \frac{\cos(k_2 y)}{\cos(k_2 h)}e^{j\beta_z}, E_y = -\frac{\beta}{k_0}Z_0 H_x,$$

$$E_z = j\frac{k_2}{k_0\varepsilon}Z_0 H_x \tan(k_2 y)$$

inside the layer 0 ≤ y ≤ h. In these equations, $Z_0 = \sqrt{\mu_0/\varepsilon_0}$ is the impedance of the free-space. The wave number in free-space is denoted as $k_0 = \omega\sqrt{\varepsilon_0\mu_0} = 2\pi/\lambda_0$ where ω is the angular frequency of harmonic oscillations and λ_0 is the free-space wavelength.

The wave numbers by the relations are connected

$$\kappa_1^2 + \beta^2 = \kappa_0^2 \text{ and } \kappa_2^2 + \beta^2 = \kappa_0^2\varepsilon\mu$$

Trough the Helmholtz wave equations. It follows that

$$\kappa_2^2 - \kappa_1^2 = \kappa_0^2(\varepsilon\mu - 1), \ \kappa_1\varepsilon = jk_2\tan(k_2 h).$$

This transforms into the dispersion equations by TE and TM waves are respectively

$$D^{TM}(k_0,\beta) \equiv \sqrt{k_0\varepsilon\mu - \beta^2}\tan\left(h\sqrt{k_0^2\varepsilon\mu - \beta^2}\right) + j\varepsilon\sqrt{k_0^2 - \beta^2} = 0$$

$$D^{TE}(k_0,\beta)\equiv\sqrt{k_0\varepsilon\mu-\beta^2}\,ctg\left(h\sqrt{k_0^2\varepsilon\mu-\beta^2}\right)$$
$$+\,j\mu\sqrt{k_0^2-\beta^2}=0$$

Above the layer, the time-averaged Poynting vector of TE waves contains the components

$$P_y=\frac{k_1^{'}}{2\omega\varepsilon_0}e^{-2\left[k_1^{''}(y-h)+\beta^{''}z\right]},$$
$$P_z=\frac{\beta^{'}}{2\omega\varepsilon_0}e^{-2\left[k_1^{''}(y-h)+\beta^{''}z\right]}$$

for TM waves and

$$P_y=\frac{k_1^{'}}{2\omega\mu_0}e^{-2\left[k_1^{''}(y-h)+\beta^{''}z\right]},$$
$$P_z=\frac{k_1^{'}}{2\omega\mu_0}e^{-2\left[k_1^{''}(y-h)+\beta^{''}z\right]},$$

$$k_1=k_1^{'}+jk_1^{''}\ \text{ and }\ k_2=k_2^{'}+jk_2^{''}$$

for TE waves.

Thus, in the case of TE waves, the Poynting vector is also perpendicular to the phase front.

III. Analysis Method

In this paper, some modifications of radiating elements in an antenna arrays are presented. The goal is reducing power propagated as surface wave. In most configurations, the main task is to be repressing TM_0 surface waves. The propagation of this wave can be reducing by change of the parameters at environments between the resonators.

The electromagnetic simulations are made by the method of moments. Dividing the models in groups is for making the analysis easier. This division will help for the better study of the single characteristics, configurations, and general conclusion between the groups.

The material which is used for dielectric substrate in this analysis is *Rogers RT/Duroid 6010* with ε_r=10.2, $tg\delta$=0.0023 and thickness 1.5mm. The feed of the microstrip resonators is with probe feed. This feeding method is chosen because of its minimal influence toward radiation of elements and easy manufacturing.

1. Basic model

This is the classical model (fig. 1) used for constructing microstrip antenna arrays. It is a base for comparison with another type models.

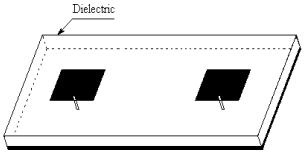

Fig.1. Basic model

In short, the main characteristics of the method with relation to mutual coupling are:

1. the increasing of the permittivity leads to reduce sizes of the resonators, but enhances the mutual coupling and stronger excitation of surface wave;
2. the increasing of the height of the dielectric substrate leads to expand of the frequencies band, but there is stronger surface wave again;
3. the increasing of the distance between the resonators reduces the mutual coupling, but after an optimal value the gain begins to decrease and the diagram pattern starts to disturbance (the power of side lobe is increase).

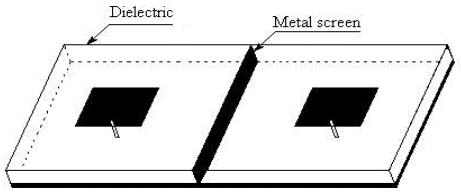

Fig. 2 Reducing mutual coupling between two resonators wit metal wall

The pointed disadvantages limit the area of their applications in the different antenna configurations. By this reason, there was made a simulative investigation on other configurations in the paper. These configurations can be used in different antenna arrays.

2. *Reducing of mutual coupling by screening of resonators each other*

The first shown method of the approach is trough screening of resonators each other with metal wall or metal via-hole. The first way guarantee a better result, but is more difficult for manufacturing. In the second way, the requirement is to choose optimal distance between the via-holes. In the current paper it is accepted for such kind of optimum to be used a distance between the via-holes 2-2,5mm [2]. From a simply technological point of view it is also defined a minimal diameter of the via-holes 6mm.

3. Cell model

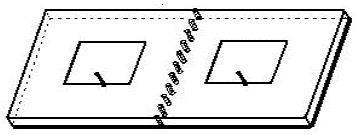

Fig. 3 Reducing mutual coupling between two resonators wit via hole

The other method of decreasing of the mutual influence, considered in the paper, is consisted of separating each resonator from the others by placing in an own cell. In this case, the optimizing task can become very complicated. Because of the thickness of the dielectric substrate the relative dielectric permittivity, and the distance between the

resonators is also necessary to be defined, the sizes of the cavity backed, its shape and dielectric permittivity of the material in and out of it.

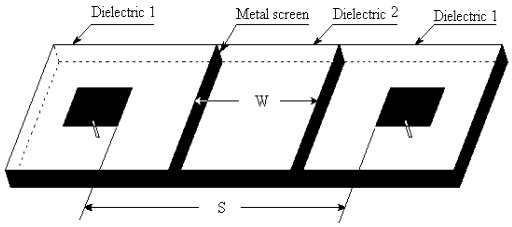

Fig. 4 Reducing mutual coupling between two resonators by dielectric barrier with different permittivity or metal

In fig. 4, it is shown that the screening can be done in immediate proximity to the resonator or in distance, which is defined from the exact requirements. In other words, it is necessary to be optimized the desired effect (wider frequency band, bigger reinforcement, less mutual influence, etc.).

The reducing of mutual coupling between resonators with separating each cell is shown. The variants, are computed, as it is shown below:

1. Dielectric barrier between cell one and cell two is put. In this case the high of dielectric substrate is *h=const*, permittivity ε_r changes from ε_r = 1…20, width *W* changes from W=0…S. The cells are not screening;
2. The single cells are not screening, but dielectric barrier between them is covered with metal. The parameters ε_r and W are the same like these in case one;
3. The cells are screening by metal walls. The parameters ε_r and W are the same like in case one;
4. The area between cells is fully metal. The width of the metal is changing from W=0…S.

In this modification, the distance between two adjacent resonators remains unaltered – S=0,5λ_0. This value of S is preferred because it is used frequently in antenna applications and in that way a maximum gain reaches with it.

IV. Result of the Calculations

Electromagnetic simulations are made with the help of high-frequency electromagnetic simulator working by the moment method. All of the researches are for the same resonance frequency (10,9GHz). With the goal of decreasing the error in the analysis of the results in all of the researches, it is observed the rule – the coefficient of the mutual coupling S12 to be accounted at S11=const. Because of this reason, there is made preliminary impedance matching of all researched structures and the values of S11 are equal or close to the shown in fig.5

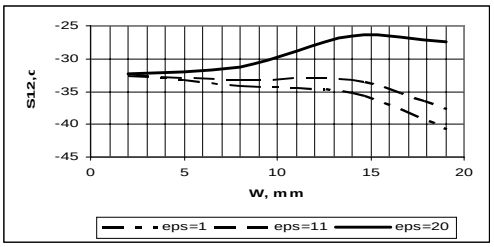

Fig. 6 Mutual coupling without metal strips

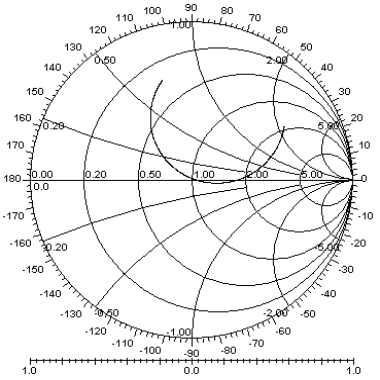

Fig. 5 S11 in Smith chart

It is shown in fig. 6 that when ε_r =1 and ε_r= 11 then W=13-14 S12 (dB) changes negligible but after this value there is an exponential decrease. It can be seen that when ε_r =20 there is a noticeable mutual coupling. S12 has a maximum when W=15 mm.

It can be seen that when each particular cell is put in a private metal screen the parameters S12 do not change essentially. Not only the character of change stays the same but also the values of S12 are reserved.

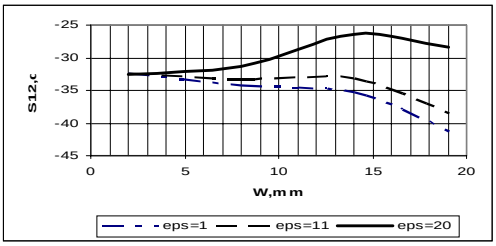

Fig. 7 Mutual coupling with metal strips between dielectric one and dielectric two

Using a metal strip (fig. 7) over the dielectric barrier the graphic has a different form. When W=8 there can be seen a resonance. At this value of W there is a lowest mutual coupling between the resonators. Reducing the mutual coupling between resonators is better than each other cases and it is over 10 dB. These characteristics of the metal strip can be used in designing of microstrip antenna arrays with a low mutual coupling.

Over a defined value of the width of W many parasite

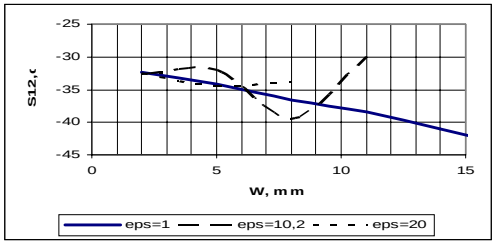

Fig. 8 Using metal strip over dielectric between the cells

resonances can be seen which is typical for this structure. This is the reason for the graphics, when ε_r=10,2 и ε_r =20, not to be finished.

When a metal is put instead of dielectric (fig. 9) it can be seen that the mutual coupling between the resonators reduces with a linear law. When this metal is put, the mutual coupling reduces faster with the increasing of the width of W, as a comparison with the described models. If fig. 8 and fig.9 are compared it can be seen that this type of screening does not have a resonance character and when W=8mm the value of S12 is nearly the same as in the previous case (horizontal metal strip).

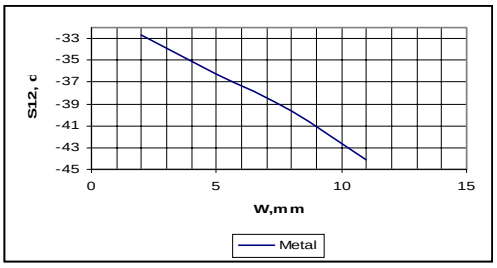

Fig.9. Mutual coupling (S12) between the patches with metal barrier between the cells

On fig. 10 is shown the variation of frequency bandwidth like a function of change in the area W with and without vertical metal strip. When the width W= 7mm all graphics

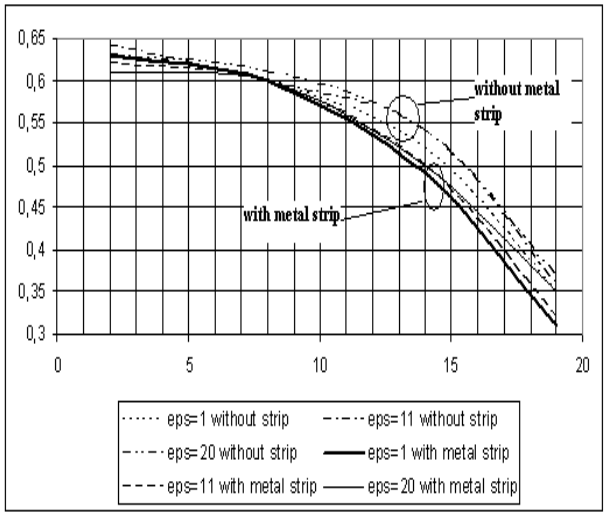

Fig.10 Bandwidth with and without metal strips between dielectric one and dielectric two

are crossed. Over this value, the structures, which has not metal strip, are more bandwidth.

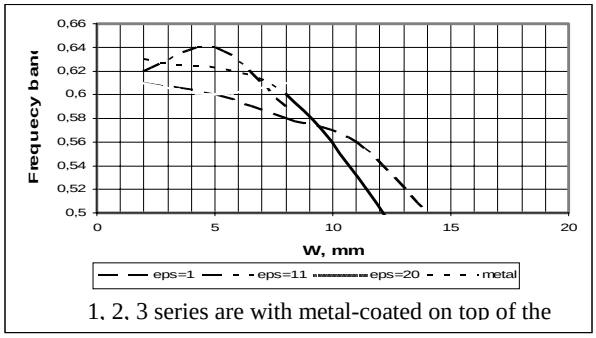

1, 2, 3 series are with metal-coated on top of the

Fig. 11 Bandwidth with metal strip over the dielectric barrier

On fig. 11 are depicted dependencies of bandwidth with metal over the dielectric, which is between two cells and the case when the cells are divided fully with metal. When metal strip is used over the dielectric with width W>7mm there are undesirable parasitical resonances but they are not shown. It is obvious that when the metal strip is used with width W=3-6mm and ε_r =11 the largest bandwidth appears.

V. CONCLUSION

In the paper is made simulative investigation of mutual coupling between patches with constant distance between them. The changes of the characteristics in the area between resonators exert influence over the mutual coupling. These specific changes can be used of reduce the mutual coupling, surface wave or to increase the bandwidth in determinate area.

In the paper are shown some advantages and disadvantages of the described structures. The resonators can be used in design of antenna arrays with reducing mutual coupling.

REFERENCES

[1] D. M. Pozar, “The active element pattern,” *IEEE Trans. Antennas Propagat*.,vol. 42, pp. 1176–1178, Aug. 1994.

[2] H. Steyskal and J. Herd, “Mutual coupling compensation in small array antennas,” *IEEE Trans. Antennas Propagat*., vol. 38, pp. 1971–1975,Dec. 1990.

[3] Linear Pattern Correction in a Small Microstrip Antenna Array Salonen, I.; Toropainen, A.; Vainikainen, P.; *IEEE Trans. Antennas Propagat*.,Volume: 52, Feb. 2004 pp.578-586

[4] K. R. Dandekar,H. Ling, and G. Xu, “Experimental study of mutual coupling compensation in smart antenna applications,” *IEEE Trans. Wireless Commun*., vol. 1, pp. 480–487, July 2002.

[5] Efficient full-wave analysis of mutual coupling between cavity-backed microstrip patch antennas Rubio, J.; Gonzalez, M.A.; Zapata, J.; *Antennas and Wireless Propagation Letters*, Volume: 2, Issue:11, 2003 pp. 155 - 158

Mutual Coupling between the Resonators in the Planar Microstrip Antennas Part II. Antenna Arrays

Nikola Ivanov Dodov[1] and Nikolay Mitrev Stoyanov[2]

Abstract – In Part two of this paper the basic structures are presented which are investigated in part one and on their basic analysis is extended to antenna arrays with finite size. The gain, radiation pattern, and directivity of antenna array with different number of resonators depending on scan angle had been shown. This result can be use for designing of finite size antenna arrays.

I. Introduction

In the resent years the planar microstrip antenna arrays are widely known, as well as their increasing number of applications [1], [2]. In addition to conformability, microstrip antennas have desirable features such as low cost and light weight which makes them extremely attractive for use in a variety of applications. The principal disadvantage of microstrip patch antennas is their narrow impedance bandwidth, which results from the small separations between the resonators and the ground plane [2]. The most straightforward way to improve the bandwidth is to use a thicker substrate. Unfortunately, the grounded dielectric slab supports tightly bound surface wave modes, which represent a loss mechanism. As the substrate becomes thicker, the bandwidth of the antenna increases. Recently, it has been demonstrated that the metal walls placed between the elements of printed phased arrays prevent mismatch and blindness as the array is scanned. A similar concept can be used to improve performance of microstrip patch face arrays. By placing metal walls between the patch elements, the guided wave modes in the substrate can be suppressed. Thus, the substrate thickness can be increased substantially to improve the bandwidth without corresponding decrease in scan coverage.

In this part of the paper the analysis of the structure that are described in Part I is developed, but emphasis is upon the variation that can be seen in the radiation pattern of the antenna arrays. The variation of the parameters of the antenna arrays with different number of resonators are investigated because of the models that were described in Part I. In particular, the variation of the directivity and the great side lobes are investigated.

[1]Nikola Ivanov Dodov - Technical University, Department of Radiocommunications, Sofia, Bulgaria
[2]Nikolay Mitrev Stoyanov - Technical University, Department of Radiocommunications, Sofia, Bulgaria, e-mail: n_m_stoyanov@abv.bg

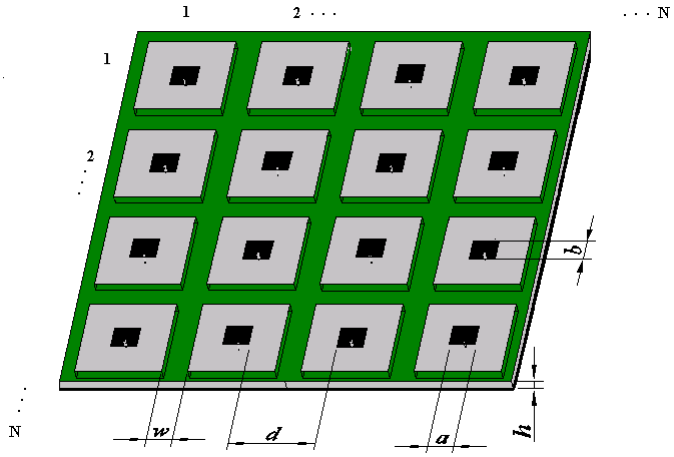

Fig. 1 Antenna array

The objective of this paper is to make an estimation of the performance of the various practical methods used for decreasing of the mutual coupling between the patches.

On the other hand, decreasing of the mutual coupling between the patches can give unlike variations of the radiation pattern and scanning possibilities of the antenna. Also the mutual coupling between the patches has dependence of the number of the resonators that constitute the antenna. This is the other problem that is partly investigated.

Another problem with the scanning antenna arrays is that when the scanning angle increases then the width of the main lobe is changed, the mutual coupling between the patches is increased etc.

The antenna arrays described in this paper are periodical and equidistant. As a result of that the theorems for the periodical structures can be used.

II. Analysis Method

Because microstrip antenna problems are not amenable to closed-form solution, some degree of modeling must be used in their design and analysis. While simple approaches such as the transmission line and cavity models are often used to design microstrip antennas, the deficiencies of these models become increasingly serious, as greater performance is demanded from the antenna.

The most accurate solutions for printed antennas utilize fully electromagnetic techniques such as the finite-difference time-domain (FDTD) method, finite element method (FEM) or integral equation (IE) approach. In this paper, the finite element method is used. This method cannot be used for large structures because of the consumed great computer memory. This requires a settlement by compromise such as dividing the arrays of subarrays, using of symmetric plain and etc. This method can lessen the accuracy of computations, but allows the dedicated computer memory to decrease and larger structures to be estimated [3], [4]. Here, the dividing of the array of subarrays is used to be estimated an NxN antenna array.

For the estimation of the radiation pattern of the antenna arrays is used estimated before radiation pattern of particular radiator. The analytical expression of the radiation pattern is

$$F_A(\phi,\theta) = S(\phi,\theta)F_e(\phi,\theta),$$

where

$S(\phi,\theta) = \sum_{n=1}^{N} W_n e^{jk\vec{r}_n\vec{r}_s}$ is the factor of the arrays

and $F_e(\phi,\theta)$ is the radiation pattern of particular radiator.

(ϕ,θ) are angular coordinates of the current point in spherical co-ordinates

$k=2\pi/\lambda_0$ – wave number in the free space

r_n is the vector determined by the current point and the position of the element *n*,

$W_n = A_n e^{j\psi_n}$ is complex weight of element *n*.

The scanning of a regular antenna array with a step of phase variation per an element ψ_n is defined by

$$\psi_n = -k\vec{r}_n\vec{r}_j$$

r_j is the vector that defined the direction of scanning.

The basic cell used in this investigations is shown on Fig. 2.

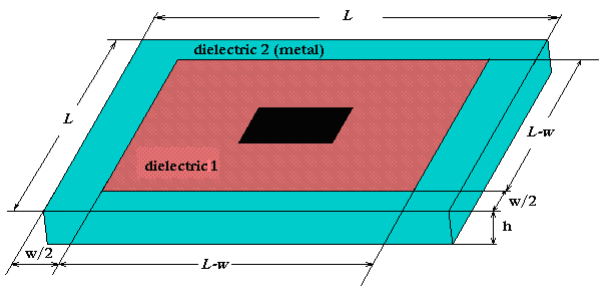

Fig. 2 The isolated microstrip radiator (cell)

It can be seen that the substrate is composed of two parts - dielectric 1 and dielectric 2 (metal). A special case, when the width *w/2*=0mm (without dielectric 2/metal) then this result in the conventional microstrip resonator. This model is used as a template for the other models. The dimensions of dielectric 1 decreases significantly when the values of the width *w/2* is great and this can result in mismatch or undesirable resonances can appear. In this paper are not represented the cases when these effects occur.

The shape of the cell is quadratic with dimensions LxL.

As in part I different cases are described:

1. The barrier between cells is entirely constituted of dielectric;
2. The vertical walls of the barrier are metal-coated;
3. The upper side of barrier is metal-coated;
4. The barrier is entirely constituted of metal.

Also, in the first three cases permittivity is changed εr = 1; 10; 20. These great differences of ε_r give an idea of the differences in the particular cases. The distance between the patches in this paper is $d=const=0{,}55\lambda_0$. The thickness of barrier between different cells is changed in the interval *W=0, 2…10mm*, the height of the substrate is h=1,5mm, permittivity of the substrate in the area of the resonators is $\varepsilon_r = 10{,}2$.

About the structure of the antenna arrays is performed comparison between the two cases for the antenna arrays with sizes: 1x1; 5x5 patches.

III. Results of the Calculations

Electromagnetic simulations are made with the help of high-frequency electromagnetic simulator working by the moment method. All of the investigations are for the same resonance frequency (10,9GHz).

On the next figures is represented the gain of the patch *G* [dBi] versus the width *w* of dielectric2/metal.

First, for the permittivity ε_r of the substrate is assigned the values 1, 11 and 20. The gain significantly decreases for great values of ε_r and *w*. It can be seen that the gain for ε=1 (in air) slightly increases when the area of dielectric 1 become smaller. Variation of the gain when ε_r=11 is negligible due to the permittivity of dielectric 2 that become quite close to that of dielectric 1.

When the permittivity is ε_r=20, *w* has high values and the border area between dielectric 1 and dielectric 2 is metal-coated, it is obvious that the gain decreasing is significantly greater in comparison to the case when the border is not metal-coated (Fig.3 and Fig.4).

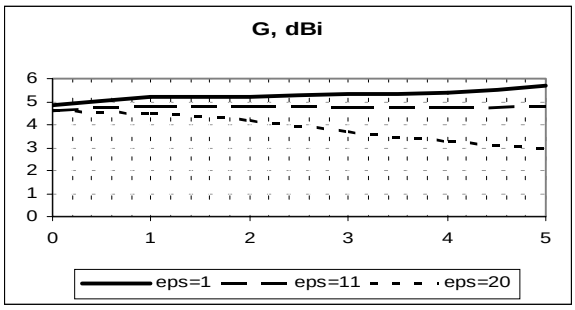

Fig. 3 Gain versus the width w[mm] for different values of the permittivity of the dielectric 2

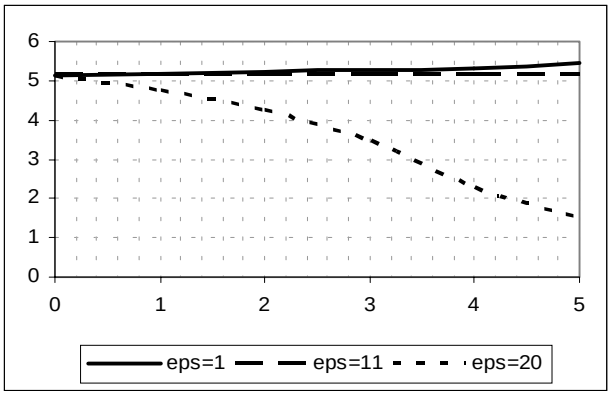

Fig. 4 Gain versus the width w[mm] for different values of the permittivity of the dielectric 2 with metallization between dielectric 1 and dielectric 2

The next simulation is performed with metallization of the top side of dielectric 2. The results are shown on Fig.5. There is not remarkable change of the gain. As the previous cases one can observe greatest gain for εr=1 and smallest for ε_r=20.

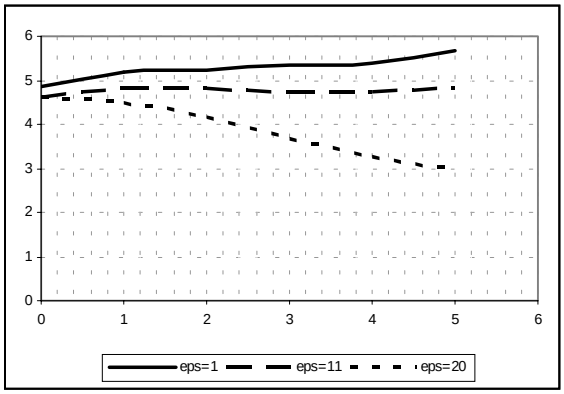

Fig. 5 Gain versus the width w[mm] for different values of the permittivity of the dielectric 2 with metallization on the top of dielectric 2

In the cases described above the parameter that is used for comparison is ε_r. On Fig. 6 are shown four curves for ε_r=1: the dielectric 1 is not metalized; there is a metallization between dielectric 1 and dielectric 2 (vertical strips); the top side of dielectric 2 is metalized (horizontal strips); instead of dielectric a perfect conductor is used. The curve of gain is smoother when the top side of dielectric 2 is metalized. Further, the gain is smaller than this one in the other cases when the values of width *w* are great. It is deeply impressed that the gain significantly increases for all values of *w* when the metal is used instead of dielectric 2. Other special feature is that the gain has resonance (G_{max} =5,78 when *w*=2mm).

The variation of the width of the main lobe of the radiation pattern is also investigated. Because of the same nature of the variations in all investigated structures only the simulation results for the cases with dielectric (without metallization)

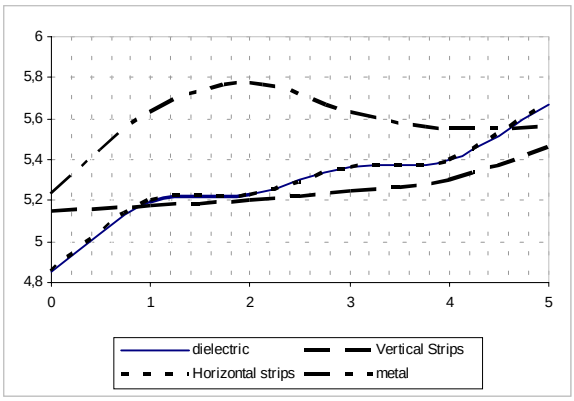

Fig. 6 Gain versus the width w [mm]

and perfect conductor (metal) used instead of dielectric 2 are shown (фиг.7).

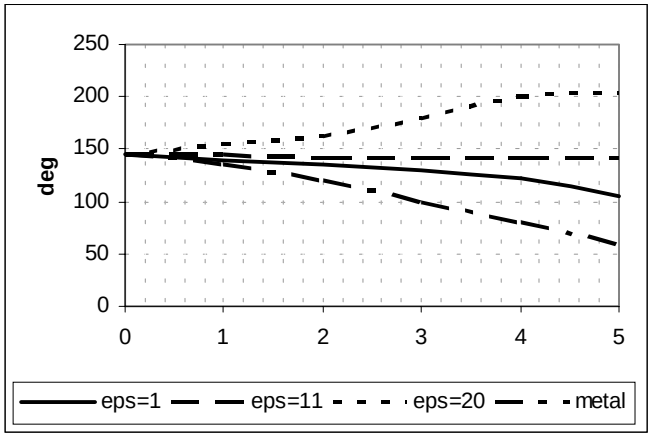

Fig. 7 Main lobe width versus the width of dielectric 2

It is obvious that the increasing of the value of permittivity results in widening of the radiation pattern; despite the inherent low directivity of the isolated radiator, (the main lobe is wide). The use of a metal box can significantly narrow the main lobe and to increase the directivity. This effect can be used in design of microstrip antennas when the main requirement is high directivity.

On the next drawings are represented the simulation results for an 5x5 antenna array in order to get an idea about the variation of the gain and the radiation pattern (Fig.8, Fig.9).

The level of the first side lobe is -13dB that is standard value for the microstrip antennas. When the permittivity of dielectric 2 increases then the backside lobe level decreases. For example, for the great values of width *w* and the permittivity ε=20 the backside lobe is suppressed about 25dB.

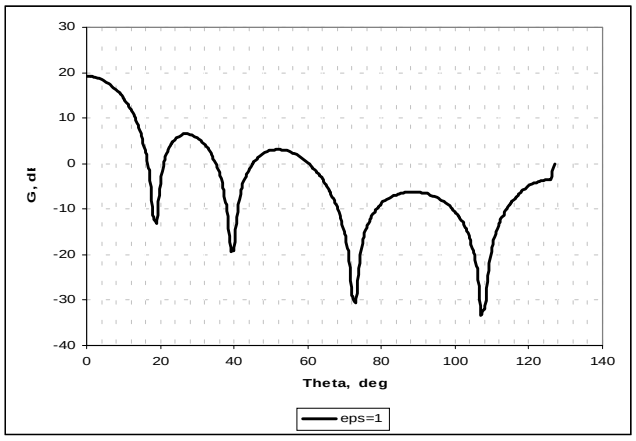

Fig. 8 The radiation pattern for the permittivity of dielectric 2 ε=1

The curves of the gain are similar to these of the isolated radiator (Fig.9). As in the previous simulations on the axes X is the width *w* [mm]. It is noticeable that the difference between the curves is greater for the higher values of the width *w* (more than 2 .5 dB for ε=1 and ε=20).

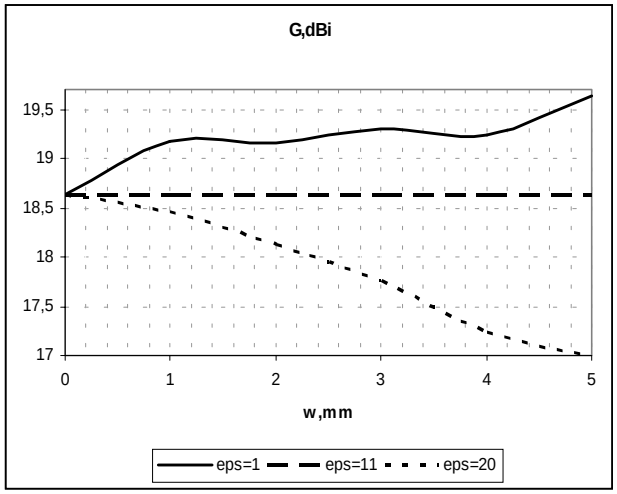

Fig. 9 The gain of a 5x5-antenna array versus the width of dielectric 2

IV. Conclusions

In this paper were represented the gain and main lobe width of the isolated radiator. The computed radiation pattern of isolated radiator is used for the simulation of radiation pattern of an 5x5-antenna array. A comparison between gains for different values of the permittivity ε_r was performed.

When the permittivity of dielectric 2 increases then the backside lobe level decreases. Putting the radiator in a metal box can increase the gain.

Reference

[1] Mutual coupling in conformal microstrip patch antenna arrays
Sangster, A.J.; Jacobs, R.T.;
Microwaves, Antennas and Propagation, IEE Proceedings -
, Volume: 150 , Issue: 4 , 8 Aug. 2003
Pages:191 - 196
[1] A. Ishimaru, R. J. Coe, G. E. Miller, and W. P. Geren, "Finite periodic structure approach to large scanning array problems," *IEEE Trans. Antennas Propagat.*, vol. 33, pp. 1213–1220, Nov. 1985.
[2] A. K. Skrivervik and J. R. Mosig, "Finite phased array of microstrip patch antennas: the infinite array approach," *IEEE Trans. Antennas Propagat.*, vol. 40, pp. 579–582, May 1992.
[3] A. Neto, S. Maci, G. Vecchi, and M. Sabbadini, "A truncated Floquet wave diffraction method for the full-wave analysis of large phased arrays. Part I: Basic principles and 2D case," *IEEE Trans. Antennas Propagat.*, vol. 48, Apr. 2000
[4] , "A truncated Floquet wave diffraction method for the full-wave analysis of large phased arrays. Part II: Generalization to the 3D case," *IEEE Trans. Antennas Propagat*., vol. 48, Apr. 2000.

Influence of the atmospheric turbulence over the optical cosmic investigations with ground based telescopes

Ervin S. Ferdinandov[1] and Kalin L. Dimitrov[2]

Abstract **- A research on the influence of the atmospheric turbulence over the optical images of cosmic objects, formed in the focal planes of ground-based telescopes is presented. Explicit final expressions about the average optical intensity, the contrast of the fluctuations and about the correlational radii of the fluctuations in front of the entrance aperture of the telescope and in its focal plane, are derived.**

Keywords **- Atmospheric turbulence, Atmospheric optics**

I. INTRODUCTION

The processing and interpretation of the data from the research of cosmic objects, using ground-based optical receiving systems and the relevant registration devices, are a very important scientific and scientifically applicable issue. These objects are sources of thermal radiation or disperse light falling diffusely on them. In both cases the stochastic structure of the radiations changes along with the distance from the objects that determine them. Their initial spatial coherece (SC) is practically zero. Their propagation in the cosmic space and in the atmosphere is accompanied by the "birth" and development of SC with diffraction origin. Exactly because of this SC the passing of the radiation through the turbulent earth atmosphere is related to the appearance of specific increasing phase and amplitude fluctuations, cross spatial ones in particular. As a general result, the images of the cosmic object which are formed in the focal plane of the receiving optical system, are strongly influenced by the atmospheric turbulence [1,2]. What is more, not only do significant declinations of the optical intensity of the images from its average distribution take place, but there are also important changes of the very average distribution, compared to what corresponds to non-turbulent atmosphere.

The influence of the turbulence over the images of the separate one-dimension sections of a cosmic object is different. It is stronger if the level of SC is higher along the axes of these sections, and the latter is inversely proportional to the size of the sections(of the plane angles in which they are seen). That is why, the influence of the turbulence can only be expressed in a different "dilution" of each section along the relevant axes in the image, i.e. in a decrease in resolution (in long expositions) - Fig. 1a, or in breaking the image into pieces (in short expositions) - Fig. 1b (by using dashed lines, an example image while turbulence is missing, is presented).

[1]Ervin S. Ferdinandov is with the Technical University of Sofia, 8 Kl.Ohridski , 1756, Sofia, Bulgaria
[1]Kalin L. Dimitrov is with the Technical University of Sofia, 8 Kl.Ohridski , 1756, Sofia, Bulgaria, E-mail:kld@tu-sofia.bg

Fig.1.Examle of influenced of atmospheric turbulence image

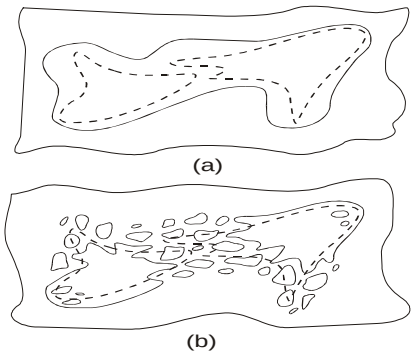

(a - acase of long exposures; b - a case of short exposures)

Therefore, in order to restore the actual shape of the object on the basis of its image, it is necessary to know the character of the ifluence of the turbulence as well as its quantitative expressions.

The theoretical research of the process of the forming of the optical image when there is no turbulence, is done using methods which origin in the theory about diffraction and partial coherence [3], respectively in the theory about coordinate-invariant and frequence-ivariant linear systems [4]. The conclusions, however, do not lead to an explicit analytic solution even in the simplest geometrical configurations of the radiating object. The reason why this happens is the large number of consequent integrations with special functions.

When there is a turbulence layer in the transmission medium, the theoretical analysis becomes more complex. As a rule, the Rytov method of smooth perturbations (called MR - Method of Rytov) is used [5]. Of course, the derived results are not explicit analytical formulae, either [6,7]. What is more, these results concern only the distribution of the average optical intensity in the focal plane. In the last few years the interest to these problems has grown. This is related to the processing of the data derived from the experimental investigations of the solar corona during the total solar eclipse on 11th August 1999, which were done at the same time in many countries, including Bulgaria. This is also related to the improvement of adaptive optics systems [8]. The difficulties mentioned above, however, have not been overcome yet.

II. METHODS OF RESEARCH

The presented method has a higher analytical effectiveness

- it provides explicit analytical results, which is used in the next sections.

It is rational to use a current one-dimensional section of the two-dimensional projection of the object in the plane of observation, and then, to restore the two-dimensional image. The corresponding setup is shown in Fig. 2.

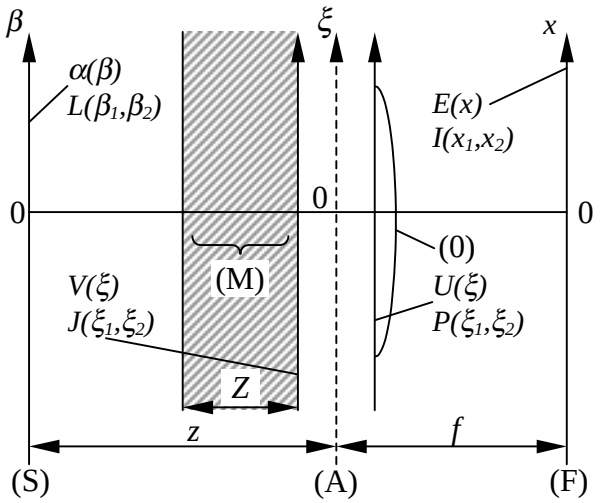

Fig. 2. Setup of the research

β denotes the axis of the one-dimensional cosmic object (S), (M) denotes the layer with width Z, which corresponds to the turbulence atmosphere, ξ denotes the axis of the one-dimensional input aperture (A) of the receiving telescope, (0) is the lens equivalent to the telescope, x is the axis of the one-dimensional focal plane (F), in which the image is formed. The complex amplitudes and the mutual intensities of the optical planes along the axes β, ξ before (A), ξ after (A), x are respectively $\alpha(\beta)$ and $L(\beta_1,\beta_2)$, $V(\xi)$ and $J(\xi_1,\xi_2)$, $U(\xi)$ and $P(\xi_1,\xi_2)$, $E(x)$ and $I(x_1,x_2)$. The methods known so far are used only for derivation of the distribution of the average optical intensity. What is more, they cannot lead to practically usable results, even in the simplest configurations of the radiation objects – mostly because of the large number of necessary consequent integrations of expressions which contain special functions. The aim of the method presented here is to deal with these disadvantages. Its most important part is the opportunity found for analytical representation of the influence of the turbulence as a "correction multplier" of the images which would be formed if turbulence was missing.

$$\langle J(\xi_1,\xi_2)\rangle = \langle J_0(\xi_1,\xi_2)\rangle Turb(\xi_1,\xi_2) \qquad (1)$$

To do this, we introduce mathematical models, the descriptions of which allow integrations with elementary quadratures.

In compliance with the latter we assume that the average intensity of $\alpha(\beta)$ can be described by Gaussian function of β , i.e.

$$\langle L(\beta)\rangle = \langle L(\beta_1,\beta_2)\rangle\big|_{\beta_1=\beta_2=\beta} = L_m \exp\left(-2\frac{\beta^2}{b^2}\right) \qquad (2)$$

where b is the half-size of the cosmic object.

Using [9] and [10] we derive

$$\langle J_0(\xi_1,\xi_2)\rangle = C_z^2 q L_m \int_{-\infty}^{\infty} \exp\left(-2\frac{\beta^2}{b^2}\right)\times$$

$$\times \exp\left[-j\frac{k}{z}(\xi_2-\xi_1)\beta\right] d\beta \ , \qquad (3)$$

where $q=\frac{\lambda}{\sqrt{\pi}}$, $C_z=\sqrt{\frac{k}{2\pi z}}$, $k=\frac{2\pi}{\lambda}$ [4,7].

We use this result which is subject to double integration. We deal with it as a marked integral over third variable and , by changing the sequence of the integral operators, we derive division of the first two integration variables.

When we use [9,10] the derivation of $\langle I_0(x)\rangle$ implies not complex, but continuous calculations and transformations. Here we will show only the final result. It is expressed by using new parameters which, however, have explicit physical sense. So we derive

$$\langle I_0(x)\rangle = \frac{aL_m}{\sqrt{2}f}\frac{1}{\sqrt{1+r^2}}\exp\left(-2\frac{x^2}{x_0^2}\right) \qquad (4)$$

where

$$r=\frac{\lambda}{\pi a\theta} \ , \ \langle I_0(x_0)\rangle = \frac{\langle I_0(0)\rangle}{e^2} \ , \ x_0=\sqrt{1+r^2}x_b \ , \ x_b = f\theta \ .$$

In the cases of strongly hindered analytical moving on, appropriate mathematical approximations are used, and the areas of their validity are carefully assessed.

III. DISTRIBUTION OF THE AVERAGE OPTICAL INTENSITY

The subject of the analysis in this section is the distribution of the mathematical expectation of the optical intensity, which is a major interest in registration with long exposures. The aim of the analysis is to derive practically usable results about the distribution of the average temporal intensity in an explicit way, which can also be used as initial basis for future research into the statistical structure of this intensity. The analysis is done with the help of the method suggested and developed in the previous section. The main part of the research here is the realization of our idea for analytic presentation of the influence of turbulence as a multiplicative correction of the images which would be formed if turbulence was missing.

The "multiplier of turbulence", which corresponds to this correction, is defined

$$Turb(\xi_1,\xi_2)=\langle\exp[\chi(\xi_1)+\chi(\xi_2)]\times$$

$$\times\exp\{-j[\Phi(\xi_1)-\Phi(\xi_2)]\}\rangle\ , \qquad (5)$$

where $\chi(\xi)=\ln\frac{V_m(\xi)}{V_{0m}(\xi)}$ and $\Phi(\xi)=\varphi_V(\xi)-\varphi_{0V}(\xi)$ are, respectively, the random perturbations of the logarithm of the amplitude and the phase variation at the point ζ [5,6].

We use the MR of the optical field [5] as well as the "heuristic" theory about the distribution of partially coherent optical radiation in turbulence medium and we derive an expression about "the multiplier of turbulence"

$$Turb(\Delta\xi)=\exp(-\gamma^2)+[1-\exp(-\gamma^2)]\exp\left[-\eta\frac{(\Delta\xi)^2}{\rho_{cV_0}^2}\right]\ , \quad (6)$$

where γ^2 is determined by MR [5,9,10], and η is a function of γ, i.e.

$$\eta=\ln\left\{[\exp(\gamma^2)-1]\left[\exp\left(\frac{\gamma^2}{e^2}\right)-1\right]^{-1}\right\}\ . \qquad (7)$$

By using [10] we quantitatively define the margins of physical validity of the analysis concerning the angle of observation of the object. These margins are compared to the interval of values of the angle in question, in which the influence of turbulence is essential (Fig.3)

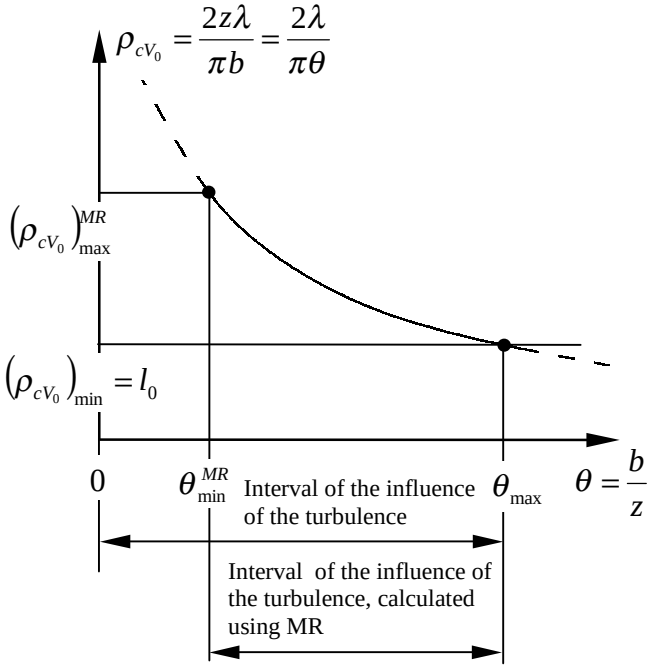

Fig. 3. Margins of the physical validity of the analysis

Explicit final formulae are derived about the distribution of the average temporal optical intensity in the focal plane in the telescope. In these formulae parameters take part as independent variables. They have explicit physical sense and they are easily calculated.

$$\langle I(x)\rangle=\langle I_0(x)\rangle\exp(-\gamma^2)+\frac{aL_m}{\sqrt{2}f}\times$$

$$\times\sqrt{\frac{\frac{2}{\eta}}{1+\frac{2}{\eta}(1+r^2)}}\quad[1-\exp(-\gamma^2)]\times$$

$$\times\exp\left[-2\frac{\frac{2}{\eta}(1+r^2)}{1+\frac{2}{\eta}(1+r^2)}\frac{x^2}{x_0^2}\right]\ . \qquad (8)$$

By making example calculations () using (8) it is shown that turbulence has a stronger influence over the images of the sections of the objects whose angle sizes are smaller – exactly these images undergo larger turbulence expansions (Fig.4).

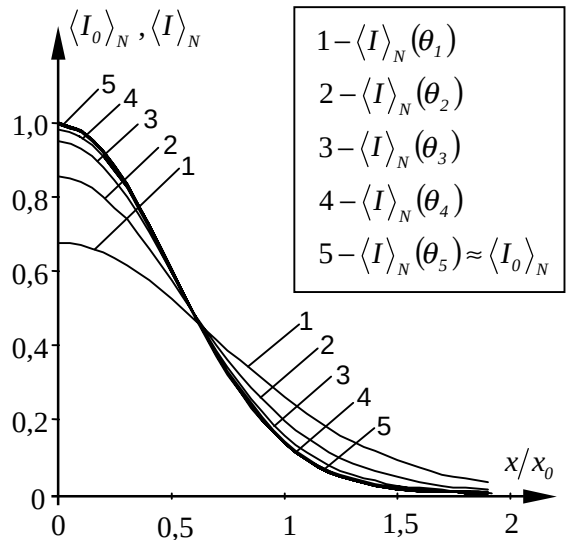

$\theta_1=\theta_{\min}=0{,}93.10^{-5}$; $\theta_2=1{,}89.10^{-5}$; $\theta_3=3{,}85.10^{-5}$;
$\theta_4=7{,}82.10^{-5}$; $\theta_5=\theta_{\max}=1{,}59.10^{-4}$.

Fig. 4. Distribution of the average optical intensity

IV. FLUCTUATIONS OF THE OPTICAL INTENSITY

The subject of the analysis in this section are the fluctuations of the optical intensity determined by turbulence, which are a major interest in registration with short exsposures and they have not been dealt with in the literature so far. The aim of the analysis is to derive practically applicable results which describe the statistical characteristics of the intensity in an explicit way.

The dispersion of the fluctuations of the optical intensity along the radial axis *x* in the focal plane is determined by the expression

$$\sigma_I^2(x) = \left\langle I^2(x) \right\rangle - \left\langle I(x) \right\rangle^2 , \qquad (9)$$

where

$$I(x) = E(x)E^*(x) = \left|E(x)\right|^2 \qquad (10)$$

is the intensity itself, and $E(x)$ is its corresponding optical field. The analysis is based on a method presented in section two. By using the results about the average intensity from the previous paragraph and, assuming some approximations and simplifying concepts with quantitatively assessed consequences, which at the same time contribute to the engineering effectiveness of the analytical results, we derive explicit final expressions about the contrast of fluctuations (about the distribution of the mean quadratic deviation, compared with the distribution of the mathematical expectation), about the correlational radii of the fluctuations in front of the entrance aperture of the telescope and in its focal plane [11]:

$$\sigma_I^2(x) = \left\langle I(x) \right\rangle^2 - \left[\exp\left(-2\gamma^2\right)\right] \left\langle I_0(x) \right\rangle^2 , \qquad (11)$$

$$\rho_{cE} = \frac{\lambda f}{\pi} \frac{2}{a} \sqrt{\frac{1}{2} + \frac{1}{\left(1 - 0{,}2\gamma^2\right)^2} \left(\frac{a}{\rho_{cV_0}} \right)^2} . \qquad (12)$$

By exemplary calculations it is shown that even in medium turbulence, the marginal part of an image (not only the one that corresponds to the turbulent expansion, but also the one that is determined by diffraction) can be registered with relatively reduced brightness, or not be registered at all, in a large number of short exposures (Fig.5).

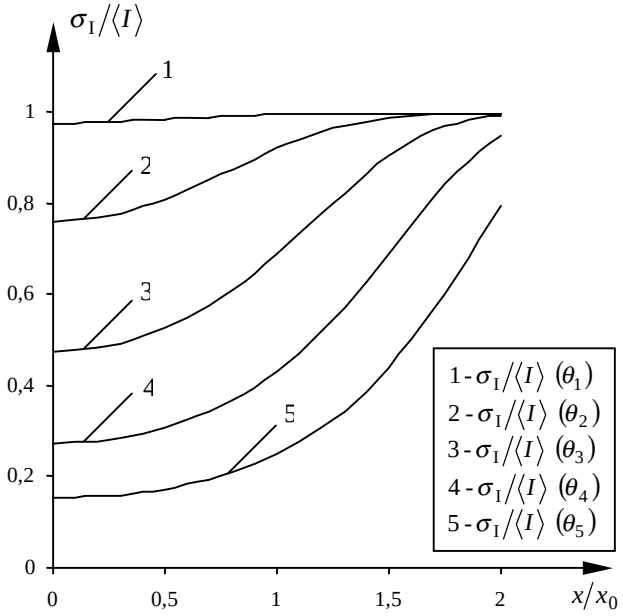

$\theta_1 = \theta_{\min} = 0{,}93.10^{-5}$; $\theta_2 = 1{,}89.10^{-5}$; $\theta_3 = 3{,}85.10^{-5}$;
$\theta_4 = 7{,}82.10^{-5}$; $\theta_5 = \theta_{\max} = 1{,}59.10^{-4}$.

Fig. 5. Distribution of the contrast of of fluctuations

What is more, it is most probable that, at the same time, in the diametrically opposed marginal part of the same image, the opposite result be observed - increase of the brightness of the image compared to the average brightness.

V. CONCLUSIONS

A conclusion can be made, that the presented research has a much wider compass than its application in processing the images of cosmic objects. The derived results can successfully be used in the research of the distribution of laser radiation in the atmosphere, laser communication systems, satellite communications, etc. For this expansion of the research, some additional assumptions are necessary, which correspond to the specifics of the spatial structure of the researched radiation.

REFERENCES

[1] D.L. Hutt, Modeling and measurements of atmospheric optical turbulence over land, Opt.Eng., 38, №8 p.p.1288-1295, 1999.

[2] S.D. Ford , B.M. Welsh, M.C.Roggemann, Reconstruction of turbulence - degraded images using the vector Wiener filter, Opt.Eng., 37, №9, pp.2491-2500,1998.

[3] M.Born, E.Wolf, *Principles of optics*, Oxford, Pergamon Press Ltd., 1964.

[4] E. Ferdinandov, *Fundamentals of optoelectronics*, Sofia,Tehnika, 1993.

[5] V.I. Tatarskii, *Wave propagation in a turbulent medium*,New York, McGraw-Hill, 1961.

[6] P. Lawson (Ed.), *Principles of long baseline interferometry*,JPL Publication, Chapter 5, p.71, 2000.

[7] J.W. Goodman, *Statistical Optics*, New York, Wiley, 1985.

[8] N. Ageorges, C. Dainty (Eds.), *Laser Guide Star Adaptive Optics for Astronomy*, Netherlands, Kluwer Academic Publishers, 2000.

[9] E.S. Ferdinandov, K.L. Dimitrov, V.I. Tsanev, T.N. Arabadjiev, Influence of the atmospheric turbulence over the images over the images of cosmic objects - methods of research, Elektrotehnika&elektronica, 38, № 7-9, pp.25-30, 2003.

[10] E. Ferdinandov, K. Dimitrov, V. Tsanev, Influence of the atmospheric turbulence over the images over the images of cosmic objects - distribution of the average optical intensity, Elektrotehnika&elektronica, 38 , №10-12, pp.36-41, 2003 .

[11] E. Ferdinandov, K. Dimitrov, V. Tsanev, Influence of the atmospheric turbulence over the images over the images of cosmic objects - fluctuations of the optical intensity, Elektrotehnika&elektronica, (in print) , 2004.

Influence of Fluctuations of Laser Beam Direction on the Bit-Error Rate in Digital Space Communication Systems

Erwin Ferdinandov[1], Tsvetan Mitsev[2], Slavyan Saparev[3], Boryana Pachedjieva[4]

Abstract – **BER dependence for ground-to-space digital communication systems on the dispersion of laser beam axis random deviations from the center of receiving antenna aperture due to the turbulence degree of the atmosphere are presented. An account is given on the influence of distance, atmospheric attenuation, and background spectral radiance. The effects of the turbulence noise and photo detection quantum noise on *BER* are compared.**

Keywords – **Free space optics, Bit-error rate, Atmospheric attenuation, Atmospheric turbulence, Quantum noise.**

I. INTRODUCTION

The deep space expansion of contemporary civilization is accompanied from growing interest to the ground-to-satellite, satellite-to-ground and intersatellite free-space communication systems. Special attention is paid on the laser space communications that offer narrow beam divergence and possibilities to create multichannel systems with extraordinary high data rate [1-4]. In our work [5] is presented a general model analytical description of such a communication system.

It is very important the fact that narrow field of view and respectively too small cross-section of laser beam in the field of the receiving antenna aperture increase significantly influence of random fluctuation of laser light direction on the quality of system parameters. This is quite essential for the ground-to-satellite systems in which turbulized atmosphere is an initial section of the propagation medium. Atmospheric turbulence determines laser beam extension analytically described in [6]. Most important are random angular deviations of the laser beam from its central axis. Due to the great length of the space section of propagation medium as well as the relatively small general (diffraction and turbulence) beam scattering result, even small angular fluctuations of direction of laser beam can cause major cross linear deviations of laser beam in relation to receiving antenna aperture. Since the optical intensity in the beam periphery is smaller than the one in its centre, turbulence cross deviations will cause random changes of the optical flow through receiving aperture. Therefore, a peculiar turbulence noise will be added to the pulse-code signal, i.e. there will be increase of the possibility of erroneous recovery of the binary code pulse in a particular one-bit time interval of the signal. This means that the value of bit-error rate (*BER*) will rise.

Here we provide theoretical research work of the relationship between *BER* and the dispersion of fluctuation of laser light direction in different atmospheric and background conditions for the ground-to-space digital laser communication system. Using the theory of turbulence and the theory of laser beam propagation in turbulent medium, basically presented in [7-9], an analytical quantity evaluation of the influence of turbulence noise on BER value is obtained. The developed analytical model describing connection between *BER* and fluctuations of laser beam direction, independently of their origin, one can use in design of digital space communication systems.

[1] Erwin Ferdinandov is with the Faculty of Communication Techniques and Technologies, Kliment Ohridski blvd. 8, 1797 Sofia, Bulgaria.

[2] Tsvetan Mitsev is with the Faculty of Communication Techniques and Technologies, Kliment Ohridski blvd. 8, 1797 Sofia, Bulgaria, E-mail:Mitzev@tu-sofia.bg.

[3] Slavyan Saparev is with the Technical University-Branch Plovdiv, Canko Diustabanov St. 25, 4000 Plovdiv, Bulgaria.

[4] Boryana Pachedjieva is with the Technical University-Branch Plovdiv, Canko Diustabanov St. 25, 4000 Plovdiv, Bulgaria, E-mail: Pachedjieva@yahoo.co.uk.

II. THEORY

The intensity of Gaussian laser beam which corresponds to binary 1 is given by expression

$$I(z,y)=\frac{2\Phi_L\tau_T\tau_A}{\pi\varepsilon r^2(z)}\psi(z,y),\quad \psi(z,y)=\exp\left[-2\frac{y^2}{r^2(z)}\right], \quad (1)$$

where z is the transmitter-receiver antennas distance, y is the random linear deviation of the cross section laser beam centre from the receiving antenna aperture centre, Φ_L is the laser pulse energy, τ_T is the transmitter antenna efficiency, τ_A is the atmosphere transmittance, $\varepsilon = 1 - e^{-2} = 0{,}865$, and the expression

$$r(z)=r_0\sqrt{1+\left(\frac{K\lambda}{\pi r_0^2}\right)^2 z^2} \quad (2)$$

describes the diffraction radius of laser beam on distance z from the emitting aperture, $r_0 = r(z = 0)$, $K > 1$ is the experimentally determined coefficient to give an account for additional broadening of laser beam in the Fraunhofer field due to the incomplete initial cross-spatial coherence of the laser radiation.

For the atmospheric transmittance determination the Elterman model for extinction is used. As a rule in this model light extinction in the optical wavelength range is mainly determine from the troposphere and we have

$$\tau_A = \tau_{aer}.\tau_{mol}, \quad (3)$$

and

$$\tau_{aer}=\exp\left\{-\frac{3{,}92}{S_m b(S_m)}\left[1-\exp\left(-b(S_m)z_A\right)\right]\right\}, \quad (4)$$

where $b\left[\text{km}^{-1}\right]=1{,}44\left(S_m\left[\text{km}\right]\right)^{-0{,}2}$, S_m is the meteorological visual range for $z = 0$, z_A is the troposphere upper limit, and $\tau_{mol}(t_{z=0} = 20^oC, p_{z=0} = 900$ mbar, $z_A = 15$ km) $\approx 0{,}9$.

The laser beam current diameter of $2r$ is significantly influenced by two groups of spatial turbulence inhomogeneities of the refraction index n of atmosphere air: relatively small inhomogeneities of $l<<2r$ and relatively big inhomogeneities of $l>>2r$. The influence of small inhomogeneities on beam structure expression in its not large additional extension with no change of the initial laser beam direction z. Quite essential to our analysis appear to be the big inhomogeneities, which determine the random angular deviations γ of laser beam from the axis z and practically do not affect $r(z)$. We shall ignore the influence of small inhomogeneities on the beam as well as the relatively weak connection between turbulence and diffraction changes of the spatial configuration of radiation. On one hand, the two currently ignored effects do not determine essential quantity changes, and on the other, their consequences are partially made up for.

The physical reason for the γ deviations lies in the turbulence determined random phase difference $\Delta\varphi_t$ between the optical oscillations in the central point $\rho = 0$ and the peripheral points $\rho = r(z)$ of the beam cross section. This difference is accumulated by radiation distribution through turbulent atmosphere layer. It can be localized equivalently in the conditional upper border plane $z = z_t$ of this layer and described by the structural function of cross phase distribution, calculated for $z = z_t$:

$$D_{\Delta\varphi_t} = \left\langle \left[\Delta\varphi_t(z_t, r(z_t))\right]^2 \right\rangle = \left\langle \left[\varphi_t(z_t, \rho = 0) - \varphi_t(z_t, \rho = r(z_t))\right]^2 \right\rangle . \quad (5)$$

The random phase difference $\Delta\varphi_t$ has a corresponding random cross plane oriented and random size deviation of the normal to the wave front of the beam at γ angle in relation to the axis z, i.e. one random oriented turn of the wave front of the random angle γ in relation to its centre. Of course, this turn is simply connected to the longitudinal shift $r(z_t)\gamma$ in the laser beam periphery. Therefore, introducing the wave vector module $k = 2\pi/\lambda$ we can write down

$$\Delta\varphi_t = kr(z_t)\gamma . \quad (6)$$

Replacing Eq.(6) in Eq.(5) results in

$$D_{\Delta\varphi_t} = k^2 r^2(z_t)\left\langle \gamma^2 \right\rangle = k^2 r^2(z_t)\sigma_\gamma^2 , \quad (7)$$

where σ_γ^2 is the γ dispersion (we have $\langle\gamma\rangle = 0$).

We use the well known formula for $D_{\Delta\varphi_t}$ of a spherical wave in homogeneously turbulized atmosphere. i.e. $C_n^2(z) =$ *const* in the interval $z \in [0, z_t]$ (with C_n^2 standing for the structural constant of n). For $z = 0$ this interval appears to be

$$D_{\Delta\varphi_t} = 1{,}095 C_n^2(0) k^2 z_t \left[r(z_t)\right]^{5/3} . \quad (8)$$

In real atmosphere, however, the following gradient is observed

$$C_n^2(z) = C_n^2(0) f(z), \quad (9)$$

where $f(z)$ is a fast decreasing function (example $f(z) \in [1; 0{,}1]$ for $z \in [0, 1\ \text{km}]$). Accepting the Gaussian model

$$f(z) = \exp\left(-\frac{z^2}{a^2}\right) \quad (10)$$

in Eq.(9) and replacing real atmosphere with an equivalent homogeneously turbulized layer at $C_{n,\text{eq}}^2 = C_n^2(0)$, we find out

$$z_{t,\text{eq}} = \int_0^\infty \exp\left(-\frac{z^2}{a^2}\right) dz = \frac{\sqrt{\pi}a}{2} . \quad (11)$$

With the condition $f(1\ \text{km}) = 0{,}1$ in Eq.(10), the calculation of Eq.(11) results in $z_{t,\text{eq}} \approx 0{,}6$ km.

Equalizing Eqs.(7) and (8) leads to

$$\sigma_\gamma^2 = 1{,}095 C_n^2(0) z_{t,\text{eq}} \left[r(z_{t,\text{eq}})\right]^{-1/3} . \quad (12)$$

For y we have the following relation

$$y = (z - z_{t,\text{eq}})\gamma , \quad \langle y \rangle = 0 , \quad (13)$$

where z stands for the distance to space correspondent. Based on Eq.(13) we can write down

$$\sigma_y^2 = (z - z_{t,\text{eq}})^2 \sigma_\gamma^2 \quad (14)$$

and replacing Eq.(12) in Eq.(14) we receive

$$\sigma_y^2\left(z, C_n^2(0)\right) = 1{,}095 C_n^2(0) z_{t,\text{eq}} (z - z_{t,\text{eq}})^2 \left[r(z_{t,\text{eq}})\right]^{-1/3} . \quad (15)$$

The expression for signal power in the receiver aperture is $\Phi_L(z, y) = \pi R^2 \tau_R I(z, y)$. Here τ_R is the receiver antenna efficiency and R is the radius of the receiver aperture. Using Φ_L the cathode signal current of photomultiplier (PMP) is calculated by

$$i_S(z, y) = W(z)\psi(z, y), \quad (16)$$

where

$$W(z) = \frac{2}{\varepsilon r^2(z)} S_i \Phi_L \tau_T \tau_A \tau_R R^2 , \quad (17)$$

and

$$S_i = \frac{e}{hc}\eta\lambda . \quad (18)$$

In Eqs.(17) and (18) S_i is the light output-current efficiency of PMP cathode, η is the quantum efficiency of PMP, $e = 1{,}6.10^{-19}$ C, $h = 6{,}626.10^{-34}$ Js, $c = 3.10^8$ m/s.

As the distance y fluctuate, the function $\psi(z, y)$ in Eqs.(1) and (16) is random and the current $i_S(z, y)$ fluctuate too. We accepted that the probability distribution of y is Gaussian with mean value $m_y = 0$ and dispersion σ_y^2. Using the expression for $\psi(z, y)$ given in Eq.(1) we find [6]

$$m_\psi\left(z, \sigma_y^2\right) = \frac{1}{\sqrt{1 + \dfrac{4\sigma_y^2}{r^2(z)}}} ,$$

$$\sigma_\psi^2\left(z, \sigma_y^2\right) = \frac{1}{\sqrt{1 + \dfrac{8\sigma_y^2}{r^2(z)}}} - m_\psi^2\left(z, \sigma_y^2\right), \quad (19)$$

and from Eq.(16)

$$m_{i_S}\left(z,\sigma_y^2\right)=W(z)m_\psi\left(z,\sigma_y^2\right),\ \sigma_{i_S}^2\left(z,\sigma_y^2\right)W^2(z)\sigma_\psi^2\left(z,\sigma_y^2\right),\quad(20)$$

where $m_{i_S}(z)$ is the mean signal current for the one bit time interval when we have binary 1.

Dispersion of current quantum fluctuations in the PMP cathode circuit is expressed as

$$\sigma_j^2\left(z,\sigma_y^2\right)=\sigma_{j_S}^2\left(z,\sigma_y^2\right)+\sigma_{j_b}^2+\sigma_{j_d}^2,\qquad(21)$$

where

$$\sigma_{j_S}^2\left(z,\sigma_y^2\right)=2em_{i_S}\left(z,\sigma_y^2\right)\Delta f,$$

$$\sigma_{j_b}^2(z)=2ei_b\Delta f,\quad \sigma_{j_d}^2(z)=2ei_d\Delta f\qquad(22)$$

are the dispersions of quantum fluctuations of signal current, background current, and dark current respectively, i_b is the mean value of background current, and i_d is the mean value of dark current, both last for the time interval with binary 1.

The mean dark current is defined by

$$i_d=\frac{i_{da}}{G_i},\qquad(23)$$

where i_{da} is the PMP anode dark current, and G_i is the PMP current gain. They are catalogue parameters.

It is easy to find the expression

$$i_b=\pi^2L_{b\lambda}\tau_R(\Delta\lambda)_{IF}S_iR^2R_p^2\frac{1}{f_{eq}^2},\qquad(24)$$

where $L_{b\lambda}$ is the background spectral radiance, $(\Delta\lambda)_{IF}$ is the optical bandwidth of the interference filter before the PMP, R_p is the radius of the PMP aperture, f_{eq} is the equivalent focal length of the receiver antenna.

As we mentioned above $i_S(z, y)$ is the random function of y. That is why $m_{i_S}\left(z,\sigma_y^2\right)$ is figured in (11) instead of $i_S(z, y)$.

To calculate *BER* we use the expression

$$BER\left(z,\sigma_y^2\right)=\frac{1}{2}\operatorname{erfc}\left[\frac{m_{i_S}\left(z,\sigma_y^2\right)}{2\sqrt{2}\sqrt{N\sigma_j^2\left(z,\sigma_y^2\right)+\sigma_{j_S}^2\left(z,\sigma_y^2\right)}}\right],\quad(25)$$

where

$$\operatorname{erfc}(x)=\int_x^\infty\exp\left(-\xi^2\right)d\xi$$

is the tabulated function, and N is the excess-noise factor of the PMP due to the amplification.

In order to estimate the effect of turbulence noise for the increase of *BER* we use the Eqs.(15) and (25). The following relation is made up

$$\beta\left(z,C_n^2(0)\right)=\frac{BER\left(z,C_n^2(0)\right)}{(BER)_0(z)},\qquad(26)$$

where $(BER)_0$ corresponds to *BER* without considering turbulence. The Turbulent-to-Quantum Noise Ratio (*TQNR*) is estimated by the formula

$$TQNR\left(z,C_n^2(0)\right)=\frac{\sigma_{i_S}\left(z,C_n^2(0)\right)}{\sqrt{N}\sigma_j\left(z,C_n^2(0)\right)}.\qquad(27)$$

III. CALCULATIONS

On the basis of the relations (1-25) an example calculation was done. The input parameters are: τ_T = 0,8; τ_R = 0,6; r_0 = 10 cm; Φ_L = 0,5 W; λ = 0,53 μm (yttrium aluminium garnet with 3-valent neodymium); Δf = 100 MHz; K = 6; $(\Delta\lambda)_{IF}$ = 20 Å; R = 4 cm; η = 0,1; R_p = 3 mm; i_{da} = 10 nA; G_i = 10^7; f_{eq} = 0,5 m; N = 1,5.

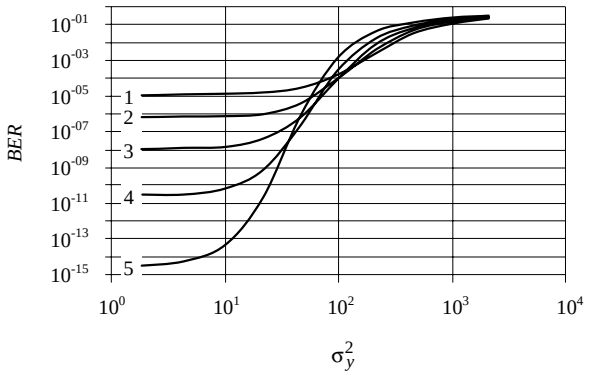

Fig. 1. *BER* as a function of σ_y^2 of random deviations y for S_m = 10 km, $L_{b\lambda}$ = 10^{-2} W/(m^2.sr.Å) and distances z: 1 - 6200 km; 2 - 5600 km; 3 - 5000 km; 4 - 4400 km; 5 - 3800 km

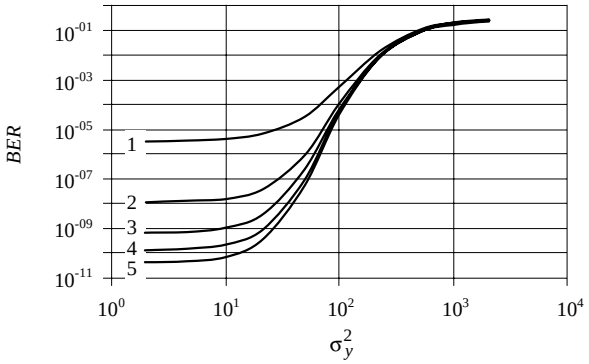

Fig. 2. *BER* as a function of dispersion σ_y^2 of random deviations y for z = 5000 km, $L_{b\lambda}$ = 10^{-2} W/(m^2.sr.Å) and visibilities S_m: 1 - 5 km; 2 - 10 km; 3 - 15 km; 4 - 20 km; 5 - 25 km

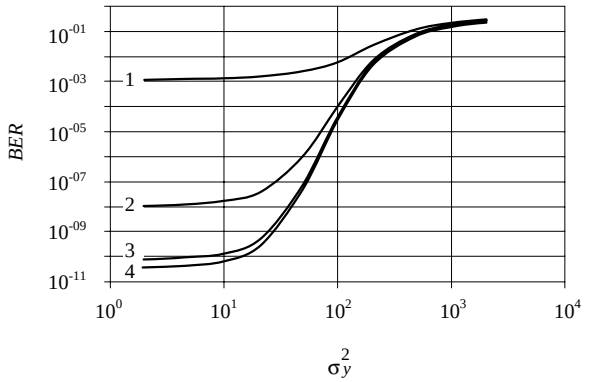

Fig. 3. *BER* as a function of dispersion σ_y^2 of random deviations y for z = 5000 km, S_m = 10 km and background spectral radiances $L_{b\lambda}$: 1 - 10^{-1} W/(m^2.sr.Å); 2 - 10^{-2} W/(m^2.sr.Å); 3 - 10^{-3} W/(m^2.sr.Å); 4 - 10^{-4} W/(m^2.sr.Å)

The *BER* results are shown plotted as a function of dispersion of random deviations *y* for different distances *z* (Fig.1), different meteorological visual ranges S_m (Fig.2), and different background spectral radiances $L_{b\lambda}$ (Fig.3). The dependence of *BER* on $C_n^2(0)$ for different distances *z* is shown in Fig.4. Plots of the function Eqs.(26) and (27) are shown in Fig.5 and Fig.6 respectively.

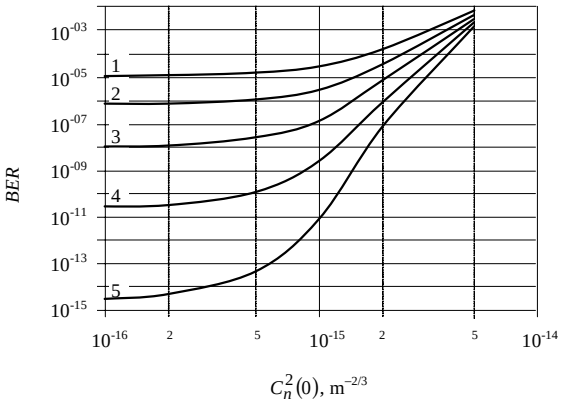

Fig. 4. *BER* as a function of structural constant $C_n^2(0)$ of the atmospheric turbulence for distances *z*:
1 - 6200 km; 2 - 5600 km; 3 - 5000 km; 4 - 4400 km; 5 - 3800 km

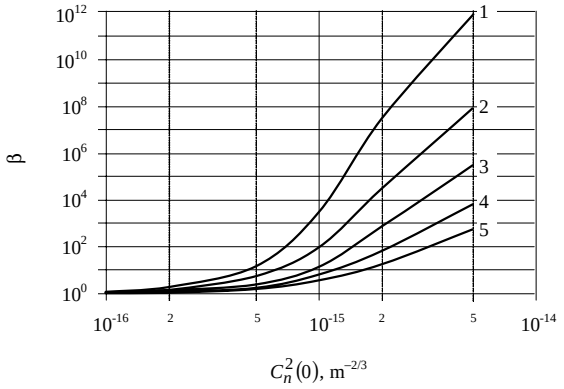

Fig. 5. β as a function of structural constant $C_n^2(0)$ of the atmospheric turbulence for distances *z*:
1 - 3800 km; 2 - 4400 km; 3 - 5000 km; 4 - 5600 km; 5 - 6200 km

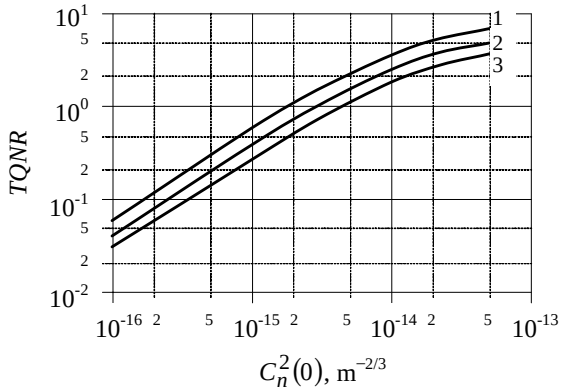

Fig. 6. Turbulent-to-Quantum Noise Ratio as a function of structural constant $C_n^2(0)$ of the atmospheric turbulence for distances *z*:
1 - 3800 km; 2 - 5000 km; 3 - 6200 km

IV. CONCLUSION

The *BER* values increase significantly with increase of the dispersion of random linear deviation *y* of the cross section laser beam centre from the receiving antenna aperture centre as is seen from the plots. It is easy to explain *BER* increase with change for the worse of the meteorological conditions and with reinforcement of the background spectral radiance (Fig.2 and Fig.3). Peculiar behavior of the curved lines $BER(\sigma_y^2)$ with *z* = vary on Fig. 1 is due to the circumstance that for small values of *z* the diffraction broadening of the laser beam is more weak and its peripheral parts more probably fall into receiver antenna aperture. Fig.4 and Fig.5 clearly show that *BER* and β increase with $C_n^2(0)$ relatively slowly in the example interval $C_n^2(0) < 5.10^{-16}$ m$^{-2/3}$. However, further increase of turbulization extent results in sharp increase of both gradients. Quite interesting appears to be the fact that the relative effect of turbulence noise is bigger at small distances. Such strange at first sight behavior of β can be easily explained if bearing in mind that, for example, for $C_n^2(0) \approx 10^{-15}$ m$^{-2/3}$ we have $(BER)_0 \approx 10^{-12}$ for *z* = 3800 km and $(BER)_0 \approx 10^{-5}$ for *z* = 6200 km. The curves in Fig.6 show that at relatively weak turbulence the quantum noise dominates over the turbulence one while at relatively strong turbulence it is the other way round. The two types of noise are commensurable for $C_n^2(0) \approx 3.10^{-15}$ m$^{-2/3}$.

REFERENCES

[1] H. Hemmati, at al., "Comparative Study of Optical and Radio Frequency Communication Systems for a Deep Space Mission", JPL TDA Prog. Rep., pp. 42-128, February 1997.

[2] R. Strickland, M. Lavan, E. Woodbridge and V. Chan, "Effects of Fog on the Bit-Error Rate of a Free-Space Laser Communication System", Applied Optics, vol. 38, no. 3, pp. 424-431, 1999.

[3] D. Begley, "Laser Cross-Link Systems and Technology", IEEE Comm. Mag., Free Space Laser Comm., pp. 126-132, August 2000.

[4] K. Wilson, M. Enoch, "Optical Communications for Deep Space Missions", IEEE Comm. Mag., Free Space Laser Comm., pp. 134-139, August 2000.

[5] E. Ferdinandov, Ts. Mitsev, "Link Range of Free Space Laser Communication System", IEEE Trans., Microwave Review, vol 9. no. 2, pp. 41-42, 2003.

[6] S. Arnon, "Effects of atmospheric turbulence and building sway on optical wireless-communication systems", Optics Letters, vol. 28, no. 2, pp. 129-131, 2003.

[7] S. Panchev, *Random Functions and Turbulence*, New York, Toronto, Sydney, Braunschweig, Pergamon Press Oxford, 1971.

[8] A. Gurwich at al., *Laser radiation in turbulized atmosphere*, Moscow, Science Press, 1974. (russian)

[9] E. Ferdinandov, *Laser radiation in radiotechnics*, Sofia, Science Press, 1981. (bulgarian)

3D TLM Simulator Application for an Analysis of the EM Field Distribution Inside Metallic Cavity with Real Feed

J. Joković[1], B. Milovanović[2], T. Randjelović[3] and M. Stojanović[4]

Abstract - **In this paper, by using 3D TLM simulator, the analysis of real feed probe influence to electromagnetic field distribution inside the rectangular metallic cavity is examined. According to the wanted type of mode in the cavity, an excitation is achived through a small wire conductor, placed into the cavity on the top wall, along the z-axis, establishing TM_{mnp} modes. In order to investigate the influence of feed and receiving probe to the field distributions in the cavity, field strength versus probe length, are presented.**

Keywords - **TLM method, microwave applicator, cavity, TLM wire node, electromagnetic field distribution**

I. Introduction

Rectangular metallic cavities represent a configuration very suitable for good modeling of some practical heating and drying applicators. The knowledge of the mode tuning behavior has important significance and would help in designing these applicators. For this reason, some researches of the metallic cavities, based on using the different approaches, were presented by a number of authors [1,2,3].

TLM (Transmission Line Modeling) method is a general, electromagnetic based numerical method that has been applied very successfully in the area of metallic cavities modeling [3,4,5]. By using an real feed probe for establishing desired field distribution in the modeled cavity all the deficiencies of impulse excitation could be avoided [6,7]. The difference in the cavity excitation causes that the TLM results in the case of impulse excitation being different from the experimental ones. With some recent improvements in TLM method, it is possible to model a probe inside the cavity using TLM wire node [8] and to investigate the influence of the real excitation to the resonant frequencies and field distributions in the cavity [6,7].

In practice, depending on the position and dimensions excitation, the number of modes will be different [9]. This situation is made worse when many modes are present.

In practical realization of the microwave applicators one of the most important issues is the electromagnetic field distribution inside the metallic cavity, in order to achieve equally material drying. The goal of this paper is to describe the possibilities of TLM method for the analysis of the electromagnetic field distribution inside the metallic cavity for different probe length. TLM method is applied to the rectangular metallic cavity. As an excitation form straight wire conductor loaded in the cavity is used.

Feed probe is connected with voltage source and placed on the top wall along the *z*-axis, establishing TM_{mnp} modes with E_z component. The resonant frequencies and field distribution inside the metallic cavity is analyzed for the excitation probe placed in the middle of the top wall (*a/2,b/2*), along the *z*-axis, and for different feed probe length. Also, in the case of both feed and receiving probe presence, field distribution for TM_{mnp} modes for different probe length is analyzed. The analysis is incomplete, as empty cavity only is considered, but some important conclusions can be drawn that are still valid for the loaded cavity.

II. Problem Modeling

In TLM method, an electromagnetic (EM) field distribution in three dimensions, for a specified mode of oscillation in a microwave cylindrical cavity, is modeled by filling the field space with a network of transmission lines and exciting a particular field component in the mesh by voltage source placed on the excitation probe. EM properties of a medium in the cavity are modeled by using a network of interconnected nodes (Fig.1), a typical structure being the symmetrical condensed node (SCN). To operate at a higher time-step, a hybrid symmetrical condensed node (HSCN) [10] is used. An efficient computational algorithm of scattering properties, based on enforcing continuity of the electric and magnetic fields and conservation of charge and magnetic flux [11] is implemented to speed up the simulation process.

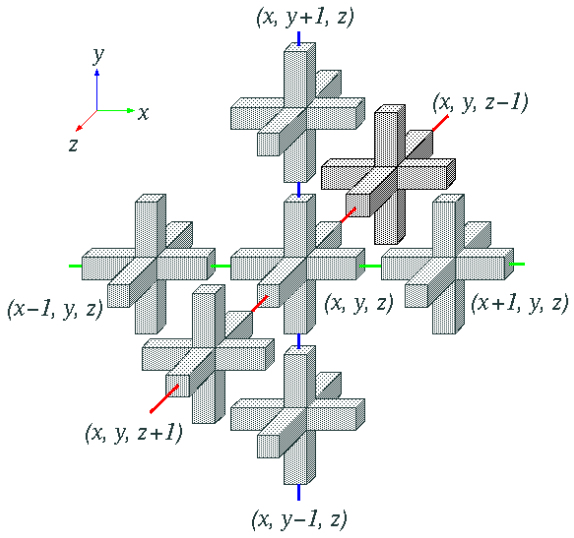

Fig. 1. Network of interconnected TLM nodes

[1]Jugoslav Joković, [2]Bratislav Milovanović, [3]Tijana Randjelović and [4]Mila Stojanović are with the Faculty of Electronic Engineering, Beogradska 14, 18000 Nis, Serbia and Montenegro, E-mail: [jugoslav, bata, tijana, milas]@elfak.ni.ac.yu

III. TLM WIRE NODE

In TLM wire node, wire structures are considered as new elements that increase the capacitance and inductance of the medium in which they are placed [12]. Thus, an appropriate wire network needs to be interposed over the existing TLM network to model the required deficit of electromagnetic parameters of the medium. In order to achieve consistency with the rest of the TLM model, it is most suitable to form wire networks by using TLM link and stub lines.

Equivalent radius of fictive cilindre for calculating the capacitance and inductance, r_{Ci} and r_{Li}, respectively, for wire segment spreading along i direction ($i \in \{x,y,z\}$) are:

$$r_{Ci} = k_{Ci}\ i_c \quad (1)$$

$$r_{Li} = k_{Li}\ i_c \quad (2)$$

where i_c represents mean dimensions of the node cross-section in i direction (for example, $x_c=(y+z)/2$), while k_{Ci} and k_{Li} are factors empirically obtained by using known characteristics of TLM network [13].

Distributed capacitance and inductance per unit length, needed for modeling of wire segments, may be expressed as:

$$C_{wi} = \frac{2\pi\varepsilon}{\ln(r_{Ci}/r_w)}, \quad (3)$$

$$L_{wi} = \frac{\mu}{2\pi}\ln(r_{Li}/r_w) \quad (4)$$

where r_w is real wire radius.

IV. NUMERICAL ANALYSIS

The numerical results obtained by using 3D TLM software, which illustrate the effect of the real feed probe on the field distribution, are presented for a cavity with rectangular cross-section. Dimensions of the investigated cavity are chosen to be $a=35cm$, $b=37cm$ i $c=26.9cm$. (Fig. 2). As homogeneous lossless dielectric inside the cavity is used air ($\varepsilon_r=1$). TLM network with dimensions $x\ y\ z=35\ 37\ 27$ nodes is used for modeling considered cavity. Feed probe, with radius r=0.5mm, is placed in the middle of the top wall of the cavity ($x=a/2$, $y=b/2$) along the z-axis. The probe is connected with voltage source V_{source} =1V, R_{source} =50Ω.

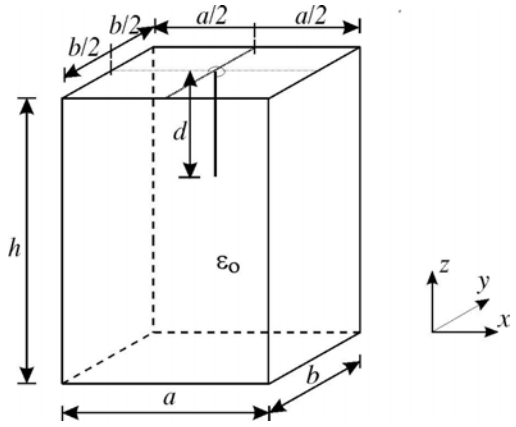

Fig. 2. Rectangular metallic cavity

First, in order to investigate the influence of the feed probe presence to the resonant frequencies and the field strength in the cavity, simulation is done for different probe length in the range d=[2,12] cm. In the Fig. 3. the resonant frequencies and strength of Ez field component in TLM node (18,19,10) versus probe length for TM_{110} i TM_{111} modes is shown.

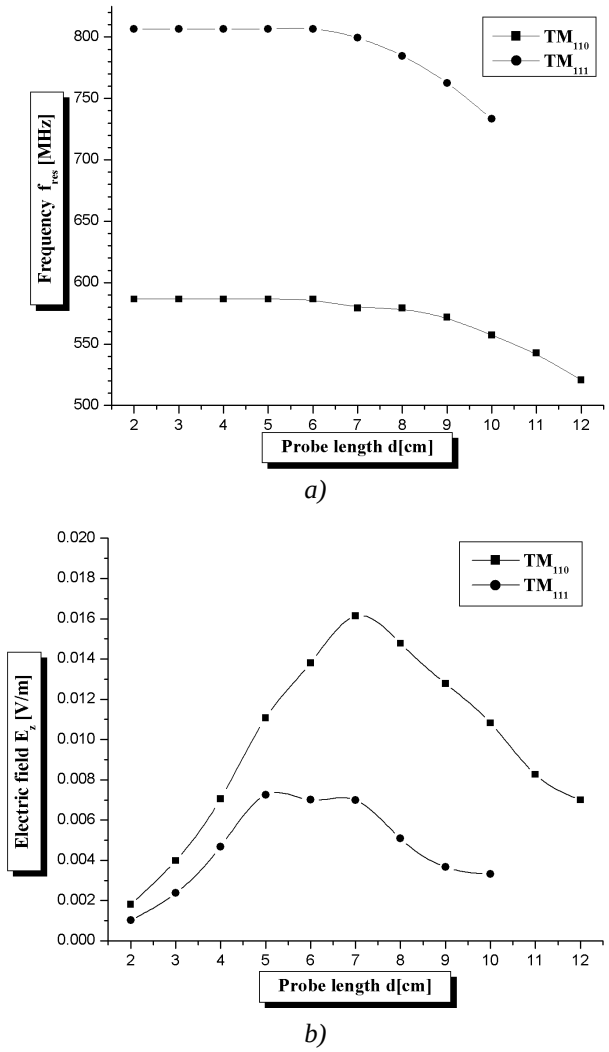

Fig. 3. *a)* Resonant frequencies, *b)* z component of electric field, versus feed probe length for TM_{110} and TM_{111} modes

As it can be seen from Fig. 3, the results of both resonant frequencies and field strength calculated by using TLM method, where a probe inside the cavity is used as an excitation, significantly depends on the probe length. Due to increasing of wire conductor length, the values of resonant frequencies shift to the lower ones. On the other hand, the strongest electric field for TM_{110} and TM_{111} is obtained for the probe length $d=7cm$ and $d=5cm$, respectively.

Further, for chosen probe length $d=5cm$ and same position of the probe ($x=a/2$,$y=b/2$), electric field distribution is investigated. By using 3D TLM*scn* software [4], *Ez* field component distribution inside the rectangular metallic cavity is analyzed for considered modes. Fig. 4 shows 3D presentation of electric field distribution, as well as corresponding presentation in *x-y* plane for TM_{110}. In similar way, field distribution for TM_{111} mode can be obtained.

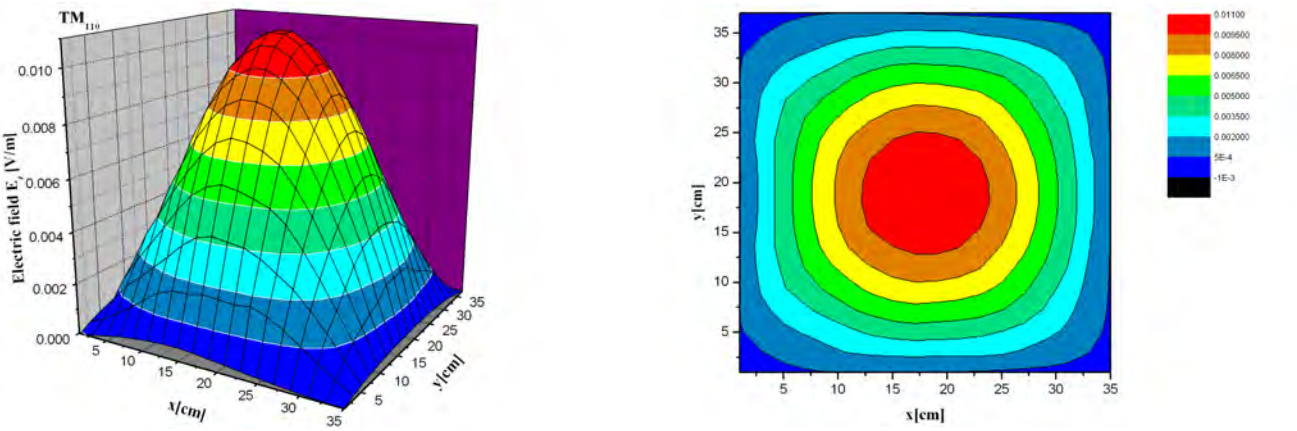

Fig.4. The field distribution of *Ez* component for TM_{110}, mode, for feed probe position (*a/2,b/2*) and probe length *d=5cm*

Also, in the case of both feed and receiving probe presence, field distribution for TM_{110} and TM_{111} modes for different probe length is analyzed. In Fig. 5 distribution of inducted current in the receiving probe $i_c(x,y)$, $x \in (1,35)$, $y \in (1,37)$ for TM_{110} mode versus feed and receiving probe length is shown.

As it can be seen from Fig. 5 values of inducted current in the receiving probe depends on the probe length. In fact, due to increasing probe length, values of the inducted current i_c, determining TM_{110} and TM_{111} modes, increase. Also, deviation of inducted current appears, that is two maximum values in corresponding direction appear instead of one. This deviation is related with the coupling of the probes.

To the aim of illustrating of obtained TLM results, Fig. 6 shows 3D presentation of inducted current distribution, as well as corresponding presentation in *x-y* plane for TM_{110} in the case of probe length of *d=6cm*. As it is shown, the shape of TM_{110} in this case is different from the case shown in Fig. 4. According to the obtained results, influence of the probe presence to establishing modes can be seen.

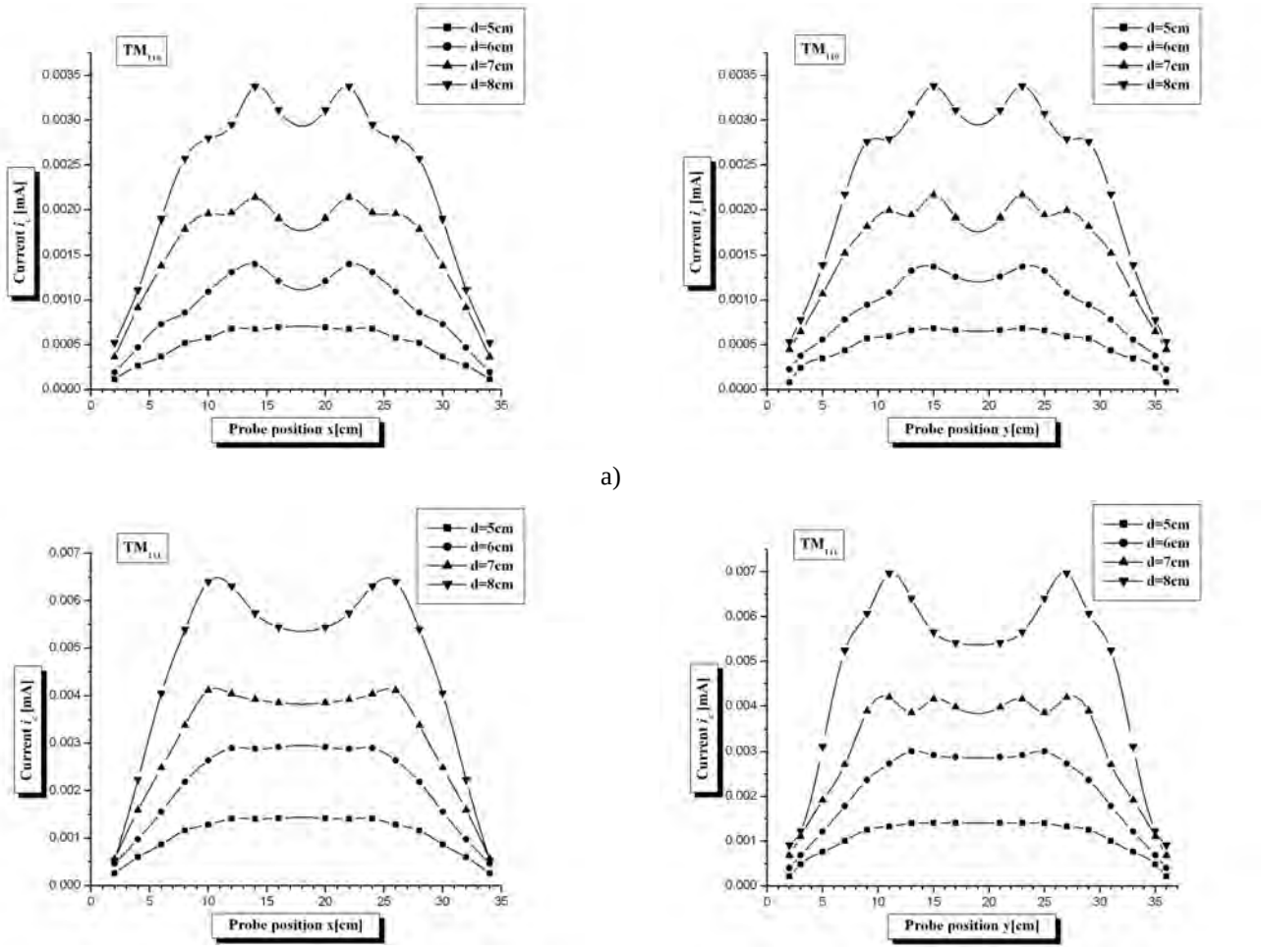

a)

b)

Fig. 5. Inducted current for a) TM_{110} mode b) TM_{111} mode

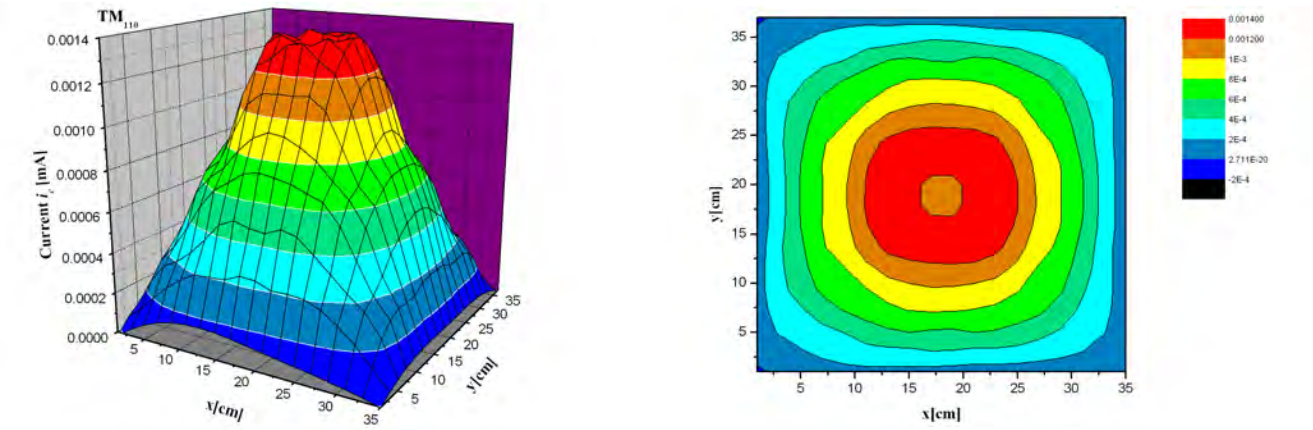

Fig. 5. Inducted current for TM_{110} mode, for probe length d=6cm

V. Conclusion

In this paper, using TLM method, for the example of the rectangular metallic cavity, influence of probe presence to the resonant frequencies and field distribution in the cavity is analyzed. Numerical results of resonant frequencies and field strength calculated by using TLM method, where the probe inside the cavity is used as an excitation, significantly depends on the probe length. The probe presence tends to shift the resonant frequencies of TM_{110} and TM_{111} modes. To the aim of illustrating TLM method application to field strength, distribution of E_z field component for probe length $d=5cm$, is presented.

Further, 3D TLM method is applied to determine field distribution in the real case, when both feed and receiving probe are used. According to the obtained results, influence of the feed and receiving probe presence to establishing modes can be seen. Due to increasing the probe length, values of inducted current i_c, determining TM_{110} and TM_{111} modes, increase. Also, deviation of inducted current is observed, that is two maximum values in corresponding direction appear instead of one. This deviation is related with the coupling of the probes.

Obtained results show possibilities of applying TLM method for analysis of field distribution inside the cavity versus probe dimensions and position.

References

[1] A. Baysar, J.L. Kuester and S. El-Ghazaly, "Theoretical and Experimental Investigations of Resonance Frequencies in a Microwave Heated Fluidized Bed Reactor", *IEEE MTT-S Digest*, pp.1573-1576, 1992.

[2] M. Mladenović, A. Marinčić, B. Milovanović, "Mode Tuning of Microwave Resonator Loaded with Losses Multilayer Dielectric", *Journal of Microwave Power and Electromagnetic Energy* 24, 3: 166-177, 1989.

[3] B. Milovanović, N. Dončov, V. Trenkić and V. Nikolić, "3-D TLM Modelling of the Circular Cylindrical Cavity Loaded by Lossy Dielectric Sample of Various Geometric Shapes", *Proc. of the Third International Workshop on TLM Modelling-Theory and Applications*, Nice, France 187-195, 1997.

[4] N. Dončov, "Microwave structures analysis using 3-D TLM method", M.Sc thesis, *Faculty of Electronic Engineering, University of Niš*, 1999.

[5] B. Milovanović, N. Dončov, A. Atanasković, "Tunnel Type Microwave Applicator Modelling using TLM Method", *Problems in Modern Applied Mathematics, A Series of Reference Books and Textbooks: Mathematics and Computers in Science and Engineering, WSES (World Scientific and Engineering Society) Press*, pp.327-332, 2000.

[6] B. Milovanović, A. Marinčić, N. Dončov, V. Marković, J. Joković, A. Atanasković "Analysis of Real Feed Probe to the Resonant Frequencies and Field Distribution in the Cylindrical Metallic Cavity Using 3-D TLM Method", *Proc. of the 6th IEEE TELSIKS 2003 Conference*, Niš, Yugoslavia, 223-228, 2003

[7] B. Milovanović, A. Marinčić, J. Joković, A. Atanasković, "Modeling of a Loaded Cylindrical Metallic Cavity with Real Excitation Using 3-D TLM Method", *Proc. of the XXXVIII ICEST 2003 Conference*, Sofia, Bulgaria 16-18. October 2003, 79-82

[8] V. Trenkić, A.J. Wlodarczyk, R.A. Scaramuzza, "Modelling of Coupling Between Transient Electromagnetic Field and Complex Wire Structures", *International Journal of Numerical Modelling: Electronic Networks, Devices and Fields*, Vol.12, No.4, pp.257-273, 1999.

[9] T.V.C.T. Chan, H. C. Reader "*Understanding Microwave Heating Cavities*", Artech House, Boston, London, 2000.

[10] C. Christopoulos, "The Transmission-Line Modelling Method", *IEE/OUP Press*, 1995.

[11] V. Trenkić, "The Development and Characterization of Advanced Nodes for TLM Method", *Ph.D. Thesis*, University of Nottingham, 1995.

[12] V. Trenkić, C. Christopoulos, "An Efficient Implementation of Wire Nodes in TLM", *Proceedings of the 2nd International Workshop on TLM Modelling-Theory and Applications*, Munich, Germany, pp.60-67, 1997.

[13] N. Dončov, "Development and Application of 3-D TLM Method for Modeling Coupling between Microwaves and Complex Wire and Dielectric Structures", *Ph.D. Thesis*, Faculty of Electronic Engineering, University of Niš, 2002.

Influence of dispersion and non-linear effects in optical fiber on the parameters of CATV system

Lidia T. Jordanova[1] and Dobri M. Dobrev[2]

***Abstract* – The object of this paper is the analysis of the influence of dispersion and several non-linear effects in the fiber optic on the parameters of the transmitted digital and analog signals. Plot for an estimation of the maximum transmitted bandwidth, i.e. the symbol rate, is given taking into account the restriction caused by the chromatic and polarization mode dispersion. Thresholds that ensure acceptable received signal quality are determined. The worsening of the signal quality is explained as a result of stimulated scattering, self-phase and cross-phase modulation, and intermodulation.**

***Keywords* – Chromatic and polarization mode dispersion; Stimulated Brillouin and Raman scattering; Self-phase and cross-phase modulation; four-wave modulation.**

I. INTRODUCTION

The trends in the CATV system development are related to the inculcation of digital and fiber-optic technologies. This allows a growth of the system traffic, additional services (Internet, e-commerce, interactive TV, VoIP), and expansion of the distribution system coverage area.

Modern CATV systems are hybrid fiber/coax (HFC) systems. The main part of such system is build up by fiber-optic and the peripheral part by coax. The parameters of the signals transmitted through the fiber-optic are worsening as a result of the dispersion and non-linear effects in the fiber and this put restrictions on the signal bandwidth (the symbol rate), the maximum allowed fiber-optic length, the optical transmitter output power etc. The design of the optical part of HFC system requires knowledge of the relations between the system and the fiber-optic parameters. The last are the main object of this work.

II. INFLUENCE OF THE DISPERSION

In the CATV systems a single mode fiber is established. This fiber has chromatic and polarization dispersion. Estimation of the chromatic dispersion is performed through the pulse spread τ_{chr} that is given by

$$\tau_{chr} = \sqrt{\tau_{out}^2 - \tau_{in}^2} = D_{chr}(\Delta\lambda)_S l\,, \qquad (1)$$

where τ_{in} and τ_{out} – optical pulse width in the input and the output of the fiber, respectively; D_{chr} – chromatic mode dispersion coefficient; $(\Delta\lambda)_S$ – spectral width of the laser; and l – the length of the fiber. The chromatic dispersion coefficient D_{chr} is defined as a spread (in picosecond) of an optical pulse with length of 1 nanometer in the fiber end that is 1 kilometer long i.e. the dimension is ps/(nm·km).

It is obvious that the laser is necessary to have narrow spectral width and the fiber to be with a small coefficient D_{chr} in order to decrease the pulse spread τ_{chr} and to increase the data rate. The relation between the coefficient D_{chr} and the optical wavelength for the frequently used in the CATV system fiber-optic is shown on Fig. 1.

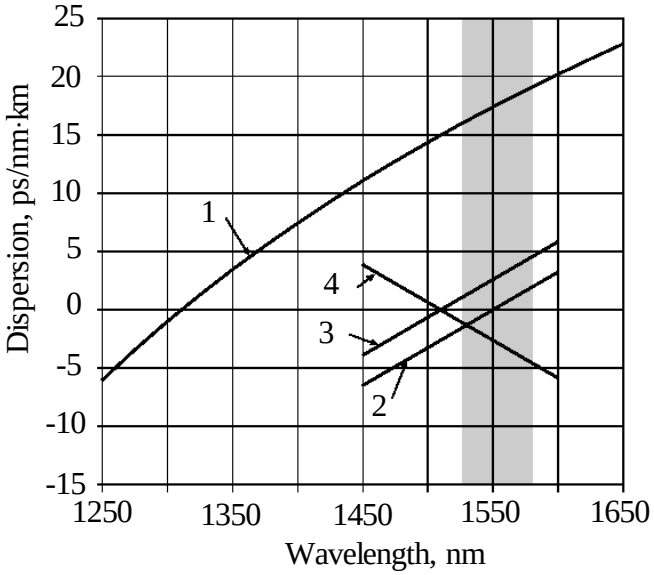

Fig.1 Influence of the optical wavelength on the coefficient D_{chr} for single mode fiber

The single mode fiber (SMF) is denoted by (1) and it is suitable for the wavelength λ about 1310 nm, where the chromatic mode dispersion coefficient D_{chr} is zero. Recently, the dispersion-shifted fiber (DSF), that is with D_{chr} = 0 for λ = 1550 nm (the curve denoted by 2), is used for 1550 nm fiber-optic network. In the present, the Dense Wavelength-Division Multiplexing (DWDM) is used and SMF fiber is

[1]Lidia T. Jordanova is with Faculty of Telecommunications of TU-Sofia, 8 "Kl. Ohridski" Blvd., 1756 Sofia, Bulgaria, e-mail: jordanova@tu-sofia.bg
[2]Dobri M. Dobrev is with Faculty of Telecommunications of TU-Sofia, 8 "Kl. Ohridski" Blvd., 1756 Sofia, Bulgaria, e-mail: dobrev@tu-sofia.bg

unsuitable because of the great non-linear effects. This imposed a development of the fiber-optic and the result is so called Non-Zero Dispersion-Shifted Fiber (NZ-DSF). The chromatic dispersion coefficient D_{chr} is zero in the outside of 1550 nm range. By (3) and (4) is denoted on Fig. 1 the relations between D_{chr} and λ for this type of fiber. The first is related to the fiber with positive and the second with negative coefficient D_{chr}. It can be seen that the coefficient D_{chr} of fiber (+D) NZ-DSF and (–D) NZ-DSF has small values for the wavelength λ about 1550 nm.

The polarization mode dispersion is caused by the property of the fiber-optic to divide the ray in two mutual perpendicular rays. The fiber is not perfectly round and it is exposed to various mechanical forces and climatic conditions. Therefore, the two rays travel in the fiber with distinct velocities and have different delays at the fiber end. The described above phenomenon is the reason for the polarization mode dispersion.

The polarization mode dispersion is estimated by the deference between the delays of the two orthogonal components of the optical pulse at the fiber end or so called polarization mode dispersion pulse spread τ_{pol}. The pulse spread τ_{pol} is determined by the following expression:

$$\tau_{pol} = \sqrt{\tau_{out}^2 - \tau_{in}^2} = D_{pol}\sqrt{l}\ , \qquad (2)$$

where by D_{pol} is denoted the polarization dispersion coefficient of the fiber in ps/√km. The typical values of D_{pol} for standard single mode fiber (SMF) varies in the interval 0,01...0,8 ps/√km and for the dispersion-shifted fiber (DSF) D_{pol} = 0,2...1,6 ps/√km.

III. LIMITATION DUE TO THE DISPERSION

In consequence of the chromatic mode dispersion, the signal spectral component has different delays at the fiber end. This result in decreasing of demodulated signal level P_{RF} at the optical receiver output by

$$P_{RF}/P_{RF\max} = \cos\left(\frac{\pi D_{chr}\, l}{c}\lambda^2 f_{RF}\right), \qquad (3)$$

where λ is wavelength of the optical carrier, c – the velocity of lights in vacuum and f_{RF} – the frequency of the *RF* signal. If analog signals are transmitted then the acceptable losses due to chromatic mode dispersion are in order of 1 to 3 dB. It is obvious that the chromatic mode dispersion restricts the signal bandwidth and the length of the fiber.

According to the equation (3) on Fig. 2 are shown relations between the fiber length and the maximum frequency of the modulating RF signal. These plots can be used in the design of analog optical link intended for 1550 nm range and realized by standard single mode fiber (S-SMF) or Non-Zero Dispersion-Shifted Fiber (NZ-DSF) with D_{chr} = 3,5 ps/nm·km.

The bandwidth B_{RF} (in GHz) of optical CATV system with limitation due to chromatic dispersion can be roughly estimated by

$$B_{RF} \le 500(\Delta\lambda)_S/(D_{chr}\, l)\ . \qquad (4)$$

In the digital optical link, the chromatic mode dispersion results in pulse spread, hence intersymbol interference is occurred and the probability of error is increasing. The "eye-diagram" is used for an estimation of the intersymbol interference and bit error rate (BER) in On-off keying (OOK) system.

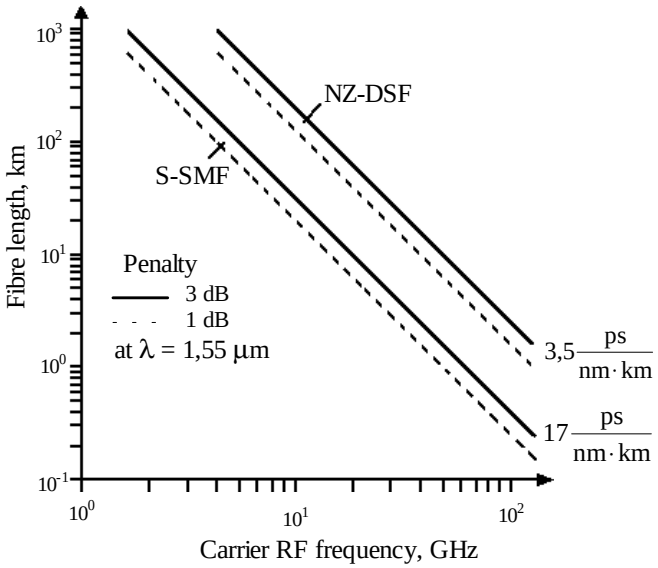

Fig. 2 Plots used for a design of analog optical link build by S-SMF and NZ-DSF

The acceptable distortions are these that correspond to the shrinkage of "eye-diagram" by 1 dB (as an exception 2 dB). This is indirectly estimated by the parameter p_{chr} that depends on the symbol bit rate (BR), the optical wavelength λ, the velocity of light in vacuum c, the length of the fiber l and the dispersion coefficient D_{chr}

$$p_{chr} = \frac{1}{\pi} BR^2 D_{chr}\, l\, \frac{\lambda^2}{c}. \qquad (5)$$

It can be shown that the shrinkage of eye-diagram by 1 dB is achieved when the value of p_{chr} is equal to 0,252 and shrinkage by 2 dB for p_{chr} = 0,321. As plots shown above can be drawn by an equation (5) and the design of digital optical link could be performed by them.

The polarization mode dispersion restricts the maximum length of the fiber and the data rate. In that case, the main criterion for acceptable signal distortions is also the shrinkage of the "eye-diagram" by 1 dB. In order to confirm this requirement the pulse spread due to polarization mode dispersion τ_{pol} must fulfil the condition $\tau_{pol} \le T/10$, where T ($T = 1/BR$) is the symbol repetition time. Taking into account

this requirement and equation (2) the length of the fiber can be given by

$$l \le \frac{1}{100\,BR^2 D_{pol}^2}\,. \qquad (6)$$

If the fiber length is given then the maximum data rate can be estimated by the expression (6).

IV. LIMITATIONS ORIGINATED FROM THE STIMULATED SCATTERING

According to the represented principles we can conclude that for a transmission of wideband signals (with high data rates) on a long distance it is necessary to employ lasers with narrow spectral line and great output power. Exactly, this is the objective of the research work in the recent years. At present, lasers on the market transmit optical signals with very narrow band about 10 MHz and at that the power is over 10 mW. The reduction of the optical signal spectrum and the increasing of the power result in several nonlinear effects in the fiber. Especially, that is the stimulated Raman scattering (SRS) and the stimulated Brillouin scattering (SBS). These effects must be taking into account when the design of optical CATV system is performed.

When the power is over a given threshold the SRS scattering is happened and in the fiber are excited undesirable molecular oscillations. These oscillations interact with the optical field and as a result a part of the signal is reflected and the spectral line shifts to the longer wavelength. In the WDM systems, this result in transfer of signal power from short-wave to long-wave channels.

The stimulated Raman scattering (SRS) can be described by so called SRS gain g_R that depends on the frequency shift Δf toward the channel central frequency. When the shift Δf is increased then the coefficient g_R grows and reaches its maximum value of $g_R \approx 7.10^{-14}$ m/W for $\Delta f \approx 13{,}2$ THz (respectively $\Delta\lambda = 100$ nm) after that it decreases. In other words, if the SRS scattering is occurred then the maximum optical power is transferred in the channel with a central frequency that is 13,2 THz lower than the desirable channel and the wavelength is 100 nm greater, respectively. The stimulated Raman scattering can be observed in a very wide frequency band Δf_R, to 40 THz, hence it makes problems in WDM systems where the channel spacing is 100 GHz. This effect has no influence over the single channel optical systems.

In a single channel the power scattering owing to the nonlinear effect described above result in a decreasing of the received optical power and a growth of the noise floor. In other words, the signal-to-noise ratio in the optical receiver output decreases; consequently, the received signal quality is made worse. The maximum power that can be fed to the fiber with absence of unacceptable signal quality worsening, owing to SRS scattering, is restricted by the threshold power $P_{Th}(SRS)$. This threshold is selected in such a way that the power loss in a single channel to be under 3 dB and it can be determined by following expression:

$$P_{Th}(SRS) \approx 16\,S_{eff} \,/\, g_R\, l_{eff}\,, \qquad (7)$$

where S_{eff} is effective area of the fiber core section and l_{eff} is the fiber length.

Usually in the fiber optic specifications is included the mode field diameter (MFD) and then $S_{eff} = \pi(MFD/2)^2$. The length l_{eff} is given by

$$l_{eff} = \frac{1}{\alpha^*}\left(1 - e^{-\alpha^* l}\right), \qquad (8)$$

where l is the actual fiber length in km and α^* is attenuation constant in 1/km. In order to transform the dimension of α, its value in dB/km is divided by the term $10\lg e$ ($e = 2{,}718$).

The typical values of the SRS threshold power $P_{Th}(SRS)$ are close to 1 W (30 dBm), but with N amplifiers included in the optical link this threshold decreases N times.

The stimulated Brillouin scattering (SBS) is occurred when the power fed to the fiber approach a specifically threshold. At that threshold power, acoustic vibrations are excited in the fiber. Because of the interaction between the light and the acoustic wave, the part of the transmitted power is reflected backward to the laser. This results in a growth of the noise floor and decreasing of the received signal level. The SBS scattering is observed in a narrow band Δf_B ($\Delta f_B < 100$ MHz) and it makes problems only in one channel.

This scattering is estimated by the SBS gain g_B that varies in frequency band Δf_B as the SRS gain g_R. The maximum scattering is observed at frequency that has a small shift upward with respect to the channel frequency. For example, at optical frequency band about 1550 nm, respectively 193 THz, the maximum gain g_B is shifted 10 GHz upward to the channel frequency and has a value approximately 5.10^{-11}, m/W.

The threshold power $P_{Th}(SBS)$ in that case is given by

$$P_{Th}(SBS) \approx 21\,S_{eff} \,/\, g_B\, l_{eff}\,. \qquad (9)$$

That is significantly lower (about three orders) than the Raman threshold power.

V. INFLUENCE OF OTHER NONLINEAR EFFECTS

In addition to the described above, in the fiber can be observed the following nonlinear effects: self-phase and cross-phase modulation and four-wave modulation. These are owing to the relation between the index of refraction n of the fiber core and the launch power P (so called Kerr effect) that can be represented by

$$n = n_1 + n_1^* P / S_{eff}\,, \qquad (10)$$

where n_1 is the index of refraction at low power levels and n_1^* - nonlinear index of refraction (for silicon its value is about $3{,}2\cdot10^{-20}$ m^2/W).

Self-phase modulation (SPM) is owing to the fluctuations of the index of refraction n that decreases the phase velocity

of the pulse rise edge and increases the phase velocity of the pulse fall edge. These phase variations cause a parasitic frequency modulation (chirp) that spread the pulse spectrum. At the rise edge, the spread is toward the longer wave ("red" shift) and at the fall edge – the shorter wave ("blue" shift). The value of the phase shift for SPM depends on the launch power P, the effective length l_{eff} and the nonlinear propagation coefficient γ and this is given by

$$\Phi(SPM) = \gamma P l_{eff}\,, \tag{11}$$

where $\gamma = 2\pi n_1^*/\lambda S_{eff}$ ($n_1^* = 3{,}2\cdot10^{-20}$ m^2/W). In order to avoid unacceptable distortions of the transmitted NRZ signals the maximum phase shift Φ(SPM) is restricted to $\pi/2$.

The cross-phase modulation (XPM) is as the SPM modulation but in that case the phase variation in a given channel depends on the optical power carried by the other channels. Hence, this nonlinear effect is typical for WDM systems. The estimation of the phase shift due to the XPM modulation in a single channel is performed by the following expression:

$$\Phi_i(XPM) = \gamma l_{eff}\left(P_i + 2\sum_{i\neq j} P_j\right), \tag{12}$$

where P_i is the launch power in the channel and by P_j is denoted the power in the i^{th} channel. Here, the requirement $\Phi(\text{XPM}) \le \pi/2$ is also valid.

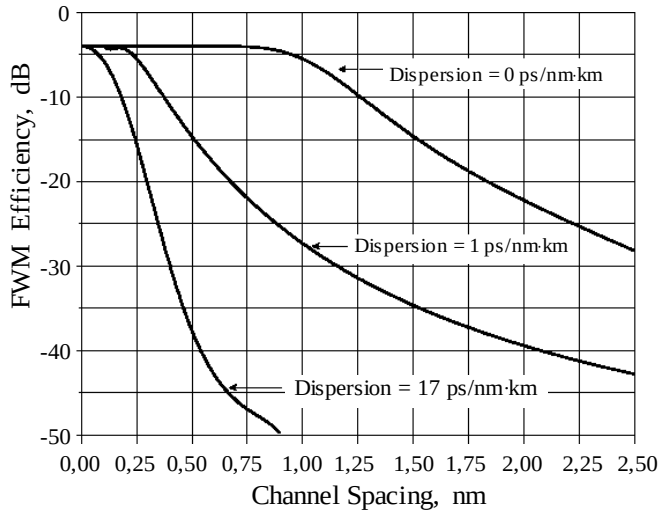

Fig. 3 A relation of the FWM efficiency from the dispersion and the channel spacing

The four wave mixing (FWM) is inherent to the fiber-optic systems that use the technology *DWDM*. This nonlinear effect arises due to the interaction between the signals from three channels with wavelength λ_i, λ_j и λ_k that result in intermodulation component $\lambda_F = \lambda_i + \lambda_j - \lambda_k$. For M-channel system the indexes *i*, *j* and *k* vary from 1 to M and the number of the intermodulation components rises by law $(M^3 - M^2)/2$. Part of these components fall in the main channel bandwidth and can significantly make worse the signals. The FWM modulation is obtained as the composite triple beat (CTB) distortion in the CATV systems.

The four-wave modulation efficiency η depends on the phase relations between the different signals and it has a maximum value when the signals are in-phase. The dispersion in the fiber results in a difference between the group velocity of the transmitted signals and due to the efficiency η decreases. Furthermore, the efficiency depends on the channel spacing, when the channel spacing increases then the efficiency decreases. These relations are shown on Fig. 3 and they are plot in accordance to expressions given in [3].

VI. CONCLUSIONS

The represented results allow the correct selection of the fiber. This is performed when the following parameters are given: the fiber length; the signal bandwidth or the data rate; the output signal-to-noise ratio or BER and the acceptable levels of intermodulation components.

REFERENCES

[1] G. P. Agrawal, Nonlinear Fiber Optics. Third edition, Academic Press Limited, 2001.

[2] E. Iannone, et al., Nonlinear Optical Communication Networks, John Wiley & Sons, Inc., 1998.

[3] T. Baldwin, St. Durand, IF Fiber Selection Criteria EVLA Memorandum No. 32, Version 7, 2001, evlamemo32.pdf

[4] J. A. Buck, Fundamentals of Optical Fibers, John Wiely & Sons, Inc., 1995.

[5] F. Forghieri, R. W. Tkach, and A. R. Chraplyvy, "Fiber Nonlinearities and Their Impact on Transmission Systems" in Optical Fiber Telecommunications IIIA, Academic Press, 1997.

[6] M. Shtaif, "Analytical description of cross-phase modulation in dispersive optical fibers," Optics Letters, vol.23, no.15, pp.1191-1193, August 1998.

[7] Jong-Hyung Lee, Analysis and Characterization of Fiber Nonlinearities with Deterministic and Stochastic Signal Sources. Dissertation for the degree of Doctor of Philosophy in Electrical Engineering, Blacksburg, Virginia, February, 2000.

New Approach to Applying the Transistor Neural Models within Microwave Circuit Simulators

Zlatica Marinković, Vera Marković

Abstract- **This paper deals with the implementation of microwave transistor signal and noise neural models into standard microwave circuit simulators. Models based on neural networks were proposed earlier and presented in the previous authors' papers. Models were implemented as user-defined library elements and are valid for the whole operating range of transistor biases.**

Keywords - **Neural network, microwave transistor, noise parameters, S-parameters, microwave circuit simulator**

I. INTRODUCTION

The development of reliable small-signal and noise device models is very important task required for the design of microwave circuits, especially for the wireless applications, [1].

A drawback of most existing empirical or physical models is that they are limited to one bias point. Authors of this paper have been proposed new transistor models valid in the whole operating range of biases and frequencies, [2]-[5]. Neural networks have been chosen as a modeling tool because they have capability to extract very complex relationships between two sets of data, which is very interesting for problems not fully mathematically described, [6]. They have found application in many areas. Recently, an interest in neural networks has arisen in the microwave area as well [7].

This papers deals with implementation of the proposed transistor models into standard microwave simulators.

II. MULTILAYER PERCEPTRON (MLP) NEURAL NETWORK

MLP neural network [6] is most often used neural network structure for modeling of microwave devices. MLP network consists of an input layer, output layer and a number (usually one or two) of so-called hidden layers. Each neuron from one layer is connected to all neurons from the next layer. Neurons are characterized by their activation functions. The connections between neurons are characterized by weighting factors. Input vectors are presented to the input layer and fed through the network that then yields the output vector. The *l*-th layer output is:

$$\mathbf{Y}_l = F(\mathbf{W}_l \mathbf{Y}_{l-1} + \mathbf{B}_l) \quad (1)$$

where $\mathbf{Y}_l$ and $\mathbf{Y}_{l-1}$ are outputs of *l*-th and (*l*-1)-th layer, respectively, $\mathbf{W}_l$ is weight matrix between (*l-1)*-th and *l*-th layer and $\mathbf{B}_l$ is bias matrix between (*l-1)*-th and *l*-th layer. Function *F* is an activation function of each neuron and, in our case, is linear for input and output layer and sigmoid for hidden layers: $F(u) = 1/(1+e^{-u})$.

Network training is an iterative process of adjusting of network parameters (activation function thresholds and connection weights) in order to minimize the difference between a network response and reference values. Here, for training purposes, *Levenberg-Marquardt* algorithm (a modification of "backpropagation" algorithm) is used.

Once trained, neural network is expected to generate correct responses for all inputs even they are presented to the network during the training or not (generalization ability).

III. TRANSISTOR SIGNAL AND NOISE CHARACTERISTICS

A microwave transistors is usually represented as a two-port circuit characterized by its scattering ([*S*]) matrix, that define so-called transistor signal performance, and that contains four complex scattering parameters, S_{ij}, *i,j* = 1,2 described by their magnitudes and phases. It is common that the manufacturers provide S-parameters' data at certain number of frequencies from the specified frequency range, where these data are related to only one or, infrequently, to a few bias conditions. In addition to the signal performance, transistor noise performance is of a great importance for the low noise applications. Any two-port noisy component can be characterized by a noise figure *F*, which is a measure of the degradation of the signal-to-noise ratio between input and output of the component, [8], and can be expressed as

$$F = F_{\min} + \frac{4R_n \left|\Gamma_g - \Gamma_{opt}\right|^2}{Z_0 \left(1 - \left|\Gamma_g\right|^2\right) \left|1 + \Gamma_{opt}\right|^2}, \quad (2)$$

where Z_0 is normalizing impedance. In (1), minimum noise figure $F_{\min}$, equivalent noise resistance R_n, and magnitude and angle of the optimum reflection coefficient Γ_{opt} represent a set of four noise parameters that describe inherent behavior of the component and their frequency dependences are required for low-noise circuit design.

IV. MICROWAVE LOW-NOISE TRANSISTOR MODELING USING NEURAL NETWORKS

The basic idea of neural network application in microwave transistor modeling is developing models that can predict transistor signal and noise performance accurately in a wide frequency range for all bias points from the operating range.

Authors are with the Faculty of Electronic Engineering, Beogradska 14, 18 000 Niš, SERBIA AND MONTENEGRO
e-mail: [zlatica,vera]@elfak.ni.ac.yu

MLP networks were applied with the aim to model the HEMT transistor S and noise parameters dependence on frequency and bias conditions (*dc* drain-to-source voltage and *dc* drain-to-source current), as it is presented in Figs 1 and 2, respectively, [3].

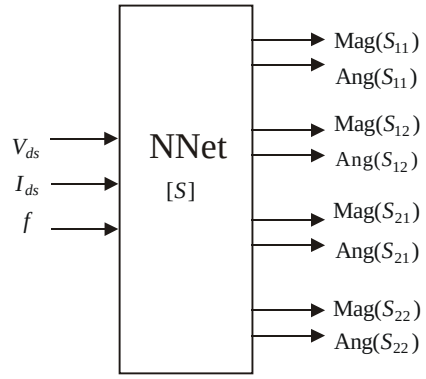

Fig. 1. *Neural model for S- parameters dependence on bias conditions and frequency*

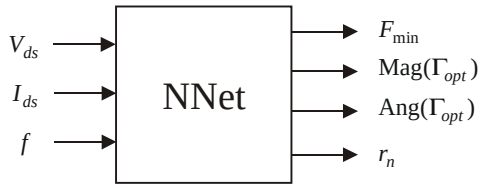

Fig. 2. *Neural model for noise parameters dependence on bias conditions and frequency*

Both neural networks have three neurons in the input layer corresponding to

- dc drain-to-source voltage V_{ds} ,
- dc drain-to-source current I_{ds} and
- frequency *f*.

The output layer of a network that models S-parameters has eight neurons corresponding to magnitudes and phases of all four scattering parameters.

The output layer of a network which models noise parameters consists of four neurons corresponding to:

- minimum noise figure,
- magnitude of optimum reflection coefficient,
- angle of optimum reflection coefficient and
- normalized equivalent noise resistance (50 Ω normalizing impedance).

The number of hidden neurons can be one or two, depending on the number of training data.

The proposed models are able to predict signal and noise parameters for any bias point including those not presented in the training process, without additional computation or change in the network structure.

Further, with the aim to increase the accuracy of modeling additionally, some improvements in model structure have been introduced, as it has been reported in [2]-[5].

V. New Approach to Neural Model Implementation into a Standard Circuit Simulator

Practical using of once developed neural models for transistor signal and noise parameters requires their implementation in some of standard packages for analyzing, optimization and design of microwave circuits, like Libra [9], ADS [10], etc.

One possible way is to represent a low-noise transistor within the circuit simulator as a two-port circuit with assigned so-called *s2p* file. An *s2p* file contains table values of S-parameters in the operating frequency range and the noise parameters in a number of frequency points as well. This approach is shown in Fig 3, and described in detail in [11].

The procedure is as following: *S*- and noise parameter data are generated using transistor neural models, and an *s2p* file is formed according to the specified syntax. It can be done within the environment where neural models were trained (e.g. MATLAB environment).

Since one s2p file corresponds to only one specified bias point, it is necessary to go back to "training environment" and generate a new *s2p* file for any other bias point. This is the main drawback of this procedure.

Here, a new way of neural network implementation is proposed, Fig 4, where the prediction of transistor signal and noise parameters is completely performed in the microwave simulator. Namely, instead of generating *s2p* files, the sets of equations are generated in the "training environment". Actually, these equations are mathematical representation of the developed neural models, according to Eqn (1).

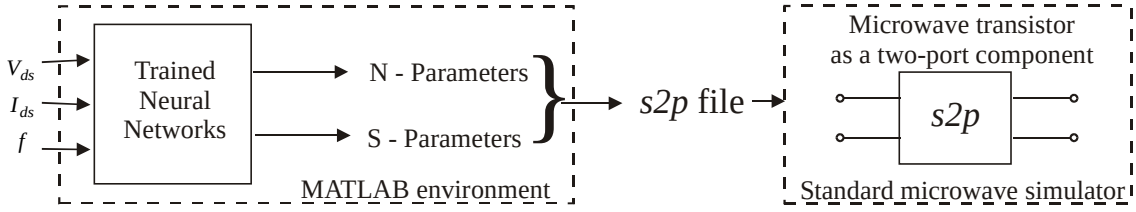

Figure 3. Implementation of signal and noise neural models by *s2p* file generating

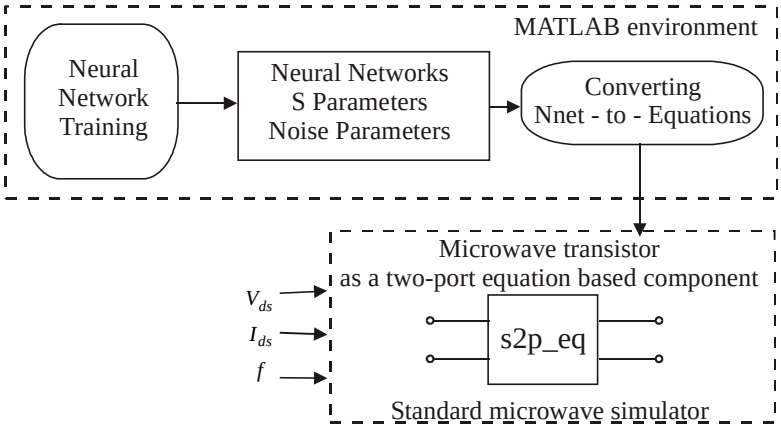

Figure 4. Implementation of signal and noise neural models by equation generating

.

Further, these equations are used in the VAR blocks within the microwave simulators. The outputs of these VAR blocks, magnitudes and phases of S-parameters and four noise parameters, are assigned to specified, so-called S2P_EQN, item. This item represents a two-port component whose S-parameters and noise parameters are equation based. In that way, signal and noise characteristics, for any operating bias point and any frequency from the operating range can be obtained within the simulator, i.e. model can be used apart from the "training environment".

VI. Modeling Example

The proposed procedure can be illustrated by an example of implementation of transistor neural models in ADS, the standard software tool widely used for microwave design. A *Hewlett Packard* microwave pHEMT transistor ATF35143 has been modeled.

First, appropriate signal and noise neural models for this transistor have been developed, [3]. The models were trained within MATLAB program package environment using the data from the manufacturer's catalogue over the (0.5-10) GHz frequency range and for different bias conditions. The both of developed neural models, sp_10_10 model for S-parameters and bf_10_10 model for noise parameters, have ten neurons in each of two hidden layers. A procedure for generating mathematical equations corresponding to neural models has been developed within MATLAB environment as well. Using this procedure, models, sp_10_10 and bf_10_10 were converted to blocks of equations that have been further used within the appropriate VAR blocks in the simulator.

In the ADS simulator, the transistor is defined as a new user-defined library element, ATF35143_bf_sp, Fig. 5. Schematic design of the library element structure is shown in Fig. 6.

The neural model incorporated within ADS package enables fast and efficient simulation of *S* and noise parameters for different bias conditions, for instance for optimization purposes.

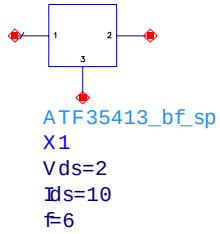

Fig. 5. Transistor model as user defined library element

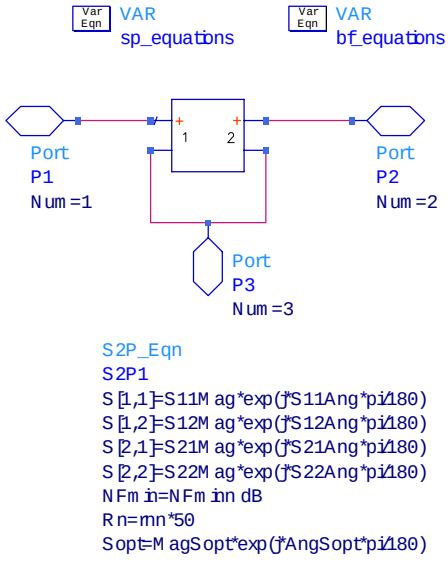

Fig. 6. Transistor model - Schematic Design

For illustration, the minimum noise figure characteristics for the considered pHEMT for two bias points are presented in Fig.7. It can be seen that predicted data (solid line) are very close to referent data not only for bias point used for network training (crosses) but also for bias point not used for network training (squares). Further, the results of simulation of the parameter S_{21}, minimum noise figure, and optimum reflection coefficient for several different biases conditions are presented in Fig. 8 (a), (b) and (c), respectively.

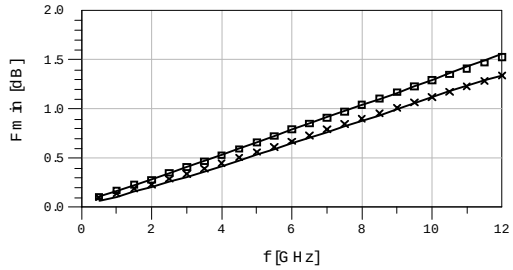

Fig. 7 Prediction of the minimum noise figure by the neural model for two bias points, comparing with the referent data

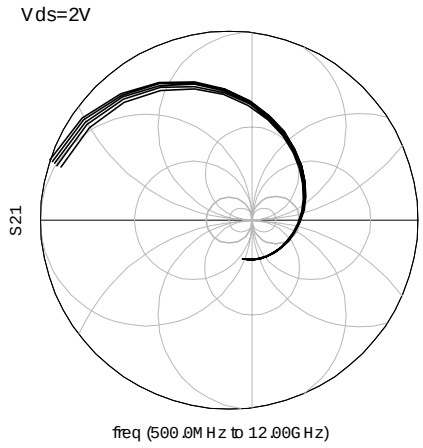

(a) Parameter S_{21} for V_{ds} =2V and I_{ds} =(10-40) mA

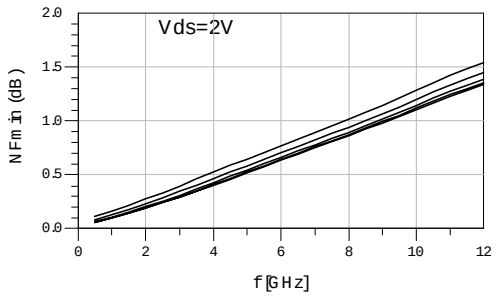

(b) Minimum noise figure for V_{ds} =2V and I_{ds} =(10-40) mA

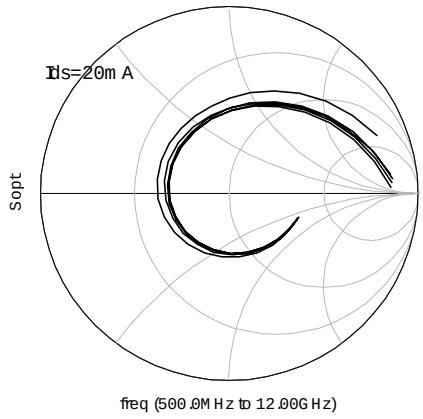

(c) Γ_{opt} for I_{ds} =20mA and V_{ds} =(2-4) V

Fig. 8 Prediction of some transistor parameters for different bias points

VII. CONCLUSION

Neural networks can be successfully used for microwave low-noise transistor modeling. Once trained neural models can predict transistor *S* - and noise parameters in the whole operating range without changes in model structure. This is their main advantage comparing to most of the existing transistor signal and noise models, which are valid for only one bias condition. Namely, the extraction of elements of transistor equivalent circuit and/or model parameters, that is necessary in most of the standard transistor models, is avoided, i.e. on-line optimization is shifted in off-line training of neural networks.

The developed models can be implemented in microwave simulator in two ways. The first one is forming an *s2p* file in the training environment and its assigning to a two-port circuit representing the transistor. The disadvantage of this approach is a need for going back from the simulator to the training environment for each bias point not used before, in order to form *s2p* file. The approach suggested here is converting neural models to corresponding mathematical expressions and their direct implementation into the simulator. In this way, a completely new library element for transistors that include bias conditions can be defined. All computations for any new bias point will be done within the simulator, which enables very efficient further analysis of circuits containing this active device.

ACKNOWLEDGEMENT

This work was supported in part by Ministry of Science, Technologies and Development of Republic of Serbia, under project 1351: "*The development of physically based noise models for micro- and millimeter wave range*".

REFERENCES

[1] J. M. Golio, *Microwave MESFETs & HEMTs*, Artech House, Ma, U.S.A., 1991.

[2] V. Marković, Z. Marinković, "Neural Models of Microwave Transistor Noise Parameters Based on Bias Conditions and S-parameters ", *Proceedings of the Conference TELSIKS 2001*, Nis, September 2001, pp. 683-686.

[3] B. Milovanović, V. Marković, Z. Marinković, Z. Stanković, "Microwave circuits modeling using neural networks - overview of the results achieved at the Faculty of Electronic Engineering in Niš" - invited paper, *Neurel 2002*, Belgrade, September 2002, pp. 177-184

[4] V. Marković, Z. Marinković, "Signal and Noise Neural Models of pHEMTs", *NEUREL2002*, Belgrade, 2002, pp. 177-184

[5] V. Marković, Z. Marinković, B. Milovanović, "New Neural Models of Microwave Transistor Noise Parameters Based on Bias Conditions", *23rd Conference on Microelectronics - MIEL 2002*, May 2002, pp.405-408.

[6] S. Haykin, *Neural networks*, New York, IEEE, 1994.

[7] Q. J. Zhang, K. C. Gupta, *Neural Networks for RF and Microwave Design*, Artech House, 2000

[8] D. Pozar, *Microwave Engineering*, J. Wiley&Sons, Inc.,1998.

[9] Touchstone and Libra Users Manual, EEsof, Inc. 1990.

[10] "Advanced Design Systems-version 1.5", Agilent EEsof EDA, 2000

[11] V. Marković, Z. Marinković "Implementation of Microwave Transistor Neural Noise Models into Standard Microwave Simulators", *ICEST 2003*, October 2003, Sofia, Bulgaria, pp.83-86.

Accuracy of a Processing Algorithm, Using the Space Correlation of Satellite Movement in GPS

Marin S. Marinov[1] and Georgi V. Stanchev[2]

Abstract– **This paper discuses using of Kalman filtering to improve the accuracy of user locating when GPS is used. The state and observation equation are derived. The improvement of the accuracy by proposed algorithm is more than 80 percent. An analysis of model parameter influence is made.**

Keywords– **GPS, Kalman filtering, GPS accuracy.**

I. INTRODUCTION

In the present days the use of Global Positioning System (GPS) increases in daily life and often the locating of slow moving objects is needed. In this case the alteration of distances between the user and satellites depends on satellites orbital movement, when short time period is considered. The satellites transmit ephemeris data and some of them are related to the orbital parameters. Thus the user can calculate coordinates of satellites not only at the current but also at future moments in Earth-Centered-Earth-Fixed (ECEF) coordinate system [4]. This information can be used in the processing algorithm in order to increase the accuracy of the locating.

The locating of slow moving users through use of Kalman filtering is considered in this paper. The measurement equation and state equation of Kalman filter are derived.

II. PROCESSING ALGORITHM

Pseudoranges are measured in real GPS receivers and then they are used to calculate user coordinates. The measurements are always accompanied with errors. When the statistical distribution of these errors is not known the method of Least Mean Squares appears to be useful to determine the user location [2], [3].

The distance errors in GPS are supposed to possess Gaussian distribution with zero mean value and variance σ_D^2 [4]. The coordinate errors hold the same distribution as the distance errors. Kalman filter is a very good tool for parameter estimation in presence of additive errors with normal distribution [1]. An observation and a state equation have to be determined before Kalman filtering can be used.

The distance between the ECEF coordinate system origin and the n^{th} satellite at the moment $k\Delta t$ is given by:

$$R_n(k) = \sqrt{\mathbf{C}_n(k)\mathbf{C}_n^T(k)}\,, \tag{1}$$

where:

$$\mathbf{C}_n(k) = [x_n(k), \quad y_n(k), \quad z_n(k)] \tag{2}$$

is a vector of satellite coordinates; Δt is the time step of the measurement.

The distance from user to a given satellite is:

$$D_n(k) = \sqrt{[\mathbf{C}_n(k) - \mathbf{C}_c(k)][\mathbf{C}_n(k) - \mathbf{C}_c(k)]^T}\,, \tag{3}$$

where:

$$\mathbf{C}_c(k) = \mathbf{C}_0(k) + \mathbf{C}_\delta(k) \tag{4}$$

is a vector of calculated user coordinates;

$$\mathbf{C}_0(k) = [x_0(k), \quad y_0(k), \quad z_0(k)] \tag{5}$$

is a vector of true user coordinates;

$$\mathbf{C}_\delta(k) = [\delta_x(k), \quad \delta_y(k), \quad \delta_z(k)] \tag{6}$$

is a vector of the errors in the calculated user coordinates.

Both sides of Eq.(3) are raised to the second power then as a result the root in Eq.(3) disappears. However this leads to appearance of the second power of coordinate errors. The difference of the distance squares between the user and two satellites is obtained in order to avoid the squares of errors:

$$\begin{aligned}\Delta_{nm}(k) &= D_n^2(k) - D_m^2(k) = \\ &= R_n^2(k) - R_m^2(k) + 2[\mathbf{C}_m(k) - \mathbf{C}_n(k)]\mathbf{C}_c^T(k)\end{aligned}\,. \tag{7}$$

The distances $R_n(k)$ and $R_m(k)$ can be derived from ephemeris data, i.e. they are known and can be moved on the left side in Eq.(7):

$$\begin{aligned}E_{nm}(k) &= \Delta_{nm}(k) - [R_n^2(k) - R_m^2(k)] = \\ &= 2[\mathbf{C}_m(k) - \mathbf{C}_n(k)][\mathbf{C}_0(k) + \mathbf{C}_\delta(k)]^T\end{aligned}\,. \tag{8}$$

The coordinates that should be estimated are three and consequently three observations like this described by Eq.(8) have to be used. Every GPS receiver uses constellation of four satellites at least and as a result there is no problem to obtain these observations. The matrix form of the observation equations in Kalman filtering can be obtained by Eq.(8):

$$\mathbf{E}(k) = \mathbf{H}(k)\boldsymbol{\xi}(k) + \mathbf{v}(k) = [E_{12}(k), \quad E_{34}(k), \quad E_{13}(k)]^T\,, \tag{9}$$

where: $\mathbf{H}(k) = 2[\mathbf{C}_D(k), \quad \mathbf{0}]$; $\mathbf{0}$ is zero matrix 3 by 3 dimensions; $\boldsymbol{\xi}(k) = [\mathbf{C}_0(k), \quad \dot{\mathbf{C}}_0(k)]^T$ is the state vector;

[1]Marin S. Marinov, PhD is with the Aviation Faculty, National Military University, 5856 Dolna Mitropolia, Bulgaria, e-mail: mmarinov2000@yahoo.com.

[2]Georgi V. Stanchev, PhD is with the Aviation Faculty, National Military University, 5856 Dolna Mitropolia, Bulgaria, e-mail: gstanchev@af-acad.bg.

$$\mathbf{C}_D(k) = \left[\mathbf{C}_2(k) - \mathbf{C}_1(k), \mathbf{C}_4(k) - \mathbf{C}_3(k), \mathbf{C}_3(k) - \mathbf{C}_1(k)\right]^T;$$

$$\mathbf{V}_v(k) = 4\sigma_D^2 \begin{bmatrix} D_1^2(k) + D_2^2(k) & 0 & D_1^2(k) \\ 0 & D_3^2(k) + D_4^2(k) & -D_3^2(k) \\ D_1^2(k) & -D_3^2(k) & D_1^2(k) + D_3^2(k) \end{bmatrix}$$

is the covariance matrix of the measurement error; σ_D^2 is the variance of distance errors.

The error elements on the right side of Eq.(9) are expressed by the distance errors:

$$\delta_{nm} = 2D_{0n}\delta_n - 2D_{0m}\delta_m, \quad (10)$$

where $D_{0n}(k)$ is the true distance to the n^{th} satellite and $\delta_{Dn}(k)$ is the measurement errors.

A model for user motion is needed to use Kalman filtering. The following model is useful for slow moving objects [5]:

$$\frac{d\xi(t)}{dt} = \mathbf{\Phi}\left[\mathbf{C}_0^T(t), \quad \dot{\mathbf{C}}_0^T(t)\right]^T + \mathbf{w}(t), \quad (11)$$

where: $\mathbf{w}(t) = \left[0,\ 0,\ 0,\ w_x(t),\ w_y(t),\ w_z(t)\right]$ is normally distributed noise component; $\mathbf{\Phi} = \begin{bmatrix} \mathbf{I} & \mathbf{0} \\ \mathbf{0} & -\alpha\mathbf{I} \end{bmatrix}$ is the transition matrix; α is coefficient reciprocal to the correlation time of the velocities in each coordinate; $\mathbf{I}$ is an identity matrix with 3 by 3 dimensions.

The state equation of Kalman filter is obtained directly from Eq.(11):

$$\xi(k) = \mathbf{F}\xi(k-1) + \mathbf{w}(k), \quad (12)$$

where: $\mathbf{F} = \begin{bmatrix} \mathbf{I} & \left(1 - e^{-\alpha T}\right)\alpha^{-1}\mathbf{I} \\ \mathbf{0} & e^{-\alpha T}\mathbf{I} \end{bmatrix}$ is the state transition matrix; T is the sampling time interval; $\mathbf{V}_w = \alpha T\sigma_v^2 \begin{bmatrix} \frac{2}{3}T^2\mathbf{I} & T\mathbf{I} \\ T\mathbf{I} & 2\mathbf{I} \end{bmatrix}$ is the covariance matrix of normally distributed noise component in Eq.(12); σ_v is standard deviation (STD) of the user velocity that is assumed to be equal for each of the coordinates.

The state vector estimate is given by equation:

$$\hat{\xi}(k) = \tilde{\xi}(k) + \mathbf{K}(k)\left[\mathbf{E}(k) - \mathbf{H}(k)\tilde{\xi}(k)\right]. \quad (13)$$

The Kalman gain $\mathbf{K}(k)$ is described by:

$$\mathbf{K}(k) = \tilde{\mathbf{V}}_\xi(k)\mathbf{H}^T(k)\left[\mathbf{H}(k)\tilde{\mathbf{V}}_\xi(k)\mathbf{H}^T(k) + \mathbf{V}_v(k)\right]^{-1}, \quad (14)$$

where:

$$\tilde{\mathbf{V}}_\xi(k) = \mathbf{F}\mathbf{V}_\xi(k-1)\mathbf{F}^T + \mathbf{V}_w \quad (15)$$

is the predicted covariance matrix of the state vector.

The error covariance matrix is obtained by:

$$\mathbf{V}_\xi(k) = \left[\mathbf{I} - \mathbf{K}(k)\mathbf{H}(k)\right]\tilde{\mathbf{V}}_\xi(k). \quad (16)$$

The error covariance matrix is independent of the state vector estimate. It defines the time after which Kalman filter is in the stationary state. Diagonal elements of matrix $\mathbf{V}_\xi(k)$ are the variances of coordinate and velocity errors.

The most complex mathematical operation which has to be done during filtering is inverting of the matrix in Eq.(14). However the dimensions of the matrix are only 6 by 6 and there is no difficulty in inverting it.

III. RESEARCHES

The accuracy of proposed algorithm is studied at different standard deviations of distance errors σ_D. Different values for standard deviation of user velocity σ_v are used in order to estimate the influence of this parameter of user motion model. The sampling time Δt=0.01 sec. is used. Some of the results are shown in the following figures.

Standard deviations of estimates are shown in Fig.1. The results displayed in the figure are at STD of distance errors σ_D=18 m and the following values of model parameters: σ_v=6 m/s; α=0.2. These results are obtained by computer simulation of Eq.(16).

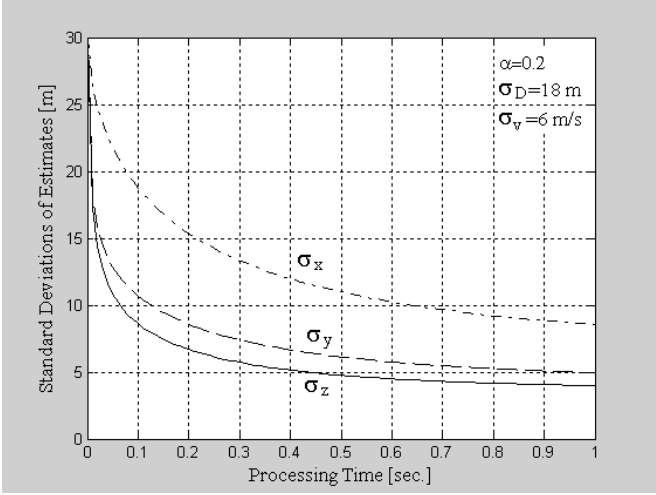

Fig.1. STD of estimates.

As one can see in Fig.1 the values of standard deviations first decrease fast and then the slopes of curves are smooth. The results indicate that the relative differences between STDs of estimates, when the processing time is T=0.5 sec. and when it is T=1 sec., are less than 3 dB. The studies show that the values of STDs of estimates are highest when the STD of velocities in the model is σ_v=6 m/s. The differences between minimal and maximal values of STDs of estimates for different velocity STDs are small.

The results for STD of z-coordinate estimate σ_z as a function of parameter α and STD of distance errors σ_D are shown in Fig.2. The worst case for velocities STD of σ_v=6 m/s is chosen. The STD of z-coordinate estimate is calculated for two values of processing time: T=0.05 sec. and T=1 sec. respectively.

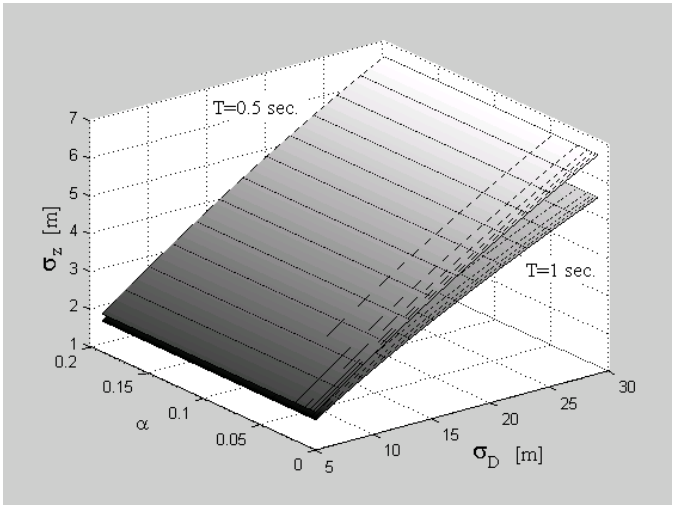

Fig.2. STD of z-coordinate estimate at σ_v=6 m/s.

The results indicate that the influence of parameter α is insignificant. The STD of *z*-coordinate estimate increases when the STD of distance errors increases. The relation between both STDs is not proportional. It is obvious that the accuracy is better when the processing time is longer.

The fact that the STDs of estimates for different coordinates are not equal is due to the user relative geometry. The influence of the geometry on accuracy can be estimated, using concept of dilution of precision (DOP) [4]. If the user's location is calculated directly from measured distances then the STDs of coordinate estimates are calculated by the following equations:

$$\sigma_x=\text{XDOP}\ \sigma_D;\ \sigma_y=\text{YDOP}\ \sigma_D;\quad \sigma_z=\text{ZDOP}\ \sigma_D, \qquad (17)$$

where XDOP, YDOP and ZDOP are delusion of precisions of each coordinate respectively. The results shown in all figures are at the following values of DOPs: XDOP=4.2407; YDOP=2.0134; ZDOP=1.8466.

The improvement in accuracy (in percent), when the proposed Kalman filter is used, is shown in Fig.3 and Fig.4.

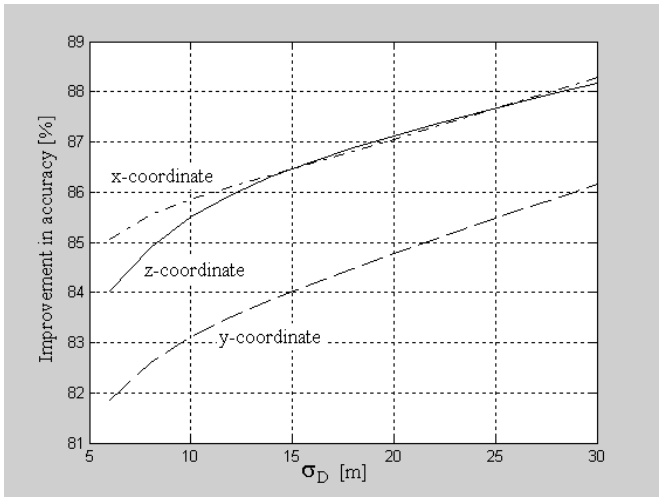

Fig.3. Improvement in accuracy at σ_v=6 m/s and T=0.5 sec.

The improvement is more than 80% in case of processing with proposed Kalman filter. The improvement grows when STD of distance errors increases.

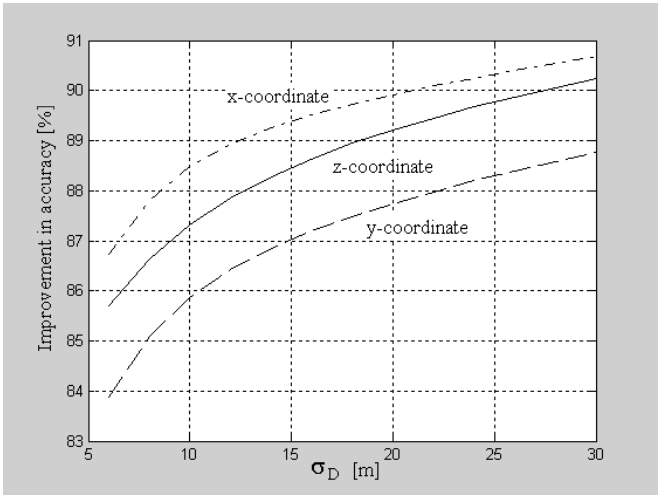

Fig.4. Improvement in accuracy at σ_v=6 m/s and T=1 sec.

The improvement at processing time *T*=1 sec. is bigger in comparison with processing time *T*=0.05 sec. The values of accuracy improvement reach more than 90% for *x* and *z* coordinates. The studies display that the user's relative geometry does not affect on the improvement degree in accuracy.

The results from a computer simulation are shown in the following figures. A user motion is generated for the equal values of velocities in each coordinate, i.e. $V_x=V_y=V_z$. These results are obtained by simulation of Eq.(13) and Eq.(15).

Mean values of estimate errors as a function of user velocity at σ_v=0.1 m/s and α=0.2 are displayed in Fig.5.

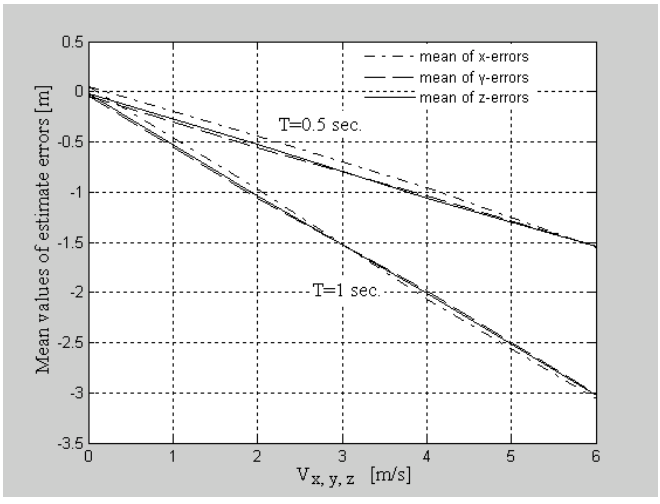

Fig.5. Mean values of estimate errors at σ_v=0.1 m/s and α=0.2.

It is clearly seen that the bias of estimates grows up when the user velocity increases. This is because of differences between model and real user motion. The bias at processing time *T*=1 sec. is bigger than at processing time *T*=0.5 sec. Maximal bias is about -3 m and -1.5 m for processing time *T*=1 sec. and *T*=0.5 sec. respectively. The mean values of estimate errors

are almost equal for all three coordinates. Even with these model parameters the bias is small enough.

The STD of *x*-coordinate estimate at σ_v=0.1 m/s and α=0.2 is shown in Fig.6.

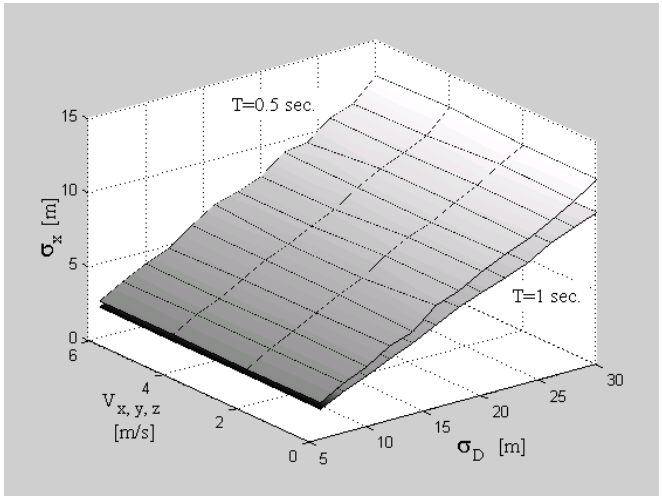

Fig.6. STD of x-coordinate estimate at σ_v=0.1 m/s and α=0.2.

It is obvious that the influence of user velocities $V_{x,\,y,\,z}$ on the STD of *x*-coordinate estimate is insignificant. The standard deviation is smaller when the processing time is longer. The results from simulation indicate that the improvement of accuracy, when processing time is *T*=1 sec., is below 3 dB in comparison with the case of processing time *T*=0.5 sec. The STD of *x*-coordinate estimate is less than 15 m.

Mean values of estimate errors as a function of user velocity at σ_v=6 m/s and α=0.2 are displayed in Fig.7 for two values of processing time.

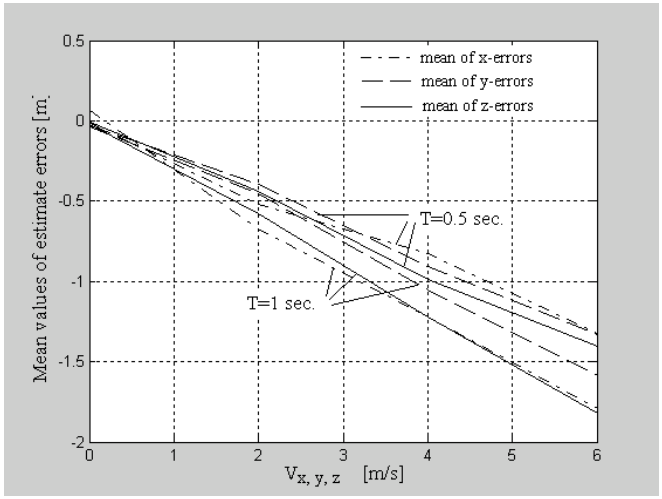

Fig.7. Mean values of estimate errors at σ_v=6 m/s and α=0.2.

It is readily seen that the bias of estimates grows up when the user velocity increases. The difference between biases at processing times *T*=1 sec. and *T*=0.5 sec. is not so much. The bias of coordinate estimates is less significant than in the case shown in Fig.5. The bias is below 1 m when the user velocities are less than 3 m/s. The mean values of estimate errors are almost equal for all three coordinates.

The STD of *x*-coordinate estimate at σ_v=6 m/s and α=0.2 is shown in Fig.8.

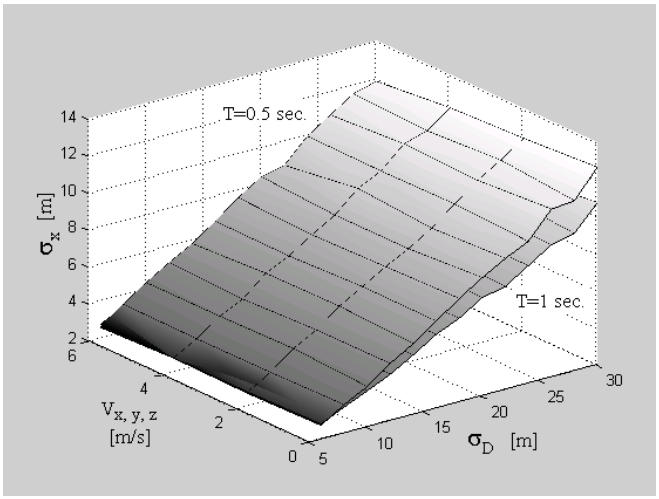

Fig.8. STD of x-coordinate estimate at σ_v=6 m/s and α=0.2.

The influence of user velocities $V_{x,\,y,\,z}$ on the STD of *x*-coordinate estimate is small but clearly seen in Fig.8. The accuracy increases for bigger values of user velocities. The results from simulation indicate that the improvement of accuracy, when processing time is *T*=1 sec., is below 3 dB in comparison with the case of processing time *T*=0.5 sec. The STD of *x*-coordinate estimate is below 14 m. The studies show that the grater value of σ_v in the model better matches the real user motion.

IV. Conclusion

The proposed model of user motion and the formed observation equation permit using of the Kalman filtering. The general advantage of formed observation is that any approximation is not implemented and thus any additional errors are not introduced in the processing algorithm. The results prove that the improvement in accuracy is great in comparison with direct user's location calculating. The studies show that by careful choosing of the model parameters an additional improvement in accuracy can be achieved. The DOPs usually are less than 2.5 and in the most cases the use of proposed algorithm will lead to errors of a few meters only.

References

[1] A. P. Sage, J. L. Melse, *Estimation Theory with Application to Communication and Control*, Moscow, 1976.

[2] M. Marinov, G. Stanchev, *Use of Space Correlation of Satellite Move in GPS*, Proceeding of XXXVII International Scientific Conference ICEST, 16-18 October 2003, Sofia, Bulgaria, 2003, pp.132-135.

[3] M. Marinov, G. Stanchev, *Use of Joint Space Correlation of Satellite Constellation Move in GPS*, Proceeding of XXXVII International Scientific Conference ICEST, 16-18 October 2003, Sofia, Bulgaria, 2003, pp.128-131.

[4] *Understanding GPS Principles and Applications*, Editor E. D. Kaplan, Artech House, London, 1996.

[5] V. Ivanov, M. Marinov, *Stochastic Theory of Aircraft Radio Engineering Devices*, Sofia, Bulgaria, 1999.

CAD of Trisection and Cascaded Triplet Microstrip Square Open-Loop Resonator Filters

Marin V. Nedelchev

Abstract: This paper proposes a method for calculation of the coupling coefficients in trisection and cascaded triplet filters. Formulas for coupling coefficients are derived. Synthesis results, obtained by the design technique, are shown.

Keywords: Microstrip bandpass filter, Cross-coupled resonators, coupling coefficients.

I. INTRODUCTION

In the modern communication systems, high selectivity and low passband loss are the main requirements for the microstrip filters. Low passband loss increases the system sensitivity and the high selectivity decrease the guard interval between two channels in a communication system. A better spectrum efficiency is achieved. High filter selectivity requires high filter order and more resonators. Because of the low unloaded Q factor of the microstrip resonators, the passband loss increases. Both requirements become contradictory for cascaded microstrip filters. Filters satisfying the increased requirements are the cross-coupled filters. They have non-adjacent resonator coupling.

The simplest cross-coupled filters are the trisection filters, proposed in [1,2]. They have asymmetric characteristics and one transmission zero (TZ) out of the passband. Quadruplet filters with one cross-coupling produces a pair of TZs symmetrically around the passband. These sections may be the core of cascaded triplet (CT) or cascaded quadruplet (CQ) filters [3,4,5] shown respectively on Fig.1a and Fig.1b. The authors of [6] proposed box section filters (Fig.1c), where the box is a four-resonator core with one cross-coupling, having asymmetric characteristic and asynchronously tuned resonators. Another filter topology, proposed in [6] is called cul-de-sac (Fig1d). These filters use a core of four cross-coupled resonators and the other resonators are "straight" coupled. One of the couplings in the core quartet must be negative. Cul-de-sac filters may have either symmetric or asymmetric characteristic and are generally asynchronously tuned..

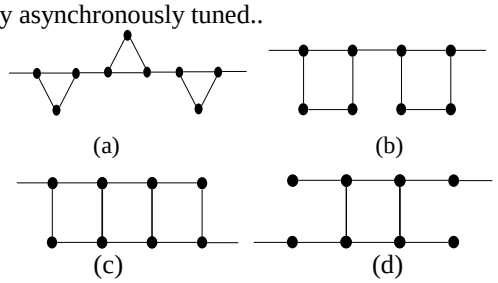

Fig.1. Coupling and routing diagrams for cross-coupled filters. (a)Cascaded triplet. (b) Cascaded Quadruplet (c) Eight degree box section. (d) 8-3 cul-de-sac

Marin Veselinov Nedelchev – PhD student in Dept. of Radiotechnic in Faculty of Communications and Communication Technologies in TU –Sofia E-mail mnedelchev@abv.bg

The maximum TZs they produce are N-3 and the number of the couplings is at its absolute minimum for a given filtering function. A drawback of the cul-de-sac filters is their high temperature sensitivity.

The microstrip filter synthesis includes calculating the coupling coefficients for a given approximation (a method for Chebyshev approximation is presented in [7]) and their realization. The theory of coupling for synchronously and asynchronously tuned resonators is given in [8,9]. A full-wave electromagnetic (EM) simulator is used to calculate the couplings in the papers [1,2,4,8], which is an expensive and time-consuming method. The use of EM simulator is not a flexible way for computation of the coupling coefficients. A design technique for synthesis of CQ filters without the use of EM simulator is given in [10]. A closed form formulas are derived for the basic couplings in the CQ filters.

Fig.2 Trisection filters. (a) produces a TZ on the upper side of the passband. (b) produces TZ on the lower side of the passband

In this paper is proposed a design technique for synthesis of trisection and CT filters (Fig.2) without full-wave EM simulator. Closed form formulas are derived for the coupling coefficients in the trisection and CT filters. Two filters are synthesized and analyzed with their electrical parameters. A comparison between the theoretical and the synthesized characteristics is done and a good correlation is observed. For eliminating the error, an optimization process may be performed.

II. COUPLING COEFFICIENTS FOR DIFFERENT RESONATOR CONFIGURATIONS IN CT FILTERS.

The three microstrip square open-loop resonators in the trisection filter are asynchronously tuned. The self-resonant frequency of each resonator is f_{0i}, which is different from the filter's central frequency f_0. Resonators 1 and 3 are tuned on an equal frequency, i.e. $f = f_{01} = f_{03}$. For the microstrip square open-loop resonators their electrical length is $\theta_i \approx \frac{\pi}{2}$ *rad* for $f = f_{0i}$, *i=1,2,3.*

A. *Electrical coupling*

The cross-coupling between resonators 1 and 3, shown on Fig.2a, is electrical in nature, because the open ends of the lines are close and the electric fringe field is much stronger near the open ends. The coupled resonators are tuned on equal frequency and a closed form formula for the coupling coefficient is derived in [10] (Fig.3):

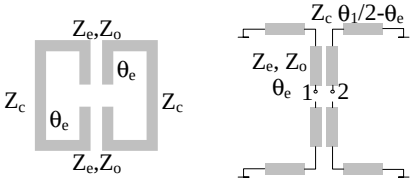

Fig.3 Electric coupling. (a) Resonator topology (b) Equivalent scheme

$$k_e = \frac{1}{2b}\left(\frac{1}{Z_o}\frac{Z_o - Z_c tg\theta_e tg\left(\frac{\theta_1}{2}-\theta_e\right)}{Z_c tg\left(\frac{\theta_1}{2}-\theta_e\right)-Z_o tg\theta_e} - \frac{1}{Z_e}\frac{Z_e - Z_c tg\theta_e tg\left(\frac{\theta_1}{2}-\theta_e\right)}{Z_c tg\left(\frac{\theta_1}{2}-\theta_e\right)-Z_e tg\theta_e}\right) \quad (1),$$

where Z_c is the characteristic impedance of the transmission line,

Z_e и Z_o are the even and odd impedances of the coupled lines

θ_1 is the electrical length of the resonators

θ_e is the length of the coupled lines

b is the admittance slope of the resonators.

B. *Magnetic coupling*

The cross-coupling between resonators 1 and 3, shown on Fig.2b is magnetic in nature, because of the virtual ground in the middle of the resonator. A closed form formula for the coupling coefficient is derived in [10]. Figure 4 shows the resonator configuration and their equivalent scheme.

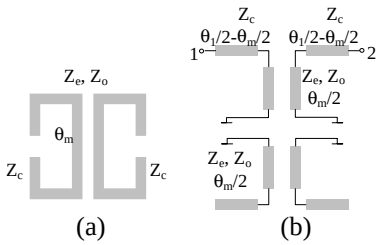

Fig.4 Magnetic coupling. (a) Resonator topology (b) Equivalent scheme

$$k_m = \frac{1}{2bZ_c}\left(\frac{Z_c - Z_o tg\frac{\theta_m}{2}tg\frac{\theta_1-\theta_m}{2}}{Z_o tg\frac{\theta_m}{2} - Z_c tg\frac{\theta_1-\theta_m}{2}} - \frac{Z_c - Z_e tg\frac{\theta_m}{2}tg\frac{\theta_1-\theta_m}{2}}{Z_e tg\frac{\theta_m}{2} - Z_c tg\frac{\theta_1-\theta_m}{2}}\right), \quad (2)$$

where $\boldsymbol{\theta_m}$ is the coupled line length.

C. *Hybrid coupling.*

Hybrid coupled resonators are shown on Fig.5a and Fig.6a. For this type of coupling none of the electromagnetic field components is much stronger than the other. It is important for these case that the resonators are asynchronously tuned. Their self-resonant frequencies are f_{01} и f_{02} and the electrical lengths are respectively θ_1 and θ_2 for the central frequency f_0.

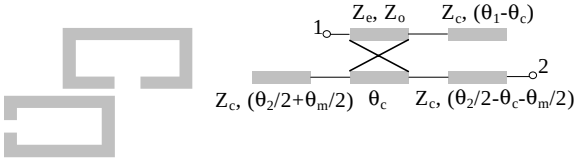

Fig.5 Hybrid coupling 1 (a) Resonator topology (b) Equivalent scheme

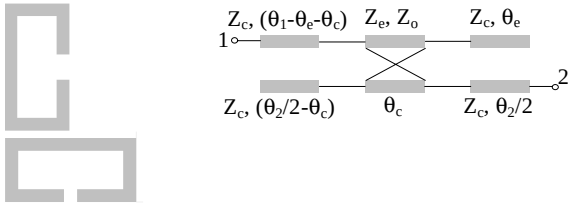

Fig.6 Hybrid coupling 2. (a) Resonator topology (b) Equivalent scheme

For the hybrid coupling shown on Fig.5a and using the equivalent scheme on Fig.5b for the coupling coefficient is derived:

$$k_{hyb1} = \frac{y_{21}}{\sqrt{b_1 b_2}} \quad (3)$$

$$d_2 = \left[\frac{\cot g\theta_c}{w} - y_c tg\left(\frac{\theta_2}{2}+\frac{\theta_m}{2}\right)\right]\left[\frac{\cot g\theta_c}{w} + y_c tg\left(\theta_1-\theta_c\right)\right] - \frac{\csc^2\theta_c}{v^2}$$

$$y_{41} = j\frac{\csc\theta_c}{v} - j\frac{\csc\theta_c}{d_2 w}\left[\begin{array}{l} -\frac{\csc^2\theta_c}{vw} + \\ +\frac{\cot g\theta_c}{v}\left(\frac{\cot g\theta_c}{w} - y_c tg\left(\theta_1-\theta_c\right)\right)\end{array}\right] -$$

$$-j\frac{\cot g\theta_c}{d_2 v}\left[\begin{array}{l} -\frac{\cot g\theta_c \csc\theta_c}{v^2} + \\ +\frac{\csc\theta_c}{w}\left(\frac{\cot g\theta_c}{w} - y_c tg\left(\frac{\theta_2}{2}+\frac{\theta_m}{2}\right)\right)\end{array}\right]$$

$$y_{44} = j\frac{\cot g\theta_c}{w} - j\frac{\csc\theta_c}{d_2 w}\left[\begin{array}{l} -\frac{\cot g\theta_c \csc\theta_c}{v^2} + \\ +\frac{\csc\theta_c}{w}\left(\frac{\cot g\theta_c}{w} - y_c tg\left(\theta_1-\theta_c\right)\right)\end{array}\right] -$$

$$-j\frac{\cot g\theta_c}{d_2 v}\left[\begin{array}{l} -\frac{\csc^2\theta_c}{vw} + \\ +\frac{\cot g\theta_c}{v}\left(\frac{\cot g\theta_c}{w} - y_c tg\left(\frac{\theta_2}{2}+\frac{\theta_m}{2}\right)\right)\end{array}\right]$$

$$y_{21} = \left[jZ_c\frac{y_{44}}{y_{41}}\sin\left(\frac{\theta_2}{2}-\frac{\theta_m}{2}-\theta_c\right) - \frac{1}{y_{41}}\cos\left(\frac{\theta_2}{2}-\frac{\theta_m}{2}-\theta_c\right)\right]^{-1}$$

$$\frac{1}{v} = \frac{1}{2}\left(\frac{1}{Z_o}-\frac{1}{Z_e}\right) \quad \frac{1}{w} = \frac{1}{2}\left(\frac{1}{Z_e}+\frac{1}{Z_o}\right)$$

$$b_i = \frac{\pi}{2}y_c, \text{ за } i=1, 2.$$

For the hybrid coupling shown on Fig.6a and using the equivalent scheme on Fig.6b for the coupling coefficient is derived:

$$k_{hyb2} = \frac{y_{21}}{\sqrt{b_1 b_2}} \qquad (4)$$

$$d_1 = \left[\frac{\cot g\theta_c}{w} - y_c tg\left(\frac{\theta_2}{2} - \theta_c\right)\right]\left[\frac{\cot g\theta_c}{w} + y_c tg\theta_e\right] - \frac{\csc^2\theta_c}{v^2}$$

$$y_{11} = -j\frac{\cot g\theta_c}{w} + j\frac{\cot g\theta_c}{d_1 v}\left[\begin{array}{l} -\dfrac{\csc^2\theta_c}{vw} + \\ +\dfrac{\cot g\theta_c}{v}\left(\dfrac{\cot g\theta_c}{w} - y_c tg\theta_e\right)\end{array}\right] +$$

$$+ j\frac{\csc\theta_c}{d_1 w}\left[\begin{array}{l} -\dfrac{\cot g\theta_c \csc\theta_c}{v^2} + \\ +\dfrac{\csc\theta_c}{w}\left(\dfrac{\cot g\theta_c}{w} - y_c tg\left(\dfrac{\theta_2}{2} - \theta_c\right)\right)\end{array}\right]$$

$$y_{41} = j\frac{\csc\theta_c}{v} - j\frac{\csc\theta_c}{d_1 w}\left[\begin{array}{l} -\dfrac{\csc^2\theta_c}{vw} + \\ +\dfrac{\cot g\theta_c}{v}\left(\dfrac{\cot g\theta_c}{w} - y_c tg\theta_e\right)\end{array}\right] -$$

$$- j\frac{\cot g\theta_c}{d_1 v}\left[\begin{array}{l} -\dfrac{\cot g\theta_c \csc\theta_c}{v^2} + \\ +\dfrac{\csc\theta_c}{w}\left(\dfrac{\cot g\theta_c}{w} - y_c tg\left(\dfrac{\theta_2}{2} - \theta_c\right)\right)\end{array}\right]$$

$$y_{14} = -y_{41}$$

$$y_{44} = j\frac{\cot g\theta_c}{w} - j\frac{\csc\theta_c}{d_1 w}\left[\begin{array}{l} -\dfrac{\cot g\theta_c \csc\theta_c}{v^2} + \\ +\dfrac{\csc\theta_c}{w}\left(\dfrac{\cot g\theta_c}{w} - y_c tg\theta_e\right)\end{array}\right] -$$

$$- j\frac{\cot g\theta_c}{d_1 v}\left[\begin{array}{l} -\dfrac{\csc^2\theta_c}{vw} + \\ +\dfrac{\cot g\theta_c}{v}\left(\dfrac{\cot g\theta_c}{w} - y_c tg\left(\dfrac{\theta_2}{2} - \theta_c\right)\right)\end{array}\right]$$

$$y_{21} = \left[\begin{array}{l} jZ_c \sin\dfrac{\theta_c}{2}\cos(\theta_1 - \theta_c - \theta_e)\dfrac{y_{44}}{y_{41}} - \\ -Z_c^2 \sin\dfrac{\theta_c}{2}\sin(\theta_1 - \theta_c - \theta_e)\left(\dfrac{y_{11}y_{44}}{y_{41}} + y_{14}\right) - \\ -\dfrac{1}{y_{41}}\cos\dfrac{\theta_2}{2}\cos(\theta_1 - \theta_c - \theta_e) - \\ -jZ_c \cos\dfrac{\theta_2}{2}\sin(\theta_1 - \theta_c - \theta_e)\dfrac{y_{11}}{y_{41}}\end{array}\right]^{-1}$$

$$\frac{1}{v} = \frac{1}{2}\left(\frac{1}{Z_o} - \frac{1}{Z_e}\right) \quad \frac{1}{w} = \frac{1}{2}\left(\frac{1}{Z_e} + \frac{1}{Z_o}\right)$$

$$b_i = \frac{\pi}{2} y_c \text{, за } i=1, 2$$

D. Tapped input/output electrical length

The tapped electrical length θ_t is found in [11] (Fig.7).

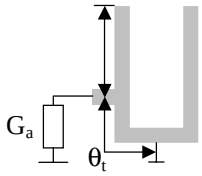

$$\theta_t = \sin^{-1}\left(\sqrt{\frac{G_a}{b_1 Q_e}}\right), \quad (5)$$

Fig.7. Tapped microstrip open-loop resonator

III. Design technique for trisection and CT filters.

1.Calculating the coupling matrix M and the external Q factor [6].

2.Finding the resonator parameters and the resonator self-resonant frequency. The main diagonal elements in the coupling matrix (M_{ii}) show the frequency deviation of each resonator. The angular self-resonant frequencies are the positive root of the equation:

$$\omega_{0i}^2 - M_{ii}\omega_0\omega_{0i} - \omega_0^2 = 0$$

Choosing the transmission line characteristic impedance Z_c and calculating the admittance slope parameter b_i.

3. Calculating the even and odd impedances of the coupled lines for different couplings Eqs. (1-4), the tapped input/output line length Eq. (5).

4.Computing the geometric dimensions of the filter for a given substrate.

5.Optimisation of the filter parameters.

IV. Design examples.

Two trisection filters are designed using the proposed formulas for the coupling coefficients. The analysis is performed using the electrical parameters of the filter. Both filters have central frequency f_0=*1GHz*, and fractional bandwidth *FBW=0.08.*

A. The first filter has a TZ on a frequency f_0=*850MHz* (Fig.2b). The coupling matrix is:

$$M = \begin{pmatrix} -0.00888 & 0.0936 & -0.03248 \\ 0.0936 & 0.02864 & 0.0936 \\ -0.03248 & 0.0936 & -0.00888 \end{pmatrix}$$ and the external Q factor is

$Q_e = 15.275$.

The self-resonant frequencies are computed as follows: $f_{01}=f_{03}$=*1004.37MHz* и f_{02}=*985.94MHz.*

The frequency response of the filter is shown on Fig.8a.

B. The second filter has a TZ on a frequency f_0=1150MHz (Fig.2a). The coupling matrix is:

$$M = \begin{pmatrix} 0.00872 & 0.09376 & 0.03216 \\ 0.09376 & -0.02832 & 0.09376 \\ 0.03216 & 0.09376 & 0.00872 \end{pmatrix}$$ and the external Q factor is $Q_e = 15.275$.

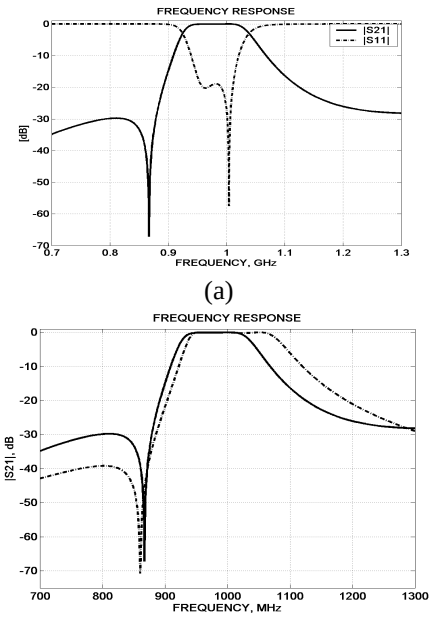

(a)

(b)

Fig.8.Filter 1 simulated frequency responses. (a) – Rejection and return loss. (b) Comparison between the synthesized and theoretic responses (solid line-synthesized, dash-dotted line-theoretical)

The self-resonant frequencies are computed as follows: $f_{01}=f_{03}$=995,57MHz и f_{02}=1014,42MHz.
The frequency response of the filter is shown on Fig.9a.

Figures 8b and 9b show plotted together the theoretically computed and synthesized frequency responses. It is clear that the proposed design technique leads to filters with the desired characteristics. The initially designed filter may be a start point for further optimization of the filter. A drawback of the proposed technique is widening the passband, small shifting of the central frequency in the direction of the TZ.

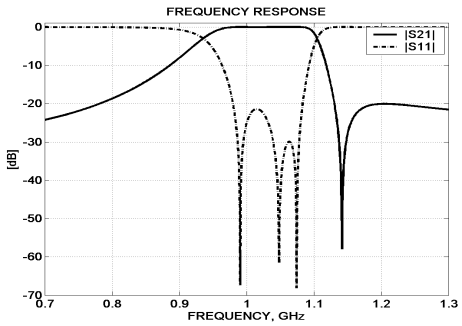

(a)

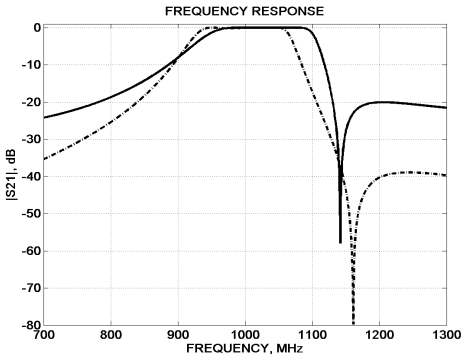

(b)

Fig.9.Filter 2 simulated frequency responses. (a) – Rejection and return loss. (b) Comparison between the synthesized and theoretic responses (solid line-synthesized, dash-dotted line-theoretical)

V. CONCLUSION

The paper proposes a method for synthesis of trisection or CT filters. Closed-form formulas for different type of couplings are derived. The computation of the coupling coefficients is carried out without using a full-wave EM simulator. The proposed method drawbacks may be eliminated performing an optimization process.

ACKNOWLEDGEMENT

The author is grateful to PhD Ilia G. Iliev, Technical University Sofia, for the helpful discussion that aided considerably in the development of the method presented in this paper.

REFERENCES

[1] J.S.Hong, Lancaster, M, Microstrip Cross-Coupled Trisection Bandpass Filters with Asymmetric Frequency Characteristics, IEE Proc.-Microwave, Antennas, Propagation 146, Feb, 1999, pp.84-90
[2] Chih-Ming Tsai et al, Microstrip Trisection Cross-coupled Bandpass Filter with I-Shaped Resonator,
[3] Levy, R, Filters with Single Transmission zeros at Real or Imaginary Frequencies, IEEE Trans. On MTT-24, April 1976, pp.172-181
[4] J.S.Hong, Lancaster, M, Theory and Experiment of Novel Microstrip Slow-Wave Open Loop Resonator Filters, IEEE Trans. On MTT-45, Dec.1997, pp.2358-2365
[5] J.S.Hong, Lancaster, M, Cross-Coupled Microstrip Hairpin-Resonator Filters, IEEE Trans on MTT-46, Jan.1998, pp.118-122
[6] Cameron, R., et al, Synthesis of Advanced Microwave Filters Without Diagonal Cross-Coupling, IEEE Trans on MTT-49, Dec.2002, pp.2862-2871
[7] Cameron, R., Advanced Coupling Matrix Synthesis Techniques for Microwave Filters, IEEE Trans on MTT-50, Jan.2003, pp.1-10
[8] Rosenborg, U., Amari, S., Novel Coupling Schemes for Microwave Resonator Filters, IEEE Trans on MTT-49, Dec.2002, pp.2896-2902
[9] J.S.Hong, Couplings of Asynchronously Tuned Coupled Microwave Resonators, IEE Proc. Microwave, Antennas, Propagation 147, Oct. 2000, pp.354-358
[10] Iliev, I, Nedelchev, M, CAD of Cross-Coupled Miniaturized Hairpin Bandpass Filters, ICEST, Nis, Yugoslavia, 2002
[11] Wong, J, Microstrip Tapped-Line Filter Design, IEEE Trans on MTT-27, Jan.1979, pp.44-50

Determinating the amplitudes of intermodulation products of higher order by means Volterra kernels

Oleg Borisov Panagiev[1]

Abstract **- Nonlinear distortions and the resulting nonlinear products in the systems for cable television present a fundamental problem for the quality receiving of the transmitted signals by such systems. In this paper we describe an algorithm for computation of the amplitudes of the nonlinear products of higher order.**

Key words **- intermodulation distortions, nonlinear products, cable television products, binomial coefficients, Volterra kernels.**

I. INTRODUCTION

The quality receiving of transmitted products in a current CATV system is mainly determined by the possibility for nonlinear distortions in such a system. In many papers /1,2,3/ the resulting nonlinear products are considered up to distortions of third order and limited number of frequencies /channels/.

In the general case the combination frequencies are determined by the formula:

$$f = r_1 f_1 + r_2 f_2 + r_3 f_3 + ... = \sum_{i=1}^{N} r_i f_i \qquad (1)$$

where r_i are arbitrary integers, possibly equal to zero. If the transmission characteristic of the system is of n-th order, then the coefficients $r_1, r_2, r_3 ...,$ need to satisfy the inequality $|r_1| + |r_2| + |r_3| + ... \le n$

When it is needed to compute the amplitudes of the intermodulation products of a very high order n, in the case of many frequencies (channels) N, using trigonometric formulas and solving multiple integrals is too complicated and cumbersome.

Below we describe an algorithm for computation of the amplitude of each nonlinear intermodulation product in the presence of arbitrarily large number of sinusoidal signals at the input. Our treatment of the relation between each intermodulation product and the parameters of the input signals for the system (as well as its transfer characteristics, given by the Volterra kernels of the related order) is based upon the use of binomial coefficients.

[1]O. B. Panagiev is a system engineer at the Technical University of Sofia, e-mail: ctv@alpha.tu-sofia.bg

II. DESCRIPTION OF THE ALGORITHM.

Assume that the nonmodulated signal at the input of the system is given by the formula

$$x(t) = \sum_{i=1}^{N} A_i \cos(\omega_i t + \theta_i), \qquad (2)$$

and its nonlinearity is described by the polynomial

$$y(t) = \sum_{n=1}^{\infty} |H_n(f)|.x^n(t) \qquad (3)$$

The amplitudes of each nonlinear product of the intermodulation satisfy the following equation:

$$A = \frac{S}{2^{n-1}} |H_n| . \prod_{i=1}^{N} A_i^{d_i} \qquad (4)$$

where A_i is the amplitude of the i-th input frequency;

d_i - is the coefficient of the i-th input frequency in the nonlinear product;

i - taking values from 1 to N, labels the input frequencies;

$|H_n|$ - is the Volterra kernel of n-th order for the corresponding nonlinear product;

$|H_n| \equiv |H_n(f)|$

n -is the degree of the polynomial, describing the nonlinearity of the system /coincides with the order of the nonlinear product/;

S - is the coefficient that characterizes the number of the nonlinear products with equal frequency at the output of the system.

$$S = \prod_{i=1}^{N} C_{p_i}^{d_i} \qquad (5)$$

which represents a product of binomial coefficients [5], obtained by the following formula:

$$C_{p_i}^{d_i} = \frac{p_i(p_i - 1)(p_i - 2)....[p_i - (d_i - 1)]}{d_i!} \qquad (6)$$

$$p_i = n - \sum_{i=1}^{i} d_{i-1} \qquad (7)$$

$$|H_n| = \frac{y_n^{(n)}(t)}{n!} \qquad (8)$$

where $y_n^{(n)}(t)$ is the n-th derivative of the n-th output signal with respect to x(t).

III. AN EXAMPLE:

Let n=3 and N=3, and let the nonlinear product be $f_1 \pm f_2 \pm f_3$.

Then:

1. First we determine the numbers d_i for each frequency

$$d_1 = 1; d_2 = 1; d_3 = 1$$

2. Second we compute the values of p_i. Since the nonlinear product is composed from three frequencies, we look for p_1, p_2, and p_3.

$p_1 = 3-(d_{1-1}) = 3 - d_0$ but $d_0 = 0$

Therefore $p_1 = 3$

$$p_2 = 3-(d_{1-1}+d_{2-1}) = 3-(d_0+d_1)$$
$$= 3-(0+1) = 2$$
$$p_3 = 3-(d_{1-1}+d_{2-1}-d_{3-1})$$
$$= 3-(d_0+d_1+d_2) = 3-(0+1+1) = 1$$

3. Next we compute the binomial coefficients $C_{p_i}^{d_i}$

$$C_{p_1}^{d_1} = C_3^1 = \frac{3}{1!} = 3;\ C_{p_2}^{d_2} = C_2^1 = \frac{2}{1!} = 2;$$
$$C_{p_3}^{d_3} = C_1^1 = \frac{1}{1!} = 1$$

4. We compute the coefficient S:

$$S = C_{p_1}^{d_1} C_{p_2}^{d_2} C_{p_3}^{d_3} = C_3^1 C_2^1 C_1^1 = 6$$

5. Next we compute the Volterra kernel for the corresponding nonlinear product. From formula (3) with $n = 3$ we deduce

$y_3(t) = |H_3(f)| x^3(t)$, therefore

$y_3^{(3)}(t) = \left[|H_3(f)| x^3(t)\right]^{(3)}$, that is

$y_3^{(3)}(t) = 6|H_3(f)|$. This is substituted in (8) and gives

$$|H_3| = \frac{6|H_3(f)|}{3!} = \frac{6|H_3(f)|}{1.2.3} = |H_3(f)|$$

6. Finally we compute the amplitude of the nonlinear product with frequency $f = f_1 \pm f_2 \pm f_3$.

$$A = \frac{6}{2^{3-1}} |H_3(f_1 \pm f_2 \pm f_3)| A_1 A_2 A_3$$
$$= \frac{6}{2^2} |H_3(f_1 \pm f_2 \pm f_3)| A_1 A_2 A_3$$
$$= \frac{3}{2} |H_3(f_1 \pm f_2 \pm f_3)| A_1 A_2 A_3 \qquad (9)$$

The expression /8/ is identical with the corresponding expression in Table 1,[1], determined by using trigonometric identities and by evaluating multiple integrals.

TABLE I

nonlinear products		frequency	amplitudes
order	type		
4	composite	$2\mathbf{f}_1 \pm 2\mathbf{f}_2$	$3/4\|H_4\|.A_1^2.A_2^2$
		$2\mathbf{f}_1 \pm 2\mathbf{f}_3$	$3/4\|H_4\|.A_1^2.A_3^2$
		$2\mathbf{f}_2 \pm 2\mathbf{f}_3$	$3/4\|H_4\|.A_2^2.A_3^2$
		$3\mathbf{f}_1 \pm \mathbf{f}_2$	$1/2\|H_4\|A_1^3.A_2.$
		$3\mathbf{f}_1 \pm \mathbf{f}_3$	$1/2\|H_4\|A_1^3.A_3$
		$3\mathbf{f}_2 \pm \mathbf{f}_1$	$1/2\|H_4\|A_2^3.A_1$
		$3\mathbf{f}_2 \pm \mathbf{f}_3$	$1/2\|H_4\|A_2^3.A_3$
		$3\mathbf{f}_3 \pm \mathbf{f}_1$	$1/2\|H_4\|A_3^3.A_1$
		$3\mathbf{f}_3 \pm \mathbf{f}_2$	$1/2\|H_4\|A_3^3.A_2$
		$2\mathbf{f}_1 \pm \mathbf{f}_2 \pm \mathbf{f}_3$	$3/2\|H_4\|.A_1^2.A_2.A_3$
		$\mathbf{f}_1 \pm 2\mathbf{f}_2 \pm \mathbf{f}_3$	$3/2\|H_4\|.A_1.A_2^2.A_3$
		$\mathbf{f}_1 \pm \mathbf{f}_2 \pm 2\mathbf{f}_3$	$3/2\|H_4\|.A_1.A_2.A_3^2$

In a similar manner, following the above algorithm, one can determine the amplitudes of each combination of frequencies for arbitrary values of n and N without the need of complicated trigonometric computations. Same intermodulation products for n=4 and N=3 are presented in Table I.

IV. CONCLUSION

The suggested algorithm can be applied to determine the amplitudes of intermodulation products for large values of n and N for arbitrary combinations of frequencies (see Eq.1). A program presenting in a tabular and a graphical form the results from formula (4) will be the subject of a forthcoming publication.

REFERENCES

[1] O.B Panagiev, "Non-linear distortions and methods of their limitation and reduction in the cable television systems", IX NSASC Electronics'2000, Sozopol, 20–22 sept.2000.

[2] J. Vulevi, "Analysis, measurement and cancellation of the bandwidth and amplitude dependence of intermodulation distortion in rf power amplifiers", Academic Dissertation Oulu, 2001.

[3] C. Evans, D. Rees, L. Jones and M. Weiss, "Periodic signals for measuring non-linear Volterra kernel", IEEE Trans. Instrumentation and Measurement, vol.45, no.2, 1996.

[4] A. P. Volkoedov, Academic Dissertation, Moskow, 1970.

[5] www.mathworld.wolfram.com

Algorithm for defining the limits possibilities of a system for cable television with the aim of minimal nonlinear distortions

Oleg Borisov Panagiev[1]

Abstract: **An algorithm, by which it is possible to explore the limits possibilities of a system for cable television, depending on the number of the transmitted programs (channels) and number of the amplifiers connects in series in the cable distribution network (CDN), is created. The defining of the maximum number of the channels and the amplifiers lead to minimizing of the nonlinear distortions. The results from algorithm are presented graphically (three-dimensional graphics), by using the program product MAPLE**.

Key words: **cable television, nonlinear distortions, tolerance, optimization, nonlinear products (NP).**

I INTRODUCTION

When designing the system for cable television with the aim of minimal nonlinear distortions, it is necessary to optimize the number of the transmitted programs (channels) and the number of the amplifiers connected in series from the Head End to any point of CDN. It is know that, with the increase of the number of programs, the level in the exit of every amplifier has to decrease with:

$$\Delta U_N = x \lg(N-1) \quad (1)$$

x = 10 with asynchronous of carrier frequencies
x = 7.5 with PLL
x = 5 with synchrony of the carrier frequencies (HRC – Harmonically Related Carrier)
N – nummber of the programes (channels).
Also, with the increase of the number of amplifiers connected in series it is necessary to decrease the output level of the respective amplifier by

$$\Delta U_M = y \lg M \quad (2)$$

M – number of amplifiers connected in series to the point, including which the output level of the signal of the amplifier (or following number of the amplifier) is measured.
y - coefficient, depending on the abstand used when designing.
y = 10 with IMA2 and CSOA;
y = 17 with XMA and IMA3;
y = 18 with CTBA;
y = 20 with CXMA;
A criterion is introduced, by which the values of the parameters N and M are optimized so that, with a given value of each of them (N or M), the other one can be defined, according to this criterion, and then the nonlinear distortion are minimal

[1]O. B. Panagiev is a system engineer at the Technical University of Sofia, e-mail: ctv@alpha.tu-sofia.bg

II. CRITERION AND ALGORITHMUS FOR DEFINING THE LIMITS POSSIBILITIES

1. Criterion for one amplifier

The maximum output level of the cable amplifier is defined by the formula

$$U_{out\,\max,1} = U_{out,2} - \Delta U_n [dB\mu V] \quad (3)$$

where $U_{out,2}$ is the output level of the amplifier with two programs (it is given in the catalogue of the producer of the amplifier).

The minimal level of the cable amplifier is given by the formula.

$$U_{out\,\min,1} = N_{75} + NF + G + \tfrac{S}{N}\ ,[dB\mu V] \quad (4)$$

where N_{75} is the channel thermal noise
NF- the noise figure of merit
G - Gain of the amplifier in dB.
S/N - Signal-to-noise ratio dB.

The difference between the maximum and minimum output levels is the criterion for minimal nonlinear distortions.

$$T_1 = U_{out\,\max,1} - U_{out\,\min,1,}[dB] \quad (5)$$

$$T_1 = U_{out,2} - x \lg(N-1) - N_{75} - NF - G - S/N, [dB] \quad (6)$$

this criterion is called tolerance and its connection with the other parameters of the system is given in fig.1.

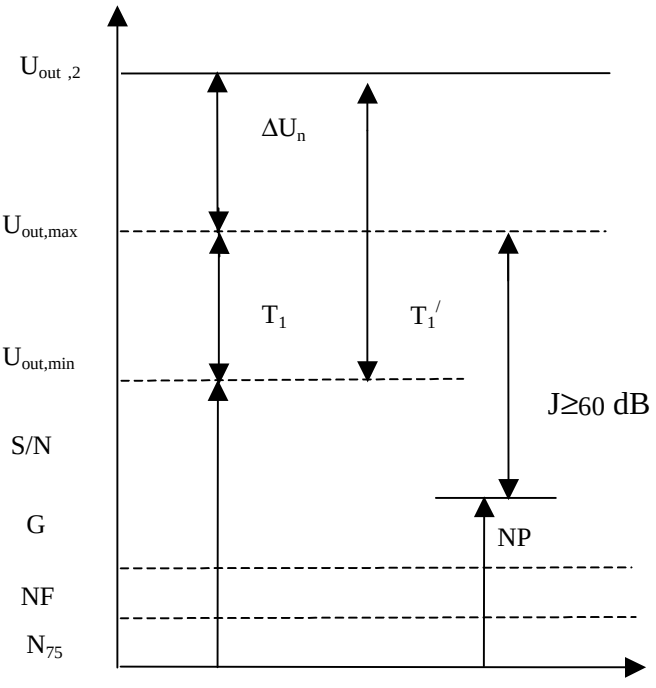

Fig.1.

2. Criterion for M amplifiers when there are a large number of cable amplifiers connected in series (fig.2), the formulas for their output level are.

$$U_{out\max,M} = U_{out,2} - \Delta U_N - \Delta U_M, [dB\mu V] \quad (7)$$

$$U_{out\min,M} = N_{75} + NF + G + S/N + 10\lg M, [dB\mu V] \quad (8)$$

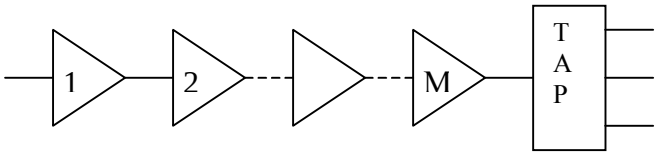

Fig .2.

$$T_M = U_{out\max,M} - U_{out\min,M}, [dB] \quad (9)$$

$$T_M = U_{out,2} - \Delta U_N - \Delta U_M - N_{75} - NF - G - S/N - \Delta U_{S/N}, [dB]$$

where $\Delta U_{S/N} = 10\lg M$.

$$T_M = T_1 - \Delta U_M - \Delta U_{S/N}. [dB] \quad (10)$$

By T_M=0 the maximum number of the amplifiers connected in series can be defined (fig.3), i.e.

$$U_{out\max,M} = U_{out\min,M} = U_{out,opt} \quad (11)$$

Then (10) turns into this:

$$0 = T_1 - \Delta U_M - \Delta U_{\frac{S}{N}}, [db] \quad (12)$$

$$T_1 = \Delta U_M + \Delta U_{\frac{S}{N}} = y\lg M + 10\lg M = (y+10)\lg M$$

i.e. (13)

$$= \lg M^{y+10}, [db]$$

$$T_1 = \lg M^{(y+10)}, [dB] \quad (14)$$

After the antilogaritming of (14), for the number of the amplifiers connected in series, it is derived.

$$M = 10^{\frac{T_1}{y+10}} \quad (15)$$

As in the expression for T_1 the number of programs is present, the connection between M and N is given by using (15), with defined parameters of the amplifiers.

3. Criterion for n channels in number.

For the derivation of an analytical expression for N, the expression (10) will be used, the equation calculated in relation to N, with the assumption of M=const.

$U_{out\max,M} = U_{out\min,M}$, in order to be $T_M = 0$. (16)

$$U_{out,2} - \Delta U_M - \Delta U_n = N_{75} + NF + G + \frac{S}{N} + \Delta U_{\frac{S}{N}} \quad (17)$$

$$U_{out,2} - \Delta U_M - N_{75} - NF - G - \frac{S}{N} - \Delta U_{\frac{S}{N}} = \Delta U_n \quad (18)$$

After replacing:

$$U_{out,2} - N_{75} - NF - G - \frac{S}{N} = T_1', \quad (19)$$

it is derived:

$$T_1' - T_1 = \Delta U_n, [dB] \quad (20)$$

It is replaced by /1/ in the above expression

$$T_1' - T_1 = x\lg(N-1), [dB] \quad /\kappa/ \quad (21)$$

the logarithmic equation is calculated in relation to N.

$$\frac{T_1' - T_1}{x} = \lg(N-1) \quad (22)$$

$$(N-1) = 10^{\frac{T_1' - T_1}{x}} \quad (23)$$

$$N = 10^{\frac{T_1' - T_1}{x}} + 1 \quad (24)$$

4. Algorithm

On the basis of the formulas derived above, an algorithm (fig.4) is created for defining of the boundary potentialities of the system in relation to N and m with.

$T_M = 0$ and the parameters of the amplifiers: $N_{75}, NF, G, S/N, U_{out\max,2} = U_{02}$.

It is assumed that the amplifiers are equal parameters.

In fig.5. is given a graphic of the dependence $T_M = func(N,M)$ in the three-dimensional space for the following values of:

N_{75}=2 dBμV; NF=6 dB; G=27 dB; S/N=46 dB; M=100; N=100; x=7.5; y=10.

The calculation of T_M and the drawing of the graphic is done by the program product MAPLE.

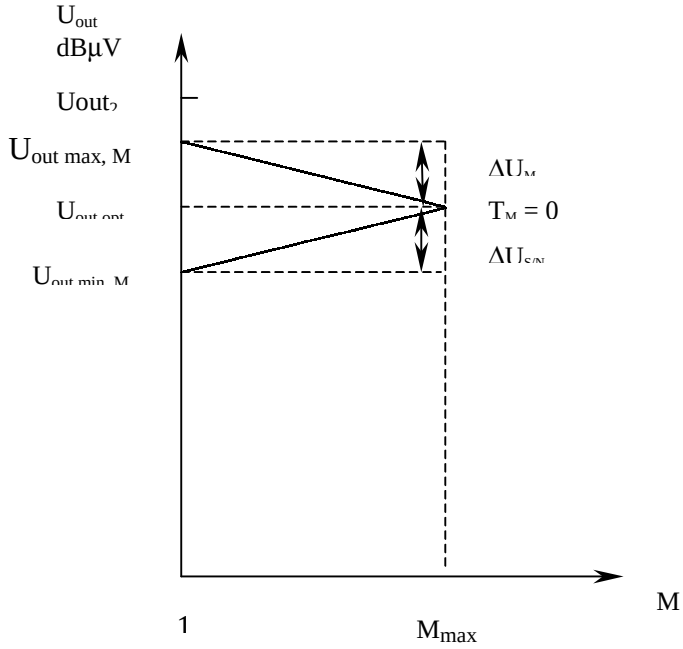

Fig. 3

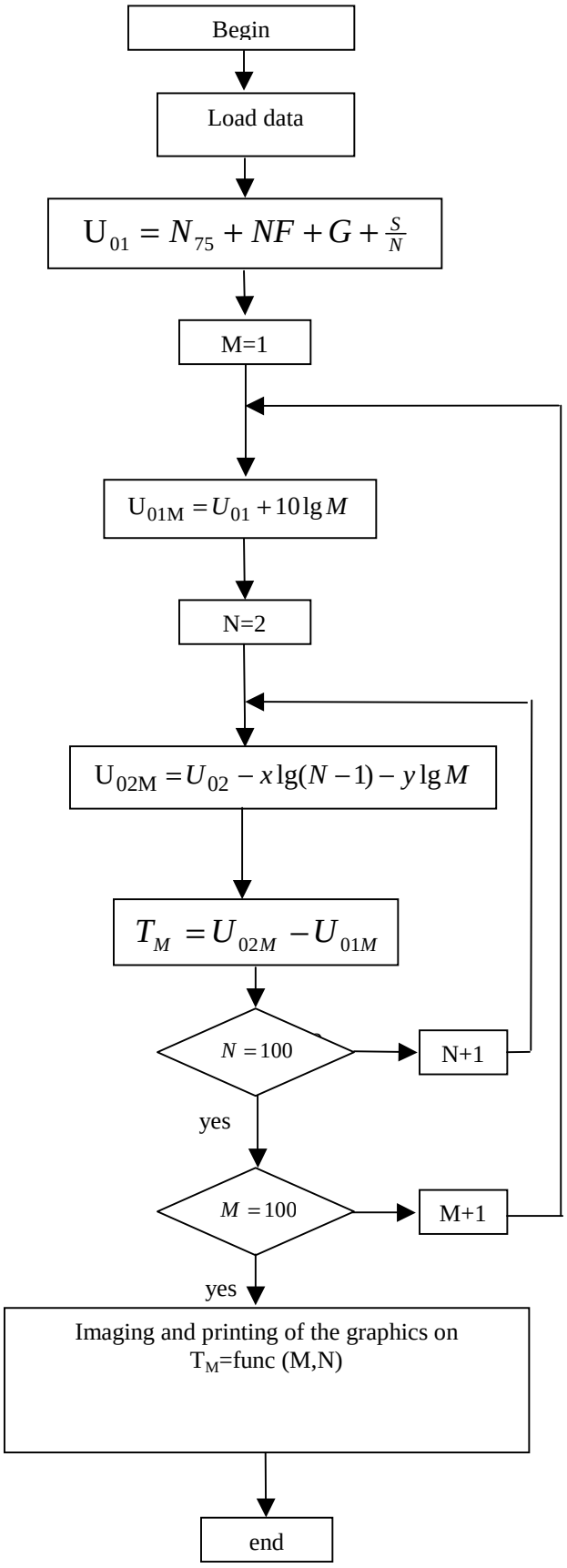

Fig.4.

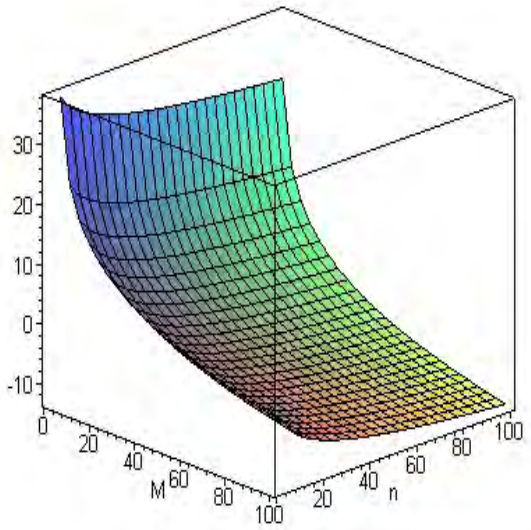

Fig.5.

III. Conclusion

The defining of maximum number of channels and amplifiers, lead to minimizing of the nonlinear distortions.

With the increase of the number of the channels in CATV, the maximum output level decreases.

By asynchronous carrier frequencies of image, transmitted in CATV, $U_{out,opt}$ decreases compared to HRC and IRC systems. To get a larger optimal level, it is necessary to work with an amplifier, the nominal output voltage of which is the highest possible and at the same time with a high gain.

The optimal output level of a given amplifier does not depend on its following number, or the number of amplifiers, but it depends on their parameters: nominal output voltage, Gain and noise figure of merit.

IV. References

[1] D. Dobrev , L.Yordanova," Receiving on radio- and TV programs by means satellite and cable", Electron – invest, 1996

[2] Kathrein antenen. Electronic CTV – U 11.92

[3] Simons K.A. The optimum gain for a CATV line amplifier. Proc. IEEE, 1970.

[4] www.analog.com

Application of the Volterra kernels for calculation of the crossmodulation and modulation distortions

Oleg Borisov Panagiev[1]

Abstract **- In this article the crossmodulation (CMD) and modulation distortions (MD) will be viewed, because they have more significant influence on the quality of the image. The sequences of Volterra will be used as a mathematical apparatus, particularly the Volterra kernels, which are the coefficients of the polynomial of third order in the mathematical model.**

Key words **- crossmodulation (CMD), modulation distortions (MD), nonlinear products, Volterra kernels, Hybrid Fiber Coaxial(HFC) network.**

I. INTRODUCTION

During the service of the contemporary cable television (CATV) systems under certain conditions [1] in the active devices, used in the system, non-linear products (HP) are emerging. Thus the subscribers receive except the useful signal also parasitic (disturbing) signals, which in a number of cases of high non-linearity are prevailing over the useful signal (especially in case of transmitting of digital signals, as well as digital and analogue – Hybrid Fiber Coaxial network-HFC). Non-linearity is approximated most often with polynomial of third power, because the theoretical researches through mathematical models are comparatively feasible. The availability of HP leads to worsening of the ratio C/N and hence to decreasing of BER, what is with special importance in transmitting of digital signals [2].

Crossmodulation (CMD) and modulation distortions (MD) will be viewed, because they have more significant influence on the quality of the image. The Volterra kernels, which are the coefficients of the polynomial of third order in the mathematical model, will be used as a mathematical apparatus,. For the active devices (mostly the cable amplifiers and laser diodes), the Volterra kernels are their transfer functions of the corresponding order for the particular combination frequency.

II. CHARACTER OF THE CROSSMODULATION AND MODULATION DISTORTIONS

When the non-linear distortions in the system are described with polynomials of third and upper order, at specific amplitude and phase ratios useful information (image) is transferred from the carrying frequency of one channel to the carrying frequency of another channel. In case of signals, transferring an image, on the screen of the television receiver are seen both the desired and the disturbing images - and at specific quantitative ratios - just the disturbing. In addition to problems in the brightness signal, such are displaying in the color-different signals, as the color is worsened, changed or lost at all. In a number of cases the horizontal and/or vertical synchronization could be disrupted.

Object of the present article further down will be the qualitative ratios in cases of cross-modulation and modulation distortions (products).

1. Crossmodulation distortions

They appear when the non-linearity of CATV systems is from third and upper order, i.e. n=3,4....Their study is made for one tested channel [1], through which is transferred just carrying signal (harmonious), and all other signal are modulated with one and the same frequency (fig.1). Let the tested channel frequency is f_s, and the modulated frequencies are $(f_r \pm \Omega)$, $r = 1,2,3....(N-1) \neq s$.

At fig.1a is shown part of the spectrum of CATV systems until the moment of occurrence of cross-modulation distortions. The tested channel has higher frequency.

Fig.1b illustrates the spectrum of CATV systems after occurrence of CMD. Around f_s two new signals appear with frequencies $f_r \pm \Omega$ that are the disturbing (unwanted) signals. The most severe case is presented when all signals have equal phases, i.e. amplitudes are summed up.

If we assume that n=3 than the inter-relation could be written as follows:

$$f_s \pm (f_r \pm \Omega) \pm f_r \qquad (1)$$

We open the parenthesis consecutively and perform the mathematical operations and as a result we get four new signals that fall into the test channel:

$$f_s + (f_r + \Omega) + f_r = f_s + f_r + \Omega + f_r = f_s + \Omega + 2f_r \qquad (2)$$

$$f_s + (f_r - \Omega) + f_r = f_s + f_r - \Omega + f_r = f_s - \Omega + 2f_r \qquad (3)$$

$$f_s - (f_r - \Omega) - f_r = f_s - f_r + \Omega - f_r = f_s + \Omega - 2f_r \qquad (4)$$

$$f_s - (f_r + \Omega) - f_r = f_s - f_r - \Omega - f_r = f_s - \Omega - 2f_r \qquad (5)$$

[1]O. B. Panagiev is a system engineer at the Technical University of Sofia, e-mail: ctv@alpha.tu-sofia.bg

$$f_s-(f_r+\Omega)+f_r=f_s-f_r-\Omega+f_r=f_s-\Omega \quad (6)$$

$$f_s-(f_r-\Omega)+f_r=f_s-f_r+\Omega+f_r=f_s+\Omega \quad (7)$$

$$f_s+(f_r+\Omega)-f_r=f_s+f_r+\Omega-f_r=f_s+\Omega \quad (8)$$

$$f_s+(f_r+\Omega)-f_r=f_s+f_r+\Omega-f_r=f_s+\Omega \quad (9)$$

Resulting frequencies obtained from formulae (2) ÷ (5) fall out of the tested channel and will not be object of further considerations.

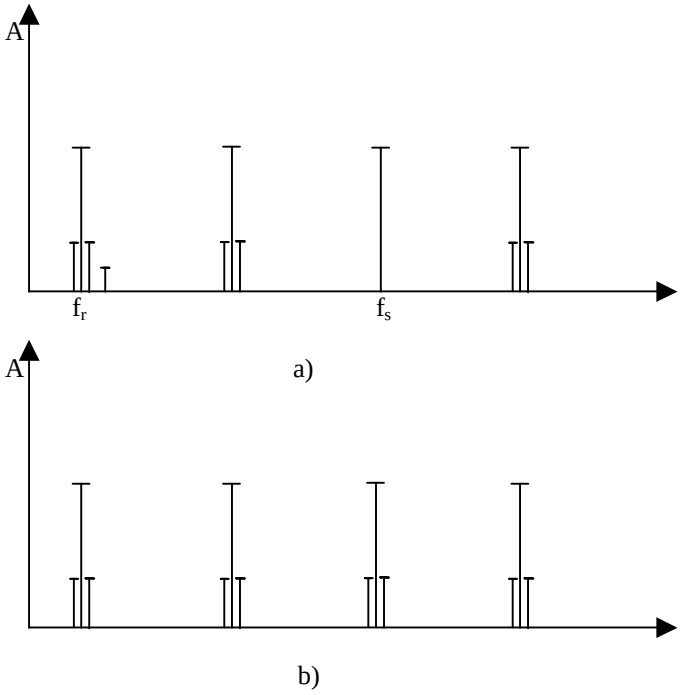

Fig.1.

Frequencies obtained from formulae (6) ÷ (9) fall into the tested channel and present nonlinear products of cross-modulation. In case of equal phases they superposition and their joint presentation is given on fig.1b.

2. Modulation distortions

These distortions arise when the carrier frequency (f_s) of a given channel aggregates with a signal from other channel with double modulation frequency (f_r), that is $f_s \pm 2\Omega$ (fig.2a.). These are wide-band distortions that influence both the tested channel and the adjacent channels. This fact is especially embarrassing for the present-day CATV systems where the channels are transmitted one next to other (channel beside channel) and especially for HFC network (fig.2b.), where analogue channels are transmitted up to about 470 MHz, and digital channels with M-QAM - above 470 MHz [2].

fig.2

When modulation distortions arise in CATV systems at n=3, the interrelation between the carrier frequency of the tested channel and the modulated carrier frequency of the disturbing channel is shown by the expression:

$$f_s \pm (f_r \pm \Omega) \pm (f_r - \Omega) \quad (10)$$

After consecutive performance of the mathematical operations in (10), four new signals are derived with frequencies as follows:

$$f_s+(f_r+\Omega)+(f_r-\Omega)=f_s+2f_r \quad (11)$$

$$f_s-(f_r+\Omega)+(f_r-\Omega)=f_s-2f_r \quad (12)$$

$$f_s+(f_r+\Omega)+(f_r-\Omega)=f_s+2\Omega \quad (13)$$

$$f_s-(f_r+\Omega)+(f_r-\Omega)=f_s-2\Omega \quad (14)$$

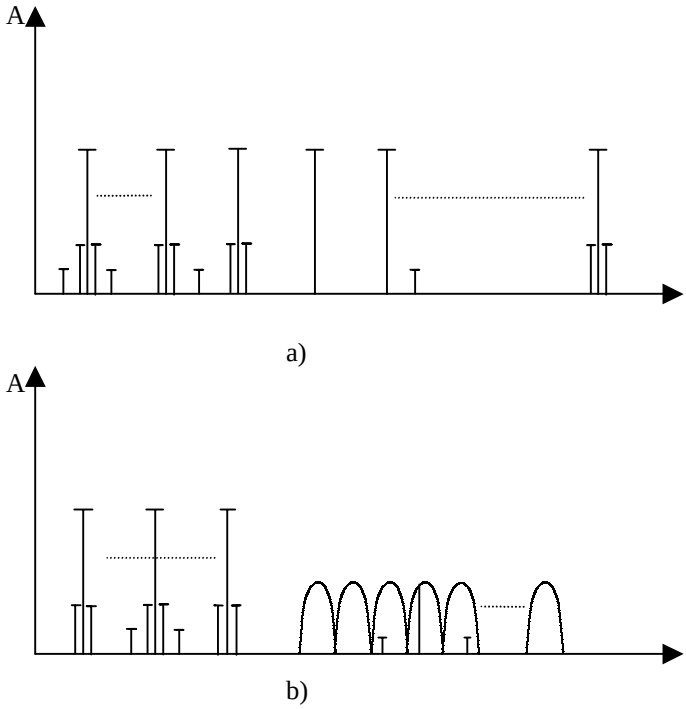

Fig.2.

Expressions (11) and (12) are of no interest because the signals are out of the tested channel while expressions (13) and (14) are signals with frequencies falling into the tested channel and its adjacent channels (fig.2).

III. CROSSMODULATION AND MODULATION DISTORTIONS AT TWO MODULATED FREQUENCIES FOR N=3

In order to determine CMD and MD during signal transmitting in CATV systems, trigonometrical transformations and Volterra kernels of the appropriate level will be used. Let non-linearity is described by polynomial of degree 3 (Eq.15) and the nonlinear products that fall into the tested channel are as a result of two modulated channels.

$$y(t)=\sum_{n=1}^{3} y(t)=y_1(t)+y_2(t)+y_3(t)=\sum_{n=1}^{3}|H_n(f)|x^n \quad (15)$$

where $|H_n(f)|$ is the Volterra kernel

$x(t)=\sum_{N=1}^{3} X_N(t)$ is the input signal with one non modulated and two modulated frequencies.

$$x_N(t)=A_s\cos\omega_s t+\sum_{r=1}^{2} A_r(1+m\cos\Omega t)\cos\omega_r t \quad (16)$$

Because CMD and MD are of third or higher order, only $y_3(t)$ is of interest

$$y_3(t)=|H_3(f)|x(t)^3 \quad (17)$$

$$y_3(t)=|H_3(f)|\begin{bmatrix} A_s\cos\omega_s t+ \\ A_1(1+m\cos\Omega t)\cos\omega_1 t+ \\ A_2(1+m\cos\Omega t)\cos\omega_2 t \end{bmatrix}^3 \quad (18)$$

Direct raise to the third power of the expression enclosed in parentheses leads to complex and numerous addends. For this reason the author proceed in the following way:

- addends in (18) are replaced as follows:

$$A_s\cos\omega_s t=a \quad (19)$$

$$A_1(1+m\cos\Omega t)\cos\omega_1 t=b \quad (20)$$

$$A_2(1+m\cos\Omega t)\cos\omega_2 t=c \quad (21)$$

- the expression enclosed in parentheses is raised to the third power and (18) take the following form:

$$y_3(t)=|H_3(f)|\begin{pmatrix} a^3+b^3+c^3+3a^2b+3a^2c+ \\ 3b^2a+3b^2c+3c^2b+6abc \end{pmatrix} \quad (22)$$

- Each addend from the parentheses in (22) is calculated separately by using the relations from trigonometric formulae. New replacements are made in order to simplify and visualize mathematical operations. All addends that are not object of this article are omitted from the final results.

1. CROSSMODULATION DISTORTIONS

$$[b]^3_{CMD}=\tfrac{9}{8}A_1 m\left(A_1^2+m^2\right)\cos(\omega_1\pm\Omega)t \quad (23)$$

$$[c]^3_{CMD}=\tfrac{9}{8}A_2 m\left(A_2^2+m^2\right)\cos(\omega_2\pm\Omega)t \quad (24)$$

$$\left[3b^2c\right]_{CMD}=\tfrac{9}{3}A_1^2A_2\left(4m+m^3\right)\cos\left(2\omega_1\pm\omega_2\pm\Omega\right)t+\tfrac{3}{16}A_1^2A_2\left(12m+m^3\right)\cos\left(2\omega_2\Omega\right)t \quad (25)$$

$$\left[3c^2b\right]_{CMD}=\tfrac{9}{32}A_2^2A_1\left(4m+m^3\right)\cos\left(2\omega_2\pm\omega_1\pm\Omega\right)t+\tfrac{3}{16}A_2^2A_1\left(12m+m^3\right)\cos\left(2\omega_1\pm\Omega\right)t \quad (26)$$

$$\left[3b^2a\right]_{CMD}=\tfrac{3}{4}A_1^2A_2 m\cos\left(2\omega_1\pm\omega_s\pm\Omega\right)t+\tfrac{3}{2}A_1^2A_s m\cos\left(2\omega_s\pm\Omega\right)t \quad (27)$$

$$\left[3c^2a\right]_{CMD}=\tfrac{3}{4}A_2^2A_3 m\cos\left(2\omega_2\pm\omega_s\pm\Omega\right)t+\tfrac{3}{2}A_2^2A_s m\cos\left(2\omega_s\pm\Omega\right)t \quad (28)$$

$$\left[3a^2b\right]_{CMD}=\tfrac{3}{8}A_s^2A_1 m\cos\left(2\omega_s\pm\omega_1\pm\Omega\right)t+\tfrac{3}{4}A_s^2A_1 m\cos\left(2\omega_1\pm\Omega\right)t \quad (29)$$

$$\left[3a^2c\right]_{CMD}=\tfrac{3}{8}A_s^2A_2 m\cos\left(2\omega_s\pm\omega_2\pm\Omega\right)t+\tfrac{3}{4}A_s^2A_2 m\cos\left(2\omega_2\pm\Omega\right)t \quad (30)$$

$$[6abc]_{CMD}=\tfrac{3}{2}A_sA_1A_2 m\cos\left(\omega_s\pm\omega_1\pm\omega_2\pm\Omega\right)t \quad (31)$$

Amplitudinal and frequency ratios obtained in expressions from (23) to (31) are CMD in the system for assigned initial conditions. Most of them are out of the tested channel, others are there only for particular conditions and the rest are in the tested channel.

Analyzing (23), (24) and the second addends in (25), (26), (29) and (30) we see that CMD concern the channels whose signals are modulated that is they are of no interest for the current work.

Analyzing the first addends in (25) and (26), a conclusion could be made that under some conditions these CMD could be in the tested channel. These conditions are as follows:

$$2\omega_1\pm\omega_2=\omega_s \quad (32)$$

$$2\omega_2\pm\omega_1=\omega_s \quad (33)$$

The second addends in (27) and (28) fall completely in the tested channel and represent the main CMD. Considering this fact, expression (22) get the following form:

$$y_{CMD}(t)=\tfrac{3}{2}A_s\left(A_1^2+A_2^2\right)m|H_3(\omega_s\pm\Omega)|\cos(\omega_s\pm\Omega)t \quad (34)$$

When conditions (32) or (33) are fulfilled, the generalized expression for CMD is:

$$y_{CMD}(t)=\tfrac{3}{2}\left[\left(A_1^2+A_2^2\right)m+\tfrac{3}{16}A_{1(2)}^2A_{2(1)}\left(4m+m^3\right)\right]|H_3(\omega_s\pm\Omega)|\cos(\omega_s\pm\Omega)t \quad (35)$$

2. MODULATION DISTORTIONS

In the solution of expression (22) along with the other non-linear distortions there are modulation distortions distributed the following way in the addends:

$$\left[b^3\right]_{MD}=\tfrac{9}{16}m^2A_1{}^3\cos(\omega_1\pm2\Omega)t \quad (36)$$

$$\left[c^3\right]_{MD}=\tfrac{9}{16}m^2A_2{}^3\cos(\omega_2\pm2\Omega)t \quad (37)$$

$$\left[3b^2c\right]_{MD}=\tfrac{9}{16}A_1^2A_2m^2\cos\left(2\omega_1\pm\omega_2\pm2\Omega\right)t+\tfrac{9}{8}A_1^2A_2m^2\cos\left(2\omega_2\pm2\Omega\right)t \quad (38)$$

$$\left[3c^2b\right]_{MD}=\tfrac{9}{16}A_2^2A_1m^2\cos\left(2\omega_2\pm\omega_1\pm2\Omega\right)t+\tfrac{9}{8}A_2^2A_1m^2\cos\left(2\omega_1\pm2\Omega\right)t \quad (39)$$

$$[3b^2a]_{MD} = \frac{3}{16}A_1^2A_s m^2\cos(2\omega_1 \pm \omega_s \pm 2\Omega)t + \frac{3}{8}A_1^2A_s m^2\cos(2\omega_s \pm 2\Omega)t \quad (40)$$

$$[3c^2a]_{MD} = \frac{3}{16}A_2^2A_s m^2\cos(2\omega_2 \pm \omega_s \pm 2\Omega)t + \frac{3}{8}A_2^2A_s m^2\cos(2\omega_s \pm 2\Omega)t \quad (41$$

$$[6abc]_{MD} = \frac{3}{8}A_1A_2A_3 m^2\cos(\omega_s \pm \omega_1 \pm \omega_2 \pm 2\Omega)t \quad (42)$$

Modulation products (MP) in expressions (36), (37) and (42) are out of the tested channel but the ones in (36) and (37) fall in the channels adjacent to the channels with modulated carrier, and the non-linear products in (42) in some cases could fall out of CATV systems frequency range. Assertions concerning MP in expression (42) apply fully to the first addends in expressions (38), (39), (40) and (41). Only in (38) and (39) under some conditions MP could fall in the spectrum of the tested channel.

The main modulation products that fall into the tested channel are given by the second addends in (40) and (41).

Taking into account the above considerations it could be written:

$$y_{MD}(t) = \frac{3}{8}A_s\left(A_1^2 + A_2^2\right)m^2\left|H_s(\omega_s \pm 2\Omega)\right|. \cos(\omega_s \pm 2\Omega)t \quad (43)$$

When condition /32/ or /33/ are fulfilled, the generalized expression for MD is the one below:

$$y^*_{MD}(t) = \frac{3}{8}\left[A_s\left(A_1^2 + A_2^2\right) + 3A_1^2A_2\right]m^2 \left|H_3(\omega_s \pm 2\Omega)\right|\cos(\omega_s \pm 2\Omega)t \quad (44)$$

IV. CONCLUSION

Expressions /35/ and /44/ show the products of CMD and MD of third order. Obtaining NP (of higher order) that are of special importance for HFC network, by trigonometric transformations is rather complex and sluggish calculation process.

A method will be proposed in a subsequent publication that uses the relation between inter-modulation, cross-modulation and modulation distortions, which is interpreted using Volterra kernels applied during calculation of corresponding coefficients.

REFERENCES

[1] O.B Panagiev, ”Nonlinear products, spring up active devices by transferring of modulated video signals”, Proc.of Intern. Scient. Confer. EIST’ 2001, vol.II, Bitola, June 7-8, 2001

[2] O.B. Panagiev, “Some Capabilities of the Optical Technologies in the Cable Television Systems”.,IX NSASC "Electronics'2000, Sozopol 20-22 sept. 2000.

[3] K.Konov, “Digital television”, Dios,Sofia,2004.

[4] A. Oppenheim, “Signals and systems”,Prentice Hall,Inc.,Englewood Cliffs, New Jersey,1978.

[5] www.mathworld.wolfram.com

Magnetic Field Influence on Some Microwave Characteristics of Rubber Based Thin Films

R.I. Shtarkova[1], I.V. Petrova[2], N.T. Dishovsky[3], G.I. Krunev[4]

Abstract - **Thin films based on chloroprene rubber (CR) unfilled and filled with magnetite have been produced by magnetic modification method. Reflection and attenuation coefficients of the experimental films obtained were measured in the 8 - 12 GHz frequency range.**

Keywords - **Microwave Absorber, Magnetic Modification**

I. INTRODUCTION

The development and wide spread usage of microwave absorbers starts in the middle 30s of the previous century. The first absorber was patented in 1936 in Holland. In the Second World War absorbing materials were used for camouflage of military objects, especially submarines. After 1955 microwave absorbers start their market penetration. Nowadays microwave absorbers are mainly used for:

- protection of the environment and people from the adverse influence of high frequency electromagnetic radiation due to industrial and other sources;
- technical purposes like eliminating undesired signals and noise in radio- and television technique; in anechoic chambers;
- antiradar camouflage of mobile and fixed military structure and objects for reducing or altering the radar signature.

The main microwave absorbers' requirements are minimum reflection and maximum absorption of the electromagnetic energy. The ideal absorber has broad frequency range of the absorbing energy, excellent weather stability, light weight, characteristic reliability and capability to work in a broad temperature range.

Most of the contemporary microwave absorbers are produced of dielectric polymer matrix and specific functional fillers with high values of the imaginary part of the complex dielectric permittivity and magnetic permeability that absorb high frequency energy.

Nowadays in the making of microwave absorbers a lot of methods for physical impact exist, which help improving the properties of the final material. Such a method is so called magnetic modification, which modifies the properties of the material using external magnetic field. In our previous paper [1] a lot of properties of magnetically modified CR based films were investigated.

[1]R.I. Shtarkova is with Technical University, 8 Kl. Ohridsky blvd, 1000 Sofia, E-mail: rchtarko@tu-sofia.bg
[2]I.V.Petrova is with University of Chemical Technology and Metallurgy, 8 Kl. Ohridsky blvd, 1000 Sofia, E-mail: irena_parvanova@yahoo.com
[3]N.T. Dishovsky is with University of Chemical Technology and Metallurgy, 8 Kl. Ohridsky blvd, 1756 Sofia, E-mail: dishov@uctm.edu
[4]G.I.Krunev is with Tumbleweed Communications, 8 Khan Asparuh, 1000 Sofia, E-mail: georgi.krounev@tumbleweed.com

The purpose of the present paper is to investigate the magnetic field influence on the reflection and attenuation coefficients of unfilled and magnetite filled CR based films.

II. SAMPLE PREPARATION

Chloroprene Rubber Baypren 320 (product of Bayer) was used as rubber matrix. Natural magnetite (particle size below 10 μ) was used as absorption active filler. The mixing process of the rubber with the filler was carried out by Brabender Plasticorder at 50ºC.

The rubber-filler ratio was 10-60 phr. The films (average thickness of 100 μ) were prepared from 2 mass % 1,2-dichloroethane solution of the rubber-filler composition. A paper with special treated surface was used as a substrate. Magnetic field with an induction of 0,60 T were applied for the period of 20 minutes during the film formation process. The magnetic field induction was controlled by teslameter. The samples were placed parallel and perpendicularly to the magnetic field lines of force.

Special experimental equipment was used for creation of constant magnetic field (Fig.1). The samples were conditioned for the period of 72 hours (for evaporation of the solvent and achievement of constant weight of the samples) before starting the measurement procedure.

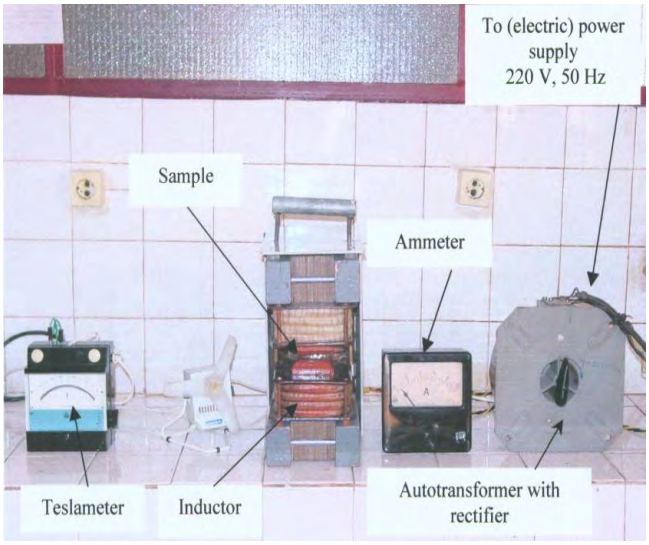

Fig.1. Experimental equipment for creation of constant magnetic field

III. SAMPLE TESTING

The scheme used to perform the measurements of the reflection coefficient (Fig.2) consists of:

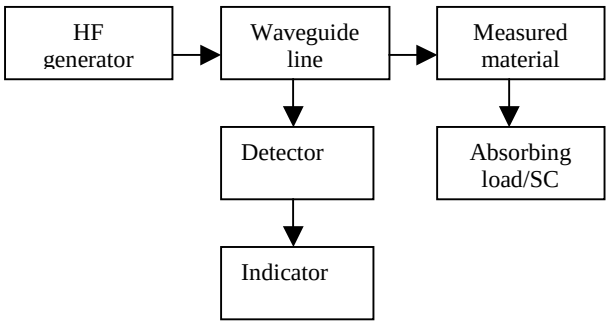

Fig.2. Experimental equipment for measurements of the reflection coefficient

The usage of short circuit (SC) is caused by the fact that most of the materials will be used over metal surfaces. In the same time measuring of the radio transparent materials (with few attenuation and suitable characteristic resistance) with short circuit at the end of the line will cause a lot of reflection coefficient. To avoid this the same measurement should be performed with absorbing load at the end of the line.

Measurements of the attenuation coefficient were performed in waveguide line (Fig.3):

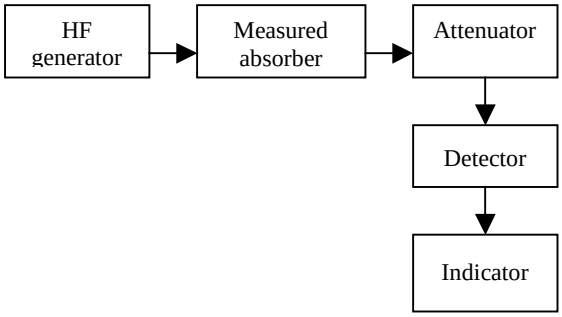

Fig.3. Experimental equipment for measurements of the attenuation coefficient

Measurement steps:

1. Without any absorber and using etalon power of the generator is measured the zero level of the indicator.
2. The absorber is placed and the level of the indicator changes.
3. The absorber is removed and using an attenuator the power of the generator's electromagnetic radiation is reduced while reaching the same level of the indicator.
4. The transition factor can be calculated using the attenuator's scale:

$$g = 10 \lg \frac{P_1}{P_2} [dB] \qquad (1)$$

Here P_1 is the passed through the absorber power and P_2 is the generated initial power.

The attenuation of the absorber can be calculated using the following formula:

$$\Delta\alpha = 10 \lg \frac{P_1}{P_2 \left(1 - p^2\right)} [dB] \qquad (2)$$

Here p is the reflection coefficient.
The relative attenuation depending on the thickness of the absorber is:

$$\alpha = \frac{\Delta\alpha}{d} [dB / mm] \qquad (3)$$

Here d is the thickness of the absorber in millimeters.

IV. RESULTS AND DISCUSSION

The external magnetic field influence on the polymer matrix properties is shown measuring test simples of CR without active fillers introduced in the matrix. Two types of samples were measured – the first one - magnetically modified and the second - with the same composition, but without magnetic treatment. In the 8 - 12 GHz frequency range the reflection and absorption coefficients of the samples are shown in figures 4-5:

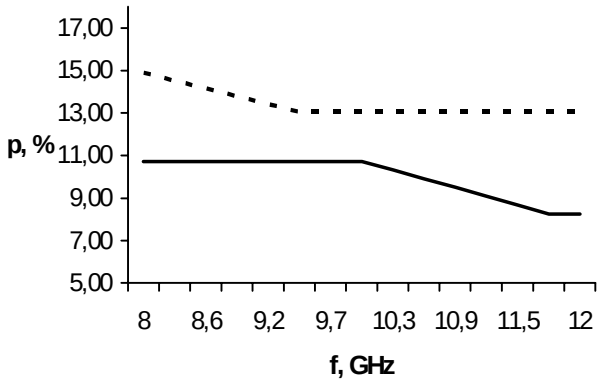

Fig.4 Reflection coefficient frequency dependence for the samples prepared without (…..) and with (____) magnetic field application during their preparation

It may be seen from the figure that the reflection coefficient of the magnetically modified CR is 20% lower than the coefficient of the control matrix.

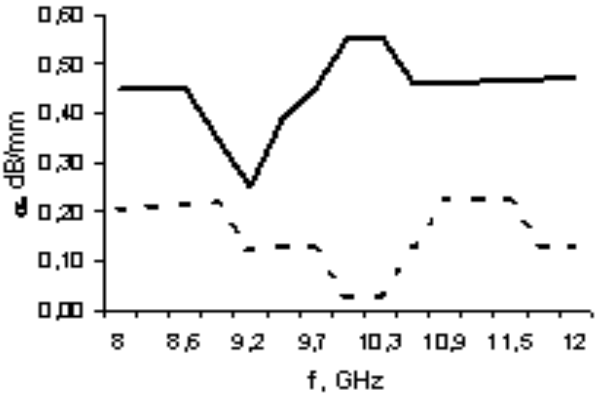

Fig.5. Absorption coefficient frequency dependence for the samples prepared without (…..) and with (____) magnetic field application during their preparation

The absorption coefficient of the magnetically modified matrix has increased two times in compared to those of the control matrix. It is clear that the magnetic field demonstrates an orientation activity on the rubber macromolecules, containing polar functional groups and sensitive to magnetic field action chemical bonds. It is due to the fact that macromolecules containing such type of structures have exactly fixed values of their magnetic susceptibility [2]. The applied external magnetic field changes the susceptibility of these macromolecules and as a result the macromolecules may be easily orientated in the direction of magnetic field lines of force [2]. The orientation effects, described also in our previous publications [1] cause structural and supermolecular microheterogeneities strongly influencing on all properties of the rubber [3], including the ratio between crystal and amorphous phase. In the absence of magnetic field the amorphous phase is localized in large areas, irregular distributed. When an external magnetic field is applied the dimensions of crystal and amorphous domain decrease and increase their numbers. A higher degree of organization and an increasing of the amount of the crystal phase may be observed as a final result. This is the reason for the changes observed in the values of the absorption and reflection coefficients.

The influence of the magnetic modification on the microwave absorbers may be assessed also measuring CR based samples filled with magnetite. The effects here mainly concern the influence of the magnetic field on the magnetite distribution in the rubber matrix. That material is magnetically soft and its particles orientation is highly dependant on external magnetic fields. The measurements were performed in a waveguide line. There were three measured absorbing samples - one control and two magnetically modified. For the first modified sample the direction of the external magnetic field is parallel with the H_{10} wave in the waveguide. For the second sample it's perpendicular (Fig.6).

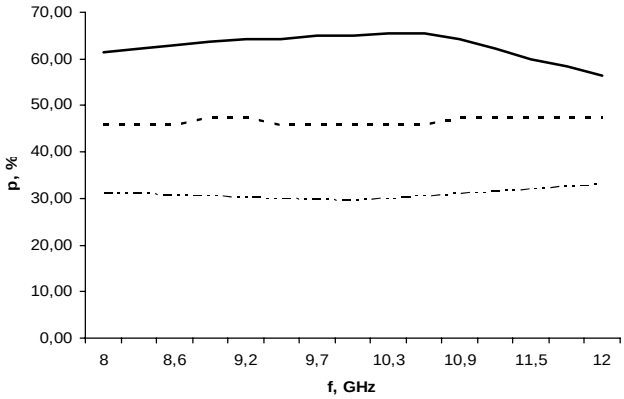

Fig.6. Reflection coefficient frequency dependence for the samples prepared without (…..) and with magnetic field application parallel (.._.. _..) and perpendicular (____) during their preparation.

The reflection coefficient of the sample modified with perpendicular field is higher than those of the non modified simple. The reflection coefficient of the sample modified with parallel field is lower than those of the non modified sample.
The absorption coefficient - frequency dependence of the samples investigated is shown on Fig. 7.

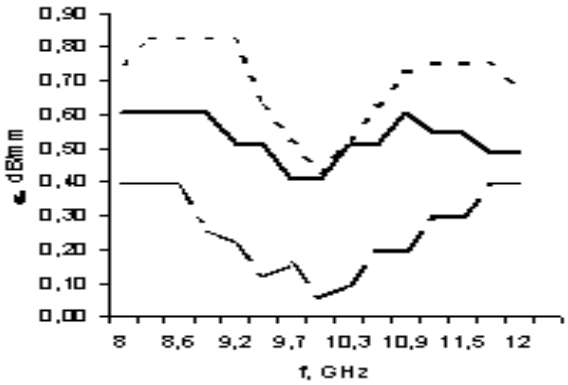

Fig.7 Absorption coefficient frequency dependence for the samples prepared without (…..) and with magnetic field application parallel (.._.. _..) and perpendicular (____) during their preparation.

The absorption coefficient of the no modified sample is the highest. The sample modified with a parallel magnetic field has the lowest absorption.
The application of magnetic field during sample preparation affects the filler particles ordering causing secondary structures formation guided by the direction of the magnetic field lines of force (Fig.8). That way the properties of the

material (including microwave ones) could be changed in a direction assigned in advance.

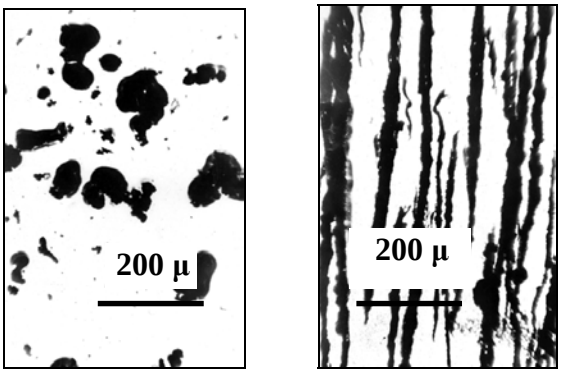

a) 10 phr Fe_3O_4, H=0 b) 10 phr Fe_3O_4, H>0

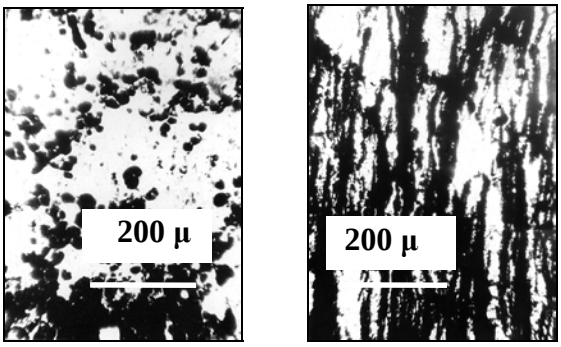

c) 50 phr Fe_3O_4, H=0 d) 50 phr Fe_3O_4, H>0

Fig.8. Optical microscope pictures (x 70) of CR films, containing different concentrations of magnetite (H=0, without magnetic field application; H>0- with magnetic field application)

V. Conclusion

All measurements performed illustrate how dependable are the properties of the rubber investigated from the direction of the external magnetic field applied during their modification. It causes artificial structuring of the dispersed particles of the filler in chain structures oriented in the direction of the magnetic field. This change the properties of the composite material and it assessed as anisotropy. More complete interpretation of these processes is possible in the case of measure the imaginary part of the complex dielectric permittivity and magnetic permeability in different directions, but that is out of sphere of this work.

References

[1] I.Petrova, N. Dishovsky, R. Dimitrov, “Structure Investigations of Chloroprene Rubber Thin Films Modified in Constant Magnetic Fields”, Technomer 2003, 13-15 November 2003, Chemnitz, Germany, ISBN 3-00-012510-8

[2] 2. A. Alekseev, A. Kornev, “Magnitnie elastomeri”, Moscow, Khimia, 1987 (in Russian)

[3] U. Molchanov, “Mehanika Polimerov”, 4 (1978) 583 (in Russian)

Model of a Differential BPSK Decoder with Matched Filter Included, Providing a Minimal ISI

Georgi V. Stanchev[1] and Marin S. Marinov[2]

Abstract– **This paper sets out a model of a differential BPSK decoder which includes a matched filter in order to provide a minimal inter-symbol interference and maximal signal to noise ratio at its output. This model is designed to reject the phase difference between the received carrier and the recovered one, too. The influence of the roll-off factor and impulse response limiting over system performance is indicated.**

Keywords– **differential BPSK decoder, minimal inter-symbol interference, matched filter, phase difference rejection.**

I. INTRODUCTION

The digital methods for information exchange have established themselves in the field of communications because of their decisive superiority to analogue ones. Besides building of LAN and WAN wire networks, these methods are increasingly employed in mobile and satellite communications [1]. One of the main criteria of information transfer quality is the error probability, and values of this criterion depend on transmitted information – voice; images; video and data [4]. Because of increasing requirements to quality of the communications services it is necessary appropriate methods for digital signal processing to be researched. Attention should be paid to the special features of propagation medium as well as to the enforced limits on the frequency resources. Some useful methods are differential encoding/decoding and matched filtering. To obtain good results the models of transmitter and receiver should be designed and considered together [5].

II. TRANSMITTER MODEL

The diagram shown in Fig.1 describes frequency band limiting of the transmitted digital signals in conditions of limited frequency resources.

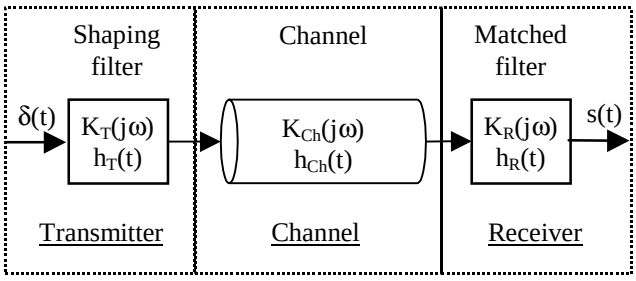

Fig.1. Band limiting of transmitted digital signals

.

The following notations are used in Fig.1: $K_T(j\omega)$ and $h_T(t)$ are respectively the frequency and the impulse responses of the shaping filter in the transmitter; $K_{Ch}(j\omega)$ and $h_{Ch}(t)$ are respectively the frequency and the impulse responses of the channel; $K_R(j\omega)$ and $h_R(t)$ are respectively the frequency and the impulse responses of the matched filter in the receiver.

The lack of inter-symbol interference (ISI) can be obtained if the impulse response of whole system is [3, 4]:

$$h(t) = \frac{\sin\left(\pi\frac{t}{T_C}\right)\cos\left(\pi\rho\frac{t}{T_C}\right)}{\pi\frac{t}{T_C}\left[1-\left(2\rho\frac{t}{T_C}\right)^2\right]}, \quad (1)$$

where ρ is the roll-off factor with values from 0 to 1, and T_C is the period of the impulse sequence. This impulse response corresponds to the raised-cosine frequency response of whole system:

$$K(f) = \begin{cases} 1, & \frac{f}{R_C}-\frac{1}{2} < -\frac{\rho}{2} \\ \cos^2\left[\frac{\pi}{2\rho}\left(\frac{f}{R_C}-\frac{1}{2}+\frac{\rho}{2}\right)\right], & \left|\frac{f}{R_C}-\frac{1}{2}\right| \le \frac{\rho}{2} \\ 0, & \frac{f}{R_C}-\frac{1}{2} > \frac{\rho}{2} \end{cases}, \quad (2)$$

where R_C is the rate of the impulse sequence and

$$K(f) = K_T(f)K_{Ch}(f)K_R(f). \quad (3)$$

If $K_{Ch}(f)$ is much wider than $K_T(f)$ and $K_R(f)$ the following approximation takes place:

$$K(f) \approx K_T(f)K_R(f). \quad (4)$$

The matched filtering in the receiver requires that:

$$K_T(f) = K_{0T}K_0(f); \qquad K_R(f) = K_{0R}K_0(f), \quad (5)$$

and

$$h_T(t) = K_{0T}h_0(t); \qquad h_R(t) = K_{0R}h_0(t). \quad (6)$$

Without loss of any generality it can be assumed that $K_{0T} = K_{0R} = 1$ and consequently $K_0(f) = \sqrt{K(f)}$. The impulse response, as it is shown in [2], can be derived by means of Fourier transform and Eq.7 and Fig.2 describe it:

[1]Georgi V. Stanchev, PhD is with the Aviation Faculty, National Military University, 5856 Dolna Mitropolia, Bulgaria, e-mail: gstanchev@af-acad.bg.

[2]Marin S. Marinov, PhD is with the Aviation Faculty, National Military University, 5856 Dolna Mitropolia, Bulgaria, e-mail: mmarinov2000@yahoo.com.

$$h_0(t) = R_C \frac{\sin\left[\pi(1-\rho)\frac{t}{T_C}\right] + 4\rho\frac{t}{T_C}\cos\left[\pi(1+\rho)\frac{t}{T_C}\right]}{\pi\frac{t}{T_C}\left[1-(4\rho\frac{t}{T_C})^2\right]}. \quad (7)$$

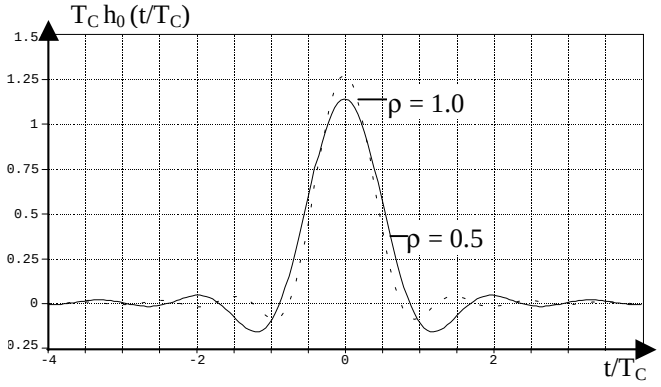

Fig.2. Impulse responses of the shaping and matched filters.

It is important to keep the joint phase characteristic of the shaping and matched filters linear.

These filters are not realizable because their impulse responses are infinite and they are not causal. An window-function *w(t)* is used in order to limit the impulse response:

$$w(t) = \begin{cases} 1 & , -kT_C \le t \le kT_C \\ 0 & , -kT_C > t > kT_C \end{cases} \quad (8)$$

and impulse response of a realizable filter is given by:

$$H(t) = h_0(t)w(t). \quad (9)$$

The particular impulse response that every single impulse b_n causes on the shaping filter output is:

$$H_n(t) = h_0(t - nT_C)w(t - nT_C)b_n, \quad n = 0, \pm 1, 2, 3, ... \quad (10)$$

The block-diagram, where the general processes in the transmitter are described, is shown in Fig. 3. The transmitter includes a differential encoder, a shaping filter with impulse response *H(t)* and a modulator.

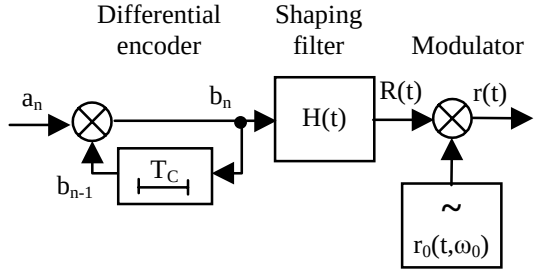

Fig.3. Model of the transmitter.

The total impulse response at the shaping filter output is:

$$R(t) = \sum_{n=-\infty}^{\infty} H_n(t);$$
$$R(t) = \sum_{i=-[k]}^{[k+1]} H_{n+i}(t), \quad nT_C \le t \le (n+1)T_C. \quad (11)$$

At the modulator output, where the signal is up-converted to the carrier frequency, the output signal is:

$$r(t) = R(t)\cos(\omega_0 t). \quad (12)$$

For the time being a single path Gaussian channel is presupposed.

III. Receiver model

The examined model of the receiver includes the following processes: band converting; matched filtering; sampling and differential decoding. Because of non-coherent band converting, two channels of signal processing, an in-phase I-channel and a quadrature Q-channel, are used – Fig. 4. The carrier is recovered at accuracy to phase.

$$r_I(t) = 2\cos(\omega_0 t + \psi); \qquad r_Q(t) = 2\sin(\omega_0 t + \psi). \quad (13)$$

After down converting of the received signal *r(t)* into base-band signal it becomes $R_I(t)$ and $R_Q(t)$ respectively in the in-phase and quadrature channels:

$$R_I(t) = R(t)\cos\psi + R(t)\cos(2\omega_0 t + \psi);$$
$$R_Q(t) = R(t)\sin\psi + R(t)\sin(2\omega_0 t + \psi). \quad (14)$$

The matched filters have the same limited impulse response as the shaping filter in the transmitter. The signals at the filter outputs are:

$$S_I(t) = R_I(t) * H(t) = \int_{t-kT_C}^{t+kT_C} R_I(\tau)H(t-\tau)d\tau;$$
$$S_Q(t) = R_Q(t) * H(t) = \int_{t-kT_C}^{t+kT_C} R_Q(\tau)H(t-\tau)d\tau. \quad (15)$$

In essence the matched filter is low-pass filter and components with doubled carrier frequency are not presented at its output. In fact the roll-off factor of 0 is corresponding to an ideal low-pass filter. It is taken for granted that the synchronization system is working in an ideal manner. Moreover the symmetric impulse response of the applied filters, i.e. *H(t)=H(-t)*, is taken into consideration. Then the signal of the model output, at the moments of interest, is:

$$S(nT_C) = S_I(nT_C)S_I[(n-1)T_C] + S_Q(nT_C)S_Q[(n-1)T_C] =$$
$$= (\cos^2\psi + \sin^2\psi)\int_{(n-k)T_C}^{(n+k)T_C} \sum_{i=-[k]}^{[k+1]} H_{n+i}(\tau)H(\tau - nT_C)d\tau \quad (16)$$
$$\times \int_{(n-1-k)T_C}^{(n-1+k)T_C} \sum_{i=-[k]}^{[k+1]} H_{n-1+i}(\tau)H[\tau - (n-1)T_C]d\tau.$$

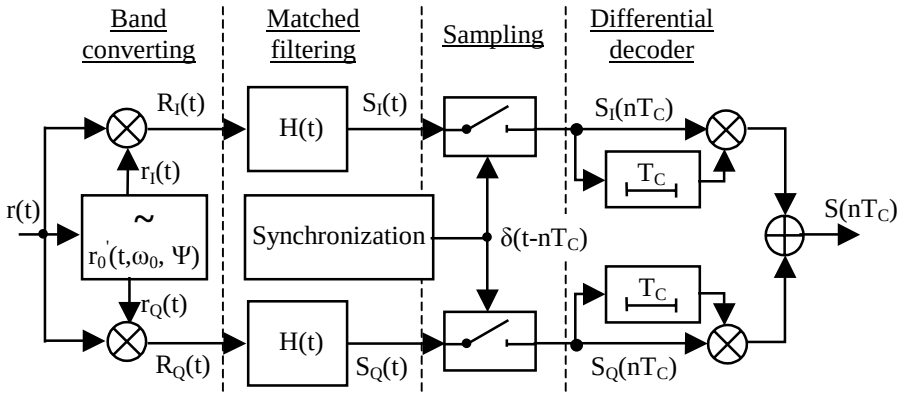

Fig.4. Model of the receiver.

In this way the rising to the second power of the signals in the channels, in order to reject the random phase difference between the received and recovered carrier, and the differential decoding are combined in one and the same process.

IV RESEARCHES

In order to study the models, described above, two computer programs were created. Walsh sequences were used as a kind of impulse sequence and the influence of the roll-off factor and "windowing" to system performances was examined.

Some of the results are presented in the following figures.

In the Fig. 5 the magnitude of output signal is shown, when the volume of the Walsh functions is 8, the roll-off factor is 0.5 and the relative window width is 6. Every element of the sequence is evaluated separately. Minimal, maximal and average magnitudes of the output signal are calculated, too.

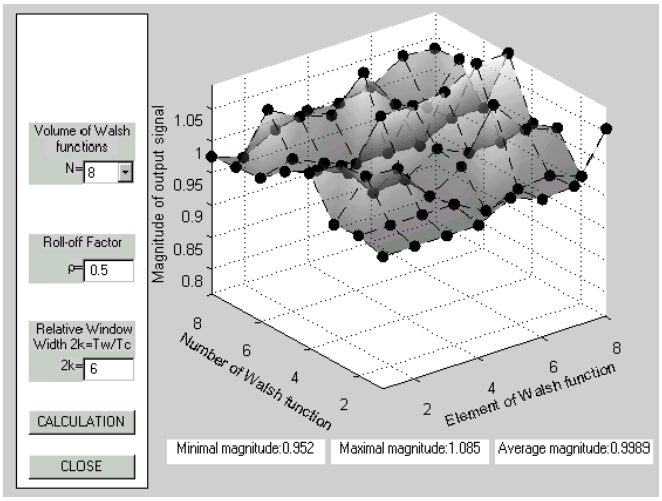

Fig.5. Magnitude of the output signal.

The program interface allows other values of the Walsh functions volume, the roll-off factor and the relative window width to be examined. The studies showed that the magnitude of the output signal depends on the values of the roll-off factor and the window width. For example if only the roll-off factor is changed to 0, the minimal magnitude becomes 0.4124, maximal magnitude becomes 1.5 and the average magnitude becomes 1.012.

The magnitude of the output signal for all possible numbers of Walsh functions at the determinate volume of 32 was examined and the results are shown on following figures.

In Fig. 6 the results for minimal magnitude of the output signal as a function of the roll-off factor and the relative window width are presented. Program interface shows the minimal and maximal values of all minimal magnitudes and the calculated average magnitude, too. The minimal magnitude is the most important one because it is closely related to the risk the output signal to be wrong.

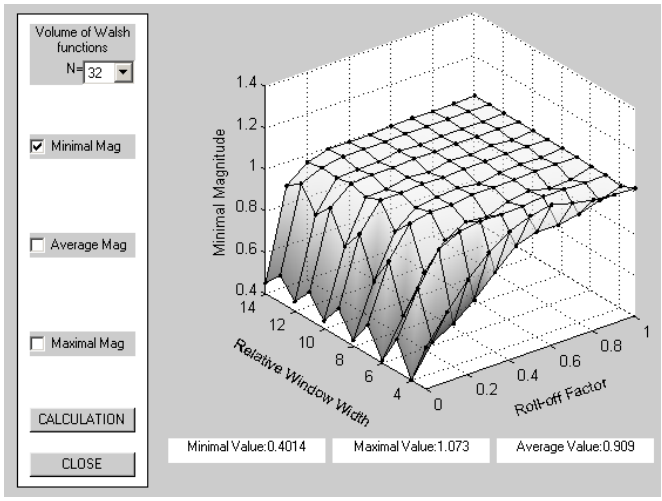

Fig.6. Minimal magnitude of the output signal.

The results show that the minimal magnitude is the lowest when the roll-off factor is zero. The value of the minimal magnitude increases when the roll-off factor grows in value.

The changes of minimal magnitude with the window width changing are due to the rejection of the impulse response tails. Because of finite time duration of the impulse response the perfect conditions are not satisfied and there is a residual inter-symbol interference. The studies show that at values of the roll-off factor greater than 0.2 the changes of the minimal magnitude are too small. The minimal, maximal and average values of minimal magnitude at other volumes of the Walsh functions slightly differ from these above.

In Fig.7 the results for maximal magnitude of the output signal as a function of the roll-off factor and the relative window width are presented. The studies show that alterations of maximal magnitude are more significant at the lowest values of the roll-off factor.

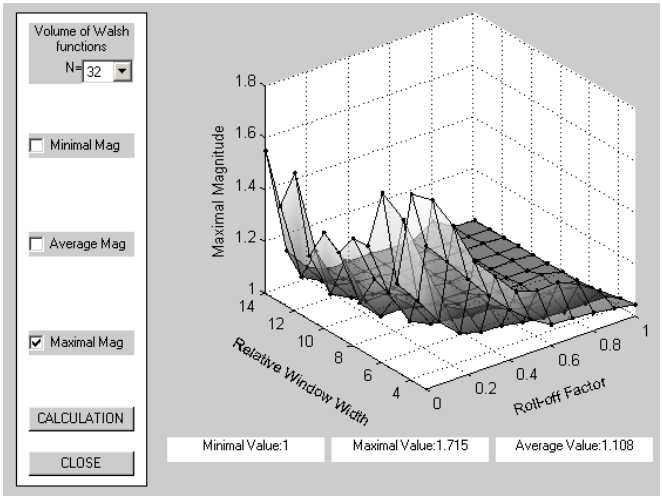

Fig.7. Maximal magnitude of the output signal.

It is obvious that the values of maximal magnitude are smaller for relative window widths from 7 to 9, when the roll-off factor is below 0.3. The minimal, maximal and average values of maximal magnitude at other volumes of Walsh functions slightly differ from these shown in Fig.7.

In Fig.8 the results for average magnitude of the output signal as a function of the roll-off factor and the relative window width are presented.

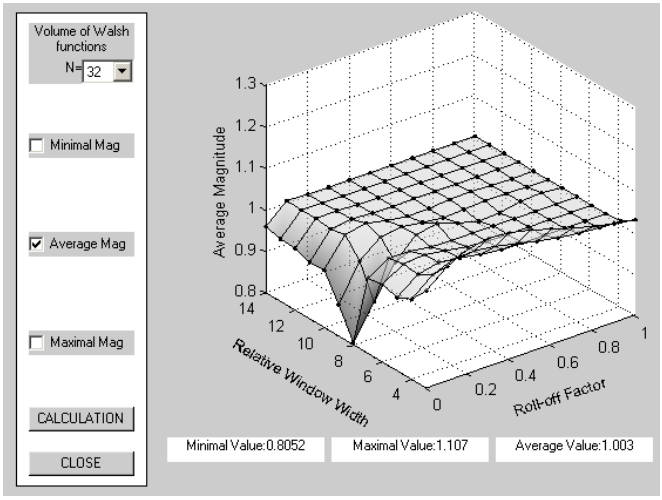

Fig.8. Average magnitude of the output signal.

The studies show that when the roll-off factor is below 0.3 there is a significant decreasing of the average magnitude at relative window widths from 7 to 9. Some decreasing of average magnitude occurs at all window widths if the roll-off factor is below 0.1.

In Fig.9 the lines of the worst and the best cases of the average magnitude are shown. It is clearly seen that the worst case should be taken in account when the roll-off factor is less than 0.3, because when it is greater than 0.3 the values of the average magnitude in the worst case differ very slightly from the other ones. The best case is always when the window width is minimal, but this means maximal frequency bandwidth of the signal which is not often acceptable.

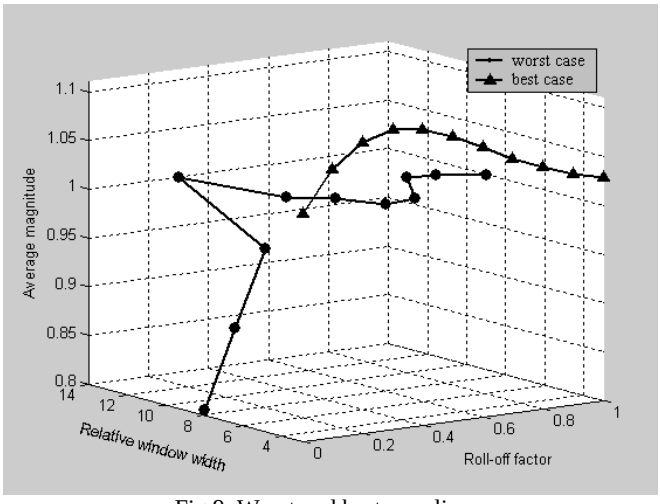

Fig.9. Worst and best case lines.

The results from Fig.9 prove once again that it is better to use roll-off factor greater than 0.3 if it is possible.

V. Conclusion

The attained results prove that the proposed model of decoder can be used successfully for decoding of differential binary phase shift keying signals. It combines the advantages of matched forming and filtering of signals, providing a maximal signal to noise ratio.

The shaping filter and matched filter possess finite impulse responses and consequently these filters can always be made realizable. The limiting of the impulse responses in time domain makes the decoder performance worse, but by proper choice of the roll-off factor and relative window width a performance slightly different from the perfect one can be achieved.

The results show that the roll-off factor should always be chosen to be more than 0.1. When this factor is between 0.1 and 0.3 the relative window width should not be between 7 and 9.

Because both the roll-off factor and the relative window width influence on the frequency bandwidth of the emitted signals they should match the channel bandwidth requirements.

References

[1] D. Roddy, *Satellite Communication,* New York, McGraw-Hill, 1995.

[2] G. Stanchev, *Doctoral thesis: Study of Satellite Digital Communication System Stability, Using Spread Spectrum Signals,* Dolna Mitroplia, 2000.

[3] N. Durchev, G. Bichev. *Telecommunications Systems with Pulse Code Modulation,* Sofia, Tehnika, 1986.

[4] S. Haykin, *Communication Systems,* New York, John Wiley & Sons Inc., 1994.

[5] Y. Okunev, *Phase and Phase-Difference Modulation in Digital Communications,* Artech House, London, 1997.

Study of Clutter Influence on a Differential BPSK Decoder, Providing a Minimal Intersymbol Interference

Georgi V. Stanchev[1] and Marin S. Marinov[2]

Abstract– **This paper studies both Doppler shift and additive white Gaussian noise influence on a differential BPSK decoder which includes matched filters in its in-phase and quadrature channels. Results about probability density function of the output signal and probability of error at the output are obtained.**

Keywords– **differential BPSK decoder, minimal inter-symbol interference, matched filter, phase difference rejection, Doppler shift, AWGN.**

I. INTRODUCTION

The mobile communication channels suffer from additional influences in comparison with the wire channels. Some of them are Doppler shift, high level noise and multipath. These phenomena and to be more precise their stochastic nature makes equipment performance estimation difficult to access. But in present days with the frequency spectrum overloading and object speed increasing, the demands and requirements to service quality of communications in mobile environment grow, too. Realistic and practical applicable results can be obtained only if the joint clutter influence of the damaging factors and technical limits are considered together.

Here the performance of a differential BPSK decoder, described in [2], suffering from clutter influence of Doppler shift and additive white Gaussian noise (AWGN) is researched. The single path propagation of the signal through the radio-channel is presupposed.

II. SIGNAL PROCESSING IN THE RECEIVER

The mixture of a useful digital modulated signal $r(t)$ and AWGN at the front end of the receiver is described as:

$$r(t) = R(t)\cos(\omega_0 t) + n_G(t). \quad (1)$$

The diagram shown in Fig.1 describes the main elements of the signal processing in the receiver.

The receiver design in any case requires the frequency band of the receiver to be limited and this is taken into account by band-pass filer (BPF) including. In this manner the noise after BPF can be described as a narrow-band process:

$$r(t) = [R(t) + n(t)]\cos(\omega_0 t). \quad (2)$$

The Doppler shift is introduced by a frequency offset ω_D of the receiver local oscillator. In this manner frequency recovery inaccuracies can be marked, too.

The results from down converting in the in-phase I-channel and quadrature Q-channel are:

$$\begin{aligned} R_I(t) &= [R(t) + n(t)]\{\cos(\omega_D t + \psi) + \cos[(2\omega_0 + \omega_D)t + \psi]\}; \\ R_Q(t) &= [R(t) + n(t)]\{\sin(\omega_D t + \psi) + \sin[(2\omega_0 + \omega_D)t + \psi]\}. \end{aligned} \quad (3)$$

The matched filters are low-passed filters by nature and hence they reject the components around doubled carrier frequency effectively. The signals at the filter outputs are:

$$\begin{aligned} S_I(t) &= R_I(t) * H(t) \approx \{[R(t) + n(t)]\cos(\omega_D t + \psi)\} * H(t); \\ S_Q(t) &= R_Q(t) * H(t) \approx \{[R(t) + n(t)]\sin(\omega_D t + \psi)\} * H(t). \end{aligned} \quad (4)$$

These signals are sampled in order to reject the inter-symbol interference and then they are differentially decoded.

III. RESEARCHES

The studies of the decoder, which is described above, in presence of Doppler shift show that the influence of Doppler shift is hardly seen and there is no need to take it in account, when practical system is considered – Globalstar for example.

Studies of the output signal distribution at different values of signal to noise ratio (SNR) are done. In [1] is shown that the energy of signal is equal to the chip duration value T_C. This value is used in order to calculate the variance of the continuous AWGN. When the noise is simulated this one is a discrete process and its variance is related to that of continuous process by the Eq. 5:

$$\sigma_d^2 = \frac{\sigma^2}{\Delta t}, \quad (5)$$

where $\Delta t = \pi/\omega_0$ is the sampling period.

In order to obtain results about the distribution of the output signal at each SNR 10 000 realizations are used. The values of the window width and the roll-off factor are chosen in keeping with recommendations produced in [2]. Enough statistics is provided by rounding off to 0.02 of the output signal values. The designed software uses numerical integration in order to calculate the convolution between the input signals and impulse responses of the matched filters in both of quadrature channels. The frequency of occurrence for each output signal value at concrete SNR is calculated. Actually it is the distribution of the output signal. Some of the results are presented in the following figures

The output signal distributions at values of 1 and 3 for the roll-off factor and the relative window width respectively are shown in Fig.2.

[1]Georgi V. Stanchev, PhD is with the Aviation Faculty, National Military University, 5856 Dolna Mitropolia, Bulgaria, e-mail: gstanchev@af-acad.bg.

[2]Marin S. Marinov, PhD is with the Aviation Faculty, National Military University, 5856 Dolna Mitropolia, Bulgaria, e-mail: mmarinov2000@yahoo.com.

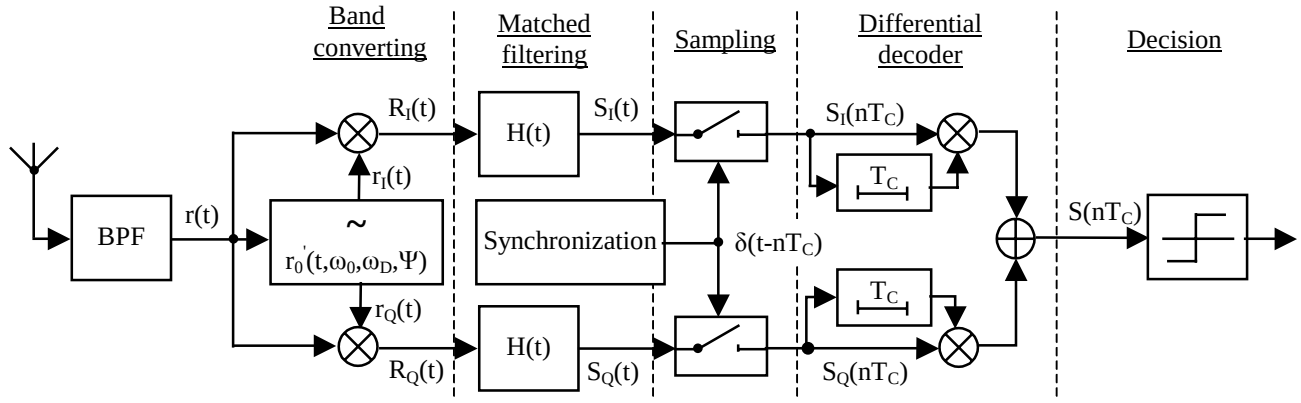

Fig.1 Model of the receiver.

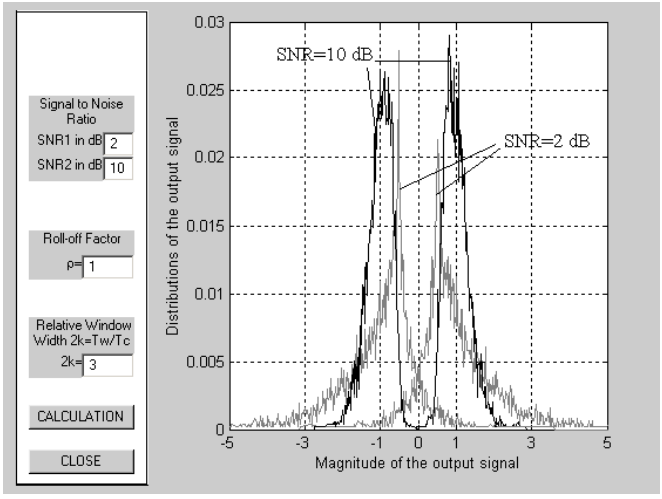

Fig.2. Distributions of output signal at ρ=1 and 2k=3.

The results show that the lower SNR leads to a wider output signal distribution. The values with the highest frequency of occurrence are far enough from zero even at SNR of 2 dB. It is obvious that the distribution at SNR of 10 dB is much narrower than this one at 2 dB. The values with the highest frequency of occurrence are closer to -1 and +1 respectively at the higher SNR.

Many more than 10 000 realizations are needed to calculate the probability of error. This is unpractical because too much time would be wasted to obtain results. It is advisable to approximate the probability density function (PDF) of output signal by using its distribution obtained from realizations.

In case of Gaussian channel the distribution of output signal possesses a Gaussian (normal) distribution. The normal probability density function is given by:

$$p(S) = \frac{1}{\sqrt{2\pi}\sigma} \exp\left\{-\frac{(S-m)^2}{2\sigma^2}\right\}, \qquad (6)$$

where m is the mean value and σ^2 is the variance. This is the continuous distribution and it is used in order to obtain the discrete distribution by next equation:

$$P(S_i) = \int_{S_i-\Delta S/2}^{S_i+\Delta S/2} p(S)dS, \qquad (7)$$

where S_i are the discrete values of the output signal and ΔS is the discrete step between two adjacent values.

The integral of normal probability density function in Eq.7 can be solved by means of famous error function [3]:

$$\mathrm{erf}(S) = \frac{2}{\sqrt{\pi}} \int_0^S \exp\{-x^2\}dx. \qquad (8)$$

The discrete distribution is derived from Eq.7 and Eq.8:

$$P(S_i) = \frac{1}{2}\left[\mathrm{erf}\left(\frac{S_i+\Delta S/2}{\sqrt{2}\sigma}\right) - \mathrm{erf}\left(\frac{S_i-\Delta S/2}{\sqrt{2}\sigma}\right)\right]. \qquad (9)$$

The optimal mean value m and the root mean square σ at which the equation (9) best fits the obtained distribution of the output signal are calculated. Then they are substituted in (6) and the probability density functions which best fit to the output signal distribution are obtained.

The approximated probability density functions of output signal at values of the roll-off factor 1 and the relative window width 3 are shown in Fig.3.

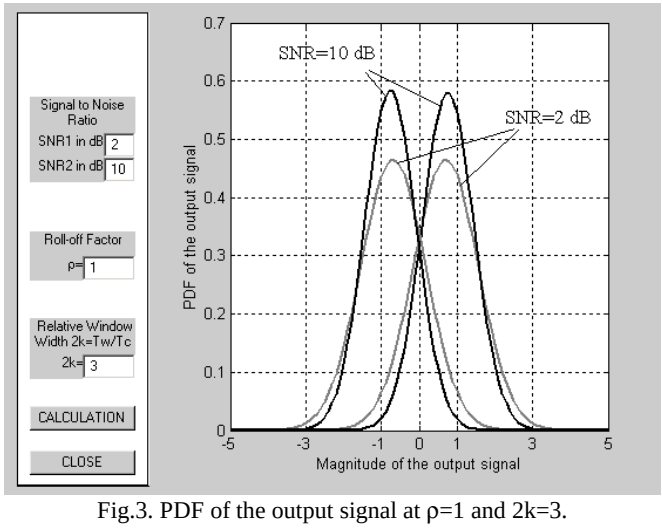

Fig.3. PDF of the output signal at ρ=1 and 2k=3.

It is clearly seen that the probability for output signal to exceed zero, when -1 is transmitted, is higher at lower SNR. The probability for output signal to be below zero, when +1 is transmitted, is higher at lower SNR, too. These two cases determine the error level at the decoder output.

The distributions of the output signal at values of 0.5 and 6 for the roll-off factor and the relative window width respectively are shown in Fig.4.

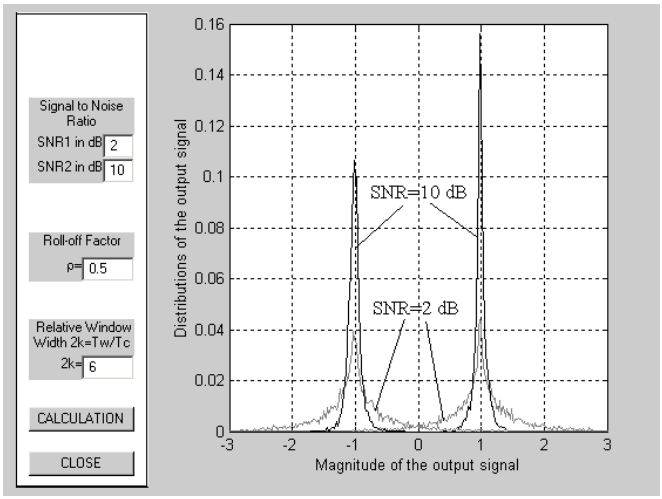

Fig.4. Distributions of the output signal at ρ=0.5 and 2k=6.

The results show that the distribution of output signal in this case is narrower than in the previous one. Thus the output signal values are more concentrated around -1 and +1 respectively. This leads to lower error level at the decoder output.

The approximated probability density functions of output signal at values of the roll-off factor 0.5 and the relative window width 6 are shown in Fig.5.

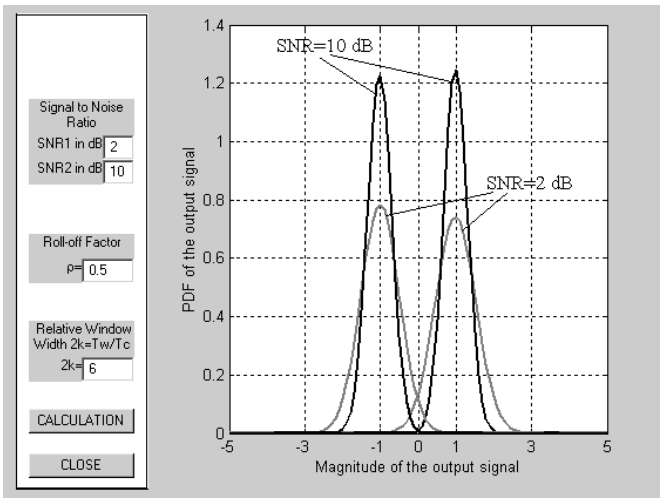

Fig.5. PDF of the output signal at ρ=0.5 and 2k=6.

Fig.5 shows that the mean values of probability density functions are closer to -1 and +1 respectively in comparison with the previous case. The variances of probability density functions are smaller and consequently the probability of error is lower.

The distributions of the output signal at values of 0.4 and 9 for the roll-off factor and the relative window width respectively are shown in Fig.4. The comparison between these distributions of the output signal and previous distributions shows that they are wider than these at the roll-of factor 0.5 and the relative window width 6, but they slightly differ from those ones at the roll-of factor 1 and the relative window width 3. This is a result from windowing of the impulse responses of the shaping and matched filters in the transmitter and the receiver respectively [2].

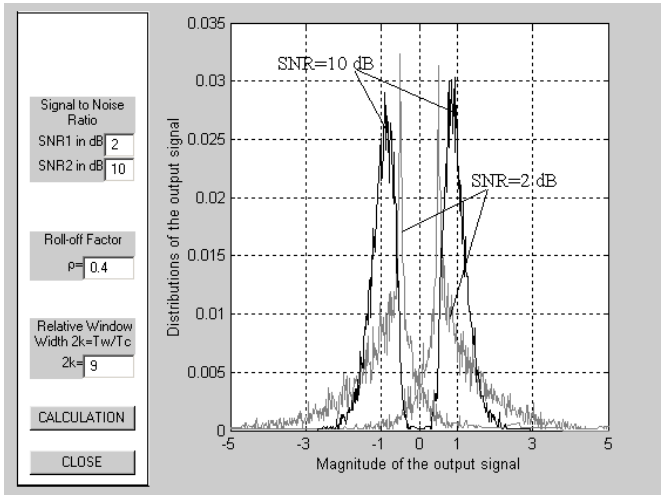

Fig.6. Distributions of the output signal at ρ=0.4 and 2k=9.

The approximated probability density functions of output signal at values of the roll-off factor 0.4 and the relative window width 9 are shown in Fig.7.

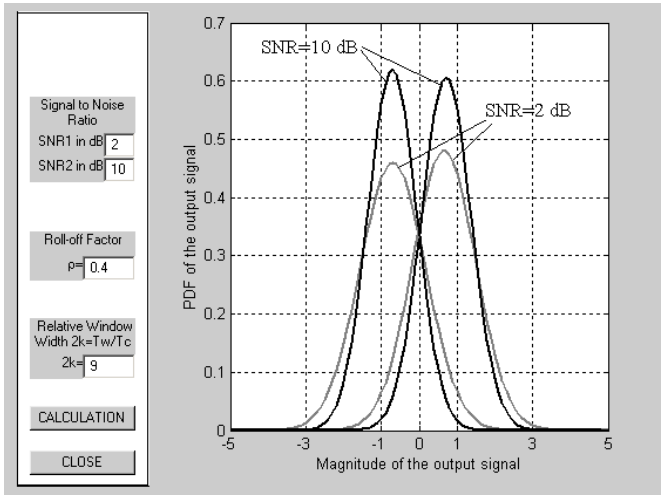

Fig.7. PDF of the output signal at ρ=0.4 and 2k=9.

The more precise analysis of the results indicates that the approximated probability density functions in Fig.7 are narrower than these in Fig.3. This means that the error levels are lower at cases displayed in Fig.6 and Fig.7 than these displayed in Fig.2 and Fig.3, but the differences between them are too small. A conclusion that the even number of the relative window width leads to lower error level than cases of odd such number can be done. The results shown in the following figures confirm this inference.

The distributions of the output signal at values of 0.4 and 4 for the roll-off factor and the relative window width respec-

tively are shown in Fig.8. It is obvious that these distributions are more concentrated around -1 and +1 respectively than those in Fig.6. This leads to narrower probability density functions and consequently to lower error levels.

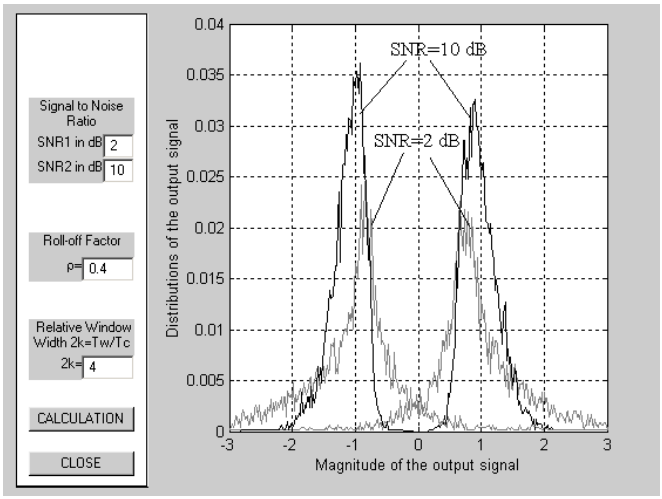

Fig.8. Distribution of the output signal at ρ=0.4 and 2k=4.

The approximated probability density functions of the output signal at values of the roll-off factor 0.4 and the relative window width 4 are shown in Fig.9.

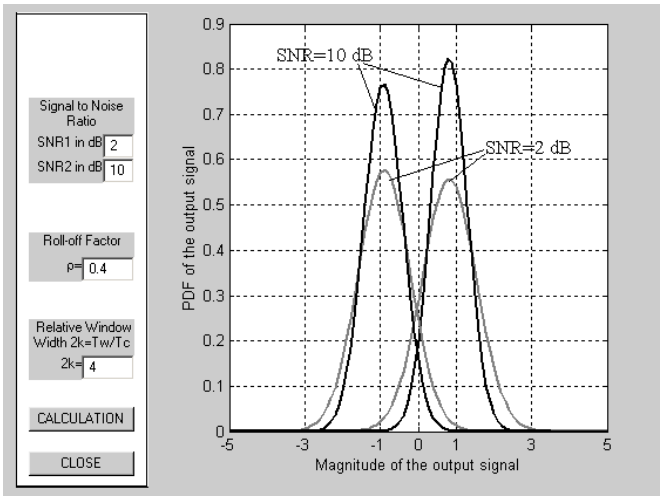

Fig.9. PDF of the output signal at ρ=0.4 and 2k=4.

It is easy to find that if +1 is transmitted, the area under this part of the probability density function where the output signal magnitude is below 0, is much smaller than in the case shown in Fig.7. The same one is valid for the part of probability function where the output signal magnitude exceeds 0 when -1 is transmitted. The value of PDF at output signal magnitude 0 and SNR 10 dB in Fig.9 is below 0.2, while the corresponding PDF in Fig.7 exceeds 0.3 i.e. it is almost twice greater. Furthermore it is obvious that the values of PDF at output signal magnitudes -1 and +1 in Fig.9 are higher than these in Fig.7.

The probability of error can be calculated by obtained quantities of the mean values and the variances and Eq.6:

$$P_{err} = 1 - \frac{1}{2}\left[\operatorname{erf}\left(\frac{-m_2}{\sqrt{2}\sigma_2}\right) - \operatorname{erf}\left(\frac{-m_1}{\sqrt{2}\sigma_1}\right)\right], \qquad (10)$$

where m_1 and σ_1^2 are the mean value and the variance when +1 is transmitted; m_2 and σ_2^2 are the mean value and the variance when -1 is transmitted.

The examination of the error probability as a function of SNR at different combinations of the roll-off factor and the relative window width values is done, too. Some of the obtained results are shown in Fig.10.

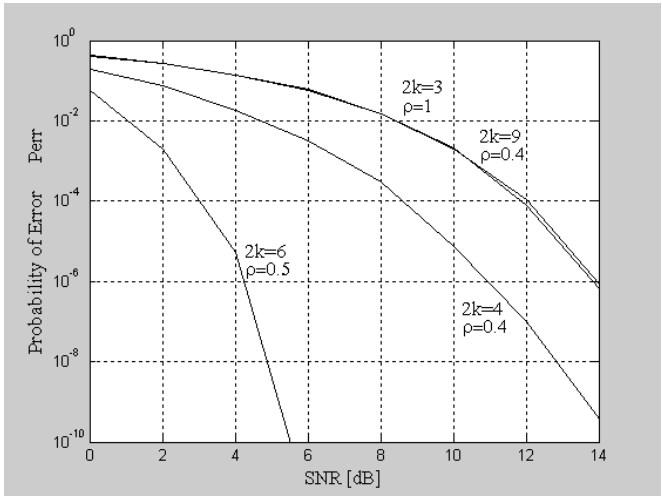

Fig.10. Probability of error as a function of SNR.

It is obvious from the results that the behavior of the probability of error at the parameter pairs *2k*=3, ρ=1 and *2k*=9, ρ=0.4 is the same. The steepest slope of the function is at pair *2k*=6, ρ=0.5 and very likely this is the optimal parameter pair.

IV. Conclusion

The studies of the differential BPSK decoder show that it possesses good characteristics in the presence of additive white Gaussian noise. It is better an even value of the relative window width to be used. Thus the lower error probability is provided in comparison with the case of an odd value. The results display that for even value the error probability decreases when the relative window width increases. The decoder provides the error probability below 10^{-6} when SNR exceeds 14 dB in the worst case. Obtained results prove that the practical development of such decoder is useful.

The recommendations in [2] should be kept in mind when the decoder parameters are chosen. Detailed studies and analysis of the influence of different factors and parameters should be done during development of a practical scheme of the pair encoder/decoder. Thus the best parameters can be chosen and the best results can be reached.

References

[1] G. Stanchev, *Doctoral thesis: Study of Satellite Digital Communication System Stability, Using Spread Spectrum Signals*, Dolna Mitroplia, 2000.

[2] G. Stanchev, M. Marinov. *Model of a Differential BPSK Decoder with Matched Filter Included, Providing a Minimal ISI*, ICEST 2004, Conference Proceedings, Bitola, Macedonia 2004.

[3] *Handbook of Mathematical Functions*, edited by Milton Abramowitz and Irene A. Stegun, Moscow, 1979.

Electromagnetic Field Strength Level Prediction by Neural Model – Application to Broadcasting

Zoran Stanković[1], Bratislav Milovanović[1], Anđelija Đorđević[1] and Marija Veljković[1]

Abstract - **This paper presents the neural model for efficient prediction of the electromagnetic field strength level for a UHF/VHF transmitter based on a multilayered perceptron (MLP) network. The proposed neural model has four input parameters, the distance from the transmitter, the effective antenna height, the terrain irregularity factor, and the clearance angle of the receiving antenna, and one output parameter, the field strength level for certain azimuth. According to the training set values, this neural model enables fast and accurate computing of the field strength level for any given effective antenna height between 37.5 m and 1200 m, terrain irregularity factor from 10 m to 500 m, clearance angle of the receiving antenna from – 20° to 1°, and for all distances from the transmitter in 10 km to 250 km range.**

Keywords - **Neural model, electromagnetic field level, ITU-R P370-7 recommendation.**

I INTRODUCTION

The efficient prediction of EM field strength is essential for modern telecommunication systems design. A propagation of EM wave is influenced by a large number of global and local parameters, such as relief, objects in the line of sight, clime area, atmosphere refraction index, multiple paths propagation, etc. The methods that are being used for the prediction of EM field strength do not take all of these parameters into account. Generally these methods are statistic, deterministic or pseudo-deterministic.

Statistic method recommended by ITU-R, recommendation 370-7 [1, 2], is used most often in prediction of the electric field strength level. This method is based on a visual reading of the electric field strength directly from the curve which gives the dependency of the field strength in dB(μV/m) from the distance and effective antenna height, Fig 1. Afterwards the correction factor, directly read from the curve which gives its dependency from the terrain irregularity, and the correction factor, directly read from the curve which gives its dependency from the clearance angle, must be added to this value. The biggest problem with this method is that the values of the effective antenna height are discrete, and for the other values the appropriate interpolation [2] must be applied, so if the large number of readings is in question this job can be very long and tedious.

The good alternative to this method is modeling the propagation curves with neural networks. The first neural models, based on the multilayer perceptron (MLP) network

[1]With the Faculty of Electronic Engineering,
Beogradska 14, 18000 Nis, Serbia and Montenegro, E-mail: zoran@elfak.ni.ac.yu, bata@elfak.ni.ac.yu, andjelija@elfak.ni.ac.yu marija@elfak.ni.ac.yu

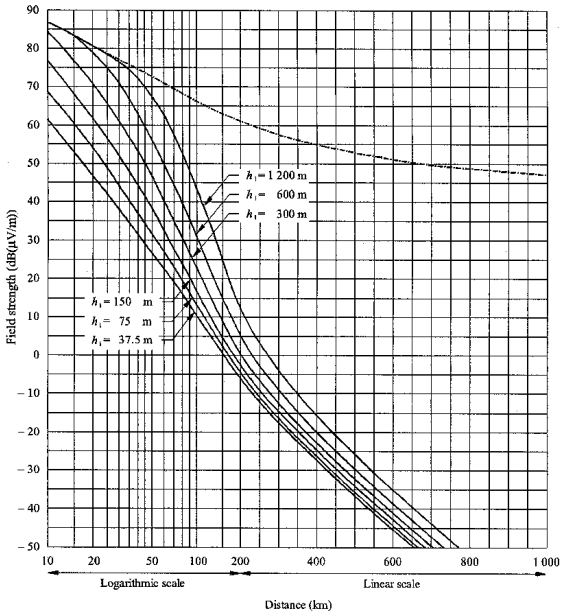

Fig. 1. Electric field strength level in dependence from the distance and the effective antenna height (the curves are given for half wave dipole antenna with 1kW power, and the 450-1000 MHz band, for 50% time and 50% locations.

[3-7], developed in [6, 7, 8] have shown a great speed and good accuracy in predicting the electric field strength level of the transmitter. These MLP models had two inputs, the distance from the transmitter and the effective antenna height. In [9] the terrain irregularity is the third input of the MLP model. Here, the more complex MLP model, with the clearance angle as the fourth input, is elaborated. The first results of this model were given in [10].

II NEURAL MODEL FOR THE ELECTRIC FIELD STRENGTH LEVEL PREDICTION

Problem that is being modeled is finding the electric field strength level as the function of the distance from the transmitter, the effective antenna height, the irregularity factor, and the clearance angle:

$$E = f(r, h_e, \Delta h, \theta) \qquad (1)$$

The complex neural model is composed of three multilayer perceptron networks. The first MLP network models the ITU-R P.370-7 propagation curves shown in Fig.1. The second MLP network models the electric field strength level correction due to the effect of the terrain irregularity, and the third MLP network models the electric field strength level

TABLE I - TESTING RESULTS FOR PROPAGATION CURVES

MLP network	Two-phase training	
	WCE[%]	ATE[%]
M4-5-5	1.65	0.45
M4-6-6	1.97	0.48
M4-7-7	1.6	0.45
M4-8-8	2.74	0.61
M4-8-5	3.21	0.84
M4-8-8	12.94	0.77
M4-9-5	4.13	1.14
M4-9-8	3.34	1.03

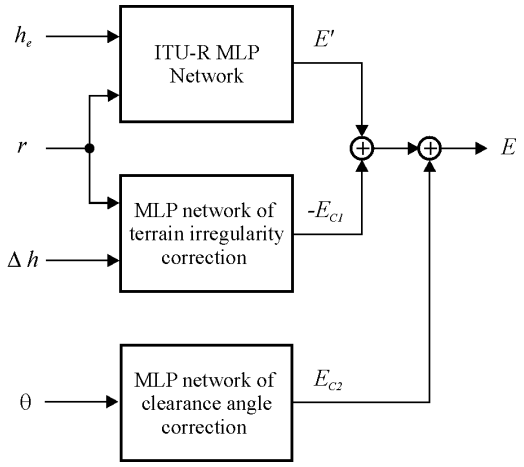

Fig. 2. The complex integrated neural model for the electric field strength level prediction for UHF/VHF transmitter.

correction caused by the effect of the clearance angle. As shown in Fig.2. the final neural model forms the resulting electric field strength level E [dB(μV/m)], according to

$$E = (E' - E_{c1}) + E_{c2} \qquad (2)$$

The output of the first MLP network is the electric field strength level E'[dB(μV/m)]. The terrain irregularity correction factor E_{C1}[dB], is output of the second MLP network, whereas the clearance angle correction factor, E_{C2}[dB], is the output of the third MLP network.

The first two neural networks both have two neurons in the input layer, and one neuron in the output layer. The third neural network has one neuron in the input as well as in the output layer. All three networks have two hidden layers of neurons, which is optimal according to [6, 7]. The activation functions of the hidden layers are sigmoid, while the neurons of the output layers have linear activation functions. In notation of the neural networks we used M_n-l_1-l_2-…-l_{n-2}, where n is the number of layers, and l_1, l_2, …, l_{n-2} are the numbers of neurons in corresponding hidden levels.

In order to model the required function more accurately, the training procedure of the first (ITU-R) neural network had two phases [6, 8]. In the first phase, called "the coarse training" the neural networks are trained on a large training set of 10000 samples generated by the approximate method [2] in range 30 m ≤ h_e ≤ 1400 m and 1 km ≤ r ≤ 650 km, using the

TABLE II - TESTING RESULTS FOR TERRAIN IRREGULARITY CORRECTION

MLP network	Classic training	
	WCE[%]	ATE[%]
M4-4-2	10.64	3.30
M4-4-4	11.35	3.32
M4-9-7	9.4	3.64
M4-10-7	11.48	3.58
M4-10-10	8.93	3.68
M4-14-11	13.44	3.58
M4-16-10	13.51	3.33
M4-22-20	9.76	2.82

TABLE III - TESTING RESULTS FOR CLEARANCE ANGLE CORRECTION

MLP network	Classic training	
	WCE[%]	ATE[%]
M4-3-2	2.94	0.87
M4-4-4	2.46	0.49
M4-5-5	2.82	0.58
M4-6-5	2.63	0.57
M4-7-4	2.07	0.57
M4-9-9	2.53	0.63
M4-10-10	2.46	0.61
M4-12-12	2.08	0.54

Quasi-Newton training method with the accuracy of 10^{-3}.This method is less efficient than the Levenberg-Marquart method, but more applicable on a large training set.

In the second phase ("the fine training"), ITU-R networks from "the coarse training" indicating the best performance were retrained on a smaller training set of 155 samples, obtained directly from the ITU-R P.370-7 curves, Fig. 1. The Levenberg–Marquart method (with the maximum absolute error of 10^{-4}) was applied in this training phase, because it is very efficient for a small training set. Testing of the networks after the final phase of training was fulfilled on a set of 73 samples, also obtained from the propagation curves. The pre-knowledge from the first training phase has improved the accuracy and the neural network learning rate. Training of the second and the third MLP networks (modeling the terrain irregularity correction and the clearance angle correction, respectively) was carried out on a classic manner, applying the Levenberg-Marquardt method with the given accuracy of 10^{-4}. The second neural network is trained on a set of 187 samples in range 10 km ≤ r ≤ 250 km and 10 m ≤ Δh ≤ 500 m and tested on 47 samples, both directly obtained from the ITU-R correction diagram [1]. A training set for the third neural network comprised 50 samples in range $-20^o \le \theta \le 1^o$ obtained from the appropriate ITU-R diagram [1], while the test set of 20 samples was used for network testing. Testing results of successfully trained neural networks are presented in Tables I, II and III, together with the average test error (*ATE*) and the worst case error (*WCE).* The minimum of the average test error was the basic criterion for selection of the best MLP network.

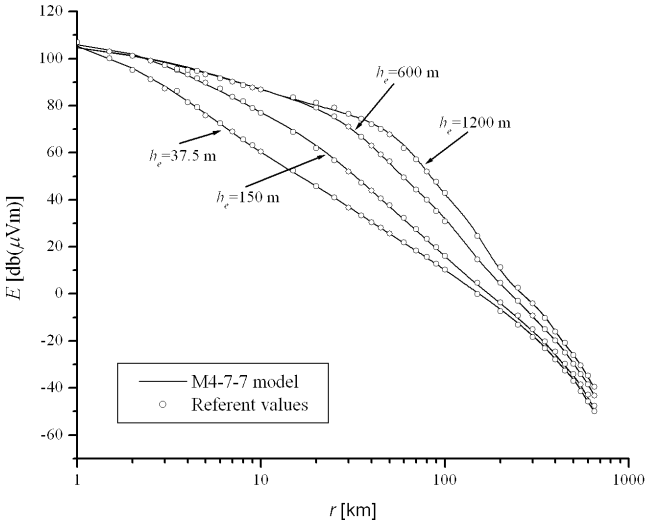

Fig. 3. Comparison of the propagation curves generated by M4-7-7 network and referent values.

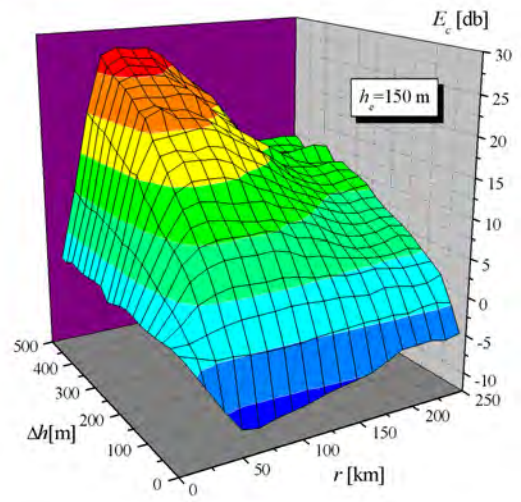

Fig. 4. Three-dimensional presentationof the correction depending on the terrain irregularity Δh and the distance r, generated by the M4-22-20 network.

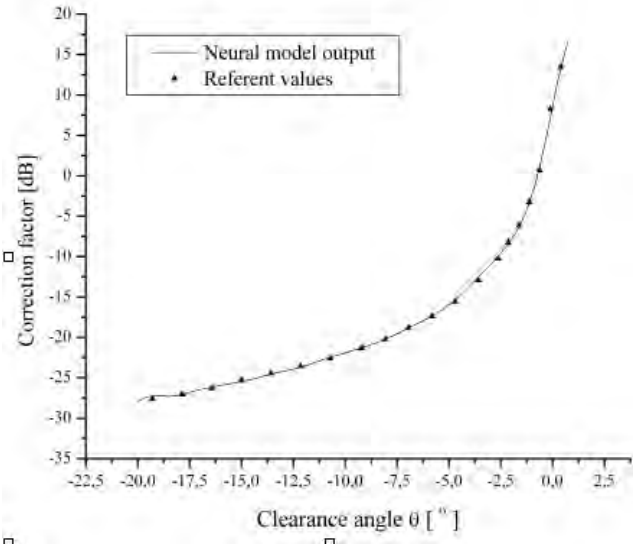

Fig 5. Comparison of the correction depending on clearance angle of the receiving antenna obtained by M4-4-4 model with referent values.

III Simulation Results

After the error analysis, we chose a neural network with the best performances from each of the Tables I, II and III. These three networks are used in the integrated neural model, as shown in Fig. 2. Selected networks are:

- M4-7-7 for the prediction of the electric field strength level depending on the effective antenna height h_e and the distance from the transmitter r,
- M4-22-20 that gives the electric field strength level correction as the function of the terrain irregularity factor Δh and the distance from the transmitter r,
- M4-4-4 for the receiving antenna clearance angle (θ) correction.

The neural network M4-7-7 is employed for the simulation of the electric field strength level depending on the effective antenna height h_e and the distance from the transmitter r. Propagation curves for several values of the effective antenna height, generated by this network, are presented in Fig. 3, together with referent values obtained from the ITU-R diagrams. It is obvious that modeled curves are very close to the referent values, which emphasizes high accuracy of the neural network.

Fig. 4 is a three-dimensional presentation of the correction depending on the terrain irregularity factor Δh and the distance from the transmitter r, for the constant effective antenna height h_e=150 m, generated by the M4-22-20 neural network.

The receiving antenna clearance angle correction, generated by the M4-4-4 network is shown in Fig.5. Referent values, obtained directly from the ITU-R correction diagram, are consistent with the neural network output values.

Fig. 6 shows the resulting electric field strength level on the output of the complex neural model depending on the distance from the transmitter when there is no receiving antenna clearance angle correction (θ = -0.73˚) and when this correction is present (θ = -10˚, θ = -5˚ and θ = 0.5˚), with the constant effective antenna height h_e = 150 m and the terrain irregularity factor Δh = 20 m. It is obvious that the output values of the neural model are very close to referent values from the ITU-R diagrams.

Complete 3D functions $E = f(r, h_e = 150$ m, $\Delta h, \theta = -5^\circ)$ and $E = f(r, h_e, \Delta h = 300$ m, $\theta = -0.73^\circ)$ are shown in Figs. 7 and 8, respectively.

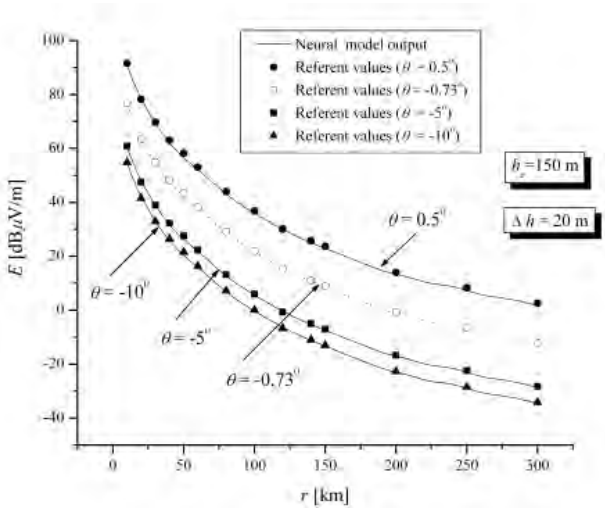

Fig 6. Comparison of the resulting electric field strength level generated by the complex neural model with referent values for different receiving antenna clearance angle values.

IV CONCLUSION

The widespread statistical method for the electric field strength level calculation in broadcasting systems is based on visual determining of the electric field strength level from the ITU-R P.370-7 curves. The electric field strength level, in this way, is estimated with sufficient accuracy, but the method itself is too complicated and time-consuming. Modeling the ITU-R propagation curves by neural models based on MLP networks could be a convenient alternative to the classic method. This conclusion results from the fact that the output values of the developed neural model are in excellent agreement with the electric field strength levels assessed from the ITU-R diagrams, while generating of the output values is extremely fast (values in 15 000 points are calculated in less than 5 seconds on PIII 450MHz hardware platform with 128 MB RAM).

Due to the high calculation rate, proposed neural model can be applied in systems for automatized determination of the service area for a VHF/UHF transmitter.

V REFERENCES

[1] Recommendation ITU-R P.370-7, VHF and UHF Propagation Curves for the Frequency Range from 30 MHz to 1 000 MHz, Broadcasting services.

[2] B. Milovanović, N. Vasić, V. Stanković, A. Atanasković, J. Joković, "Approximation of the Propagation Curves from the Recommendation ITU-R P. 370-7", TELSIKS 2001 Conference Proceedings, Niš 2001, pp.699-702.

[3] S. Haykin, *Neural Networks*, New York, IEEE, 1994.

[4] J. Hertz, A. Krogh and R. Palmer, Introduction to the Theory of Neural Computation, Addison-Wesley, 1991.

[5] B. Milovanović, Z. Stanković, S. Ivković, "Modelling of the Cylindrical Metallic Cavity Loaded by Lossy Dielectric Slab Using Neural Networks", NEUREL 2000 Conference Proceedings, Beograd 2000, pp. 141-145.

[6] Z. Stanković, B. Milovanović, J. Jovković, J. Antonijević, "Modeling of the ITU-R P.370-7 Propagation Curves by Neural Network", ICEST 2002 Conference Proceedings, Niš 2002, pp. 103-106.

[7] Z. Stanković, B. Milovanović, J. Antonijević, J. Jovković, "Neural Model of the Propagation Curves from ITU-R P.370-7", NEUREL 2002 Conference Proceedings, Beograd, September 2002, pp. 191-196.

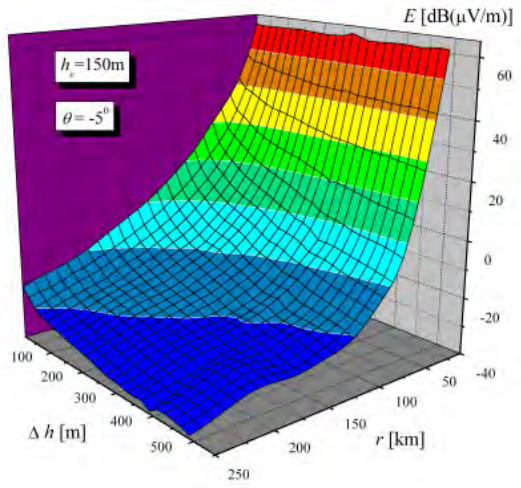

Fig. 7. Three-dimensional representation of the electric field strength level, depending on the distance from the transmitter *r* and the terrain irregularity factor *Δh*, generated by the complex neural model.

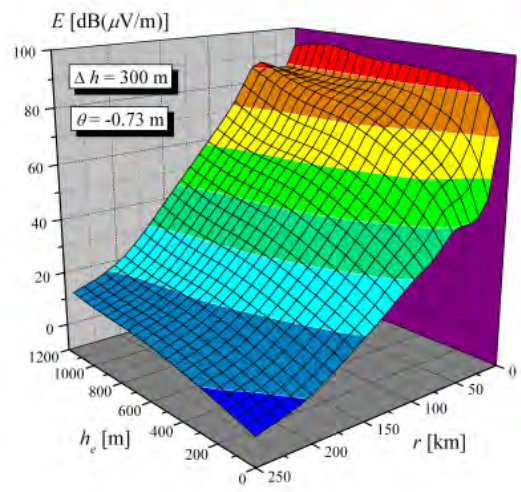

Fig. 8. Three-dimensional representation of the electric field strength level, depending on the distance from the transmitter *r* and the effective antenna height h_e, generated by the complex neural model

[8] Z. Stanković, N. Vasić "Neural Approach in Modelling of the Propagation Curves from Recommendation ITU-R P.370-7", ETRAN 2003 Conference Proceedings, H. Novi 2003.

[9] B. Milovanović, Z. Stanković, A. Stošić "Prediction of the Electromagnetic Field Strength Level using Neural Model", TELSIKS 2003 Conference Proceedings, Niš 2003, pp.457.

[10] B. Milovanović, Z. Stanković, A. Đorđević, M. Veljković "Neuronski model za predikciju nivoa elektromagnetnog polja u radio-difuziji", YUINFO 2004, Conference Proceedings, Kopaonik 2004.

Stable Soliton Propagation Over the Fiber-optic System with Losses

B. Stojanović[1], D. Milović[2] , M. Stefanović[3] and N. Spasojević[4]

***Abstract* – This paper investigates the stable soliton propagation over the realistic fiber-optic system when fiber losses are taken into the consideration. The motivation for this paper is a fact that the fiber losses can be compensated by suitable amplification scheme. Periodically amplified signal yields stable pulse propagation over a long-haul distances.**

***Keywords* – Fiber-optic transmission, soliton, amplification scheme.**

I. INTRODUCTION

In a fiber-optic communication system information is transmitted over a fiber by using a coded sequence of optical pulses whose width is determined by the system bit rate R. The drawback of the fiber-optic transmission is a fiber loss. The fiber exhibits a minimum loss of about 0.2 dB/km near 1550 nm which has to be compensated.

There are several factors that contribute to the loss spectrum; material absorption and dominantly contributed Rayleigh scattering. The loss is considerably higher at shorter wavelengths [1].

The development of erbium-doped-amplifier (EDFA) has eliminated loss as a fundamental limit to achievable fiber optic transmission distance. This has rapidly led to the construction of all-optical long-haul communication systems. Before invention of optical amplifiers, optical transmission systems typically consisted of a digital transmitter and receiver separated by spans of transmission optical fiber interspersed with optoelectronic regenerators.

The application of optical amplifiers eliminated the problem of signal attenuation over the link, but the effect of fiber dispersion is still rising. Fiber dispersion is serious problem particularly in systems with large bandwidths and long distance lengths. Consequently, the extensive research on compensating techniques is present, including the soliton technique which eliminates the fiber dispersion effects by utilizing nonlinear fiber effects, namely, by balancing them for a sufficiently high levels of transmitted signal. Soliton technique is quite complex but very powerfull as it was implemented and utilized in many system designs.

[1]Bratislav D. Stojanović is with the Faculty of Electronic Engineering, Beogradska 14, 18000 Niš, Serbia and Montenegro, E-mail: batas@ni.ac.yu

[2]Daniela M. Milović is with the Faculty of Electronic Engineering, Beogradska 14, 18000 Niš, Serbia and Montenegro, E-mail: dacha@elfak.ni.ac.yu

[3]Mihajlo Č. Stefanović is with the Faculty of Electronic Engineering, Beogradska 14, 18000 Niš, Serbia and Montenegro, E-mail: misha@elfak.ni.ac.yu

[4]Nebojša D. Spasojević is with the NIS Jugopetrol, Milentija Popovića 1, 11000 Belgrade, Serbia and Montenegro, E-mail: nebojsa.spasojevic@jugopetrol.co.yu

II. OPTICAL LOSSES VS EDFA'S GAIN

A very important fiber parameter that should be taken into consideration is a measure of power loss during transmission of optical signals inside the fiber. If P_0 is the power launched at the input of a fiber of length L, the transmitted power P_T is given by [1]

$$P_T = P_0 \mathrm{e}^{-\alpha L} \tag{1}$$

where α is attenuation constant, commonly referred to as the fiber loss.

The fiber attenuation is mainly caused by absorption and scattering. Absorption arises from impurities and atomic effects in the fiber glass. Scattering is mainly due to intrinsic refractive index variations of fiber glass with distance (Rayleigh scattering) and imperfections of the cylindrical symmetry of the fiber. The Rayleigh-scattering loss varies as λ^{-4} and is dominant at short wavelengths. Since this loss is intrinsic to the fiber, it sets the ultimate limit on the fiber loss. The loss level can reach values below 0.2 dB/km at around 1550 nm.

As a result of the power loss, the pulse width of the soliton also increases with propagation. To overcome the effect of fiber loss, solitons needs to be reshaped and amplified periodically to recover their original width and pick power. In a simple scheme, an optical amplifier boosts the soliton energy to it's input level. The soliton then readjusts its width to it's input value. However, it also sheds a part of its energy as a dispersive wave during the contraction phase.

The EDFA is an optical amplifier that amplifies signal purely in the optical domain. EDFAs can be used as a power amplifiers to boost transmitter power, as repeaters or in-line amplifiers to increase system reach, or as preamplifiers to enhance receiver sensitivity. The most far-reaching impact of EDFAs has resulted from their use as repeaters in place of conventional optoelectronic regenerators to compensate the transmission loss and extend the span between digital terminals. EDFAs amplifies light at wide range of wavelengths. In addition, optical amplifiers support the use of wavelength division multiplexing (WDM), whereby signals of different wavelengths are combined and transmitted together at the same transmission fiber.

Range of wavelengths when EDFA's gain is around 30 dB is 20-30 nm. With this kind of optical amplifiers, the overall gain is decreasing with the level of the output power and reaches 10 dB at +20 dBm of output power.

The gain of EDFA is varying with the distance from the location of pump signal, hence the gain is represented as follows [2]

$$G = \exp\left[\int_0^2 [\Gamma g(z) - a_i]dz\right] \quad (2)$$

where Γ represent limitation factor of propagating field, $g(z)$ is an inline amplification of a doped fiber that is changing over the axis of a propagating, pump wave, a_i is a total inline attenuation through the amplifying zone in doped fiber. Inline amplification can be represented as [2]

$$g(z) = \frac{g_0}{1 + I_{pro}(z)/I_{sat}} \quad (3)$$

where g_0 is a small signal gain, $I_{pro}(z)$ is the intensity of propagating signal and I_{sat} is the intensity at the saturation level.

III. SIMULATION RESULTS

A single-channel transmission system is investigated, where timing jitter effects are negligible. Pulses are propagated with a bit rate of 40 Gbit/s. The transmission link consists mainly of SSMF with a nominal dispersion of 0.2 ps/nm·km and fiber losses of 0.2 dB/km. The RZ pulses are launched with peak power of 6 mW and FWHM duration of 12.5 ps. No extra phase modulation is applied. It should be noted that the pulse energy do not correspond with the solution of the fundamental soliton; it was significantly increased to provide the stable soliton propagation [3].

A single RZ signal stream is transmitted over 2,500 km, applying optical inline amplifiers and a periodic spacing of 50 km. Figure 1. shows the power profile and a portion of first three amplified spans (out of 50 spans) of fiber link. It is clearly noticable that the pulse power is rapidly decreasing but after each amplifier the soliton regains it's original peak.

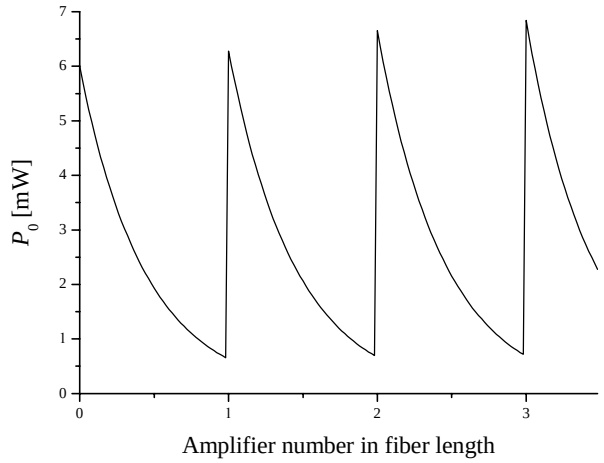

Fig. 1 Portion of power profile with first three spans

In this simulation, the doped fiber length was 30 m. Amplifiers gain was calculated to be the exact amount of the fiber loss in a single span.

Fig. 2 represents the evolution picture of stable soliton propagation over the 2500 km long fiber link with 50 amplified spans.

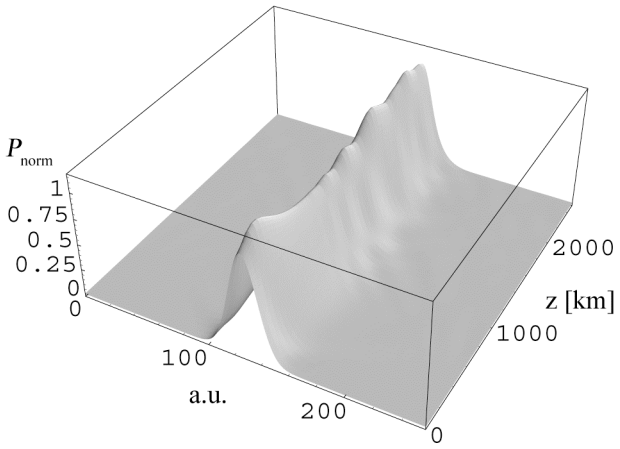

Fig. 2. Stable soliton propagation over periodically amplified fiber link

Fig. 2 is very descriptive as it shows soliton propagation that is slightly changing it's power and width. The figure encounters only the snap shots after each erbium doped amplifier (50 km), so it should be noted that the pulse is rapidly changing its peak power (nonlinear effect) and width (dispersive fiber effect) over one amplification span but readjusts itself after the amplifier. That should be taken into account in order to reduce the possible ISI effect when designing the real system.

IV. CONCLUSION

With the invention of Erbium-doped fiber amplifiers, the development of fiber-optic communication systems accelerated rapidly. Electro-optic repeaters could be replaced by the more robust, flexible and cost-efficient EDFAs, allowing all-optic links over transoceanic distances. The goal of this paper was to verify the necessity of the fiber amplifiers in the long distance link. In this simple simulation, it is shown that with the suitable amplification scheme fiber losses can be totally compensated. It should be also noted that the main drawback of the EDFA amplification is the induced ASE noise that should be considered at the receiver input.

REFERENCES

[1] Govind P. Agrawal, *Nonlinear Fiber Optics*, The Instityt of Optics, University of Rochester, Rochester, New York.

[2] A. Marinčić, *Optičke telekomunikacije*, Univercity of Belgrade, Belgrade, 1997.

[3] W. Xue, G. Zhou, Z. Li, and S. Guo, "Stable Propagation of Solitons in Strongly Dispersion-Managed Unequal-Lenght Optical Fiber Link with Loss," *Journal of Lightwave Technology*, vol. 18, pp. 926-932, No. 7, July 2000.

Long-haul Fiber-optic Transmission Utilizing DMS Modulation Format

B. Stojanović[1], D. Milović[2], M. Stefanović[3] and N. Spasojević[4]

***Abstract* – This paper investigates the stable soliton propagation over the long-haul fiber-optic system. Soliton system design provides transmission of undistorted pulses over a long distances through the SSMF. The similar effect on pulse dynamics is accomplished if a periodic dispersion compensation is applied on fiber-optic transmission. It has been shown that the so-called dispersion-managed soliton (DMS) can propagate over long-haul distances.**

***Keywords* – Long-haul transmission, soliton, DMS map.**

I. INTRODUCTION

Long distance fiber-optic telecommunication systems carry digital information over terrestrial distances ranging from 3,000 km to 5,000 km and transoceanic distances ranging from 5,500 km to 12,000 km. During the last 10 years these systems have evolved significantly.

Wavelength Division Multiplexing (WDM) [1], is a technology that allows multiple information streams to be transmitted simultaneously over a single fiber at data rates as high as the fiber plant will allow. WDM technology utilizes a composite optical signal carrying multiple information streams, each transmitted on a distinct optical wavelength. By allowing multiple WDM channels to coexist on a single fiber, one can tap into the huge fiber bandwidth with multiple, simultaneous, extremely high frequency signals of terahertz (THz) range.

The performance of high-speed fiber-optic communication systems is generally limited by GVD effect that broadens the pulse and disperses its energy. Solitons are useful to improve the performance of such dispersion limited communication systems since they can maintain their width over long distances by balancing the effect of GVD through the nonlinear phenomenon of SPM. In the soliton system design, many unavoidable limiting factors are to be considered and understood like the effect of fiber loss, mutual interactions between two neighboring pulses and the Gordon-Haus effect.

[1]Bratislav D. Stojanović is with the Faculty of Electronic Engineering, Beogradska 14, 18000 Niš, Serbia and Montenegro, E-mail: batas@ni.ac.yu

[2]Daniela M. Milović is with the Faculty of Electronic Engineering, Beogradska 14, 18000 Niš, Serbia and Montenegro, E-mail: dacha@elfak.ni.ac.yu

[3]Mihajlo Č. Stefanović is with the Faculty of Electronic Engineering, Beogradska 14, 18000 Niš, Serbia and Montenegro, E-mail: misha@elfak.ni.ac.yu

[4]Nebojša D. Spasojević is with the NIS Jugopetrol, Milentija Popovića 1, 11000 Belgrade, Serbia and Montenegro, E-mail: nebojsa.spasojevic@jugopetrol.co.yu

Dispersion-managed soliton wavelength-division multiplexed (WDM) transmission with 20 Gbit/s per channel is a promising way to realize long-haul systems with an aggregate transmission capacity greater than 100 Gbit/s. Optimizing the performance of such dispersion-managed system is of crucial importance, and requires lunching properly shaped and chirped pulses into the fiber to minimize the shedding of energy into a dispersive pedestal [2].

II. SOLITON PROPAGATION

It is well known that the pulse propagation in an nonlinear dispersive medium [3], as the optical fiber is, can be described with the Generalized Nonlinear Schrödinger's partial differential Equation (GNLS),

$$\frac{\partial A}{\partial z}+\frac{1}{v_g}\frac{\partial A}{\partial t}+\frac{i}{2}\beta_2\frac{\partial^2 A}{\partial t^2}+\frac{\alpha}{2}A=i\gamma|A|^2A \qquad (1)$$

where β_2 is dispersion coefficient, v_g is group velocity, γ is nonlinearity coefficient defined as

$$\gamma=\frac{n_2\omega}{cA_{\mathrm{eff}}} \qquad (2)$$

and A_{eff} represents the effective core area (typically 10-20 μm^2 in visible region), c is speed of light, ω is the pulse central frequency and n_2=3,2×10^{-16}cm^2/W for silica fiber.

Ignoring fiber loss (α = 0), and introducing normalized units, the GNLS in Eq. (1) can be written as

$$j\frac{\partial}{\partial\xi}u=\frac{1}{2}\mathrm{sgn}(\beta_2)\frac{\partial^2}{\partial\tau^2}u-\frac{L_D}{L_{NL}}|u|^2u \qquad (3)$$

where u is the normalized field amplitude given by

$$u=A/\sqrt{P_0}\ ,$$

with P_0 peak power at fiber input,
ξ is the normalized transmission distance given by

$$\xi=z/L_D\ ,$$

L_D is the dispersion length, L_{NL} and is nonlinear length, τ is the normalized, retarded time given by

$$\tau=T/T_0=(t-z/v_d)/\sqrt{L_D|\beta_2|}$$

Using the inverse scattering method [4], Eq. (3) can be solved analytically for a launched pulse shape, which satisfies the equation at any distance point.

Among others, so-called soliton [4,5] solutions exist in the anomalous dispersion regime ($\beta_2 < 0$), which satisfy the criterion

$$N = \sqrt{\frac{L_D}{L_{NL}}} = 1,2,... \qquad (4)$$

Of special interest is the fundamental soliton solution, as its pulse shape is not altered during propagation. It is given for the case $L_D = L_{NL}$ as

$$u(\xi,\tau) = \mathrm{sech}(\tau)\, e^{j\xi/2} \qquad (5)$$

Only the phase of the fundamental soliton is undergoing a circular change with period. Other, higher order soliton solutions of interest for fiber-optic communications are those of the same initial pulse shape as the fundamental one

$$u(0,\tau) = N\,\mathrm{sech}(\tau) \qquad (6)$$

At the fiber input, the peak power and width of the soliton are related by (4). Using definitions for dispersion and nonlinear lengths, $L_D = T_0^2/|\beta_2|$ and $L_{NL} = 1/(\gamma|A|^2)$, one gets [4]

$$P_0 = N^2 \frac{|\beta_2|}{\gamma T_0^2} \approx N^2 3{,}107 \frac{|\beta_2|}{\gamma T_{FWHM}^2} \qquad N = 1,2,... \qquad (7)$$

where T_0 is the pulse duration (half-width 1/e-intensity) and T_{FWHM} is the FWHM (full-width at half maximum) pulse duration.

Figure 1 shows the pulse shape evolution of the fundamental soliton in comparison with a Gaussian pulse. For both pulses, the peak power is 8.141 mW and the FWHM duration is 20 ps. It can be seen how the fundamental soliton retains its shape, while the Gaussian pulse shape is changing rapidly as it tries to balance linear (pulse-spreading) and nonlinear (pulse-compressing) forces.

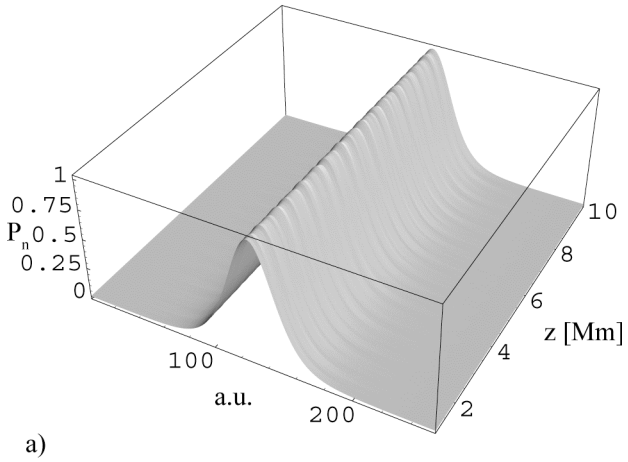

a)

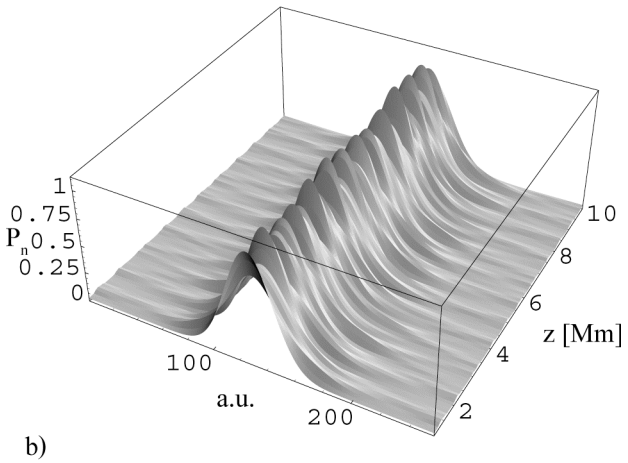

b)

Fig. 1 Evolution of sech (a) and Gaussian (b) shaped pulses of equal FWHM duration, (no fiber attenuation).

The similar effect on pulse dynamics is accomplished if a periodic dispersion compensation is applied in the pulse propagation. It has been shown that the so-called dispersion-managed soliton (DMS) can be propagated over long-haul distances. Inside each dispersion map, the characteristics of DMS evolution is governed by local dispersion values. Thus, the DMS changes its width and peak power inside each dispersion map (it "breathes" with local dispersion) [2,6].

III. DMS MODULATION FORMAT

The study of propagation in optical fibers with non-uniform dispersion has recently become a key topic in long-haul optical transmission. Dispersion management is the term for a technique in which the transmission path is constructed from section of two or more fibers or other elements with different dispersion. We can represent this with a dispersion map below

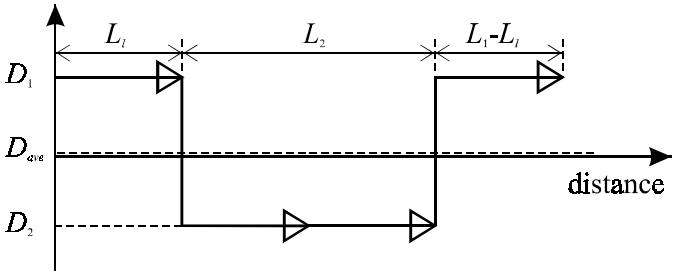

Fig. 2 Dispersion map

If the map contains both anomalous ($\beta_2 < 0$) and normal ($\beta_2 > 0$) dispersion sections (in the map, D_1 is anomalous and D_2 is normal dispersion), then, although at any point in the system the dispersion is substantial, the path-average dispersion (D_{ave}) over the whole system can be close to zero. This procedure strongly modifies the nonlinear transmission properties of the system compared to one constructed with uniform low-dispersion fiber. In addition, it produces a high local dispersion at any given point, and yet a low path-average dispersion. By adopting a suitable dispersion management

scheme for soliton transmission, it is possible to substantially increase the soliton energy compared to the equivalent uniform fiber with equal path-average dispersion.

Design of initial pulse power and width is critical for successful propagation of DMS. One important parameter determining the DMS behavior is the dispersion map strength S_D, given as

$$S_D = \frac{\lambda^2}{2\pi c}\frac{(D_1 - D_{ave})L_1 - (D_2 - D_{ave})L_2}{T_0^2} \qquad (8)$$

where D_1, D_2 are the dispersion coefficients, and L_1, L_2 are the lengths of the anomalous and normal dispersion spans, respectively, and

$$D_{ave} = \frac{D_1 L_1 + D_2 L_2}{L_1 + L_2} \qquad (9)$$

is the average dispersion of the dispersion map.

Utilizing the advantages of DMS propagation in the anomalous dispersion regime on the one hand, and avoiding interactions with neighboring pulses on the other hand, the dispersion map strength should be in the range of $4 \le S_D \le 10$.

Dispersion-managed solitons are not sech-shaped anymore; they tend to be more Gaussian-shaped. In general, it is difficult to determine the proper pulse shape, width and power for a DMS, as these parameters depend strongly on the applied dispersion map and amplifier positioning. There are three main rules for launching the proper DMS into a system, and thus avoiding energy shedding throughout the propagation. Firstly, the path-average dispersion mast be anomalous (as it is in Fig. 2), so that there is a net dispersion of the right sign to balance the nonlinearity of fiber. Secondly, the period of the dispersion compensation cycle must be short compared to nonlinear length (L_{NL}) of the system. Finally, dispersion maps in which one of the fibers is much closer to zero dispersion than the other should be avoided, or energy is rapidly coupled out of the pulse into dispersive waves. This effectively implies the need of fibers with opposite sign dispersion. It should be taken into consideration, that, the energy of the launched pulse should match the energy of the true DMS solution for the particular dispersion map.

A typical single channel DMS system with a bit rate of 10 Gbit/s is considered here. The initially Gaussian pulses are launched. The dispersion map consists of a span of anomalous DSF with dispersion D_1 (2,80 ps/nm·km) and length L_1 (100 km) and a span of normal DSF with dispersion D_2 (-2,40 ps/nm·km) and length L_2 (100 km). Pulses are launched in each channel at L_l, ($L_l = L_1/2 = 50$ km) here, from the middle of the anomalous dispersion span. Figure 2 illustrates graphically the meaning of parameters of dispersion map.

Figure 3 shows typical DMS pulse evolution over a symmetric dispersion map, e.g., anomalous and normal dispersion fiber spans are of equal lengths ($L_1 = L_2 = 100$km). Here the DMS is found to be approximately of Gaussian shape with 20 ps FWHM duration and 1.63 mW peak power at the middle of the anomalous dispersion fiber, where it is launched. Note that no chirp is added.

At each optical amplifier, spontaneous emission adds photons of white noise to the signal. This results in a small random change of the central frequency of each pulse. Due to velocity dispersion, these frequency changes are translated into velocity shifts, and hence, cause timing jitter. In a uniform dispersion system, reducing Gordon-Haus timing jitter can only be done by lowering the signal power, which is clearly detrimental to the received SNR. Dispersion management provides an escape from this problem by providing an extra degree of freedom in design. As the strength of the dispersion map (S_D) is increased, soliton energy is enhanced without any increase in either the optical bandwidth or the path-average dispersion. The increased number of photons in the soliton renders the addition of any given number of noise photons less significant, and so produces a smaller frequency shift (timing jitter). In addition, the increase of power for DMS systems compared to classical soliton systems using pulses of comparable duration results in an increased optical signal-to-noise ratio (OSNR) without the need to increase the average dispersion. This is advantageously as it allows higher robustness against ASE-noise induced timing jitter and amplitude fluctuations.

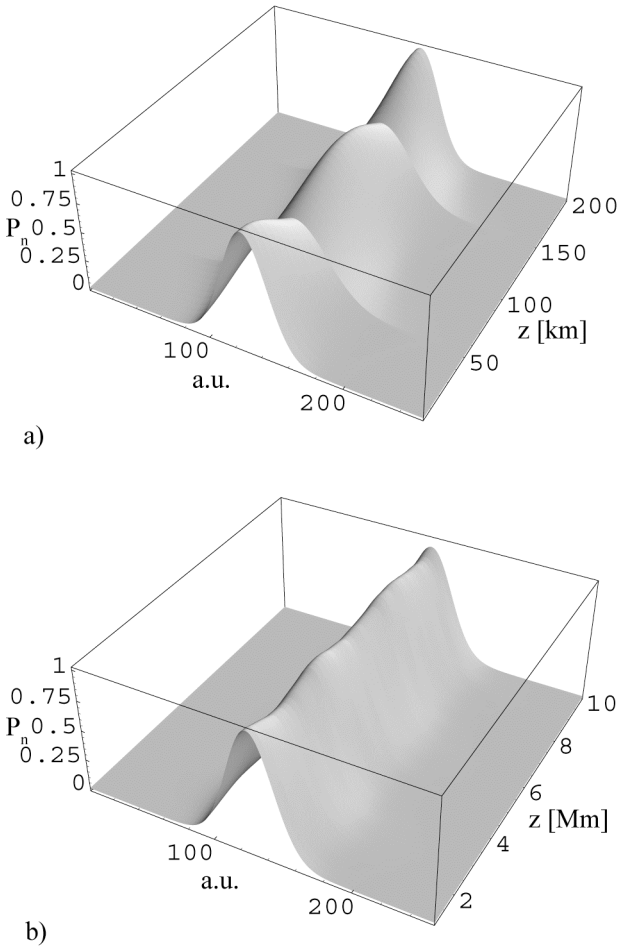

Fig. 3 Evolution of dispersion-managed soliton. (a) over one dispersion map of 200 km, (b) over 10,000 km with snap shots after each dispersion map (200 km), (no fiber attenuation).

The graph 3.a shows pulse dynamics inside the map, where pulse 'breathing' is recognizable. The DMS pulse width is smallest in the middle of the spans, and widest at the edges between anomalous and normal dispersion fiber spans, where chirp is broadening the spectrum as well. The graph 3.b shows stable evolution over 10,000 km, where snap shots are taken after each dispersion map. Slight modifications of pulse peak power and width are recognizable over the distance, which results from the fact that the launched Gaussian pulse is not the true solution of the propagation equation.

IV. CONCLUSION

The advantage of DMS system compared to classical soliton systems is the possibility to utilize larger local dispersion values, which results in increased robustness against disturbing fiber nonlinear effects (such as FWM, XPM) and timing jitter due to ASE-noise. It allowed the usage for high-capacity long-haul system applications.

Another highly novel feature of these solitary waves is that their pulse shapes are not the hyperbolic secants of regular optical fiber solitons. The pulse profile changes with different dispersion maps chosen, that is, with different couple of values D_1 and D_2. As the dispersion variation is increased there is a transition from the uniform fiber hyperbolic secant solitons to the Gaussian form, and to super Gaussian form.

And finally, as previously mentioned, dispersion managed systems also reduce the timing jitter compared to uniform dispersion systems.

REFERENCES

[1] L. Bergman, J. Morookian, and C. Yeh, "An All-Optical Long-Distance Multi-Gbytes/s Bit-Parallel WDM Single-Fiber Link," *Journal of Lightwave Technology*, vol. 16, pp. 1577-1582, September 1998.

[2] T-Sh. Yang, W. Kath, and S. Turitsyn, "Optimal dispersion maps for wavelength-division multiplexed soliton transmission systems," *Opt. Letters*, vol. 23, pp. 597-599, 1998.

[3] A. R. Chraplyvy, "Limitations of lightwave communications imposed by optical fiber nonlinearities," *Journal of Lightwave Technol.*, vol. 8, pp. 1548–1557, 1990.

[4] Govind P. Agrawal, *Nonlinear Fiber Optics*, The Instityt of Optics, University of Rochester, Rochester, New York.

[5] G. L. Lamb, Jr., *Elements of Soliton Theory*, New York, Wiley,1980.

[6] W. Xue, G. Zhou, Z. Li, and S. Guo, "Stable Propagation of Solitons in Strongly Dispersion-Managed Unequal-Lenght Optical Fiber Link with Loss," *Journal of Lightwave Technology*, vol. 18, pp. 926-932, No. 7, July 2000.

Multipanel Concept for Wide-Angle Scanning of Phased Array Antennas

Alexander G. Toshev[1], Nikola I. Dodov[2], Ilian Stoyanov[3]

Abstract — **A method for scanning of the main beam of phased array antennas in wide angular range is presented. The method utilizes several smaller flat antenna panels working at boresight and pointed in the direction of the main beam of overall antenna. The output signal of the overall antenna is summation of the signals from all antenna panels. Investigation of the array performance of such structure with respect to the distance between panels is presented.**

Keywords — **Phased arrays, scanning antennas, sub array architecture of a phased array**

I. INTRODUCTION

Commercial scanning phased array antennas has gained significant role in the last decade since the advent of high power satellites. Their main application is mobile TV reception. Mobile applications require wide angle scanning low cost arrays. Sub-array architecture is one of the approaches for decreasing the cost of the array, because one phase control device is used for a group of radiators called sub-array [1], [2]. Difficulties in realization of wide angle scanning flat phased arrays with sub-array architecture are mainly connected with scan losses at low elevation angles due to the pattern of the sub-array [1], [3] and grating lobe level due to the sub-array architecture [3], [4], [5], [6].

This paper emphasizes on a different approach for wide angle scanning phased arrays. The flat aperture of the array is divided of number of smaller parts or panels. Each panel is separate sub-array with its main beam mechanically slanted in the direction of the main beam of the antenna and all sub-arrays form the aperture of overall phased array. Distance between panels is changed each time when direction of the main beam of the antenna is changed, so that parasitic grating lobes due to equivalent array of panels are suppressed. Phase control is applied on panels for steering of the array factor of the equivalent array of panels.

II. MATHEMATICAL BACKGROUND AND ANALYSIS

Further in the analysis linear array of slanted panels is considered for simplicity of the derivations. Transition to 2D slanted panels is straightforward. Schematic diagram of the considered phased array is presented on Fig. 1.

[1]Alexander G. Toshev is with the faculty of Communications and Communications Technologies, TU Sofia, "Kl. Ohridsky" blvd. N8, 1756 – Sofia, Bulgaria, E-mail: toshev_a@skygate.bg

[2]Nikola I. Dodov is with the faculty of Communications and Communications Technologies, TU Sofia, "Kl. Ohridsky" blvd. N8, 1756 – Sofia, Bulgaria, E-mail: ndodov@tu-sofia.bg

[3]Ilian Stoyanov is with "SkyGate", Ltd. , 2A "Mogilata" str., 1700 – Sofia, Bulgaria, E-mail: stoyanov_i@skygate.bg

Expression for the electric far field using the principle of superposition of the radiations from the radiating elements is as follows [1]:

$$\vec{\mathbf{E}} = \sum_{n=1}^{N} \dot{A}_n \left[E^e_{\theta_n}(\theta,\varphi)\vec{i}_\theta + E^e_{\varphi_n}(\theta,\varphi)\vec{i}_\varphi \right] exp\left(j\,\vec{\mathbf{k}}.\vec{\mathbf{r}}_\mathbf{n} \right) \quad (1)$$

where $\vec{\mathbf{k}}$ is the wave vector, $\vec{\mathbf{r}}_\mathbf{n}$ is the position vector of each radiating element, $E^e_{\theta_n}(\theta,\varphi)$ and $E^e_{\varphi_n}(\theta,\varphi)$ represent radiation pattern of the n[th] radiating element for the two orthogonal components of the field. The following expressions are valid for $\vec{\mathbf{k}}$ and $\vec{\mathbf{r}}_\mathbf{n}$:

$$\begin{aligned} \vec{\mathbf{k}} &= k\,sin(\theta)\vec{i}_x + k\,cos(\theta)\vec{i}_z \\ \vec{\mathbf{r}}_\mathbf{n} &= x_n\,\vec{i}_x + z_n\,\vec{i}_z \end{aligned} \quad (2)$$

where x_n and z_n are coordinates of the radiating elements; $\vec{i}_x$ and $\vec{i}_z$ are unity vectors.

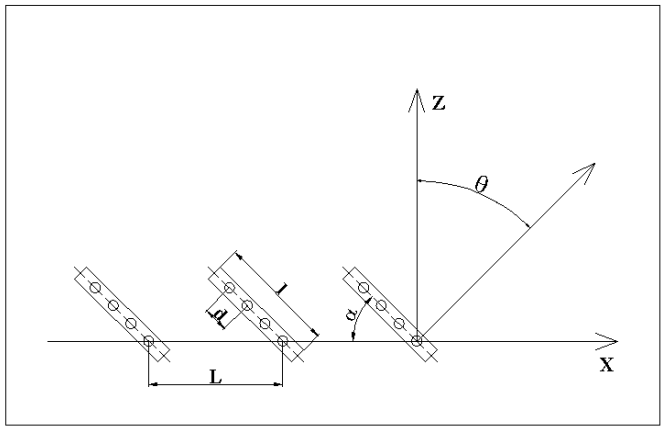

Fig. 1: Shematic diagram of multipanel linear phased array antenna

If all patterns of the radiating elements in are the same, array factor can be extracted from Eq. (1) in the form [1]:

$$F = \sum_{n=1}^{N} \dot{A}_n \, exp\left(j \vec{\mathbf{k}} . \vec{\mathbf{r}}_{\mathbf{n}} \right) \tag{3}$$

where $\dot{A}_n$ are complex coefficients comprising amplitude and phase excitation of the radiating elements.

For further analysis lets assume that the number of radiating elements for each panels is P and total number of antenna panels is S. If α is the angle, shown on Fig. 1, the following expression for the coordinates of the radiating elements is valid:

$$\begin{aligned} x_n &= -mL - qd\cos(\alpha); \\ z_n &= qd\sin(\alpha) \\ m &= 1...S; q = 1...P \end{aligned} \tag{4}$$

Using relations given with Eq. (4), expression for the array factor could be written in the form:

$$\begin{aligned} F(u) = \left\{ \sum_{q=1}^{P} \dot{E}_q \, exp[2\pi j(q-1)u] \right\} \times \\ \left\{ \sum_{m=1}^{S} \dot{S}_m \, exp[2\pi j(m-1)u_s] \right\} = Fe(u)Fs(u_s) \end{aligned} \tag{5}$$

where

$$u = \frac{d}{\lambda}\sin(\theta - \alpha); u_s = \frac{L}{\lambda}\sin\theta \tag{6}$$

Eq. (5) has two terms. The term $Fe(u)$ describes array factor of the single panel slanted on angle α, whilst $Fs(u_s)$ describes array factor of equivalent array of slanted panels separated at distance L. Since distance between slanted panels is far greater than distance between radiating elements in each panel ($L >> d$), oscillations of the function $Fs(u_s)$ are much more than those of $Fe(u)$ as it can be seen on Fig. 2 a). Maximum of the array of the single panel $Fe(u)$ appears at angle α, which is the slanted angle of the panels. There are not additional maximums caused by the term $Fe(u)$. The term $Fs(u_s)$ has one main beam and normally more than one grating lobes, because distance L is far greater than wavelength. Principle of operation of the array of slanted panels is that grating lobes caused by the array factor of the equivalent array of panels, with distance L between elements ($Fs(u_s)$), are suppressed by the pattern of the array factor of the single panel ($Fe(u)$). In order to obtain good shape of overall pattern of the antenna, additional phase should be applied on each slanted panel so that position of the main beam of the array factor $Fs(u_s)$ to coincide with the peak of the function $Fe(u)$. Phase difference between adjacent slanted panels is easily calculated having the distance between panels L and angle α:

$$u_s^0 = \frac{L}{\lambda}\sin\alpha \tag{7}$$

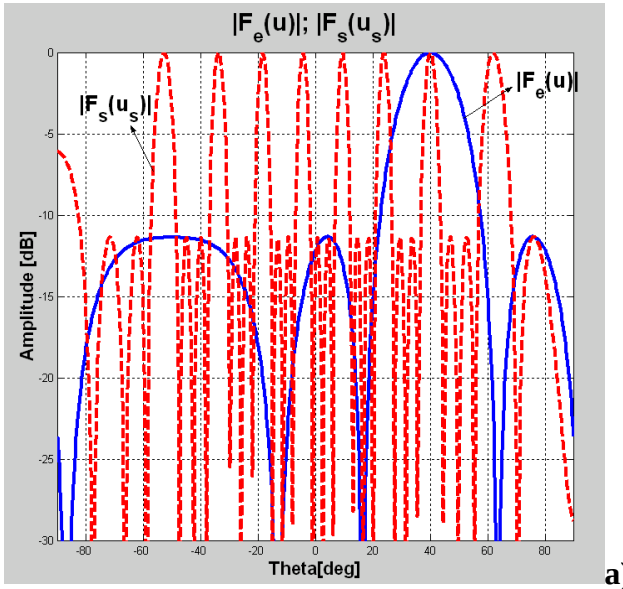

a)

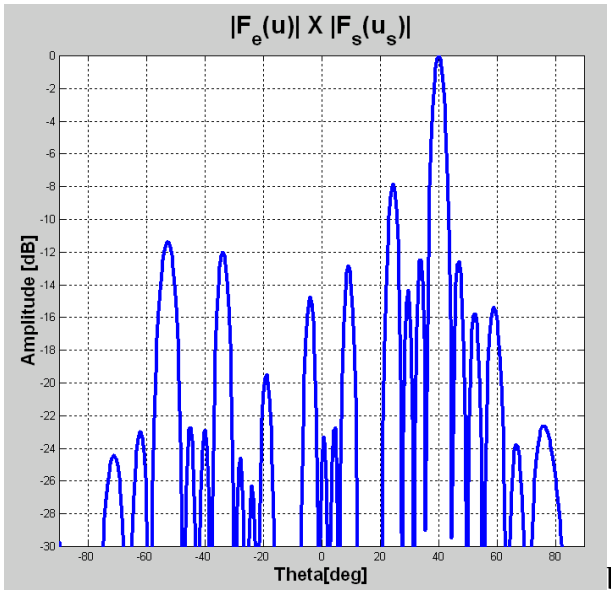

b)

Fig. 2: Graphs of the partial array factors and overall array factor for $d = 15[mm]$, $\lambda = 24[mm]$, $L = 100[mm]$, $P = 4$, $S = 4$: a) - $Fe(u)$ and $Fs(u_s)$; b) - $F(u)$

Using the phase difference defined by Eq. (7) the array factor of overall antenna can be written in the form:

$$F(u)=\left\{\sum_{q=1}^{P}\left|\dot{E}_q\right| exp[2\pi j(q-1)u]\right\}\times \left\{\sum_{m=1}^{S}\left|\dot{S}_m\right| exp\left[2\pi j(m-1)\left(u_s-u_s^0\right)\right]\right\} \quad (8)$$

where $\left|\dot{E}_q\right|$ and $\left|\dot{S}_m\right|$ take into account magnitude excitation of radiating elements within panel and magnitude excitation of each panel respectively.

An important question is determination of the distance between slanted panels - L, corresponding to a given angle α so that good shape of the pattern to be obtained. A criterion for good pattern shape could be ratio between main beam and the highest sidelobe (peak sidelobe) - b_m, given in [dB]. Since the pattern of the single panel - $Fe(u)$, is relatively sharp, the first grating lobe of the function $Fs(u_s)$ is of importance for the peak sidelobe level of overall antenna – Fig. 2 a). Positions of the grating lobes of the function $Fs(u_s)$ are determined from the periodicity of the sine function:

$$2\pi\left(u_s^p-u_s^0\right)=-2p\pi \quad (9)$$

where p is the number of the grating lobe. The position of the first grating lobe is obtained from Eq. (9), substituting $p=1$:

$$\theta_s^P=arcsin\left(sin\alpha-\frac{\lambda}{L}\right) \quad (10)$$

Having determined the position θ_s^P of the first grating lobe of $Fs(u_s)$ and given the ratio b_m, the equation for determination of the distance between panels could be written in the form:

$$\frac{F(u)_{\theta=\alpha}}{F(u)_{\theta=\theta_s^P}}=\left|\frac{1}{Fe(u)_{\theta=\theta_s^P}}\right|\geq 10^{\frac{b_m}{20}} \quad (11)$$

It is taken into account in Eq. (11) that $Fs(u_s)_{\theta=\theta_s^P}=Fs(u_s)_{\theta=\alpha}=F_e(u)_{\theta=\alpha}=1$. For uniform excitation of the array, Eq. (11) takes the form:

$$\frac{P\,sin\left(\pi u_{\theta=\theta_s^P}\right)}{sin\left(\pi P u_{\theta=\theta_s^P}\right)}-10^{\frac{b_m}{20}}\geq 0 \quad (12)$$

which together with Eq. (10) is used for determination of the distance between panels for uniform excitation. The function for determination of the distance between panels could be designated as W, which is the left side of the Eq. (12):

$$W=\frac{P\,sin\left(\pi u_{\theta=\theta_s^P}\right)}{sin\left(\pi P u_{\theta=\theta_s^P}\right)}-10^{\frac{b_m}{20}} \quad (13)$$

For values of W greater than zero, sidelobes of the array factor are less than the value specified by b_m.

There is one more restriction when determining the distance between panels L. Looking from the direction α in order not to exist overshadowing between panels, the following condition should be satisfied for the distance L:

$$L\geq\frac{l}{cos\,\alpha} \quad (14)$$

where l is transversal dimension of the panel. It may happen that value of L determined using (12) to be less than that determined by (14). This normally happens when desired level of the sidelobes is very low. This leads to placement of the panels close to each other and overshadowing is significant. Practically overshadowing of 20% could be accepted for normal operation of the array, which leads to values of b_m of order of -10÷-12 dB.

III. Simulation Results

The theory above has been used for simulation and determination of the distance between panels L of an array antenna comprised of four slanted panels according to Fig. 1. The antenna has been simulated at 12.5GHz. The single panel contains four radiating elements with distance between them $d=0.625\lambda$. Array factor of the single panel ($Fe(u)$) slanted at angle $\alpha=40[deg]$ is shown on Fig. 2 a). On the same figure is shown also array factor of the equivalent array of slanted panels ($Fs(u_s)$) for the distance between slanted panels $L=4.17\lambda=100[mm]$. On Fig. 2 b) multiplication of the two array factors is shown, which is the total array factor of the array.

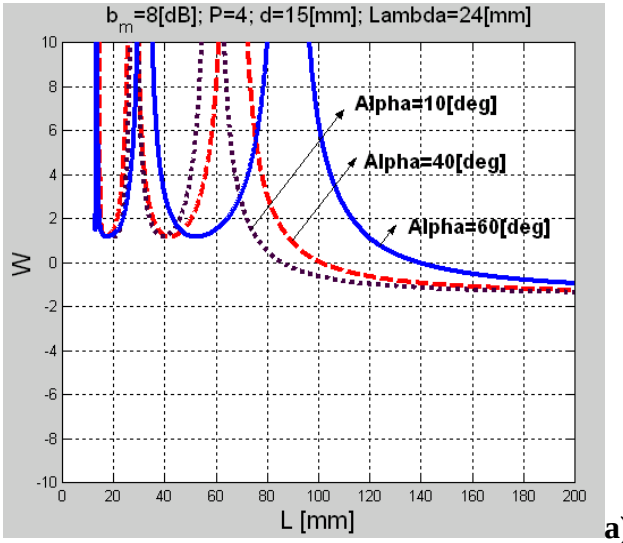

a)

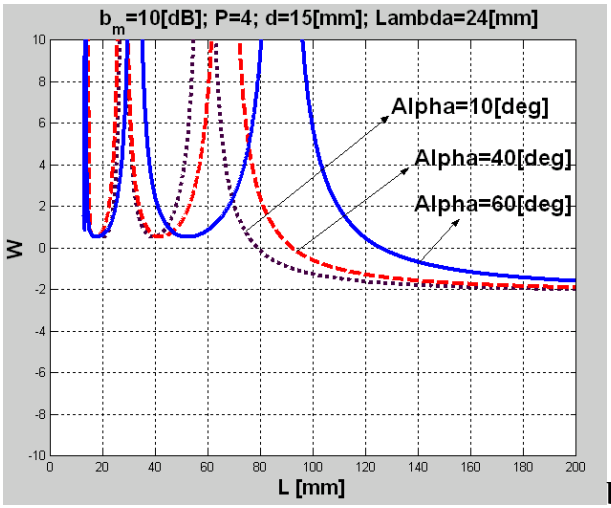

b)

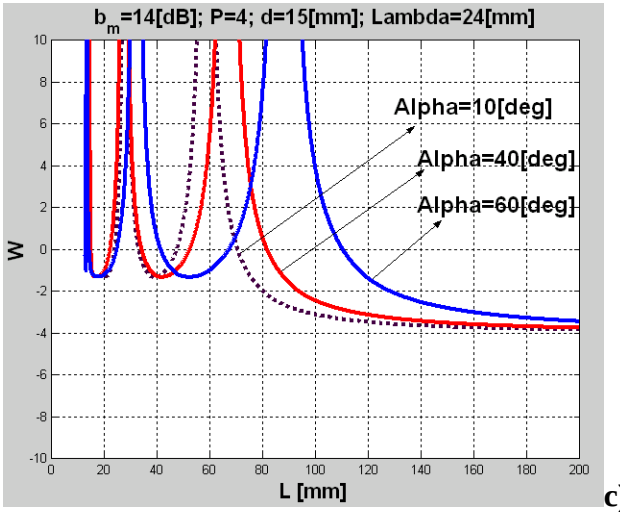

c)

Fig. 3: Graph of the function W for different values of slant angle α, $d = 15[mm]$, $P = 4$, $\lambda = 24[mm]$ for the values of the ratio b_m as follows: a) - $b_m = 8[dB]$; b) - $b_m = 10[dB]$; c) - $b_m = 14[dB]$

Graph of the function W, given with Eq. (13), for the simulated array is shown on Fig. 3 a), b) and c) for different values of the slant angle α and different ratios b_m. Crossing between W curve and x-axes gives the distance L, for which sidelobes of the array factor are exatly the value specified by b_m. For values of b_m lower than the level of sidelobes of the function $Fe(u)$ there are several crossings of the x-axes and the function W. This could be explained having in mind that the grating lobe follows the shape of the pattern of one panel ($Fe(u)$). On Fig. 3 a) and b) ratio b_m is above the peak sidelobe level of the single panel, while on Fig 3 c) b_m is below that level.

IV. Discussion and Conclusion

An effective method for scanning of the main beam of phased array antennas containing several slanted flat panels has been presented. Analysis of the array factor of such construction of a phased array has been performed. Dependence of the array factor of overall array with respect tot the distance between slanted antenna panels has been investigated. Equation has been proposed for determination of the distance between antenna panels given the ratio between main beam of the array and the first grating lobe levels. Simulation results utilizing the theory have been presented.

References

[1] Robert J. Mailloux, *Phased Array Antenna Handbook*, Artech House, 1994

[2] R. C. Hansen, *Phased Array Antennas*, Wiley, 1998

[3] R. J. Mailloux, "Grating lobe characteristics of arrays with uniformly illuminated contiguous subarrays," 1984 IEEE Int. Antennas Propagat. Symp. Dig. vol. 22, pp. 511 - 514, June 1984.

[4] D. M. Pozar, "Scanning characteristics of infinite arrays of printed antenna subarrays," IEEE Trans. Antennas Propagat., vol. 40, pp. 666 - 674, June 1992.

[5] J. A. Smolko, "Optimization of pattern sidelobes in arrays with regular subarray architectures," 1998 IEEE Int. Antennas Propagat. Symp. Dig. vol. 36, pp. 756 - 759, June 1998.

[6] R. J. Mailloux, "Constrained feed techniques for limited field of view scanning or time delay steering," 1998 IEEE Int. Antennas Propagat. Symp. Dig. vol. 36, pp. 740 - 743, June 1998

Diversity Systems in the Presence of Correlated Shadowing

Milan Živković, Nenad Milošević, Bojan Dimitrijević, Zorica Nikolić

Abstract - **In this paper we describe micro- and macrodiversity reception systems in an additive white Gaussian noise channel in the presence of Rayleigh fading and correlated log-normal shadowing employing BPSK signaling. The SC and MRC microdiversity system with various number of branches, *L*, along with dual macrodiversity system with correlated, power unbalanced branches is analyzed. System performances is analyzed using MGF (moment-generating function) approach where the dependence to BER of the average SNR/bit is used as the measure of the performances.**

Keywords – **BPSK signaling, Rayleigh fading, correlated log-normal shadowing, diversity combining.**

I. INTRODUCTION

Mobile communication channel can be modeled as additive white Gaussian noise channel subject to Rayleigh fading (received amplitudes has Rayleigh distribution) and log-normal shadowing (the mean of signal-to-noise ration has log-normal distribution). This scenario is typical for congested downtown areas with a large number of slow-moving pedestrians and vehicles. A powerful communication receiver technique that provides wireless channel improvement at relatively low cost is a well-known as diversity reception. Supplying to the receiver several replicas of the same information signal transmitted over independently fading channels, the probability that all the signal components will fade simultaneously is reduced considerably [1] and therefore, instant and mean SNR can be increased. The diversity reception is categorized as micro- and macrodiversity.

Microdiversity is a method for reducing the effect of instantaneous fading in which several uncorrelated faded signals are received at a radio port. There are several techniques for evaluating transmitted signal at the receiver. In this paper we consider MRC (*Maximal Ratio Combining*) and SC (*Selection Combining*) techniques for microdiversity combining. When SC is employed, among the *L* diversity branches, the branch providing the largest signal-to-noise ratio (or largest fading amplitude) is selected. Using MRC, the signals from all the branches are co-phased and individually weighed by fading factor to provide the optimal SNR at the output. Macroscopic diversity, again, is a method for reducing for reducing the effect of shadowing, in which several signals are received at different radio-ports, with differently experienced long-term shadowing. The most commonly used Macrodiversity technique is macrodiversity selection where selected signal originates from the port where the smallest long-term shadowing (the largest mean SNR) is present.

In this paper we will analyze systems with implemented micro- and macrodiversity techniques in an additive white Gaussian noise channel in the presence of Rayleigh fading with dual correlated, power unbalanced, log-normal shadowing and compare different microscopic selection methods where the dependence to BER of the average SNR/bit is used as the measure of the performances. Numerical evaluations of performances will be done using MGF (moment-generating function) approach [2], which represent a power tool that simplifies numerical calculations.

Milan Živković, Nenad Milošević, Bojan Dimitrijević, and Zorica Nikolić are with the Faculty of Electronic Engineering, Beogradska 14, 18000 Nis, Yugoslavia, E-mail: zivkovic8@ptt.yu

II. SYSTEM MODEL

Consider the system with two different radio-ports forming the microscopic diversity group. In order to mitigate the effect of shadowing (long-term attenuation) one can select signal originated from those port where the largest mean SNR is present. Consider, again, *L* independent microdiversity branches at every radio-port employ one of considered microdiversity techniques. If the transmitted signal is $x(t)$, the low-pass equivalent received signal in the *l*th branch of the *k* th port [3]

$$\omega_{kl} = \alpha_{kl} e^{j\phi_{kl}} \cdot x + \eta_{kl} \quad k = 1,2 \quad l = 1,\cdots,L \qquad (1)$$

where

α_{kl} - fading amplitude (factor) in the *l*th branch of the *k* th port (nonnegative number).

x - $\sqrt{E_b}$ ili $-\sqrt{E_b}$ with *a priori* probability 1/2.

ϕ_{kl} - fading phase in the *l* th branch of the *k* th port

η_{kl} - additive complex Gaussian noise in the *l*th branch of the *k* th port

E_b - bit energy.

Corresponding signal in the *l*th branch of the *k* th port after cophasing is

$$r_{kl}(t) = \mathrm{Re}\left\{\omega_{kl} e^{-j\phi_{kl}}\right\} = \alpha_{kl} \cdot x + n_{kl} \quad k = 1,2 \quad l = 1,\cdots,L \qquad (2)$$

where $n_{kl} = \mathrm{Re}\left\{\eta_{kl} e^{-j\phi_{kl}}\right\}$. We assume that $E\left\{n_{kl}^2\right\} = N_0 / 2$ for every *k* i *l*.

Let's $a_{k1}, \alpha_{k2}, \cdots, \alpha_{kL}$ denote fading amplitudes correspondent to microdiversity branches of the *k* th port. We assume that they are statistically independent with Rayleigh probability

density function (pdf) of the instant SNR, $\gamma_{kl} = \alpha_{kl}^2 \frac{E_b}{N_0}$, which has the form

$$p_{\gamma_{kl}}(\gamma_{kl}/\gamma_k) = \frac{1}{\gamma_k} e^{-\frac{\gamma_{kl}}{\gamma_k}} \tag{3}$$

which is conditioned on the local mean SNR at the k th port $\gamma_k = E\{\alpha_k^2\}\frac{E_b}{N_0} = z_k \frac{E_b}{N_0}$, where $z_k = E\{\alpha_k^2\}$ denotes mean-square amplitude values at the k th port. We assume dual branch, correlated, power unbalanced, macrodiversity system where the mean-square amplitude values follow a log-normal pdf [2]

$$p_{z_k}(z_k) = \frac{10/\ln 10}{\sqrt{2\pi}\sigma_{S_k} z_k} \exp\left(-\frac{(10\log_{10} z_k - \mu_k)^2}{2\sigma_{S_k}^2}\right) \tag{4}$$

where $\mu_k\,(dB)$ denotes mean, and $\sigma_S\,(dB)$ denotes standard deviation of the quantity $10\log_{10} z_k$. Let $z_{k\max}$ be the larger local mean-square value selected from the considered radio-ports, that is $z_{k\max} = \max\{z_1, z_2\}$. One can show that the pdf of $z_{k\max}$ has the form [4]

$$\begin{aligned} p_{z_{\max}}(z_{\max}) = {} & \frac{10/\ln 10}{\sqrt{2\pi}\sigma_{S_1} z_{\max}} \times \exp\left(\frac{(10\log_{10} z_{\max} - \mu_1)^2}{2\sigma_{S_1}^2}\right) \\ & \times \left(1 - Q\left(\left(\frac{1}{\sqrt{1-\rho^2}\sigma_{S_2}} - \frac{\rho}{\sqrt{1-\rho^2}\sigma_{S_1}}\right)10\log_{10} z_{\max} \right.\right. \\ & \left.\left. - \frac{\mu_2}{\sqrt{1-\rho^2}\sigma_{S_2}} + \frac{\rho\mu_1}{\sqrt{1-\rho^2}\sigma_{S_1}}\right)\right) \\ & + \frac{10/\ln 10}{\sqrt{2\pi}\sigma_{S_2} z_{\max}} \times \exp\left(\frac{(10\log_{10} z_{\max} - \mu_2)^2}{2\sigma_{S_2}^2}\right) \\ & \times \left(1 - Q\left(\left(\frac{1}{\sqrt{1-\rho^2}\sigma_{S_1}} - \frac{\rho}{\sqrt{1-\rho^2}\sigma_{S_2}}\right)10\log_{10} z_{\max} \right.\right. \\ & \left.\left. - \frac{\mu_1}{\sqrt{1-\rho^2}\sigma_{S_1}} + \frac{\rho\mu_2}{\sqrt{1-\rho^2}\sigma_{S_2}}\right)\right) \end{aligned} \tag{5}$$

Where ρ is correlation coefficient, and $Q(x)$ is Gaussian Q-function

$$Q(x) = \frac{1}{\sqrt{2\pi}} \int_x^\infty e^{-t^2/2} dt\,. \tag{6}$$

II. The System Performance

The average bit error probability (BER) of overall system is derived by averaging bit error probability conditioned on instantaneous γ_b, over the corresponding pdf

$$P_b(e) = \int_0^\infty P_b(e/\gamma_b)\, p_{\gamma_b}(\gamma_b) d\gamma_b \tag{7}$$

where the conditioned BPSK BER is given as

$$P_b(e/\gamma_b) = Q\left(\sqrt{2\gamma_b}\right) \tag{8}$$

We use MGF approach to analyze the proposed system performance, which is based on using the moment-generating function of instantenous γ_b [2]

$$M_{\gamma_b}(s) = \int_0^\infty p_{\gamma_b}(\gamma_b) e^{s\gamma_b} d\gamma_b \tag{9}$$

Moreover, a finite integral form of Gaussian Q-function is used for system analysis [2]

$$Q(x) = \frac{1}{\pi}\int_0^{\pi/2} \exp\left(-\frac{x^2}{2\sin^2\phi}\right) d\phi \tag{10}$$

where argument of the function becomes integrand of the finite integral, instead of lower limit of infinite integral as it is in the classical form (6). Substituting (8) in (7), using modified form of Gaussian Q-function (10) we get

$$P_b(e) = \frac{1}{\pi}\int_0^{\pi/2}\int_0^\infty e^{-\frac{\gamma_b}{\sin^2\phi}} p_{\gamma_b}(\gamma_b) d\gamma_b d\phi \tag{11}$$

where the inner integral presents familiar form of moment-generating function (9), so we have

$$P_b(e) = \frac{1}{\pi}\int_0^{\pi/2} M_{\gamma_b}\left(-\frac{1}{\sin^2\phi}\right) d\phi\,. \tag{12}$$

As we consider system with both macro- and microdiversity reception, pdf of instantaneous γ_b has the form

$$p_{\gamma_b}(\gamma_b) = \int_0^\infty p(\gamma_b/z_{\max})\, p(z_{\max})\, dz_{\max} \tag{13}$$

The corresponding moment-generating function one can get as

$$M_{\gamma_b}(s) = \int_0^\infty \left(\int_0^\infty p(\gamma_b/z_{\max}) e^{s\gamma_b} d\gamma_b\right) p(z_{\max})\, dz_{\max} \tag{14}$$

which is according to (9)

$$M_{\gamma_b}(s) = \int_0^\infty M_{\gamma_b}(s/z_{\max}) p(z_{\max})\, dz_{\max} \tag{15}$$

where $p(z_{\max})$ is given in (5).

The form of $M_{\gamma_b}(s/z_{\max})$ depends on applied microdiversity technique. When MRC is applied, it has form

$$M_{\gamma_b}(s/z_{\max}) = (1 - s\gamma_{\max})^{-L} \tag{16}$$

In order to simplify the further evaluations we assume, without the loss of generality, that $\mu_1 = \mu_2 = 0$. Then, MGF in (15) has form

$$\begin{aligned} M_{\gamma_b}(s) = \int_0^\infty (1 - s\gamma_{\max})^{-L} & \left\{ \frac{10/\ln 10}{\sqrt{2\pi}\sigma_{S_1} z_{\max}} \times \exp\left(\frac{(10\log_{10} z_{\max})^2}{2\sigma_{S_1}^2}\right) \right. \\ & \times \left(1 - Q\left(\left(\frac{1}{\sqrt{1-\rho^2}\sigma_{S_2}} - \frac{\rho}{\sqrt{1-\rho^2}\sigma_{S_1}}\right)10\log_{10} z_{\max}\right)\right) \\ & + \frac{10/\ln 10}{\sqrt{2\pi}\sigma_{S_2} z_{\max}} \times \exp\left(\frac{(10\log_{10} z_{\max})^2}{2\sigma_{S_2}^2}\right) \\ & \left. \left(1 - Q\left(\left(\frac{1}{\sqrt{1-\rho^2}\sigma_{S_1}} - \frac{\rho}{\sqrt{1-\rho^2}\sigma_{S_2}}\right)10\log_{10} z_{\max}\right)\right)\right\} \end{aligned} \tag{17}$$

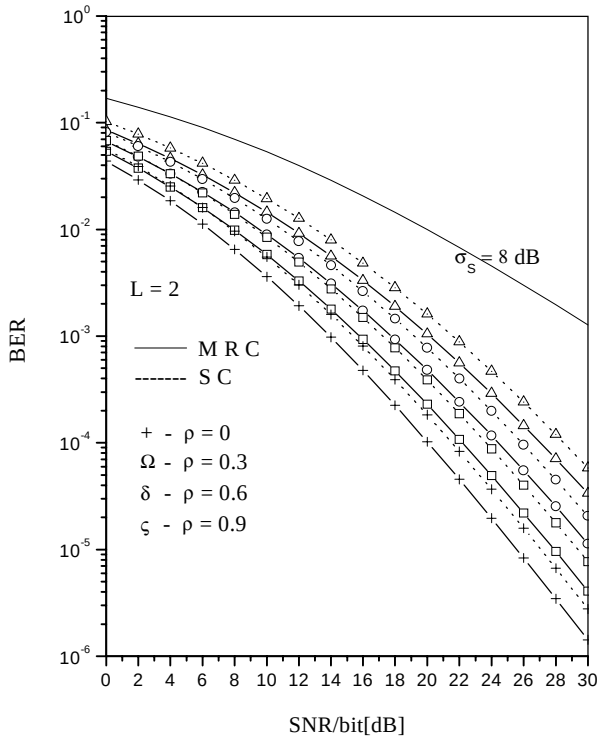

Fig. 1 Dependence of the BER of the SNR/bit for the diversity system with $L = 2$ SC and MRC combined micro branches with different values of correlation coefficient.

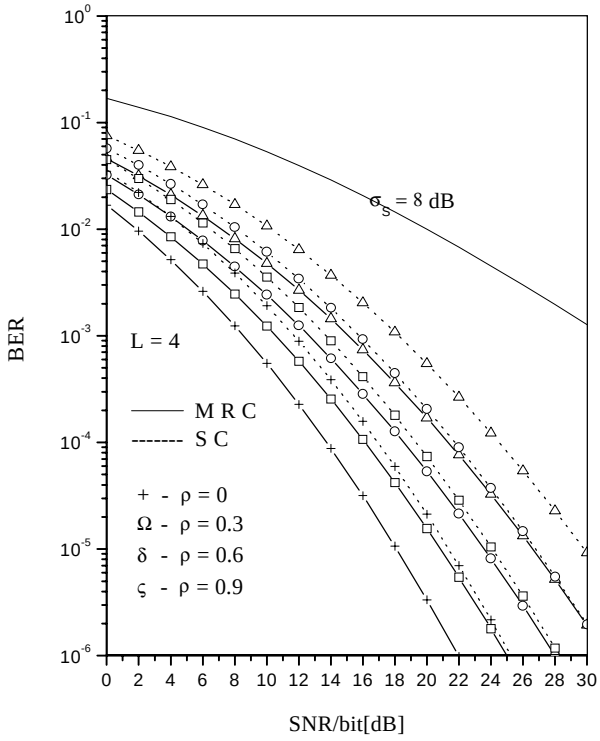

Fig. 2 Dependence of the BER of the SNR/bit for the diversity system with $L = 4$ SC and MRC combined micro branches with different values of correlation coefficient.

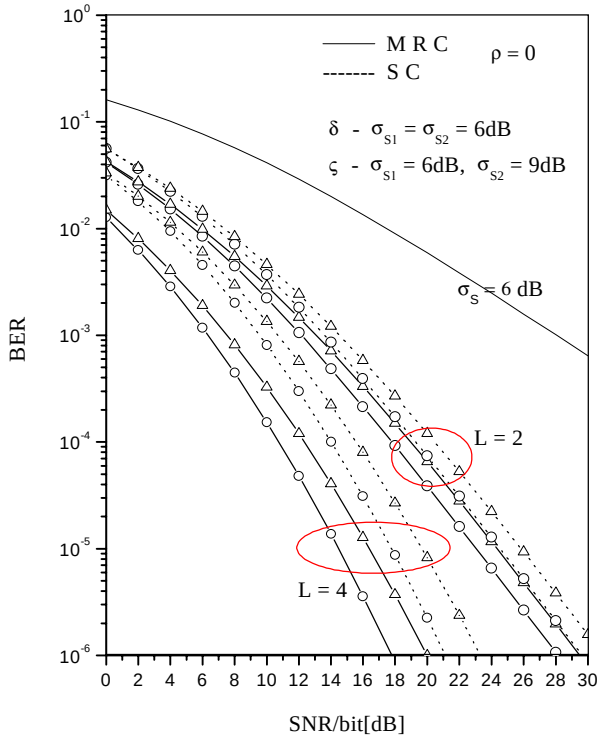

Fig. 3 Dependence of the BER of the SNR/bit for the diversity system with SC and MRC combined micro branches with equal and unequal power in uncorrelated macro branches ($\rho = 0$).

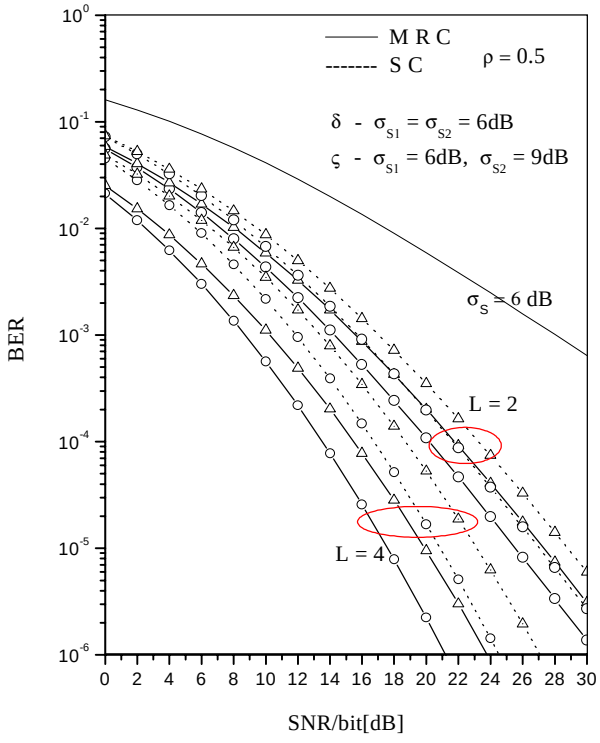

Fig. 4 Dependence of the BER of the SNR/bit for the diversity system with SC and MRC combined micro branches with equal and unequal power in correlated macro branches ($\rho = 0.5$).

Making the changes of variables $x_k = \frac{10\log_{10} z_{\max}}{\sqrt{2}\sigma_k}$, $k = 1,2$ and using a Gauss-Hermite quadrature integration [6], $M_{\gamma_b}(s)$ will have a form

$$M_{\gamma_b}(s) = \frac{1}{\sqrt{\pi}} \sum_{i=1}^{n} A_i \cdot \left\{ \left(1 - s \cdot 10^{\frac{\sqrt{2} x_i \sigma_{S_1}}{10}} \right)^{-L} \times \left(1 - Q\left(\left(\frac{1}{\sqrt{1-\rho^2}\sigma_{S_2}} - \frac{\rho}{\sqrt{1-\rho^2}\sigma_{S_1}} \right) \cdot x_i \sqrt{2}\sigma_1 \right) \right) \right. \quad (18)$$
$$\left. + \left(1 - s \cdot 10^{\frac{\sqrt{2} x_i \sigma_{S_2}}{10}} \right)^{-L} \times \left(1 - Q\left(\left(\frac{1}{\sqrt{1-\rho^2}\sigma_{S_1}} - \frac{\rho}{\sqrt{1-\rho^2}\sigma_{S_2}} \right) \cdot x_i \sqrt{2}\sigma_2 \right) \right) \right\}$$

Where $\{x_i\}, i = 1,2,\ldots,n$ are the zeros of the *n*th-order Hermite polynomial, and $\{A_i\}, i = 1,2,\ldots,n$ are corresponding weight factors. The sufficient value of *n* is 20.

Substituting (20), using $-1/\sin^2\phi$ as argument of $M_{\gamma_b}(s)$, in (14), we get expression for average BER in system with employed MRC micro- and dual, correlated, power unbalanced macrodiversity system with BPSK signalling.

Similar, when SC is applied, corresponding form of $M_{\gamma_b}(s/z_{\max})$ has a form

$$M_{\gamma_b}(s/z_{\max}) = L \sum_{j=0}^{L-1} \binom{L-1}{j} (-1)^j \left(1 - s\gamma_{\max} + j\right)^{-1} . \quad (19)$$

Substituting this expression in (15) we can get

$$M_{\gamma_b}(s) = \frac{L}{\sqrt{\pi}} \sum_{i=1}^{n} A_i \cdot \left\{ \sum_{j=0}^{L-1} \left[\binom{L-1}{j} (-1)^j \left(1 - s \cdot 10^{\frac{\sqrt{2} x_i \sigma_{S_1}}{10}} + j \right)^{-1} \right] \right.$$
$$\times \left(1 - Q\left(\left(\frac{1}{\sqrt{1-\rho^2}\sigma_{S_2}} - \frac{\rho}{\sqrt{1-\rho^2}\sigma_{S_1}} \right) \cdot x_i \sqrt{2}\sigma_1 \right) \right) \quad (20)$$
$$\left. + \sum_{j=0}^{L-1} \left[\binom{L-1}{j} (-1)^j \left(1 - s \cdot 10^{\frac{\sqrt{2} x_i \sigma_{S_2}}{10}} + j \right)^{-1} \right] \times \left(1 - Q\left(\left(\frac{1}{\sqrt{1-\rho^2}\sigma_{S_1}} - \frac{\rho}{\sqrt{1-\rho^2}\sigma_{S_2}} \right) \cdot x_i \sqrt{2}\sigma_2 \right) \right) \right\}$$

where $\{x_i\}$ and $\{A_i\}$ are defined as in (18).

Again, substituting (22) in (14), we get expression for average BER in system with employed SC micro- and dual, correlated, power unbalanced macrodiversity system with BPSK signalling.

III. Numerical Results

Figs. 1 and 2 illustrate performances of diversity receiver employing MRC and SC microdiversity reception, and dual macrodiversity reception with different values of correlation coefficient ρ, and equal branch powers ($\sigma_{S_1} = \sigma_{S_2}$). The performances decrease as the ρ gets bigger value for both of microdiversity cases, as it is expected. Degradation of performance due to correlation of macrodiversity branches becomes more evident when the number of microdiversity branches is greater. Furthermore, Figs. 3 and 4 depict dependence of the BER of the SNR/bit for the diversity system with SC and MRC combined microdiversity branches with equal and unequal power in uncorrelated and correlated macrodiversity branches, respectively. It is noticed that performances decrease when the power in macrodiversity branches is unbalanced, which is more noticeable when ρ has biger value.

IV. Conclusion

In this paper we analyze systems with implemented MRC and SC microdiversity and dual macrodiversity selection techniques in an additive white Gaussian noise channel in the presence of Rayleigh fading with dual correlated, power unbalanced, log-normal shadowing and compare different microscopic selection methods where the dependence to BER of the average SNR/bit is used as the measure of the performances. Numerical evaluations of performances are done using MGF (moment-generating function) approach [2], which represent a power tool that simplifies numerical calculations. It is noticed that performances decrease as the ρ gets bigger value for both of microdiversity cases, especially for greater number of microdiversity branches. Also, the effect of power unbalancing is is more evident ρ has biger value.

References

[1] J.G. Proakis, *Digital Communications*, 3rd ed. New York: McGraw-Hill, 1995.

[2] M. G. Simon, M.-S. Alouini, Digital Communication over Fading Channels: A Unified Approach to Performance Analysis, New York: Wiley, 2000.

[3] M. Živkovic, N. Milošević, Z. Nikolić, "Performanse BPSK diverziti sistema u prisustvu fedinga i efekta senke", *Zbornik radova, TELFOR*, Beograd, Novembar 2002.

[4] M. G. Simon, M.-S. Alouini, "Dual Diversity Over Correlated Log-Normal Fading Channels", *IEEE Trans. Commun.*, vol. 50, pp. 1946-1959, December 2002.

[5] J. Zhang, V. Aalo, "New Effect of Macrodiversity on Average-Error Probabilities in a Rician Fading channel with Correlated Lognormal Shadowing", *IEEE Trans. Commun.*, vol. 49, pp. 14-18, January 2001.

Session CSIT:

Computer Systems and Internet Technologies

Systematic Implementation Of Virtual Product On The Example of *DriveSets*

Angel Bachvarov[1]

Abstract **– The Virtual Product concept is explained as an internal rationalization and facilitation of the engineering process in the small-scale companies. A systematic design approach for implementation of modular positioning systems as a Virtual Product is presented. The implementation of the concept is discussed on the example of a case study.**

Keywords – virtual product, systematic design, modular positioning system

I. INTRODUCTION

In the last decade a significant number of research projects deal with closing the gap in the production chain beginning from the planning stage up to the putting the technical products in operation within a common infrastructural framework of software tools with compatible interfaces and "virtualization" of the manufacturing [1].

The Virtual Manufacturing is based on following three main principles:

- **Model and Simulate**, which means to do manufacturing activities „virtualy in the computer";
- **Predict and Evaluate**, which means to determine what would happen if the activities were actually carried out;
- **Make Improvements**, before the actual manufacturing is done.

The different VM-models are discussed in details in [1,2]. A simplified schematic comparison between the Virtual and Classical Manufacturing could be obtained from Fig. 1. It is obviously that the Virtual Manufacturing could be used for enhancement and optimization of the real Manufacturing as far as the VM could be observed as an image of the "real-world" manufacturing processes and its output could be applied directly for improvement of the existing production practice. Introduction of the virtual production strategies has as consequence a lot of benefits for the vendor which could help him to ensure his market share. The most important among there are:

[1]Angel G. Bachvarov is with the Faculty of German Engineering and Management Education, TU – Sofia, Building 10, Room 10214, 8 Kliment Ohridski, 1756 Sofia, Bulgaria, e-Mail: a_bachvarov@tu-sofia.bg

- **Adaptation and quick reaction** on changed market conditions;
- **Customization and utilization** of manufacturing resources selected for their abilities;
- **Higher efficiency** allowing low cost, and low volume production;
- **Better management** of the supply chain trough on-time deliveries, lead time compression, inventory and costs reduction.

Implementation of such production strategies for life-cycle management of the technical products is a very complex task and demands significant financial and research resources. It raises some issues related to a new corporate culture, data protection, information infrastructure, complex engineering knowledge communication, standards development, etc. Due all this they are presently an exclusive privilege of the large production companies, clusters of companies, global partnerships and big research institutes. Their introduction in the small and medium-scale companies is still problematic.

Different scenarios for the use of VM in the small and medium-scale companies are reasonable, e.g. Component catalogues, Digital procurements, Electronic bids, Partner selection, Customisation etc. Recently a trend for developing of so-called Virtual Products is established.

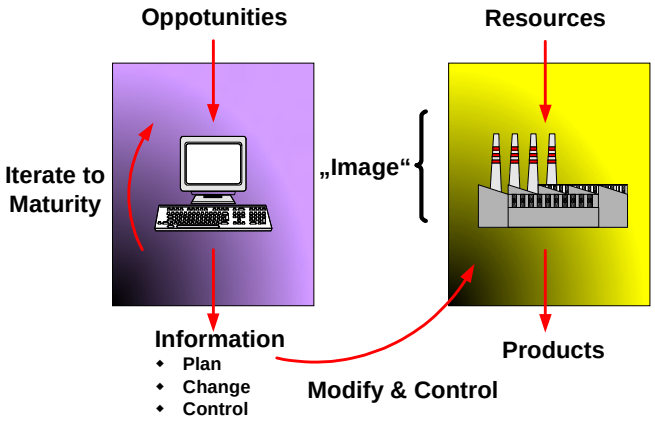

Fig. 1 Model of VM and "classical" Manufacturing

Here the concept of "*the virtual product*" concerns not only the conventional computer aided planning and simulation of the developed products. According to the adopted definition "the virtual product" is a technical system, which allows instant and direct access and management from every PC, everywhere and on every stage and level of its production

cycle in order to increase the competitiveness and to guarantee the market share of the vendor through high diversity of the covered technical parameter ranges and possibility for promptly development and "materialisation" of pre-engineered "custom-tailored" solutions according to the individual clients needs. In this sense the Virtual Product could be seen as an important engineering technique for internal rationalization and facilitation of the engineering process in the small-scale companies.

According to the market research carried out by the authors in 2002 covering Germany, Austria and Switzerland a significant number of the small-scale production companies acts mostly only as integrators of OEM modules in fully functional technical systems [3]. The application of the "Virtual Product" concept is especially favourable in such cases. A common approach for development of Virtual technical products is still missing.

II. Systematic Design Approach

The strong competition on the global market creates a need for precise selection of production devices with optimal technical and economical characteristics and their best possible adaptation to the specific requirements of the customers. The electric driven modular positioning and handling systems offer opportunity for this. The available on the market systems are limited in respect of diversity of their operational properties [3]. In consequence of this fact significant additional efforts are required every time in order to customise these systems to the constraints and technological limitation for every single automation problem.

As a design object the modern modular positioning and handling systems have the following features:

- they are complex technical systems;
- they are described with diverse sub-systems, structures and parameters;
- their development imposes observance of a large number of requirements and constraints and is developed with significant financial and temporal resources.

The importance of timely and efficient product development requires quickly and directly determination of the possible solutions. That could be achieved by adopting design procedure, which is flexible, transparent, and capable of being planed, optimized and verified. As Pahl, G., Beitz,W. [4] claim the systematic design approach provides an effective way to rationalize the development and production processes. Such design method is also prerequisite for continuous computer support using stored data. Systematic processing [5] makes possible consideration of cost and quality of the designed products on early stage, which enables better market chances. In order to implement a modular positioning systems as a Virtual Product range a special design procedure was proposed.

The method has three stages and includes following elements:

- Virtual Product framework;
- Functional structure of a modular handling system;
- Classification of the functional units performing the the functional structure;
- Morphological matrix for composing the functional units set of the single sub functions;
- Algorithm for generating (syntheses) the possible system structures;
- Selection of the optimal handling system;
- Validation procedure.

Within ***first stage*** sets of functional entities performing the sub-functions are combined through a morphological matrix technique in complete functional structures (see Table 1 and Fig. 2). The first column of the scheme contains the sub-functions of the functional structure and the instances of the correspondent functional entities (sub-modules) are entered in the rows. The possible solutions could be obtained by combination trough systematic variation of the modules (functional entities) performing the single sub-functions according to the resolved functional structure entered in the morphological matrix.

The main problem with such combinations is ensuring the physical and geometrical compatibility of the functional entities to be combined. The compatibility of functional entities is tested through an additional compatibility matrix. If compatibility (full or partial) between two functional entities exists, the instance of the required connecting element (mechanical, electrical or software) is mapped in the correspondent cell of the scheme. This enables the combination only of the compatible instances of the correspondent sub-solutions.

TABLE I
MORPHOLOGICAL MATRIX

Sub-function	Functional Entity	Instances of functional entities			
		1	2	...	m
1. Control	*Control unit*	E_{11}	E_{12}	..	E_{12m1}
2. Amplification of the control signals	*Motor driver*	E^1_{21}	E^1_{22}	...	E^1_{2m2}
3. Transformation of the electrical energy in torque	*Electric motor*	E^1_{31}	E^1_{32}	...	E^1_{3m3}
4 Amplification of the mechanical energy	*Gear*	E^1_{41}	E^1_{42}	...	E^1_{4m4}
5. Transformation of the torque in force	*Linear actuator*	E^1_{51}	E^1_{52}	...	E^1_{5m5}
6. Fixing the load position	*Sensor*	E^1_{61}	E^1_{62}	...	E^1_{6m6}

where: E^i_{nm} – functional entity; i – indicates axis No.; n – sub-function No.; m – functional entity instance No.

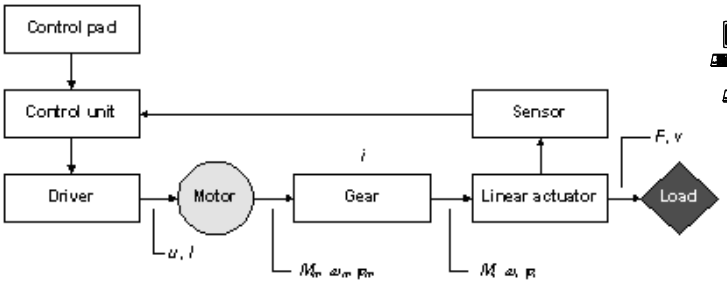

Fig. 1. Simplified symbolic model of a linear positioning system

Within ***second stage*** a selection of the optimal positioning and handling system have to be done. For the systematic approach the solution field is very wide. The task is to find the optimal combination of the available functional entities performing the system sub-functions under preliminary requirements and constraints related to the technical and economical characteristics of the system (price, weight, long-life etc). That is a multi-objective optimization problem (MOP) and with following mathematical representation:

$$\textit{Minimize}\ F(\vec{x}) = (f_1(\vec{x}),\ldots f_p(\vec{x})) \tag{1}$$

$$\textit{under constraints}\ g_i(\vec{x}) \le O, i = 1,\ldots,m, \vec{x} \in \Omega$$

The analysis of the problem has found its following special features:

- huge number of possible variant solutions;
- discrete character;
- need of evaluation of the evolved structures based on a set of technical and economical system characteristics of different physical meanings and dimensions;
- optimisation goals of different priority level.

In order to obtain diverse results three essentially different optimization techniques were studied [6,7], e.g.:

- Weighted sum method;
- Minimax Goal Programming;
- Vector Evaluated Genetic Algorithm (VEGA) based optimisation by switching objectives.

Within ***third stage*** a graphic form model describing the physical characteristics of the proposed structure: e.g. spatial, geometric and topological data is built. Tests are run through simulation to determine whether the intended purposes are satisfied by the found structure.

A web-based tool for computer aided selection of modular linear drive systems with up to three axes to support development of the virtual product was developed based on the presented approach excluding third stage, which is not yet implemented as web-based function. It has a classical 3-layer model: data input interface (front end client), computing algorithm (server) and database at back-end. Fig. 3 shows the software architecture and data flow within the system.

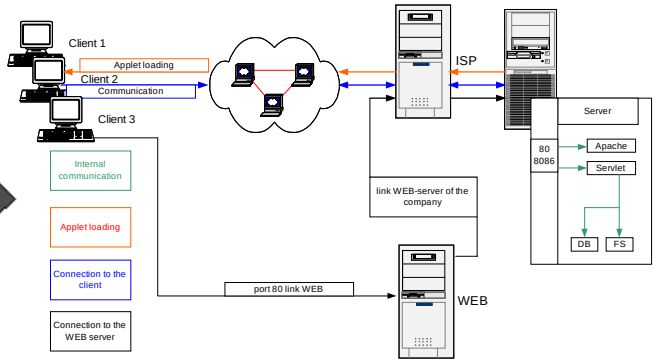

Fig. 3. System architecture and data flows

At the end of the work cycle a graphic 3D form model is generated with *Autodesk Inventor* and is used for crash-tests, FEM-analysis etc. Presently a migration to *SolidWorks* is undertaken.

III. Case Study Drive Sets

The aforesaid method and tool were used as a core element in the development of ***DriveSet***-family as a part of an R&D project studying feasibility of the introduction of a virtual production model in ***Systec E+S GmbH***. ***Drive Sets*** were designed in a scalable framework as parametric range of modular linear positioning and handling systems with application in the industrial and laboratory automation, evolved through the integration of OEM-modules. The framework of the parametric range was built by systematic variation and full combination of 6 technical and structure system parameters (load carrying capacity, maximum speed, repeatability, operating area, design type, stroke) mapping every combination as unique ***DriveSet***-family member.

For the purposes of an unique identification of the single entities of the ***DriveSet***-family a convention for the following the system properties groups was adopted (Table 2):

- ***operating properties*** – all parameters defining the system input and output;
- ***structure properties*** – they describe the spatial structure of the system and geometric relations between the system elements.

The defined system properties, excluding the stroke, are coded with an art of semantic code. Through their systematic variation the set of the possible variants is generated. These possible variants build the framework in which the **DriveSets**-family evolves. Every unique property combination obtains a single number identifying the correspondent representative of the family (see Fig. 4). The network model of the **DriveSets**-family could be seen on Fig. 5. In this manner some 144 basic structures were specified.

TABLE 1
SYSTEM PROPERTIES OF THE DRIVE SETS-FAMILY

Operating properties	Structure properties
Load carrying capacity: describes the capacity of the system to carry a definite load. That is the maximal paying load which the system could accelerate up to the maximal speed in 100 ms.	**Operating area:** describes the shape of the operating area where the system TCP could be positioned. The shape of the operating area is related to the type of the kinematical structure and number of the spatial axes.
Speed: indicates the maximal system speed.	**Design type:** indicates the spatial arrangement and fixing of the single mechanical modules: e.g. gentry.
Repeatability: indicates the repeatability class of the system.	**Stroke:** indicates the maximal stroke along a single spatial axis.

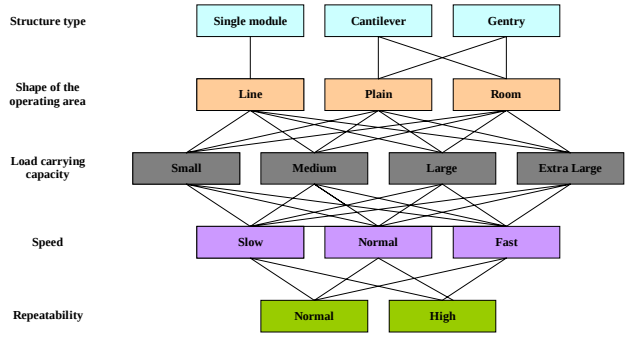

Fig. 4. Network model of *DriveSets*

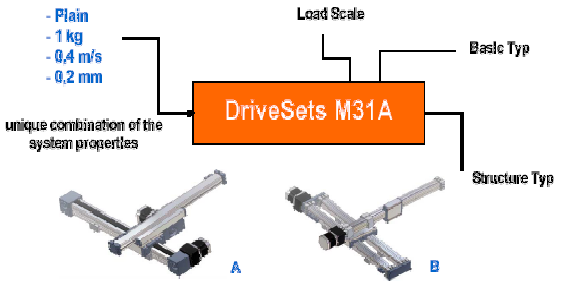

Fig. 5. Identification of *DriveSets*

The values corresponding to the used semantic code are determined on the ground of statistic processing and analysis of the market figures for the past three years delivered by ***Systec E+S GmbH*** as well as an inquiry made among 114 companies from EU, identified as potential customers. The optimal solutions for 98 of the predefined within the frame positioning and handling systems were found and implemented as "virtual products", 3D-models and product specifications needed for the fast production is stored in the database. Now the customer could select among the offered pre-engineered basic structures and find the system most appropriate for his specific needs using a simple selection procedure (with hard copy catalogue or online). Further he can choose the stroke for every single axis of the system. 10 standard stroke lengths are available.

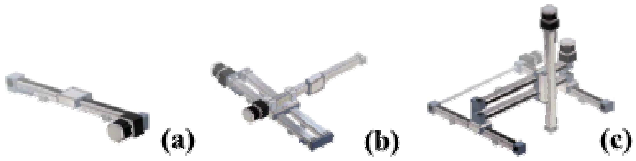

Fig. 2 3D-models of *DriveSets*-family representatives:

(a) M2 (single module; line; 1kg; 0,1m/s; 0,025mm), (b) M31B (cantilever; plain; 1kg; 0,4m/s; 0,2 mm), (c) M90 (gentry; room; 0,4 m/s; 0,2 mm)

More detailed information about *DriveSets* is available from <http://www.drivesets.de>.

IV. CONCLUSION

The Virtual Product are an important engineering technique for internal rationalization and facilitation of the engineering process in the small-scale companies.

An approach for systematic design of modular handling system applicable in the industry for the purposes of an attempt for introduction virtual manufacturing practices in small-scale companies is developed.

The adoption of the systematic design method for development of Virtual Products:

- ensures the determination of an optimal solution due its systematic nature;
- reduces the effort and saves time in respect to the solving of the design problem;
- cuts off the cost within development stage up to 40%;
- possesses improving potential and wide application field;
- was successfully applied in the solving of real-world design.

REFERENCES

[1] P. Banerjee, ,D. Zetu, *Virtual Manufacturing***.** John Wiley & Sons Inc. NY, 2002.

[2] D.S.Nau, J.W.Herrmann, W.C.Regli *Virtual Factories*, Institute for System Research, University of Maryland, 2002.

[3] A. Bachvarov, T. Wolter, „Neue Strategie für systematische Entwicklung von Antriebssystemen", Automation & Design Kompendium. München. pp. 214 – 218, 2003.

[4] G. Pahl, , W. Beitz, *Konstruktionslehre*, Springer-Verlag. Berlin Heidelberg, 2000.

[5] *VDI 2221: Systematic Approach to the Design of Technical Systems and Products*, VDI-Verlag GmbH. Dusseldorf, 1998.

[6] I. Boyadjiev, I. Malakov, "Selection of Optimal Structure Variant of Assembly Systems", Машиностроене 2-3, Sofia, pp.18-24, 1999.

[7] K. Deb, *Multi-Objective Optimization using Evolutionary Algorithms*, John Wiley & Sons Inc. NY, 2002.

Three-dimensional terrain visualisation on the Internet using VRML, Java, and JavaScript

Dusan Dacic[1] and Dejan Rancic[2]

Abstract – **This paper presents technologies applied to design of three-dimensional GIS systems on the Internet. VRML descriptive language is described as a suitable platform for system development and possibilities of procedural programming using Java and JavaScript are also presented. At conclusion, we present Web 3D Modeler, three-dimensional terrain visualization system on the Internet**

Keywords – **terrain visualization on the Internet, VRML, Java, JavaScript**

I. INTRODUCTION

The complexity of modern Geographical Informational Systems (GIS), and tasks that they are meant to perform, demand integration of three-dimensional spatial information, semantics, and all the necessary tools to work with and analyze relationships between them. Currently, existing systems lack either three-dimensional analysis capabilities, as do the majority of commercial GIS systems, or are missing tools for analysis of information related to spatial objects, like CAD (Computer-Aided Design) software [1]. There are still only a few systems that have the capabilities to process 3D spatial queries that seem simple enough: "mark all landscape areas that are not covered by radar network", or "mark all available apartments in Central Street having windows NOT looking at the newest discotheque". For a while, it's justifiable to develop systems with above described capabilities. Remote access to these systems over the Internet is a challenge yet to meet. There are three basic problems to be solved when designing this functionality, data structuring on the server side, ways to organize communication and queries between client and server side, and query result visualization on the client computer.

World Wide Web (WWW) is based on standard data formats, such as HTML and XML, JPEG and GIF image formats, and GML for 2D vector graphics images. These standards enable the use of "thin" client-server model in heterogeneous environment that the Web is.

The goal of this paper is to present technologies and standards that are setting direction for the development of three-dimensional GIS systems on the Internet, having very low development cost, multiplatform support, that are very easy to maintain and expand, and intrinsically enable easy integration into other systems.

Dusan Dacic is with the Electronic Faculty Nis, Beogradska 14, 18000 Nis, Serbia e-mail: dusandacic@elfak.ni.ac.yu
Dejan Rancic is with the Electronic Faculty Nis, Beogradska 14, 18000 Nis, Serbia e-mail: ranca@elfak.ni.ac.yu

The use of VRML standard in development of 3D client-server GIS systems is not an unknown idea, VRML exists since year 1994 [2], and it is no longer considered a new and immature standard, but until recently the widespread use of this standard was limited by narrow bandwidths, and also by the cost of powerful 3D graphics subsystems that could enable real-time rendering of VRML's three-dimensional objects. With lower prices of graphics hardware, and constant increase of average bandwidth, we now have the possibility to construct 3D GIS systems for wide use, lowering the price for end-users, and thus increasing user population and justifying development effort. .

II. VRML

VRML [2] stands for *Virtual Realty Modeling Language*. Similarly as HTML and XML are used to describe data with predefined fields, that describe structure and attributes, VRML has predefined nodes and statements that describe structure, appearance and interaction in 3D environment. Unlike existing 3D graphics languages and libraries, that are procedural, like OpenGL and DirectX, VRML is object-oriented descriptive language, and much more. VRML is neither typical Virtual Reality language, neither real modeling format. It is common that VR systems include complicated display systems and HUD displays, state-of-the art non-standard input devices such as gloves, movement tracking sensors, voice interaction systems, and VRML has standard support only for mouse interaction, and standard displays. For CAD modeling purposes, VRML has only minimal capabilities.

Many authors consider VRML to be the 3D analogue for HTML. This actually means that VRML has become a standard media for publishing 3D multimedia data on the Internet. VRML supports different multimedia formats for sound, video and animation.

By definition, VRML is file format for integration of 3D graphics and multimedia, an international ISO/IEC-14777 standard that offers efficient way to exchange 3D data. Many modern modeling and programming tools have support for import/export for VRML. Good examples are 3D Studio Max by Discreet, World ToolKit by Sense8 and Java 3D [3].

VRML Consortia is a community gathered around defining an open standard for VRML. This consortium defines VRML as an "Open standard for three-dimensional multimedia on the Internet". Open standard means that VRML is publicly available, like Java.

To view VRML content, one must use plug-ins for Internet browsers, or stand-alone software that enable loading and rendering of VRML files. Most used plug-ins are Cortona VRML Client by Parallel Graphics [4], Cosmo Player by

Computer Associates [5], and Blaxxun Contact by Blaxxun interactive [6] (Fig 1.)

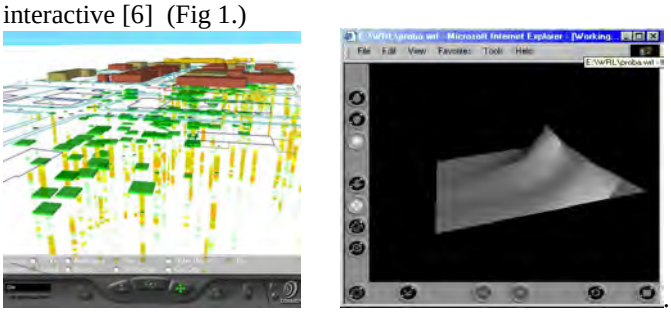

Fig. 1. VRML browsers

III. VRML PROGRAMMING

VRML is very useful for developing service for interactive three-dimensional visualization on the Internet. VRML describes 3D object by using scene graph structure. Scene graph is hierarchical tree-like structure that describes the entire 3D scene, including geometrical object representation, object attributes and relations between objects [2]. Scene graph makes it easy to build complex objects composed of simple objects. Separate models and scenes could be easily combined in order to build complex virtual environment. Each object is presented by a node or a sub-tree, and it can be only one entity or composition of spatially or logically related entities. Each object in the scene has its own unique name. Primitive objects can be enhanced by additional attributes as material, texture or some other attribute, by using attribute-defining nodes. Attributes defined in one node are applied to all children of that node.

An example of object attribute definition is given in Fig 2. The code models the scene graph.

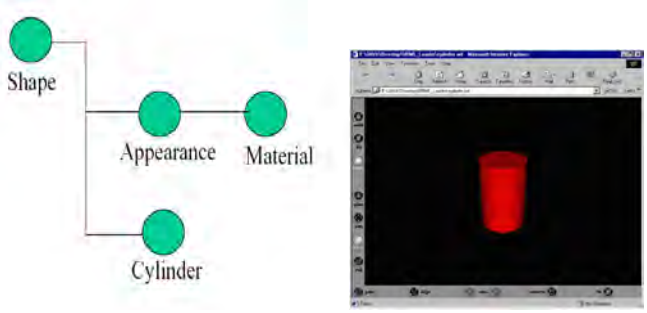


```
#VRML V2.0 utf8
Shape {

      appearance Appearance {
          material Material {
              diffuseColor  1 0 0  # R G B -comment
          }
       }

      geometry Cylinder {
          height 3
      }
}
```

Fig. 2. VRML code example

The given example shows that the graph scene is defined by object instantiation. *Shape* node contains a reference to an *Appearance* object that defines material from which the virtual object is built.

A VRML node can be compared with object or class in OO (Object Oriented) languages like C++ or Java. Objects are generated after the browser parses the VRML file. VRML has 54 nodes that cover almost every aspect of 3D modeling.

In order to model terrain, *ElevetionGrid* node is used together with *QuadLOD* node to model LOD functionality (Level Of Detail) as shown in Figs. 3 and 4.

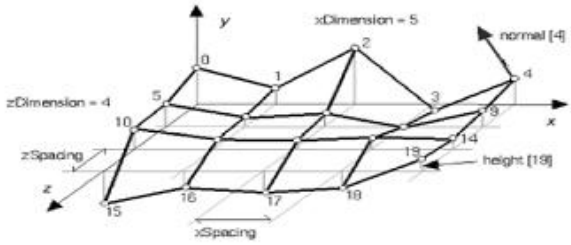

Fig. 3. *ElevationGrid* node model

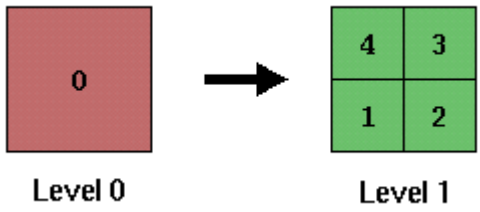

Fig. 4. *QuadLOD* node model

QuadLOD node is derived node type developed in order to enable implementation of level-of-detail algorithm. LOD algorithm enables the viewer to transfer and render only the detail that can be seen on the raster display, depending on the virtual viewpoint. One node can only contain data for two levels of detail, but using the quad-tree-like structure multiple level of detail can be achieved.

LOD algorithm should be able [1]:

1. To form a terrain view with varying detail level, based on viewpoint location and terrain configuration, meaning that areas with small or none height variation can be represented with fewer polygon count than areas with high level of variations, such as canyons, cliffs, and mountains.
2. To solve appearance of *cracks* in terrain rendering that appear due to resolution mismatch of neighboring quadratic areas at different levels of detail
3. To enable smooth and seamless transition between terrain tiles that present the same area but at different level of detail.

To achieve such functionality, it's not enough to use only VRML descriptive language; therefore, we looked for possibility of introducing procedural described behavior. VRML standard enables procedures to be defined through the use of External Authoring Interface (EAI) system, basically a framework of Java base classes that are to be sub-classed or

used directly, and when linked dynamically with VRML browser, used as a behavioral description of VRML objects and scenes. To access these classes, one could use Java or JavaScript programming languages.

VRML node used to link Java or JavaScript with VRML world is *Script* node. This node has input and output ports like almost every node in VRML. These ports or *events* are used to enable communication between VRML objects: it's possible, for example, for proximity sensor to switch the light on in a virtual environment when the virtual viewpoint reaches the certain threshold. The same logic is used to incorporate a *Script* node into virtual environment. Script has no body, but it can be used to receive events, pass them to Java code for processing, and pass generated events back to the virtual world.

Java code can also be used to access *Factory* engine of the VRML browser that has the ability to introduce new objects into the VRML scene.

JavaScript can be used for simple world scripting, and for processing user input from an environment external to a VRML world, such as a web page that has VRML world embedded in it. The best thing about JavaScript is that it can be coded directly into the VRML scene or HTML environment that surrounds the VRML.

In Fig. 5 is shown a snippet of JavaScript code that is used to model a simple behavior together with a VRML code that links it with a scene.

```
DEF MoveObject Script {
        eventIn SFFloat set_timeFraction
        eventOut        SFVec3f  location
        url "javascript:
        function set_timeFraction  (time_fraction, tm)
{
        location[0]   =   0.0;
        location[1]   =   4.9*(1-time_fraction);
        location[2]   =   0.0;
}" }
DEF Timer TimeSensor {
                loop TRUE
}

ROUTE Timer.fraction_changed TO
MoveObject.set_timeFraction

ROUTE MoveObject.location_changed TO
MovingObject.set_translation
```

Fig. 5. Script sample

Java stands out as a complicated but powerful medium for programming VRML objects behavior. It enables a powerful programming environment, and executes a lot faster then a JavaScript code. Java has advanced network communication abilities, and can be used efficiently to model user interface into a VRML world, that intrinsically has no interface but one that enables us to move in virtual space.

IV. GINIS WEB 3D MODELER

Ginis Web 3D Modeler is a Web application developed at *Geographic Informational Systems and Computer Graphics Laboratory* with *Electronic Faculty* in Nis. It is an experimental application for testing the possibilities of presenting virtual world on the Internet containing GIS informative capabilities.

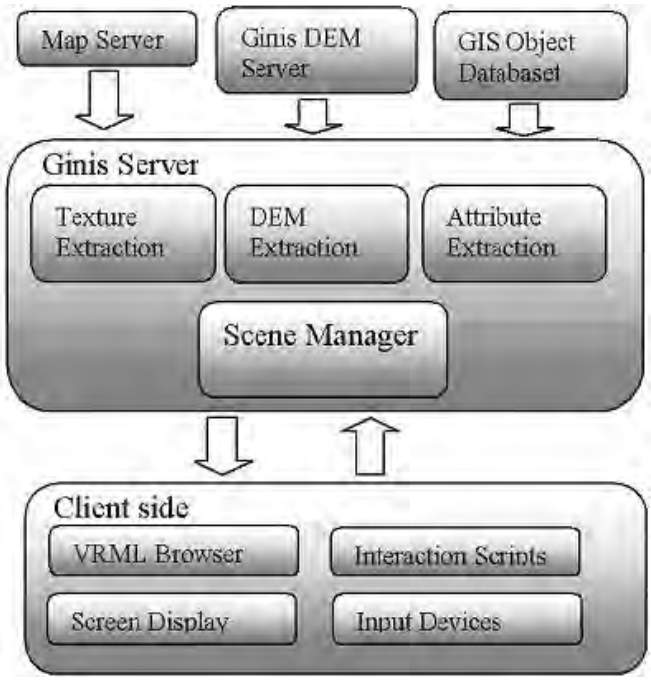

Fig. 6. Ginis Web 3D Modeler

Conceptual model of the system is shown on Fig 6. By using VRML methodology, all of the actual 3D graphics rendering process is done solely on the client side. Interaction with the user is done inside the virtual environment, or through the scripts embedded in the web page that has access inside the virtual world. To access virtual environment, user selects geographic area of a special interest, and gets directed to a page with 3D rendering (Figs. 7 and 8)

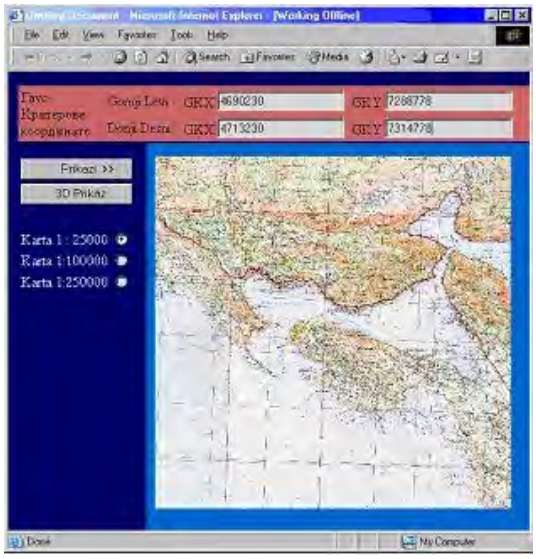

Fig. 7. Selection of special interest area

When the user approaches some part of the terrain, the tile used for that area is being replaced with a tile that has a higher resolution per measure unit (Figs. 8 and 9).

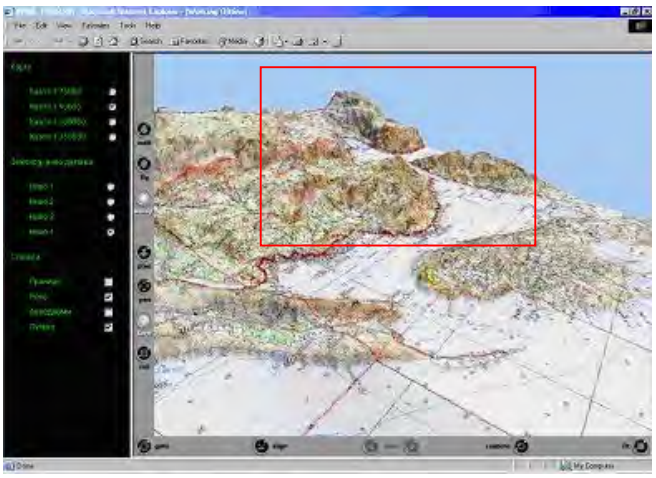

Fig. 8. Terrain viewed from a distance

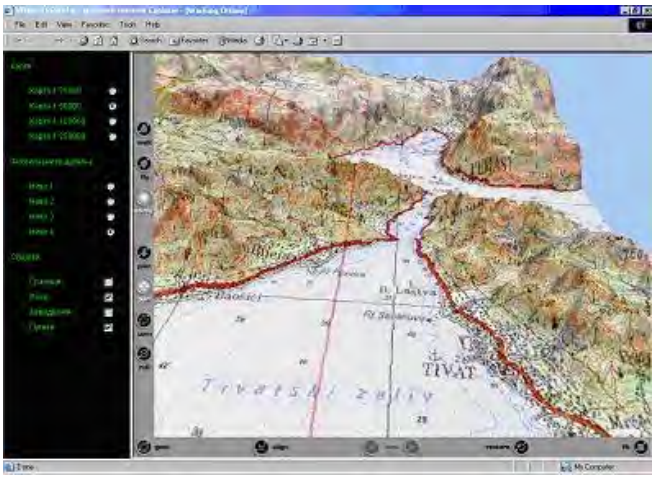

Fig. 9. Close-up look with a different LOD

Table I shows average measured frame rates with LOD functionality on and off, and also with static or dynamic viewpoint. Measured terrain sample had 60000 height points, and was textured with 1024x1024 24-bit bitmap. Test configuration was Athlon 1GHz CPU, 512 MB DDR RAM, GeForce 2 Graphics card, Windows 2000 OS, MS Internet Explorer 6.0, Cortona VRML browser.

It can be observed that we gained an average of 10 frames per second, which can be considered a small gain by static camera, but makes almost 50 percent gain with dynamic camera, and together with optimized bandwidth requests justifies the introduction of LOD algorithms.

TABLE I
MEASURED AVERAGE FRAME RATES

	Static camera	Dynamic camera
LOD switched OFF	80	23
LOD switched ON	88	34

V. CONCLUSION

In the paper, we tried to explain the ways of developing a system that has all the benefits of the two worlds: organized geographical and georeferenced information capability of a full-featured GIS system, and an easy-to-use three-dimensional presentation of GIS information. There are numerous applications of such system. System like this can be used for a public-place automatic-information desk, or with a recent increase in small mobile devices performance, it could be easily executed on any mobile device that has a ported version of VRML browser. Cortona has developed a Pocket Cortona Client for PocketPC devices [4], and it is expected for the other companies in the business to do the same.

Java and JavaScript programming languages enable us to expand existing capabilities of VRML, and are powerful tools for design of user interaction system and performance optimization algorithms.

Ginis Web 3D Modeler is a step toward designing a truly powerful interface to existing GIS datasets, available to larger population of users.

VRML is an open standard, but recently, X3D as an XML-compatible standard has gained its position in a WWW community [7]. X3D is by all concepts similar to VRML, and also has same basic nodes with same structuring rules, and it is an easy task to convert existing VRML-based systems in a way to support X3D, only disadvantage of X3D is the slow response of VRML browser manufacturers. Implementation of X3D should be the first step in developing this system as a full-featured Web service.

ACKNOWLEDGEMENT

The research was partially supported by the project “Geographical Information System Designed to Improve the Local Municipal Function based on Internet/WWW Technologies”, funded by Ministry of Science, Technology and Development, Republic of Serbia and Municipality of Niš, Contract No. IT.1.23.0249A.

REFERENCES

[1] Zlatanova, S., A. Rahman, M. Pilouk, “3D GIS: current status and perspectives”, Proceedings of ISPRS, 8-12 July, Ottawa, Canada, 2002
[2] Rikk Carey and Gavin Bell, “The annotated VRML 97 reference”. URL: http://www.best.com/rikk/Book, 1999
[3] Coors, V. and V. Jung, “Using VRML as an Interface to the 3D Data Warehouse”, Proceedings of VRML'98, New York
[4] PARALLELGRAPHICS,2003 url:http://www.parallelgraphics.com/products/
[5] COSMOSOFTVARE,2003 url:http://www.cosmosoftware.com
[6] BLAXXUN,2004 url: http://www.blaxxun.com
[7] WEB3D,2004: http://www.web3d.org/x3d/

WEB-based Controller for Monitoring of Yoghourt Process Making

Rosen S. Ivanov[1] and Ivan S. Simeonov[2]

Abstract – **This paper presents a WEB-based controller that enables remote monitoring of yoghoutrt process making via HTTP browser, WAP browser or Java 2 Micro Edition application (MIDlet). The moment of ending the process of souring of the milk is estimated indirectly, by analysis of the reflected from yoghourt ultrasound signal in frequency domain.**

Keywords – **Remote Process Monitoring, fuzzy classification**

I. INTRODUCTION

Milk acid products are known from the ancient times. Milk acid products are those, who have endured milk acid fermentation as a result of their sours with milk acid bacteria. It is characteristic for them, that they are obtained from fresh milk, put under fermentation. The fermentation technology is the main domain, where the biotechnology finds application [1-3].

One of these milk acid products is the Bulgarian sourly milk. It is known also under the name yoghurt. It is prepared mainly in the areas of the Balkan Peninsula and the Caucasus. It is very important the process of souring of the milk to run properly for the sake of receiving the product with necessary chemical composition and properties. That's only way the received yoghourt to represent perfect, easy digestible and refreshable dietetic food. The process of the souring is watched, as the acidity and the consistence of the soured milk are determined regularly. The moment of the souring is determined when the acidity of the souring milk reaches 75–80ºT, but the consistence and the density are determined by shaking of the jar or plastic pail. When during the shaking of the jar only the middle part of the surface layer is shaking, but the edge remains still, this means that the souring milk had received enough density. If the so prepared soured milk is pull out of the thermostat too early it will remain with a rare consistence [2]. That's from the technological point of view and with the aim of receiving souring milk with the necessary composition and properties is very important to determine properly the moment of the souring.

For avoiding the subjectivity during the control of this process and its fully automation we suggest a developed controller, which determines more precisely the process of the souring of the milk. Its description follows.

[1] R. Ivanov is with the Department of Computer Systems and Technologies, TU of Gabrovo, BULGARIA, E-mail: rs-soft@ieee.org.

[2] I. Simeonov is with the Department of Computer Systems and Technologies, TU of Gabrovo, BULGARIA, E-mail: isim@tugab.bg.

II. HARDWARE REALIZATION

The controller is realized with minimal number of components because of the use of he System-On-Chip (Soc) IPC@CHIP SC12 firm Beck GmbH [4]. The use SC12 modules are as follows:

- Micro controller AMD186;
- Ethernet controller for IEEE 802.3 with integrated 10Base-T transceiver;
- 512 KB FLASH disk;
- 512 KB DRAM;
- Programmable Interrupt Controller;
- Two programmable 16-bits timers (Timer 0, Timer 1);
- Programmable digital inputs and outputs;
- I2C interface;
- Watchdog timer.

The integrated in AMD186 microprocessor 8086 works at frequency 20 MHz (50 ns). The network controller and 10base-T transceiver enables the connections of SC12 to LAN to be realized only with one external component - 10Base-T filter (FB2022). Via RJ-45 connector the controller has a connection to HUB, Switch or Wireless Ethernet Bridge. The network configuration can be static or dynamic when DHCP server is used.

The external components, necessary for the realization of the controller are as follows:

A. Ultrasound transmitter and receiver

We use UST40T as an ultrasound transmitter and UST40R as a receiver. The recommended frequency for the driving of the transmitter is 40 kHz. The distance between the transceiver and the analyzed object is 30 cm. The control of the module for the driving of UST40T (CMOS invertors 4069) is realized with digital outputs P9 and P10 of the SC12 SoC.

B. Analog-to-Digital-Converter (ADC)

An integrated circuit AD976A from Analog Devices, Inc. [5] is used. AD976A is a 16-bit ADC, working at a maximum sampling frequency of 200 kHz. The circuit requires single supply voltage of +5V. When the internal reference voltage of +2.5V is used, the range of input signal is ±10V.

The connection between SC12 and AD976A is realized trough the following signals:

- Data bus - the result after the conversion (16-bit) is read in two cycles, because the SC12 data bus is 8-bit (AD0-AD7). When signal BYTE is 0 the lower 8 bits of the result (D0-D7)

are read, and when BYTE is 1 the last 8 bits (D8-D15) are read.

- R/C# - falling edge on R/C# starts conversion, a rising edge enabled the output data bus. R/C# signal is controlled by the output of the Timer 1 (TMROUT1 pin of SC12);
- BUSY# - this signal goes low when a conversion is started. Output data will be valid when BUSY# goes high. It is connected directly to the input INT0 of SC12 - after conversion an interrupt request is generated. The Interrupt Service Routine (ISR) reads data from ADC and writes this information into the DRAM.

C. Sensor for relative humidity and temperature

An integral sensor SHT11 from the Sensirion AG [6] is used. This sensor requires single power supply of +5V. The communication between SC12 and SHT11 is realized trough a specialized two-wire serial synchronous interface. The accuracy of the sensor is:

- ±0,9°C in the range 0°C to 40°C when the temperature is measured;
- ±3,5% when the relative humidity in the range 20 % to 80 % is measured;

The communication with SHT11 is realized trough the programmable inputs-outputs P7 and P8. Because of the high relative humidity during the process of the souring of the milk, integrated in SHT11 heating element is switched on. It will increase the temperature of the sensor by approximately 5°C.

D. Real-Time Clock (RTC)

The date and time are needed when software generates a report for process status. As RTC an integrated circuit PCF 8583 from Philips [7] is used. The communication between SC12 and RTC is realized trough the interface I2C.

E. Power Supply

The controller is powered with +12V/800mA. LM340 and 7809 integral voltage regulators are used to obtain +5V and +9V.

III. ALGORITHM REALIZATION

The main goal of the controller is to detect the exact moment of terminating the process of souring of the milk. The goal is indeed to measurement of the density of the milk. For that purpose the reflected ultrasound signal is analyzed. The analysis is performed in the frequency domain. It is established experimentally, that the interest is for the spectral components in the narrow band, included the frequency of the transmitter (40 kHz). If sampling frequency is F_s=100kHz and number of discrete is N=2048 the spectral components with indexes from N_a=775 (37842 Hz) to N_b=865 (42236 Hz) are analyzed. 91 spectral components are included in that frequency band. To reduce the number of spectral coefficients and to increase the noise immunity of the system a filtration in the frequency domain is realized. We use 22 filters with coefficients **h**={0,25; 0,5; 0,75; 1,0; 0,75; 0,5; 0,25}. If *PS*(*i*) is the *i*-th spectral component, the reaction of the *k*-th filter *PSF*(*k*) is calculated according to the equation:

$$PSF(k) = \sum_{j=-3}^{3} PS\left[\left(N_a - 1\right) + 4k + j\right] h\left(j + 3\right),\ 1 \le k \le 22\ . \qquad (1)$$

During the training of the system the coordinates of the centers of the every one of the following 3 classes are calculated:

- Class 1 – the training vectors are obtained just after the heal treatment of the milk (start of the souring);
- Class 2 – the training vectors are obtained at the end of the process of the souring (usually from 2,5 to 3 hours after the start of the process, if temperature is in the range 44-46 °C);
- Class 3 – the training vectors are obtained in the interval 15 to 30 minutes after the terminating of the souring.

As a result of the training three 22-dimension features vectors $\mathbf{c}_k$ (k=1, 2, 3) are obtained and used during the classification. The classification is realized in on-line mode. Its aim is to give a qualitative estimation of the probability every new test vector to belong to every one of the defined classes. The evaluation is received according to the following equation:

$$\mu_i = \frac{\left[1 \Big/ \left(\left\|\mathbf{x},\mathbf{c}_i\right\|_G\right)\right]^{\frac{1}{m-1}}}{\sum_{j=1}^{Nc}\left[1 \Big/ \left(\left\|\mathbf{x},\mathbf{c}_j\right\|_G\right)\right]^{\frac{1}{m-1}}}\ ,\ \text{if}\ \mathbf{x} \ne \mathbf{c}_i\ ,\ 1 \le i \le N_c\ \text{ and,} \qquad (2a)$$

$$\mu_i = \begin{cases} 1, j = i \\ 0, j \ne i \end{cases}\ ,\ \text{if}\ \mathbf{x} = \mathbf{c}_i\ \text{where:} \qquad (2b)$$

N_c is the number of the cluster centers;

$\left\|\mathbf{x} - \mathbf{c}_i\right\|_G$ is G-estimation of the distance between the test vector ***x*** and center of class *i* - $\boldsymbol{c}_i$, ;

$d\left(\mathbf{x},\mathbf{c}_i\right) = \left\|\mathbf{x} - \mathbf{c}_i\right\|_G = \left(\mathbf{x} - \mathbf{c}_i\right)^T G\left(\mathbf{x} - \mathbf{c}_i\right)$. If G=I Euclidean distance is calculated;

m is a parameter that influences the degree of fuzziness between classes. Usually 1.25≤m≤ is chosen [8].

IV. SOFTWARE DESCRIPTION

The software is developed on Borland C++ v. 5.2 and is compiled to an EXE file, which is started automatically after the switching on of the power supply. The program code works under the control of the multi-task Real Time Operation System (RTOS) of the SC12. The tasks switching interval is 1 ms. RTOS

The description of the software is as follows:

A. Main Task

This program module realizes the initialization of the hardware and software modules.

The initialization is realized in the following sequence:

- load information for centers of classes;
- initialize digital inputs and outputs;
- Activate internal security system: install a User Error Handler for processing the fatal errors (invalid operation code,

system stack overflow, TCP/IP fatal error and etc.) and activate a Watchdog timer. If fatal error has been occurred the controller is rebooted;

- Enable interrupt request for input INT0 and set the edge-triggered interrupt request mode (low-to-high).
- Install Interrupt Service Routine (ISR) for handling the INT0 requests;
- Init Timer 1: continuous mode, internal clock use, enable TMROUT1 pin. We use TMROUT1 to start of the ADC - 100 KHz clock (10μs), 50% duty cycle;
- Create task that communicate with the ADC (ADCC). After the creation the task is suspended;
- Create task that controls the ultrasound transmitter (USTT). After the creation the task is suspended;
- Install CGI CallBack functions for HTTP, WAP and J2ME clients. Information for the status of the technological process can be received by three ways: from HTTP browser started on a personal computer, from WAP browser started on GSM terminal or from MIDlet, started on a mobile terminal with integrated Java Virtual Machine.

After the initialization Main task performs in loop following algorithm:

1. Activate task USTT.
2. Waiting until the task USTT is ended - flag USTTready=true.
3. Activate task ADCC (2048 ADC conversions).
4. Waiting until the task ADCC ended - flag ADCCready=true.
5. Calculate Power Spectrum and Filtered Power Spectrum (functions getSpectrum and frequencyFiltering).
6. Classification - function fuzzyClassifier.
7. Measure temperature and relative humidity - function getTHinfo.
8. Update values of global variables, necessary a report is generated.
9. Sleep the task for 1 minute.

B. Task ADCC

The task is activated with the function RTX_wakeup from RTOS API. The Timer 1 is started with function StartTimer. After 2048 analog-to-digital conversions flag ADCCready is set, and the task is suspended (RTX_Sleep_Request). Conversion timing diagram using BYTE signal is shown in Fig. 1.

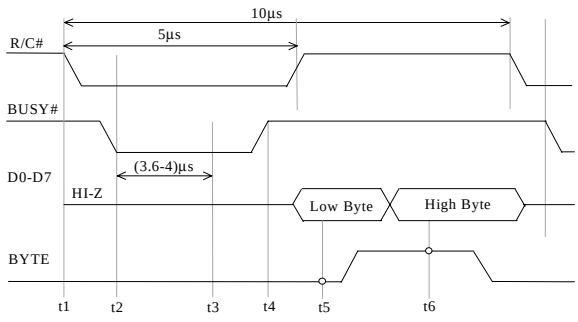

Fig. 1. Conversion Timing diagram using BYTE signal

C. Task USTT

After task wake-up a packet of 6 impulses (40kHz) for driving of the ultrasound transmitter UST40T is generated. For that purpose the digital outputs P9 and P10 are used.

The time diagrams of the signals, which control the ultrasound transmitter, are shown in the Fig. 2.

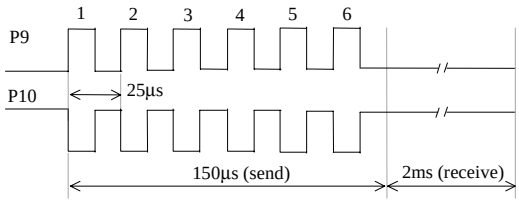

Fig. 2. UST40T driving diagram

When the working temperature is in the range (44–46)°C and distance between the receiver and the controlled medium is 30 cm, the time needed for waiting the reflected signal is about 1.7 ms. USTT task waits 2 ms, after which sets the flag USTTready and enters in suspend state.

D. ISR for serving the requests from ADC

The procedure reads the result after ADC conversion. When signal BYTE is 0 the lower 8 bits of the result are read, and when BYTE is 1 - the last 8 bits (D8-D15) are read. The received data are written in the buffer (receivedData).

E. Function getSpectrum

This function calculates Power Spectrum of the discrete signal, written in the buffer receivedData. Radix 4, Decimation in Frequency Fast Fourier Transform (R4 DIF FFT) is used.

F. Function frequency Filtering

A filtration of the spectral components, obtained trough the function getSpectrum is realized. For that purpose the equation (1) is used. The test vector *PSF* is obtained.

G. Function fuzzyClassifier

This function classifies every new test vector *PSF* to one of the defined classes. The equation (2) is used.

H. CGI CallBack functions

Since the buildin in SC12 WEB server doesn't assure access to the value of the field "User-Agent" from the HTTP requests header, on-line identification of the client is not possible. For that reason different CGI functions for serving different clients are installed:

- Request from HTTP browser, started on the personal computer or mobile terminal, supporting XHTML;
- Request from WAP browser, started on mobile terminal;

- J2ME application, started from a mobile terminal.

In dependence from the type of request, the WEB server answer is in different format: HTML, WML or Base 64 encoded data. Independently from the type of the client, the returned information is:

- Temperature in °C or °F;
- Relative humidity in % RH;
- The process "ready status" in %;
- Date and time of the report generation.

It is accepted, that the process of the souring of the milk ends, when maximum in the "ready status" (the probability the test vector to belongs to class 2 in %) is detected. The system gives the possibility for sending a SMS via an Email-to-SMS Gateway and SMTP server at the time of the detecting the end of the process of souring and when the temperature is out of range. For that purpose the function sendSMS is used.

V. Experimental results

The proposed controller is experimented in laboratory conditions and in the milk processing plant "ELVI" Ltd. in the village "Velkovci". On the basis of the experimentally data, received from 5 consequently circles of yoghourt making, off-line training is realized. As a result, the coordinates of the centers of the every one of the defined classes are obtained. They are recorded into a file CLASS.DAT.

The information which WEB server returns after an authorized (user name and password) HTTP request, generated from HTTP browser (HTML format) is shown in Fig. 3.

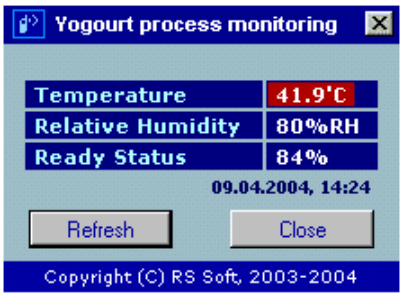

Fig. 3. HTML report

The access to this information, but trough WAP browser and Java 2 Micro Edition application (GSM terminal Samsung SGH-C100) is shown in the Fig. 4.

Fig. 4. Access to WEB server via WAP and MIDlet

The renewal of the information occurs automatically at every minute or by pressing the button "Refresh". When client is mobile terminal it is desirable to use WAP over GPRS. In this case only the really exchanged with the controller information will be paid.

Possibilities for choice of the measure for the temperature (°C, °F) and fixing the interval, after which the information is renewal automatically, are given from the menu of the MIDlet. In this case, the access to the controller is realized with POST request and base authorization (the name and password of the user are encoded with the algorithm Base64). The returned data is also encoded with the algorithm Base64. The aim is to guarantee the authenticity of the received data.

VI. Conclusion

A controller, automatically permitting precise determination of the moment of ending the process of souring of the milk, is developed. The estimate is realized indirectly, on the base of analysis of the density of the product.

The controller enables remote monitoring of the process from every point of the world, due to the buildin WEB server. Information for the status of the process of souring can be received trough HTTP browser, WAP browser or a J2ME application. As an additional possibility, automatically sending of SMS via an Email-to-SMS Gateway and SMTP server is provided.

Cooling of the components of the controller by means of fan (+12V) is needed for its correct functioning.

In our plans we anticipate realizing the connection between the proposed controller and the temperature and ventilation controller. This connection will be realized by means of interface RS485. In that way, the possibility will be given for setting different temperature profiles with the aim of finding the optimal results.

References

[1] Smith J. E., Biotechnology, Zemizdat, Sofia, 1987.
[2] Dimov, H., J. Shalichev, P.Chernev, L. Bakalova, H. Chomakov. The milk. Sofia, State Publishing Company for Agriculture Literature, 1971.
[3] Zudin, D.V., G.A. Ugodchikov, V. M. Kantere. Automation of the biotechnological investigations. Moskow, The High School, 1987.
[4] Bech GmbH, IPC@CHIP SC12 Hardware Menual, 2003.
[5] Analog Devices, Inc., Data Sheet "AD976/AD976A 16-bit 100kSPS/200kSPS BiCMOS A/D Converter", 1999.
[6] Sensirion AG, Data Sheet "Humidity & Temperature Sensor SHT11", Rev.1.00, 2002.
[7] Philips Semiconductor, Data Sheet "PCF8583 Clock/Calendar with 240x8-bit RAM", 1997.
[8] R. Ivanov, N-dimensional vector clustering algorithm based on self-organizing ANN with fuzzy output layer, International Workshop on Intelligent Systems INCON'97, pp.85-88, Sofia, 1997.

Modeling of the Software for System of Currier Service

Predrag R. Janićijević[1] and Zoran Ž. Avramović[2]

Abstract: **In this paper, we describe modeling of the software for system functioning of currier service based on Dial-a-Ride. Rational Rose with UML is used for working of the model. Description of the software development is given in phases of defining project requests, analysis of requests, planning and implementation with the accent on the planning phase.**

Key words: **Modeling, OOM, UML, OOP, Dial-a-Ride**

I. INTRODUCTION

In order to organize adequate courier service according to up-to-date principles of informative society, it is necessary to develop and implement the software that includes the following elements:

- Vehicle communication - dispatching centre,
- Monitoring (positioning and supervising of vehicles),
- Tracing of parcels,
- Routing and
- Data base on users.

A special kind of routing problem - dynamic systems Dial-a-Ride are used for this service's requirements. Its elementary features are collecting and dispatching of passengers and goods as well as non-existence of fixed routes and the need for their adapting to new requests during the time.

In order to reach its highest efficiency, quantity and profitability, it is necessary for this service to be based on highest standards of information communication technology. The link between several systems based on completely different techniques are supposed. Here belong the transport system as a base, telecommunication system (GPS, 3Ap or cellular network) for communication and stating of current locations of courier service vehicles and information system with the address base, GIS (Geographic Information System) elements, computer software which makes a choice and routing of vehicles according to certain algorithm and, at the end, the software that joins all cited subsystems and synchronize all activities necessary for functioning of this complex totality.

The development of these complex softwares using the techniques for object-oriented programming (OOP) became even more efficient with the method for object-oriented modeling (OOM). After a great amount of researching in this field, UML was established.

[1]Predrag R. Janićijević is with the PTT of Serbia, Takovska 2, 11000 Belgrade, SCG, E-mail: pjanicijevic@ptt.yu

[2]Zoran Ž. Avramović is with the Faculty of Transport and Traffic Engineering - University of Belgrade, POBox 26-48, 11010 Belgrade-48, SCG, E-mail: zoran.avramovic@sf.bg.ac.yu

II. PROJECT REQUESTS FOR THE COURIER SERVICE SOFTWARE

The system of this kind is very complex and experts in different fields must be engaged in order to get a product that will function irreproachably.

In this phase, it is necessary to describe what this system should do, not the way it will be done. That will be defined in the proceeding phases of development. It is important that the contents of data undoubtfully give instructions to every member of the project team for making certain models.

A. Contents of the documents with projects requests

Project requests of the system of courier service contain description of the software that will enable:

- monitoring (positioning and supervising of vehicles),
- tracing vehicles and parcels,
- dynamic routing according to Dial-a-Ride,
- communication between dispatchers and service users and
- connection between mentioned subsystems and data base containing necessary data for working of the whole system.

The document contains elementary requests, description of functions and basic abstraction of the system.

B. The role and the environment of the system

The software system that has to be made must give high efficiency to the service as well as the user. Good communication (phone connection and interactive Internet communication) must exist between the service and the user. Having delivered service request and receiving it automatically and/or entering necessary data on the user (civic data, the address, current locations) by a dispatcher, his location must be marked on the digital city map. Simultaneously the current location of courier vehicles (coordinates have to be obtained by GSM or GPS system) must presented together with former routes, as well as the locations of served and unserved users (these locations should be marked in different colors). After words, the choice of vehicles that will be send to new locations with updated route has to be made by using certain routine (by the most appropriate algorithm of the dynamic system Dial-a-Ride). This procedure is being repeated with every new request for service.

It would be useful that the system works in environment of PostNet and business LAN with 100BaseX Ethernet standard with the possibility of expanding and adapting to other networks. The work in Windows and two-layer client - server architecture (the possibility that the belonging database is located on one of the servers) is also advisable.

C. Description of the domain

Domain is described by its key abstractions (classes). In this problem, we can see the following four totalities (packages) with their key abstractions:

- data base "Addresses",
- digital city plan "Map",
- locating system "Positioning" and
- dynamic routing system "Routing".

Database "Addresses" must include all relevant data of users, their addresses, courier vehicles and parcels. "Map" (in vector's format) is the elementary means for monitoring and has to afford graphic illustration of most elements from database. The system "Positioning" is located out of the PostNet and its task is to give data on vehicle positions in certain time intervals. The abstractions regarding dynamic Dial-a-Ride system are placed in "Routing" package.

D. Functioning requests

Use case can be divided into following groups:

- data base operations,
- graphic objects operations,
- geolocation system operations and
- route optimization operations.

"Data base operations" are the data input of users and vehicle locations, creating of certain queries that afterwards generate necessary graphic presentations.

"Graphic objects operations" relate to object selection (users addresses, courier vehicles and their routes) on digital map and their presentation.

"Geolocation system operations" belong to the external system that should do the service of inserting data on courier vehicles locations in certain time intervals.

"Route optimization operations" have to be generated according to the algorithm of route optimization and vehicle choice and then these data should be put on the city map.

III. The Analysis of Project Requests

In the analysis phase, the use case model and the domain model are being defined according to the project requests.

According to the project requests, four packages can be clearly noticed and they should include all structural elements and the ones describing system functioning (fig. 1).

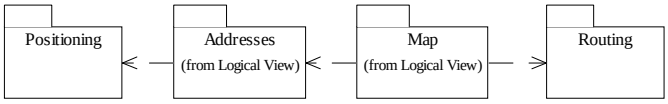

Fig. 1. Use Case View/Main

A. Analysis of functionality

The package "Positioning" will be presented by the symbol of an actor (performer) because this automated system is out of PostNet and does the service of inserting data into the system. In this section, we show the most striking diagrams, which give the description of the system performance according to the functional requests.

In Fig. 2, we present the main diagram of use cases for the package "Addresses" which consists of use cases, actors and navigable associations.

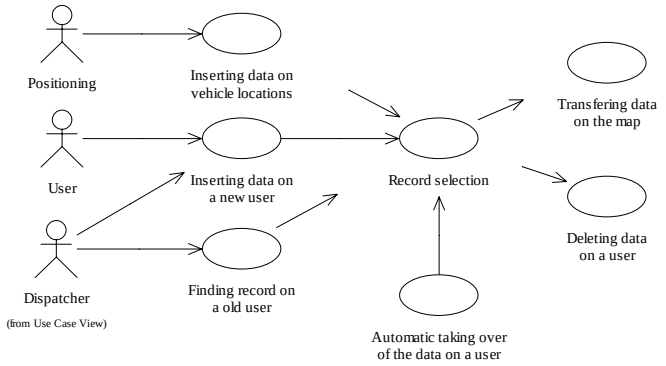

Fig. 2. Use Case Diagram: Addresses/Main

Fig. 3 shows the use case diagram of the package "Map" with all functionalities (use cases) regarding graphical presentation and all the details performing in reality.

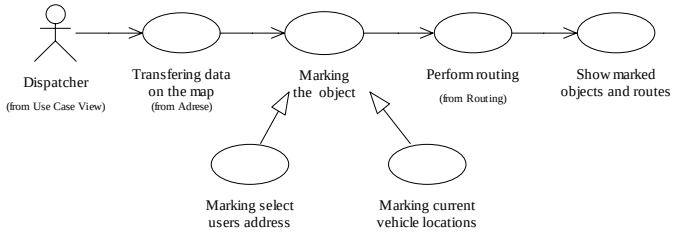

Fig. 3. Use Case Diagram: Map/Main

In Figs. 4 and 5, we present diagrams of activities and interaction (sequence) belonging to certain use cases on preceding diagrams.

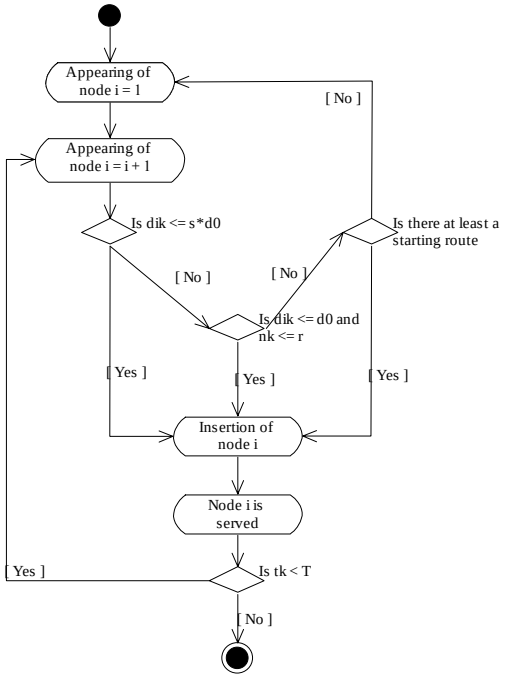

Fig. 4. Activity Diagram: Do the routing/Routing

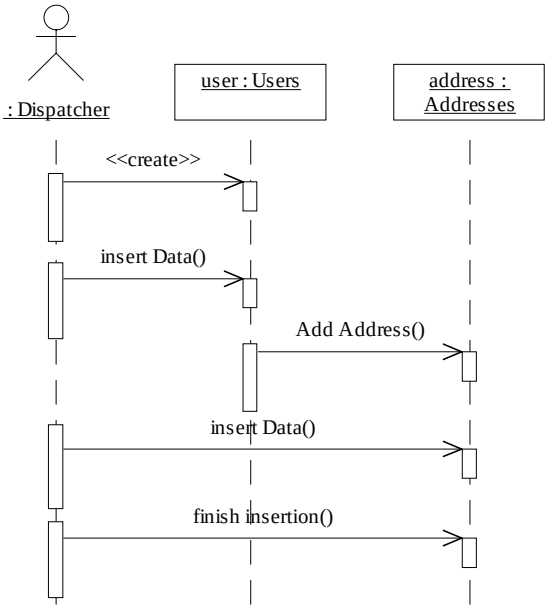

Fig. 5. Sequence Diagram: Insertion of data on a new user/Insertion

B. Domain analysis

In further analysis, we can notice the two diagrams of key classes giving domain description.

In Fig. 6, we give a diagram of classes for package "Addresses" that represent the database.

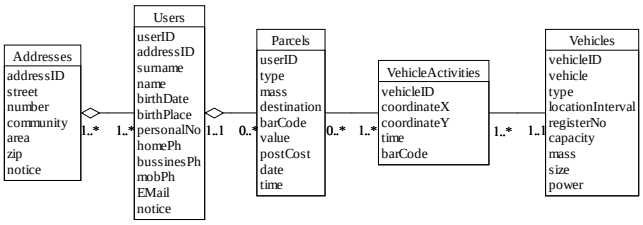

Fig. 6. Class Diagram: Addresses/Main

In Fig. 7, we give a diagram of classes for the package "Map" representing a city plan with its objects.

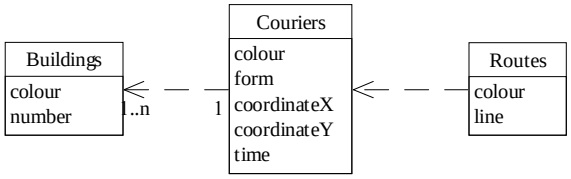

Fig. 7. Class Diagram: Map/Main

IV. PROJECTION PHASE

In this section according to the project request, we present a project model of first iteration for use case "Data input on new customer" and "Transferring objects on the map". It is done by certain collaborations (fig. 8).

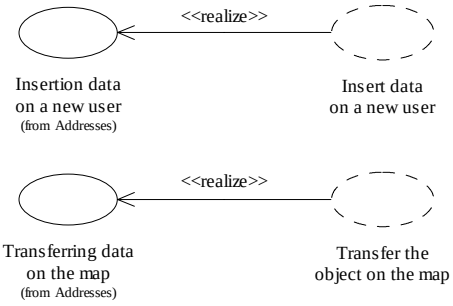

Fig. 8. Collaborations/Main

Fig. 9 shows a diagram of classes taking part in accomplishing use cases relating the database on a user with his first request for service.

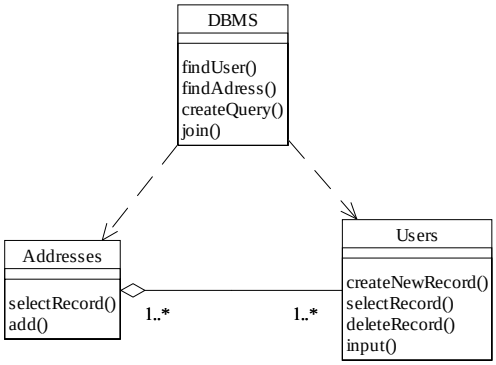

Fig. 9. Class Diagram: Collaborations/Users and addresses

In Fig. 10, we can notice messages and flows of data between instances of classes from the previous diagram. We can also see the marks showing the features of objects relating to each other.

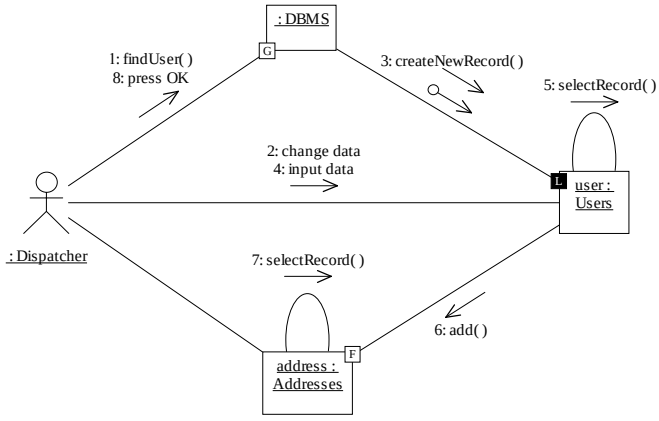

Fig. 10. Collaboration Diagram: Insertion of data on a new user/Insertion

The classes used for marking a graphical presentation of users' addresses and courier vehicles on the city map are shown in Fig. 11 and the appropriate diagram of collaboration is shown in Fig. 12.

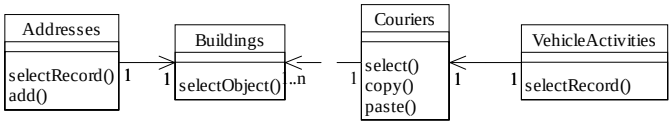

Fig. 11. Class Diagram: Collaborations/Transferring

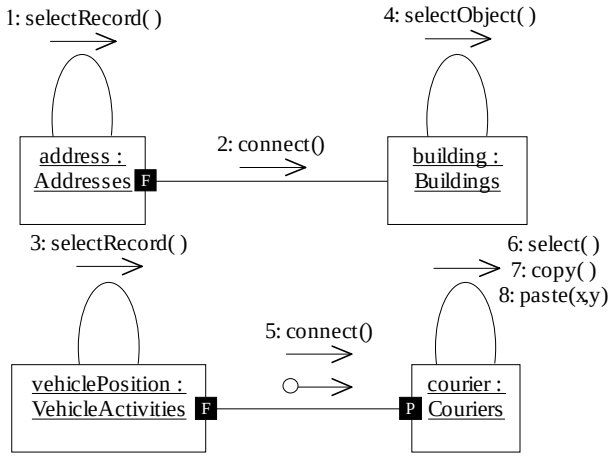

Fig. 12. Collaboration Diagram: Objects transferring on the map/Transferring

V. Implementation Phase

The phase of implementation is (like previous phases) presented in one (first) iteration. The presentation of implementation is given in the package "Component View" on component diagrams. In the main diagram, we can see packages containing all components implementing the classes of the package "Logical View" (fig. 13).

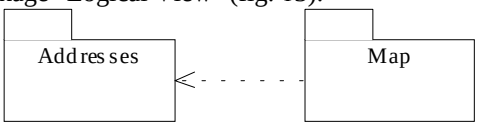

Fig. 13. Component Diagram: Component View/Main

In Fig. 14, we present the components of the package "Addresses" and in Fig. 15, the components of the package "Map" are presented. Both packages are added to the packages with the same names from logical view.

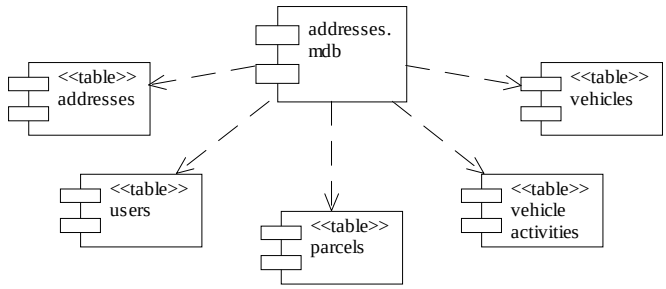

Fig. 14. Component Diagram: Addresses/Main

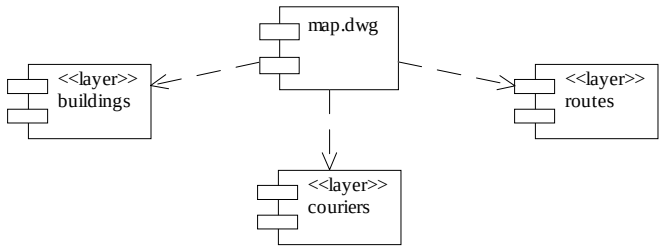

Fig. 15. Component Diagram: Map/Main

In physical sense, the shown components are tables of database and layer maps in vector format.

Generated source code in C++ language for the components of these two packages is placed in implementation files *.cpp and heading files *.h. The given source code depends on the specification of components and other features of the model.

VI. Conclusion

In the area of Serbia so far does not exist any courier service that works according to the principles of modern information communication technology, even though there is the need for it. Since a high level of communication and computer technology is accomplished, as well as a great number of experts, neither a long period of time nor great financial resources are necessary for applying of these technologies.

As for as domestic market is concerned, we can say that the most important data necessary for software support to courier service are accessible. That means that we already have digital maps of Belgrade and other big cities of Serbia. It is also possible to take over some data from other users' bases as well as the data on telephone subscribers. There is the possibility of applying location systems based on the mobile network of "Telekom" of Serbia.

The presented software model can be used as the starting one and be improved in practice in further iterative incremental procedure. Depending on changes of environment and market conditions, new improved versions would be accomplished. This dynamic approach (fast development, implementation, reversible engineering) just makes UML possible. So it is quite justified to consider the development and the implementation of courier service software in Serbia.

It is also necessary to make preliminary simulation models on the base of conducting a query of potential users and market research and thus make favorable service costs possible.

VII. References

[1] Booch, G., Jacobson, I., Rumbaugh, J.: "The Unified Modeling Language User Guide", Addison Wesley Longman, Inc., 1999.

[2] Janićijević P.: "Mogućnost primene geolokacijskih sistema u kurirskim službama", PTT saobraćaj, ZJPTT, Beograd, april - jun 1999.

[3] Janićijević P.: "Primena CAD tehnika u kurirskim službama", PTT saobraćaj, ZJPTT, Beograd, oktobar - decembar 2000.

[4] Janićijević P.: "PostNet i njegova uloga u kurirskoj službi", poslediplomske studije, seminarski rad, Saobraćajni fakultet, Beograd, mart 2001.

[5] Janićijević P.: "Modelovanje sistema kurirske službe", poslediplomske studije, seminarski rad, Saobraćajni fakultet, Beograd, mart 2002.

[6] Milićev, D., Zarić, M., Pirićanac, N.: "Objektno orijentisano modelovanje na jeziku UML, skripta sa praktikumom", Mikro knjiga, Beograd (2001).

[7] Milićev, D., Lazarević, Lj., Marušić, J.: "Objektno orijentisano programiranje na jeziku C++, skripta sa praktikumom", Mikro knjiga, Beograd (2001).

The Redesign of the Software of the DKTS 30 Switching System to Support Extended Capacity

Branko Kolašinović[1], Dimitar Komlenović[1], Milan Jovanović[1]

Abstract – **Some software solutions implemented in the project of extending capacity of the DKTS 30 switching system were presented in this paper. This project includes: a redesign of the system image, a redesign of the interprocessor communication, more natural integration of the remote subscriber unit into the system, algorithms for distributed systemsupervision, appropriate changes in the system data base and the graphical user interface.**

Keywords – **switching system, embedded real-time software, DKTS 30**

I. INTRODUCTION

The DKTS 30 public digital telephone exchange is the newest product from the series of DKTS digital telephone switching systems. Although it has been successfully commercially exploited since 1999, it is still under development in order to achieve better quality, provide new services and reduce the production price.

II. PROBLEM

The first DKTS 30 public digital telephone exchange was designed to provide the capacity of 15872 subscribers. However, this number was shown to be insufficient with the uprising market demands. Therefore, the project of extending the capacity was undertaken. The project goal was to provide the maximum capacity of 174592 subscribers. All the necessary changes in the hardware were presented in [1]. This paper presents software changes, while hardware changes were presented in a degree of detail that was necessary to understand the presentation to follow.

The project requirement was not only to trivially provide capabilities for a larger number of blocks in the system, but also to pay specific attention to the system performance. It was highly unlikely that the algorithms that were shown to be efficient with one traffic load would be efficient in the same way with much heavier traffic load.

The project of extending capacity comprised changes in several categories of the DKTS 30 software. The categories that needed changes were: the system image, the interprocessor communication, the interprocessor communication monitoring, the system database and the graphical user interface. Furthermore, with these redesigned categories, it was necessary to implement new algorithms for distributed system monitoring and to obtain a more natural integration of remote subscriber blocks.

As far as software compatibility is concerned, it was decided to obtain compatibility of the newly designed software with the old hardware, but not with the old software. This means that the new software may run on all DKTS 30 platforms, but it must not be mixed with old software. The goal was to move beyond some obstacles that were present in previous software solutions due to required compatibility with the DKTS 20 system, which was put aside in the meanwhile. Special attention was payed to the intermediate period in order to make it possible to add new funcionalities to the software of the old system as well as to the software of the system with extended capacity.

[1] PUPIN TELECOM DKTS, Batajnički put 23, Belgrade, Serbia
E-mail: {brankok, dimitark, milanj}@ dkts.co.yu

III. SYSTEM ARCHITECTURE

The DKTS 30 system architecture is given in Figure 1. The system consists of central blocks, peripheral blocks, and terminals. The central blocks are: administration (ADM), switching (KOM), synchronization (OSC), source of speech information (GGI) and USP (*Universal Signaling Processor*). The USP unit consists of a UCP (*Universal Communication Processor*) unit and a signaling processor, connected via an HDLC link. The UCP unit distributes messages among central and peripheral blocks. In order to increase system reliability, central blocks are duplicated. Central blocks are connected via a local Ethernet, which is doubled, too All central blocks, except USP units, are connected to both Ethernet networks. The terminals can be local or remote. The local terminals are connected to the administration blocks via a separate local Ethernet.

Peripheral blocks are connected to UCP blocks via serial HDLC links. A pair of UCP units works in a load-sharing mode for a group of six peripheral units. Each of these six peripheral units is connected to each of two UCP units by its own separate link. Peripheral blocks (PB) are subscriber blocks and interexchange trunks. Peripheral blocks are originally developed boards based on the Motorola 68302 family of processors and on the originally developed operating system. Voice transmission is achieved by the PCM multiplex that connects peripheral blocks to the switching block.

A remote subscriber unit is realized using an IUUB4 block which combines 4 subscriber blocks with 128 subscribers on each. That gives the maximum capacity of 512 subscribers. The function of the remote subscriber unit is to map subscriber block interfaces. In this way, software of the central UCP module does not make a difference whether a block is a local or a remote one.

The administration unit is an industrial PC. The DKT3 30 application for the administration unit may run under various operating systems, such as Windows NT/XP or Linux. Other central blocks are originally developed boards based on the Motorola 68360 family of processors. Software for these boards may also run under different real-time operating systems, such as pSOS and RTEMS. The terminal unit is a common PC. The operating system used on this unit is Windows NT. The application that runs on this unit is called GUI (*Graphical User Interface*) and represents the interface between the operator and the DKTS 30 system.

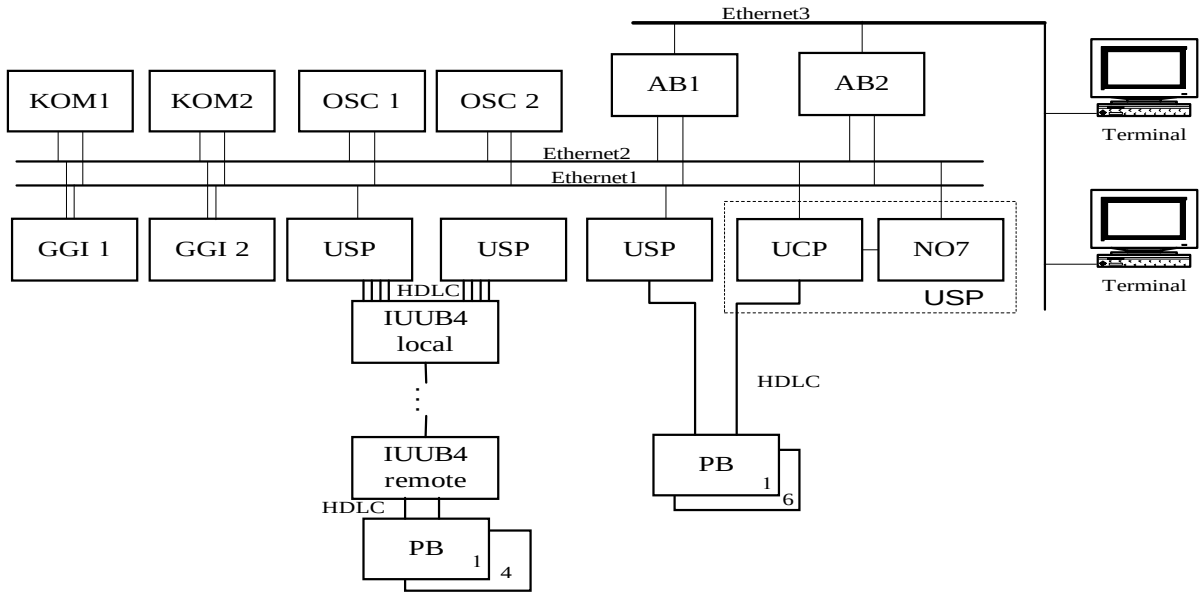

Figure 1: The DKTS 30 system architecture

IV. SOFTWARE ORGANIZATION

The DKTS 30 software is based on object-oriented principles. [2] It is developed using UML notation, and implemented in C++ programming language. Software is organized hierarchically into layers. Each layer provides a service to the layer above it, and simultaneously it is a client of the layer below it.

One of the main challenges facing DKTS 30 software engineering is the variety of microprocessors (Motorola 68360 and Intel family are present, processors from the PowerPC family are planned for future use), as well as the variety of operating systems that run on different parts of the DKTS 30 switching system (WinNT, Linux, pSOS, RTEMS).

The software is organized as a collection of server objects that are distributed among processors. Main system abstractions are modeled with server objects. These servers are implemented as finite state machines (FSM), which is a common approach in design of embedded real-time systems [3]. Each FSM is designed according to the *Bridge* template [4], and consists of an interface and an implementation object. Interface and implementation objects may reside on the same processor or on different processors, and the only connection between them is their unique identifier.

The well known CVS (Control Version System) tool is being used to control file versions. CVS lets a developer maintain a detailed revision history of a file that is under its control.. In this way, it makes the reconstruction of any previous version possible. Since there is typically more than one developer who works on the same file, CVS is of great help, because it allows multiple users to work on a file concurrently.

V. NUMERATION OF BLOCKS

Software of the first DKTS 30 system was developed in order to be flexible within the requested maximum capacity. Each block in the system had its determined identification which depends on the block's position. Blocks of the same type have successive identifications. The first DKTS 30 system can host the maximum number of 256 blocks, where the numeration for peripheral blocks starts from 128. According to the request of the project, the existing numeration had to be changed, which was the source of incompatibility difficulties. In order to simplify the routing algorithm, it was decided that every potential position in the topology of the system with maximum capacity had its own identification representing block's physicall address. Therefore, it was necessary to provide space for a number of 3000 blocks, where the numeration for peripheral blocks is agreed to start from 1000. Of course, the possability that the real system would have each position filled is relativelly small.

Another problem were 4-bytes long internet addresses that represented blocks' network interfaces. In the first system, one byte held processor identification, another byte held network identification, while two bytes held identification of a switching system in a WAN network. In the system with extended capacity, the 4-bytes internet address were retained. Also, two bytes of the address are used for the switching system identification. Since the unique recognition of each block implies the number of 12 bits, the byte that was assigned to the network identification was devided into two nibbles. Since the identification of blocks that are connected to the Ethernet is held in one byte, in order to make switching system's internet addresses equal to internet addresses of network interfaces of blocks that are connected to the Ethernet, it was decided to add the higher nible of the network byte to the procssor identification byte (in total, 12 bites that are not near-by), while the lower nibble should represent network identification.

VI. SYSTEM IMAGE

In order to monitor system behavior as easy as possible and to use collected information in the most efficient manner, a software category called system image is developed. The system image represents the database with all the relevant information regarding state of each resource needed for the interprocessor communication. The system image consists of two subcategories. The central image subcategory represents the image of the whole system with all the necessary

information and it is only located on processors with the administrative function. It consists of a map of processors and a map of network interfaces. The local image subcategory is a part of the system image that is located on each processor. It contains all the data structures needed for the implementation of the efficient interprocessor communication. The local image consists of a map of physical processors, a map of internet addresses, and a routing map.

The initialization of data structures within local image is performed according to the central image of the master administrative processor immediately after software has been downloaded to the specified processor and just before the processor starts to communicate with other processors. The local image states are being brought up to date by sending and processing messages that contain information on activation or failure of processor units and network interfaces. Furthermore, local image states are also being made current by sending of central image from the administrative processor. In the first DKTS 30 switching system, this was done according to the defined pattern for the system with the highest capacity. Although the procedure was optimized, the problem of adding new block types remained present during the evolution of the system. Every time a new block type was added, the software for all boards had to be changed, even for boards that were not communicating with the newly added block type. That is why a new procedure was developed for the system with extended capacity. According to this procedure, every block first receives the message that precisely specifies the format of messages that will be used for local image update. By adding this message, the repetition of information in the header of messages that are send in order to make local image current was avoided. Furthermore, dynamic adding of new block types was made possible. Finally, messages that are sent for the purpose of bringing local image up to date may be as long as it is needed, since the information on boards that are not configured are not being sent.

VII. INTERPROCESSOR COMMUNICATION

A basic requirement for the design of interprocessor communication was to reduce the number of messages passing through the system, as well as to provide higher reliability of interprocessor communication. In order to fullfil these requirements, it was necessary to make some changes in a message header. The message header remained of the same length as it was. It contains the same fields as in the previous implementation: message type, source and destination internet address, message identification, destination object's identification. However, some changes were inevitable. First of all, the format of internet address had to be changed. Next, the way message type is marked was also changed. As a result of these changes, incompatibility with the previous software implementation became unavoidable. Among other things, with the new message caracterization, it became possible for clients in upper software layers to supress acknowledgement messages on the protocol layer when functional messages are used to acknowledge an application layer acknoledgement request.

In the aim of acchieving faster interprocessor communication, the SP protocol was abandoned. The SP protocol was used for communication between peripheral and UCP blocks via HDLC links [5]. The reason for the presence of this protocol in the previous implementation lay in requested compatibility with DKTS 20 peripheral blocks. Since the concept has been abandoned in the meanwhile, the NLC layer of the interprocessor communication protocol stack was eliminated. In adition to this, another historical role of the UCP board, which also existed due to requested compatibility with DKTS 20 peripheral blocks, became unnecessary in the new software environment. That was the NLB layer whose task was to perform message format conversion between DKTS 20 and DKTS 30, and vice verse.

The design of the first DKTS 30 switching system did not support communication between UCP and No7 boards belonging to one Ethernet with UCP/No7 boards that belong to another Ethernet. However, during the exploitation phase, the need for communication between No7 peer boards was brought to attention. In addition to this, there was the need to put interprocessor communication under software supervision. Accordingly, it was decided to correct this defect by allowing software routing from one Ethernet to another. Central blocks that have available network interfaces belonging to both Ethernets became potential routers. It was more than likely that this task would be commited to the OSC board, since the OSC board is the processor that is not overloaded with interprocessor communication responsibilities. The routing is now supported in system image. In addition to everything else, this routing may be used in the case of a failure of a network interface on boards with two network interfaces. For example, in previous software versions, the KOM board with an inactive network interface that belongs to the Ethernet A could not send a message to a UCP or No7 board connected to the DKTS 30 WAN network via network interfaces belonging to the Ethernet A.

A reduction of the number of messages passing through the system is acheived by the use of multicast techniques [6]. Instead of sending a large number of single messages to different destinations, it is now possible to send only one multicast message that is received by all procesors that are members of the specified multicast group. The great problem was the presence of several operatin system in the DKTS 30 switching system, each of which providing similar (but different) programming interface towards the multicast facilities. In addition to this problem, it was important to provide that all processors in the group receive a multicast message, but also to avoid duplicated messages, which may be the consequence of the use of alternative routes. Periodical updating of local image, sending information on block or network interface failure or activation, periodical checking of block states, sending error reports to terminals are cases in which it is evident that significant improvements in speed and efficiency are achieved.

VIII. SOFTWARE SUPERVISION

Software supervision is responsible for timely and reliable detection of block failure and activation, failure and activation of network interfaces, software download to peripheral blocks, efficient monitoring and error recording, as well as undertaking actions in order to cope with irregularities or to alarm error conditions to operators.

Previous software versions were based on a centralized approach, according to which the administrative unit was collecting information and performing actions. This was an acceptable solution. However, with the extention of the capacity of the public telephone exchange, it was necessary to migrate from centralized to decentralized algorithms. The administrative unit has nevertheless the main role in software supervision, yet it delegates some software supervision functionalities to other central blocks in the system.

For example, in the previous implementation, the administrative unit was checking processor states for all blocks in the system. As a result of the use of decentralized algorithms, periodical checking of the activity of peripheral processors is now delegated to UCP processors. This means that the administrative unit sends request messages to UCP processors ordering them to perform the inspection of peripheral blocks connected to UCP boards. As a result, the number of messages needed to provide some funcionalities is decreased, which contributes to decreasing system overload and shortening time needed for obtaining information of the overall system status.

IX. IUUB4 BLOCK

The IUBB4 block is maybe one of the most important element in the project of extending capacity of the DKTS 30 switching system. As a result of the use of the IUUB4 block, significant increase in the number of subscribers is provided. The new IUUB4 block is connected to the UCP block by only one HDLC channel, instead of four, as it was in the previous solution, where IUUB4 blocks were transparent both on the side of the telephone exchange and on the side of subscriber blocks, which means that other blocks in the system were not aware of their existance. Software on this block was running from the EPROM memory. However, this concept was changed. The IUUB4 software is now being downloaded to the IUBB4 board from the administrative unit, as well as it is performed for other boards in the system. Not only does the administrative unit perform download, but also it inspects IUUB4 processor activity, informs IUUB4 blocks on failure or activation of other blocks in the system. In other words, the IUUB4 block is being treated the same way as any other block. The algorithm for the IUUB4 software download is distributed. That means that the IUUB4 executable is firstly downloaded from the administrative unit to the UCP board, and then it is uploaded to the IUUB4 block.

X. SYSTEM DATABASE

Modern switching systems require storing of huge amounts of data very economically and reliably. These data are necessary for handling calls, i.e. establishing and terminating connections, as well as for different periodical data processing performed by an operator. The database of switching system is used for storing specific system parameters needed for the functionality of the overall system. The system database contains parameters that describe hardware configuration (blocks configuration, their physical and logical addresses), parameters needed for establishing connections with other switching systems, as well as data needed for performing different functionalities, such as users data, billing prices, information services, etc.

The database software, apart from storing large amounts of data, must enable fast searching through the database and finding the data needed to satisfy the request for establishing connections in real-time. Apart from that, this software has to offer consistent data at anytime, to guarantee protection of data and to prevent unauthorized access. It is obvious that the capacity extension of the DKTS 30 switching system imposed changes in the DKTS 30 database in order to qualify this software category for the heavier traffic load.

XI. GRAPHICAL USER INTERFACE

Together with the changes in other parts of the DKTS 30 software, the changes were needed in the GUI application. Not only were there the need to change the graphical representation in order to show a large number of blocks, but also it was needed to adapt the GUI application to the situation of more intense traffic load, i.e. increased amounts of data coming from the administrative unit, processing larger files quickly and efficiently, etc.

XII. TESTING

Because of the large number of different processor types, different hardware platforms, various operating systems, situations in which it is necessary to perform potential error corrections in the field and in laboratory conditions, concurrently with adding new funcionality to the fisrt DKTS 30 system, a great attention was payed on developing methodologies for software testing. As a result, a set of tests was designed. The set comprised different testing techniques: from the partial to the integral testing, with and without the use of call generator, etc. In the testing phase, the use of error information is increased. However, the great part of this code will be excluded from the final version in order to assure executable programs with the minimal time of execution. In addition to this, finite state machines whose only purpose is testing are designed. The FSM whose only task is to generate desired traffic is instantiated on every processor. This is an example of how interprocessor communication is tested.

XIII. CONCLUSION

A flexible base for the switching system with extended capacity was provided. The change of the maximal capacity required a redesign of some critical algorithms and transition to distributed and heterogenous solutions. A lot has been done in order to decrease the number of messages passing through the system, which, in the last instance, may make the response time to certain events significantly shorter.

Because of the decision to abandon compatibility with DKTS 20 peripheral blocks, it was convenient to undertake a redesign of the system software on peripheral blocks, which was shown to be a complex task contributing to the slowdown of the entire project.

Once the project of extending capacity has been completed, it is expected that the work on the DKTS 30 system in order to increase its performance will continue. It remains interesting to see the results of the quality analysis of the behavior of the first DKTS 30 and the DKTS 30 with extended capacity.

XIV. LITERATURE

[1] S. Laketa, P. Vidić, N. Nikolić, "Extending capacity of the DKTS system," *Telfor 2003*, Beograd, 2003.

[2] Booch G., *Object-Oriented Analysis and Design*, Second Edition, Benjamin-Cummings, 1994.

[3] Selic B., Gullekson B., T.Ward P., *Real-Time Object-Oriented Modeiling*, Willey Professional Computing, 1994.

[4] Gamma E., Helm R., Johnson R., Vilsides J., *Design Patterns – Elements of Reusable Object-Oriented Software*, Addison-Wesley, 1994.

[5] M. Jovanović, V. Hiršl, "Interprocessor communication in DKTS 30 switching system," *YU INFO 1999*, Kopaonik, 1999.

[6] Deering, S., "Host Extensions for IP Multicasting," *RFC 1112*, 1989.

System Modeling via Databases

Geo Kunev[1], Valentina Antonova[2], Pavlina Vladimirova[3]

Abstract: **Today we have terabytes of data, gathered in databases, and dozens of mathematical methods for searching models in these data – applicable in form of data mining tools. The fusion of both is union of data and models, based on the same approaches.**

Keywords: **System, Modeling, Database, Induction, Data mining**

I. Introduction

The main human reasoning task is to search regularities in the world's phenomena, which can help in comprehending this infinite variety. The task of scientific research is to find laws describing classes of systems. Modeling is such a task. Once discovered, the model simplifies such variety in forms of laws, formulae or patterns. This is not only scientific, but an everyday mental effort, and it is highly efficient to use computers, and the most fundamental computer structures – databases.

II. Systems: a Recursive Definition

A generalized recursive definition, rendering in account that systems are built from sub-systems is given here:

"A system is a dynamic wholeness, built up from systems".

The wholeness, (holistic) of systems is expressed by:

"The whole is more than sum of its parts" [1]:

$$\text{System} > \text{Sum (Sub-System)} \qquad (1)$$

Almost all technical systems are directed systems and can be represented in terms of input ⇒ output:

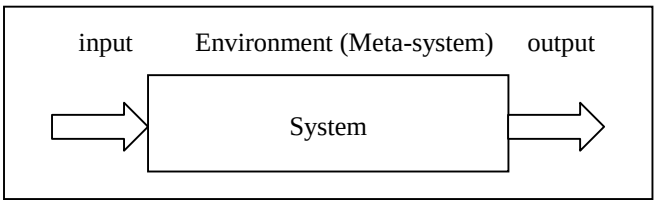

Fig. 1. Directed system

[1]Geo Kunev, [2]Valentina Antonova, [3]Pavlina Vladimirova are with the Department of Computer Sciences and Engineering, Technical University - Varna, 1 Studentska St., Varna 9010, Bulgaria, E-mail: geo_qnew@hotmail.com

III. Modeling

Modeling approaches [2]:

- knowledge and insight of the system (white box component)
- experimental data of system inputs and outputs (black box component).

Table 1. Comparison of the two main modeling approaches

	Knowledge based	Data based
approach:	modeling	system identifying
	top-down	bottom-up
reasoning:	deduction	induction
uncover:	inner structure	system behavior
task:	analysis	synthesis

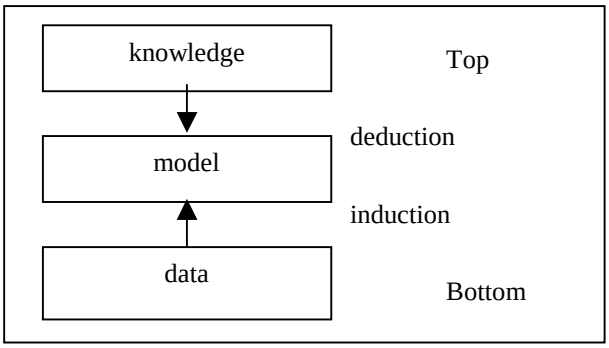

Fig. 2. Two main modeling approaches

IV. Data Mining

The current approach of inductive model searching, based on data, is Data Mining. It uses several techniques [3]:

Classical techniques such as:

- statistics,
- neighborhoods,
- clustering;

Advanced techniques such as:

- trees,
- networks,
- rules;

But, this is only one stage of the process, called KDD (Knowledge Discovery in Databases):

- Data
- Data selection
- Preprocessing
- Transformation

- Data mining
- Knowledge

The computer community had already developed:

- Conventional databases: usually in form of RDB (Relational Data Bases);
- Deductive databases: They add capabilities for drawing deductive consequences to a database through using rule-bases.
- Data mining and knowledge discovery: Current methods for deriving knowledge from data. They use simple knowledge representations; are not integrated in database management systems; employ limited domain knowledge [4].

Current methods strengths:

- Simple to be implemented
- Easy to use
- Efficient to apply
- Can scale-up

Current methods weaknesses:

- Are able to find only simple patterns
- Not integrated with the database
- Unable to employ sophisticated domain knowledge
- The generated knowledge may be difficult to interpret

V. Knowledge Mining

The most promising direction is to integrate data and models, and to provide common access to both: data and model (interpreted like meta-data, with appropriate functionality).

So, the next promising step can be developing inductive databases: They aim at answering queries that require drawing inductive inferences and deriving plausible conclusions; data bases are integrated with knowledge bases and inductive inference capabilities.

Having a union of data and knowledge and unification of approaches, based on current database techniques, we can expect achieving of the following:

- User's goals (knowledge needs) can be defined abstractly;
- Knowledge generation in more "natural forms," that is, in forms similar to those used by experts, more understandable and easy for interpretation;
- A memorized prior knowledge usage.

Today there are two main types of databases: relational and object. The object databases are in the early stage of development, and usually they have some object additions to the standard relational functionality. But, we can expect more and more developments, like the shifts in the programming languages paradigms. Thus, we have two ways to develop such inductive data/knowledge databases – relational, and object (or object-relational).

The relational approach has already been treated in some pilot projects [5], as an answer to:

- The need for effective and efficient using both data and background knowledge, and reasoning with more advanced knowledge representations than the currently used
- Since data may be insufficiently relevant to the task, there is a need for constructive induction
- In many applications, knowledge generated needs have to be easy to interpret and understand: this calls for natural induction
- The process of knowledge discovery needs to be more automated: this leads to the concept of a knowledge scout.

Using object-oriented databases as a basis for an inductive union is more perspective, despite of their problem-focused nature. This approach allows modeling complex (hierarchical) systems, rendering in account that systems are built from sub-systems, and combining the knowledge about the sub-systems with the knowledge about the (whole) system. The object-oriented paradigm can be spread beyond the programming itself.

VI. Conclusion

Memorizing the knowledge in the same database with raw data allows achieving not only faster results, but also a qualitative improvement in data/knowledge treatment. The two main branches are: upgrading standard relational database functionality, and/or developing advanced object structures and appropriate methods in a form of object (object-relational) databases.

References

[1] Klir G.J., An Approach to General System Theory. Van Nostrand Reinhold, 1969.

[2] Zeigler B.P., Theory of Modeling and Simulation. John Wiley & Sons, 1976.

[3] Van Welden D. Tree Classifiers as Data Mining Tools, Catholic University of Leuven, Belgium, 1998.

[4] Kunev G., Nedev A, Wild W. Application of Infrared Thermography Technical Diagnostics: Holistic Approach, Telecom 2002, p.689-696, Varna, Bulgaria

[5] Michalski, R.S. and Kaufman, K., "Building Knowledge Scouts Using KGL Metalanguage," Fundamenta Informaticae, Vol. 40, pp. 433-447, 2000

Effectiveness Evaluation Methods of Multimedia Learning Courses

Kalin H. Monov[1], Oleg D. Asenov[2] and Raycho T. Ilarionov[3]

Abstract – **The dynamical changes of the social environment the conditions for professional realization impose the use of intensive learning methods. The possibility for the realization of numerous multimedia learning systems imposes certain requirements to the developers concerning the effectiveness of the courses. A model for effectiveness evaluation of MMLC (Multimedia Learning Courses), using indirect methods and interface technologies presented in this paper.**

Keywords – **effectiveness, model, MMLC, direct and indirect evaluation methods.**

I. Introduction

The use of IT technologies as a means of development and progress of intensive learning methods is important because the information is a basic element of every learning technology. The intensive methods involve the use of IT technologies.

The progress of the forms and the migration to a continuous learning is a prerequisite for the appearance of uniform learning environments. They are result of the synthesis of the particular forms. The use of uniform learning environments is prompted by the possibility for a full and complete cycle of preparation.

The implementation of the learning environments in different fields of application imposes the use of different types of document models and modeling the data base [1].

The realization of learning courses is directly bound with a series of requirements and norms organized in s.c. Standards. The strict fulfillment of the standards is a prerequisite for successful realization of each learning course. The statistics concerning the feedback – learnee-learner is of great importance. In this case the role of the learner is performed by the learning system. The accumulation of statistics is possible by means of information. The information is possible to accumulate by means of two main methods: direct and indirect. The indirect methods are realized on the basis of metrical evaluations in respect of the perception from the user's aspect, accumulated by two main approaches – event approach and time approach.

[1]Kalin H. Monov is with the Technical University of Gabrovo, 4 H. Dimitar Str., 5300 Gabrovo, Bulgaria, E-mail: monov@tugab.bg

[2]Oleg D. Asenov is with the Technical University of Gabrovo, 4 H. Dimitar Str., 5300 Gabrovo, Bulgaria, E-mail: oleg@lirex.bg

[3]Raycho T. Ilarionov is with the Technical University of Gabrovo, 4 H. Dimitar Str., 5300 Gabrovo, Bulgaria, E-mail: ilar@tugab.bg

II. Main Topics

The life cycle of the development of a MMLC is directly bound with the time [2]. The time necessary for development, introduction and exploitation is of great importance. The idea of the presented model is by using of indirect methods to realize a module, which will register, analyze and actualize the effectiveness of the MMLC. For that purpose a limited finite set of criteria and parameters, tracking and analyzing the multi-modality (the modality) of the particular MMLC can be used [1].

Let us present the life cycle of the development of a particular MMLC in function of time (Fig. 1). Let us assume, that t_1 is the time, for which the learning course is fully finished. Let Δt_{21} is the time interval, for which the course is introduced for exploitation. Let Δt_{32} is the time interval necessary for adjustment of the course and Δt_{43} is the time for exploitation of the already improved course.

The purpose of this development is: increasing the effectiveness of the course by decreasing the total time for product actualization, where the total effectiveness is a function of the time (1).

$$\Delta Q_i = F(\Delta T_j) \tag{1}$$

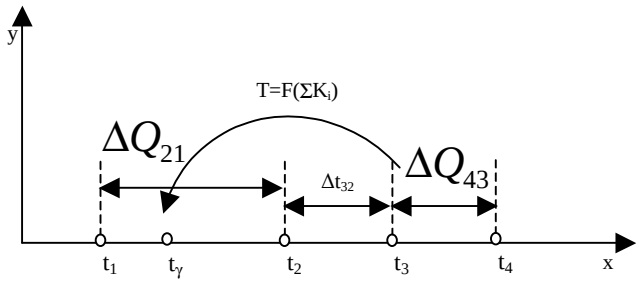

Fig. 1. Life cycle of MMLC

Let us assume that the relation of the effectiveness ΔQ_{ij} to the time factor Δt_{ij} is a value which determines the quality of the MMLC, readed in the time interval Δt_{ij}. Then the following relation can be deduced from the formed intervals in Fig. 1:

$$\frac{\Delta Q_{21}}{\Delta t_{21}} = \Delta \gamma_{21} \tag{2}$$

$$\frac{\Delta Q_{43}}{\Delta t_{43}} = \Delta\gamma_{43} \quad (3)$$

where it is assumed, that condition (4) is satisfied.

$$\Delta\gamma_{21} < \Delta\gamma_{43} \quad (4)$$

An additional reservation that equality (5) is fulfilled can be made the obtained relations (2) and (3).

$$\Delta t_{21} = \Delta t_{43} \quad (5)$$

The fulfillment of the upgrade of the life cycle of the course presented in fig. 1 is carried out by means of direct feedback, i.e. by using of direct methods as: intermediate tests and tasks, control tasks and questions. The time interval Δt_{32} is of great importance for the development of the course.

The idea of the model for the evaluation the effectiveness of MMLC is through indirect methods and new interface technology to translate the point t_3 to the point t_γ - an arbitrary point from the interval $[t_1, t_2]$. The translation of the point of the practice ignore the time interval $[t_2, t_3]$. The upgrade of the course is done here in parallel with the passing of $[t_1, t_2]$.

Let us assume every of the intervals from fig. 1 is divided to a set of equal number intervals δ, which for the fake of brevity we will call step (Fig.2).

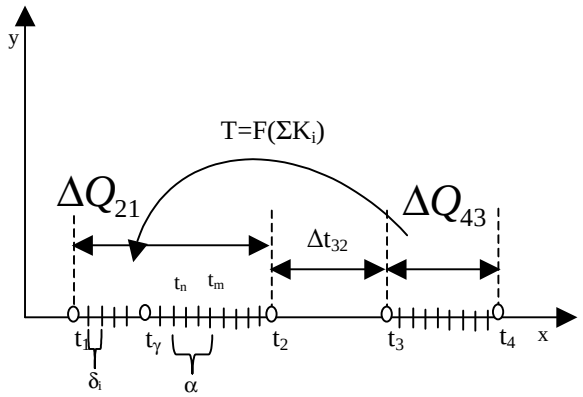

Fig. 2. Discredited life cycle of MMLC

Let $\alpha = [t_n, t_m]$ is a specified finite set of step for the realization of the course upgrade on the basic of a metric evaluation. The effectiveness of the MMLC in the interval $[t_1, t_2]$ is (6)

$$\Delta Q_{21} = Q\sum\delta_1 + \alpha \quad (6)$$

The effectiveness of the course in the interval $[t_3, t_4]$ is (7)

$$\Delta Q_{43} = Q\sum\delta_1 + \alpha \quad (7)$$

which satisfies the inequality (8)

$$\Delta Q_{43} > \Delta Q_{21} \quad (8)$$

After the transformation of point t_3 to point t_γ, the effectiveness ΔQ_{43} to automatically transferred over the step of the interval $[t_n, t_m]$. Hence the aggregate effectiveness of $[t_1, t_2]$ is the following:

$$\Delta Q_{21} = Q\sum\delta_1 + Q_{43}\sum\delta_i + \alpha \quad (9)$$

which satisfies the following condition:

$$\Delta Q_{43} < \Delta Q_{21} \quad (10)$$

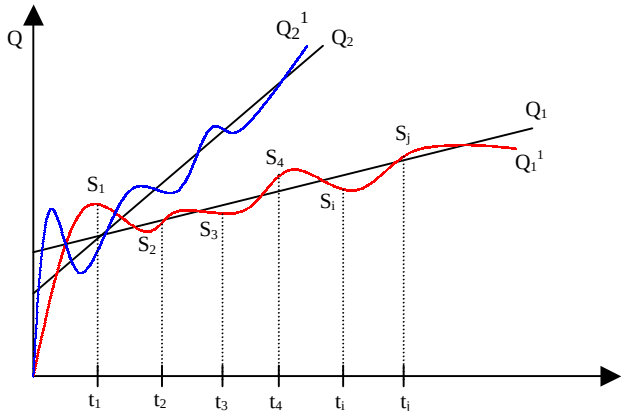

Fig. 3. Expected effectiveness for different group of users

The effectiveness of each learning course is different for the particular groups of learnees (user) - Q_i. The straight lines Q_1 and Q_2 represent the expected effectiveness for different group of users. When using the metrical methods for the effectiveness evaluation in the realcase, these straight lines would have looked in the following way – Q_1^1, Q_2^1. This is due to the following facts: on one hand the different concentration of users in the particular time intervals (t_i) and on the other hand of the single effectiveness of the particular screens (S_i).

It is seen from fig. 3 that Q_1^1 and Q_2^1 are a function, as of t_I as well as of S_i. If we assume that the learning course in not realized by a linear algorithm, i.e. the condition for the moduleness of the screens is not fulfilled, then let represent the user actions, by which he does navigation between the particular screens in the application in a band. Let call this band "band of a learning course" – fig. 4.

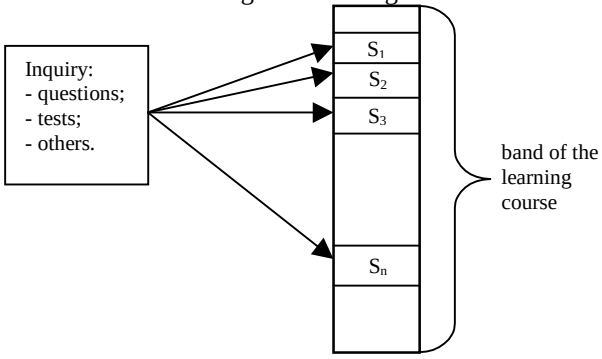

Fig. 4. Band of the learning course

In the cases when direct methods for the evaluation of the effectiveness of a given learning course are used, the most frequently encountered mean is the use of a questionnaire. The questionnaire can be a set of questions, test or expressing the user's opinion about the product given to him.

From the questionnaire made, which can be given in an arbitrary moment of time, belonging to the interval of work of the user in a system or after it, an evaluation is made which concerns the product as a whole. That is the effectiveness of the course, but as an unity. Let us represent the process of the evaluation in function of time – fig. 5.

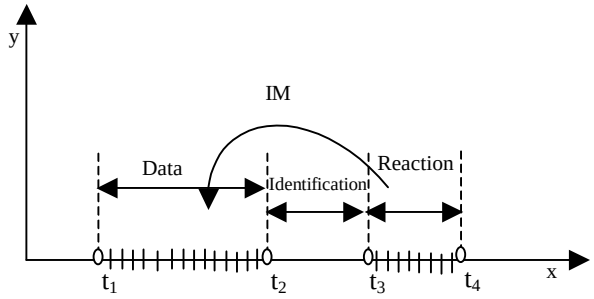

Fig. 5. Time for direct evaluation of a learning course.

The process consists of three stages: Data, Identification and Reaction. The data represent the questionnaire. Then an identification stage follows, whose aim is to generalize the results from the questionnaire and at the end is the reaction.

If indirect evaluation methods are used then it is possible practically to ignore the identification stage. Why? An advantage of the indirect methods is that it is possible to obtain more detailed information. An information concerning the particular screens, even the behavior of the particular user. The information becomes objective and has a direct attitude with respect to the effectiveness of the course.

Identification stage is actually not ignored but it takes a quite ting value in time in order not to have an leading effect on the process of indirect evaluation. The identification is known in every moment of time i.e. the evaluation system has a possibility in every moment to determine the following parameters: screen, time, and modality.

The model described above is based on so called indirect methods for the effectiveness evaluation. It is possible the process of building of indirect methods of evaluation to be realized on the basis of two main approaches: event approach and time approach.

- *event approach* – by this approach a set of the events is defined (e_1, e_2, … e_n) , as well as control intervals Δt_e. Within the framework of every control interval an information about the number of event that have taken place is accumulated by types e_1, e_2, … e_n . For each event type an area of a "guaranteed success" is determined. If the number of the events is such, that for every one the intervals Δt_e, the events registered as a number are in the area, it is accepted that an effectiveness of the interface influence with indirect metrical evaluation with parameter - event e_i is achieved - fig.6.

- *time approach* – the time, "consumed" for passing the atomical interface objects – the screens – S_1,S_2, … S_m , is registered by this approach. For each screen S_i a control

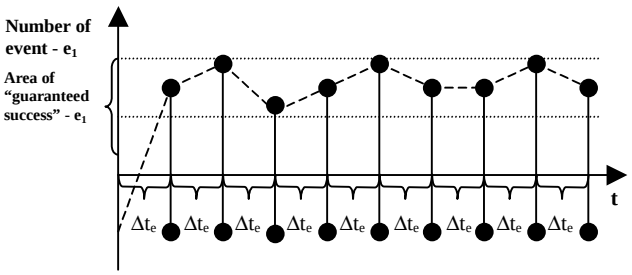

Fig. 6. Event approach for indirect feedback

interval for successful passing is defined - Δt_i. For each user an individual profile about passing the screens is accumulated. In case of completely falling into the control intervals for all screens, it is accepted that for the concrete user the learning effect is expected to be effective – fig. 7. It is of great importance by this approach the selection of a representative excerpt of learnees about implementing of an experimental testing. The process of an indirect feedback is possible to continue after the introducing of the interface environment in the real environment. The indirect methods for metrical evaluation ere usually used about off-line corrections of the learning effect since this necessitates statistical processing of the results for more than one learnee.

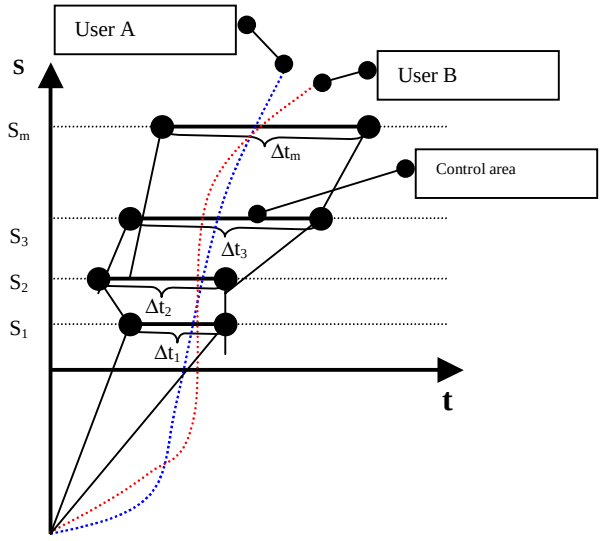

Fig. 7. Time approach for indirect feedback

III. Conclusion

The use of the effectiveness model of MMLC involves the use of so called Modality Pads. These are different peripheral devices for reading of subjective user factors such as concentration, concentration of the eyesight over the learning course and others.

The effectiveness model of a MMLC has the following advantages: it concedes the developers of the course a quick possibility by for actualization, reducing the total time for corrections, possibility for better realization of the particular MMLC.

Some disadvantages are: conforming of the model with a great number of subjective factors, concerning different objective fields of application, a complex algorithm.

The suggested model is a possibility for correction and eliminating of errors in different by type and structure MMLC.

References

[1]. http://www.learningcircuits.org

[2]. Blattner, M.M. and Glinert, E.P., “Multimodal Integration,” *IEEE Multimedia*, 4(3), IEEE Press, 14-24, 1996.

The Interaction Of The Web Technologies In Integrated Marketing Information System

Veselina Ivanova Nedeva[1]

Abstract: **The report presents the different approaches of interaction of the information technologies, which now have their place in the integrated marketing information system. They are defined as wall as the script language so as the tasks of IMIS. In this report we have presented a few basic variants of the interaction, which reflect the specific features IMIS.**

Keywords: **Data Warehouse, Data Mining, OLAP, architecture of information system.**

I. INTRODUCTION:

The report presents different approaches of the interaction of the information technologies, which now have their place in the integrated marketing information system. The script language and the tasks of Integrated Marketing Information System (IMIS) define them.

In the process of analysis the main objects and their relations are defined. We explain the reflecting behavior on the main objects. Diagrams of the interaction objects are developed. The determination of the objects and scenarios is connected to information technologies and consumer services.

The specialists, participating in the creation of IMIS, have their place and role in process of the designing and making the information systems. IMIS creates the balance between information necessities and needs on one side and information technologies and necessities on the other side. If the information technologies are not adapted to the condition of the company, they will be inefficient and the money than have been put for their introduction are of no use. On other side Data warehouse (DW), Data Mining (DM) and OLAP (Online Analytical Processing) might be based on these data, thus creating seriously problems for the information security.

II. THE SOURCES OF INFORMATION FOR MARKETING INFORMATION SYSTEM

To comply with the requirements of the users concerning the preparation and the decision making, IMIS must give information from different sources - an operative system, geodemographics systems and historical data from the system from past reporting period. They should support high quality of data in order to give support for the purpose of making decisions and using the possibility of online analysis. The extraction, transformation and consolidation of the data from operative systems require much time and resources. Creating the multi-objective, consolidated and spreader over the territory of the corporation information archives requires coordination of the different data models. Also the data from the operative systems have to be standardized in order to make them stable.

In IMIS the technology DW is used. The obvious advantage of the DW is the quality of the data – it is prematurely “filtered” (the unnecessary and doubled information is removed); it is complete, because it consists of the whole available data from the operative systems of the external sources – GDIS and the succeeded systems; DW is constantly updating; it consists of details and summarized data, which is a good base for study and analysis and shortens the time for their conduct; DW is consolidated over a single star – scheme; it is integrated in a common information data base of IMIS; DW is available on-line for all users.

[1]Veselina Iv.Nedeva, Assist.Prof.Ph.D., Technical college – Yambol, Gr.Ignatiev Str. 38, Yambol 8600, BULGARIA,
e-mail: vnedeva@tk.uni-sz.bg

III. THE ARCHITECTURE OF MARKETING INFORMATION SYSTEM

The architecture and technology that evolved to answer this demand in IMIS was client/server, in the guise of a two-tiered approach. By replacing the file server with a true database server, the network could respond to client requests with just the answer to a query against a relational DBMS. One benefit to this approach, then, is to significantly reduce network traffic. Also, with a real DBMS, true multi-user updating is now easily available to users on the PC LAN.

A. 2-tier architecture

In a 2-tier client/server architecture, SQL are typically used to communicate between the client and server. The server is likely to have support for stored procedures and triggers. These mean that the server can be programmed to implement business rules that are better suited to run on the server than the client, resulting in a much more efficient overall system. 2-tiered client/server approach is a good and economical solution for certain classes of problems.

The 2-tiered client/server architecture has proven to be very effective in solving workgroup problems. "Workgroup", as used here, is loosely defined as a dozen to 100 people interacting on a LAN. For bigger, enterprise-class problems and/or applications that are distributed over a WAN, use of this 2-tier approach has generated some problems.

What typically happens with client/server in large enterprise environments is that the performance of a 2-tier architecture deteriorates as the number of on-line users increases. If something happens to the connection, the client must go through a session reinitiating process. With 50 clients and today's typical PC hardware, this is no problem. When one has 2,000 clients on a single server, however, the resulting performance isn't likely to be satisfactory.

The data language used to implement server procedures in SQL server type data base management systems is proprietary to each vendor. Oracle, Sybase, Informix and IBM, for example, have implemented different language extensions for these functions. Proprietary approaches are fine from a performance point of view, but are a disadvantage for users who wish to maintain flexibility and choice in which DBMS is used with their applications.

Another problem with the 2-tiered approach is that current implementations provide no flexibility in "after the fact partitioning". Once an application is developed it isn't easy to move some of the program functionality from one server to another. This would require manually regenerating procedural code. In some of the newer 3-tiered approaches to be discussed below, tools offer the capability to "drag and drop" application code modules onto different computers.

The response to limitations in the 2-tier architecture has been to add a third, middle tier, between the input/output device (PC on your desktop) and the DBMS server. This middle layer can perform a number of different functions - queuing, application execution, database staging and so forth. The use of client/server technology with such a middle layer has been shown to offer considerably more performance and flexibility than a 2-tier approach.

Just to illustrate one advantage of a middle layer, if that middle tier can provide queuing, the synchronous process of the 2-tier approach becomes asynchronous. In other words, the client can deliver its request to the middle layer, disengage and be assured that a proper response will be forthcoming at a later time. In addition, the middle layer adds scheduling and prioritization for the work in

process. The use of an architecture with such a middle layer is called "3-tier" or "multi-tier".

B. 3-Tier With a TP Monitor

The client connects to the TP monitor (transaction processing monitor) instead of the database server. The transaction is accepted by the monitor, which queues it and then takes responsibility for managing it to correct completion.

On-line access to mainframes was available through one of two metaphors – time-sharing or transaction processing (OLTP). Time-sharing was used for program development and the computer's resources were allocated with a simple scheduling algorithm like round robin. OLTP scheduling was more sophisticated and priority driven.

TP monitors (TP Heavy) have staged a comeback because their queuing engines provide a funnelling effect, reducing the number of threads a DBMS server needs to maintain. The client connects with the monitor, which accepts the message and queues it for processing against the database. Once the monitor has accepted the message, the client can be released for further processing. The synchronous session based computing of a 2-tier architecture, then, becomes asynchronous through the insertion of the TP monitor into the equation. The monitor smoothes out and lowers the overhead of accessing the database server.

Some other key services a monitor provides are: the ability to update multiple different DBMS in a single transaction; connectivity to a variety of data sources including flat files, non relational DBMS, and the mainframe; the ability to attach priorities to transactions; and robust security.

C. 3-Tier With a Messaging Server

Messaging provides still another technology to implement 3-tier computing. Messages are processed asynchronously with the appropriate priority level. And, like a TP monitor, a

Messaging server provides connectivity to data sources other than RDBMS. A message is a self-contained object that carries information about what it is, where it needs to go, and what should happen when it reaches its destination. There are at least two parts to every message; the header contains priority, and address and an ID number. The body of the message contains the information being sent, which can be anything-including text, images or transactions.

A primary difference from TP Monitors is that message server architecture is designed around intelligence in the message itself as opposed to a TP monitor environment, which places the system intelligence in the monitor or the process logic of the application server.

Messaging systems are designed for robustness. By using store and forward logic, they provide message delivery after and around failures. They also provide independence from the enabling technologies such as wired or wireless or protocols. They don't require a persistent connection between the client and server. They are robust because message delivery can be programmed to occur after or around failures. Because messaging systems support an emerging wireless infrastructure, they should become popular for supporting mobile and occasionally connected workers.

D. 3-Tier With an Application Server

When most people talk of 3-tier architectures, they mean the approach of an application server. With this approach most of the application's business logic is moved from the PC and into a common, shared host server. The PC is basically used for presentation services - not unlike the role that a terminal plays on a mainframe. Of course, because we are talking about a real PC here, it still has the advantages of being used for client side application integration (via OLE or other Approach) if desired.

The approach of putting business logic on a server offer a number of important advantages to the application designer: When less software is on the client, there is less worry about security since the important software is on a server in a more controlled environment. The resulting application is more scalable with an application server approach. With a middle application server tier it's much easier to design the application to be DBMS- agnostic. If you want to switch to another DBMS vendor, it's more achievable with reasonable effort with a single multithreaded application than with thousands of applications on PC's.

E. 3-Tier With an Object DBMS

A variation on this theme of application server is the idea of using an object DBMS (ODBMS) as the middle layer. Data in a relational DBMS is usually stored in normalized fashion across many tables and for access by different applications and users. This generalized form of storage may prove inadequate (performance wise) for the needs of any one particular application. An ODBMS can be used to retrieve the data from the common store, assemble it for efficient usage by your application, and provide a persistent store for that data as long as your application might need it.

Since extended data types like video or voice are not typically supported in today's RDBMS, those data types might also be stored in the ODBMS, which could then associate the appropriate multimedia data with the data retrieved from the RDBMS.

F. Distributed Components & the 3-Tier Architecture

This brings us to distributed object computing and components. Many software specialists are predicting a software future with the creation of application systems through assembly of software components. That kind of software approach is available today in a few proprietary object environments. The emergence of a broad based industry for component-based software will require the prior emergence of industry standards for interchangeable parts.

The distributed object implementation of client/server computing is going to change the way applications are built.

There should be some very interesting advantages to observe. If we needed fault tolerant computing, we could implement copies of objects onto multiple servers. That way if any were down, it would be possible to go to another site for service. With distributed objects being self contained and executable (all data and procedures present) it will be possible for a systems administrator to tune the performance of the network by moving those objects from overloaded hardware to under utilized computers.

Distributed object architecture should also offer other benefits for application developers. The same interface will be used for building a desktop, single location application or a fully distributed application. The application can be developed and tested locally and you'll know that it will work fine when it's distributed – you depend on the known services of an object request broker for distribution.

Since the application developer is dealing with an object request broker for transmission services, technical issues like queuing, timing and protocols aren't an issue for the application developer.

G. Data Warehouse & 3-Tier

A 3-tier architecture is also useful for data mining or warehouse types of applications. These applications are characterized by unanticipated browsing of historical data. The databases supporting this type of application can sometimes be huge (up to a few terabytes -10(12) bytes) and have to be structured properly for adequate performance (a few second turnaround).

Data mining and decision support applications typically need response times of a few seconds. If the system can't provide that kind of performance, the thought process of the human analyst is disrupted and the overall purpose of the system is foiled. A production database established for multiple users isn't typically in a form that can support ad-hoc inquiries. IT systems and operations managers usually don't want access to those tables to be on the mainframe.

Often this server is called OLAP - on-line analytical processor. In other circumstances this server can be a symmetric or massively parallel processor running an RDBMS.

IV. THE INTERACTION OF THE WEB TECHNOLOGIES

There are a number of technologies for data transformation and filtering techniques, which comply with these requirements. They examine the data preparation for DW while maintaining the quality and minimizing the risk during the process. The complexity of extracting, transforming and integrating of the data depends of the number and the variety of the sources. The process of extracting and integrating is almost impossible to be conducted with the traditional methods, because of the large amount of resources and the complex multi-step processing.

The connection between the user and DW is done by Meta-data. The meta-data has special status of meta-class, which does not posses other class or object in the system. Once we have finally transferred the data to the DW, then we must have metadata, including:

- DBMS system tables
- Partition settings
- Indexes
- Disk striping specifications
- Processing hints
- DBMS-level security privileges and grants
- View definitions
- Stored procedures and SQL administrative scripts

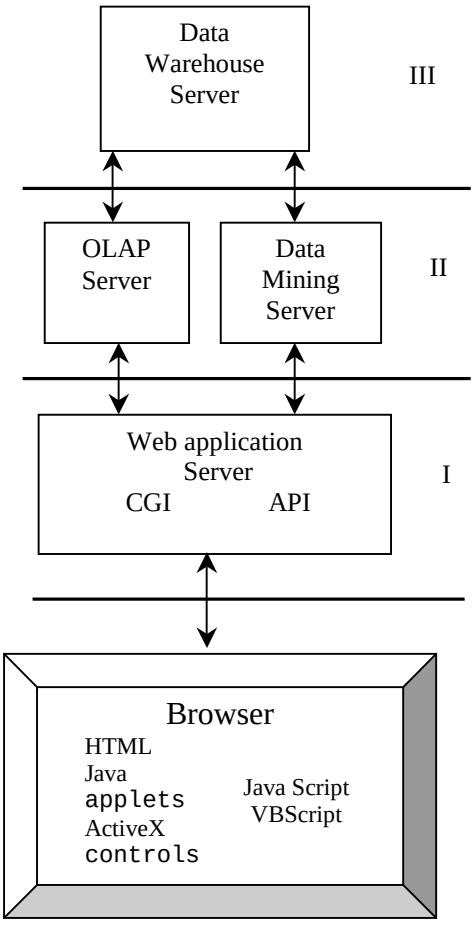

Fig.1. Approach to access uses Web Application server in 3-Tier architecture.

The data in these dimensions, called measurable, are in most cases aggregated. Detailed 'raw' data are used for the analysis needed by the marketing specialists. Because of this both non-aggregated data and different summarized level data (like that used for OLAP analysis) are stored in the repository of the DW.

The information system has a user-friendly interface, because the users examine the DW data using browsers. This way most of the data is very easy integrated and provided in any place in the Internet. By the same token the moving in the Web ensures independent platform mechanism for remote users, group application and consumer services. In this case the server's task is to build the processes that on one side use HTML and HTTP and on other side communicate with OLAP applications and DB server. The Web server controls the communications between browsers and applications or the DB server. In this process the following server options are used: CGI script, API Web server, API application and API DW. On the client side – combination of HTML, Java applets, ActiveX controls, Java Scripts and VBScripts and interface (Fig.1).

OLAP is working in this mix through its installation in the net as an application server. The application server can be reached by any client application, including that spread by web browser. By this means the developer can use the 'best fitting' technology for every part of the program of the widespread Web-based applications.

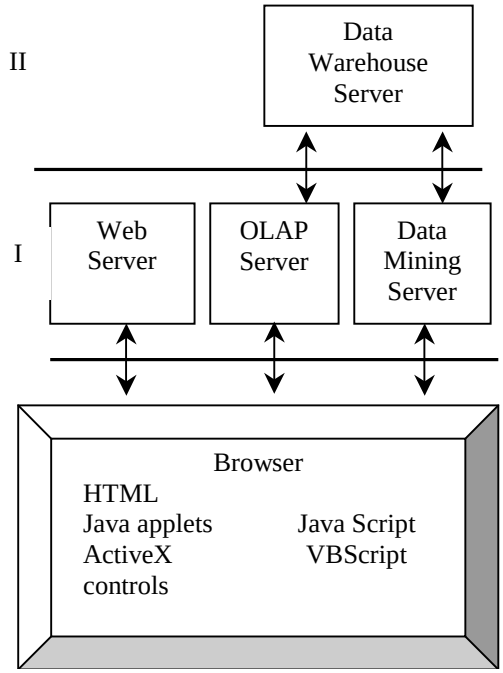

Fig.2. Approach to communicate directly to the application server without the use of the web server in 2-Tier architecture.

From the browser (Fig.2) the application components communicate directly to the application server without the use of the web server. Protocols like Distributed Component Object Model (DCOM, formerly Network OLE), Distributed System Object Model (DSOM), or Common Object Request Broker Architecture (CORBA) are used for finishing the communication. In such a way the productivity is increased and better functionality and security are ensured.

The necessity for providing information through the browsers is the basic philosophy of OLAP and Web application. We can conclude that this process requires HTTP access to the MDB server and the Data Mining server. The possibilities of data analysis are very important for the users of IMIS. Different levels of the OLAP reports, ranging over a large number of statistic's reports with dynamic dimensions and drilling down the reports through the data.

The interface provided by the standard HTML presents plain text and stability features. The user must make several selections of two

or three dimensions that are represented data. Only after that the user can watch the rotation after a selection.

Some product and time position changes can be made after which the user must wait for the updated report.

The approaches for granting access to the OLAP function in the Web can be presented in three categories:

- Static HTML reports, made in packet mode;
- HTML data patterns on-the-fly;

Java and ActiveX components, supported by the browsers.

The first approach uses preliminary lists for extracting OLAP data in packet mode, making static HTML reports using HTML templates. The templates are prepared in such a way that they can be used for all reports, no matter of their content. Then the reports are being controlled and sent to the browsers by Web server. The static reports are very convenient, fast and easy to transport to the browser. The disadvantage of the static reports is that they are not allowed to interact with DW data during the process. Some static reports simulate research of dimensions by navigation through the reports. In the browser list field a number of a report could be assigned that links it to the data using a hypertext.

In the 'on-the-fly approach' templates of the reports and the metadata are created in the browser. These metadata show the browser, which data are to be loaded in a HTML file, before sending them to the browser. There are two formats of metadata on the server – in the application tags and in the HTML templates. An alternative is storing them in the DB field in binary format. There is a possibility of another format for storing the metadata. Using its own HTML tags, the report presents the metadata already existing in the HTML file.

HTML also exists in two formats on the server. If off-the-shelf educator is used for creating templates they exist as HTML files on the server. By single user click on the name the report, both the HTML template and the data from the report are joined and sent as HTML reply to browser.

Web toolkits can also be used for making and storing metadata models in a binary format. In this case both the reports and the templates can be made using on-the-fly Web server processes. Web maintenance toolkit allows designing and formatting the report's pages. The obtained information is stored in a Web DB. Using this information it makes HTML templates, joins the data in a single report and presents it in the browser.

Regardless of the way the templates and reports are stored on the Web server, the server obtains the information, which is based on the code of the report sent by the browser. This information is merged with the template and all packets are sent to the browser as a HTML response. The default report offers several levels of OLAP functions. If the user is in dialog with an interactive report mode, user's code is sent with the rest of the information to the Web server. The application server starts a program that extracts and sends data to the browser. The alternative is if the code exists as values in the hidden HTML control of HTML file. Using this kind of project the program on the Web server identifies the user by reading the value of the user code as a control. Using this code and other information from the browser's session, the server downloads and formats the necessary MDB information and directs it towards the browsers.

Depending on the way the web server's applications are built the project can be used for multiple computer platforms. The CGI specification is mobile, but most servers don't use API.

The Java and ActiveX approaches use Java applets and ActiveX controls in order to minimize the communication between the browser and the web server and to improve the interface. There are two methods for their usage. In the first, the web server uses binary file with data from the reports and interface's controls are sent to the browser with an HTML files together. Using the client, the characteristics and the requirements of the control show the name of the corresponding data file to the browser. In this project the components provide functionality using deepening the data and changing the common format with "tricky" interface – with no need of communication with the server. Also, since the data are transferred in binary format between the client and the server, this method is more secure.

In the second method the interface's components communicate directly with the browser, transferring data to the user as result of a search. The interface components download the results from the server using HTTP stream. When the components present the result to the server, it makes selection and moves the data towards the object for visualization. This method has advantages similar to the ones of the first method. Nonetheless, in order to achieve the same level of security as for the first method HTTP protocols should be used. This method has its disadvantages as well - the JAVA work execution is faster, but it is not as easy transferred as HTML.

Generation of reports can be applied, based on browsers, presenting WEB based applications; mixing other web protocols with HTTP for direct communication with the same server process, used for the usual client/server applications. These network transport protocols can be used with HTTP for improvement in the communication characteristics. These reports include DSOM and DCOM, both based on CORBA. This design can improve the customer's experience, when browser is used and the abilities for growth, in order to make the systems usable in multiple environments.

V. CONCLUSIONS

In the development of the Web based marketing information system several conclusions can be drawn:

The applications directed to information adjust better to the web and obtain more advantages from their architecture.

The information systems that present the information use multiple formats and user friendly.

Using a browser for adjustment to the environment, the applications increase with a little bit their intensity, but this way difficulty for the users and the developers are created. The users need to administer additional software on the web server and the users obtain fewer possibilities from the interface if HTML is used.

REFERENCES:

1. Inmon W.H., Building The Data Warehouse (Second Edition). - NY, NY: John Wiley, 1993

2. Kimball, Ralph, "The Data Warehouse Toolkit: Practical Techniques for Building Dimensional Data Warehouses", John Wiley & Sons, 1996

3. Архипенков С.Я., Завьялов Б.П., Шеховцов А.И. Object-oriented approach in the task of modeling complicated systems. Сб. Вопросы кибернетики, серия "Моделирование сложных систем и виртуальная реальность", Москва, 1997

4. Асадуллаев, С., Architectural corporative Data Warehouse, PC Week/RE'98

5. Буч, Гради, Object-oriented analysis and design, Second Edition, Пер.с англ. под ред. И.Романовского и Ф.Андреева, Издателтьство Бином, 1998

6. Вавилов К., С.Щербина, Web-integration of the corporative systems, http://www.profi-club.kiev.ua/, 2001

The New Technology and Information Society in Bulgaria

Galina St. Panayotova[1], Nikolay Iv. Petrov[2]

Abstract: **In this paper we investigate the human and scientific components of the information society in Bulgaria. The contemporary pragmatization and the influence of the so called computer revolution.**

In this paper we describe too, different national innovations in the field of information and high technology in high school.

The results of made inquiry is presented.

Key words: **Information society, new technology, computer revolution**

HISTORICAL PERSPECTIVES

The worldly democratic aspect of education as it has been left us by testament from the time of Alexander Humbolt, has a humanitarian foundation. After the 18th Century Industrial Revolution a number of elements from natural sciences has been added to enrich education. In that respect the role of mathematics has become much more significant for the scientific research work as well as for education in general. The intensive development of the natural sciences in 19th – 20th centuries, especially that of physics, chemistry biology, mathematics and engineering brings essential changes in the general notion of the world. Science being closely bound up with politics, causes real problem and one of them is the danger of self-destruction due to the availability of nuclear weapon. This is a question that has been raised for discussion and fiercely debated by humanitarian and cultural and cultural workers, philosophers and sociologist. Here is what the French philosopher Jian Francoif Liotard answered when asked to define the connection between science and philosophy in human society: "The balance the philosopher in me strikes is disaster". A great number of humanitarian workers share the opinion that science today is burdened with great responsibility before humanity.

INTRODUCTION

We are living today in the century of information. We are gradually building a new type of community, a community of information where it is of major importance. Regardless of its opponents it has become a fact, and its distinctive features have turned it into an inseparable part of the daily routine of modern people. Some old ways of communication have long ago been replaced with new ones. The traditional methods and ways of learning have also been changed with new ones, more flexible and mobile. It all concerns use of modern computer systems and technologies which are no longer the privilege of only highly qualified specialists, but are also used by all modern people.

1. Galina St. Panayotova, (*g_panayotova@abv.bg*)
2. Nikolay Iv. Petrov (*nikipetrov@lycos.com*)

University "Prof. Dr. Asen Zlatarov"Burgas, Bulgaria

INFORMATION TECHNOLOGIES IN EDUCATION

In the period of 1995-1999 in a number of countries there have been introduced educational strategy programs for the for the active use of Information and Communication technologies in the system of education on all levels. Some of them comprise even the kindergartens (Great Britain, Israel, Portugal). It shows how significant the role of these new technologies in education is.

Is the computer of use science? Definitely yes! The computer is of use for the scientific research work as well as for pedagogic which is much concerned with teaching. The variety here is boundless because it has do with personal tastes, preferences and capabilities. The teacher is one to decide what to use – the computer or Internet.

THE INTERNET COMMUNITY IN BULGARIA AND CREATING IT.

You can't foresee the future if you don't know the present well. Plain as it may be, the truth of this statement is something that worries all instructors from the Internet branch in Bulgaria. For how could they plan the future development of the branch when the statistics now is unable to answer the simplest question – what is number of Internet users in Bulgaria?

There follow a few consequences that directly concern the community and the greater use of Internet.

- The main motor of computerization and spreading of computer learning – the corporative economics in our country – is either in rudimentary or lethal stage.
- There hasn't been completely fulfilled one main condition – the one when Internet communication becomes not only widely spread but also of first necessity – anonymous, atomized community and a wide range of interests and tastes.
- The Bulgarians today are not in the same need as consumers of electronics services as the people in the developed consumer societies (USA and Western Europe).

Even the valuation of the maximum possible Internet consumers turns out to be of great difficulty. The main groups of users can be divided into three:

- Company and departments employees actively engaged in working on computers and well aware of the Internet atmosphere in the office system.
- The technical ragamuffin intellectuals.
- The computer – learned young people – school and university students (the group of the latter ones being almost entirely included in the contingent of youth sub-cultures).

There isn't an exact or approximately average statistics for either of these groups. They most probably number 350 000 – 500 000 people – this is the presumable range of our Internet users. Besides that we have to bear in mind that the computer

– learned Bulgarians are gradually leaving the country. We even don't know whether the outgoing flow of computer – learning Bulgarians is greater or smaller compared to that of complete beginners. And this is very important because it will show whether what we have in store of computer – learning people as our potential Internet users is increasing or decreasing in number.

It is quite probable that in the next 10 years there'll come the time when the majority of the Bulgarian users will be living abroad and will enter Internet from there (that's the case with the Russian Interned today). An account of this fact should be rendered as it will restrict the clientele of our Internet sellers, and it can also influence the revenue brought by commercials in our sites.

Let's have now a closer look at the third group: the computer - learned young people, that is to say the group of students. An inquiry has been held 70 students who are studying different subject: 35 - marketing, 20 – tourism, 15 – chemistry (30 girls and 40 boys). The charts below show the results.

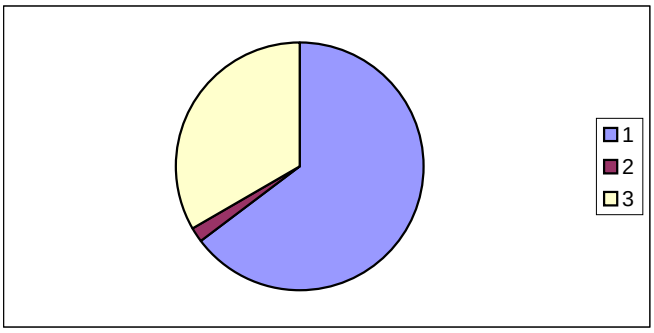

Chart 1: Do you use a computer? (1 – yes; 2 – no; 3 – rarely)

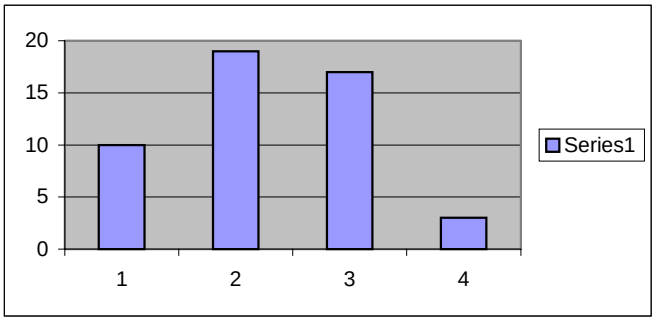

Chart 2: Where did you learn how to work on the computer? (1-home, 2-school, 3-computer club, 4 with friends)

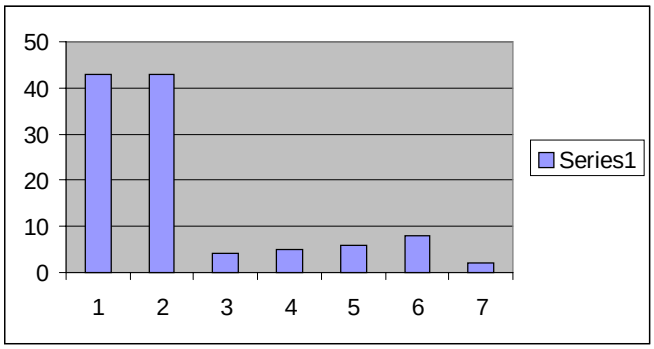

Chart 3: Software (1-word, 2-excel, 3-Photoshop, 4-corel draw, 5-p.point, 6-etc., 7-no)

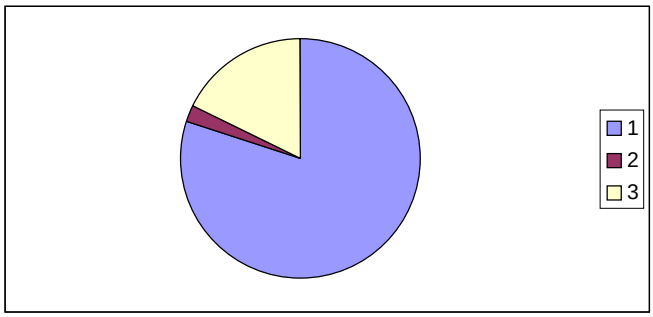

Chart 4: Do you use Internet for the purposes of study? (1 – yes; 2 – no; 3 – rarely)

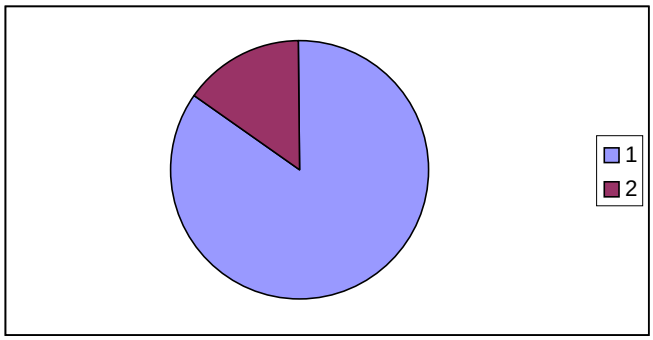

Chart 5: Do you have e-mail? (1-yes, 2- no)

CONCLUSION

To create an Internet community we need to have acquired a good knowledge of the subject of information technologies, which means: operating thee computer and using computer systems and technologies, Internet, different program products, etc,. In the future that'll be something compulsory for every technically literate person. The existing good results are the achievement of personal enthusiasm rather than of national policy.

REFERENCES:

[1]. National Innovation – European School Net, hthp://www.en.eun.org/eun.org2/eun/ni/inovation/sub_area.cfm

[2]. Shishcov D. "Philosophy of Computer Informatics", Sofia, Tangra TanNakRa, 2002.

[3]. Nedeva V. "Information Technologies for WEB marketing of equation services", HC, Stara Zagora, 2003, ISBN 954-9329-03-8, v. 2.

[4]. Иван Попов , "СВЕТЛО БЪДЕЩЕ ЗА БЪЛГАРСКИЯ ИНТЕРНЕТ?", (стратегически доклад)

[5]. Tabov J. "Multiple choice style informatics", Mathematics Competitions, vol 16, No 2, 2003.

Object Oriented Web Client for Content Management System

Ivan Petković[1], Milena Stanković[2]

Abstract – **Data redundancy is usual on the client side of the contemporary Web applications. Eliminating the redundancy can significantly improve Web site performance and maintenance. For that purpose, we propose a new efficient method which eliminates redundancy on the client side.**

Keywords - **object oriented, client side, content management system**

I. INTRODUCTION

Managing content has always been one of the primary needs for using the computer. At the earlier stages of the Internet evolution, Web sites contained primarily static content. Another problem was lack of separation between presentation and actual content. This lead to the fact that only people who knew the actual code implementation of the Web site could change the content. Now days, as technology advanced, both the types of content and the way people manage and use it have greatly changed. New content types such as continuous multimedia streams have become commonplace due to the constantly improving storage, encoding, and networking technologies. This combination has allowed users to access and share multimedia content in both local and remote area networks with the network itself acting as a huge data repository [1]. Two issues became very important: how to efficiently find and use Web content, and how to produce and make them accessible to users. Solution to the first issue is to design a good Web client interface, and for the second issue is to make a content management system.

In section II we will discuss about the needs for content management systems, and afterwards, in section III, we will describe the Web content lifecycle in. Section IV will explain the architecture of the general-purpose content management system, and section V will be more specific about the client side of the content management system. In section VI we will describe proposed Web client.

[1] Ivan Petković is with the Faculty of Electronic Engineering, Beogradska 14, 18000 Niš, Yugoslavia, E-mail: ivanp@elfak.ni.ac.yu

[2] Milena Stanković is with the Faculty of Electronic Engineering, Beogradska 14, 18000 Niš, Yugoslavia, E-mail: mstankovic@elfak.ni.ac.yu

II. NEEDS FOR CONTENT MANAGEMENT SYSTEMS

A content management system is a system used to manage the content of a web site. It typically consists of two elements: the content management application and the content delivery application. First one allows the authors, to manage the creation, modification, and removal of content from a web site, while the other is focused on the content delivery to the users.

The need for the content management systems (further referred as CMS) evolved for the series of reasons, but we should state the major ones:

- Site visitors have difficulties to find what they need
- Content must be updated often
- Content must be modified by a different people
- Content must be extracted from the various sources (database, XML, other applications, etc.)
- Content must be available to the different types of clients (PDA, WAP, Web of other)

There is also a set of requirements CMS should meet. Two fundamental requirements every CMS should provide are separating the way of presenting contents (layout) from the actual content, and separating the site map ("where it is stored") from content. This enables content redeployment to different locations and devices, with changeable "look and feel" of the client interface. Because a large number of people should be able to use the CMS, it must operate on a large number of heterogeneous systems. It should also be flexible enough to support content management policy (what content should be obtained, how it will be integrated, and under what circumstances should it be discarded).

III. ARCHITECTURE OF THE CMS

There are different opinions on the architecture of the content management system, but we can define fundamental model which can be modified according to the specific needs (Fig. 1). This model is divided into three sections:

- client
- CMS engine
- source

We should state that the presented model is for general-purpose CMS, not only for Web. Web content management

systems are more specialised since their primary focus are Web clients. Clients represent target platforms which receive the content. Since the client platforms can drastically differ (e.g. cell phones, Web pages and PDF documents), content must be specialy adapted for each of them. As we stated earlier, this can acheived by following the "golden rule of CMS" – separation of storage, presentation and content.

Content sources can be very different, and they can also be distributed. Most frequently used type of source is database, which is often used in Web content management systems. Besides database, there are other types of sources: Web services, structured and unstructured documents, and even input from machines.

In order to acheive univesal data interchange, inputs from all the sources must be transformed (adapted) to the standardized form. Nowdays, the most promising solution is using XML as an open standard based on common synax and with infinite semantics.

Our primary focus will be on Web clients and their design and implementation using the proposed object oriented approach.

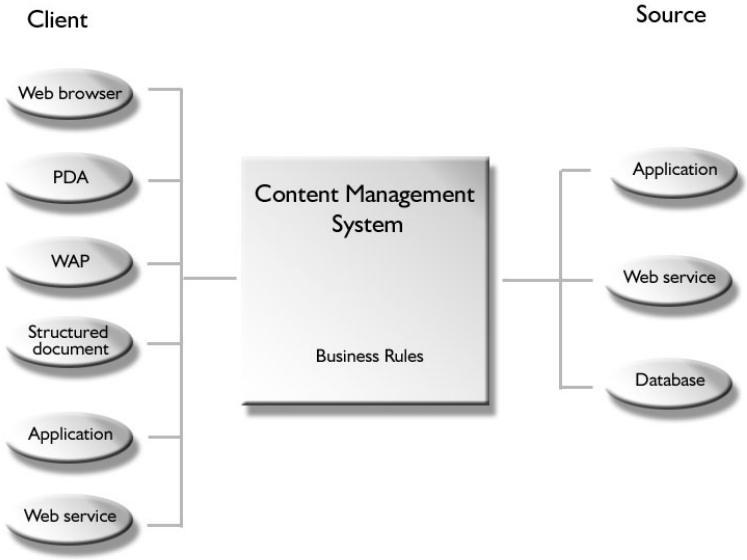

Fig. 1 Architecture of the CMS

IV. THICK WEB CLIENT

There are two Web Client patterns used in Web development:

- Thin, and
- Thick Web Client.

Thin client usually refers to a system that runs on a resource-constrained machine. The client only requires a standard web browser. All of the business logic is executed on the server.

In principal, Thick Web Client pattern include the dynamic of the Thin Web Client pattern plus the ability to execute all or some parts of the business logic on the client. As with the Thin Web Client pattern, all communication between the client and server is done during page requests. The business logic however, can be partially executed on the client with scripts, controls or applets.

Page sent to a client may contain scripts, controls and applets. They may be used simply to enhance the user interface, or contribute to the business logic. The example of the simple business logic is a form validation. In this case, script checks every field in the form to prevent incompatible input before the page is sent to the server. Scripts can also respond to various events (user interactions and browser events), which gives them ability to define the behavior of the user interface (page).

Sometimes, page contains Java Applets or ActiveX controls. These controls and applets can work independently of any scripts in the page, but can also communicate with them (form of interdependency).

Scripts have access to the Web page content via Document Object Model (DOM) interface [2]. This interface is a W3C standard. At the core of the Document Object Model is a set of interfaces that specifically handle XML documents. XML is a flexible language that enables designers to create their own special purpose tags. The DOM interface enables client scripts to access XML documents through ActiveX controls or Java Applets. The main disadvantage of using controls or applets is requirement for the additional software to be installed. In the past, when every browser had its own logic of accessing page contents, thick client pattern was not popular. The reason was that developers had to write different code for every browser, which resulted in Web sites working only on the most popular browser at the moment.

Today, as DOM interface standardized page contents access, future for the thick client got brighter. Moreover, processor power of the client machines has increased, enabling more complicated scripts to be executed on Web client.

We must state that term "rich client" as a middle layer between thick and thin client patterns is becoming popular lately. Its purpose is to distinquish above mentioned type of thick client from the clients working independetly from Web browsers – standalone applications which must be installed on each client system.

V. Proposed Web Client

As World Wide Web Consortium defined several important standards (DOM, CSS, HTML 4.0), we can say that browsers war calmed down. These standards united browsers in some way, defining how to write code which will run on every browser (DOM compatible). They are also the baseline for proposed Web client.

Current client-server communication can be presented on the diagram on Fig. 2:

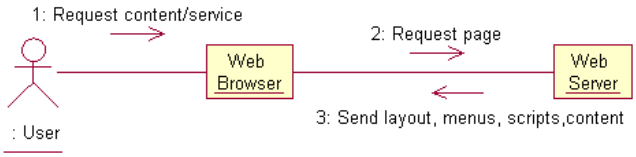

Fig. 2 Common client-server communication model

User is requesting content or a service through some form of interaction (clicking on the link). After that, Web browser will send a page request to the Web server. Server will gather complete page code (layout, menus, scripts and requested content) and send back as a complete page. Problem with this approach is that every time new content is requested, user gets a whole page. Very often, Web content can be only small part of the page. That leads to conclusion that communication is not always optimized. In case of content management systems, with a large number of content requests, this approach makes unnecessary extra network traffic and extra page download time. So, how can we achieve better results?

If Web server could send back only the requested piece of information, that would improve efficiency and decrease network traffic [3] (see Fig. 3).

We propose an approach based on object oriented paradigm. Object oriented thinking is most natural to human thinking. We have developed the framework which acts like a layer between page (HTML) and the Web server. It uses JavaScript syntax, but has its own set of objects.

Purpose of the framework is that developers can think in the more abstract way. Instead of thinking on the level of HTML tags, they can think on the level of objects. To be more specific, this framework recognizes following types of objects:

- resources
- scripts
- contents
- modules

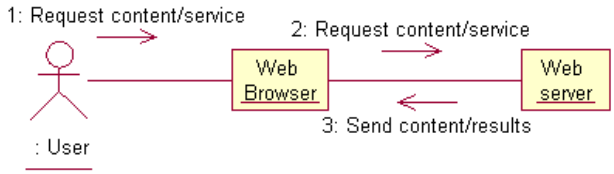

Fig. 3 Improved communication model

Resources are mostly static elements which are used by the Web pages. They can be:

- multimedia files (images, video, audio, Flash, ...),
- menu objects, and
- layout objects

There are two types of menu objects (see Fig. 4):

- menu data objects,
- menu presentation objects, and
- menu controller objects.

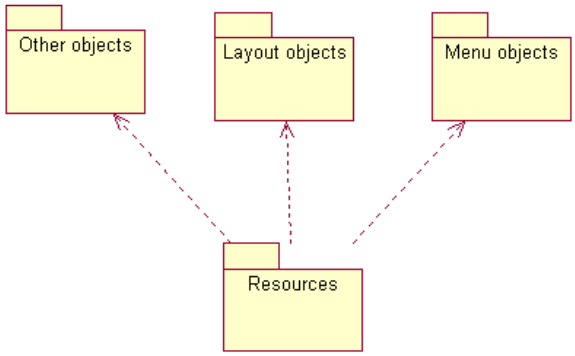

Fig. 4 Resources hierarchy

Menu data object is a structure (most likely tree), which contains all or most of the links to the other pages or options. It does not define the presentation of the menu object (popup, dropdown ...), only its structure.

Menu presentation object defines a visual appearance and behavior of the specified menu data object. In other words, it defines what form will menu data object take – for example popup menu. If a page contains some type of menu (e.g. popup menu), it can be changed to other type of menu, let's say to dropdown menu, even in run-time by calling only one function.

Menu controller object connects one menu data object with one menu presentation object. Together they make MVC (Model-View-Control) framework. Changes in one of them will not influence other two. Also, if we want two representations of the same menu structure, we only have to create two menu controller objects which will be attached to the same menu data object on the one side, and to the different menu presentation objects on the other side.

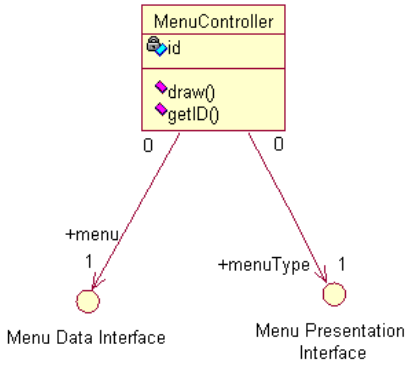

Fig. 5 Model-View-Control framework

Layout object represents visual appearance of the page. It structures the page layout by splitting it onto parts, and it defines their behavior. Those parts (called layout components) can be nested into other parts of the same kind. It is important to say that implementation of the component is abstracted using Bridge design pattern [4]. Than means developers will not need to use tags (<DIV> or <TABLE>) to design layout, but only to define structure by calling layout class methods. Design and behavior of the layout object can be changed in the run-time, simply by calling an appropriate class method. Layout object acts like a "window" to the client – users will experience Web site through it. Thet means we can adapt whole CMS to every Web client only by creating one layout object for each type of client (e.g. for PDA users, users with high resolution displays, etc.).

Scripts define behavior and the dynamics of the Web page. They can be client side or server side. Client side usually defines behavior of the page (user interface and additional layout object behavior, menu object implementations and other). The proposed framework recommends that all client side script code should be embedded into classes, and not as unstructured code. We can clearly see frameworks orientation on object models, and not on data-flow models [5]. Server side scripts dynamically create contents and resources like layout and menu objects.

Contents are actual data the user wants – they can be structured documents (XML, HTML), but also a simple text.

Module is an independent or interdependent component which can be consisted of other modules, resources, scripts and contents. There is an analogy to the folder on the computer file system. It can be independent in a way that it uses only elements from itself, or can be interdependent – if uses elements from the other modules.

VI. Conclusion

By implementing the proposed Web client pattern, we achieved better performance (network traffic and download time) obtained by decrease of the data sent back to a client. Redundant data (data common to all or most of the pages on the site) are not sent, but only desired content. Web client is robust and flexible, since its every element can be changed in the runtime. Here is the list of some possibilities that can be achieved in the runtime:

- Content can be seamlessly loaded or changed in the layout component
- Content can be loaded into every (not only one) layout component.
- Layout design can be changed (in runtime)
- Menu presentation (type) can be changed (in runtime)
- Menu structure can be changed (adding, editing and removing menu items).

Our future work will be based on further integration of the object oriented paradigm into both CMS and Web client, in order to achieve more flexible platform. That would provide advantages like online graphic and layout design and "skinable" Web sites (sites with more layouts which can be switched by one click). These advantages would also enable CMS personalization, modern and very important concept in the process of CMS development.

References

[1] C. D. Cranor, R. Ethington, A. Sehgaly, D. Shur, C. Sreenanz and J.E. van der Merwe, *Design and Implementation of a Distributed Content Management System*, Proceedings of the ACM International

[2] World Wide Beb Consortium, *Document Object Model Level 3*, http:/ /www.w3.org/TR/2004/REC-DOM-Level-3-Val-20040127/

[3] I. Petković: *Component Development of the Client Side of the Web Applications*; Proceedings of 6th International Conference on Telecommunications in Modern Satellite, Cable and Broadcasting Services, Telsiks 2003, October 2003

[4] E. Gamma, R. Helm, R. Johnson, J. Vlissides: *Design Patterns*, Addison-Wesley, 1997

[5] I. Sommervielle, *Software Engineering***,** Sixth Edition, Addison-Wesley, 2001

Problems In Creation Of The Mathematical Insurance Of High Technology Systems

Nikolay Iv. Petrov[1], Galina St. Panayotova[2]

Abstract: **In this paper we investigate technical difficulty for creating by mathematical insurance of high technology systems, function in limited interval of time. These difficulties according to authors represent basic reason for realize by enterprise for this systems.**

We make analysis by basic arguments for followers and opponents of realization for these systems.

Key words: **mathematical insurance; function in limited interval of time; high technology systems**

INTRODUCTION

Lately the interest about the problems in creating reliability working mathematic insurance of High Technology Systems (HTS) for security of the society increase suddenly. In row publication on the West and on the East appeared developments of that problem. Those questions became subject of discussions in the committee about strategic and tactics nuclear forces in the Senate in the USA and in the Public word in Russia.

PROBLEM FORMULATION

Main difficulty in creating of that mathematical insurance is it's huge volume. Even the small programs for computers are rarely written without mistakes and they usually demand a lot of time for control and remove the errors in them. In the American press different valuations about the capacity of the mathematical insurance of HTS were citationed – from some millions to ten millions lines (operator for „Fortran", C^+, C^{++} in and other program languages).

Different valuations about the number of the possible errors in one thousand lines from the program were adduced – from 300 to 1 mistake. No arguments were emphasized for proving these dates. Paying the necessary attention on the traditional American love to the ciphers, we have to mark that the work is not only in them. One mistake in one thousand lines – is it many or not? And one mistake in ten thousand lines? One million lines for the program – how difficult is that to be done?

It seems that the questions, which are brought up in the American press, are not asked correctly. But, of course, the most important thing is not how many lines there are in the program, but how much work of high-qualified specialists is necessary for it's writing. Neither is important how many mistakes there are, but what could happen if there is only one mistake in the program.

[1]Nikolay Iv. Petrov**,** Assist.Prof.Dr.Sc. ***"Prof. Dr. Asen Zlatarov" University,*** 8000, Burgas, BULGARIA, nikipetrov@lycos.com

[2]Galina St. Panayotova, Assist.Prof.Ph.D. ***"Prof. Dr. Asen Zlatarov" University,*** 8000, Burgas, BULGARIA

Nowadays there are scientific methods [2], which give the possibility to be valuated the volume of the program and the possible number of the mistakes in it. Of course, such valuations have statistic character. The comparisons of theoretical prognosis with parameters of really written programs in [2] show good condition.

PROBLEM SOLUTION

Let's try to value the volume of the program for mathematical insurance, the volume of the operation system in the central processor and the number of the mistakes in the mathematical insurance of HTS, using Holsted's methods [2]. If the total number of the independent incoming and outgoing parameters η_2 is known, then the number of the operators in the program is calculated by deciding the following equations:

$$\eta_2 = \eta_2^*.\log_2\left(\eta_2^*/2\right)\left(\eta_1 - 2\right)/\left(\eta_2^* + 2\right) + \eta_2^*, \qquad (1)$$

$$\left(\eta_2^* + 2\right).\log_2^2\left(\eta_2^* + 2\right) =, \\ \lambda\left(\eta_1 \log_2 \eta_1 + \eta_2.\log_2 \eta_2\right).\log_2\left(\eta_1 + \eta_2\right) \qquad (2)$$

where: λ - parameter, which characterize the program language (for "Fortran", C^+, C^{++} the middle value of $\lambda = 1{,}14$); η_2 - number of the operands in realization of the program (collective number outgoing, incoming and middle parameters, initiated during the process of realization of the program); η_1 - number of the operators in the program.

For better understanding the meaning of the initiated variable we will mark that on the operators in the program can be put in the appropriate verb tenses from the spoken language, and on the operands – the nouns. If we зададем $\hat{\eta}_2$ and λ, after we calculate equations (1) and (2), we can find the value of η_1 and η_2 and after that the total number of the symbols in the program (the dictionary of the program) $\eta = \eta_1 + \eta_2$ and the length of the program N:

$$N = \eta_1.\log_2 \eta_1 + \eta_2.\log_2 \eta_2 \ . \qquad (3)$$

Let's investigate what will happen, if we examine utmost decentralized case of the processor, connected to group of five sensors, and think, that the mathematical insurance of the whole HTS is integrated. From that assumption follows that the number of the incoming and outgoing parameters will increase about 50 times [1], i.e. we calculate that:

$\eta_2^* = 303.10^3$; $\eta_1 \approx 1{,}4.10^9$; $\eta_2 \approx 2{,}4.10^{10}$; $N \approx 8{,}4.10^{11}$. (4)

By that way it is received absolutely unthinkable for realization length of the program of ten milliard lines. From the shown values we can see, that for creating of mathematical insurance with sensible sizes is necessary utmost decrease of the parallelism of the operations. If we examine, what will be the volume of the work in programming and how many mistakes must be expected in programs with similar size, we will receive the time for programming $T_{ПР}$ formula [2]:

$$T_{PR} = \frac{N^2.\log_2[(\eta_1+\eta_2)/2]}{4S}, \quad (5)$$

where: N, η_1 and η_2 are defined from (3), and S is parameter of Straud, which is changeable from 4 to 20 [2].

Formula (4) gives the possibility to be received for the first of the examined cases, where $\eta_2^* = 6060$, time for programming is $T_{ПР} \approx 10^{12}$ man's lives. The number of the mistakes in programming can be defined from [2] following:

$$B_{MIS} = \frac{N.\log_2(\eta_1+\eta_2)}{3000}. \quad (6)$$

For The first of the inspected cases we get $B_{MIS} \approx 5.10^5$. For elimination of such number of mistakes will be necessary time exceed the time for writing the programs. Recently in the American press and in many European governmental it is militant discussed the problem with the mistakes in programming, and the principal possibility of creating a HTS. To that problem were devoted statements in the Subcommittee of the Senate of the USA about the tactical and strategic nuclear powers of two eminent specialists in the field of the communications and their program insurance – doctor David Koen (from the institute in informatics) and Salomon Buksbaum (from the laboratory of company "Bel"). They have announced themselves in protection of the program for construction of HTS for security [3; 4].

Let's scrutinize their arguments. Doctor Koen, disproving the dates, published in an article in newspaper "New York Times" from 1995 (where is made an valuation of the number of the mistakes in mathematical insurance – 300 in 1000 lines from the program), says that real relative number of the mistakes must be valuated with magnitude from 1 to 3 in 1000 lines from the program. In very attentive control of the program that number can be decrease to 0,1 mistakes in 1000 lines in the program.

Holsted's theory shows, that the relative number of the mistakes depends on the length of the program: in big lengths it increase approximately proportionally to the logarithm of the its length. The computations made earlier shows that in length of the program $\approx 10.10^6$ lines the relative number of the mistakes is 60 in 1000 lines from the program, i.e. is considerably higher from the number pointed from D. Koen. From Holsted's theory it turned out, that the numbers pointed from D. Koen, are valid only for relatively small programs, but nothing is said about the real lengths of the programs which insures the mathematical cover of HTS. However only one mistake in the program (without talking any more about 10^4 mistakes) can be reduced to zero effectiveness of HTS. Simultaneously Koen expresses certainty, that the huge difficulties which stands on the way of creation of the system in question can be surmounted, by the methods for creation of auspicious elements, used especially in the telecommunication's nets [5].

Analogical idea develops in his statements Solomon Baksbaum. He suggests HTS to be examined as a similarity of telephone net. And talking about the reliability of a work of the telephone centrals, which functioning is ensured from big computer programs with volume some millions lines, Baksbaum mentions, that exists methods for decreasing the number of the mistakes in the work of the telephone net. They reduce to duplicate of the elements and their own control.

Based on that he makes the conclusion, that the creating of auspicious mathematical insurance of HTS is possible, but he doesn't reject the extraordinary complexity of the task. Actually, the ideas of Karl Shanon and John von Noyman [6] about creating of reliable devices from reliable elements, by reserving the systems, are also well known. Wonderful example about that are the over fast computers, where the problem for the reliability of the triggers in integral execution is considerable.

But when Buksbaum talks about the trustworthiness of the big technical systems, he substitutes the task. The main difficulty in that case is the dependability of the material part (the hardware), not the mathematical provision and it's programming (the software), so it's the availability of algorithmic and program mistakes (failure in the meaning of reliability). For the present there are no means for fully excluding of the algorithmic mistakes, which are known. The elimination of the program mistakes is a constructive work, which demand very good, qualification of the programmers.

Here is the moment for making the analysis with a purpose-composing an analytical model of the effectiveness of functioning of HTS compound of N_{HTS} on number HTS. The whole HTS undoubtedly is an adaptive complicated system. The time t_i for advent of another failure in the whole system can be expressed by the time $t_i(H_i)$ for staying in relevant condition H_i, in agreement with formulas:

$$\begin{cases} t_1 = t(H_0), \\ t_2 = t(H_0) + t(H_1), \\ \ldots\ldots\ldots\ldots\ldots\ldots \\ t_N = t(H_0) + t(H_1) + \ldots + t(H_{N-1}). \end{cases} \quad (7)$$

For random i number of the failure ($0 < i \le N$), we get:

$$t_i = \sum_{j=0}^{i-1} t(H_j), \tag{8}$$

which permit us, in constant interval for normalize, to write an formula for effectiveness $E[T_{R\max}(N_{HTS})]$ of HTS considering N_{HTS} in number HTS in their maximal technical resource $T_{R\max}(N_{HTS})$:

$$E[T_{R\max}(N_{HTS})] = \frac{1}{N_{HTS}.T_{R\max}(N_{HTS})} \sum_{i=1}^{N} \sum_{j=0}^{i} \bar{t}(H_j) \tag{9}$$

where: $\bar{t}(H_j)$ is the mathematical hope of the time for staying of the complicated system from HTS in j condition.

For lineal process of maturing of HTS (which must be supported by respective service, considering the responsibility of the system), can be written:

$$\bar{t}(H_j) = \overline{T}(H_j) = \frac{1}{\varpi_{N_{HTS}}(\Delta t)}, \tag{10}$$

where: $\varpi_{N_{HTS}}(\Delta t)$ - middle intensity of the flow of failures in N_{HTS} for observing interval of time Δt.

Respective for the maximal technical resource $T_{R\max}(N_{HTS})$ of the system from N_{HTS} on number HTS can be written:

$$T_{R\max}(N_{HTS}) = \sum_{i=0}^{N} \frac{1}{\overline{\omega}_{PER}(\Delta t)}, \tag{11}$$

where: $\varpi_{PER}(\Delta t)$ - permissible intensity of the flow of failures in N_{HTS} for examined for interval of time Δt.

Therefore the effectiveness $E[T_{R\max}(N_{HTS})]$ of HTS will be defined from formula

$$E[T_{R\max}(N_{HTS})] = \frac{\sum_{i=1}^{N} \sum_{j=1}^{i} \frac{1}{\varpi_{HTS}(\Delta t)}}{N_{HTS} \cdot \sum_{i=0}^{N} \frac{1}{\varpi_{PER}(\Delta t)}} \to \frac{\overline{T}_{0,HTS}}{T_{R\max}(N_{HTS})} \tag{12}$$

Consequently the effectiveness of HTS will be defined asymptotic from the attitude:

$$E[T_{R\max}(N_{HTS})] = \frac{\overline{T}_{0,HTS}}{T_{R\max}(N_{HTS})}, \tag{13}$$

where: $\overline{T}_{0,HTS}$ - middle time for flawlessly work of one HTS from the whole observing extract.

Formula (13) is an analytical model of the effectiveness of functioning of HTS made from N_{HTS} on number HTS. From if follows a conclusion, that it is inefficient creating of a complicated system like HTS, functioning in unlimited interval of time.

Simultaneously on the increasing of the relative number of the mistakes in rising length of the programs must be paid attention, because it's extremely dangerous tendency, which put under doubt the principle possibility for formulation of programs with length above 10^8 lines. Until now that fact was skipped. The requirement for calculating tasks, connected with writing of program with similar length is a new approach to the programming, and may be a new method to the architecture of computers. The human brain is easily coping with such tasks, but in all probability it works on completely different principles and is self programming biological pattern.

Another approach for building of HTS is by using contemporary technologies for their construction. Data Mining (DM) is similar technology where implicit information with a huge volume database is pulling up. This is a new mighty technology with a big potential, which must help to the creating process where the attention is focused on the most important information from their database [7].

DM uses technologies like neuron nets, tree of resolutions and statistic techniques, for finding the biggest quantity of useful information – knowledgee. In HTS can be found techniques like [7]:

- Artificial Neural Networks (ANN);
- Classification and Regression Trees (C&RT or CART);
- Memory-Based Reasoning (MBR).

A new direction in the methodology of the projecting and constructing of such tape systems is the automation of that process using different types CASE (Computer Added System Engineering) means [8]. CASE means allows the time for development of the information systems to be curtailed many times, significantly to decrease the possibility for mistakes, by automation the first stage of constructing of the information system, to be insured the possibility for coordination and management of the work in a team.

By the medium of using CASE can be used the advantages of the structure approach in the detached stage in the vital cycle of the system. This is very common for the complicated information HTS [7]. That can be systems with multilayer architecture; the information systems based in the Internet, the information systems that use the contemporary technologies Data Warehouse, Data Mining, OLAP and others. Besides the

process of projecting is quiet shortened, automation the activity of the system-analysers and the designers of the information systems; the documentation of the project of the information system is made easier; the value of the project is tracking. The connection between the different stage of the vital cycle are followed unstoppable, automatically a part from the program code during the creating of the diagrams and others is generated. These instrumental devices are common for projecting of existing information systems also.

CONCLUSION

1. In this paper is compound analytical model of the effectiveness of functionality of High Technical Systems. New approaches for their construction are suggested.

2. Because of the particular complexity of the programs for mathematical insurance, of the electronic chains, of their mutual connections inside the single component and between them, of High Technical Systems with big degree of probability is typical inner instability.

3. The creation of complicated systems like High Technology Systems, functioning in unlimited interval of time is ineffective.

REFERENSES:

[1]. Space-Based Missile Defense. A Report by the Union of Concerned Scientists. Cambridge, Mass., March 1984.

[2].Halstead M. Elements of Software Science. N.Y.-Oxford-Amsterdam, 1977.

[3]. Cohen. D. Statement on the Software for the Battle Management of the Strategic Defense System. United States Senate Committee on Armed Services. Subcommittee on Strategic and Theater Nuclear Forces, 3-rd Dec. 1995.

[4]. Buchsbaum. S. Statement of Solomon. United States Senate Committee on Armed Services. Subcommittee on Strategic and Theater Nuclear Forces, 3-rd Dec. 1995.

[5]. Gindev E. Introduction in theory and practice by relaebility. Part 2, Publ. "Prof. Marin Drinov", Sofia, 2002.

[6]. Gindev E. Relaebility by complex sistems. Institute for special optics and elektroniks, Sofia, 1976.

[7]. Nedeva, V. Iv., Technology Data Mining in contemporary information systems, Mikolav, Ukraina, 2002, p.p. 71-78.

[8]. Nedeva, V.Iv., Contemporary instrumental devices for the construction of informational systems, Scientific - diligent conferences whit international participation "Information technology. Science, technique and technologies", Yambol, 2003, p.p. 39-45

MapInfo Based Infrastructure -presentation and updating-

A.Popovska[1], A.Hristova[2], B.Lozanovski[3], A.Kulakov[4], D.Davcev[5]

Abstract – **MapInfo represents software designed to support the management, manipulation, analysis, modeling and display of spatially-referenced data for solving complex planning and management problems. In this paper we present it as a powerful tool for updating and producing thematic maps (layers) with high graphical and geometrical quality. By implementing the updating layers over the old maps, we have produced new updated maps.**

Keywords – **MapInfo, thematic layer, updating.**

I INTRODUCTION

The development of the computer technology and the high quality digital data disposal leads to new forms and ways of graphical data processing thus allowing a new effective kind of public/private institutions/enterprises management.

The Geographical Information System or GIS is an integral computer system capable of capturing, controlling, storing, analysing and displaying geographically referenced information [1].

The MapInfo is the GIS software used to create maps, design and develop digital spatial databases as well as to perform complex spatial analyses and reports [2]. It also provides combining many layers of different thematic information into one level in order to find their correlations. It is possible to link, or integrate, information that are difficult to associate through any other means. Thus, a GIS can use combinations of mapped variables to build and analyze new variables. Simply, the MapInfo is able to produce images – not just maps but drawings, animations and other cartographic products which allow researchers to view their subjects in a way that they never could before. The power of MapInfo comes from its ability to relate different information in a spatial context and to reach a conclusion about their relationship.

As a fundament for the spatial and thematic processing, the digital topographic maps are used most often. However, besides archived data (whether in analogue or digital form), the real world data can also come from other sources like satellite images and field measurements (Global Positioning System – GPS) for example. Nevertheless, the maps are generally easy to use with MapInfo and they are often the most effective in identifying the objects, their absolute location on the Earth's surface and their spatial relationships.

To more realistically analyze the effect of the Earth's terrain, three-dimensional models are available to display the Earth in realistic, three-dimensional perspective views and animations that convey information more effectively to wider audiences than traditional, two-dimensional, static maps.[3]

In few words, this technology can be used for scientific investigations, resource and situation management, and development planning. As a precondition, there is a need of accurate, precise and quickly produced data as well as of high quality maps to be use for various applications such as spatial planning, urbanism, waterworks, electrification, environment studies and many other fields.

To convey the results of analyses to the people who make decisions about resources, there are possibilities to produce graphics on the screen or on paper. Thus, wall maps, Internet-ready maps, interactive maps, and other graphics can be generated, allowing the decision makers to visualize and thereby understand the results of analyses or simulations of potential events.

Many countries have already established appropriate systematic registration of their socio-economical infrastructure inconstancy. Organizations around the world are using MapInfo products and solutions to view and analyse location based data overlaid on digital maps. The result is a better business intelligence, improved customer relations and much better bottom line performance. From this point of view our public and private sectors are just queuing up.

In section II in this paper we represent the concept of the project, section III includes description of the documentation used and the process of digitising, furthermore section IV illustrates the up-dating of the thematic layers as well as the database, while section V concludes the project.

[1] Andrijana Popovska is with the Faculty of Electrical Engineering, "St.Cyril and Methodius" University - Skopje, E-mail : andrijana_222@yahoo.com

[2] Ana Hristova is with the Faculty of Electrical Engineering , "St.Cyril and Methodius" University - Skopje, E-mail : ana_aleks@yahoo.com

[3] Borce Lozanovski is with the Public Corporation for Spatial and Urban Planning E-mail : blozan@mt.net.mk

[4] Andrea Kulakov is with the Faculty of Electrical Engineering, "St.Cyril and Methodius" University - Skopje, E-mail : kulak@etf.ukim.edu.mk

[5] Danco Davcev is with the Faculty of Electrical Engineering, "St.Cyril and Methodius" University - Skopje, E-mail : etfdav@etf.ukim.edu.mk

II The Project

The Project represented in this paper is initiated by and realized in cooperation with the Public Corporation for Spatial and Urban Planning.

The project's concept consists of producing several basic thematic layers for a city area (specific regions of the city area - industrial zones, settlements, lakes, parks ; lines - rail and road networks, rivers ; characteristic points - churches, mosques, trigonometric points) as well as of connecting the objects of these thematic layers with the database to be made.

So, the Project represents a summary of graphical and alpha numerical database connected in a functional wholeness. The database of the geographical information system includes data organized as themes, database tables and links to relevant existing documentation.

The expected results should provide a variety of possibilities starting from thorough analyses needed for spatial urban planning, through monitoring and predicting the pollution, socio-economical and demographic analyses, up to the construction and maintenance of the infrastructure.

In this paper we've chosen to present a part of the work done for the town of Bitola which includes updating of the existing documentation.

III The Fundament and Digitizing

As a fundament for the layers in this case, as an existing documentation, we use a military topographical map produced in 1983, scaled as 1:25000 with the Gauss-Kruger projection as shown on Fig.1.

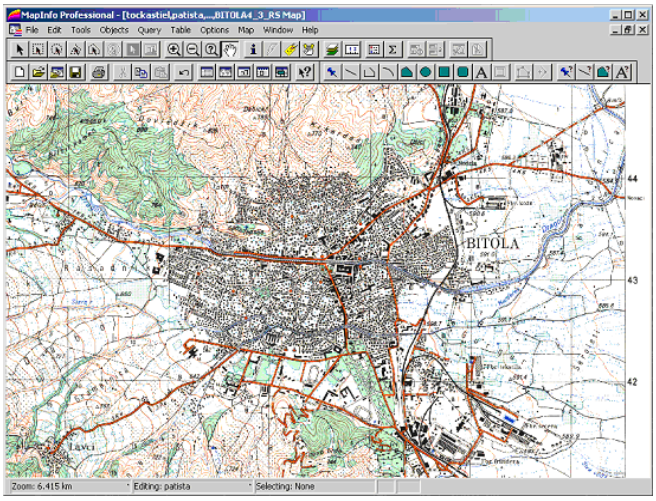

Fig.1. 1:25000 map of Bitola

There is a need to mention that the projection is a very basic element of map-making. It is a mathematical way of transferring information from the Earth's three-dimensional curved surface into a two-dimensional medium – a peace of paper or computer screen. There are many different types of projections according to the employed system of coordinates which are appropriate for a particular case. For example, a projection that accurately represents the shape of a continent will greatly distort its relative size [3].

The objects on the map and their spatial relationships in the city of Bitola are organized on several thematic layers:

1. Constructions: Settlements, Plants, Cemeteries, Archaeological zones, etc;
2. Traffic and transport : Railroads, Roads Bridges;
3. Hydro-geography : Rivers, Lakes, Dams, Channels.

For this presentation we've chosen two layers : Road layer (because we know there is a new, recently built up road) shown on Fig. 2, and Settlement layer presented on Fig.3. As we can see on Fig.2. the existing roads are digitised and separated from map. In the same time, a table with all the characteristic attributes, as a part of the database, is associated to this thematic level.

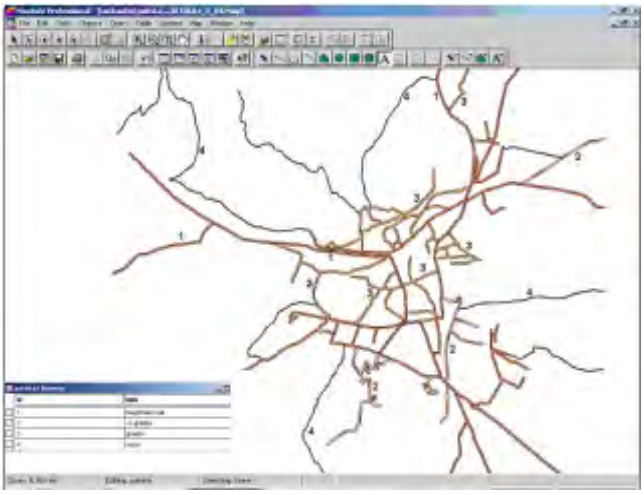

Fig.2. Road Layer

The same is done for the Settlement layer on Fig.3. The purpose of this one is to show the city's dynamic environment, to notice the rapid growth of the city as a result of increasing population and to stress the need for spatial urban planning. By this, the balance between the environment and the possibilities for surveys and services that maintain the city will be controlled thus allowing high-quality decisions for managing the space in the city area.

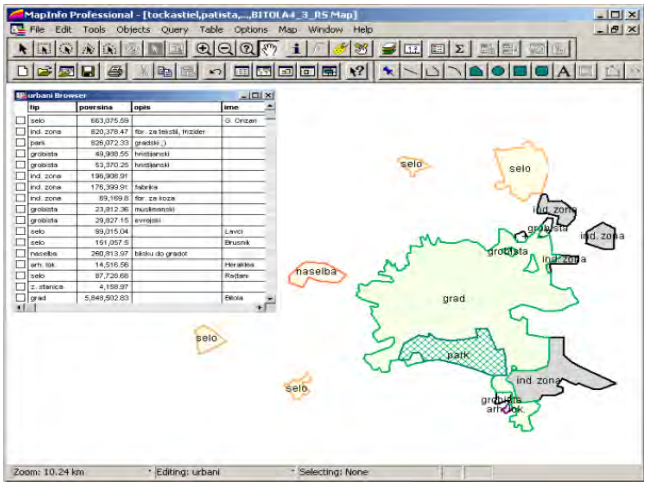

Fig.3. Settlements Layer

To digitise the map we can use various techniques that can capture information : hand-tracing with a computer mouse on the screen or on a digitising tablet to collect the coordinates of features (like in our case), electronic scanners can also convert maps to digits, coordinates from GPS receivers can be directly up-loaded into a GIS and so on.

Anyway, software tools that automatically extract features from satellite images or aerial photographs are gradually replacing what has traditionally been a time-consuming capture process. In each case, the spatial objects from the real world are identified and approximated by points, lines or areas combined with their alpha numeric attributes.

So, after organizing the thematic levels, tables of attributes have been created and the captured objects are identified in a series of attribute tables - the "information" part. This significantly minimizes the number of attributes assigned to every spatial object and provide better and faster accessibility. Spatial relationships, such as whether features intersect or whether they are adjacent, are the key to all GIS-MapInfo based analysis.

This represents the first step of making a consistent database. After these relations are explicitly established, data browsing, updating, analysing and displaying can be done.

Before digitizing the map it is necessary to register some geographical control points. This provides that geographical objects on any thematic level will be registered on the same, mutual system of coordinates which later will provide correct overlaying of all thematic layers.

To ensure consistency and compatibility of the spatial information used in this project, a unique nomenclature is defined. Sometimes extra information(meta) are needed for the database. In order to reach additional data, there is a possibility of connecting to an already existing, standardized, external databases. (In this project access data base is used). This is possible if the nomenclature is standardized.

Standardization also helps to stretch data collection funds further by allowing data sharing, and, in many cases, gives users access to data that they could not otherwise collect for economic or technical reasons. Unifying in accordance with the European standards enables incorporation of the database on European level allowing its connection on International level with other thematic databases. Nowadays spatial data can be accessed and analysed over the Internet through Internet map server technology.

IV UP-DATING

Updating the thematic levels is done by marking (registering) the spatial units on the Earth's surface, which do not exist on the topographic map.

This is accomplished by overlaying the layers over a more recent satellite image (in this case the satellite image dates from 95/96 and is taken by the French satellite SPOT). The satellite image is shown on Fig.4.

As it can be seen on the satellite image (concerning the two mentioned layers) the difference between the map and the current situation (the satellite image) is quite obvious.

To update the map we got to update the layer of concern. So, overlaying the layers one by one, the digitisation of the new detected elements is done for every thematic layer separately, followed by updating the database. This provides registration of the infrastructure changes during the given time period.

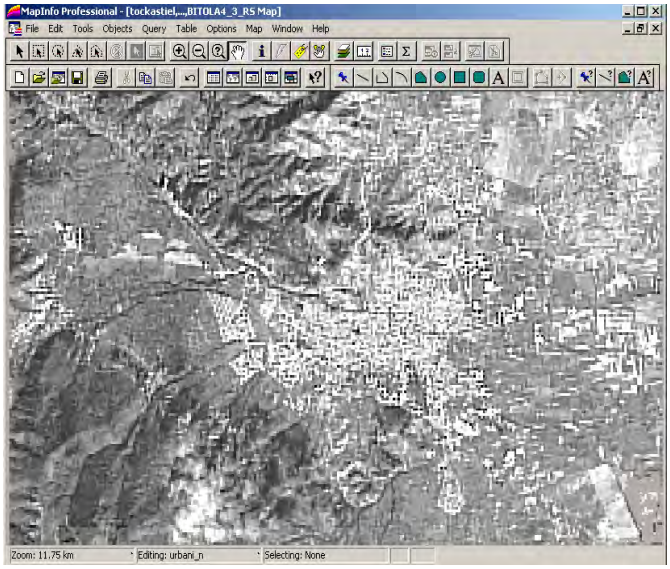

Fig.4. Satellite image of Bitola

On Fig.5. we can see the road layer overlaid on the satellite image and that the new magistral road is detected and drawn on the layer.

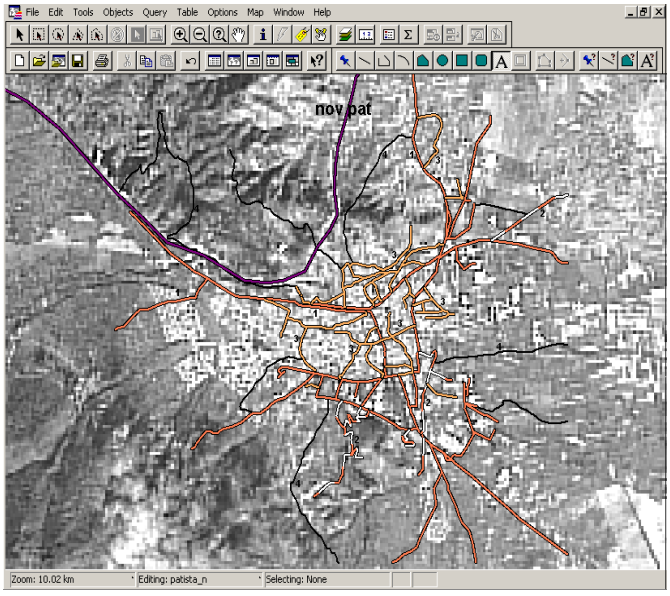

Fig.5. Overlaying the road layer

The consistence of the spatial relationship is obtained or provided by the MapInfo from the previously registered control geographical points. That is the reason why the layer will match any image taken from any distance and why the new inserted drawings will match the scale.

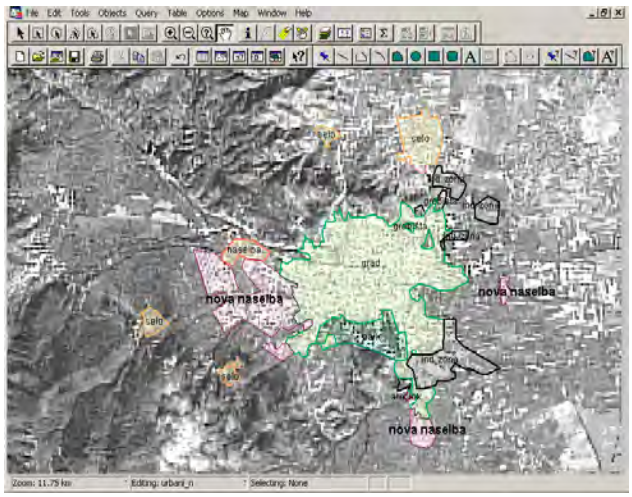

Fig.6. Overlaying the settlement layer

On Fig.6. the settlement layer is overlaid and the new areas of constructions are registered. As it can be notified, this satellite image offers a good registration of an area but it can not be said for the spot elements (houses in that area).
Mainly it is a consequence of the bad resolution of the image that we have on our disposal. Contemporary satellite images can offer quite better resolution which is much bellow one square meter. Unfortunately, the cost of such images are much more above the price of this one.

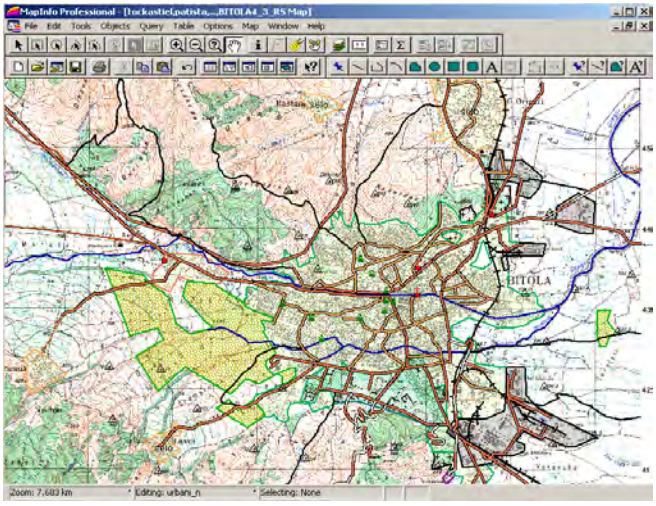

Fig.7. Final Map

So, the most appropriate solution is to obtain aero-photos taken above the areas of concern. Certainly it is possible to use the data from the urban planning office but usually they are not quite accurate.

The final map clearly shows the value of the MapInfo and updated database.

We can see that the new road and the settlements consisting of not registered constructions are placed on the final map in proper, corresponding spatial relationship with the other objects on the map which have already existed in the old map.

V CONCLUSION

In this paper, satellite image data are used to update an old topographic map. By processing the image according to the described technique thematic maps are produced with high graphical and geometrical quality. They represent graphical base which entirely enables quality analysis of the target area.
Finally, by implementing the updated layers over the old map we can print and produce a new updated map which is presented on Fig.7.

It is also noticed that updating of specific layers requires adequate quality of the input data according to the customer requirements.

The results can be used for production of standardized thematic maps in various scales, contents and levels of generalization provided for integration with other data on national and international level.

Although this system is usually associated with larger state or local administration, it makes the spatial information more available and makes the decision process more transparent, dynamic and easy to control.

REFERENCES

[1] Jeffrey Star and John Estes: ”Geographic Information Systems: An Introduction”, Prentie Hall, 1990
http://www.gis.com

[2] MapInfo-MapX Developers Guide, Version 5.0, MapInfo Cooperation Troy New York, June 2002
http://www.mapinfo.com

[3] http://erg.usgs.gov

[4] http://www.GISdevelopment.net

Turbo codes: matched MAP decoders

Zafir Popovski[1] , Tatjana Ulcar Stavrova[2]

Abstract – **In analysing wireless channels we most often assume that we exactly know the variance of the channel. However, in real applications this is usually not tha case. The variance needs to be derived from the received data and hence is only an approximation. In this paper we tackle the question on how will a non-accurate variance affect the performance of an iterative turbo decoder, test a variance estimation method and present the performances.**

Keywords – **Matched decoders, variance estimation.**

I INTRODUCTION

The turbo codes are a new class of FEC (forward error control) coding shemas that have been first intraduced by Berrou et al.[1] in 1993 and have received a lot of attention because they exhibit extremely good performance. For a bit error rate (BER) of 10^{-5}, the first TC was only 0.7 dB away from the theoretical Shannon's limit.

The turbo codes represent a parallel concatenation of two or more recursive systematic convolutional codes (RSCC), produced by a turbo encoder composed of two or more constituent RSC encoders (CEs) with input to each but one constituent encoder permuted by an interleaver of length N as shown on Fig.1.

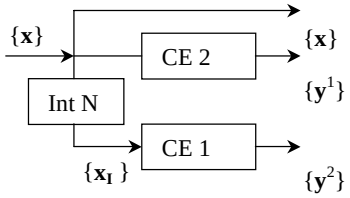

Fig.1. Turbo encoder structure

Such a composition allows for replacement of the optimal but rather complex maximum likelihood decoding algorithm by two (or more) relatively simple constituent decoders to decode corresponding constituent codes one by one.

A simple SISO (Soft-In Soft-Out) maximum a posteriori (MAP) decoder which minimise the probability of bit error appears to be a good solution for component decoders (CDs).

As an output, the MAP algorithm provide a real number which is a measure of probability of error in decoding a particular bit. Since both CDs decode the same information bit x_i, coded twice but in different order, it becomes possible this extra information, so-called extrinsic information, λ_i, to be passed as an input to the second CD allowing it to improve its own output extrinsic which will be passed to the first CD in the next iteration. The process is than iterated until reaching a satisfactory degree of confidence regarding the received noisy examples contained in length N sequence. The iterative TD shematicaly is presented on Fig.2.

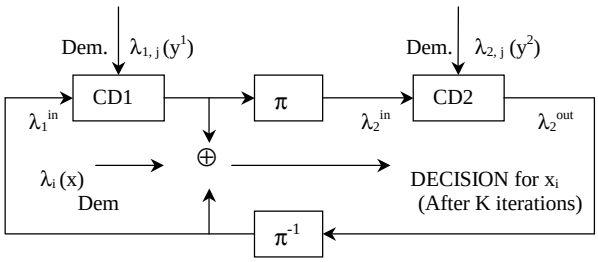

Fig.2 : Iterative TD with two MAP CDs

As the most promising one, the TC sheme is very likely to be implemented in various applications - one of which beeing the second generation of broadband satellite systems utilised on Ka band such as WEST from Matra Marconi Space, EuroSkyWay by Alenia Aerospazio, ASTROLINK by Locheed Martin, CYBERSTAR from Space Systems/Loral and SPACEWAY from Hughes Communications.

The system requirement constraints in such an application require to address the TC performances from several aspects.

First, the TC proposed by Berrou uses very large interleaving blocks (65536 bits) which would be very problematic for satellite applications since this would entail large delays and buffer sizes. The results from different researchers show that with an appropriate interleaving algorithm, good porformances can be achieved even with an interleaving length equal to the ATM-like cell. As an average of the known results, on Fig.3. we present the Eb/No required to achieve a BER of 10^{-3} for different values of the code memory and interleaving length.

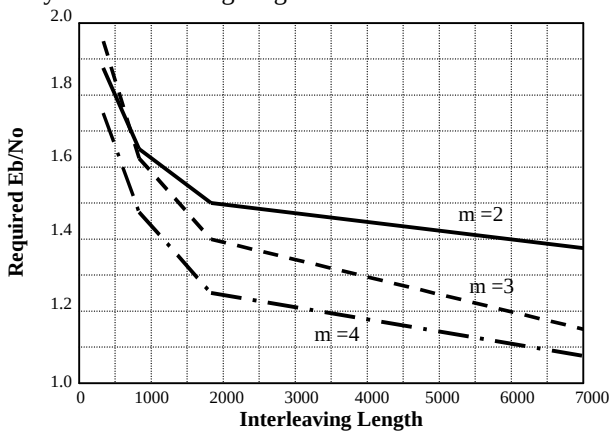

Fig.3. Eb/No to achieve a BER of 10^{-3}

[1] Zafir Popovski is with the Faculty of Electrical Engineering , "St.Cyril and Methodius" University - Skopje, E-mail : zpopovski@yahoo.com

[2] Tatjana Ulcar - Stavrova is with the Faculty of Electrical Engineering , "St.Cyril and Methodius" University - Skopje, E-mail : tanjaus@etf.ukim.edu.mk

As can be seen on Fig.3 on previous page, the performance degradation due to a reduction in the interleaving length from about 7000 to 1700 bits is lower than 0.2 dB. When the length is further reduced to about 440 bits (one ATM-like cell) the additional loss is limited to about 0.5 db which means that the TC can be successfully applied even when the interleaving length must be kept at very law value.

The second issue that needs to be addressed for the implementation of the TC is the decoding complexity which depends on both the SISO (Soft Input – Soft Output) algorithm used for the decoding of the constituent codes and the number of required iterations.

The modified *Maximum A Posteriori* (MAP) algorithm offers the best performance but is rather complex. A simplified version which does not show any performance degradation has been already proposed. Further simplification is achieved by performing the computations in the log domain and is reffered to as LogSMAP.

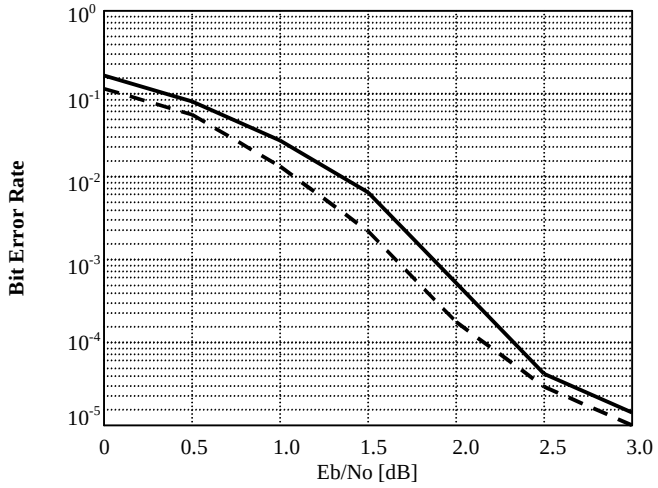

Fig.4. Log & Sub SMAP algorithm comparison

From the LogSMAP base, the SubSMAP algorithm has been developed which uses an approximation for the calculation of the logarithm of a sum of exponential terms.

Fig.4. presents the performance of the TC for different SISO decoding algorithms – LogSMAP and SubSMAP in this case, for the memory length of constituent codes equal to 2, interleaving lengths equal to 440 bits and number of iterations equal to 8. The dashed line corresponds to the performance of the LogSMAP while the plane line is associated with the SubSMAP algorithm. We can see that the performance degradation of the SubSMAP is limited to about 0.15 dB.

Better power efficiency could be achieved with constituent codes having a larger memory size. However, it was shown that increasing the memory size beyond 4 did not provide any performance gain. From the other side, increasing the memori size from 2 to 4 is very limited in view of the increased decoding complexity.

As far as the number of iterations is of concerne, this figure is set to 10 as standard. However, by implementing one of dynamic stopping rules the average number of iteration can be reduced to about from 6 to 8 iterations. Certainly, such a stopping rule should increase the decoding speed while not sacrifacing the BER performance. The soft stopping rule that is based on the evolution of the probability density function of the extrinsic information [5] shows a significant increase in the average decoding speed at almost no cost concerning the performance. The negligible computational requirements give this rule an advantage.

The speed and BER performances of this rule are shown on Figs.5 and 6, respectively.

From Fig.5 we can tell the speeds for different tresholds for the same rule to achieve the same BER.

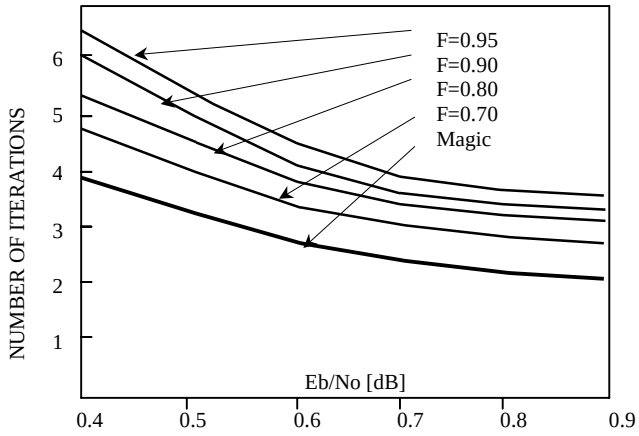

Fig.5. Average number of iterations

From the other side, Fig.6.indicates that the overall error rates are very close to each other and together to these for 10 fixed iterations. In fact they are nearly equal to the error rates achieved by a decoder using 20 iterations. In this case, 20 iterations are set as an endless loop protective treshold.

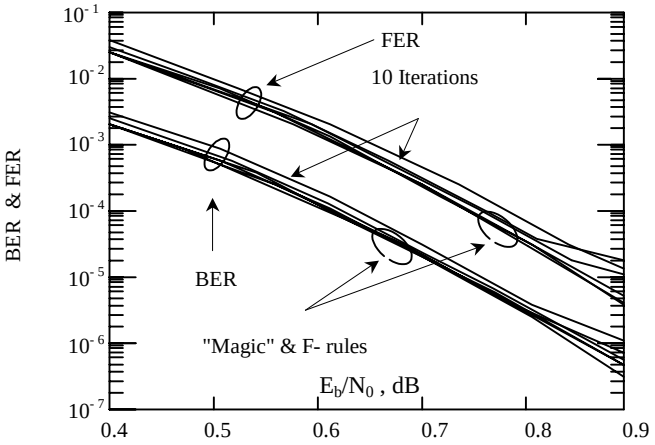

Fig.6. BER & FER with stopping rules

Finaly, the derivation of the exact a posteriori probabilities by the implemented decoding algorithm requires detailed knowledge of the channel. The problems arise when the channel varies with time requiring a continuous update of its parameters which may not be avaluable at all (some mobile applications). In practical systems, suboptimal metrics that take into account the range of channel variations are often used with the added benefit that they are often much simpler to implement than optimal metrics.

In this case, the resulting decoder is said to be mismatched with respect to the channel which results in performance reduction from that mismatch. It should be noted that asymptotically optimal decoders that operate without any knowledge of the channel statistics do exist. However, these asymptotically optimal decoders are often too complex to be used in practice.

Since the Ka band satellite channels (uplink, downlink and interlink) are proved to be slow-varying AWGN channels and that the estimates of the variance for such channels could be estimated 'on-line' thus resulting in a channel-matching decoder, we tried to implement a variance estimator which will be suitable in regard with the above mentioned system constraints.

In this paper we first evaluate the robustness of both the single constituent and turbo logRMAP decoders, then present some variance estimation methods and finaly implement one which we found suitable for logRMAP turbo decoder and present the result for 10 iterations performed by 4 memory length, 440 bits (ATM cell like) of interleaving length, rate 0.324 turbo code expresed by $(1,33/23,33/23)_8$

II Variance sensitivity

First we test the effect of variance mismatch on the performance of the constituent RSC (Recursive Systematic Convolutional) code $(1,33/23)_8$ since it is an integral part of the TC. There is a need to stres that we looked at the performance just for different values of Eb/No offset. We use the Eb/No because we can directly relate the results back to simulated BER results and actual variance since the Eb/No is inversely proportional to the variance of the channel. Note that the Eb/No of the channel can be converted to σ^2 (for an overall code rate of R) for a BPSK AWGN channel by using the following relationship :

$$\sigma^2 = (2REb/No)^{-1} \qquad (1)$$

Since the En/No is inversely proportional to the variance σ^2, if the offset is negative then the variance used by the decoder is greater than that of the actual noise variance, i.e. $\sigma^2_{MAP} > \sigma^2_{noise}$, and, if the offset is positive then the variance of the decoder is less than that of actual noise : $\sigma^2_{MAP} < \sigma^2_{noise}$.

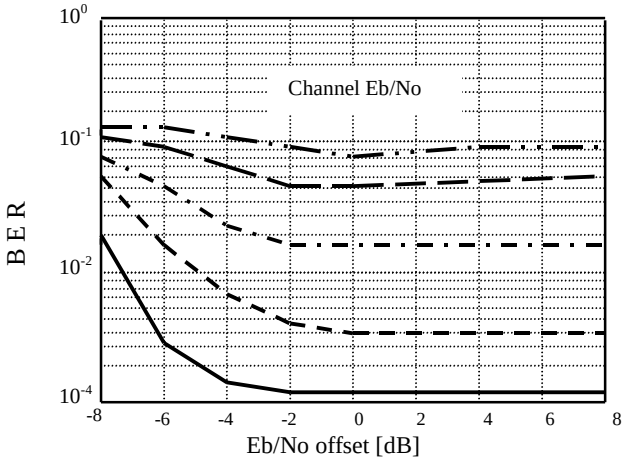

Fig.7. CC BER performance versus decoder offset

As we can see from the Fig.8 the RSC constituent performs quite well if the estimated variance is less than the actual noise variance or, in other words, when the decoder underestimate the actual condition of the channel. On the other hand the performance does not degrade until the Eb/No offset is at least 2 db under the actual Eb/No.

The robustness of the overall paralel composition is similar and is presented on fig.9.

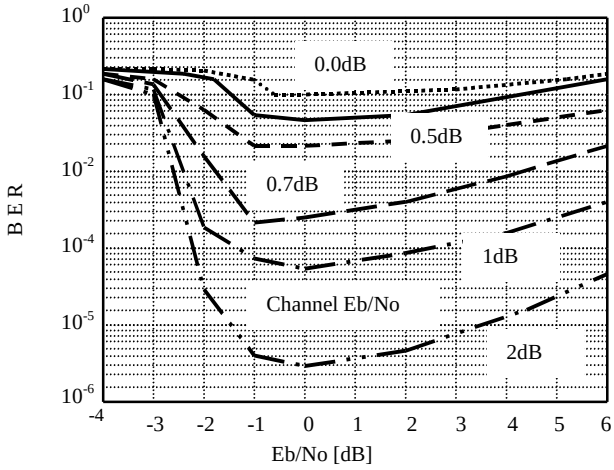

Fig.8. TC BER versus decoder Eb/No offset

We see that an overestimate of the noise power is much more problematic than an underestimate. We further see that the turbo decoder is quite robust, i.e. performance remains invariant, over an surprisingly wide range of mismatch values.

III Variance estimation methods

Nonetheless, the issue of robustness is moot if the estimation of the channel parameters is included within the decoding process. We present here two different variance estimation methods which, although different, both are suitable for online estimation of the channel variance.

The Summer Variance Estimator estimates the variance directly from the magnitude of the received simbol r_n by finding the ratio between $E(r_n^2)$ and $E(|r_n|)^2$ which is a function of E_s/No. We have

$$E(r_n^2) = E_s + \sigma^2 \qquad (2)$$

and

$$E(|r_n|)^2 = \sigma\sqrt{\frac{2}{\pi}}e^{-(E_s/2\sigma^2)} + \sqrt{E_s}\left[erf\left(\sqrt{\frac{E_s}{2\sigma^2}}\right)\right] \qquad (3)$$

so, the ratio becomes :

$$\frac{E(r_n^2)}{[E(|r_n|)]^2} = \frac{1+\frac{E_s}{\sigma^2}}{\left(\sqrt{\frac{2}{\pi}}e^{-(E_s/2\sigma^2)} + \sqrt{\frac{E_s}{\sigma^2}}\left[erf\left(\sqrt{\frac{E_s}{2\sigma^2}}\right)\right]\right)^2}$$

$$= f(E_s/\sigma^2) \qquad (4)$$

As we can see it is not easy to find the variance from the ratio by using Eq.(4). A practical approach is to find the ratio and its related channel variance σ^2 for the operational range of the decoder and express it as a look-up table. By using this look-up table we can find the variance of the channel by obtaining the ratio from the received data.

Another way as suggested in [4] is to find an n^{th} order polynomial that can approximate the above mentioned ratio for a fixed channel variance range that is related to the decoder's Eb/No operating range. For this purpose we can use the MatLab *polifit* function to find the polynomial that fits the function *f*(x) in the least squares sense. The coefficients of the polynomial generated by MatLab are then used in the estimator to estimate the channel variance for the given $E(r_n^2)/E(|r_n|)^2$ ratio.

In our simulations, assuming an AWGN channel and BPSK signaling, we used the next estimate of the channel variance as developed in [2] :

$$\sigma^2 = [\frac{1}{k}\sum_{t=1}^{k} y_t^j]^2 + [\frac{1}{k}\sum_{t=1}^{k}(y_t^j - \frac{1}{k}\sum_{t=1}^{k} y_t^j)^2] - 1 \qquad (5)$$

where y_1^j, y_2^j,…, y_k^j, is a steam of soft values of the received sequence.

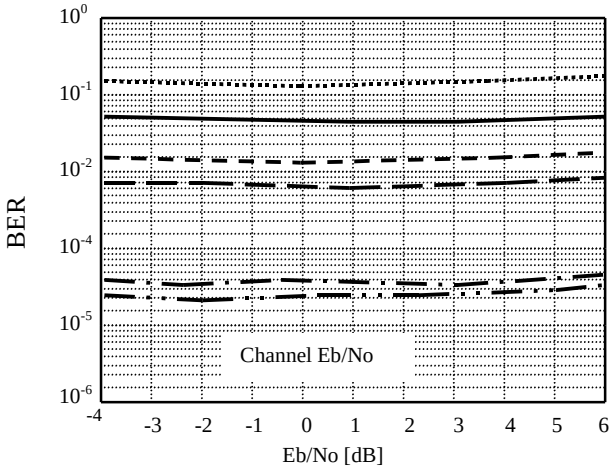

Fig.9. Performance of channel matching TC

By incorporating this estimate into the decoding process, as can be seen on Fig.9, any impact of initial error in estimating the channel variance is rapidly eliminated and the initial mismatch is no longer a factor in performance degradation.

IV Conclusion

We presented all the aspects which must be considered when the turbo codes are to be implemented into the newcoming generation of a global, Ka band satellite communications and showed that these codes are still powerfull even with small, ATM cell like interleaving length.

In this paper we emphasized the robustness of the turbo codes to the channel variations and also showed the results of a practical implemntation of a channel variance estimation model which is easy to implement and gaves very good results flatening the performance degradation due to the channel mismatching.

References

[1] C.Berrou, A.Glavieux and P.Thitimajshima,"Near Shannon Limit Error Correcting Coding: Turbo Codes", *Proceedings 1993 IEEE Int.Conf. on Comm.*,pp.1064 - 1070,Geneva, May 1993.

[2] S.Kim and S.B.Wicker, " On Mismatched and Self-Matching Turbo Decoding " - *Submitted to IEEE Transactions on Information Theory*, 1998.

[3] S.Kim, "Probabilistic Reasoning, Parameter Estimation and Issues in Turbo Decoding "-*PhD dessertation*, Cornell University, 1998.

[4] T.A.Summers and S.G.Wilson,"SNR mismatch and online estimation in turbo decoding ", *IEEE Transactions on Communications*, vol.46, pp 421-423, April 1998.

[5] Z.Popovski, T.U.Stavrova,"A New Stopping Rule for Turbo Decoders", *In Proc. XXXV International Conference on communications*, Dubrovnik 2003.

[6] M.Reed and J.Asenstorfer, " A novel variance estimator for turbo-code decoding", *in Proc. ICT'97, Melbourne, Australia, pp.173-178, April 1997.*

Generating Dynamic Questions in Distributed eTesting Cluster - DeTC

Olga D. Rahneva[1]

***Abstract* – This paper describes how dynamic questions with engineering and mathematical contents are being created, generated and applied into practice at a Distributed eTesting Cluster – DeTC. As a result, the learners receive unique testing questions, while the database with tests does not grow significantly in size, and the size of the information transferred is minimized.**

***Keywords* – Electronic Testing, eTesting, DeTC, Dinamic Question, Free Answer**

I. Introduction

Testing examination is one of the most popular and well-developed assessment instruments in higher education [1]. The classic test is a sequence of precisely defined questions, with each question suggesting a simple answer, which can be easily checked and assessed as correct, incorrect or partially correct (for example, incomplete).

Questions are often split in types, according to the expected answer:

- classic type of question – with a "yes/no" answer;
- multiple-choice question – one answer (MC/SA, Multiple-Choise/Single-Answer);
- multiple-choice question – more than one correct answer (MC/MA, Multiple-Choise/Multiple-Answer);
- free-type questions- with the answer being a number or a text;
- others.

Most of the existing Web-based systems for testing and assessment provide technologies and tools for creation, submission and assessment of questions of the first three types [2-6]. A certain number of systems process all types of questions [7,8].

However, most of the latter support materials with insufficient mathematical contents. The tests authors have to create the formulae and equations with a separate tool and convert them into a GIF/JPEG format and include them in the testing system as a graphic, when more complex mathematical or engineering content is required.

[1]Olga D. Rahneva is with the department of Informatics and Statistics at the University of Food Industries, 26 Maritza blv., Plovdiv, Bulgaria, E-mail: rahneva@yahoo.com.

This approach significantly increases the size of the database, which stores the testing questions, as well as the size of the information transferred to the learners, because of the large number of images.

On the other hand, it does not provide a solution to the problem for dynamic creation of questions, which forces the development of a large set of test versions, in order to prevent the test from being learned by heart.

It is described below how dynamic free-type questions with engineering or mathematical contents are created, generated and applied in practice at a Distributed eTesting Cluster – DeTC. Learners are given unique testing questions by generating random values for the variables in the question. This does not increase the number of the preliminary created questions, decreases the size of the database with tests, and minimizes the size of the transferred information.

DeTC [9-11] is being developed as a joint project of the University in Limerik – Ireland, the Laboratory for Electronic Trade, and the department of Computer Technologies at the University of Plovdiv, Bulgaria, and the department of Informatics and Statistics at the University of Food Industries, Plovdiv, Bulgaria.

II. Example Questions

Fig. 1 shows a sample multiple-choice (MC/SA) question in Electrical engineering.

The resistance R of a conductor, which dissipates an amount of heat Q, for time t, with amperage I, is determined with the following formula:

$$R = \frac{Q}{I^2 \cdot t}$$

Determine the resistance R in ohms (Ω) of the conductor, which dissipates heat of 10 000 J for a time of 2 seconds, at amperage of 10A.

a) 10 b) 20 c)50 d)100

Fig.1 Sample question MC/SA

In order to provide the learners with different questions, the authors must create many versions of such as question with different values for Q, t and I. Of course, they have to perform a lot of calculations to mark the correct answers.

This disadvantage can be overcome if the question is redefined as dynamic, a free answer is requested from the

learners, and the answer is automatically analyzed for being correct or not by the system.

Fig.2 demonstrated how the sample question from fig. 1 can be transformed into a dynamic free-type question.

The resistance *R* of a conductor, which dissipates an amount of heat *Q*, for time *t*, with amperage *I*, is determined with the following formula:

$$R = \frac{Q}{I^2 \cdot t}$$

Determine the resistance R in ohms (Ω) of the conductor, which dissipates heat of 10000J for a time of 2 seconds, at amperage of 10A.

R = I

Fig. 2. Sample dynamic question

III. System details

At DeTC, each dynamic question is described in a number of sections.

The first section describes the dynamic variables in use. In the example from fig. 2, those are Q, I and t. Each variable receives a name, a type (integer or real) and one or more ranges of possible values, which are dynamically set by a random generator. In the same example, the variable t is of type integer and its value is set in the range (0,12). The value is an integer or real number with specified precision and depends on the type of the numeric variable.

The second section defines the dynamic answers. Each answer is given a name, a type (integer or real), a formula for calculation and a method for comparison with the correct answer. The formula can contain only the dynamic variables, defined in the first section, numeric constants and arithmetic functions.

Fig. 3 shows the formula for calculating the correct answer of the dynamic question from fig. 2.

$$R = \frac{Q}{I^2 \cdot t}$$

Fig. 3. Sample formula for the dynamic question

Two methods for comparison of the learner's answer with the correct answer are provided – by calculating an absolute or a relevant error.

The third section describes the body of the question – as a text with mathematical formulae. The body is a template, in which dynamic variables are defined by putting a "@" before their names.

Fig. 4 shows how the body of the dynamic question from fig. 2 is described:

The resistance *R* of a conductor, which dissipates an amount of heat *Q*, for time *t*, with amperage *I*, is determined with the following formula:

$$R = \frac{Q}{I^2 \cdot t}$$

Determine the resistance R in ohms (Ω) of the conductor, which dissipates heat of @Q J for a time of @t seconds, at amperage of @I A.

Fig. 4. The body of a Sample dynamic question

The fourth section describes the dynamic answer form for of the questions to the learner. For each answer, the name of the dynamic variable is defined, as well as the sign = (equals) and a form for the free answer with a certain number of characters allowed. It can be specified whether preliminary formal control will be exercised over the input.

The fifth section is not mandatory. It allows extended formatting of the questions screen with sound, pictures, animations, etc.

IV. Authoring tool

A syntactically oriented editor is created to facilitate the authors of tests – Dynamic Test Development Tool (DTDT), as an extension of the existing in DeTC editor Test Development Tool (TDT) [10]. DTDT features an easy and convenient dialog-based user interface for writing engineering and mathematical formulae; for defining the dynamic variables used; for defining the dynamic answers; for defining the body of the dynamic questions and for additional design of the questions screen.

DTDT saves each testing question in a file in XML (eXtensible Markup Language) format. The file contains the logical data as contained in the question – keywords, general information, the question type, question itself, variables, ranges, type of answers supported, possible answers, information about the correct answer, and extra information.

XML is chosen as a technology for storing the testing questions, because it allows the transformation of the basic data into virtually any other format by using XSL (XML Style-sheet Language) – HTML, MathML, XHTML, WML, PDF, Microsoft Word document, etc.

Fig. 5 shows a principal diagram for development and generating of tests with dynamic questions.

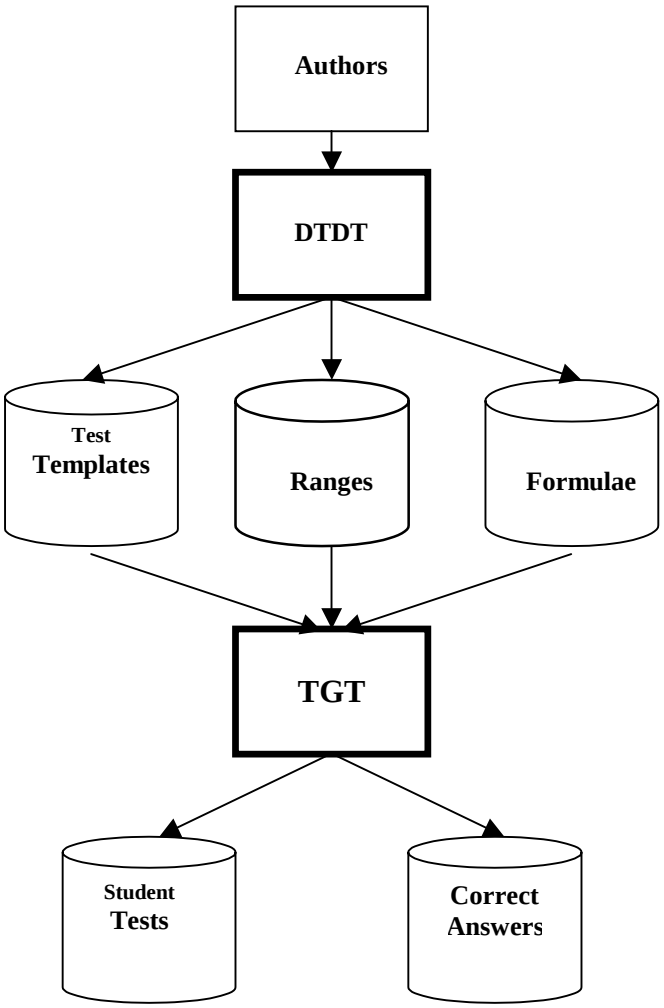

Fig. 5. Development and Generating of Dynamic Tests

DTDT is a multi-language editor – all its menus and buttons are parameterized and the dialog with the author of the test can be conducted in any one of the specified (and defined in the database, of course) languages – Bulgarian, English, French, even Macedonian.

V. Assessment tool

Tests are assessed with the Dynamic Test Assessment Tool (DTAT), which analyzes the free-form answers, given by the learners and determines whether they are correct or incorrect. DTAT parses the answer, evaluates it and compares it to the author specified answer.

Depending on the chosen approach, DTAT will seek zero or close to zero difference between the learner's answer and the author's answer, to mark a question as correctly answered. The error tolerance level can be specified with the definition of the question (for example, tolerance level is 10^{-5}).

The lecturers, instructors and assessors can receive various reports on the results of the conducted tests. Apart from that they can follow the performance of each learner and check his knowledge and skills, to measure up his progress. DTAT allows the creation of various personal, local and global (for the cluster) statistics of the results of the tests.

That feedback is very useful for the lecturers, so that they can estimate the success rate of each test and each question. In this way they can modify the tests or the questions in them or just the difficulty level of one or more questions.

Fig. 6 shows a principal diagram of the assessment process of dynamic questions.

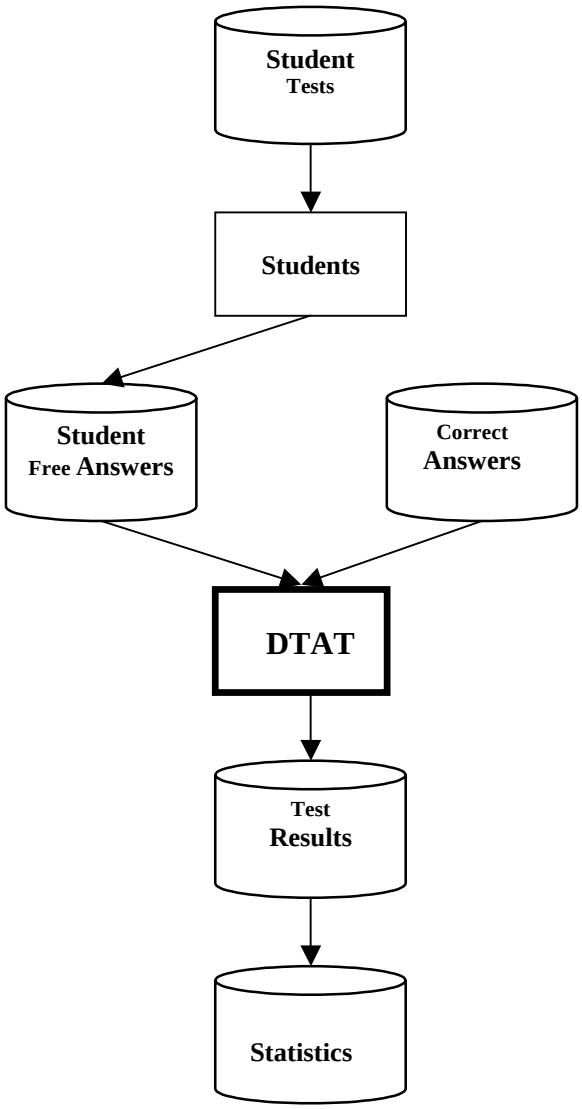

Fig.6. Assessment of Dynamic Tests

References

[1] Peter Brusilovsky, Philip L. Miller, “Web-based Testing for Distance Education”, WebNet 1999, pp. 149-155.

[2] http://wdo.uni-svishtov.bg.

[3] http://estudy.iccs.bas.bg.

[4] http://www.nbu.bg.

[5] http://www.infoguard.net/education/test/.

[6] Gusev M., G.Armenski, “A New Model of On-line Learning”, Proceedings of SSGRR Advances in Infrastructure for Electronic Bussiness, Education, Science and Medicine. Roma, 2002.

[7] http://arcade.fmi.uni-sofia.bg:8080/arcade/index.jsp

[8] Maomi Ueno & Keizo Nagaoka, "Web based Computerized Testing System for Distance Education", Proc of ICCE 2001, pp. 547-554, (2001), Korea.

[9] Rahneva, O., DeTC – Distributed Electronic Testing Cluster, Scientific and Practical Conference “New Technologies in Education and Professional Learning”, Sofia, 16-17 May 2003, pp. 84-91.

[10] Rahneva O, eTesting Tools, First Bulgarian-Irish E-learning Workshop, Plovdiv, August 2003.

[11] Rahneva, O., Testing and Assessment in Distributed Electronic Testing Cluster - DeTC, 12th International Conference Electronics '2003, Sozopol, 24-26 Sept. 2003, Conference Proceedings, v. 4, pp. 214-219.

Electronic Patient Record As A Basis Of Medical Information System

Petar J. Rajković[1], Dragan S. Janković[2]

Abstract: **Quality medical information systems realization is, nowadays, one of the most important areas in IT business. This paper presents some electronic patient record (EPR) design principles as well as important international standards. Also, paper includes one specific solution for realization of EPR considering human, technological and institutional factors both existing and yet undeveloped. In addition to offering a detailed implementation plan this paper recommends effective and comprehensive developing methodology.**

Keywords: **Electronic Patient Record, EPR, Medical Information System, Healthcare, Standard.**

I. INTRODUCTION

The leading idea of healthcare information systems (HCIS) realization is collecting and processing medical data in order to make them available for the best possible medical decision in urgent situation. Electronic patient record, as a main building block of medical IS, formats patient's and other data, and prepares them for processing and/or interchanging with other computer based systems.

The main improvement of medical service quality is done by creating "patient's electronic medical history". This set of data that can be easily accessed by the web or in the other way contains all relevant information about patient such are previous injuries, diseases, allergies, etc. In urgent situation, quick access to these data can be critical for medical staff to make right decision [1]. Reducing clinical costs, through avoiding non-necessary actions in the process of healthcare, is also important advantage done by medical information system (MIS). Managing medical resources in proper way, as well as reducing paper documents using, saves a huge percent of clinical material goods.

Availability of medical data makes educational and scientific work easier. All kinds of analysis can be done instantly, and data about "rare cases" cannot be loosed or forgotten. Researchers, students and other medical staff can access them to improve their work. In the same time, data access must be restrictable enough to avoid misusage.

Data, stored by EPR, can be used in any kind of medical institutions, both public and private, in order to improve healthcare in general. Except medical and healthcare institutions other users can be dental clinics, pharmacies, as well as related insurance and home health agencies. Analyzing key capabilities of different HCIS's it can be considered that the main uses of EPR based systems are:

- patient care delivery,
- patient care management,
- patient care process support,
- education and research,
- improving policy and regulations,
- public health improvement and
- Patient self-management.

EPR based systems process medical data which reliability, in some cases, could be life-important. Otherwise, there are a lot of potential users for MIS, from clinical staff to patients, students, researchers and the other interested persons. So, we can assume that developing of the medical information system is very important process for every society.

In its main part, this paper presents a solution for specific realization of EPR based MIS considering human, technological and institutional factors of public Serbian healthcare system. Also, both detailed MIS realization plan and an overview on existing standards and solutions are given by this paper.

II. EXISTING STANDARDS AND SOLUTIONS-OVERVIEW

EPR system implementation and its continuing development is a critical element of the establishment of an IT infrastructure for health care. In the process of electronic patient record developing there were some problems with poor domestic standards in the area of medical information systems. In that reason, following important international standards [2] [3] were considered during the process of EPR development:

- HL7, standard developed since year of 1987 by consortium of several companies mostly from United States,
- Guidance on the key care delivery-related capabilities of an electronic health record system, by Institute of Medicine (IOM) of National Academies of United States,
- eEurope 2005, an action plans presented by European Council in June 2002 for implementation various areas of informatical society including e-health.

After analysis of existing international standards, the next step was choosing appropriate strategy for development of EPR and MIS, according to potential users. To implement any

[1] Petar J. Rajković is from Faculty of Electronic Engineering, Beogradska 14, 18000 Niš, Serbia & Montenegro, E-mail: rajkovicp@elfak.ni.ac.yu

[2] Dragan S. Janković is from Faculty of Electronic Engineering, Beogradska 14, 18000 Niš, Serbia & Montenegro, E-mail: gaga@elfak.ni.ac.yu

strategy for development, one must first clearly define a functional model of key capabilities for an EPR system.

Generally, EPR systems can contain different sets of data, which can be organized on different ways. Some EPR systems include all kind of patient data, while others are limited to certain types of data, such as demographics, medications and ancillary results. Advanced EPR systems provide some simple types of decision support like preventive service reminders, alerts concerning possible drug interactions. But, for the most of contemporary EPR systems one can tell that they are medical institution-specific because they operate within a specific national health system in single or multi-hospital organization [4].

Weak point of number of MIS is the fact that they are not connected, and not provide stronger support for communication and interconnectivity across the healthcare providers in a community. The implemented functionalities of EPR systems also varies from one to the other solution, because some systems have been developed locally and others by commercial vendors. In summary, EPR systems are actively "under construction" and will remain so for next several years.

III. REQUESTED EPR FUNCTIONALITIES AND THEIR REALIZATION

The IOM Committee on Standards formulated following criteria in order to guide the process of identifying core functionalities of EPR [2] [3]:

- Improve patient safety.
- Support the delivery of effective patient care.
- Facilitate management of chronic conditions.
- Improve efficiency.

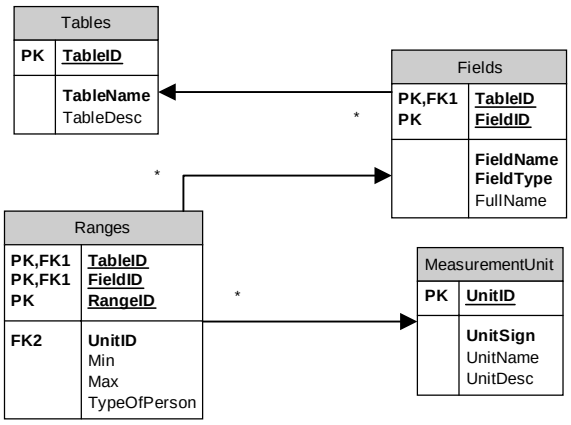

Figure 1. The structure of the healthcare related metadata

According analyzed standards, client medical institution needs and previously described guidance we consider developing EPR system that main schemas are given on figures 1, 2, 3 and 4. Figures related to data models are drawn in MS Visio as *database diagram*.

Metadata model is shown on figure 1. This part of EPR is important for more efficient creating database system for single healthcare facility. In the same time metadata model allows faster database recovery.

The most important data in system are healthcare related (both medical and non-medical data) that are grouped in adequate database (DB) tables, described in metadata model. Each of these tables corresponds to some medical analysis, treatment, diagnostic or similar. Every table consists of fields, and values of each filed are connected with specific ranges. Those ranges are values that are the most adequate for single group of patient. Every value can correspond to more ranges.

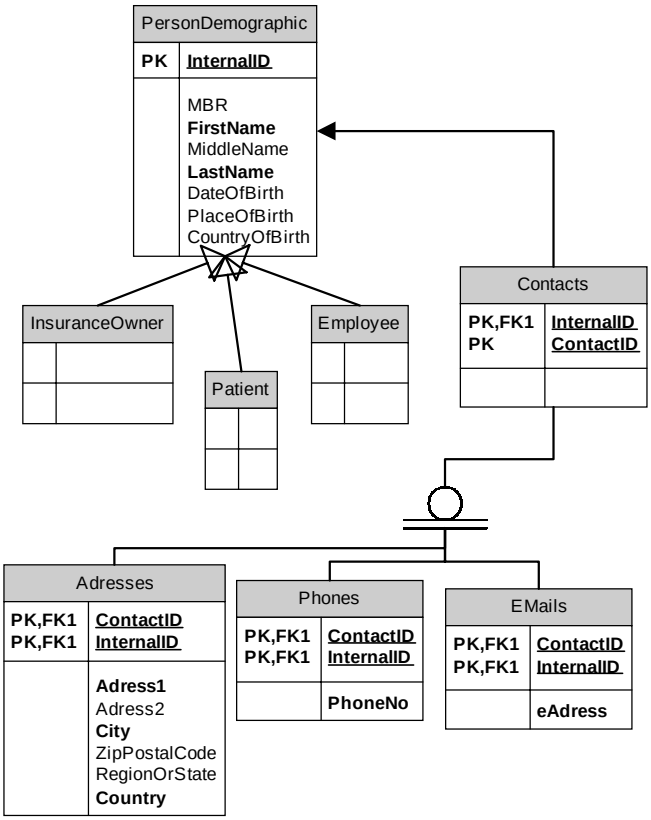

Figure 2. Demographic and other person related data model

The EPR system deals with data different types of persons. Three main classes of them are patients, employees (e.g. physicians) and insurance owner persons (e.g. parents). In the system, all of them are identified using internal ID that is consisted from 13 characters. First character describes type of person, next four are code of clinic and last 8 characters are unique number of patient in specific clinic. The other identification number in system is personal ID (in Serbia it is a 13-digit number which first 7 digits are derived from date of birth, next digit is region ID, and last 5 makes special code). The model of their demographic data and contacts is shown on figure 2.

The figure 3 represents relationships between patient demographic and insurance data as well as demographic data medical record. Internal ID, as primary key in table with demographic data and main key in system, is foreign key in every insurance related table. Patient medical record table has its own ID, and its foreign identification keys are patient ID as well as clinic identification code.

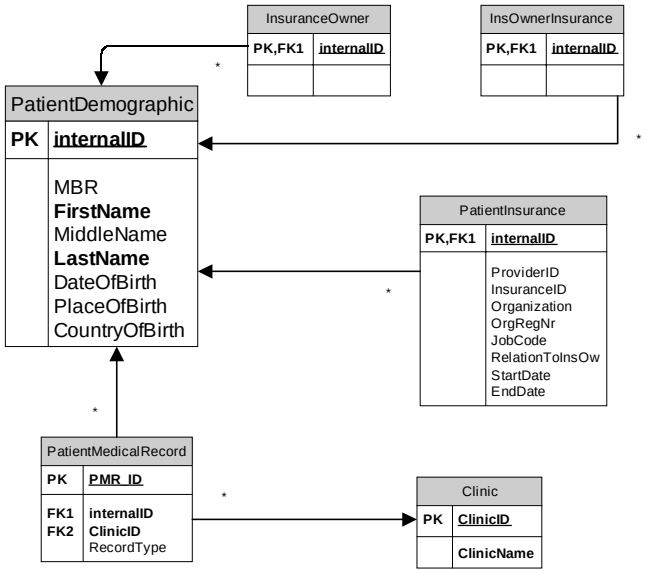

Figure 3. Relations between different types of patient related data

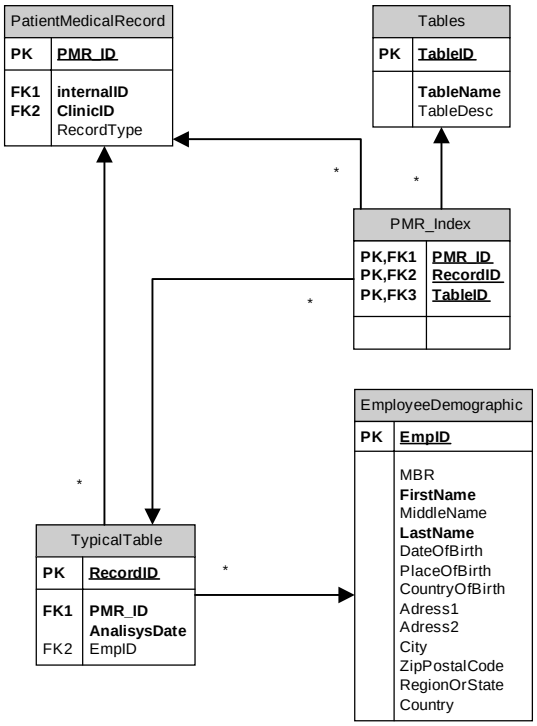

Figure 4. Patient medical record and related tables

Patient medical record and related tables that make base of EPR are shown on figure 4. Medical data, in this system are stored in typical tables, which are created on the base of metadata model. Except the fields described in metadata model, those tables have also the following fields: RecordID, PMR_ID (medical record ID), date of analysis and identification of responsible member of staff. There is a table named PMR_index, too. This table represents a list of pointers to every analysis that is made as a part o single medical record. The existence of this table helps in faster searching for specific data. Table EPR_index consists of RecordID and table ID for each of mentioned analyses.

Patient identification methods include patient's name, partial name, social security number, date of birth, MBR and internalID. Once the patient is selected, updates or edits can be made to the demographic recall file from any user with adequate privilege.

IV. MEDICAL INFORMATION SYSTEM IMPLEMENTATION PLAN

Provider of medical information system's applicative software should realize versions for different types of operation systems. In our realization, we develop software versions for Windows and Linux using Borland CLX technology. The main advantage of this technology is that one CLX project can be compiled under different Borland development tools – Delphi and Kylix. The result of CLX project compiling under Delphi environment is Windows, and under Kylix Linux application. The functionallities of the resulted applications are completly equivalent [5].

The hart of the system is database and it should be the most stabil part of the system. The database is realized according to previously described electronic patient record model. In a perspective DBMS will be exposed to large quantity of different data, as well as different attacks through the web. From these reasons we propose databases infrastructure as it is shown on figure 5. During software testing Interbase 6 was used as the main DBMS, but for system exploatation some more robust DBMS, such are Oracle or Intersystems Cache, should be installed.

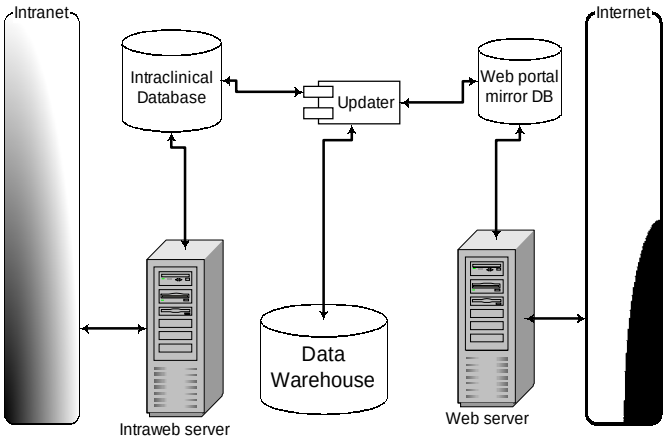

Figure 5. Database system structure

Our realization considers medical information systems that are consisted of many different parts, called modules, with a number of different roles. Each module can be treated as independent software component, but common objects for all of them are networks that bind them together physically, databases that concentrate data and security modules that control data access. These common objects make central part of system, called the core [6].

This kind of system organization allows its modular implementation, and brings more results in shorter time. General strategy for development of such system is implementation one by one part. The main part of the system, the core, should be realized and tested before implementation

of any other module. The core must be very stabile and secure system because all the other components use network infrastructure, databases, database management applications and security modules for their work. It should allow proper environment for the rest of the system. The rest of the MIS is a set of applications that provide access to database system, such are:

- **Security module** consists of two parts: main security module, directly connected to databases, and additional extranet security module. The purposes of extranet security module are guarding system from unauthorized access and keeping patients' privacy. Also, the main job of this module is creating user accounts and profiles and defining access privileges.
- **Medical documentation management module (MDMM)** is a part of system implemented as intraweb application that allows clinical staff more effective work with medical documents.
- **Electro medical instrumentation data collecting module (EIDCM)** is Intranet application for transferring data from medical instruments to database.
- **Material resources management module (MRM)** is intranet application for clinic material goods management. The job of this module is to avoid "disappearing" of medicaments and other material resources.
- **Medical insurance module (MIM)** is extranet application that allows flowing of data between clinic and institutions such are government's Health department and different social insurance funds.
- **Research and education improvement module (RIM)** is a part of system implemented as extranet/internet application that is consisted from more elements, such are telemedicine and different applications for extracting data from databases, suitable for researchers, students and other interested persons.
- **Internet module** is one of the most important elements in the system. Mainly part of this module is web-portal that allows to registered users viewing some data they are interested in. Also it provides different forums and discussion groups.
- **WAP module** is extension internet module**.** In some critical cases, it allows communication with members of medical staff that can help by advice or similar way.

The price of realization of such web-oriented MIS is more than reasonable corresponding to improvements that bring in whole healthcare systems. Investments in network equipment, hardware and software are equal to costs for paper documents and "loosed" medical material during 12 to 18 months.

V. CONCLUSION

Medical information systems simplify almost every process in complex healthcare system. Their targets are all activities connected with healthcare. From the process of patient scheduling, over medical documentation management and telemedicine to using stored data for scientific work, these systems help reducing errors and misunderstandings.

The importance of such complex and voluminous informatical product can be viewed through support of the government. The results, presented by this paper, were made under project of MIS developing for Clinical center in Niš. This project is supported by Serbian ministry of Sciences and Ecology. Realized EPR should become a model for realization of similar systems that would be realized for other Serbian public health facilities.

Summarizing main electronic patient record's characteristics it can be considered that EPR:

- is electronic and replaces existing paper records,
- supports all patient care processes,
- is patient – centric model of public health organization,
- is generated by health care providers as a business record,
- Can be longitudinal across providers, care settings and time.

One characteristic that become more actual today is ability of sharing data between medical institutions. But, in wide number of countries there are no relevant paper-based model of patient record. The new standards, which can be brought with development of EPR and MIS, can improve whole health – related public sector.

The quality EPR is main factor in integration of different medical information systems. This fact, together with development of medical expert systems and improving of medical instrumentation, can help further advance in healthcare, and generally in medicine.

ACKNOWLEDGES

The writing of this paper was supported by the Ministry of Sciences and Ecology, Goverment of Republic of Serbia (Project No. IT.1.23.0047).

REFERENCES

[1] *Realizing Our Vision For an Interconnected, Electronic Health Information Infrastructure*, e-Health Initiative News, Volume 1, Number 3, July 2002

[2] Jeffrey S. Blair: *An Overview of Healthcare Information Standards*, IBM Healthcare Solutions, Atlanta 2003, Georgia

[3] Commission of the European Communities: *eEurope 2005: An Information Society for All*, Brussels, June 2002

[4] *Electronic Medical Record - Why Their Time Has Come*, article taken from http://www.healthcare-informatics.com

[5] Marco Cantú: *Mastering Delphi 6, Sybex*, 2001

[6] Petar Rajković, Dragan Janković: *Web-Oriented Medical Information Systems*, Proc. of Workshop on CIIT pp.73-76, Niš, Serbia & Montenegro, October 13, 2003

GIS And Virtual Reality Systems Integration

Dejan Rančić[1], Aleksandar Dimitrijević[2], Aleksandar Milosavljević[3], Vladan Mihajlović[4]

Abstract - **The paper describes virtual reality and geographical information systems integration methodology. Described virtual GIS is based on OO methodology and uses original continuous georeferenced raster map, developed by CG&GIS Lab, as texture source, and DEM obtained from georeferenced raster map. While VR part uses Microsoft DirectX technology, GIS functionality is based on the original GIS framework developed by CG&GIS Lab.**

Keywords – **VR, GIS, Integration, Virtual GIS**

I. INTRODUCTION

The representation of the world surrounding us have been changed during past centuries from drawings on the pottery, through geographic paper maps, to the electronic maps. The representation becomes more realistic as humans improved their knowledge. Nowadays, it is made possible to improve these representations, in such way that they look more realistic, due to the hardware and the software evolution. The new trend of reliable modeling of real world is known as ***Virtual Reality*** (***VR***). Virtual Reality is still on its beginning, but the results are already impressive. The development of ***Geographic Information Systems*** (***GIS***) follows this progress. Nowadays, the scientific researches are oriented to exploring new virtual **three-dimensional** (***3D***) GIS systems, which provide 3D interactive topographic maps, without space, time or context limitations.

The two-dimensional (2D) GIS and 3D ***CAD*** (***Computer Added Design***) systems are the most common systems that use spatial data. CAD systems are usually designed to work with small 3D models, but the performance of their execution on huge 3D models is very poor. One example of this is a terrain modeling. From the GIS point of view, the CAD and the VR systems have two major disadvantages: lack of the semantic metadata and limited 3D analyses.

One way of enhancing CAD and VR systems is to add capability of working with databases and assigning attributes to the geometric objects [1,2]. However, these new systems cannot perform complex analyses using the object's attributes.

Further enhancement can be achieved by integrating GIS, CAD and VR, i.e. their geometric and semantic data in order to enable complex 3D analyses and more realistic visualization and the interactivity.

The rest of the paper is organized in the following way. The second part contains the existing solutions and current research efforts to improve geometric and semantic data integration. Third section describes the methodology of GIS and VR systems integration into a monolite Virtual GIS, developed in Computer Graphics and GIS Laboratory (***CG&GIS Lab***) on the Faculty of Electronic Engineering, Niš. The usability of VR GIS and the short description of its appliance are described in the fourth part. The conclusions and directions for further research are presented at the end of the paper.

[1]ranca@elfak.ni.ac.yu, [2]aks@elfak.ni.ac.yu, [3]alexm@elfak.ni.ac.yu, [4]wlada@elfak.ni.ac.yu
All authors are with the Faculty of Electronic Engineering, Beogradska 14, 18000 Nis, Serbia and Montenegro

II. EXISTING SOLUTIONS AND RESEARCH TRENDS

First attempts to solve the problem of GIS and VR integration are appearance of hybrid systems such as AutoCAD, ArcView and ArcCAD. The drawback is isolation of database due to different data formats, causing either incomplete analyses or inefficient visualization. Intensive researches are performed in the computer graphics and GIS area to overcome this problem. In the computer graphics area, the research is focused on discovering the algorithms and structures for processing huge amount of 3D data (geometry and texture) in real time, photorealistic visualization, algorithms for 3D data generalization and manipulation of the ***Level of Detail*** (***LOD***).

The objectives of research provided in the GIS domain are:

1. Development of conceptual 3D GIS models,
2. Data acquisition,
3. Spatial analyses,
4. Visualization, navigation and user interface.

The development of conceptual 3D models capable to integrate semantic data, 3D geometry and 3D topology, mostly consider 3D topology or 3D visualization in real time, and only some of them consider 3D analyses and visualization integration.

The 3D data acquisition is more complex and costly in comparison with 2D data acquisition. Some successful methodologies and algorithms for automatic 3D data acquisition are presented in Gulch et al. [3]. However, the manual approaches are still predominant.

3D GIS should make possible measuring operations (distance, length, area, volume, etc.) and set operations (intersection, union, difference, etc.). Third dimension increases complexity of spatial relations. The researches in this domain are involved in discovering the formalisms for detecting spatial relationships [4] and definition of spatial query languages for 3D analyses or extending existing 2D languages [5].

Advances in the area of visualization, navigation and user interface have made visual media a major ingredient of the current interface and it is likely that graphics will play a dominant role in the communication and interaction in the future. Researches in this area are focused on revelation the new modes for 3D spatial analyses visualization, tools for navigation through large 3D models in real time and texture the geometry [6].

CG&GIS Lab has also taken part in solving problems mentioned above. The main objective of the researches is integration of the Virtual Reality systems and 3D GIS. There are four levels of integration [7]:

1. Rudimentary level.
2. Operational level.
3. Functional level.
4. Complete integration.

Minimal data sharing between two technologies is provided on the rudimentary integration level. On the operational level the data consistency between VR and GIS is established, and the redundancy is minimized. Communication transparency between GIS and VR technologies was achieved on the functional level. The fourth level represents merged system – a complete integration of the technologies into monolite Virtual GIS. The cost-effective alternative of Virtual GIS is usage of WWW and VRML technologies.

The examples of systems with high level of integration are:

1. ***Virtual 3D GIS*** [8], which is not real 3D GIS, because it uses 2.5D data,
2. ***3D GIS*** [9], which performs fast 3D visualization and gives the contribution to real time navigation, but it hardly can be classified as 3D GIS.

Currently, in this area, the most important competitors on the commercial market are:

1. ***ArcView 3D Analyst***, product of ESRI that uses only 2.5D data and is oriented to the 3D visualization, but not to 3D analyses.
2. ***Imagine VirtualGIS***, product of ERDAS, which provides excellent 3D visualization, fly-through functionality, but 3D GIS function are still on the rudimentary level.
3. ***GeoMedia Terrain***, product of Intergraph Inc. that provides 3D terrain model generation using DEM data, fly-through functionality and some simple 3D analyses.

In general, there are a lot of software environments that visualize 3D terrain efficiently, but 3D GIS functions are at rudimentary level. 3D data structures, 3D data manipulation and 3D GIS analysis has been neglected. Current researches attempt to offer monolithic Virtual GIS that provides complete 3D GIS functionality and the capability of visualization and interactive work like the VR systems. The popularity of this topic is confirmed by the numerous projects that are developed in last few years. Most of those projects have appliance in the telecommunication domain, mainly in the propagation of electromagnetic waves through space, prediction and visualization. These applications can be found in FP5 (finished in 2002.) and FP6 (will be finished in 2006.) founded by European Union, as the topic in the most preferential research domain – IST (Information Society Technologies).

III. VR AND GIS INTEGRATION METHODOLOGY

CG&GIS Lab has also given its contribution to the efforts mentioned before developing its own methodology. This methodology is based on the original continual georeferenced raster map, developed in CG&GIS Lab [10] that is used for the terrain textures and 3D digital elevation model. The elevation model is result of digitalization of contour according to preset grid from the continual georeferenced raster map. The software is built on object-oriented paradigm. A VR part of the system is implemented using Microsoft DirectX technology. GIS functionality is based on original GIS framework developed in CG&GIS Lab. Graphical representation of the global system architecture is shown in Fig. 1.

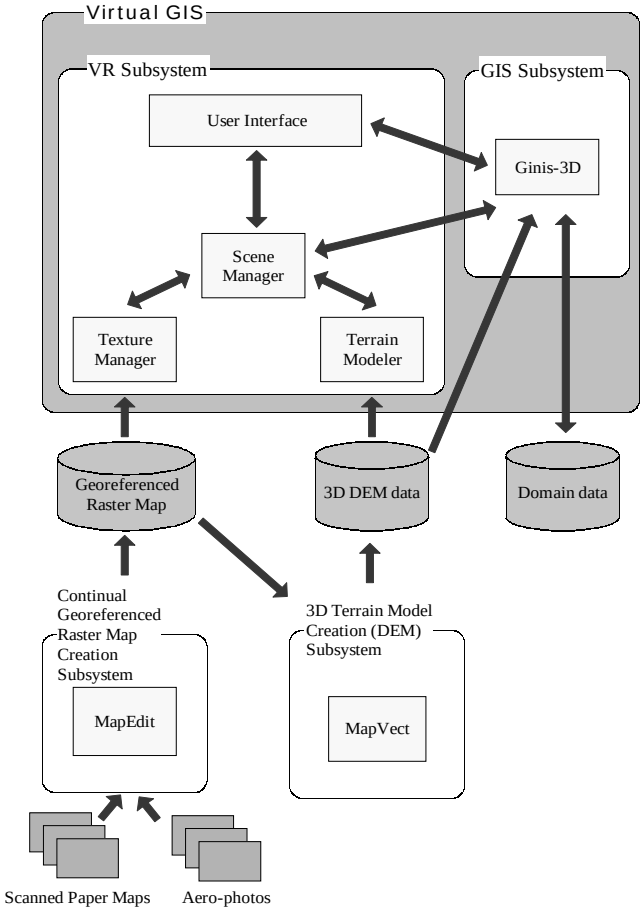

Fig. 1. VR and GIS integration methodology

The complete methodology is developed and it starts from geographic data acquisition. This can be done using commercially available DEM data and georeferenced raster data for the texturing. If these data are not available, the methodology offers the possibilities to create them from the scanned raster maps or orthophotos. These data are the input to the subsystem for continual georeferenced raster map creation, which major component is ***MapEdit***, software for georeferencing and rectification of the raster data. The output of the subsystem is georeferenced raster map divided in small sections for easier manipulation in texture creation process and DEM data computation.

The basic part of the subsystem that computes 3D data for particular terrain is software MapVect, which perform vectorization of georeferenced raster map data [11].

The data computed in such way (georeferenced raster map and 3D DEM data), altogether with data from the problem domain, are the input data for Virtual GIS.

Virtual GIS is monolithic application that integrates VR subsystem and GIS subsystem. The basic component of the GIS subsystem is **Ginis-3D** – 3D GIS, developed in CG&GIS Lab [12]. This component performs georeferencing of all data in system and 2D and 3D spatial query processing. Ginis-3D is hybrid GIS (georeferenced raster map + vector layers) with possibility to generate 3D terrain representation, gathering

information about altitude of arbitrary point and some aspects of 3D analyses (e.g. terrain profile).

VR subsystem consists of the following components:

1. User Interface.
2. Scene Manager.
3. Texture Manager.
4. Terrain Modeler.

User Interface component provides user-system interaction on the VR manner. This means that user can "jump" to certain position in the space and to analyze the perspective. Moreover, the VR interface provides flying over the terrain and six degrees of freedom: moving upward, sliding along the scene, rotation and three-dimensional translations. This component also provides possibility of visual motion and 2D and 3D spatial queries that are parameterized and passed to the GIS subsystem. The GIS subsystem executes queries and retrieves 2D and 3D results needed for visualization.

Scene Manager is main component of the VR subsystem. The role of the component is dynamic scene creation, depending on position of camera. During scene rendering, Scene Manager use the texture formed by the Texture Manager, 3D terrain model created by the Terrain Modeler and data from problem domain, which are georeferenced by the GIS subsystem.

Texture Manager is component that dynamically creates texture after the Scene Manager request. For the texture creation, Texture Manager uses continual georeferenced raster map.

Terrain Modeler creates the terrain model using the 3D DEM data when Scene Manager requests it.

The complete algorithm of 3D representation generation is as follows:

1. According to the user request, the User Interface computes the region, which will be created the 3D model, and forward the request to the Scene Manager.
2. The Scene Manager forwards the request to the Texture Manager, Terrain Modeler and GIS subsystem.
3. The Terrain Modeler extracts the DEM data of the specified region and constructs the regular grid.
4. The Texture Manager extracts the part of the georeferenced raster map defined by the region specified earlier and use it as a texture.
5. The GIS subsystem performs spatial query on the domain data, georeferences the data and forwards them to the Scene Manager.
6. The Scene Manager performs space triangulation, i.e. calculate triangular surfaces as details in the 3D representation.
7. The Scene Manager locates the parts of the texture corresponding to the each of the triangular surfaces and applies them to the particular surfaces.
8. The Scene Manager calculates the normal for each node in the grid that will be used later in the rendering of the scene.
9. The Scene Manager does the rendering using Gouraud rendering model. The color and intensity of the adjacent nodes are interpolated along the surfaces among them and the created representation is seamless.
10. The Scene Manager performs the color interpolation inside the triangles. The linear interpolation is used among all three points.
11. The Scene Manager is involved in texture filtering. It uses linear interpolation among four adjacent pixels, which improve the quality of the representation.
12. The Scene Manager places the light. Two types of light are used: directional and ambient.
13. The Scene Manager locates the viewing point.
14. The Scene Manager renders 3D terrain model using the parameters that have been computed earlier and if it is needed adds some visual elements to create more realistic representation (e.g. fog).

At the end, user can see the visualization results (3D model of the terrain as well as 3D data from the problem domain). The terrain model provides capability to change the real time position of the light and the camera. This feature makes the impression of flying over the terrain. The GIS subsystem provides 3D model with the current geographical location, azimuth and elevation, in real time.

The outlined methodology integrates VR and GIS subsystems forming one monolith application. In this way, the forth level of integration – Merged systems (according to [7]) is reached. This enables both subsystems to use the same set of data. The complete data integration is achieved by developing the both subsystems as single application. The overall communication between the subsystems is carried out throw the local procedure calls, which represent the component interface. The realization performed in that way ensures fast system response and reduce the environment influence to minimum.

IV. VIRTUAL GIS APPLICATION

The Virtual GIS can be used in every domain in which the traditional GIS are used – urbanism, aqueduct, mining, hydrology, telecommunication etc. The Virtual GIS can also have a military application, for example for monitoring dynamic battlefields. Also, these systems are irreplaceable for different kind of trainers and simulators.

VR GIS make available real representation of the data without leaving the office, which minimize the frequency of the terrain work, and also the cost. This is especially significant in the telecommunication domain, where this kind of systems perform different type of simulations in the process of development wireless telecommunication networks (mobile telephone network, radio-relay links, radar networks etc.).

In the purpose of testing and verification of developed methodology, one system is designed in the CG&GIS Lab. The system provides the prediction of the radar coverage zone and verification of radar network configuration. The system uses the model of the radar, the parameters of the target, which can be discovered by the radar, model of atmosphere and 3D terrain model to precisely determine the coverage zone of particular radar. Besides, the system creates reliable 2D and 3D visualization of the calculated zone, and possibility of interactive work between user and the system. The examples of 2D and 3D visualization are shown in Fig. 2 and Fig. 3.

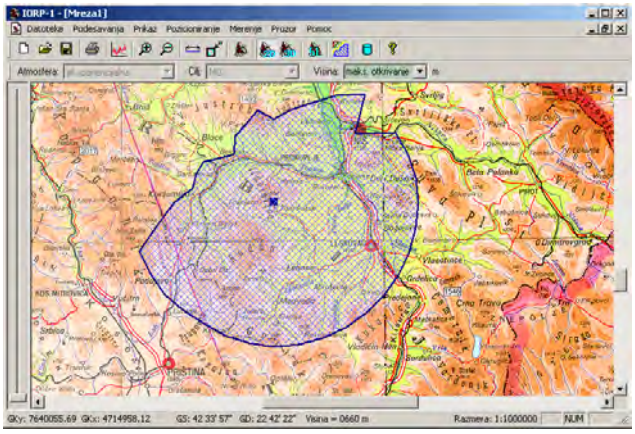

Fig. 2. 2D visualization of radar coverage zone

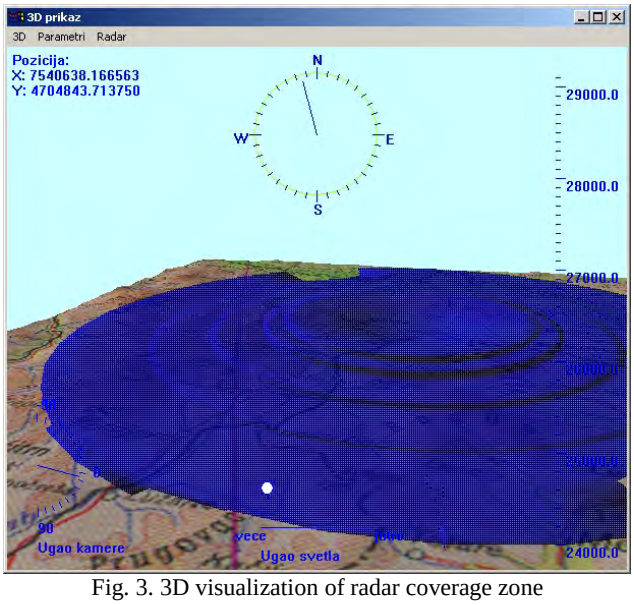

Fig. 3. 3D visualization of radar coverage zone

V. CONCLUSIONS

The earlier version of the GIS provided the information about third dimension – the altitude of arbitrary point on the map. The further evolution of the computers and adequate software has created the new possibilities for improving the representation of the world surrounding us. The Virtual Reality has been introduced into the GIS application allowing more reliable representation of the real world. The researches in the GIS domain are immediately oriented to the closer integration of two technologies. The researches on this topic are carried out in the CG&GIS Lab. The result of the researches is the integration of VR and GIS into monolite Virtual GIS. The complete methodology is developed and it begins from the spatial data acquisition and ends with the creation of reliable 3D representation. This paper presents detailed description of the methodology and overview of the application of the Virtual GIS in the telecommunication domain, developed in order to verify the developed methodology.

Further research trends in this domain are involved in improvement of the performance of the developed methodology. The component capable to predict user movements through the scene and dynamically prepare the 3D scene according to these movements prior to its visualization is under development. This component will afford the impression of the continuous motion through the scene in real time, regardless to the size of the scene, giving the user more natural way of viewing the surrounding space, which is the final goal of the Virtual GIS.

ACKNOLEDGEMENT

The research was partially supported by the project “Geographical Information System Designed to Improve the Local Municipal Function based on Internet/WWW Technologies”, funded by Ministry of Science, Technology and Development, Republic of Serbia and Municipality of Niš, Contract No. IT.1.23.0249A.

REFERENCES

[1] Bentley, 1999, http://bentley.com.
[2] Intergraph, 1999, http://intergraph.com.
[3] Gulch, E., H. Muller and T. Labe, “Integration of automatic processing into semiautomatic building extraction”, Proceedings of ISPRS: Automatic extraction of GIS objects from digital imagery, Vol. 32, Part 3-2W5, pp.8-10., Munchen, Germany, September 1999.
[4] Pullar, D.V. and M.J. Egenhofer, ”Toward formal definition of topological relations among spatial objects”, Proceedings of the Third International symposium on SDH, pp. 225-241, Sydney, Australia, 1988.
[5] Mattos, N. and L. DeMichiel, ”Recent design trade-offs in SQL3”, ACM SIGMOD record, Vol. 23, No. 4, pp.6, 1994.
[6] Zlatanova, S., *3D GIS for urban development*, PhD thesys, University of Technology, Gratz, Austia, 2000.
[7] Rhyne T., ”Going Virtual with Geographic Information and Scientific Visualization”, Computers & Geosciences, vol.23, no. 4, 1997.
[8] Koller, D., P. Lindstrom, W. Ribarsky, L. Hodges, N. Faust and G. Turner, ”Virtual GIS: a real-time 3D geographical information system”, Proceedings of IEEE Visualization, pp. 94-100, 1995.
[9] Kofler, M., *R-trees for the visualisation of large 3D databases*, PhD Thesis, TU, Gratz, Austria, 1998.
[10] Rančić, D., Đorđević-Kajan, S, “Mapedit: solution to continuous raster map creation", Computer and Geosciences, Elsevier Science, Vol. 29, No. 2, pp.115-122, 2003.
[11] Stoimenov L, Đorđević-Kajan S., Stojanović D., “The vectorisation process in GinisNT system”, Primena informatike u Vojsci Jugoslavije - VJINFO 2001, Beograd, April 2001.
[12] Rancić D., Đorđević-Kajan S., Milenović D., Stoimenov L, “3D Geographic Information Systems”, INFO Science 3, pp. 27-30, 2000.

Adaptive License Plate Extraction

Vladimir Shapiro[1], Stefan Bonchev[2], Veselin Velichkov[2] and Georgi Gluhchev[2]

***Abstract*—The paper presents the automatic plate localization component of a Car License Plate Recognition system. The approach includes stages of preprocessing, edge detection, filtering, detection of the plate's position, slope evaluation, and character segmentation. In the experiments Israeli and Bulgarian plates were used. The obtained results have shown that the approach is robust to illumination, plate slope, scale and is insensitive to the country's peculiarities.**

***Keywords*—License plate, Image processing, Segmentation**

I. INTRODUCTION

While the first industrial automatic systems of Car License Plate Recognition (CLPR) started emerging in 80-ies [9], an outburst of commercial systems occurred in 90-ies. Nevertheless that hundreds of CLPR systems are available in the market worldwide, the research and development still continues and new sophisticated solutions to plate localization, character segmentation and recognition appear. This is due to the growing demand for the automatic vehicle identification required for traffic control, border control, access-control, calculation of parking time and payment, search for stolen cars or unpaid fees, and the requirement for reliable identification at different lighting conditions, presence of random or structured noise in the plate, and nationality specific features, concerning plate's size and type of characters.

A system for automatic CLPR consists of a camera (color or gray level), frame grabber, computer and specially designed software for image processing and analysis. A system should be ready to work with alternative image acquisition equipment, as well as with previously or remotely captured and stored images. It should be capable of:

- working indoor and outdoor
- working in a wide range of illumination conditions
- being invariant to size, scale and stroke thickness
- being robust to broken strokes, printing defects, noise, etc.
- being robust to camera-car relative movement
- giving a real-time response [1,5,7]

[1]Vladimir Shapiro is with Orbograph Ltd., Israel, E-mail: Vladimir.shapiro@orbograph.com

[2]Stefan Bonchev, Veselin Velichkov and Georgi Gluhchev are with the Institute of Information Technologies, Acad. G. Bonchev Str.
Bl. 2, Sofia 1113, Bulgaria, E-mail: gluhchev(bonchevs, vesko)@iinf.
bas.bg

A CLPR system can be conceptually considered as containing two separate processing stages:

- License Plate Localization (LPL)
- License Plate Character Recognition (LPCR).

In practice, LPCR serves also as a verifier [2], providing an indication that the clipped image fragment, referred to below as a "plate candidate", at the LPL stage is the actual plate, otherwise LPL iterates in an attempt to find better candidates.

The most popular approach, which seems to become dominating since 2nd half of 90-ies, is based on edge detection, gradient and other variants of intensity derivatives [4,5,6]. These techniques are sensitive to noise and illumination variation, therefore they need to be supported or complemented by other methods.

This paper represents the LPL component of a CLPR system, which works with single frame gray-level images, obtained at different daytime and weather conditions, as an input. It is organized in the following way: Section II describes preprocessing procedures; Section III considers the image segmentation the effect of which is verified as described in Section IV. Section V presents some experimental results. Discussion and conclusion are included in Section VI.

II. PREPROCESSING

The preprocessing has to improve the image and facilitate its analysis. Below, a series of preprocessing steps, involved in our research, is described in the order they are applied.

The original image might be quite large (up to 1M pixels and even larger), as the image size might vary depending on the image acquisition equipment in use, and require much processing work. Because of trade-off between the size and processing time, we first undersample the image to about 120 columns using simple and fast pixel decimation while preserving the original aspect ratio.

A. Vertical Edge Detection

There are two basic assumptions about the CLPR systems: 1) plates are oriented horizontally and 2) the plate zone is characterized with relatively high density of sharp contrast alterations between the characters and plate's background [3,6]. Having these two assumptions in mind, we apply Roberts' edge operator to the log-intensity image in order to emphasize vertical edges (Fig. 1b).

B. Rank Filtering

As seen in Fig. 1b, there is a clearly visible cluster of high density of bright edges in the plate zone. To detect it, a horizontally oriented rank-filter of *MxN* – element size (the horizontal size *M* is much larger than *N*) is applied to the whole image. Each image pixel is replaced with 80%-percrntile of pixel intensity in the area covered by the filter

mask. This step leads to the creation of a bright spot of ellipsoidal shape in the plate's zone (Fig. 1c).

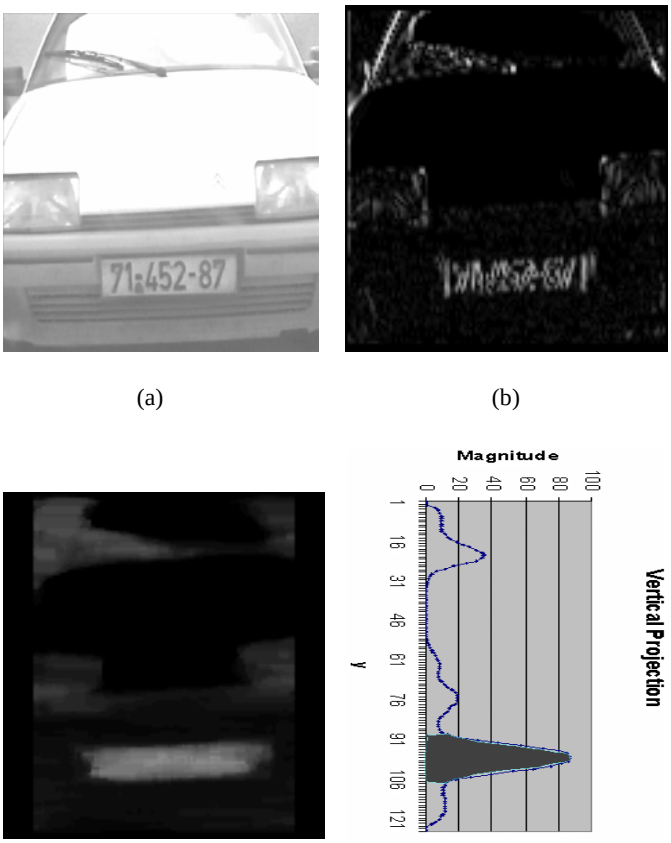

(a) (b)

(c) (d)

Fig. 1. (a) Condensed original image; (b) vertical edges; (c) rank-filtered image; (d) vertical projection.

II. PLATE SEGMENTATION

A. Vertical Projection Acquisition

The preprocessor ends up with obtaining a vertical projection, as shown in Fig. 1d. To decrease the random noise the projection is smoothed by a 5-element uniform filter.

B. Prime Clipping of the Plate

The forthcoming segmentation works in phases. The first stage consists in finding a horizontal strip loosely locked on the plate. To compute its vertical bounds, we find the y-coordinate for which $P(i)_{Iw}$ has a maximal value, i.e.

$$i_{plate} = ArgMax[P(i)_{Iw}] \quad (1)$$

Then the bounds i_{top} and respectively i_{bottom} are found as:

$$i = ArgMax[P(i)_{Iw} = 0.2 \max[P(i)_{Iw}] \quad (2)$$

C. Plate Skew Evaluation

After the plate's vertical bounds evaluation according to Eqs (1) and (2), the strip is clipped from the image (Fig. 2a).

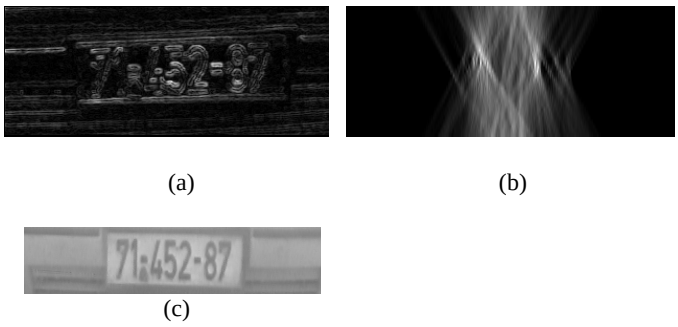

(a) (b)

(c)

Fig. 2. Skew detection and deskewing. (a) extended image strip; (b) Radon transform space of (a), θ; (c) deskewed image strip (skew of -3^0 was detected)

Due to the vehicle's position and orientation with respect to the camera, a plate zone might appear skewed. The skew may prevent LPL from accurately finding and clipping the plate zone, therefore the skew, if present, must be eliminated. The applied technique is similar to the described one in [11], where Hough transform (HT) is used for acquiring angular projections. Dealing with grey-level imagery in this work we have used Radon transform (RT) instead of HT. The following equation was found to be applicable to the radon space:

$$\theta_{plate} = ArgMax[\mathrm{var}\, R(\rho)_\theta], \quad (3)$$

where $\theta \in [-\theta_{start}, \theta_{end}]$, ($\theta_{start} = \theta_{end} = 8^o$ was chosen for this research) and $R(\rho)_\theta$ is the angular projection under θ.

In this work we have modified the RT in the HT style, attempting to save computation time and making it more robust for the plate skew measurement. Namely, the RT was applied to those edge pixels the intensity of which exceeded a certain threshold.

Having θ_{plate} evaluated according to Eq. (3) and i_{top}, i_{bottom} determined from Eq. (2), the strip is cut from the original image and deskewed by rotating it by $-\theta_{plate}$ (Fig. 2c).

D. Horizontal Segmentation

The clipped and deskewed image is processed by horizontal edge detection operator (Fig. 3a). It is again possible to use rank filter but this will be a costly solution because this time the processed image is of original size. The use of a series of morphological erosions [3] with primarily horizontally oriented structured elements would be much simpler and cheaper solution. The obtained result is shown in Fig. 3a.

For the horizontal segmentation we evaluate first the horizontal projection $P(j)$ as a convolution with a filter of a length equal to the roughly estimated plate length. The convolution maximum is then used for the refinement of the plate's boundaries. The search is based on the localization of significant gaps while moving from the convolution maximum

x-coordinate outwards (Fig. 3b). The gap horizontal coordinates of the strip x_{left} and x_{right} respectively should satisfy the following conditions:

$$x_{left} = ArgMax[P(x) < T_1]; x_{right} = ArgMax[\sum_{j=0}^{x-1} P(j) < T_2 \quad (4)$$

where $T_1 = 0.005\sum_{j=0}^{N-1} P(j)$, i.e. 0.5% of the total projection volume, and $T_2 = 0.5\sum_{j=0}^{N-1} P(j)$, which is half of the total volume. The idea behind Eq. (4) is to find an x-coordinate with low enough magnitude, and not to "cut" while x is still within the plate area. Here is the place to use heuristics determined by the application constraints such as plate size, aspect ratio, etc.

(a)

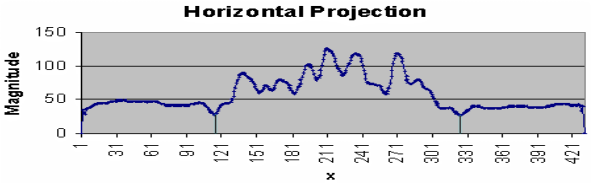

(b)

Fig. 3. Horizontal segmentation and plate zone refinement (a) edge image after erosion; (b) vertical projections of (a) with left and right boundaries designated.

III. Verification

Ideally, a CLPR system should not impose any restrictions on image content. The background is entirely beyond developer's control and any prediction or assumption about the background behavior might lead to the localization failure. The exception is a smallest subset of CLPR tasks, when the system works indoors in such static environment as, say, a parking lot. Working outdoors in a non-predictable environment, a system often encounters situations when the actual plate is either not presented at all, or is present but is not necessarily the leading candidate. The verification stage aims at checking a given plate candidate feasibility. For this the following context-dependent conditions are tested: geometrical constraints, such as width, height, aspect ratio, and gray-level distribution considerations (the plate background is expected to be lighter than the characters). If the plate candidate passes all these tests, it is presented to the LPCR.

A. Cray-level Distribution Consistency Considerations

The edge-based approach, adopted in this work, does not differentiate between the intensity transition sign. Therefore, there is a need to distinguish between the regular and the reverse intensity situation, when characters are lighter than the background (Fig. 4a).

Our approach is based on image intensity analysis. First we try to separate the image into dark and light parts. Otsu algorithm [8] is applied for that purpose. In case of a feasible plate candidate there will be larger number of light pixels (intensities above the threshold), than those lying below. This condition is verified by comparing the threshold with the intensity median. The plate candidate is plausible when the intensity median of the plate zone is higher than the threshold.

When the test fails the current plate candidate strip is eliminated and the system goes back to the segmentation stage to look iteratively for the next plate candidate.

(a) (b)

Fig. 4. (a) a source image; (b) wrong plate candidate with dominating dark levels.

IV. Experimental Results

Extensive testing has been conducted with more than 150 Israeli and Bulgarian vehicles. Images have been captured from various distances and viewing angles. Image size has varied from 64K to 1M pixels. JPEG and PNG image compression was tried along with a raw uncompressed gray level imagery. Different daylight conditions were examined, from bright sunlight illumination to foggy winter half-darkness. Very frequently the plate zone has been in a shadow and the contrast of characters has been poor with regard to the plate's background. Situations of mixed illumination, where certain portions of the plate were shadowed, while the others were brightly illuminated, caused problems and sometimes led to rejection of the whole plate.

The true license plate zone was correctly located and approved on more than 90% of the images. The rest of the cases were rejected by one of the consistency tests. It is important to stress that there have been zero false positive errors, which explain the relatively high share of rejected plates due to the conservative tests while approving plate "candidates".

V. Discussion and Conclusion

The basic elements of the LPL system are presented in this paper. The goal of the research is to investigate the possibility to create a comprehensive system for multinational vehicle

identification based on the license plate recognition. In that case no additional hardware such as transmitters mounted on the vehicle or additional sensors are required.

The preliminary results obtained on real data are quite satisfactory. They could be summarized as follows:

- Reliable verification of the plate candidate generated at the phase of localization is achieved

- Accurate plate segmentation under varying illumination and various image distortions is obtained.

In vast majority of classes the plate was contained into one of the detected prospective horizontal strips (plate candidates). Only few images of extremely poor quality (poor contrast and missing part of the plate) attempted more than three prospective strips. The conclusion is that in case of reasonably good images the above-described plate localization approach yields excellent results.

License plate imagery is equivalent to very low text scanning resolution and non-homogeneous background and lighting conditions in addition. Use of an RGB camera would allow higher precision of the plate's position detection and segmentation.

VI. Acknowledgements

The authors are grateful to M. Goldstein and D. Barkan for supporting preliminary stages of this work. Also, the work was partially supported by the Institute of Information Technologies of the Bulgarian Academy of Sciences, Grant #010042/2003.

VII. References

[1] Cohen, H.,Bergman, G., Erez, J., "Car License Plate Recognition", Project Report, Vision and Image Sequence Laboratory, Technion, Israel, 2002

[2] Hsieh, J.W., Yu, S.H., Chen, Y.S.,Morphology-based License Plate Detection from Complex Scenes, ICPR, Quebec C, vol.3, pp.176-179, 2002

[3] Huang, Y.S., Suen C.Y.,"Combination of Multiple Experts for the Recognition of Unconstrained Handwritten Numerals", PAMI 17, pp. 90-94, 1995

[4] Jilin, L., Hongqing, M., Peihong, L., "A High Performance License Plate Recognition System Based on the Web Technique", IEEE Int. Conference on Intelligent Transportation Systems, Oakland, CA, pp. 14-18, 2001

[5] Kim, S., et al., "A Robust License- Plate Extraction Method under Complex Image Conditions", ICPR, Quebec City, CA, pp. 216-219, 2002

[6] Lee, S-H.,Seok, Y-S., Lee, E-J., " Multi-National Integrated Car-License Plate Recognition System Using Geometrical Feature and Hybrid Pattern Vector", Int. Conference Circuits/Systems, Computers and Communications, Phuket, Thailand, 2002

[7] Nelson, L.J., "Vehicle Recognition: Putting an Image Technology on the Road", Advanced Imaging, pp. 53-55, 1995

[8] Otsu, N., "A Thresholding Selection Method from Gray Level Histograms", *IEEE Trans, Syst., Man, Cybern*., 9, pp. 62-66, 1979

[9] Sgurev, V., G. Gluhchev, D. Mutafov, et al., Recognition of Car Registration Numbers", *Problems of Engineering Cybernetics and Robotics*, 27, Sofia, Bulgaria, pp. 79-85, 1987

[10] Shapiro, V., G. Gluhchev., V. Sgurev., "Preprocessing for Automatic Examination of Handwritten Documents", Proc. of 7th Scandinavian Conference on Image Analysis SCIA, Aalborg, Denmark, pp. 790-797, 1991

[11] Srihari, S. N., Govindaraju, V., "Analysis of Textual Images Using the Hough Transform", *Machine Vision and Applications*, 2, pp. 141-153, 1989

Electronic Business and PKI System of the Post Serbia

Dragan M. Spasić[1]

Abstract - **Public enterprise of PTT communications "Srbija" (Post Serbia) has decided to make the PKI system and establish the public Certification Authority. Therefore, new technologies such as e-commerce, e-banking and e-government demand protected Internet communication, and PKI system is the basis for the application of the most various mechanisms of electronic transaction protection. The services and digital certificates of PKI system and Certification Authority of the Post Serbia are intended for the internal use in the framework of the Post Serbia as well as for all the external participants of electronic business, regardless whether they are legal or natural persons.**

Keywords - **Public Key Infrastructure (PKI), Certification Authority (CA), digital certificates.**

I. INTRODUCTION

The success of electronic business depends completely on the protection of business transactions on Internet. As a matter of fact, Internet gives large possibilities in the field of electronic business, but on the other hand, creates problem of data protection. Among problems that appear, the following must be emphasized: unauthorized connection to the network, unauthorized access to network resources, revealing content of messages that are exchanged by network – problem of the secrecy of inventions, unauthorized modification of messages – problem of integrity of messages, forging the messages, forecast of the activities performed, etc. In order to prevent appearance of the problems mentioned, it is necessary to apply various mechanisms of protection, i.e. it is necessary to maintain the appropriate system of protection.

The existence of the Public Key Infrastructure – PKI system is the precondition for the successful conducting of various methods of protection of electronic business. Actually, PKI system is the basis for the application of various solutions of protection that are based on technology of symmetry and asymmetry cryptography systems and technology of digital (electronic) signature.

The solutions of protection of electronic business that are based on PKI system secure four (4) basic functions of protection:

1. Confidentiality – guarantees that the content of the message shall be revealed to the intended receiver of message only.
2. Authentication – verifies the identity of the user that communicates over the network.
3. Integrity – guarantees that the message has not been changed while transferred.
4. Nonrepudiation – does not allow the denial of the transaction performed.

The protection of the secrecy of the message (confidentiality) is enforces by encrypting the message by the application of the suitable cryptographic system, while the other three functions of protection are realized by the technology of digital signature.

II. COMPONENTS OF PKI SYSTEM

The most important components of the PKI system are the following:

1. Certification Authority (CA),
2. Registration Authority (RA),
3. Public directory,
4. User (client) applications.

Certification Authority performs the following activities:

- issuing, renewal, suspension and revoking of digital certificates,
- configuration of various types, life cycles or other parameter of certificates,
- renewal of CRL (Certificate Revocation List),
- cross-certification with other Certification Authority, and other.

Registration Authority represents a connection between the users that pass demands for issuing certificates and the Certification Authority. Tasks of the Registration Authority are the following:

- accepting demands of the users for issuing certificates,
- verifying identity of users and collecting the necessary data on the users,
- transfer of the demands of users for issuing certificates towards the Certification Authority, and other.

Public directory is the location where the Certification Authority publishes and keeps the following public data:

- Data on the users,
- Digital certificates,
- CRL (Certificate Revocation List).

User applications enable the users to take advantage of the digital certificates to perform protected on-line transactions.

[1]Dragan M. Spasić is with the Public enterprise of PTT communications "Srbija" (Post Serbia), Katićeva 14-18, 11000 Belgrade, SCG, E-mail: dspasic@ptt.yu

III. DIGITAL CERTIFICATES

Digital certificate is an electronic document that is issued by the Certification Authority. Digital certificate can be perceived as the digital personal identity card, since it contains the data on the user (owner) of the certificate and data on the publisher. It contains (Fig. 1.):

1. data on identity of the user to whom the certificate has been issued, such as the name and surname, e-mail address, etc,
2. public cryptographic key of the user of certificate,
3. data on the entity that has issued the certificate or the Certification Authority.

Within this framework of the digital certificate that is issued to the user, there is, among other, also the user's public cryptographic key, representing a pair to his private cryptographic key. Certification Authority guarantees accuracy of the data in the certificate, i.e. guarantees that the public key situated in the certificate belongs to the user whose data has been mentioned in the same certificate. Therefore, the other users on Internet, if they have confidence in the Certification Authority, can be sure that a certain public key really belongs to the user who is the owner of the private key. Digital certificate is impossible to forge, because it has been signed by the private key of the Certification Authority.

Digital certificate is electronic document that is publicly available on Internet. Therefore, in framework of certificates, there are public keys of the owner of certificate, and the distribution of certificate is also distribution of the public keys. For that reason, we have enabled the competent exchange of public keys by means of Internet between the users that have never met, with the possibility of verification of the identity of users.

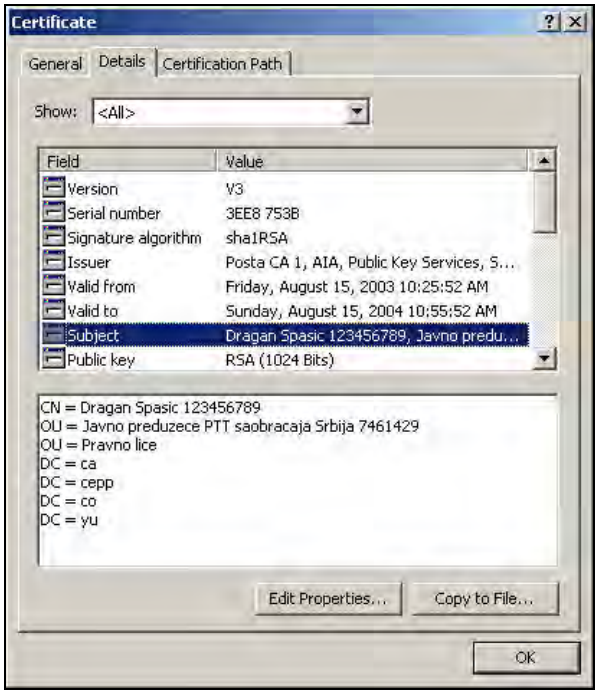

Fig. 1. Digital certificate, tab Details

IV. PKI SYSTEM AND CERTIFICATION AUTHORITY OF THE POST SERBIA

The Post Serbia has decided to make the PKI system and establish the public Certification Authority (CA). Therefore, new technologies such as e-commerce, e-banking and e-government demand protected Internet communication, and PKI system is the basis for the application of the most various mechanisms of electronic transaction protection.

PKI system of the Post Serbia has been made in accordance with the Entrust technology [1]. Company Entrust is world acknowledged producer of PKI solutions, that, in accordance with the realized PKI systems, is dominant in the world.

PKI Post Serbia system has hierarchical organization (Fig. 2.). In the first phase of production of PKI system, there are installed two CA servers:

- Root CA server ("Posta CA Root"),
- Issuing CA server ("Posta CA 1").

In the second phase, Post Serbia have planned to install two more servers:

- Issuing server ("Posta CA 2"),
- Timestamp server ("Posta TS").

Hierarchical organization of the PKI Post system consist of the two levels of CA server (Fig. 2.), that are placed in the relation of superior - subordinate CA servers. Such organization of PKI system with the greater number of CA servers enables: increased availability of PKI services (if one CA server fails, the others are available), flexible organization of PKI services, distribution of administrative authorities and duties, application of the various forms of protection in accordance to levels.

Root CA server is in the off-line regime of operations. This minimizes the risk of compromising the root CA private key. However, private key of the root of CA server is the most critical element of the entire PKI system. Apart from that, there are all measures taken in order to keep the private keys, of the issuing CA servers that work in the on-line regime, remain secret. The protection of CA servers is executed by the application of the following measures of protection:

1. Physical security,
2. Protection of communications,
3. Protection on the level of operation system and communications,
4. Organizational measures of protection.

Apart from the CA servers, PKI system of the Post Serbia consists also of the following servers and administrative workstations.

- Main Directory server where the Master Directory Service pertains.
- Public Server where a copy of the Public Directory is situated – Shadow Directory Server.

- Web server with the application for the reception of the requests of the Registration Authorities for the issue of certificates.
- Web server with the application (Entrust Web Connector) for the issue of certificates to the users through Internet.
- Workstations for the administration of CA servers and the issue of certificates.
- Workstations for the supervision and configuration of firewalls.

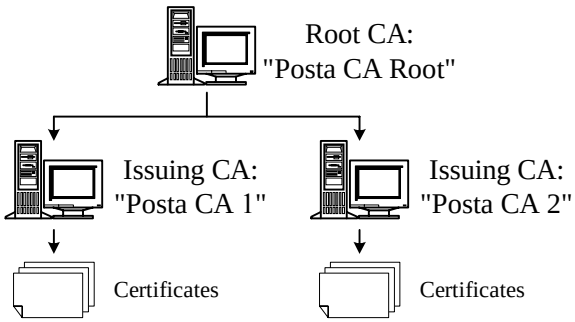

Fig. 2. Hierarchical organization of CA servers in the Post Serbia

V. Digital Certificate of the Post Serbia Certification Authority

PKI system of the Post Serbia is the commercial PKI system that shall, after being released into production, offer to the interested buyers the services of the issuing of the digital certificates. Certification Authority of the Post Serbia has at the disposal the following four (4) types of certificates [2-4]:

1. Entrust Enterprise certificate for more applications (Multiple application ID),
2. Entrust Enterprise certificate for one application (Single application ID).
3. Web certificate.
4. Certificate for Web server.

Entrust Enterprise certificates are standard X.509 version 3 certificates that have been adjusted to the Entrust applications, and they can be used also by the "Entrust-Ready" applications. There are two (2) types of the Entrust Enterprise certificates:

1. Enterprise certificate for more applications (MID). The user with this certificate can obtain the client application Entrust Entelligence and the possibility of using certificates with the unlimited number of applications and plug-ins.
2. Enterprise certificate for one application (SID). The user with this certificate obtains the client application Entrust Entelligence and the possibility of using the certificates with only one application or plug-in.

Client application Entrust Entelligence is delivered with every Entrust Enterprise certificate and it enables the following:

- Obtain and renewal of Entrust Enterprise certificate, survey of content of certificates and exporting of certificates in the files of the various formats (Public Encryption Certificates for Entrust Users – file .key, Public Encryption Certificate for S/MIME Users - file .p7c, Certificates and Keys using the PKCS#12 – file p.12).
- Encrypting / decrypting files and signing /verification of the signed files (Fig. 3.).

Considering the fact that there is a compatibility with Microsoft CryptoAPI, it has been enabled to use Entrust Enterprise certificates in the framework of the Microsoft applications (Internet Explorer, Outlook, Outlook Express, Word,...), as well as applications of the other vendors. Microsoft applications are using Entrust Enterprise certificate through Microsoft CryptoAPI interface that is completely transparent for end users.

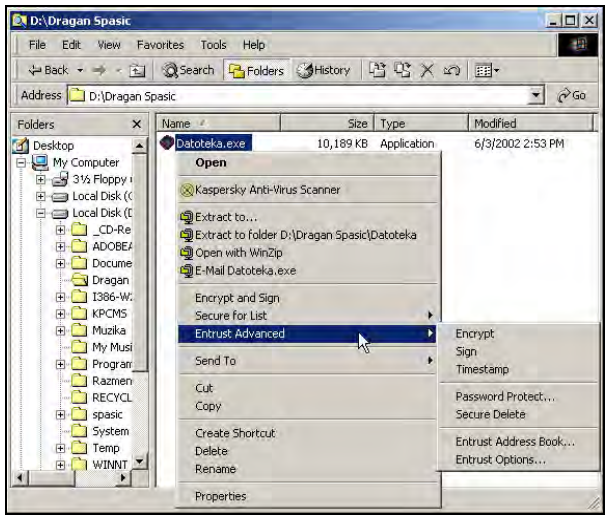

Fig. 3. Options of client application Entrust Entelligence

Web certificates are standard X.509 version 3 certificates that can be used in the framework of Microsoft applications (Internet Explorer, Outlook, Outlook Express, Word,…) and applications of other vendors. Apart from that, Certification Authority of the Post Serbia can be adjusted to the Web certificate in accordance to the demands of the users (applicants) of the certificate. For example, Certification Authority of the Post Serbia can adjust the Web certificate for the needs of the bank that intends, in process of electronic banking, to implement utilization of certificate, and in such a way, secure the protected communication.

Web administrator can install certificate for Web server on Web server, configure Secure Sockets Layer (SSL) and/or Transport Layer Security (TLS) protocol and provide confidential communication between Web server and clients [5].

Apart from the certification, the Post Serbia is able to offer to the interested users also plug-ins for the Entrust Enterprise certificates:

1. File plug-in titled Entrust ICE. It enables the creation of folders where the files are automatically encrypted after the copying in that folder (Fig. 4.).

2. E-mail plug-in titled Entrust Express. After the installation, it has been completely integrated in the framework of E-mail client application Microsoft Outlook (Fig. 5.) and it enables the encrypting / decrypting and signing / verification of signed e-mails.

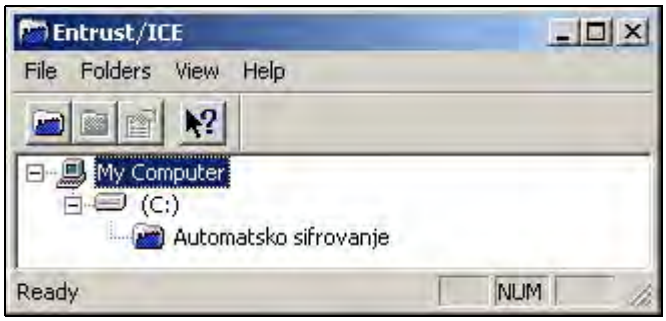

Fig. 4. File plug-in Entrust ICE

Fig. 5. Options of the E-mail plug-in Entrust Express

VI. Protection of On-Line Transactions

Post Serbia plans to offer to the potential users applications and solutions which by using digital certificates enable the protected on-line communication:

- Signing and encrypting of transactions of e-banking and e-commerce that are exchanged by Internet.
- Protected E-mail communication.
- Protected Web communication.
- Log in on the computer, computer network or application.
- Signing code of software packages.
- Signing and encrypting of files, either to store them on hard-discs of the computer or to exchange them by computer network.

VII. Potential Users

The most important potential users of the Post Serbia certificates and applications are the following:

- Post Serbia (internal user),
- Banks and other financial institutions.

Apart from the mentioned most important potential users of the Post Serbia certificates and applications, the Post takes care of the needs for the certificates and other potential users:

- Internet providers,
- Providers of e-banking,
- Providers of e-commerce,
- Providers of telecommunication services,
- Government institutions,
- Individual users.

VIII. Conclusion

Post Serbia pretends to become the first public Certification Authority in the Republic of Serbia that shall issue the digital certificates to the participants in electronic business (institutions, organizations, companies and individuals). The services of PKI system and Certification Authority of the Post Serbia are intended for the internal use in the framework of the Post as well as for all the external participants of electronic business, regardless whether they are legal or natural persons.

Difficulty in becoming public Certification Authority in the Republic of Serbia is the lack of the Law on Electronic Signature. That law should be introduced to establish the use of electronic signature in administrative, judicial and other procedures, business and other actions, as well as rights, obligations and responsibilities with regard to the digital certificates.

References

[1] Entrust Web site: http://www.entrust.com.
[2] "Entrust Authority Security Manager Comprehensive", Entrust Technologies, 2002.
[3] D. Spasić, "Digital Certificates of the Post Certification Authority", X Conference "YU Info 2004", Conference Proceedings (CD-ROM), Kopaonik, SCG, march 2004.
[4] D. Spasić, "Obtaining Entrust Digital Certificates", IV Conference "E-trgovina 2004", Conference Proceedings (CD-ROM), Palić, SCG, april 2004.
[5] D. Spasić, "Secure Web Communication and Digital Certificates", VIII Conference "JISA 2003", Conference Proceedings (CD-ROM), Herceg Novi, SCG, june 2003.
[6] D. Spasić, "Cryptosystems and Digital Certificates", IX Conference "YU Info 2003", Conference Proceedings (CD-ROM), Kopaonik, SCG, march 2003.
[7] "Microsoft Windows 2000 Server Resource Kit", Microsoft Corporation, 2000.
[8] R. Housley, W. Polk, W. Ford, D. Solo, "Internet X.509 Public Key Infrastructure Certificate and Certificate Revocation List (CRL) Profile", RFC 3280, April 2002.
[9] "DIRECTIVE 1999/93/EC OF THE EUROPEAN PARLIAMENT AND OF THE COUNCIL of 13 December 1999 on a Community framework for electronic signatures", Official Journal of the European Communities, L 13/12, 19.1.2000.

Design of Symbol Table by using Design Patterns

Miloš Stamenović[1] and Suzana Stojković[2]

***Abstract* – This paper presents an object-oriented approach in symbol table design. Symbol tables are data structures storing data about symbolic names in the program. Symbolic names are names of different kinds of items in the programs. Because of that, symbol tables contain very heterogeneous structures of data. In this solution symbol table is divided on: type table, symbol table (storing only variable names) and function table.**

Design patterns are used often in object-oriented design. Composite, factory method and singleton patterns are used in symbol table design presented in this paper.

***Keywords* – Symbol tables, compiler design, object-oriented design, design patterns**

I. INTRODUCTION

Symbol tables are data structures that are used for identifiers storing in compile time [1],[2]. Symbol tables are used for identifying syntax and semantics errors and warnings within a program. Identifier in the program can be the name of: variable, constant, type, function, etc. For different types of tokens (that are named by identifiers), different data must be stored in the symbol table. For example:

- for a variable - name, type, dimension (for array variable), last value definition, last using, etc;
- for a function - name, returned type, number of formal arguments, types of arguments, types of argument passing, etc.

There are three basic methods manipulating with a symbol table: method for inserting new symbol in the symbol table, method for deleting symbol from the symbol table and symbol lookup method (method for searching the symbol within the symbol table). The symbol lookup method is very often used and because of that, it must be very fast. Therefore, symbol tables are obligatory realized as a hash tables.

It is obvious that structure of the symbol table is very complex. Because of that, symbol table construction is one of the most significant problem in the compiler construction.

Object-oriented approach in software design and implementation enables reusing of the existing source and reusing of existing the design details (known as the design patterns [3],[4],[5]). In the last years, design patterns are often applied in compiler construction and in the symbol table design, too [6],[7]. Design patterns usage in symbol table design for a simple script language interpreter will be shown in this paper. The script language is very specialized, but proposed design is general and applicable for the other interpreters and compilers.

II. DESIGN PATTERNS

"Design pattern systematically names, explains and evaluates an important and recurring problem in object-oriented systems" [3]. Each pattern is defined by 4 elements:

- name (identifies the pattern),
- problem (describes when pattern is applied),
- solution (describe design elements making up the pattern and relationships between them),
- consequences (describe results and trade-off of using the pattern).

In the next section we will give a brief sketch of design patterns which are used in our symbol table design.

A. *Composite pattern*

The Composite pattern [3], [5] models composition of objects into tree structure. This pattern is used for representation of part-whole hierarchies of objects when clients should not know about difference between composite and leaf objects. Structure of the Composite pattern is shown on Fig. 1.

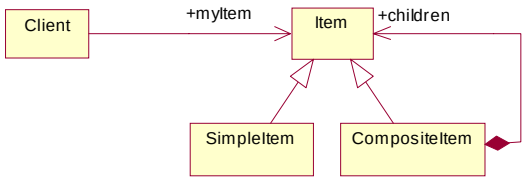

Fig. 1 Class diagram of the Composite pattern

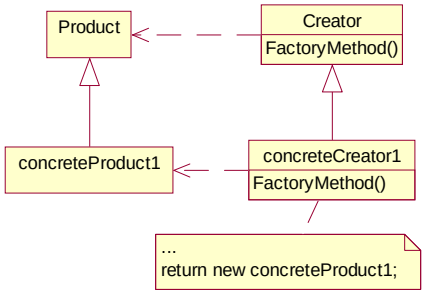

Fig. 2 Structure of the Factory method

[1] Miloš Stamenović emploied in the Troxo d.o.o, Dusanova 55, 18000 Niš, Serbia and Montenegro, e-mail: milostam@eunet.yu.

[2] Suzana Stojković emploied in the Faculty of Electronic Engeneering, Beogradska 14, 18000 Niš, Serbia and Montenegro, e-mail: suza@elfak.ni.ac.yu

B. *Factory method*

The Factory method [3] (known as Virtual Constructor) models an interface for creating an object. Derived classes "know" which class to instantiate. Structure of the Factory method pattern is shown on Fig. 2.

C. *Singleton*

The Singleton pattern [3] models a class that has exactly one instance. The Singleton class is responsible for creating its unique instance and contains an *Instance()* operation. Clients access Singleton instance through the *Instance()* operation. Structure of Singleton pattern is shown on Fig. 3.

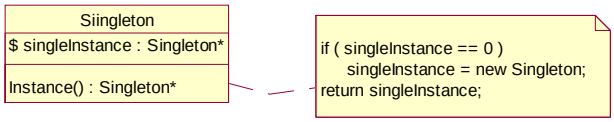

Fig. 3 Structure of the Singleton pattern

III. SCRIPT LANGUAGE CHARACTERISTICS

We have requirement to create a C++ documentation generator. Documentation generation is based on usage of documentation templates. Documentation templates describe how the generated software documentation will look like. Documentation templates are Word documents containing certain scripts. The base problem in documentation generator development is to realize interpreter of the scripts. The symbol table, presented in this paper, is a part of that interpreter. Characteristics of the script language important for symbol table design are:

- The script language has limited number of types build-in the language definition. It is not possible to define any new type. There are three kinds of types: simple types (*integer*, *string*, *image*, *float*), structures (sset of data of different types) and collections (set of data of the same type).
- The script language does not contain declarations of script variables. Thus, types of variables are determined by the context of their using.
- The script language has limited number of functions build-in the language definition, too. Those functions generate data about C++ project that can be integrated in generated documentation.
- The script language has *for each* iteration statement,. Therefore we have to involve a special type – collection type.

In the following text, we will emphasize some main components of the specific script interpreter and recommend our approach in symbol table design.

IV. SYMBOL TABLE DESIGN

Symbol table in general, has to store type names, function names and variable names. As it was mentioned before, our implementation of script language has limited number of types and functions included in definition of the language. Type names never appear in the scripts. New functions cannot be defined within the scripts. Symbol table is divided into three tables: type table, symbol table and function table because set of data describing the functions, types and variables are very different. Since, all types and functions are well known in design phase, type table and function table are initialized and filled before interpreting starts.

Architecture of our script language interpreter is shown on Fig. 4. Every table is represented as class package. Every package has one main class that is designed like singleton class. Thus, type table has TypeTable singleton class, symbol table has SymbolTable singleton class and function table has FunctionTable singleton class.

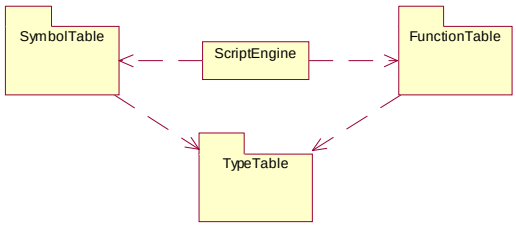

Fig. 4 Architecture Overview

A. *Type table*

A limited number of types allow us to define data structures for all types that will be used in the script language. Data structure including all script language types definitions is called Type table. Basic demand for type table is to allow maintainability and extensibility. We will use some combination of design patterns to accomplish these requirements. Class diagram of the Type table is shown on Fig. 5.

We define generic *type* with the Type class and all other kinds of types as subclasses of the Type class. The following classes are derived from Type:

- SimpleType
- StructureType
- CollectionType

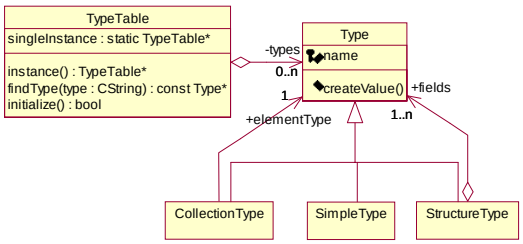

Fig. 5 Type table class diagram

The SimpleType class encapsulates simple types like *integer*, *string*, *imagee*, *float*, *etc.* StructureType has various fields, and every field has its own *type*. For example, some instance of StructureType can have one field of an *integer* type, one field of any StructureType and one field of any CollectionType. The CollectionType class represents collection of elements where all elements have the same type.

We want to describe this types hierarchy and treat all objects uniformly. Also this types structure could be very complex. This consideration leads us to *composite design pattern* as obvious choice. The types objects are used by one very complex object, called ScriptEngine. Composite design pattern separates ScriptEngine class from types hierarchy, which is liable for changes.

TypeTable is a singleton class and its findType method is used to find type in hash table where the key is a function of type name. Certain symbol can be created when its type is determinated. First, we have to get *type* object by type name, then we create *value* for this *type* and, finally, create *symbol* with this *value*

B. Symbol table

The Symbol table, in our interpreter, contains only data about variables in the scripts. The Symbol table includes the following classes:

- SymbolTable class. The SymbolTable class is implemented as hash table of symbol objects. As it was mentioned before, this class is designed like a singleton class.
- Symbol class. The Symbol class represents a variable in the scripts. Symbol has the following attributes describing variable in a program: *name, lastUsed, defined, DTName* (name of documentation template in which variable is defined) and *value.* Atribut *value* is necessary because Symbol table is used in interpreter, i. e. Symbol table exists in a run-time.
- Values class hierarchy. This hierarchy includes Value class and Value subclasses (SimpleValue, StructureValue and CollectionValue). It is designed by using composite pattern, too. When we expand this composite object structure we will get tree structure with SimpleValue-s as leafs. Only SimpleValue contains data in the *value* attribute. The *value* attribute is implemented as string, because all simple types *integer, date, float* etc could be represented as strings.

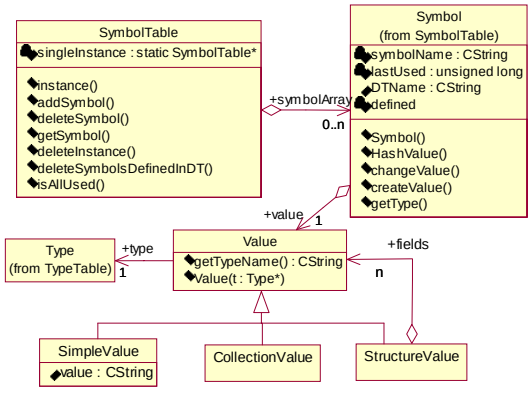

Fig. 6 Symbol table class diagram

SymbolTable structures are shown on the *Symbol table* class diagram (see Fig. 6). It is important to note a connection between Value and Type. Value object always "has knowledge" of its own type by using this connection. Also, the StructureValue knows types of its fields via the StructureType object. Similarly, the CollectionValue knows type of its elements via the CollectionType object.

Imagine that Type subclasses are added on the *Symbol table* class diagram. The result diagram would contain parallel class hierarchies connected with *type* relationship. This relationship is realized with createValue method and we can notice similarity between this Value-Type structures and FactoryMethod (Creator-Product) design pattern. FactoryMethod design pattern is useful when we want to delegate creation responsibility to derived classes. It means that, for example, only StructureType class knows how to create its value (StructureValue).

Fig. 7 shows scenario intending to explain process of creating values. This scenario covers interpreting of a script with a function call containing certain StructureType script variable. First, ScriptEngine gets function from FunctionTable by function name in order to get type of out function argument. Second, new empty symbol has to be added in SymbolTable. Third, StructureValue object has to be created with all its fields. Finally, StructureValue object has to be filled in with real data by using the Function object. Process of creating StructureValue object have to be explained with more details. Creating of StructureValue object implies creating of all its fields. According to that, StructureValue object gets type for each field from its StructureType object and requires from these types to create value by using factory method *createValue*.

Creating value does not mean coping real data to symbol. Symbol is added in symbol table when declaration of some variable is detected, but there is possibility that declared variable would not be used in the following script. For example, CollectionValue object could contain many elements, copying all elements can be an expensive operation, but there is not guaranty that all elements would be used. Therefore, current design could be improved by using virtual proxy technique. It means that only reference to data source is placed in CollectionValue object so CollectionValue object is used like proxy to real data source. Thus, when parsed script requires value of some CollectionValue element, real data will be obtained via proxy.

C. Function table

It was mentioned before, that we had limited number of functions build-in the language definition. Therefore, we can gather definition of all functions in the FunctionTable structures.

FunctionTable class is designed like Singleton class, because there must be only one instance of the FunctionTable. Every function is identified by its name (arguments are not considered like they do many object oriented languages). As it is shown on Fig. 7, when the ScriptEngine detects a function in script it starts creating value based on type of the function out argument. It means that symbol with empty Value object is created. The Value object has to be filled in with information extracted from project for which documentation will be generated. For this purpose, ScriptEngine gets function by its name from FunctionTable and calls the function (*call*

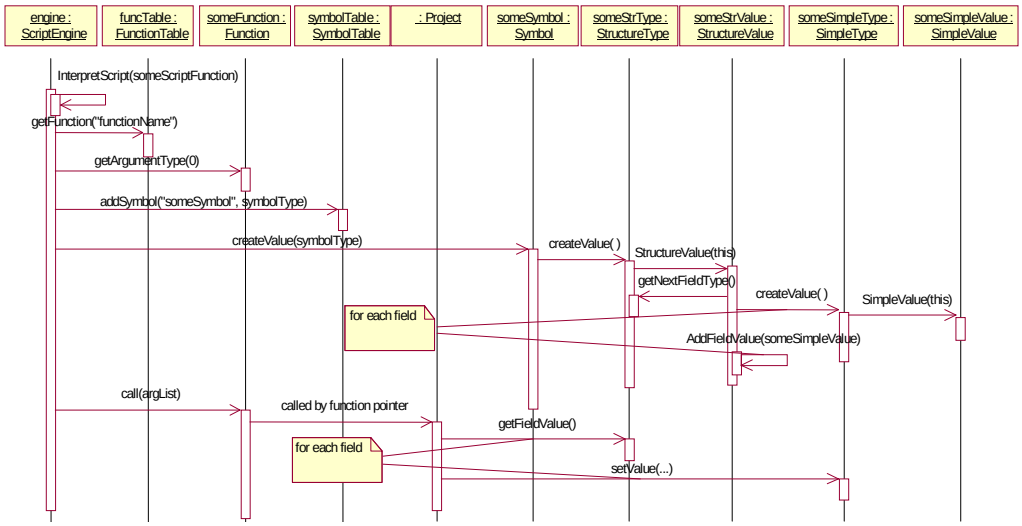

Fig.7 Scenario of interpreting certain script

member of Function class) to fill Value object. Method *call* is generic because it is used for every symbol. During the initialization of FunctionTable, *implementation* property of Function class is set. *implementation* property represents function pointer on real function. Thus, ScriptEngine calls real function via Function object, i.e., via *implementation* property.

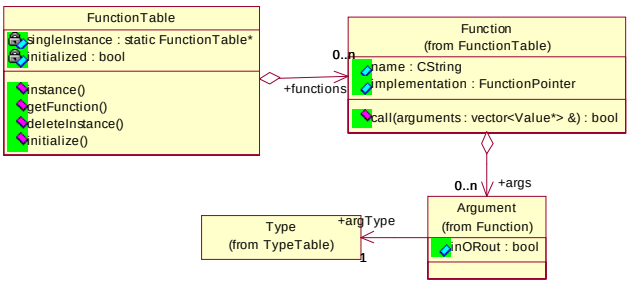

Fig. 8 Function table class diagram

Finally, class Argument defines function parameter or argument. Argument maintains a pointer to Type which is used by ScriptEngine for detecting incorrect parameters.

V. CONCLUSION

In this paper we have presented an object-oriented approach in development of a script language interpreter. We were focused on symbol table design. The Symbol table is the most important part of language interpreters and compilers. Our basic idea was to create a symbol table independent of script engine implementation and applicable in various interpreters. Therefore, we have used design patterns.

In the presented design, symbol table was divided in three tables: type table, symbol table and function table. Each table has a main class designed as singleton class. For designing of types and variables values, composite pattern was used. It enables that other parts of system do not have to know about differences between types and appropriate values. It provides easy adding new types in the language, or replacing existing type. For creating variable value, the factory method pattern was used.

Usage of UML language and design patterns increased speed and quality of presented design. It enables vary easy extansion of existing script language and application of implemented symbol table in other interpreters or compilers.

REFERENCES

[1] A. V. Aho, R. Sethi, J. D. Ullman, *Compilers – Principles, Techniques and Tools*, Addition-Wesely, 1986.

[2] D. Grune, H. E. Bal, C. J. H. Jacobs, K. G. Langendeon, *Modern Compiler Desing*, New York, John Wiley & Sons, 2002.

[3] E. Gamma, R. Helm, R. Johnson, J. Vlissides, *Design Patterns: Element of Reusable Object-Oriented Software*, Addition-Wesely, 1995.

[4] D. Milićev, M. Zarić, N. Pirоćanac, *Objektno orijentisano modelovanje na jeziku UML: skripta sa praktikumom*, Beograd, Mikro knjiga, 2001.

[5] R. Riechle, "Composite Design Patterns", Proceedings of the 12th ACM SIGPLAN conference on Object-oriented programming, systems, languages, and applications , pp. 218-228, Atlanta, Georgia, United States, 1997.

[6] J. F. Power, B. A. Malloy, "Symbol Table Construction and Name Lookup in ISO C++", Proceedings of the 37th Conference on Technology of Object-Oriented Languages and Systems, pp. 57-69, Sydney, Australia, 2000.

[7] M. Hind, A. Pioli, "Traveling Through Dakota: Experiences with an Object-Oriented Program Analysis System" , Proceedings of the 34th Conference on Technology of Object-Oriented Languages and Systems, pp. 49-60, Santa Barbara, California, 2000.

Geodata integration in distributed environment using OLE DB data provider

Aleksandar Stanimirović[1], Leonid Stoimenov[2] and Slobodanka Đorđević-Kajan[3]

Abstract - **This paper describes implementation of OpenGIS standards for uniform access to heterogeneous and distributed data sources. These standards are based on Microsoft Universal Data Access specification and OLE DB technology. The basic architecture of Ginis OLE DB Data Provider and schema definition for GIS data is also shown in this paper.**

Keywords – GIS, OLE DB, OpenGIS, Ginis, provider

I. INTRODUCTION

Research in information systems interoperability is motivated by the ever-increasing heterogeneity of the computer world. Heterogeneity in GIS is not an exception, but the complexity and richness of geographic data and the difficulty of their representation raise specific issues for GIS interoperability. Interoperability means openness in the software industry, because open publication of internal data structures allows GIS users to build applications that integrate software components from different developers.

Integrating geodata from various sources increasingly becomes important because of growing environmental concerns, pressures on governments and businesses to perform more efficiently, and simply because of the existence of a rapidly growing body of useful geodata and geoprocessing tools [1] Increasing number of geodata producers and users have expressed the need for the integration of geodata from distributed information sources and for interoperable GISs [2]. The systems that own this data must be capable of interoperation with systems around them, in order to make access to this data to become feasible.

Process of designing that kind of systems can become very complicated. It is very useful, in order to avoid this complication, to realize data access in separate component. In this way, application becomes completely independent from underlying data access technique. That kind of components will provide means for development of new applications, capable to interchange data with systems from distributed environment. At the same time this component must provide standard interfaces for data access. In that way existing applications can also use this component without any change.

[1]Aleksandar Stanimirović is with the Faculty of Electronic Engineering, Beogradska 14, 18000 Serbian and Montenegro, E-mail: alex@elfak.ni.ac.yu

[2]Leonid Stoimenov is with the Faculty of Electronic Engineering, Beogradska 14, 18000 Serbian and Montenegro, E-mail: leni@elfak.ni.ac.yu

[3]Slobodanka Đorđević-Kajan is with the Faculty of Electronic Engineering, Beogradska 14, 18000 Serbian and Montenegro, E-mail: sdjordjevic@elfak.ni.ac.yu

The paper is structured as follows. In the second section, we shortly describe related work. The goals of our research activities and **`GinisFrame`** component framework along with are described in the third section. Fourth section of this paper describes our efforts in defining schema definition for GIS metadata information.

II. RELATED WORK

In the past few years the OpenGIS Consortium (OGC), as a consortium of GIS vendors, agencies, and academic institutions, has emerged as a major force in the trend to openness. According to OpenGIS Abstract Specification for Features and OpenGIS Simple Feature Specification access to spatial data should be seen in the context of database problems [3]. Spatial geometry should be seen as one of the object attributes and feature collections could be easily represented as tables in relational database. Several feature collections (tables) also form one relational database.

This point of view is supported by current trends in database systems. Modern relational database management systems introduce new technologies for spatial data storage. OpenGIS Consortium has proposed OpenGIS Simple Features Specification For SQL [4] to standardize storing geo-spatial data in relational databases. Unfortunately there exists large base of spatial data stored in proprietary formats (mostly binary data in various GIS formats). Chances that this data will be converted to some standard database format are very small. For this reason OpenGIS Simple Feature Specification For OLE/COM provides unified method for accessing data spatial data stored in both databases and proprietary formats. This technology is based on Microsoft OLE DB standards. This standard provides data in unified table-oriented manner to any system or application.

Universal Data Access (UDA) is the Microsoft strategy for providing access to all types of data across information system [5]. Microsoft UDA provides access to a variety of information sources including relational and non-relational data (e-mail and file system stores, text, graphical, geographical data and more).

The Universal Data Access provides component architecture. This kind of architecture allows components to implement only required set of functionalities over data sources. UDA also assumes existence of service components that implements additional functionalities on the top of less capable components.

The Microsoft UDA strategy is based on OLE DB. Microsoft defines OLE DB as a specification for a set of data access interfaces [6]. This set of interfaces expose data from a variety of sources using OLE Component Object Model (COM). These interfaces provide applications with uniform access to data stored in diverse information sources.

OLE DB architecture distinguish three kinds of database components:

- *Data providers* – components that represent various data sources. Providers expose information uniformly using a common abstraction called the rowset,
- *Data consumer* – applications or tools that consumes data exposed by data providers and
- *Data services* – components that consume and produce data at the same time. Data services retrieve data from existing providers, transform data and expose it, using the same set of interfaces, to other components.

The Data provider is basic component that must be implemented in order to allow data to be exposed to and shared among different applications. Data providers are only required to implement minimal set of OLE DB interfaces. Data providers wishing to allow simple creation and modification of data must implement additional OLE DB interfaces. Sophisticated data providers may also expose custom COM interfaces in order to implement functionalities specific for their data sources.

III. GINISFRAME – COMPONENT BASED FRAMEWORK

Component-oriented programming is the predominant software development methodology today [7][8]. Components can be considered as stand-alone service providers. When a system needs some service, it calls on a component to provide that service. In that case system doesn't take care about where component is executing or about programming language that was used for component development. Component could be considered as a completely independent executable entity. Components publish their interfaces and all interactions are through that interfaces. Components may exist at different level of abstraction, from a simple library subroutine to an entire application.

Basic architecture of **`GinisFrame`** component framework [9] is shown in Fig. 1. This framework is part of **`GeoNis`** framework for interoperability of GIS applications. **`GinisFrame`** component framework was used for development of **`GeoJP`** application, which is part of **`GeoNis`** framework.

`GinisFrame` is component-based framework developed in CG&GIS Laboratory at Faculty of Electronic Engineering in Nis. This framework provides greater flexibility and efficiency in development of desktop and Internet GIS applications. GIS applications can utilize services provided by components from framework using standard interfaces. In this way GIS application is completely independent from implementation of a component.

`Ginis OLE DB Provider` is part of **`GinisFrame`** component framework, and is responsible to provide access to diverse data sources. In order to achieve this functionality this component use existing commercial OLE DB providers. This component is also responsible for providing data consumers with GIS specific functionality.

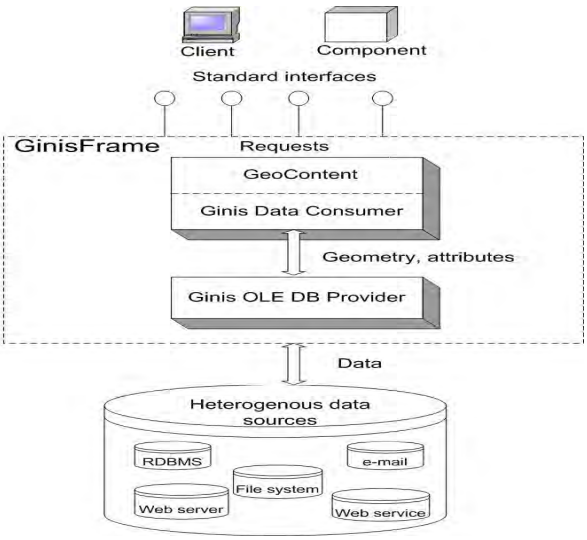

Fig. 1 Architecture of GinisFrame component framework

The basic architecture of **`Ginis OLE DB Provider`** component [9][10] is shown in Fig. 2.

GIS OLE DB provider consists of three components:

1. **`Data Manager Component`** – read and writes data from various data sources,
2. **`OLE DB Component`** - implements Data Source, Session, Command and Rowset objects that expose standard interfaces to data consumers according to Microsoft specification and
3. **`GIS DB Component`** – provides GIS specific functionality extending or implementing new interfaces besides interfaces defined by Microsoft specification.

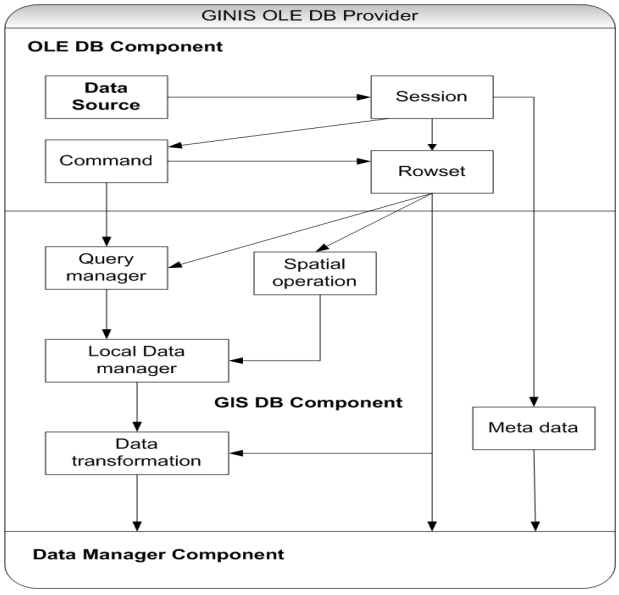

Fig. 2 Basic architecture of Ginis OLE DB Provider component

OLE DB standard defines facilities by which consumers and providers communicate. In order to achieve interoperability OGC has defined standard that allows GIS consumers and GIS providers to exchange GIS information (OpenGIS Consortium Inc., 1999). This standard makes a GIS data consumer capable to determine the GIS capabilities of a GIS data provider. Using this

standard GIS data consumer can also retrieve GIS data in predictable manner.

These standards involve:

- *Open GIS data provider registry entries* – data provider must register his support for GIS data so that consumer can distinguish him from common data providers,
- *GIS metadata* – required and optional GIS metadata that describes to clients that GIS data exists and how to get it,
- *IColumnsRowset* – additional GIS columns are defined for the Rowset returned by calling GetColumnsRowset method,
- *Geometry* – methods are described for acquiring geometry from Column or Field as WKBGeometry,
- *Spatial Reference Information* – methods are described for acquiring Spatial Reference Information from Session and Rowset objects and
- *Spatial Filter* – standard spatial filter parameters are defined for use with Command object. Parameters are spatial filter, spatial operator and Geometry Field/Column name.

Although this standard is needed for communication between GIS consumer and GIS provider there is no strict level of compliance for Open GIS OLE DB providers. The minimum level of support is that a provider must provide registry entries for Open GIS OLE DB provider. Clients are supposed to use standard techniques to determine which functionalities provider supports and to take actions according to that.

V GIS METADATA

Ginis OLE DB Provider component must provide additional GIS Metadata information in order to tell consumers that GIS data exist and to explain how to get this data and how to interpret it. This additional metadata contains following information:

- which tables are considered GIS *feature tables*,
- which columns contain geometry, type and spatial reference of the geometry,
- spatial references of the Data Source and
- spatial operators supported by the provider.

According to OpenGIS Simple Feature Specification For SQL Simple geospatial feature collections conceptually can be stored as tables with geometry valued columns in a Relational DBMS (RDBMS). Each feature will be stored as a row in a table. A table whose rows represent Open GIS features is referred to as a *feature table*. In order to support this specification OpenGIS Simple Feature Specification For OLE/COM has extended schema information provided by standard OLE DB provider.

Ginis OLE DB Provider component contains three additional *SchemaRowsets* and one additional *PropertySet*:

- *DBSCHEMA_OGIS_FEATURE_TABLES Rowset* - this rowset indicates those tables that the consumer can query as features,
- *DBSCHEMA_OGIS_GEOMETRY_COLUMNS Rowset* - this rowset identifies the feature columns in the *feature table* that contains geometry information,
- DBSCHEMA_OGIS_SPATIAL_REF_SYSTEMS Rowset – contains information of *Spatial Referent Systems* supported by data provider and
- *OGIS Property Set* – contains information of spatial operator supported by data provider.

In order to provide this kind of information to consumers **Ginis OLE DB Provider** must obtain this data in the first place. If GIS application use **Ginis OLE DB Provider** on the top of relational database, designed according to OpenGIS Simple Feature Specification For SQL, this data can be obtained from additional tables that extends standard database Schema Information. But in **Ginis OLE DB Provider** cannot rely on this.

Modern GIS applications have to deal with distributed data sources. *Feature table* is not necessary located in one data source. Columns that forms *feature table* can be distributed in great number of data sources. Also *feature* data is not necessary in relational databases. Spatial data can be stored in great number of heterogeneous data sources. Ginis OLE DB provider must access all this data sources in order to build up *feature table* and to provide data from it to his consumers. In this situation obtaining GIS metadata information is very difficult and sometimes impossible.

In order to solve this problem we extended **Ginis OLE DB Provider** in the way that he can receive GIS metadata information from consumer during his initialization. **Ginis OLE DB Provider** still fully supports OpenGIS Simple Feature Specification For SQL. When Ginis OLE DB Provider is used for accessing data in relational database, designed according to this specification, additional schema information from database can be used if not specified different. In all other cases **Ginis OLE DB Provider** relies on data provided by consumer during initialization.

Ginis OLE DB Provider expects this GIS metadata information in the form of XML document. This XML document is built according to schema in Fig. 3.

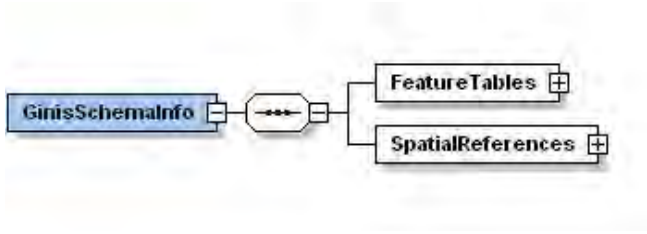

Fig. 3 Schema for document with GIS Metadata information

Every schema element contains information specified in OpenGIS specification [3] plus some additional information that are specific for **Ginis OLE DB Provider** component.

Metadata XML document contains collection of *feature table* and *spatial reference system* definitions. *Spatial reference system* is defined according to schema in Fig. 4.

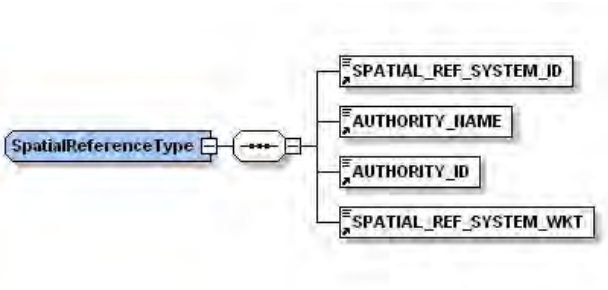

Fig. 4 Definition of Spatial Reference System

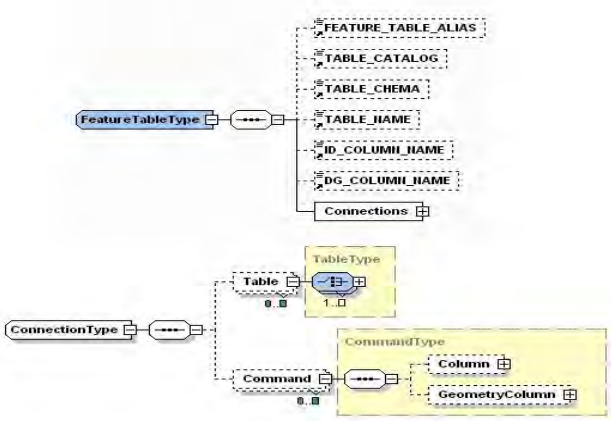

Fig. 5 Definitions of Feature table and Connections

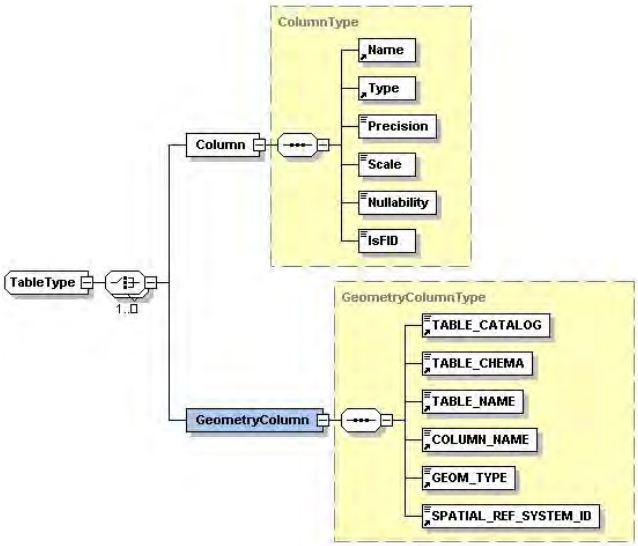

Fig. 6 Definition of columns and geometry columns

Every *feature table* is defined as a collection of connections. Each connection defines one data source and contains tables from that data source or commands that can be executed against data source. Each table or command contains collection of columns and geometry columns.

Schema for this definition is shown in Fig. 5 and Fig. 6. Feature table is treated as distributed table partitioned vertical. Every distributed source only has certain columns of *feature table*. Every vertical fragment includes primary key so that full feature table can be reconstructed. For this reason some columns can be defined to participate as a part of feature identifier (FID).

VI Conclusion

To provide integrated access to various distributed geo-information sources, we have developed Ginis OLE DB Provider component. This component is a part of GinisFrame component framework. Component is based on OLE DB technology and OpenGIS specification. OLE DB technology provides system architecture model related to interoperability. This model specifies uniform paradigm for accessing spatial and non-spatial data in distributed data sources. We also developed schema definition for specifying data sources and metadata information in distributed environment.

Acknowledgement

This research was partially supported by the project “Geographic Information System for Local Authorities based on Internet/WWW Technologies”, funded by Ministry of Science, Technology and Development, Republic of Serbia, Contract No. IT.1.23.0249A.

References

[1] Buehler R., and McKee L., 1998, The Open GIS Guide, Third Edition, OpenGIS Consortium, Inc, http://www.OpenGIS.org/techno/specs.htm

[2] Stoimenov L., and Đorđević-Kajan S., 2002. Framework for semantic GIS interoperability, FACTA Universitatis (Niš), Series: Mathematic and Informatics, 17(2002), pp.107-125.

[3] OpenGIS Consortium Inc, OpenGIS Simple Features Specification For OLE/COM, 1999, http://www.opengis.org

[4] OpenGIS Consortium Inc, OpenGIS Simple Features Specification For SQL, 1999, http://www.opengis.org

[5] Rauch S., Manage Data from Myriad Sources with the Universal Data Access Interfaces, Microsoft System Journal, September 1997

[6] Microsoft Press, Microsoft OLE DB 2.0 Programmer’s Reference and Data Access SDK, 1998

[7] Stojanovic Z., and Dahanayake A.N.W., 2002, "A New Approach to Components", accepted for the 2002 Information Resources Management Association (IRMA) International Conference, to be held in Seattle Washington, USA, May 19-22, 2002.

[8] Szyperski, C., 1998, "Component Software: Beyond Object Oriented Programming", ACM Press, Addison-Wesley.

[9] Stoimenov L., Stanimirović A., Đorđević-Kajan S., Realization of Component-Based GIS Application Framework, Accepted for 7th Agile Conference on Geographic Information Science, Heraklion, Crete, 29 April-1 May, 2004

[10] Stanimirović A., Đorđević-Kajan S., Stoimenov L., Ginis OLE DB data provider, accepted for Etran conference, Čačak, May 2004

Notification Systems: Basic Concepts and an Example

Milena Stanković[1], Milan Rajković[2]

Abstract – **In this paper we discuss software systems for user notification, underlying functional and architecture requirements. We also present an example of a notification system, which is developed and deployed at the Faculty of Electronic Engineering in Niš.**

Keywords – **Notification systems, Internet SMS gateways**

I. Introduction

Notification systems are software products used for notifying and alerting users about the events they have subscribed for. Nowadays, they are usually a part of more general information systems, but they can also exist independently if they are used for advertising purposes.

The importance of these systems has been spot by many software vendors. One of them is *Microsoft*, which offers Web Services called *.Net Alerts* that can be integrated into the third party applications. The main disadvantage of these high level solutions for developers is their price and the lack of flexibility, which is why most programmers prefer to implement the whole system from the scratch.

In order to enable efficient alerting, these applications provide multiple alternative ways for sending messages. That is why these systems require using and integrating different technologies. The most frequently used alerting methods are sending E-mail, SMS, ICQ or Microsoft Messenger messages. Of course, users can choose the way they receive the notifications.

In this paper we focus on functional and architecture requirements these systems have to fulfill. In the second part, a notification system called *StudentAlerts* is presented. It is developed and deployed at the Faculty of Electronic Engineering in Niš.

II. Functional requirements

In this section we will present common functional requirements for a notification system.

There are three typical roles that can be identified in the system. The first is *client*, which represents a person who subscribes for a notification(we also use the term *alert*) on a specific *event*. The client can choose from all events that currently exist, and has to specify the notification method (E-mail, SMS etc.). Figure 1 shows a use case for this scenario.

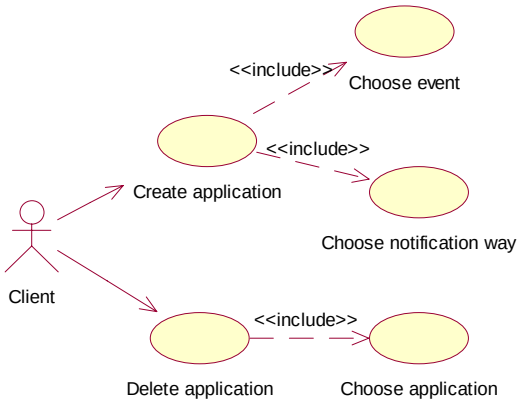

Fig. 1. Use case: subscribing for an event

The second role is *Sender*, which represents a person that creates and sends alerts. There can be many types of alerts, but the most common are personal and group alerts. Latter ones are used for notifying all clients that has subscribed for a specific event. *Sender* also creates new events and delete the old ones. Use case which explains the process of creating and sending alerts is presented in figure 2.

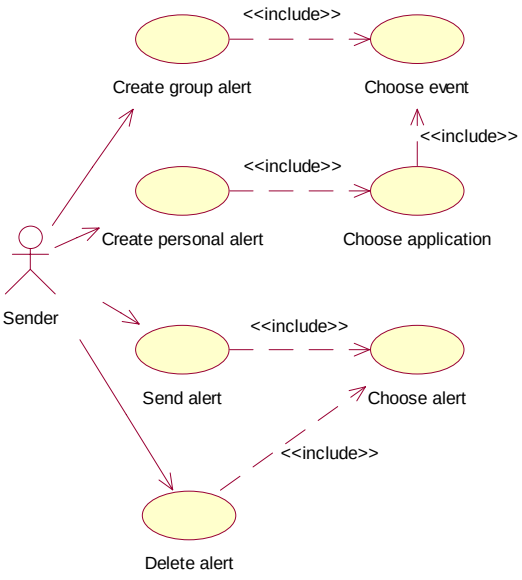

Fig. 2. Use case: creating and sending alerts

The third role is *Administrator*, which represents a person that adds *users* or changes their data. Of course, *users* are *clients* and *senders*. Administrator is also responsible for setting user privileges. Use case which explains the process of managing users is presented in figure 3.

[1] Milena Stanković is with the faculty of Electronic Engineering, Beogradska 14, 18000 Niš, Serbia and Montenegro, E-mail: mstankovic@elfak.ni.ac.yu

[2] Milan Rajković is with the faculty of Electronic Engineering, Beogradska 14, 18000 Niš, Serbia and Montenegro, E-mail: mrajkovic@elfak.ni.ac.yu

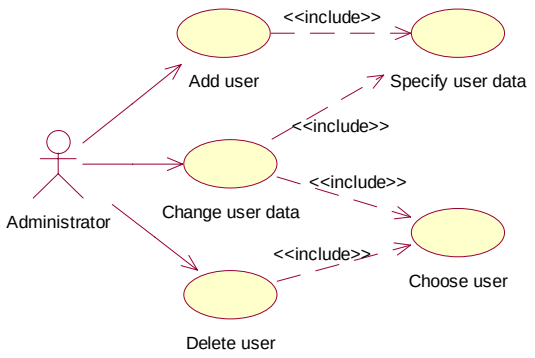

Fig. 3. Use case: managing users

III. Architecture requirements

In this section we will present the most important architecture requirements that notification systems have to carry out.

In order to provide multiple ways for sending alerts, notification systems are implemented as a mixture of different technologies. As we have already mentioned, typical ways for sending messages are SMS, E-mail, ICQ etc. We will here discuss in more details how SMS messages can be sent from a notification application to a client, this being the most complicated and frequently used way.

Basically, there are two different approaches for sending SMS messages from an application. The first one involves using an Internet SMS gateway, which is an interface to an SMS center (SMSC). Many telecommunication companies provide access to their SMSCs via SMPP, SMTP, HTTP or FTP protocols, allowing programmers to include SMS features into their applications. Of course, these companies charge for the service, and the price differs depending on the target mobile network. Figure 4 shows how SMS messages are sent using an Internet SMS gateway. [1]

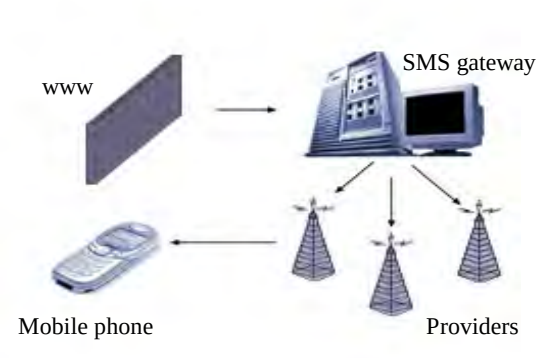

Fig. 4. Sending messages using SMS Gateway

The second approach is a local solution and it involves using a GSM modem or a mobile phone connected to the COM port. There are free software solutions that support many mobile phones, providing a simple, high level interface for programmers. One of these is a server *VisualGSM Lite*, which was developed by company *Visualtron.* [2]

Sending E-mail messages is very simple from most of programming languages. In the next chapter we will show how E-mail messages are sent from a Delphi application. Sending ICQ messages can also be accomplished using ICQ API for developers, which can be found at www.icq.com.

IV. Notification system *StudentAlerts*

In this chapter we will describe an example of a notification system which was developed at the Faculty of Electronic Engineering in Niš. This system called *StudentAlerts* is intended for alerting and notifying students about events they have subscribed for.

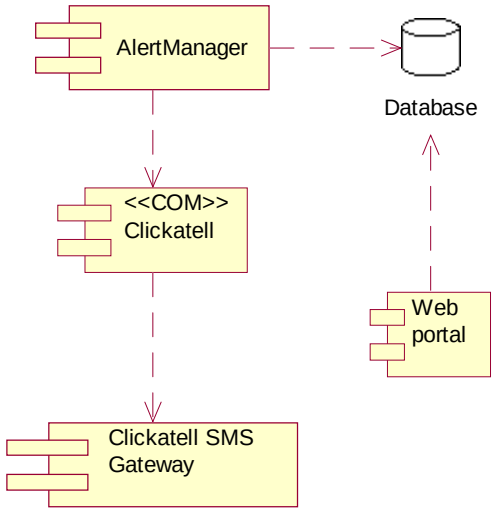

Fig. 5. Basic components of the system *StudentAlerts*

Figure 5 shows the basic components of the system. Students apply for events using Web portal, which is a PHP application. They can change their personal data, like their cell phone number or E-mail address, or they can create new application or delete the old ones. In order to logon to the Web portal, students have usernames and passwords, which can also be modified on the Web site.

All the information important for the application is saved into MySQL database. This is a relational data base, which can be used as a freeware product. Besides, MySQL is very fast and reliable medium for keeping application data. Unfortunately, it has a few problems, like poor user interface and impossibility to automatically maintain the referential integrity. [3]

For setting new events or sending notifications as for maintaining the student data, application *AlertManager* is used. It is created using Delphi7, and has a two-tier , client-server architecture which connects to MySQL database server using *dbExpress* drivers.

Currently, we provide only two ways of alerting: via SMS or E-mail, but we plan to enable alternative ways of notification. For sending E-mails we use *Indy* components, made by company *Nevrona*, which implement SMTP protocol and provide simple interface for developers.

In the system we use *Clickatell*'s SMS gateway [1]. It provides access to its SMS centre using SMPP, SMTP, HTTP, FTP and XML interface. Moreover, programmers of Windows applications can use a COM component that implements HTTP interface and represents a simple and safe way for accessing the SMSC. This option is used in application *AlertManager*, and this is shown in Figure 5.

V. Application *AlertManager*

Application *AlertManager* is a part of the system *StudentAlerts*, and it is used for sending notifications and administration. As we have already mentioned, it is implemented using Delphi 7, with *dbExpress* drivers for accessing *MySql* database via unidirectional cursors. [4]

For sending SMS messages we use *Clickatell* COM component. However, application is designed in a way which enables an easy integration of alternative ways of sending SMS messages (for example, using a different Internet gateway or a local solution like *VisualGSM*). The class diagram which shows how this is accomplished is shown in Figure 6.

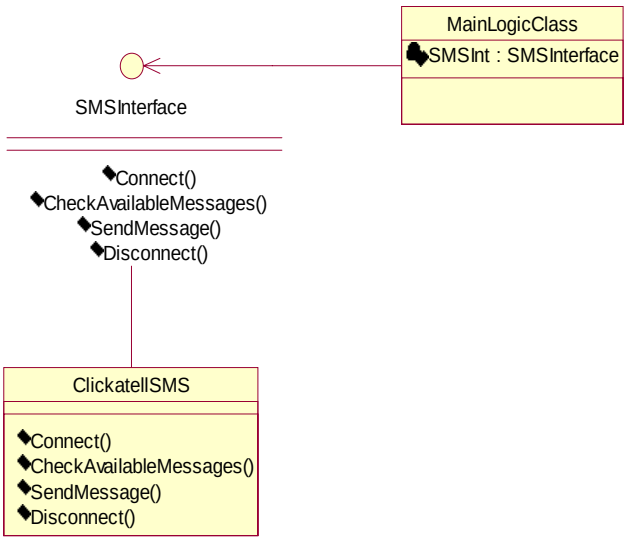

Fig. 6. Classes used for sending SMS messages

Methods for sending SMS messages are grouped into *SMSIneterface*. For every alternative way of sending SMS messages it is necessary to create a separate class that implements *SMSInterface*. Because the client code calls only the interface methods, it is possible to switch between the implementations even during the run time. In this way, a user can choose which provider or gateway he wants to use.

Currently, there is only one way of sending SMS messages, meaning that there is one class that implements *SMSInterface*. Its name is *ClickatellSMS*, and it creates a class *TSMS* which is just a Delphi container for *Clickatell's* COM component.

Application *AlertManager* has very intuitive, *office like* interface and it is very easy to use. It is intended for professors and administrative workers, and its interface varies depending on user privileges.

Figure 7 shows the main application window. On the left side of the main form there is a menu containing categories, while on the right side there are lists showing the elements of the chosen category. Double click on any element of a list opens a detail dialog, which enables changing and saving data. Above every list, there is a toolbar, which is used for adding or deleting the list elements. The toolbar buttons differ depending on the current category.

Categories *Teachers*, *Students* and *Events*, are used for manipulation of data belonging to the respective entities. The most complicated for handling are events and this case is shown on figure 7. Events and student applications are grouped into the master-detail structure. Considering that for one application there can be multiple notifications, applications and notifications are also in the master-detail relation. Toolbar shown on the figure is connected to the currently selected list, although the toolbar actions are a part of a pop-up menu which belongs to the list.

Category *Sent messages* shows all successfully sent messages, where the time of delivery and the codes received from the Clickatell's gateway can be seen in dialog shown on the figure 7. Category *Messages for sending* shows all the messages that have not been sent which are all messages with status *not delivered* or *error on delivery*.

Conclusion

In this paper we presented some basic concepts behind notification systems, and we described common functional and architectural requirements. In the second part, we described a system for student notification, developed at the Faculty of Electronic Engineering in Niš.

It was also shown here that implementation of a notification system involves integration of different technologies. SMS messages are only one example of this. The way this issue is resolved influences the quality of the system itself. That is why it is very important to carefully choose providers or gateways in order to get a reliable application.

References

[1] Clickatell Mobile Solutions, http://www.clickatell.com/brochure/index.php

[2] Visualtron company, http://www.visulatron.com

[3] MySQL Reference Manual, http://www.mysql.com/documentation/manual.php

[4] Marco Cantu, *Mastering Delphi 6*, Sybex, 2001

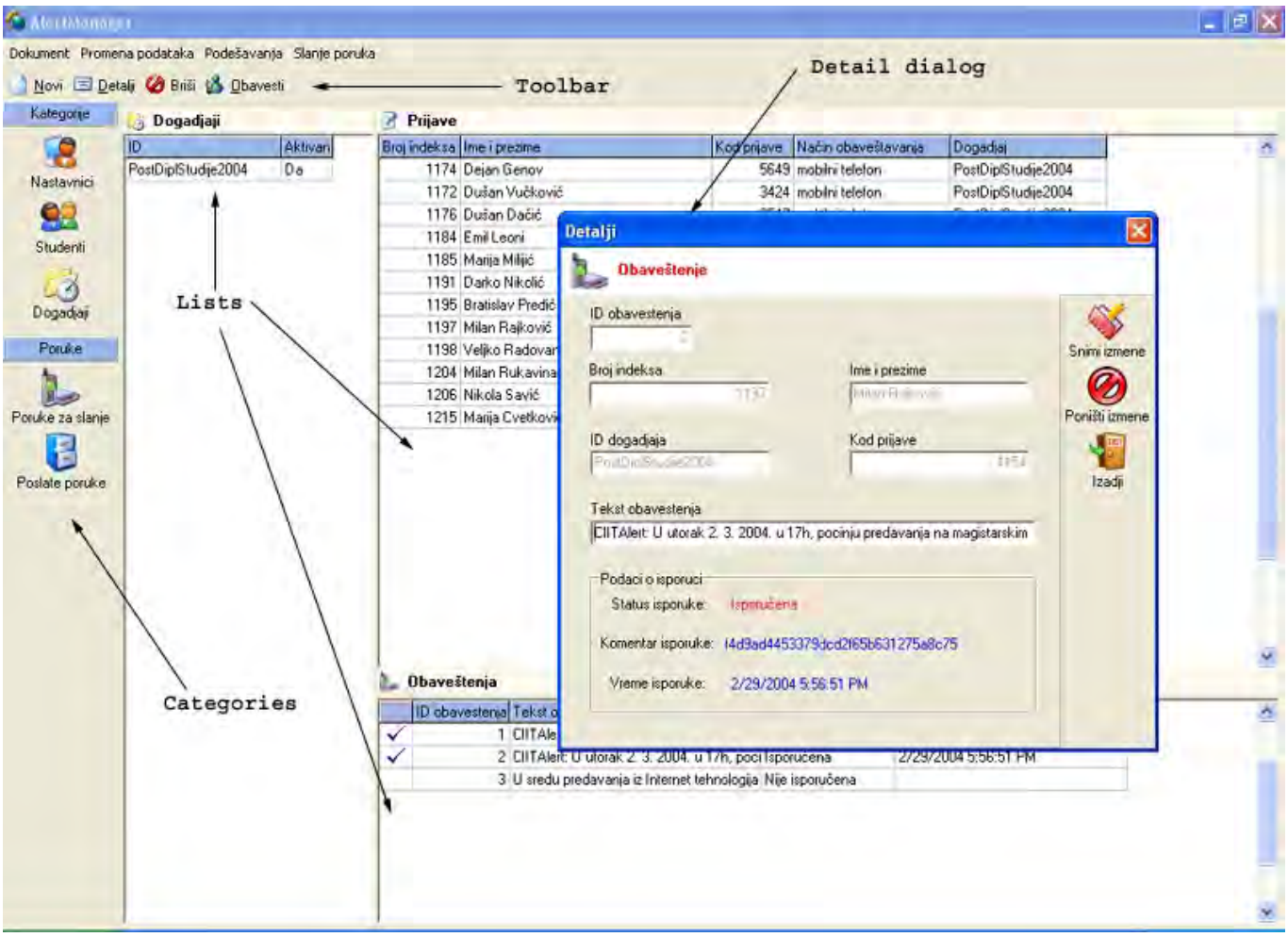

Fig. 7. Application *AlertManager*

Optimal assignment of multi-valued and binary nodes in heterogeneous DDs

Suzana Stojković[1] and Radomir Stanković

Abstract – **Decision diagrams (DDs) are a data structure for representation and manipulation of discrete logic functions efficiently in terms of space and time. Binary Decision Diagrams (BDDs) are the most widely used for representation of Boolean functions. Complexity of BDD representations is usually estimated through the number of nodes in BDDs, usually denoted as the size of BDD. Minimization of size of BDDs is a greatly considered problem in the literature. One of the solutions is the usage of multi-valued and heterogeneous DDs for representing Boolean functions. In this paper, an approach for determination of optimal assignment of multi-valued and binary nodes in heterogeneous DDs is proposed. The paper presents experimental results that verify usefulness of the proposed method.**

Keywords – **Boolean functions, Decision diagrams, Heterogeneous decision diagrams, Minimization of size of decision diagram**

I. INTRODUCTION

Decision diagrams (DDs) are graph-based data structures for representation of discrete functions permitting to represent functions of large number of variables efficiently in terms of space and time [11]. For representing Boolean functions, Binary Decision Diagrams (BDDs) are widely used [2]. Compactness of BDD representations is usually estimated through the number of nodes in the BDDs denoted as the size of BDD. The size of BDDs depends on the order of variables in functions represented by BDDs. Minimization of the size of BDD by reordering of variables is a widely discussed problem, see for example [4], [5], [6], [7] and references therein. Majority of the proposed algorithms for BDD minimization are heuristic and express common disadvantages of heuristic algorithms that does not garantee the quality of solutions provided. Another approach to BDD minimization is by using linear transformations of input variables [5], [6]. Third way for minimization of DD representations of Boolean functions is by using multi-valued DDs (MDDs) [10]. MDDs, in general case, represent multi-valued functions $f:\{0,1,...,q-1\}^n \rightarrow \{0,1,...,q-1\}$. Boolean functions are represented by MDDs by encoding subsets of binary variables by a single multiple-valued variables.

Recently, heterogeneous MDDs are used for Boolean function representation [7], [8], [9]. In heterogeneous DDs, nodes at different levels can have different number of outgoing edges. It is shown that heterogeneous DDs are useful for representation of Boolean functions when priority is: minimization of size and cost of DDs expressed as the number of nodes and cost of nodes, minimization of the average path length in DDs, etc.

In this paper, we propose a method to determine an optimal assignment of multi-valued and binary nodes in heterogeneous DDs when the size of DD should be minimized.

II. MINIMIZATION OF DD SIZE

A. Minimization of DD by reordering of variables

Size of DD is defined as the number of non-terminal nodes in the DD. The size of a DD depends on the order of variables assigned to the levels of the DD.

Example 1. 1Fig. 1 and shows BDDs for a function $f(x_1,x_2,x_3)=x_1x_3+x_2$ for the order of variables (*a*) (x_1,x_2,x_3), and (*b*) (x_2,x_1,x_3). These BDDs have 4 and 3 non-terminal nodes, respectively. Thus, in this example, permutation of variables x_1 and x_2 permits reduction of a non-terminal node.

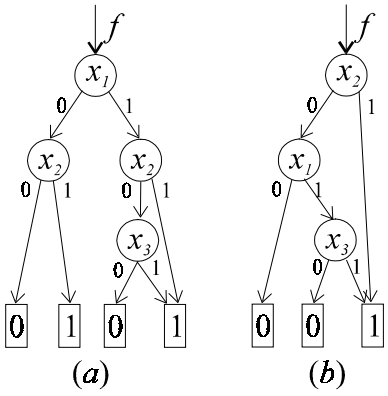

Fig. 1 BDDs for the function f in Example 1.

Exact algorithms for optimal order of variables reuce to brute search methods. Heuristic algorithms are based on dynamic reordering and sifting of variables [3].

B. DD Minimization by using of MDDs

Boolean function of *n*k* binary variables can be alternatively viewed as a binary-valued function of *n* 2^k-valued variables. In this approach, a subset of *k* binary-valued variables is replaced by a single 2^k-valued variable. Due to

[1] The authors are with Dept. of Computer Science, Faculty of Electronic Engeneering, Beogradska 14, 18000 Niš, Serbia and Montenegro, e-mail: suza@elfak.ni.ac.yu.

this encoding, Boolean functions can be represented by MDDs.

Example 2. Fig. 2 shows that a Boolean function

$$f(x_1,x_2,x_3,x_4)= x_1x_2 + x_2x_3 + x_3x_4 + x_4x_1$$

can be represented by BDD with 6 non-terminal nodes and or by a 4-valued MDD with four non-terminal nodes.

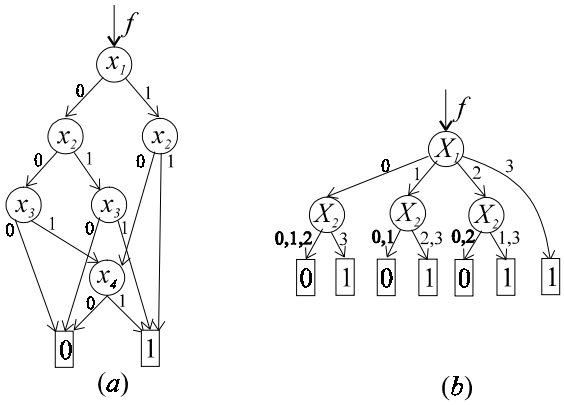

Fig. 2 BDD and 4-valued MDD for the function *f* in Example 2.

In estimation of the const of a DD, it is usually assumed that the cost of a node is proportional to the number of outgoing edges. In this setting, the cost of a multi-valued node (the node with *q* outgoing edges) is greater then the cost of a binary-valued node. Due to that, the usage of MDDs is not always efficient. If we assume that the cost of a non-terminal node is *K*number of edges*, where *K* is the size of the DD, the cost of the BDD in Fig. 2 (*a*) is a *12K*, but the cost of MDD in Fig. 2 (*b*) is *16K*. It follows that usage of MDD, in that case, is not justified. Another disadvantage of representation of Boolean functions by MDDs is the requirement for the relationship between the number of binary variables and the number of outgoing edges of multiple-valued nodes that must be satisfied. In particular, MDDs with 2^k-valued variables can be applied for representation of Boolean functions with *n*k* binary variables.

III. HETEROGENEOUS DDS

When a Boolean function is represented by a MDD, the set of input variables is partitioned into subsets of the same cardinality. In heterogeneous DDs, the set of input variables is partitioned in subsets of different cardinality. Therefore, in heterogeneous DDs non-terminal nodes at different levels can have different number of outgoing edges.

Example 3. Fig. 3 shows three heterogeneous DDs representing the function f in Example when the set of input variables (x_1,x_2,x_3,x_4) is partitioned into subsets (X_1,X_2,X_3), where:

(a) $X_1 = (x_1)$, $X_2 = (x_2)$ and $X_3 = (x_3,x_4)$.

(b) $X_1 = (x_1)$, $X_2 = (x_2,x_3)$ and $X_3 = (x_4)$.

(c) $X_1 = (x_1,x_2)$, $X_2 = (x_3)$ and $X_3 = (x_4)$.

Size of the first DD is 6 and number of its 4-valued non-terminal nodes is 3 (its total cost is *18K*). Size of the second DD is 4 and number of its non-terminal 4-valued non-terminal nodes is 2 (its total cost is *8K*). Size of third DD is also 4, but the number of 4-valued non-terminal nodes is 1 (its total cost is *6K*). It shows that heterogeneous DD shown in Fig. 3 (*c*) is the most efficient for representing the considered Boolean function.

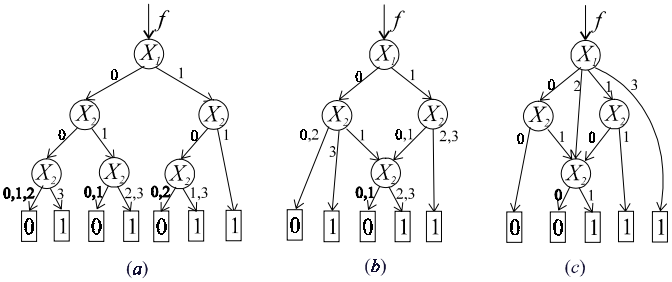

Fig. 3 Three different heterogeneous DDs for f in Example 3.

From the considerations in Example, the following question arises. Which assignment of multi-valued and binary-valued nodes produces a heterogeneous DD with the smallest cost for a given Boolean function *f*? When a subset of binary-valued variables $(x_j,\ldots x_{j+k-1})$ is replaced by a 2^k-valued variable, nodes at the levels j+1,...,j+k-1 are deleted from DD. For determination of subsets of variables which should be replaced by multi-valued variables, two criteria are imposed:

- Replacement is reasonable when the number of new nodes (that must be created at the level *j*) is smaller than the number of deleted nodes.
- Heterogeneous DD will be of the minimum size if levels with the maximal number of non-terminal nodes will be deleted.

IV. MAXIMAL POSSIBLE SIZE OF LEVELS IN BDD

Consider an *n*-variable Boolean function *f*. Denote the number of non-terminal nodes at the level *k* in a BDD by *width*(BDD,*k*). Then, *width*(BDD,*k*) is limited by two ways:

1. *width*(BDD,*k*)≤*width*(BDT,*k*), where BDT denotes a Binary Decision Tree from which BDD is derived by the application of the BDD reduction rules [11]. Recall that the number of non-terminal nodes at the *k*-th level in the BDT is equal to 2^{k-1}. It follows that:

$$width(\text{BDD},k) \le 2^{k-1} \quad (1)$$

i.e.,

$$max\_wl(\text{BDD},k) = 2^{k-1} \quad (2)$$

2. *width*(BDD,*k*) is also limited by the number of possible successors. A successor of a node at the level *k* can be any node from the levels *k*+1, ... , *n*, *n*+1. Number of possible nodes at the level *n*+1 is 2 (these are terminal nodes 0 and 1). Number of possible nodes at the levels *n*, *n*-1,...,1 can be calculated by:

$$width(\text{BDD},k) \le \left(\sum_{i=k+1}^{n+1} width(\text{BDD},i) \right)^2 - \sum_{i=k+1}^{n+1} width(\text{BDD},i) \quad (3)$$

i. e.,

$$maxw2(\text{BDD},k) = \left(\sum_{i=k+1}^{n+1} maxw2(\text{BDD},i) \right)^2 - \sum_{i=k+1}^{n+1} maxw2(\text{BDD},i)$$
$$= 2^{2^{n-k+1}} - 2^{2^{n-k}} \quad (4)$$

Generally:

$$max\_width(\text{BDD},k) = \mathbf{min(}maxw1(\text{BDD},k)\mathbf{,}maxw2(\text{BDD},k)\mathbf{)}$$
$$= \min(2^{k-1}, 2^{2^{n-k+1}} - 2^{2^{n-k}}) \quad (5)$$

It follows that the level with the maximum possible size in a BDD (denoted by $L_{\max}$) is:

$$L_{\max} = n - k \text{ , for } n \in \left[2^k + k + 1, 2^{k+1} + k + 1\right]. \quad (6)$$

Values of $L_{\max}$ for different number of variables are shown in Table 1. In this table, [i,j] shows the values i=2^k+k+1 and j=2^{k+1}+k+1 determined in (6).

TABLE 1
VALUES OF L_{MAX} FOR DIFFERENT VARIABLES NUMBER

N	[2,3]	[4,6]	[7,11]	[12,20]	[21,37]	[38,70]	[71,135]
$L_{\max}$	n	n-1	n-2	n-3	n-4	n-5	n-6

max_width(BDD,k) for the levels less than $L_{\max}$ is equal to *maxw*1(BDD,k) and for the levels great then $L_{\max}$ is equal to *maxw*2(BDD,k).

V. DETERMINATION OF OPTIMAL ASSIGNMENT OF MULTI-VALUED AND BINARY NODES

In a BDD, multi-valued variables are introduced by attempting to replace the maximum possible number of binary nodes by the minimum number of multi-valued nodes. Due to that, the level $L_{\max}$ has to be deleted obligatory. If 4-valued variables are used, one partition of input variables must be ($x_{L\max-1}$,$x_{L\max}$). If one multi-valued variable replaces more than two binary variables, many partitions of the set of input variables containing $x_{L\max}$ can be defined. DD will be of the minimum size when the partition ($x_{L\max-k+1}$,…,$xL_{\max}$) is replaced by one 2^k-valued variable, because *max_width*(BDD,k) quickly decreases from the level $L_{\max}$ to the terminal level, then from the level $L_{\max}$ to the root level.

If in a given function f the set of binary variables $(x_j,\ldots x_{j+k-1})$ is replaced by a 2^k-valued variable, then max*w*1(DD,j), could not be changed (it is equal to 2^{j-1} independently of the cardinalities of other partitions of the set of input variables). In that case, max*w*2(DD,j) would be:

$$maxw2(\text{DD},j) = \left(\sum_{i=j+k}^{n+1} maxw2(\text{BDD},i) \right)^{2^k} - \sum_{i=j+k}^{n+1} maxw2(\text{BDD},i)$$
$$= 2^{2^{n-j+1}} - 2^{2^{n-j-k+1}} = \sum_{i=j}^{j+k-1} maxw2(\text{BDD},i). \quad (7)$$

Equation (7) shows that after replacement of binary nodes by multiple-valued nodes, the maximum number of 2^k-valued nodes at the level j (for j great then $L_{\max}$) is equal to the sum of maximum number of binary nodes at all levels which are changed. It follows that by replacing binary variables from levels greater than $L_{\max}$ by multi-valued nodes is not reasonable. It follows that, when multi-valued nodes are introduced, partitions of the set of input variables should be done by starting from the level $L_{\max}$ to the root node.

VI. EXPERIMENTAL RESULTS

Theoretical considerations, presented in sections IV and V were verified by experimental results. We performed two groups of experiments. In the first, we represented 100 randomly generated functions of 10 variables by different heterogeneous DDs. It is assumed that a function can take the value 0 or 1 with equal probability. **TABLE 3** shows average sizes and average numbers of multi-valued nodes (MVNN) in DDs with the specified assignment of nodes. In the second group, we performed experiments on representing functions of four variables. TABLE 2 shows numbers of functions of defined size for different types of heterogeneous DDs.

In the first, in both groups of experiments, heterogeneous DDs with one multi-valued variable were generated. Rows 2-10 of **TABLE 3** contain data about heterogeneous DDs of functions of 10 variables with one 4-valued node. In that group, DD of minimal size is the DD in which multi-valued variable replaces pair of input variables (x_7,x_8), i. e. ($x_{L\max-1}$,$x_{L\max}$) because $L_{\max}$=8 for n=10. The same proposition is verified by comparison of sizes of DDs with one 8-valued non-terminal node. Data about those DDs are shown in rows 11-18. Minimal size in that group has the DD where the 8-valued variable replaces input variables (x_6,x_7,x_8).

In BDDs with four levels, $L_{\max}$=3. It follows that the optimal partition of input variables when 4-valued nodes are used in heterogeneous DDs is: X_1=(x_1), X_2=(x_2,x_3), X_3=(x_4); and when 8-valued nodes are used: X_1=(x_1,x_2,x_3), X_2=(x_4). TABLE 2 shows that for these partitions the size of DDs is minimum.

Then, we have generated heterogeneous DDs with maximal number of multi-valued non-terminal nodes. We performed experiments by using 4-valued and 8-valued non-terminal nodes. The conclusion is that partitioning should be done from the level $L_{\max}$ to the root level. The optimal partitions of the set of 10 input variables when 4-valued 8-valued variables are used are, respectively:

X_1=(x_1,x_2), X_2=(x_3,x_4), X_3=(x_5,x_6), X_4=(x_7,x_8), X_5=(x_9), X_6=(x_{10});

and

X_1=(x_1), X_2=(x_2), X_3=(x_3,x_4,x_5), X_4=(x_6,x_7,x_8), X_5=(x_9), X_6=(x_{10}).

Rows 19 and 20 show that the homogeneous 4-valued MDD and heterogeneous DD with induced optimal assignment of multi-valued and binary nodes have equal sizes. Heterogeneous DD is a better solution in that case, because the cost of binary nodes is smaller. Proposition that changing binary variables from levels greater than $L_{\max}$ by multi-valued variables has no effect on the size of the DD is confirmed by comparison of sizes of BDD and heterogeneous DD with one

TABLE 2
NUMBERS OF FUNCTIONS OF 4 VARIABLES REQUIRING DDS OF THE SPECIFIED SIZES

nodes arrangement \ size	0	1	2	3	4	5	6	7	8	9
2-2-2-2	2	8	48	236	960	3248	8928	17666	23280	11160
2-2-4	2	18	120	758	3304	11102	26208	24024		
2-4-2	2	18	192	1118	12784	51422				
4-2-2	2	18	264	2054	8056	18542	25440	11160		
2-8	2	256	1016	64262						
8-2	2	256	12608	52670						

4-valued variable (by replacing variables x_9 and x_{10}) (see rows 1 and 2 in **TABLE 3**).

At the end, sizes of determinated optimal heterogeneous DD with 8-valued variables was compared with sizes of heterogeneous DDs with maximum possible number of 8-valued variables, i.e., with DDs having three 8-valued variables and one binary variable (see rows 21-25 in **TABLE 3**). It was verified that theoretically determined optimal solution is really optimal.

TABLE 3
AVERAGE SIZES OF DIFFERENT HETEROGENEOUS DDS REPRESENTING FUNCTIONS OF 10 BINARY VARIABLES

No.	Nodes arrangement	DD size	MVNN
1.	2-2-2-2-2-2-2-2-2-2	235.49	
2.	2-2-2-2-2-2-2-2-4	235.49	14
3.	2-2-2-2-2-2-2-4-2	228.09	99.26
4.	2-2-2-2-2-2-4-2-2	140.96	63.96
5.	2-2-2-2-2-4-2-2-2	171.66	32
6.	2-2-2-2-4-2-2-2-2	203.49	16
7.	2-2-2-4-2-2-2-2-2	219.49	8
8.	2-2-4-2-2-2-2-2-2	227.49	4
9.	2-4-2-2-2-2-2-2-2	231.49	2
10.	4-2-2-2-2-2-2-2-2	233.49	1
11.	2-2-2-2-2-2-2-8	226.84	100.01
12.	2-2-2-2-2-2-8-2	128.97	63.97
13.	2-2-2-2-2-8-2-2	77	32
14.	2-2-2-2-8-2-2-2	139.66	16
15.	2-2-2-8-2-2-2-2	187.49	8
16.	2-2-8-2-2-2-2-2	211.49	4
17.	2-8-2-2-2-2-2-2	223.49	2
18.	8-2-2-2-2-2-2-2	229.49	1
19.	4-4-4-4-4	98.96	98.96
20.	4-4-4-4-2-2	98.96	84.96
21.	2-8-8-8	119.01	118.01
22.	8-2-8-8	125.01	117.01
23.	8-8-2-8	172.84	109.01
24.	8-8-8-2	74.97	72.97
25.	2-2-8-8-2-2	53	36

VII. CONCLUSION

In this paper, we presented principles for determination of the optimal assignments of multi-valued and binary nodes in heterogeneous DDs. This principle proposes that partition of the set of binary-valued input variables into subsets of variables (that will be replaced by multi-valued variables) has to be done by starting from the level with the maximum possible number of nodes to the root level. A formula for computation of the level with maximal possible number of non-terminal nodes in BDD is determined.

Experimental results that verify all the presented theoretical considerations are provided.

REFERENCES

[1] K. S. Brace, R. L. Rudell, R. E. Bryant, "Efficient implementation of a BDD package", In Design Automation Conference, pp. 417-421, San Francisko, Juny 1991.

[2] R. E. Bryant, "Graph-based algorithms for Boolean functions manipulation", IEEE Trans. on Computers, Vol. C-35, No. 8, 677-691, August 1986.

[3] R. E. Bryant, "Binary Decision Diagrams and Beyond: Enabling Tehnologies for Formal Verification", International Conference on Computer-Aided Design ICCAD '95, pp. 236-243, November, 1995.

[4] S.W. Jeong, T.S. Kim, and F. Somenzi, "An efficient method for optimal BDD ordering computation" In *International Conference on VLSI and CAD (ICVC'93)*, Taejon, Korea, November 1993.,

[5] W. Gunther, R. Drechler, "BDD Minimization by Linear Transformations", International Workshor on Boolean Problems, Freiberg, 1998.

[6] W. Gunther, R. Drechler, "Linear Transformations and Exact Minimization of BDDs", IEEE Great Likes Symposium on VLSI, pp. 325-330, Lafayette, 1998.

[7] S. Nagayama, T. Sasao, "Minimization of Memory Size for Hetrogeneous MDDs", ASP-DAC 2004 (Asia and South Pacific Design Automation Conference 2004) , pp. 872-875, Yokohama, Jan. 27-30, 2004.

[8] S. Nagayama, T. Sasao, "Compact Representation of Logic Functions using Hetrogeneous MDDs", 33rd International Symposium on Multiple-Valued Logic, pp. 247-255, Tokyo, May 16-19, 2003.

[9] S. Nagayama, T. Sasao, "Compact Representation of Logic Functions using Hetrogeneous MDDs", IEICE Transactions on Fundamentals of Electronics, Vol. E86-A, No. 12, pp. 3168-3175, Dec. 2003.

[10] T. Sasao, J. T. Butler, "A design Method for Look-up Table Type FPGA by Pseudo-Kronecker Expansion", Proceedings of 24-th International Symposium on Multiple-Valued logic, pp. 97-106, Boston, MA, May 25-27, 1994.

[11] T. Sasao, M. Fujita, Representatiosn of Discrete Functions, Kluwer Academic Publishers, 1995.

Computation Model of *p*-adic Arithmetic

Borislav P. Stoyanov[1], Borislav Y. Bedzhev[2] and Zhivko S. Zhekov[3]

***Abstract*—The classical computing with floating point data presentation accumulates small errors at every step. As a consequence some times the final result of a complex program is entirely false. With regard to this, our paper suggests a computation model of *p*-adic arithmetic using exact Hensel code presentation in Visual C++ environment. It could be applied successfully for developing of stream ciphers with *Feedback with Carry Shift Register* architecture and for synthesis of pseudorandom sequences with variety of statistical properties.**

***Keywords*—Programming, Cryptography, Communication system signaling.**

I. INTRODUCTION

The classical computing algorithms, based on floating point data presentation, accumulate small errors at every step. As a consequence some times the final result of a long and complex program is much distorted or even so entirely false. This situation motivated active researches directed to finding more powerful and accurate computing tools able to interpret with insight a given science or technical problem. The efforts in this area leaded to developing of new methods of computer programming and data expressing. One of them proposed recently, is the method of the so-named *p*-adic arithmetic [1], [4], [6], [7], [8]. It seems to be very effective in some applications such as orthogonal signal synthesis, cryptography, spread spectrum systems and so on. The positive features of this method will be clarified with following example. Let us consider the recursive filter which output u_i in time moment $i.\tau$ (τ denotes the clock period of the filter) is:

$$u_i = u_{i-1} + u_{i-2};\ \ u_0 = u_1 = 1. \tag{1}$$

The output can be determined using two approaches. The simpler one consists in recursive (step by step) computing of the consecutive outputs u_2, u_3, …, u_i. This way needs *i* steps and hence a lot of time for large i. The second possible approach is that of using the Eq. (2):

$$u_i = \frac{1}{\sqrt{5}}.\left[\frac{(1+\sqrt{5})^i}{2} - \frac{(1-\sqrt{5})^i}{2}\right] \tag{2}$$

The Eq. (2) gives the result directly (in $\lfloor \log_2 i \rfloor + 1$ steps), but here a problem is the impossibility to represent the irrational number $\sqrt{5}$ exactly. This obstacle can be avoided applying the method of *p*-adic arithmetic. For instance, the number $\sqrt{5}$ has the following 11-adic exact representation (7606, 0) [7]. Hence, the filter output u_i can be calculated using Eq. (2) and 11-adic arithmetic in $\lfloor \log_2 i \rfloor + 1$ steps. The final result will be obtained with great accuracy after transforming in usual arithmetic.

With regard to the all above cited, this paper aims to suggest a computation model of *p*-adic arithmetic using exact Hensel code presentation in Visual C++ environment.

The paper is organized as follows. First, the basics of *p*-adic arithmetic are recalled. After then, the computation model of *p*-adic arithmetic using exact Hensel code presentation in Visual C++ environment is described. Finally, the advantages and possible areas of application of our model are discussed.

II. BASICS OF *P*-ADIC ARITHMETIC

We will explain the bases of the *p*-adic arithmetic refer to [1], [4] , [6].

For any positive integer *m*, denote $\mathbf{Z}_m$ the ring of integers modulo *m* and by |.| - the canonical ring homomorphism from $\mathbf{Z}$ to $\mathbf{Z}_m$. Let $\mathbf{N}$ be the set of natural numbers. For a given prime *p*, a rational number $\alpha = a / b$ can be represented in a unique way as is Eq. (3):

$$\alpha = (c/d) * p^e, \tag{3}$$

where *c*, *d* and *e* are integers, *c*, *d* and *p* pairwise relatively prime, *d* and *p* positive. This kind of representation of rational numbers is called the normalized form.

The function in Eq. (4)

$$\|.\|_p : Q \to R \tag{4}$$

[1]Borislav P. Stoyanov is with the Faculty of Mathematics, Informatics and Economics, Shumen University, 1 Universitetska Str., 9700 Shoumen, Bulgaria, E-mail: bpstoyanov@abv.bg

[2]Borislav Y. Bedzhev is with the Faculty of Artillery, Air Defense and Communication Information System, National Military University, 1 Karel Shkorpil Str., 9713 Shoumen, Bulgaria, E-mail: bedzhev@mail.pv-ma.bg

[3]Zhivko S. Zhekov is with Space Research Institute, Bulgarian Science Academy, PIO Box 118, 9700 Shoumen, Bulgaria, E-mail: zhekov@yahoo.com

from the rational numbers Q to the real numbers R, defined as in Eq. (5)

$$\| \alpha \|_p = \begin{cases} p^{-e}, if\ \alpha \neq 0 \\ 0\ \ , if\ \alpha = 0 \end{cases} \quad (5)$$

is a norm on Q, called the p-adic norm [4]. Furthermore α can be uniquely expressed in the following form in Eq. (6):

$$\alpha = \sum_{i \geq e} a_i p^i, \quad (6)$$

where $a_i \in \mathbf{Z}_p$. The infinite sequence $(a_e a_{e+1} \ldots a_{-1} a_0 a_{+1} \ldots)$ is called *p-adic representation* of α. The p-adic expansion of a rational number is periodic and it can also assume the following form: $\alpha = (a_e a_{e+1} \ldots a_{-1 \ldots} a_{k-m-1}{}' a_{k-m} \ldots a_{k-1} a_k)$, where the m digits from a_{k-m} to a_k constitute the period.

For instance, above mentioned 11-adic representation (7606, 0) of the irrational number $\sqrt{5}$ means that $a_0 = 7,\ a_1 = 6,\ a_2 = 0,\ a_3 = 6,\ a_4 = a_5 = ... = 0$ in Eq. (6).

We use *truncated representation*, defined as follows.

Definition *1* **(Hensel Code).** Given a prime number p, a Hensel code of length r of any rational number $\alpha = (c / d)*p^e$ is a pair of Eq. (7):

$$\left| c * d^{-1} \right|_{p^r} = \sum_{i=0}^{r-1} a_i \cdot p^i \in \mathrm{Z}_{p^r} \cdot \quad (7)$$

Let $\mathbf{H}_{p,r}$ denote the set of all Hensel codes where subscripts mean the prime p and the approximation r respectively, and let $\mathbf{H}(p, r, \alpha)$ indicate the Hensel code representation of the rational number $\alpha = (a / b)*p^e$.

The forward mapping between rational numbers and Hensel codes can then be defined on the bases of the following theorem.

Theorem *1* **(Forward Mapping)**. Given a prime p, an integer r and a rational number $\alpha = (c / d)*p^e$, such that c, d and p pairwise relatively prime integers, the mantissa $mant_\alpha$ of the code related to the rational number α, is computed by the Extended Euclidean Algorithm (EEA) [10] applied to p^r and d as: $mant_\alpha \equiv c \,.\, y \pmod{p^r}$, where y is the second output of the EEA.

Definition *2* **(Farey Fraction Set).** Let

$$\mathrm{N}_{(p,r)} = \left\lfloor \sqrt{\frac{p^r - 1}{2}} \right\rfloor \quad (8)$$

The Farey fraction set $\mathbf{F}_{p,r}$ of order $\mathbf{N}_{(p,r)}$ is the subset of rational numbers a / b such that: a,b $\in \mathbf{N}$, $0 \leq a \leq \mathbf{N}_{(p,r)}$, $0 < b \leq \mathbf{N}_{(p,r)}$.

Arithmetic operations on Hensel codes are carried out, digit by digit, starting for the leftmost digit, as in the usual base-p arithmetic operations. An addition (or subtraction) can give a result in which some leftmost digits are equal to zero. In this case we make the addition (or subtraction) produced in a *pseudo-Hensel code*.

Definition *3* **(Pseudo-Hensel codes)**. A pseudo-Hensel code is a code such that $a_0 = \ldots = a_k = 0$, for some k with $0 < k \leq r$-1.

Theorem *2*. Given a prime p, an approximation r, given an arithmetic operator Φ in Q and the related arithmetic operator $\Phi' \in \mathbf{H}_{p,r}$, if $\mathbf{H}(p, r, \alpha_1)\ \Phi'\ \mathbf{H}(p, r, \alpha_2) = \alpha_3'$, then there exists only one $\alpha_3 \in \mathbf{F}_{p,r}$, such that $\alpha_3' = \alpha_3$.

Now let us consider the arithmetic operations in $\mathbf{H}_{p,r}$.

Addition. Given two Hensel codes $\mathbf{H}(p, r, \alpha) = (mant_\alpha , exp_\alpha)$ and $\mathbf{H}(p, r, \beta) = (mant_\beta , exp_\beta)$, first of all we must remove the smaller mantissa to the right side in order to obtain $exp_\alpha = exp_\beta$. After that perform the addition taking into account that all the operations are carried out from left to right.

Subtraction. The subtraction could be performed using two approaches.

First, we can compute the complement *mod* p^r of the minuend and then to carry out the addition.

Second, if the minuend is a pseudo-Hensel code, then the subtraction can be carried out in the usual way, without using the complement of the minuend (except in the case when the subtrahend is the Hensel code which represents zero). In this situation in order to carry out the subtraction we must get a p-adic unit from the right digit (instead of from the left digit, as usually happens in subtraction between two integer numbers).

Multiplication. When we perform multiplication we must operate by multiplying the respective mantissas of the codes, and then we must add their exponents. Also in this case the code result is truncated to r digits.

Division. In order to perform division we must operate by dividing the respective mantissas of the codes, and then we must subtract the respective exponents.

If the first digit of the divisor is zero, we cannot compute the modular inverse as stated in the classical algorithm. Nevertheless we can carry on with the computation, because the code approximation has not been decreased, but if we want to compute a division in which the dividend belongs to $\mathbf{H}_{p,r}$ and the divisor is a pseudo-Hensel code of order k, with $k < r$. We can appropriately manipulate these codes with algorithm "Lim92" [7], in order to apply the division algorithm. In this way we can avoid the loss of significant digits and we can manipulate the pseudo-Hensel codes in the same way as the Hensel codes.

III. COMPUTATION MODEL OF *P*-ADIC ARITHMETIC

We propose a computation model of the p-adic arithmetic in exact Hensel code presentation in Visual C++ environment. The model is based on two files *p_adic.h* and *p_adic.cpp*. Our class *p_adic* has the following structure:

```
class p_adic : CObject{
public:
    long a;                    //numerator
    long b;                    //denominator
    long sign;                 //sign of the rational number
    long c;                    //numerator after elimination
    long d;                   //denominator after elimination
    long base;                 //p-adic base
    long ord;                  //exponent in the elimination
    long prec;                 //precision
    long cd_pr;                //c*d^-1 mod p^r
    CArray<int, int>mantisa;     // mantisa
}
```

The class *p_adic* has two constructors.

The first is *p_adic(CString &m, long e, long s, long p, long r)*. It creates expansion from *CString*, where *e* is the exponent, *s* – the sign of the exponent, *p* means the *p*-adic base and *r* – the approximation. For example, if the initial parameters are *m* = "4333", *e* = 2, *s* = -1, *p* = 5 and *r* = 4 then after execution of this constructor the next elements receive the values: *base* = 5, *ord* = -2, *prec* = 4, *mantisa* = (4, 3, 3, 3).

The second constructor is *p_adic(long x, long y, long p, long s, long r)*. It creates expansion from rational number, where *x* is the numerator, *y* – denominator, *p* – *p*-adic base, *s* – sign of the rational number, *r* - the approximation. If we have *x* = 4, *y* = 3255, *s* = -1, *p* = 3, *r* = 10 then the created object will have *a* = 4, *b* = 3255, *sign* = -1, *c* = 4, *d* = 1085, base = 3, *ord* = -1, *prec* = 10, *cd_pr* = 53389, *mantisa* = (1, 0, 1, 0, 2, 0, 1, 0, 2, 2).

The obtaining of the class elements depends on few auxiliary member functions.

The member function *void elimination(long &x, long &y,long &e, long p)* creates from a given rational number *a / b* the rational number from Eq. (3) with the help of the member function *long gcd(long x, long y)*. It returns the greatest common divisor [10] from *x* and *y* and *long fract_ord(long *x, long *y, long p)* returns the exponent *e* from Eq. (3).

The member function *long integer_part(long c, long d, long s, long pr)* calculates the long number *cd_pr* by computing of $c*d^{-1} \bmod p^r$, with the help of the member function *long inverse(long a, long n)*, which returns $a^{-1} \bmod n$.

The member function *void expansion(long cd_pr)* creates the *p*-adic expansion from *cd_pr* and put it in *mantisa*.

We have realized in the class *p_adic* the following four basic operations:

Addition - void sum(p_adic y, p_adic z)*. For example, if we have 34/4 + 2/7 in $\mathbf{H}_{2,5}$, the result is (1 0 1 1 0, -1).

Subtraction - void sub(p_adic y, p_adic* z)*. For example, if we have 15/9 – 2/28 in $\mathbf{H}_{3,7}$, the result is (2 2 2 2 1 0 0, -1).

Multiplication - void mul(p_adic y, p_adic* z)*. For example, if we have 50/7 * 2/23 in $\mathbf{H}_{7,6}$, the result is (1 2 1 5 2 6, -1).

*Division – void div_norm(p_adic *y, p_adic *z)*. For example, if we have 2/3 / (-51/9) in $\mathbf{H}_{7,9}$, the result is (4 6 4 3 4 1 1 6 2, 0).

The class *p_adic* with the *p*-adic member functions can be included as a part in projects with *p*-adic calculations. To illustrate this we propose an application "Hensel exact calculation" - hcalc.exe for executing *p*-adic arithmetic in Hensel code.

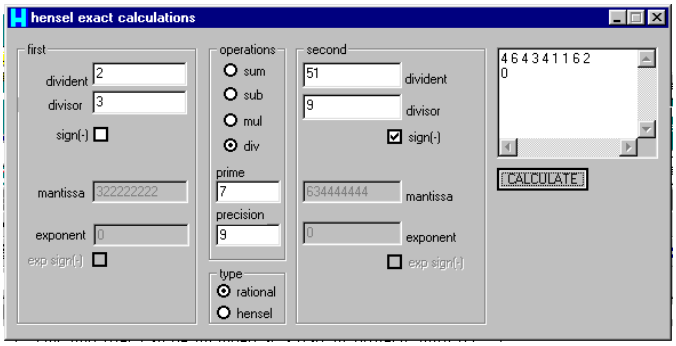

Fig. 1. Expansion from rational numbers

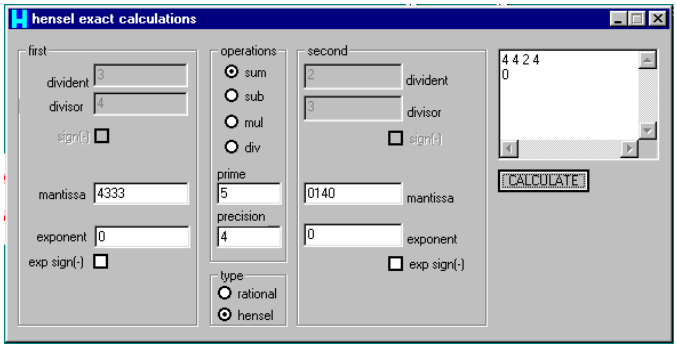

Fig. 2. Expansion from string

Here, according to the two constructors, we have two kind of *p*-adic expansion obtaining: first, from rational numbers as it is shown on Fig. 1 and second, from string (see Fig. 2).

IV. Conclusion

The advantages of proposed in our work *p*-adic computation modeling will be clarified by following example. Let us consider the modern stream ciphers, which are designed by combining the outputs of several *Linear Feedback Shift Registers* (*LFSR*). Here one new direction of development was proposed from Klapper and Goresky recently [5]. It will be explained using Fig. 3.

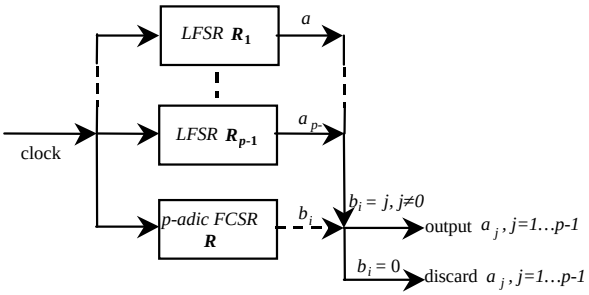

Fig 3. The Shrinking Generator with *p*-adic controlling *FCSR*

How it is shown, the Klapper & Goresky's stream cipher uses a controling *p*-adic *Feedback with Carry Shift Register (FCSR) R* to select a portion of the output sequences of *LFSRs* from R_1 to R_{p-1}. Therefore, the produced keystream is a *shrunken and mixed* version of the output sequences of *LFSRs* R_1 to R_{p-1} as it is specified in Fig. 3.

The algorithm of shrinking generator with controlling *p*-adic *FCSR* consists of the following steps:

1. All *LFSRs* from R_1 to R_{p-1} and *FCSR R* are clocked.

2. If the *p*-adic output $b_i = j$ of control register *R* is not equal to 0, the output bit of register R_j forms part of the keystream. Otherwise, if the output $b_i = 0$ of control register *R* is equal to 0, the all output bits are discarded.

In the origin papers of Klapper and Goresky only the case $p = 2$ is studied comprehensively [5]. It is shown [3], that the shrinking generator from Fig. 3 could use a generalization of *FCSRs* with stage contents and feedback coefficients in $\mathbf{Z}_p$ where *p* is a prime number, not necessarily 2. It is shown [5], that the work of the controlling *FCSR* depends on the initial loading of the register. Namely, the controlling *FCSR* ought to calculate the *p*-adic expression of a certain rational number $\alpha = (c/d) * p^e$, where *c*, *d* and *e* are integers, according to conditions in Eq. (3). Moreover, the initial loading of the *FCSR* register have to be:

$$a_0 + a_1.p + \ldots + a_{r-1}.p^{r-1} = \frac{c}{d} \bmod p^r . \qquad (9)$$

Here *r* is the number of cells tapped in the controlling *FCSR*.

It is not hard to see that usage of our class *p_adic*, proposed above, provides the finding of the necessary initial loading of the controlling *FCSR*.

From all the above stated and from [2], it is easy to see that the computation modeling of *p*-adic arithmetic, proposed in the paper, could be applied successfully for:

- developing of stream ciphers with *Feedback with Carry Shift Register* architecture;

- synthesis of pseudorandom sequences with variety of statistical properties such high linear span, low autocorrelation side-lobes and pair wise cross-correlation values, pair wise hamming distance.

ACKNOWLEDGEMENT

Authors would to thank Professor Carla Limongelli, who kindly give us opportunity to use her PhD thesis. We also acknowledge to Professor Rusin Petrov, whose observations made the drafting of the paper the best possible.

REFERENCES

[1] A. J. Baker, "An Introduction to *p*-adic Numbers and p-adic Analysis", Departament of Mathematics, University of Glasgow G12 8QW, Scotland, 2003.

[2] B. Y. Bedzhev, Zh. N. Tasheva, V. A. Mutkov, "CDMA Codes for the Next Generation Mobile Communication Systems", XII International Symposium of Theoretical Electrical Engineering ISTET 03, Warsaw, Poland, 6-9 July, 2003, Conference Proceedings, vol.I, pp. 78-82

[3] B. Y. Bedzhev, Zh. N. Tasheva, V. A. Mutkov, "An Shrinking Data Encryption Algorithm with *p*-adic Feedback with Carry Shift Register", XII International Symposium of Theoretical Electrical Engineering ISTET 03, Warsaw, Poland, 6-9 July, 2003, Conference Proceedings, vol.II, pp. 397-400.

[4] F. Q. Gouvea, "*P*-adic Numbers, an Introduction", Springer-Verlag, 1997.

[5] A. Klapper , M. Goresky, "2-adic shift register. Fast Software Encryption", Second International Workshop. (Lecture Notes in Computer Science, vol. 950, Springer Verlag, N. Y., 1994.) pp.174-178

[6] C. K. Koc, "A Tutorial on *p*-adic Arithmetic", Technical Report, Oregon State University, Corvallis, Oregon, USA, 2002.

[7] C. Limongelli, "The Integration of Symbolic and Numeric Computation by *p*-adic Construction Methods", Ph.D. thesis, University of Rome "La Sapienza", Italy, 1993.

[8] C. Limongelli, R. Pirastu, "Exact Solution of Linear Equation Systems over Rational Numbers by Parallel *p*-Adic Arithmetic", No.94-25, Johannes Kepler University, Linz, Austria, 1994.

[9] B. Schneier, "Applied Cryptography", John Wiley & Sons, New York, 1996.

[10] P. van Oorshot, A. Menezes, S. Vanstone, "Handbook of Applied Cryptography", CRC Press, 1996

Algorithm for *p*-adic Combiner Generator Synthesis

Borislav P. Stoyanov[1] and Borislav Y. Bedzhev[2]

***Abstract*— The stream ciphers have large application in the practice. As a result, they ought to satisfy great number of necessary conditions. The most significant of them are: resistance to crypto attacks, high performance velocity and cost-effective hardware implementation. It is impossible to meet all of these conditions if the stream cipher has a structure similar to the classical *Linear Feedback Shift Registers (LFSR)*. Due to this reason, recently some new stream cipher architectures have been proposed. One of them is the so-named shrinking generator, introduced in 1993. With regard to its positive features, our paper is focused on the problem of synthesis of a derivative structure, named *p*-adic combiner generator.**

***Keywords*—Programming, Cryptography, Communication system signaling.**

I. INTRODUCTION

The stream ciphers are an important class of encryption algorithms, which have large application in the practice. As a result, the stream ciphers ought to satisfy great number of necessary conditions. The most significant of them are: resistance to crypto attacks, high performance velocity and cost-effective hardware implementation. Unfortunately, these conditions are in contradiction, because if the structure of the stream cipher is simple in order to provide high performance velocity and cost-effective hardware implementation, then the crypto reliability is low. For instance, the classical fast and cheap *Linear Feedback Shift Registers (LFSR)* are vulnerable to the so - named "Berlekamp – Massey crypto attack" [4]. This attack allows finding of all bits of a *LFSR* output sequence, if *2n* its consequent bits are known. Here *n* is the number of the cells tapped in the *LFSR*. Having in mind the advantages of the stream ciphers with simple structure, recently some theoreticians [8] proposed a new approach to stream cipher design. The basic idea of this approach is building devices with high crypto reliability combining in some appropriate way crypto vulnerable, but fast and cheap elements (including *LFSR*). This meaning of stream cipher design leaded to introducing of a few new architectures. One of them is the so-named shrinking generator [2], introduced in 1993. It is a promising candidate for high-speed encryption applications due to its simplicity and provable properties.

With regard to positive features of the shrinking generator, our paper is focused on the problem of synthesis of a derivative structure, named *p*-adic combiner generator.

The paper is organized as follows. First, the basics of *p*-adic Feedback with Carry Shift Register *(FCSR)* are recalled. After then, an algorithm for automatic synthesis of *p*-adic combiner generator is presented. It is practically realized in Visual C++ environment. Finally, the advantages and possible areas of application of our algorithm are discussed.

II. BASICS OF *FCSRS*

In the shrinking generator, a control *LFSR* R_0 is used to select a portion of the output sequence of a second *LFSR* R_1. The keystream produced is, therefore, a *shrunken* version (also known as an *irregularly decimated subsequence*) of the output sequence of R_1, as depicted in Fig. 1.

The algorithm of shrinking generator consists of the following steps:

1. Registers R_0 and R_1 are clocked.
2. If the output of R_0 is 1, the output bit of R_1 forms part of the keystream.
3. If the output of R_0 is 0, the output bit of R_1 is discarded.

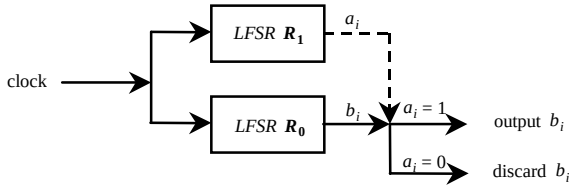

Fig. 1. The shrinking generator

Let R_0 and R_1 be maximum-length *LFSRs* of lengths L_0 and L_1, respectively, and let x be an output sequence of the shrinking generator formed by R_0 and R_1. If $\gcd(L_0, L_1) = 1$, the x has period $(2^{L_1} - 1).\ 2^{L_0-1}$ [8]. The linear complexity $L(x)$ of x satisfies Eq. (1) [8]:

$$L_1.2^{L_0-2} < L(x) \le L_1.2^{L_0-1} \qquad (1)$$

Suppose that the connection polynomials for R_0 and R_1 are chosen uniformly at random from the set of all primitive

[1]Borislav P. Stoyanov is with the Faculty of Mathematics, Informatics and Economics, Shumen University, 1 Universitetska Str., 9700 Shoumen, Bulgaria, E-mail: bpstoyanov@abv.bg

[2]Borislav Y. Bedzhev is with the Faculty of Artillery, Air Defense and Communication Information System, National Military University, 1 Karel Shkorpil Str., 9713 Shoumen, Bulgaria, E-mail: bedzhev@mail.pv-ma.bg

polynomials of degrees L_0 and L_1 over $\mathbf{Z_2}$. Then the distribution of patterns in x is almost uniform [8].

For maximum security, R_0 and R_1 should be maximum-length *LFSRs*, and their lengths should satisfy $gcd(L_0, L_1) = 1$. Moreover, secret connection should be used. Subject to these constraints, if $L_0 \approx m$ and $L_1 \approx m$, the shrinking generator has a security level approximately equal to 2^{2m}. Thus, if $L_0 \approx 64$ and $L_1 \approx 64$, the generator appears to be secure against all presently known attacks [2], [6], [8].

The above presented classical concept of shrinking generator has been extended from Klapper and Coresky in [3]. How it is shown on Fig. 2, in the derivative shrinking generator the controlling *LFSR* from Fig. 1 is replaced with a p-adic Feedback with Carry Shift Register *(FCSR)* R_0. It selects a portion of the output sequences of *LFSRs* $R_1 \div R_{p-1}$. Therefore, the produced keystream is a *shrunken and mixed* version of the output sequences of *LFSRs* R_1 to R_{p-1}. Due to this reason, the derivative structure of shrinking generator is named *p-adic combiner generator*.

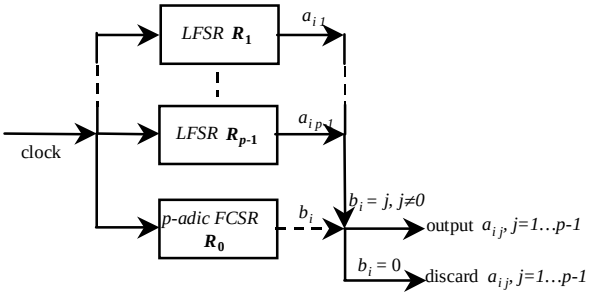

Fig 2. The p-adic combiner generator

The algorithm of p-adic combiner generator consists of the following steps:

1. All *LFSRs* from R_1 to R_{p-1} and *FCSR* R_0 are clocked.

2. If the p-adic output $b_i = j$ of control register R_0 is not equal to 0, the output bit of register R_j forms a part of the keystream. Otherwise, if the output $b_i = 0$ of control register R_0 is equal to 0, the all output bits are discarded.

In the origin papers of Klapper and Goresky only the case $p = 2$ is studied comprehensively [3]. It is shown [1], that the shrinking generator from Fig. 2 could use a generalization of *FCSRs* with stage contents and feedback coefficients in $\mathbf{Z}_p$, where p is a prime number, not necessarily 2. Due to this reason, we will explain the bases of the Feedback Shift Registers with Carry, assuming the common case $p \geq 2$ [1].

The *FCSRs* provide a simple and predictable method for the fast generation of pseudorandom sequences with good statistical properties and large periods. The *FCSRs* have an algebraic theory that parallels of *LFSRs*, in the case based on the 2-adic numbers.

Let we fix an odd positive integer $d \in \mathbf{Z}$ and let $r = \lfloor \log_p(d+1) \rfloor$ (where $\lfloor\ \rfloor$ denotes the floor or integer part). Write

$$d + 1 = d_1 p + d_2 p^2 + \ldots + d_r p^r \qquad (2)$$

for the p-ary representation of the integer $d + 1$ (so $d_r \neq 0$). The shift register uses r stages and $\lfloor \log_p(r) \rfloor$ additional p-its of memory (or less). The feedback connections are given by the p-its $\{d_1, d_2, \ldots, d_r\}$ appearing in Eq. (2).

Definition *1* **(Feedback with Carry Shift Register).** A Feedback with Carry Shift Register (*FCSR*) with connection integer d is the register depicted in Fig. 3.

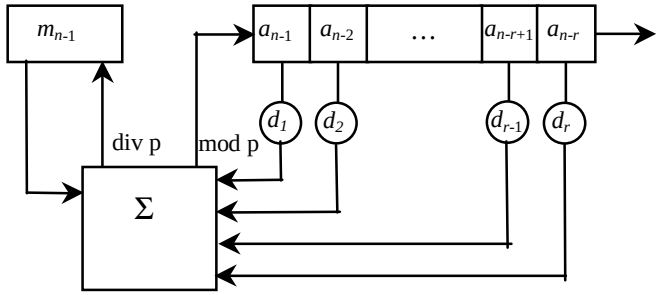

Fig. 3. Feedback with Carry Shift Register

Notice that $d_0 = -1$ does not correspond to a feedback tap, and that the coefficients of high powers of p are close to the output cell. In Fig. 3, Σ denotes integer addition. The contents of the register at any given time consists of r p-its, denoted a_{n-1}, a_{n-2}, …, a_{n-r+1}, a_{n-r}. The operation of the shift register is defined as follows:

1. Form the integer sum in Eq. (3):

$$\sigma_n = \sum_{k=1}^{r} d_k a_{n-k} + m_{n-1}. \qquad (3)$$

2. Shift the contents one step to the right, outputting the rightmost p-it a_{n-r}.

3. Place a_n from Eq. (4)

$$a_n = \sigma_n \pmod p \qquad (4)$$

into the leftmost cell of the shift register.

4. Replace the memory integer m_{n-1} with

$$m_n = (\sigma_n - a_n) / p = \lfloor \sigma_n / p \rfloor. \qquad (5)$$

We refer to d as the *connection integer* because its p-ary expansion gives the analog to the connection polynomial in the usual theory of linear feedback shift registers.

III. Algorithm for *p*-adic Combiner Generator Synthesis

From all stated in above parts of our paper (especially from Eq. (1)), it is easy to see that crypto resistance of the p-adic combiner generator depends essentially on the period of the

sequence, created from it. Due to this reason in [3] have introduced the following definition:

Definition *2* **(*l*-sequence).** An *l*-sequence is an *FCSR* sequence of maximum possible period *T*.

Klapper and Goresky have proved in [3] that the *l*-sequences are generated by *FCSR's* with connection integers *d* for which 2 is a *primitive root* of the finite Galois field *GF*(*d*). In this case, the period of the sequence is $T = d\text{-}1$ (and a single period of an *l*-sequence is a cyclic shift of the sequence formed by *reversing* a single period of the binary expansion of the fraction 1/*d*).

The results of Klapper and Goresky are generalized in [1] as follows:

Theorem *1*. If *c* and *d* are relatively prime, $-d < c \le 0$, and *d* is a prime for which *p* is *primitive root*, then the period *T* of the *p*-it sequence, presented the *p*-adic expansion of the rational number $\alpha = c / d$, is maximal.

In this case $T = \mathrm{ord}_d(p) = d\text{-}1$ (where *d* is the connection integer of the *FCSR*).

The Theorem 1 shows that the synthesis of combiner generator is reduced to the problem of proper determining of integers *p*, *c*, and *d*. With regard to this conclusion, we propose an algorithm for period calculations of *p*-adic expansion of an arbitrary rational number $\alpha = c / d$. It is realized in Visual C++ environment and is consisted of the following steps:

INPUT: The rational number in the form $\alpha = (c / d)*p^e$, where *c*, *d* and *e* are integers, *c*, *d* and *p* pairwise relatively primes and *d* positive.

OUTPUT: The period of the *p*-adic expansion of α.

1. Compute for *d* the Euler phi function $\varphi(d)$ [8].
2. Find the divisors $T_1, T_2, \ldots,$ of $\varphi(d)$.
3. The smallest T_i from the sequence $T_1, T_2, \ldots,$ such that

$$p^{T_i} \equiv 1 (\mathrm{mod}\, d) \qquad (6)$$

is the length *T* of *p*-adic expansion of $\alpha = c / d$.

In order to realize the above algorithm we are created in the class *p_adic*, described in [7], a new member function named *long period()*. It returns the period of given rational number. The member function uses an other member function, named *long powmod(long x, long n, long m)*, created in Visual C++ environment also. It executes "repeated square-and-multiply algorithm" (see [8]) to find an exponent in $\boldsymbol{Z_m}$ and returns $x^n \bmod n$.

The abilities of above mentioned member function for period calculation will be explained with following example. Let the rational number is $\alpha = (1/37)*3^0$, where the prime number is $p = 3$. Then we have:

1. $\varphi(37) = 36$.
2. The divisors of 36 are 1, 2, 3, 4, 6, 9, 12, 18 and 36.
3. The smallest divisor satisfying Eq. (6) is 36.

Analogously, the period of every rational number, satisfying conditions, showed in the Theorem 1, could be calculated. As an illustration, the periods of a few others (except $\alpha = (1/37)*3^0$) rational numbers are listed in the Table I. Our class member function *long period()* work properly if the size of *long integer* in Visual C++ is in the range $[0 \div 2^{31} - 1]$.

TABLE I
RESULTS FROM THE ALGORITHM FOR PERIOD CALCULATIONS

Rational number	Prime number	Period
-23/16	3	4
32/45312	5	58
-1/71927	13	2256

On the base of our new member function we propose an application "Period calculations"- period.exe, realized in Visual C++ environment. Its interface is shown on Fig. 4.

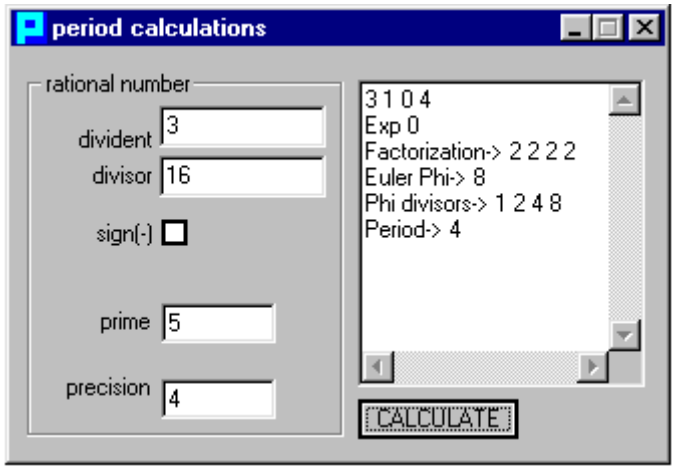

Fig. 4. Period calculations

The application calculates a Hensel code of a given rational number and corresponding period of *p*-adic expansion [5].

The program products, presented above and in [7], automate all procedures during the process of *p*-adic combiner generator synthesis. Actually, let us consider a variant of *p*-adic combiner generator, where *LFSRs* from R_1 to R_{p-1} (see Fig. 2) are replaced with analogous *FCSRs*. Then, the algorithm for *p*-adic combiner generator synthesis will consist the following steps.

1. Using our *p*-adic member function *long period()*, we can find *p* positive prime integers $d_0, d_1, \ldots, d_{p-1}$ for which *p* is a primitive root.

2. We determine the number r_j, $j = 0, 1, \ldots, p\text{-}1$ of cells tapped in every *FCSRs* $R_0, R_1, \ldots, R_{p-1}$:

$$r_j = \lfloor \log_p (d_j + 1) \rfloor. \qquad (7)$$

3. The feedback connections of every *FCSR* R_j from the sequence $R_0, R_1, \ldots, R_{p-1}$, are found in an analogous way to Eq. (2):

$$d_j + 1 = d_{1j}\, p + d_{2j}\, p^2 + \ldots + d_{rj}\, p^{r_j}\,; \qquad (8)$$

4. The proper initial loadings of every *FCSR* register are calculated applying our *p*-adic library [7] to Eq. (9):

$$a_{0j} + a_{1j}.p + \ldots + a_{r-1j}.p^{r_j-1} = \frac{c_j}{d_j} \bmod p^{r_j}\,. \qquad (9)$$

In Eq. (9) all c_j ought to satisfy the following conditions:
- c_j, d_j and p pairwise relatively primes;
- $(-d_j) < c_j \leq 0$;
- $|c_j| < d_j$.

IV. Conclusion

From all the above stated, it is easy to see that the algorithm of synthesis of *p*-adic combined generator, proposed in the paper, could be applied successfully for:

1. Developing of great number of stream ciphers, based on the *Feedback with Carry Shift Register* architecture;

2. Synthesis of pseudorandom sequences with variety of statistical properties such high linear span, low autocorrelation side-lobes and pair wise cross-correlation values, pair wise hamming distance.

It is necessary to emphasize that if the pseudorandom sequences, created with *Feedback with Carry Shift Register* architectures, are used to manipulate radio signals of some perspective communication systems, then the electromagnetic spectrum will be exploit very effectively. This conclusion follows from the fact that the low autocorrelation side-lobes and pair wise cross-correlation values of these pseudorandom sequences provide small radio interference among the consumers. Consequently, *FCSR* sequences may play a key role in the process of new generation personal communication system developing.

Acknowledgement

Authors would to thank Professor Rusin Petrov, whose observations made the drafting of the paper the best possible.

References

[1] B. Y. Bedzhev, Zh. N. Tasheva, V. A. Mutkov, "An Shrinking Data Encryption Algorithm with *p*-adic Feedback with Carry Shift Register", XII International Symposium of Theoretical Electrical Engineering ISTET 03, Warsaw, Poland, 6-9 July, 2003, Conference Proceedings, vol.II, pp. 397-400.

[2] D. Coppersmith, H. Krawczyk, Y. Mansour, "The Shrinking Generator", Proceedings of Crypto 93, Springer-Verlag, 1994, pp 22-39

[3] A. Klapper , M. Goresky, "2-adic Shift Register. Fast Software Encryption", Second International Workshop. (Lecture Notes in Computer Science, vol. 950, Springer Verlag, N. Y., 1994.) pp.174-178

[4] R. Lidl, H. Niederreiter, "Finite Fields", Addison – Wesley Publishing Company, London, England, 1983

[5] C. Limongelli, "The Integration of Symbolic and Numeric Computation by *p*-adic Construction Methods", Ph.D. thesis, University of Rome "La Sapienza", Italy, 1993.

[6] B. Schneier, "Applied Cryptography", John Wiley & Sons, New York, 1996.

[7] B. Stoyanov, B. Bedzhev, Zh. Zhekov, "Computation Model of *p*-adic Arithmetic", XXXIX International Scientific Conference on Information, Communication and Energy Systems and Technologies, ICEST 2004, 16-19 June 2004, Bitola, Macedonia, submitted for publication.

[8] P. van Oorshot, A. Menezes, S. Vanstone, "Handbook of Applied Cryptography", CRC Press, 1996

Artificial Neural Networks - State-of-the-Art *

Hristo I. Toshev[1], Chavdar D. Korsemov[2], Stefan L. Koynov[3] and Vesselin P. Velichkov[4]

Abstract: - **The paper is a review of the state-of-the-art for the artificial neural networks. The background for their application begins with comparisons with the biological prototypes and the classical von-Neuman architecture. Artificial neural networks prototypes in biology and their technological equivalent are presented Advantages and disadvantages of neural networks are given.**

Keywords - **artificial neural networks; artificial neural network properties; artificial neural network applications.**

I. INTRODUCTION - MATHEMATICAL EQUATIONS, NEURAL NETWORKS AND FUZZY SYSTEMS

The description of (and knowledge of) a system, according to [1] can be done in three different ways, namely: with mathematical equations, distributed parameters (neural networks – NNs), and linguistic rules.

Despite their obvious simplicity mathematical equations are not applicable to complex systems because of some similarly complex reasons. In this approach, besides defining the exact relationship between the varying parameters, also the time variable has to be taken into account (speaking of time-dependent systems).

The latter inconvenience seems to be overcome in the case of linguistic rules, which can be easily modified. They include even badly defined languages, which allow controversial conclusions from one and the same fact.

Mathematical equations and "crisp" rules of the type "if-then" describe an algorithm of a process manifestly. NNs describe an algorithm of a process in a hidden way. They are atypical example of distributed data processing. Artificial NNs can be examined as iterative systems in two different typical example of distributed data processing. Artificial NNs can be examined as iterative systems in two different ways.On one hand they are structurally - iterative, as their structure is a simple iteration of their components; in this way they can be interpreted as a structured graph. On the other hand artificial NNs are algorithmically -iterative, the aim of the algorithm being to define the centroids of different classes if the system is self-organizing. If the system is not self-organizing, the centroids of its classes are "taught" by a teacher. The drawbacks of NNs come from the unpredictability of the system for every moment in time, as well as from the non-implicit convergence for every separate case (because of which, instead of global convergence**,** an asymptotic convergence is usually pursued); even small variations of input data cause new knowledge to be learned by the network. Finally, it must be said that NNs give in to fuzzy systems in terms of ease of development. However, in spite of its disadvantages, NNs along with fuzzy systems are much more suitable for solving badly defined problems, compared to the systems with mathematical equations.

The merging of fuzzy systems and NNs into so-called "adaptive fuzzy systems" is a comparatively old technique in the field ([2]-[11]). Contemporary tendencies are towards merging fuzzy logic with chaos and NNs. Example of a fuzzy system is the modeling of human brain and an example of chaos in terms of informatics and NNs are the nonlinear dynamic processes of the complex neural nets in the human brain.

II. ANN ARTIFICIAL NEURAL NETWORKS PROTOTYPES IN BIOLOGY AND THEIR TECHNOLOGICAL EQUIVALENT

Comparison between biological neural network system and Fon Neumann computer

The upper equivalence follows from [12]. Next are listed the main components of the Fon Neumann architecture (fNA), followed by the characteristics of the classical computer architecture and of the biological neural system (BNS).

Processor. While the fNA-processor is complicated, BNS processor is simple.

Memory. While fNA-memory is divided from fNA-processor and is localized and content addressable, BNS-memory is integrated into the BNS-processor and is distributed and content addressable.

Processing. While fNA-processing is centralized, sequential and is based on the programs in memory, BNS-processing is distributed, parallel and self-learnt.

Reliability. While fNA-reliability is very vulnerable, BNS-reliability is robust.

* This study is partly supported by the Ministry of Education and Science, National Science Fund, contract No. I-1302 / 2003, Sofia, Bulgaria.

[1] Hristo I. Toshev is with the Institute of Information Technologies, Bulgarian Academy of Sciences, Acad. G. Bonchev str., bl. 29A, 1113 Sofia, Bulgaria, E-mail: toshev@iinf.bas.bg

[2] Chavdar D. Korsemov is with the Institute of Information Technologies, Bulgarian Academy of Sciences, Acad. G. Bonchev str., bl. 29A, 1113 Sofia, Bulgaria, E-mail: korsemov@iinf.bas.bg

[3] Stefan L. Koynov is with the Institute of Information Technologies, Bulgarian Academy of Sciences, Acad. G. Bonchev str., bl. 29A, 1113 Sofia, Bulgaria, E-mail: baruch@iinf.bas.bg

Vesselin P. Velichkov is with the Institute of Information Technologies, Bulgarian Academy of Sciences, Acad. G. Bonchev str., bl. 29A, 1113 Sofia, Bulgaria, E-mail: vesko@iinf.bas.bg

Information representation and basic tasks. Information in fNA is in the form of numbers and symbols and this is why the main problems of fNA are in the data representation. In contrast to fNA, information in BNS has impulse-analog representation, and the main problems come from analysis/recognition of input data.

Work environment. While in fNA it is well defined, the work environment in BNS is badly defined and its limits have to be accepted by default.

Models of evolutionary computation in NNs

According to the approach of evolutionary computation, which has gathered much popularity lately, NNs are one of the main representatives of the FOE-model (filogenesis, ontogenesis, epigenesis) of simulated computation [13].

After they reach a certain level of complexity, living organisms develop highly specialized processes, which allow an individual to integrate the huge amount of interactions with environment. In relation to living organisms such processes are referred to as epigenesis.

Three systems in living organisms represent epigenesis: nervous system, immune system and endocrine system. From the three systems, the one receiving greatest attention from researchers is the nervous system. A typical example in that respect is the nervous system, which according to [14] includes 10^{10} neurons and 10^{14} synapses, if compared to the four symbol genome, which has length $3 \bullet 10^9$, according to [13]. The immune system is a prototype of systems for finding software bugs [15], of mobile robots controllers [16], and of immune systems of computers [17]. The endocrine system is composed of a large number of gland tissues, which release directly into the blood stream, hormones, controlling bodily functions as reproduction, etc. From functional point of view this system is similar to some extent to the nervous system in the sense that both of them help the individual's adaptation to changes in environment.

Artificial NNs are the technical equivalent of the three above mentioned biological systems, their synaptic weights and their topology changing in response to outside influence. The paradigm of artificial NNs is a technical realization of the epigenetic axis of the FOE-model and as such it acquires amazing results, which very often are equal to, if not exceeding, the results of the traditional methods. Artificial NNs are applied mainly in programming and in small number of cases in hardware equipment. Some of their applications in practice are: data analysis, function approximation, associations, inter- and intra class categorizations, recognition and classification of images, data compression, prediction and control [12].

In recent years the attention of researchers has been centered around evolutionary artificial NNs, which beside the epigenetic axis of the FOE-model also include its filogenetic axis. According to [18] and [19], filogenesis in living nature covers the evolution of the species itself. The technical solution from NNs's theory point of view is a population of NNs, in which the evolution is realized on global (population's) level, while learning is realized on individual level (i.e. single NN level). Examples in that respect are the works of Liu and Yao [20], Nolfi et al. [21] and Yao [22], although they are completely out-of-date. Another interesting example is the effect of Baldwin, who demonstrates the complex interaction between filogenesis and epigenesis.

The application of the latter process for the uses of simulated computation is examined in [23] and [24]. The FE-plane (filogenesis-epigenesis) in nature is also connected with the process of human linguistic learning i.e. to what extent the linguistic ability is inbred (filogenetic) or acquired (epigenetic).

A short historical review on the subject discussed can be found in [25], and information on this process applied in artificial systems is given in [26]-[28].

Concept of artificial NN

The artificial neural network (NN) is a high-level parallel structure of interconnected simple elements (neurons), which are hierarchically organized. The information in NN is stored in distributed way as weights and links between neurons, and its acquisition is realized through association. The algorithms defining the changes in weights are called training rules. The main models of NNs are examined in [29-31]. The trainable networks have possessed the flexibility, necessary for solving of complex dynamic problems. Such NNs have to be able to adapt on two clearly separable levels: by changing of the dynamics of the inter-neuronal interactions (which is normally achieved through change of the synaptic weights) and by changing the actual topology of the network. Topology modification proves to be a successful solution to the stability-flexibility dilemma, i.e. how a trainable system may remember the already acquired knowledge, while at the same time it continues to add new knowledge [32].

III. ADVANTAGES AND DISADVANTAGES OF NN

Advantages

The strongest, and at the same time the most specific features of a NN are: adaptivity, robustness to fuzzy and noisy input, reliability:

Adaptivity. There is no inlaid, concrete algorithm in a NN; the training of a NN is done by example and it can continue during the use of the NN in real applications.

Robustness to fuzzy and noisy input. The NN finds the "true" path by association.

Reliability. Even the removing of some neurons is not fatal as the information in the NN is distributed.

Disadvantages

The main problems when working with artificial NNs are: the curse of dimensionality, number of layers and number of neurons in each layer (network design problems), selection of energy (step) function along with interpretation on physical level, convergence of the network in case of complex definition domains of input vectors (classification problems), time for training/self-organization.

Curse of dimensionality. In most of the cases in practice, the input vectors of the NN are composed of hundreds or even thousands of components. This makes necessary a reduction of dimensions to be made. The latter is realized during preprocessing, when the highly informative components are separated from the less informative ones; data compression is a synonym of preprocessing. (There are situations in which it

is necessary to artificially generate additional samples, as in the case of image recognition). Other methods for dimensionality decrease is the use of some symmetry in the training sequence or to use the principle of unification, i.e. to use the knowledge for a single object as valid for the rest of the objects of the respective class as well.

Network design problem. Another fundamental problem appears to be the problem of defining the number of hidden neurons, i.e. the number of the neurons positioned between the input and output layers. What makes this problem so crucial for the design of the NN is the fact that from the number of hidden neurons the properties of the network are defined in respect to the concrete application. If theoretically the addition extra neurons results in settling into a local minimum, then the removing of neurons corresponds to the case of convergent network.

Selection of energy function (physical level interpretation). Also very important proves to be the problem of how to escape the local minimums in our search of the global one. A number of physical in their essence methods are used. The more popular of them are the Hebb training and the Bolzman; beside them other methods are also used, among which – statistical, binary, neuro-dynamical, etc. On mathematical level the physical method can be explained as the selection of the type of the energy function.

Convergence of the network in complex definition domains of the input vectors (classification problems). From samples' classification/recognition point of view the problem of the complex definition domains of the input data is very essential. Very often instead of looking for absolute convergence, it is looked for asymptotic.

Training/self-organizing time. The training of a NN can be realized in two ways, each of them characterized by its own training time. Training can be done "per sample" (guarantees quicker result acquisition) or over the whole sample sequence – packet training (slower than the first case). Although in the case of packet training the weights' changes for each sample have to be kept in memory through the whole epoch, it is guaranteed that the error will slide down over the weight-plane. The time for packet training is called "epoch".

IV. Conclusions

The paper is a review of the state-of-the-art for the artificial neural networks. The background for their application begins with comparisons with the biological prototypes and the classical von-Neuman architecture. Artificial neural networks prototypes in biology and their technological equivalent are presented. Advantages and disadvantages of NN are given.

References

[1] T. Yamakawa, A fuzzy inference engine in nonlinear analog mode and its application to a fuzzy logic control, *IEEE Trans. on Neural Networks*, V. 4, N. 3, pp. 496-521, May 1993.

[2] T. Yamakawa, Japanese Patent Applications, Tokuganhei, No. 1-043600, Feb. 23, 1989, No. 1-133690, May 26, 1989

[3] T. Yamakawa A fuzzy neuron and its application to pattern recognition, Proc. Third IFSA Congress, Seattle, WA, Aug. 6-11, 1989, pp. 30-38, 1989

[4] T. Yamakawa Pattern recognition hardware system employing a fuzzy neuron, Proc. Int. Conf. Fuzzy Logic & Neural Networks, Iizuka, Japan, July 20-24, 1990, 943-948, 1990.

[5] T. Yamakawa A fuzzy neuron and its application to a hand-written character recognition system, Proc. IEEE Int. Symp. Circuits and Systems, Singapore, June 11-14, 1991, 1369-1372, 1991.

[6] Proc. Int. Conf. Fuzzy Logic and Neural Networks, Iizuka, Japan, July 20-24, 1990.

[7] T. Yamakawa A design algorithm of membership functions for a fuzzy neuron using example-based learning, Proc. IEEE Int. Conf. Fuzzy Systems, San Diego, CA, Mar. 8-12, 1992, pp.75-82, 1992.

[8] B. Kosko, Neural networks and fuzzy systems, Englewood Cliffs, NJ, Prentice Hall, 1992.

[9] B. Kosko, Neural networks for signal processing, Englewood Cliffs, NJ, Prentice Hall, 1991.

[10] Proc. A Second Int. Conf. Fuzzy Logic and Neural Networks, Iizuka, Japan, July 17-22, 1992.

[11] T. Yamakawa , *et al.*, A neo fuzzy neuron and its applications to system identification and prediction of the system behavior, Proc. Second Int. Conf. Fuzzy Logic & Neural Networks, Iizuka, Japan, July 17-22, 1992, pp. 477-484, 1992.

[12] A. Jain, A. K., Artificial neural networks: a tutorial, *IEEE Computer*, Mar. 1996, pp. 31-44, 1996.

[13] M. Sipper, *et al.*, A phylogenetic, ontogenetic, and epigenetic view of bioinspired hardware systems, *IEEE Trans. on Evol. Comput.*, Apr. 1997, V. 1, N. 1, pp. 83-97, 1997.

[14] G. M. Shepherd, C. Koch, Introduction to synaptic circuits, The Synaptic Organization of the Brain (G. M. Shepherd, ed.), N.Y., Oxford University Press, 1990, 3-31, 1990.

[15] S. Xanthakis, ,*et al.*, Immune system and fault-tolerant computing, Evolution artificielle 94, 1995, Cepadues, cop., 1994.

[16] A. Ishiguro, *et al.*, Immunoid: an immunological approach to decentralized behavior arbitration of autonomous mobile robots, Parallel Problem Solving from Nature - PPSN IV (*Lecture notes in Computer Science*, V. 1141), H.-M. Voigt, W. Ebeling, I. Rechenberg, H.-P. Schwefel, Eds., Heidelberg, Springer-Verlag, 1996, 666-675, 1996.

[17] J. O. Kephart, A biologically inspired immune system for computers, Artificial Life IV, R. A. Brooks, P. Maes, Eds., Cambridge, MA, MIT Press, 1994, pp. 130-139, 1994.

[18] A. Danchin, A selective theory for the epigenetic specification of the monospecific antibody production in single cell lines, *Ann. Immunol. (Institut Pasteur)*, V. 127C, 1976, 787804, 1976.

[19] A. Danchin, Stabilization fonctionelle et epigenese: une approche biologique de la genese de l'identite individuelle, L'identite, J.-M. Benoist, Ed., Paris, France, Grasset, 1977, 185-221, 1977.

[20] Y. Liu, X. Yao, Evolutionary design of artificial neural networks with different nodes, Proc. IEEE Int. Conf. Evol. Comput. (ICEC'96), 1996, 670-675, 1996.

[21] S. Nolfi, *et al.*, Learning and evolution in neural networks, Adaptive Behavior, V. 3, N. 1, 1994, 5-28, 1994.

[22] X. Yao, Evolutionary artificial neural networks, *Int. J. Neural Syst.*, V. 4, N. 3, 1993, 203-222, 1993.

[23] G. E. Hinton, S. J. Nowlan, How learning can guide evolution, *Complex Syst.*, V. 1, 1987, 495-502, 1997.

[24] D. Ackley, M. Littman, Interactions between learning and evolution, *Artificial Life II (SFI Studies in the Sciences of Complexity*, V. X), C. G. Langton, C. Taylor, J. D. Farmer, S. Rasmussen, Eds., Redwood City, CA, Addison-Wesley, 1992, 487-509, 1992.

[25] D. Dennet, C., Darwin's dangerous idea: evolution and the meanings of life, N.Y., Simon & Schuster, 1995.

[26] G. M. Werner, M. G. Dyer, Evolution of communication in

artificial organisms, *Artificial Life II (SFI Studies in the Sciences of Complexity*, V. X), C. G. Langton, C. Taylor, J. D. Farmer, S. Rasmussen, Eds., Redwood City, CA, Addison-Wesley, 1992, 659-687, 1992.

[27] B. MacLennon, Synthetic ethology: an approach to the study of communication, *Artificial Life II (SFI Studies in the Sciences of Complexity*, V. X), C. G. Langton, C. Taylor, J. D. Farmer, S. Rasmussen, Eds., Redwood City, CA, Addison-Wesley, 1992, 631-658, 1992.

[28] L. Steels, A self-organizing spatial vocabulary, *Artificial Life*, V. 2, N. 3, 1995, 319-332, 1995.

[29] S. Grossberg, The adaptive brain I: cognition, learning, reinforcement, and rythm; The adaptive brain II: vision, speech, language and motor control, Elsevier/NorthHolland, Amsterdam, 1986.

[30] R. P. Lippmann, An introduction to computing with neural nets, *IEEE ASSP Magazine*, April 4-22, 1987.

[31] P. Wasserman, Neural computing - theory & practice, N.Y., 1989.

[32] G. Carpenter, S. Grossberg, The ART of adaptive pattern recognition by a self-organizing neural network, *IEEE Computer*, Mar. 1988, 77-88, 1988.

Artificial Neural Networks - Classification and Technical Applications *

Hristo I. Toshev[1], Chavdar D. Korsemov[2], Stefan L. Koynov[3] and Vesselin P. Velichkov[4]

Abstract: - **The paper is a review of the classification and applications of the artificial neural networks. The basic properties of these networks are viewed thus pointing to the governmental programs for their research and applications.**

Keywords - **artificial neural networks; artificial neural network properties; artificial neural network applications.**

I. Classification of Neural Networks

According to [1], neural networks (NN) may be divided in two large groups: *feed-forward networks* and *recurrent/feedback* networks.

1.Types of feed-forward networks:

One-layer perceptron. All inputs are connected to each of the output neurons.

Multilayer perceptron, NN with radial basis functions. Outputs from all neurons of a layer are connected to each of the neurons of the next layer.

2.Recurent networks (feedback networks). According to the type of the links between their neurons, the NNs can be classified as:

NNs with competitive training. Each neuron from a given layer is connected to all other neurons of the same layer.

Kohonen's self-organizing maps (SOM). Each neuron from a layer is connected his nearest neighbors from the same layer.

Hopfield network. Each neuron from a layer has as an input all outputs of all other neurons of the same layer.

Adaptive Resonance Theory Networks (ART). Each output neuron is connected to all other output neurons as well as with all input neurons.

Training algorithms

The NNs training rules may be classified according to the following features: training paradigm, training rule, training algorithm, NN architecture and application area [1].

1.Training paradigm: supervised learning, unsupervised learning, hybrid.

2.Training rules:

Error correction;

Competitive training;

Hybrid training – competitive and error correction;

Rules based on principles from physics. On their part they are classified as: Hebb's training (supervised and unsupervised), Boltzman's training (supervised).

3.Architecture: NN's architecture is closely dependent upon its training rule.

With error correction: multiplayer perceptrons are used. In case of supervised learning, perceptrons may be multiplayer as well as one-layer.

Competitive training: in this case the following architectures are possible- architecture for standard competitive training, SOM (unsupervised), ART-networks (supervised or unsupervised).

With error correction and competitive (for hybrid training) - NNs with radial basis functions.

Rules based on principles from physics: Hebb training (feed-forward networks architecture is used. In case of supervised learning, it is possible that the number of layers is more than 1. For unsupervised learning Hebb's rule competitive structures and Hopfield networks are possible); Boltzman's training (it has it's own unique architecture).

4.Training algorithm: it depends on the area of application, i.e. on the type of the given problem. First two points listed next describe the specific algorithms used with the two main types of training; the third point lists the most popular algorithms used with NNs:

Supervised learning. Characteristic algorithm is the within-class categorization. It is realized with adaptive vector quantization; ART-networks.

Unsupervised learning. The specific training algorithms are chosen according depending on the area of application: associative memories (on boundary between automats and NNs; trained according to a unique principle); classification (realized with vector quantization, SOM-networks, ART1- and ART2-networks).

Popular training algorithms (starting from most widely-used); perceptron algorithms (supervised) (perceptron

* This study is partly supported by the Ministry of Education and Science, National Science Fund, contract No. I-1302 / 2003, Sofia, Bulgaria.

[1] Hristo I. Toshev is with the Institute of Information Technologies, Bulgarian Academy of Sciences, Acad. G. Bonchev str., bl. 29A, 1113 Sofia, Bulgaria, E-mail: toshev@iinf.bas.bg

[2] Chavdar D. Korsemov is with the Institute of Information Technologies, Bulgarian Academy of Sciences, Acad. G. Bonchev str., bl. 29A, 1113 Sofia, Bulgaria, E-mail: korsemov@iinf.bas.bg

[3] Stefan L. Koynov is with the Institute of Information Technologies, Bulgarian Academy of Sciences, Acad. G. Bonchev str., bl. 29A, 1113 Sofia, Bulgaria, E-mail: baruch@iinf.bas.bg

Vesselin P. Velichkov is with the Institute of Information Technologies, Bulgarian Academy of Sciences, Acad. G. Bonchev str., bl. 29A, 1113 Sofia, Bulgaria, E-mail: vesko@iinf.bas.bg

training, back-propagation, Adaline/Madaline); competitive training algorithms (supervised or unsupervised)(algorithms for vector quantization or ART networks; SOM are also allowed, provided the training is unsupervised); radial basis functions algorithms; algorithms for networks based on physical rules. Hebb's rule for supervised learning is realized with linear discriminant analysis, and for unsupervised learning – with principal component analysis (in addition to associative memories training). Boltzman's rule for unsupervised learning has its own training algorithm.

II. Applications of neural networks

Survey shows, that NNs are one of the most-actively researched and most perspective fields in artificial intelligence. They are object of massive research in EEU (Eureka) and in some of the most developed countries, such as Germany (ITR-8800-G9, Ministry Of Science), France (DGA/DRET/SDR), USA, Japan.

The areas of application of NNs, according to [2] are known as "soft computing" for badly defined problems, in which constant adaptation and evolution are necessary. They are successfully used for diagnostics, image recognition, classification, optimization and control.

Types of NNs applications

Generally speaking, the applications of NNs can be classified using three different criteria, depending upon: whether the grouping follows the natural NN paradigm, whether the classification is done in view to use in industry or some very complex applications are envisaged.

Natural applications

1.Function approximation. A special place in this group is held by the radial basis functions, which synthesize in their structures supervised and unsupervised NN learning [1]; this class NNs, have their own specific training algorithm [1].

2.Associative memories (AM). The distinction between NNs and Ams is not strict and often is a question of personal favor: many NNs work as Ams (for example Hopfield network associates images with themselves, while some Ams function as NNs. Some of the more popular Ams are [3]: Willshaw associative memory, Advanced Distributed Associative Memory (ADAM), Sparse Distributed Memory (SDM), Bidirectional Associative Memory (BAM).

3.NNs for coding. Not depending upon its concrete technical implementation, coding is used in image compression. NNs are used for finding an effective field of samples, represented through hidden neurons, coding a great number of input-output samples.

4.Data compression.

5.Image compression. It is based upon the low transmitting capacity of TV channels (beside intensity and pixel color, there is also big information surplus during video signal transmission). This is why, before transmission, the picture is compressed by coding and after transmission it is decoded in the receiver. In those cases NNs are used (Kortel, for exmpl.) for coding by the sensors and the hidden layer and for decoding by the hidden layer and output layer; the NN is trained by teacher using the bach-propagation method.

6.Image and speech recognition.

7.Cell NNs. Used in hardware for modeling electrical circuits.

Application of NNs in the industry

1.Synthesis and prediction of time sequences. [4, 5]

2.Identification and modeling of dynamic no stationary processes. [6-8]

3.Optimization and control of dynamic systems. These NNs are used in economy, ecology, industry, etc. For example in the industry, NNs have two main applications – improvement of technology and application on control level. NNs improve technology if they are used in computer vision (for automatic quality control), in robot control systems, inspection of difficultly accessible areas. On the control level, NNs are very effective in optimization of production schedules, etc.

Complex applications

1.Image recognition with NNs

-Problems in image recognition:

1)Image analysis – an image is input to the NN and its output is a combination of image description parameters (feature vector). The problem which image analysis solves is classification of the object in the input image.

2)Synthesis of artificial images – input is the feature vector of an image (see p.1)). Classical optics and computer graphics are problems of visual synthesis. An important term is the field of optical flow. It takes part in the synthesis of new images, with known transformation parameters and given input image.

-Visual perception and recognition:

1)Object representation: through lines or photographic representation (through arrey of values, corresponding to levels of grey), most realistic or closest to human vision.

2)Main problems: separating image from background, and visualizing object independently of its position.

Typical applications of visiual perception and recognition are criminology, banking, communications and medicine; image editing, video editing, virtual reality, multimedia databases, computer graphics; human-computer interaction (HCI) interfacesface and object recognition; image animation for cartoons; mdelling of visual processes in humans and animals; character recognition [9]; signature classification for identification; greyscale image segmentation.

A HCI interface for example is described with 10 parameters, more or less, plus several global parameters. In medicine, NNs are used for obtaining and storing of medical data, from specialized medical technology (for example computer tomograph, etc), which is eventually processed in certain way (ex. Diagnose formulation, visualization of scanned images, etc). In banking and finances a main problem is the risk evaluation and this is why for the moment only straight, small-sized NNs are used.

-NNs for image recognition – applications:

1)Pose-independent face recognition. 15 different poses of a face are used.

2)Classical approach to visual perception. In this approach the information is divided in two parts – position independent –"what" and viewpoint for object representation – "where". The NN has an input layer , a hidden layer and an output

layer. The two parts of the output layer characterize the object position. The training of the network is realized through random image sequence.

3)Segmentation. (Kienker) Specific parts of the network are described – a layer represents object's boundaries in the image, a layer defines if a pixel belongs to the object. Training is done according to Bolzman-machines rule and the test forms vary from triangle to spiral. The NN interprets correctly even figures which are represented only with their angles.

4)Problems of computer vision (Koch). They are solved through standard regulation theory by minimization of quadratic energy functions corresponding to Hopfield networks. For example when only some of the points are provided or if there is noisy data, a smooth surface is reconstructed by linear processes.

5)Object position and orientation independence (Logotetis and Pauls). The different object's views are recognized by three, instead of one, neurons.

6)Nondeformable 3d object generation. (Pojo, Bauhmer, Shashua).One of the samples if set to serve as reference. The optical field flow defines the correspondence between the pixels of the base and the other samples. From some input data – pose parameters – multiple output data is received. Each output data corresponds to an attribute for a given pixel in the image.

7)Face template construction. Templates are applied for the different parts of face – eyes, nose, mouth.

8)View-tuned and view invariant neurons; setting of the form of psychophysical recognition fields (Pojo, Brokolo, Logotetis). The input image data is passed through filters, after which is compared with patch of the target object.

9)Training by line drawings (Pojo, Brunelli, Librand).

10)Face verification (Romano, Bauhmer)

11)Face recognition using several views.

2.Speech recognition

-General scheme for speech recognition (SR). The SR process basically consists of two parts: noise reduction of the input signal and linguistic processing of the cleared signal. Noise can be either specific for the sound input (empl. Microphone) or a part of the sound background. The process of noise reduction is realized through acoustic modeling. Linguistic modeling includes word recognition, choosing of most probable word candidate and word processing of the recognized words; word recognition is composed of acoustic modeling and linguistic modeling. The acoustic analysis produces a list of words, having similar sounds, and linguistic modeling defines the probability that a given word is among, before or after other words, so that the list of most probable words may be reduced in size.

-Sound and speech characteristics.Vowels (different harmonics of one frequency can be distinguished; this base frequency is defined from the tone of talking); voiceless consonants (no harmonics can be distinguished, though noise appears in certain frequency intervals); voiced consonants (a combination of light harmonics and nose in some frequency intervals).

-Difficulties in speech recognition

1)speech is a key to human memory

2)subjective factors (pronunciation, etc)

3)speech intermittency (often no pauses between words)

4)contextual dependency of word meaning [10, 11]

-Speech recognition with NNs

1)General settings. SR with NNs can be divided into following stages: preprocessing, selection of most probable candidates, postprocessing. During preprocessing the input signal cleared from noise or the dimentions of the input vector are reduced. Postprocessing allows, the cleared signal to be saved in suitable form and to be integrated with other applications. The role of NN here is in the process of noise reduction as well as in the formation of robust to noise representations and similarity functions and in the construction of methods describing classes in case of badly structured data. [12,13]

2)Basic scheme of SR with NN. NN solve two types of problems in SR. The first one is the minimization of the topology of the NN through matrix-vector representation of the NN and synthesis of fast converging methods and algorithms for training of NN with minimized topology. For the solution of the second problem, systems of NN are used, modeling various subtasks of the SR task, rather than one single NN for recognition [14].

-Types of NN for SR:

1)Straight networks for separation of different words with limited dictionaries (have restricted use)

2)Recurrent networks

-Use temporal structure of language

-Store the contextual history of a sequence in natural language

3)Systems of NNs:

-The input NNs have to cluster / classify input vectors according to tone, so that similar sounds can be recognized

-On upper level are NNs for letter recognition, with temporal processing output

-On highest level are NNs for word recognition, with context reference for better recognition.

IV. CONCLUSIONS

The paper is a review of the classification and applications of the artificial neural networks. The basic properties of these networks are viewed thus pointing to the governmental programs for their research and applications.

REFERENCES

[1] A. Jain, A. K., Artificial neural networks: a tutorial, *IEEE Computer*, Mar. 1996, pp. 31-44, 1996.

[2] R. R. Yager, L. A. Zadeh, Fuzzy sets, neural networks, and soft computing, N.Y., Van Nostrand Reinhold, 1994.

[3] R. Beale, T. Jackson, Neural computing: an introduction, Dptmt. of Comp. Sci., Univ. of York, Adam Hilger, 1990.

[4] M. J. Cosculluela, *et al.*, Day type identification for electric hourly load demand forecasting using SOM, Prepr. of the 6-th Int. Conf. on NN - NEURO NIMES'93, France, 25-29, 1993.

[5] A. Jain, A. K., Artificial neural networks: a tutorial, *IEEE Computer*, Mar. 1996, pp. 31-44, 1996.

[6] A. Jain, A. K., Artificial neural networks: a tutorial, *IEEE Computer*, Mar. 1996, pp. 31-44, 1996.

[7] K. S. Narendra, K. Parthasarathy, Identification and control of dynamic systems using neural networks, *IEEE Transactions on*

Neural Networks, V. 1, 4-27, 1990.A. Jain, A. K., Artificial neural networks: a tutorial, *IEEE Computer*, Mar. 1996, pp. 31-44, 1996.
[8] S. A. Billings, *et al.*, Properties of NN with application to modelling nonlinear dynamical systems, *Int. J. Control*, V. 55, No. 1, 13-224, 1992.
[9] S. Mori, *et al.*, Historical review of OCR research and development, *IEEE Proc.*, V. 80, No. 2, 1029-1057, 1992.
[10] M. Zeidenbeerg, Neural network models in AI, Ellis Horwood, 1990.
[11] R. Reilly, N. Sharkey, Connectionist approaches to natural language processing, Lawrence Erlbaum Associates, Publishers, 1992.
[12] H. Hattori, Text-independent speaker recognition using neural networks, Proc. of the ICASSP'92, V. II, 153-156, 1992.
[13] M. Hunt, C. Lefebvre, A comparison of several acoustic representation for speech recognition with degraded and undegraded speech, Proc. of ICASSP'89, 262-265, 1989.
[14] Artieres, T., *et al.*, Connectionist and conventional models for free-text talker identification tasks, Universite de PARIS-SUD, Rapport de Recherche No 677, 1991.
[15] D. Williams and J. B. Gomm, "The introduction of neural network projects in a degree of electrical and electronic engineering", *12th Int. Conf. on Systems for Automation of Engineering and Research SAER'98, Proc.* 19-20 September 1998, Varna - St. Konstantin resort, Bulgaria, pp. 102-106, 1998.
[16] I. Baruch, A. Martinez and B. Nenkova, "Adaptive Neural Control with Integral-Plus-State Action", *Cybernetics and Information Technologies*, Vol. 2, No. 1, Sofia, pp. 37-48, 2002

Ad Hoc Networks Routing Protocols Efficiency With Respect To Connection Availability

Trajanov Dimitar[1], Filiposka Sonja[2], Cilku Bekim[3], Aksenti Grnarov[4]

Abstract—One of the most important issues in the main applications of mobile ad hoc networks (as rescue and military operations) is to know the availability of the system. We developed an analytical model in order to investigate the routing protocol efficiency using real measurable parameters that concern the performances of mobile ad hoc networks. We analyzed the routing protocol efficiency with respect to connection availability for rescue mission example application.

Keywords—Ad hoc Network, Connection Availability, Routing Protocols Efficiency, Availability Model

I. INTRODUCTION

One of the most vibrant and active "new" fields today is that of mobile ad hoc networks (MANET). Within the past few years, though, the field has seen a rapid expansion of visibility and work due to the proliferation of inexpensive, widely available wireless devices as well as of the network community's interest in mobile computing. An ad hoc network is a collection of wireless mobile nodes dynamically forming a temporary network without the use of any existing network infrastructure or centralized administration. The nodes are expected to act cooperatively to establish the network "on-the-fly" and route data packets possibly over multiple hops. As a result of the multihop environment, the routing protocol has become a very important part of the ad hoc network layered architecture. Its primary goal is correct and efficient route establishment between pair of nodes so that messages can be delivered in a timely manner. MANETs are often used in critical mission applications, in which fault tolerance is of great importance. For wireless (and wireline) networks, the network's ability to avoid or cope with failure is measured in three ways: reliability, availability and survivability, all of which have long been important areas of research [1]. Because of their importance, in this paper we investigate the impact of routing protocols to connection availability in ad hoc networks.

The previous work of ad hoc networks availability includes work on link availability model for enhancing the performance of routing algorithms that is proposed in [2]. In [3] prediction about the average link expiration times for a simple network scenario is investigated. In [4] the continuous time Markov chain (CTMC) is used in order to represent a connection availability model for a simple ad hoc network. The proposed connection availability model incorporates the physical faults that affect the end-to-end connection in communication systems, however not incorporating any characteristics of ad hoc routing protocols. In [5] an improved connection availability model based on commonly used ad hoc reactive routing protocols like the Dynamic Source Routing Protocol (DSR) [7] and the Ad hoc On-demand Distance Vector routing protocol (AODV) [8] is designed. In [6], based on the ad hoc network connection availability model, the connection resilience to nodes failures is evaluated.

The main motivation for this work is to analyze the impact of routing protocols to ad hoc network connection availability. In order to make this analysis we define two measures: routing protocol efficiency (RPE) and relative routing protocol efficiency (RRPE).

II. AD-HOC NETWORK MODEL DESCRIPTION

We use a common ad hoc network model that corresponds to the models used in the referenced papers. In order to give a simplified, but reasonable model we assume that the terrain is perfectly flat while all the mobile nodes have the same fixed transmission power and are equipped with omni directional antenna. Hence, the node radio coverage shape is a perfect circle with radius r. In our model we have N+2 nodes placed in area A. Two of them are the source and the destination nodes for the end-to-end connection. The rest-N nodes can be part of a connection path between the source and the destination, therefore playing the part of routers in this end-to-end connection. In order to establish a communication between the two nodes, MN_s and MN_d (l is the distance between MN_s and MN_d $r<l<2r$), the communication path has to go through one of the nodes (MN_1, MN_2) that are currently located in the intersection area B between MN_s and MN_d (see Figure 1.). While moving around in A, a node can enter the B area and, after a certain period of time, leave B and enter area C defined as A-B. This process is continuously repeated. In order to simplify the modeling of the node mobility we place the coordinate system origin in MN_s, while MN_d lays on the x-axis as shown on Figure 1. According to this assumption we only consider the distance between MN_s and MN_d and the mobility of the rest of the nodes relative to this coordinate system. Similary to [4] and [3] we use a two-hop scenario because of the complexity of an analytical model development for multihop scenario.

[1]Trajanov Dimitar is with the e-Technology Center, Faculty of Electrical Engineering, Skopje, Ss. Cyril and Methodius University, R. Macedonia, e-mail: mite@etf.ukim.edu.mk

[2]Filiposka Sonja, is with the e-Technology Center, Faculty of Electrical Engineering, Skopje, Ss. Cyril and Methodius University, R. Macedonia, e-mail: filipos@etf.ukim.edu.mk

[3]Cilku Bekim is with Institut für internationale Zusammenarbeit des IIZ/DVV, Skopje, R. Macedonia, e-mail bekim@iiz-dvv.edu.mk

[4]Grnarov Aksenti is with the e-Technology Center, Faculty of Electrical Engineering, Skopje, Ss. Cyril and Methodius University, R. Macedonia, e-mail: grnarov@etf.ukim.edu.mk

III. Routing Protocols Efficiency With Respect To Connection Availability

In order to analyze the impact of the routing protocols to connection availability, we start with the connection availability model proposed in [5] and enhanced in [6]. Availability is a network's ability to perform its functions at any given instant under certain conditions. Steady state availability is a function of how often something fails and how long it takes to recover from a failure [1]. The connection availability model [5] includes the influence of ad hoc routing protocols in the moments when a change of route is needed, given that the previously used route becomes unavailable. Hence, connection availability includes availability of possibly different source-destination paths each existing in their own time period.

The routing protocols like AODV and DSR react on all physical faults in the same fashion, that is by issuing route-error and, afterwards, activating the route discovery mechanism. According to this behavior, node and link faults can be modeled in the same way, considering only the average switching delay $1/\delta$. When there are no nodes in the intersection area, the routing protocols react in a different way than the one previously described: if no available route can be found after a short while, in order to limit the rate at which new route discoveries for the same destination are initiated, the protocols use an implementation dependent back-off algorithm. In this case, the average time needed for connection reestablishment is modeled with the connection reestablishment delay $1/\delta_r$.

The connection availability model is a parallel system of N components with N repair facilities. It depends on the leaving rate λ (failure rate), returning rate μ (repair rate), number of participants in the network N, average switching delay $1/\delta$ and connection reestablishment delay $1/\delta_r$. For the purposes of simplifying the CTMC model the following assumptions are made: all entering and leaving events in the intersection region are mutually independent, exponential distribution is assumed for time of occurrence of each enter and leave event, and the average switching delay is small compared to the average time a routing node spends in the intersection region.

The states of the CTMC model (see Fig. 2) are labeled with tuple (i,j) where $i \in \{0,1,2,\ldots,N\}$ represents the number of nodes currently in the intersection region (the total amount of nodes is N+2), and $j \in \{0,1,2,3\}$ represents the state of the connection (j=0 no fault, connection is up, j=1 route discovery state, j=2 waiting for route reestablishment, j=3 no routing nodes available). The failure rate λ is the rate of leaving the intersection region B, while the repair rate μ, is

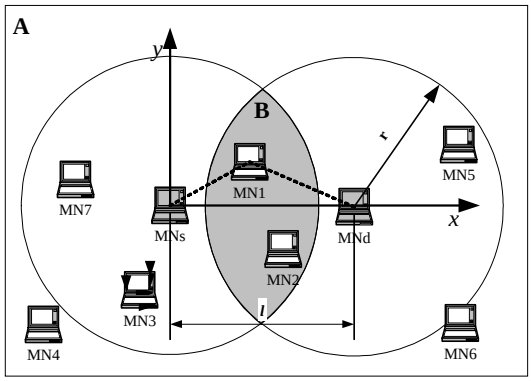

Figure 1. Ad hoc network model

the rate of the nodes returning into the B region. The steady state connection availability is given by summation of all no faulty states (states whose second index equals 0):

$$A_s = \sum_{k=1}^{N} \frac{N!}{k!(N-k)!} \left(\frac{\mu}{\lambda}\right)^N \left(\frac{\delta_r}{\lambda+\delta_r}\right) \pi_{0,3} \qquad (1)$$

$$\pi_{0,3} = \frac{(\lambda+\delta_r)/\delta_r}{\left(1+\frac{\lambda}{\delta}\right)\left(1+\frac{\mu}{\lambda}\right)^N + \lambda N \mu \left(\frac{1}{\delta_r}-\frac{1}{\delta}\right)} \qquad (2)$$

In order to evaluate the efficiency of the routing protocols to connection availability we must make model for ideal ad hoc network routing protocol behavior. The ideal routing protocol should have the average switching delay and connection reestablishment delay equal to zero. This means that when the routing node leaves intersection region the switching to a new available routing node is made immediately. Also, when there are no nodes in the intersection region and the connection is down, the connection reestablishment is made immediately when the new node enters the intersection region. The CTMC model for ideal routing protocol is shown on Fig. 3. The connection availability for ideal routing protocol is:

$$A_I = 1 - \frac{1}{(1-\mu/\lambda)^N} \qquad (3)$$

We define two measures in order to express the impact of routing protocols to ad hoc network connection availability: routing protocol efficiency (RPE) and relative routing protocol efficiency (RRPE). The routing protocol efficiency is defined as 1 minus the difference between the ideal routing protocol availability and real routing protocol availability:

$$RPE = 1 - (A_I - A_S) \qquad (4)$$

This measure gives the decreasing of availability as a result of the routing protocol. The values of RPE close to 1 represent efficient routing protocol and the lower values show that the routing protocol is not so efficient with respect to the connection availability.

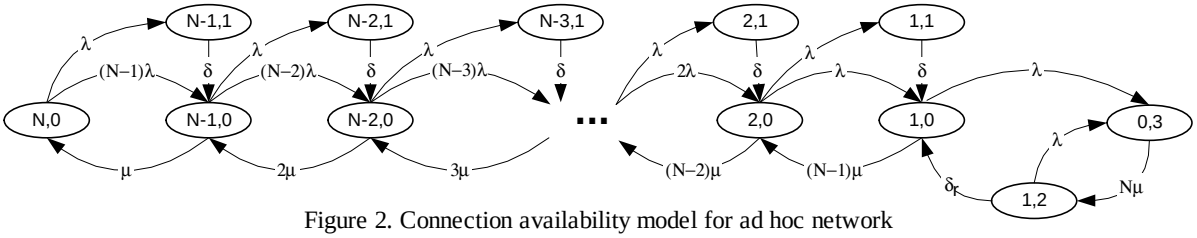

Figure 2. Connection availability model for ad hoc network

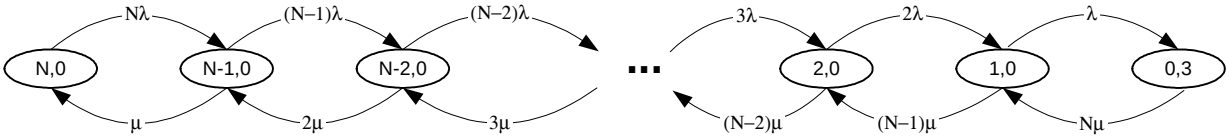

Figure 3. Connection availability model for ad hoc network (Ideal Case)

The relative routing protocol efficiency represents the relative efficiency of the routing protocol with respect to the connection availability:

$$RRPE = 1 - \frac{A_I - A_s}{A_I} \qquad (5)$$

It has values between 0 and 1. The values close to 1 represent great effectiveness of the ad hoc routing protocol network, while the values close to 0 represent the routing protocol ineffectiveness.

IV. Mobility Parameters Modeling

Connection availability of ad hoc networks depends on many factors: routing protocol, number of participants in the network, distance between source and destination, nodes velocity, mobility model, transmission range and size of the area wherein the participants in the ad hoc network are scattered. One of the main goals of this paper is to obtain the influence of these factors over the ad hoc network routing protocols efficiency.

The influence of the routing protocol is represented through the average link switching delay $1/\delta$ and the average connection reestablishment delay $1/\delta_r$ parameters. By the means of series of simulations using the NS2 [11] network simulator the numerical values of these parameters for AODV and DSR routing protocol are obtained in [6].

Both, transmission range and distance between nodes, affect the size of the intersection area B:

$$B = r^2 (2ArcCos(\frac{a}{2}) - a\sqrt{1 - \frac{a^2}{4}}) \qquad (6)$$

where r is transmission radius, a is relative distance between the nodes $a=l/r$ and l is distance between the nodes ($l \in [r,2r]$, $a \in [1,2]$).

The nodes mobility affects the leaving rate and returning rate. In order to obtain the leaving rate, we must obtain the average time $\bar{t}_B$ that a MN spends in the intersection region. The MN movement is described by a given Mobility Model (MM). There are several MM that are used in performance evaluation simulations for ad hoc networks. The most commonly used models are Random Walk and Random Waypoint [9]. In the both mobility models linear motion and uniformly distributed speed is used. In order to simplify analytical modeling we can presume that no changes of direction happen in the intersection region, namely the node passes the intersection region in a straight line with constant speed. Presuming these conditions, the time needed to pass the intersection region is given by $t = d/v$, where d is the path length that MN passes, while moving through the intersection region and v is the MN speed. The speed v is an uniformly distributed random variable. The path d is a random variable and its value depends only on the entry point into the intersection region and the entry angle. The average time that a node passes into the intersection region [6]is given by

$$\bar{t}_B = \frac{\ln(\bar{v} + \sigma\sqrt{3}) - \ln(\bar{v} - \sigma\sqrt{3})}{2\sigma\sqrt{3}} \bar{d} \qquad (7)$$

where $\bar{d}$ is the average path length, $\bar{v}$ is the average speed of the node and σ is the standard deviation. The average time that a MN passes outside the intersection region B [6] is

$$\bar{t}_C = \frac{p_C}{p_B} \bar{t}_B \qquad (8)$$

The leaving rate for intersection area B is $\lambda = 1/t_B$ and the leaving rate for area C (returning rate for area B) is $\mu = 1/t_c$.

V. Routing Protocol Efficiency Analysis

The analysis of the routing protocol efficiency with respect to connection availability is made for an example rescue mission application of ad hoc networks. The mobile nodes are located in area A=1km^2, while the use of IEEE 802.11 protocol results in transmission range r=250m. In order to be sure, with a probability of at least p, that no node in an ad hoc network with N>>1 nodes and homogeneous node density $\rho=N/A$ nodes per unit area is isolated, the node transmission radius r according [10] must be set to

$$r \geq \sqrt{\frac{-\ln(1 - p^{1/N})}{\pi} \cdot \frac{A}{N}} \qquad (9)$$

The no-isolated-node probability is a measure of the ad hoc network connectivity and here it is used to calculate the number of nodes needed to achieve connected ad hoc network for a given area A and transmission range r. Solving equation (8) for A=1km^2 and r=250m we get N=42 nodes (because of the border effects we use N=50). The value of the relative distance between MN_s and MN_d nodes is a=1.5 (average distance) in all cases. The node speed standard deviation σ is 0.01, hence the node speed is nearly constant.

The dependence of RPE on the relative node distance for AODV and DSR routing protocols is shown on Fig. 4. It can be seen that the AODV routing protocol has greater efficiency than DSR. The routing protocol efficiency drops with the increasing relative distance until it reaches a minimum value after which it again rises as a result of the very small values of the connection availability. On Fig. 5 the dependence of RRPE on the relative distance between the communication nodes for different values of the average node speed is shown. The increasing relative distance decreases the RRPE. This is a consequence of the smaller intersection region because of which there are more route requests for new routes and the protocol frequently enters the connection reestablishment stage. The delays between the subsequent route requests do not allow immediate discovery of the nodes that entered the intersection region. The increasing average node speed decreases the RRPE.

Fig. 6 represents the RRPE depending on the number of

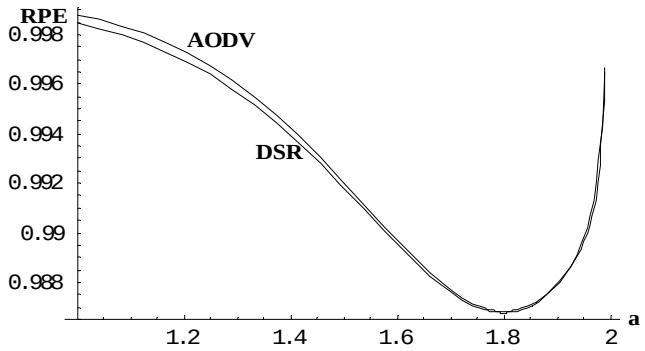

Figure 4. RPE depending on the routing protocol and relative distance between communicating nodes.

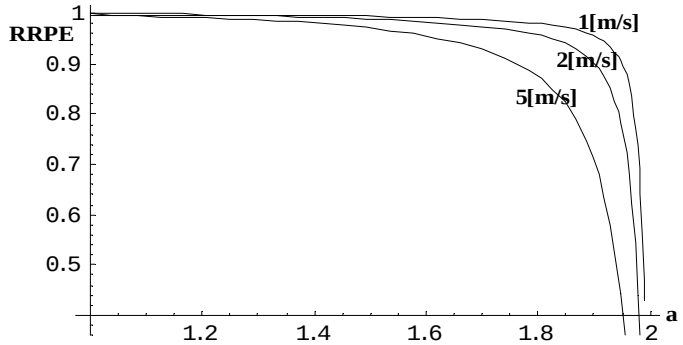

Figure 5. RRPE depending on the average node speed and relative distance between communicating nodes.

nodes in the ad hoc network for various average node speeds. The increasing number of nodes increases RRPE, while the increasing average node speed decreases RRPE. When the number of nodes increases, the routing protocol seldom enters the connection reestablishment stage which yields to improved routing protocol efficiency. RRPE depending on the node transmission radius for various average node speeds is given on Fig. 7. The increasing node transmission radius increases the RRPE, while the increasing average node speed leads to decreased RRPE, just like in the other examples. Larger transmission radius leads to larger intersection region which decreases the need for frequent route reestablishment.

VI. CONCLUSION

In this paper the impact of routing protocols to connection availability for ad hoc networks is presented. Firstly, the model of connection availability for ad hoc networks is presented and the parameters affecting this model are defined. The model includes measurable parameters like routing protocol, number of participants in network, source destination distance, node velocity, mobility model, transmission radius and size of the area wherein the MANET participants are scattered. In order to quantify the impact of the routing protocols we introduced two new measures: routing protocol efficiency and relative routing protocol efficiency. RRPE and RPE are evaluated for one important mobile ad hoc networks application, the rescue mission. According to the obtained results, the AODV routing protocol shows better performance than DSR. The increased node velocity leads to poorer RRPE. The node mobility must be considered when some level of connection availability is needed. This is especially the case, when transmission radius

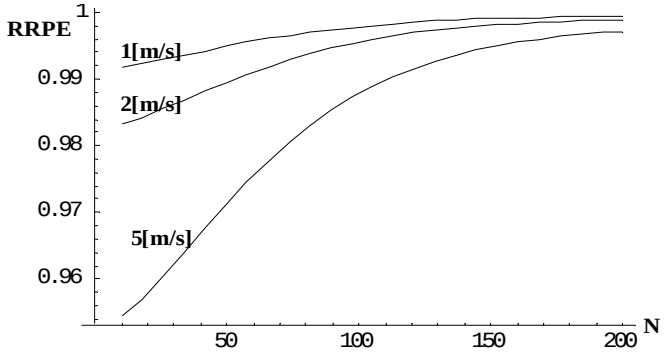

Figure 6. RRPE depending on the node speed and number of nodes in the ad hoc network.

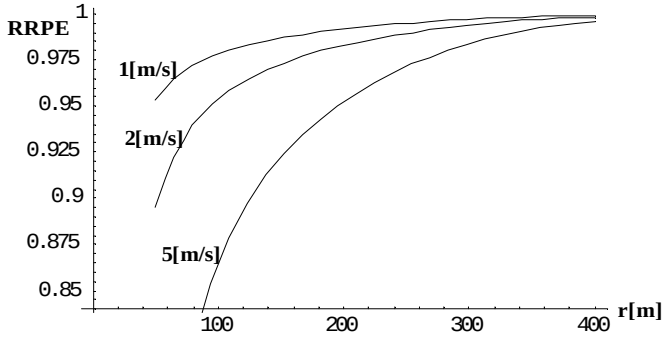

Figure 7. RRPE depending on the node speed and transmission radius.

is smaller and thus the impact of mobility is significant.

VII. REFERENCES

[1] Andrew P. Snow, Upkar Varshney, Alisha D. Malloy, "Reliability and Survuvability of Wireless and Mobile Networks", *IEEE Computer*, July 2000, pp 49-55

[2] McDonald B. and Znati T., "Predicting Node Proximity in Ad-Hoc Networks: A Least Overhead Adaptive Model for Selecting Stable Routes", *Proc. of The First Annual ACM Workshop for MobiHOC*, Boston, MA, 2000, pp. 29-33.

[3] Ingo Gruber, Hui Li, "Link Expiration Times in Mobile Ad Hoc Networks", *Proceedings of the 27th Annual IEEE Conference on Local Computer Networks*, 2002

[4] Dongyan Chen, Sachin Garg, Kishor S. Trivedi, "Network Survivability Performance Evaluation: A Quantitative Approach with Applications in Wireless Ad-hoc Networks", *MSWiM '02*, 2002, Atlanta, USA

[5] Dimitar Trajanov, Filiposka Sonja, Aksenti Grnarov, "Connection Availability Model For Mobile Ad Hoc Networks Using Reactive Routing Protocols", *IASTED*, USA, 2003

[6] Trajanov Dimitar, Filiposka Sonja, Makraduli Jani, Grnarov Aksenti, "Connection Resilience to Nodes Failures in Ad Hoc Networks", *MELECON 2004*, Croatia, May, 2004

[7] David B. Johnson, The Dynamic Source Routing Protocol for Mobile Ad Hoc Networks (DSR), internet draft, February 2002

[8] Charles E. Perkins, Ad hoc On-Demand Distance Vector (AODV) Routing, internet draft, November 2002

[9] Tracy Camp, Jeff Boleng, Vannesa Davies, "A Survey of Mobility Models for Ad Hoc Network Research", *WCMC: Special issue on Mobile Ad Hoc Networking*, vol. 2, no. 5, pp. 483-502, April 2002

[10] Christian Bettstetter, "On the Minimum Node Degree and Connectivity of a Wireless Multihop Network", *MOBIHOC'02*, EPF Lausanne, Switzerland, 2002

[11] *The network simulator – NS-2*, http://www.isi.edu/nsnam/ns

Cisco IOS Features used for QOS analysis and implementation

Tsvetomir Tsvetanov[1] and Nikolay Manolov[2]

Abstract - **IT managers and network administrators are constantly faced with managing critical business applications across their network infrastructure. Management tasks include troubleshooting network performance problems, capacity analysis and planning, internal accounting of service usage and service billing to company departments. The key to effectively managing network performance and utilization is the ability to measure, quantify and analyze enterprise traffic across the network. This paper describes the use of Cisco NetFlow and network probes for building analysis charts, as well as a practical example of easiest way to utilize protocol information.**

Keywords – **Cisco IOS NetFlow feature, network management**

I. INTRODUCTION

The trends in information and communication technologies to transfer multimedia data, including online audio and video conference streams, in same way of batch interactive data streams raise new problem field waiting for fast and adequate decisions. In the end of 90-es dominating type of services was text and graphical web contents. New age of communications enjoined new technologies in addition of standard e-mail, web-forum, IRC and other similar.

Enhancing effective management and utilizing internetworks Cisco Systems Company offers an ability to measure, quantify, and analyze enterprise traffic across the network.

Typically, such information is gained via 2 methods built-in Cisco IOS:

1. Network probes are used to continuously collect RMON2 statistics (such as, volume, rate, Top N Talkers, etc) about network and application traffic as it flows through the network. This raw data is then mined and analyzed in order to extract information to guide engineering and administrative processes.
2. Cisco's NetFlow data collection technology provides the data necessary to effectively analyze, trend and baseline application data as it passes through the network. NetFlow data can be created by Cisco routers and switches within the network and exported to a reporting package to provide the information necessary to manage critical business applications.

[1] Tsvetomir I. Tsvetanov is with Bulgarian Telecommunication Company – Intranet Department, blvd.Sh.Prohod #69, 1574 Sofia, Bulgaria, z_zvetanov.cits@btk.bg

[2] Nikolay D. Manolov is with Bulgarian Telecommunication Company – Intranet Department, blvd.Sh.Prohod #69, 1574 Sofia, Bulgaria, ndm_w@abv.bg

II. IMPORTANCE OF TRAFFIC ANALYSIS

Traffic analysis builds the foundation upon which successful and proactive network management is possible. It provides precise information as to the existence and behavior of applications and network protocols including the following key elements:

- Volume and rate measurements by application, host and conversation. These measurements allow network administrators to trend growth and to identify abnormal occurrences within the network. (e.g. virus attacks performing Denial of Services on network devices)
- Customizable groupings of network traffic by business units, geography, IP subnets, etc. These groupings of network traffic allow network administrators to associate network traffic with business entities and functions, and trend growth per grouping.
- Customizable filters and exceptions based on network traffic. Such filters and exceptions provide network administrators with alarm notifications in the event of abnormal occurrences in the network.
- Baselining to identify and trend usage statistics and report changes in network or application usage.
- Customizable time-periods to support workday reporting. This provides network administrators the ability to schedule recurring network tasks (such as data backups, database synchronizations, batch processes, etc.) at off-peak hours and to analyze statistics for a given set of business hours.

This information can be used to identify, plan and execute network based projects such as capacity planning and management, network readiness assessments for new business application rollouts, accounting functions on network usage, removing unwanted traffic, managing necessary and optional applications, planning and implementing QoS, and performing budget assessments for future network equipment and support. Without precise and comprehensive knowledge of the presence and behavior of application protocols on a network, network and application performance can be unpredictable, unacceptable and costly. Network administration and engineering changes become reactive. Additionally, costs for rolling out new applications, or adding new sites could well exceed projected values. This could wreak havoc on IT budgets, which could be avoided with usage based planning and accounting.

III. CISCO NETFLOW

Cisco has taken a novel approach to network instrumentation by adding the NetFlow feature set to its routers. NetFlow gives a Cisco router the ability to collect IP network traffic data. Utilizing a router as a probe to gather NetFlow data has the following advantages:

- Low capital investment – The majority of networks are already instrumented with Cisco routers. Customers must simply turn NetFlow on each of the routers in order to start measuring traffic to those routers.
- Simple configuration – configuring NetFlow involves a few global commands and an interface command for each interface running NetFlow.
- Completeness of data – NetFlow measures and reports automatically on all application traffic (most probe solutions require that each probe be configured to look for each traffic type).
- Low lifecycle maintenance - NetFlow capabilities are tied to Cisco router hardware/software maintenance.

However, the following should also be considered when looking to deploy NetFlow:

An increase in CPU utilization on the configured routers (The amount of increase on router CPU utilization varies by router platform and the number of flows traversing the router.)

- An increase in network traffic along the path between the configured routers and the NetFlow harvesters.
- A less significant increase in network traffic along the path between the NetFlow harvesters and the management/reporter console.
- Only IP traffic is supported!

IV. HOW CISCO'S NETFLOW WORKS

NetFlow enables Cisco routers to track unicast IP packets as they enter the router through an interface. As the name implies, NetFlow tracks IP packets on a "per flow" basis. A flow is made up of unidirectional flow of data having two endpoints as individually identified by a combination of the following seven criteria items:

- Source IP address
- Destination IP address
- Source port number (TCP, UDP)
- Destination port number (TCP, UDP)
- Layer 3 protocol type (IP, ICMP)
- Type of Service (ToS) byte (0-7)
- Input logical interface

Any difference in these seven criteria distinguishes one flow from another.

When enabling NetFlow on a Cisco router, a NetFlow cache is built by the router to track flows as they enter the router. The NetFlow cache contains 64-byte records (one per flow) that describe each respective flow. The default size of the NetFlow cache is dependent on the router platform and/or the amount of memory in the router. The information contained in each NetFlow record is somewhat similar, but varies by NetFlow version number.

V. NETFLOW SYSTEM FOR TRAFFIC ANALYSIS

According to Cisco, a complete NetFlow system should contain the components as shown in Figure 1.

Figure 1 : NetFlow Infrastructure

- **NetFlow data export devices** – Cisco switches and routers. Captures NetFlow statistics for ingress IP traffic and export data to a collection device.
- **NetFlow data collector –** Software performing data collection, filtering and aggregation.
- **NetFlow analyzer –** The user interface to collected data. Enables user to retrieve and display NetFlow collected data, based on several criteria.

There are number of commercial NetFlow collectors and analyzers available from Cisco, NetQoS, Apogee, HP and Concord.

VI. EXPORTING NETFLOW DATA

The routing device checks the NetFlow cache once per second and expires the flow in the following instances:

- Transport is completed (TCP FIN or RST).
- The flow cache has become full.
- The inactive timer has expired after 15 seconds of traffic inactivity.
- The active timer has expired after 30 minutes of traffic activity.

NetFlow data is exported in one of four formats: Version 1, Version 5, Version 7, and Version 8. In all versions, the datagram consists of a header and one or more flow records (see Table 1 and Table 2). The Version 5 format adds BGP AS information and flow sequence numbers. The Version 7 format is used only on Catalyst switches. Cisco IOS NetFlow aggregation maintains one or more extra flow caches with different combinations of fields that determine which traditional flows are grouped together. These extra flow caches are called aggregation caches. Version 8, a new data export version format, has been added to support data exports from aggregation caches. This leads to reduced bandwidth requirement and reduced NetFlow workstation requirements. In version 9 Cisco will implement flexible export format and support for MPLS, multicast and BGP Next Hop.

TABLE 1
VERSION 1 HEADER FORMAT

Bytes	Content	Description
0-1	version	NetFlow export format version number (in this case, the number is 1).
2-3	count	Number of flows exported in this packet (1 to 24).
4-7	sysUptime	Number of milliseconds since the routing device was last booted.
8-11	unix_secs	Number of seconds since 0000 UTC 1970.
12-15	unix_nsecs	Number of seconds since 0000 UTC 1970.

TABLE 2
VERSION 1 FLOW RECORD FORMAT

Bytes	Content	Description
0-3	srcaddr	Source IP address.
4-7	dstaddr	Destination IP address.
8-11	nexthop	IP address of the next hop router.
12-13	input	Simple Network Management Protocol (SNMP) index of the input interface.
14-15	output	SNMP index of the output interface.
16-19	dPkts	Packets in the flow.
20-23	dOctets	Total number of Layer 3 bytes in the flow's packets.
24-27	first	SysUptime at start of flow.
28-31	last	SysUptime at the time the last packet of flow was received.
32-33	srcport	TCP/UDP source port number or equivalent.
34-35	dstport	TCP/UDP destination port number or equivalent.
36-37	pad1	Pad 1 is unused (zero) bytes.
38	prot	IP protocol (for example, 6 = TCP, 17 = UDP).
39	TOS	IP ToS.
40	flags	Cumulative OR of TCP flags.
41	tcp_retx_cnt	Number of mis-sequenced packets with delay > 1 second.
42	tcp_retx_secs	Cumulative seconds between mis-sequenced packets.
43	tcp_misseq_cnt	Number of mis-sequenced packets seen.
44-47	reserved	Unused (zero) bytes.

VII. NETFLOW APPLICATION

As NetFlow is activated on appropriate router interfaces and export function is up and running, using a simple command application (Figure 2) NetFlow data is collected within a period of time and is stored into relational database or into plain text file/s. Result analysis performs, aided by relations of data stored, which is the way to trend and monitor enterprise traffic. All information presents in a user-friendly graphic style by web application or other GUI. Graphics and text result summaries the points and time, where and when is recommended applying prioritization techniques performed in router IOS.

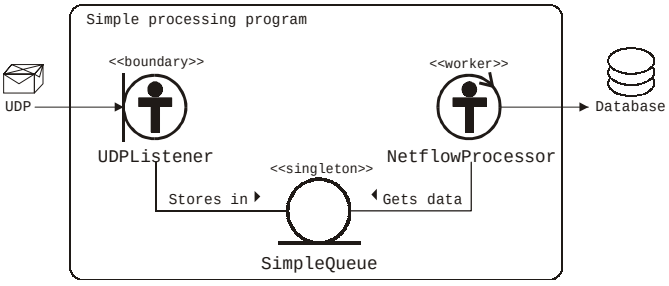

Figure 2 : Application UML diagram

Data storage and monitoring can be done via two scenarios:

- Data is stored within a 24-hour period and using additional processes stored data is aggregated following previously well defined plan for creating significant sections (database table joins). Aggregated in that manner data leaves for additional trending within a larger periods of time: couple of days, a week or a month.
- Data is stored into a relational database within a longer time period, e.g. month, and finally the NetFlow application generated interactively online DB queries for significant table joins.

Based on NetFlow data collection and aggregated data network managers get a picture which kind of internetwork and enterprise applications is used between sets of subnetworks and specific nodes. In enterprises implemented policy-based routing network engineers and administrators can have real information of load in logical circuits. In that way NetFlow analyzer application is a tool for designing a reliable and load balanced network. Assume that we chance on a multiple interconnections at core/backbone network as shown in Figure 3. As the network grows and changes its topology it is possible to misbalance the traffic shaping doesn't matter it was previously well balanced. Adding or modifying services supplied by enterprise servers attached at stub subnetworks of backbone routers can be reason of change of traffic characteristics, so policy-routing is no more properly working. In enterprises quickly growing and altering, in cases of designing new network implementation, when preparing test plans for innovations, NetFlow application analyzer helps engineers to commit trends, points of weakness, and fields of redesign.

Furthermore, modern networks transfer still more multimedia content. Audio, video and telephony services are routed together with batch interactive data. Having NetFlow collection process engineers can afford designing more intelligent software that provides an advisory capabilities such as report suggestion for QoS implementation, for new load balance design, and for bandwidth utilization.

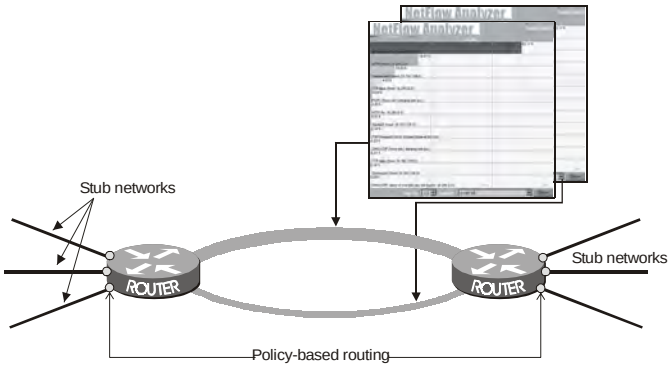

Figure 3: Multiconnected backbone network

VIII. BENEFIT FOR BILLING/ACCOUNTING

NetFlow captures and exports detailed measurements including intra-company, supplier and customer traffic volume and application usage patterns for billing/accounting and network planning purposes.

Customer benefits by pay for only the required bandwidth being utilized. The customer (and the service provider) also benefits by receiving detailed usage measurements via NetFlow data export and by easy reconfiguration to higher service levels when required. For example - time and usage based billing via NetFlow measurements provide the service provider with a means of encouraging (or shifting) demand during periods of light network loading by offering off peak discount pricing. Traffic classes and prioritization allow the network operator to encourage the customers to classify their traffic and then to transport the highest value bits during peak usage periods and heavy congestion conditions.

IX. CONCLUSION

Cisco IOS QoS services and NetFlow data collection and export capabilities provide a new paradigm for ISP's to efficiently monitor network operations, drilldown to diagnose and resolve network troubles and provide both internal personnel and customers with data concerning service level agreement metrics. ISPs may now utilize a flow-based paradigm to visualize traffic flows in the network including aggregate traffic flows, flows by application and flows by class of service. Enhanced network monitoring based on layer 3 services MIBs will also provide the capability to observe bandwidth allocation and excess usage.

In addition with IP Account and RMON2 features of Cisco IOS NetFlow is a powerful tool for monitoring and management of complex enterprise networks. It gives managers and engineers a key for flexible and vivid trend and performance management and utilization of their enterprises internetworks.

REFERENCES

[1] Cisco® NetFlow or RMON2: NetQoS White Paper, http://www.netqos.com

[2] Advanced QoS Services for the Intelligent Internet, Cisco White Paper, www.cisco.com

Watermark Algorihm for JPEG2000

Georgi B. Varbanov[1]

Abstract - **A lot of research work had been carried out recently in the field of copyright protection of multimedia documentation-images, videos, and audio files and etc. In this article a specific method for preventing images' copying is presented. In previous work we discussed for embedding and delectation of watermark had been done using wavelets algorithm using JPEG. Now we proposed method for watermark still images based on the JPEG2000 compression standard.**

***Keywords*: watermark, wavelets, compression, JPEG2000.**

I. INTRODUCTION

In recent years a lot had been done in the field of technologies for compression of static and dynamic images and multimedia files transmission over Internet and warless sets. The well-known standards JPEG and MPEG had undergone many changes. Two years letter ago the JPEG2000 was introduced. Modern hardware solutions, such as digital video cameras, digital photo cameras, multimedia players etc. implement to a certain degree the new standards due to the usage of smaller files' size or memory reduction possibilities. Copyrights protection in a global plan becomes more and more important due to the increased dissemination of multimedia files in the world wide web.

Until recently research activities in the field of multimedia data protection were quite a few. Nowadays they have increased a lot..New qualitative solutions are investigated, new algorithms for watermarking second and third generation are developed. In this article a method for water marking of still images is presented on the basis of an improved algorithm using JPEG and JPEG2000 standards of compression.

II. DECOMPOSITION

The submit algorithm itself is a combination of the well known algorithms of blind Dugad [7][1][14] and non blind algorithm Xie [6][1], but now we adapt to new standard and add new features. After research and a lot of experiments we chose this combination, implementing a new modification, calculating results of non-overlapping blocks when watermark is represented as a binary sequence.

The watermark length is two bytes when is binary. The length the pseudo random watermark (when generated in a copyright mode) is variable and depends on the threshold array [Tj] and images' dimensions of selected polygons. It depends upon the wavelet decomposition levels as well as upon the various sub-bands.

Initially selected coefficients are normalized by vector factor *a*. This vector is experimentally chosen and set in the range of 0.1-1(Default 0,33). As a result of using a combination of blind and non-blind methods we've got the possibility of improving results in water mark extraction and increase the stability of the algorithm against deformation, compression, cropping etc. attacks..

III. WATERMARK EMBEDDING

The modified algorithm of Dugad [***] and Xie [***] is used aiming at the least visible changes in images.

Watermarking is embedded in the JPEG2000 algorithm. Initially a 7/9 bi-orthogonal filter is used with 5 levels of decomposition. Data are fed in LH2, HL2, HH2 sub ranges at second and third decomposition wavelet level. The overall level is divided apriori into non-overlapped blocks of 32X32 elements. A combination of three cells is used (as in the Xie algorithm Fig[1]).

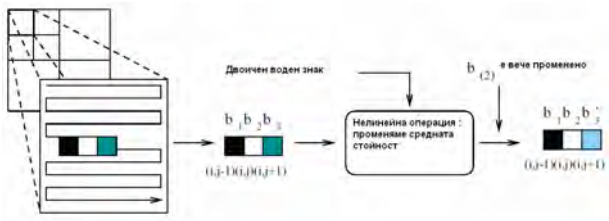

Fig. 1 Method Watermark by Xie

Where:

B1,b2,b3 was pixel 1,2,3 and second b was sorted and mark mean with formula Δ Eq(1);

$$\Delta = \frac{\alpha.(\max|bj| - \min|bi|)}{2} \qquad (1)$$

α Is scaling factor

Δ-Mean of the bj ,bi of array 3x3

The watermark is a Gauss function, generated by three Pseudo random generators. The watermark has got a variable length and it depends upon the number of selected points, having threshold values, set into an array. The values depend upon the specific image and may vary from 15 to 60. It depends of levels sub-bands. We use a technique for selection and marking, similar to the Dugad method [7], selecting groups of cells in 3 (in the frame of the Xie[6] algorithm) Fig. 2

[1] Georgi. B. Varbanov is with the Faculty of Computer Science and Automation , Studentska STR. 1 9000 Varna , Bulgaria, E-mail: gvarbanov@hotmail.com , varbanov@mbox.digsys.bg

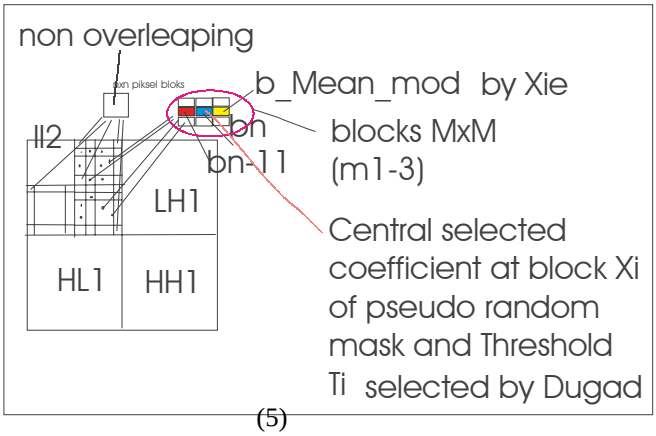

(5)

Fig.2 Blocks and coefficients located in the Wavelet levels by the modified methods

The embedding formula is shown in Eq(2), whilst the schemes of embedding are shown in Fig. 2

$$f^{'}(m,n) = f(m,n) + \alpha.\Delta(m,n).wi \tag{2}$$

Where m,n is selected coefficient by the thresholds array Ti and m,n < x,y(where x,y size of images(blocks) Defaults level is 8x8 for binary . Every blocks in this case embedded one bits of watermark sequences wi* . When images uses for copyright protection blocs was 256x256 min up to blocks K(i) where K(i) is number of array of Thresholds(i)/3

We don't need the original images in order to extract the watermark. This modified algorithm is a "blind" algorithm. After the reverse IDWT wavelet JPEG2000 transformation and extracting the colors and luminance components of the image the watermark is being extracted. First we determine non-overlapping blocks sized 16x16 (when watermark has been binary), and then we select coefficients by mask of Pseudo random sequences [-1,1] and component threshold array Tj.

$$T_i = \frac{\alpha}{S.N}\sum_{i}^{N}\left|f^{i}\right| \tag{3}$$

Where S is Standard deviation

The routine for checking the availability of watermark starts with the evaluation on the correlation between the embedded watermark wi* and the extracted one wi with formula Eq (4), setting the group coefficients 3X3

$$wi^{*} = \frac{f^{*}(m,n) - f(m,n)}{\alpha.f(m,n)} \tag{4}$$

Where m,n is the number of current selected (masking) point

The results from the separate blocks are compared to a standard correlation function – Eq [5]

$$\delta = \frac{w_i^{*} \bullet w_i}{\left\|w_i^{*}\right\| \bullet \left\|w_i\right\|} \tag{5}$$

The number of cells for watermarking may be additionally set to 1, 2x2 3x3. Extraction is shown in Fig. (4). It is similar a lot of know additive algorithms for watermarks images

As a complementary protection we foresee a change of the coefficients of the wavelet filter for image decomposition. Coefficients equal to 6, 5 and 4 are used for the one to tree levels. All experiments had been carried out at second and third levels of decomposition wavelets. Software developments are JAVA2 based, using JJ2000 [15][14]

In [1] was given others schemes for watermarking schematic connections that produced others selected coefficients by irregulars mechanism watermark

IV. Results.

Results are based on an overall number of 1000 tests. Due to the improved Dugad-Xie algorithm we get an improved exposure of watermarking in 80 % of all case studies in the event of attacks, done by StirMark[1] layout compared to other algorithms[1]. For other types of attacks, such as (still not for all Crop & Rotation) the algorithm yields very good results (very robust) on the condition that parameters of image deformation are known beforehand. Described above algorithm has been used to create a program, that embedded and detect watermark in still colors images. It s was release by Java2 and JJ2000[] coder and encoder()

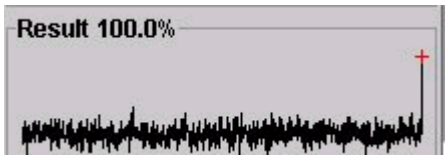

Fig. 7 Result FMLR –attack StirMark new method

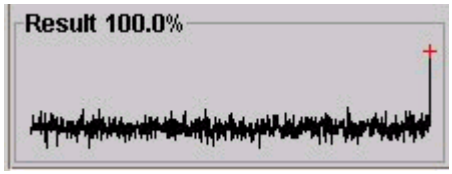

Fig. 8 Result Gaus –attack StirMark new method

Fig. 9 Result Median 4x4 –attack StirMark new method

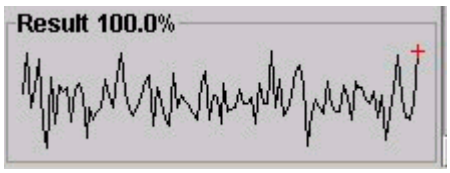

Fig. 10 Result Shearing 5x5 –attack StirMark new method

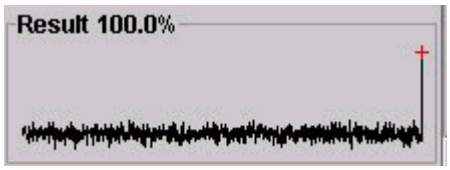

Fig. 11 Result Remuve 17 columns and 5 rows –attack

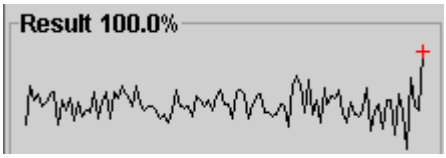

Fig. 12 Result Median 3x3–attack StirMark old method

Fig.13 Original 14 Fig. Marked jp2

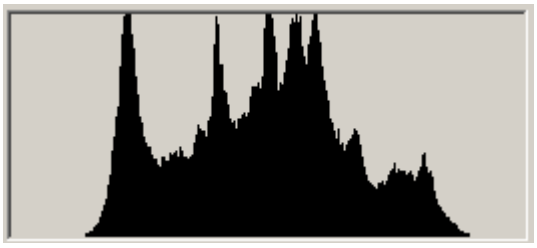

Fig. 15 Marked image Lena.jp2 Histogram fig.

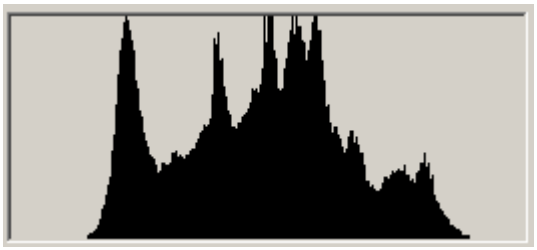

Fig. 16 Histogram Original Histogram fig.

Different images can be obtained after casual modulation of other parameters. On fig. 3 you can see the same diferenses original and marked images..

The multiple embedding of water signs in result in more stability and robustnes against geometric distortion of the selected image, cropping and compression ratio high diapason

V. Conclusion

The next step for the improvement of the algorithm should be the implementation of an algorithm for automatic recognition of applied image's attack (e.g. using feature point or some other well known algorithms for embedding reconstruction functions)[9,10,11,1,2,3,5], whose deformation can reconstruct the image after attacks) or a manual adaptive definition of the level of deformation by the software and then searching for the watermark.

The second option is too complicated and needs a lot of time and resources in processing bigger data arrays (as specified in images' database), which in its turn is not applicable for Internet applications for automatic registration and images watermarking

References

[1] "Digital Image Watermarking in the Wavelet Transform Domain" - Peter Meerwald, Salzburg, January 2001, University Salzburg

[2] "Digital Image Watermarking Techniques" - Christopher G. Martin, 23 May 2000, Rochester Institute of Technology

[3] "Attack Modelling: Towards a Second Generation Watermarking Benchmark" – S. Voloshynovskiy, S. Pereira, V. Iquise, T. Pun, University of Geneva

[4] "Attacks on Copyright Marking Systems" – Fabien A.P. Petitcolas, Ross J. Anderson and Markus G. Kuhn, University of Cambridge, Computer Laboratory

[5] "Robust Digital Image Watermarking" - Shelby Pereira, Thesis, Geneva 2000

[6] "Liehua Xie , Charles G. Boncelet, and Gonzalo R. Arce. "Wavelet transform based watermark for digital images". *Optocal Expres, 3.(120:467, December 1998*

[7] "A new Wavelet – Based Scheme for Watermarking Images" – Rakesh Dugad, Krishna Ratakonda and Narenda Ahuja, Department of Electrical and Computer Engineering Beckman Institute, University of Illinois, Urbana, IL 61801

[8] "WaveMark:Digital Image Watermarking Using Daubechies'Wavelets and Error Correcting Coding" – James Ze Wang and Gio Wiederhold, Stanford University, Stanford, CA 94305, USA

[9] "Signal compression based on human perception" – N. Jayant, J. Johnston and R. Safranek, Proceeding of the IEEE, 81(10):1385 – 1422, October 1998

[10] "Optimized wavelet domain watermark embedding strategy using linear programing" – Shelby Pereira, Sviatoslav Voloshynovskiy and Thiery Pun, University of Geneva, Switzerland

[11] "Geometrically Invariant Watermarking Using Feature Points" – P. Bas, J-M. Chassery and B. Macq, 5-AUTH Authentication and Watermarking

[12] "Thinking in Java" Bruce Eckel 2&4 Edition

[13] Java 2 Ръководство на програмиста, Herbert Schildt, Софтпрес

[14]"Wawelet based watermarking algorihm for still images" G. Varbanov, V.Naumov, D. Ilieva, Technical Universiti

of Varna,Bulgaria Meet/Marind'2002 volume IV 201-207
[15]"JPEG2000 part 1 final commtteee draft –version 1,0 " tech.rep, ISO/IEC FCD15444-1, March 2000
[16] http://cosimo.die.unifi.it/~piva/Watermarking
[15]http://www.bearcave.com/misl/misl_tech/wavelets/daubechies

Intelligent Transportation Infrastructure For Traffic Incident Management System Support

m-r Kostandina Veljanovska, MASc[i]

Abstract **- Actual trends in the computer science, neural networks and artificial intelligence at all have become inseparable part of our daily life. Transportation systems are also under that influence. A broader view of the research in the field of implementation of the new technologies in freeway traffic management and freeway traffic incident management is given in the paper. The research was done at the Faculty of Technical Sciences - Bitola and the University of Toronto, Canada.**

Keywords **- intelligent transportation systems (telematics), intelligent transportation infrastructure, ITS architecture, incident detection.**

I. Introduction

Traffic congestion are very often caused by incidents - accidents, vehicle malfunctioning, road maintenance, or other unpredictable or predictable events… Video surveillance and sensors on the road can help for rapid incident detection. Computerized emergency vehicles scheduling enables fast reaction on site. Changeable Message Signs (CMS) can re-route drivers on the alternative routes.

These technologies can shorten travel time for 10 to 45 % in the congested case.

Republic of Macedonia, trying to provide safer roads is among the countries - beginners in designing its own traffic incident management system (TIMS) applying intelligent transportation systems (ITS). This state of the art is motivation factor for engaging scientists in the filed of traffic engineering and information sciences. In that direction is the effort of this paper - to give a complete picture of intelligent transportation infrastructure (ITI) for TIMS, i.e. picture of the information organization, processing, transfer and management in a complete system in Europe and in the world. Our efforts to approach EU would have the meaning of following the standards in traffic and integration in the European transportation infrastructure.

II. ITS

The answer of the many of our traffic and transportation problems lies in a broad range of various technologies known as ITS - intelligent transportation systems. ITS - a multidimensional approach towards satisfying our transportation needs consists of a substantial number of technologies, information processing, communications, control and electronics. Connecting these technologies to transportation systems can save lives, energy and money. Implementation of these technologies means real revolution the way traffic has been understood. In this paper implementation of intelligent transportation systems (ITS) in traffic incident management research done at University of Toronto and Sv Kliment Ohridski - Bitola is presented.

A. Definition

ITS is a system that gives services for the customers using the information system, adapted to the customer. ITS are open and adaptable, offering implementation of different technologies for interactive and multimedia work and on the other side complete coverage starting from micro-location, street, city, region, nation and the world as a whole.

B. Aim

The aim of ITS creation is to improve traffic and transportation quality by avoiding traffic congestion, travel time savings, drivers and passengers safety and commodity improvements, goods and services exchange, improvement of the total information transparency. As a result we get higher level of customer satisfaction and overall environment prosperity. Among the key aims in ITS creation are today's science imperatives lower pollution and lowering energy dissipation.

III. ITI

ITS domain comprises systems starting with control systems till automatic freeways. But, the starting point in implementation is the core of the systems. The implementation could be done step by step. **Intelligent transportation infrastructure (ITI**) is the core of ITS.

Intelligent transportation infrastructure (ITI) is the key element necessary for a complete implementation of ITS. It is an integrated system from nine synergetic connected systems of traffic components.

Basically, ITI is the ITS infrastructure and these component have to be developed first. ITI consists of these integrated components:

- Traffic signal control
- Freeway management
- Public transportation management
- Incident management
- Electronic fare collection
- Electronic tool collection
- Railway crossings
- Emergency management services
- Regional multi-modal traveler information

ITI refers to the part of ITS which deals with hardware, software, services etc., which now and especially in the future will complete and support all traffic related activities.

Usually, ITI is implemented in the urban areas, and afterwards it includes commercial vehicles and rural needs.

IV. ITS ARCHITECTURE

Every system initially has its own architecture. Architecture means common starting point and common language. In USA and Canada there is National ITS architecture. It is the frame that refers to 29 ITS user services. Architecture defines subsystems and data flow (information that has to be exchanged among subsystems) needed for proper ITS operation. ITS architecture does not define the actual design or what to purchase. It is a subject of a local choice.

Terminology is important, as well as the basic structure of the architecture. On the basic level, architecture defines series of functions. Those are different activities that system has to perform. For example, traffic surveillance or public transport vehicles surveillance. There is a substantial number of complex functions or high level functions and they are divided in sub-functions. For example, low - level functions are HOV lane usage surveillance (HOV = High Occupancy Vehicles). On a higher level, functions are defined graphically as Data Flow Diagrams DFD. Every low-level function is precisely defined with Process Specification (P-spec).

Architecture is indeed software, which enables simple and easy designing of ITS services, needed to be implemented on site, depending on the local circumstances, user requirements and constraints. Both logical and physical architecture contain implementation constraints depending on the local circumstances in the real world. For example, in the Canadian ITS architecture there are constraints from the point of view of the environment (environment, road, potential obstacles etc.), human factor (driver, traveler, maintenance personal, pedestrians, etc), systems (company user, financial institution, governmental administration, media, etc.) and other systems (other vehicles, other TMC etc.).

One of the basic tasks of the architecture is to assign functions to the different components or ITS subsystems, which operate together. Examples of subsystems are information services providers, traffic management etc. Traffic incident information, as well as all other relevant information have to be exchanged among specific subsystems if we want coordinate and integrated ITS operation. So, ITS architecture defines links, i.e. the way of connection among subsystems. This is done at the logical level as a **data flow**.

Logical architecture defines data flow diagrams and process specifications. According to the Canadian National ITS architecture, logical architecture defines functions, for example, incident detection, or incident verification; while physical architecture defines where those functions could be found, for example, in traffic management center (TMC).

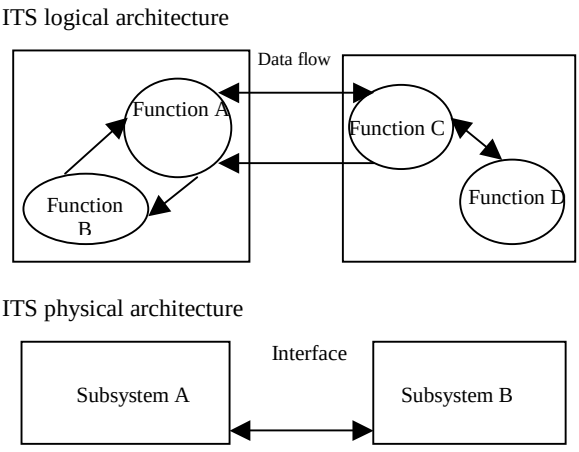

Fig.1 Logical and physical ITS architecture

Figure 1 shows scheme of ITS logical and physical architecture. Logical architecture defines functions which have to be performed in the subsystems i.e. data exchange. Physical architecture defines the way the functions defined in the logical architecture are realized, i.e. the way the subsystems are connected (interface).

Physical architecture defines subsystems, assigns functions to the process specifications (p-spec) and documents the interface (the way of connection) for the data flow among subsystems. In the Canadian ITS architecture physical architecture contains three levels: communication (how the information is transferred among transportation subsystems), transportation (which are the transportation systems that transfer specific information) and institutional (institutional structure, politics and supporting strategies).

A. National ITS architecture - ITI connection

Architecture documentation gathers highly detailed technical documentation. How the architecture operates can be seen in the ITI component connections diagram. Figure 2 shows simplified diagram of ITI components and their basic connections, the way they are defined in the National ITS Architecture.

Figure 2 shows type of the data that have to be exchanged among different ITI components (shown with arrows). Arrow peak shows in which direction data have to be transferred. These data definition and exchange direction are defining the interface (the way the components communicate). Technically speaking, almost all interfaces are bi-directional because computer systems have to communicate that way so the data transfer can be performed.

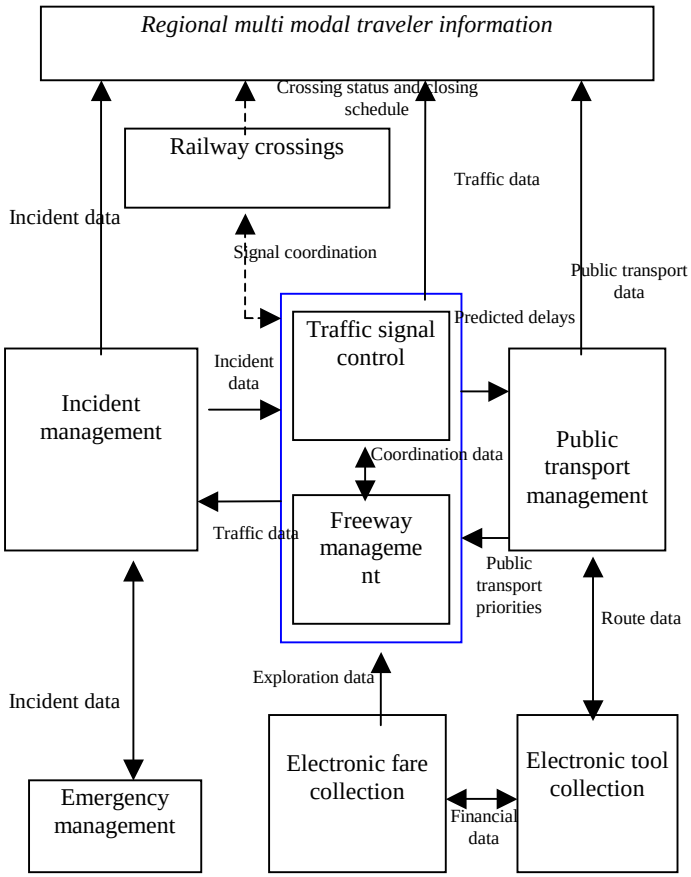

Figure 2. ITI components and connections among them

V. Freeway Traffic Management System (FTMS)

Traffic management means congestion management which results of

- Geometry design inconsistency of a freeway and
- Traffic regulation (including insufficient capacity),

that appeared as recurrent reasons and non-recurrent or random reasons:

- Incidents,
- Maintenance and reconstruction, and
- Weather conditions,

According to FHWA non-recurrent reasons can cause about 60% of congestion.

Freeway traffic management system (FTMS) consists of infrastructure elements chosen to satisfy the aims of the function, which they perform together. They include hardware (video, variable message signs - VMS, electronic vehicles identifiers, etc.), communication equipment, Traffic management center (TMC) (with appropriate hardware and software), people that work in the center. And the regulations and procedures established in order to provide continual operation of the all traffic related events on the freeway.

Freeway traffic management system (FTMS) consists of several subsystems (information system for the drivers, ramp metering system, etc.), which communicate among each other.

VI. Incident Management (IM)

Incident management is the most needed and from the safety point of view the most useful freeway traffic management system function.

Experienced drivers have learned to deal with recurrent congestion, planning their travel time lost in the congested traffic. However, non-recurrent congestion is unexpected and dangerous. In spite of the fact that it is unsafe, it can cause additional delay for the non-informed drivers.

Almost all non-recurrent or random congestion can be considered as traffic incidents, because they are potentially dangerous and can lead to conflicts.

Incident management needs coordinated operation and beforehand planned usage of human and technological resources, so the freeway can restore its complete capacity shortly after the incident occurred.

A. Incident Management Phases

As a first phase in incident management design characteristics of the incident have to be known. The incident influence on the freeway traffic in a certain region has to known also.

Rapid incident detection is a critical element in the incident management process. The faster the incident is detected, the faster the response and clearance would be. There is a substantial number of available technologies, starting with cheap manual methods, going to sophisticated automatic surveillance techniques which require high investments from the public agencies (probably governmental). The most significant factor is that ITS often promise dramatic improvement of the detection possibilities.

Rapid and on time response from the appropriate subjects can substantially reduce duration of the incident. So, in the second phase of the incident management usage of the computer technology is essential.

B. AID Algorithms

At the beginning of incident management system creation commonly used technique is telephone calls from the drivers or manual surveillance.

Automatic incident detection techniques surveillance use:

- Inductive loops
- Magnetometers
- Microwaves/radar
- Laser
- Infrared
- Ultrasound
- Sound
- Vehicles exploration (AVI, AVL).
- Closed - circuit television

Automatic incident detection technique efficacy depends partly on the type of the algorithm used for analysis of the detected data.

During the research, two types of algorithms for automatic incident detection were tested: conventional McMaster Algorithm (MMA) and non-conventional Neural Network Algorithm (NNA). The research was completely computerized with algorithms testing done on the database from QEW freeway in Toronto. Comparative results are shown in Table 1. Automatic incident detection algorithm testing has shown that neural network is far better for automatic incident detection than the McMaster algorithm. Both algorithms initially need parameters setting for the particular freeway or freeway section (MMA), i.e. initial training of the neural network and then testing and implementation.

Table 1. AID algorithms testing results

	Results	
	MMA	NNA
Correct classification (%)	70.47	66.84
Normal states detected (%)	94.83	62.48
Total detection rate (%)	20.90	57.98

VI. CONCLUSION

Existing FTMS research and analysis, as well as AID algorithms analysis has shown that implementing new computer technologies in traffic accident and /or incident management as potential accidents the number of accidents would decrease, damage would be less and the number of killed and wounded would decrease.

One of the key components in incident management subsystem as part of the FTMS are algorithms for automatic incident detection algorithms.

On the other hand, immediately establishing National ITS architecture is needed according to the developed countries examples.

Education and training as well as information for the users, i.e. potential users of the freeway traffic management system and freeway traffic incident management system are needed.

LITERATURE

[1]. Вељановска, К., Функционални аспекти на интелигентната транспортна инфраструктура за поддршка на системот за управување со сообраќајни инциденти во РМ, Магистерски труд, Универзитет "Св. Климент Охридски" - Битола, 2002

[2]. Apogee/Hagler Bailly, Intelligent Transportation Systems: Real World Benefits. US DOT, Washington, DC, 1998

[3]. Carvel, J.D. and others, Freeway Management Concepts. Freeway Management Handbook, Texas Transportation, U.S.DOT, FHWA, 1997

[4]. Building the ITI: Putting the National Architecture into Action. US DOT, Washington, DC, 1996

[i] Kostandina Veljanovska, REK Bitola, 7000 Bitola, Makedonija, kostandina@rocketmail.com

Software Aspects of Intel Pentium Simulator Development

Elena I. Zaharieva-Stoyanova[1], Radoslav At. Atanasov[2], Erkan Sh. Shakir[3]

Abstract **- The simulation technique is often used in computer architecture development. The software simulators could be used as a tool for studying the architectures' models and functionality. In this paper a software simulator named PipeSimul is represented. It shows the Intel Pentium processors' structure and functionality. This paper treats the software problems related with simulator development. The simulation of instructions execution is realized by independent module, represented in this paper. The Graphics User Interface is represented, too.**

Key words **- simulators, computer architecture, Intel Pentium processor, pipelining**.

I. INTRODUCTION

The simulation technique is often used in computer architecture development. The software simulators could be used as a tool for studying the architectures' models and functionality.

The software simulation method is used because of the following reasons:

- Through the circumstances it is the one way of observing of insupportable processes
- Software simulation is cheaper; its realization is faster than hardware execution.
- It has more flexibility
- Software simulation allows to investigate and to modify the simulating object through its design.
- The simulator is a tool for a dynamic optimization of the models, who are not able to be analysed by theirs mathematic description.
- The simulation allows viewing processes hidden into big and complex modules.
- The simulation technique allows realizing virtual, not existed models used for an education.

The development of up-to-date processors' architecture is closely related with instruction-level parallelism and superscalar concepts [2]. Studying of these concepts for theirs application in a real architecture needs a software simulation. This paper treats the problem of software simulator development. The simulator represents Intel Pentium architecture.

[1]Elena I. Zaharieva-Stoyanova is with the Department Computer Systems and Technologies, Technical University of Gabrovo, 4 H. Dimitar, 5300 Gabrovo, Bulgaria, E-mail: zaharieva@tugab.bg.

[2]Radoslav At. Atanasov is a student with the Department Computer Systems and Technologies, Technical University of Gabrovo, 4 H. Dimitar, 5300 Gabrovo, Bulgaria

[3]Erkan Sh. Shakir is a student with the Department Computer Systems and Technologies, Technical University of Gabrovo, 4 H. Dimitar, 5300 Gabrovo, Bulgaria

The Intel Processors are among of most used processors in the computer systems. Developing IA-32 architecture, Intel Corporation introduces superscalar technique in the Pentium processor. The Intel Pentium is the first processor with superscalar architecture. The next steps of IA-32 architecture development are coming of P6 and NetBurst processor architectures [1],[3],[7],[8].

In this paper a software simulator named PipeSimul is represented. It shows the Intel Pentium processors' structure and functionality. The objective of new simulator creation is to show the base concepts of the Intel Pentium processors working by means of short assembler programs. This simulator could be used also for the evaluation of source code efficiency. It will be applied in the hirer-school education to show how superscalar architecture works [4],[5],[6].

This paper treats the software problems related with simulator development. The simulation of instructions execution is realized by independent module, represented in this paper. The Graphics User Interface is represented, too.

II. THE PIPELINE EXECUTION IN INTEL PENTIUM PROCESSOR

The Intel Pentium processor is the first Intel processor with a superscalar architecture. It has two execution pipelines to achieve superscalar performance. Two 5-stages pipelines, known as U and V, together can execute two instructions per clock. In comparison with 80486, the on-chip first-level cache was doubled, with 8 KB devoted to code, and another 8 KB devoted to data. Branch prediction with an on-chip branch table was added to increase performance in looping constructs. The Pentium processor also implements 8-stages pipeline for float-point instructions [9].

The U pipeline is known as a main pipeline. It can execute all 80x86 and Pentium instructions. The V pipeline is used just for hardware executed instructions. The pipelines structure in given on fig. 1. The U and V pipelines have 5 stages:

- Instruction Fetch (IF) stage is a common for both pipelines. It fetches two instructions from the first-level (L1) cache. The active buffer attempts to be filling with 16 bytes code. If there is a JUMP or CALL instruction (JMP, Jcc, and CALL), the branch prediction is activated.
- Decode 1 (D1) stage is common for both pipelines, too. D1 stage consists of two parallel decoders. The Pentium processor determines whether two consequent instructions can execute together. If it is possible, the first instruction is loaded into U pipeline and the second instruction is loaded into V pipeline.
- Decode2 (D2) is separate for U and V pipeline. It determines data addresses.

• Execution (EX) stage executes instructions. The instructions run to this stage together but it is not necessary to leave it together. In this case, the instruction in U pipeline has to leave this stage first.

• Write Back (WB) is the last stage, where the results are written into registers and the flags are changed.

The results from the branch prediction could be controlled at the stage EX (for JMP and CALL instructions), or at the stage WB (for conditional branches).

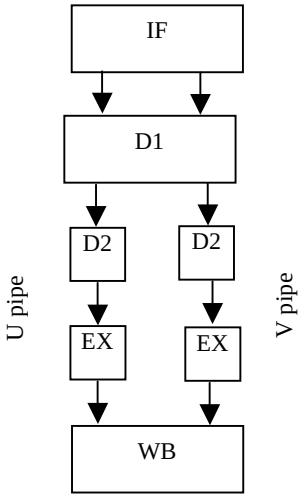

Fig. 1 The structure of pipelines

III. Base structure of Intel Pentium simulator

PipeSimul is a program simulating the superscalar architecture of Pentium processors. Its purpose is to visually show the work of the Pentium's pipes and maintain execution of assembly sources step by step, showing the state of registers, flags, data and stack segments.

PipeSimul is MDI based application. Using MDI architecture the application might be structured according to the information for the different needs of the user. The information is placed in the child windows of the program. These child windows are based on separate View classes and Document classes. This provides additional flexibility in resizing, rearranging, closing and showing windows, which are in relevance. For example, scrolling of code window PipeSimul automatically scrolls the window showing the pipes' structure. Certain Windows can be closed or minimized, when not in use. In this way the application benefits from tiling and cascading. The base structure of PipeSimul is introduced on fig. 2.

PipeSimul is compiled on Microsoft Visual C++. It's based on an open-source project called SoftWire [10].

It is a class library written in object-oriented C++ for compiling assembly code. It can be used in projects to generate x86 machine code at run-time as an alternative to self-modifying code. Its classes are used to parse the assembly source code and to generate the internal structures of the assembler. Then they are used to emulate Pentium's work, especially the pipeling, simulating the execution of the instructions as represented in the internal structures (classes).

PipeSumul is a program demonstrating the work of pipes with its specific features. This application is not a full Pentium simulator. It is not necessary to show all processes in Intel Pentium [6]. In the first version the simulator assumes the following restrictions:

- Simulator executes only real mode applications.
- Simulator uses near program model, so only one code segment and therefore only near jumps and calls. Only one data and stack segment are shown, too.
- Simulator can execute the most used instructions. Only the following instructions: Data transfer: MOV, PUSH, PUSHA, PUSHAD, PUSHF, PUSHFD, POP, POPA, POPAD, POPF, POPFD; Arithmethical instructions: ADD, ADC, SUB, SBB, INC, DEC, CMP, NEG, MUL, IMUL, DIV, IDIV;Logical instructions: AND, OR, XOR, NOT, TEST; Shift and rotation: SHL, SAL, SHR, SAR, ROR, ROL, RCR, RCL, SHLD, SHRD;Instruction flow control: JMP, CALL, RET, Jcc, LOOP, LOOPZ, LOOPNZ; Flag manipulation: STC, CLC, CMC, STD, CLD, STI, CLI, SAHF, LAHF.

These instructions are included in Reduced Instruction Set Computer (RISC). Pipelining is a feature of RISC architecture. Therefore, there is no reason to simulate complex instructions execution.

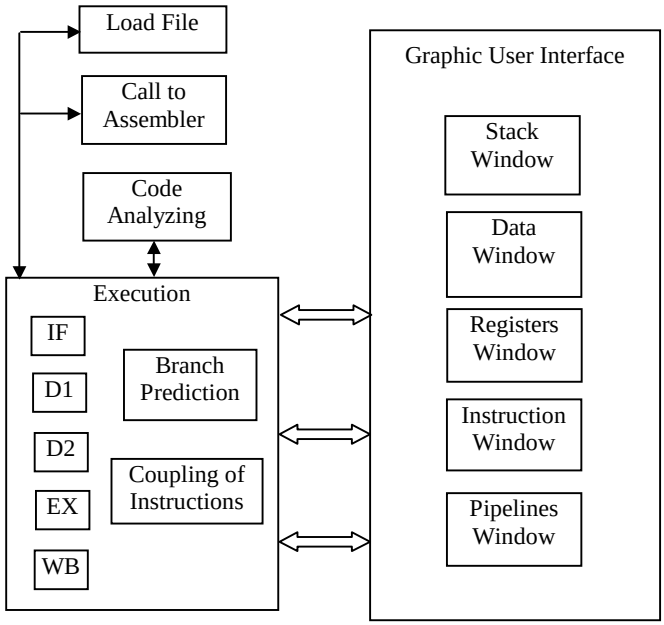

Fig. 2 The base structure of the simulator

IV. Simulation of instruction execution in Intel Pentium

Instruction execution simulation is realized by software module named PS. This module is a part of PipeSimul application. PS is realized as C++ source files closed in namespace Simulator. It this manner the integration of PS module in another software module is easer because the conflicts between identifiers are avoided.

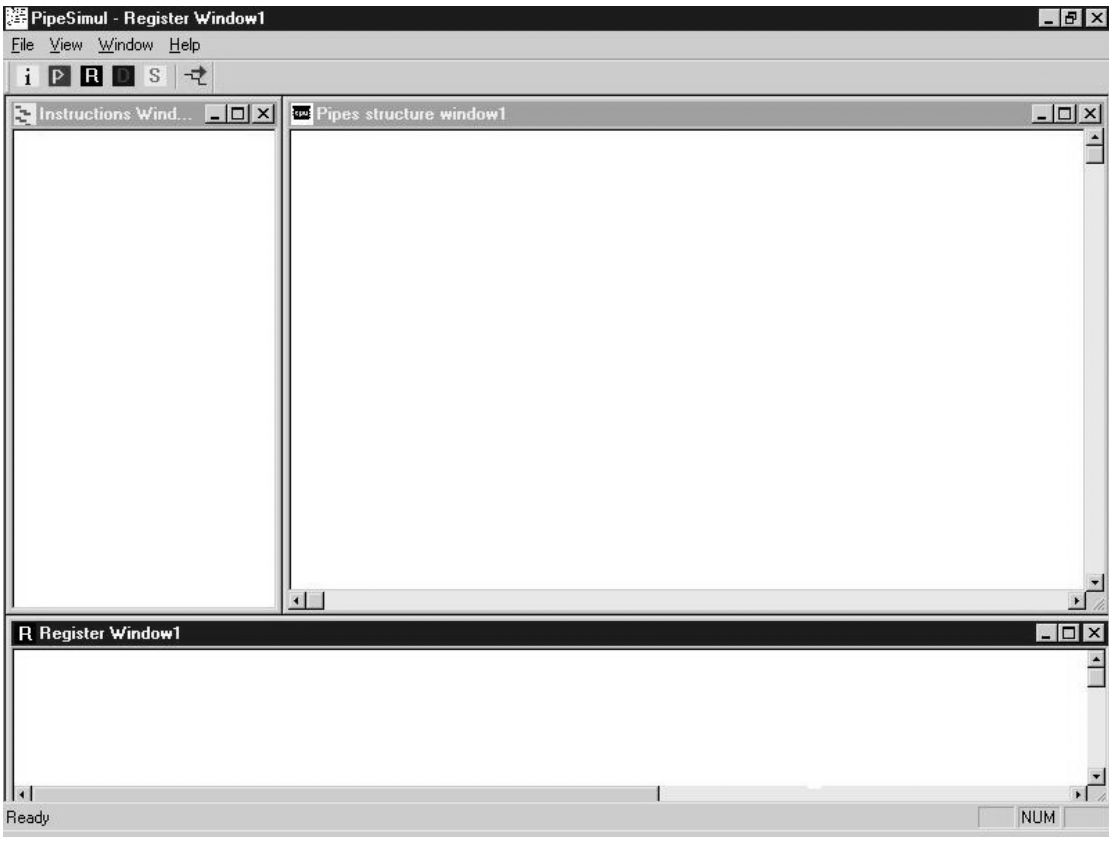

Fig. 3. The PipeSimul application window

The PS module is designed as independent on PipeSimul application. Thus, its integration to another software simulator or to the other similar application is possible.

To use the PS module, it is necessary to instant the object of class Simulator::TSimulator. The constructor finds the path the base module directory.

Simulator::TSimulator object creates an object of class Simulator::TProcessor. Class TProcessor has an array of pointers to class Simulator::TPipe. Class TPipe represents pipelines. In this case, the pipeline numbers is two. When the code has to know this number, it might to bring the value of the constant named Simulator::TProcessor::PIPES_COUNIt is possible to change the source code for more than two pipelines. In this stage of the application development, the most parts of the code rely that the number of pipelines is two.

The instances of class Simulator:TRAM and class Simulator::TIOSpace are created additionally. They serve like as a simulation memory and an I/O address space.

They inherit the base class Simulator::TAbstractDataSpace.

The method Simulator::TSimulation::LoadFile() has as parameter the path to a source file consisted assembler file. The method loads file to memory and prepares it for simulation. It includes: call to Assembler, code analyzing, and program loading to memory as binary code.

The method Simulator::TSimulator::Clock() simulates one cycle. It is all needed for an instruction stream control by the software application.

The pipelines software realization is divided between classes Simulator::TProcessor and Simulator::TPipe. It includes five virtual methods: DoIF, DoD1, DoD2, DoEX, DoWB. The first two methods belong to class Simulator::TProcessor, the other three methods belong to class Simulator::TPipe. These functions correspond to the fifth pipeline stages in Intel Pentium.

This development stage of the simulator executes the instructions simultaneously. The development provides to simulate U and V-pipeline functionality by using classes Simulator::TUPipe and Simulator::TVPipe.

IF stage working represented by DoIF method is to fill 16-bytes buffer memory.

D1 stage realized by DoD1 creates an object of TInstructionSet class. This class loads the instruction codes. At D1 stage, the object of Simulator::TDecoding class is created to decode the instruction according to the Simulator::TInstruction object definition.

This approach saves the creation of an extra source code, it also allows dynamic changing of instruction set.

The method DoD2 computes the addresses and extracts the operands for an instruction execution.

Methods DoEX and DoWB are realized particularly at this development stage.

V. Simulator Graphics User Interface

The Graphics User Interface of the simulator as software application is given on fig 3. The most used windows are given:

- Instruction Window - it contains the executed program code

- Pipelines Window - it represents instruction execution through pipes.
- Register Window - it shows the registers' content.

There is possibility to open Data segment Window and Stack segment Window.

The names of created classes and theirs base classes are given at the table 1.

TABLE 1

Class	Base Class	File
DataSegment	CView	DataSegment.h DataSegment.cpp
DataSegmentDoc	CDocument	DataSegmentDoc.h DataSegmentDoc.cpp
InstrFrame	CMDIChild Wnd	InstrFrame.h InstrFrame.cpp
Instruction	CView	Instruction.h Instruction.cpp
InstructionDoc	CDocument	InstructionDoc.h InstructionDoc.cpp
RegFrame	CMDIChild Wnd	RegFrame.h RegFrame.cpp
Register	CScrollView	Register.h Register.cpp
RegisterDoc	CDocument	RegisterDoc.h RegisterDoc.cpp
Stack	CView	Stack.h Stack.cpp
StackDoc	CDocument	StackDoc.h StackDoc.cpp

VI. CONCLUSION

Software simulation is often used technique in computer architecture development. This paper represents Intel Pentium simulator development. The key points of simulator creation as software tool are: Graphics User Interface development; instruction execution simulation; simulation of branch prediction logic.

This paper represents the solution of instruction execution simulation and Graphics User Interface creation.

The execution of assembler instructions is simulated by module named PS. It uses an open-source object called SotfWire for an assembler code compiling. The PS is designed as independent module. It may be used in another software simulator or similar application.

REFERENCES

[1] Hinton G., D. Sager, M. Upton, D. Boggs, D.Carmean , A. Kyker, P. Roussel, The Micro architecture of the Pentium 4 Processor, *Intel Technology Journal Q*, 2001.

[2] Hlavicka J, Computer Architecture, CVUT Publishing house, 1999.

[3] Keshava J., Vl. Pentkovski, Pentium III Processor Implementation Tradeoffs, *Intel Corp., Intel Technology Journal Q2*, 1999.

[4] Zaharieva-Stoyanova E., Simulation Models Of Pipelining in Intel Pentium Processors, IEEE-TTTC International Conference on Automation, Quality and Testing, Robotics, Cluj-Napoca, Romania, 2002, pp. 373-378.

[5] Zaharieva-Stoyanova E., Simulation of Pipelined Data Processing in Intel Pentium Processor, CompSysTech, Sofia, 2002, pp I.14-1 –I.14-5.

[6] Zaharieva-Stoyanova E., R. Atanasov, E. Shakir, V. Frunze, Software simulator of Intel Pentium Architecture, Advanced Control Theory and Applications, June 16 – 29, Plovdiv – Gabrovo, Bulgaria, 2003, pp. 91-95

[7] A Detailed Look inside the Intel NetBurst Micro-Architecture of the Intel Pentium 4 Processor, Intel Corporation, 2000.

[8] IA-32 Intel Architecture Software Developer's Manual, Intel Corporation, 2001.

[9] Pentium, NiSoft Ltd ,1998.

[10] Capens N., http://softwire.sourceforge.net.

Generating Textures Algorithm using Causal Modulation of Shapes.

Ognyan I. Zhelezov[1]

***Abstract*-In this paper is proposed one algorithm for generating synthetic texture based on modulation of shapes, that covers the two-dimensional surface. The modulation gives as a result a different textures, composed by two-dimensioned regions. Using different modulation finctions it is possible to create different pattern images. Additional parameters are the color of lines and fill color of rectangular element.**

***Keywords*: texture generation, shapes modulation, covering of surface**

I. INTRODUCTION

Pattern images (textures) are useful in computer graphics, especially in object's synthesis. They give realistic appearance of artificial generated surfaces. Digital textures can be obtained using different sources, but usually obtained texture hasn't needed dimensions and shape. If we use a simple repetition of given piece of textured surface, we will obtain unacceptable defects - well visible transitions and. repetitions. Better results give methods, which generate textures using direct synthesis by computation. These methods can be separated in two groups

Methods that create textures, using given pattern.
Methods, that create textures, using given casual or determined function.

In this paper is proposed one algorithm for generating synthetic textures, based on modulation of shapes, that covers the two-dimensional surface. Method is development of offered in [1] method for texture generation based on modulation of apexes of polygons, that covers given two-dimensional surface.

II. COVERING OF TWO-DIMENSIONAL SURFACE BY POLYGONS

As it is known in mathematics, full covering of plain by regular polygons is possible only for triangles, rectangles, pentagons and hexagons. Many full coverings by different shapes are known, including shapes of birds, animals and others. All these coverings, regardless of used shapes, can be classified as a generation of some determined function.

As a result this generation gives co-ordinates of polygon's apexes, which covers the surface.

Textures, created by determined function look like artificial, while the others, created, using casual functions, look more realistic, like obtained from existing object's surface.

III. PROBLEM DESCRIPTION

Many of known algorithms for casual texture generation perform arrange of pixels from given pattern to larger surface or use some spectral analysis of pattern and generate texture having given dimensions and similar spectrum. Textures, generated in this way, haven't distinguished objects despite of they have look like similar.

On the other hand, can be found many real textures that have "grain" surface, including objects with casual variation of dimensions or other parameters. One of the problems of texture generation is to discover algorithm that can obtain textures with "grain" surface and given variation of parameters.

IV. COVERING BY CASUAL SHAPES

Proposed algorithm use described in [1] algorithm for covering of two-dimensioned surface with casual polygons. This algorithm uses a determined function for covering of two-dimensional surface by given regular polygons and modulation of polygon's parameters by casual function. Generated function (GF) gives co-ordinates of polygon's apexs. Co-ordinates of apexes will look as follows:

$$\begin{cases} x(n) = F_x(n) \\ y(n) = F_y(n) \end{cases} \quad (1)$$

where n is the number of current point
Type of functions $F_x(n)$ и $F_y(n)$ and scheme of apexes connections determine the polygons, that will be obtained.. For description of scheme for apexes connections it is useful to describe apexes by two decartian co-ordinates n1 (as x co-ordinate) and n2 (as y co-ordinate , $n1 \in [0,N1]$, $n2 \in [0,N2]$., which are related with n as follows:

$$n = n1 + N1 * n2 \quad (2)$$

where N1 и N2 are dimensions (in number of points) of

[1] Ognyan. I. Zhelezov is with the Faculty of Computer Science and Automation , Studentska STR. 1 9000 Varna , Bulgaria, E-mail: ognyanz@yahoo.com

rectangular area D, in which functions x(n1,n2) и y(n1,n2) are defined.

In example, the covering by rectangles with dimensions A*B can be obtained using functions x(n1,n2) , y(n1,n2) and connections L1, L2, L3 и L4, given as follows.

$$\begin{aligned} x(n1,n2) &= A*n1 \\ y(n1,n2) &= B*n2 \end{aligned} \tag{3}$$

$$\begin{aligned} &L1:(n1,n2)-(n1+1,n2) \\ &L2:(n1+1,n2)-(n1+1,n2+1) \\ &L3:(n1+1,n2+1)-(n1,n2+1) \\ &L4:(n1,n2+1)-(n1,n2) \end{aligned} \tag{4}$$

In [1] was given others schemes for apexes connections that produced others coverings by regular polygons

V MODULATION OF POLYGONS

Modulation is non-linear transformation of signal that changes some parameter of given signal in according of modification of other signal, named modulator [3]. In our case we consider functions Fx(n1,n2) и Fy(n1,n2), that describes co-ordinates of polygon's apexes, as digital signals. As a modulators, that gives modification of co-ordinates of polygon's apexes we will use functions Mx(n1,n2) и My(n1,n2) as follows:

$$\begin{cases} x(n1,n2) = Mx(n1,n2) + Fx(n1,n2) \\ y(n1,n2) = My(n1,n2) + Fy(n1,n2) \end{cases} \tag{5}$$

For prevent cut across borderlines of polygons, the deviation of apexes co-ordinates can be not greater then a half of initial dimension of corresponding border line. Using casual function as a modulator will give as a result covering by polygons, which dimensions are functions of casual variable (fig. 1)

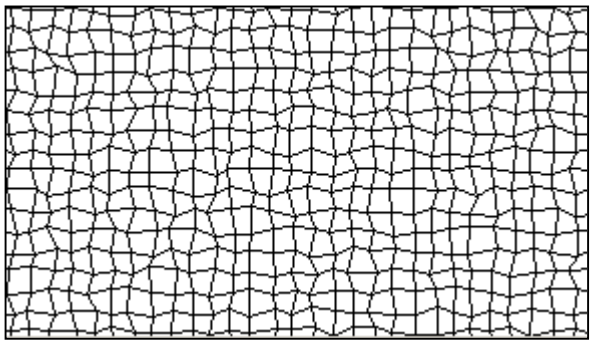

Fig. 1 Covering by polygons using casual function as a modulator

VI. SMOOTHING OF CONTOURS USING LF FILTER

Textures, composed by polygons look like artificial created. For obtain more realistic behavior of texture it is useful to smooth the contours of shapes. Smoothing can be obtained, using Low frequency (LF) filter as the apexes of polygons corresponds to the height frequencies in spectrum, while the smooth curves corresponds to the low frequencies in spectrum of contour functions n1(n) и n2(n).

As it is known, the calculation of output of digital filter can be given as [2].

$$y(n) = \sum_{m=-\infty}^{\infty} h(m).x(n-m) \tag{6}$$

where:
h(m) is impulse response of digital filter.
x(n) - input signal
y(n) - output signal
In this case it is useful to use non-recursive

filter, which impulse function has limited length, because it's transitional process has limited length too. This will make the smoothed contour independent from start point of smoothing. So, for offered method smoothed contour functions $n1_s(n)$ и $n2_s(n)$ will be obtained using non-recursive filter as follows:

$$\begin{cases} n1_s(n) = \sum_{m=-N/2}^{N/2} h(m).n1(n-m) \\ n2_s(n) = \sum_{m=-N/2}^{N/2} h(m).n2(n-m) \end{cases} \tag{7}$$

where:
n1(n) and n2(n) are contour functions
n1s(n) и n2s(n) are contour functions, obtained after smoothing
h(n) is impulse response of filters

As LF filter can be applied simple average filter, which length N of impulse response can be selected by operator. Because the value of N can't be too big (less then full length of contour) can't be found big difference between simple average filter and better filters, using known window functions like Haming's or Kaiser's functions. Smoothing of contours, using linear filters ids described in [5].

VII. RESULTS.

Described above algorithm has been used to create a program, that generate textures , giving possibility to select the parameters of created image – line and background colors and initial shape's dimensions. On fig. 2 is shown

one result of execution of this program using casual function as modulator. And smoothing using average window functions dimension, having dimension of 41 points.

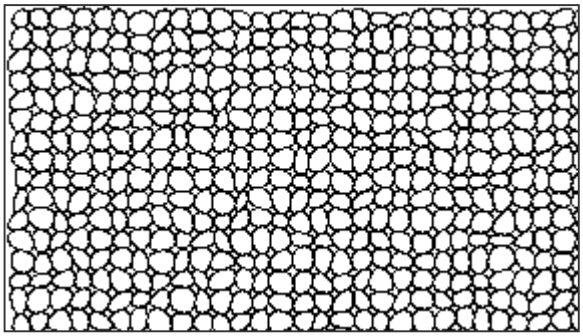

Фиг. 2 Texture, obtained after smoothing of contours.

Different textures can be obtained after casual modulation of other parameters. On fig. 3 you can see the same texture after casual modulation of shape's colors.

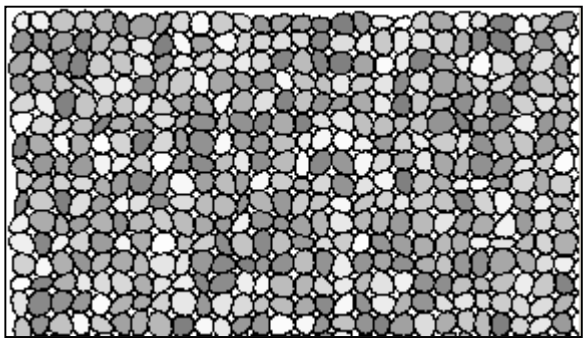

Фиг. 3 Texture, obtained from previous, using casual modulation of shape's colors.

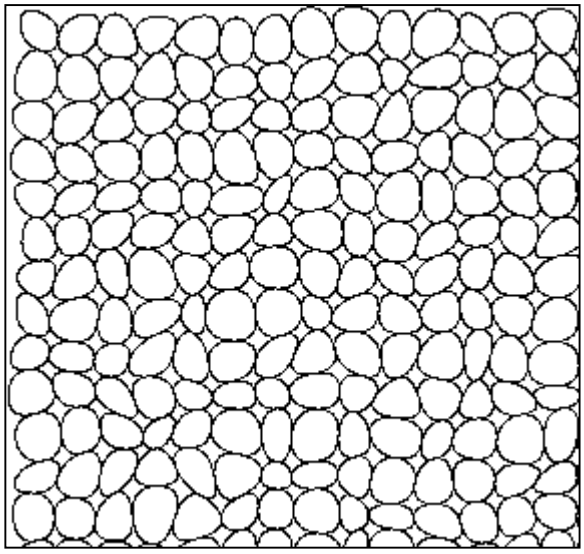

Фиг. 4 Texture with bigger initial dimension of shapes

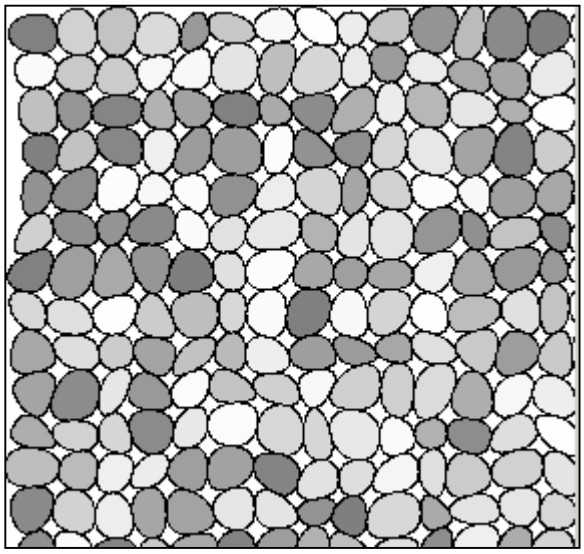

Фиг. 5 Texture, obtained from previous, using casual modulation of shape's colors.

VIII. Conclusion

The proposed algorithm for texture generation is based on modulation of apexes of polygons using a casual function and smoothing of shapes using LF digital filter. The next development of this algorithm can be generating of textures using randomly ordered different shapes and next modulation of parameters of obtained texture using casual function. This will give possibility to generate many different realistic textures.

References

[1] О. И. Железов, Даниела Д. Илиева, Алгоритъм за генериране на текстурни изображения, Юбилейна научна сесия ТУ-Варна 1991г.

[2] M. Gardner, Mathematical Games from Scientific American, Prentice Hall, Inc. 1977

[3] В. Халачев, Г. Стоянов, Теория на сигналите, С. "Техника", 1980.

[4] L. R. Rabiner , B. Gold , Theory And Application of Digital Signal Processing, Prentice Hall, Inc. 1975

[5] T. Pavlidis , Algorithms for Graphics and Image Processing, Computer science press, 1986.

[6] О. Железов, Метод за изглаждане на контури. Научна сесия "Дни на науката - Варна", 1998г

[7] Ashikhmin, M., " Synthesizing Natural Textures**",** The Proceeding of 2001 ACM Symposium of Interactive 3D Graphics, Research Triangle Park, North Carolina, pages 217-226, March, 2001.

Traffic Road Section Investment Risk Modelling and Computer Simulation

Gjorgji Manceski[1] and Gjorgi Kokalanov[2]

Апстракт – In this work, the model for determination of the coefficient for estimation of investment risk is presented as well as its application when choosing the optimal variant of a traffic road.

Key words – modeling, investments, a confidence interval, traffic, simulation

INTRODUCTION

There are various motives for a construction of a traffic road which are economic, political or military ones. Regardless of which of these is the motive for a construction of a certain traffic road, the variants should depend upon economic evaluation. The choice of a multicriterial evaluation based on economic, investment, environmental and functional evaluation. Setting a unique analytical function and its optimizing is practically impossible. Accordingly, the approach of a choice of an optimal variant is a choice of partial functions for each evaluation and defining of their importance. Moreover, it is known that a great part of the environmental and functional evaluation has an impact on the economic indicators. In order to realize the influence and to decrease the influence of the "untouchable" influences, two hypotheses have been in relation to the environmental and functional evaluation.

1. In each of the variants, supplementary investments will be made so that the negative environmental effects are brought to the same level. Such a hypothesis eliminates the need for an environmental evaluation.
2. The indicators of the functional evaluation, such as the length of the traffic road, the number and the types of accidents, the practical capacity etc., have an impact on the economic indicators and through them they certainly influence the economic evaluation. If these influences are considered to be enough, the functional evaluation may also be eliminated.

The acceptance of these hypotheses means an importance of the economic or the investment evaluation. To determine the economic and the investment evaluation is an interest of two parties: the social community and the investor. The effects of these two evaluations can be seen through the previsibility and visibility studies. Such studies are made by the institutions of the social community as a social Cost-Benefit analysis and by the investor as a financial Cost-Benefit analysis. These two analyses are in opportunity to each other and their opposition can be solved by appropriate legal act.

1. Faculty of Economics, St. Climent Ohridski University, Gjorce Petrov b.b., 7500 Prilep, Macedonia gmanceski@mt.net.mk
2. Faculty of Civil Engineering, St. Cyril and Methodius University, Partizanski odredi 24 1000 Skopje kokalanov@gf.ukim.edu.mk

DEFINITION OF IRAC (INVESTMENT RISK ASSESSMENT COEFFICIENT)

Investment indicators can be found in the function of the economic indicators expressed through economic costs and benefits. The basic investment indicators are the opportunistic price of capital, the Net Present Value and the Internal Rate for Return. A real analysis of these indicators is complex. The definition of an Internal Rate of return is expressed in the following expression:

$$\sum_{t=1}^{n} \frac{NI_t}{(1+r)^t} - \sum_{j=-m}^{0} \frac{I_j}{(1+r)^j} = 0$$

where:

NI_t - net incomes in the t-year,

I_j - investment in the j-year,

n - planned period for a traffic road exploitation,

m - investment period.

By solving this expression according for r, the internal profitability rate of a traffic road is found.

On the other side, the Net Present Value is defined according to the following expression:

$$NPV = \sum_{t=1}^{n} \frac{NI_t}{(1+OCC)^t} - \sum_{j=-m}^{0} \frac{I_j}{(1+OCC)^j} = 0$$

In this expression it is obvious that NPV (Net Present Value), which is the aim of the investor, is in the function of NI (Net Income), the investments, OCC (Opportunity Capital Cost) and IRR (Internal Rate of Return). The determining presentation of these dimensions does not correspond with the reality. Also, a presentation of a pessimistic, probably and optimistic scenario, too, does not correspond with the reality because each of them is realized with "0"-probabiliyy. According to that, the real approach could present NPV probability, it could belong to a certain interval or a marginal case of an investment efficacy NPV, not to get a negative value and be indefinite (not positive). The probability for NPV to be negative has been called a coefficient for the evaluation of the investment risk. The definition of this coefficient starts from the probability distribution is IRR and OCC. To determine the probability law of IRR, we should start from the following expression:

$$\sum_{t=1}^{n} \frac{NI_t}{(1+r)^t} - \sum_{j=-m}^{0} \frac{I_j}{(1+r)^j} = 0$$

It turns out that NI_1 are in the function of the traffic intensity in the planned period which means that $NI_t = f(AADT_t)$ (AADT – Average Annual Daily Traffic). If this is correct, the traffic intensity depends on a great number of factors, such as: economic potentials of the zones of direct or indirect influence, development strategy of the zones, demographic characteristics

etc. As the number of the independent variables is big and, certainly, with unknown distributions for a distribution according to the central marginal theorem, we can accept that the AADT distribution law a gauss one. Determination of the intensity and structure of the traffic is based on prediction. Determination of the confidence intervals of AADT with some certainty coefficient (for economics problems, 0.95 or 0.99) leads determination of confidence interval of NPV and then, through the section of confidence intervals with the axis, confidence intervals of the IRR are

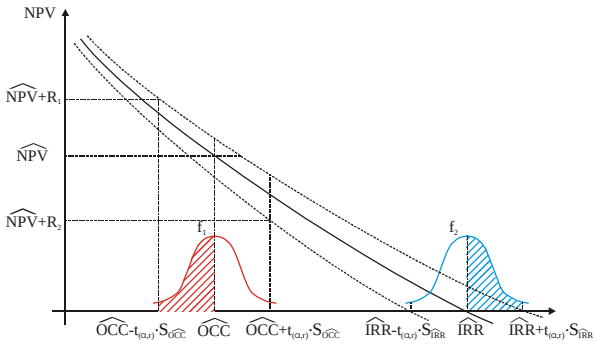

Figure 1. The relation IRR, NPV and OCC as well as their probability distribution and confidence intervals.

defined.

The complex real relation, NPV-IRR-OCC, is shown in the Figure 1:

OCC also depends on a big number of factors. According to their central marginal theorem, its distribution depends on the gauss distribution.

According to this Figure, if we define a partial coefficient for the evaluation of the investment risk is accordance with the expression:

$$P(NPV<0)=P(OCC\in\Delta r)\cdot P(IRR<r_1)$$

and Figure 2.

The analytical expression of the partial coefficient for evaluation of the investment risk is:

$$P(NPV<0/OCC\in[r_1,r_1+\Delta r])=f_1(r_1)\cdot\Delta r\cdot\int_{-\infty}^{r_1}f_2(r)\cdot dr$$

If we want this expression to be useful in the whole interval

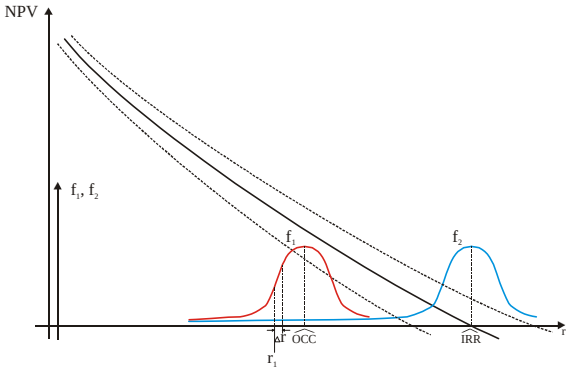

Figure 2. Partial Investment Risk Assessment Coefficient

of possible values of the discount rate, it must be supplemented which means that the sum of all partial coefficients must be determined.

$$IRAC=P(NPV<0)=\sum_i f_1(r_i)\cdot\Delta r\cdot\int_{-\infty}^{r_i}f_2(r)\cdot dr$$

when $\Delta r\to 0$ sum turns into an integral and Δr turns into a differential dr. So, the final expression for determination of the coefficient for evaluation of the investment risk gets the following form:

$$IRAC=P(NPV<0)=\int_{-\infty}^{\infty}f_1(r)\cdot dr\cdot\int_{-\infty}^{r}f_2(l)\cdot dl$$

or

$$IRAC=P(NPV<0)=\int_{-\infty}^{\infty}f_1(r)\cdot F_2(r)\cdot dr\,.$$

The interval of possible values of IRAC is [0,1], where if the value is closer to "0", the risk for the project to get a negative net present value is smaller, and vice versa. If the IRAC value is closer to 1, the risk for the net present value not to be positive is bigger.

The evidence of the multitude of values of this coefficient happens in three cases:

- The first case is shown in a figure,

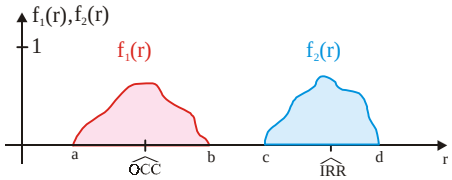

Figure 3. IRR and OCC situations with their distribution.

- The second case is shown in a figure,

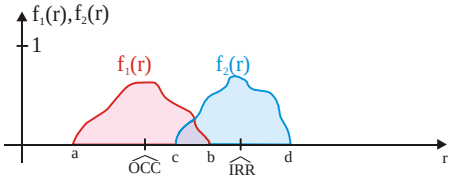

Слика 4. IRR and OCC situations with their distributions.

- The third case is shown in a figure.

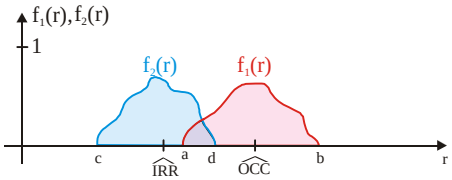

Figure 5. IRR and OCC with their distributions.

Here, we will come to the evidence (proof) of only the second case:

If we develop the expression for IRAC, we get:

$$IRAC = P(NPV < 0) = \int_{-\infty}^{\infty} f_1(r)\cdot\left(\int_{-\infty}^{r} f_2(l)\cdot dl\right)\cdot dr = \int_{-\infty}^{c} 0\cdot\left(\int_{-\infty}^{r} 0\cdot dl\right)\cdot dr + \int_{c}^{d} 0\cdot\left(\int_{-\infty}^{c} 0\cdot dl + \int_{c}^{r} f_2(l)\cdot dl\right)\cdot dr +$$

$$+\int_{d}^{a} 0\cdot\left(\int_{-\infty}^{c} 0\cdot dl + \int_{c}^{d} f_2(l)\cdot dl + \int_{d}^{r} 0\cdot dl\right)\cdot dr + \int_{a}^{b} f_1(r)\cdot\left(\int_{-\infty}^{c} 0\cdot dl + \int_{c}^{d} f_2(l)\cdot dl + \int_{d}^{r} 0\cdot dl\right)\cdot dr +$$

$$+\int_{b}^{\infty} 0\cdot\left(\int_{-\infty}^{c} 0\cdot dl + \int_{c}^{d} f_2(l)\cdot dl + \int_{d}^{r} 0\cdot dl\right)\cdot dr =$$

of all the intervals which participate in the sum, only the fourth one is not zero

$$= \int_{a}^{b} f_1(r)\cdot\left(\int_{-\infty}^{c} 0\cdot dl + \int_{c}^{d} f_2(l)\cdot dl + \int_{d}^{r} 0\cdot dl\right)\cdot dr = \int_{a}^{b} f_1(r)\cdot\left(\int_{c}^{d} f_2(l)\cdot dl\right)\cdot dr$$

But from the hypothesis in the beginning of the expression, that $\int_{-\infty}^{\infty} f_2(r)\cdot dr = 1$, and it has an important value only in the interval $[c,d]$ т.е. $\int_{-\infty}^{\infty} f_2(r)\cdot dr = \int_{c}^{d} f_2(r)\cdot dr = 1$, follows

$$IRAC = \int_{a}^{b} f_1(r)\cdot dr .$$

What has previously been said about $f_2(r)$ is also valid for $f_1(r)$, which means that $\int_{-\infty}^{\infty} f_1(r)\cdot dr = 1$, It has an important value only in the interval $[a,b]$, or

$\int_{-\infty}^{\infty} f_a(r)\cdot dr = \int_{a}^{b} f_1(r)\cdot dr = 1$ It means that

$IRAC = 1$, so that $IRAC = 100\%$.

The expression for IRAC does not have analytical solution so a numerical solving of this expression is used. Reaching the IRAC value is a long process. We have created an appropriate software solution which contains a great number of models mutually connected with their interactive connection. From the definition of this coefficient, we can see that it has a general use value when the investment risk is estimated. In this research work, models are directed to a determination of this coefficient when the investment risk is estimated and when a choice of an optimal variant for a traffic road is made.

MODULES OF THE SOFTWARE SOLUTION

The software solution of these models will be connected with the existing programming tools which are used in the process of planning and projecting road. AUTO-CAD is one of the widely used software solution which gives an opportunity for the basis of a development of various applications in it. This software contains the PLAEIA application which is used to project roads in almost all Europe, in about 7000 patterns. This software is also used in the projecting companies, in the Republic of Macedonia. This was the reason for us to let this project support for the form of this software. The Software solution consists of the following modules:

1. Module for determination of the speed in a free traffic flow,
2. Module for determination of the direct exploitation costs of a traffic road,
3. Module for determination of costs which depend on the weather,
4. Module for determination of accident costs,
5. Module used to update construction data, maintenance of traffic roads, cost for decreasing the environmental consequences and costs for the protection of the environment.
6. Module for determination of costs for the traveling time of the passengers,
7. Module for estimation of the costs of the lost profit,
8. Module for determination of the incomes gained by payment of special tolls when a traffic road is used,
9. Module for estimation of IRR, IRAC и NPV,
10. Module for a final ranking of variants.

The most important model is the one used to determine the speed in a free traffic flow the diagram of which is presented in the Figure 8.

Prediction for the future AADT has an important influence for determination of IRAC and choosing the optimal variant of the traffic road.

Prediction is made by extrapolation the traffic trend. The trend

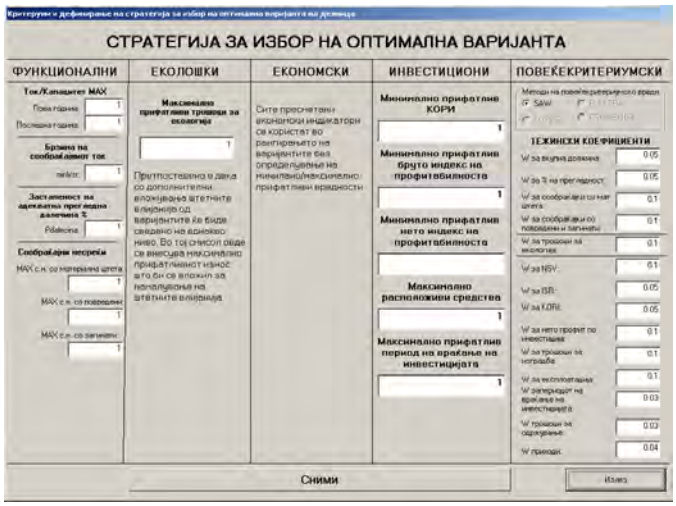

Figure 6. A screen of the module used to define the strategy

prediction is according to a degree or a linear function depending on the correlation coefficient and the average square aberration. A screen of this model is presented in figure 8.

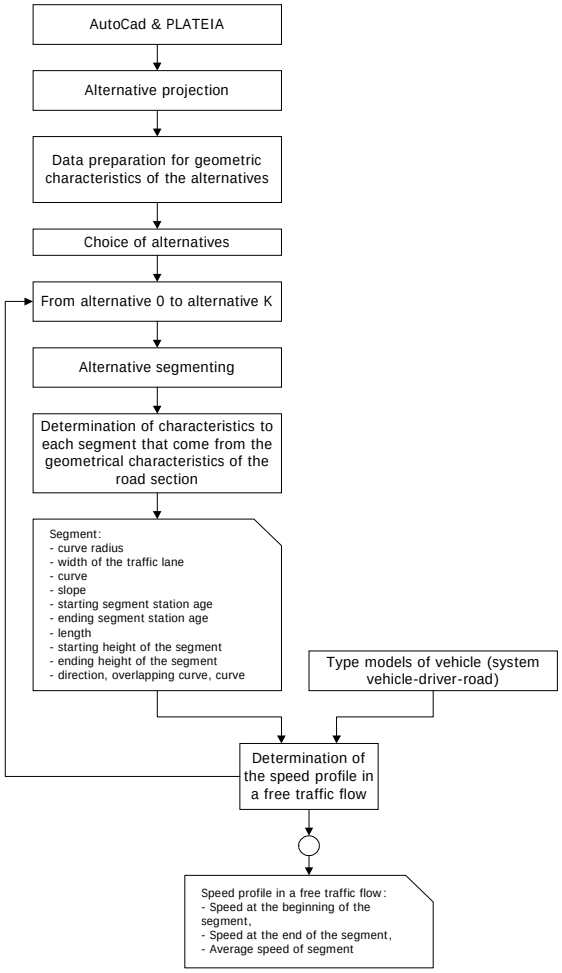

Figure 7. A block diagram of the module used to determine the speed in a free traffic flow.

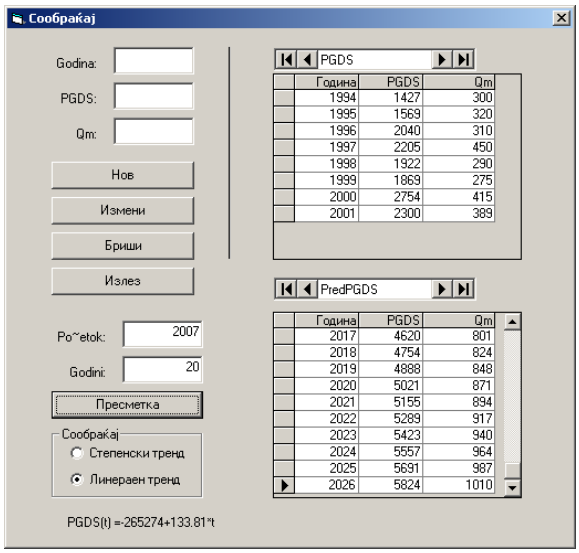

Figure 8.A screen of the model used to predict the future/next AADT

4.

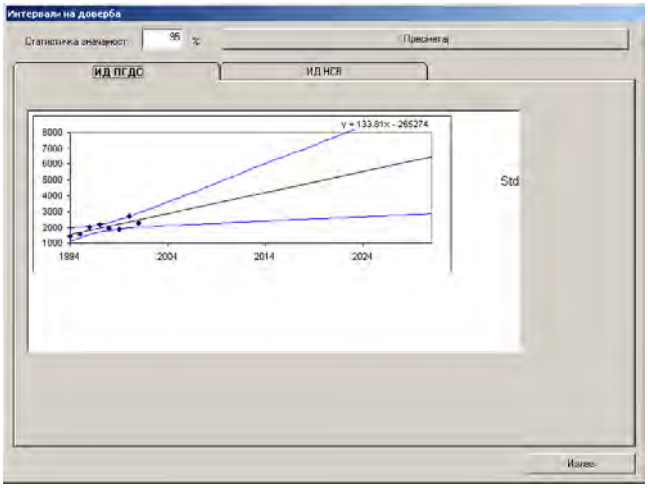

5. Figure 9. A screen of the module used to estimate the confidence interval

CONCLUSION

The Investment Risk Assessment Coefficient has been included as quantitative indicator to estimate the risk investing in general. This coefficient has also been specially analyzed for the filed of investments in roads and the choice of the optimal variant of a traffic road considering, construction, maintenance and exploitation. The interval of values [0, 1] and one part of its proof has been presented here. A software solution has been made for the purpose of this coefficient and the models necessary for the choice of the optimal variant of a traffic road. Data adaptation is quite possible in the software which makes it be widely used for certain regions. This software and this coefficient might be used in previsibility and visibility studies as a quantitatively qualitative indicator of the investment risk. This coefficient is also suitable when variants are ranked.

REFERENCES

1. Bennett R. Christopher, Greenwood D. Ian, “Modelling Road User and Environmental effects in HDM-4”, volume Seven, © 2000 HTC Infrastructure Management Ltd. Version 1.0 – DRAFT 28.04.2000 15:48,
2. Berger Louis, Study of Transport Investment and Impact on Distribution of Income in Remote Area: Phase I, A report prepared for the United States Agency for International Development, p.1-17. , International Inc., 1979,
3. Damjanović d-r Dragorad, "Uticaj elemenata puta na brzinu u slobodnom toku", doktorska disertacija, GAF-Niš, 1980 god,
6. Кокаланов Ѓорѓи, Манчески Ѓорѓи, "Софтверско решение за определување на профилот на брзината", зборник, Градежен факултет, Скопје, книга 13, ноември 2002,
7. G. Manceski, P. Mitrevski, "A Model and Software Solution for Determining the Economic Indicators for Construction, Exploitation and Maintenance of a Traffic Road Section", 4th International Conference on Informatics and Information Technology, Bitola, December 11-14, 2003 (Book of Abstracts, p.36),

M-Government

Ljupco Antovski[1], Marjan Gusev[1], Pece Mitrevski[2]

Abstract. **M-government is defined as the strategy and its implementation involving the utilization of all kinds of wireless and mobile technology, services, applications and devices for improving benefits to the parties involved in e-government. The main effort of m-government is to become a complement to e-government. The 3P Value Model for m-government application has three dimensions of evaluations: prime value, pleasure value and post value. There are four major factors concerning citizens and the use m-government applications: awareness, ease of use, real added-value/benefit and price.**

Keywords. **E-government, democracy, transactions, mobility**

I. INTRODUCTION

Many governments have engaged in the process of developing a wide range of electronic (e-government) services by using information technologies, particularly, web-based internet applications. Nonetheless, as governments increase the use of information and communications technologies, demands by the public for more effective services increase. In response, governments are aiming to meet the rising expectations of citizens for better, more comprehensive services using innovative information technologies and various service delivery channels in addition to the web.

E-government efforts aim to benefit from the use of most innovative forms of information technologies, particularly web-based Internet applications, in improving governments' fundamental functions. These functions are now spreading the use of mobile and wireless technologies and creating a new direction: mobile government (m-government). M-government is defined as the strategy and its implementation involving the utilization of all kinds of wireless and mobile technology, services, applications and devices for improving benefits to the parties involved in e-government including citizens, businesses and all government units [Kushchu, 2003].

M-government seems to have a substantial influence on the generation of set of complex strategies and tools for e-government efforts and on their roles and functions. M-government is inevitable. The number of people having access to mobile phones and mobile internet connection is increasing rapidly. The mobile access is becoming a natural part of daily life, and the governments will have to transform their activities according to this demand of convenience and efficiency of interactions for all parties.

[1]Ljupco Antovski and Marjan Gusev are with the Institute of Informatics, Faculty of Natural Sciences and Mathematics, "Ss. Cyril and Methodius" University, Arhimedova 5, P.O Box 162, 1000 Skopje, Macedonia, Email: anto@ii.edu.mk, marjan@ii.edu.mk

[2]Pece Mitrevski is with the Faculty of Technical Sciences, University "Sv. Kliment Ohridski", I. L. Rebar bb, 7000 Bitola, Macedonia, E-mail: pece.mitrevski@uklo.edu.mk

Information delivery to public is a key task of government and often not an easy job. It is the responsibility of the government to keep their citizens informed of what is happening around them. Citizens need this information and sometimes are critical for them in making decisions and forming any opinions. Timely information delivery to public promotes democracy in the country and creates accountability. Mobile technologies prove to be a critical channel for governments to provide timely information for citizens [Zalesak, 2003].

II.E-GOVERNMENT MOBILITY

Even considered segregate, e-government and m-government are not two separate entities. E-Government encompasses usage of all technologies to deliver services to citizens and improve the activities of government and streamline their processes. On the other hand, m-government is an add on to the e-government confined to use of mobile technologies such as mobile phones, PDAs (Personal Digital Assistant), Wi-Fi enabled devices, Bluetooth, wireless networks in delivering services. In addition, m-government is a better option compared to e-Government in delivering services and public information to citizens due to its nature of being available anywhere, anytime and from any internet enabled device [Lallana, 2004].

The main effort of m-government is not to provide a replacement for e-government but to become a complement to e-government. While the mobile devices provide a faster and timely way of delivering information to citizens, it has some limitations. Mobile phone is considered as the most common medium or enabler of m-government but lacks the ability to transfer large volume of information, especially complex information. In addition they lack several features that the normal internet enabled personal computer has. Examples of this limitation are the Short Message Service (SMS) which can transmit up to 160 characters only while email can transmit large amount of information and the mobile internet channels throughput while the implemented fix line internet protocols already provide gigabit transfers [Ghyasi, 2003]. These limitations limit m-government services to simple but most critical applications. In case of developing countries, delivering critical information to citizens is one of the most beneficial applications of m-government.

The service quality will follow the technological evolution of the Internet, and the future development of e-government applications will be evaluated based on mobility, interactivity and intelligence. Among these three dimensions, mobility is expected to gain more attention than the other two.

- *Increased expectations:* Often, people want services to be more readily available with a high standard. When people are aware that some new service is available in the commercial sector, they will expect for more in governmental services. This in turn requires more efficient civil servants who need

more accurate and timely information readily available regardless of where they are working. This contributes to the forces driving mobile government applications.

- *Emergence of mobile internet:* With the development of 3G mobile network services, the capability of providing services through mobile devices are greatly improved. This development makes the provision of mobile government applications possible and more accessible than using the wired Internet.
- *Improvement on e-government effort:* Mobile government is not a replacement to e-government but complementary to it. People can access the applications from a new platform in case they do not have access to the wired internet.

Extending from the definition, mobile government applications may be considered as different from e-government applications in terms of the followings [Arazyan, 2002]:

- *Personalized information:* Computer can be shared among different users, but mobile devices are designed to be used by a single user. This means that personalized information can reach the same user at any time through that one specific device.
- *Always on:* Different from personal computers, most mobile devices are always switched on. Usually, these devices stay at an inactive state, but applications can "wake up" the device. This is very different from e-government applications.
- *Mobility:* As mobile devices are always carried around by the user, applications can be designed to provide instant information to the users. An example is to send out warnings during emergencies. The development of mobile government applications can simply be migrating e-government applications to a new platform, or to develop new applications according to the characteristics of mobile devices. There is no definite answer to which approach is better, and that depends wholly on the provisions of particular applications.

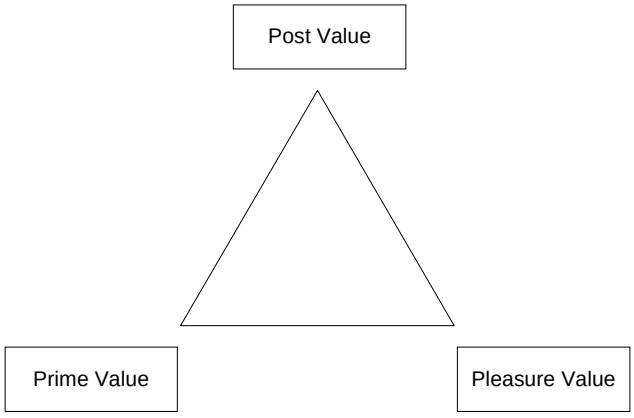

Figure 1. 3P Model for m-government applications

In terms of technology involved, currently many mobile government applications make use of SMS (short messaging service). Other technology includes WAP, MMS and mobile internet. It is expected that mobile internet will play a much more significant role in near future due to the development of 3G technologies and the capabilities to process more information faster.

III. M-Government Application's Value

Analyzing other researcher's studies, reports and news from different countries, we have agreed on using the Yu model to evaluate the value of the emerging m-government applications. According to [Yu, 2004], the 3P Value Model for m-government application (Fig. 1) has three dimensions of evaluations: prime value, pleasure value and post value.

We will use 3P Model to identify the key elements of what is valuable in some emerging m-government applications. This analysis aims to improve our understanding of m-government applications and services and to help application developers and government officials to identify applications that are worthwhile to invest in.

Table 1

Prime Value

A. Instant information release		
Service	**Place**	**Description**
SMS for people with hearing disabilities	Great Britain	Citizens with hearing problems can be contacted by the police with SMS
Special notification cases	California, USA	SMS are sent to citizens in case of energy black-outs
SMS floods warning systems	Malaysia	When the water level rises to certain level, the control centre sends a message to all the affecting citizens
B. Mobile warning		
Fight against mobile phone theft	Holland	SMS messages are sent to the mobile number of stolen phone every 3 minutes. Application can still work even when original SIM card is removed
Prevention of false phone calls on emergency lines	Denmark	When false calls are initiated through mobile phones, SMS messages will be sent to that mobile number to interfere the phone
C. Quick Information Collection		
Fire fighting	Germany	Firemen receive critical information on their way to the site using mobile devices
Search for missing citizens and criminals	Germany	When police are searching for missing person or criminals, SMS message will be sent to registered bus and taxi drivers.

Prime value means satisfying a real need for the users. Satisfying the real need does not simply imply providing users with what they want, but to solve a particular problem they are facing. For m-government applications, prime value is concerned with providing a solution to problems that could not be solved easily by the wired technologies. The prime value emerges in the cases of:

- Instant information release
- Mobile warning
- Quick information collection

Mobile devices are often carried by users and are always turned on. This characteristic enables mobile devices to serve as a warning or reminder to users with quick and specific information release. The Table 1 A presents several examples concerning the instant information release.

The instant information release model targets a wide range of users and is suitable in mass crisis situations that affect everyone in a specific community.

Another way of using messaging service is to target at particular persons and give them specific warnings. Refer to Table 1 B for specific cases.

TABLE 2
PLEASURE VALUE

A. MOBILE TRANSACTIONS		
Service	**Place**	**Description**
Mobile automobile parking	Serbia, Belgrade	Driver can log in and log out a parking space using a mobile phone. Fee is automatically charged to the driver's account. Receipt is sent via SMS
Tax declaration	Norway	Citizens via SMS message with specific code can complete the entire tax declaration procedure.
B. FASTER INFORMATION EXCHANGE		
Mobile hospital staff	Sweden	Mobile technology enables hospital staff to have faster information flow
Mobile care workers	Norway	Ability to access data from service site allows care workers to spend more time on their job rather than traveling around for information
Fight against higher rate of employment	Australia	Allows job seekers to reach information in a timely manner
C. FIGHT AGAINST CRIME		
Reporting crime	Philippines	Can report suspicious activities via SMS
Criminals Identification	Italy	Couple of thieves are caught after photos of criminal act were taken by others and sent as MMS to the police

The possibility of retrieving information while on the move is one of the major characteristics of mobile government applications. This allows civil servants to collect necessary information to provide more efficient and effective service to the public (Table 1 C).

The pleasure dimension of 3P model represents provision of better services to make citizen-government interaction more enjoyable. This dimension may come about in different forms, such as ease of getting service, or clarity of information. The possibility of receiving service through mobile phone is an improvement in experience already. The pleasure dimension is mainly identified in:

- Mobile transactions
- Faster information exchange
- Fighting against crime

Transaction is a very important part in doing business and how to improve that experience for customers can be an interesting issue. Currently, many companies are exploring the possibility of mobile commerce and some governmental organizations have already taken the initiative to utilize this opportunity (Table 2 A).

In case the speed of information exchange is important but not critical, applications are defined as enhancing the pleasure value for users (Table 2 B).

To fight against crime, law enforces need citizens' corporation to provide information. The reports from citizens can increase the chance for police to arrest, find missing people and better investigate cases. Table 2 C presents some examples.

Value is a comparative relationship between benefits and costs; clearly the issue of costs can have a significant impact on the users' perception of value. Besides the cost in terms of money, other costs may include potential privacy issues and possible danger in security. Post value, the third dimension deals with these issues. This value is the perception of users towards government services and how users feel after they use the services. This serves as a foundation to the 3P model and differentiates applications that are welcomed and easily adopted by citizens. Applications that provide this value should make users feel that their privacy or security issues are handled properly. The post value is identified in:

- Location Identification
- M-Voting

GPS can be a very powerful tool to identify users' location. The proper use of it can allow users to be located and shortens the time to find services at a particular location (Table 3 A).

TABLE 3
POST VALUE

A. LOCATION IDENTIFICATION		
Service	**Place**	**Description**
Police GPS	USA	All police are equipped with GPS enabled mobile devices
Emergency black box in Car	Europe	Cars are equipped with on demand black box that identifies the cars location in case of accident
B. M-VOTING		
Local elections	Czech Republic	lack of confidence in mobile technology has greatly affected the post value
Eurovision contest voting	Europe	Voting for singer, minor privacy issues arise

Mobile voting via SMS has been used in some local government elections, but is especially popular for private commercial use in conducting polls and receiving customer comments, often for entertainment events (Table 3 B).

Several issues arise from the pilot experiences that influence on its negative popularity. The system is fully appropriate for commercial use, considering the lack of privacy issues in entertainment opinion research. On the contrary, the use of the m-voting system in political elections arises the question of undisputable personal identification over the mobile phone's number, more clearly presenting the users political belief that is by law considered only as an intimate matter.

IV. USERS' READINESS

Readiness refers to the situation in which people are able to access and use Information Communication Technologies and Internet regularly. While the readiness is high in many developed countries, the situation is different in developing and under developed countries. People in many developing and under developed countries are unable to access ICT with sufficient regularity and use and in some places people are unable to access it at all [Gashghai, 2002].

M-government brings lots of opportunities which e-government couldn't succeed. Mobile government applications are accessed using mobile devices such as mobile phones and PDA's. The cost of owning these mobile devices are low. In addition, use of these devices is fairly simple thus making it easy for any common person to use it to access information. Governments can use this opportunity to better reach out to their citizens. Considering the lack of readiness for e-government and increasing use of mobile phones in developing countries and factors such as wide availability of mobile phones, ease of use, low cost of ownership and use, m-government seems to be a better way to reach citizens and interact with them.

V. MACEDONIAN CASE

In order to present a clear picture about the user's readiness to adopt the m-government channels, we realized an electronic survey about the citizen's opinion in the Macedonian society.

TABLE 4
SURVEY-BENEFITS FORM M-GOVERNMENT

Benefit	% participants
Better Information	41%
Save time	33%
Better communication	29%
Freedom	23%
Mobility	21%
Democracy	21%
Transparency	16%

The electronic survey was anonymous. The survey was intended mainly for the employees and the student at the Institute of Informatics in Skopje.

101 participants answered the questions in the survey, 63% males and 37% females. The participants were mainly young people, in the age group 20-35 years old with strong IT knowledge.

According to the results, the major part of the participants were not informed about e-government (66%) and even more 68% did not have a clear picture what is m-government. From the rest, 55% saw m-government as an addition to e-government and 45% considered them completely diverse.

The participants numbered several issues as benefits form implementing m-government services in Macedonia. The mostly addressed issues are presented in Table 4.

When it comes to the State's strategy about implementing m-government services, the participants clearly identified that it should involve pilot projects, implementation of balanced services with democracy/cost and services that are profitable in nature.

At the end, the participants pointed out that the issues as: lack of knowledge in the government, lack of technical infrastructure, lack of initiative and inexistence of ministry of information technology should be considered as major obstacles when implementing m-government services in Macedonia.

VII. RECOMMENDATIONS AND CONCLUSION

There are four major factors concerning citizens and the use m-government applications: awareness, ease of use, real added-value/benefit and price.

As the survey showed, the users should be carefully educated in order to feel comfortable with m-government. It involves public campaign and benefits that the citizens can clearly see and understand.

When implementing new technologies, governments should not force citizens to upgrade their current devices, but rather start small with applications using current technologies and current bandwidth for data transfers or services.

Starting small, but thinking big – basic m-government applications should be cornerstones of wireless strategies for governments worldwide.

On the other hand, such systems should be open to handle new technologies and the strategy should have a clear, long-term vision for the provision of the service and information relating to it.

Governments should prepare a complex strategy document in close cooperation with the public and private sectors. Governments should not see businesses as just business partners, but as true team players with a common goal – serving citizens in the best possible way.

REFERENCES

[Kushchu, 2003] Kushchu, I. and Kuscu, H (2003), "From E-Government to M-Government: Facing the Inevitable", in the proceedings of European Conference on E-Government (ECEG 2003), Trinity College, Dublin

[Zalesak, 2003] Zalesak M., (2003), "m-government: more than a Mobilized Government", web: http://www.movlab.org, accessed: 10.04.2004

[Lallana, 2004] Lallana, E (2004), "eGovernment for Development, M-Government Definitions and Models", web: http://www.egov4dev.org/mgovdefn.htm, accessed: 12.04.2004

[Ghyasi, 2003] Ghyasi, F. (2004), "Uses of Mobile Government in Developing Countries", web: http://www.movlab.org, accessed: 04.04.2004

[Arazyan, 2002] Arazyan H. (2002) "m-Government: Definition and Perspectives", web: http://www.developmentgateway.org/download/143909/mGov_Interview_2.doc, accessed: 17.03.2004

[Gashghai, 2002] Ghashghai, E. and Lewis, R. (2002), "Issues affecting Internet use in the developing countries in Middle East", Rand Corporation

Session IE:

Industrial Electronics

Modeling of a Control System of a Transistor Resonant Inverter

Nikolay D. Bankov [1], Tsvetana Gr. Grigorova [2]

Abstract - **The paper presents a control system of an induction heating transistor resonant inverter operated above the resonant frequency. The self-oscillating control system allows deep control of the inverter output power, by varying the duration of the transistors turn-on time. Control system is described using Analog Behavioral Modeling (ABM) feature provided in OrCAD PSPICE.**

Simulation and experimental results from the investigation of the induction heating transistor inverter are shown.

Keywords – **transistor resonant inverter, control system, induction heating, OrCAD PSpice.**

I. INTRODUCTION

There are modern methods for deep regulation of the output power inside the resonant inverter [2], [4], [5]. At the same time the input DC source can be uncontrolled. A method for output power control of resonant inverters, belonging to this group of methods, which has not been thoroughly studied, is based on the change in the transistors turn-on time [2], [4].

The block-diagram of the inverter control system is presented in [2], by which can be realized the given control principle.

In this paper the investigations are extended and the specific variant of the induction heating transistor resonant inverter controls system operated above resonant frequency is proposed.

The control system is described using Analog Behavioral Modeling (ABM) feature provided in OrCad PSpice [3].

II CIRCUIT DESCRIPTION AND OPERATION

Fig.1 shows the full-bridge induction heating transistor resonant inverter. The power switches used in the circuit are MOSFET transistors.

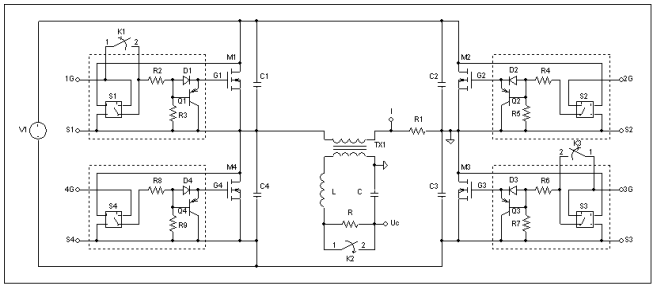

Fig.1. Full-bridge induction heating transistor resonant inverter

The series compensation of the inductor R-L is achieved with the capacitor C and by means of the high-frequency transformer TX1 is obtained a proper match between the inverter and the load.

The inverter circuit is operated above resonant frequency. The transistor individual control circuits are introduced.

These circuits feed the gate drive pulses of the corresponding transistor, if at the individual circuit input has drive signal and the transistor drain-source voltage is practically zero. This control method can be better understood by looking at the waveforms shown in fig.2.

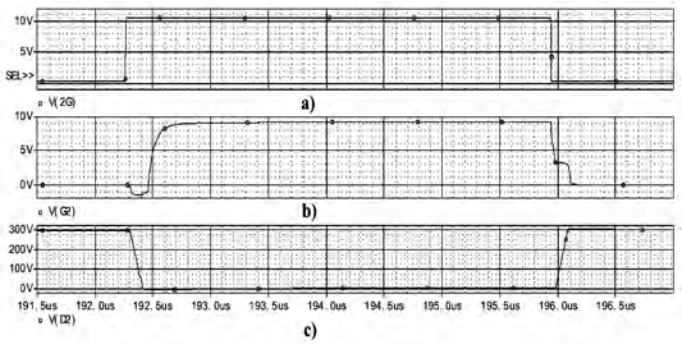

Fig.2. Individual control circuit – a) input driving signals and b) output driving signals. c) The transistor M2 drain-source voltage.

The drive pulse appears on the transistor M2 individual circuit input (fig.2a) immediately after the transistor M3 is turned off, because the two transistors are operated with the voltages, dephased at 180^0.

The drain-source voltage of the M2 (fig.2c) becomes practically zero, after the snubber capacitors C2 and C3 are recharged.

In this way, only by zero voltage of the transistor M2 (ZVS), the gate drive pulse (fig.2b) is ensured.

Like a parameter for deep control of the inverter output power is used normalized transistor turn-on time t'_{VT} [2].

[1] Nikolay Dimitrov Bankov is with the University of Food Technologies, 26 Maritza Blvd., 4002 Plovdiv, Bulgaria, E-mail: nikolay_bankov@yahoo.com

[2] Tsvetana Grigorova Grigorova is with the Technical University of Sofia, Branch Plovdiv, 61 Sankt Petersburg Blvd., 4000 Plovdiv, Bulgaria, E-mail: c_grigorova@abv.bg

The inverter has fixed characteristics typical for a voltage source, when $1>t'_{VT}>0,45$. In this interval of the parameter's t'_{VT} change, measures should be taken to limit the current in the resonant circuit, in the case of an overload or a short-circuit. The inverter can be considered as a current source, stable at short-circuit mode, when $t'_{VT}<0,45$.

III. CONTROL SYSTEM OF THE INVERTER

The control system is described using Analog Behavioral Modeling (ABM) [6]. The ABM feature provided in OrCad PSPICE allows for flexible descriptions of electronic components in terms of transfer function or lookup table. In other words, a mathematical relationship is used to model a circuit segment so the segment need not be designed component by component. Moreover, the combination of significant calculation efficiency with adequate component's modeling is achieved [3].

Fig.3 shows the proposed control system (CS) and fig.4 – the waveforms in significant points, which explain the system operation.

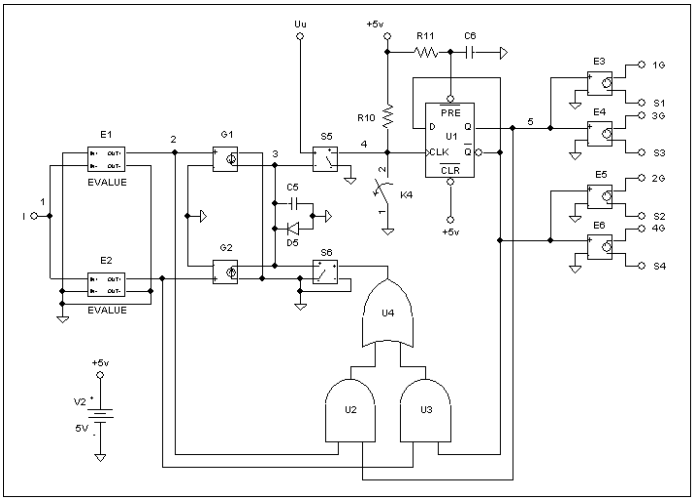

Fig.3. Inverter control system

The operation of the CS is synchronized with the current **i** in the primary transformer winding.

The resistor R1 senses the current trough the resonant link. This information is delivered of the controlled voltage sources (E1, E2), realizing a zero detector, which tracks the resonant current zero crossing.

The shaped pulses (fig. 4a) start the sawtooth voltage generator (fig. 4b), formed by the capacitor C5 and controlled current sources G1 and G2.

The voltage increasing time is equal to the transistors turn-on time - t_{VT}. It by the voltage Uu is formed (fig. 4b).

Uu is delivered on the comparator input, designed with voltage-controlled switch S5. The sawtooth voltage generator (SVG) output is sent to another comparator input. The comparator output shaped pulses (fig. 4c) are used to zeroing SVG and at the same time, are fed to the flip-flop trigger U1. The pulse distributor U1 forms two channels of the control pulses, dephased at 180^0 (fig. 4d). The dependent voltage sources E3÷E6 provide the required power, amplitudes and galvanic separation of the control signals.

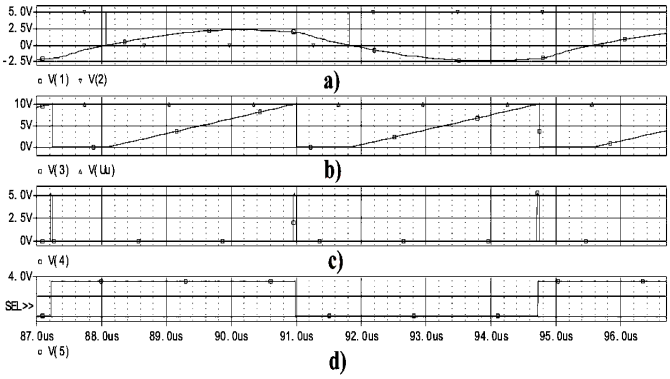

Fig.4. Control system main waveforms

Fig.5 circuit realizes the peak current limit of the inverter, which is fixed through V3 (signal Limit-I), in an advance specified level. The turn-on time of the transistors is achieved through V4, R14, and C9 -signal Time-VT. The peak detector current is formed on S7-S9, U5, E7 and C7, as the current peak value for each half period is stored in the capacitor C7. In fact, this storage is obtained at the moment that corresponds to the zero crossing of the compensating capacitor voltage.

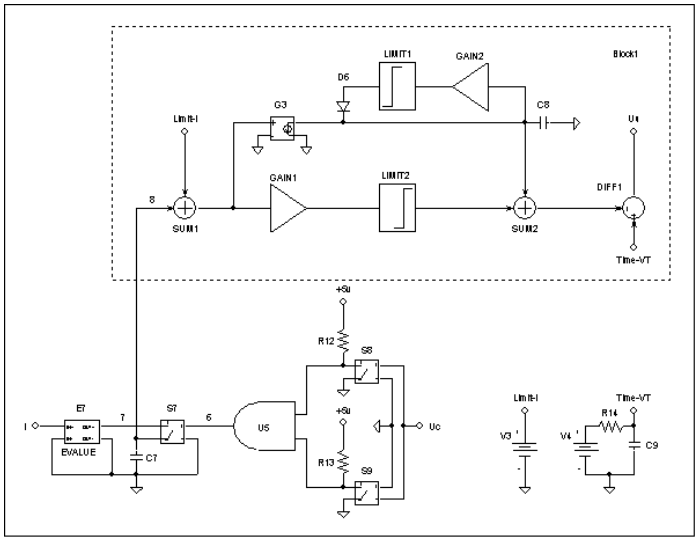

Fig.5. Peak current limited circuit of the inverter

The voltage of the capacitor C7 is compared to the signal Limit-I and according to the PI low (realized by means of the Block1 circuit) changes control signal Uu, thus the transistors turn-on time is decreased. The signal Uu is equal to the signal Time-VT, if the peak current is smaller than the previously specified value.

The peak current limited circuit operation is illustrated, as in the inverter from fig.1 the short circuit mode is simulated by switch K2. Fig.6 and fig.7 show the waveforms, explaining these processes.

From the waveforms are seen that the transistors turn-on time is decreased automatically (fig.7c), after the failure mode has occurred. This is the reason for the limitation of the resonant current.

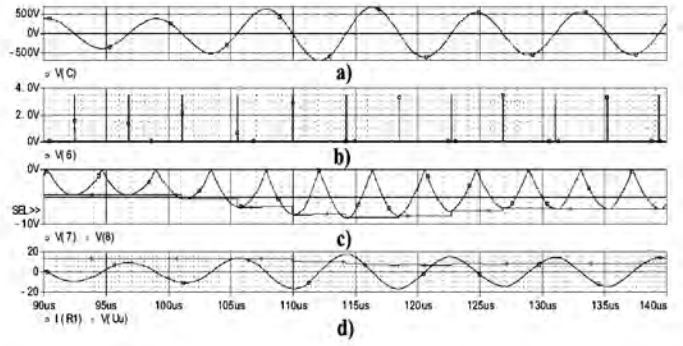

Fig.6. Inverter peak current limited circuit main waveforms

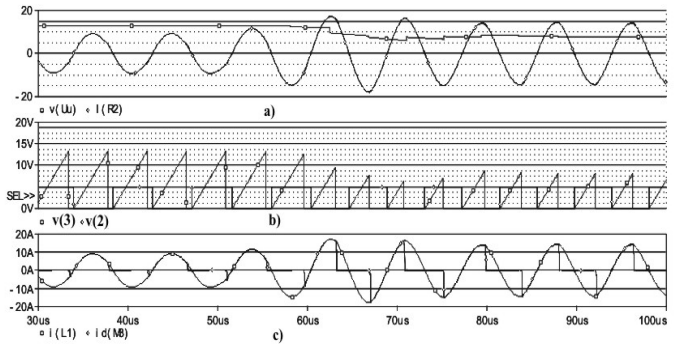

Fig.7 Transistor resonant inverter and control system waveforms in short circuit mode

IV. EXPERIMENTAL RESULTS

Based on the above consideration, the stomatology purposes induction melting resonant inverter of the small quantity of Ni-Cr-Co alloys and noble metals was built up and tested. The inverter dc power supply voltage is the rectified single-phase ac supply, the output power is 3kW and the operation frequency at the rated load is 115kHz. MOSFET transistors, type IRFP450 have been used. The heating inductor has inside diameter 40mm, height 40mm and number of turns – 4.

About 50g of melting Ni-Cr-Co alloy is put on the ceramic pot. Under these condition the inductor parameters from [1] are L=1,54μH and R=0,13Ω.

A series compensation and a proper match between the heating inductor and the load are obtained by the capacitor C=0,95μF and reducing transformer (ferrite core section $S=840mm^2$ and number of turns $w_1=20$; $w_2=2$).

Fig.8 shows the working point trajectory during the semiconductor switches commutation. This trajectory is favourable, because it is found near the i(u) coordinate axis.

The transistor commutation losses are proportional to the area enclosed by the trajectory and they reduce with increasing the snubber capacitors value. During the experiment snubbers' value is 1nF.

Fig.9 shows transistor voltage and resonant link current at the rated load.

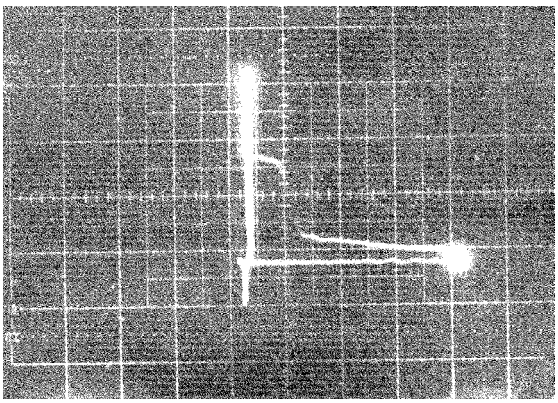

Fig.8. Trajectory of the working point at commutation of the transistor (x=50V/div.; y=5A/div.).

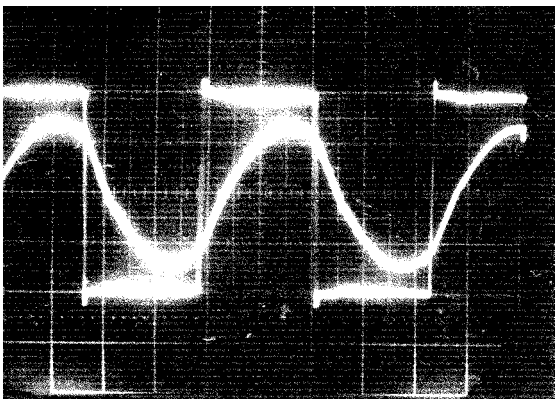

Fig.9. Voltage of the transistor-50V/div and current through the resonant circuit-10A/div. (x=2μs/div.).

V. CONCLUSIONS

The proposed control system ensures deep regulation of the inverters output power, by varying the duration of the transistors turn-on time.

Each transistor owns an individual control circuit, which allows the devices turn-on only by zero voltage (ZVS). As a result of the introduced current limited system, the inverter stays efficient even nearly short circuit mode.

REFERENCES

[1] Bankov, N., "Parameters measuring of a real heating inductor", The National Conference with International Participation "Electronika'2002", 17-18. 10. 2002, Sofia, Proceedings of the conference, pp. 38-42.

[2] Bankov, N.D., V.A. Kostova, "A Method for Power Control of Transistor Resonant Inverter", XXXVII International Scientific Conference on Information, Communication and Energy Systems and Technologies "ICEST2002", 02-04. 10. 2002, Nis, Yugoslavia, Proceedings of Papers, Volume 1, pp. 389-392.

[3] OrCAD PSpice A/D User's Guide, OrCAD Inc., USA, 1999

[4] Cheron, Y., "La commutation douce dans la conversion statique de l'energie electrique", Technique et Documentation - Lavoisier, 1989.

[5] Cheron, Y., H. Foch, J. Roux, “Power transfer control methods in high frequency resonant converters”, PCI Proceedings, Munich, 1986, pp.92-103.

[6] Kunov, G., E. Gadjeva, I. Eftov, “Modeling of a Selfoscillating Control System of a Transistor Oscillator for Tube Welding Using Spice”, XXXVII International Scientific Conference on Information, Communication and Energy Systems and Technologies “ICEST2002”, 02-04. 10. 2002, Nis, Yugoslavia, Proceedings of Papers, Volume 1, pp. 381-384.

Investigation of a Method for Power Control of a DC/DC Transistor Resonant Converter

Nikolay D. Bankov [1], Tsvetana Gr. Grigorova [2]

Abstract – **A deep power control method of a transistor DC/DC converter has been suggested. The method is based on varying the duration of the inverter transistor turn-on time operated above the resonant frequency. A family of the converter load characteristics has been drawn. The control system block-diagram and converter main steady-state equations, which allow fast engineering design, are proposed.**

The main theoretical results are proved by computer simulation using OrCAD PSpice.

Keywords – **resonant DC/DC converter, control method**

I. INTRODUCTION

The transistor DC/DC converter operated above the resonant frequency becomes more favorable as the feed source for the different electrotechnological purposes, by reason of unique energetic factors and high reliability of operation.

The large number of publications in this area is a good evidence of increased interests- [1], [2], [4] etc.

A method for output power control of transistor resonant inverters, which has not been thoroughly studied, based on varying the duration of the transistor turn-on time, have been reported in the literature [3] and [4]. This method is completely applicable by DC/DC converters.

In this paper an output power approach of the transistor resonant DC/DC converter operated above resonant frequency by varying the duration of the transistors turn-on time is presented. A family of the inverter load characteristics during the supply of the strongly variables loads has been drawn. The block-diagram of one version of a control system is proposed.

The converter main steady-state equations are presented, which allow fast engineering design.

II ANALYSIS AND LOAD CHARACTERISTICS OF THE DC/DC CONVERTER

Fig.1 shows proposed DC/DC converter and a control system block-diagram.

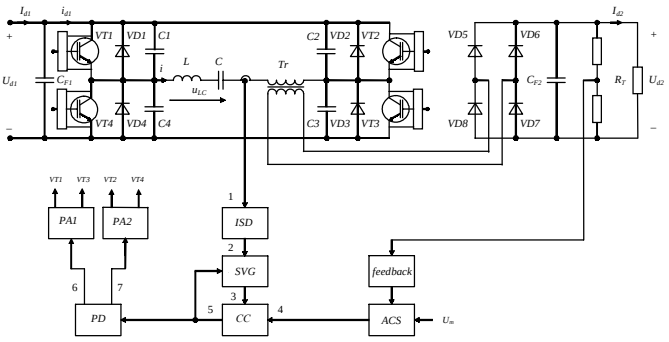

Fig.1. DC/DC converter and a control system block-diagram

The analysis and design of such converter are presented in [1] and [2]. The analysis is made under the following assumptions: the matching transformer is ideal; transformer turn ratio is one, the converter elements are ideal; the effect of snubber capacitors and the ripples of input and output voltages are neglected.

The results from the analysis are shown in table 1, where the following common symbols are used:

$\omega_0 = 1/\sqrt{LC}$ - resonant frequency; $Z_0 = \sqrt{L/C}$ - intrinsic impedance;

ω - switching frequency;

u_{LC} – voltage across resonant link *L*-*C* for each stage of the converter operation Eq. (3);

$i(0)$, $u_C(0)$ – initial values of the resonant link current and voltage across series capacitor for each stage of the converter operation - Eqs. (4) and (5);

$\theta_{VT} = \omega_0 \cdot t_{VT}$ - transistors conduction angle;

$\theta_{VD} = \omega_0 \cdot t_{VD}$ - diodes conduction angle.

For unifying purposes all units are presented as relative ones: the voltages to the supply voltage U_{d1}; the currents to the current $I = U_{d1}/Z_0$; the input power to the power $P = U_{d1}^2/Z_0$.

[1] Nikolay Dimitrov Bankov is with the University of Food Technologies, 26 Maritza Blvd., 4002 Plovdiv, Bulgaria, e-mail: nikolay_bankov@yahoo.com

[2] Tsvetana Grigorova Grigorova is with the Technical University of Sofia, Branch Plovdiv, 61 Sankt Petersburg Blvd., 4000 Plovdiv, Bulgaria, e-mail: c_grigorova@abv.bg

TABLE I
RESULTS FROM ANALYSIS

Quantity	Expression	
$i(\omega_0 t)$	$\frac{u_{LC}-u_C(0)}{Z_0}\cdot\sin\omega_0 t + i(0)\cdot\cos\omega_0 t$	(1)
$u_C(\omega_0 t)$	$u_{LC}-[u_{LC}-u_C(0)]\cdot\cos\omega_0 t + i(0)\cdot Z_0\cdot\sin\omega_0 t$	(2)
u_{LC}	1. $U_{d1}+U_{d2}$ 3. $-U_{d1}-U_{d2}$ 2. $U_{d1}-U_{d2}$ 4. $-U_{d1}+U_{d2}$	(3)
$i(0)$	1. $-I_0$ 3. I_0 2. 0 4. 0	(4)
$u_C(0)$	1. $-U_{C0}$ 3. U_{C0} 2. $-U_{Cm}$ 4. U_{Cm}	(5)
I'_0	$\frac{I_0}{U_{d1}/Z_0}=\frac{(1-U'_{d2})\cdot\sin\theta_{VT}}{U'_{d2}+\cos\theta_{VT}}$	(6)
U'_{C0}	$\frac{U_{C0}}{U_{d1}}=\frac{U'_{d2}\cdot(1-U'_{d2})\cdot(1-\cos\theta_{VT})}{U'_{d2}+\cos\theta_{VT}}$	(7)
U'_{Cm}	$\frac{U_{Cm}}{U_{d1}}=\frac{(1-U'_{d2})\cdot(1-\cos\theta_{VT})}{U'_{d2}+\cos\theta_{VT}}$	(8)
θ_{VT}	$\frac{\pi}{\omega/\omega_0}-\theta_{VD}$	(9)
θ_{VD}	$arctg\frac{(1-U'^2_{d2})\cdot\sin\theta_{VT}}{2U'_{d2}+(1+U'^2_{d2})\cdot\cos\theta_{VT}}$	(10)
I'_{d2}	$\frac{2\cdot(1-U'_{d2})\cdot(1-\cos\theta_{VT})}{(U'_{d2}+\cos\theta_{VT})\cdot(\theta_{VT}+\theta_{VD})}$	(11)
$I'_{d1}=P'_d$	$\frac{2U'_{d2}\cdot(1-U'_{d2})\cdot(1-\cos\theta_{VT})}{(U'_{d2}+\cos\theta_{VT})\cdot(\theta_{VT}+\theta_{VD})}$	(12)
$I'_{VT_{AV}}$	$\frac{(1-U'^2_{d2})\cdot(1-\cos\theta_{VT})}{2\cdot(U'_{d2}+\cos\theta_{VT})\cdot(\theta_{VT}+\theta_{VD})}$	(13)
$I'_{VD_{AV}}$	$\frac{(1-U'_{d2})^2\cdot(1-\cos\theta_{VT})}{2\cdot(U'_{d2}+\cos\theta_{VT})\cdot(\theta_{VT}+\theta_{VD})}$	(14)
I'_m	$\frac{1-U'^2_{d2}}{U'_{d2}+\cos\theta_{VT}}$	(15)

When a parameter for converter output power control is angle, respectively the transistors turn-on time, the latter in relative units should be presented in the following way:

$$\theta'_{VT}=\frac{\theta_{VT}}{\pi}=\frac{t_{VT}}{T_0/2}=t'_{VT} \tag{16}$$

Solving equations from Table 1 can be drawn an inverter family of load characteristics. Those are the relationships of the converter main variables as a function of the output current I'_{d2} and angle, respectively the transistors turn-on time θ'_{VT} in relative units.

The following relations can be of great interest: the converter output voltage $U'_{d2}(I'_{d2},\theta'_{VT})$, the input power and the input current $I'_{d1}=P'_d(I'_{d2},\theta'_{VT})$, the transistors average current $I'_{VT_{AV}}(I'_{d2},\theta'_{VT})$ and the freewheeling diodes average current $I'_{VD_{AV}}(I'_{d2},\theta'_{VT})$, the peak capacitor voltage $U'_{Cm}(I'_{d2},\theta'_{VT})$ and the switching frequency ratio $\nu(I'_{d2},\theta'_{VT})$, where $\nu=\omega/\omega_0$.

Fig. 2 ÷ 7 show corresponding graphs by θ'_{VT} = 0,80; 0,60; 0,45 and 0,30.

The description of the DC/DC converter load characteristics is identical to these that are referred only to the resonant inverter [3].

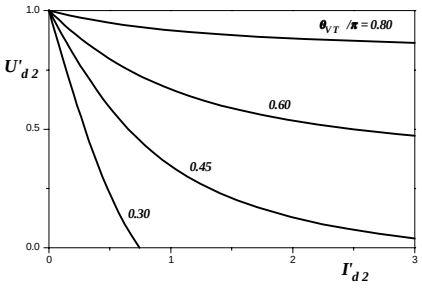

Fig.2. Normalized output characteristics of the converter

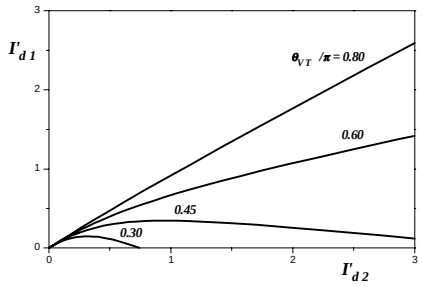

Fig.3. Normalized input current I'_{d1} (input power) as a function of output current I'_{d2}

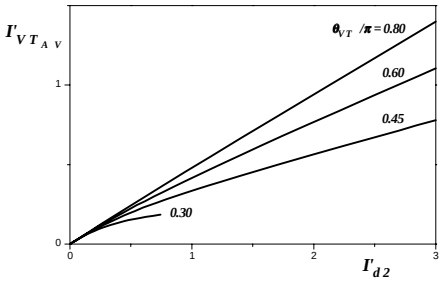

Fig.4. Normalized transistors average current $I'_{VT_{AV}}$ versus normalized output current I'_{d2} for different values of normalized transistors turn-on time θ'_{VT}

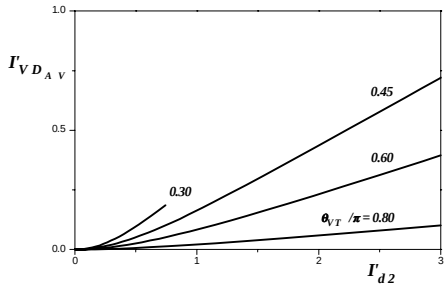

Fig.5. Normalized antiparallel diodes average current $I'_{VD_{AV}}$ against normalized output current I'_{d2} for different values of normalized transistors turn-on time θ'_{VT}

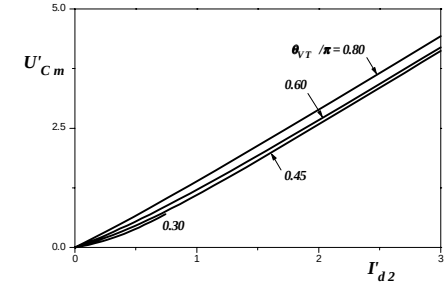

Fig.6. Normalized peak capacitor voltage U'_{Cm} as a function of normalized output current I'_{d2} for different values of normalized transistors turn-on time θ'_{VT}

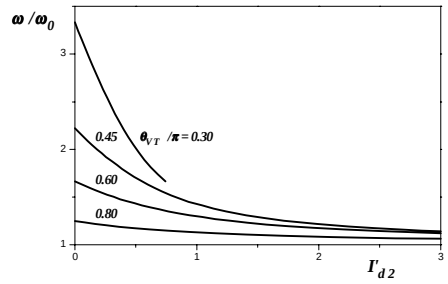

Fig.7. Switching frequency ratio as a function of normalized output current I'_{d2} for various normalized transistors turn-on time θ'_{VT}

III. CONTROL SYSTEM OF THE INVERTER

Fig.1 shows proposed control system block-diagram with the considered DC/DC converter. The operation of the control system (CS) is synchronized with the resonant link current **i**.

The input synchronizing device (ISD) shapes pulses, which give information when the resonant current crossing zero. These pulses start the sawtooth voltage generator (SVG). The voltage increasing time is equal to the transistors turn-on time.

SVG output voltage is sent to the one input of the comparison circuit (CC). The automatic control system (ACS) output voltage is delivered to another CC input.

The shaped pulses of the CC output zeroing SVG and are fed to the pulse distributor (PD). Pulse distributor forms 2 channels of control pulses, dephased at 180^0. The pulse amplifiers (PA1 and PA2) provide the required power, amplitudes and galvanic separation of the control signals.

ACS provides the necessary change of the CC control function, aiming to stabilize or regulate the inverter parameters according to a certain rule under the feedback.

Fig.8 shows the waveforms in significant points, which explain the system operation.

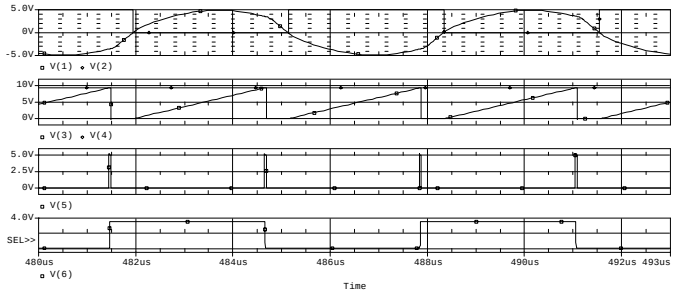

Fig.8. Control system waveforms

IV. DESIGN AND COMPUTER SYMULATION

Based on the analysis we have made and the load characteristics by given input and output voltages U_{d1} and U_{d2}, switching frequency f and output power P, the following design method can recommend.

1. The normalized output voltage is found from - $U'_{d2} = U_{d2}/U_{d1}$.

2. The normalized transistors turn-on time θ'_{VT} value is chosen, which determined the type of the output characteristics depending on industrial process requirements. In this way the operating points on the load characteristics at the rated load are determined. All the base converter quantities in relative units become known.

3. The value of Z_0 can be expressed as:

$$Z_0 = \frac{U_{d1}^2}{P} \cdot P'_d \tag{17}$$

4. The resonant frequencyω_0 can be calculated as:

$$\omega_0 = (2 \cdot \pi \cdot f)/\nu \tag{18}$$

5. The values of L and C from Z_0 and ω_0 can be evaluated as:

$$L = Z_0/\omega_0 \tag{19}$$

$$C = 1/(Z_0 \cdot \omega_0) \tag{20}$$

6. The base quantity values in real units, necessary to choose the converter elements are calculated.

The computer simulation of the DC/DC converter without matching transformer is given by the following conditions: power supply U_{d1}=300V; output voltage U_{d2}=260V; switching frequency f=150kHz; output power P=3kW; and resonant link elements L= 33.975μH and C= 44.937nF. The value of the θ_{VT}=0,75π rad is determined.

Fig.9 sows simulation results, which are compared with theoretical results in table2. A good coincidence between theoretical and simulation results can be seen.

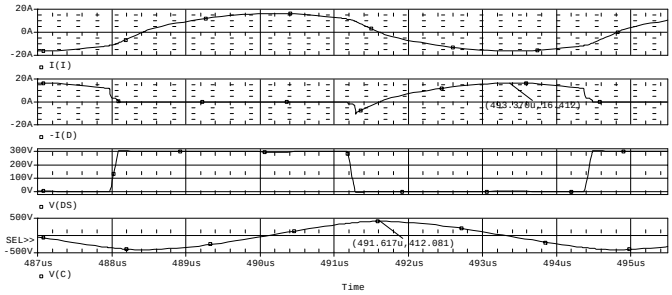

Fig.9. Simulation results

TABLE II
COMPARISON BETWEEN THEORETICAL AND SIMULATION RESULTS

	t_{VT}	t_{VD}	I_{d1}	I_{d2}	I_m	U_{Cm}
	µs	µs	A	A	A	V
Evaluation	2.9113	0.4220	10.00	11.538	17.019	427.95
From PSpice	2.8736	0.4592	10.06	11.550	16.412	412.08

V. CONCLUSIONS

A method has been suggested for a deep regulation of the DC/DC converter operated above the resonant frequency by varying the duration of the transistor turn-on time. A version of a control system is shown. Converter analysis known from literature has been used and its load characteristics have been built. They allow to evaluate the behavior of the considered converter when the load is changed strongly during the operation process. The main steady-state equations are presented, which allow fast engineering design. A very good coincidence has been obtained between theoretical results and those from computer simulation.

REFERENCES

[1] Al Haddad, K., Y.Cheron, H.Foch, V.Rajagopalan, “Static and dynamic analysis of a series resonant converter operating above its resonant frequency”, SATECH'86 Proceedings, Boston, 1986, pp.55-68.

[2] Anchev, M.Ch., G.J. Maleev, “Transistor inverter analysis functioning at frequencies higher than the resonance one”, E+E, 2000, 5-6, pp. 12-17.

[3] Bankov, N.D., V.A. Kostova, “A Method for Power Control of Transistor Resonant Inverter”, XXXVII International Scientific Conference on Information, Communication and Energy Systems and Technologies “ICEST2002”, 02-04. 10. 2002, Nis, Yugoslavia, Proceedings of Papers, Volume 1, pp. 389-392.

[4] Cheron, Y., “La commutation douce dans la conversion statique de l'energie electrique”, Technique et Documentation - Lavoisier, 1989.

Real Time Kernel for Embedded Systems

Emil N. Dimitrov[1] Stanimir D. Mollov[2], Kristian Dilov[3]

Abstract – **The paper presents the problems connected with a real-time kernel for embedded systems. The system kernel building, the system process building and the interactions between the applied tasks and processing of external events have been discussed. The developed real time kernel MSPIX, which is intended for embedded systems, has been analyzed. The results of the analysis have given an opportunity to state that MSPIX possesses most of the contemporary real time-kernels features.**

Keywords – **real-time kernel, dispatcher, system process, applied task, descriptor.**

I. INTRODUCTION

The high requirements to contemporary control systems are the main precondition for their continuous improvement and modernization. To decrease the necessary time and resource expenses, the control systems are realized with a possibility of quick and easy configuration, reconfiguration and adjustment. These possibilities are supplied by software of the system. Its main purpose is to distribute the system expenses among the control processes. Such a system s is called Operating System (OS)[1].

Each applied system is designed on the base of OS and given user's tasks. On the base of the user's tasks the functional purpose of the system is formed. The time of changing the functional action of the system is reduced. Only the user's tasks are replaced, while the basic platform is unchanged.

II. BASIC CONCEPTS IN REAL-TIME SYSTEMS

The Real Time Operating System (RTOS) is a combination of the system software, which allows performing a large number of user's programs at one and the same time. The user's software can interact with external environment as well as exchange some data with another software.

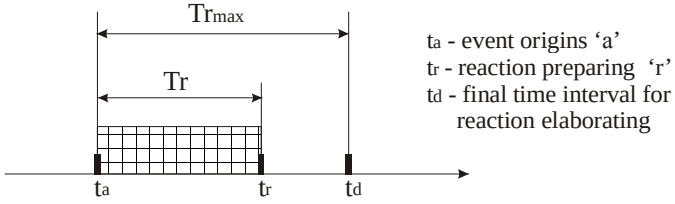

Fig. 1. Requirement for work in real time

[1]Emil N. Dimitrov is with the Faculty of Electronic Engineering, & Technologies, TU – Sofia, 1797, Sofia, Bulgaria, E-mail: edim@tu-sofia.bg

[2]Stanimir D. Mollov is with the Faculty of Electronic Engineering, & Technologies, TU – Sofia, 1797, Sofia, Bulgaria, E-mail: smollov@abv.bg

[3]Kristian Dilov is with the Faculty of Electronic Engineering, & Technologies, TU – Sofia, 1797, Sofia, Bulgaria

The term "real time" means that the system responds to each external event in a fixed time interval (Fig.1). The period T_r, which determines reaction R of the input influence A, is a variable because of asynchronous character and unpredictable influence on the computing process. The requirement of work in real time is reduced to the inequality:

$$t_r = (t_a + T_r) < t_d \quad (1)$$

where t_d is the final time interval for elaborating the reaction from Real Time System (RTS) [2]. The violation of this inequality is equal to the system failure.

The problems, which are solved during design of a real-time system, increase with adding the time co-ordinate. Under this condition it is necessary to create the real-time operating system as a multitask system. The multitask system consists of many asynchronous tasks and communication environment between them. Each task represents an active logical process, which is performing a kind of work within the system. In the common case each event is connected with a definite task.

The real time operating system provides a virtual process for each task. The virtual process performs the task in parallel to the others in the system. In the single processing systems this performance is a pseudo one – parallel or competitive. An actual parallelism can exist only between the tasks in multi processing or distributive real-time systems.

The hierarchical structure of the applied system (Fig. 2) can be divided into two components: a real-time operating system and applied tasks.

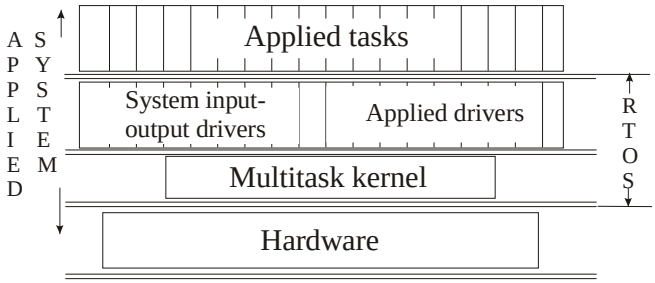

Fig. 2. Hierarchical structure of an applied system

The multitask kernel is located on the lowest level of the hierarchy. It implements all mechanisms, which support the multitask mode: task dispatching, the interaction between the tasks and events control. The kernel "services" are given to the upper levels in the form of system primitives and system macro. The system input-output drivers are an additional component and are used to control the standard peripheral devices. In contrast to the system drivers, the applied ones are additionally developed according to the used hardware.

The applied tasks are located on the highest level of the hierarchy. Their number, composition and character depend on the specificity of the applied system application.

III. SOFTWARE

A. System kernel

The main function of the kernel is to support the multitask mode. The code of the kernel is the most intensively used component in the system and in contrast to most of the drivers, it is a mandatory part of each applied system. Therefore the kernel must be effective enough with the requirements of a small memory size.

The purpose of the presented system kernel is to control the industrial controllers, which are built on the base of MSP 430 produced by Texas Instrument. The system kernel must create a possibility for competitive tasks performance in real time. The distribution of the processing time among the tasks is realized on a priority base by a dispatcher, which consists of two parts: a system clock dispatcher and an events dispatcher. The system clock dispatcher used Timer_A built in the microcontroller. It counts to a defined value and having reached it, generates a request for interrupt. This request is used for switching between tasks. After this counting starts again. The events dispatcher transforms the external influences in internal circuit events. The effectiveness of this transformation determines the field of the real-time system application. There are different methods to implement these reactions, but the most suitable one is that described above, which is used to interrupt from input port.

B. Applied tasks and their states

At the time of self-existing the processes in the real-time system have different states. The change of their state is done by the system kernel. This process is connected with the system losses – the processing time, the resource expenses. Because of this it is necessary to create exact rules for serving the tasks by the kernel.

At a given time each task in the applied system can be in one of these states:

- IDLE – the task uses only the memory area, in which its code is written as a resource;
- READY –the task has at its disposal the necessary conditions for its performance without the central processing unit;
- RUN – the task is being performed;
- BLOCK – the task is waiting for setting in some kind of event or resource discarding;
- WAIT – the task is waiting to pass a period of time;

At the beginning all tasks are in IDLE state. The procedure for establishment the task in READY state includes: creating the necessary data structures and stack segment organizing.

The tasks can be interpreted by the kernel as system tables – descriptors (fig.3). The manipulations, which the kernel can perform with system tables, are reduces to modify their fields. Each task has a unique *ID*, which is stored in the kernel work area. The kernel defines this *ID*, when the task is created. In fact this *ID* is the pointer to the task source in program memory. The current state of the task is written in field – *Type* and can be one of these enumerated above. The next field contains the task priority. The contemporary real-time system has 64 user's tasks. Because of this the maximum value, which can be written here is 64. The connection between the value and priority is straightforward (higher value – higher priority).

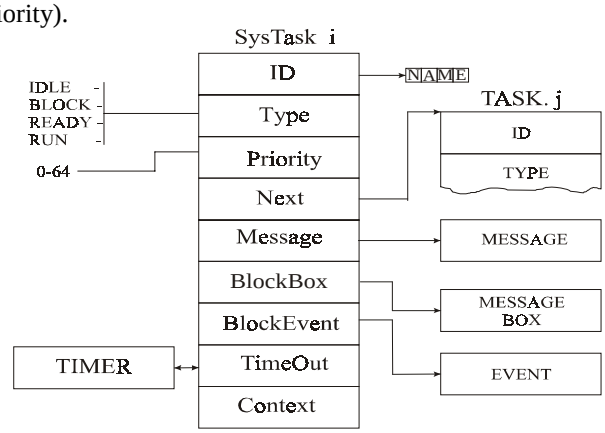

Fig. 3. Task descriptor

The arrangement of the tasks in the queue depends on the task priority – field *Next*. The beginning point of the queue contains the address pointer to the descriptor of the task of the highest priority. The fields *Message* and *BlockBox* in the task descriptor are used for communication between tasks, while the field *TimeOut* is used to definite the time interval in WAIT state. In the last field of the task descriptor named *Context* the work registers contents is written. These registers are: program counter, stack pointer, status register and accumulators.

C. System process

Before inserting a number of applied tasks, a system process is started in the system that in consequence originates them. This system process exists and is performed together with the applied task. Analogous to the applied tasks, the system process has a descriptor as well (Fig.4).

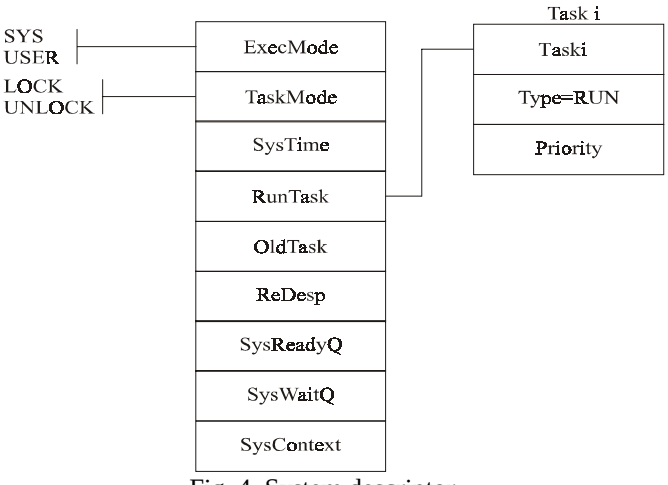

Fig. 4. System descriptor

The first field of the system descriptor indicates the current operating mode and can be:

- USER – the interrupts are enabled and there are premises for task dispatching;

- SYSTEM – the system manipulations are performed.

The field *TaskMode* defines the mode of the active task, which is usually UNLOCK. The task, which is in LOCKED mode, cannot be switched by another task and therefore it is working in a monopoly mode.

The system quantums are generated by Timer_A and heaping in the 32-bits counter –*SysTime* field. The system descriptor contains a pointer to the active task – *Runtask* field. It is possible that there is no active task at the moment (*RuntTask* = NULL). The pointer *OldTask* and *Redesp* are used for re-dispatching.

The system kernel keeps two system queues. The first one is the queue of ready tasks, which contains pointers to the tasks in READY state– *SysReady* field (fig.5). The second is the queue of holding tasks (Fig. 6). The arrangement of the tasks here occurs according to the contents of *TimeOut* field of their descriptors. The task with the shortest timeout stays at the beginning.

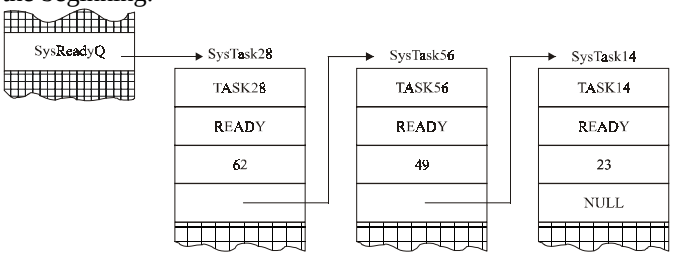

Fig.5. Ready task queue

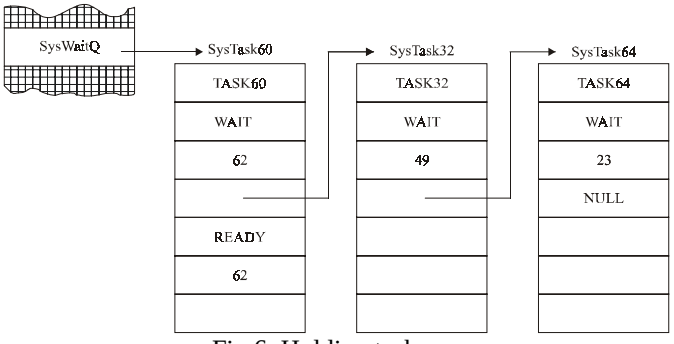

Fig.6. Holding task queue

The last field of the system descriptor contains pointer to system stack and status register.

D. Dispatchiring

The multitask kernel of the real time operating system supports a virtual processing unit for each task. Immediately after starting in the system exists only one virtual processing unit, which is intended for system process. When the applied task is creating the system process adds its virtual processing unit, which is executing in parallel with another tasks. In the single processing systems the processing unit is only the resource, which is distributing from the multitasking kernel. Therefore the dispatcher is a kernel component, which is distributing the time of processing unit between the ready for execution tasks.

There are two main strategies for system time distribution:

- Strategy without interrupts of the current executing task;
- Strategy with priority interrupts of the active task.

The strategy with priority interrupts gives privileges of the high priority tasks in processing time distribution. Because of this it is a more suitable strategy for realize the real time operating system.

It is possible several tasks to be with same priority. In this case they are switching alternate. The switching will continue while the change in the system occurs. The changes may be:

- An event, which is changing the state of the current task and removing it from list of the ready tasks;
- An event, which is setting the task with higher priority from the active task (fig. 7).

When the system quantum is time out, the dispatcher is checking whether there is a task with higher priority and if absence of such, the current task execution will continues in the next system quantum.

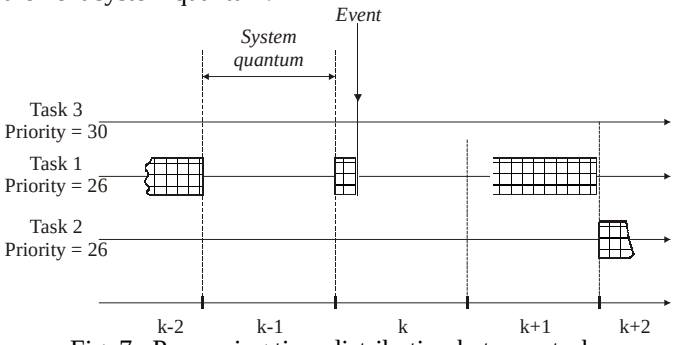

Fig. 7. Processing time distribution between tasks

The system quantum is creating on the base of interrupts from the Timer A. During the interrupt service procedure the content of the current performed task is stored. Afterwards the processing unit registers are loaded with the contents of system virtual processing unit and the current mode is changed from USET to SYSTEM. The first task is loaded from the ready tasks queue. The content of the system process is stored and the registers of the physical processing unit are loaded with the contents of the first task from the list of ready tasks. After this the system mode is changed from SYSTEM to USER by modification of *ExecMode* field in the system descriptor.

E. Interaction between tasks

The interaction between the processes in the real-time operating system consists of data exchange between them. The data exchanged between the processes can be examined as a message of a defined format. The same idea is grounded on the base of the message box mechanism. The message boxes are used as a buffering message as well as for including the synchronizing methods between the processes: process transmitter and process receiver.

The message box descriptor is shown in Fig. 8. The flag FULL accepts FALSE if the message box does not contain any massage, and TRUE if the message is received by it. The *BlockTask* field contains the blocked task *ID* from the message box. This can be the task receiver, which is waiting for a message or the task transmitter, which is waiting for the message transmits. The message box buffer

is pointed by the pointer MsgPtr. When the box is empty (Full=FALSE), its contain is indefinite.

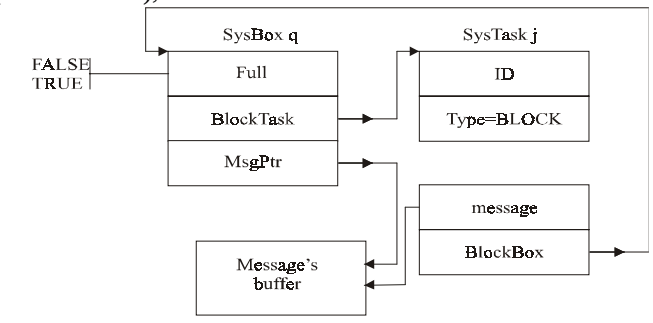

Full - flag full/empty Message box
BlockTask - blocked task identifier
SysBox - message box descriptor
SysTask - task descriptor

Fig.8 Message box descriptor

F. Registration of external events

One of the main functions of the multitask kernel is to transform the external influences into internal events. This transformation, which defines the area of the real-time system application, is performed by the embedded events mechanism (Fig.9). On the external event ei replays the system event Eventi, which is serving by Taski. It is possible that some events are served by one task, but each event can be served by one task.

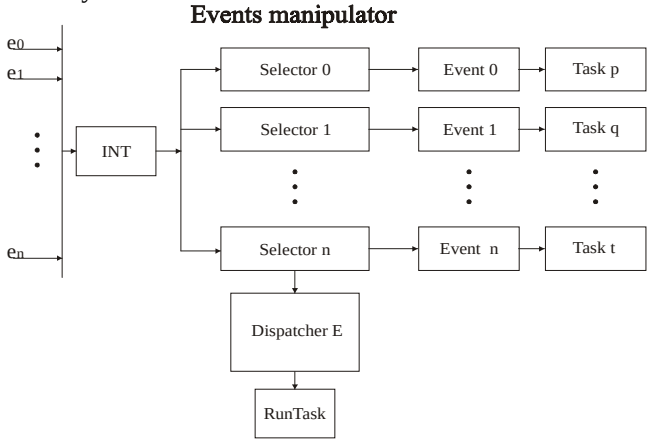

Fig. 9. Model of the event mechanism

When the event ei occurs, the hardware interrupt mechanism returns the control to events manipulator. The Selector identifies ei and establishes a connection with the system event Eventi. After this the system manipulator generates a request to the dispatcher. The events dispatcher distributes the processing unit time on the base of the strategy with priority interrupts: the blocked task on Eventi is activated if its priority is higher from the current performed task. In the opposite case, the task is included in the ready task queue.

The realization of the events mechanism depends on the architecture of MSP430 microcontrollers. To determinate the external influence two ports are used: Port 1 and Port 2 of the microcontroller. These ports have different interrupt vectors. The connection between the influence and the internal event is set by the system manipulator functions Selector0 – Selector.

IV. Real Time Operating System MSPIX

MSPIX is a priority multitask operating system, which is designed for use in embedded system built in on the base of MSP430 microcontrollers. Its parameters include: the necessary volume of data and software memory and some basic time parameters. The first parameter group is necessary for the microcontroller choice. The limitations here are a result of data memory size. It varies from 256 to 10240 bytes. It is recommended to use the microcontrollers with minimum 1024 bytes of data memory. The system expenses for a user's task are connected with creating its descriptor in the memory and with organizing its stack area. The task descriptor consists of 8 fields with a size of 16 bits (one word) and a field with twenty words for task content. The additional system expenses are created from the system descriptor (generally 34 words), message box descriptors (6 words) and event descriptors (2 words). Another basic feature of the real-time operating system is the time switching. These are quite important parameters characterizing the system. The switching between the tasks is done when the system process is activated. The system is in SYSTEM mode and the mask-like interrupts are not allowed. At this moment a risk of event service delaying can occur. The time parameters are shown in Table 1.

Table 1

Expenses	Cycles	In seconds
Maximum switching time between the tasks	496	66.10^{-6} sec
Minimal switching time between the tasks	344	43.10^{-6}sec

V. Conclusions

The developed real-time operating system possesses most of the contemporary real-time operating system features.To analysis the main system parameters, it is developed a system on base of MSP430F149 microcontroller. In this system the maximum switching time between the tasks is **66us**, and the system quantum is 66ms. The developed system is characterized with low processing time expenses. The results of the developed system are near to the contemporary real-time operating systems.

V. References

[1] Henzinger T.The Embedded Machine:Predictable, Portable Real-Time Code, EECS, University of California, Berkeley.

[2] Дилов К. Дипломна работа на тема: Операционна система за реално време за фамилия микроконтролери MSP430, София 2004.

[3] MSP430X1XX Family User's Guide - Texas Instruments.

[4] Single-chip Microcontroller real-time operating system – Digital Cellular Magazine 2002.

[5] J.K Stankovic, J. K. Ramamritham. The design of the spring kernel. Real-time systems symposium, San Jose, 1987.

Analysis of an Asymmetric Inverter in Phase Space

Hristo P. Hinov and Valentina V. Rankovska[2]

Abstract – **A model of an asymmetric inverter in the Phase space (PSM) have been build-up. By the means of the respective theoretical basis the main connections of the circuit parameters have been represented, with the mode parameters in PSM. The main dynamic conditions have been specified as in inverters definition. The common differential structure of the inverters is offered to your attention.**

Keywords – **inverter, model, phase space**

I. Introduction

The asymmetric inverter (AI) is a spreaded frequency converter and it is found in many variants. The electromagnetic processes in it are defined by differential equations similar to those of the serial inverter [1]. They are also a model for some more complex circuits at definite conditions [2]. The base circuit of an asymmetric inverter is shown in Fig. 1.

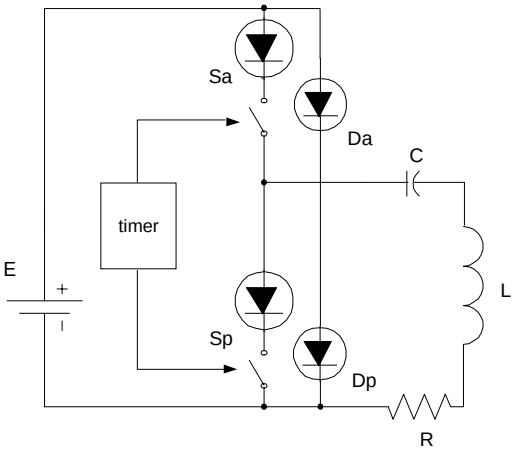

Fig 1 Base circuit of AI

It's load chain is a serial resonant CLR circuit. The equivalent parameters of the load are included in it.The load is usually an induction heating system, it could be also a ultrasonic converter or other consumer. The load circuit is connected to a DC source – E by driven and single-pole switch and a diode – S_aD_a, called "active". The second couple of switch and diode – S_pD_p, close the load chain directly and they are called "passive". The switches are electronic devices, for instance transistors. They are driven by a device, called "timer" for short. It implements an inverse control of the switches – when the first is active (closed), the other is not active (opened). The change of these states is made by tacts, by equal intervals called one-half periods - $T_\tau/2$.

The goal of this report is to define a phase-space model of the inverter and also to structure the major connections between the elements of the model, respectively of the inverter. Making active the switch S_a leads to current in the load chain and voltage across the capacitor. A differential dependence exists between the capacitor voltage and the current which determines the space of their interaction as in the PS is called Phase Model (PM). The model includes Phase Vector (PV) and it's specific kinematics. The vertex of Phase space (PS). It is a plane marked by a Cartesian coordinate system. The interpretation of the inverter processes the PV traces the Phase Trajectory (PT). It is a closed curve consisting of two spiral arcs – segments – active and passive. The general view of the Phase Model is presented in Fig. 2. It is related to inverters with Q-factor q=2. The one-half

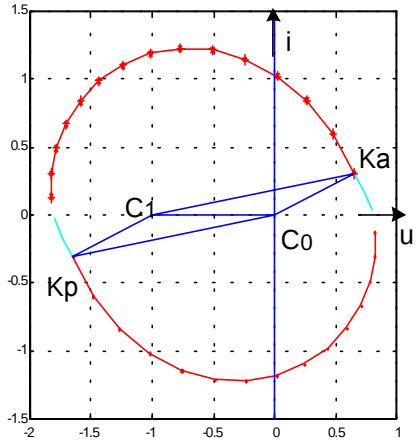

Fig 2 Phase model of AI

period development angle is set by the timer: θ_s = 3,4 radians which is about 195°. The upper arc is the active segment of the PT. It's start is the commutation point with coordinates u_0 = 0,79 and i_0 = 0,32. The commutation point will be an object of special attention.

II. Theoretical Basis

The generalization and universalization of the particular circuit parameters is made using well-known procedure. The x-axis shows the voltage across the capacitor divided by the constant E. The source voltage – E [V] with it's dimension (volts) is treated as a scale for the x-axis. Thus the x-axis markers are relative and universal values released from the dimension of the particular voltage. The y-axis presents the current across the inductunce again in universal relative units. As a dimensional scale a current – E/ρ [A] is applied, where ρ = $\sqrt{L/C}$ is the wave resistance of the load circuit.

The following equations (Eqs. 1) present the voltage and current in the PS:

$$\begin{aligned} u(\theta) &= 1 - u_s \exp(-\varepsilon\theta) \cos\theta \\ i(\theta) &= i_s \exp(-\varepsilon\theta) \sin\theta \end{aligned} \qquad (1)$$

The angle θ = ωt is the phase argument limited by the frames of the one-half period $0 \le \theta \le \theta_s$, where it's boundary value "development angle" is $\theta_s = (T_\tau/T_0)\pi$.

[1] Hristo P. Hinov is from the Technical University, 4 H. Dimitar str. 5300 Gabrovo, Bulgaria, E-mail: hinov@abv.bg

[2] Valentina V. Rankovska is from the Technical University, 4 H. Dimitar str. 5300 Gabrovo, Bulgaria, E-mail: rankovska@tugab.bg

The frequency is $\varpi = \sqrt{(CL)^{-1} - \delta^2}$;the fade $\delta = R/2L$; the relative fade $\varepsilon = \delta/\omega$ or approximately: $\varepsilon = 1/2q$, where the Q-factor: $q = \sqrt{L/C}/R$. T_τ is the period set by the timer; $T_0 = 2\pi/\omega$ is the period of the free oscillations. It is important to notice that the inequality:$T\tau > T_0$ is always true. The inverter always works at development angle $\theta_s > \pi$.

III. Phase Model Elements

The voltage is marked on the real axis and the current on the imaginary axis when treating the phase plane as complex. This gives the PV suitable complex form (Eq. 2):

$$F(\theta) = - 1 + (1+ Ka)*\exp((-\varepsilon+j)*\theta) \qquad (2)$$

The complex function (Eq. 2) is a spiral segment. The spiral start point k_a by it's coordinates $k_a(u_0,i_0)$ determines the commutation mode of the inverter. The start and the commutation processes are typical for the zero value of the argument $\theta = 0$. At the consequent rising of the argument the vertex of the PV – $F(\theta)$ traces the active segment of the Phase trajectory. The center of this spiral arc is on the x-axis at the point -1. The end of the segment is at the borderline value of the argument $\theta = \theta_s$. This is the other commutation point – passive k_p where the connection between the active and passive arc of the PT is realized

The typical for the inverters change of the PV centering is made at the commutation point. This transferring of the PV at the beginning of the coordinate system where the center of the passive arc is, is made discrete at the moment when it's vertex is at the commutation point.

The energy interpretation of this phenomenon gives an opportunity for a more different approach toward the inverters. The transferring of the vector beginning at the new center determines the new analytic definition of the PV valid for the passive one-half period – Eq. 3:

$$F(\theta_s+\theta) = Kp*\exp((-\varepsilon+j)*\theta) \qquad (3)$$

The spiral of the passive segment starts from the point k_p, develops according Eq. 3 and ends at the active commutation point $k_a(u_0,i_0)$. The center transferring of the PV is made at the both commutation points.

Another type of commutation is implemented at the cross points of every spiral arc with the x-axis. The current is transferred from the appropriate switch to it's diode at these points. This is an apparatus-device commutation and it is not of special energy importance. The functions of the inverter stay fluent and unchanged.

The components of the PM can be treated also as a conventional functions of the time. The inverter current – imaginary component of the PV is developed in Fig. 3. It is related to inverters with Q-factor q = 2 and one-half period angle $\theta_s = 4{,}4$ radians or 252°.

The commutation point where the active sub-circuit diode current is "transferred" to the passive sub-circuit transistor is marked as broken arc. At the end of the function of the current the another commutation is made with which the active transistor starts the next period "accepting" the current. At the "zeros" of the current function where it crosses the x-axis the diode commutations are made. The current is "transferred" from the transistor to it's corresponding diode there.

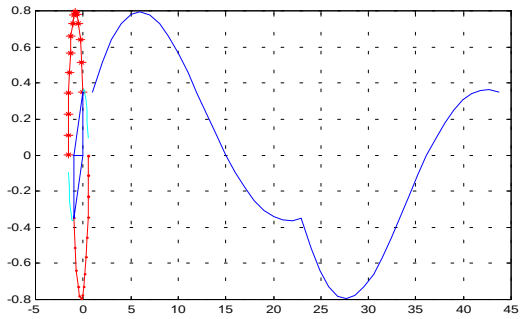

Fig 3 Current of AI

IV. Phase Model Recurrent Dependencies

The inverter processes development matching to the passive arc is nearly the same as for the active segment and it is due to the functional similarity between Eqs. (2) and (3). The imaginary part of the phase vector – current by modulus repeats the former one-half period. The real part of the PV – voltage differs only with a constant of "one" which is the distance between the two spiral centers. There is a distinct symmetry between the passive and active sectors of the PM and this will be proved by the analysis of the stationary mode of the inverter.

Let us examine the inside of the PM. There is a rhomboid between the active and the passive sectors marked by the spiral centers C1 and C0 and commutation points k_a and k_p. The outside angles of the rhomboid at the centers are the spiral one-half period angles $\theta_s = \pi + \alpha$. The diagonal between the centers divides it to two identical triangles.

Each of the triangles is characterized with:

1. It's base is the single segment of the x-axis.
2. Opposite the single base of the triangles at the commutation points resides the complain component of the spiral angle α ($\theta_s = \pi + \alpha$).
3. The other faces of the triangles are respectively the start and the final values of the PV. The reduction connection between the start and final modules of the PV is valid also for the lengths of the other two faces:

$$CoKa = C1Ka * \exp(-\varepsilon\, \theta_s) \qquad (4)$$

That is enough to build-up the triangle which apex completely defines the whole stationary mode of the inverter. That is the direct solution of the stationary mode without using the connections with the former transitional process. The problem will be especially treated comprehensively.

V. Phase Model Dynamics

The vertex of the PV traces the PT by rotation with permanent angle velocity. The permanent reduction of it's modulus expresses the realized or so called "active" energy. This is only the one side of the dialectical energy parity at he inverters. The discrete periodical transferring of the beginning of the PV from the first spiral center to the other is **the typical for the inverters** transferring to another subsystem with **increased energy potential**. The PM represents accurately the rise of the potential energy with the increased modulus

immediately after the commutation. Thus the energy realization which the PM expresses as a permanent modulus reaction of the PV corresponds to the discrete post-commutation modulus rise. This gives an ability for an alternative approach by the means of which the inverter processes and parameters can be predicted and designed in a untraditional way.

VI. Phase Model Accents

The mentioned spiral centers are the steady solutions images of the differential equations which are valid during the various one-half periods of the inverter. Their positioning in the Phase Space presents a specific classification of the inverter types. They reside on the x-axis of the PS for all inverters which load circuit includes a serial capacitor as it is at the examined object.

The described single-round distance between the spiral centers stay also at the so called “half-bridge” inverter and in the various pseudo symmetrical circuits too. At them the PM and the inverter processes have the form shown in Fig 2, with the difference that the y-axis is in a symmetrical position expressing a symmetry at the voltage too. The spiral centers are positioned respectively at the points +0,5 and -0,5 on the real axis.

The PT at the bridge inverters is not much different too. It’s centers are only at a double distance on the x-axis points ±1. This makes possible and stable the operation of the bridge inverters also at an increased fading in the load circuit.

Could be said that he presented Phase Model is valid not only at the asymmetric inverter but it includes the processes in a wilder class of inverters.

It excites interest a wider classification of the inverters made not only by circuit parameters but especially by the steady solutions of their differential systems which at the present PM figure as centers of the spiral arcs. Such position is typical for all inverters which have serial capacitor in the load circuit. However many inverters exit where these centers reside at other – alternative position. Such type of inverter is for instance the known Parallel inverter. Another alternative is the “Inverter with inductive commutation” [3].

VII. Conclusion

The Phase Model presents the dynamic connection between the circuit and mode parameters of the inverters. The voltage, the current, the time and the energy of the inverter are scaled in one drawing. This gives opportunities for:

- General classification of the inverters by the steady solutions of their differential equations;
- Structuring the dynamic model and thus defining the noun “inverter” determining it from the other powerful generators;
- Implementing the element connections at the PM for application aims which was only demonstrated by the direct “incoming” in a stationary mode.

References

[1] Х. П. Хинов. “Векторно моделиране на елктромагнитните процеси в последователен резонансен инвертор”, сп.”Техническа мисъл”, кн.1/1978г., БАН, София.

[2] Н. П. Градинаров, Х. Л.Хинов, Д. Д.Арнаудов, П. Т. Горанов, “Товарни характеристики на резонансни инвертори с обратни диоди, работещи в режим с подрезонансна честота”, сп.”Е+Е”, 3-4/2003 г., София.

[3] Х. П. Хинов, “Инвертор с индуктивна кумулация”, сп.”Е+Е”, 2004 г., София (под печат).

Diagnostic Functions Embedding in Industrial Control Systems

Stanimir D. Mollov[1], Georgy Sl. Mihov[2], Ratcho M. Ivanov[3], Stoyan N. Jilov[4]

Abstract – **In the paper problems of diagnostic functions embedding in industrial control systems have been discussed. The idea for co-operation between control functions and functions related with loading, diagnostics and adjustment of the software in a single communication channel has been developed. The realization of this idea requires some conditions to be determined. In respect on these particular conditions, the rules for industrial networks building with embedded diagnostic functions are defined. Possibilities for existing conflict situations have been analyzed. The variants for their overcoming are offered.**

Keywords – **Industrial control system, Programmable Logical Controller, communication channel, debugger, networking.**

I. INTRODUCTION

One of the main features of Programmable Logical Controllers (PLC) or Industrial Controllers is a capability of networking. Usually each PLC is provided with a primary local area network trough which it is able to exchange information with controllers of the same rang and with the central computer [1].

However, in many applications, it is necessary to support secondary communication channel, which is used for diagnostic purposes. The main diagnostic function is software adjustment and diagnostics. Usually the secondary communication channel is different kind from the primary. More over, different channels may support different physical and logical levels.

The family controllers SIMATIC of SIEMENS is an example for PLCs with divided diagnostic and control functions (fig.1). Functions of loading and adjustment of the software are accomplished by Multi Point Interface (MPI). This interface is specially developed for connection between PLC and programmable station and may serve up to 126 correspondents. Control functions are accomplished by another interfaces: ProfiBus, Industrial Ethernet and AS-Interface. Usually these interfaces are built as additional modules [2].

MODICOM controllers produced by Telemechanique use similar strategy. These controllers are provided by an embedded primary interface, which is used for loading and adjusting of the software. However, this interface is Point- to-Point kind and does not have a capability of networking. Modbus interface is used for control functions between the same type of controllers.

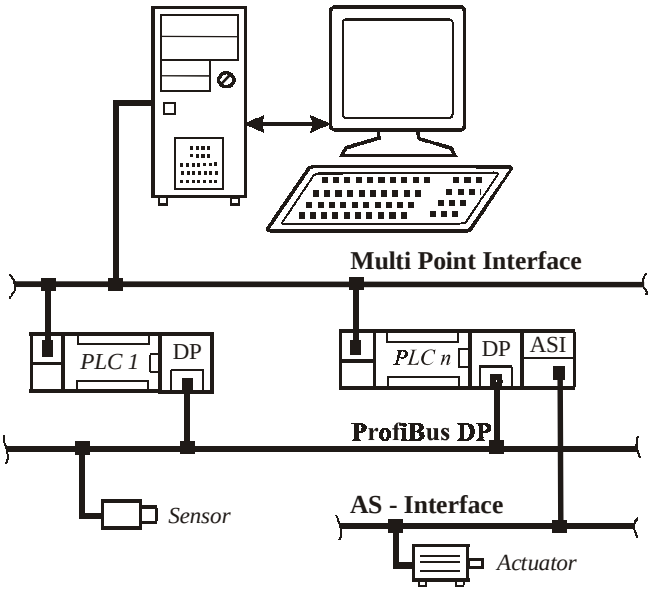

Fig.1 Communication options via the integrated interfaces of the SIMATIC

In the present paper, a solution is applied where the primary and the secondary communication channels are united in just one common channel. This solution allows controllers, having only one communication port, to use the control information network for loading, adjusting and diagnosing of the software. For this purpose, the functions for loading of the operation system and for loading, adjusting and diagnosing of the software have to be realized via the common channel, using common communication environment for different protocols.

II CONTROL INFORMATION SYSTEM

Functionally, the control information system may be divided into two main parts. The first part is the control part and it consists of a personal computer. The personal computer may combine the functions of an operation station and of a diagnostics station as well. According to those purposes, the

[1]Stanimir D. Mollov is with the Faculty of Electronic Engineering, and Technologies, TU – Sofia, 1797, Sofia, Bulgaria, E-mail: smollov@abv.bg

[2]Georgy Sl. Mihov is with the Faculty of Electronic Engineering, and Technologies, TU – Sofia, 1797, Sofia, Bulgaria, E-mail: gsm@tu-sofia.bg

[3]Ratcho M. Ivanov is with the Faculty of Electronic Engineering, and Technologies, TU – Sofia, 1797, Sofia, Bulgaria, E-mail: rmi@tu-sofia.bg

[4]Stoyan N. Jilov is with the SPV Ltd. Rakovsky 135, 6000, St. Zagora, Bulgaria, E-mail: spv@abv.bg

personal computer is mainly characterized with a powerful processing unit, and with embedded interfaces RS232 and USB. Thanks of the powerful processing unit of the computer, the main part of the network's protocol have to be realized in the computer environment. At the same time, a suitable hardware module has to be used to connect the embedded interfaces to the industrial interface.

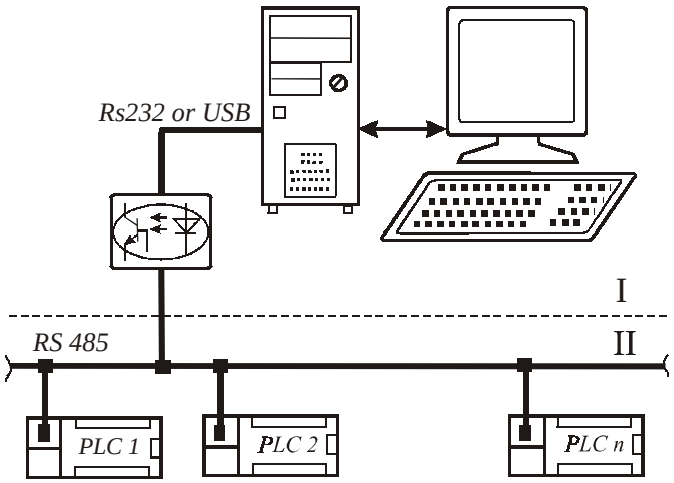

Fig. 2. Control information system

The secondary part of the control information system is a group of slave modules. The group includes intelligent sensors, PLCs and intelligent actuators. They are characterized by low power processing units. In most cases they are provided an embedded serial communication interface (SCI). This interface allows the network's protocol to be built easier and the connection to the industrial network to be realized directly via a suitable hardware adapter.

For the presented control information system is applied so called centralized management. This management is characterized with a request sending from the master station to the some slave station. By this way, the task of the slave module is to identify the request from the master station and to replay at a fixed time interval. The master station, considering the specified necessity defines the order of requests.

A. Hardware realization of a communication environment

The communication of the presented control information system is based on a serial communication interface, which is embedded in most controllers. To achieve maximum noise immunity it is necessary to use a differential transmission and a galvanic isolation. In the present case, the physical standard RS485 is used for a communication between correspondents. The using of a half duplex line requires an additional control signal for the data direction exchange.

B. Software realization of a communication environment

Due to the high noise level in the communication environment, it is necessary the transferred data to be blocked in comparatively short packets. Single data packet of the local area network has the following structure (fig. 3):

1. *SOH* – 'start of header' (1 byte). This is the leading symbol, which indicates the start of the data block transmission. There are two types of leading symbols: *SOH1* (start of message transmission) and *SOH2* (start of data block transmission). The first symbol is located at the start of the message. The second one is located at the beginning of the second and the following blocks of the multi-block message.
2. *RCV* (1 byte). It indicates the address of the message receiver (destination address).
3. *TRN* (1 byte). It indicates the address of the message transmitter (source address).
4. *COL* (1 byte). It may have value 0 or 0xFF, which is alternatively changed each other in the multi-block message transmission.
5. *LENGTH* (1 byte). It indicates the block length, e.g. the number of bytes in the informative part.
6. *DATA*. This is an informative part and can be sized from 0 to 255 (0xFF).
7. *CKSUM* (1 byte for a check sum). It is the least byte of the sum of all transmitted bytes, from *SOH* to end of *DATA*. It is used to check the block receive accuracy.
8. *EOT* (1 symbol 'end of transmission'). It indicates the end of the data block transmission. There are two types of end symbols: *EOT1* (end of message transmission) and *EOT2* (end of data block transmission). The first symbol is located at the end of the last block of the message. The second one is located at the end of the first and following blocks (except the last block) of multi-block message.

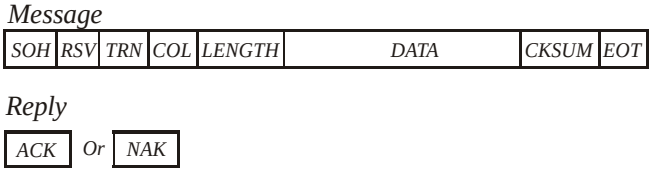

Fig. 3 Transmitting a single data packet

After the transmitter sends the message, the receiver sends back a positive or negative acknowledges (fig.4). Positive acknowledge (ACK) means that the transmission had finished successfully and the calculated checksum equals to the received checksum. Negative acknowledge (NAK) means that the transmitter have to resend this message, because an error occurs. All actions in the local area network have own protected times. If the transmitting station had not received the acknowledgment at a fixed time interval, it repeats the transmission of the current data block. If the acknowledgment from the receiving station was positive, but it had not received, due to the noises in the network, the transmitting station have to repeat the same message. By the value of the *COL* field of the message the receiving station understands that the transmitting sequence is destroyed. The sending a *BREAK* signal causes the transmission interruption. All users, including the sender recognize the *BREAK* signal like an error in the format of the transmission data. After that, all users are listening to the line continuously and start transmitting a message only when the line is not busy. The time for one symbol's transmission is limited. The users of the network

will know, that the line is busy after the time of a one symbol's transmission.

A conflict situation is possible to appear when more than one station from local area network start transmission at the same time. Each sender listens to the line (receives its own transmission) and compares the sent and the received information. In case of a difference (someone transmits over the line too) the sender interrupts the transmission and sends a *BREAK* signal to inform the others users for the conflict situation. After that each user continues to receive, but does not start transmission before a certain time, that depends on user's address in the network. By this way the conflict situations in the local area network are solved.

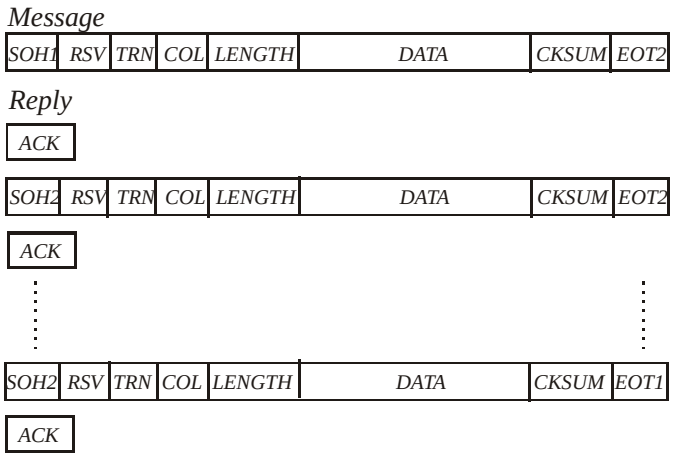

Fig. 4 Multi-block message transmission

III. Program Environment for Adjustment and Diagnostics

One of the main software tools for developing, adjustment and diagnostics of the micro processing systems is so called Debugger. The debugger's quality depends on used system resources. The main functions of the debugger are: program loading and executing, including break points, executing a single instruction, disassembling, reading and modification memory and registers.

One part of debugger functions is related with the specific of the central processing unit. The specification depends on the number, the kind and the structure of central processing unit registers as well as on the addressing mechanism.

Another part of debugger functions is related with the specific hardware realization of the controller. There are functions, which provide an access to the hardware resources. Most important of them are: inputs reading, writing and modification of controller's outputs, access to keyboard, indication, etc.

The adjustment and the diagnostics may be accomplished either by the control panel or by the terminal station via communication environment. Due to the limited information, which could be shown on the control panel, its application is limited. The terminal station, used for adjustment and diagnostics is built on a personal computer, as a rule. Using appropriate software, it can provide a full control over the slave controllers and also it is able to execute full or particular changes of the controller's applied program and parameters.

IV. Diagnostic Functions of the Information System Based on SPV-4xx Industrial Controllers

The main idea, developed in the building of an industrial network with SPV-4xx, is that all operations, related with control, adjustment and diagnostics, to be performed in the same network. The realizing of the idea requires:

– the control program and the debugger to be switched;

– the control program and the debugger to work independently.

To perform these conditions, it is necessary the debugger to be provided with own network driver and to does not use the network driver of the control program.

The industrial controller SPV 4xx is built on microcontroller MC68HC11. For the 'first time' loading the controller is set in Bootstrap mode. In this mode a small Boot program is enabled, which is located in its internal ROM memory. After the microcontroller is run, this program initializes the serial communication port, receives a program up to 256 bytes throw which and writes them in the internal RAM. The manufacture requirements, defined for bootstrap mode, must be strongly kept. They include data format and transmission speed. The bootstrap loading uses binary format. After each received byte, the microcontroller sends an acknowledgment. These special futures must be taken into account when the special software for the programmable station is developed.

After the bootstrap loading, the program in the internal RAM is started. This program has to provide the followed possibilities:

– the SCI interface to be initialized, if it is necessary;

– the execution operation cod of the debugger to be received via the network and to be loaded into the FLASH memory of the microprocessor system.

Including diagnostic functions in the network requires keeping exact rules, e.g. so called 'discipline of work'. These rules determine the conception: each correspondent in network has to have an own name. The main station has the name 'A'. The control information part of the information system is organized between controllers used capital letters from D to Y as a name. The controller, which enters into diagnostic functions, is identified as a controller with name 'C'. Such controller cannot perform control and information functions at the same time. The name 'Z' is reserved for future applications, like a calibration function controller.

In this paper the diagnostic functions are minded as an adjustment and a diagnostics of the applied software. If the diagnostic functions have to be performed at same time when the user program is run, they should be embedded in it.

The debugger commands are different from commands of the control information program. The main station may run them but it is not desirable. Especially for diagnostics function using, a new station is included in the network. It is called 'service station' and has got the name 'B' (fig. 5). Run in the

diagnostic mode controller responds to the one, which asks him. From security point of view, just one controller in the network is allowed running in the diagnostic mode.

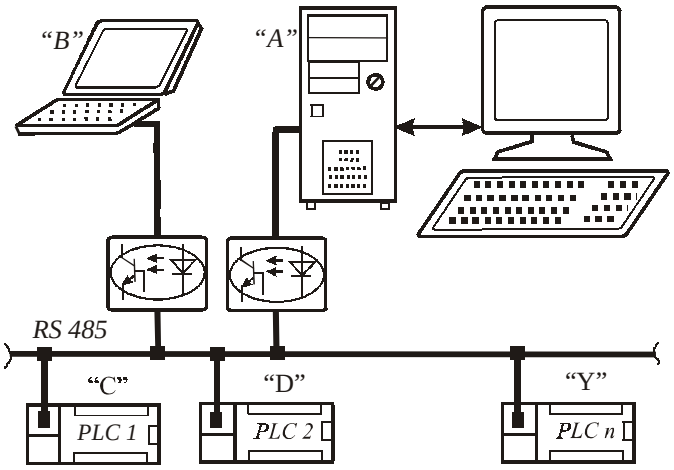

Fig. 5 Conception for correspondents naming

A proper mechanism for switching between the debugger and the applied program is built. The hardware realization of this mechanism consists of the program memory division in two banks (fig. 6). These banks are located in the same area of the addresses. The user program is loaded is loaded in the first bank, while the debugger is loaded in the second one. The switching between the banks is provided by a special command in the network protocol. By this way, the simultaneous running of the debugger and the applied program is excluded.

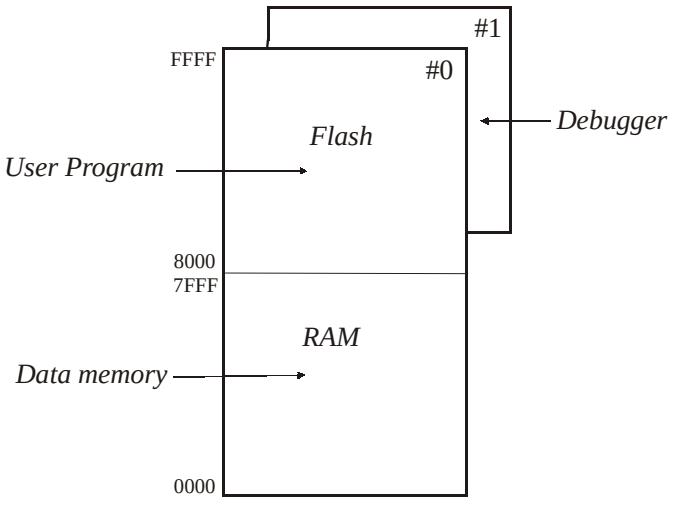

Fig. 6 Address memory map

The bootstrap loading of some controller may provoke a conflict situation if it is done using the network, at the same time, when the network is used by another controller for an normal (control and information) work. It may occur when some controller, loaded in advance, is laid and caught the information for the bootstrap loading as a valid for it. There are some ways to avoid this conflict situation:

1. The information for original loading is analyzed and checked for a stream of symbols sequence, which is the same as the sequence *SOH* and *RCV* (fig. 3). If there is such sequence, it must be avoided. Mostly, it is done including an empty operation cod between these symbols.

2. If it is not possible to include an empty operation cod in the program of the bootstrap operation code, it is necessary to exclude the controller and to do the bootstrap loading out the network.

Another way to avoid generally conflict situations is the bootstrap loading to be controlled by additional device (mediator). Ordinary it is also a microcontroller, which listens the network information. If the mediator detects the command for the bootstrap loading, it disconnects the controller from the network, gets the bootstrap information and translates it to the controller's processor. In this case, the bootstrap information has to be formatted according the network protocol.

V. CONCLUSIONS

In the paper the idea for co-operation between the operations related with loading, adjustment and diagnostics software in common communication channel is developed. The necessary conditions for its realization are discussed. As a result, a conclusion that the control program and debugger must have their own network protocol is done.

Including the diagnostic functions in the industrial network requires specific rules to be kept. They bring a conception for the naming of controllers. In additional, a protected mechanism, which does not allow the debugger and the control program to be run simultaneous, is created.

It the present paper the possibility for conflict situations are discussed. The variants for their solving are offered.

REFERENCES

[1] Mihov, G., E. Dimitrov, S. Jilov, A. Kostadinov. Composing of Different Local Area Networks for Industrial Controllers on Common Physical Layer. XXXVII International Scientific Conference on Information, Communication and Energy Systems and Technologies ICEST '2002. vol. 2 pp. 406-409, October 1-4, 2002, Niš, Yugoslavia.

[2] SIMATIC Programmable Controller System Manual, SIEMENS Berlin, Siemens Aktiengesellschaft 1999, C79000-G7076-C230-02

[3] Mihov G., I. Tashev. Industrial Controller For Discrete Manufacture National Scientific Conference "Electronics '96", book I, 31-36, Sozopol, Bulgaria, September, 1996.

[4] Dimitrov E., G. Mihov, I. Tashev, M. Mitev. Local Area Network for Industrial Controller. The International Scientific Conference ENERGY AND INFORMATION SYSTEMS AND TECHNOLOGIES. vol. III, pp. 608-613. Bitola, Macedonia, June 7-8, 2001.

[5] http://www.schneiderelectric.com/

MOSFET Bridge Switch Converter for Pulse Reverse Plating

Mincho Ph. Peev[1], Anastassia P. Krusteva[2], Milko G. Yordanov[3]

***Abstract*: In the present work it is presented the block-structural diagram of a bridge switch converter of pulse reverse current for electroplating, which is built on the basis of MOSFET transistors. The output pulse frequency is regulated within the range of 1 Hz to 50 kHz. The regulation range of the output voltage is within 2 V to 12 V for the maximal value of the output current equal to 15 A. A simulation model of the MOSFET switch converter in MicroSim DesignLab software environment is developed by taking into account the equivalent circuit of the electroplating bath. A maximal value of the shearing strength of a nickel coating electroplated at current frequency 500 Hz is obtained experimentally. The converter developed enables the performance of investigations with the purpose of obtaining electroplated coatings with improved properties.**

***Keywords* – Pulse Reverse Plating, Electrodeposition, MOSFET Pulse Generator.**

I. INTRODUCTION

Today's level of development in the fields of electronics, instrument production and machine-tool industry is closely connected with the achievements in the area of electroplated coatings. Many processes of metallization through deposition of pure metals and alloys are being constantly improved with the purpose of obtaining increasingly better coating parameters (electric conductivity, magnetic properties, equalizing ability, porosity, internal voltages, hardness, wear resistance). In known literature references [1-4] the authors discuss problems related to potentials of exerting influence and improving the physico-chemical parameters of electroplated coatings by applying pulsed power supply. Its broadest application is connected with the use of rectangular pulses [1-4], where it is sought to optimize the electrodeposition regime by varying: - the pulse frequency; - the duration of forward and reverse pulses; - the pulsed value of the current.

[1]Mincho Ph. Peev is with the Technical University of Sofia, Faculty of Engineering and Pedagogy of Sliven, 59 Bourgasko Shaussee Str., 8800 Sliven, Bulgaria, e-mail: mfpeev@abv.bg,

[2]Anastassia P. Krusteva is wit the Technical Uneversity of Sofia, Department of Power Electronics, 8 Kliment Ohridski Blvd., 1000 Sofia, Bulgaria e-mail: krusteva@tu-sofia.bg.

[3]Milko G. Yordanov is with the Technical University of Sofia, Faculty of Engineering and Pedagogy of Sliven, 59 Bourgasko Shaussee Str., 8800 Sliven, Bulgaria, e-mail: myordanov@abv.bg.

II. ANALYSIS OF THE TECHNOLOGICAL REQUIREMENTS

In electroplating metal coatings in a d.c. regime the process is controlled through the magnitude of the current (within close limits) as well as through the concentration of surface-active substances in the electrolyte. Applying unipolar current pulses (Fig. 1) enables the simultaneous regulation of three independent parameters [5]: pulsed current density j_p, pulse duration t_{ON}, and pause duration t_{OFF}. This conditions the following features of the process of electroplating:

- using of a high instantaneous current density, which permits to attain a high degree of cathode polarization. The high value of overpotential at the cathode is the cause for a change in the speed of electrochemical reactions with different kinetics. This is one of the reasons that the current effectiveness in pulsed metallization may be rather different from that performed with direct current. The high value of overpotential influences to a great extent the rate of forming new metal nuclei, an along with this it leads to coating structure of finer grain size.
- during the pause there occur phenomena of adsorption and desorption, as well as a re-crystallization of the metal deposited.

The average value of current density j_m in pulsed regime is equal to the current density in d.c. regime [5].

A positive effect on coating properties in pulse reverse regime of electroplating (Fig. 2) is exercised by the electrochemical processes during the anode (reverse) period t_{REV} of the current, which is expressed in prevailing dissolution of the coating microprotrusions and ionization of hydrogen atoms adsorbed in the coating.

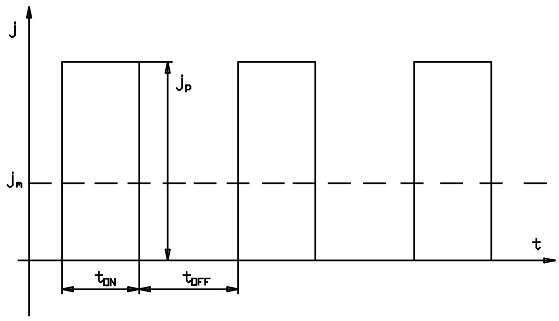

Fig. 1

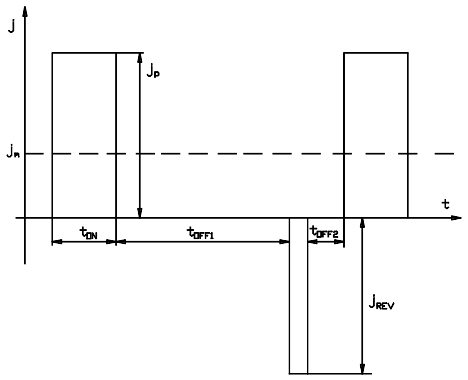

Fig. 2

The performed analysis of the technological requirements permits to synthesize the circuit of a power supply source for pulse reverse plating with the potential of regulating within broad limits the output parameters: - the pulsed value of the current; - the pulse frequency; - independent regulation for the whole frequency range of the duration of forward and reverse pulses; - the duration of the pause between forward and reverse pulses.

III. BRIDGE CONVERTER FOR PULSE REVERSE PLATING

The block-structural diagram of the produced power supply source of pulse reverse current for the deposition of electroplated coatings, realized with MOSFET transistors of BUZ10 type, is shown in Fig. 3. The output voltage of the

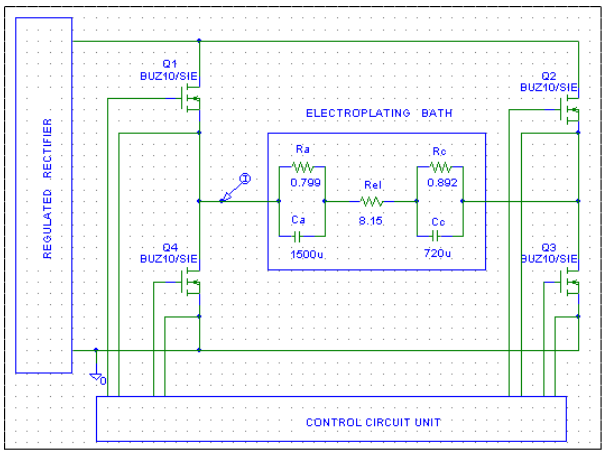

Fig. 3

power source is regulated from 2 V to 12 V. This is specified in the requirements for the realization of electrochemical processes in the electroplated deposition of metal coatings [6]. The output current is determined by the current density during the process and by the working area of the cathode:

$$i = j_F \cdot S_c \text{, A} \qquad (1)$$

where: j_F is the density of Faraday current, A.dm^{-2};

S_c – the cathode area, dm^2.

A maximal value of 15 A for the output current is assumed for the purposes of laboratory investigations.

The circuit includes regulated stabilized rectifier. By using it the supply voltage can be reduced to the necessary value, transformed into direct voltage, and stabilized with the possibility of regulation from 2 V to 12 V.

The stabilized voltage obtained in this manner is transformed into pulsed voltage by means of the bridge switch converter built-up with MOSFET transistors Q1 – Q4 (Fig. 3), and fed to the electroplating bath. Turning-on transistors Q1 and Q3 leads to obtaining the positive current pulse. Transistors Q2 and Q4 provide the reverse current pulse.

Controlling the MOSFET bridge switch converter is carried out by the *control circuit* unit. This unit is used for setting the parameters of output current pulses:

- frequency f – it can be regulated from 1 Hz to 20 kHz;
- duration of the forward pulse t_{ON} – it can be regulated from 0.01 to 0.9 of the duration of the pulse period τ ($\tau = \frac{1}{f}$);
- duration of the reverse pulse t_{REV} – it can be regulated from 0.01 to 0.5 of the period τ;
- duration of pauses t_{OFF1} and t_{OFF2} – they can be regulated within the range from 0.01 to 0.99 of the value of τ.

In such a way it is possible to regulate within broad limits the technological parameters in the deposition of electroplated coatings. It should be kept in mind that in metal deposition the duration of the forward pulse must be greater than that of the reverse one.

In Fig. 3 the electroplating bath is represented by its equivalent RC-circuit [7, 8]. Resistors R_a and R_c correspond to the resistances of the electrode surfaces (anode and cathode, respectively) in the transfer of electric charges between the respective electrode and the electrolyte. C_a and C_c are capacitors determined by the capacitance of the double electric layer at the "electrode–electrolyte" boundary for the anode and cathode. R_{el} is the ohmic resistance of the electrolyte**.**

The analysis, presented in [7], concerning the charging and discharging of the double electric layer in pulsed electrolysis is used for determining R_a, R_c, C_a, and C_c. The resistance of the electrode surface during transfer of electric charges, determined per unit area, is assumed not to depend on the value of the current flowing through it. It is obtained in accordance with the expression [7]:

$$R = \frac{d\eta}{dj_F} \text{, } \Omega.\text{dm}^2 \qquad (2)$$

where: η is the overpotential of the electrode, V;

Determining the electrode overpotential may be performed according to the expression [9]:

$$\eta = a + b \cdot \ln j \qquad (3)$$

where: a and b are constants depending on the character of the reactions, the material of the electrode, and the electrolyte;

j - density of the current flowing through the electrode, A.dm^{-2}.

The capacitance of the double electric layer per unit area of the electrode varies from 10 to 100 μF.cm^{-2} [7]. For rough

nickel surface it is determined as 80 μF.cm^{-2} (the real area of the electrode may be 2 to 3 times greater than the geometrical one if the surface roughness is taken into consideration).

IV. EXPERIMENTAL AND SIMULATION INVESTIGATIONS

The presented MOSFET bridge switch converter is used for depositing an electroplated nickel coating with thickness of 10 μm. Specimens are produced at various pulse frequencies within the range from 100 Hz to 20 kHz. The filling factor of the forward pulse is 0.4. The duration of the reverse pulse is $t_{REV} = 0.25\ t_{ON}$.

Sulphate electrolyte of the following composition is used: nickel sulphate ($NiSO_4.7H_2O$) – 145 g/l; sodium sulphate ($Na_2SO_4.10H_2O$) – 45 g/l; boric acid (H_3BO_3); sodium chloride (NaCl) – 7 g/l. During the process the temperature of the electrolyte is maintained at 25 °C (298 K) and the value of pH at 5.5. The recommended range of the current density in d.c. regime is from 0.8 to 2.0 A.dm^{-2}.

The conditions for coating deposition are as follows:

- pulsed value of current density: $j_p = 3.6$ A.dm^{-2};
- the density of Faraday current is equal to the pulsed current density in the circuit: $j_F = j_p$;
- area of the cathode: $S_c = 0.24$ dm^{-2};
- area of the anode: $S_a = 0.50$ dm^{-2};
- distance between anode and cathode = 3 dm;
- electrolyte volume = 6 dm^3.

A. Electric parameters and time diagrams

A simulation model of the MOSFET bridge switch converter of Fig. 3 is created in MicroSim DesignLab software environment.

Realizing the model requires the calculation of elements in the equivalent circuit of the electroplating bath.

For the capacitance of the double electric layer, per unit area of the electrode, it is assumed the value [7] $C_{Ni} = 3000$ μF.dm^{-2} (it is operated with a cathode of smooth surface). The values of capacitors C_c and C_a from the equivalent electric circuit of the electroplating bath are determined as follows:

$$C_c = S_c \cdot C_{Ni} = 720\ \mu\text{F};$$

$$C_a = S_a \cdot C_{Ni} = 1500\ \mu\text{F}.$$

The overpotential at the cathode (η_c) and anode (η_a) is determined in accordance with equation (3), the constants a and b in electroplating deposition of nickel being [9] a = 0.63, and b = 0.11:

$$\eta_c = a + b \cdot \ln j_p = 0.771\ \text{, V};$$

$$\eta_a = a + b \cdot \ln j_a = 0.690\ \text{, V},$$

where: j_a is the anodic current density.

The current in the circuit and the anodic current density are calculated:

$$i = j_F \cdot S_c = j_p \cdot S_c = 0.864\ \text{, A};$$

$$j_a = \frac{i}{S_a} = 1.728\ \text{, A.dm}^{-2}.$$

The values of resistors R_a and R_c are obtained from the equivalent circuit of the electroplating bath in accordance with equation (2):

$$R_c = \frac{\eta_c}{j_F \cdot S_c} = 0.892\ \ \Omega;$$

$$R_a = \frac{\eta_{ac}}{j_a \cdot S_a} = 0.799\ \ \Omega.$$

The electrolyte resistance is determined from the experimental investigations as: $R_{el} = 8.15\ \Omega$.

Time diagrams of the voltage and current at the output of the bridge switch converter, plotted from the simulation model at pulse frequency of 100 Hz, are shown in Fig. 4.

Figs. 5 and 6 represent oscillograms from experimental investigations of the current and voltage at pulse frequency of 100 Hz.

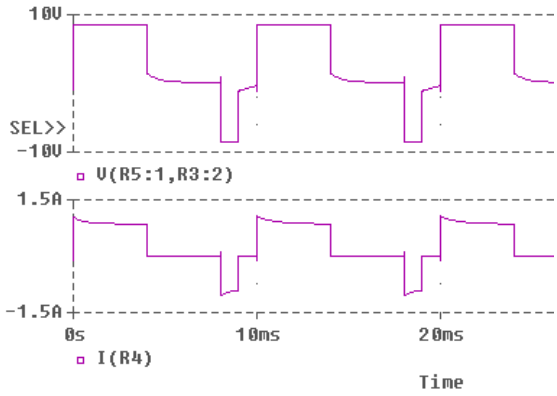

Fig.4

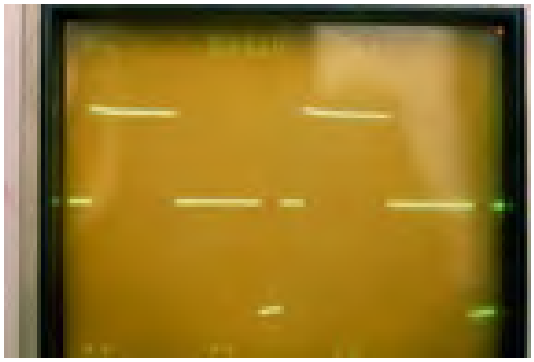

Fig. 5

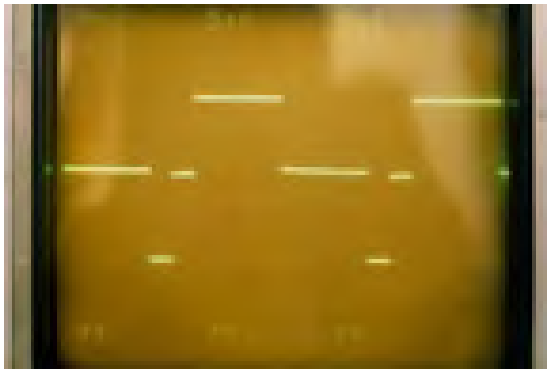

Fig. 6

B. Mechanical properties of the coating deposited depending on the frequency

The influence of pulse frequency upon the shearing strength of an electroplated nickel layer is determined.

Shearing strength σ_{sh} can be obtained from tension strength Rm in accordance with the relationship [10]:

$$\sigma_{sh} = 0.6 \times Rm \text{ , MPa} \quad (4)$$

The tension strength can be determined through the measured Rockwell hardness (HRC) in accordance with the relationship [11]:

$$Rm = 325 + 207 \times e^{0.0377 \cdot HRC} \text{ , Mpa} \quad (5)$$

The hardness is measured by means of a FISCHERSCOPE H100 nanotester (made in Germany) by the method of Vickers at a load of 100 mN.

Upon performing the measurement, Vickers hardness (HV) values obtained are re-calculated in hardness according to Rockwell's method [12]. Results are shown in Table 1.

TABLE I

f	logf	HRC	Rm	σ_{cp}
Hz	-	-	MPa	MPa
100	2,0	39,00	1225,6	735,3
200	2,3	39,25	1234,1	740,4
500	2,7	46,00	1497,5	898,5
1000	3,0	41,50	1314,6	788,7
10000	4,0	39,00	1225,6	735,3
20000	4,3	39,50	1242,7	745,6

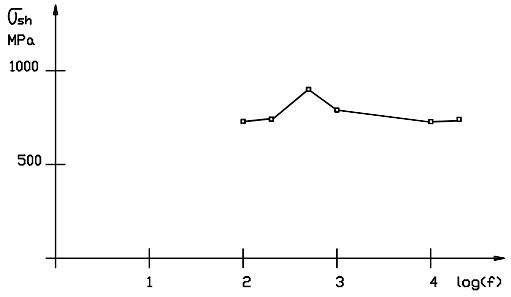

Fig. 7

The diagram of shearing strength variation for a nickel layer, deposited by electroplating, with the pulse frequency during coating deposition is shown in Fig. 7.

V. CONCLUSIONS

The experimental power source for pulse reverse deposition of electroplated coatings, developed on the basis of MOSFET transistors, provides output voltage regulation within the range from 2 V to 12 V at maximal value of the current in forward and reverse direction equal to 15 A. The pulse frequency is regulated within the range from 1 Hz to 50 kHz. Durations of the forward and reverse pulses as well as that of pauses between pulses are regulated independently all over the frequency regulation range.

A simulation model of the MOSFET switch converter in MicroSim DesignLab software environment is developed by taking into account the equivalent circuit of the electroplating bath.

The method of combined analysis presented, simultaneously taking into consideration the circuit components and load parameters, may be useful for the engineering practice.

The mechanical parameter of shearing strength of the nickel coatings deposited by electroplating is studied in the frequency variation range from 100 Hz to 20 kHz. A maximal value of the shearing strength of the nickel layer deposited at current frequency 500 Hz is found.

The power supply source developed allows the performance of experimental investigations with the purpose of obtaining electroplated coatings with improved properties

VI. REFERENCES

[1] A. Marlot, D. Londold, "Pulse Plating of Ni-Mo Alloys from a Citrate Bath", 5th International Pulse Plating Symposium, Chicago, June 2000.

[2] M. Aroyo, N. Tzonev, "Pulse Periodic Reverse Plating – New Possibilities for Electrodeposition of Metal Coatings with Improved Properties: Part 1", Plating & Surface Finishing, July 2002, pp. 48-53.

[3] S. Frant, A. Marlot, D. Londolt, "Pulse Plating of Ni-W Alloys", The Electrochemical Society, Inc., 204 Meeting, 2003.

[4] Shan Guan, Bradley J.Nelson, "Residual Stress and Magnetic Properties of Pulse – Reverse Electrodeposited High Aspect Ratio CoNiP Micro Array Magnets", The Electrochemical Society, Inc., 204 Meeting, 2003.

[5] N. Ibl, "Some Theoretical Aspects of Pulse Electrolysis", Surface Technology, 10 (1980), pp. 81-104.

[6] Conrad Harry, R. Krampitz, "Electrotechnologie", Berlin, 1983 (in German).

[7] J. Cj. Puippe, N. Ibl, "Influence of Charge and Discharge of Electric Double Layer in Pulse Plating", Journal of Applied Electrochemistry, 10 (1980), pp. 775-7784.

[8] Ernest Yeager, Alvin J. Salkind, "Techniques of Electrochemistry, Volume 1", Cleveland, Ohio, 1972.

[9] Hristo Petrov, S. Yordanova, "Chemistry", Sofia, 1990 (in Bulgarian).

[10] I. Kisyov, "Tables in Strength of Materials", Tekhnika, Sofia, 1977 (in Bulgarian).

[11] K. Kostov at al., "Choice of Materials and Strength Dimensioning in Machine-Tools Design", Tekhnika, Sofia, 1988 (in Bulgarian).

[12] Yu. Sedov, A. Adaskin, "Handbook of the Young Heat-Treatment Specialist", Vissha Shkola, Moscow, 1986 (in Russian).

[13] Elena Shoykova, S. Tsanova, D. Kolev, I. Pandiev, "Methodology of Designing Electronic Circuits with PSpice", Sofia, 2000 (in Bulgarian).

Galvanomagnetic Current-Frequency Converter

Anatoliy Aleksandrov

Abstract **– A current-frequency converter has been synthesized on the basis of experimental specimens of a digital magneto-sensitive IC, its sensitive element being a two-collector magneto-transistor. Experimental investigations have been carried out of the conversion characteristic, as well as of the factors affecting it. Different versions have been developed for temperature stabilization of the converter.**

Keywords – magnetic-field galvanomagnetic sensor, magneto-sensitive IC, current-frequency converter.

I. INTRODUCTIO*N*

Current-frequency converters are applied in the field of electrical engineering, instrumentation, in intelligent sensor mocrisysytems, robotics, automatics and instrument engineering as sensor devices with high sensitivity. There exists a magnetosensitive integrated sensor with a frequency output [3] for converting magnetic induction into a frequency signal, as well as a device for energy reading on the basis of a Hall element, the output signal being modulated by means of a multivibrator [7]. These converters have been developed using galvanomagnetic discrete components.

The magnetosensitive ICs are the latest and the most promising magnetic sensor. They incorporate a magnetosensitive element and an electronic circuit for signal processing, which are accomplished in one technological cycle [4, 2], and achieve multisensor properties as well [5]. Their main advantages are: low cost, high noise immunity, reduced dimensions, complete electrical disconnection between the input and the output circuits.

The present paper describes a new galvanomagnetic current-frequency converter on the basisi of a digital magneto-sensitive IC.

II. CURRENT-FREQUENCY CONVERTER:

A current-frequency converter has been developed for the realization of the new device, on the basis of experimental specimens of a digital magnetosensitive IC of the type CM 701 AM 5.1 [6], its sensitive element being a two-collector magneto-transisitor.

Anatoliy T. Aleksandrov. Department of Electronics, Technical University – Gabrovo, Street “Hadji Dimiter” No. 4, 5300 Gabrovo, Bulgaria, phone: +359 66 801064, e-mail: alex@tugab.bg.

The schematic electric circuit of the converter, realized with an electronic switch of a bipolar transistor connected in the common emiter circuit, is presensted in Fig. 1.

When the supply voltage of the IC is switched on its output in logical ”1” state, and the bipolar transisitor VT passes into a saturation mode. Current I begins to flow through the coil of the electromagnet W. When the magnetic induction in the magnetic circuit reaches the magnetic induction of switching on $B=B_{ON}$ the output of the magnetosensitive IC switches to the state of logical ”0”. The transisitor is turned off. The current and the magnetic induction, respectively, decrease, and when $B=B_{OFF}$, the output of the magnetosensitive IC switches again to the state of logical ”1”and the processes are repeated. A saturated operating mode of the transisitor switch must be ensured for stable operation of the generator circuit. Square pulses are generated at the IC output, having a certain pulse-repetition rate, which depends on the magnitude of the current I and the number of the windings W, i.e. $f=\varphi(I,W)$. The transisitor switch functions as a positive feedback in the square pulse generator.

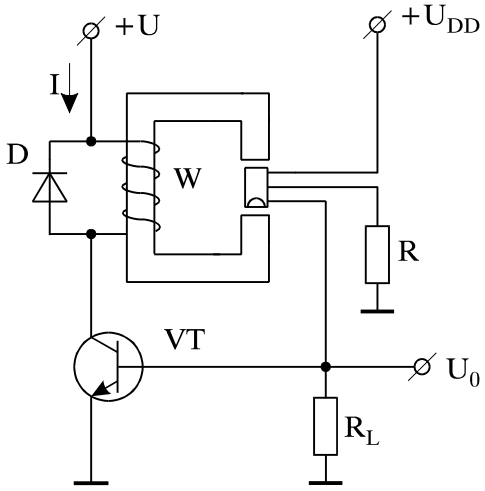

Fig. 1. Schematic Electrical Circuit of the Current-Frequency Converter

Experimental investigations have been carried out to determine the influence of I and W over the converter frequency f, an electromagnetic system being used for that purpose, having the following parameters: $\mu=400$; $\delta=10$mm; $S=1600$mm^2.These parameters have been chosen for design reasons, and they guarantee a linear and uniform magnetic field. The range of the conversion characteristic is determined by the condition that the transisitor switch should be saturated and the induction in the magnetic circuit should be greated than the magnetic induction of switching on B_{ON} of the magneto-sensitive IC.

Figure 2 presents the family of conversion characteristics $f=\varphi(I)$ taken experimentally when W=const.

In order to determine the analytical form of the dependence $f = c.I^n$ of the frequency f on the magnitude of the converted

current I when W=const, the least-squares method has been applied [1].

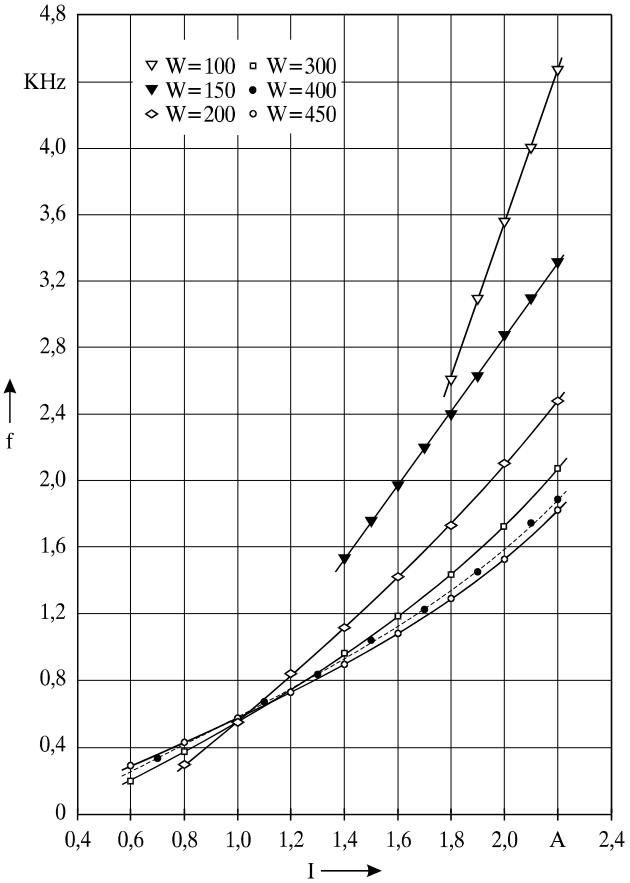

Fig. 2. Conversion Characteristic f=φ(I) when W=const.

The form of the theoretical-experimental models obtained is:

$$f = 0{,}5389.I^{2{,}016}$$ when W=200 windings;

$$f = 0{,}6018.I^{1{,}3899}$$ when W=450 windings.

The analysis of the graphical and empirical dependences obtained shows that when W=const the frequency f is a function of the current flowing, the increase in current causing an increase in frequency. The nature of this change in f in accordance with the change in current corresponds to the converter operating principle. When the number of widings is great the conversion characteristics is non-linear. When the number of widings decreases the converter switching on current increases, and the conversion characteristics become linear. With greater current the magnetization is carried out along a curved line having a steeper slope, the result of this being that the period of output-pulse repetition decreases, and the output frequency f increases. Therefore, the steepness of the conversion characteristic depends on the number of windings in the electromagnetic. In this particular converter optimum steepness from the point of view of the sensitivity parameter is observed when W=100 windings. On the basis of the characteristics taken experimentally (Figure 2) the following parameters have been determined for the current-frequency converter discussed here: measuring range-(1,8÷2,2)A; differential sensitivity S=3790 Hz/A; relative sensitivity S_{00}=2,37.

The conversion characteristics are non-linear when the number of windings is greater (W > 150). In order to realize a measurement convertor it is necessary to linearize the function f=φ(I,W) or to choose a characteristic range with sufficient linearity. The coversion characteristic is linear in a measurement range (0,8÷2,1)A when W=200 windings. The following parameters are determined for this case: differential sensitivity S=1446 Hz/A; relative sensitivity S_{00}=1,7965.

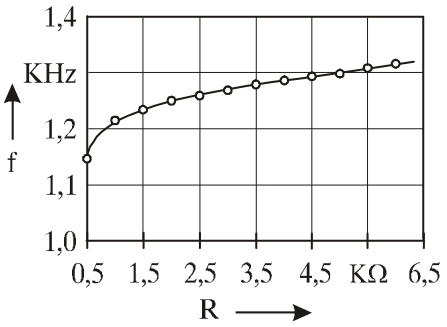

Fig. 3. Influence of R over frequency

In order to achieve a complex and plausible assessment for operation of the current-frequency converter it is necessary to investigate not only the influence of the number of windings W and the current I, but also the effect of the voltage U_{DD} and the resistance R over the frequency f of the current-frequency converter. The experimental dependences obtained f=φ(R) when U_{DD}=12V and f=φ(U_{DD}) when I=1,5A, W=250, R=4,7kΩ and R_L=10kΩ are presented in Fig. 3 and 4, respectively. When R increases the frequency f increases, too, the extent of change in f being greater with smaller values of R=(0,5÷2,5)kΩ. The frequency f decreases with the increase in the supply voltage.

Fig. 4. Influence of U_{DD} over frequency

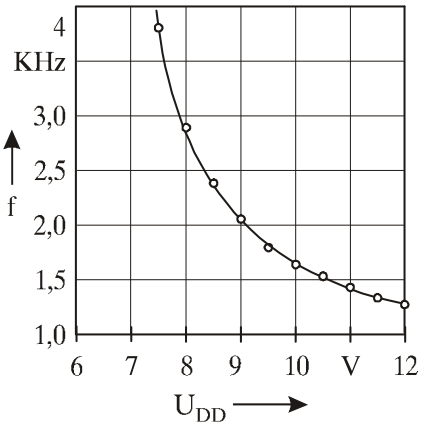

Temperature investigations of the current-frequency converter have also been carried out. The characteristic f=φ(T) obtained experimentally is shown in figure 5 (curve 1). The rise in temperature from 25 to 65 °C causes a decrease in frequency by 9%. Therefore temperature stabilization must be carried out for the converter discussed.

The nature of the change in the frequency f according to the resisitance and the supply voltage f=φ(R) (Figure 3) and

$f=\varphi(U_{DD})$ (figure 4) shows that these dependences can be used for temperature stabilization.

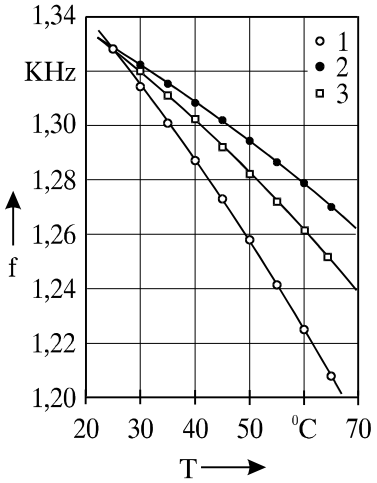

Fig. 5. Influence of Themperature over Frequency

Two circuits for temperature stabilization of the converter have been realized: with a posistor R′=300Ω connected in series to the resisitance R, and with a posistor connected in series to the supply circuit. The respective experimental characteristics f=φ(T) for the two circuits for temperature stabilization are shown in Figure 5 (curve 2 - for the circuit with a posistor connected in series to the resisitance R ; curve 3 - for the circuit with a posistor connected in series to the supply circuit). Better temperature stabilization is achieved by applying the circuit with a posistor connected in series to the resisitance R , the frequency f of the converter changing within 5% when the temperature rises in the range investigated (25÷65)°C.

The experimental results obtained show that following the approaches proposed and with a properly chosen posistor the desired temperature stability can be achieved.

III. ANALYSIS AND CONCLUSIONS:

A galvanomagnetic current-frequency (voltage-frequency) converter has been developed on the basis of a digital magnetosensitive IC with a simple circuit solution.The output frequency is stable, provided the transistor switch operates in a saturated mode. With a selected design version of the magnetic system the conversion characteristic can change within certain limits by changing the values of the resistor resistance R and of the supply voltage U_{DD}.

The practical possibility of the temperature stabilization of the conversion characteristic has been proved experimentally by means of a thermo-dependent element - posistor. A stable operationn mode of the converter can also be ensured by thermostating.

The current-frequency converter discussed here can also be used for realizing converters with a frequency output of linear displacement and current measurement.

REFERENCES

[1] Adler,Y.P., E.V.Markova, Y.V.Granovskii. Experiment Planning in Search of Optimum Conditions. (in Russian). Moscow, Naouka, 1976.

[2] Rosenblat, M.A. Galvanomagnetic sensors. State of the Art and Prospects for Development. (in Russian). Avtomatika i telemehanika, Moscow, 1997, No 1, 3-44.

[3] Roumenin, Ch.S., P.T.Kostov. A magnetosensitive Planar Device with a Freguency Output . Inv.Cert. Reg. No 61825, 30.11, 1984

[4] Roumenin, Ch. S. Solid State Magnetic Sensors, ELSEVIER, 1994

[5] Roumenin, Ch.S. Functional Magnetic-field Microsensors: An overview, Sensors and Materials,5(5) (1994) 285-300.

[6] Todorov, P. Zh., A.T.Alexandrov. Investigation of Magnetosensitive Integrated Circuits CM701AM-5.0 and CM701AM-5.1. Research Work of Rousse University, Vpl. XXXV, ser. VI, Rousse, 1994, 48-53.

[7] Homeriki, O.K. Application of Galvanomagnetic Sensors in Devices for Automatics and Measurements. Moscow, Energija, 1971.

Mathematical Model of a Current-FrequencyGalvanomagnetic Converter

Anatoliy T.Aleksandrov

***Abstract* – A current-frequency converter has been synthezited on the basis of a digital magnetosensitive integrated circuit (IC). The paper studies the complex influence of the number of winding W, current I, voltage U_{DD} and resistance R over frequency f of the converter developed and it presents the respective theoretical-experimental models obtained, which reflect their influence. The dependencies obtained form the basis of the practical application of the current-frequency converter and set prerequisites for choosing an optimum mode of operatin.**

Keywords – magnetic field galvanomag-netic sensor, magneto-sensitive IC, current-frequency conversion system.

I. INTRODUCTION:

On the basis of a digital magnetosensitive IC a galvanomagnetic current-frequensy converter has been developed [1]. It exhibits a stable conversion characteristic, high noise immunity and low power consumption.

With a view to the practical use of this device and in order to obtain a complex and reliable assessment of its operation, it is necessary to investigate the complex influence of the number of windings W, current I, voltage U_{DD} and resistance R over frequency f and to obtain the respective theoretical-experimental models reflecting this influence.

II THEORETICAL-EXPERIMENTAL MODEL:

In order to obtain the dependence $f=f(W,I,U_{DD},R)$ complete factor experiments of the type $N=2^4$ have been conducted, each experiment having been repeated (n=4), with simultaneous variation of the variable factors W, I, U_{DD}, R, according to a predeterminated plan of the experiment. The planning of the experiments and the processing of the results obtained have been carried out following the methodology presented in [2]. The type and levels of varying the factors are shown in Table 1. The areas of change in the parameters W and I, indirectly reflecting the effect of the magnetic field B on the converter operation, as well as in voltage U_{DD} and resistance R, have been determined after conducting preliminary single-factor experiments and they guarantee the normal operation of the current-frequency converter.

Anatoliy T. Aleksandrov. Department of Electronics, Technical University – Gabrovo, Street "Hadji Dimiter" No. 4, 5300 Gabrovo, Bulgaria, phone: +359 66 801064, e-mail: alex@tugab.bg.

The experimental investigations have been carried out at a constant ambient temperature T = 25°C. The magnetic curcuit has been solved experimentally and it exhibits constant values of magnetic permeability μ=400, air gap 8÷10 mm and magnetic circuit area S = 1600 mm^2.

The relation between the natural and code values of the factors is set by the equation [2, 3, 4]:

The relation between the natural and code values of the factors is set by the equation [2]:

$$x_i = \frac{2.\left(\ell nz_i - \ell nz_{iup}\right)}{\ell nz_{iup} - \ell nz_{ilw}} + 1, \quad (1)$$

where: x_i - code value of the factor;

z_i - natural value of the factor.

The plan of the experiment, as well as the results of measuring f of the current-frequency converter and the values of the target function $y_1 = \ell nf$ have been pointed in Table 2. The presented values of the measured frequency logarithm are the average of the four observations carried out at each point: $\ell nf = \frac{\ell nf_1 + \ell nf_2 + \ell nf_3 + \ell nf_4}{4}$. The experimental setting presented in [1] has been used to measure f.

The dependence between frequency f of the converter and the parameters W, I, U_{DD}, R is power function of the type:

$$f = c.W^p.I^q.U_{DD}^s.R^t. \quad (2)$$

In order to simplify the mathematical processing this power equation is linearized (converted into a first power polynomial) by taking logarithms:

$$\ell nf = \ell nc + p.\ell nW + q.\ell nI + s.\ell nU_{DD} + t.\ell nR \quad (3)$$

There are correlational links between the parameters W, I, U_{DD}, R, as a result of which the equation reflecting the dependence $f=f(W, I, U_{DD}, R)$ is presented in a general form by means of the polynomial:

$$y_1=b_0+ b_1x_1+ b_2x_2+ b_3x_3+ b_4x_4+ b_{12}x_1x_2+ b_{13}x_1x_3+ b_{14}x_1x_4+ +b_{23}x_2x_3+b_{24}x_2x_4+b_{34}x_3x_4+ b_{123}x_1x_2x_3+ b_{124}x_1x_2x_4+ b_{234}x_2x_3x_4+ +b_{134}x_1x_3x_4+ b_{1234}x_1x_2x_3x_4, \quad (4)$$

To check the reliability of the experimental results obtained, the dispersion of reproductivity (the experimental error) is determined $S_y=5,7.10^{-3}$. It has been calculated after determining the dispersions of all experiments consisting of n=4 repeated observations and exhibiting the deviation of the repeated experiments significance from the arithmetic mean value of the output parameter, the sum of all dispersions

Table 1. Values of the Factors

Level	Natural values				Coded values			
	W	I	U_{DD}	R	x_1	x_2	x_3	x_4
	wind.	mA	V	kΩ				
Upper	450	2200	12	5,5	+1	+1	+1	+1
Zero	350	1450	10	3	0	0	0	0
Lower	250	700	8	0,5	-1	-1	-1	-1

Table 2. Plan of the Experiment

Coded values of the factors					Values of the Output Parameters					$\hat{y}_1$
x_0	x_1	x_2	x_3	x_4	f_1	f_2	f_3	f_4	$y_1=\ell n\, f$	
+1	-1	-1	-1	-1	445	446	445	446	6,0986	6,0999
+1	+1	-1	-1	-1	487	488	488	488	6,1898	6,1885
+1	-1	+1	-1	-1	3205	3203	3190	3196	8,0704	8,0717
+1	+1	+1	-1	-1	2389	2401	2408	2425	7,7856	7,7843
+1	-1	-1	+1	-1	285	284	283	281	5,6463	5,6476
+1	+1	-1	+1	-1	384	382	380	380	5,9441	5,9428
+1	-1	+1	+1	-1	2477	2461	2478	2480	7,8136	7,8149
+1	+1	+1	+1	-1	1938	1952	1957	1982	7,5793	7,5780
+1	-1	-1	-1	+1	633	633	636	637	6,4532	6,4545
+1	+1	-1	-1	+1	719	720	720	722	6,5796	6,5783
+1	-1	+1	-1	+1	3762	3779	3818	3822	8,2415	8,2428
+1	+1	+1	-1	+1	2987	2996	3018	3022	8,0083	8,0070
+1	-1	-1	+1	+1	266	265	262	261	5,5740	5,5753
+1	+1	-1	+1	+1	428	426	426	427	6,0562	6,0549
+1	-1	+1	+1	+1	2832	2835	2838	2844	7,9541	7,9554
+1	+1	+1	+1	+1	2251	2265	2289	2292	7,7294	7,7281

$\sum_{u=1}^{16} S_u^2 = 5.10^{-4}$, the maximum dispersion $S^2_{umax} = 10^{-4}$ and a check of dispersions uniformity according to Kohren's criterion (G_R=0,1686<G_{Rtable}=0,2674) at a significance level α=0,05.

The coefficients in the mathematical model (4) have been determined in a coded form:

$$b_i = \frac{\sum_{u=1}^{N} y_{1u}}{\sum_{u=1}^{N} x_{iu}^2}; \qquad b_{ij} = \frac{\sum_{u=1}^{N} y_{1u} \cdot x_{iu} \cdot x_{ju}}{N};$$

$$b_{ijg} = \frac{\sum_{u=1}^{N} y_{1u} \cdot x_{iu} \cdot x_{iu} \cdot x_{gu}}{N};$$

$$b_{ijgk} = \frac{\sum_{u=1}^{N} y_{1u} \cdot x_{iu} \cdot x_{ju} \cdot x_{gu} \cdot x_{ku}}{N}, \qquad (5)$$

where: n = 1 - N; N - number of the experiment;

i, j, g, k - 1, 2, 3, 4 - number of the factir.

The significance of the coefficients in the regression equation (4) has been determined according to Student's criterion. The confidence interval of the regression coefficients Δb_i=1,4.10^{-3} at a level of significance α = 0,05.

After removing the insignificant coefficients of the equation the following theoretical model is obtained:

$$\hat{y}_1 = 6,9828+0,915x_2 - 0,1956x_3 - 0,0918x_4 - 0,1234x_1x_2 +$$
$$+ 0,0388x_1x_3 + 0,0176x_1x_4 + 0,0689x_2x_3 - 0,0062x_2x_4 -$$
$$- 0,0505x_3x_4 - 0,0315x_1x_2x_3 - 0,0099x_1x_2x_4 - 0,0067x_2x_3x_4 +$$

$+ 0{,}0376x_1x_3x_4 - 0{,}0119x_1x_2x_3x_4$ (6)

The theoretical model obtained satisfies the requirements of the adequacy check according to Fisher's criterion at a significance level α=0,05: $F_R = 3{,}2086 < F_{Rtable} = 4{,}051$. This check shows that the dispersion of the experimental results obtaiined compared to the theoretical dependence does not exceed the present value. The dispersion of inadequacy characterizing the model accuracy is S_{AD}=0,0102.

The process guality of description is good and it is assessed using the multiple correlation coefficient r=0,9998. The significance of the multiple correlation coefficient is determined according to Fisher's criterion (F_R=30660> F_{Rtable}=1,991).

After passing from coded to natural values of the variable quantities the followng empirical dependence is obtained, which reflects the complex influence of W, I, U_{DD}, R over the converter frequency f.

ℓn f=56,6834-8,9485. ℓn W-5,5601. ℓn I-39,5986. ℓn U_{DD} + +31,5508. ℓn R+1,059. ℓn W. ℓn I+6,1218. ℓn W. ℓn U_{DD}- -4,5645. ℓn W. ℓn R+4,9442∗ ℓn I. ℓn U_{DD}-4,2177. ℓn I. ℓn R- -14,7804. ℓn U_{DD}. ℓn R-0,7745. ℓn W. ℓn I ℓn U_{DD}+ +0,6177. ℓn W. ℓn I. ℓn R+2,175. ℓn W. ℓn U_{DD}. ℓn R+ +1,9691. ℓn I∗ ℓn U_{DD}. ℓn R-0,2922. ℓn W. ℓn I. ℓn U_{DD}. ℓn R (7)

When U_{DD}=12V and R_2=5kΩ the theoretical-experimental model has the form:

$$f = e^{-50{,}0402}.W^{7{,}6247-1{,}0401.\ell nI}.I^{7{,}8127} \quad (8)$$

Since with W<250 the converter switches on at I>1900mA, to obtain the dependence f′=*f*(W, I, U_{DD}, R), with the change in W=100÷400 windings, complete factor experiments of the type $N=2^4$ have been conducted, each experiment having been repeated (n=4), with simultaneous variation of the variable factops W, I, U_{DD}, R, according to a predetermined plan of the experiment. The areas of change in the parameters W, I, U_{DD}, R: W=(100÷400) windings, I=(1800÷2000)mA, U_{DD}=(10÷12)V, R=(0,5÷5,5)kΩ, have been determined after conducting preliminary single-factor experiments and they guarantee the normal operation of the current-frequency converter.

The form of the theoretical-exprimental model obtained, which reflects the complex influence of the parameters W, I, U_{DD}, R over frequency f′ under these conditions, is:

ℓn f′=188,5906-25,3304. ℓn W-22,0062. ℓn I-89,4842∗ ∗ ℓn U_{DD} + 324,2198 ℓn R+3,0857. ℓn W. ℓn I+ +12,1223. ℓn W. ℓn U_{DD}-47,3797. ℓn W. ℓn R+11,1825. ℓn I∗ ∗ ℓn U_{DD}-2,9998. ℓn I. ℓn R-134,4424. ℓn U_{DD}. ℓn R-1,5196∗ ∗ ℓn W. ℓn I ℓn U_{DD}+6,304. ℓn W. ℓn I. ℓn R+17,8401 ℓn W∗ ∗ ℓn U_{DD}. ℓn R+19,7871. ℓn I. ℓn U_{DD}. ℓn R- -26335. ℓn W. ℓn I. ℓn U_{DD}. ℓn R (9)

When U_{DD}=12V and R=5kΩ the theoretical-experimental model has the form:

$$f' = e^{-49{,}6336}.W^{7{,}6723-1{,}0767\ell nI}.I^{7{,}868} \quad (10)$$

III. ANALYSIS AND CONCLUSIONS

The theoretical-experimental models obtained describe the conversion characteristic of the current-frequency converter with a high degree of accurasy and enable the working out of an assessment on the degree of influence of the parameters W, I, U_{DD}, R over the frequency f.

The frequency f of the converter discussed depends to the greatest extent on the magnitude of the current I, the increase in current causing an increase in frequency, the conversion characteristic being linearized above a certain value of I. With the increase in the number of windings W, rise in R and decrease in voltage U_{DD}, the influence of current over the frequency f weakens.

The frequency of the converter depends on the number of windings W of the electromagnet, their increase causing the frequency to decrease following an exponential law. The influence of W is most significant when I>1800 mA. When I=1500 mA the number of windings does not influence f. When I>1500 mA the freguency decreases with the increase in W, and when I<1500 mA the tendency is reversed.

The converter frequency depends on the supply voltage of the magnetosensitive IC, the increase in U_{DD} causing a decrease in freguency. The degree of influence of U_{DD} over f rises with the reduction in the number of windings W, the change being 1,6 times when W=100 windings , and 1,3 times when W=400 windings. This dependence of f on U_{DD} can be used for temperature stabilisation.

The converter frequency depends on the resistor resistance R, its increase causing the frequency to increase according to an exponential law. The degree of influence of R decreases with the decrease in the number of windings W.

REFERENCES

[1] Alexandrov, A.T. Gallvanomagnetic Current-frequency Converter (forthcoming).

[2] Александрова, И.С. Основи на инженерните изследвания. УИ "В.Априлов", Габрово, 2003

[3] Александров, А.Т. Изследване на галваномагнитен преобразувател за линейно преместване. – Електротехника и електроника, София, 2001, кн. 3-4, 2001, с.36-39.

[4} Стоянов, С.К. Методи и алгоритми за оптимизация. С. Техника, 1990

AUTHOR INDEX